Medical Radiology
Series Editors: H.-U. Kauczor · H. Hricak · M. Knauth

U. Joseph Schoepf
Felix G. Meinel *Editors*

Multidetector-Row CT of the Thorax

Second Edition

Springer

Medical Radiology

Diagnostic Imaging

For further volumes:
http://www.springer.com/series/4354

U. Joseph Schoepf • Felix G. Meinel
Editors

Multidetector-Row CT of the Thorax

Second Edition

Springer

Editors
U. Joseph Schoepf
Department of Radiology and
Radiological Science
Medical University of South Carolina
Charleston, SC
USA

Felix G. Meinel
Institute for Clinical Radiology
Ludwig-Maximilians-University Hospital
Munich
Germany

ISSN 0942-5373 ISSN 2197-4187 (electronic)
Medical Radiology
ISBN 978-3-319-30353-6 ISBN 978-3-319-30355-0 (eBook)
DOI 10.1007/978-3-319-30355-0

Library of Congress Control Number: 2016944609

Printed on acid-free paper

This Springer imprint is published by Springer Nature
The registered company is Springer International Publishing AG Switzerland

To Our Patients

Foreword

The first edition of "MDCT of the Thorax" was published in 2004 when the new capabilities and clinical applications of MDCT were met with excitement and explored with great enthusiasm. Since then, much has happened – the excitement has persisted and has even grown. While 16-row scanners were once celebrated as the peak of innovation in 2004, 64-row computed tomography is now considered to be standard technology with 128 and even 320-row scanners available in the high-end sector. However, the technical innovations are by no means limited to the number of detector rows. Iterative reconstruction methods, new detector materials, automated tube current modulation and tube voltage selection have substantially reduced the radiation exposure to patients. These improvements mitigate and perhaps invalidate the primary argument against the widespread use of CT angiography of the coronary arteries in particular.

For the second edition, editors Joseph Schoepf and Felix Meinel have kept important features essential to the success of the first edition while revising and updating each chapter to capture the rapidly advancing developments in CT and their clinical applications. New chapters have been added, including: "Dual Energy CT of the Thorax", "Comprehensive CT Imaging in Acute Chest Pain", and "Imaging of the Heart-Lung Axis". In contrast, chapters from the first edition which have since lost their importance have been excluded.

The editors are to be congratulated on assembling an authorial team of highly recognized, international experts. Furthermore, one has to thank the authors for illustrating that the technical and methodological advancements of the recent past are not just improvement for improvement's sake, but significantly increase the clinical applicability and the diagnostic value of MDCT.

It can be asserted with good reason that MDCT of the thorax is one of the most interesting and exciting fields of radiology. Few topics in medical imaging arouse such heated discussion as lung cancer screening with CT or the use of CT in acute chest pain. This work provides detailed, comprehensive information on these and many other topics that capture the cutting-edge of innovation while remaining valuable for everyday practice.

I would like to sincerely thank the editors, authors, and Springer for promoting this important work and I wish them much deserved success. I have no doubt that readers will not only enjoy the book, but also find it a significant help in their daily practice.

Munich, Germany
March 2016

Maximilian F. Reiser

Preface

...δὶς ἐς τὸν αὐτὸν ποταμὸν οὐκ ἂν ἐμβαίης...

It has been more than a decade since the first edition of this tome – and what an amazing 12 years it has been for a spectacular medical imaging modality and those who harness its power! Not only is CT not dead, as it was quite ubiquitously predicted and accepted at the eve of the last millennium, but rather it has piled triumph upon roaring triumph in our conquest of disease. And hardly any other area of CT imaging has seen more dramatic evolution, more spectacular victories, or more profound disruption than the evaluation of the cardiothoracic system. The scourges of the past were utterly and effectively vanquished: Pulmonary embolism has found its match, eradicating the diagnostic uncertainties from days past. Heart disease is increasingly tackled by the new, imposing kid on the block – cardiac CT. Doubts over the effectiveness of CT lung cancer screening have all but disappeared and this test is shaping up as a powerful weapon in our war on cancer. And the list goes on…

Our exploits can in part be ascribed to the ingenuity, curiosity, and zeal of the radiological community in the pursuit of ever more refined strategies to better the fate of our patients. But our intellect and our passion alone would have stood little chance to overcome our formidable adversaries. To our aid came the brilliance of engineers, thinkers, technical innovators, who gave us the means, gave us the tools, the very instruments of success. Zooming through the chest in a split second, freezing the heart's motion, obtaining tissue signatures of organs healthy and diseased, smoking out pathology with micrometer precision – what a feat!

As with the first edition, we were able to assemble a stellar team of global experts, fabled bards to sing the stories of our exploits, to chronicle our journey, and to take tally of the spoils of war on human ailment. Again, the result of our collective musing has become a shining testimony to the prowess of our profession and a reflection of our ever increasing abilities in medicine. Our deep gratitude goes out to our many friends who dedicated their precious time and their genius to the success of this work. We thank the editorial team at Springer, who again so expertly steered the publication of this new edition. Lastly, we salute our patients, who are the reason for it all.

Charleston, South Carolina, USA — U. Joseph Schoepf
Munich, Germany — Felix G. Meinel
March 2016

Contents

Part III Lung Nodules/Lung Cancer

Part IV Cardiovascular Applications

Part V Data Management

Part VI Miscellaneous

Contributors

Vartika Appiah Department of Radiology, Epicura – Hopital de la Madeleine, Ath, Belgium

Edwin J.R. van Beek Clinical Research Imaging Centre, University of Edinburgh, Edinburgh, Scotland, UK

Clinical Research Imaging Centre, The Queen's Medical Research Institute, Edinburgh, UK

Catherine Beigelman-Aubry Diagnostic and Interventional Radiology, University Hospital Lausanne, Lausanne, Switzerland

Chandra Bortolotto Department of Thoracic Imaging, Hospital Calmette (EA 2694), University of Lille Nord de France, Lille, France

Yolonda L. Colson Division of Thoracic Surgery, Brigham and Women's Hospital and Harvard Medical School, Boston, MA, USA

Anand Devaraj Department of Radiology, Royal Brompton Hospital, London, UK

Julien Dinkel Institute for Clinical Radiology, Ludwig-Maximilians-University Hospital, Munich, Germany

Shannon G. Farmakis St. Louis University School of Medicine, SSM Health Cardinal Glennon Children's Hospital, Saint Louis, MO, USA

John Field Department of Molecular and Clinical Cancer Medicine, The University of Liverpool, Institute of Translational Medicine, Liverpool, UK

Dominik Fleischmann Department of Radiology, Stanford University School of Medicine, Stanford, CA, USA

Thomas G. Flohr Siemens Healthcare GmbH, Computed Tomography, CT Concepts Department, Forchheim, Germany

Department of Interventional Radiology, Eberhard-Karls-University, Tübingen, Germany

Matthew K. Fuld Diagnostic Imaging, Computed Tomography, Collaborations, Siemens Medical Solutions, Inc, Malvern, PA, USA

Stephen R. Fuller Department of Radiology and Radiological Science, Medical University of South Carolina, Charleston, SC, USA

Camilo A. Garcia Service de Médecine Nucléaire, Université Libre de Bruxelles, Institut Jules Bordet, Brussels, Belgium

Victor H. Gerbaudo Division of Nuclear Medicine and Molecular Imaging, Brigham and Women's Hospital, Harvard Medical School, Boston, MA, USA

Pierre Alain Gevenois Department of Radiology, Hôpital Erasme, Université libre de Bruxelles, Brussels, Belgium

Lucas L. Geyer Institute for Clinical Radiology, LMU Ludwig-Maximilians-University Hospital Munich, Munich, Germany

Ritu R. Gill Department of Radiology, Brigham and Women's Hospital and Harvard Medical School, Boston, MA, USA

Jin Mo Goo Department of Radiology, Seoul National University Hospital, Jongno-gu, Seoul, South Korea

Jochen M. Grimm Department of Medical Radiology, University Hospital Center and University of Lausanne, Lausanne, Switzerland

University Center of Legal Medicine Lausanne/Geneva, Lausanne, Switzerland

Maxime Hackx Department of Radiology, Hôpital Erasme, Université libre de Bruxelles, Brussels, Belgium

Richard L. Hallett Cardiovascular Imaging, Northwest Radiology Network, Indianapolis, IN, USA

Division of Cardiovascular Imaging, Department of Radiology, Stanford University School of Medicine, Stanford, CA, USA

Ethan J. Halpern Department of Radiology, Thomas Jefferson University, Philadelphia, PA, USA

Marieke Hovinga Department of Radiology, Meander Medical Center, Amersfoort, The Netherlands

Bertram Jobst Department for Diagnostic and Interventional Radiology, University Hospital Heidelberg, Heidelberg, Germany

Willi A. Kalender Institute of Medical Physics, University of Erlangen-Nürnberg, Erlangen, Germany

Rashmi Katre Department of Radiology, The University of Texas Health Science Center at San Antonio, San Antonio, TX, USA

Hans-Ulrich Kauczor Department of Diagnostic and Interventional Radiology, University Hospital Heidelberg, Heidelberg, Germany

Tatiana Kelil Department of Radiology, Brigham and Women's Hospital and Harvard Medical School, Boston, MA, USA

Suonita Khung Department of Thoracic Imaging, Hospital Calmette (EA 2694); Univ Lille Nord de France, Lille, France

Chang Hyun Lee Department of Radiology, College of medicine, Seoul National University, Seoul, South Korea

Michael M. Lell Department of Radiology, Friedrich-Alexander University Erlangen-Nürnberg, Erlangen, Germany

Ulrich Linsenmaier Institute for Diagnostic and Interventional Radiology, HELIOS Kliniken München WEST and HELIOS Kliniken München Perlach and Klinikum Augustinum München, Munich, Germany

Stefanie Mangold Department of Radiology and Radiological Science, Medical University of South Carolina, Charleston, SC, USA

Department of Diagnostic and Interventional Radiology, University Hospital of Tuebingen, Tuebingen, Germany

Felix G. Meinel Institute for Clinical Radiology, Ludwig-Maximilians-University Hospital, Munich, Germany

Hagen Meredig Department of Diagnostic and Interventional Radiology, University Hospital Heidelberg, Heidelberg, Germany

Saeed Mirsadraee Clinical Research Imaging Centre, University of Edinburgh, Edinburgh, Scotland, UK

Clinical Research Imaging Centre, The Queen's Medical Research Institute, Edinburgh, UK

Amy Mumbower Department of Radiology, The University of Texas Health Science Center at San Antonio, San Antonio, TX, USA

Matthijs Oudkerk Department of Radiology, University of Groningen, University Medical Center Groningen, Center for Medical Imaging – North East Netherlands, Groningen, The Netherlands

Julien Pagniez Department of Thoracic Imaging, Hospital Calmette (EA 2694); Univ Lille Nord de France, Lille, France

Narinder S. Paul Department of Medical Imagining, Toronto General Hospital, University Ave, University of Toronto, Toronto, ON, Canada

Robin Peters Department of Radiology, University of Groningen, University Medical Center Groningen, Center for Medical Imaging – North East Netherlands, Groningen, The Netherlands

Jim Potchen Department of Radiology, Michigan State University, East Lansing, MI, USA

Juan Carlos Ramirez-Giraldo Diagnostic Imaging, Computed Tomography, Collaborations, Siemens Medical Solutions, Inc., Malvern, PA, USA

James G. Ravenel Department of Radiology and Radiological Science, Medical University of South Carolina, Charleston, SC, USA

Jacques Remy Department of Thoracic Imaging, Hospital Calmette (EA 2694); Univ Lille Nord de France, Lille, France

Martine Remy-Jardin Department of Thoracic Imaging, Hospital Calmette (EA 2694); Univ Lille Nord de France, Lille, France

Carlos S. Restrepo Department of Radiology, The University of Texas Health Science Center at San Antonio, San Antonio, TX, USA

Carole A. Ridge Department of Radiology, Mater Misericordiae University Hospital, Dublin, Ireland

Beth A. Ripley Department of Radiology, Brigham and Women's Hospital and Harvard Medical School, Boston, MA, USA

Geoffrey D. Rubin Department of Radiology, Duke University School of Medicine, Durham, NC, USA

Cornelia Schaefer-Prokop Department of Radiology, Meander Medical Center, Amersfoort, The Netherlands

Department of Radiology, Radboud University Nijmegen, Nijmegen, The Netherlands

Sabine Schmidt Diagnostic and Interventional Radiology, University Hospital Lausanne, Lausanne, Switzerland

Bernhard Schmidt Siemens Healthcare GmbH, Computed Tomography, CT Concepts Department, Forchheim, Germany

U. Joseph Schoepf Department of Radiology and Radiological Science, Medical University of South Carolina, Charleston, SC, USA

Marilyn J. Siegel Mallinckrodt Institute of Radiology, Washington University School of Medicine, St Louis, MO, USA

Stephen B. Solomon Department of Radiology, Memorial Sloan Kettering Cancer Center, New York, USA

Ralf Sprengers Department of Radiology, Meander Medical Center, Amersfoort, The Netherlands

Denis Tack Department of Radiology, Epicura – Hopital de la Madeleine, Ath, Belgium

Rozemarijn Vliegenthart Department of Radiology, University of Groningen, University Medical Center Groningen, Center for Medical Imaging – North East Netherlands, Groningen, The Netherlands

Julian L. Wichmann Department of Radiology and Radiological Science, Medical University of South Carolina, Charleston, SC, USA

Department of Diagnostic and Interventional Radiology, University Hospital Frankfurt, Frankfurt, Germany

Mark O. Wielpütz Department for Diagnostic and Interventional Radiology, University Hospital Heidelberg, Heidelberg, Germany

Amelia M. Wnorowski Department of Radiology, Thomas Jefferson University, Philadelphia, PA, USA

Long Jiang Zhang Department of Medical Imaging, Jinling Hospital, Medical School of Nanjing University, Nanjing, China

MDCT – Technical Background, Radiation Protection

CT Technology for Imaging the Thorax: State of the Art

Thomas G. Flohr and Bernhard Schmidt

Abstract

We review the basics of CT system design, scan, and image reconstruction techniques, as well as scan protocols for imaging of the thorax with multidetector row CT (MDCT) systems. In addition, we discuss CT systems with wide area detectors and dual-source CT (DSCT). We briefly describe different techniques to reduce the radiation dose in thoracic CT, and we discuss dual energy CT acquisition techniques which have the potential to provide combined functional and morphological information, e.g., to depict local perfusion deficits in the lung parenchyma in patients with pulmonary embolism.

1 Introduction

The advent of spiral computed tomography (CT) in 1990 and the broad introduction of multidetector row computed tomography (MDCT) in 1998 were significant steps in the ongoing refinement of CT-imaging techniques of the thorax.

With the first generation of 4-slice CT systems, high-resolution imaging of the entire thorax within one breath-hold of the patient became feasible, and CT was quickly recognized as the gold standard for the diagnosis of pulmonary embolism up to the level of sub-segmental arteries (Schoepf et al. 2002; Remy-Jardin et al. 2002).

T.G. Flohr (✉)
Siemens Healthcare GmbH, Computed Tomography, CT Concepts Department, Forchheim, Germany

Department of Interventional Radiology, Eberhard-Karls-University, Tübingen, Germany
e-mail: thomas.flohr@siemens.com

B. Schmidt
Siemens Healthcare GmbH, Computed Tomography, CT Concepts Department, Forchheim, Germany

ECG-synchronized data acquisition (Ohnesorge et al. 2000), which proved to be sufficient for adequate visualization of the coronary arteries at low to moderate heart rates (Achenbach et al. 2000; Becker et al. 2000; Knez et al. 2001; Nieman et al. 2001), could unfortunately not be extended to the entire thorax because of slow scan speed.

The generation of 16-slice MDCT systems (Flohr et al. 2002a, b) provided simultaneous acquisition of 16 submillimeter slices and faster gantry rotation with rotation times down to 0.375 s. CT scans of the entire thorax with submillimeter spatial resolution were now possible in about 10 s. As a consequence, central and peripheral pulmonary embolism could be reliably and accurately diagnosed even in dyspneic patients with limited ability to cooperate (Remy-Jardin et al. 2002; Schoepf et al. 2003). The combined assessment of pulmonary embolism and deep venous thrombosis, first demonstrated in 2001 (Schoepf et al. 2001), entered clinical routine. The faster scan speed of ECG-gated cardiac scanning with 16 slices enabled motion-free visualiza-

U.J. Schoepf, F.G. Meinel (eds.), *Multidetector-Row CT of the Thorax*, Medical Radiology,
DOI 10.1007/978-3-319-30355-0_1

tion of the lung and the cardiothoracic vessels as well as cardiac functional evaluation in one scan, even though detailed visualization of the coronary arteries was still limited (Coche et al. 2005).

Sixty-four-slice CT systems, available since 2004, enabled CT imaging of the thorax with isotropic submillimeter spatial resolution in less than 5 s scan time. This facilitated the examination of uncooperative patients and emergency patients, e.g., with suspicion of acute pulmonary embolism. The improved temporal resolution due to gantry rotation times down to 0.33 s increased the clinical robustness of ECG-gated scanning at higher heart rates, even though most authors still proposed the administration of beta-blockers (Leber et al. 2005; Raff et al. 2005). Sixty-four-slice CT scanners enabled comprehensive diagnosis of morphology and cardiac function within one integrated CT examination, including high-resolution imaging of the coronary arteries (Salem et al. 2006; Bruzzi et al. 2006a, b; Delhaye et al. 2007). ECG-gated 64-slice CT was also used for rapid triage of patients with acute chest pain in the emergency room and for diagnosis of pulmonary embolism, aortic dissection or aneurysm, or significant coronary artery disease in one scan. This application is often referred to as "triple rule out" (Schoepf 2007; Johnson et al. 2007a). As a downside, ECG-gated MDCT scanning of the entire thorax can result in considerable radiation exposure, which is of particular concern in patients with low likelihood of disease.

Even with 64-slice CT, motion artifacts remained an important challenge for cardiothoracic imaging. In 2005, a dual-source CT (DSCT) system, i.e., a CT system with two x-ray tubes and two corresponding detectors offset by 90°, was introduced (Flohr et al. 2006). It provided improved temporal resolution of 83 ms independent of the patient's heart rate as compared to 165–190 ms with MDCT systems at that time. DSCT scanners proved to be well suited for integrated cardiothoracic examinations even in acutely ill patients and for the triage of patients with acute chest pain (Johnson et al. 2007b). The introduction of dual-energy scanning with DSCT enabled tissue characterization and provided combined functional and morphological information, e.g., to depict local perfusion deficits in the lung parenchyma in patients with pulmonary embolism (Pontana et al. 2008; Thieme et al. 2008).

The second and third generations (introduced in 2009 and 2013, respectively) of DSCT systems offer high-pitch scan modes which enable high-resolution CT scans of the entire thorax in less than 1 s scan time with an acquisition time per image better than 100 ms (Lell et al. 2009; Tacelli et al. 2010). These scan modes are potentially advantageous for evaluating the lung parenchyma and vascular structures in patients who have difficulty complying with breath-holding instructions (Schulz et al. 2012). High-pitch scan modes have been used for fast CTA scans of the aorta (Beeres et al. 2012). Combined with ECG triggering, they provide adequate visualization of the coronary arteries, the aorta, and the iliac arteries in one scan at low radiation dose, which is beneficial in the planning of transcatheter aortic valve replacement (TAVR) procedures (Wuest et al. 2012; Plank et al. 2012).

Since 2009, iterative reconstruction techniques have been used to significantly reduce the radiation dose in CT examinations of the thorax (e.g., Prakash et al. 2010; Leipsic et al. 2010; Pontana et al. 2011a, b, 2015; Singh et al. 2011; Baumueller et al. 2012). With the latest generation of iterative reconstruction and dedicated pre-filtration of the x-ray beam, radiation dose values of 0.1 mSv and less have been reported for non-enhanced CT scans of the thorax (Newell et al. 2015).

Yet another challenge for CT is the visualization of dynamic processes in extended anatomical ranges, e.g., to characterize the inflow and outflow of contrast agent in the arterial and venous systems in dynamic CT angiographies or to determine the enhancement characteristics of the contrast agent in volume perfusion studies. One way to address this problem is the introduction of area detectors large enough to cover organs such as the heart, the kidneys, or the brain in one axial scan. Meanwhile, two vendors have introduced CT scanners with 16 cm detector coverage at isocenter, providing 320×0.5 mm collimation at 0.27 s rotation time or 256×0.625 mm collimation at 0.28 s rotation time. These scanners have the potential to acquire dynamic volume data by repeatedly scanning the same anatomical range without table movement (e.g., Ohno et al. 2011; Willems et al. 2012; Motosugi et al. 2012). An alternative to provide time-resolved CT data of larger anatomical volumes is a periodic shuttle movement of the patient table while scan data are acquired (e.g., Goetti

et al. 2012; Morhard et al. 2010; Sommer et al. 2010, 2012). This technique is realized in several CT systems with smaller detector *z*-coverage.

Overall, the greatest challenge of evolving CT technology is the explosion of information now available to physicians. Standardizing the display of post-processed images will be increasingly important to preserve efficient workflow and optimum patient care.

2 CT System Technology

2.1 Multi-Detector Row CT (MDCT)

In this section, we review the basics of CT system design, scan, and image reconstruction techniques, as well as scan protocols for imaging of the thorax with multi-detector row CT (MDCT) systems. In our terminology, these are CT systems with 2–128 detector rows and a detector *z*-coverage of up to 8 cm at isocenter. CT systems with wider detectors (e.g., 320×0.5 mm or 256×0.625 mm, both covering 16 cm) and dual-source CT (DSCT) systems will be discussed in a separate section because of their different clinical protocols.

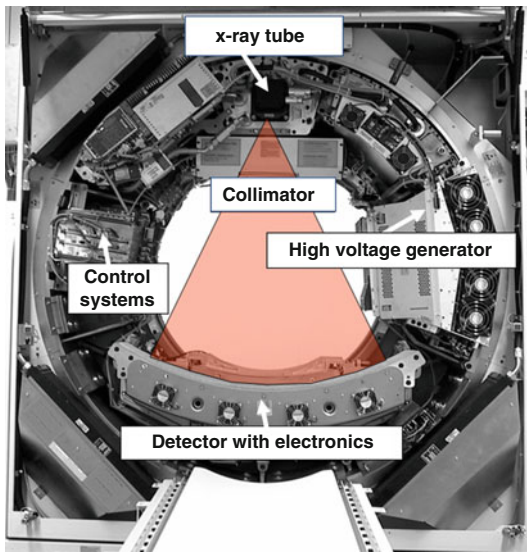

Fig. 1 Basic system components of a modern MDCT system. The x-ray fan beam is indicated in red; it covers a SFOV of typically 50 cm in diameter. The data measurement system consists of detector and detector electronics

2.1.1 MDCT System Design

The basic system components of a modern MDCT system are shown in Fig. 1. Today, the third-generation fan-beam CT design is used by all manufacturers, characterized by an x-ray tube and an opposing detector which are mounted on a rotating gantry ring. The detector is a two-dimensional array, consisting of 2–128 rows aligned in the *z*-axis direction (the *z*-axis is the patient's longitudinal axis) with 700 and more detector elements in each row. The fan angle of the detector is wide enough (approximately 45–55°) to cover a whole-body scan field of view (SFOV) of usually 50 cm in diameter. In a CT scan, the detector array measures the x-ray attenuation profile of the patient at about 1000–2000 different angular positions during a 360° rotation. All measurement values acquired at the same angular position of the measurement system are called a "projection" or "view." Slip-ring designs which pass the electrical signals across sliding contacts allow for continuous rotation of the measurement system.

State-of-the art x-ray tubes are powered by onboard generators and provide peak powers of 60–120 kW at different user-selectable voltages ranging from 80 to 140 kV. Recently, the available voltage range was extended to enable new clinical applications, and other tube voltages such as 70 kV became available. Scanning at low tube voltage is favorable for dose-efficient pediatric CT (Niemann et al. 2014; Durand and Paul 2014). In addition, contrast-enhanced examinations can be performed at reduced radiation dose and potentially reduced amount of contrast agent, because the x-ray attenuation of iodine significantly increases at lower kV (Meyer et al. 2014). This technique will be described in detail in Sect. 3.1.

All modern MDCT systems use solid-state scintillation detectors. The x-rays hit a radiation-sensitive crystal or ceramic (such as gadolinium oxide, gadolinium oxysulfide, or garnets) with suitable doping. They are absorbed, and their energy is converted into visible light which is detected by a Si photodiode attached to the backside of the detector. The resulting electrical current is amplified and converted into a digital signal.

Key requirements for a detector material are good detection efficiency, i e., high atomic number, and very short afterglow time to enable fast

readout at the high gantry rotation speeds that are essential for cardiothoracic CT.

The image noise in a CT image is caused by the quantum noise of the x-ray photons and the electronic noise of the detection system. In high-dose scanning situations, the image noise is dominated by quantum noise. Electronic noise significantly contributes to the image noise when bigger patients are scanned or in examinations at low radiation dose, e.g., in low-dose thorax scans. In addition, electronic noise degrades image quality and the stability of CT values. Recently, a detector with integrated electronics was commercially introduced (STELLAR, Siemens Healthcare, Forchheim, Germany), with the goal to reduce electronic noise and detector cross talk. In this design, photodiodes and analog-to-digital converters are combined and directly attached to the ceramic scintillators, without the need of noise-sensitive analog connection cables (see Fig. 2). In a recent study, image noise reduction by up to 40 % for a 30 cm phantom corresponding to an average abdomen was demonstrated with the use of a detector with integrated electronics at 80 kV (Duan et al. 2013). According to the authors, this noise reduction translated into up to 50 % in dose reduction to achieve equivalent image noise.

A CT scanner must provide different slice widths to adapt scan speed and through-plane (z-axis) resolution to the clinical requirements of different scan protocols. In MDCT, detectors with a larger number of detector rows than finally read-out slices are used to provide slices

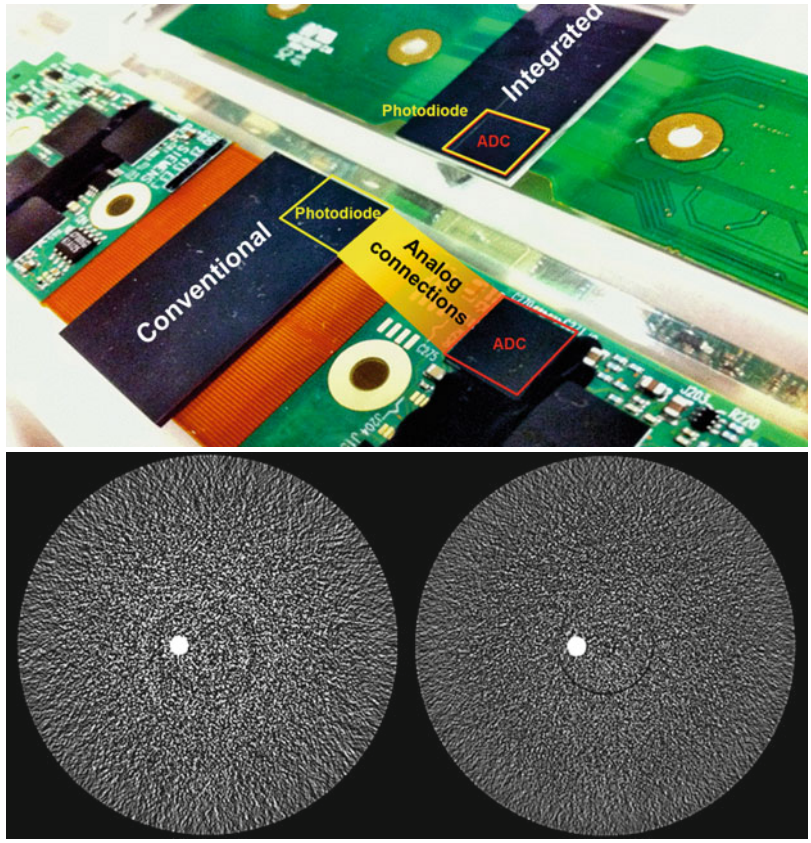

Fig. 2 *Top*: Principle of an integrated CT detector compared to a conventional CT detector. The Si tile is shown without the scintillation ceramics. Integrated detectors do not use distributed electronics with analog connections. As a consequence, electronic noise and cross talk are reduced. *Bottom*: Image quality improvement in a 40 cm phantom with an integrated detector (*right*) as compared to a conventional detector (*left*). Scan parameters: 80 kV, 100 mAs

at different collimated slice widths. The total beam width in the *z*-direction is adjusted by pre-patient collimation, and the signals of every two (or more) detectors along the *z*-axis are electronically combined to thicker slices.

The detector of a 16-slice CT (Siemens SOMATOM Emotion 16) as an example comprises 16 central rows, each with 0.6 mm collimated slice width, and four outer rows on either side, each with 1.2 mm collimated slice width – in total, 24 rows with a *z*-width of 19.2 mm at isocenter (Fig. 3). By adjusting the x-ray beam width such that only the central detector rows are illuminated, the system provides 16 collimated 0.6 mm slices (Fig. 3, top). By illuminating the entire detector, reading out all rows, and electronically combining the signals of every two central rows, the system provides 16 collimated 1.2 mm slices (Fig. 3, bottom). The 16-slice detectors of other manufacturers are similarly designed, with slightly different collimated slice widths (0.5, 0.6, or 0.625 mm, depending on the manufacturer).

MDCT detectors with 64 detector rows provide 64 collimated 0.5, 0.6, or 0.625 mm slices. They allow acquisition of 32 collimated 1.0, 1.2,

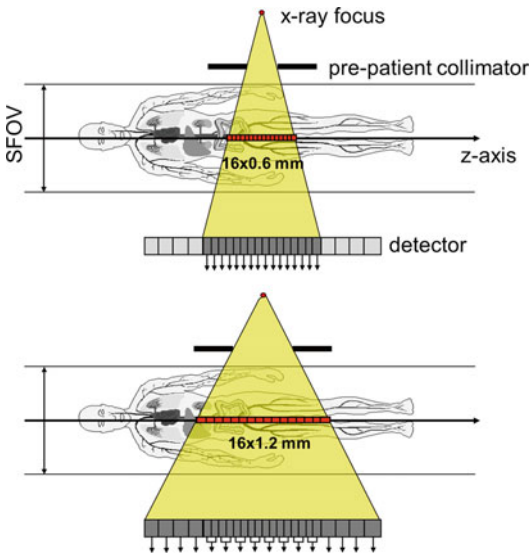

Fig. 3 Example of a 16-slice detector, which consists of 24 detector rows and provides either 16 collimated 0.6 mm slices (*top*) or – by combination of the signals of every two central rows – 16 collimated 1.2 mm slices (*bottom*)

or 1.25 mm slices by electronic combination of every two detector rows. One CT system has a detector with 128 collimated 0.625 mm slices (total *z*-width 8 cm at isocenter). The widest commercially available CT detectors cover 16 cm at isocenter; they acquire 320 collimated 0.5 mm slices (Aquilion ONE, Toshiba Medical, Japan) or 256 collimated 0.625 mm slices (Revolution, GE Healthcare, USA).

All modern MDCT scanners enable reconstruction of images with different slice widths from the same raw data – typically, the scan data are acquired at submillimeter collimation (e.g., 64×0.6 mm, or 64×0.625 mm), and different sets of image data are reconstructed with different target slice widths according to the clinical needs (e.g., 3 or 5 mm for initial viewing and additional submillimeter slices or 1 mm slices for post-processing).

Some CT systems double the number of simultaneously acquired slices by using special "conjugate" interpolation schemes during image reconstruction or by means of a *z*-flying focal spot (Flohr et al. 2004, 2005). The focal spot in the x-ray tube is periodically moved between two *z*-positions on the anode plate by electromagnetic deflection. As a consequence, the measurement rays of two readings are shifted by half a collimated slice width at isocenter and can be interleaved to one projection with double the number of slices, but half the *z*-sampling distance (Fig. 4). Two 64-slice readings with 0.6 mm slice width and 0.6 mm *z*-sampling distance, as an example, are combined to one projection with 128 overlapping 0.6 mm slices at 0.3 mm *z*-sampling distance.

The *z*-flying focal spot provides improved data sampling in the *z*-direction for better through-plane resolution and reduced spiral windmill artifacts (see Fig. 5).

2.1.2 MDCT Scan and Image Reconstruction Techniques

With the advent of MDCT, axial "step-and-shoot" scanning has remained in use for only few clinical applications, such as ECG-triggered cardiac scans at low radiation dose. For the vast majority of all MDCT examinations, spiral (helical) scanning is the method of choice.

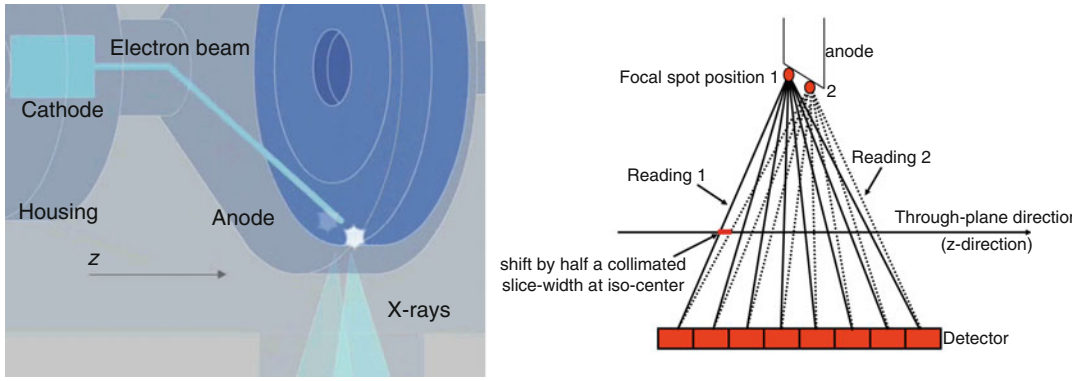

Fig. 4 Principle of a *z*-flying focal spot. Consecutive readings are shifted by half a collimated slice width (at isocenter) by means of a periodic motion of the focal spot on the anode plate. Every two readings are interleaved to one projection with double the number of slices and half the *z*-sampling distance

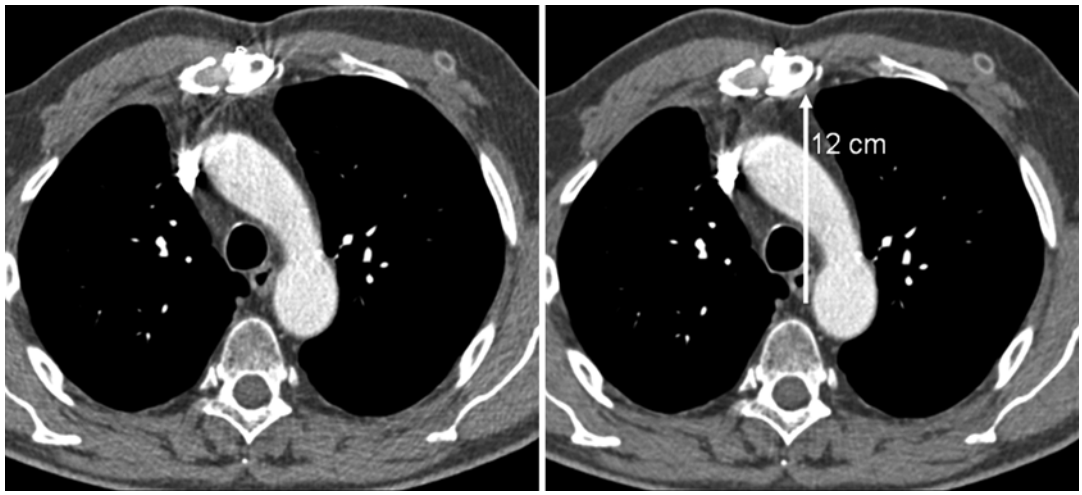

Fig. 5 Reduction of spiral windmill artifacts in a 64-slice CT scan (*left*) with the *z*-flying focal spot technique (*right, white arrow*). The distance of the sternum from the isocenter is about 12 cm

An important parameter to characterize a spiral scan is the pitch p. It is given by p = tablefeed per rotation/total z-width of the collimated beam at isocenter

This definition applies to single-slice CT as well as to MDCT. It indicates whether scan data are acquired with gaps ($p > 1$) or with overlap ($p < 1$) in the through-plane direction. If the x-ray tube current is left unchanged, radiation dose increases with decreasing pitch due to the overlapping radiation. Some CT scanners (e.g., Siemens MDCT systems) compensate for this increase by automatically lowering the tube current with decreasing pitch such that a constant; pitch-independent "reference mAs" and radiation dose are applied.

Many technical challenges of MDCT image reconstruction, such as the complicated z-sampling patterns or the cone-angle problem, have been addressed in the past 15 years. In two-dimensional image reconstruction approaches used for single-slice CT, all measurement rays are perpendicular to the z-axis. In MDCT systems, however, the measurement rays are tilted by the so-called cone angle with respect to a plane perpendicular to the z-axis. The wider the

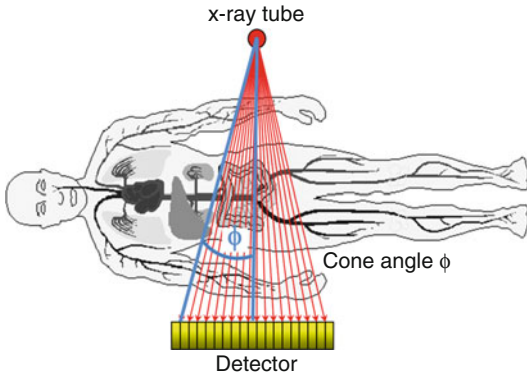

Fig. 6 Geometry of a MDCT scanner demonstrating the cone-angle problem: in the patient's longitudinal direction (z-direction), the measurement rays are tilted by the so-called cone-angle ϕ with respect to a plane perpendicular to the z-axis

detector is in the z-direction, i.e., the more detector rows it has, the larger is the cone angle of the outer detector rows (Fig. 6).

For CT systems with up to eight simultaneously acquired slices, cone-beam artifacts stay at a clinically acceptable level if the cone angle of the measurement rays is simply neglected in the image reconstruction algorithms. The rays are then treated as if they were perpendicular to the z-axis. For CT systems with more than eight slices, the cone angle has to be taken into account at least approximately. Pertinent reconstruction methods considering the cone-beam geometry are nutating slice algorithms (e.g., Flohr et al. 2003) and 3D-filtered back projection (Stierstorfer et al. 2004). Nowadays, 3D-filtered back projection is the reconstruction method of choice for most MDCT systems (Grass et al. 2000; Hein et al. 2003; Stierstorfer et al. 2004). 3D-filtered back projection is a natural extension of the 2D-filtered back projection used in single-slice CT reconstruction: the measurement rays are back projected into a 3D volume along the lines of measurement, in this way accounting for their cone-beam geometry. 3D-filtered back projection, even though it is an approximate algorithm, can significantly reduce cone-beam artifacts. In most MDCT scanners, 3D-filtered back projection is enhanced by z-filtering techniques which enable the reconstruction of images with different slice widths from the same CT raw data. The user can then trade off z-axis resolution with image noise.

2.1.3 Scan Protocols for MDCT Imaging of the Thorax

CT imaging of the thorax benefits from MDCT technology in several ways:

- *Shorter scan time*. Examination times for standard protocols can be significantly reduced. With modern MDCT systems, the entire thorax can be scanned at submillimeter isotropic resolution in less than 5 s. CT angiographic examinations benefit from these short scan times, because a compact contrast bolus may be used.
- *Extended scan range*. Larger scan ranges can be examined within one breath-hold time of the patient. This is relevant for CT angiography with extended coverage and for oncological staging. The chest and abdomen, as an example, can be examined in one scan with one contrast bolus.
- *Improved through-plane resolution*. The most important clinical benefit is the ability to scan a region of interest, e.g., the chest, within a breath-hold time of the patient with substantially thinner slices than in single-slice CT. The significantly improved through-plane resolution is beneficial for all reconstructions, in particular when 3D post-processing is part of the clinical protocol.

In clinical practice, most scan protocols benefit from a combination of these advantages. The close-to or true isotropic spatial resolution in routine examinations – depending on the number of detector rows – enables 3D renderings of diagnostic quality and oblique multiplanar reformations (MPRs) with a resolution comparable to the axial images. The wide availability of MDCT systems has transformed CT from a modality acquiring cross-sectional slices of the patient to a volume imaging modality. In many scan protocols, the use of narrow collimation is recommended independently of what slice width is desired for primary viewing. In practice, different

slice widths are commonly reconstructed by default: thick slices for PACS archiving and primary viewing and thin slices for 3D post-processing and evaluation.

MDCT imaging of the thorax also greatly benefits from the shorter gantry rotation times of modern MDCT scanners and the reduced acquisition times per image. The better the temporal resolution of the images, the less pronounced are motion artifacts in CT images of the thorax, which typically appear as double contours or blurring of thoracic structures close to the heart. The best possible temporal resolution in a single-source CT scan is half the rotation time of the respective scanner, because half a rotation of scan data is the minimum needed for image reconstruction close to the isocenter. CT scanners used for thoracic imaging should therefore enable short gantry rotation times – at the moment, rotation times of 0.25–0.3 s result in a best possible temporal resolution of 125–150 ms. A further significant improvement of the temporal resolution to values below 100 ms can be achieved with dual-source CT systems (see Fig. 7) (Adapted from Hutt et al. 2016).

It is interesting to note that the temporal resolution in a spiral scan, which is the basic scan mode for MDCT scanning of the thorax, depends on the pitch of the scan: the higher the pitch, the better the temporal resolution. At a pitch of 1, a full rotation of scan data typically contributes to an image. Temporal resolution is therefore not better than the gantry rotation time. The higher the pitch, the less data contribute to image reconstruction, and the temporal resolution approaches half the gantry rotation time. On the other hand, even lower pitch will lead to even worse temporal resolution: at a pitch of 0.5, almost two rotations of scan data contribute to an image. Therefore, to reduce motion artifacts, it is mandatory to perform MDCT examinations of the thorax at fast gantry rotation and high pitch >1. Another option, in particular when the heart and the coronary arteries are also targeted in the planned examination, is the use of ECG-gated scan protocols. As a downside, these protocols result in longer scan times and increased radiation dose to the patient. ECG-triggered high-pitch scan protocols are a potential way out of this dilemma – they will be discussed in Sect. 2.3.

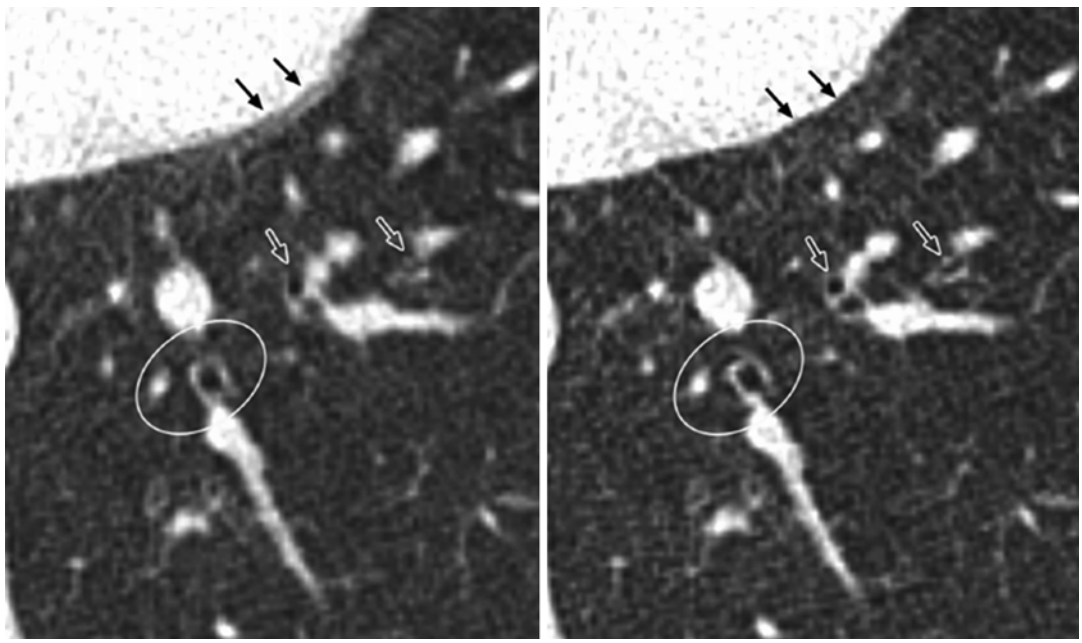

Fig. 7 Lung image acquired with a dual-source CT and reconstructed at a temporal resolution of 140 ms (*left*) and 75 ms (*right*). Note the double contour of the left ventricular wall due to cardiac motion (*fine arrows*) and the blurry appearance of the bronchi (*arrows*) in the image at 140 ms temporal resolution (Modified from (Hutt et al. 2016))

2.2 CT Systems with Area Detector

An area detector is a CT detector wide enough in the through-plane (z-axis) direction to cover entire organs, such as the heart, the kidneys, or the brain, in one axial scan without table movement. Two commercially available CT systems provide 16 cm detector coverage at isocenter, either with a collimation of 320×0.5 mm and 0.27 s rotation time (Aquilion ONE, Toshiba Medical Systems, Japan) or with 256×0.625 mm and 0.28 s rotation time (Revolution, GE Healthcare, USA). The SFOV is cone shaped in the z-axis direction (see Fig. 8).

CT scanners with area detectors are optimized for axial scanning without table movement – this scan technique has benefits in ECG-controlled cardiac imaging and in the acquisition of dynamic CT data, e.g., of the brain. Larger scan volumes in the z-direction, e.g., the entire thorax, have to be covered by "stitching," i.e., by appending axial scans shifted in the z-direction. With increasing SFOV, more overlap in the z-direction is required for gapless volume coverage. Another option is standard spiral scanning. Then, however, only a smaller detector coverage of, e.g., 80 mm is typically available because of image reconstruction challenges, and the maximum table feed is limited to, e.g., 300 mm/s.

In ECG-controlled cardiac CT imaging, an image stack with an anatomical coverage corresponding to the detector z-width is acquired in each heartbeat. Typical MDCT detectors provide a z-coverage of 40 mm (and recently up to 80 mm) at isocenter, so two to four of these image stacks acquired in two to four consecutive heartbeats have to be put together to a volume image of the heart (Flohr et al. 2007). These image stacks can be blurred or shifted relative to each other as a consequence of insufficient temporal resolution or variations of the heart motion from one cardiac cycle to the next, resulting in stair-step or banding artifacts. CT systems with 16 cm detector coverage avoid these artifacts, because they can scan the entire heart in one axial scan without table movement (Rybicki et al. 2008). As a downside, all images will be affected in case of arrhythmia or ectopic beats during data acquisition. Another challenge of larger detectors is increased x-ray scatter. Scattered radiation may cause hypodense cupping or streaking artifacts, and the scatter-induced noise may reduce the contrast-to noise-ratio (CNR) in the images (Flohr et al. 2009a). Meanwhile, successful use of CT systems with 16 cm detector coverage for coronary CTA and other cardiac applications has been demonstrated (Rybicki et al. 2008; Steigner et al. 2009; Dewey et al. 2009). The application spectrum has been extended to, e.g., scanning of patients with atrial fibrillation (Kondo et al. 2013)

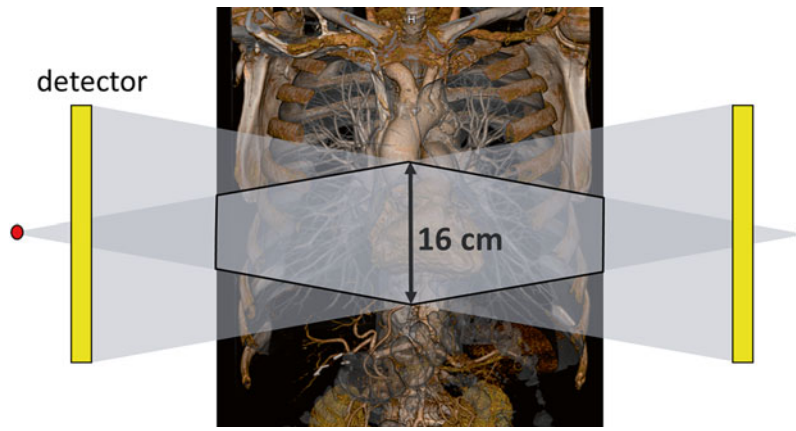

Fig. 8 Schematic illustration of axial CT scanning with a CT system with an area detector wide enough to cover entire organs such as the heart. Two commercially available CT systems provide 16 cm z-coverage at isocenter

and coronary CTA combined with the first-pass perfusion evaluation (George et al. 2015; Sharma et al. 2015). The second generation of 320-row CT scanners has been shown to enable coronary CTA at reduced radiation dose compared to the first generation (Tomizawa et al. 2013; Chen et al. 2013).

As a second benefit, CT systems with area detectors can acquire dynamic volume data by repeatedly scanning the same anatomical range without table movement. This is useful in dynamic CT angiographic examinations, e.g., in patients with brain arteriovenous malformations (Willems et al. 2012) or in volume perfusion studies, e.g., of the brain (Manniesing et al. 2016). In the context of thoracic scanning, 320-detector row first-pass perfusion scanning has been used to differentiate between malignant and benign pulmonary nodules (Ohno et al. 2011).

In triple-rule-out acute chest pain evaluation, the use of the sequential wide-volume mode proved to be more dose efficient than standard spiral scanning (Kang et al. 2012).

2.3 Dual-Source CT

A dual-source CT (DSCT) is a CT system with two x-ray tubes and two detectors at an angle of about 90° (see Fig. 9). Both measurement systems acquire CT scan data simultaneously at the same anatomical level of the patient (same *z*-position).

The first generation of DSCT scanners with 2×64 slices and 0.33 s gantry rotation time was introduced in 2006 (Somatom Definition, Siemens Healthcare, Forchheim, Germany), the second generation with 2×128 slices and 0.28 s gantry rotation time in 2009 (Somatom Definition Flash, Siemens Healthcare, Forchheim, Germany), and the third generation with 2×192 slices and 0.25 s gantry rotation time in 2014 (Somatom Definition Force, Siemens Healthcare, Forchheim, Germany).

DSCT systems provide significantly improved temporal resolution for cardiothoracic imaging. The shortest data acquisition time for an image corresponds to a quarter of the gantry rotation time. Close to the isocenter, 180° of scan data is the minimum needed for image reconstruction. Due to the 90° angle between both x-ray tubes, each of the measurement systems needs to acquire only 90° of scan data. The two 90° segments at the same anatomical level are put together to the 180° scan. Using this technique, a temporal resolution of 83, 75, and 66 ms, respectively, is achieved for the three generations of DSCT systems. With the dual-source approach, temporal resolution is independent of the patient's heart rate, because data from one cardiac cycle only are used to reconstruct an image. This is a major difference to single-source MDCT systems, which can provide similar temporal resolution by combining data from several heart cycles to an image in a multi-segment reconstruction. Then, however, temporal resolution strongly depends on the relation of heart rate and gantry rotation time. Meanwhile, several clinical studies have demonstrated the potential of DSCT to reliably perform coronary CT angiographic studies in patients with high and even irregular heart rates (e.g., Sun et al. 2011; Lee et al. 2012; Paul et al. 2013). DSCT is sufficiently accurate to diagnose clinically significant coronary artery disease in some or all difficult to image patients (Westwood et al. 2013). The good temporal resolution is also beneficial to reduce motion artifacts in cardiothoracic studies (e.g., Hutt et al. 2016).

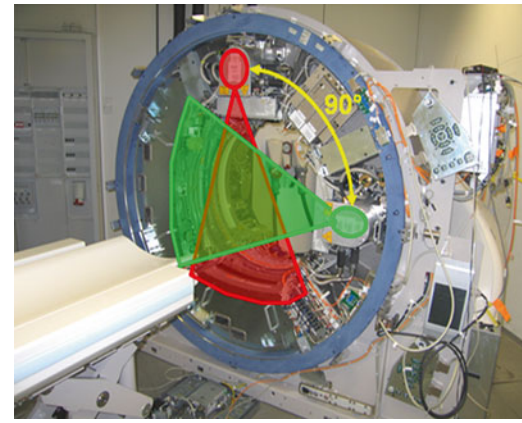

Fig. 9 DSCT with two independent measurement systems. The image shows the first-generation DSCT with an angle of 90° between both measurement systems. To increase the SFOV of detector B, a larger system angle of 95° was chosen for the second and third generations

With a DSCT system, both x-ray tubes can be operated at different kV settings, e.g., 80 and 140 kV, to acquire dual-energy CT data. The advantages and disadvantages of different techniques to acquire dual-energy CT data as well as clinically relevant applications will be discussed in Sect. 4.

While the maximum spiral pitch in single-source CT images is limited to about 1.5 to ensure gapless volume coverage, DSCT systems can be operated at double the pitch. Data acquired with the second measurement system, a quarter rotation after the first measurement system can be used to fill the sampling gaps up to a pitch of about 3.2 in a limited SFOV that is covered by both detectors (Petersilka et al. 2008; Flohr et al. 2009b). At maximum pitch, no redundant data are acquired, and a quarter rotation of data per measurement system is used for image reconstruction. Temporal resolution is then a quarter of the gantry rotation time. At decreasing pitch, temporal resolution worsens because of the increasing angular data segment that corresponds to an image. At a pitch of 2, as an example, temporal resolution is about 0.4 times the rotation time – this is 100 ms with the third-generation DSCT (Flohr et al. 2009b).

With the high-pitch scan mode, very high scan speed is achieved – up to 450 mm/s with the second-generation DSCT (38.4 mm detector coverage, 0.28 s gantry rotation time) and up to 737 mm/s with the third-generation DSCT (57.6 mm detector coverage, 0.25 s gantry rotation time). This is beneficial for the examination of larger anatomical ranges in very short scan times, e.g., for chest CTA at high temporal resolution (Tacelli et al. 2010), for the evaluation of pulmonary embolism and visualization of most cardiac structures and proximal coronary arteries (Hou et al. 2013), for fast CTA scans of the aorta at low radiation and contrast doses (Apfaltrer et al. 2012), or when the patient has limited ability to cooperate, such as in pediatric radiology (Lell et al. 2011; Bridoux et al. 2015) (see Fig. 10).

The high-pitch scan mode can also be used in combination with ECG triggering – the patient's ECG triggers both table motion and data acquisition. The patient table is positioned, and table acceleration is started in a way that the table arrives at the prescribed start z-position (e.g., the base or the apex of the heart) at the requested cardiac phase after full table speed has been reached (see Fig. 11). Then data acquisition begins.

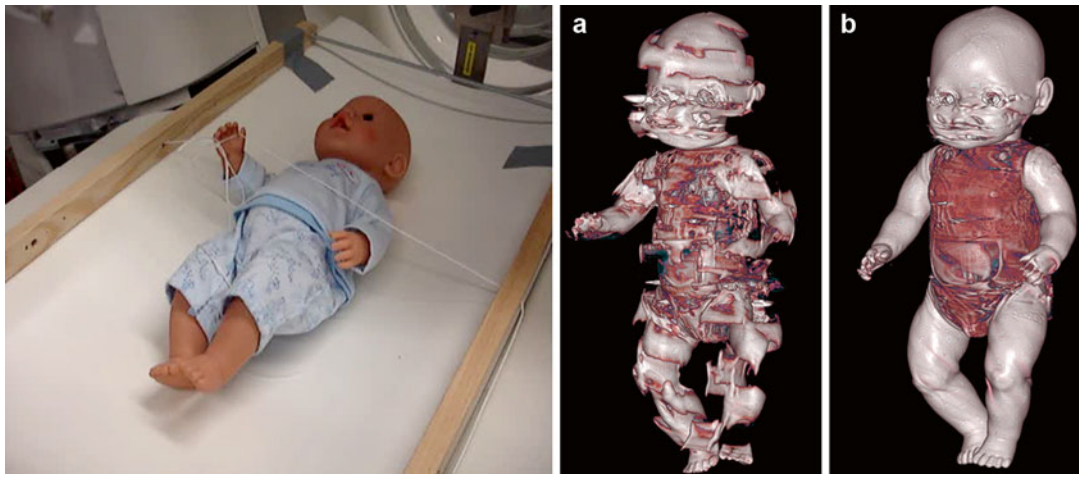

Fig. 10 CT scans of a moving doll phantom simulating motion of a child without sedation. (**a**) VRT of the phantom scanned with a standard spiral (pitch 1, 0.33 s rotation time) shows significant motion artifacts. (**b**) Using the high-pitch spiral (pitch 3.2, 0.33 s rotation time) motion artifacts are significantly reduced because of the very short scan time and the good temporal resolution per image (Courtesy of C. McCollough, Clinical Innovation Center, Mayo Clinic Rochester, Mn, USA)

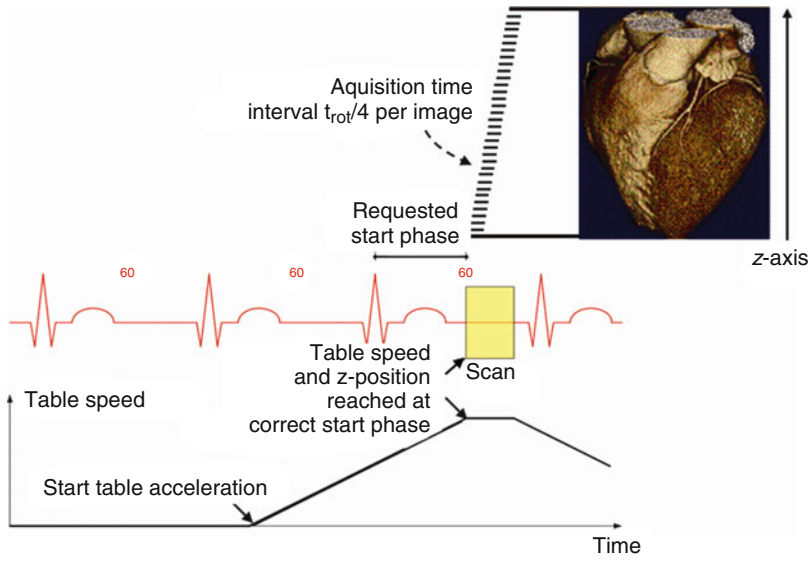

Fig. 11 ECG-triggered start of table movement and data acquisition for the high-pitch DSCT spiral

The scan data for images at adjacent *z*-positions are acquired at slightly different phases of the cardiac cycle. Meanwhile, several clinical studies have demonstrated the successful use of the high-pitch scan technique for coronary CT angiography in patients with sufficiently low and stable heart rate (<65 bpm with the second-generation DSCT, <73–75 bpm with the third-generation DSCT), with the potential to scan the entire heart in one beat at very low radiation dose (Achenbach et al. 2009; Lell et al. 2009; Leschka et al. 2009, Gordic et al. 2014a, Morsbach et al. 2014).

ECG-triggered high-pitch scans can be used for comprehensive thorax examinations in the emergency room and in the planning of TAVR procedures, because they provide adequate visualization of the coronary arteries, the aorta, and the iliac arteries in one scan at low radiation dose. The very short total scan time may potentially allow for a reduction of the amount of contrast agent (see, e.g., Wuest et al. 2012; Azzalini et al. 2014). Figure 12 shows an ECG-triggered high-pitch CTA of the aorta as an example.

Despite their clinical benefits, DSCT systems have to cope with some challenges. One challenge is the presence of cross-scattered radiation, i.e., scattered radiation from x-ray tube B detected by detector A and vice versa. Cross-scattered radiation – if not corrected for – can result in image artifacts and degraded CNR of the images (Petersilka et al. 2010). Another challenge is the limited SFOV of the second detector, which was increased from 25 cm in the first-generation DSCT to 35.5 cm in the third-generation DSCT.

3 Radiation Dose Reduction

3.1 Low-kV Scanning

Most CT scans are performed with the use of iodinated contrast agent. The x-ray attenuation of iodine and as a consequence, its CT number in a CT image increases with decreasing mean energy of the x-ray beam, i.e., with the use of lower x-ray tube voltages (kV) (see, e.g., McCollough et al. 2009). This behavior is caused by the k-edge of iodine at 33 keV. The x-ray attenuation of soft tissue depends only very weakly on the x-ray tube voltage. Therefore, the image contrast of tissues and vessels that take up iodinated contrast agent increases relative to other surrounding tissues at lower x-ray tube voltage. If the same radiation dose is applied to the patient when using lower kV, the increased contrast of iodine in the image translates into increased iodine contrast-to-noise ratio (CNR) (see Fig. 13).

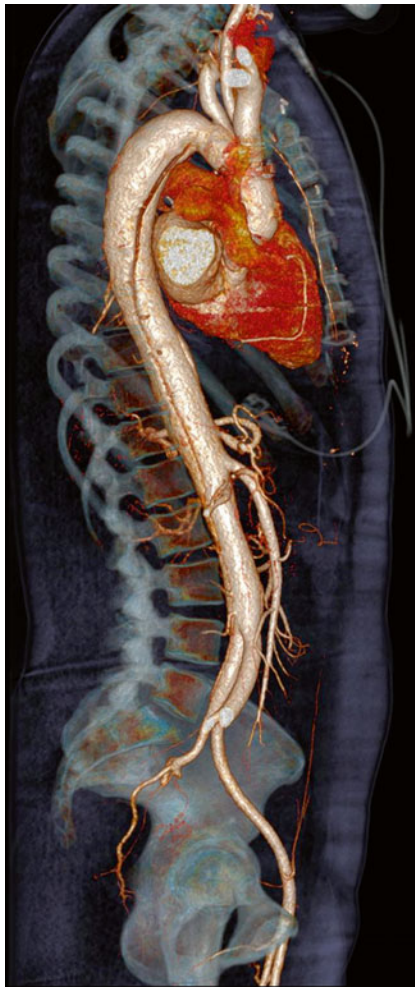

Fig. 12 ECG-triggered high-pitch spiral scan of the aorta and the iliac arteries in a patient with aortic dissection. Scan parameters: 0.25 s rotation time, pitch 3.2, 90 kV, DLP = 177 mGy cm. Total scan time 0.8 s. Note the clear visualization of the right coronary artery (Courtesy of Klinikum Großhadern, Munich, Germany)

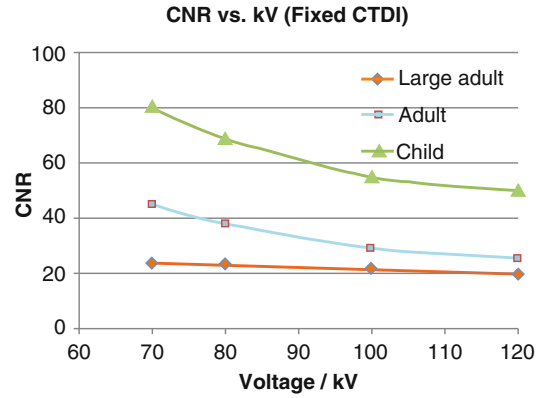

Fig. 13 Iodine contrast-to-noise ratio (*CNR*) at equal radiation dose (*equal CTDI*) as a function of the x-ray tube voltage (*kV*) for phantoms representing the attenuation of children, adults, and large adults, on a second-generation DSCT. A small tube filled with diluted iodine solution was placed at the center of the phantoms; the iodine concentration was chosen to provide the typical contrast of the aorta in a CT angiographic examination. Note the increase of the CNR with decreasing x-ray tube voltage

The increased CNR at lower x-ray tube voltage may either be exploited to reduce the radiation dose to the patient or to reduce the amount of iodinated contrast agent.

Unfortunately, with decreasing x-ray tube voltage, the tube current–time product mAs has to be significantly increased to provide adequate radiation dose in particular for larger patients. Because of missing tube power reserves, low-kV imaging has been mainly used for children and small patients. Meanwhile, new technologies are available that automatically adapt the x-ray tube voltage to the size and shape of the patient and the planned examination, taking into account the tube power reserves of the respective CT system (e.g., CAREkV, Siemens Healthcare, Forchheim, Germany). According to Niemann et al. (2013), automatic tube voltage selection reduced the radiation dose delivered during chest CT angiograms by 38.5 % compared to the standard 120 kV protocol while improving the CNR of the examinations.

Recently, new x-ray tubes with significantly increased mA reserves and significantly increased power at low kV were introduced (VECTRON, Siemens Healthcare, Forchheim, Germany), which have the potential to extend low-kV scanning at reduced radiation dose and/or reduced contrast dose also to adult and obese patients (Meyer et al. 2014; Meinel et al. 2014). Meyer et al. (2014) observed that coronary CTA with a third-generation DSCT at 70 kV resulted in up to 52 % lower radiation dose as well as up to 45 % less contrast medium volume in nonobese adults (see Fig. 14 as an example).

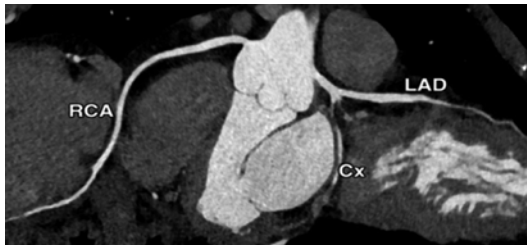

Fig. 14 Coronary CTA in an adult patient at 70 kV. ECG-triggered high-pitch scan at 64 bpm. Total radiation dose 0.21 mSv (Courtesy of Mannheim University Hospital, Germany)

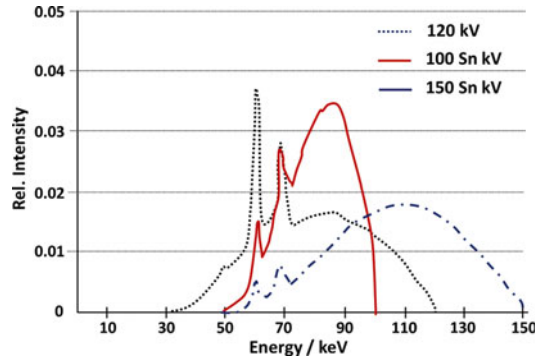

Fig. 15 Spectral shaping by Sn (tin) pre-filtration. Standard 120 kV spectrum as compared to 100 and 150 Sn kV. The tin filter removes x-ray quanta at lower energies (lower keV) from the spectra. Note the onset of the tin-filtered spectra at about 50 keV as compared to about 30 keV for the standard 120 kV spectrum and the very narrow, almost "mono-energetic" shape of the 100 Sn kV spectrum

3.2 Spectral Shaping

In CT examinations of the lung without contrast agent, spectral shaping may be used to significantly reduce the radiation dose to the patient. A tin filter, which can be moved into the x-ray beam in the pre-patient tube collimator box if needed, removes lower-energy x-ray photons from the x-ray spectrum and hardens it– these photons would otherwise mainly be absorbed in the patient without contributing to the image and would degrade the dose efficiency of the CT scan[1]. Third-generation DSCT systems are equipped with 0.6 mm thick tin filters, which can be used with 100 or 150 kV x-ray tube voltage. Figure 15 demonstrates the effect of the tin filter on the shape of the spectra for 100 kV + tin filter (100 Sn kV) and 150 kV + tin filter (150 Sn kV). The novel scan mode offers a potential radiation dose reduction in non-enhanced lung examinations compared to standard 120 kV scans.

Gordic et al. (2014b) evaluated the image quality and sensitivity of low-dose CT with spectral shaping and iterative reconstruction for the detection of pulmonary nodules in a phantom setting. They concluded that radiation dose levels of non-enhanced chest CT for the detection of pulmonary nodules can be lowered down to a level of 0.06 mSv when using 100 kV with tin pre-filtration in combination with advanced iterative reconstruction techniques. Image quality remains diagnostic and sensitivity remains high. This is potentially interesting for the use of CT in the context of lung cancer screening. According to Newell et al. 2015, quantitative CT lung imaging can be performed with spectral shaping and third-generation iterative reconstruction methods with acceptable image noise at very low-dose levels of 0.15 mGy (corresponding to about 0.07 mSv for a scan range of 350 mm). It remains subject of further studies how well subtle features of the lung parenchyma can be evaluated at such a low radiation dose. Figure 16 shows a representative example of a non-enhanced thorax scan with spectral shaping (100 Sn kV) at a radiation dose of 0.07 mSv.

3.3 Iterative Reconstruction

As an add-on to the dose reduction approaches described above, iterative image reconstruction has found its way into routine CT scanning after it had been proposed in 2007 as a method to improve image quality, enhance image resolution, and lower image noise in CT (Thibault et al. 2007).

1 Please note that this is valid for non-contrast scans. In contrast-enhanced examinations, the increased x-ray absorption of iodine at lower energies overcompensates this effect.

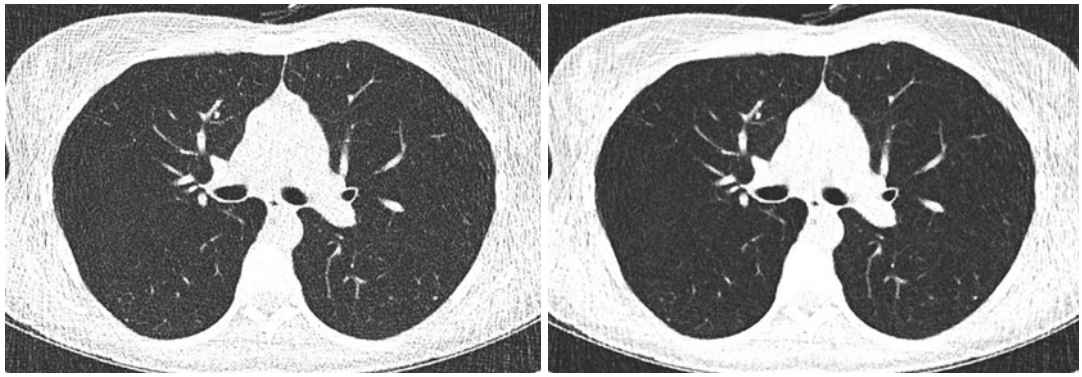

Fig. 16 Non-enhanced lung image acquired with spectral shaping (100 Sn kV) and two levels of iterative reconstruction (ADMIRE level 3, *left*, and level 5, *right*) at a radiation dose of 0.07 mSv (Courtesy of Universitätsspital Zürich, Switzerland)

While increased spatial resolution is directly correlated with increased image noise in filtered back projection, the standard image reconstruction approach in all medical CT scanners today, it is to a certain extent decoupled from image noise in an iterative reconstruction.

With iterative reconstruction, a correction loop is introduced into the image reconstruction process (Thibault et al. 2007). After an image has been reconstructed from the measured projection data, synthetic projections are calculated from that image by ray tracing. Because image reconstruction is not exact, the synthetic projections are not fully identical to the measured projections. The deviation is used to reconstruct a correction image and update the original image in an iterative loop. Each time the image is updated, nonlinear image processing is used to stabilize the solution. It maintains or enhances spatial resolution at higher object contrasts and reduces image noise in low-contrast areas. This step, called regularization, is essential for the image noise reduction claimed with most iterative reconstruction approaches. The repeated calculation of correction projections mainly removes image artifacts introduced by the approximate nature of the filtered back projection reconstruction when applied to multi-row CT data. In some approaches, a statistical raw-data weighting is added in the reconstruction loops which assigns low weights to measured raw data with high noise. This step reduces image noise in particular in low-dose situations, but at the expense of a certain loss of spatial resolution.

There is a variety of different iterative reconstruction techniques commercially available, such as ASIR, VEO and ASIR-V (GE Healthcare, USA), IRIS, SAFIRE and ADMIRE (Siemens Healthcare, Forchheim, Germany), iDose (Philips), and AIDR3D (Toshiba). While the technical realization is highly vendor specific, using some or all of the steps described above, all approaches aim at including the statistical properties of the acquired measurement data into the image reconstruction process in a better way than traditional filtered back projection.

The reduced image noise in low-contrast areas is the prerequisite for a potential radiation dose reduction, which is the main goal when using iterative reconstruction. Iterative reconstruction has been widely used for chest CT examinations (see Fig. 16), and a potential for substantial radiation dose reduction has been reported (see, e.g., Kim et al. 2015; Wang et al. 2015; Pontana et al. 2011a, b, 2015; Padole et al. 2014; Vardhanabhuti et al. 2013). By analyzing 24 studies using iterative reconstruction for chest CT, den Harder et al. (den Harder et al. 2015) found that by means of iterative reconstruction, radiation dose can be reduced to less than 2 mSv for contrast-enhanced chest CT, while non-contrast-enhanced chest CT is possible at a sub-mSv dose.

However, as a downside, it has also been shown that iterative reconstruction may alter

both the qualitative and quantitative assessment of smoking-related lung disease (Hague et al. 2014) and may affect quantitative CT measures in the assessment of emphysema and air trapping and should therefore be used with caution (Mets et al. 2012).

4 Dual-Energy CT (DECT)

CT imaging shows the patient's anatomy; however, it cannot provide information about the chemical composition of the examined structures. CT is only sensitive to the x-ray attenuation coefficients μ of the examined objects. Tissues of different chemical composition but with the same μ will appear with the same Hounsfield number in the CT image. Additional information obtained by measurements at different x-ray energies *E* can help overcome this limitation. Alvarez and Macovski observed that in the typical energy range of the CT x-ray spectra, ranging from 30 to 140 keV, only two absorption processes are relevant, the Compton effect and the photoelectric effect (Alvarez and Macovski 1976). Both have a characteristic energy dependence which is almost independent of the atomic number *Z*. As a consequence, all materials in the examined scan volume can be decomposed into two different base materials, e.g., water and bone or water and iodine. The relative contributions of these two base materials to each voxel of interest can be determined if the x-ray absorption by the object of interest is measured with two different spectra. In some cases, by observing a volume conservation constraint, decomposition into three materials is possible, e.g., water, bone, and iodine. Because there are only two different absorption mechanisms, however, it is not possible to e.g., separate *N* different materials by measurements at *N* different energies.

4.1 Instrumentation

There are several methods to acquire CT data with spectral information. In single-source CT systems, the kV setting of the x-ray tube can be changed either between different CT scans (slow kV switching) or more rapidly between the different projections of a CT scan (fast kV switching (see Fig. 17). Slow kV switching is problematic for chest imaging because cardiac motion causes registration problems between the two data sets acquired at different kV.

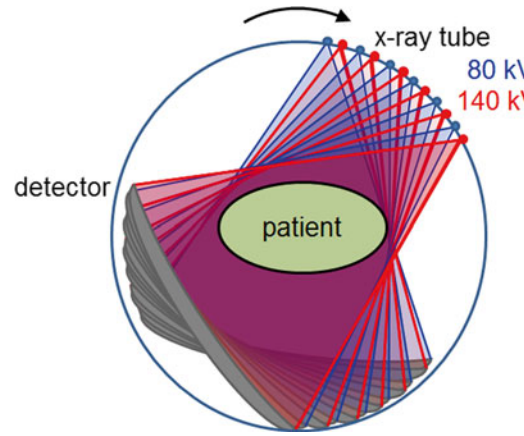

Fig. 17 Schematic drawing illustrating the principle of dual-energy CT data acquisition by means of fast kV switching. The x-ray tube voltage is rapidly switched from 80 to 140 kV and vice versa between two projections

Fast kV switching, usually between 80 and 140 kV, is per se well suited for thoracic imaging because of the nearly simultaneous acquisition of low-energy and high-energy projections which avoids registration problems and allows the use of raw-data-based dual-energy algorithms. Fast kV switching was commercially reintroduced in 2009 (Gemstone Spectral Imaging, GE Healthcare, USA) (see, e.g., Zhang et al. 2011). As a downside, current tube technology doesn't allow switching the tube current between two projections. Equal radiation dose at 80 and 140 kV can only be achieved if each 80 kV projection is two–four times longer than the corresponding 140 kV projection. This reduces the number of projections per rotation and may cause sampling artifacts in the images. Another drawback is the fixed and relatively high tube current that is required to obtain stable switching between both tube potentials, which prevents the use of anatomical dose modulation

techniques to adapt radiation dose to the patient's size and shape.

Dual-layer detectors consisting of two conventional scintillation detectors on top of each other enable the acquisition of spectral CT data with a single polychromatic x-ray spectrum and without further modifications of the CT system. A CT scanner with dual-layer detector was commercially introduced in 2013 (IQon, Philips Healthcare, the Netherlands). Dual-layer detectors enable the acquisition of dual-energy data in the full SFOV and with perfect registration between the high- and low-energy data. However, spectral separation is not as good as with the use of two different x-ray spectra (Tkaczyk et al. 2007).

Another alternative for dual-energy data acquisition is the use of dual-source CT systems, which have the potential to acquire DE data by operating both x-rays tubes at different kV settings. The scan parameters can be individually adjusted for both measurement systems, resulting in a flexible choice of scan protocols. In combination with online anatomical dose modulation (CAREDose 4D, Siemens Healthcare, Forchheim, Germany), the radiation dose to the patient can be fine-tuned to patient's size and the planned examination. As a drawback, DE data acquisition is limited to a smaller, central FOV covered by both detectors. Cross-scattered radiation has to be carefully corrected for in order not to degrade the stability of the Hounsfield numbers and – as a consequence – the quality of the image-based DE evaluation. Furthermore, images of moving objects may show slightly different motion artifacts due to the 90° offset between both measurement systems, which may result in registration problems affecting material decomposition. In practice, however, this problem is mitigated by the good temporal resolution of DSCT and – if necessary – by nonrigid image registration.

The quality of dual-energy CT examinations relies on the effective separation of the energy spectra. More spectral overlap and worse energy separation mean less efficient and less precise tissue differentiation, which has to be compensated by increased radiation dose. With DSCT systems spectral separation can be optimized by introducing additional pre-filtration into the high-kV beam, e.g., by means of a filter that can be moved in when needed and moved out for non-DE applications. In the second-generation and third-generation DSCT systems, additional tin filters (Sn) with a thickness of 0.4 mm (second-generation DSCT) and 0.6 mm (third-generation DSCT) are used. They shift the mean energy of the 140 kV spectrum and the 150 kV spectrum (third-generation DSCT) to higher values, which increases spectral separation (see Fig. 18).

Spectral pre-filtration of the high-kV beam is beneficial for DECT at low radiation dose. Several authors have meanwhile demonstrated dual-source DECT scanning with no dose penalty compared to standard single-energy CT. Schenzle et al. (2010) report the feasibility of dual-source DECT without increasing radiation dose in chest CT. Bauer et al. (2011) compare radiation dose and image quality of 64-slice CT and dual-source DECT for CT pulmonary angiography (CTPA). They conclude that the use of the second-generation DECT in 80/140 Sn kV configuration allows for significant dose reduction with image quality similar to 120 kV CTPA. A comprehensive overview on radiation dose in DECT can be found in (Henzler et al. 2012).

4.2 Applications

For thoracic DECT, dedicated scan protocols are available that aim at high scan speed and good temporal resolution by using fast gantry rotation (e.g., 0.28 or 0.25 s). For dedicated cardiac examinations, both ECG-triggered DE sequential "step-and-shoot" scanning and ECG-gated DE spiral scanning are provided, both at the fastest gantry rotation speed of the respective CT scanner.

Clinically relevant applications for thoracic and cardiothoracic scanning are the computation of pseudo mono-energetic images or iodine distribution maps of the lung parenchyma as a surrogate of the local blood volume and lung perfusion

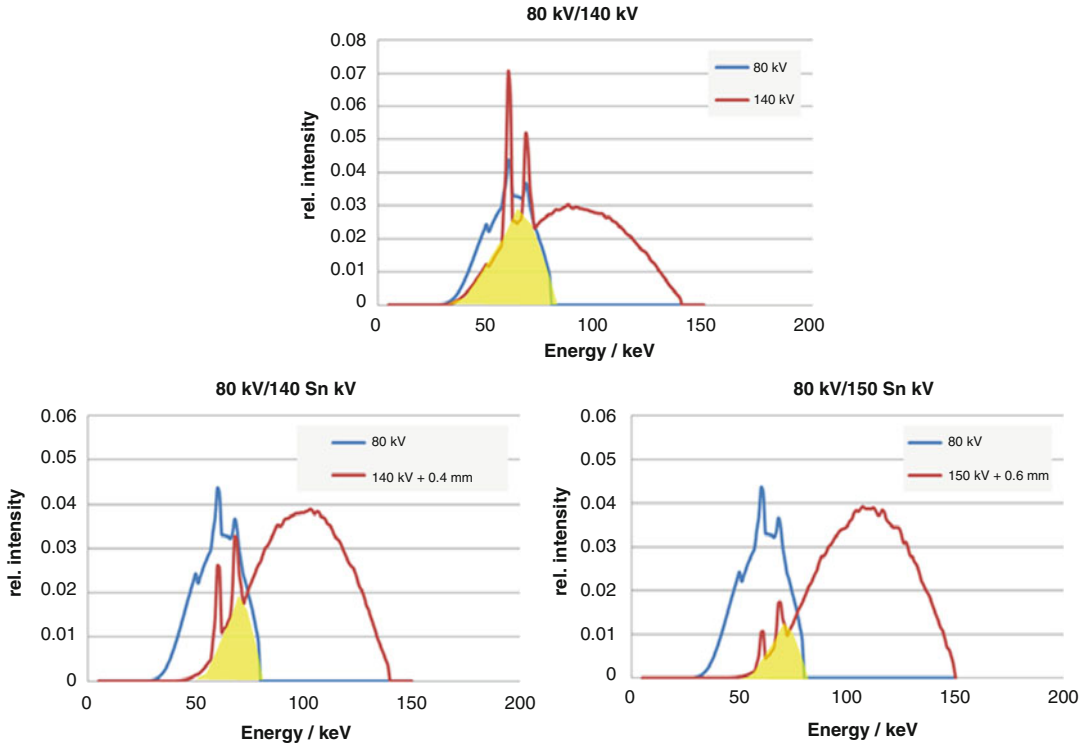

Fig. 18 *Top*: Standard 80 and 140 kV spectra. The mean energy is 69 keV for the 140 kV spectrum and 52 keV for the 80 kV spectrum. Both spectra overlap significantly (indicated in *yellow*). *Bottom left*: Standard 80 kV spectrum and 140 kV spectrum with additional 0.4 mm tin pre-filtration. Note the shift of the 140 kV spectrum to higher energies. The mean energy is now 89 keV. *Bottom right*: Standard 80 kV spectrum and 150 kV spectrum with additional 0.6 mm tin pre-filtration. Note the further reduced spectral overlap

Pseudo mono-energetic images at arbitrary energies can be obtained from the polychromatic low-kV and high-kV images, if we assume that the object consists of only two base materials in variable concentrations, e.g., water (soft tissue) and iodine. The concentrations of both materials in each image pixel are calculated by means of an image-based material decomposition. They are multiplied with predicted CT numbers per concentration at the desired energy and summed up to the final mono-energetic image. Other materials will contribute to both base material images, their CT numbers may therefore not reflect the actual enhancement of the respective material at the desired energy.

Pseudo mono-energetic images may be used to benefit from the increased iodine contrast at lower keV in CT angiographic studies. With conventional decomposition approaches, optimum CNR in contrast-enhanced thoracic scans has been observed at 60 keV for the aorta, pulmonary arteries, and veins. For the superior vena cava and brachiocephalic veins, the reconstructions at 100 keV with reduced iodine contrast enabled reduction of beam-hardening artifacts (Delesalle et al. 2013).

Performance can be improved by means of recently introduced algorithms (e.g., mono+, Siemens Healthcare, Forchheim, Germany) that efficiently reduce image noise at low and high keV (Grant et al. 2014). Using these techniques, images at the target keV and images at optimal keV from a noise perspective (typically, minimum image noise is obtained at approximately 70 keV) are computed. For the final images, the lower spatial frequencies (that contain most of the object structure) from the images at the target keV are combined with the higher spatial frequencies (that contain most of the image noise) from the images at optimal keV from a

noise perspective. It has been shown (Grant et al. 2014) that use of the mono+–technique at 40 keV may be more efficient to optimize iodine CNR than low-kV scans, which has been the established and recommended method to improve iodine CNR to date (see also Fig. 19). Recent publications demonstrated that mono+images at 40 keV improve the contrast of dual-energy CT pulmonary angiography (Meier et al. 2015). Figure 20 shows a clinical example for illustration.

The polychromatic low-kV and high-kV images can also be used for the subtraction of iodine from a contrast-enhanced CT scan, to compute both a virtual non-enhanced CT image and an iodine map showing the iodine content per image pixel. In lung imaging, the iodine content is a surrogate parameter for the perfused blood volume in the lung parenchyma or in lung tumors. The underlying technique is a modified three-material decomposition. In a diagram showing the CT number of each image pixel at low kV as a function of its CT number at high kV, image pixels containing mixtures of air and soft tissue (these are the relevant two "base materials" in lung imaging) are located along a line between air and soft tissue (see Fig. 21). If iodine is added, the respective data points in the CT-number diagram move in the direction of the iodine enhancement vector. To extract the iodine, each pixel is projected onto the line between air and soft tissue along the direction of the iodine enhancement vector. The length of the displacement vector represents the enhancement attributed to iodine in that pixel (see the two examples "Pixel 1" and "Pixel 2" in Fig. 21). The iodine map can provide quantitative information about the iodine content in mg/ml.

Iodine maps have been frequently used in patients with pulmonary embolism to assess perfusion defects, which show up as hypodense areas with reduced iodine content (see, e.g., Pontana et al. 2008; Thieme et al. 2008, 2009; Ferda et al. 2009). Figure 22 shows a clinical example.

Dual-energy CT of the lung has also other clinical applications, such as the evaluation of regional perfusion according to the presence of emphysematous changes in the lung parenchyma in patients with chronic obstructive pulmonary disease (Remy-Jardin and Remy 2008), the depiction of regional alterations of lung perfusion in

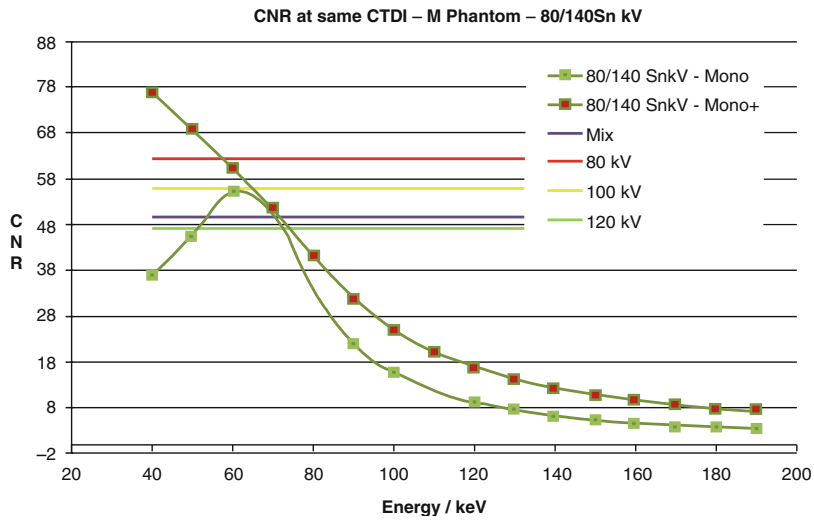

Fig. 19 Iodine CNR as a function of the energy (in keV) of pseudo mono-energetic images computed with a standard two-material decomposition (mono) and with an advanced algorithm (mono+). In addition, CNRs from single-energy scans (at 80, 100 and 140 kV) for the same medium-sized body phantom at the same radiation dose are shown (From (Grant et al. 2014)). Note the better iodine CNR with mono+even compared with 80 kV scans in the energy range 40–50 keV

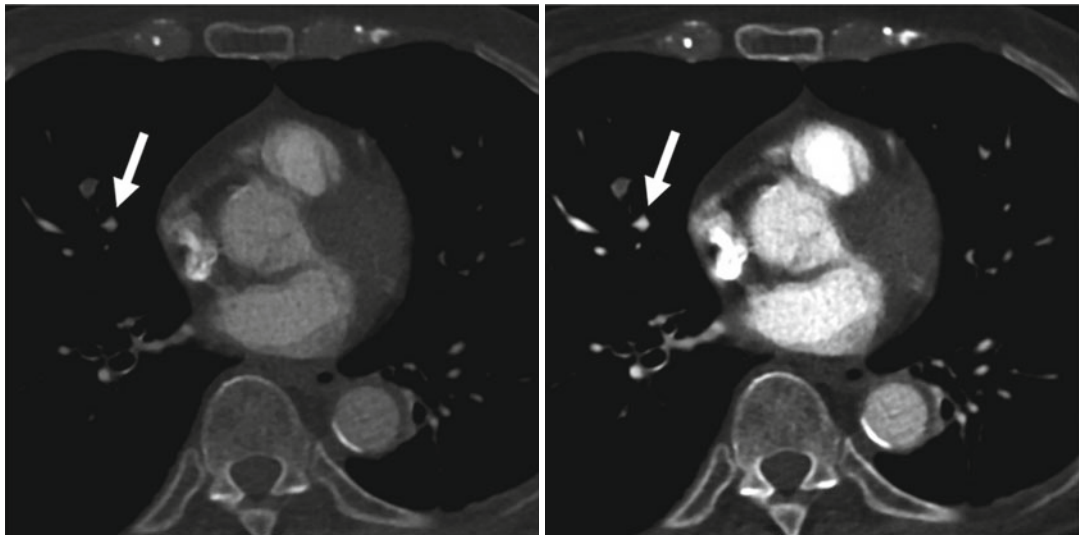

Fig. 20 Image example from a DE pulmonary CTA examination. *Left*: In the standard mixed image (corresponding to a 120 kV scan), opacification of peripheral pulmonary arteries is suboptimal (*arrow*), and the examination is of limited diagnostic value. *Right*: Reconstruction of pseudo mono-energetic images at 40 keV with an advanced algorithm (mono+) demonstrates increased iodine contrast and allows for a reliable exclusion of PE (Adapted from (Meier et al. 2015))

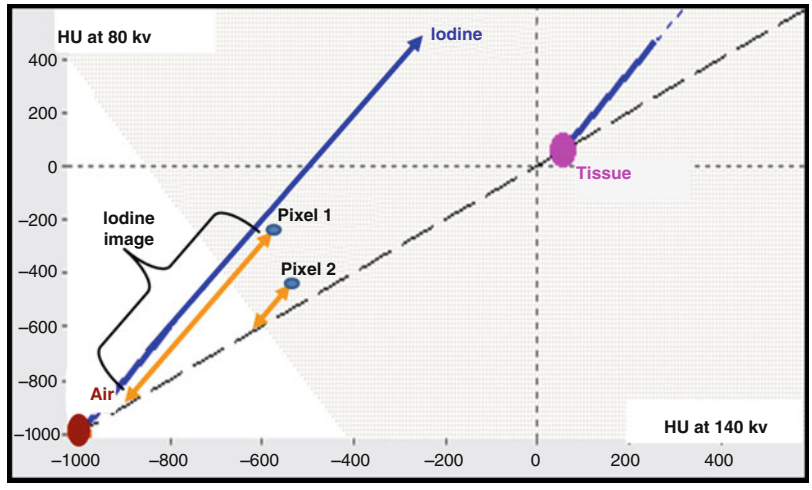

Fig. 21 Principle of a modified three-material decomposition: subtraction of iodine from contrast-enhanced DECT images to compute both an iodine map ("iodine image") and a virtual non-enhanced image

smokers with predominant emphysema (Pansini et al. 2009), or the characterization of lung tumors (Aoki et al. 2014; Wang et al. 2014). According to Lu et al., (2012) dual-energy CT of the lung can improve the diagnosis of acute and chronic PEs, other vascular disorders, lung malignancies, and parenchymal diseases.

In xenon lung ventilation studies, dual-energy CT allows extracting the amount of inhaled xenon gas per voxel without the need for a pre-scan without xenon. Hence, limitations in the quantification of Xe enhancement by ventilation mismatch, i.e., by the variability of lung attenuation caused by different lung volumes between scans, can be avoided.

With ongoing technical refinements, DECT has the potential to provide complementary information in a variety of chest disorders. An overview of dual-energy imaging of the thorax is, e.g., available in (Lu et al. 2012) or (Remy-Jardin et al. 2014).

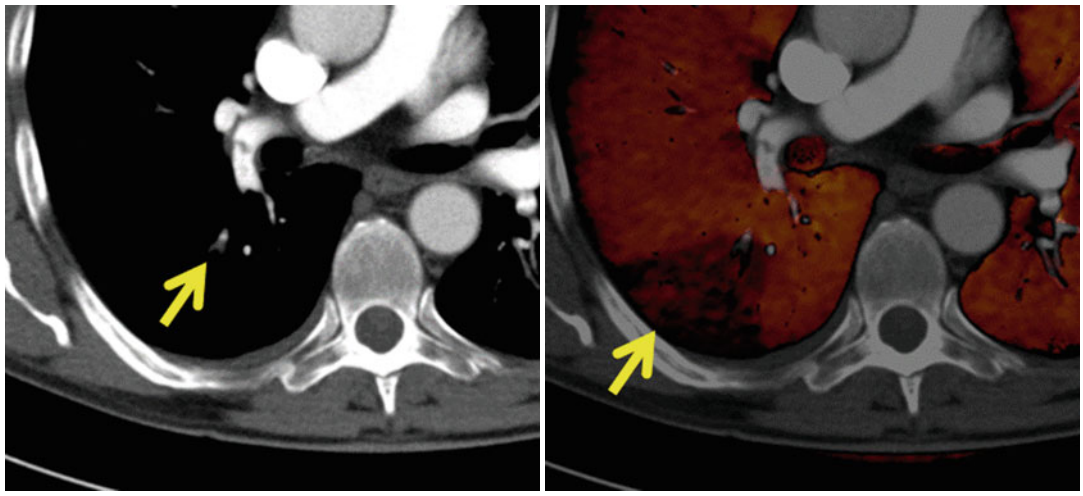

Fig. 22 Visualization of perfusion defects in the lung parenchyma caused by pulmonary embolism. DECT angiography using a second-generation DSCT, scan parameters 80 kV/140 Sn kV, rotation time 0.28 s. *Left*: Mixed low-kV/high-kV axial image corresponding to a standard 120 kV image shows small embolus that occludes a sub-segmental vessel in the right lower lobe (*arrow*). *Right*: DE iodine map of the lung parenchyma as a colored overlay (*red*) shows the corresponding typical wedge-shaped perfusion defect (*dark zone*, *arrow*) (Courtesy of Klinikum Großhadern, Munich, Germany)

References

Achenbach S, Marwan M, Schepis T, Pflederer T, Bruder H, Allmendinger T, Petersilka M, Anders K, Lell M, Kuettner A, Ropers D, Daniel WG, Flohr T (2009) High-pitch spiral acquisition: a new scan mode for coronary CT angiography. J Cardiovasc Comput Tomogr 3:117–121

Achenbach S, Manolopoulos M, Schuhbäck A, Ropers D, Rixe J, Schneider C, Krombach GA, Uder M, Hamm C, Daniel WG, Lell M (2012) Influence of heart rate and phase of the cardiac cycle on the occurrence of motion artifact in dual-source CT angiography of the coronary arteries. J Cardiovasc Comput Tomogr 6(2):91–98

Alvarez RE, Macovski A (1976) Energy-selective reconstructions in X-ray computerized tomography. Phys Med Biol 21(5):733–744

Aoki M, Takai Y, Narita Y, Hirose K, Sato M, Akimoto H, Kawaguchi H, Hatayama Y, Miura H, Ono S (2014) 23. Correlation between tumor size and blood volume in lung tumors: a prospective study on dual-energy gemstone spectral CT imaging. J Radiat Res 55(5): 917–923

Apfaltrer P, Hanna EL, Schoepf UJ, Spears JR, Schoenberg SO, Fink C, Vliegenthart R (2012) Radiation dose and image quality at high-pitch CT angiography of the aorta: intraindividual and interindividual comparisons with conventional CT angiography. AJR Am J Roentgenol 199(6):1402–1409

Azzalini L, Abbara S, Ghoshhajra BB (2014) Ultra-low contrast Computed Tomographic Angiography (CTA) with 20-mL total dose for Transcatheter Aortic Valve Implantation (TAVI) planning. J Comput Assist Tomogr 38(1):105–109

Bauer RW, Kramer S, Renker M et al (2011) Dose and image quality at CT pulmonary angiography: comparison of first and second generation dual energy CT and 64-slice CT. Eur Radiol 21:2139–2147

Baumueller S, Winklehner A, Karlo C, Goetti R, Flohr T, Russi EW, Frauenfelder T, Alkadhi H (2012) Low-dose CT of the lung: potential value of iterative reconstructions. Eur Radiol 22(12):2597–2606

Becker C, Knez A, Ohnesorge B, Schöpf U, Reiser M (2000) Imaging of non calcified coronary plaques using helical CT with retrospective EKG gating. AJR 175:423–424

Beeres M, Schell B, Mastragelopoulos A, Herrmann E, Kerl JM, Gruber-Rouh T, Lee C, Siebenhandl P, Bodelle B, Zangos S, Vogl TJ, Jacobi V, Bauer RW (2012) High-pitch dual-source CT angiography of the whole aorta without ECG synchronisation: initial experience. Eur Radiol 22(1):129–137

Bridoux A, Hutt A, Faivre JB, Flohr T, Duhamel A, Pagniez J, Remy J, Remy-Jardin M (2015) Coronary artery visibility in free-breathing young children on non-gated chest CT: impact of temporal resolution. Pediatr Radiol 45(12):1761–1770

Bruzzi JF, Rémy-Jardin M, Delhaye D, Teisseire A, Khalil C, Rémy J (2006a) When, why, and how to examine the heart during thoracic CT: Part 1, basic principles. AJR Am J Roentgenol 186(2):324–332

Bruzzi JF, Rémy-Jardin M, Delhaye D, Teisseire A, Khalil C, Rémy J (2006b) When, why, and how to examine the heart during thoracic CT: Part 2, clinical applications. AJR Am J Roentgenol 186(2):333–341

Chen MY, Shanbhag SM, Arai AE (2013) Submillisievert median radiation dose for coronary angiography with a second-generation 320-detector row CT scanner in 107 consecutive patients. Radiology 267(1):76–85

Coche E, Vlassenbroeck A, Roelants V, D'Hoore W, Verschuren F, Goncette L, Maldague B (2005) Evaluation of biventricular ejection fraction with ECG-gated 16-slice CT: preliminary findings in acute pulmonary embolism in comparison with radionuclide ventriculography. Eur Radiol 15:1432–1440

Delesalle MA, Pontana F, Duhamel A, Faivre JB, Flohr T, Tacelli N, Remy J, Remy-Jardin M (2013) Spectral optimization of chest CT angiography with reduced iodine load: experience in 80 patients evaluated with dual-source, dual-energy CT. Radiology 267(1):256–266

Delhaye D, Remy-Jardin M, Salem R, Teisseire A, Khalil C, Delannoy-Deken V, Duhamel A, Remy J (2007) Coronary imaging quality in routine ECG-gated multidetector CT examinations of the entire thorax: preliminary experience with a 64-slice CT system in 133 patients. Eur Radiol 17(4):902–910

den Harder AM, Willemink MJ, de Ruiter QM, Schilham AM, Krestin GP, Leiner T, de Jong PA, Budde RP (2015) Achievable dose reduction using iterative reconstruction for chest computed tomography: a systematic review. Eur J Radiol 84(11):2307–2313

Dewey M, Zimmermann E, Deissenrieder F, Laule M, Dübel HP, Schlattmann P, Knebel F, Rutsch W, Hamm B (2009) Noninvasive coronary angiography by 320-row computed tomography with lower radiation exposure and maintained diagnostic accuracy: comparison of results with cardiac catheterization in a head-to-head pilot investigation. Circulation 120(10):867–875

Duan X, Wang J, Leng S, Schmidt B, Allmendinger T, Grant K, Flohr T, McCollough CH (2013) Electronic noise in CT detectors: impact on image noise and artifacts. AJR Am J Roentgenol 201(4):W626–W632

Durand S, Paul JF (2014) Comparison of image quality between 70 kVp and 80 kVp: application to paediatric cardiac CT. Eur Radiol 24(12):3003–3009

Ferda J, Ferdová E, Mírka H, Baxa J, Bednářová A, Flohr T, Schmidt B, Matějovič M, Kreuzberg B (2011). Pulmonary imaging using dual-energy CT, a role of the assessment of iodine and air distribution. Eur J Radiol 77(2):287–93

Flohr T, Stierstorfer K, Bruder H, Simon J, Schaller S (2002a) New technical developments in multislice CT, part 1: approaching isotropic resolution with sub-mm 16-slice scanning. Röfo Fortschr Geb Rontgenstr Neuen Bildgeb Verfahr 174:839–845

Flohr T, Bruder H, Stierstorfer K, Simon J, Schaller S, Ohnesorge B (2002b) New technical developments in multislice CT, part 2: sub-millimeter 16-slice scanning and increased gantry rotation speed for cardiac imaging. Röfo Fortschr Geb Rontgenstr Neuen Bildgeb Verfahr 174:1022–1027

Flohr T, Stierstorfer K, Bruder H, Simon J, Polacin A, Schaller S (2003) Image reconstruction and image quality evaluation for a 16-slice CT scanner. Med Phys 30(5):832–884

Flohr T, Stierstorfer K, Raupach R, Ulzheimer S, Bruder H (2004) Performance evaluation of a 64-slice CT-system with z-flying focal spot. Röfo Fortschr Geb Rontgenstr Neuen Bildgeb Verfahr 176: 1803–1810

Flohr TG, Stierstorfer K, Ulzheimer S, Bruder H, Primak AN, McCollough CH (2005) Image reconstruction and image quality evaluation for a 64-slice CT scanner with z-flying focal spot. Med Phys 32(8): 2536–2547

Flohr TG, McCollough CH, Bruder H, Petersilka M, Gruber K, Süß C, Grasruck M, Stierstorfer K, Krauss B, Raupach R, Primak AN, Küttner A, Achenbach S, Becker C, Kopp A, Ohnesorge BM (2006) First performance evaluation of a dual-source CT (DSCT) system. Eur Radiol 16(2): 256–268

Flohr T, Schoepf UJ, Ohnesorge B (2007) Chasing the heart – new developments for cardiac CT. J Thorac Imag 22(1):4–16

Flohr TG, Raupach R, Bruder H (2009a) Cardiac CT: how much can temporal resolution, spatial resolution, and volume coverage be improved? J Cardiovasc Comput Tomogr 3(3):143–152

Flohr TG, Leng S, Yu L, Allmendinger T, Bruder H, Petersilka M, Eusemann CD, Stierstorfer K, Schmidt B, McCollough C (2009) Dual-source spiral CT with pitch up to 3.2 and 75 ms temporal resolution: image reconstruction and assessment of image quality. Med Phys 36(12):5641–53.

George RT, Mehra VC, Chen MY, Kitagawa K, Arbab-Zadeh A, Miller JM, Matheson MB, Vavere AL, Kofoed KF, Rochitte CE, Dewey M, Yaw TS, Niinuma H, Brenner W, Cox C, Clouse ME, Lima JA, Di Carli M (2015) Myocardial CT perfusion imaging and SPECT for the diagnosis of coronary artery disease: a head-to-head comparison from the CORE320 multicenter diagnostic performance study. Radiology 274(2):626

Goetti R, Reiner CS, Knuth A, Klotz E, Stenner F, Samaras P, Alkadhi H (2012) Quantitative perfusion analysis of malignant liver tumors: dynamic computed tomography and contrast-enhanced ultrasound. Invest Radiol 47(1):18–24

Gordic S, Husarik DB, Desbiolles L, Leschka S, Frauenfelder T, Alkadhi H (2014a) High-pitch coronary CT angiography with third generation dual-source CT: limits of heart rate. Int J Cardiovasc Imaging 30(6):1173–1179

Gordic S, Morsbach F, Schmidt B et al (2014b) Ultralow-dose chest computed tomography for pulmonary nodule detection: first performance evaluation of single energy scanning with spectral shaping. Invest Radiol 49(7):465–473

Grant KL, Flohr TG, Krauss B et al (2014) Assessment of an advanced image-based technique to calculate virtual monoenergetic CT images from a dual-energy examination to improve contrast-to-noise ratio in examinations using iodinated contrast media. Invest Radiol 49(9):586–592

Grass M, Köhler T, Proksa R (2000) 3D cone-beam CT reconstruction for circular trajectories. Phys Med Biol 45(2):329–347

Hague CJ, Krowchuk N, Alhassan D, Ho K, Leipsic J, Sin DD, Mayo JR, Coxson HO (2014) Qualitative and quantitative assessment of smoking-related lung disease: effect of iterative reconstruction on low-dose computed tomographic examinations. J Thorac Imaging 29(6):350–356

Hein I, Taguchi K, Silver MD, Kazarna M, Mori I (2003) Feldkamp-based cone-beam reconstruction for gantry-tilted helical multislice CT. Med Phys 30(12):3233–3242

Henzler T, Fink C, Schoenberg SO, Dual SUJ, Energy CT (2012) Radiation dose aspects. AJR 199:S16–S25

Hou DJ, Tso DK, Davison C, Inacio J, Louis LJ, Nicolaou S, Reimann AJ, Hou DJ, Tso DK, Davison C, Inacio J, Louis LJ, Nicolaou S, Reimann AJ (2013) Clinical utility of ultra high pitch dual source thoracic CT imaging of acute pulmonary embolism in the emergency department: are we one step closer towards a non-gated triple rule out? Eur J Radiol 82(10):1793–1798

Hutt A, Tacelli N, Faivre JB, Flohr T, Duhamel A, Remy J, Remy-Jardin M (2016) Is bronchial wall imaging affected by temporal resolution? comparative evaluation at 140 and 75 ms in 90 patients. Eur Radiol 26(2):469–477

Johnson TR, Nikolaou K, Wintersperger BJ, Knez A, Boekstegers P, Reiser MF, Becker CR (2007a) ECG-gated 64-MDCT angiography in the differential diagnosis of acute chest pain. Am J Roentgenol 188(1):76–82

Johnson TR, Nikolaou K, Busch S, Leber AW, Becker A, Wintersperger BJ, Rist C, Knez A, Reiser MF, Becker CR (2007b) Diagnostic accuracy of dual-source computed tomography in the diagnosis of coronary artery disease. Invest Radiol 42(10):684–691

Kang EJ, Lee KN, Kim DW, Kim BS, Choi S, Park BH, Oh JY (2012) Triple rule-out acute chest pain evaluation using a 320-row-detector volume CT: a comparison of the wide-volume and helical modes. Int J Cardiovasc Imaging 28(Suppl 1):7–13

Kim Y, Kim YK, Lee BE, Lee SJ, Ryu YJ, Lee JH, Chang JH (2015) Ultra-low-dose CT of the thorax using iterative reconstruction: evaluation of image quality and radiation dose reduction. AJR Am J Roentgenol 204(6):1197–1202

Knez A, Becker CR, Leber A, Ohnesorge B, Becker A, White C, Haberl R, Reiser MF, Steinbeck G (2001) Usefulness of multislice spiral computed tomography angiography for determination of coronary artery stenoses. Am J Clin Pathol 88:1191–1194

Kondo T, Kumamaru KK, Fujimoto S, Matsutani H, Sano T, Takase S, Rybicki FJ (2013) Prospective ECG-gated coronary 320-MDCT angiography with absolute acquisition delay strategy for patients with persistent atrial fibrillation. AJR Am J Roentgenol 201(6):1197–1203

Leber AW, Knez A, von Ziegler F, Becker A, Nikolaou K, Paul S, Wintersperger B, Reiser M, Becker CR, Steinbeck G, Boekstegers P (2005) Quantification of obstructive and nonobstructive coronary lesions by 64-slice computed tomography. JACC 46(1):147–154

Lee AM, Engel LC, Shah B, Liew G, Sidhu MS, Kalra M, Abbara S, Brady TJ, Hoffmann U, Ghoshhajra BB (2012) Coronary computed tomography angiography during arrhythmia: radiation dose reduction with prospectively ECG-triggered axial and retrospectively ECG-gated helical 128-slice dual-source CT. J Cardiovasc Comput Tomogr 6(3):172–183.e2

Leipsic J, Nguyen G, Brown J, Sin D, Mayo JR (2010) A prospective evaluation of dose reduction and image quality in chest CT using adaptive statistical iterative reconstruction. AJR Am J Roentgenol 195(5): 1095–1099

Lell M, Hinkmann F, Anders K, Deak P, Kalender WA, Uder M, Achenbach S (2009) High-pitch electrocardiogram-triggered computed tomography of the chest: initial results. Invest Radiol 44(11):728–733

Lell MM, May M, Deak P, Alibek S, Kuefner M, Kuettner A, Köhler H, Achenbach S, Uder M, Radkow T (2011) High-pitch spiral computed tomography: effect on image quality and radiation dose in pediatric chest computed tomography. Invest Radiol 46(2):116–123

Leschka S, Stolzmann P, Desbiolles L, Baumueller S, Goetti R, Schertler T, Scheffel H, Plass A, Falk V, Feuchtner G, Marincek B, Alkadhi H (2009) Diagnostic accuracy of high-pitch dual-source CT for the assessment of coronary stenoses: first experience. Eur Radiol 19(12):2896–2903

Lu GM, Zhao Y, Zhang LJ, Schoepf UJ (2012) Dual-energy CT of the lung. AJR Am J Roentgenol 199(5 Suppl):S40–S53

Manniesing R, Oei MT, van Ginneken B, Prokop M (2016) Quantitative dose dependency analysis of whole-brain CT perfusion imaging. Radiology 278(1):190–197

McCollough CH, Primak AN, Braun N, Kofler J, Yu L, Christner J (2009) Strategies for reducing radiation dose in CT. Radiol Clin North Am 47(1):27–40

Meier A, Wurnig M, Desbiolles L, Leschka S, Frauenfelder T, Alkadhi H (2015) Advanced virtual monoenergetic images: improving the contrast of dual-energy CT pulmonary angiography. Clin Radiol 70(11):1244–1251

Meinel FG, Canstein C, Schoepf UJ, Sedlmaier M, Schmidt B, Harris BS, Flohr TG, De Cecco CN (2014) Image quality and radiation dose of low tube voltage 3rd generation dual-source coronary CT angiography in obese patients: a phantom study. Eur Radiol 24(7):1643–1650

Mets OM, Willemink MJ, de Kort FP, Mol CP, Leiner T, Oudkerk M, Prokop M, de Jong PA (2012) The effect of iterative reconstruction on computed tomography assessment of emphysema, air trapping and airway dimensions. Eur Radiol 22(10):2103–2109

Meyer M, Haubenreisser H, Schoepf UJ, Vliegenthart R, Leidecker C, Allmendinger T, Lehmann R, Sudarski S, Borggrefe M, Schoenberg SO, Henzler T (2014) Closing in on the K edge: coronary CT angiography at 100, 80, and 70 kV-initial comparison of a second-

versus a third-generation dual-source CT system. Radiology 273(2):373–382

Morhard D, Wirth CD, Fesl G, Schmidt C, Reiser MF, Becker CR, Ertl-Wagner B (2010) Advantages of extended brain perfusion computed tomography: 9.6 cm coverage with time resolved computed tomography-angiography in comparison to standard stroke-computed tomography. Invest Radiol 45(7):363–369

Morsbach F, Gordic S, Desbiolles L, Husarik D, Frauenfelder T, Schmidt B, Allmendinger T, Wildermuth S, Alkadhi H, Leschka S (2014) Performance of turbo high-pitch dual-source CT for coronary CT angiography: first ex vivo and patient experience. Eur Radiol 24(8):1889–1895

Motosugi U, Ichikawa T, Sou H, Morisaka H, Sano K, Araki T (2012) Multi-organ perfusion CT in the abdomen using a 320-detector row CT scanner: preliminary results of perfusion changes in the liver, spleen, and pancreas of cirrhotic patients. Eur J Radiol 81(10):2533–2537

Newell JD Jr, Fuld MK, Allmendinger T, Sieren JP, Chan KS, Guo J, Hoffman EA (2015) Very low-dose (0.15 mGy) chest CT protocols using the COPDGene 2 test object and a third-generation dual-source CT scanner with corresponding third-generation iterative reconstruction software. Invest Radiol 50(1):40–45

Nieman K, Oudkerk M, Rensing BJ, van Ooijen P, Munne A, van Geuns RJ, de Feyter PJ (2001) Coronary angiography with multi-slice computed tomography. Lancet 357:599–603

Niemann T, Henry S, Faivre JB, Yasunaga K, Bendaoud S, Simeone A, Remy J, Duhamel A (2013) Clinical evaluation of automatic tube voltage selection in chest CT angiography. Eur Radiol 23(10):2643–2651

Niemann T, Henry S, Duhamel A, Faivre JB, Deschildre A, Colas L, Santangelo T, Remy J, Remy-Jardin M (2014) Pediatric chest CT at 70 kVp: a feasibility study in 129 children. Pediatr Radiol 44(11): 1347–1357

Ohnesorge B, Flohr T, Becker C, Kopp A, Schoepf U, Baum U, Knez A, Klingenbeck Regn K, Reiser M (2000) Cardiac imaging by means of electro- cardiographically gated multisection spiral CT – initial experience. Radiology 217:564–571

Ohno Y, Koyama H, Matsumoto K, Onishi Y, Takenaka D, Fujisawa Y, Yoshikawa T, Konishi M, Maniwa Y, Nishimura Y, Ito T, Sugimura K (2011) Differentiation of malignant and benign pulmonary nodules with quantitative first-pass 320-detector row perfusion CT versus FDG PET/CT. Radiology 258(2):599–609

Padole A, Singh S, Ackman JB, Wu C, Do S, Pourjabbar S, Khawaja RD, Otrakji A, Digumarthy S, Shepard JA, Kalra M (2014) Submillisievert chest CT with filtered back projection and iterative reconstruction techniques. AJR Am J Roentgenol 203(4):772–781

Pansini V, Remy-Jardin M, Faivre JB et al (2009) Assessment of lobar perfusion in smokers according to the presence and severity of emphysema: preliminary experience with dual-energy CT angiography. Eur Radiol 19(12):2834–2843

Paul JF, Amato A, Rohnean A (2013) Low-dose coronary-CT angiography using step and shoot at any heart rate: comparison of image quality at systole for high heart rate and diastole for low heart rate with a 128-slice dual-source machine. Int J Cardiovasc Imaging 29(3):651–657

Petersilka M, Bruder H, Krauss B, Stierstorfer K, Flohr TG (2008) Technical principles of dual source CT. Eur J Radiol 68(3):362–368

Petersilka M, Stierstorfer K, Bruder H, Flohr T (2010) Strategies for scatter correction in dual source CT. Med Phys 37(11):5971–5992

Plank F, Friedrich G, Bartel T, Mueller S, Bonaros N, Heinz A, Klauser A, Cartes-Zumelzu F, Grimm M, Feuchtner G (2012) Benefits of high-pitch 128-slice dual-source computed tomography for planning of transcatheter aortic valve implantation. Ann Thorac Surg 94(6):1961–1966

Pontana F, Faivre JB, Remy-Jardin M, Flohr T, Schmidt B, Tacelli N, Pansini V, Remy J (2008) Lung perfusion with dual-energy multidetector-row CT (MDCT): feasibility for the evaluation of acute pulmonary embolism in 117 consecutive patients. Acad Radiol 15(12):1494–1504

Pontana F, Pagniez J, Flohr T, Faivre JB, Duhamel A, Remy J, Remy-Jardin M (2011a) Chest computed tomography using iterative reconstruction vs filtered back projection (part 1): evaluation of image noise reduction in 32 patients. Eur Radiol 21(3):627–635

Pontana F, Duhamel A, Pagniez J, Flohr T, Faivre JB, Hachulla AL, Remy J, Remy-Jardin M (2011b) Chest computed tomography using iterative reconstruction vs filtered back projection (part 2): image quality of low-dose CT examinations in 80 patients. Eur Radiol 21(3):636–643

Pontana F, Henry S, Duhamel A, Faivre JB, Tacelli N, Pagniez J, Remy J, Remy-Jardin M (2015) Impact of iterative reconstruction on the diagnosis of acute pulmonary embolism (PE) on reduced-dose chest CT angiograms. Eur Radiol 25(4):1182–1189

Prakash P, Kalra MK, Digumarthy SR, Hsieh J, Pien H, Singh S, Gilman MD, Shepard JA (2010) Radiation dose reduction with chest computed tomography using adaptive statistical iterative reconstruction technique: initial experience. J Comput Assist Tomogr 34(1):40–45

Raff GL, Gallagher MJ, O'Neill WW, Goldstein JA (2005) Diagnostic accuracy of noninvasive coronary angiography using 64-slice spiral computed tomography. JACC 46(3):552–557

Remy-Jardin M, Remy J (2008) Vascular disease in chronic obstructive pulmonary disease. Proc Am Thorac Soc 5(9):891–899

Remy-Jardin J, Tillie-Leblond I, Szapiro D et al (2002) CT angiography of pulmonary embolism in patients with underlying respiratory disease: impact of multislice CT on image quality and negative predictive value. Eur Radiol 12:1971–1978

Remy-Jardin M, Faivre JB, Pontana F, Molinari F, Tacelli N, Remy J (2014) Thoracic applications of dual energy. Semin Respir Crit Care Med 35(1):64–73

Rybicki FJ, Otero HJ, Steigner ML, Vorobiof G, Nallamshetty L, Mitsouras D, Ersoy H, Mather RT, Judy PF, Cai T, Coyner K, Schultz K, Whitmore AG, Di Carli MF (2008) Initial evaluation of coronary images from 320-detector row computed tomography. Int J Cardiovasc Imaging 24(5):535–546

Salem R, Remy-Jardin M, Delhaye D, Khalil C, Teisseire A, Delannoy-Deken V, Duhamel A, Remy J (2006) Integrated cardio-thoracic imaging with ECG-Gated 64-slice multidetector-row CT: initial findings in 133 patients. Eur Radiol 16(9):1973–1981

Schenzle JC, Sommer WH, Neumaier K et al (2010) Dual energy CT of the chest: how about the dose? Invest Radiol 45:347–353

Schoepf UJ (2007) Cardiothoracic multi-slice CT in the Emergency Department. In: Ohnesorge BM, Flohr TG, Becker CR, Knez A, Reiser MF (eds) Multi-slice and dual-source CT in cardiac imaging, 2nd edn. Springer, Berlin/Heidelberg/New York

Schoepf UJ, Kessler MA, Rieger CT et al (2001) Multislice CT imaging of pulmonary embolism. Eur Radiol 11:2278–2286

Schoepf UJ, Holzknecht N, Helmberger TK et al (2002) Subsegmental pulmonary emboli: improved detection with thin-collimation multidetector row spiral CT. Radiology 222:483–490

Schoepf UJ, Becker CR, Hofmann LK, Das M, Flohr T, Ohnesorge BM et al (2003) Multislice CT angiography. Eur Radiol 13:1946–1961

Schulz B, Jacobi V, Beeres M, Bodelle B, Gruber T, Lee C, Bauer R, Kerl M, Vogl T, Zangos S (2012) Quantitative analysis of motion artifacts in high-pitch dual-source computed tomography of the thorax. J Thorac Imaging 27(6):382–386

Sharma RK, Arbab-Zadeh A, Kishi S, Chen MY, Magalhães TA, George RT, Dewey M, Rybicki FJ, Kofoed KF, de Roos A, Tan SY, Matheson M, Vavere A, Cox C, Clouse ME, Miller JM, Brinker JA, Arai AE, Di Carli MF, Rochitte CE, Lima JA (2015) Incremental diagnostic accuracy of computed tomography myocardial perfusion imaging over coronary angiography stratified by pre-test probability of coronary artery disease and severity of coronary artery calcification: The CORE320 study. Int J Cardiol 201:570–577

Singh S, Kalra MK, Gilman MD, Hsieh J, Pien HH, Digumarthy SR, Shepard JA (2011) Adaptive statistical iterative reconstruction technique for radiation dose reduction in chest CT: a pilot study. Radiology 259(2):565–573

Sommer WH, Helck A, Bamberg F, Albrecht E, Becker CR, Weidenhagen R, Kramer H, Reiser MF, Nikolaou K (2010) Diagnostic value of time-resolved CT angiography for the lower leg. Eur Radiol 20(12):2876–2881

Sommer WH, Becker CR, Haack M, Rubin GD, Weidenhagen R, Schwarz F, Nikolaou K, Reiser MF, Johnson TR, Clevert DA (2012) Time-resolved CT angiography for the detection and classification of endoleaks. Radiology 263(3):917–926

Steigner ML, Otero HJ, Cai T, Mitsouras D, Nallamshetty L, Whitmore AG, Ersoy H, Levit NA, Di Carli MF, Rybicki FJ (2009) Narrowing the phase window width in prospectively ECG-gated single heart beat 320-detector row coronary CT angiography. Int J Cardiovasc Imaging 25(1):85–90

Stierstorfer K, Rauscher A, Boese J, Bruder H, Schaller S, Flohr T (2004) Weighted FBP—a simple approximate 3D FBP algorithm for multislice spiral CT with good dose usage for arbitrary pitch. Phys Med Biol 49:2209–2218

Sun ML, Lu B, Wu RZ, Johnson L, Han L, Liu G, Yu FF, Hou ZH, Gao Y, Wang HY, Jiang S, Yang YJ, Qiao SB (2011) Diagnostic accuracy of dual-source CT coronary angiography with prospective ECG-triggering on different heart rate patients. Eur Radiol 21(8):1635–1642

Tacelli N, Remy-Jardin M, Flohr T, Faivre JB, Delannoy V, Duhamel A, Remy J (2010) Dual-source chest CT angiography with high temporal resolution and high pitch modes: evaluation of image quality in 140 patients. Eur Radiol 20(5):1188–1196

Thibault JB, Sauer KD, Bouman CA, Hsieh J (2007) A three-dimensional statistical approach to improved image quality for multislice helical CT. Med Phys 34(11):4526–4544

Thieme SF, Becker CR, Hacker M, Nikolaou K, Reiser MF, Johnson TR (2008) Dual energy CT for the assessment of lung perfusion–correlation to scintigraphy. Eur J Radiol 68(3):369–374

Thieme SF, Johnson TR, Lee C, McWilliams J, Becker CR, Reiser MF, Nikolaou K (2009) Dual-energy CT for the assessment of contrast material distribution in the pulmonary parenchyma. AJR Am J Roentgenol 193(1):144–149

Tkaczyk JE, Rodrigues R, Shaw J, Short J, Du Y, Wu X, Walter D, Leue W, Harrison D, Edic P (2007) Atomic number resolution for three spectral CT imaging systems. Proc of SPIE Vol 6510:651009

Tomizawa N, Maeda E, Akahane M, Torigoe R, Kiryu S, Ohtomo K (2013) Coronary CT angiography using the second-generation 320-detector row CT: assessment of image quality and radiation dose in various heart rates compared with the first-generation scanner. Int J Cardiovasc Imaging 29(7):1613–1618

Vardhanabhuti V, Loader RJ, Mitchell GR, Riordan RD, Roobottom CA (2013) Image quality assessment of standard- and low-dose chest CT using filtered back projection, adaptive statistical iterative reconstruction, and novel model-based iterative reconstruction algorithms. AJR Am J Roentgenol 200(3):545–552

Wang G, Zhang C, Li M, Deng K, Li W (2014) Preliminary application of high-definition computed tomographic Gemstone Spectral Imaging in lung cancer. J Comput Assist Tomogr 38(1):77–81

Wang R, Sui X, Schoepf UJ, Song W, Xue H, Jin Z, Schmidt B, Flohr TG, Canstein C, Spearman JV, Chen J, Meinel FG (2015) Ultralow-radiation-dose chest CT: accuracy for lung densitometry and emphysema detection. AJR Am J Roentgenol 204(4):743–749

Westwood ME, Raatz HD, Misso K, Burgers L, Redekop K, Lhachimi SK, Armstrong N, Kleijnen J (2013) Systematic review of the accuracy of dual-source cardiac CT for detection of arterial stenosis in difficult to image patient groups. Radiology 267(2): 387–395

Willems PW, Taeshineetanakul P, Schenk B, Brouwer PA, Terbrugge KG, Krings T (2012) The use of 4D-CTA in the diagnostic work-up of brain arteriovenous malformations. Neuroradiology 54(2):123–131

Wuest W, Anders K, Schuhbaeck A, May MS, Gauss S, Marwan M, Arnold M, Ensminger S, Muschiol G, Daniel WG, Uder M, Achenbach S (2012) Dual source multidetector CT-angiography before Transcatheter Aortic Valve Implantation (TAVI) using a high-pitch spiral acquisition mode. Eur Radiol 22(1):51–58

Zhang D, Li X, Liu B (2011) Objective characterization of GE discovery CT750 HD scanner: gemstone spectral imaging mode. Med Phys 38(3):1178–1188

Strategies for Dose Reduction and Improvement of Image Quality in Chest CT

Narinder S. Paul

Abstract

The last two decades have witnessed a dramatic escalation in the utilization of computed tomography (CT) for diagnostic purposes, and there has been a corresponding increase in patient and physician concern regarding the potential for long-term carcinogenesis. Therefore it is essential to embrace the ALARA principle in which radiation exposures are maintained "as low as reasonably achievable" and progressive improvements in CT design and software algorithms have facilitated significant reductions in radiation exposure while maintaining diagnostic image quality. This chapter is not meant to provide an exhaustive review of all these advances but instead will focus on the advances that are applicable to a wider scope of clinical applications in adult chest CT. The material will be discussed under the following sections: appropriateness guidelines, x-ray tube assembly, patient-related factors, and x-ray detector and post-processing algorithms.

1 Introduction

The last two decades have witnessed a dramatic escalation in the utilization of computed tomography (CT) for diagnostic purposes (Brenner and Hall 2007; Hricak et al. 2011), and there has been a corresponding increase in patient and physician concern regarding the potential for long-term carcinogenesis (Einstein et al. 2007). Therefore it is essential to embrace the ALARA principle in which radiation exposures are maintained "as low as reasonably achievable" and progressive improvements in CT design and software algorithms have facilitated significant reductions in radiation exposure while maintaining diagnostic image quality. This chapter is not meant to provide an exhaustive review of all these advances but instead will focus on the advances that are applicable to a wider scope of clinical applications in adult chest CT. The material will be discussed under the following sections: appropriateness guidelines, x-ray tube assembly,

N.S. Paul
Department of Medical Imagining, Toronto General Hospital, University Ave, University of Toronto, Toronto, ON, Canada
e-mail: Narinder.Paul@uhn.ca

U.J. Schoepf, F.G. Meinel (eds.), *Multidetector-Row CT of the Thorax*, Medical Radiology,
DOI 10.1007/978-3-319-30355-0_2

patient-related factors, and x-ray detector and post-processing algorithms.

2 Appropriateness Guidelines

Clinical practice is conventionally based on experience and the best clinical opinion; however, there is increased focus on appropriateness guidelines supported by evidence-based practice. Organizations such as the American College of Radiology (www.acr.org) and the Royal College of Radiologists (www.rcr.ac.uk) provide access to a wide scope of appropriateness guidelines. More chest-focused imaging tasks are addressed through the use of specific "rules" based on clinical algorithms such as the Wells score (Wells et al. 1998) and the modified Wells score (Wells et al. 2001) for pulmonary embolism. These guidelines should be used to inform local practice in utilization of imaging resources, especially modalities that issue ionizing radiation.

3 X-Ray Tube Assembly

The x-ray tube consists of a negatively charged cathode aligned with a positively charged anode placed within a glass vacuum tube. Mobile electrons are generated in the cathode filament by the x-ray tube current and accelerated to the anode by the x-ray tube potential. Photoelectric and Compton's interactions in the anode produce x-ray photons that are transmitted through the object (patient) and registered on the detector elements. The width of the x-ray beam is controlled by the aperture of the x-ray beam collimator.

The x-ray tube current determines the number of x-ray photons that are produced, and the x-ray tube potential determines the energy of these photons. The combination of the x-ray tube current and tube potential determines the x-ray exposure to the patient and, depending on the radiation sensitivity of the irradiated tissues, the effective dose to the patient.

Initial strategies at radiation dose reduction focused on reducing the x-ray tube current as the tube current has a linear relationship with radiation exposure and there is a predictable increase in image noise with decrease in the tube current. However, more recent approaches have targeted reductions in x-ray tube potential (Fanous et al. 2012) due to the almost exponential relationship between x-ray tube potential and radiation dose. Consequently, a decrease in x-ray tube potential results in a relatively large change in image noise and image quality, as assessed by the contrast-to-noise ratio. It is important to reiterate that reductions in x-ray tube current do not fundamentally change the energy spectrum of the x-ray beam, merely the amount of x-ray photons generated at each energy level. Alteration of the x-ray tube potential, however, does affect the maximum energy level of the x-ray beam and the transmission of x-rays through the patient. Therefore, there needs to be careful matching of the x-ray tube potential setting to the x-ray absorption characteristics of the patient.

Early attempts to optimize the x-ray exposure parameters to the patient body habitus resulted in bodyweight-based prioritization of x-ray tube potential, followed by using body mass index (Bendaoud et al. 2011) and then by using anthropomorphic measurements of chest dimensions (Rogalla et al. 2010). As the largest constituent organ in the thorax is the lung tissue, with minimum x-ray absorption from the normal lungs, the surrounding chest wall tissues play an important role in determining the absorption of x-ray photons and therefore in image quality (Paul et al. 2011). Therefore, the closest approximation of required x-ray exposure parameters and patient body habitus is achieved through assessment of x-ray absorption at specific anatomic levels (Odedra et al. 2014). This approach facilitates minimization of x-ray exposure parameters while maintaining diagnostic image quality (Newton et al. 2011). Modern CT scanners assess the x-ray absorption profile of the patient's thorax from the scout projections that are acquired to plan the study. Once the absorption profile has been assessed, the system will automatically prioritize the lowest x-ray tube potential for the patient and for the selected protocol; the x-ray tube current will automatically be adjusted to ensure a constant image quality at every anatomical level as

described later. The CT dose index (CTDI) is a measure of the radiation dose per unit of tissue.

Targeting a low x-ray tube potential (70–80 kVp) is of benefit in children and small adults due to the lower x-ray absorption profile. A lower x-ray tube potential (80–100 kVp) is also beneficial in larger patients if the target of interest is enhanced by intravascular injection of iodinated contrast material (CM), as the increased efficiency of x-ray photons to generate signal increases as the x-ray tube potential decreases due to increase in the photoelectric effect and approximation of the set x-ray tube potential to the "K edge" of iodine (Nakayama et al. 2005; Murakami et al. 2010). Therefore, for CT studies that focus on the thoracic aorta or the pulmonary arteries, for an equivalent CTDI, a CT study performed using a lower x-ray tube potential will have an ~30% increase in measured signal from the enhanced structures (Fanous et al. 2012). This facilitates the use of lower x-ray tube potential settings in these examinations. As diagnostic utility of CT is related to the signal-to-noise ratio (SNR) in an image, if the target structures have increased signal from the enhanced CT protocol, diagnostic utility can be maintained at a higher image noise and therefore a lower x-ray tube current setting.

Many body tissues exhibit an increase in x-ray absorption with a decrease in x-ray photons; at the x-ray potentials used in diagnostic imaging, this change is relatively small for the cortical bone and for body fluids but is substantially larger for injected iodinated CM (Godoy et al. 2009). Therefore, for CT scans enhanced with intravascular iodinated CM, if image data is acquired using low and high settings of x-ray tube potential (kV), post-processing of image data can result in several different images: a low- and a high-kV image, a weighted average image, a virtual non-contrast image, a virtual contrast image (iodine predominant), and a bone subtraction image (Godoy et al. 2009). The weighted average CT image provides a comparable image to a conventional CT acquisition; if there are technical difficulties causing suboptimal contrast enhancement or increased image noise, then the increased iodine signal in the low-kV image can maintain the diagnostic utility of a study. The virtual non-contrast study can be used to obviate the need for a prior non-contrast study (thus saving radiation dose). The iodine predominant study can be used to display the distribution of iodine (blood) in an organ and has been used to demonstrate pulmonary blood distribution in patients with acute and chronic pulmonary embolism (Pontana et al. 2008; Dournes et al. 2014). Dual energy acquisitions can be performed in several ways: using a dual-source CT with each x-ray tube set to different tube potentials, with a single x-ray detector using fast switching between high- and low-kV acquisitions, and with the use of sequential high- and low-kV data acquisitions (Ko et al. 2012; Kaza et al. 2012). Finally, this data could also be provided through modification of the detector system with dual-layer detectors or with detectors sensitive to multiple energy spectra.

Cross-sectional image data is produced as the x-ray tube-detector system rotates around the patient while emitting x-ray projections that transmit through the patient. The radiation exposure from each gantry rotation is a function of the radiation dose per projection and the number of x-ray projections. The radiation exposure can be reduced either by reducing the dose per projection (reduction in x-ray tube potential or current) or by reducing the number of projections. Assuming that the frequency of emitting x-ray projections is constant, an increase or decrease in the speed of the gantry rotation will cause a corresponding increase or decrease in radiation dose. This can be a useful strategy to adjust radiation exposure in situations where the desire is to maintain tissue contrast. For example, in CT pulmonary angiography or aortography, if a low x-ray tube potential is set, but the required x-ray tube current setting exceeds the system capacity for the patient body habitus. In this situation, instead of increasing the kV setting and losing the advantage of extra iodine signal at the lower kV, the tube rotation could be slowed to enable the appropriate tube current flux (tube current x time) to be used and otherwise maintain the exposure settings. A conventional CT image is produced from ~1200 x-ray projections; as the gantry rotation gets faster, there is a corresponding reduction in the number of projections acquired and the subsequent image

quality. This can be offset by increasing the dose per x-ray projection or by using image reconstruction methods other than filtered back projection (FBP). There is considerable interest using a smaller number of x-ray projections to achieve diagnostic image quality at significantly reduced radiation doses by utilizing limited angle data and compressed sensing algorithms in CT (Idky et al. 2006). However, at present these algorithms remain under research evaluation.

The width of the x-ray beam is controlled by the collimator diaphragm. In older CT systems, the position of the diaphragm is fixed during image acquisition; this leads to increased radiation exposure at the beginning and end of helical acquisition due to over-ranging with multidetector CT systems (Schiham et al. 2010). Modern CT systems use dynamic collimator diaphragms that move independently such that the collimator opens asymmetrically at the start and end of a helical acquisition to eliminate the irradiation of tissues outside the range of reconstructed image data.

4 Patient-Related Factors

The CT scout projections acquire data that map the x-ray attenuation profile of the patient in the region of interest. Modern CT systems utilize x-ray scan protocols that maximally optimize x-ray exposure to the x-ray absorption profile of the patient and prioritize the use of the lowest possible x-ray tube potential. As the x-ray absorption profile of the thorax is variable, with increased absorption of x-ray photons at the thoracic inlet and at the thoracoabdominal junction and least absorption at the carina, the x-ray tube current is modulated in the X-Y-Z planes to match this pattern. This dose modulation delivers consistent image quality regardless of patient size or shape and individualized or a personalized CT scan profile (Kalra et al. 2005). However, there are two essential prerequisites; the first is the determination of the level of acceptable image noise, measured as standard deviation in Hounsfield units (HUs), for each scan protocol, and the second is optimal patient positioning. Each CT system is delivered with manufacturer-determined levels of image noise for specific clinical applications. Individual radiology groups may choose more aggressive levels of image noise to drive lower radiation dose levels. The patient needs to be positioned centrally on the CT table, and ideally the patient should be in the isocenter of the CT gantry prior to image acquisition. The use of automatic dose modulation software in patients who are offset by as little as 3 cm from the isocenter of the CT gantry can result in 30 % more radiation dose.

5 X-Ray Detectors and Post-processing Algorithms

Although anti-scatter grids have been used in chest radiography for several decades, the use of an anti-scatter grid has only recently been incorporated into the design of a CT scanner. The mechanism of action is similar to that in chest radiography and is anticipated to be more advantageous in improving image quality in obese patients. Anti-scatter grids are also likely to be more useful in CT systems that have larger detector systems.

Another key determinant of patient radiation dose is related to the efficiency with which the x-ray detector converts incident x-ray photons into light. The transition from gas-filled (e.g., xenon) detectors to solid-state detectors has resulted in ~23 % increase in dose efficiency (Fuchs et al. 2000). There is continued focus on production of low profile-high efficiency detectors and reduction in the background electronic noise that limits contrast resolution for ultralow-dose CT.

Once the x-ray detector has converted the x-ray photons into light, a CT sonogram is formed in the raw data space and translated into the image data space where the trans-axial CT images are formed. Filtered back projection (FBP) has been the cornerstone of CT image processing for decades; the images are of high resolution and require little computation time and resources. However, FBP requires a significant amount of x-ray data in order to produce diagnostic quality images. Therefore, despite the fact that diagnostic quality ultralow-dose (0.2 mSv) lung images can be acquired using FBP, the mediastinum is poorly assessed (Hanna et al. 2014). This interest in low-dose and ultralow-dose CT has,

however, precipitated interest in alternative image post-processing algorithms, in particular iterative reconstruction. Iterative reconstruction (IR) algorithms have been extensively used in modalities such as nuclear medicine in order to produce diagnostic images despite the paucity of image data. However, the prolonged image reconstruction time and the infrastructure cost of the required computational resource were prohibitive for consideration of IR in CT imaging. The recent focus on low-dose imaging combined with a precipitous decrease in cost of computer graphics processing units has made implementation of IR into clinical CT a reality. The first-generation IR algorithms, image-based IR, provided relatively little compromise in image reconstruction times and modest reductions in radiation dose. The subsequent generation of IR algorithms, statistical weight-based algorithms, was a hybrid algorithm located in raw data and image-based domains. The potential reduction in radiation dose was greater, but the image quality compared to conventional FBP remained suboptimal. The latest IR algorithms, model-based IR, are located more in the raw data domain and have improved image quality, but the image reconstruction times remain a challenge. The continued development and refinement of IR algorithms will result in significant improvements in image quality with ultralow-dose thoracic CT (Beister et al. 2012; Yuki et al. 2014; Wang et al. 2014; Spears et al. 2014; Leipsic et al. 2010; Gosling et al. 2010; Di Cesare et al. 2014; Williams et al. 2013; Fujimoto et al. 2013).

Image quality and quantity of x-ray projections

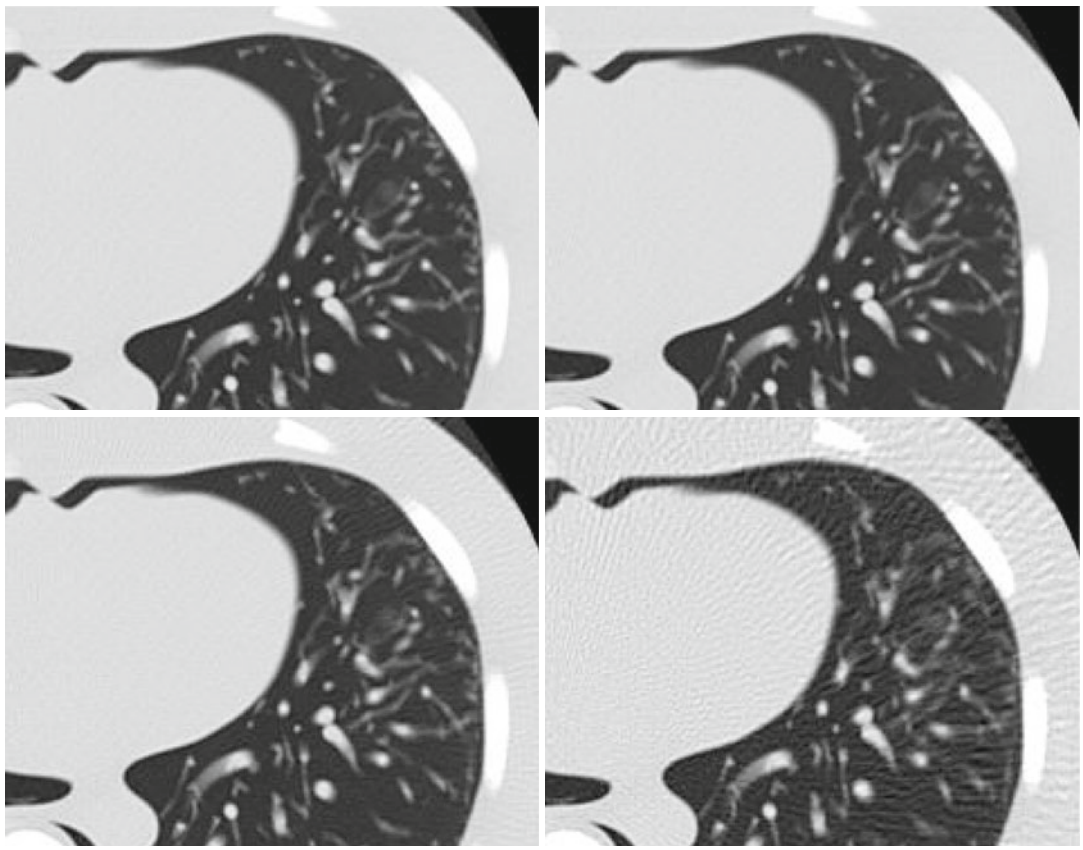

A 10 mm ground glass nodule measuring -800 HU was placed in the left lung of an anthropomorphic chest phantom (Lungman, Kyoto Kagaku) and scanned using 64×0.5 mm detector configuration (AQONE, Toshiba Medical Systems, Japan) with fixed x-ray tube exposure parameters (120 kV, 200 mAs), but the images were reconstructed with a different number of x-ray projections: (**a**) 1200, (**b**) 900, (**c**) 600, and (**d**) 300 projections. Note how artifacts start to appear when the image is reconstructed using 600 projections or less

Ultralow-dose thoracic computed tomography (0.2 mSv)

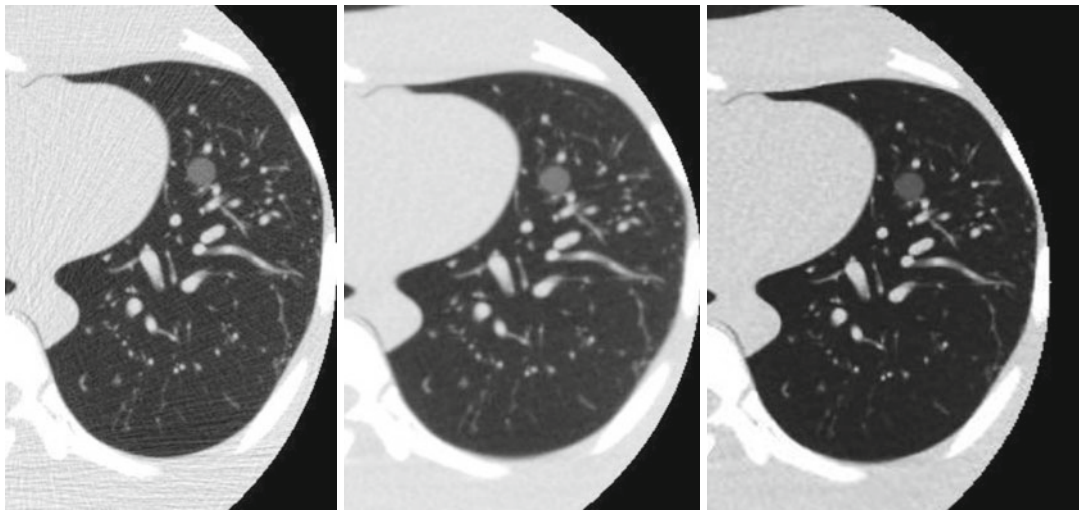

A 10 mm ground glass nodule measuring -800 HU was placed in the left lung of an anthropomorphic chest phantom (Lungman, Kyoto Kagaku) and scanned using 64×0.5 mm detector configuration (AQONE, Toshiba Medical Systems, Japan) with fixed x-ray tube exposure parameters (120 kV, 5 mAs), and the images were reconstructed with filtered back projection, FBP (**a**); third-generation iterative reconstruction, IR (**b**); and model-based IR, MIR (**c**). Note the lack of beam-hardening artifact in the MIR image compared to the FBP image and the improved edge sharpness of the MIR image compared to the IR image

Ultralow-dose thoracic computed tomography (0.2 mSv)

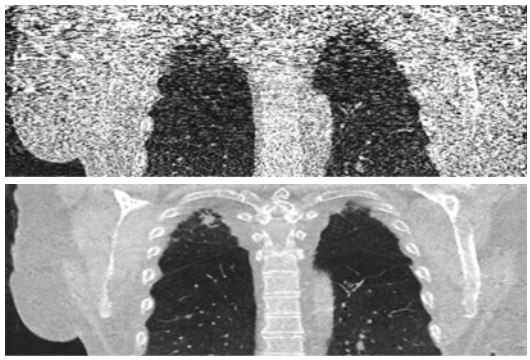

Coronal thin-slice (0.5 mm) CT reconstructions of a patient performed with 64×0.5 mm detector configuration (AQONE, Toshiba Medical Systems, Japan) using fixed x-ray tube exposure parameters (120 kV, 5 mAs), and the images were reconstructed with filtered back projection, FBP (**a**), and model-based IR, MIR (**b**). The 10 mm irregular nodule in the apex of the right lung is clearly visualized on the MIR image but obscured by image noise on the FBP image

6 Summary

Sequential advances in CT scanner design and reconstruction algorithms, adaptation of x-ray exposure parameters to the individual x-ray absorption profile of the patient, and prioritization of lower x-ray tube potentials in combination have resulted in dramatic reductions in patient radiation dose from thoracic CT. The introduction of iterative reconstruction algorithms has resulted in unprecedented reductions in radiation dose with preservation of diagnostic image quality. However, the fundamentals of good clinical practice such as the use of appropriateness criteria and correct patient positioning remain essential to maintaining radiation doses as low as reasonably achievable.

References

Beister M, Kolditz D, Kalender WA (2012) Iterative reconstruction methods in X-ray CT. Phys Med 28:94–108

Bendaoud S, Remy-Jardin M, Wallaert B et al (2011) Sequential versus volumetric computed tomography in the follow-up of chronic bronchopulmonary diseases: comparison of diagnostic information and radiation dose in 63 adults. J Thorac Imaging 26(3):190–195

Brenner DJ, Hall EJ (2007) Computed tomography- an increasing source of radiation exposure. N Engl J Med 357:2277–2284

Di Cesare E, Gennarelli A, Di Sibio A et al (2014) Assessment of dose exposure and image quality in coronary angiography performed by 640-slice CT: a comparison between adaptive iterative and filtered back-projection algorithm by propensity analysis. Radiol Med 2014(119):642–649

Dournes G, Verdier D, Montaudon M, Bullier E et al (2014) Dual-energy CT perfusion and angiography in chronic thromboembolic pulmonary hypertension: diagnostic accuracy and concordance with radionuclide scintigraphy. Eur Radiol 24(1):42–51

Einstein AJ, Moser KW, Thompson RC et al (2007) Radiation dose to patients from cardiac diagnostic imaging. Circulation 116:1290–1305

Fanous R, Kashani H, Jiménez L, Murphy G, Paul NS (2012) Image quality and radiation dose of pulmonary CT angiography performed using 100 and 120 kVp. AJR Am J Roentgenol 199(5):990–996

Fuchs TOJ et al (2000) Direct comparison of a xenon and a solid-state CT detector system: measurements under working conditions. IEEE Trans Med Imaging 19(9):941–948

Fujimoto S, Matsutani H, Kondo T et al (2013) Image quality and radiation dose stratified by patient heart rate for coronary 64- and 320-MDCT angiography. Am J Roentgenol 200(4):765–770

Godoy M, Naidich D, Marchiori E, Assadourian B et al (2009) Basic principles and postprocessing techniques of dual-energy CT: illustrated by selected congenital abnormalities of the thorax. J Thoracic Imag 24(2):152–159

Gosling O, Loader R, Venables P et al (2010) A comparison of radiation doses between state-of-the-art multislice CT coronary angiography with iterative reconstruction, multislice CT coronary angiography with standard filtered back-projection and invasive diagnostic coronary angiography. Heart 96:922–926

Hanna WC, Paul NS, Darling GE, Moshonov H, Allison F, Waddell TK, Cypel M, de Perrot ME, Yasufuku K, Keshavjee S, Pierre AF (2014) Minimal-dose computed tomography is superior to chest x-ray for the follow-up and treatment of patients with resected lung cancer. J Thorac Cardiovasc Surg 147(1):30

Hricak H, Brenner DJ, Adelstein SJ, Frush DP, Hall EJ et al (2011) Managing radiation use in medical imaging: a multifaceted challenge. Radiology 258(3):889–905

Idky EY, Kao CM, Pan X (2006) Accurate image reconstruction from few-views and limited-angle data in divergent-beam CT. J Sci Tech 14(2):119–139

Kalra M, Rizzo S, Maher M, Halpern E et al (2005) Chest CT performed with Z-axis modulation: scanning protocol and radiation dose. Radiology 237(1):303–308

Kaza RK, Platt JF, Cohan RH, Caoili EM, AlHawary MM, Wasnik A (2012) Dual-energy CT with single- and dual-source scanners: current applications in evaluating the genitourinary tract. Radio Graph 32:353–369

Ko JP, Brandman S, Stember J, Naidich DP (2012) Dual energy computed tomography: concepts, performance, and thoracic applications. J Thorac Imaging 27:7–22

Leipsic J, Labounty TM, Heilbron B et al (2010) Estimated radiation dose reduction using adaptive statistical iterative reconstruction in coronary CT angiography: the ERASIR study. AJR Am J Roentgenol 195(3):655–660

Murakami Y, Kakeda S, Kamada K, Ohnari N, Nishimura J, Ogawa M, Otsubo K, Morishita Y, Korogi Y (2010) Effect of tube voltage on image quality in 64-section multidetector 3D CT angiography: evaluation with a vascular phantom with superimposed bone skull structures. AJNR Am J Neuroradiol 31(4):620–625

Nakayama Y, Awai K, Funama Y, Hatemura M, Imuta M, Nakaura T, Ryu D, Morishita S, Sultana S, Sato N, Yamashita Y (2005) Abdominal CT with low tube voltage: preliminary observations about radiation dose, contrast enhancement, image quality, and noise. Radiology 237(3):945–951

Newton TD, Mehrez H, Wong K, Menezes R, Wintersperger BJ, Crean A, Nguyen E, Paul N (2011) Radiation dose threshold for coronary artery calcium score with MDCT: how low can you go? Eur Radiol 21(10):2121–2129

Odedra D, Blobel J, Alhumayyd S et al (2014) Image noise-based dose adaptation in dynamic volume CT of the heart: dose and image quality optimisation in comparison with BMI-based dose adaptation. Eur Radiol 24(1):86–94

Paul NS, Kashani H, Odedra D, Ursani A, Ray C, Rogalla P (2011) The influence of chest wall tissue composition in determining image noise during cardiac CT. AJR Am J Roentgenol 197(6):1328–1334

Pontana F, Faivre JB, Remy-Jardin M, Flohr T et al (2008) Lung perfusion with dual-energy multidetector-row CT (MDCT): feasibility for the evaluation of acute pulmonary embolism in 117 consecutive patients. Acad Radiol 15(12):1494–1504

Rogalla P, Blobel J, Kandel S, Meyer H, Mews J, Kloeters C, Kashani H, Lembcke A, Paul N (2010) Radiation dose optimisation in dynamic volume CT of the heart: tube current adaptation based on anterior-posterior chest diameter. Int J Cardiovasc Imaging 26(8):933–940

Schiham A, Molen AJ, Prokop M, de Jong HW (2010) Overranging at multisection CT: an underestimated source of excess radiation exposure. Radiographics 30(4):1057–1067

Spears JR, Schoepf UJ, Henzler T et al (2014) Comparison of the effect of iterative reconstruction versus filtered back projection on cardiac CT postprocessing. Acad Radiol 21(3):318–324

Wang R, Schoepf UJ, Wu R et al (2014) Diagnostic accuracy of coronary CT angiography: comparison of filtered back projection and iterative reconstruction with different strengths. J Comput Assist Tomogr 38(2):179–184

Wells PS, Ginsberg JS, Anderson DR et al (1998) Use of a clinical model for safe management of patients with suspected pulmonary embolism. Ann Intern Med 129:997–1005

Wells PS, Anderson DR, Rodger M et al (2001) Excluding pulmonary embolism at the bedside without diagnostic imaging: management of patients with suspected pulmonary embolism presenting to the emergency department by using a simple clinical model and d-dimer. Ann Intern Med 135:98–107

Williams MC, Weir NW, Mirsadraee S et al (2013) Iterative reconstruction and individualized automatic tube current selection reduce radiation dose while maintaining image quality in 320-multidetector computed tomography coronary angiography. Clin Radiol 68(11):e570–e577

Yuki H, Utsunomiya D, Funama Y et al (2014) Value of knowledge-based iterative model reconstruction in low-kV 256-slice coronary CT angiography. J Cardiovasc Comput Tomo 8(2):115–123

Contrast Medium Injection Technique

Dominik Fleischmann and Richard L. Hallett

Abstract

The general goal of intravenous contrast medium (CM) delivery in computed tomography (CT) is to achieve adequate enhancement of the organ or vessels within the anatomic territory of interest, synchronized with the CT acquisition. This apparently simple goal is increasingly difficult to achieve with rapidly and continuously evolving multiple detector-row CT (MDCT) technology. Given that acquisition times have substantially decreased with each new generation of MDCT scanners, correct scan timing and tailoring clinical injection protocols are ever more challenging and less forgiving. Thus, a working understanding of early contrast medium dynamics has become a prerequisite for the rational design of current and future injection strategies. The selection of CM type, CM iodine concentration, considerations regarding the interrelated effects of injection flow rates, CM injection duration and injection volume, new injection devices, and individual patient factors all have to be integrated to optimize acquisition of a diagnostically meaningful MDCT examination. The purpose of this chapter is to provide the reader with the basic tools for designing rational contrast medium injection protocols for various applications of thoracic MDCT. This will encompass a review of physiologic and pharmacokinetic principles, as well as a discussion of contrast media properties, injection devices and tools for accurate scan timing. Topics of current interest, including CM strategies for patients with chronic kidney disease

D. Fleischmann, MD (✉)
Department of Radiology, Stanford University School of Medicine, Stanford, CA, USA
e-mail: d.fleischmann@stanford.edu

R.L. Hallett, MD
Cardiovascular Imaging, Northwest Radiology Network, Indianapolis, IN, USA

Division of Cardiovascular Imaging, Department of Radiology, Stanford University School of Medicine, Stanford, CA, USA

U.J. Schoepf, F.G. Meinel (eds.), *Multidetector-Row CT of the Thorax*, Medical Radiology,
DOI 10.1007/978-3-319-30355-0_3

(CKD) and low-kVp image acquisition, will be discussed. In addition, practical examples of injection protocols will be provided.

1 Introduction

The general goal of intravenous contrast medium (CM) delivery in computed tomography (CT) is to achieve adequate enhancement of the organ or vessels within the anatomic territory of interest, synchronized with the CT acquisition. This apparently simple goal is increasingly difficult to achieve with rapidly and continuously evolving multiple detector-row CT (MDCT) technology. Given that acquisition times have substantially decreased with each new generation of MDCT scanners, correct scan timing and tailoring clinical injection protocols are ever more challenging and less forgiving. Thus, a working understanding of early contrast medium dynamics has become a prerequisite for the rational design of current and future injection strategies. The selection of CM type, CM iodine concentration, considerations regarding the interrelated effects of injection flow rates, CM injection duration and injection volume, new injection devices, and individual patient factors all have to be integrated to optimize acquisition of a diagnostically meaningful MDCT examination.

The purpose of this chapter is to provide the reader with the basic tools for designing rational contrast medium injection protocols for various applications of thoracic MDCT. This will encompass a review of physiologic and pharmacokinetic principles, as well as a discussion of contrast media properties, injection devices and tools for accurate scan timing. Topics of current interest, including CM strategies for patients with chronic kidney disease (CKD) and low-kVp data acquisition, will be discussed. In addition, practical examples of injection protocols will be provided.

2 Contrast Media for Multiple Detector-Row CT

All currently used angiographic x-ray CM are water-soluble derivates of symmetrically iodinated benzene. They are either negatively charged ionic molecules (ionic CM) or nonionic molecules (nonionic CM). The diagnostic use of x-ray contrast media is based on the physical ability of iodine to absorb x-rays, not on pharmacological effects, and is similar for all angiographic CM. Although small differences have been demonstrated in the rate of diffusion of different contrast media into organ parenchyma, the magnitude of these differences is not such as to affect the choice of CM in practice.

The selection of intravenous contrast medium for MDCT is not so much governed by physicochemical properties, such as osmotic pressure, viscosity, and electrical charge, but primarily by safety considerations and rate of expected adverse reactions. Nonionic CM are generally safer than ionic contrast media, with fewer adverse reactions (Katayama et al. 1990). In addition, CM delivery for MDCT requires the use of a power injector and comparably high injection rates – notably for CT angiography. Injection rates greater than 2.0–2.5 ml/s have a greater potential to cause acute nausea and vomiting and – as a result – motion, if ionic CM are used. Furthermore, extravasation of ionic CM is less well tolerated than nonionic CM. Therefore, nonionic CM are probably the best choice for contrast-enhanced MDCT in general (Hopper 1996).

Because of the unique anatomy of large vessels in the chest and the complexity of early contrast medium dynamics, an increased awareness toward the iodine concentration of the contrast agent is critical in thoracic MDCT applications.

3 Pharmacokinetic and Physiologic Principles

From a pharmacokinetic point of view, all angiographic x-ray contrast media represent extracellular fluid markers. After intravenous administration, these agents are rapidly distributed between the vascular and interstitial spaces (Dawson and Blomley 1996a). The volume of

distribution is about 0.25 l/kg body weight, which typically represents the extracellular fluid space. The main process of elimination is renal glomerular filtration. In general, kinetics were found to be linear or proportional to the dose. Because relative CT attenuation values (ΔHU – Δ Hounsfield units), derived by subtracting background attenuation before administration of contrast medium, are linearly related to the concentration of contrast medium (iodine), contrast medium dynamics may be expressed in these units (Dawson and Blomley 1996a, b).

Pharmacokinetic studies on CM have typically concentrated on the phase of elimination (following CM injection) rather than on the very early phase of CM distribution (during CM administration). For thoracic CTA, however, it is the particularly complex phase of early contrast medium dynamics, which determines vascular enhancement, perivenous artifacts, and, to a lesser degree, parenchymal enhancement.

It is important to recognize that early vascular enhancement and subsequent tissue enhancement phases utilized in MDCT are affected by different pharmacokinetics, which will be reflected in the timing and composition of injection techniques. Early vascular enhancement is essentially determined by the relationship between iodine administration per unit of time (mg I/s) versus blood flow per unit of time (i.e., cardiac output [l/min]). Parenchymal enhancement is governed by the relationship of total iodine dose (mg I) versus total volume of distribution (i.e., body weight [kg]).

3.1 Early Contrast Medium Dynamics in the Chest

The sequence of early vascular enhancement effects in the thorax following intravenous administration of CM is particularly complex, because it differs between the great veins, the heart, and the pulmonary and systemic arteries. This is illustrated in Fig. 1. Figure 1a shows a series of non-incremental dynamic images obtained every 2 s at the level of the pulmonary artery during the injection of a small test bolus. CM appears 4 s after the beginning of the injection, relatively undiluted and incompletely mixed, in the superior vena cava (which collects approximately one-third [~25 ml/s] of the cardiac output [~80 ml/s]). This causes both bright enhancement and perivenous streak artifacts. The subsequent enhancement of the pulmonary arteries and of the thoracic aorta is less strong, because it has mixed in the right atrium and ventricle with blood from the inferior vena cava and coronary sinus. The magnitude (in HU) and the time course (in seconds) of opacification for each vascular territory are plotted in Fig. 1c. Note that pulmonary arterial enhancement begins immediately (2 s) after enhancement of the superior vena cava. The bolus, which is subsequently delayed and broadened in the pulmonary circulation and left heart chambers, appears in the thoracic aorta after another 10 s (14 s after initiation of the injection). Figure 1d integrates the relative enhancement effects (in ΔHU, above baseline) for a prolonged injection of 20 s for each vessel, respectively. Note that the enhancement events overlap in time. During a prolonged MDCT acquisition of, for example, 20 s, the enhancement is expected to be substantially greater in the superior vena cava than in the pulmonary vasculature and in the aorta (Fig. 1b). With respect to perivenous artifacts, it is pertinent that the time window, which shows maximum pulmonary arterial and aortic enhancement without dense opacification of the superior vena cava, is particularly narrow.

3.2 Early Arterial Contrast Medium Dynamics

Early contrast medium dynamics for a given vascular territory such as the pulmonary or systemic arteries have gained substantial interest because of their implications for CT angiography (CTA). Whereas time-attenuation responses to intravenously injected CM vary widely between vascular territories and across individuals (as discussed below), some basic principles apply to all arterial (pulmonary and systemic) vessels.

Figure 2 schematically illustrates the early arterial contrast medium dynamics as observed in the supraceliac abdominal aorta: When a 16-ml test bolus of contrast medium is injected

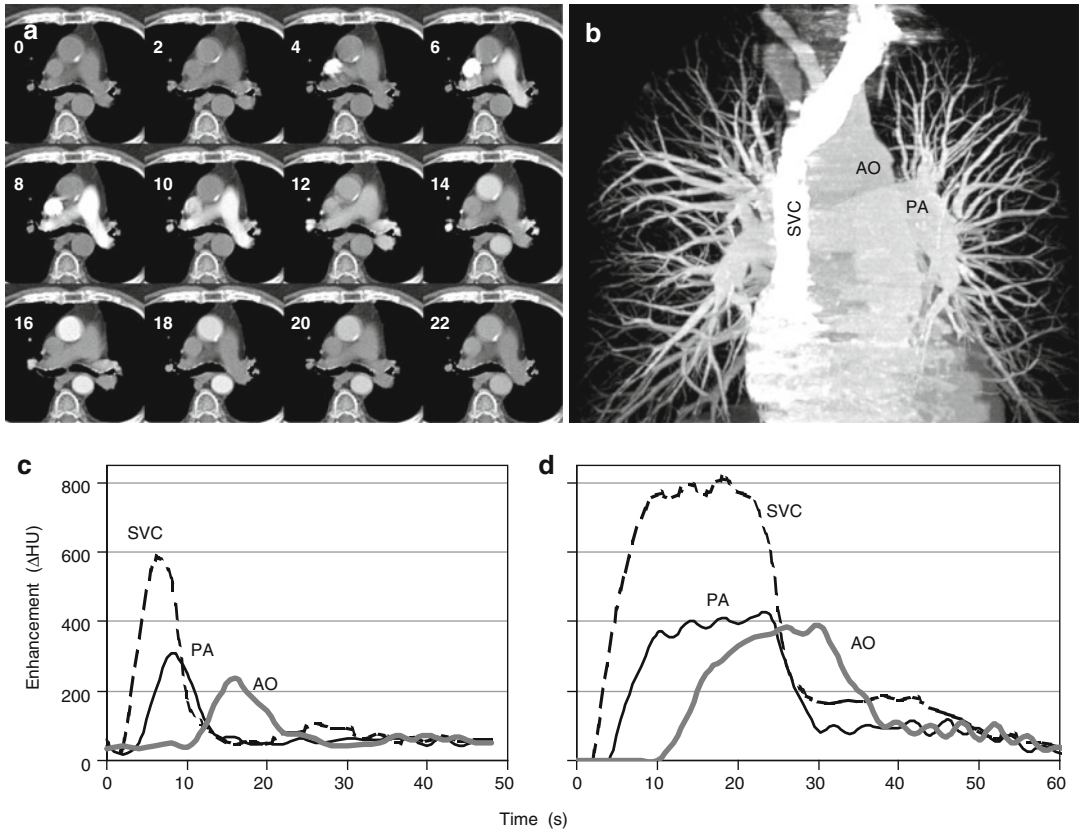

Fig. 1 Early contrast medium dynamics in the chest. (**a**) Sequence of vascular enhancement observed in a non-incremental dynamic CT acquisition following the intravenous injection of a small test bolus is shown (see text for details). (**b**) Maximum intensity projection of a MDCT pulmonary angiogram shows extensive opacification of the left brachiocephalic vein and SVC. As densely opacified blood is mixed with unenhanced blood from the inferior vena cava in the right atrium and ventricle, the pulmonary arterial enhancement is substantially smaller than the enhancement in the SVC. Aortic enhancement is again slightly less than PA enhancement. Analysis of the time-attenuation curves from a 4-s test injection (**c**) allows to predict the time-attenuation curves for a prolonged, 20-s injection (**d**). Note that the time window of maximum aortic enhancement without SVC enhancement is particularly narrow. *SVC* superior vena cava, *PA* pulmonary artery, *AO* thoracic aorta

intravenously, it causes an arterial enhancement response in the aorta. The time interval needed for the contrast medium to arrive in the arterial territory of interest is referred to as the contrast medium transit time (t_{CMT}). The first peak in the enhancement response is also referred to as the *first-pass* effect. For a given individual and vascular territory, the enhancement response is proportional to the iodine injection rate.

After the CM is distributed throughout the intravascular and interstitial fluid compartments of the body, a certain proportion of CM reenters the right heart (*recirculation*). It is important to realize that within the time frame relevant to MDCT acquisition one will not only observe the *first pass* of contrast material but also its *recirculation*. As shown in Fig. 2, a larger (128 ml), prolonged (32 s) bolus of CM can be viewed as the sum of eight subsequent injections of small "test boluses" of 16 ml each. Each of these eight "test boluses" has its own effect on arterial enhancement, respectively. Under the assumption of a time-invariant linear system, the cumulative enhancement response to the entire 128-ml injection equals the sum (time integral) of each enhancement response to their respective eight test boluses (Fleischmann 2002). Note that the recirculation effects of the earlier test boluses overlap (and thus sum up) with the first-pass effects of later test boluses.

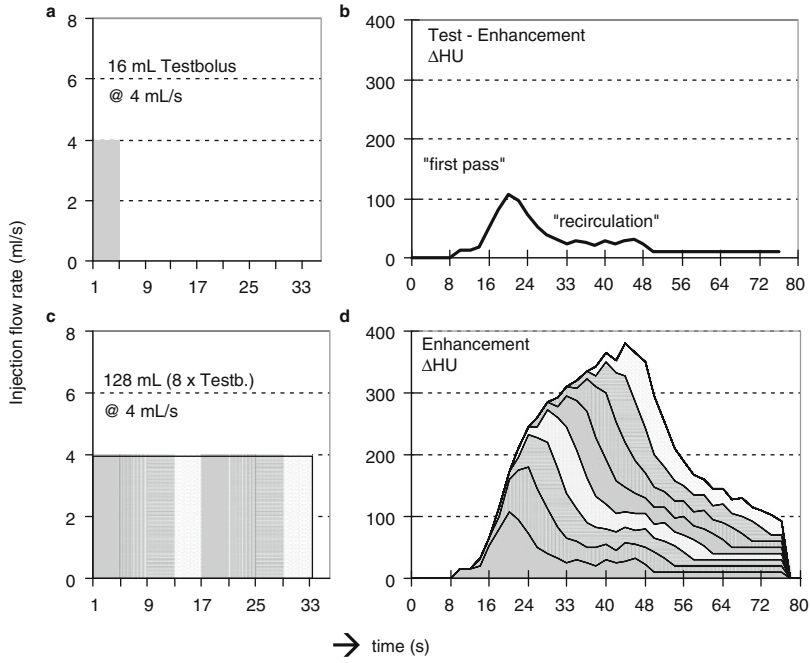

Fig. 2 Simple "additive model" illustrates the relationship between contrast medium injection (**a**, **c**) and cumulative arterial enhancement (**b**, **d**). Note that due to the asymmetric shape of the test-enhancement curve (**b**) and recirculation effects (the "tail" in the test enhancement), arterial enhancement (the "time integral of 8 test boluses") increases continuously over time (**d**). There is no enhancement plateau (Adapted from Fleischmann 2002)

In other words, when contrast medium is injected intravenously over a prolonged period of time (e.g., over 15–40 s), the arterial enhancement will continuously increase over time, before it decreases rapidly after the end of the injection. This well-documented effect is particularly important for CTA injection protocols, because it refutes the widely held misconception that continuous-rate prolonged injections lead to an arterial enhancement plateau. Biphasic (or multiphasic) injections with high initial and lower continuing flow rates lead to a more favorable plateau-like arterial enhancement (Fleischmann et al. 2000).

From the erroneous assumption that constant-rate injections cause a constant plateau enhancement comes another widely held misconception. One might intuitively assume that the average arterial enhancement from a 30-s CTA acquisition achieved with a 30-s contrast medium injection is identical to the average enhancement from a 15-s CTA acquisition achieved with a 15-s injection duration. Again, it is apparent from Fig. 2 that if only 50 % of contrast medium was injected (corresponding to the first four of eight "test boluses"), the cumulative enhancement (the sum of the first four test-enhancement curves) is substantially less compared to the cumulative enhancement from the total dose (eight "test boluses"). It follows that if one wants to achieve the same level of enhancement with shorter injection times, the injection flow rate and/or the iodine concentration of the agent has to be increased. Alternatively, the injection delay may be increased relative to the t_{CMT}. This relative increase of the delay plus the scan time should equal the injection duration (see Sect. 4.5).

3.3 Physiologic Parameters Affecting Vascular Enhancement

The vascular enhancement response to intravenously injected CM is characteristic for a given vascular territory and for a given patient. It is determined by individual physiologic parameters and beyond the control of the observer. The

contrast material transit time (t_{CMT}) from the injection site to the vascular territory of interest depends on the anatomic distance between them and also on the encountered physiologic flow rates between these landmarks. Except for the veins used for intravenous access, injection flow rates hardly affect the t_{CMT}. For systemic arteries, the t_{CMT} is primarily controlled by cardiac output. Cardiac output also accounts for most of the wide interindividual variability of the t_{CMT}. Low cardiac output prolongs and high cardiac output decreases the t_{CMT}. Obviously, the t_{CMT} can be substantially delayed in patients with venous obstructions downstream from the injection site.

The degree of arterial enhancement following the same intravenous contrast medium injection is also highly variable between individuals ("patient effect"). Even in patients considered to have normal cardiac output, midaortic enhancement may range from 140 HU to 440 HU (a factor of 3) between patients (Sheiman et al. 1996). Even if body weight is taken into account, the average aortic enhancement ranges from 92 to 196 HU/ml/kg (a factor of 2) (Hittmair and Fleischmann 2001). Adjusting the contrast medium volume (and injection rates) to body weight will therefore reduce interindividual differences of arterial enhancement, but will not completely eliminate them. The key physiologic parameters affecting individual arterial enhancement are cardiac output and the central blood volume.

Cardiac output is inversely related to the degree of arterial enhancement, particularly in first pass dynamics (Bae et al. 1998b): If more blood is ejected per unit of time, the contrast medium injected per unit of time will be more diluted. Hence, arterial enhancement is lower in patients with high cardiac output, but it is stronger in patients with low cardiac output (despite the increased t_{CMT} in the latter). This effect is illustrated in two patients with chronic thromboembolic pulmonary hypertension, in whom cardiac output was known from invasive measurements (Fig. 3).

Central blood volume is also inversely related to arterial enhancement – but presumably affects recirculation and tissue enhancement rather than the first-pass effect (Dawson and Blomley 1996a). Central blood volume correlates with body weight. If total contrast medium volumes are chosen relative to body weight, then 1.5–2.0 ml/kg body weight (450–600 mg I/kg) is a reasonable quantity for arterial CTA.

Another physiologic factor which affect the t_{CMT} but also pulmonary as well as arterial enhancement is a temporarily diminished venous return caused by a forced Valsalva maneuver of the patient in an attempt to hold his or her breath. In patients with known but also in previously undiagnosed asymptomatic individuals with a patent foramen ovale, such a maneuver may also cause a temporary right-to-left shunt with early arterial enhancement.

3.4 Physiologic Parameters Affecting Tissue Enhancement

Parenchymal and soft-tissue enhancement also diverges between different organs and tissues (Leggett and Williams 1995). Arterial blood flow, the relative proportions of intravascular to interstitial fluid compartments, and diffusion coefficients between compartments all play a role. Highly perfused tissue such as the renal cortex and the spleen, as well as hypervascular neoplasms, exhibits a similar but somewhat delayed enhancement course (e.g., 10–15 s delay relative to arterial enhancement for hypervascular liver lesions). Maximum lesion-to-background contrast between many other moderately enhancing pathological lesions (inflammatory or neoplastic) occurs 60 s or longer following CM administration (Foley 2002). It is again noted that such attenuation differences are generally dose dependent and less affected by the injection flow rate.

3.5 Perivenous "Streak" Artifacts

Streak artifacts arising from densely opacified brachiocephalic veins or the superior vena cava during CM administration are a well-known

problem in thoracic CT. Streak artifacts may obscure neighboring structures and pathology or lead to spurious abnormalities, such as a pseudointimal flap suggestive of aortic dissection. Similarly, artifacts arising from the right atrium and ventricle of the heart may obscure the right coronary artery in coronary CT angiography.

In technical terms, these artifacts are caused by beam hardening (e.g., in the vicinity of subclavian and brachiocephalic veins) or by the acquisition of inconsistent projection data (views) collected during the time window needed for the reconstruction of a given CT cross-sectional image. The latter situation occurs when densely opacified blood is incompletely mixed with unopacified blood and swirls within the superior vena cava during data acquisition.

Streak artifacts can therefore be reduced or completely avoided, if the CT acquisition is performed after contrast material is already removed from the large veins. This can be accomplished by flushing the venous system with saline immediately after the CM injection (Hopper et al. 1997; Haage et al. 2000). Hand exercising during CM administration has also been reported to exhibit this effect (Nakayama et al. 2000). It is important to keep in mind, though, that the time window exhibiting strong pulmonary and systemic arterial

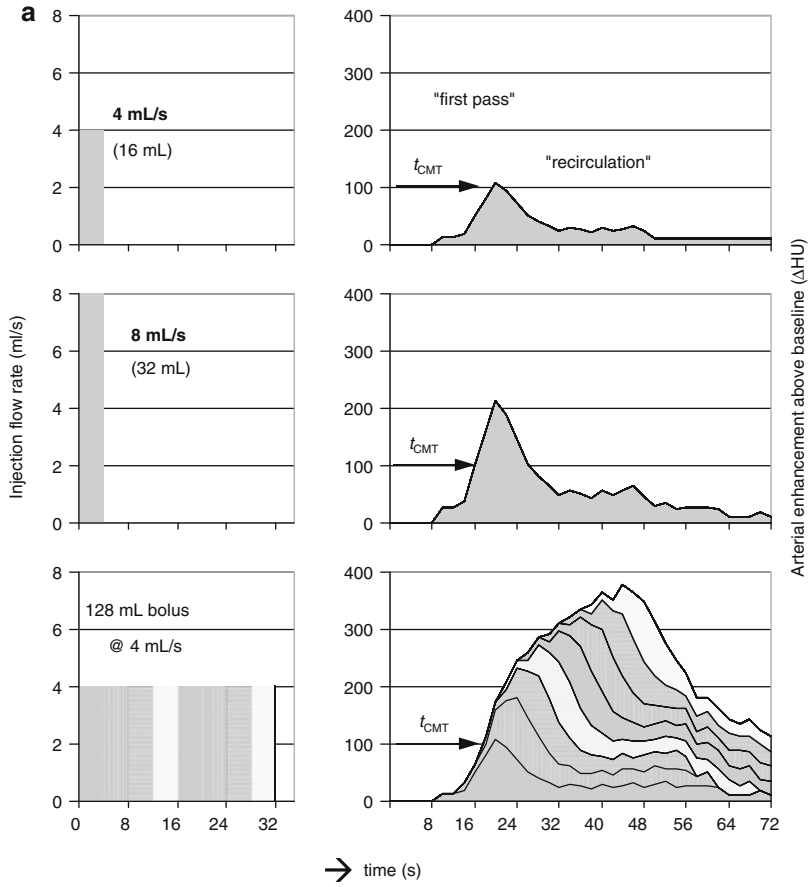

Fig. 3 Cardiac output and pulmonary arterial enhancement. (**a**) Two patients with chronic thromboembolic pulmonary hypertension (CTEPH) are compared. *PAP* pulmonary arterial pressure [systolic/diastolic (mean)], *CO* cardiac output. (**b**) Following a small test-bolus injection (16 ml at 4 ml/s), the time-attenuation response measured in the pulmonary artery is smaller in the patient with greater cardiac output. (**c**) Corresponding thin-slab volume rendered images of pulmonary vessels

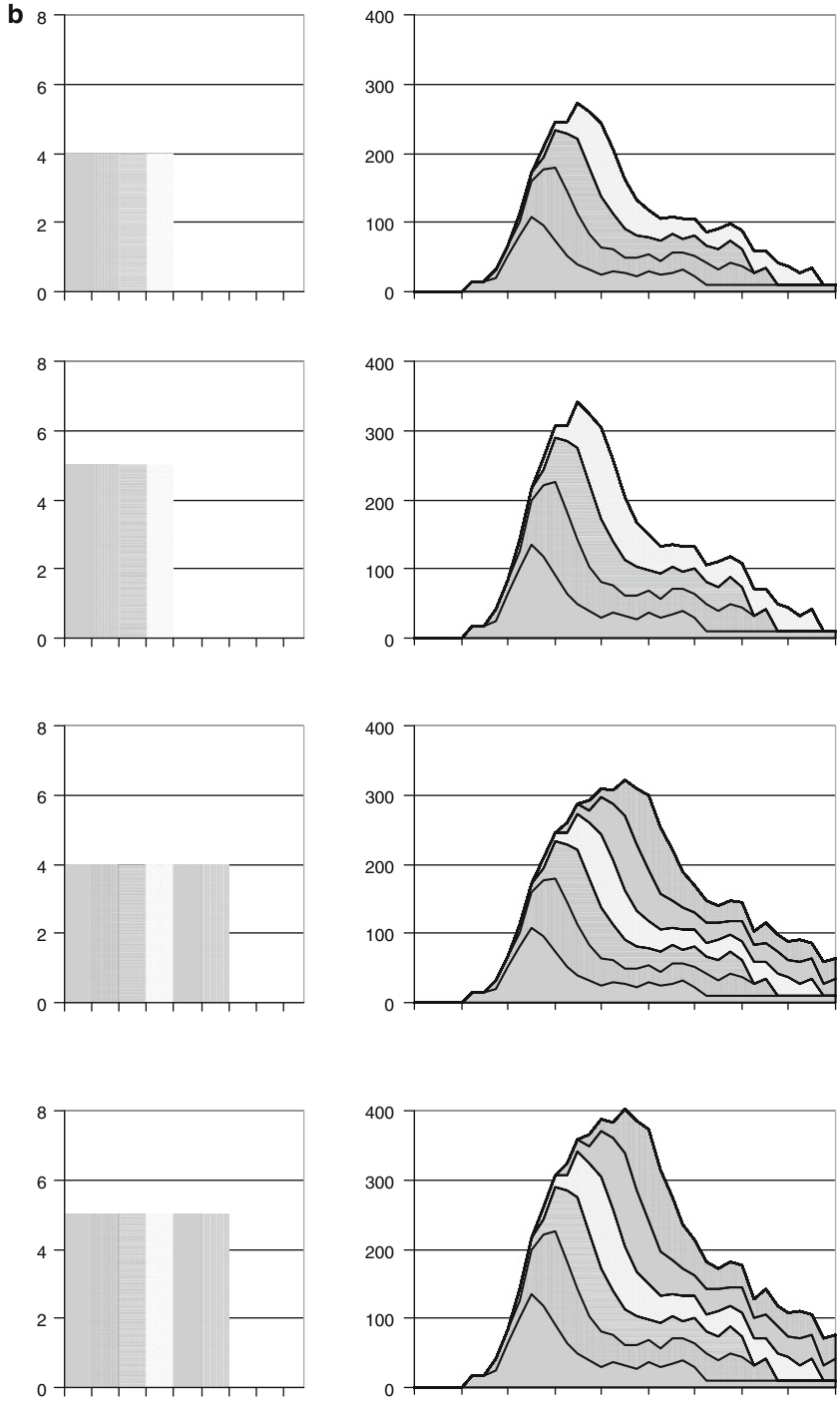

Fig. 3 (continued)

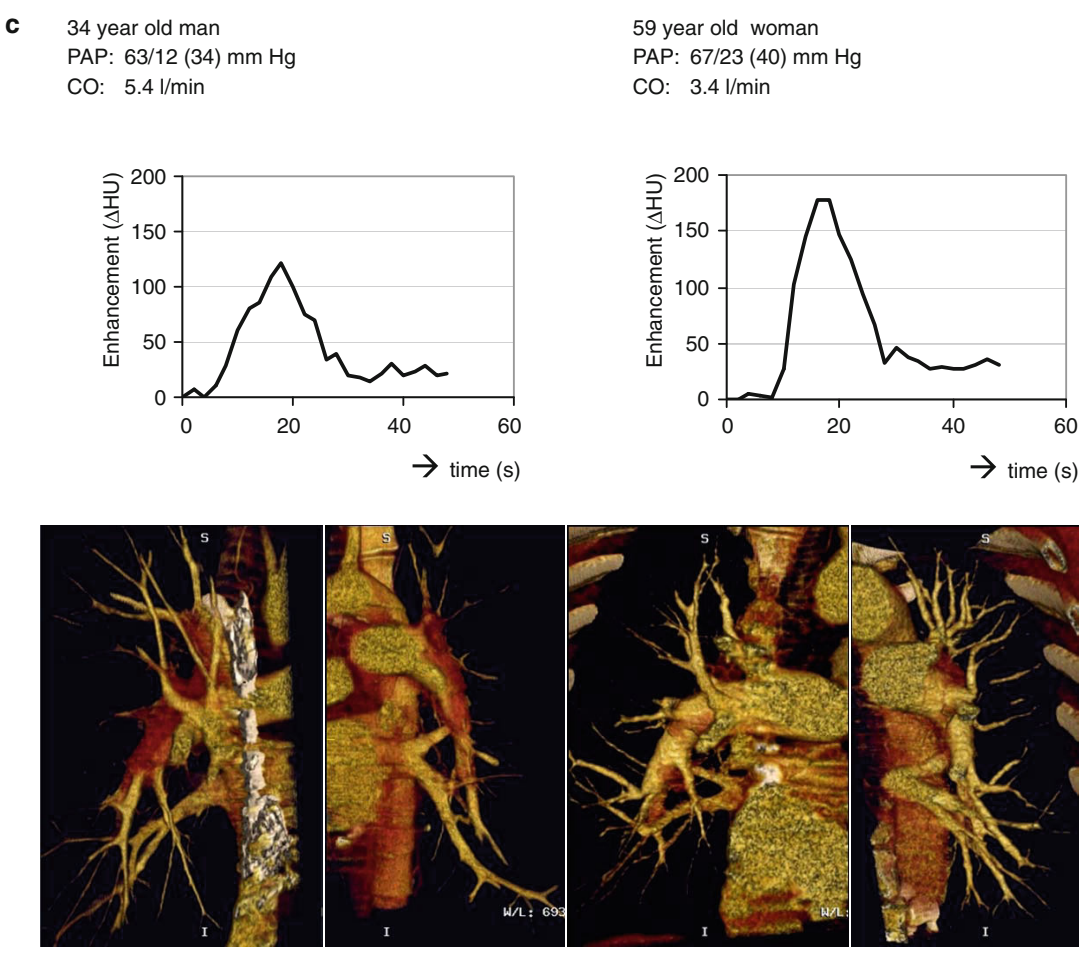

Fig. 3 (continued)

but minimal venous enhancement is remarkably short. Artifacts can also be reduced, if the attenuation difference between newly injected swirling contrast medium and blood is minimized (Fleischmann et al. 1997). This can be accomplished by using lower injection flow rates and less-concentrated contrast medium (Rubin et al. 1996) and/or by scanning during a recirculation phase. Diminished arterial opacification is a potential trade-off when such a strategy is used.

Double-piston ("dual-head") power injectors, which allow automated saline flushing and online variation of CM concentration, may be the most versatile tools for CM administration while also minimizing streak artifacts at the same time during fast MDCT acquisitions.

3.6 Mathematical Modeling

Accurate prediction and controlling of time-dependent arterial enhancement are highly desirable for MDCT, particularly with faster scanners and for CTA. Ideally, one wants to predict and control the time course and the degree of vascular enhancement in each individual – independent of

an individual's underlying physiology. Two mathematical techniques addressing this issue have been developed.

The first is a sophisticated *compartmental model*, which predicts vascular and parenchymal enhancement using a system of more than 100 differential equations to describe the transport of contrast medium between intravascular and interstitial fluid compartments of the body (Bae et al. 1998a). For CT angiography, this model suggests multiphasic injections to achieve uniform vascular enhancement. The injection flow rate is maximum at the beginning of the injection followed by a continuous, exponential decrease of the injection rate (Bae et al. 1998b).

The second *black-box model* approach is based on the mathematical analysis of a patient's characteristic time-attenuation response to a small test-bolus injection (Fleischmann and Hittmair 1999). Assuming a time-invariant linear system, one can mathematically extract and describe each individual's response to intravenously injected contrast medium ("patient factor") and use this information to individually tailor biphasic injection protocols to achieve uniform, prolonged arterial enhancement at a predefined level. The principle of this technique is outlined in Fig. 4. The method is robust and has been successfully used in clinical practice.

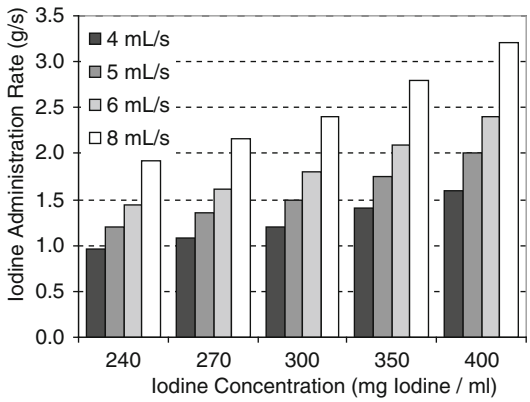

Fig. 4 Iodine administration rates and CM concentration. For a given CM concentration, the iodine administration rate (g/s) can be varied by selection of the injection flow rate (in ml/s). High-concentration agents permit greater iodine administration rates at the same injection rates

Mathematical models utilizing both the "compartmental" and "black-box" models have recently been incorporated into commercial CM power injector systems. The greatest value of these systems, however, may come from the gained insights into early contrast medium dynamics for the time frame relevant for current and future CT technology, which allows rational design and implementation of empiric and routinely applicable injection techniques.

4 Instrumentation and Technique

4.1 Intravenous Access

Adequate intravenous CM administration for MDCT requires the use of a mechanical, programmable power injector. A large cubital or antebrachial vein is the most favorable injection site. For a given vein, the largest diameter peripheral catheter, which accommodates the desired injection rate, is selected. Whereas cannula lumen diameters as small as 22 g (0.71 mm) may suffice for routine thoracic MDCT, diameters up to 17 g (1.47 mm) have been used for dedicated CTA of the thoracic aorta. If high injection flow rates are desired, a fast manual saline injection with the patient's arms in scanning position (usually above the head) before mechanical CM delivery is recommended to assure correct peripheral catheter position. Injections through a central venous catheter reduce the contrast medium transit time (t_{CMT}); injections in a peripheral vein at the dorsum of the hand slightly prolong the t_{CMT}. In both instances, the flow rates may need to be adapted in order to prevent CM extravasation or catheter rupture.

Advances in IV cannula design, including the addition of side holes/fenestrations, have resulted in lower shear force on the cannula, reduced venous wall stress, and less pressure drop across the cannulas. Radial velocities are more uniform and exiting velocity of CM from the cannula is reduced. These devices allow delivery of CM at higher flow rates at each gauge size than previously available (Weber et al. 2009). This allows the use of smaller-gauge cannulas with

preservation of high flow rates and decreased incidence of extravasation (Johnson et al. 2014).

4.2 Power Injectors and Safety Issues

The use of CM in MDCT carries the same risk of idiosyncratic (non-dose-dependent) adverse reactions as in other CM applications. These allergy-like effects are well described (Katayama et al. 1990) and their discussion is beyond the scope of this chapter. Because MDCT requires faster injections and the use of a power injector, dose-dependent (non-idiosyncratic) adverse effects and the risk of CM extravasation have recently regained interest.

Dose-dependent adverse reactions include nausea, vomiting, arrhythmia, pulmonary edema, and cardiovascular collapse. Based on clinical and experimental evidence for ionic CM, one might naturally assume that rapid injections would be less well tolerated than slower injections (Dawson 1998). However, at least for injection flow rates up to 4 ml/s, there seems to be no correlation between injection rate and the overall rate of adverse reactions (Jacobs et al. 1998).

The rate of CM extravasation during the intravenous administration of CM with power injectors is low, ranging from 0.2 to 0.6% (Bellin et al. 2002). Whereas this is presumably higher when compared to hand-injection and drip infusion technique, no correlation was found between extravasation frequency and injection rates up to 4 ml/s (Jacobs et al. 1998). Most extravasations involve only small volumes and result in minimal to mild symptoms if nonionic CM is used.

Large volumes of CM may be involved, however, in non-communicative patients such as infants and children, elderly, or unconscious patients. Monitoring of the injection site during CM administration is recommended for these patients, because severe extravasation injuries could occur without the usual patient complaints. Such extravasations have occasionally been reported, and guidelines for management of extravasation injuries should be available (Bellin et al. 2002). Recently, an automated CM extravasation device has been developed, which interrupts the mechanical injection when a skin impedance change due to fluid extravasation is detected (Nelson et al. 1998). Such a device might prove useful in high-flow-rate MDCT applications (Birnbaum et al. 1999). Newer IV cannula design may also decrease extravasation rate (Johnson et al. 2014).

4.3 Saline Flushing of the Veins

Flushing the venous system with saline immediately after CM injection pushes the CM column from the veins into the circulation. This has two desirable effects in thoracic MDCT.

First, because the CM which would otherwise remain in the arm veins after the end of the injection contributes to vascular enhancement, opacification of intrathoracic vessels is improved. This effect can also be exploited to reduce the total CM volume in routine thoracic MDCT (Hopper et al. 1997; Haage et al. 2000). Second, because saline flushing removes CM from the brachiocephalic veins and the superior vena cave, it reduces perivenous streak artifacts in thoracic and cardiac CT.

Saline flushing has been performed (a) manually – using a three-way valve – or (b) by layering saline above contrast in the syringe of a power injector or (c) by using two interconnected power injectors. The former techniques, however, are impractical for routine CT, because the manual technique may expose the radiologist or technologist to radiation, and the layering technique is time consuming and poses a risk for contamination.

The most convenient technique for routine saline flushing after CM injection is new programmable double-piston power injectors (one syringe for contrast material, one for saline) similar to those used in MR angiography. Furthermore, these devices may not only allow variation in CM injection rates but also the ability to vary the contrast material concentration during a single injection (through saline admixture). Such a strategy might allow to achieve the desired enhancement profile by initially injecting non-diluted contrast medium, followed by a phase of diluted contrast medium injection, with subsequent saline flushing to avoid artifacts.

4.4 Scanning Delay and Automated Bolus Triggering

A fixed, empiric injection-to-scan delay may be adequate for many routine thoracic and abdominal CT acquisitions, particularly if maximum vessel opacification is not of critical importance. The greatest advantage of fixed-delay protocols is obviously ease of use. As early contrast medium dynamics in patients without cardiocirculatory disease are within a comparable range and as it is easier to achieve good opacification in the pulmonary arteries compared to more distant systemic arteries, fixed scanning delays have also been employed successfully for pulmonary CTA acquisitions.

For dedicated arterial or organ (liver) MDCT imaging studies, a fixed scanning delay cannot be recommended, because the arterial CM transit time (t_{CMT}) is prohibitively variable between individual patients – ranging from 8 to as long as 40 s in patients with cardiovascular diseases. One might completely miss the bolus with a fast MDCT acquisition if the delay is not properly chosen.

In vascular MDCT, therefore the delay needs to be timed relative to the contrast transit time (t_{CMT}). It is important to realize that with the possibility of very fast MDCT acquisitions, the t_{CMT} itself does not necessarily serve as the scanning delay, but rather as a means of individualizing the delay relative to it. Depending on the vessels or organ of interest, an additional delay relative to the t_{CMT} needs to be selected. In CTA, this additional delay may be as short as 0–2 s added to the t_{CMT} ("t_{CMT} + 2 s"). For visualizing hypervascular liver lesions, this additional delay may be 10–15 s ("t_{CMT} + 15 s"). Transit times can be easily determined using either a test-bolus injection or an automatic bolus-triggering technique.

Test Bolus The injection of a small test bolus (15–20 ml) while acquiring a low-dose dynamic (non-incremental) CT acquisition is a reliable means to determine the t_{CMT} from the intravenous injection site to the arterial territory of interest (Van Hoe et al. 1995). The t_{CMT} equals the time-to-peak enhancement interval measured in a region-of-interest (ROI) placed within a reference vessel. Furthermore, time-attenuation curves obtained from one or more regions of interest can be used for individual bolus-shaping techniques using one of the previously described mathematical models. A test bolus is particularly useful to determine the t_{CMT} if unusual CM injection sites need to be used (e.g., lower-extremity veins).

Bolus Triggering Many CT scanners have this feature built into their system. A circular region-of-interest (ROI) is placed into the target vessel on a non-enhanced image. While contrast medium is injected, a series of low-dose non-incremental scans are obtained, while the attenuation within a ROI is monitored or inspected visually. The t_{CMT} equals the time when a predefined enhancement threshold ("trigger level") is reached (e.g., 100 ΔHU) or observed by the person performing the scan. The minimal trigger delay to initiate the MDCT acquisition after the threshold has been reached ("trigger delay") depends on the scanner model and on the longitudinal distance between the monitoring series and the starting position of the actual MDCT series. The minimal "trigger delay" before a scan can be initiated after the trigger threshold is reached is currently between 2 and 8 s. Bolus triggering is a very robust and practical technique for routine use and has the added advantage that it does not require an additional test-bolus injection.

4.5 Contrast Medium Concentration

Vascular enhancement (over time) is proportional to the number of iodine molecules administered (over time). This *iodine administration rate* can therefore be increased either by increasing the injection flow rate, by increasing the iodine concentration of the contrast medium used (Fig. 4), or both. Thus, to achieve a certain iodine administration rate (e.g., 1.2 g/s), a faster (e.g., 4 ml/s) injection flow rate will be needed with standard (300 mg I/ml) CM, compared to a slower (e.g., 3 ml/s) flow rate with high-concentration (400 mg I/ml) CM. Very high iodine administration rates,

up to 2.4 g/s or more, can be safely injected with a 400 mg I/ml solution at 6 ml/s, whereas an injection flow rate of 8 ml/s would be required using standard (300 mg I/ml) solution. High iodine administration rates are useful in CTA, notably in patients with low enhancement response due to underlying cardiocirculatory disease, and for avoiding high injection flow rates. Furthermore, high iodine administration rates are also desirable for specific nonvascular imaging purposes, e.g., for detecting hypervascular liver lesions, or in organ perfusion studies.

Low-concentration contrast media, on the other hand, have the advantage that they cause less perivenous artifacts at the level of the brachiocephalic veins and the superior vena cava in thoracic MDCT, particularly if no saline flushing of the veins is employed (Rubin et al. 1996).

5 Clinical Contrast Medium Injection Protocols

The following section provides an overview of clinically applicable CM injection protocols for various thoracic MDCT applications. The suggested protocols are based on pharmacokinetic considerations, published clinical and experimental data, mathematical approximations, and practical experience. An attempt is made to provide both a universal approach to injection strategies and specific examples of injection protocols.

Because of the wide variation among available MDCT scanner types (ranging from dual-channel to 320-slice MDCT systems, with substantial variation in rotation times and selectable table increments), the protocols are tabulated according to the acquisition times. Abbreviations for temporal variables are indexed as follows: t_{SCAN} = acquisition time and t_{INJ} = injection duration.

The actual CM injection protocols should be adjusted to match the suggested iodine doses and administration rates. CM doses and injection rates should also be adjusted (±20 %) in patients with a body weight smaller than 60 kg and greater than 90 kg body weight (BW).

Given the availability of wide area-detector CT and systems with very rapid gantry rotation times, scan acquisition times may be very short – for example, one gantry rotation for coronary imaging and < 2 s for the entire chest, abdomen, and pelvis. One may be tempted to use very short CM injection protocols as well; however, caution should be exercised. As discussed above, since observed enhancement continually increases during continued injection, a very short injection duration will lead to lower-level vascular enhancement. A very short injection duration will essentially serve as a "test bolus" with a narrow enhancement peak and little benefit of recirculation effects. One can compensate, to some degree, by increasing the CM injection flow rate. However, at programmed flow rates above 8 ml/s, there is no observed benefit over slower injection rates, but the risk of CM extravasation can be higher. Further, since the bolus is very short and bolus triggering includes some 3–8 s of added delays, the bolus could be easily missed, resulting in an inadequate exam. A very short injection duration also increases the likelihood of outrunning the CM bolus completely, especially if the scanner is operated at high pitch over long distances, such as peripheral runoff CTA. Finally, it is important to remember that in general at least 7 s of CM injection time is needed to assure complete filling of most vascular territories.

5.1 Routine Thoracic and Mediastinal MDCT

Indications Evaluation of various systemic or thoracic diseases; staging/follow-up malignancies (lymphoma, bronchogenic carcinoma).

Objectives Opacification of thoracic vessels for better delineation of mediastinal and hilar structures.

Strategy A small to moderate amount of iodine (20–35 g I) CM (60–120 ml of 300 mg I/ml CM) delivered at a slow injection rate (1.5–3.0 ml/s) and comparably long injection duration (>30 s) results

Table 1 Routine thoracic MDCT

Acquisition time (s)	Scanning delay (s)	Iodine dose (g)	Iodine administration rate (g/s)	CM volume (ml) [a]	Injection rate (ml/s) [a]	Injection duration (s)
20	25	30	.75	100	2.5	40
15	30	30	.75	100	2.5	40
10	28	30	.90	100	3	33
5	33	30	.90	100	3	33

[a]Volume and flow rate calculated for 300 mg I/ml concentration CM

Table 2 Routine thoracic MDCT, high CM dose protocol[a]

Acquisition time (s)	Scanning delay (s)	Iodine dose (g)	Iodine administration rate (g/s)	CM volume (ml)[b]	Injection rate (ml/s)[b]	Injection duration (s)
20	25	36	.90	120	3	40
15	30	36	.90	120	3	40
10	25	36	1.20	120	4	30
5	30	36	1.20	120	4	30

[a]Applicable if soft-tissue enhancement (e.g., chest wall) is also desired; provides good pulmonary and systemic arterial enhancement as well. Patients with >90 kg BW
[b]Flow rate calculated for 300 mg I/ml concentration CM

Table 3 Thoracic MDCT, minimum dose protocol[a]

Acquisition time (s)	Scanning delay (s)	Iodine dose (g)	Iodine administration rate (g/s)	CM volume (ml)[b]	Injection rate (ml/s)[b]	Injection duration (s)
20	25	18	.90	60	1.5	40
15	30	18	.90	60	1.5	40
10	25	18	1.20	60	2	30
5	20	18	1.20	60	2	30

[a]Suffices for vessel delineation, if saline flush is used. Saline flushing is strongly recommended
[b]Volume and flow rate calculated for 300 mg I/ml concentration CM

in sufficient opacification of thoracic vessels. Low-concentration agents or saline flushing is favorable to reduce perivenous artifacts. A fixed delay is adequate and should be determined, so that the injection ends 5 s earlier than the MDCT acquisition (delay = t_{INJ} + 5 s − t_{SCAN}). This minimizes perivenous artifacts, particularly when a saline flush and a caudocranial scanning direction are used. Examples are shown in Tables 1, 2, and 3.

5.2 Pulmonary Arteries

Indications Acute pulmonary embolism, chronic thromboembolic pulmonary hypertension (CTEPH), pulmonary arteriovenous malformations (AVM), pulmonary artery aneurysms, and arteriovenous fistulas.

Objectives High opacification of pulmonary arteries, in order to detect vascular abnormalities – notably filling defects or mural thrombus.

Strategy Moderate to large amount of iodine is required to allow distinction between opacified blood and intraluminal abnormalities. A larger amount of iodine is necessary if an additional, delayed (approx. 2 min) acquisition of the lower-extremity veins (CT venography) is desired. Moderate to high injection flow rates (3.0–4.0 ml/s) are required with a standard concentration agent; if a higher-concentration agent is used, flow rates can be slower. Saline flushing is recommended. A fixed delay is adequate in the majority of patients and should again be determined so that the injection ends 3 s earlier than the end

Table 4 Pulmonary artery CTA, fixed delay

Acquisition time (s)	Scanning delay (s)	Iodine dose (g)	Iodine administration rate (g/s)	CM volume (ml)[a]	Injection rate (ml/s)[a]	Injection duration (s)
20	23	36	.90	120	3	40
15	18	36	1.20	120	4	30
10	23	36	1.20	120	4	30
5	28	36	1.20	120	4	30

[a]Volume and flow rate calculated for 300 mg I/ml concentration CM

Table 5 Pulmonary artery CTA, with individual timing

Acquisition time (s)	Scanning delay (s)	Iodine dose (g)	Iodine administration rate (g/s)	CM volume (ml)[a]	Injection rate (ml/s)[a]	Injection duration (s)
20	$t_{CMT}+8$	30	.90	100	3	33
15	$t_{CMT}+10$	27	1.20	90	4	30
10	$t_{CMT}+15$	27	1.20	90	4	30
5	$t_{CMT}+20$	27	1.20	90	4	30

Note – t_{CMT} = contrast medium transit time, as established with a test-bolus or bolus-triggering technique
[a]Volume and flow rate calculated for 300 mg I/ml concentration CM

of MDCT acquisition (delay = $t_{INJ}+3$ s$-t_{SCAN}$). For patients with severely compromised cardiocirculatory distress (CTEPH), slower injection rates suffice (because diminished cardiac output leads to brighter enhancement). Image quality is more consistent if the delay is timed relative to the contrast medium transit time (Tables 4 and 5).

5.3 Thoracic and Coronary CT Angiography

Indications Aneurysms and dissection of the thoracic aorta and its branches, atherosclerotic or inflammatory (arteritis) arterial stenosis or occlusion, thoracic outlet syndrome, chest trauma. Coronary CT angiography.

Objectives High opacification of systemic and/or coronary arteries.

Strategy For fast acquisitions (≥64-channel MDCT), moderate amounts of iodine at high iodine administration rates are required (i.e., high injection flow rates and/or high iodine concentration agent). For slower acquisitions, larger total CM volumes (with longer injection durations and preferably biphasic injections) are optimal. Individual scan timing relative to the t_{CMT} is mandatory. Saline flushing is beneficial in thoracic outlet and coronary CTA in order to reduce artifacts in the vicinity of large veins of the right heart (Tables 6 and 7).

5.4 Thoracic Veins

Indications Assessment of venous thrombosis, obstruction, or occlusion.

Objective Delineation of venous anatomy and pathology for treatment planning

Strategy A Intravenous CM injection into the contralateral (non-diseased) arm requires large iodine doses (e.g., 100–150 ml) at slow to moderate injection rates in order to visualize the diseased venous territory during a recirculation phase. A long delay (end of MDCT acquisition should be approx. 15 s after the end of the injection) and saline flushing are recommended. This strategy also allows assessment of systemic arteries.

Table 6 Thoracic CTA, uniphasic injection

		Iodine		300 mg I/ml CM	400 mg I/ml CM
Acquisition time (s)	Scanning delay (s)	Dose (g)	Administration rate (g/s)	CM volume at injection rate (ml at ml/s)[a]	CM volume at injection rate (ml at ml/s)[b]
20	$t_{CMT}+8$	39	1.2	130 at 3	100 at 3
15	$t_{CMT}+8$	36	1.5	120 at 5	90 at 3.8
10	$t_{CMT}+8$	33	1.8	110 at 6	85 at 4.5
5	$t_{CMT}+12$	27	1.8	90 at 6	70 at 4.5

Note – t_{CMT} = contrast medium transit time, as established with a test-bolus or bolus-triggering technique
[a]Volume and flow rate calculated for 300 mg I/ml concentration CM
[b]Volume and flow rate calculated for 400 mg I/ml concentration CM

Table 7 Thoracic CTA, biphasic injection

		Iodine		300 mg I/ml CM		400 mg I/ml CM	
Acquisition time (s)	Scanning delay (s)	Total dose (g)	Biphasic administration (g at g/s)	Total volume (ml)[a]	Biphasic injections (ml at ml/s)[a]	Total volume (ml)[b]	Biphasic injections (ml at ml/s)[b]
20	$t_{CMT}+8$	34	9 at 1.8 +25 at 1.4	115	30 at 6 +85 at 4.5	90	23 at 4.5 +67 at 3.4
15	$t_{CMT}+8$	32	9 at 1.8 +23 at 1.4	105	30 at 6 +75 at 4.5	80	23 at 4.5 +57 at 3.4
10	$t_{CMT}+8$	29	9 at 1.8 +20 at 1.5	95	30 at 6 +65 at 5	75	23 at 4.5 +52 at 3.8
5	$t_{CMT}+12$	24	9 at 1.8 +15 at 1.5	80	30 at 6 +50 at 5	65	23 at 4.5 +42 at 3.8

Note – t_{CMT} = contrast medium transit time, as established with a test-bolus or bolus-triggering technique
[a]Volume and flow rate calculated for 300 mg I/ml concentration CM
[b]Volume and flow rate calculated for 400 mg I/ml concentration CM

Strategy B 200 ml of diluted CM (1:10–1:20 diluted with normal saline) injected into the diseased arm (or both arms using a Y-connector) at a slow injection rate (2–4 ml/s) is sufficient to directly opacify the thoracic veins.

5.5 Thoracoabdominal MDCT

Indications Assessment of thoracoabdominal diseases, such as staging of lymphoma.

Objectives Delineation of hilar and mediastinal structures, combined with adequate parenchymal enhancement of abdominal and pelvic organs.

Strategy Since delineation of thoracic vessels is relatively easily achieved, CM delivery is weighted toward adequate parenchymal and soft-tissue enhancement. Large iodine doses (0.5–0.6 g of iodine/kg BW) corresponding to approximately 100–150 ml (depending on the iodine concentration and on the patient's body weight) are required. Injection rates can be moderate to slow; the scan delay should be long enough to allow tissue enhancement (≥60 s).

Dedicated biphasic acquisitions (with high iodine administration rates) are also possible with MDCT, where the first acquisition includes the thorax and upper abdomen and the second acquisition includes the abdomen and pelvis (other sequences are also possible if the MDCT scanner technology permits). Timing is optimized for biphasic abdominal imaging, i.e., the first acquisition should include the liver in a late arterial phase (delay = t_{CMT} + 10 s, or delay ≅ 25 s) and the second acquisition is obtained during a hepatic parenchymal phase (delay = t_{CMT} + 40 s, or delay ≅ 60 s).

6 Advanced Contrast Medium Considerations

6.1 Contrast Medium Considerations in Patients with Chronic Kidney Disease

Chronic kidney disease (CKD) is defined as either the presence of kidney damage or glomerular filtration rate (GFR) measurement < 60 ml/min/1.73 m^2 for more than 3 months. CKD can be divided into stages of renal dysfunction based on GFR:

Stage	Description	GFR (ml/min/1.73 m^2)
I	Kidney damage with normal or increased eGFR	≥90
II	Mild CKD	60–89
III	Moderate CKD	30–59
IV	Severe CKD	15–29
V	Kidney failure	<15 (or dialysis)

Direct measurement of GFR is time consuming and may be clinically impractical. As a result, renal function is typically estimated based on laboratory tests and other variables such as age. The result is an estimated GFR (eGFR). An easy online calculator that follows the National Kidney Foundation CKD-EPI guidelines (http://www.kidney.org/professionals/KDOQI/gfr_calculator) (Levey et al. 2009) is our standard method for eGFR determination. Of note, the calculator utilizes serum creatinine, age, sex, and race and calculates results in ml/min/1.73 m^2 body surface area (BSA). This result is useful to directly compare renal function between individuals. However, to directly calculate the most appropriate CM dose, the result will need to be corrected for body weight.

Larger numbers of cardiovascular CT procedures are being performed today, including greater utilization of CT in patients with underlying CKD. Preexisting CKD has been recognized as a risk factor for contrast-induced nephropathy (CIN). The degree of potential deleterious impact from CM administration in patients with CKD remains controversial (Mcdonald et al. 2014), but the need to protect renal parenchymal function is not. There is good pharmacokinetic and clinical evidence that the ratio of the volume of CM administered to the underlying degree of renal dysfunction can predict the subsequent risk of CIN (Altmann et al. 1997; Gurm et al. 2011; Laskey et al. 2007; Nyman et al. 2008; Sherwin et al. 2005). Specifically, a CM-to-eGFR ratio of 3.7 has been found to offer optimum discrimination between patients who will develop CIN and those who will not (Laskey et al. 2007). On a practical clinical level, a ratio of <2.0 has shown no significant increased risk of CIN (Gurm et al. 2011). As such, these findings can be used to design a rational strategy for CM injection tailored to the patient's renal function and the clinical scan parameters.

Table 8 List sample calculations for three different patient sizes, all with the same eGFR of 30 ml/min/1.73 m^2

Patient body weight (kg)	eGFR-based CM volume (2 × eGFR)	Adjustment for BW (BW/75)	Final CM volume available (ml)
50	2 × 30 = 60 ml	50/75 = 0.67	40
75	2 × 30 = 60 ml	75/75 = 1.00	60
100	2 × 30 = 60 ml	100/75 = 1.33	80
Generic	(2 × eGFR)	BW/75	= total volume

In patients with CKD, lower-concentration CM (300 mg I/ml) can be utilized. The total CM volume is calculated at two times the eGFR, corrected for body weight (e.g., CM vol = 2 × eGFR × (body wt kg/75)). For example, for eGFR = 30, standard-sized (75 kg) patient would receive 2 × 30 × 75/75 = 60 ml CM for injection (Table 8).

6.1.1 Clinical Decision-Making

Once the maximal CM volume has been calculated, it is imperative to then decide whether the clinical question can be answered by utilizing only the available amount of CM. Chest CT imaging, where scan times for most applications are <10 s, lends itself well to smaller CM volume administration protocols. Other vascular territories, such as lower-extremity CTA, require longer injection profiles (FLEISCHMANN, et al. 2006) and may not be feasible to assess at very small CM volumes.

One instance deserves special mention: in the acute setting and when dealing with life-threatening emergent conditions, *the risk of CIN can be outweighed by the urgent need to obtain relevant information to guide life-saving treatment decision-making*. In these instances, standard doses and rates of CM should be utilized, irrespective of renal function status.

6.2 Low-Energy/Low-Contrast Imaging

Utilization of lower peak tube voltage (kVp) can be employed in selected patients to help maximize signal from available CM, decrease patient radiation dose, and/or provide greater arterial enhancement (Fig. 5). Among others, these techniques are valuable for pediatric patients, smaller body-size adult patients, and patients with CKD. Current-generation CT scanners allow scanning at tube potentials lower than the standard 120 kVp (e.g., 100 kVp, 80 kVp). At lower kVp, the proportional absorption of x-rays by iodine increases as the energy approaches iodine's K-edge of 33.2 keV. This phenomenon translates into higher-observed attenuation values of CM-enhanced structures (Newton and Potts 1981) However, a greater fraction of these (lower-energy) x-ray photons are also absorbed in tissue; therefore, tube current (milliampere, mA) must increase to offset the increase in image noise. It is possible, especially with older scanners, that tube current output may be insufficient alone to prevent high image-noise acquisitions. Current-generation scanners are best suited to acquire high mA exams. In older scanners, however, either slowing the pitch or gantry rotation time (e.g., to 0.5 s) has the effect of increasing photon flux per tube rotation and limiting noise (at the expense of greater patient dose).

In general, attenuation of iodine increases by 25 % from 120 kVp to 100 kVp and another 25 % from 100 kVp to 80 kVp (Table 9). Thus, by decreasing the tube voltage from 120 kVp to 80 kVp, one should observe approximately 50 % increased iodine attenuation. Conversely, increasing the tube voltage from 120 kVp to 140 kVp will decrease iodine attenuation by approximately 25 %. Although image noise also decreases at high kVp imaging, attenuation also decreases, with resultant limited benefit to signal-to-noise ratio (SNR) at the expense of higher patient dose.

The observed effects of lower kVp imaging can be leveraged to predict arterial enhancement at lower kVp and to subsequently modify CM injection protocols to obtain adequate diagnostic quality at lower CM injection rates. Using this strategy, the injection duration, scan time, and any scan delays should be kept constant. The tube current (mA) should be increased by 30–50 % for each "step"-down in kVp. Then, for each step-down in kVp (e.g., 120–100 kVp and 100–80 kVp), an increase in attenuation should allow a reduction in CM volume by 25 %. To maintain similar noise levels when manually selecting mA, depending on vendor, one could either select the same noise level on the scanner (auto/smart mA) or try to match the CTDI of the new (low-kVp) protocol to the original (120 kVp) protocol.

6.2.1 Disadvantages of Low-kVp Imaging

The expected signal gain from CM administration may not be realized if small volumes (flow rates) of CM are administered, either by design (for low-kVp imaging) or as a result of CM extravasation. Partial volume effects may also limit the iodine concentration in a given voxel. These phenomena, in addition to potentially higher image noise at lower tube voltages, can lead to significant SNR reduction if appropriate corrections are not applied.

The increased mA required for lower kVp imaging also requires a larger x-ray focal spot size, resulting in focal spot blooming beyond nominal size, which decreases spatial resolution (Oh et al. 2014). In some situations where accurate measurements are essential (e.g., TAVR planning), accuracy and interobserver agreement could be adversely affected. Newest-generation scanner technology advances may also help address this phenomenon (Oh et al 2014; Solomon et al. 2015).

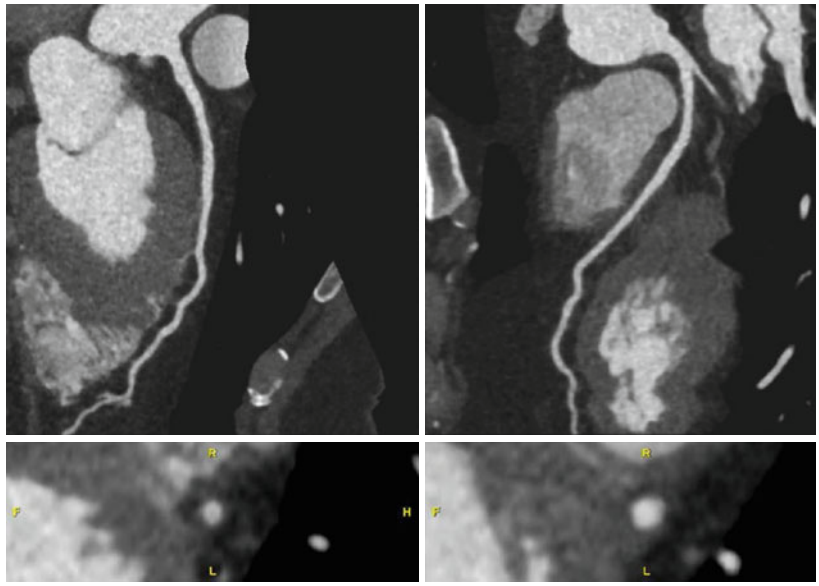

Fig. 5 The use of low-kVp scanning to decrease patient dose with preserved image quality. A 54-kg female patient with chest pain presented for CCTA. 80 kVp tube voltage was utilized, with prospective ECG synchronization and iterative reconstruction techniques. Patient dose was 0.4 mSv. High degree of vessel enhancement with relatively little background image noise is noted on both curved-planar reconstructions (*upper row*) and slice-through images (*lower row*)

Table 9 Iodine attenuation at different kVp imaging

	140 kVp	120 kVp	100 kVp	80 kVp	70 kVp
Iodine attenuation compared to 120 kVp	− 25 % attenuation	–	+25 % attenuation	+50 % attenuation	+70 % attenuation

Other limitations are also observed. At lower kVp, the "signal" from calcium is also increased, the blooming effect of vascular calcifications and metal (valve prostheses, wires, etc.) is more pronounced, and beam-hardening artifacts may appear worse. The iodine concentration in small vessels and along the periphery of vessels is also less than in the center of large vessels. Further, cardiovascular CT is usually reviewed interactively at a 3D workstation. Many of the 3D/4D post-processing and visualization techniques utilized in clinical practice, such as maximum intensity projection (MIP), inherently amplify (or sum) image noise across the slab thickness. In this scenario, small vessels can be completely obscured by surrounding image noise.

6.2.2 Iterative Reconstruction Techniques

Recent advances in computing processor speed and image reconstruction algorithms have allowed the use of iterative reconstruction (IR) techniques to improve CT image quality. A full discussion of these techniques is beyond the scope of this chapter; however, brighter vessels and borders may be more sharply defined with IR techniques, which could be a benefit for smaller vessel assessment. Poorly opacified vessels, however, may be more difficult to define or distorted by artifacts. The use of IR techniques has yielded images with lower noise to be acquired at lower patient dose (Leipsic et al. 2010). Newer model-based IR (MBIR) techniques allow

even more substantial patient dose and noise savings while maintaining diagnostic image quality (Katsura et al. 2012).

Conclusion

A basic understanding of early contrast medium dynamics provides the foundation for the design of current and future CM injection protocols for various clinical applications of thoracic MDCT. Additionally, a thorough knowledge of the technical and safety aspects of the injection equipment and CM used is necessary. Special considerations in patients with chronic kidney disease can be employed to optimize image quality and promote patient safety. Recent advances in scanner technology and image reconstruction algorithms allow further refinement of image quality and patient radiation dose. With these tools at hand, CM utilization can be optimized toward the clinical necessities while exploiting the full capabilities of latest and continuously evolving MDCT technology.

References

Altmann DB, Zwas D, Spatz A, Bergman G, Spokojny A, Riva S, Sanborn TA (1997) Use of the contrast volume to estimated creatinine clearance ratio to predict renal failure after angiography. J Interv Cardiol 10: 113–119

Bae KT, Heiken JP, Brink JA (1998a) Aortic and hepatic contrast medium enhancement at CT. Part I. Prediction with a computer model. Radiology 207:647–655

Bae KT, Heiken JP, Brink JA (1998b) Aortic and hepatic contrast medium enhancement at CT. Part II. Effect of reduced cardiac output in a porcine model. Radiology 207:657–662

Bellin MF, Jakobsen JA, Tomassin I et al (2002) Contrast medium extravasation injury: guidelines for prevention and management. Eur Radiol 12:2807–2812

Birnbaum BA, Nelson RC, Chezmar JL et al (1999) Extravasation detection accessory: clinical evaluation in 500 patients. Radiology 212:431–438

Dawson P (1998) Does injection rate affect the tolerance? In: Dawson PH, Clauss W (eds) Contrast media in practice : questions and answers. Springer Verlag, New York, pp 135–136

Dawson P, Blomley MJ (1996a) Contrast agent pharmacokinetics revisited: I. Reformulation. Acad Radiol 3(Suppl 2):S261–S263

Dawson P, Blomley MJ (1996b) Contrast media as extracellular fluid space markers: adaptation of the central volume theorem. Br J Radiol 69:717–722

Fleischmann D (2002) Present and future trends in multiple detector-row CT applications: CT angiography. Eur Radiol 12:S11–S16

Fleischmann D, Hittmair K (1999) Mathematical analysis of arterial enhancement and optimization of bolus geometry for CT angiography using the discrete fourier transform. J Comput Assist Tomogr 23:474–484

Fleischmann D, Ringl H, Nowotny R et al (1997) Streak artifacts arising from the superior vena cava in contrast enhanced CT: qualitative and quantitative assessment. Eur Radiol 7:285

Fleischmann D, Rubin GD, Bankier AA et al (2000) Improved uniformity of aortic enhancement with customized contrast medium injection protocols at CT angiography. Radiology 214:363–371

Fleischmann D, Hallett RL, Rubin GD (2006) CT angiography of peripheral arterial disease. J Vasc Interv Radiol 17(1):3–26

Foley WD (2002) Special focus session: multidetector CT: abdominal visceral imaging. Radiographics 22:701–719

Gurm HS, Dixon SR, Smith DE, Share D, Lalonde T, Greenbaum A, Moscucci M (2011) Renal function-based contrast dosing to define safe limits of radiographic contrast media in patients undergoing percutaneous coronary interventions. J Am Coll Cardiol 58:907–914

Haage P, Schmitz-Rode T, Hubner D et al (2000) Reduction of contrast material dose and artifacts by a saline flush using a double power injector in helical CT of the thorax. AJR Am J Roentgenol 174:1049–1053

Hittmair K, Fleischmann D (2001) Accuracy of predicting and controlling time-dependent aortic enhancement from a test bolus injection. J Comput Assist Tomogr 25:287–294

Hopper KD (1996) With helical CT, is nonionic contrast a better choice than ionic contrast for rapid and large IV bolus injections? AJR Am J Roentgenol 166:715

Hopper KD, Mosher TJ, Kasales CJ et al (1997) Thoracic spiral CT: delivery of contrast material pushed with injectable saline solution in a power injector. Radiology 205:269–271

Jacobs JE, Birnbaum BA, Langlotz CP (1998) Contrast media reactions and extravasation: relationship to intravenous injection rates. Radiology 209:411–416

Johnson PT, Johnson GM, Fishman EK (2014) IV contrast administration with dual source 128-MDCT: a randomized controlled study comparing 18-gauge nonfenestrated and 20-gauge fenestrated catheters for catheter placement success, infusion rate, image quality, and complications. AJR Am J Roentgenol 202:1166–1170

Katayama H, Yamaguchi K, Kozuka T et al (1990) Adverse reactions to ionic and nonionic contrast media. A report from the Japanese committee on the safety of contrast media. Radiology 175:621–628

Laskey WK, Jenkins C, Selzer F, Marroquin OC, Wilensky RL, Glaser R, Cohen HA, Holmes DR Jr (2007) Volume-to-creatinine clearance ratio: a pharmacokinetically based risk factor for prediction of early creatinine increase after percutaneous coronary intervention. J Am Coll Cardiol 50:584–590

Leggett RW, Williams LR (1995) A proposed blood circulation model for reference man. Health Phys 69:187–201

Leipsic J, Ngueyn G, Brown J et al (2010) A prospective evaluation of dose reduction and image quality in chest CT using adaptive statistical iterative reconstruction. AJR Am J Roentgenol 194(1):191–199

Katsura M, Matsuda I, Akahane M et al (2012) Model-based iterative reconstruction technique for radiation dose reduction in chest CT: comparison with the adaptive statistical iterative reconstruction technique. Eur Radiol 22(8):1613–1623

Levey AS, Stevens LA, Schmid CH, Zhang YL, Castro AF 3rd, Feldman HI, Kusek JW, Eggers P, Van Lente F, Greene T, Coresh J, Ckd EPI (2009) A new equation to estimate glomerular filtration rate. Ann Intern Med 150:604–612

McDonald JS, McDonald RJ, Carter RE, Katzberg RW, Kallmes DF, Williamson EE (2014) Risk of intravenous contrast material-mediated acute kidney injury: a propensity score-matched study stratified by baseline-estimated glomerular filtration rate. Radiology 271:65–73

Nakayama M, Yamashita Y, Oyama Y et al (2000) Hand exercise during contrast medium delivery at thoracic helical CT: a simple method to minimize perivenous artifact. J Comput Assist Tomogr 24:432–436

Nelson RC, Anderson FA Jr, Birnbaum BA et al (1998) Contrast media extravasation during dynamic CT: detection with an extravasation detection accessory. Radiology 209:837–843

Newton TH, Potts DG (1981) One of the titles. In: Newton TH, Potts DG (eds) Radiology of the skull and brain: technical aspects of computed tomography. Mosby, Saint Louis

Nyman U, Bjork J, Aspelin P, Marenzi G (2008) Contrast medium dose-to-gfr ratio: a measure of systemic exposure to predict contrast-induced nephropathy after percutaneous coronary intervention. Acta Radiol 49:658–667

Oh LC, Lau KK, Devapalasundaram A, Buchan K, Ardley N, Huynh M (2014) Efficacy of 'fine' focal spot imaging in ct abdominal angiography. Eur Radiol 24:3010–3016

Rubin GD, Lane MJ, Bloch DA et al (1996) Optimization of thoracic spiral CT: effects of iodinated contrast medium concentration. Radiology 201:785–791

Sheiman RG, Raptopoulos V, Caruso P et al (1996) Comparison of tailored and empiric scan delays for CT angiography of the abdomen. AJR Am J Roentgenol 167:725–729

Sherwin PF, Cambron R, Johnson JA, Pierro JA (2005) Contrast dose-to-creatinine clearance ratio as a potential indicator of risk for radiocontrast-induced nephropathy: correlation of d/crcl with area under the contrast concentration-time curve using iodixanol. Invest Radiol 40:598–603

Solomon J, Wilson J, Samei E (2015) Characteristic image quality of a third generation dual-source MDCT scanner: Noise, resolution, and detectability. Med Phys 42(8):4941–4953.

Van Hoe L, Marchal G, Baert AL et al (1995) Determination of scan delay-time in spiral CT-angiography : utility of a test bolus injection. J Comput Assist Tomogr 19:216–220

Weber PW, Coursey CA, Howle LE, Nelson RC, Nichols EB, Schindera ST (2009) Modifying peripheral IV catheters with side holes and side slits results in favorable changes in fluid dynamic properties during the injection of iodinated contrast material. AJR Am J Roentgenol 193:970–977

Acquisition Protocols for Thoracic CT

Denis Tack and Vartika Appiah

Abstract

Technical parameters for MDCT acquisitions of the thorax are quite numerous. These are usually set by default in acquisition protocols provided by the manufacturers. The aim of this chapter is to list and detail the parameters chosen for CT acquisitions of the chest and heart in order to adapt them accordingly to specific clinical conditions. A historical review of these protocols since the early 1980s is presented. Parameters influencing the radiation dose have been mentioned in this chapter but are detailed out further in another chapter of this edition.

1 Introduction

The remarkable improvement of CT technology over the past 20 years has enabled us to overcome the two major challenges of CT for imaging the lungs and the heart: spatial resolution in three dimensions and speed. Although this book refers to multidetector CT of the thorax, we will begin our technical description with a short historical review of the performances of single-detector CT technology for imaging the lungs. We will then proceed with the description of CT protocols for imaging on one hand the lungs and mediastinum and, on the other hand, those for imaging the heart.

D. Tack, MD, PhD (✉) • V. Appiah, MD
Department of Radiology,
Epicura – Hopital de la Madeleine,
Rue Maria Thomée, 1, Ath 7800, Belgium
e-mail: denis.tack@skynet.be

2 Historical Review of Acquisition Protocols for Thoracic CT

2.1 The Era of Single-Detector CT: 1980–1999

In the 1980s, the rotation time of single-detector scanners ranged between 2 and 5 s, and each rotation provided one slice. The cycle time between two acquisitions was approximately 25 s. Between two slice acquisitions, the table had to be moved to the next planned *z*-axis (caudocranial) position. This acquisition mode is known as being sequential. Two possible slice thicknesses could be used but were usually not combined: thick-section CT and thin-section CT.

U.J. Schoepf, F.G. Meinel (eds.), *Multidetector-Row CT of the Thorax*, Medical Radiology,
DOI 10.1007/978-3-319-30355-0_4

2.1.1 Thick-Section Chest CT

Imaging the entire chest required 30 acquisitions of 10 mm thick slices, and this was named the "standard" or "routine" chest CT protocol. The slices were contiguous and in ideal conditions, the entire chest was imaged without loss of anatomical or clinical information. There were two challenges for obtaining a perfect standard CT of the chest: the patient had to be able to take 30 consecutive breath holds of 5 s in full inspiration (total lung capacity), and the different breath holds had to be reproducible between slices. If not the case, lesions such as pulmonary nodules up to 3 cm could be missed on axial slices although seen on the topogram (scout view). The information yielded by thick-section CT imaging was also limited because of the slice thickness and its partial volume effect. Small pulmonary nodules, previously named "micronodules," could be missed because their attenuation was averaged with the air contained in the same slice. Despite all, this technology had enabled substantial advances in lung cancer staging (Frederick 1984; Graves et al. 1985; Brion 1985).

In the early 1990s, the new scanner generation was improved by a higher rotation speed, enabled by the continuous rotation of the tube and detectors and interrupted only for a scout view or by the end of the procedure. The acquisition time for obtaining one slice in the sequential mode was 1–2 s, the table movement from one position to the next one was very quick (1 s), and one was able to perform cluster acquisitions, that is, to obtain ten slices within one single full inspiration of 30 s. Thus, the entire chest could be obtained in three cluster acquisitions of 10 mm thick contiguous slices. However, in order to reduce the partial volume effect, the slice thickness usually selected was 5 mm, and six cluster acquisitions were needed to cover the 30 cm range of the adult chest.

Reducing the number of breath holds improved the patients' collaboration and minimized the risk of missing lesions by inadequate or nonreproducible breath holds.

The 1990s saw a real technical revolution that combined the advantages of the continuous rotation of the tube and detector row to perform volumetric acquisitions spirally (also known as helical mode). This technique was developed by a German physicist Willi Kalender (Wikipedia – 2006).

This technique was first applied to single-detector scanners in the 1990s and enabled the acquisition of the entire chest in one single breath hold of 17–35 s depending on the slice collimation and pitch factor used (collimation: 10 mm versus 5 mm; pitch: 1.0:1–1.5:1). Once the volume is acquired, one was able to reconstruct CT slices from the raw data with the nominal slice thickness of the acquisitions and with a free selection of the increment. This spiral mode improved significantly the detection of small pulmonary lesions (Remy-Jardin 1993).

The helical mode also introduced the option of post processing multiplanar reformats (MPR) and allowed the beginning of a 3D viewing of data. However, the resolution in the caudocranial axis (the z-axis) was still weak when scanning the entire chest because of the relatively high slice thickness used for helical acquisitions. An example of the progressive improvement of the *z*-axis resolution between the single-detector CT generation and a modern MDCT acquisition is shown in Fig. 1. Thus, 3D imaging of the lung was first developed with a restricted lung coverage, mainly for imaging pulmonary arteriovenous malformations (Remy 1994). Nevertheless, the helical mode enabled the demonstration of many new major clinical diagnoses and particularly that of thromboembolic disease (Remy-Jardin 1992; 1996a).

2.1.2 Thin-Section Chest CT

In order to investigate the lung architecture, the partial volume effect of thick-section CT had to be overcome. Researchers investigated and validated a new technique: the high-resolution CT (HRCT) characterized by a slice thickness of 1–2 mm (Mayo 1987; Zerhouni 1985; Meziane 1988). As 300 slices would have been needed with a cycle time of 25 s per slice, the technique was not based on contiguous slices but on a sample of 25–30 slices with a gap of 10 mm between slices. Correlation with pathology was very promising for the diagnosis and follow-up of interstitial lung diseases.

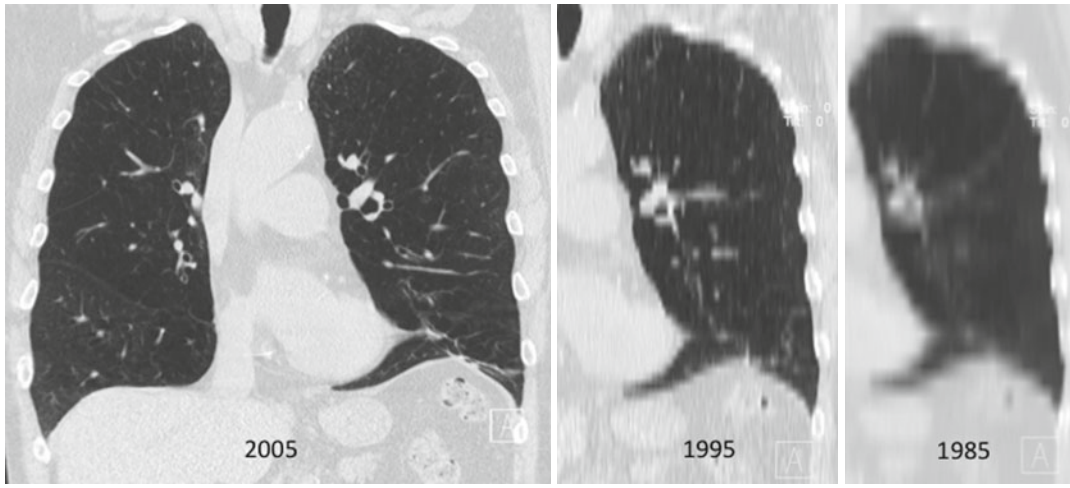

Fig. 1 Illustration of the caudocranial resolution obtained in *2005* with a multidetector CT, in *1995* with a single-detector CT reconstructing images with 5 mm thickness, and in *1985* with a single-detector CT acquiring 100 mm thick slices

In the 1990s, the thin-section helical acquisition technique was thereafter also used for obtaining 3D images and maximum intensity projections of the lung parenchyma for detecting micronodular patterns (Remy-Jardin 1996b) and for assessing vessels in CT angiography (Diederichs 1996).

2.2 The Era of Multidetector CT: From 2000

The end of year 1999 saw the dawn of a technological revolution in the multidetector CT. The new introduced CT devices were equipped with four detector rows. This enabled to provide simultaneously four slices per rotation. The rotation time had also been improved and was now reduced to 0.5 s per rotation. The typical collimations available for scanning the thorax were 4 × 1mm or 4 × 1.25 mm depending on the manufacturer and 4 × 2.5 mm. With a pitch factor of 1.5:1, the acquisition time on the entire chest (30 cm *z*-coverage) using a collimation of 4 × 1 mm and a rotation time of 0.5 s was 25 s. With this collimation, the entire chest was reconstructed with 250–300 overlapping thin sections (i.e., 1.5 mm thickness and 1.2 mm slice interval). For the first time since the invention of CTs in the 1970s, the chest could be entirely acquired with a HRCT technique. By sharing the data from two or more adjacent detector rows, these scanner devices were also able to reconstruct thick sections as used for "standard" or "routine" CT. The selection of the reconstruction section thickness was open, provided that this thickness was equal or superior to the nominal collimation at acquisition.

The radiation dose of 6 mSv delivered by a 4 × 1mm helical acquisition roughly corresponded to the sum of the doses delivered for routine (4.5 mSv) and for HRCT (1.5 mSv) examinations with the single-detector CT. However, in the case of HRCT examinations only, the multidetector scanners were not able to acquire in sequential mode with 1 mm collimation but used a 4 × 1 mm collimation with a radiation dose of 4 mSv. Thus, the sequential mode gradually gave place to the helical mode. In 2010, according to a survey on technique and radiation dose, very few of chest radiologists participating were still using the sequential acquisition mode in their routine practice (Molinari 2013).

The major breakthrough of the first generation of multidetector scanners was, therefore, to provide 3D imaging in routine with a reasonable acquisition time.

Further development in the multidetector technology was based on an increase in the num-

ber of detector rows and in the X-ray beam width. From 2 cm in 2002 with the 16 channel MDCT, the X-ray beam width rapidly increased to 4 cm (64 detector rows) and then to 8 cm (128 detector rows) and finally to 16 cm (320 detector rows) in 2007.

With a further improved rotation time (0.3 s/rotation), the 2010 scanner devices with 64 detector rows were able to scan the entire thorax in 2–3 s. This enhancement dramatically reduced the motion artifacts and the resulting number of low-quality acquisitions, as compared to the four-detector-row device from the early 2000.

The latest improvement in terms of acquisition speed was given by the dual-source technology. Using simultaneously two X-ray sources and 4 cm-wide detector rows with a 90° gap between them, and using pitch factor of 3.2:1, the entire chest could be scanned in helical mode within 0.3 s. Thus, the motion artifacts from breathing and even those from cardiac movements were almost no longer visible (Schulz 2012) while maintaining a limited radiation dose (Amacker 2012).

It is also possible to acquire the thorax using two X-ray sources with two different tube potentials: this technique is named dual-energy CT (DECT) and will be briefly discussed hereafter.

3 Acquisition Protocols for the Lungs and Mediastinum

The clinical analysis of the lungs, pulmonary vessels, and the mediastinum requires both resolution and speed. Thin sections provide the resolution, while the large detector arrays together with a high rotation speed provide the temporal resolution.

3.1 Scan Parameters of Routine CT and HRCT Examinations

3.1.1 Slice Thickness

In order to reduce the noise in reconstructed images, the general rule is to scan with thin collimation and to reconstruct images with thickness slightly greater than that of the collimation. In practice, with a 64-detector-row scanner device, the collimation is 64 × 0.6 mm, 64 × 0.625 mm, or 64 × 0.5 mm and depends on the device and manufacturer. The reconstructed images used for HRCT analysis and for volumetric analysis in 3D can, hence, be thicker than the nominal collimation and set at 1.0 mm. The reconstructed images used for the picture archiving and communicating system (PACS) and sent to the patient's record are 3–5 mm thick. This thickness is justified as being a good compromise for reducing the partial volume effect and to minimize the number of slices sent to medical records and allows to cut down on archiving costs.

3.1.2 Slice Increment

Volumetric thin-section datasets require an overlapping of 20–50 %. The reconstruction interval of thin slices is usually adjusted between 0.5 mm and 0.8 mm. Reducing this interval yields a greater number of images. A 30 cm acquisition will thus result in 400 thin-section images.

3.1.3 Reconstruction Algorithm

The reconstruction algorithms providing the best visualization of the lung architecture is the high-frequency one (Zwirewich 1989). The standard or smooth algorithm, on the other hand, provides the lowest noise and the best soft tissue resolution in the mediastinum. Each manufacturer provides many different algorithms.

Consequently, each chest CT will be reconstructed twice: firstly for the lung parenchyma and then for the mediastinum.

The principle of assigning a high-frequency algorithm to the lungs and a soft one to the mediastinum has been globally maintained when introducing iterative reconstruction techniques for CT images (Singh 2011; Pontana 2013).

3.1.4 Window Settings

As a general rule in CT, the window center (WC) has to be set at the average HU of the observed tissues, and the window width (WW) has to be large enough to visualize all the tissues of the observed organ or body region. In DICOM format, a window setting can always be modified.

Only default window settings are discussed below.

The mediastinal reconstructions with soft tissue kernel will be associated with a default window setting typically of 40/400 (WC/WW), and the lung reconstructed images in high-frequency algorithms will be associated with a default window setting typically of −600/1600 (WC/WW).

3.1.5 Tube Potential

The tube potential used for CT acquisitions of the thorax was historically set at 120 KV. Since this parameter highly influences the radiation dose delivered, it is recommended to optimize it. Radiation dose optimization is discussed further in the book by Dr Paul Narinder.

As a general rule, examinations performed with iodine contrast injection should take advantage of higher iodine absorption at lower tube potential (100 or 80 KV and even lower in pediatric patients) (Sigal-Cinqualbre 2004; Durand 2014).

3.1.6 Tube Current: Automatic Exposure Control

The tube current has to be adapted to the patient's attenuation. All modern CT scanners built after 2005 are equipped with an automatic exposure control (AEC) device. This device varies from one manufacturer to another. A good comprehension of the functioning mechanism of the device by the radiology team is important in order to maximize its efficiency. All systems are required to set default image quality parameters, expressed in "quality reference mAs" with Siemens scanners, in mAs with Philips scanners and in noise index with GE and Toshiba scanners. How AEC interacts with tube current falls outside the framework of this chapter, but the absolute rule is to switch them on to reduce the delivered mAs and, hence, dose in thin patients and to increase them in large and obese patients (Mulkens 2005).

3.1.7 Pitch Factor

According to Silverman et al., the beam pitch factor corresponds to the table feed by rotation divided by the X-ray beam width (Silverman 2001). With single-detector devices, the pitch factor could be set to 1.5:1 without significant degradation of the slice thickness and the partial volume effect of the reconstructed slices. However, the tube current has to be increased while increasing the pitch in order to compensate for reduced signal per slice. Pitch factor definition did not change between single-detector CT devices and MDCT devices. It is however very important to understand that the management of tube current while modifying the table feed (and so the pitch) differs between manufacturers. With Siemens and Philips devices, an increase in table feed (and pitch) is automatically compensated by an increase in tube current in order to maintain the same effective tube current time product (expressed in mAs eff) defined as the tube current time product divided by the pitch. With these scanners, the slice collimation, the image noise, and the radiation dose per slice are kept constant when modifying the table feed. Table feed can thus be adjusted by the user in order to adapt the acquisition duration to the patient's respiratory condition.

With GE and Toshiba scanners, the tube current is not automatically adapted to the table feed. Hence, any modification in the pitch factor has to be compensated by a manual adjustment of the tube current time product (mAs). In addition, the slice thickness is highly sensitive to pitch modifications on these devices. As this is practically quite complex and not intuitive at all, the users of these devices never change the default pitch factor of the CT acquisition protocol.

3.1.8 Use of Iodine Contrast

The use of iodine contrast injection for CT examinations of the chest depends on the clinical indication. While an iodine injection is mandatory for CT pulmonary angiography and for ruling out pulmonary embolism, it is not compulsory in numerous other indications. Iodine is also used in chest examinations combined with the abdomen and pelvis for staging of carcinoma. Iodine injections are not necessary for assessing infiltrative lung disease where the key of the image analysis relies on the high resolution of the lung parenchyma and architecture. In acute chest pain, unenhanced acquisition is required before CTA in order to detect intramural aortic hematoma (Lemos 2014).

4 Acquisition Protocols for CT Pulmonary Angiography (CTPA)

4.1 General Rules

The acquisition and reconstruction parameters suited for routine MDCT of the thorax with a modern 64-multidetector device and as listed above are sufficient to provide excellent analysis of the lung vessels. The technical success in CTPA acquisitions lies in the perfect enhancement of the pulmonary vessels. It is generally admitted that a minimum attenuation of 250 HU has to be obtained in the pulmonary arteries.

4.2 Contrast Injection Optimization for CTPA

The mechanisms of contrast injection and its effects on vessel and parenchyma enhancement are important to understand in iodine injection optimization (Fleischmann 2003). The volume of injected iodine for a CTPA examination is often too high, and in numerous instances, the contrast power injector is still running while the acquisition is already finished. With CT scanner devices necessitating 20 or 25 s for an acquisition, the volume of iodine contrast used was often 120–140 ml of 35–38 % iodine and a flow rate of 3–5 cc per second. The total iodine load seen in the literature (Remy-Jardin 1996a, b) was around 35 g. However, with modern scanners the injected volume and the corresponding iodine load have to be reduced.

4.3 Method for Reducing the Iodine Load in CTPA

Firstly, the Kilovolt has to be lowered from 120 to 100 or even 80 if the patient weighs less than 65 Kg.

Secondly, the flow rate should be adapted to the patient: an old patient with possible heart disease and altered left ventricular ejection fraction would need 3 cc/s flow rate with a high-contrast iodine (35–40 g/100 ml iodine). A young patient, and, in particular, a pregnant patient, will need a much higher flow rate of 5–6 cc/s (Litmanovich 2014).

The acquisition box should then be set on the scanner scout views (topogram), and the acquisition time needed should be noted (typically 12 s with a 16 MDCT device, 2 s with a 128 MDCT device, 1 s or less with a high-pitch acquisition).

The acquisition time, the time for breath-hold instruction (typically 5 s) duration, and a reserve of 5 s should all be added. The sum will be around 12 s.

The total time when multiplied by the flow rate (12 s × 4 cc/s = 48 cc) calculates the total volume of iodine contrast to obtain a perfect vessel enhancement.

In practice, a CTPA examination in a patient with an impaired renal function could be obtained with 30 cc iodine volume, in particular if using a tube potential of 80 KV.

The bolus tracking ROI in the main pulmonary artery should be set at a threshold of 80–120 HU, with a delay of 10 s before beginning the bolus tracking acquisition.

Finally, and most importantly, the patient must be trained in order to avoid a Valsalva maneuver. The latter is the main cause of non-enhancement (11 % of CTPA examinations) and is due to a patent foramen ovale (Henk 2003; Revel 2008). In order to avoid the opening of a patent foramen ovale from a Valsalva maneuver, the patient can be asked to simply not breathe and not to take a deep inspiration.

Note: the more the Kilovolt is lowered, the lower the iodine load is needed.

The volume of iodine can be reduced up to 44 % in a 100 KV acquisition as compared to a 120 KV acquisition (Wang 2014). Using a new scanner device capable of scanning adult patients at 70 KV allows the iodine load to be reduced to less than 20 cc for a perfect CTPA examination.

5 Acquisition Protocols for Coronary CT Angiography

Coronary CT angiography (CCTA) requires both high temporal resolution and high spatial resolution. Additionally, the ideal CCTA should also be able to get rid of the blurring next to the calcium plaques. This challenge has been overcome with

the newest CT devices. Describing acquisition protocols is non-exhaustible if we were to cover all details of all CT devices and their pitfalls. Nevertheless, the reduction of the radiation dose being a huge challenge in cardiac CT and the protocol optimization with regard to radiation dose has been addressed in a different chapter.

One common rule is shared by the CTPA acquisition protocols: they all need ECG gating (Mahesh 2007).

There are four main acquisition protocols for CCTA: prospective sequential scanning, retrospective helical scanning, high-pitch scanning, and volumetric scanning (Fig. 2). In order to obtain a perfect delineation of coronary arteries and to avoid movement artifacts, the heart rate must be as low as possible, even with the fourth generation of dual-source MDCT devices (Gordic 2014). The safety, efficacy, and indications of beta-adrenergic receptor blockers to reduce heart rate prior to coronary CT angiography have been recently reviewed (Mahabadi 2010). Unless contraindicated, the use of beta-blockers should always be considered in heart rates exceeding 60 beats per minute (BPM). This will impact on both the quality and the radiation dose optimization of the CCTA protocol.

The tube potential must be as low as possible to optimize the iodine signal in the coronary arteries, and the 2015 limit has been fixed at 30 ml iodine contract volume in a 70 KV CCTA tube potential (Meyer 2014; Zhang 2014).

In ideal conditions, i.e., in patients with low heart rate of 50 BPM, all CCTA acquisitions will provide excellent image quality, and the choice of the acquisition mode will be driven by the need for radiation dose optimization. As a general rule, high-pitch CCTA delivers lower radiation doses than sequential (step-and-shoot) acquisitions and even lower than helical acquisitions with retrospective ECG gating.

Reconstructions for CCTA will always be as thin as possible while using the same rules for noise reduction as for any CT acquisitions: the here abovementioned "scan thin–reconstruct thick" rule. In practice, the detector collimation will be of 0.6 mm and the reconstructed thickness will be set at 0.7 mm. The increment can set at 0.4 or 0.5 mm.

The tube current will be set by the AEC system. It is not recommended to lower the tube current in order to reduce the radiation dose because there is a risk of missing lesions in distal arteries.

The reconstruction algorithms are specific to each manufacturer and are optimized in order to provide a good compromise between spatial and soft tissue resolution.

Algorithms with a high frequency (more spatial resolution and more image noise) are suitable for assessing in-stent stenosis. Iterative image reconstruction algorithms in coronary CT angiography are useful to improve the detection of lipid-core plaque (Puchner 2014) and the image quality (Oda 2014).

The clinical limiting factors of CCTA are high heart rates (unless one uses a dual-source scanner), high calcium scores (long history of diabetes mellitus in elderly), obesity (need for extremely high tube power), and, most importantly, inability to collaborate for a breath hold of 10 s.

6 Acquisition Protocols for Dual-Energy CT

The principle of dual-energy CT acquisitions is to obtain data with various tube potentials. Ideally, in order to avoid movement artifacts, the two acquisitions must be obtained simultaneously. Currently, two manufacturers provide this technique. One manufacturer provides dual-energy acquisitions by using two X-ray sources and detector rows. One source uses a tube potential of 120 or 140 KV and the other source a tube potential of 80 KV. The fourth generation of dual-source scanner devices enables to select the tube potentials in a range of 70–150 KV with steps of 10 KV (Siemens Force, Forchheim, Germany). The second manufacturer, GE Healthcare, provides dual-energy technique with one single X-ray source. A generator electronically switches the tube energies from 80 KVp to 140 KVp to acquire dual-energy images. Raw data-based reconstructions enable to obtain images virtually from a single kilovolt peak source (Kang 2010).

A third manufacturer has developed the dual-energy technique by building two layers of detectors,

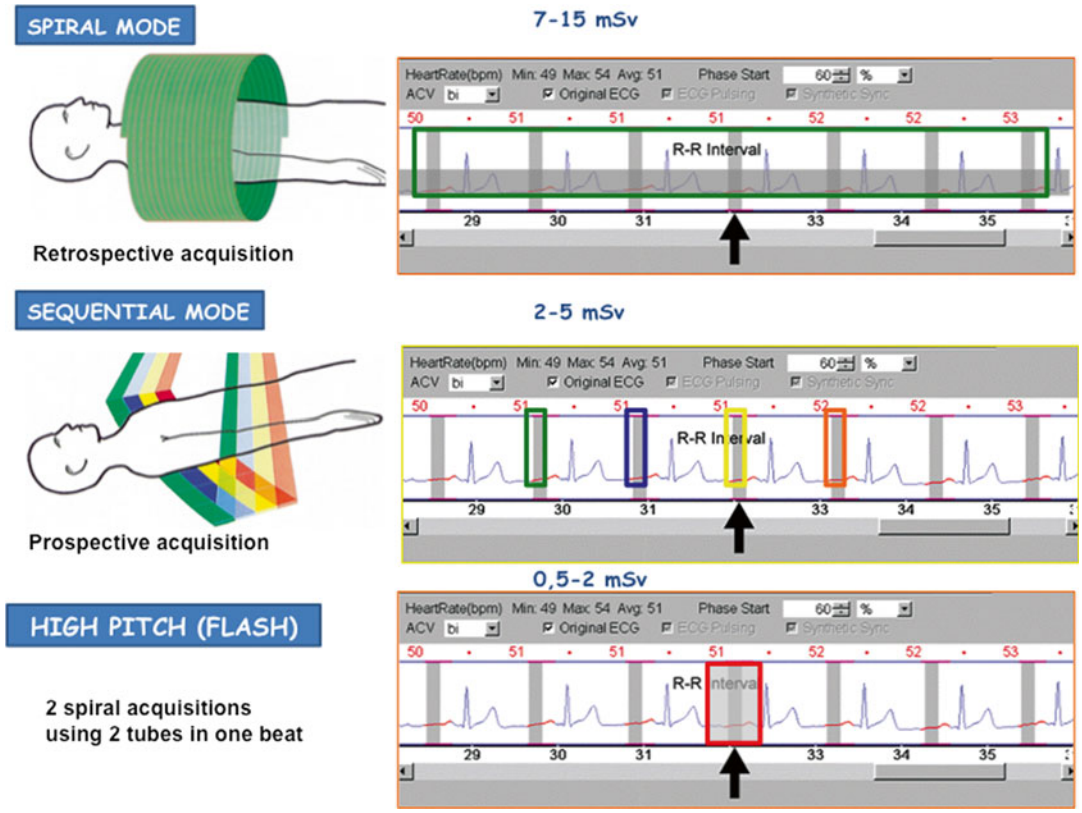

Fig. 2 Illustration of prospective (step-and-shoot) ECG gating, retrospective ECG gating (helical), and high-pitch (Flash) acquisitions for CT coronary angiography

one for soft beam located superficially and the second one for hard beam located behind the first one.

Practically, the manufacturers have prepared the dual-energy acquisition protocols and the user can adjust very few parameters. In principle, the dual-energy acquisitions are obtained with similar radiation dose, as would be single-energy CT acquisitions. This statement originally made by the manufacturers still needs to be confirmed in clinical trials.

7 Summary

Being aware of the different technical conditions with modern MDCT devices is a huge advantage. This allows having the adequate parameters to provide the best image and adapt them to specific clinical conditions when needed.

References

Amacker NA, Mader C, Alkadhi H, Leschka S, Frauenfelder T (2012) Routine chest and abdominal high-pitch CT: an alternative low dose protocol with preserved image quality. Eur J Radiol 81: e392–e397

Brion JP, Depauw L, Kuhn G, de Fracquen P, Friberg J, Rocmans P, Struyven J (1985) Role of computed tomography and mediastinoscopy in preoperative staging of lung carcinoma. J Comput Assist Tomogr 9(3):480–484

Diederichs CG, Keating DP, Glatting G, Oestmann JW (1996) Blurring of vessels in spiral CT angiography: effects of collimation width, pitch, viewing plane, and windowing in maximum intensity projection. J Comput Assist Tomogr 20:965–974

Durand S, Paul JF (2014) Comparison of image quality between 70 kVp and 80 kVp: application to paediatric cardiac CT. Eur Radiol 24(12):3003–3009

Fleischmann D (2003) High-concentration contrast media in MDCT angiography: principles and rationale. Eur Radiol 13(Suppl 3):N39–N43

Frederick HM, Bernardino ME, Baron M, Colvin R, Mansour K, Miller J (1984) Accuracy of chest computerized tomography in detecting malignant hilar and mediastinal involvement by squamous cell carcinoma of the lung. Cancer 54:2390–2395

Graves WG, Martinez MJ, Carter PL, Barry MJ, Clarke JS (1985) The value of computed tomography in staging bronchogenic carcinoma: a changing role for mediastinoscopy. Ann Thorac Surg 40:57–59

Gordic S, Husarik DB, Desbiolles L, Leschka S, Frauenfelder T, Alkadhi H (2014) High-pitch coronary CT angiography with third generation dual-source CT: limits of heart rate. Int J Cardiovasc Imaging 30(6):1173–1179

Henk CB, Grampp S, Linnau KF, Thurnher MM, Czerny C, Herold CJ, Mostbeck GH (2003) Suspected pulmonary embolism: enhancement of pulmonary arteries at deep-inspiration CT angiography—influence of patent foramen ovale and atrial-septal defect. Radiology 226:749–755

Kang MJ, Park CM, Lee CH, Goo JM, Lee HJ (2010) Dual-energy CT : clinical applications in various. Radiographics 30:685–699

Lemos AA, Pezzullo JC, Fasani P, Gullo M, Giannitto C, Lo Gullo R, Biondetti PR (2014) Can the unenhanced phase be eliminated from dual-phase CT angiography for chest pain? Implications for diagnostic accuracy in acute aortic intramural hematoma. AJR Am J Roentgenol 203:1171–1180

Litmanovich DE, Tack D, Lee KS, Shahrzad M, Bankier AA (2014) Cardiothoracic imaging in the pregnant patient. J Thorac Imaging 29:38–49

Mahabadi AA, Achenbach S, Burgstahler C, Dill T, Fischbach R, Knez A, Moshage W, Richartz BM, Ropers D, Schröder S, Silber S, Möhlenkamp S, Working group "Cardiac CT" of the German Cardiac Society (2010) Safety, efficacy, and indications of beta-adrenergic receptor blockade to reduce heart rate prior to coronary CT angiography. Radiology 257:614–623

Mahesh M, Cody DD (2007) Physics of cardiac imaging with multiple-row detector CT. Radiographics 27:1495–1509

Mayo JR, Webb WR, Gould R, Stein MG, Bass I, Gamsu G, Goldberg HI (1987) High-resolution CT of the lungs: an optimal approach. Radiology 163:507–510

Meyer M, Haubenreisser H, Schoepf UJ, Vliegenthart R, Leidecker C, Allmendinger T, Lehmann R, Sudarski S, Borggrefe M, Schoenberg SO, Henzler T (2014) Closing in on the K edge: coronary CT angiography at 100, 80, and 70 kV-initial comparison of a second-versus a third-generation dual-source CT system. Radiology 273:373–382

Meziane MA, Hruban RH, Zerhouni EA, Wheeler PS, Khouri NF, Fishman EK, Hutchins GM, Siegelman SS (1988) High resolution CT of the lung parenchyma with pathologic correlation. Radiographics 8:27–54

Molinari F, Tack DM, Boiselle P, Ngo L, Mueller-Mang C, Litmanovich D, Bankier AA (2013) Radiation dose management in thoracic CT: an international survey. Diagn Interv Radiol 19(3):201–209

Mulkens TH, Bellinck P, Baeyaert M, Ghysen D, Van Dijck X, Mussen E, Venstermans C, Termote JL (2005) Use of an automatic exposure control mechanism for dose optimization in multi-detector row CT examinations: clinical evaluation. Radiology 237:213–223

Oda S, Weissman G, Vembar M, Weigold WG (2014) Iterative model reconstruction: improved image quality of low-tube-voltage prospective ECG-gated coronary CT angiography images at 256-slice CT. Eur J Radiol 83:1408–1415

Pontana F, Pagniez J, Duhamel A, Flohr T, Faivre JB, Murphy C, Remy J, Remy-Jardin M (2013) Reduced-dose low-voltage chest CT angiography with sinogram-affirmed iterative reconstruction versus standard-dose filtered back projection. Radiology 267:609–618

Puchner SB, Ferencik M, Maurovich-Horvat P, Nakano M, Otsuka F, Kauczor HU, Virmani R, Hoffmann U, Schlett CL (2014) Iterative image reconstruction algorithms in coronary CT angiography improve the detection of lipid-core plaque – a comparison with histology. Eur Radiol 25:15–23

Remy-Jardin M, Remy J, Wattinne L, Giraud F (1992) Central pulmonary thromboembolism: diagnosis with spiral volumetric CT with the single-breath-hold technique – comparison with pulmonary angiography. Radiology 185:381–387

Remy J, Remy-Jardin M, Giraud F, Wattinne L (1994) Angioarchitecture of pulmonary arteriovenous malformations: clinical utility of three-dimensional helical CT. Radiology 191:657–664

Remy-Jardin M, Remy J, Giraud F, Marquette CH (1993) Pulmonary nodules: detection with thick-section spiral CT versus conventional CT. Radiology 187:513–520

Remy-Jardin M, Remy J, Deschildre F, Artaud D, Beregi JP, Hossein-Foucher C, Marchandise X, Duhamel A (1996a) Diagnosis of pulmonary embolism with spiral CT: comparison with pulmonary angiography and scintigraphy. Radiology 200:699–706

Remy-Jardin M, Remy J, Gosselin B, Copin MC, Wurtz A, Duhamel A (1996b) Sliding thin slab, minimum intensity projection technique in the diagnosis of emphysema: histopathologic-CT correlation. Radiology 200:665–671

Revel MP, Faivre JB, Letourneau T, Henon H, Leys D, Delannoy-Deken V, Remy-Jardin M, Remy J (2008) Patent foramen ovale: detection with nongated multi-detector CT. Radiology 249:338–345

Schulz B, Jacobi V, Beeres M, Bodelle B, Gruber T, Lee C, Bauer R, Kerl M, Vogl T, Zangos S (2012) Quantitative analysis of motion artifacts in high-pitch dual-source computed tomography of the thorax. J Thorac Imaging 27:382–386

Sigal-Cinqualbre AB, Hennequin R, Abada HT, Chen X, Paul JF (2004) Low-kilovoltage multi–detector row chest CT in adults: feasibility and effect on image quality and iodine dose. Radiology 231:169–174

Silverman PM, Kalender WA, Hazle JD (2001) Common terminology for single and multislice helical CT. AJR Am J Roentgenol 176:1135–1136

Singh S, Gilman MD, Shepard JO, Kalra MK, Hsieh J, Pien HH, Digumarthy SR (2011) Adaptive statistical iterative reconstruction technique for radiation dose reduction in chest CT: a pilot study. Radiology 259:565–573

Wang Y, Bolen M, Sydow G, Kottha A, Bullen J, Kemper C, Sydow G (2014) Adaptation of contrast injection cardiovascular CT. AJR Am J Roentgenol 203:1181–1191

Wikipedia – the free encyclopedia (2006) http://en.wikipedia.org/wiki/Willi_Kalender. Access on line on 8 Nov 2014

Zerhouni EA, Naidich DP, Stitik FP, Khouri NF, Siegelman SS (1985) Computed tomography of the pulmonary parenchyma. Part 2: interstitial disease. J Thorac Imaging 1:54–64

Zhang LJ, Qi L, Wang J, Tang CX, Zhou CS, Ji XM, Spearman JV, De Cecco CN, Meinel FG, Schoepf UJ, Lu GM (2014) Feasibility of prospectively ECG-triggered high-pitch coronary CT angiography with 30 mL iodinated contrast agent at 70 kVp: initial experience. Eur Radiol 24:1537–1546

Zwirewich CV, Terriff B, Müller NL (1989) High-spatial-frequency (bone) algorithm improves quality of standard CT of the thorax. AJR Am J Roentgenol 153: 1169–1173

CT Imaging of the Airways

Maxime Hackx and Pierre Alain Gevenois

Abstract

Abnormalities of the airways are found in a wide spectrum of diseases and conditions, with CT features that can overlap. CT features include bronchiectasis/bronchiolectasis, mucous plugging, bronchial wall thickening, and tree-in-bud pattern/centrolobular micronodules. They can be accurately assessed through image processing available on a console or workstation, such as MPR or VRT (SSD, minIP, and MIP). Recent advances in software have provided airway tree segmentation and virtual bronchoscopy navigation, as well as objective quantification of airway changes. Future developments in this objective quantification and in the reduction of the radiation dose are mandatory if CT is to play a more important role in the routine diagnosis, prognosis, and monitoring of airway diseases.

1 Introduction

During a single breath hold, computed tomography (CT) acquires volumetric raw data of the entire chest of a particular patient, including the airways from the first (i.e., the trachea) to the tenth generations (Montaudon et al. 2009). The images that are reconstructed from these raw data allow the radiologist to assess focal, diffuse, and large or small airway diseases. Small airways are defined as those with an internal diameter less than 2 mm, corresponding to airways from the fourth to the 14th generations of branching (Hackx et al. 2012), and are at least partially visible at CT. As volumetric data are acquired and as the majority of airway axes are not orthogonal to the acquisition plane, reformatted images can be obtained in various planes. On these planes, techniques to display selected voxels will increase the effectiveness of the radiologist's assessment. In addition, three-dimensional views of the airway tree and virtual bronchoscopy navigation (VBN) can also be displayed. Moreover, these three-dimensional views are sometimes coupled with dedicated algorithms that allow objective quantification of airway changes. Nowadays, objective quantification is a major area of investigation in CT of the airways, but as yet has no place in the

M. Hackx, MD • P.A. Gevenois, MD, PhD (✉)
Department of Radiology, Hôpital Erasme, Université libre de Bruxelles, 808 Route de Lennik, Brussels 1070, Belgium
e-mail: Maxime.Hackx@ulb.ac.be; pierre.alain.gevenois@erasme.ulb.ac.be

U.J. Schoepf, F.G. Meinel (eds.), *Multidetector-Row CT of the Thorax*, Medical Radiology,
DOI 10.1007/978-3-319-30355-0_5

routine assessment of airway diseases (at least partly because of radiation issues). Consequently, the other major field of investigation is radiation dose reduction.

The routine assessment of airways at CT is currently based on the depiction of several elementary airway CT features described in this chapter. As airways are involved in a wide spectrum of diseases, the depiction of a combination of various elementary airway CT features is common. However, in this chapter we detail a selection of important airway diseases and provide an overview of other conditions with airway CT features.

2 Scanning Protocol and Image Processing

2.1 Scanning Protocol

As there is no consensus on CT acquisition parameters, we provide here an example: collimation of ~0.6 mm, with tube current at 80 mA, tube potential at 120 kV, pitch of 1.4, and automatic exposure control switched on. Nevertheless, recent advances suggest that tube current could be reduced to 20 mA (Dijkstra et al. 2013) and tube potential to 80 kV when using CT of newer generation and iterative reconstructions (Kim et al. 2015).

There is also no consensus on the parameters for reconstructing the images from the raw data. Axial images with a slice thickness of ~1 mm and a reconstruction interval of ~0.5 mm obtained with a high-resolution reconstruction algorithm would probably be the most appropriate for imaging the airways. Intravenous injection of iodinated contrast material is unnecessary when the CT examination is specifically dedicated to imaging the airways.

2.2 Cine Viewing and Multiplanar Reformations

The analysis of axial images in cine mode allows the bronchial division to be followed to localize any airway lesion, and may serve as a road map for an endoscopy (Grenier et al. 2002). A recent study revealed, however, that the addition of VBN (see below) to conventional bronchoscopy improves the diagnosis performance for peripheral pulmonary lesions of 30 mm or smaller (Asano et al. 2015). Nevertheless, cine mode can also be applied to multiplanar reformations (MPR). MPR are indeed available in any plane (most frequently the coronal and sagittal planes), even along a particular airway. The MPR are immediately displayed on the console or workstation by loading the axial images. In comparison with axial images, VBN, and minimal-intensity projection (minIP), a recent study revealed that MPR are the most useful for evaluating airway stenosis and planning intervention (Sundakamura et al. 2011). For instance, they are particularly helpful in estimating the craniocaudal extension of an airway lesion (Figs. 1, 2, and 3).

2.3 Three-Dimensional Views and Virtual Bronchoscopy Navigation

Several volume-rendering techniques (VRT) allow three-dimensional views of the airways on the console or workstation: shaded surface display

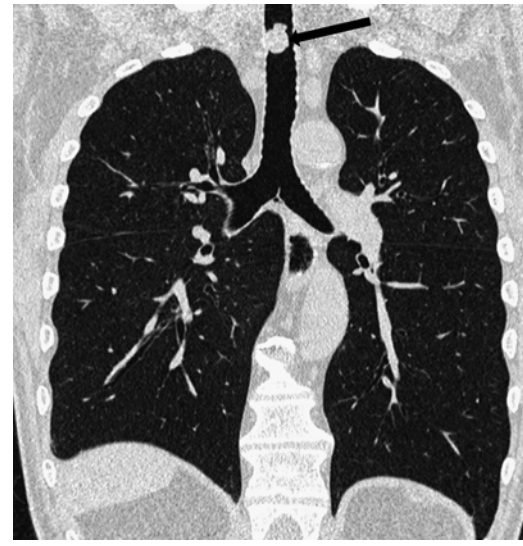

Fig. 1 Coronal reformation showing tracheal stenosis caused by a mass (*arrow*) in a 75-year-old patient

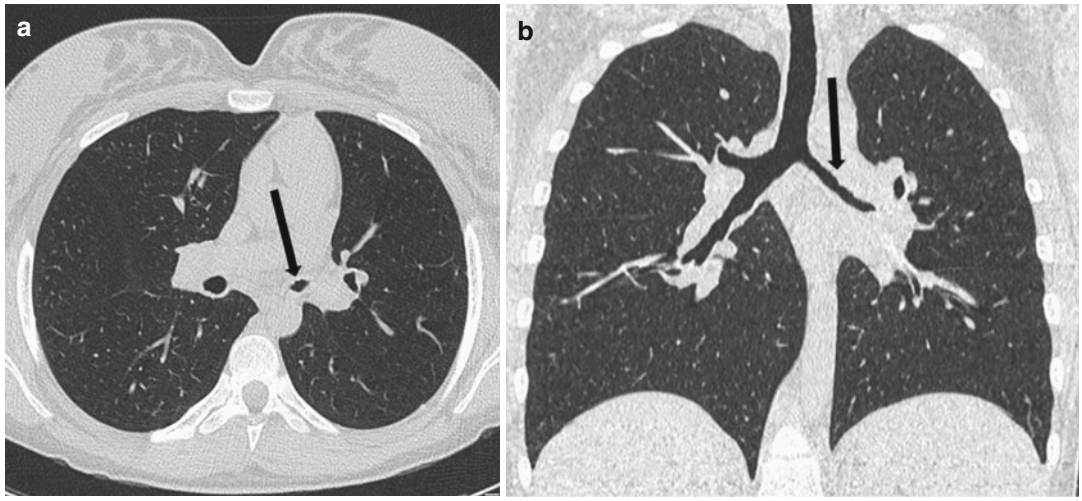

Fig. 2 (**a**) Axial image and (**b**) coronal reformation in a patient with granulomatosis with polyangiitis showing wall thickening of the left pulmonary bronchus causing bronchial stenosis (*arrows*) in a 25-year-old patient. The coronal reformation is helpful to estimate the craniocaudal extent of the stenosis

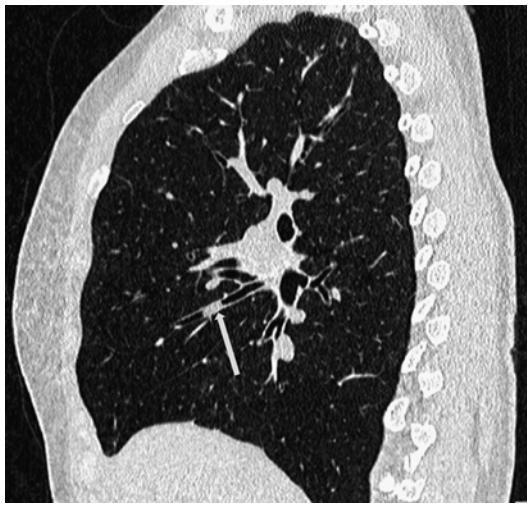

Fig. 3 Sagittal reformation showing mucous plugging (*arrow*) in a 47-year-old patient

(SSD), maximal-intensity projection (MIP), and minIP. All these VRT rely on mathematical formulas to determine for each voxel the portion of the volume data to display, and how that portion should be weighted. Differences in the images displayed are the result of variations in how voxels are selected and weighted (Calhoun et al. 1999). SSD is a process whereby apparent surfaces are determined within the volume data and an image representing the derived surfaces is displayed. For depiction of obstructive lesions in the airways, the accuracy of SSD is lower than that of axial images and MPR (Remy-Jardin et al. 1996). MIP and minIP are two processes whereby the voxels with, respectively, the maximal or minimal values are displayed. These techniques may be helpful in detecting subtle airway lesions, for instance an air bronchogram in a consolidation/ground-glass opacity (minIP), a mucoid impaction (MIP), or a tree-in-bud appearance of centrilobular nodules (MIP, Fig. 4). MinIP and MIP images can be displayed as two- or three-dimensional views (Fig. 5a). For SSD, the accuracy of MIP is lower than that of axial images and MPR for depicting airway obstructive lesions (Remy-Jardin et al. 1996). Nevertheless, VRT may increase confidence in diagnosing airway abnormalities (Ferretti et al. 2000) and should therefore be used as a complement to axial images and MPR.

Using other techniques, segmentation of the airway tree and labeling of the bronchi can be obtained. These techniques require various dedicated software not available on every console or workstation (Hackx et al. 2012). For segmentation of the airway tree, these software packages are based on different region-growing algorithms (Wood et al. 1995). These algorithms have in common that from a luminal seed point, all contiguous voxels within an

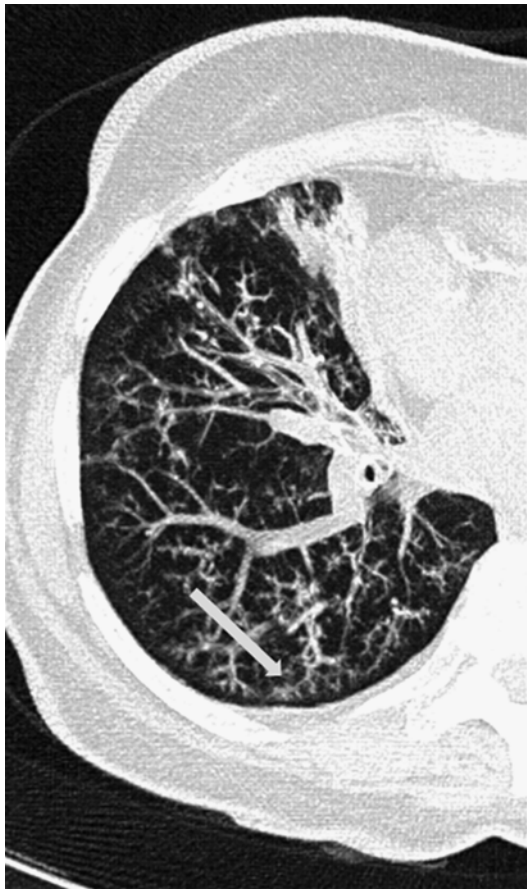

Fig. 4 Axial maximum-intensity projection of diffuse panbronchiolitis shows centrolobular micronodules in peripheral zones of the right lung in a 71-year-old patient. Note the tree-in-bud pattern (*arrow*)

attenuation value range specific for airway lumen are iteratively added. The results are then refined with mathematical formulas that differ between software suites. These results can be displayed as an airway tree (Fig. 5a) or as a bronchoscopy view allowing VBN (Fig. 6). These segmentations of the airway tree are also used as a first step before objective quantification of the airways' dimensions, as they allow determination of the axis of an airway and subsequently the determination of a plane orthogonal to this axis (measurement can be performed on a such plane) (Fig. 7). Other dedicated software shows promising results in labeling the bronchi up to the subsegmental level (i.e., fourth generation) (van Ginneken et al. 2008; Mori et al. 2009), which could be of interest for automatic quantification of airway changes.

2.4 Quantification of Airway Changes

Airway changes that occur in various diseases (see below) can be quantified subjectively or objectively by using dedicated software. In addition, this objective quantification can be direct (through measurements of morphologic changes in the airways) or indirect (through quantification of small airway obstruction).

2.4.1 Subjective Quantification

The severity of elementary airway CT features such as bronchiectasis/bronchiolectasis, mucous plugging, bronchial wall thickening, and tree-in-bud pattern/centrolobular micronodules can be graded. Such severity grading can be used, for example, in patients with cystic fibrosis (CF) or chronic obstructive pulmonary disease (COPD) (Brody et al. 2006; Hackx et al. 2015a). These grades of severity can then be converted into scores and correlated with pulmonary function (de Jong et al. 2004).

2.4.2 Objective Quantification

Measurements of Airway Morphologic Changes

Depending on the disease, morphologic changes of the airways may consist in modifications of the dimensions of their lumens, their walls, or both. These dimensions can be measured using dedicated software (Hackx et al. 2012) (Fig. 7). The majority of these software packages are based on algorithms that use the variation of the attenuation values between the bronchial lumen, the bronchial wall, and the pulmonary parenchyma. As an example, the Full-Width at Half-Maximum algorithm spreads rays 360° from a seed point in the lumen. Along each ray, the attenuation value profile is considered: as the ray enters the wall, the

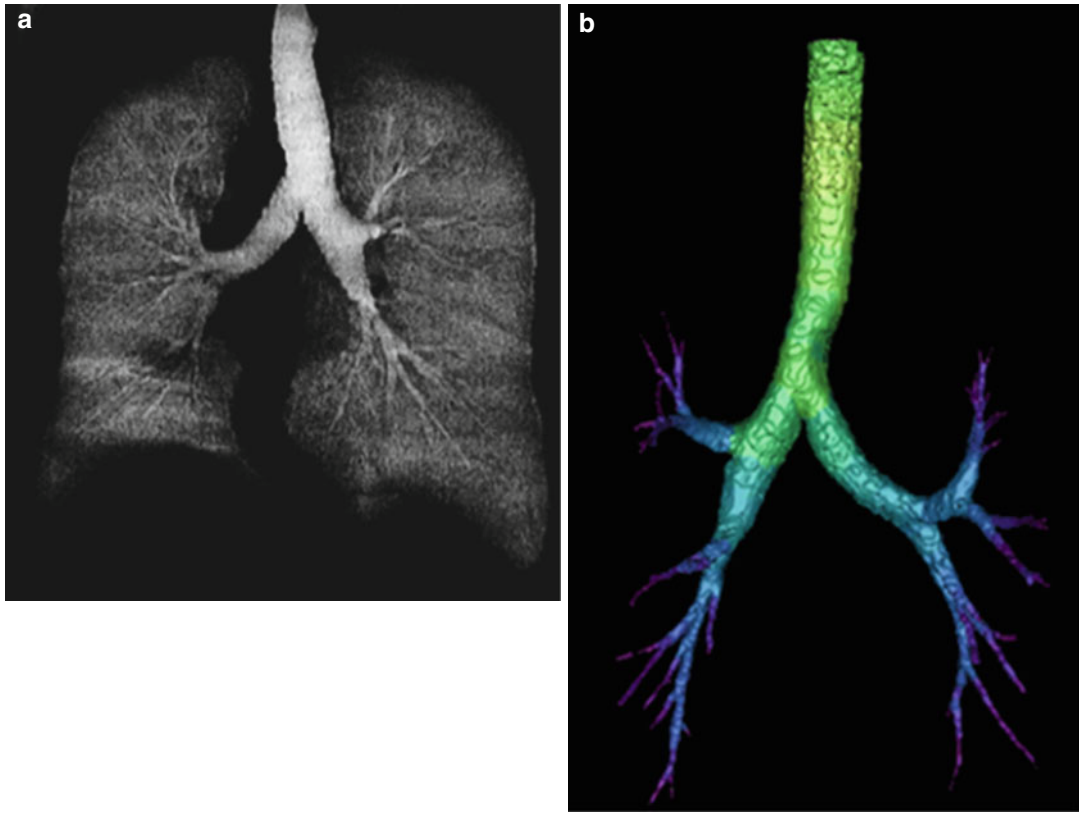

Fig. 5 Three-dimensional views of airways trees obtained with two different techniques: (**a**) minimal-intensity projection in a 78-year-old patient with tracheobronchomegaly; and (**b**) region-growing algorithm in a 25-year-old normal subject. Colors are functions of the luminal dimensions

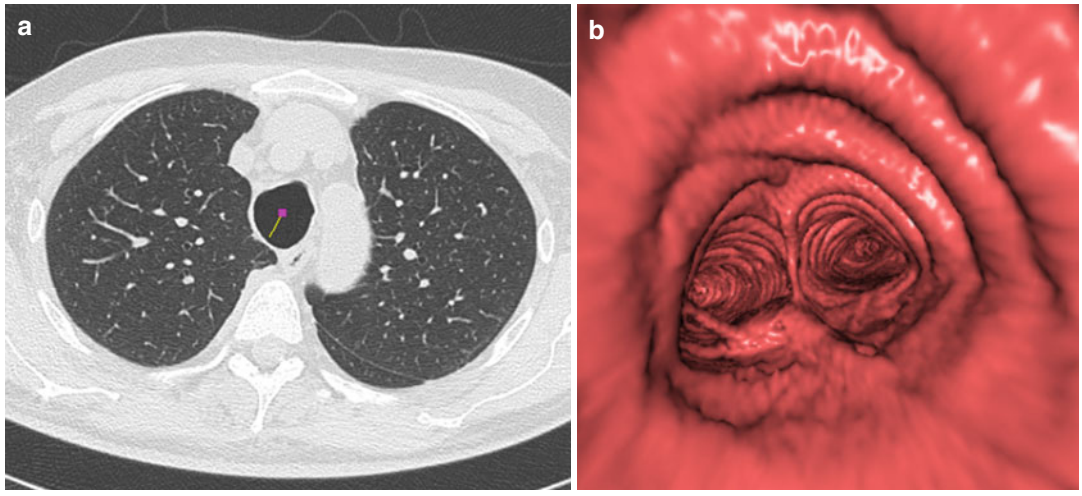

Fig. 6 (**a**) Axial image and (**b**) virtual bronchoscopy show the carina in the same 78-year-old patient as in Fig. 5a (tracheobronchomegaly)

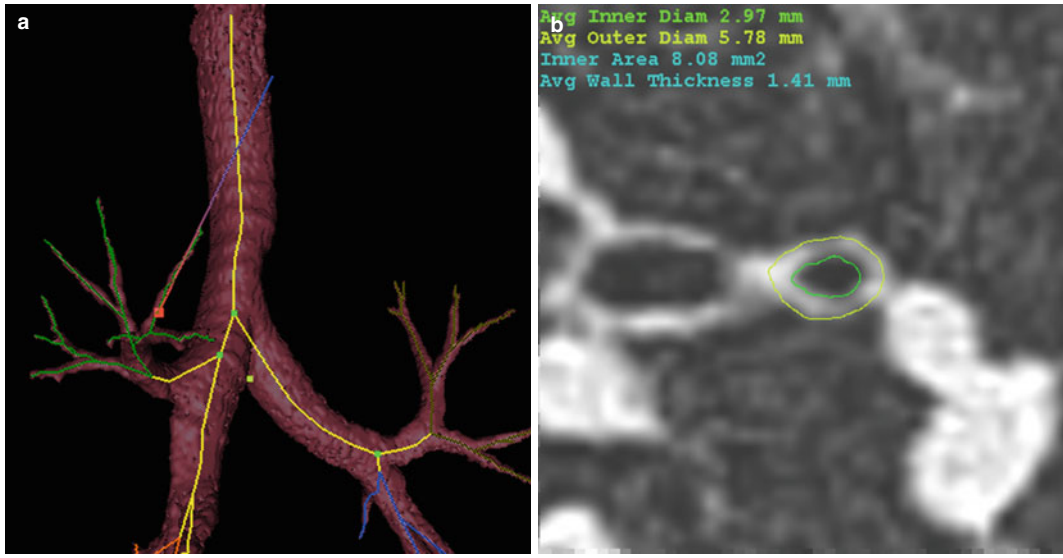

Fig. 7 Objective quantification of airway wall and lumen dimensions using dedicated software in a 25-year-old patient: (**a**) selection of a subsegmental bronchus in the right upper lobe on an airway tree obtained by a region-growing algorithm, which provides the airway axis (*green line*); and (**b**) in a plane orthogonal to this axis, computation of airway dimensions using a full-width at half-maximum-derived algorithm

attenuation will increase and thereafter decrease as it passes into the pulmonary parenchyma. The distance between the points where the attenuation is halfway between the maximal and minimum values of the wall and lumen and of the wall and the pulmonary parenchyma is considered as the airway wall thickness (Nakano et al. 2000, 2002). Other software packages are mostly based on algorithms that detect edges or abrupt changes, such as between the lumen and the wall or between the wall and the pulmonary parenchyma. To our knowledge, there is currently no consensus on which is the best dedicated algorithm.

As airway dimensions in a particular patient may be very different regarding the location and the generation of the airways, measurement indexes such as the luminal diameter or the wall thickness may differ substantially. Thus, besides one-dimensional (diameter and perimeter) and two-dimensional (area) measurement indexes, two composite indexes have been proposed. The first composite index is the percentage of the total airway area occupied by its wall (WA%). The mean WA% of the airways of a particular patient can be calculated (with its standard deviation) and used to characterize the airway tree (Nakano et al. 2000, 2005). The second composite index is the square root of the wall area corresponding to an inner perimeter of 10 mm ($\sqrt{}$WAPI10). To compute this index, each airway is plotted on a graph, with the inner perimeter along the x-axis and the square root of the wall area along the y-axis. The slope of the straight relationship between these two measurements is then calculated, and the value of the $\sqrt{}$WAPI10 is determined to characterize the airway tree of this particular patient (Grydeland et al. 2009). To our knowledge, there is currently no consensus on the best index or on the airways (number or generation) to consider. Nevertheless, $\sqrt{}$WAPI10 seems to present three advantages over WA%: it does not have to be considered by generation, it has no standard deviation when characterizing the airway tree of a particular patient, and it seems less influenced by the bronchodilation status of the patient (Hackx et al. 2015b).

Quantification of Small Airways Obstruction

Changes in dimensions of the small airways can be indirectly assessed by quantifying air trapping. Air trapping is defined as retention of air in the lung distal

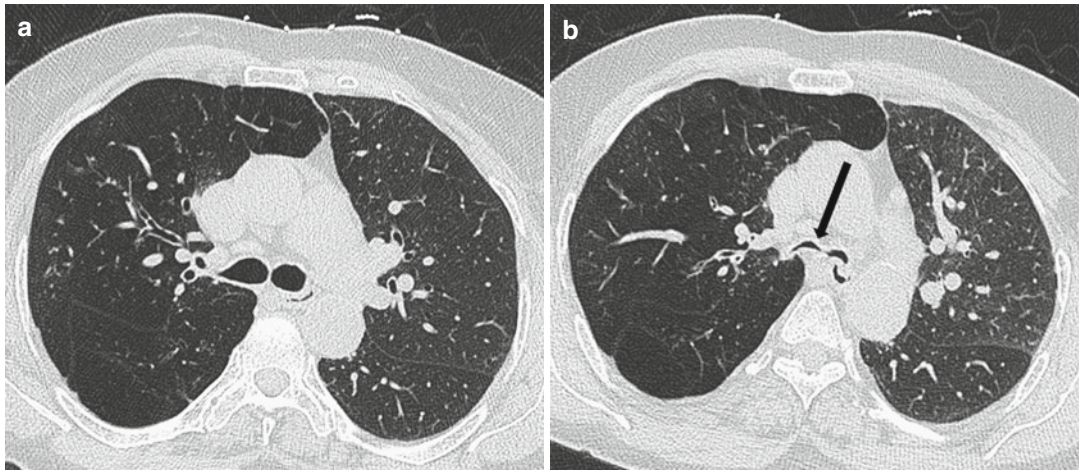

Fig. 8 (**a**) Inspiratory and (**b**) expiratory axial images show tracheobronchomalacia characterized by a decrease in cross-sectional area of the airway lumen in a 70-year-old patient. Note the crescentic shape of the lumen (*arrow*). These images also show air trapping in the right lung characterized by areas with less than normal increase in attenuation in comparison with the left lung

to an obstruction that can be seen on expiratory CT scans as lung areas with less than normal increase in attenuation (Hansell et al. 2008) (Fig. 8). Consequently, the magnitude of change in attenuation values between paired inspiratory and expiratory scans reflects the extent of air trapping and is correlated to pulmonary function. As some conditions (e.g., pulmonary emphysema) correspond also to areas of reduced lung attenuation, a precise range of low-attenuation values should be considered to minimize this confounding factor (Matsuoka et al. 2008).

3 Elementary Airway CT Features

3.1 Bronchiectasis/ Bronchiolectasis

Bronchiectasis is an irreversible bronchial dilatation that may correspond to one of the three following CT features: a bronchial dilatation with respect to the accompanying pulmonary artery, a lack of tapering of bronchi, or an identification of bronchi within 1 cm of the costal pleural surface (Fig. 9). MPR may help in the diagnosis of bronchiectasis (Chooi et al. 2003) as the lack of tapering is sometimes difficult to detect on axial images (Kang et al. 1995). Bronchiectasis may be classified as cylindrical, varicose, or cystic (Hansell et al. 2008), and its severity can be subjectively quantified in comparison with the diameter of the adjacent pulmonary artery (Brody et al. 2006).

3.2 Mucous Plugging

A mucous plugging is a mucoid impaction in the airway lumen, which is usually associated with a bronchocele (bronchial dilatation) (Fig. 10). At CT, the airway lumen is filled by mucus (generally of soft tissue attenuation values) (Hansell et al. 2008). MPR may help in distinguishing mucous plugging from a pulmonary nodule (Fig. 3).

3.3 Bronchial Wall Thickening

Bronchial wall thickening is defined as thick and less well-defined bronchial walls (Hansell et al. 2010) (Fig. 11). The severity of bronchial wall thickening can be subjectively quantified in comparison with the diameter of the adjacent pulmonary artery (Hackx et al. 2015a). To our knowledge, there is currently no objective definition of airway wall thickening. In smokers and ex-smokers, bronchial wall

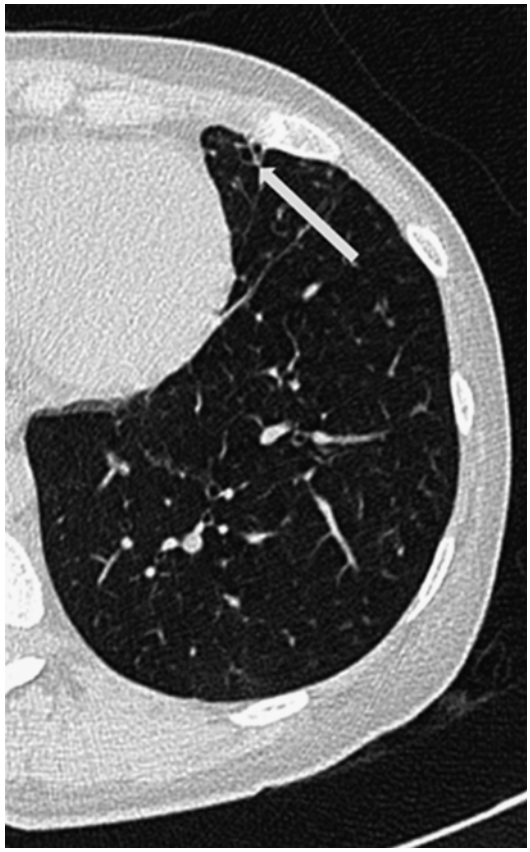

Fig. 9 Axial image of bronchiectasis: identification of bronchi within 1 cm of the costal pleural surface (*arrow*) in a 53-year-old patient

thickness is related to gender, age, and smoking habits (Grydeland et al. 2009). Nevertheless, the possible influences of weight and height remain unknown, as are the values of bronchial wall thickness in healthy subjects. Future advances in the objective quantification of airway dimensions should establish normal reference values.

3.4 Tree-in-Bud Pattern/ Centrolobular Nodules

The tree-in-bud pattern represents a centrilobular branching structure (i.e., mostly pulmonary micronodules) that resembles a budding tree. It is most pronounced in the lung periphery and is usually associated with lesions of the larger airways (Hansell et al. 2008). MIP may help in detecting the tree-in-bud pattern (Fig. 4).

4 Airway Diseases

4.1 Tracheobronchial Stenosis/ Dilation

Tracheobronchial stenosis may have various causes, for instance tumor, inflammatory diseases (Table 1), or fibrosis following surgery/radiotherapy.

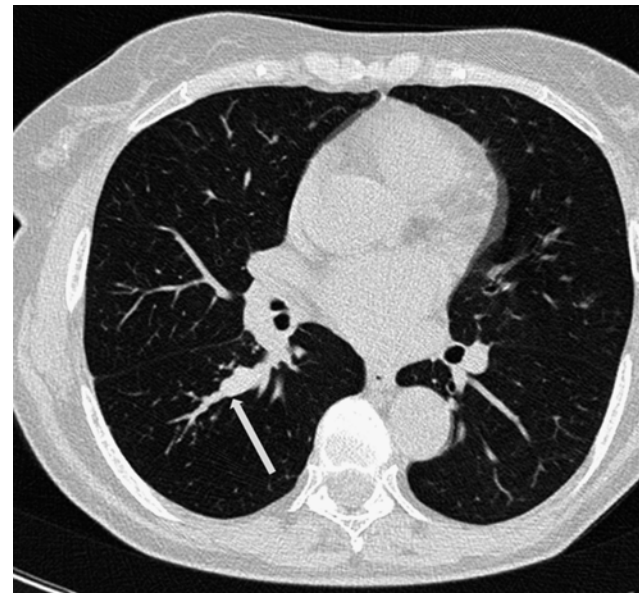

Fig. 10 Axial image shows a mucoid impaction associated with a bronchocele (*arrow*) in a 71-year-old patient

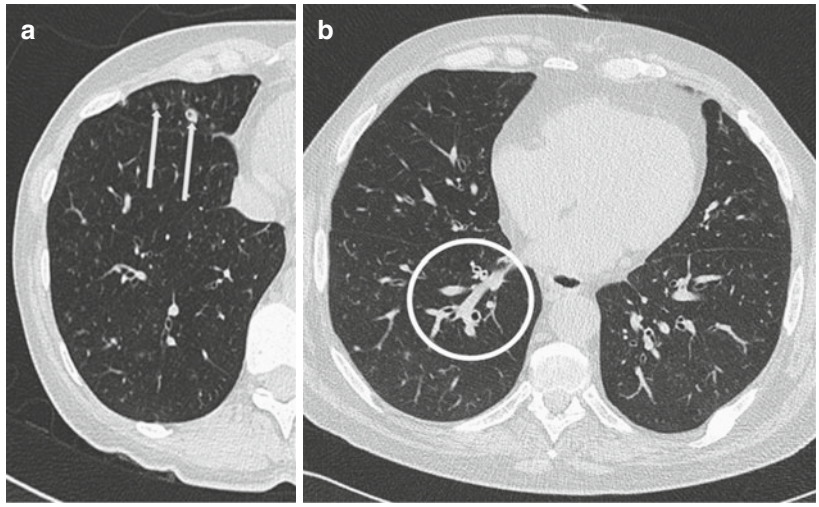

Fig. 11 (**a**, **b**) Two axial images of bronchial wall thickening: thick and less well-defined bronchial walls (*arrows and circle*) in a 71-year-old patient

Table 1 Selection of various conditions that may affect airways, with corresponding airway CT features

	Airway CT features					
Conditions	Bronchiectasis/ bronchiolectasis	Mucous plugging	Bronchial wall thickening	Tree-in-bud pattern/centrolobular nodules	Air trapping	Bronchial stenosis
Constrictive obliterative bronchiolitis	Yes, large airways	–	Yes, large airways	–	Yes	–
Diffuse panbronchiolitis	Yes	–	–	Yes, peripheral airways (lower zone initially)	–	–
Hypersensitivity pneumonitis	–	–	–	Yes	Yes	–
Sarcoidosis	–	–	–	–	Yes	Yes
Granulomatosis with polyangiitis	Yes	–	Yes	–	–	Yes
Respiratory bronchiolitis	–	–	Yes, large airways	Yes	Yes	–
Pulmonary edema	–	–	Yes	–	–	–
Ciliary dyskinesia syndrome	Yes	–	Yes	–	–	–
Allergic bronchopulmonary aspergillosis	–	Yes	–	–	–	–

CT evaluation of a stenosis is more accurate with image processing such as MPR (Figs. 1 and 2), minIP, or virtual bronchoscopy than with axial images. More precisely, such image processing might help in determining the extent of stenosis and/or its underlying cause (Sundakamura et al. 2011).

By contrast, tracheobronchomegaly (or Mounier-Kuhn syndrome) is a rare condition that is associated with recurrent respiratory tract infections, which is observed at CT as tracheal and bronchial dilation (Brody et al. 2006) (Figs. 5a and 6).

4.2 Tracheobronchomalacia

Tracheobronchomalacia is an expiratory airway collapse caused by abnormal flaccidity involving the trachea and the bronchi, owing to the loss of integrity of the airway wall structural components (usually damaged cartilage). CT shows a decrease in cross-sectional area of the airway lumen on expiratory scans, which may have an oval or crescentic shape (Gilkeson et al. 2001) (Fig. 8).

4.3 Congenital Abnormalities of the Airways

Congenital abnormalities of the airways include ectopic bronchi, bronchial atresia, and bronchial variant. These abnormalities are better depicted on three-dimensional views (VRT and segmentation of the airway tree), but some indirect signs can be depicted on axial images. For instance, bronchial atresia appears at CT as a characteristic triad: central bronchocele distal to the atretic segment, hyperlucency, and hypoperfusion of the affected segment (Hansell et al. 2008) (Fig. 12).

4.4 Chronic Obstructive Pulmonary Disease

COPD is associated with pathologic changes involving both the airways (wall remodeling and accumulation of inflammatory mucus in the lumen) and the pulmonary parenchyma (emphysema) that are related to the severity of the disease (Hogg et al. 1968, 2004). All these changes may contribute, directly or indirectly, to airway wall thickening and lumen narrowing. These changes can be quantified at CT in proximal airways, which are surrogates of morphologic changes at pathology in small airways (Nakano et al. 2005). In addition, a recent study suggested that airway wall thickening is one of the CT features associated with severe exacerbation of COPD (Hackx et al. 2015a).

4.5 Asthma

Asthma is associated with pathologic changes involving the airways through wall remodeling. While CT scans may be normal between exacerbations in patients with early asthma (Copley et al. 2002), they may later show airway wall

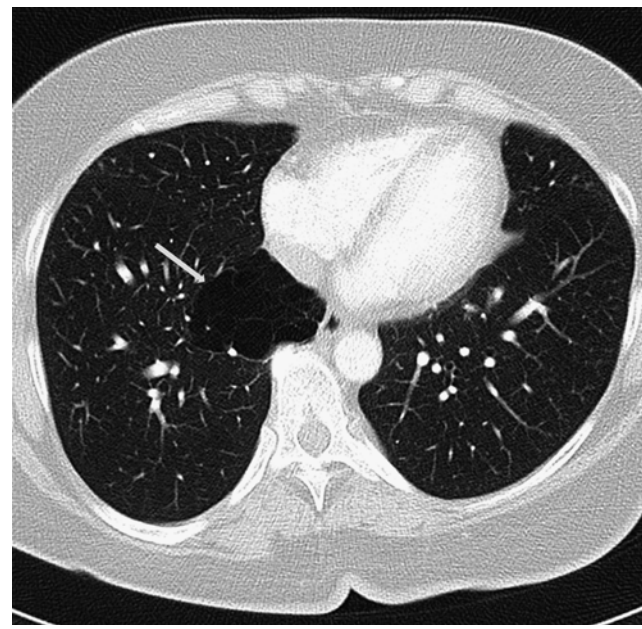

Fig. 12 Axial CT image of bronchial atresia shows hyperlucency and hypoperfusion of the affected segment (*arrow*) in a 54-year-old patient

thickening, luminal narrowing, bronchiectasis, and air trapping (Grenier et al. 1996). Similarly to COPD, objective quantification of airways has been applied to asthma and has revealed luminal narrowing but possible wall thinning (Montaudon et al. 2009; Lederlin et al. 2012).

4.6 Cystic Fibrosis

CF is an autosomal recessive disorder that affects the consistency of the mucosal secretions and leads to recurrent pulmonary infections. CT scans may show airway wall thickening, bronchiectasis, and mucous plugging. As these CT features are progressive during the disease, subjective quantification through scoring systems including these features has been developed for longitudinal assessment. In addition, these scores are correlated with pulmonary function (Brody et al. 2006; de Jong et al. 2004). Similarly to COPD and asthma, objective quantification of airways has been applied to CF, and has revealed airway wall thickening and luminal enlargement (Montaudon et al. 2007).

4.7 Overview of Various Conditions with Airway CT Features

An arbitrary selection of various conditions that may affect airways is shown in Table 1 with corresponding airway CT features (Hansell et al. 1997, 2010; Bartz and Stern 2000).

Conclusion

Airway abnormalities are found across a wide spectrum of diseases and conditions, among which CT features can overlap. They can be accurately assessed and quantified through various image processing modalities and dedicated software tools. Recent advances have focused on the objective quantification of airway changes and radiation dose reduction, two complementary fields of investigation in CT imaging of the airways. CT will continue to play important roles in the diagnosis, prognosis, and monitoring of diseases of the airways.

References

Asano F, Shinagawa N, Ishida T et al (2015) Virtual bronchoscopic navigation improves the diagnostic yield of radial-endobronchial ultrasound for peripheral pulmonary lesions with involved bronchi on CT. Intern Med 54:1021–1025

Bartz RR, Stern EJ (2000) Airways obstruction in patients with sarcoidosis: expiratory CT scan findings. J Thorac Imaging 15:285–289

Brody AS, Kosorok MR, Li Z et al (2006) Reproducibility of a scoring system for computed tomography scanning in cystic fibrosis. J Thorac Imaging 21:14–21

Calhoun PS, Kuszyk BS, Heath DG et al (1999) Three-dimensional volume rendering of spiral CT data: theory and method. Radiographics 19:745–764

Chooi WK, Matthews S, Bull MJ, Morcos SK (2003) Multislice helical CT: the value of multiplanar image reconstruction in assessment of the bronchi and small airways disease. Br J Radiol 76:536–540

Copley SJ, Wells AU, Muller NL et al (2002) Thin-section CT in obstructive pulmonary disease: discriminatory value. Radiology 223:812–819

de Jong PA, Ottink MD, Robben SG et al (2004) Pulmonary disease assessment in cystic fibrosis: comparison of CT scoring systems and value of bronchial and arterial dimension measurements. Radiology 231:434–439

Dijkstra AE, Postma DS, ten Hacken N et al (2013) Low-dose CT measurements of airway dimensions and emphysema associated with airflow limitation in heavy smokers: a cross sectional study. Respir Res 14:11

Ferretti GR, Thony F, Bosson JL et al (2000) Benign abnormalities and carcinoid tumors of the central airways: diagnostic impact of CT bronchography. AJR Am J Roentgenol 174:1307–1313

Gilkeson RC, Ciancibello LM, Hejal RB et al (2001) Tracheobronchomalacia: dynamic airway evaluation with multidetector CT. AJR Am J Roentgenol 176:205–210

Grenier P, Mourey-Gerosa I, Benali K et al (1996) Abnormalities of the airways and lung parenchyma in asthmatics: CT observations in 50 patients and inter- and intraobserver variability. Eur Radiol 6:199–206

Grenier PA, Beigelman-Aubry C, Fetita C et al (2002) New frontiers in CT imaging of airway disease. Eur Radiol 12:1022–1044

Grydeland TB, Dircksen A, Coxson HO et al (2009) Quantitative computed tomography: emphysema and airway wall thickness by sex, age and smoking. Eur Respir J 34:858–865

Hackx M, Bankier AA, Gevenois PA (2012) Chronic obstructive pulmonary disease: CT quantification of airways disease. Radiology 265:34–48

Hackx M, Ghaye B, Coche E et al (2015a) Severe COPD exacerbation: CT features. COPD 12:38–45

Hackx M, Gyssels E, Garcia TS et al (2015b) Chronic obstructive pulmonary disease: CT quantification of

airway dimensions, numbers of airways to measure, and effect of bronchodilation. Radiology 277:853–862

Hansell DM, Rubens MB, Padley SP, Wells AU (1997) Obliterative bronchiolitis: individual CT signs of small airways disease and functional correlation. Radiology 203:721–726

Hansell DM, Bankier AA, MacMahon H et al (2008) Fleischner society: glossary of terms for thoracic imaging. Radiology 246:697–722

Hansell DM, Lynch DA, McAdams HP, Bankier AA (2010) Imaging diseases of the chest, 5th edn. Mosby Elsevier, Philadelphia

Hogg JC, Macklem PT, Turlbeck WM (1968) Site and nature of airway obstruction in chronic obstructive lung disease. N Engl J Med 278:1355–1360

Hogg JC, Chu F, Utokaparch S et al (2004) The nature of small-airway obstruction in chronic obstructive pulmonary disease. N Engl J Med 350:2645–2653

Kang EY, Miller RR, Müller NL (1995) Bronchiectasis: comparison of preoperative thin-section CT and pathologic findings in resected specimens. Radiology 195:649–654

Kim Y, Kim YK, Lee BE et al (2015) Ultra-low-dose CT of the thorax using iterative reconstruction: evaluation of image quality and radiation dose reduction. AJR Am J Roentgenol 204:1197–1202

Lederlin M, Laurent F, Portron Y et al (2012) CT attenuation of the bronchial wall in patients with asthma: comparison with geometric parameters and correlation with function and histologic characteristics. AJR Am J Roentgenol 199:1226–1233

Matsuoka S, Kurihara Y, Yagihashi K et al (2008) Quantitative assessment of air trapping in chronic obstructive pulmonary disease using inspiratory and expiratory volumetric MDCT. AJR Am J Roentgenol 190:762–769

Montaudon M, Berger P, Cangini-Sacher A et al (2007) Bronchial measurement with three-dimensional quantitative thin-section CT in patients with cystic fibrosis. Radiology 242:573–581

Montaudon M, Lederlin M, Reich S et al (2009) Bronchial measurements in patients with asthma: comparison of thin-section CT findings with those in healthy subjects and correlation with pathologic findings. Radiology 253:844–853

Mori K, Ota S, Deguchi D et al (2009) Automated anatomical labeling of bronchial branches extracted from CT datasets based on machine learning and combination optimization and its application to bronchoscope guidance. Med Image Comput Comput Assist Interv 12:707–714

Nakano Y, Muro S, Sakai H et al (2000) Computed tomographic measurements of airway dimensions and emphysema in smokers. Am J Respir Crit Care Med 162:1102–1108

Nakano Y, Whittall KP, Kalloger SE et al (2002) Development and validation of human airway analysis algorithm using multidetector row CT. Proc SPIE 4683:460–469

Nakano Y, Wong JC, de Jong PA et al (2005) The prediction of small airway dimensions using computed tomography. Am J Respir Crit Care Med 171: 142–146

Remy- Jardin M, Remy J, Deschildre F et al (1996) Obstructive lesions of the central airways: evaluation by using spiral CT with multiplanar and three-dimensional reformations. Eur Radiol 6:807–816

Sundakamura DK, Bhalla AS, Sharma R et al (2011) Multidetector CT evaluation of central airways stenoses: comparison of virtual bronchoscopy, minimal-intensity projection, and multiplanar reformatted images. Indian J Radiol Imaging 21:191–194

van Ginneken B, Baggerman W, van Rikxoort EM (2008) Robust segmentation and anatomical labeling of the airway tree from thoracic CT scans. Med Image Comput Comput Assist Interv 11:219–226

Wood SA, Zerhouni EA, Hoford JD et al (1995) Measurement of three-dimensional lung tree structures by using computed tomography. J Appl Physiol 79:1687–1697

CT in Chronic Obstructive Pulmonary Disease/Pulmonary Emphysema

Hagen Meredig, Bertram Jobst, Mark O. Wielpütz, and Hans-Ulrich Kauczor

Abstract

The population of patients suffering from chronic obstructive pulmonary disease (COPD) and asthma is heterogeneous, complicating therapy management and scientific analysis. Owing to the rapid technical improvements in imaging techniques in the past years, research has succeeded in gaining further insights into the different manifestations of obstructive pulmonary disease. Whereas the main parameters for differentiation and categorization of the disease in the past were pulmonary function tests and pathologic examinations, computed tomography (CT) has now made it possible to visualize alterations in the airway and parenchymal architecture induced by COPD in vivo and in unprecedented detail. The visual differentiation of COPD is currently given by the two major radiologic phenotypes, namely the airway predominant and the emphysema predominant type of COPD. Further objective and reliable categorization and classification of the different manifestations via computer-aided analysis of pulmonary CT examinations is an important goal of recent research in pulmonary imaging. While much innovation and improvement have already been made, finding a conclusive system of parameters that allow for a reliable and quantitative classification of the different imaging features of COPD remains a task to be completed. In this chapter we provide a fundamental insight into the particular imaging patterns and provide a technical basis for the use of CT in COPD. Furthermore, we illustrate the current state-of-the-art technologies in imaging analysis and the results of recent research in typecasting COPD with clinical correlation.

H. Meredig • B. Jobst • M.O. Wielpütz
H.U. Kauczor (✉)
Department of Diagnostic and Interventional Radiology, University Hospital Heidelberg, Im Neuenheimer Feld 110, Heidelberg 69120, Germany
e-mail: Hans-Ulrich.Kauczor@med.uni-heidelberg.de

1 Introduction

The terms chronic obstructive pulmonary disease (COPD) and asthma denote a group of diseases similar in symptoms and related pathophysiologic

U.J. Schoepf, F.G. Meinel (eds.), *Multidetector-Row CT of the Thorax*, Medical Radiology,
DOI 10.1007/978-3-319-30355-0_6

changes. The underlying pathophysiology in both cases exists in inflammatory reaction of bronchial structures. In COPD the pathologic changes occur in a chronic manner, with possible additional destruction of pulmonary parenchyma, whereas in asthma exogenous or endogenous stimuli primarily lead to rather acute and (more or less) reversible bronchial reaction. While a clear stratification of asthma, especially in terms of sharp quantitative criteria, is currently lacking, COPD can be differentiated distinctly by the GOLD classification (Pauwels et al. 2001), which categorizes the severity of physiologic impairments on the basis of objective parameters measured in pulmonary function tests, such as the forced expiratory volume in 1 s (FEV_1, see Table 1) to name the most important.

However, despite this sharp quantification the group of patients suffering from COPD shows wide heterogeneity regarding the manifestation site of pathologic changes. In some individuals repetitive inflammatory bronchial reaction with consecutive airway remodeling and chronic bronchial destruction dominates the course of the disease, whereas in others parenchymal destruction leading to emphysema is the prevalent feature. Similar inhomogeneity is also found in the group of patients suffering from asthma. Characteristic symptoms and severity can vary widely in different patients but also in the individual person. Additionally, there is significant overlap in COPD and asthma, complicating both therapy management and scientific statistical analysis (Coxson et al. 2009). Recent research therefore aims at phenotyping airway disease by categorizing and quantifying pathophysiologic changes, such as either emphysema or airway affection in COPD or the presence and amount of airway wall thickening and ventilation defects in asthma. Although the recovered information might not always be useful in the differential diagnosis, it should, however, help to define distinct subgroups of patients for better therapy management and monitoring, with benefits in personalized care.

Table 1 The GOLD classification

Stage	FEV_1/FVC	FEV_1
1	<0.7	Normal
2	<0.7	<80 % predicted
3	<0.7	<50 % predicted
4	<0.7	<30 % predicted

Global Obstructive Lung Disease system used to classify the severity of airflow limitation (Rabe et al. 2007)
Abbreviations: *FEV_1* forced expiratory volume in 1 s, *FVC* forced vital capacity

While the main diagnostic tools in the past and present are physiologic parameters in pulmonary function tests as already stated, imaging features play an increasingly important role in the context of phenotyping, concerning especially the possibility of directly visualizing characteristic changes in bronchial and parenchymal structure. Magnetic resonance imaging (MRI) has proved to be very useful in functional examination of the lung such as perfusion imaging, but also, for example, in illustration of ventilation distribution using hyperpolarized noble gases (Aysola et al. 2010; Fain et al. 2010). For direct rendering of bronchial anatomy and bronchial wall thickness, and also for depiction of air trapping and interstitial alterations, computed tomography (CT) is the main workhorse in daily practice. With ongoing technical improvements, even dynamic CT examinations of tracheobronchial instability are possible and are becoming increasingly common in clinical practice (Heussel et al. 2001).

In this chapter, general technical aspects and common imaging patterns in obstructive lung disease and emphysema are discussed, with special focus on new techniques in imaging analysis and their use in typecasting different phenotypes of airway disease.

2 Pathophysiology

COPD usually originates from exogenous inhaled irritants, predominantly cigarette smoke. Chronic irritation provokes an inflammatory response in the respiratory epithelium triggered by neutrophils, CD8-positive T lymphocytes, B cells, and macrophages. The initiated inflammatory cascade is accompanied by the release of inflammatory mediators. Tumor necrosis factor alpha

(TNF-α), interleukins (IL-1, IL-6, IL-8), interferon gamma (IFN-γ), matrix metalloproteinases (MMP-6, MMP-9), C-reactive protein (CRP), and fibrinogen sustain and promote the inflammation. Locally, this process leads to tissue damage of airways on the one hand and destruction of lung parenchyma on the other (Barnes 2008).

On the airway side, the primary reaction consists in thickening of bronchial walls by hypertrophy of smooth muscle cells (Chung 2005). Driven by chronic inflammation, remodeling of the whole bronchial wall finally leads to deformation and widening of the bronchial lumen. A common feature in COPD patient is bronchial diverticula as another manifestation of bronchial remodeling. Emphysematous changes are promoted by inflammatory cells, which induce apoptosis of epithelial and mesenchymal cells. In consequence, proliferation of mesenchymal cells and synthesis of extracellular matrix is impaired. The first pathologic descriptions and also later micro-CT studies showed that emphysema is most probably initiated by a primary lesion within a single acinus consisting of destroyed respiratory bronchioles. These lesions coalesce to form centrilobular lesions supplied by one pathologic, wall-thickened bronchiole with a tortuous pathway (McDonough et al. 2011; Mc 1957a, b; McLean 1956, 1957). The centrilobular lesions may progress to form advanced types of emphysema. These findings suggest that emphysema in COPD may be initiated by small airway disease. In small airways, inflammatory scarring leads to wall thickening accompanied by peribronchiolar infiltration, which finally leads to a loss in terminal bronchioles; for example, in stage 4 COPD a loss of up to 90 % of terminal bronchioles is reported. Small airway disease is found in COPD patients suffering from emphysema-predominant disease but also in patients with predominant airway obstruction. Sometimes small airway disease is the only or the first expression of COPD, which supports the thesis that small airway disease is the initial stage of ongoing pathologic changes in COPD. Small airway disease is predominantly triggered by smoking but sometimes is also found in non-smokers, in whom it is most probably induced by environmental pollutants.

In asthma, acute attacks are characterized by rapid inflammatory reaction of bronchial epithelium to an allergic antigen but sometimes also to exogenous physical stimuli like cold air for example, or even endogenously triggered without any identifiable physical cause. Mediated by Th2 cells and B cells, mast cell degranulation is triggered within minutes, which leads to massive edema and hypersecretion of mucus glands. Vascular permeability is increased. Eosinophilic cells and neutrophils are recruited and in a later phase of the reaction (hours) lead to destruction of mucociliary glands and smooth muscle cell hypertrophy (Barnes 2008). Over time, repeated and chronic inflammation in asthmatic patients also leads to bronchial remodeling, as in COPD.

3 Scanning Protocols

3.1 Standard Settings

Modern multidetector CT (MDCT) scanners create volumetric data with isotropic voxels within 5–20 s. Because of these fast acquisition times it is possible to scan the whole thorax in one breath-hold cycle, even in dyspneic patients. The scan is usually carried out in inspiration without administration of contrast medium. For the evaluation of air trapping, an additional expiratory scan can be considered. It can be carried out in a low dose setting, e.g., with a tube current–time product of about 20–80 mAs, whereas standard dose settings should be carried out at about 50–150 mAs to achieve acceptably low image noise (Kauczor et al. 2011). Tube voltages of 100–120 kV are sufficient. Preferably low collimation should be used, as it is essential for high spatial resolution. Currently minimum achievable resolution reaches from 0.5 to 0.75 mm slice thickness, so it is possible to create a three-dimensional high-resolution CT (HRCT) volume dataset (Table 2).

Some authors promote the use of physiologic triggers to control for maximum inspiration or expiration during the scan. Especially for follow-up examinations and/or software-based image analysis, the additional accuracy and standardization may be of high importance.

Table 2 Proposed routine CT technique for COPD imaging

Detector lines	16 or more
Pitch	1–1.4
Acquisition collimation	1.25 mm or less
Tube voltage	100–120 kV
Effective tube current time product	50–150 mAs
Contrast	No
Reconstruction algorithms	Smooth and sharp
Reconstruction slice thickness	0.6–1 mm
Reconstruction interval	0.5–0.9 mm
Reconstruction field of view	Lungs only
Expiratory scan	Yes, at lower mAs, e.g. 20–50

Abbreviations: *kV* kilovolt, *mA* milliampere, *s* second, *mm* millimeter

3.2 Contrast

When contrast agents are administered, additional iodine distribution maps can be generated by subtraction of non-enhanced data from contrast scans or by dual-energy CT. Iodine maps allow for the investigation of perfusion distribution (Pansini et al. 2009; Remy-Jardin and Remy 2008; Wildberger et al. 2005). Recently even the administration of a noble gas, namely xenon, as a more sophisticated approach was reintroduced in dual-energy CT, whereby early ventilation defects and gas retention could be visualized (Chae et al. 2008; Park et al. 2010).

It is important to note that administration of iodine contrast medium affects software-based image analysis. Contrast and non-contrast scans are not comparable in longitudinal follow-up comparison, especially with regard to CT-based emphysema quantification (Heussel et al. 2009). More information on this topic is be provided in the postprocessing section.

3.3 4D Examinations

A special case is the implementation of dynamic, four-dimensional (4D) examinations to gain additional functional information on breathing mechanics (Dinkel et al. 2009). As in cardiac CT, a physiologic trigger is needed to acquire images of a specific breathing phase. As respiratory triggers external optical sensors, e.g., infrared lasers or belt-mounted pressure sensors, spirometers or nose thermometers are used for gating. Both prospective gating and retrospective sorting can be performed. A retrospective gating technique is the so-called cine mode, whereby the table is still during one breathing cycle and then moves to the next position, where the subsequent part of the lung is scanned. Afterward, all of the pieces of each respiratory phase are put together to create a total volume data set of the lung and/or tracheobronchial tree. Another technique is continuous acquisition of the whole chest in free shallow breathing with registration of the respiratory movements by a belt system, allowing for retrospective gating of the data set. Because the acquisition can be performed at the lowest possible exposure parameters and may be reconstructed with iterative reconstruction algorithms, the radiation dose is usually not higher than that used with average low-dose CT (Wielputz et al. 2014). In cardiac CT, prospective step-and-shoot acquisition as a low-dose alternative to dose-intense retrospective gating is becoming more widespread. Similarly to cine mode, the examination volume is split up into individual slices corresponding to the width of the detector. At each position, image acquisition only takes place during the desired physiologic phase. Obviously this technique has the potential to reduce radiation exposure, although dedicated reconstruction algorithms are essential for adequate image quality. As high-end state-of-the-art scanners cover 256, and sometimes 320 detector lines, the beam geometry resembles a cone, which gives rise to so-called cone-beam artifacts, which are costly to remove. At present only preliminary results on lung imaging exist using this technique.

3.4 Image Reconstruction

Standard image reconstruction should encompass sharp and smooth algorithms. The use of

iterative reconstruction algorithms has the potential for dose reduction by reducing image noise, especially in low-dose scans (Pontana et al. 2011). However, as the effects of iterative image reconstruction on quantitative parameters are still under investigation, it generally cannot be recommended in cases where post-processing with quantitative image analysis should be performed (Nishio et al. 2012; Mets et al. 2012). Reconstruction increment should be about 80 % or less of slice thickness to guarantee sufficient overlapping of slices. By targeting the reconstruction matrix onto the lungs only, spatial resolution can be further optimized. The perception of tracheobronchial anatomy and its alterations can be enhanced by multiplanar reformations (MPRs). With this technique, for instance, a set of coronal slices orientated along the longitudinal course of the trachea can be created for better depiction and measurement of tracheal stenosis. The maximum-intensity projection (MIP) technique projects the highest attenuation value of the voxels on each view through a predefined volume onto a two-dimensional image (Beigelman-Aubry et al. 2005). When inflammatory changes are present in the bronchiolar wall and lumen, the bronchioles may become visible on CT scans as small centrilobular nodular and/or linear opacities. The application of the MIP technique with the generation of 4- to 7-mm-thick slabs may increase the detection and improve the visualization of these small centrilobular opacities (Brillet et al. 2008). The minimum-intensity projection (minIP) is a simple form of volume rendering that is able to visualize the tracheobronchial air column in a single viewing plane. The pixels encode the minimum voxel density encountered by each ray. Because of lower attenuation of the air contained within the tracheobronchial tree compared with the surrounding pulmonary parenchyma, minIP is highly suitable for visualization of the airways. This technique displays only 10 % of the data set and is also an optimal tool for the detection, localization, and quantification of ground-glass and linear attenuation patterns (Beigelman-Aubry et al. 2005).

4 Distinct Imaging Patterns

4.1 Wall Thickening

In both COPD and asthma, thickening of bronchial walls is one of the main characteristics reflecting the initially dominating pathophysiologic alteration. While extensive bronchial wall thickening can sometimes be seen on a plain radiograph of the chest, CT can identify already discrete changes. Bronchial walls are depicted as hyperdense rings around the cross sections of bronchi when they meet in or near to a right angle to their long axis (Fig. 1). Wall thickness can be evaluated regarding absolute values or with respect to the ratio of wall thickness to bronchus lumen. Usually wall thickening is heterogeneously distributed in COPD patients. Subjective assessment or manual measurements are currently the usual method of evaluation in daily reporting practice, although inter-rater agreement is not particularly good. As an alternative, computer-based postprocessing analysis is able to detect wall thickening more objectively. Further detail on this topic is provided in the postprocessing section.

4.2 Remodeling and Bronchiectasis

Bronchial wall alterations and cartilage involvement resulting from chronic inflammation are common features with higher prevalence in advanced COPD than in asthma, although remodeling takes place in asthma as well, but can be more sufficiently avoided or damped by medicinal therapy. In early stages of bronchial wall remodeling, the only visible change exists in thickening of the bronchial wall from smooth muscle hypertrophy. A clear differentiation from acute, reversible changes is not possible morphologically and can only be inferred from clinical context or follow-up examinations. In advanced stages further irreversible changes occur: because of scarring of bronchial walls and destruction or atrophy of cartilage, the natural tapering of bronchus lumen from proximal to distal is lost. On

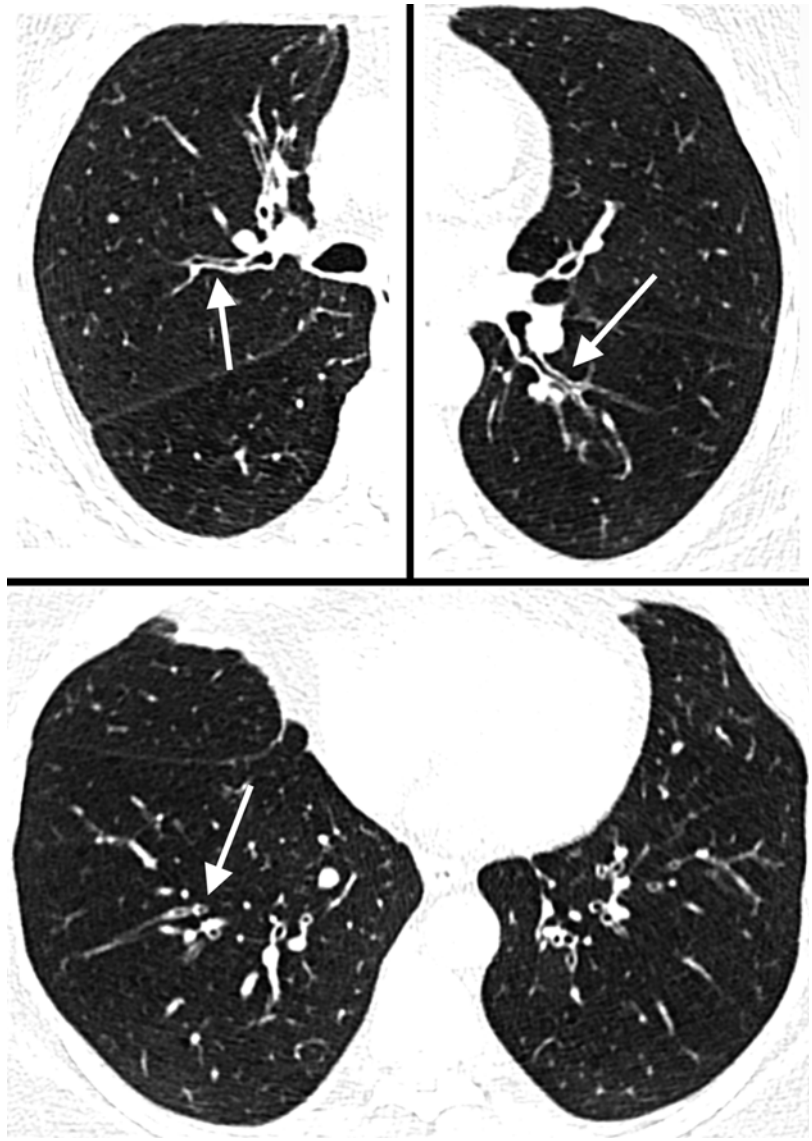

Fig. 1 Bronchial wall thickening. Transversal CT slices of a patient with bronchial wall thickening (*arrows*)

transversal slices the phenomenon is best seen in the hilar region, where segmental bronchi are cut longitudinally by the viewing plane (Fig. 2). Alternating dilatation and narrowing of the bronchial lumen can be accompanied by bronchial wall thickening but is also seen without thickening in many cases of late-stage COPD. By definition, the bronchi should have inner diameters of maximally the width of the accompanying vessel. Bronchiectasia is present when the inner lumen of a bronchus is larger than the accompanying vessel (Fig. 3). The dilated bronchi can be (partially) filled up with secretion, detritus, or pus. This finding is also referred to as mucus plugging or mucoid impaction, and can be seen in exacerbations but also as a chronic feature in COPD patients.

4.3 Tree in Bud

The aforementioned imaging findings mainly refer to the more central airway structures, but

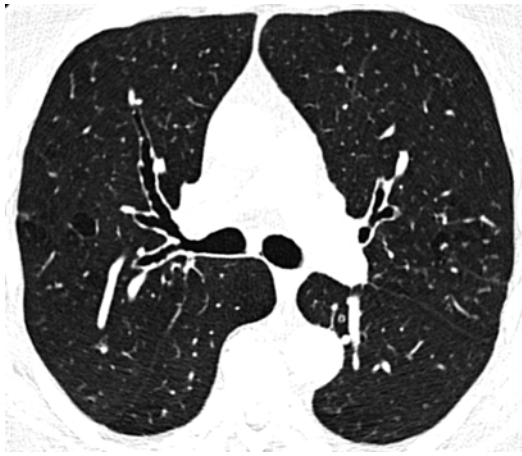

Fig. 2 Bronchial remodeling. Transversal CT slice of the right lung in advanced COPD. Ectasia and alternating widening and constriction of bronchi can be seen

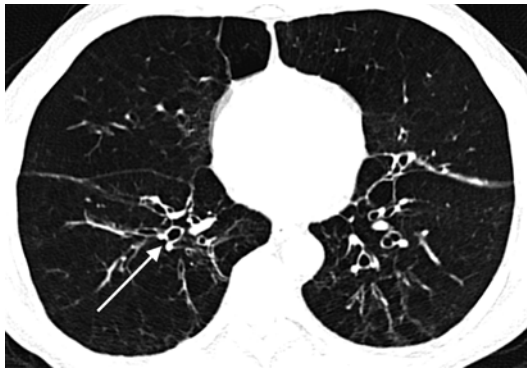

Fig. 3 Bronchial ectasia. Transversal CT slice of a patient with slight bronchial ectasia. The bronchi in the lower lobes especially have significantly wider diameters than accompanying vessels

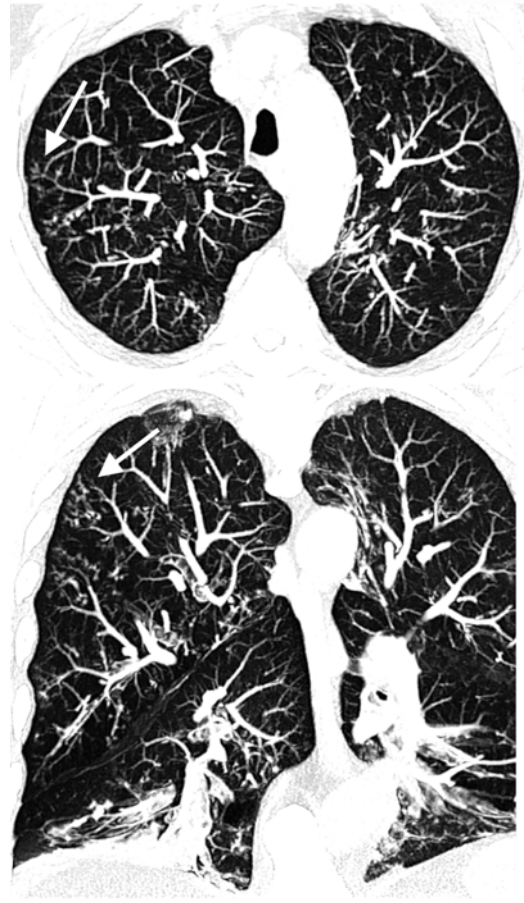

Fig. 4 Tree-in-bud sign. Transversal and coronal MIP images of a patient with centrilobular nodules at the "tips" of the arterial tree

in asthma and COPD the small airways also may be affected. In healthy lung tissue, bronchiolar structures have a diameter of less than 0.1 mm and therefore are not visible on CT. However, bronchial wall swelling and peribronchiolar infiltration become visible as condensation along the dendritic peripheral bronchi with nodular opacities on their tips in the centers of secondary lobules. The appearance resembles the geometry of a tree with buds on its branching (Fig. 4). A tree-in-bud pattern can often be found adjacent to secretion-filled bronchi.

4.4 Air Trapping/Mosaic Perfusion

An indirect sign of small airway disease is air trapping. Normally, the density of lung parenchyma increases during expiration as the volume of air declines. When airflow during expiration is impeded through narrowing or closure of bronchial lumen, the lung sections distal to the closure site remain inflated. Consequently the expiratory increase in density is missing, and the affected lung area markedly delimits as a hypodense area from the surrounding lung tissue on expiratory scans (Fig. 5a–c). The hypodensity is not solely attributable to (hyper-) inflation, but also to reduced perfusion. Owing to hypoxic

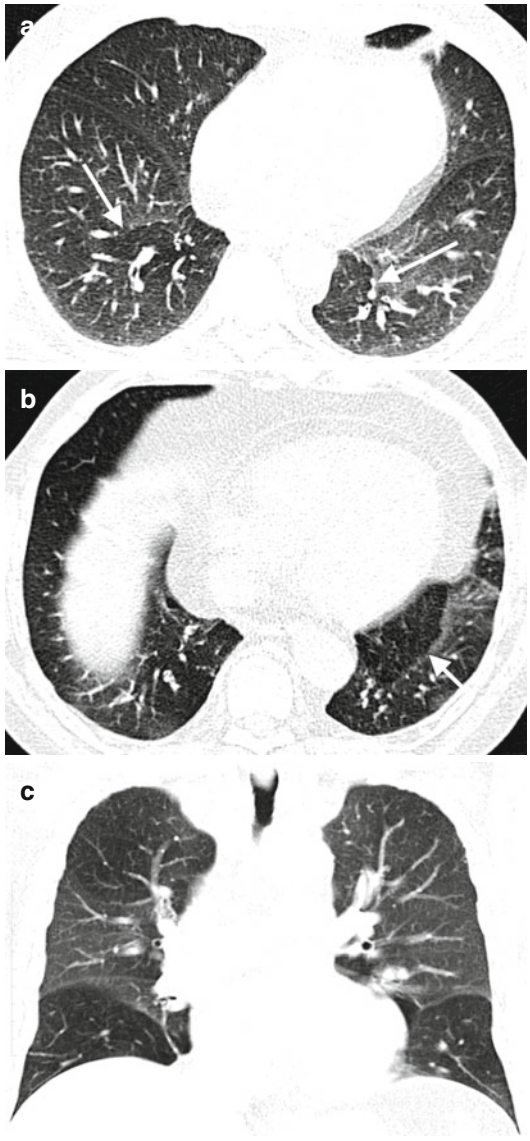

Fig. 5 Air trapping. Three examples of air trapping. Subtle demarcation of hyperinflated areas in the dorsal lower lobes in (**a**). Marked air trapping in the left lower lobe in (**b**), and in both lower lobes in (**c**)

vasoconstriction, the Euler–Liljiestrand mechanism, inadequately ventilated lung sections are less perfused than well-aerated areas. The smaller blood volume caused by the constricted vessels leads to lower regional attenuation. Clear differentiation between trapped air and hypoperfusion without contrast is not possible, particularly in view of the fact that the oxygen concentration in

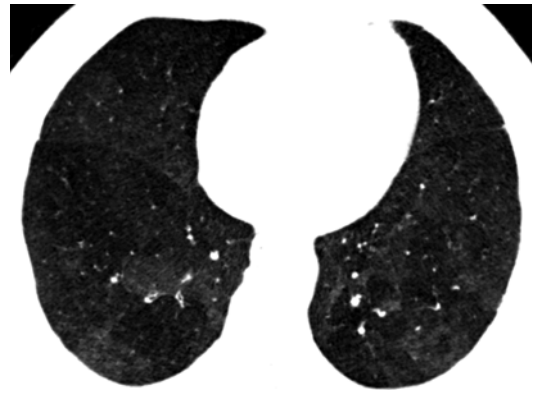

Fig. 6 Mosaic perfusion. MinIP reconstructed transversal slice of basal sections of the thorax in a patient with mosaic perfusion. *MinIP* minimum-intensity projection

trapped air is degraded. In the context of small airway disease, very heterogeneous ventilation with distribution patterns of varying density in adjacent secondary lobules can be present, which is depicted as a mosaic-like distribution of hyper- and hypodense areas on cross-sectional lung images, also known as mosaic perfusion (Fig. 6). One must note that a certain amount of air trapping, up to 25 % of affected cross-sectional lung area, is considered physiologic. Abnormal air trapping is a hallmark of small airway disease and is associated with a variety of lung diseases, including COPD, bronchiectasis, bronchiolitis obliterans, and asthma.

4.5 Emphysema

Pulmonary emphysema is characterized by a decreased attenuation of lung tissue on CT imaging. A typical cutoff value is –950 HU. An area of lung tissue with attenuation below this value is typically considered as emphysematous. Pulmonary emphysema takes different shapes and distribution patterns. Centrilobular emphysema (CLE) is distributed among the center of pulmonary lobules, and the vessel diameters are not reduced (Fig. 7a, b). As already stated in the pathophysiology section, centrilobular emphysema is thought to be the initial stage of emphysematous destruction in COPD.

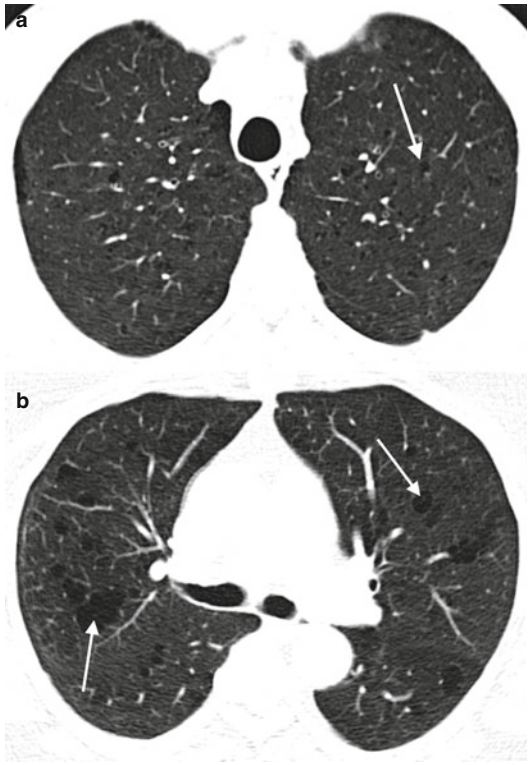

Fig. 7 Centrilobular emphysema. (**a**) Transversal CT slice of a patient with early centrilobular emphysema depicted as small, circumscript, hypodense areas (*arrow*). (**b**) Transversal CT slice with centrilobular emphysema; details magnified. Hypodense areas are less subtle than in (**a**). A greater amount of the secondary lobules is destroyed by emphysema; some of the centrilobular lesions are confluent. Vessels have normal diameters. The central arteries in some of the polygonally shaped lobules are slightly visible (*arrows*)

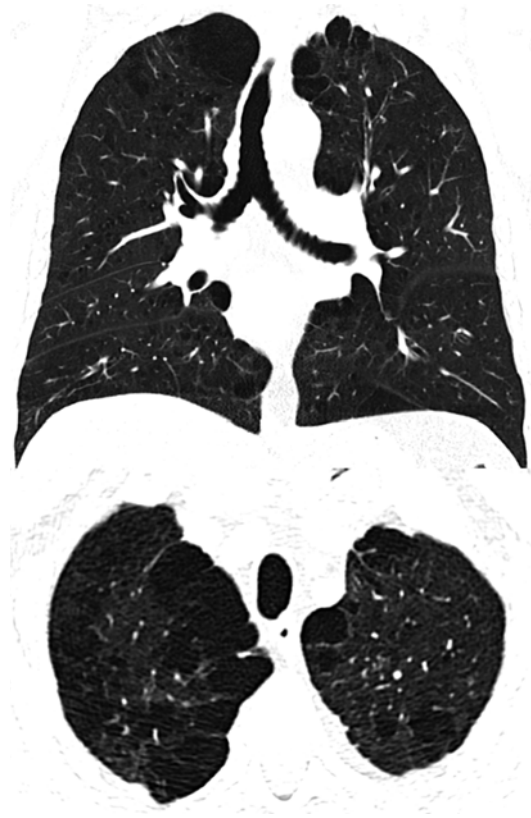

Fig. 8 Paraseptal emphysema. Coronal and transversal reconstructions of a CT scan in a patient with apical predominance of centrilobular emphysema. In both apices paraseptal emphysema is present

A special type of centrilobular emphysema, which is localized mainly in subpleural area, is called paraseptal or distal acinar emphysema because mainly the distal sections of secondary acini are affected, which leads to the dominantly subpleural distribution (Fig. 8). In combination with hyperinflation emphysematous bullae can develop, which can take small to giant diameters, sometimes covering large amounts of intrathoracic volume. Distribution patterns of emphysema show great variation: apical or basal predominance, but also localized emphysematous destruction of singular lobes or homogeneous distribution over the whole lung, are possible. A frequent depiction in smokers is a centrilobular emphysema, predominantly located in the apical lung segments, although different manifestations exist.

In advanced stages of COPD any initial type of emphysema can transform into the aspects of so-called panlobular emphysema, which is characterized by homogeneous distribution over large areas or the whole lung. Evenly distributed rarefication of small vessels and bronchial structures, reduced vessel diameters, and homogeneous degradation of lung tissue is the typical impression on CT images. It is proposed that the term panlobular emphysema should be reserved for the type of emphysema found in α1-antitrypsin deficiency, as a clear correlation with its cause is given in this case. Therefore, to describe advanced panlobular-like centrilobular emphysema in COPD the terms coalescent centrilobular and advanced destructive emphysema (ADE) are proposed (Fig. 9).

4.6 Impaired Breathing Mechanics

As progressive inflammation throughout the tracheobronchial tree may lead to malacia of cartilaginous airways, acquired tracheobronchomalacia is a common feature in COPD. It is defined as an expiratory collapse of the tracheal and/or bronchial lumen to less than 50 % of the original diameter. It has to be distinguished from excessive dynamic airway collapse, which is characterized by an excessive bowing of the posterior membranous part of the trachea. Usually the diagnosis is found via bronchoscopy, but severity estimation is not standardized and highly user dependent. With the possibility of dynamic CT examination the collapse can be made visible non-invasively and a better standardization of evaluation made possible. In advanced COPD an irregular, asynchronous ventrocranial movement of the diaphragm and chest wall has been demonstrated (Fig. 10a–c), which is thought to be a result of a rather complex mechanism induced by emphysema. When the whole thorax is covered by dynamic 4D examination, such atypical breathing mechanics can additionally be detected, which is not possible via bronchoscopy.

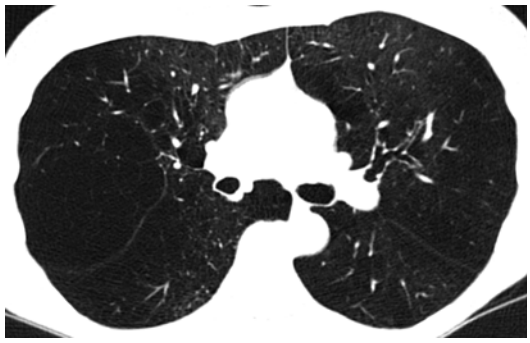

Fig. 9 Advanced destructive emphysema. Transversal CT slice of a patient with advanced COPD. Extensive destruction of pulmonary parenchyma with rarefication and reduction of vessel caliber is present in the right lung. Note bronchopathia on the left hilar region

4.7 Pulmonary Fissures

Usually the right lung is separated into three lobes, i.e., the upper, middle, and lower lobes. The margins of the distinct lobes consist of visceral pleura, which manifests as interlobular septa between the lobes. The left lung is composed of the upper and the lower lobe. The lingula, as the anatomic equivalent to the middle lobe, is normally not separated from the upper lobe of the left lung. Consequently there is a right oblique and a right horizontal septum, but only one oblique septum on the left. Recent studies showed that in practice these fissures are often incomplete (see Fig. 11a, b), and more patients than previously expected have parenchymatous connections between different lobes (Koenigkam-Santos et al. 2013a). This fact is relevant in COPD patients suffering from severe

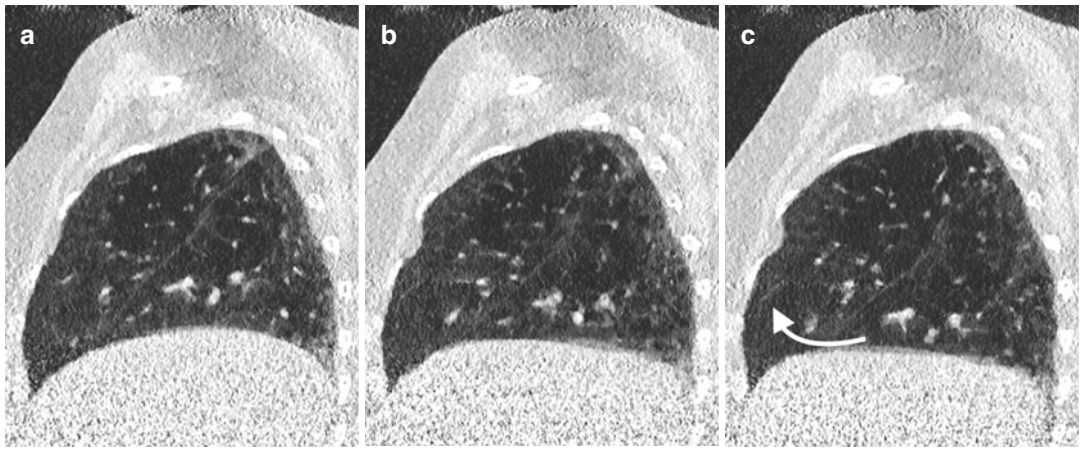

Fig. 10 Atypical movement. 4D-CT of a patient with paradoxic movement of the diaphragm with ventral and cranial dislocation (*arrow*). Expiration in (**a**), early inspiration phase in (**b**), and full inspiration in (**c**)

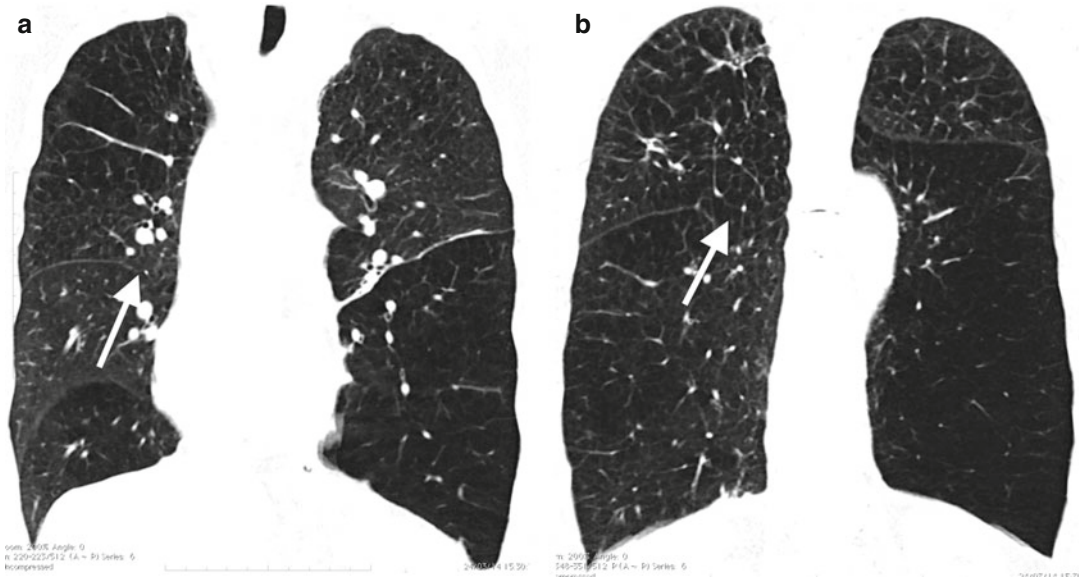

Fig. 11 Incomplete fissures. Coronal reconstruction of chest CT in a patient with a parenchymatous connection between right upper and middle lobe (**a**) and also between upper and posterior lower lobe (**b**). Defects in the corresponding septa can be seen (*arrow*)

emphysema, as the possibility of novel treatment options for emphysema, namely endoscopic lung volume reduction (ELVR), especially by the implantation of valves, may be hampered by incomplete fissures. The principle of ELVR by valves consists of the closure of a lobar bronchus belonging to a lung lobe which is severely affected by emphysema and hyperinflation. After the functional closure of the bronchus the emphysematous lobe collapses, in optimum cases giving more space to functional lung parenchyma and improving respiratory mechanics (Fig. 12). When parenchymal connections between different lobes are present, this mechanism is destined to fail partially or completely because of collateral ventilation from one lobe to the other. Thus, the radiologic evaluation of completeness of fissures is gaining relevance as ELVR is being adopted.

5 Postprocessing

5.1 Airway Analysis

The assessment of the bronchial lumen and wall geometry is part of the ongoing efforts to improve the CT evaluation of obstructive lung disease. The visual perception of airway changes is subjective and is associated with high interobserver variability (Park et al. 1997). Usually bronchi run obliquely to the axial plane, thus compromising accurate quantification (Venkatraman et al. 2006). Considering the complexity of the tracheobronchial tree and the heterogeneity of the diseases to be assessed, the need for automatic segmentation and measurements of the whole lung is evident; therefore, computer-aided analysis has become essential in objective quantitative analysis of tracheobronchial geometry. The prerequisites for such software tools, however, are challenging. High spatial resolution volumetric CT data sets with clear depiction of pulmonary structures down to the subsegmental level are needed to quantify airway geometries and dimensions. Ideally, the scan is reconstructed with a smooth reconstruction kernel, and the slice thickness is about 1 mm with an overlap of 50 %. However, high image quality is generally contrary to the desired low radiation dose and the sometimes impaired compliance of the patient attributable to the underlying disease (shortness of breath, coughing), leading to artifacts.

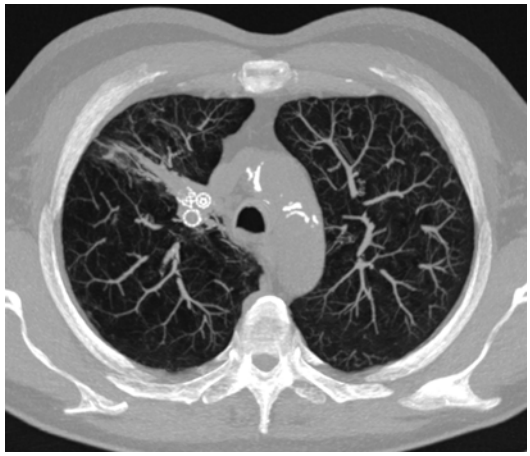

Fig. 12 ELVR with valves. MIP reconstructed transversal CT slice of a patient after ELVR. Valves have been implanted in the segment bronchi of the right upper lobe with consecutive partial atelectasis

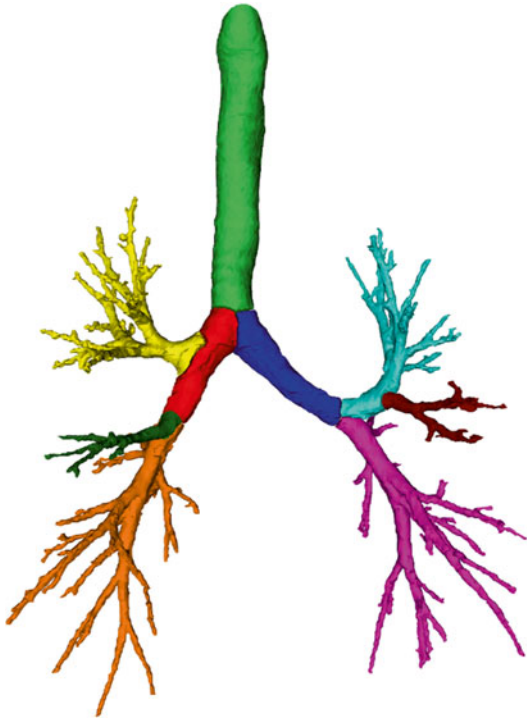

Fig. 13 3D reconstruction of an automatically segmented tracheobronchial tree. 3D volume rendering of a segmented tracheobronchial tree. Automated output of the YACTA software package, used for airway and emphysema quantification (Courtesy of O. Weinheimer, Heidelberg University; YACTA version 2.5.0.1)

Quantitative parameters of airway morphology comprise lumen area, inner and outer airway diameters, wall thickness, wall area, wall attenuation, airway segment lengths, airway taper indexes, and airway branching patterns. Volumetric MDCT data sets allow for a skeletonized visualization of the bronchial tree without overlapping parenchyma (Fig. 13). In computer-aided analysis, centerlines running through the center of the lumen of all segmented bronchi are calculated down to the subsegmental level, and depict the exact course of the bronchi. On this basis secondary reconstructions such as curved multiplanar reconstructions are made possible and allow for visualization of airway dimensions regardless of their orientation with respect to the axial CT scan (Fig. 14). To finally measure the aforementioned parameters, i.e., the bronchial wall thickness, usually the "full width at half-maximum" method is used (de Jong et al. 2005; Nakano et al. 2005; Reinhardt et al. 1997; Saba et al. 2003). In this method the centerline serves as the starting point for multiple centrifugal measurements of density profiles in Hounsfield units on images reconstructed perpendicular to the long axis of the bronchi. Half of the density value from the starting point to a maximum that is located in the bronchial wall is considered the inner circumference of the bronchus. Accordingly, the outer border is half the density between the maximum in the bronchial wall and a following minimum, usually located within the surrounding parenchyma, or a second maximum within an attached vessel. The resulting two voxels encompass the bronchial wall. Recent modifications of the simple full width at half-maximum algorithm now allow for segmentation of very distal bronchi down to diameters smaller than 1 mm (Weinheimer et al. 2008), which is important, as histopathologic studies showed that the main site of bronchial obstruction in COPD occurs in airways smaller than 2 mm in internal diameter (Hogg et al. 2004).

At present, these methods are used for stratification in clinical trials, which requires considerable effort of standardization in software analysis, CT acquisition, and reconstruction parameters. Furthermore, the management of several compli-

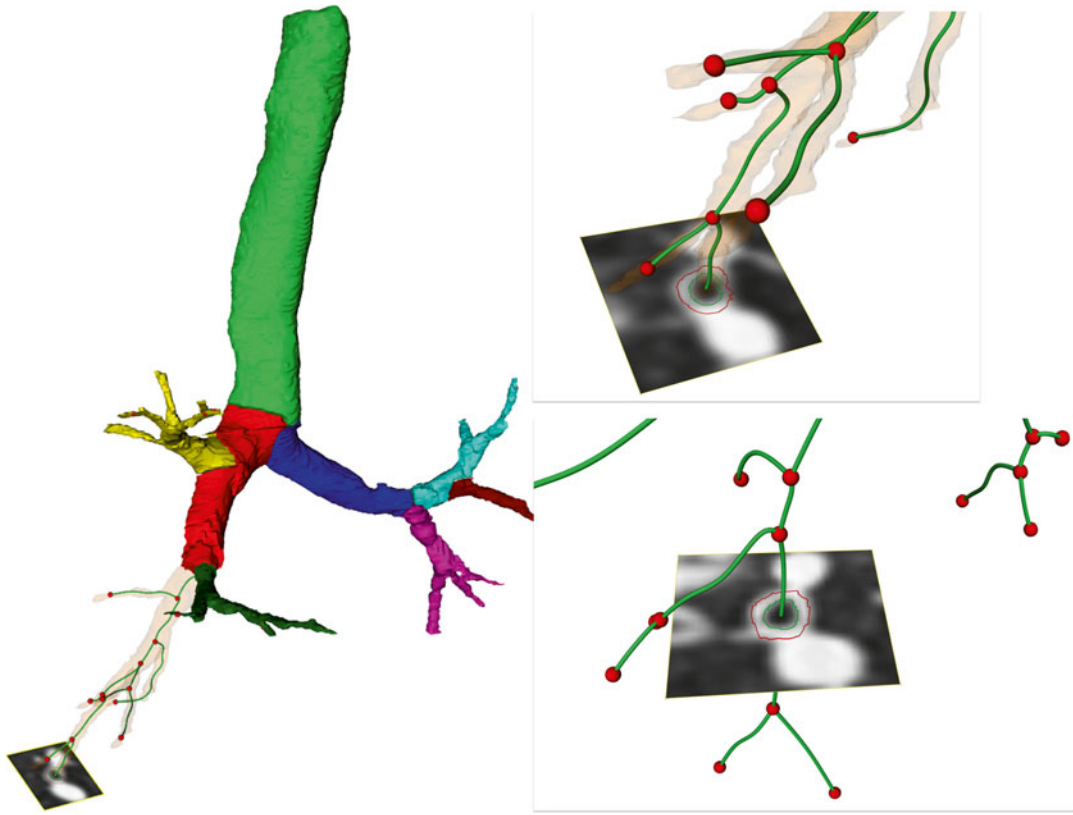

Fig. 14 Airway measurement. Visualization of centerlines of tracheobronchial tree with depiction of bronchial wall dimension measurements (Courtesy of O. Weinheimer, Heidelberg University; YACTA version 2.5.0.1)

cations in automated segmentation is still being resolved and a standard of analysis is still to be developed regarding, for example, the number and location of analyzed bronchi. Collapsed or obstructed airways generally lead to a halt in the process of segmentation, rendering the detection of distal bronchi impossible. Because the delineation of smaller bronchi is constrained by the partial volume effect, manual correction of the processed results, modifications of the algorithm, or knowledge-based simulations are required to segment the more distal branches. Moreover, the influence of iterative reconstruction algorithms on the results has yet to be clarified. Preliminary findings suggest that especially in a low-dose setting, iterative reconstruction can improve three-dimensional (3D) image analysis regarding airway dimensions (Koyama et al. 2014). Furthermore, a sensible threshold permitting consideration of certain airway dimensions as clearly pathologic still does not exist since, for example, the interscan variability of results has yet to be established (Brillet et al. 2009). In general the wall area percentage seems less suitable for reliable evaluation of bronchial wall thickening, as this parameter is influenced by the bronchial lumen, which can lead to false-negative results when bronchiectasis is present. One commonly used possibility of a generalized measure of bronchial wall dimensions is the so-called Pi10, which is the square root of the bronchial wall area of a hypothetical bronchus with an internal diameter of 10 mm, calculated from linear regression of all measured bronchi (Grydeland et al. 2011).

5.2 Quantification of Emphysema

The first studies of software-based emphysema quantification were performed on incremental

thin-section two-dimensional high-resolution CT data sets (Madani et al. 2007). The disadvantage of this method clearly lies in the lack of full coverage of the whole pulmonary volume. Regarding the variability of regional distribution patterns, an evaluation of the complete lung is desirable for a comprehensive analysis of emphysema in the individual patient. Modern software solutions perform assessment on 3D volumetric CT data sets. Quantification takes place primarily on the basis of a threshold value for the attenuation of lung parenchyma, which is usually chosen to be below 950 HU for the detection of emphysema. While this approach appears to be rather simple at first sight, it is complicated by its close relationship to airway analysis techniques: For a proper evaluation the parenchymal structures have to be clearly separated from tracheobronchial structures, which are filled with air and thus could influence the measured emphysema parameters. In practice many software tools are available as part of commercial integrated solutions, in addition to freely available software packages that perform image analysis in a fully automated or semi-automatic manner (Heussel et al. 2006) (Fig. 15). The most common parameters measured are emphysema volume and total lung volume, which are set in relation by the emphysema index (EI). Another possibility is the percentile point, which is defined by the density threshold, below which a defined percentage of lung voxels are distributed. Typical values are the 12th or 15th percentiles. Further parameters can be used to characterize emphysema in more detail, for example by registration of clusters of emphysema and the amount of different cluster sizes (Achenbach et al. 2004). All of the different software solutions show good or excellent correlations with pulmonary function tests and also with histopathologic changes, but the results of divergent software tools are not comparable with one another (Wielputz et al. 2014). Moreover, the technical parameters of the scanning protocol, especially dose settings and the use of iterative reconstruction algorithms, influence the resulting parameters (Mets et al. 2012; Gierada et al. 2010). There are also significant differences between inspiratory and expiratory scans and between contrast-enhanced and non-contrast scans (Heussel et al. 2009; Zaporozhan et al. 2005). Especially because of the influence of different inspiration levels, the evaluation of progression of emphysema in longitudinal follow-up CT examinations can be severely compromised. To account for this complication different correction techniques, such as corrections based on lung volume (Stoel et al. 2008), have been, are being, and remain to be developed.

The separation of air trapping from emphysema or, more exactly, the automated evaluation of air trapping, is another aim of recent research. In 2008, Matsuoka et al. showed that the sub-volume of lung tissue with attenuation between −950 and −900 HU in paired inspiratory and expiratory CT scans might be used to assess the amount of air trapping in individuals suffering from airway disease and emphysema (Matsuoka et al. 2008). Babosa et al. (2011) later found good correlations of their results with pulmonary function test parameters utilizing a different technique, by making use of the change of attenuation between inspiratory and expiratory scans to segment areas of air trapping. However, correlations decreased when significant emphysema was present, revealing the difficulties inherent to the problem.

Another, prospectively increasingly more important task, will be the evaluation of target lobes for ELVR. As stated earlier, ELVR aims at reducing (dysfunctional) lung volume by endoscopic implantation of closure devices into lobar bronchi, namely, valves. Patients with severe emphysema concentrated in a particular lobe are thought to benefit most from this method of lung volume reduction. Automatic emphysema qualification may become an increasingly important tool for identification of individuals suitable for ELVR, and also in determining the target lobe for intervention. An important task in this context is the evaluation of the integrity of pulmonary fissures. As already mentioned, success of valve

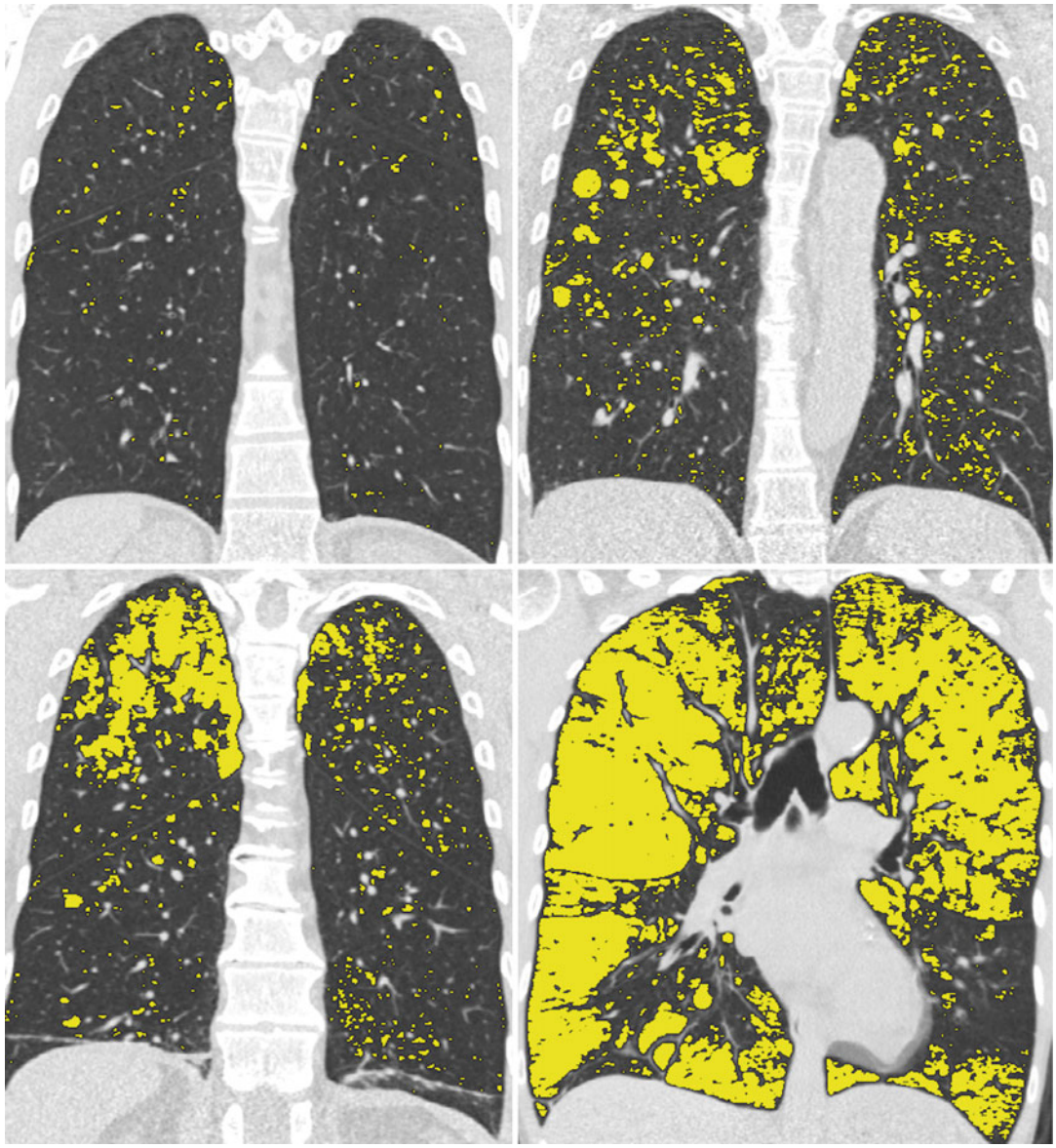

Fig. 15 Depiction of emphysema. Emphysema analysis output of the YACTA software package. Coronal CT slices of different patients. Emphysematous regions were computed threshold based and are marked in yellow. *Upper left*: No significant emphysema (<5 %). *Upper right*: centrilobular emphysema. *Lower left*: apical predominance of confluent centrilobular emphysema. *Lower right*: advanced destructive emphysema (Courtesy of O. Weinheimer, Heidelberg University; YACTA version 2.5.0.1)

implantation can be limited by collateral ventilation caused by incomplete pulmonary fissures. Present-day results for semi-quantitative evaluation of completeness of fissures read by experienced radiologists and pneumologists show good agreement on the amount of defects (Koenigkam-Santos et al. 2012, 2013b). A future task for software-based image analysis will be reliable automatic quantification of fissural defects in COPD patients.

6 Clinical Correlation and Phenotyping

6.1 COPD

As stated earlier, the two dominant features of COPD are bronchial wall thickening on the one hand and emphysematous destruction of lung parenchyma on the other. In most patients suffering from COPD both manifestations (airway remodeling and emphysema) exist in varying degree of severity. As already mentioned, current research is aimed at gaining further insight into the heterogeneity of COPD manifestations by defining subgroups of different phenotypes. There are at least two subgroups of COPD patients that have been identified in several studies, which are considered to correspond to different phenotypes of the disease, namely, emphysema predominant on the one hand and airway predominant on the other.

Not surprisingly, bronchial wall thickening is the predominant factor limiting airflow. Wall thickness is found to be higher in smokers with COPD than in smokers or nonsmokers without COPD (Berger et al. 2005). Many studies show a good correlation between a decrease in FEV_1 and airway wall thickness (Hasegawa et al. 2006; Nakano et al. 2000, 2002), whereas the extent of emphysema does not necessarily exhibit such a good correlation (Zaporozhan et al. 2005; Achenbach et al. 2008; Baldi et al. 2001). The correlation between wall thickness and FEV_1 improves with a decrease in size of the measured airways (Hasegawa et al. 2006; Achenbach et al. 2008). This is consistent with the results of histopathologic studies, which reported that the major site of airway obstruction in COPD occurs in airways smaller than 2 mm in internal diameter (Hogg et al. 2004). Acquired tracheobronchomalacia is another common feature, mostly in advanced COPD, that also influences airflow. In the setting of chronic bronchitis it has been reported in up to 44 % of patients undergoing bronchoscopy (Jokinen et al. 1976). In COPD, tracheobronchomalacia is usually diffusely distributed, and affects the whole trachea and the main bronchi. The excessive narrowing of central airways may contribute to or worsen obstructive symptoms (Loring et al. 2007). In addition, the amount of emphysema has a significant influence on the breathing dynamics. The associated loss of elastic recoil of pulmonary parenchyma promotes instability of bronchial and bronchiolar structures, and hyperinflation is thought to give rise to paradoxic diaphragmatic displacement and atypical movement of the chest wall.

Despite the correlation between bronchial wall thickness and FEV_1, a recent study showed that the amount of airway wall thickening and the amount of emphysema correlate well with the frequency of exacerbations. Moreover, those correlations are independent from the rate of airflow obstruction measured by FEV_1. Patients with >35 % emphysema reported significantly higher frequency of exacerbations than patients with less than 35 % emphysema and without significant bronchial wall thickening. Likewise, patients with significant wall thickening reported more frequent exacerbations. Furthermore, the subgroups showed differences in their comorbidity: while for the prevalence of coronary artery disease no significant differences were reported, the emphysema-predominant type showed lower prevalence of diabetes and a higher prevalence of osteoporosis (Han et al. 2011). Such results emphasize the clinical implications of phenotyping airway disease via image analysis regarding risk stratification and better possibilities in managing targeted therapy.

The increasingly important role of emphysema quantification and assessment of pulmonary fissural defects by imaging techniques in the clinical context has already been pointed out in previous sections. Regarding suitability of a patient for ELVR by valve or coil implantation and also concerning the identification of target lobes for this kind of interventional therapy, imaging techniques will be increasingly relevant.

6.2 Asthma

In patients with asthma, chronic airway inflammation induces airway remodeling. Hence, the typical CT findings are bronchial wall thickening,

narrowing of the bronchial lumen, and/or bronchiectasis accompanied by areas of decreased lung attenuation, air trapping, and, in some cases, emphysema (Aysola et al. 2010). In a large cohort of patients with severe asthma, CT scan abnormalities were present in 80 % of patients. Often they coexisted with increased bronchial wall thickness (62 %), bronchiectasis (40 %), and emphysema (8 %) (Gupta et al. 2009). Airway wall thickness in asthma patients has been evaluated in many studies using either semiquantitative or fully quantitative methods. Comparing patients with healthy individuals, all of these studies came to similar conclusions: more airway wall thickening, increased wall thickness, and increased degree of airflow obstruction (Aysola et al. 2008; Harmanci et al. 2002; Kasahara et al. 2002; Little et al. 2002; Niimi et al. 2000; Takemura et al. 2004). Furthermore, there is a positive correlation between the severity of the disease and the amount of airway wall thickening, which is fully consistent with pathologic measures of remodeling from endobronchial biopsies and the degree of airflow obstruction (Aysola et al. 2008). The coincidence of increased severity of asthma and higher prevalence of bronchiectasis was also demonstrated (Harmanci et al. 2002). Here, patients with mild intermittent asthma mostly had normal CT scans, whereas patients with severe persistent asthma more frequently had at least one abnormal airway finding. In addition, longer disease duration was presumed to cause more bronchiectasis and thick linear opacities. Besides airway remodeling, asthma can cause acute complications such as pneumothorax, pneumomediastinum, pneumonia, mucoid impaction, and atelectasis in addition to chronic complications that include allergic bronchopulmonary aspergillosis, eosinophilic pneumonia, and Churg–Strauss vasculitis (Woods and Lynch 2009).

Airway wall thickening in asthma seems to be partially reversible when treated with inhaled corticosteroid in steroid-naive patients, although the decrease was not observed in the airway dimensions of a matched asymptomatic control group (Niimi et al. 2004). After a 1-year treatment, measured airway wall thickness decreased in patients with a duration of symptoms of less than 3 years, and a minor response was recognized in patients with a duration of symptoms from 3 to 5 years. However, there was no change in airway wall dimensions for patients who had asthma for longer than 5 years (Kurashima et al. 2008). As already mentioned, air trapping is seen in patients suffering from asthma on CT, but the correlation with asthma severity was found to be variable (Gono et al. 2003; Mitsunobu et al. 2001, 2003; Paganin et al. 1996). In a recent study, air trapping in patients with asthma identified a group of individuals at high risk for severe disease. These patients were significantly more likely to have a history of asthma-related hospitalizations, intensive care unit visits, and/or mechanical ventilation. Moreover, the duration of asthma, history of pneumonia, neutrophilic inflammation, airway obstruction, and atopy were identified as independent risk factors associated with the presence of air trapping (Busacker et al. 2009), which might denote a special phenotype of asthma that could be detected by imaging examination and thus receive more thorough monitoring and treatment (Kauczor et al. 2011).

Conclusion

Technical innovations in CT and the introduction of new methods, especially regarding postprocessing analysis, in pulmonary CT have enabled a wide range of new possibilities in imaging pulmonary diseases. Whereas in the past the main diagnostic tools for COPD and asthma were pulmonary function tests, CT evaluation has gained increased importance not only in the context of clinical trials and scientific analysis but also in routine assessment and monitoring of the disease. By exactly and systematically analyzing airway remodeling on the one hand and emphysematous parenchymal destruction on the other, today's heterogeneous group of COPD patients can easily be classified in unprecedented detail. The main finding of recent studies is the confirmation of at least two different phenotypes of COPD, namely the emphysema-predominant and the airway-predominant type of disease. This differentiation not only enables better statistical evaluation in

scientific analysis, but also sets up new possibilities in personalized care and treatment. By identifying subgroups of patients at higher risk of complications and/or with a higher probability of rapid progress of the disease, therapeutic management can be adapted accordingly, enabling the chance for better patient outcomes. The feasibility evaluation of novel treatment options in emphysema patients, namely ELVR, is another field of pulmonary imaging with upcoming importance in daily clinical practice. The constant efforts in reducing radiation dose on the one hand and increasing image quality when needed on the other have furthermore enabled several new possibilities in dynamic and functional CT imaging. While many methods have already been well established in clinical routine, there are still challenges to be addressed, which in the future are expected to confirm and increase the benefit of CT in patients with COPD and emphysema.

References

Achenbach T, Weinheimer O, Buschsieweke C, Heussel CP, Thelen M, Kauczor HU (2004) Fully automatic detection and quantification of emphysema on thin section MD-CT of the chest by a new and dedicated software. Rofo 176(10):1409–1415. doi:10.1055/s-2004-813530

Achenbach T, Weinheimer O, Biedermann A, Schmitt S, Freudenstein D, Goutham E, Kunz RP, Buhl R, Dueber C, Heussel CP (2008) MDCT assessment of airway wall thickness in COPD patients using a new method: correlations with pulmonary function tests. Eur Radiol 18(12):2731–2738. doi:10.1007/s00330-008-1089-4

Aysola RS, Hoffman EA, Gierada D, Wenzel S, Cook-Granroth J, Tarsi J, Zheng J, Schechtman KB, Ramkumar TP, Cochran R, Xueping E, Christie C, Newell J, Fain S, Altes TA, Castro M (2008) Airway remodeling measured by multidetector CT is increased in severe asthma and correlates with pathology. Chest 134(6):1183–1191. chest.07-2779 [pii]. doi:10.1378/chest.07-2779

Aysola R, de Lange EE, Castro M, Altes TA (2010) Demonstration of the heterogeneous distribution of asthma in the lungs using CT and hyperpolarized helium-3 MRI. J Magn Reson Imaging 32(6):1379–1387. doi:10.1002/jmri.22388

Baldi S, Miniati M, Bellina CR, Battolla L, Catapano G, Begliomini E, Giustini D, Giuntini C (2001) Relationship between extent of pulmonary emphysema by high-resolution computed tomography and lung elastic recoil in patients with chronic obstructive pulmonary disease. Am J Respir Crit Care Med 164(4):585–589

Barbosa EM Jr, Song G, Tustison N, Kreider M, Gee JC, Gefter WB, Torigian DA (2011) Computational analysis of thoracic multidetector row HRCT for segmentation and quantification of small airway air trapping and emphysema in obstructive pulmonary disease. Acad Radiol 18(10):1258–1269. S1076-6332(11)00299-6 [pii]. doi:10.1016/j.acra.2011.06.004

Barnes PJ (2008) Immunology of asthma and chronic obstructive pulmonary disease. Nat Rev Immunol 8(3):183–192. doi:10.1038/nri2254

Beigelman-Aubry C, Hill C, Guibal A, Savatovsky J, Grenier PA (2005) Multi-detector row CT and post-processing techniques in the assessment of diffuse lung disease. Radiographics 25(6):1639–1652. 25/6/1639 [pii]. doi:10.1148/rg.256055037

Berger P, Perot V, Desbarats P, Tunon-de-Lara JM, Marthan R, Laurent F (2005) Airway wall thickness in cigarette smokers: quantitative thin-section CT assessment. Radiology 235(3):1055–1064. 2353040121 [pii]. doi:10.1148/radiol.2353040121

Brillet PY, Fetita CI, Saragaglia A, Brun AL, Beigelman-Aubry C, Preteux F, Grenier PA (2008) Investigation of airways using MDCT for visual and quantitative assessment in COPD patients. Int J Chron Obstruct Pulmon Dis 3(1):97–107

Brillet PY, Fetita CI, Capderou A, Mitrea M, Dreuil S, Simon JM, Preteux F, Grenier PA (2009) Variability of bronchial measurements obtained by sequential CT using two computer-based methods. Eur Radiol 19(5):1139–1147. doi:10.1007/s00330-008-1247-8

Busacker A, Newell JD Jr, Keefe T, Hoffman EA, Granroth JC, Castro M, Fain S, Wenzel S (2009) A multivariate analysis of risk factors for the air-trapping asthmatic phenotype as measured by quantitative CT analysis. Chest 135(1):48–56. chest.08-0049 [pii]. doi:10.1378/chest.08-0049

Chae EJ, Seo JB, Goo HW, Kim N, Song KS, Lee SD, Hong SJ, Krauss B (2008) Xenon ventilation CT with a dual-energy technique of dual-source CT: initial experience. Radiology 248(2):615–624. 248/2/615 [pii]. doi:10.1148/radiol.2482071482

Chung KF (2005) The role of airway smooth muscle in the pathogenesis of airway wall remodeling in chronic obstructive pulmonary disease. Proc Am Thorac Soc 2(4):347–354; discussion 371–342. doi:10.1513/pats.200504-028SR

Coxson HO, Mayo J, Lam S, Santyr G, Parraga G, Sin DD (2009) New and current clinical imaging techniques to study chronic obstructive pulmonary disease. Am J Respir Crit Care Med 180(7):588–597. 200901-0159PP [pii]. doi:10.1164/rccm.200901-0159PP

de Jong PA, Muller NL, Pare PD, Coxson HO (2005) Computed tomographic imaging of the airways: relationship to structure and function. Eur Respir J 26(1):140–152. 26/1/140 [pii]. doi:10.1183/09031936.05.00007105

Dinkel J, Hintze C, Rochet N, Thieke C, Biederer J (2009) Computed tomography of the lungs. A step into the fourth dimension. Radiologe 49(8):698–704. doi:10.1007/s00117-009-1879-y

Fain S, Schiebler ML, McCormack DG, Parraga G (2010) Imaging of lung function using hyperpolarized helium-3 magnetic resonance imaging: review of current and emerging translational methods and applications. J Magn Reson Imaging 32(6):1398–1408. doi:10.1002/jmri.22375

Gierada DS, Bierhals AJ, Choong CK, Bartel ST, Ritter JH, Das NA, Hong C, Pilgram TK, Bae KT, Whiting BR, Woods JC, Hogg JC, Lutey BA, Battafarano RJ, Cooper JD, Meyers BF, Patterson GA (2010) Effects of CT section thickness and reconstruction kernel on emphysema quantification relationship to the magnitude of the CT emphysema index. Acad Radiol 17(2):146–156. doi:10.1016/j.acra.2009.08.007

Gono H, Fujimoto K, Kawakami S, Kubo K (2003) Evaluation of airway wall thickness and air trapping by HRCT in asymptomatic asthma. Eur Respir J 22(6):965–971

Grydeland TB, Thorsen E, Dirksen A, Jensen R, Coxson HO, Pillai SG, Sharma S, Eide GE, Gulsvik A, Bakke PS (2011) Quantitative CT measures of emphysema and airway wall thickness are related to D(L) CO. Respir Med 105(3):343–351. doi:10.1016/j.rmed.2010.10.018

Gupta S, Siddiqui S, Haldar P, Raj JV, Entwisle JJ, Wardlaw AJ, Bradding P, Pavord ID, Green RH, Brightling CE (2009) Qualitative analysis of high-resolution CT scans in severe asthma. Chest 136(6):1521–1528. chest.09-0174 [pii]. doi:10.1378/chest.09-0174

Han MK, Kazerooni EA, Lynch DA, Liu LX, Murray S, Curtis JL, Criner GJ, Kim V, Bowler RP, Hanania NA, Anzueto AR, Make BJ, Hokanson JE, Crapo JD, Silverman EK, Martinez FJ, Washko GR (2011) Chronic obstructive pulmonary disease exacerbations in the COPDGene study: associated radiologic phenotypes. Radiology 261(1):274–282. radiol.11110173 [pii]. doi:10.1148/radiol.11110173

Harmanci E, Kebapci M, Metintas M, Ozkan R (2002) High-resolution computed tomography findings are correlated with disease severity in asthma. Respiration 69(5):420–426, doi:res69420 [pii]

Hasegawa M, Nasuhara Y, Onodera Y, Makita H, Nagai K, Fuke S, Ito Y, Betsuyaku T, Nishimura M (2006) Airflow limitation and airway dimensions in chronic obstructive pulmonary disease. Am J Respir Crit Care Med 173(12):1309–1315. 200601-037OC [pii]. doi:10.1164/rccm.200601-037OC

Heussel CP, Hafner B, Lill J, Schreiber W, Thelen M, Kauczor HU (2001) Paired inspiratory/expiratory spiral CT and continuous respiration cine CT in the diagnosis of tracheal instability. Eur Radiol 11(6):982–989

Heussel CP, Achenbach T, Buschsieweke C, Kuhnigk J, Weinheimer O, Hammer G, Duber C, Kauczor HU (2006) Quantification of pulmonary emphysema in multislice-CT using different software tools. Rofo 178(10):987–998. doi:10.1055/s-2006-926823

Heussel CP, Kappes J, Hantusch R, Hartlieb S, Weinheimer O, Kauczor HU, Eberhardt R (2009) Contrast enhanced CT-scans are not comparable to non-enhanced scans in emphysema quantification. Eur J Radiol 74(3):473–478. S0720-048X(09)00136-3 [pii]. doi:10.1016/j.ejrad.2009.03.023

Hogg JC, Chu F, Utokaparch S, Woods R, Elliott WM, Buzatu L, Cherniack RM, Rogers RM, Sciurba FC, Coxson HO, Pare PD (2004) The nature of small-airway obstruction in chronic obstructive pulmonary disease. N Engl J Med 350(26):2645–2653. doi:10.1056/NEJMoa032158350/26/2645 [pii]

Jokinen K, Palva T, Nuutinen J (1976) Chronic bronchitis. A bronchologic evaluation. ORL J Otorhinolaryngol Relat Spec 38(3):178–186

Kasahara K, Shiba K, Ozawa T, Okuda K, Adachi M (2002) Correlation between the bronchial subepithelial layer and whole airway wall thickness in patients with asthma. Thorax 57(3):242–246

Kauczor HU, Wielpütz MO, Owsijewitsch M, Ley-Zaporozhan J (2011) Computed tomographic imaging of the airways in COPD and asthma. J Thorac Imaging 26(4):290–300. 00005382-201111000-00006 [pii]. doi:10.1097/RTI.0b013e3182277113

Koenigkam-Santos M, Puderbach M, Gompelmann D, Eberhardt R, Herth F, Kauczor HU, Heussel CP (2012) Incomplete fissures in severe emphysematous patients evaluated with MDCT: incidence and interobserver agreement among radiologists and pneumologists. Eur J Radiol 81(12):4161–4166. doi:10.1016/j.ejrad.2012.06.006

Koenigkam-Santos M, de Paula WD, Owsijewitsch M, Wielputz MO, Gompelmann D, Schlemmer HP, Kauczor HU, Heussel CP, Puderbach M (2013) Incomplete pulmonary fissures evaluated by volumetric thin-section CT: semi-quantitative evaluation for small fissure gaps identification, description of prevalence and severity of fissural defects. Eur J Radiol 82(12):2365–2370. S0720-048X(13)00428-2 [pii]. doi:10.1016/j.ejrad.2013.08.029

Koenigkam-Santos M, de Paula WD, Owsijewitsch M, Wielputz MO, Gompelmann D, Schlemmer HP, Kauczor HU, Heussel CP, Puderbach M (2013b) Incomplete pulmonary fissures evaluated by volumetric thin-section CT: semi-quantitative evaluation for small fissure gaps identification, description of prevalence and severity of fissural defects. Eur J Radiol 82(12):2365–2370. doi:10.1016/j.ejrad.2013.08.029

Koyama H, Ohno Y, Nishio M, Matsumoto S, Sugihara N, Yoshikawa T, Seki S, Sugimura K (2014) Iterative reconstruction technique vs filter back projection: utility for quantitative bronchial assessment on low-dose thin-section MDCT in patients with/without chronic obstructive pulmonary disease. Eur Radiol 24(8):1860–1867. doi:10.1007/s00330-014-3207-9

Kurashima K, Kanauchi T, Hoshi T, Takaku Y, Ishiguro T, Takayanagi N, Ubukata M, Sugita Y (2008) Effect of

early versus late intervention with inhaled corticosteroids on airway wall thickness in patients with asthma. Respirology 13(7):1008–1013. RES1384 [pii]. doi:10.1111/j.1440-1843.2008.01384.x

Little SA, Sproule MW, Cowan MD, Macleod KJ, Robertson M, Love JG, Chalmers GW, McSharry CP, Thomson NC (2002) High resolution computed tomographic assessment of airway wall thickness in chronic asthma: reproducibility and relationship with lung function and severity. Thorax 57(3):247–253

Loring SH, O'Donnell C R, Feller-Kopman DJ, Ernst A (2007) Central airway mechanics and flow limitation in acquired tracheobronchomalacia. Chest 131(4):1118–1124. 131/4/1118 [pii]. doi:10.1378/chest.06-2556

Madani A, De Maertelaer V, Zanen J, Gevenois PA (2007) Pulmonary emphysema: radiation dose and section thickness at multidetector CT quantification–comparison with macroscopic and microscopic morphometry. Radiology 243(1):250–257. doi:10.1148/radiol.2431060194

Matsuoka S, Kurihara Y, Yagihashi K, Hoshino M, Watanabe N, Nakajima Y (2008) Quantitative assessment of air trapping in chronic obstructive pulmonary disease using inspiratory and expiratory volumetric MDCT. AJR Am J Roentgenol 190(3):762–769. 190/3/762 [pii]. doi:10.2214/AJR.07.2820

Mc LK (1957a) The histology of generalized pulmonary emphysema. II. Diffuse emphysema. Australas Ann Med 6(3):203–217

Mc LK (1957b) The histology of localized emphysema. Australas Ann Med 6(4):282–294

McDonough JE, Yuan R, Suzuki M, Seyednejad N, Elliott WM, Sanchez PG, Wright AC, Gefter WB, Litzky L, Coxson HO, Pare PD, Sin DD, Pierce RA, Woods JC, McWilliams AM, Mayo JR, Lam SC, Cooper JD, Hogg JC (2011) Small-airway obstruction and emphysema in chronic obstructive pulmonary disease. N Engl J Med 365(17):1567–1575. doi:10.1056/NEJMoa1106955

McLean KH (1956) The macroscopic anatomy of pulmonary emphysema. Australas Ann Med 5(2):73–88

McLean KH (1957) The histology of generalized pulmonary emphysema. I. The genesis of the early centrolobular lesion: focal emphysema. Australas Ann Med 6(2):124–140

Mets OM, Willemink MJ, de Kort FP, Mol CP, Leiner T, Oudkerk M, Prokop M, de Jong PA (2012) The effect of iterative reconstruction on computed tomography assessment of emphysema, air trapping and airway dimensions. Eur Radiol 22(10):2103–2109. doi:10.1007/s00330-012-2489-z

Mitsunobu F, Mifune T, Ashida K, Hosaki Y, Tsugeno H, Okamoto M, Harada S, Takata S, Tanizaki Y (2001) Influence of age and disease severity on high resolution CT lung densitometry in asthma. Thorax 56(11):851–856

Mitsunobu F, Ashida K, Hosaki Y, Tsugeno H, Okamoto M, Nishida N, Nagata T, Takata S, Tanizaki Y (2003) Decreased computed tomographic lung density during exacerbation of asthma. Eur Respir J 22(1):106–112

Nakano Y, Muro S, Sakai H, Hirai T, Chin K, Tsukino M, Nishimura K, Itoh H, Pare PD, Hogg JC, Mishima M (2000) Computed tomographic measurements of airway dimensions and emphysema in smokers. Correlation with lung function. Am J Respir Crit Care Med 162(3 Pt 1):1102–1108

Nakano Y, Muller NL, King GG, Niimi A, Kalloger SE, Mishima M, Pare PD (2002) Quantitative assessment of airway remodeling using high-resolution CT. Chest 122(6 Suppl):271S–275S

Nakano Y, Wong JC, de Jong PA, Buzatu L, Nagao T, Coxson HO, Elliott WM, Hogg JC, Pare PD (2005) The prediction of small airway dimensions using computed tomography. Am J Respir Crit Care Med 171(2):142–146. 200407-874OC [pii]. doi:10.1164/rccm.200407-874OC

Niimi A, Matsumoto H, Amitani R, Nakano Y, Mishima M, Minakuchi M, Nishimura K, Itoh H, Izumi T (2000) Airway wall thickness in asthma assessed by computed tomography. Relation to clinical indices. Am J Respir Crit Care Med 162(4 Pt 1):1518–1523

Niimi A, Matsumoto H, Amitani R, Nakano Y, Sakai H, Takemura M, Ueda T, Chin K, Itoh H, Ingenito EP, Mishima M (2004) Effect of short-term treatment with inhaled corticosteroid on airway wall thickening in asthma. Am J Med 116(11):725–731. doi:10.1016/j.amjmed.2003.11.026, S0002934304000464 [pii]

Nishio M, Matsumoto S, Ohno Y, Sugihara N, Inokawa H, Yoshikawa T, Sugimura K (2012) Emphysema quantification by low-dose CT: potential impact of adaptive iterative dose reduction using 3D processing. AJR Am J Roentgenol 199(3):595–601. doi:10.2214/AJR.11.8174

Paganin F, Seneterre E, Chanez P, Daures JP, Bruel JM, Michel FB, Bousquet J (1996) Computed tomography of the lungs in asthma: influence of disease severity and etiology. Am J Respir Crit Care Med 153(1):110–114

Pansini V, Remy-Jardin M, Faivre JB, Schmidt B, Dejardin-Bothelo A, Perez T, Delannoy V, Duhamel A, Remy J (2009) Assessment of lobar perfusion in smokers according to the presence and severity of emphysema: preliminary experience with dual-energy CT angiography. Eur Radiol 19:2834–2843. doi:10.1007/s00330-009-1475-6

Park JW, Hong YK, Kim CW, Kim DK, Choe KO, Hong CS (1997) High-resolution computed tomography in patients with bronchial asthma: correlation with clinical features, pulmonary functions and bronchial hyperresponsiveness. J Investig Allergol Clin Immunol 7(3):186–192

Park EA, Goo JM, Park SJ, Lee HJ, Lee CH, Park CM, Yoo CG, Kim JH (2010) Chronic obstructive pulmonary disease: quantitative and visual ventilation pattern analysis at xenon ventilation CT performed by using a dual-energy technique. Radiology 256(3):985–997. radiol.10091502 [pii]. doi:10.1148/radiol.10091502

Pauwels RA, Buist AS, Calverley PM, Jenkins CR, Hurd SS (2001) Global strategy for the diagnosis, management, and prevention of chronic obstructive pulmonary disease. NHLBI/WHO Global Initiative for Chronic Obstructive Lung Disease (GOLD) workshop summary. Am J Respir Crit Care Med 163(5):1256–1276

Pontana F, Duhamel A, Pagniez J, Flohr T, Faivre JB, Hachulla AL, Remy J, Remy-Jardin M (2011) Chest computed tomography using iterative reconstruction vs filtered back projection (part 2): image quality of low-dose CT examinations in 80 patients. Eur Radiol 21(3):636–643. doi:10.1007/s00330-010-1991-4

Rabe KF, Hurd S, Anzueto A, Barnes PJ, Buist SA, Calverley P, Fukuchi Y, Jenkins C, Rodriguez-Roisin R, van Weel C, Zielinski J (2007) Global strategy for the diagnosis, management, and prevention of chronic obstructive pulmonary disease: GOLD executive summary. Am J Respir Crit Care Med 176(6):532–555. 200703-456SO [pii]. doi:10.1164/rccm.200703-456SO

Reinhardt JM, D'Souza ND, Hoffman EA (1997) Accurate measurement of intrathoracic airways. IEEE Trans Med Imaging 16(6):820–827. doi:10.1109/42.650878

Remy-Jardin M, Remy J (2008) Vascular disease in chronic obstructive pulmonary disease. Proc Am Thorac Soc 5(9):891–899. 5/9/891 [pii]. doi:10.1513/pats.200804-036QC

Saba OI, Hoffman EA, Reinhardt JM (2003) Maximizing quantitative accuracy of lung airway lumen and wall measures obtained from X-ray CT imaging. J Appl Physiol 95(3):1063–1075. doi:10.1152/japplphysiol.00962.2002, 00962.2002 [pii]

Stoel BC, Putter H, Bakker ME, Dirksen A, Stockley RA, Piitulainen E, Russi EW, Parr D, Shaker SB, Reiber JH, Stolk J (2008) Volume correction in computed tomography densitometry for follow-up studies on pulmonary emphysema. Proc Am Thorac Soc 5(9):919–924. doi:10.1513/pats.200804-040QC

Takemura M, Niimi A, Minakuchi M, Matsumoto H, Ueda T, Chin K, Mishima M (2004) Bronchial dilatation in asthma: relation to clinical and sputum indices. Chest 125(4):1352–1358

Venkatraman R, Raman R, Raman B, Moss RB, Rubin GD, Mathers LH, Robinson TE (2006) Fully automated system for three-dimensional bronchial morphology analysis using volumetric multidetector computed tomography of the chest. J Digit Imaging 19(2):132–139. doi:10.1007/s10278-005-9240-0

Weinheimer O, Achenbach T, Bletz C, Duber C, Kauczor HU, Heussel CP (2008) About objective 3-d analysis of airway geometry in computerized tomography. IEEE Trans Med Imaging 27(1):64–74. doi:10.1109/TMI.2007.902798

Wielputz MO, Bardarova D, Weinheimer O, Kauczor HU, Eichinger M, Jobst BJ, Eberhardt R, Koenigkam-Santos M, Puderbach M, Heussel CP (2014) Variation of densitometry on computed tomography in COPD – influence of different software tools. PLoS One 9(11), e112898. doi:10.1371/journal.pone.0112898

Wildberger JE, Klotz E, Ditt H, Spuntrup E, Mahnken AH, Gunther RW (2005) Multislice computed tomography perfusion imaging for visualization of acute pulmonary embolism: animal experience. Eur Radiol 15(7):1378–1386. doi:10.1007/s00330-005-2718-9

Woods AQ, Lynch DA (2009) Asthma: an imaging update. Radiol Clin North Am 47 (2):317–329. S0033-8389(08)00219-4 [pii]. doi:10.1016/j.rcl.2008.11.008

Zaporozhan J, Ley S, Eberhardt R, Weinheimer O, Iliyushenko S, Herth F, Kauczor HU (2005) Paired inspiratory/expiratory volumetric thin-slice CT scan for emphysema analysis: comparison of different quantitative evaluations and pulmonary function test. Chest 128(5):3212–3220. 128/5/3212 [pii]. doi:10.1378/chest.128.5.3212

CT Imaging of Interstitial Lung Diseases

Marieke Hovinga, Ralf Sprengers, Hans-Ulrich Kauczor, and Cornelia Schaefer-Prokop

Abstract

Until today, computed tomography (CT) is the most important and valuable radiological modality to detect, analyze, and diagnose diffuse interstitial lung diseases (DILD), based on the unsurpassed morphological detail provided by high-resolution CT technique.

In the past decade, there has been a shift from an isolated histopathological diagnosis to a multidisciplinary acquired diagnosis consensus that is nowadays regarded to provide the highest level of diagnostic accuracy in patients with diffuse interstitial lung diseases. The 2002 ATS/ERS statement on classification of idiopathic interstitial pneumonias assigned a central role to high-resolution CT (HRCT) in the diagnostic workup of idiopathic interstitial pneumonias (ATS/ERS consensus classification 2002). The more recent 2013 ERS/ATS statement reinforced that combined clinical data (presentation, exposures, smoking status, associated diseases, lung function, and laboratory findings) and radiological findings are essential for a multidisciplinary diagnosis (Travis et al., Am J Respir Crit Care Med 188(6):733–748, 2013).

The traditional HRCT consisted of discontinuous 1 mm high-resolution axial slices. The primary focus was on visual pattern analysis demanding

M. Hovinga • R. Sprengers
Department of Radiology, Meander Medical Center, Amersfoort, The Netherlands

H.-U. Kauczor
Department of Radiology, University of Heidelberg, Heidelberg, Germany

C. Schaefer-Prokop (✉)
Department of Radiology, Meander Medical Center, Amersfoort, The Netherlands

Department of Radiology, Radboud University Nijmegen, Nijmegen, The Netherlands
e-mail: cornelia.schaeferprokop@gmail.com

U.J. Schoepf, F.G. Meinel (eds.), *Multidetector-Row CT of the Thorax*, Medical Radiology,
DOI 10.1007/978-3-319-30355-0_7

for the highest possible spatial resolution. Because of the intrinsic high structural contrast of the lung, it has been possible to substantially reduce dose without losing diagnostic information. This development has been supported by new detection and reconstruction techniques. Not only detection of subtle disease and visual comparison of disease stage but also disease classification and quantification nowadays take advantage of continuous volumetric data acquisition provided by multidetector row (MD) CT technique. The following book chapter will focus on acquisition technique with special emphasis on dose and reconstruction, advantages, and new diagnostic options of volumetric MDCT technique for interstitial lung diseases. Based on evidence from the literature, certain diseases will be covered more specifically, but it has to be noted that for the pattern analysis of the various interstitial lung diseases, the plethora of other publications and books is recommended.

1 Introduction

Until today, computed tomography (CT) is the most important and valuable radiological modality to detect, analyze, and diagnose diffuse interstitial lung diseases (DILD), based on the unsurpassed morphological detail provided by high-resolution CT technique.

In the past decade, there has been a shift from an isolated histopathological diagnosis to a multidisciplinary acquired diagnosis consensus, that is nowadays regarded to provide the highest level of diagnostic accuracy in patients with diffuse interstitial lung diseases. The 2002 ATS/ERS statement on classification of idiopathic interstitial pneumonias assigned a central role to high-resolution CT (HRCT) in the diagnostic workup of idiopathic interstitial pneumonias (ATS/ERS consensus classification 2002). The more recent 2013 ERS/ATS statement reinforced that combined clinical data (presentation, exposures, smoking status, associated diseases, lung function, and laboratory findings) *and* radiological findings are essential for a multidisciplinary diagnosis (Travis et al. 2013).

The traditional HRCT consisted of discontinuous 1 mm high-resolution axial slices. The primary focus was on visual pattern analysis demanding for the highest possible spatial resolution. Because of the intrinsic high structural contrast of the lung, it has been possible to substantially reduce dose without losing diagnostic information. This development has been supported by new detection and reconstruction techniques. Not only detection of subtle disease and visual comparison of disease stage but also disease classification and quantification nowadays take advantage of continuous volumetric data acquisition provided by multidetector row (MD) CT technique.

The following book chapter will focus on acquisition technique with special emphasis on dose and reconstruction, advantages, and new diagnostic options of volumetric MDCT technique for interstitial lung diseases. Based on evidence from the literature, certain diseases will be covered more specifically, but it has to be noted that for the pattern analysis of the various interstitial lung diseases, the plethora of other publications and books is recommended.

2 Acquisition Technique

Traditionally CT and HRCT were strongly differentiated with the latter being defined by a section thickness of <1.5 mm and the use of an edge-enhancing high-resolution reconstruction kernel. Since the advent of MDCT technique, which allows for covering the whole chest in thin section technique within one breath-hold, essentially *each* chest CT is a HRCT.

Reconstruction of 1, 3, or 5 mm thick slices determines the number of axial images to be evaluated. Besides for a given acquisition dose, a 3 mm thick slice has a better signal-to-noise ratio than a 1 mm thick slice. A 1 mm thick slice, however, offers a higher spatial resolution and thus superior morphological detail. These trade-offs therefore determine the choice of reconstruction depending on the clinical indication: analysis of an (advanced) tumor stage is mostly done with thicker slices, while analysis of diffuse interstitial lung disease or focal nodular disease requires maximum detail resolution and therefore thin slices.

Before the advent of MDCT, HRCT consisted of a thin section CT obtained with 1 mm slice thickness at 10 or even 20 mm gaps. The rationale behind such a protocol was that analysis of a diffuse parenchymal process does not require continuous coverage. Secondly, discontinuous scanning warranted the relatively high-dose use to achieve the excellent signal-to-noise, image quality, and thus detail resolution.

Several developments have contributed to the fact that over the last years, discontinuous HRCT acquisition has been increasingly replaced by volumetric data acquisition, and they will be discussed more extensively below. In short, these developments refer to:

(a) Modern MDCT scanners allow for acquisition of volumetric HRCT with high image quality at acceptable dose levels, which furthermore have been continuously decreasing over the last decades due to improved detector technology and advanced reconstruction algorithms (see also "iterative noise reconstruction").
(b) Modern scanners perform faster, allowing for a single continuous scan in deep breath-hold instead of acquiring discontinuous slices with multiple scans that require repetitive breath-hold maneuvers.
(c) Volumetric 2D and 3D display techniques such as multiplanar reconstructions (MPR), maximum and minimum intensity projections (MIP and MinIP), as well as advanced volumetric quantification techniques became only possible with continuous volumetric data acquisition.
(d) Volumetric scans allow for an easier and also more precise comparison of disease development over time in follow-up studies because slices exactly matching to each other can be compared.
(e) Volumetric scans will also capture subtle and focal disease, potentially missed when data are acquired with large gaps in between.

Nevertheless a questionnaire among members of the European Society of Thoracic Imaging carried out in 2013 revealed that a subgroup of radiologists (15 %) still uses discontinuous HRCTs for analysis of interstitial lung diseases (Prosch et al. 2013). To which extent various aspects such as the scanner technology availability, expected image quality, or unwillingness to give up the old, but familiar techniques play a role in this remains unclear.

2.1 Scan Collimation and Slice Reconstruction

There are two essential factors that constitute a "high-resolution" CT study: firstly, thin axial slices using narrow detector width (0.5–1.25 mm) and reconstruction of 1–1.5 mm thick slices (Fig. 1) and, secondly, reconstruction of the scan data with a high-spatial-frequency (sharp or high-resolution) algorithm (Muller 1991).

Whether the whole lung can be covered within one breath-hold with 1 mm collimation width depends on the speed of data acquisition. While a four-slice CT scanner still needed more than 25 s to cover a chest length of 30 cm, a 16-slice scanner provided already the technical base to cover the thorax (30 cm length) in less than 15 s when a table feed of 1.5 mm was used. A 64-slice scanner allowed for a scan time below 10 s. The most modern scanners (128-slice scanners and beyond) allow for coverage of the chest in less than 3 s while acquiring data with isotropic submillimeter resolution. Thus, speed of data acquisition within one breath-hold does not represent a limitation anymore.

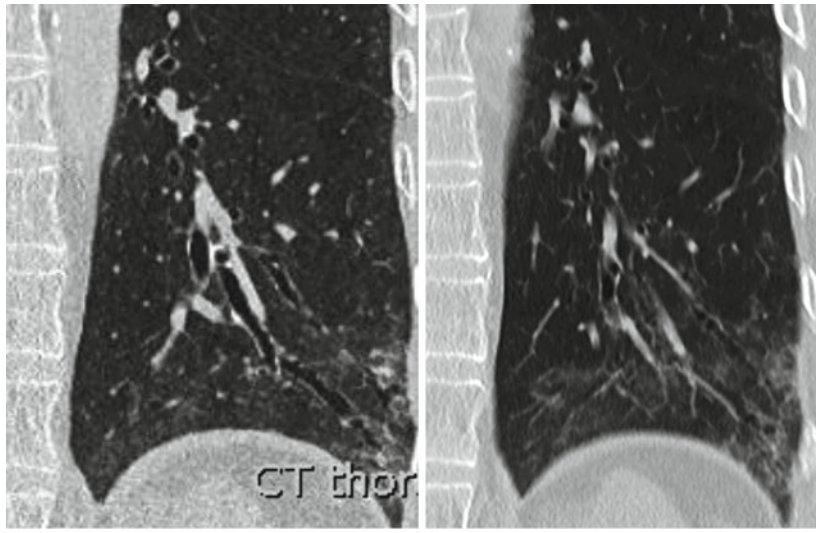

Fig. 1 Coronal reconstructions 1 mm versus 3 mm slice thickness demonstrating the impact of SL on detail resolution

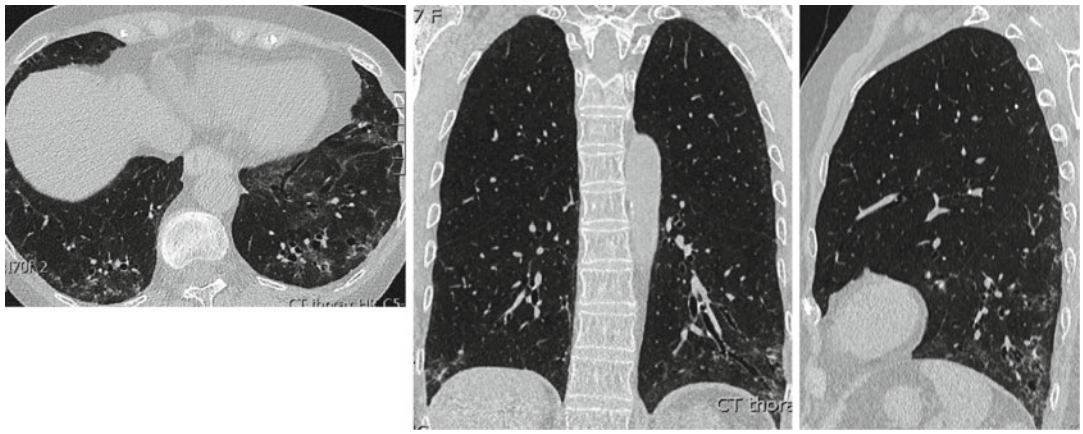

Fig. 2 Isotropic resolution in all three dimensions allows for axial, coronal, and sagittal reconstructions with equally high detail resolution. While pattern analysis is done on axial slices, the multiplanar reconstructions (MPR) nicely demonstrate the subpleural and craniocaudal distribution of disease in this patient with systemic sclerosis

The ability of HRCT to provide high morphological detail of normal and abnormal lung parenchyma is based on high-quality examinations. With optimal scan technique, the spatial resolution is as low as 0.5 mm. Due to the high contrast within the lung parenchyma, even structures as small as 0.2 mm can be visualized (Murata et al. 1989). Thus, pulmonary artery branches down to the 16th and bronchi down to the 8th generation can be depicted. Since partial volume averaging effects on the margins of such small structures are minimized, HRCT provides a very accurate image of their true size. This represents the base for CT-based quantification, e.g., of bronchial wall thickness and airway lumen in COPD patients. Since this high resolution is available isotropically, meaning in all three directions, diameters of vessels, lung nodules, or obliquely oriented bronchi are accurately reflected, irrespective of their location in or near the scan plane or even perpendicular to the scan plane (Fig. 2).

Spatial resolution is increased by the application of a high-spatial-frequency reconstruction algorithm (Mayo et al. 1987). Standard algorithms lead to smoothening of the image in respect that visible image noise is reduced and contrast resolution increased. Sharp, high-spatial-frequency, or high-resolution algorithms, on the other hand, reduce image smoothening and increase spatial resolution. Anatomic margins and tissue interfaces, such as the fissure, pleura, or septa, appear sharper. Small vessels and bronchi are seen superiorly compared to a standard algorithm.

Reducing the field of view results in smaller pixel sizes and thus increases spatial resolution. In general, the field of view should be adjusted to the size of the lungs, usually resulting in a spatial resolution of 0.5–0.3 mm. To ensure that the field of view does not cut off any parts of the lung, it is usually limited by the diameter of the external cortex of the ribs.

To further increase spatial resolution, targeting of the field of view to a single lung or particular lobes or regions can be performed. Such an approach may be used for minute evaluation of the parenchyma or peripheral bronchi beyond the regular evaluation of images demonstrating both lungs. However, with this approach, the spatial resolution will be limited by the intrinsic resolution of the detectors and whether it will gain diagnostic information will largely depend on personal preferences. There is no literature reference that generally recommends this approach, not even for certain indications. In addition, it requires additional reconstruction time, the raw data scan must be saved until targeting is performed, and it precludes the ability to compare both lungs on the same image.

2.2 Dose Aspects

One of the major arguments not to change from discontinuous HRCT (10 or 20 mm gap) to continuous volumetric data acquisition was the associated increase in dose. Since 1 mm thin sections need to have a certain signal-to-noise level to provide acceptable diagnostic image quality, it was inevitable that volumetric data acquisition would deliver a higher dose to the patient.

Table 1 Dose ranges of HRCT techniques demonstrating the potential of modern dose-reduction techniques

Effective radiation dose (mSv)	
Yearly background radiation	2.5
PA chest radiograph	0.05
Discontinuous HRCT (10 mm gap)	0.7
Volumetric HRCT	4–7
Volumetric HRCT with xyz-modulation	3–5
Volumetric HRCT with iterative noise reconstruction	1.5–3

3D dose modulation – automatically adapting the delivered dose in the transverse plane (*xy*-axis) and along patient length (*z*-axis) – is an effective means to reduce dose by about 30 % and is strongly recommended (Kubo et al. 2014) (Table 1). The abovementioned survey in 2013 confirmed that 90 % of the respondents indeed apply it. Additional options are to adapt the protocol to patient weight, patient age, or scan indication. Principally a tube voltage of 120 kV is recommended, but in young patients or patients of lower body weight, a tube voltage of 100 kV can be applied, further contributing to dose saving. The tube current is mostly set around 100 mAs. Ultimately a dose between 1.5 and 4 mSv should be aimed for (Fig. 3).

There is a multitude of publications evaluating low-dose protocols (40–60 mAs), most of them for the detection of nodules or within a screening setting. Those results cannot be directly transferred to the diagnostic workup of DILD, in which detection of ground-glass opacities and fine septal thickenings is required. Christe A et al. systematically evaluated the efficiency of a low-dose protocol for the detection of common patterns of pulmonary diseases evaluating 1 mm slices, reconstructed with filtered back projection (FBP) and a high reconstruction kernel. They concluded that a 120 kVp/40 mAs protocol was feasible for detecting solid nodules, air space consolidations, and airway and pleural diseases; however, pathologies consisting of ground-glass opacities and interstitial opacities required higher tube current or iterative noise reconstruction (Christe et al. 2013).

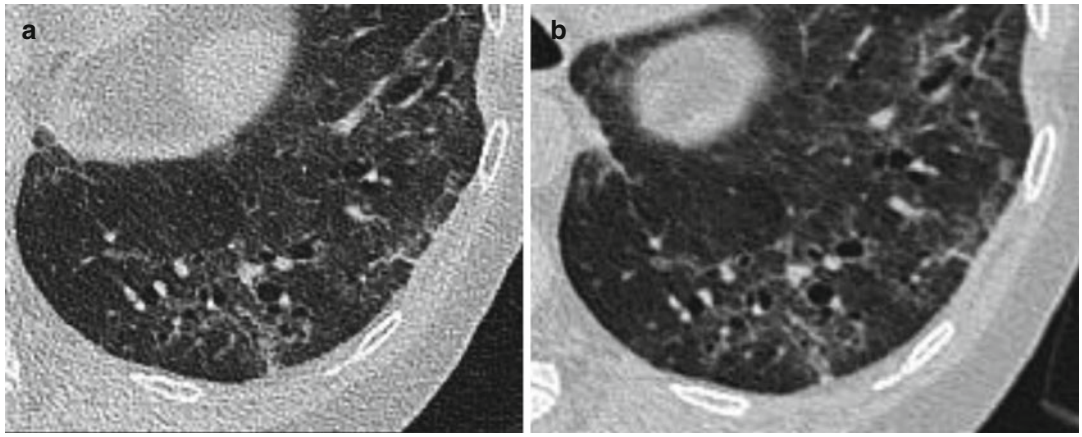

Fig. 3 Impact of dose: the right-sided image (**b**) was obtained with double acquisition dose compared to the left-sided image (**a**) (4.5 mGy versus 6.8 mGy, no iterative noise reconstruction has been applied)

New iterative reconstruction algorithms (IR) allow for greater noise reduction than standard filtered back projection (FBP) and subsequently more effective dose reduction. While increased spatial resolution is directly correlated with increase of image noise in standard filtered back projection, iterative reconstruction allows for decoupling of spatial resolution and image noise to a certain extent. Once an image has been reconstructed from measured projections, this image itself is used as "scan object" in a simulated CT measurement of the same projection, resulting in an image of calculated projections. The differences between the measured and calculated projections result in correction projections which are subsequently used to update the originally measured projections. This process is repeated until the difference between the calculated projections and measured projections is smaller than a predefined limit. With each update to the original image, image-processing algorithms enhance spatial resolution in higher contrast areas of the image and reduce noise in low contrast areas. While the first generations of IR produced images of lower noise, they were criticized for modifying the visual appearance of images, either being smoothed or pixelated especially with increased weighting of iterative noise reconstruction (Pontana et al. 2011; Prakash et al. 2010) (Fig. 4). The second generation of so-called model-based IR – active in the raw data space – aims for reducing noise and maintaining image sharpness, thus having less impact on the visual image impression.

Some studies evaluated the visualization of certain elements of lung infiltration and diffuse lung disease: an improved detection of ground-glass opacities, pulmonary nodules, and emphysema had already been reported with first-generation IR in vivo (Pontana 2011) and by experimental studies (Christe et al. 2012). Similarly an excellent inter-method agreement comparing IR and FBP images for the detection of emphysema, GGO, bronchiectasis, honeycombing, and nodules has been described (Ohno et al. 2012). No study evaluating the impact on the diagnostic evaluation of diffuse interstitial lung disease has been published yet, but nevertheless it can be anticipated that modern IR allows for substantial (around 50 %) dose reduction of volumetric HRCT for DILD, which represents an important step forward in terms of radiation protection, especially for young patients and patients with multiple follow-up studies.

2.3 Prone Position

In the normal lung with the patient supine, there is a gradual increase in attenuation and vessel size from ventral to dorsal lung regions. This attenuation gradient is caused by the effect of

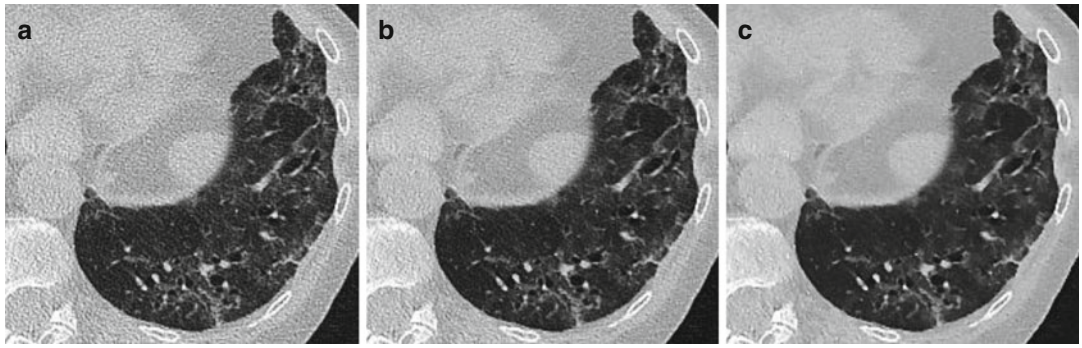

Fig. 4 Impact of iterative noise reconstruction (IR) on image noise but also on visualization of attenuation differences and detail resolution: (**a**) IR factor 1, (**b**) IR factor 3, and (**c**) IR factor 5

gravity on blood flow and gas volume as well as some non-gravity-dependent effects. This density gradient is accentuated on expiration (Verschakelen et al. 1998). Hypoventilation and atelectasis in the dependent lung can cause areas of dependent density or subpleural lines, which can mimic early lung fibrosis.

With the patient in prone position, these hydrostatic densities will immediately disappear, while abnormalities caused by real pathology will remain. Therefore, in some cases it may be necessary to obtain images in prone position to differentiate actual disease from physiologically dependent densities or atelectasis. This is especially true when the detection of ground-glass opacities or curvilinear subpleural lines are of diagnostic relevance (e.g., in patients with subtle disease or in patients with asbestosis).

Publications dating from more than 15 years ago – thus obtained with slower scanners and discontinuous HRCT technique – found that prone scanning was useful in almost 20% of patients (Volpe et al. 1997). This proportion is certainly too high, given the fast scanning technique available today. Prone scanning is not indicated routinely anymore. Some colleagues may prefer it in selected cases, e.g., patients with questionable, subtle disease exclusively in the dorsobasal area of the lung which would be decisive for the presence or absence of disease.

A questionnaire obtained in 2013 did not reveal a real consensus about the use of additional CT acquisitions in the prone position, though it was recommended to be performed on demand only (Prosch et al. 2013). This, however, requires the scans to be closely monitored or that the patient is called back for additional scanning. In patients with emphysema, airway disease, or diffuse obstructive lung disease, prone scans are usually not needed.

2.4 Expiratory Scans

Scans are routinely obtained in full inspiration with the lungs fully expanded, which optimizes the contrast between low-attenuation aerated air space and high-attenuation lung structures and various abnormalities. At the same time, full inspiration minimizes the frequency of confounding densities due to transient atelectasis.

Additional expiratory HRCT scans have proved useful in the evaluation of patients with a variety of obstructive lung diseases. Focal or diffuse air trapping may be detected and can be essential in the differentiation of large or small airway disease and emphysema (Kauczor et al. 2011).

The guidelines of the British Thoracic Society recommend the routine use of expiratory scans in patient's initial HRCT evaluation (Wells and Hirani 2008). The rationale behind this is the potential value of air trapping for the differential diagnosis that can be appreciated on an expiratory scan, even in the absence of inspiratory scan abnormalities and the fact that the functional cause of respiratory disability is not always known, especially during the initial diagnostic

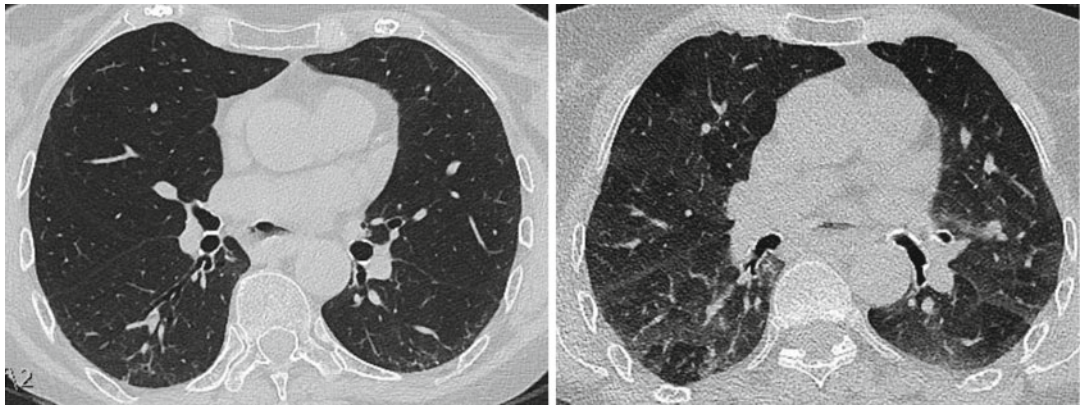

Fig. 5 Images in full inspiration and after full expiration: lobular areas of lower attenuation (*black*) demonstrate air trapping. Air trapping is more easily and sometimes exclusively seen in expiration

phase. Within the context of management of interstitial lung disease, the British Thoracic Society suggest that after a diagnosis has been set, additional expiratory CT acquisitions should only be performed to evaluate inconclusive findings on inspiratory CT.

Because of dose considerations, most investigators obtain some expiratory scans on predetermined levels or discontinuous clusters (Prosch et al. 2013). There are various ways how to plan these scans: either in areas of pathology seen in inspiration or on specific predefined levels following anatomic landmarks (e.g., carina, aortic arch) in order to facilitate reproducibility in follow-up scans. How many levels need to be covered is unclear and ranges from 2 to 5. Alternatively also the expiratory scan can be obtained with volumetric data acquisition. It has the advantage of decreasing the risk of motion artifacts frequently seen in discontinuous expiratory scans, allows for quantification on a 3D basis, and allows for more precise, level-matched follow-up. Since the only purpose of these scans is the detection, localization, and quantification of air trapping, these scans can be obtained with a drastically reduced dose. Multiple studies have shown that tube current levels as low as 40 mAs are sufficient for the diagnostic purpose intended. Bankier et al. carried out a systematic comparison of expiratory CT scans obtained with 120 kV, 80 mAs, and simulated 60, 40, and 20 mAs scans and found that – though diagnostic confidence went down with decreasing acquisition dose and interreader variability went up – diagnostic accuracy was not affected (Bankier et al. 2007). Similar results had been published also by other authors (Nishino et al. 2004).

Scans after full expiration are obtained to display lobular areas of air trapping (Fig. 5). Air trapping refers to lobular demarcated areas of hypertransparency caused by air trapped in expiration by a check valve mechanism of small airways. Consequently the involved secondary lobule will not decrease in volume and increase in attenuation during expiration compared to the surrounding uninvolved lung parenchyma. Areas of air trapping are more easily visible in expiration than in inspiration. In some patients air trapping may be seen exclusively in expiration. The finding of air trapping as indirect sign of small airway disease is an important diagnostic finding in all diseases with an obstructive or combined obstructive/restrictive lung function impairment. Diseases in which the finding of air trapping and thus expiratory CT scans represent an important part of the diagnostic workup are exogenous allergic alveolitis, collagen vascular diseases such as Sjögren's disease and rheumatoid arthritis, but also sarcoidosis and diseases with predominant airway pathology such as asthma and cystic fibrosis.

Sharply demarcated areas of air trapping need to be differentiated from ill-defined areas of varying parenchymal density in expiration. The latter

is seen frequently and has been interpreted as "inhomogeneous emptying" of the lung in expiration. Correlation of scans during inspiration and expiration illustrating the unaltered volume and density in lobuli with air trapping represents the diagnostic clue.

Expiratory CT scans are also used for interpretation of a mosaic pattern seen in inspiration. Mosaic pattern is defined as areas of varying density, sharply demarcated by interlobular septa. To differentiate whether the area of increased attenuation represents ground glass, e.g., caused by an acute alveolar or interstitial process, or that the area with hypoattenuation represents air trapping caused by bronchiolitis, expiratory CT scans are very helpful.

An increased contrast between hypo- and hyperattenuated areas in expiration demarcates air trapping as pathology and bronchiolitis as underlying disease. There are less vascular structures visible in the "black" areas of hypoattenuation due to the Euler-Liljestrand reflex, causing vascular constriction in areas of lower ventilation. Importantly there are no signs of pulmonary hypertension.

A decreased contrast between hypo- and hyperattenuated areas in expiration demarcates ground glass as pathology and an acute alveolar/interstitial process as underlying disease. There is no difference in vascular calibers in the areas of different attenuation.

Thirdly, pronounced differences in vascular diameter between the areas of different attenuation indicate true mosaic perfusion. Additional signs of pulmonary hypertension, such as dilated central pulmonary arteries and pathological arterio-bronchial ratio, may be present. The underlying disease is recurrent pulmonary emboli. Though discrimination of the different underlying diseases is also possible by analyzing the vascular diameters only, many radiologists consider the information of increased contrast differences caused by air trapping the most valuable and reassuring.

Instead of acquiring the CT scans after full expiration in suspended respiration, other authors have proposed to acquire the data during forced expiration, more specifically to perform data acquisition during the dynamic process of forced expiration. While especially end-expiratory air trapping might be seen with higher sensitivity, the risk for considerable breathing artifacts hampering image quality has to be outweighed against the potentially increased diagnostic information. Dynamic scans were firstly introduced using an electron beam CT; however, it can also be performed with any MDCT scanner with a gantry rotation time of 1 s or less. Because images can be reconstructed at any time point during the scan, the temporal resolution is even higher than with the electron beam CT. Mostly continuous imaging is performed on a single axial level for 6–8 s as the patient expires rapidly. Acquisition dose is drastically reduced (usually 40 mAs). Lucidarme et al. (2000) found a significantly higher density difference between the different areas of attenuation and a higher extent of air trapping in dynamic scans as opposed to static scans, but the number of patients for which dynamic scan acquisition changed the diagnosis has been found to be small (Gotway et al. 2000).

A detailed instruction of the patient is important to avoid motion artifacts and to assure that the scan acquisition takes part in the desired respiratory status. A visual qualitative control for the inspired or expired state is possible by analyzing the shape of the trachea: in full inspiration the trachea demonstrates a round shape, while in expiration there is bulging of the dorsal membranous part of the trachea ventrally and intraluminally to a various extent. A too strong deformation producing a considerable reduction of the tracheal area and demonstrating a moon-like (luna) shape is associated with tracheomalacia which can be a hint toward severe obstructive lung disease (O'Donnell et al. 2014).

2.5 Motion Artifacts and ECG Gating

Motion artifacts caused by non-suspended respiration are common and can severely hamper a meaningful interpretation of the images. Respiratory motion leads to blurring of normally sharp details, pseudo-ground-glass opacities, and

linear streaks or star artifacts from edges of vessels and other high-density structures.

On lung window setting, gross respiratory motion artifacts are normally easily recognizable, and while they degrade image quality, they will not cause misinterpretation because of their obviousness. Subtle motion-related unsharpness and ground-glass opacities, however, may mimic an interstitial process; doubling of vascular structures can mimic thickened interlobular septa or walls of a dilated bronchus.

A dedicated and detailed instruction of the patient how to deeply breathe in and out and especially to hold the breath before data acquisition is therefore an important step toward high image quality (Vikgren et al. 2008).

Cardiac pulsation artifacts typically affect the paracardiac regions of the left lower lobe and to a lower extent of the lingula and middle lobe. Aortic pulsation may affect lung areas adjacent to the aortic arch or the descending thoracic aorta, being the segments six and ten of the left lower lobe. In selected cases these pulsation artifacts may be misleading and can cause false positive findings. Typical artifacts are double contours of the bronchial walls mimicking bronchiectasis and hyperlucencies close to arteries mimicking emphysema. Usually they do not cause diagnostic problems if correlated to the blurred heart contour.

Options to reduce pulsation artifacts are reduced gantry rotation time, segmented reconstruction, or ECG triggering of scan acquisition. Reduced gantry rotation time and segmented reconstruction are means to increase scanning speed, but they go along with decreased dose delivery and thus increase of image noise. Prospective ECG triggering leads to a significant prolongation of measurement time, which interferes with the breath-hold capabilities of many patients. Retrospective cardiac gating would therefore be the method of choice to avoid disturbing pulsation artifacts at the expense of a markedly increased acquisition dose. In principal, techniques for coronary CT imaging can be used, without contrast administration, adaptation of the FOV to cover both lungs, and adaptation of acquisition dose. Similarly to motion-free imaging of the coronaries, motion-free imaging of the lung parenchyma would be achieved.

Nevertheless, the few studies that compared image quality with and without ECG triggering – carried out with relatively small groups of patients – found a significantly increased image quality based on artifact reduction, however, without relevant impact on diagnostic performance or confidence (Boehm et al. 2003). With the fast rotation time of most scanners used today, cardiac pulsation artifacts are significantly reduced and there appears no indication for ECG triggering for diagnostic workup of interstitial lung diseases.

3 Image Display and Processing

3.1 Windowing

There is no single correct or ideal window setting for evaluating the lung parenchyma. Window settings have to be optimized with regard to the settings of scanners and monitors. Several combinations of window level and window width may be appropriate, and individual modifications based on personal preferences play a role.

Nevertheless, it is advisable to use a chosen lung window setting consistently in all patients to optimize comparison between different patients and between sequential examinations of the same patient. It is also very important to use window settings constantly to develop a visual default and thus understanding of normal and abnormal findings. Additional window settings may be useful in specific cases, depending on what abnormality is in question.

For the assessment of a routine lung examination, window level settings ranging from −600 to −700 HU and window widths of 1000–1500 HU are recommended. Wider window width (i.e., 2000 HU) may be applied for the evaluation of overall lung attenuation and high-contrast interfaces, especially of peripheral parenchymal abnormalities along the pleural interfaces. For example, wide windows are therefore advised for the assessment of asbestosis.

Low window level settings (e.g., −800 to −900) and narrow window width (500 HU) facilitate the detection of subtle attenuation differences and are therefore suited for the detection of

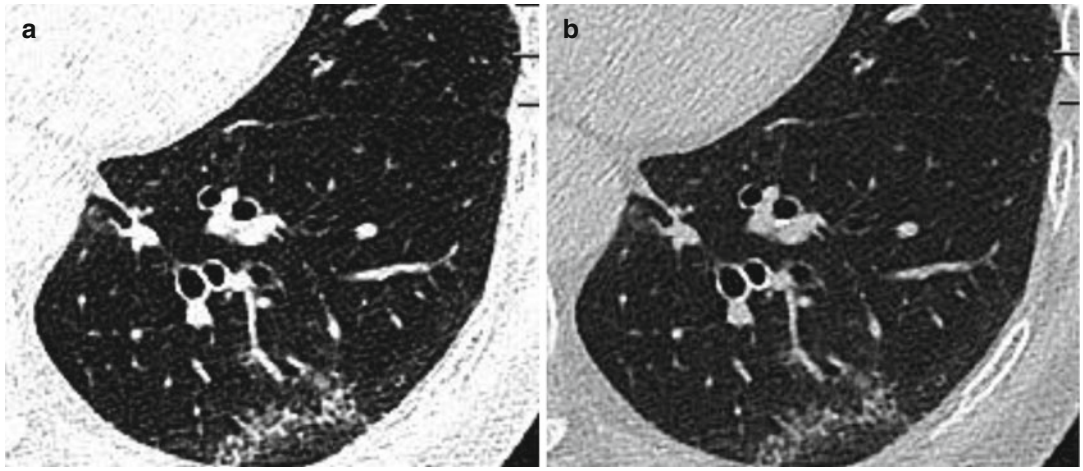

Fig. 6 Impact of window width on visualization of structures and bronchial wall thickness: (**a**) narrow window; (**b**) normal window settings

emphysema, air trapping, or air-filled cystic lesions.

The window setting has a substantial effect on the accuracy of size measurements. This is particularly important for the assessment of bronchial lumen diameter and bronchial wall thickness. It has been demonstrated that an intermediate window width between 1000 and 1400 HU together with a window level between −250 and −700 HU reflects best the true size of the bronchi and especially the thickness of the bronchial wall (Bankier et al. 1996) (Fig. 6).

As a result, it might be necessary to use different window settings for identifying pathological changes of the parenchyma or the pleura on one side and for the measurement of bronchial diameter and wall thickness on the other side. Window level settings of 40–50 HU and window width settings of 350–450 HU are generally recommended for evaluation of the mediastinum, the hili, and the pleura.

3.2 Multiplanar Reformations

Multidetector-HRCT produces an isotropic dataset that allows for contiguous visualization of the lung parenchyma in three dimensions and to create multiplanar two-dimensional (2D) reconstructions in any arbitrary plane. Mostly planar coronal and sagittal reconstructions are routinely performed and considered standard for reconstructed series of any HRCT dataset (Prosch et al. 2013; Beigelman-Aubry et al. 2005; Walsh et al. 2013) (Fig. 2).

Coronal reformations facilitate the display of disease distribution, e.g., the craniocaudal gradient representing a key finding in idiopathic pulmonary fibrosis (IPF) or the upper lobe predominance in sarcoidosis or Langerhans cell histiocytosis (LCH). Coronal MPRs are also preferred by many clinicians because they facilitate anatomic orientation (Eibel et al. 2001a) and produce images more easily comparable to chest radiographs. Advantages of sagittal MPR include the sharper delineation of the interlobar fissures and thus an improved anatomic localization of lesions close to the lobar border or for lesions with transfissural extent (Eibel et al. 2001a, b). Sagittal images also ease the evaluation of the thoracic spine and the dorsal costophrenic angle.

For the dedicated evaluation of the relationship between parenchymal lesions and airways, curved MPR can be useful following the course of the branching tubular airways (Lee and Boiselle 2010). Both coronal and sagittal MPR are superior to the axial scans alone to illustrate the location and extent of abnormalities situated in the central tracheobronchial system.

Though there is a high level of concordance between reading coronal and axial slices with regard to the identification of parenchymal disease, there is a general agreement that coronal or sagittal MPRs have a complimentary role, but are not regarded as the principle scan plane used for diagnostic evaluation.

3.3 Maximum Intensity Projection

Maximum intensity projection (MIP) is a 3D display technique, displaying the voxel of maximum intensity along the path of X-rays. To retain spatial information, MIPs are usually reconstructed with a thickness between 5 and 10 mm, dependent on the indication. Since they largely facilitate the differentiation between tubular (vascular structures) and nodular densities, their major advantage lies in demonstrating the distribution of nodules (Remy-Jardin et al. 1996; Beigelman-Aubry et al. 2005). The analysis of nodule distribution pattern in relation to the secondary lobule (e.g., perilymphatic, centrilobular, or random) is one of the key elements for the differential diagnosis; however, especially in cases with subtle findings and low numbers of nodules or on the contrary in cases with a very high number of nodules, it can be difficult to assess their distribution on axial thin slices alone, since vascular structures and nodules have the same appearance (Fig. 7).

Similarly, MIPs are very useful for the detection of (solitary) nodular densities, e.g., metastases. MIPs were found to show a large advantage especially in the central parts of the lungs; it proved to be significantly superior to regular MPR with over 25 % additional findings and increased diagnostic confidence (Peloschek et al. 2007) (Fig. 8).

In one study 103 patients with suspicion or evidence of pulmonary nodules underwent MDCT with a collimation of 1 mm. MIP and MPR were reconstructed in all three planes. The MIP were superior in the depiction of pulmonary nodules at a statistically significant level. Additional lesions were identified with MIP that were missed with transaxial slices and MPR. The improvement by MIP was based on the identification of nodules smaller than 5 mm in diameter. The improvement by MIP also led to an increase in diagnostic confidence (Eibel et al. 2001b). In a

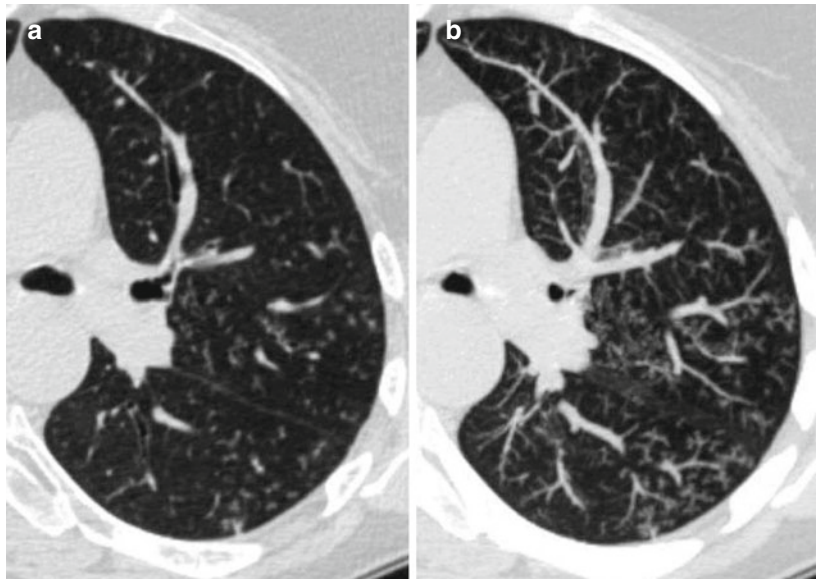

Fig. 7 1 mm axial slice (**a**) and 10 mm maximum intensity projection (MIP, **b**) demonstrating the better visualization of the distribution of a diffuse nodular pattern in MIPs in a patient with diffuse tree-in-bud due to infectious bronchiolitis nodular densities (here small granulomas) in MIPS

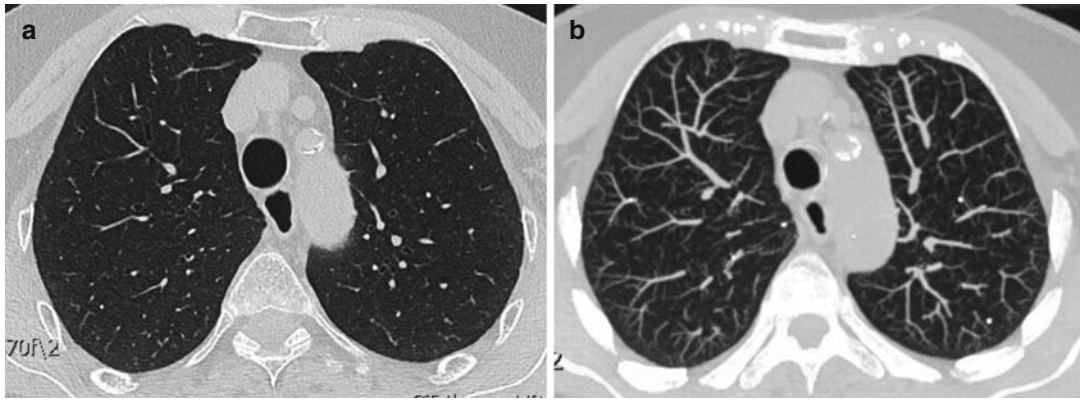

Fig. 8 1 mm axial slice (**a**) and 7 mm maximum intensity projection (MIP, **b**) demonstrating the better visualization of nodular densities (here small granulomas) in MIPs

different study, MIPs led to the detection of additional findings in 27 % of patients with nodular disease (Gavelli et al. 1998).

Finally, MIP sections of variable thickness allow assessing the size and location of pulmonary vessels. Recognizing enlarged pulmonary veins is useful in differentiating the diagnosis of pulmonary edema from other causes of diffuse ground-glass attenuation. In case of a mosaic attenuation pattern, MIP contributes to the differentiation of ground-glass attenuation (normal vascular diameter) and mosaic perfusion (altered vascular diameter). Eventually, MIP can help to differentiate between constrictive bronchiolitis and mixed emphysema (Beigelman-Aubry et al. 2005).

3.4 Minimum Intensity Projection

Minimum intensity projections (MinIPs) are less commonly used, but have been shown to facilitate the assessment of lung disease associated with decreased attenuation. MinIPs are created by projecting the voxel with the lowest attenuation value for every view throughout the volume onto a 2D image. It was demonstrated that MinIP enhances the visualization of air trapping as a result of small airway disease, yielding not only increased observer confidence but also increased interreader agreement as compared to HRCT alone (Fig. 9). MinIPs revealed additional findings in 8 % of patients with emphysema and in 25 % of cases with ground-glass opacities (Gavelli et al. 1998). These results have been confirmed by another study where MinIP improved the detection of pulmonary cysts and their differentiation from honeycombing (Vernhet et al. 1999).

There is a subtle difference in density between the endobronchial (pure) air and the lung parenchyma (HU difference 50–150). This allows visualization of the bronchi below the subsegmental level (Beigelman-Aubry et al. 2005) (Fig. 10). Recently, more attention has been paid to the options of MinIPs in facilitating the differentiation of bronchiectasis from honeycombing. The presence of honeycombing represents a key finding for the diagnosis of UIP/IPF (Raghu et al. 2011), but a relatively large interreader disagreement, even between experienced radiologists, has been described (Watadani et al. 2013).

3.5 Quantitative CT as Imaging Biomarker

CT is increasingly being used to stage and quantify the extent of DILD both in clinical practice and in treatment trials. The continuous data acquisition of CT with high isotropic resolution provides unique options for computer-supported quantification of diffuse lung disease. There has been a history in quantifying emphysema and airway disease in COPD patients with the ultimate goal to identify different phenotypes in the spectrum of

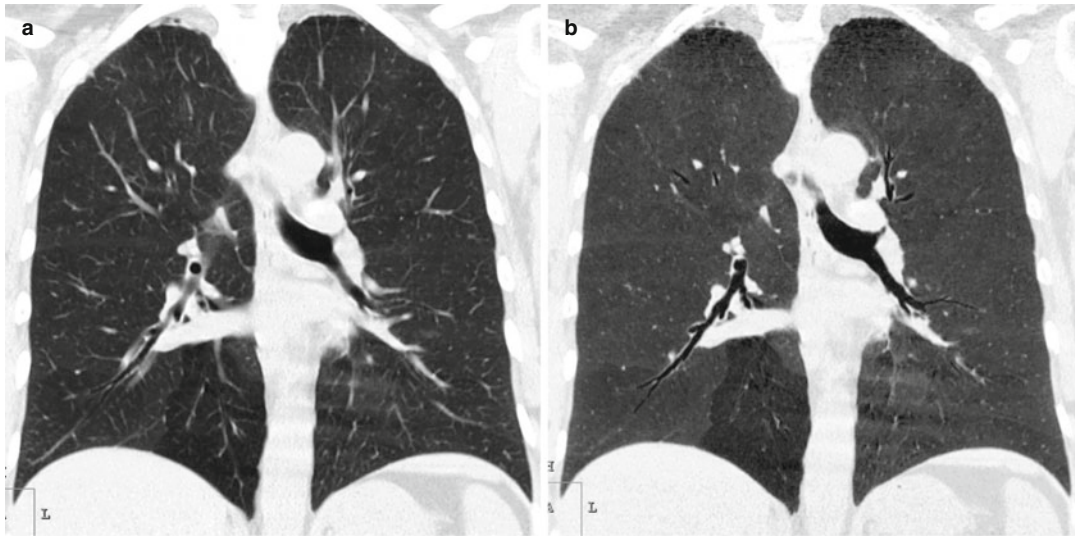

Fig. 9 3 mm coronal MPR (**a**) and 10 mm minimum intensity projection (MinIP, **b**) demonstrating the better visualization of lobular air trapping

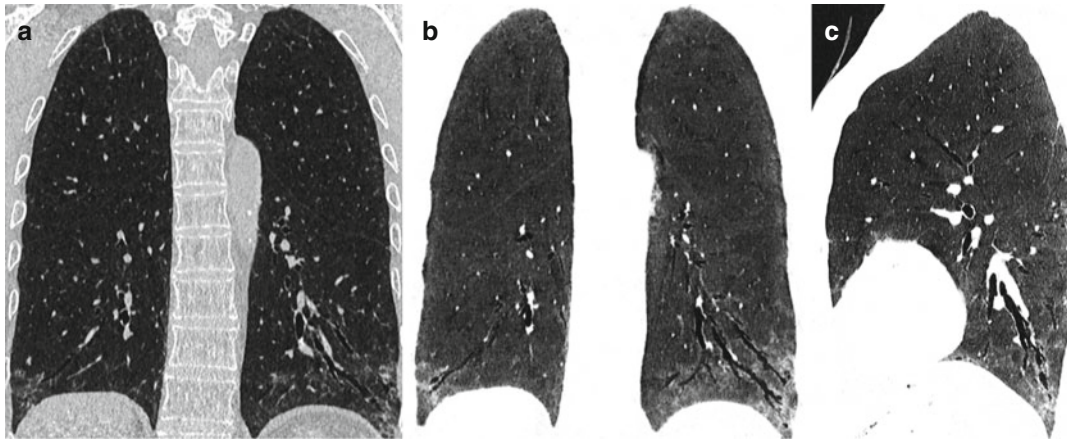

Fig. 10 1 mm coronal MPR (**a**) and 10 mm minimum intensity projection (MinIP, **b**, **c**) demonstrating the better visualization of bronchiectasis; increased peribronchial parenchymal density increases the visualization of ectatic peripheral bronchi

COPD. Recently, these efforts of computer-based analysis have been expanded to DILD.

Quantification of the extent of interstitial lung disease, both at a single time point and longitudinally, poses a challenge for several reasons:

- Mostly, DILD often consists of a mix of various patterns that show a considerable overlap between different DILD, rendering it difficult to clearly distinguish one from the other.
- The characterization of the pattern is influenced by inspiration depth, motion artifacts, and overlying other diseases such as infection.
- The extent of architectural distortions in all three spatial dimensions and within the lobular anatomy is difficult to assess.

Multiple studies have shown that type and extent of parenchymal changes, including accompanying airways pathology, correlate with lung

function, disease progression, response to therapy, and last but not least, disease prognosis. It has to be stated however that the extent of correlation is very variable for the different diseases and highly dependent on the type of pathology and thus the appreciated HRCT pattern.

Goh and colleagues proposed an interesting concept of combining a relatively simple visual quantification with pulmonary function (Goh et al. 2008). Firstly, the disease extent was differentiated into minimal or severe (less or more than 20 % involved lung area). For the subgroup of patients in which the disease extent was not readily classifiable on HRCT (so-called indeterminate), the distinction between limited and extensive was based on FVC threshold values below or beyond 70 % predicted (FVC = forced expiratory vital capacity). Using this relatively simple two-step approach, the authors were able to discriminate two groups of patients with significantly different outcomes and thus prognosis.

A similar approach of combining extent of disease on HRCT with pulmonary function tests has been successfully applied to patients with sarcoidosis and connective tissue diseases. For example, severity of traction bronchiectasis, extent of honeycombing, and DLco were found to be strongly associated with mortality in connective tissue disease related fibrotic lung disease (Walsh et al. 2014a, b). Similarly an extent of fibrosis exceeding 20 %, the diameter ratio between the aorta and main pulmonary artery, and a composite score of pulmonary function tests formed a significantly more effective prediction for mortality in sarcoidosis patients than any of the factors individually (Walsh et al. 2014a).

There has been an increasing interest for the use of automatic CT quantification as imaging biomarker to document disease response to treatment, disease progression, and eventually prognosis. Such a biomarker should be measurable but also reproducible and linked to relevant clinical outcome parameters (Goldin 2013). To meet the first two demands, rigorous standardization of imaging protocols over several sites and time points is needed, including centralized scanner and image quality checks. The underlying technique of automatic, texture analysis-based CT quantification is beyond the scope of this book chapter. There has been a number of studies evaluating the use of a computer-derived quantitative lung fibrosis score (QLF) for assessment of baseline disease extent and changes over time in patients with IPF (Kim 2015) and scleroderma patients treated with cyclophosphamide (Kim 2011). While this algorithm focuses solely on fibrotic changes, a different approach is used by the so-called CALIPER software (computer-aided lung informatics for pathology evaluation and rating), which associates a certain group of neighboring voxels to one of the basic patterns (normal, emphysema, ground glass, honeycombing, and reticular) for the complete lung volume (Bartholmai 2013). A recently published position paper by the Fleischner society (Hansell et al. 2015) acknowledges that CT has not only the potential to select the most appropriate patients to be included in treatment trials but also to represent a study end point in conjunction with other markers. This recent development has been fueled by the increasing precision with which image-processing software can quantify diffuse lung diseases.

4 Image Analysis

A widely accepted approach for analysis of HRCT in the context of DILD is based on the four patterns of pathological findings. It provides a structured and in certain ways standardized HRCT analysis and provides, together with distribution of the parenchymal changes, clinical history (acute versus chronic), and associated clinical (e.g., bronchoalveolar lavage) and imaging findings (e.g., lymphadenopathy, pleural effusion), the base for a differential diagnosis.

The four patterns differentiate between:

- Nodular opacities (I)
- Septal/reticular changes with parenchymal distortion (II)
- Diseases with increased density (III), including ground glass and consolidations
- Diseases with decreased density, mosaic pattern, and cysts (IV)

For communication with clinicians, it is important to use a cohesive terminology of signs and patterns describing the findings, so that they will know how a specific differential diagnosis has been made and what the confidence level of this diagnosis is. It has to be noted again that the final diagnosis in patients with DILD should be made within a multidisciplinary conference involving clinicians, radiologists, and pathologists and should thus be the result of a multidisciplinary approach.

A number of interstitial lung diseases are associated with such a characteristic pattern on HRCT, that diagnosis is strongly promoted by image findings, e.g., Langerhans cell histiocytosis, lymphangioleiomyomatosis, end-stage lung disease of usual interstitial pneumonia (UIP), and certain stages of sarcoidosis. Other diseases show a combination of findings that considerably overlap with a number of possible diagnoses, which is often the case in advanced disease with considerable parenchymal destruction. For example, there can be considerable overlap between sarcoidosis stage IV, UIP/IPF, and chronic exogenous allergic alveolitis.

4.1 Normal Anatomy

Localization and extent of parenchymal abnormalities are described in relation to readily appreciable anatomical structures, such as lobes and segments. The secondary lobule is the smallest anatomic unit bordered by connective tissue in the lung and represents one of the key anatomic structures in HRCT analysis that can be analyzed in its three-dimensional architecture.

In general, the secondary lobule measures between 1 and 2.5 cm in diameter, being bigger and rectangular in the periphery and smaller and more hexa- or polygonal in the central lung. The centrilobular core structures are formed by the pulmonary artery branch, the bronchiolus terminalis, lymphatics, and some connective tissue. It is important to note that under normal conditions, only the central pulmonary artery is visible on HRCT. The bronchiolus terminalis is below the spatial resolution and not visible under normal circumstances. Interlobular or perilobular septa represent the outer margin of the secondary lobule. They contain lung veins and lymphatics. In the peripheral subpleural 2 cm of lung parenchyma, only pulmonary arteries and some septal boundaries in an irregular distribution are visible. As soon as interlobular septa are regularly spaced or small airways become visible, these findings represent pathology. It is readily understandable that especially subtle pathological findings, such as an increased number of septal lines, is more easily appreciated in continuously scanned parenchyma that can be evaluated in all three projections as warranted.

4.2 Nodular Pattern

Pulmonary nodules are spherical or ovoid. They are categorized according to size, attenuation, margination, and localization. A general categorization of size results in micronodules (<3 mm), nodules (3–30 mm), and masses (>30 mm). Measurements of attenuation are problematic, but the appearance can be distinguished in being solid or of ground-glass opacity. Solid nodules may be sharply or poorly marginated, whereas ground-glass nodules are often poorly marginated. Values higher than 150 HU are typical for calcifications and indicate benign, postinflammatory granulomata. A surrounding area with increased ground-glass density is called "halo." The halo sign may be caused by acute inflammation or hemorrhage.

In general, the location or anatomic distribution of nodules is of great importance for the differential diagnosis. According to localization with regard to the anatomy of the secondary lobule, three main distribution categories of nodules are differentiated: perilymphatic, random, and centrilobular (Fig. 11). Once the predominant distribution pattern has been determined, the overall distribution within the complete lung is considered in the differential diagnosis (Fig. 12).

Perilymphatic nodules occur predominantly in relation to the lymphatic pathways within the lung, both histologically and on HRCT. They appear along the bronchovascular bundles, the

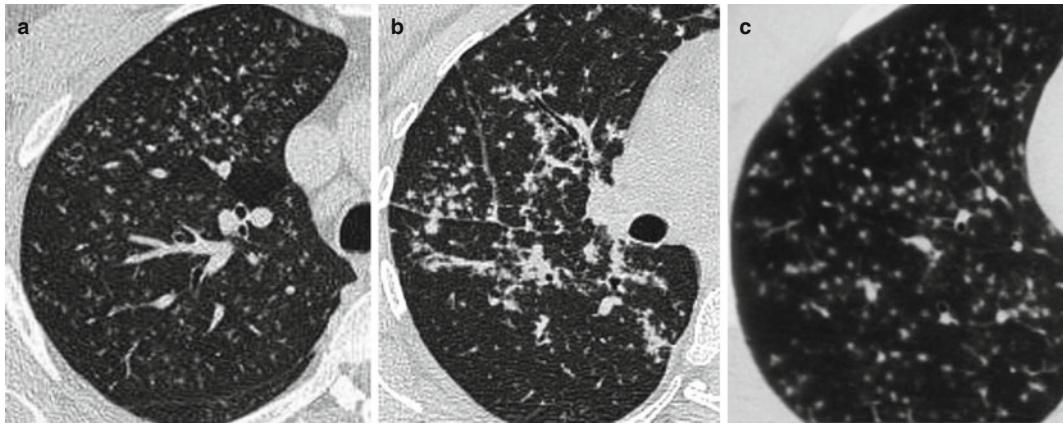

Fig. 11 Examples of a centrilobular (**a**), perilymphatic (**b**), and random (**c**) nodular distribution. (**a**) bronchiolitis, (**b**) sarcoidosis, and (**c**) miliary tuberculosis

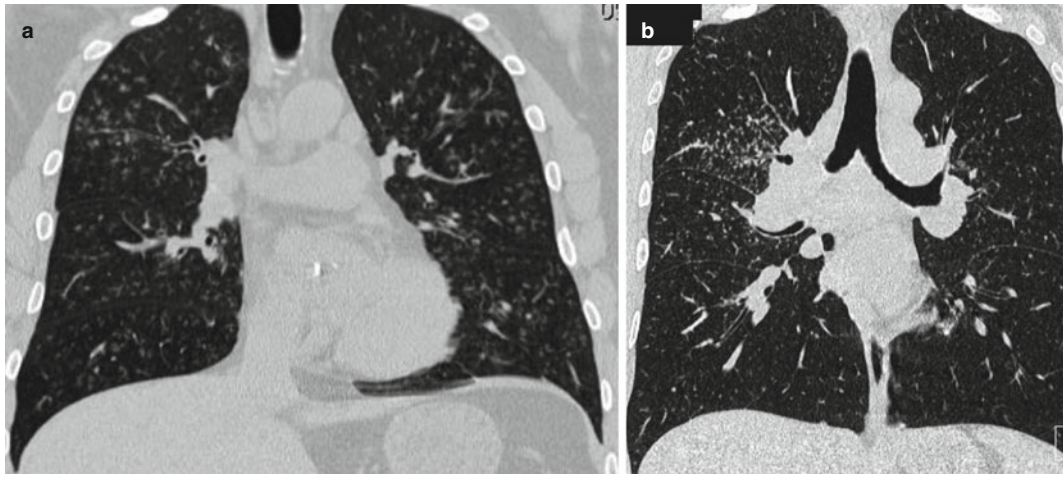

Fig. 12 1 mm coronal MPR in two patients with a nodular pattern: (**a**) shows the diffuse distribution in a patient with bronchiolitis, (**b**) shows the upper lobe predominance in a patient with sarcoidosis

interlobar fissures, the interlobular septa, and the subpleural regions. Central, perihilar nodules along the bronchovascular bundle, individually or clustered, are most typical for granuloma in sarcoidosis. The nodules usually measure less than 5 mm, are well defined, and regularly marginated. They have a predominance for the perihilar regions and the upper lobes, which is particularly well depicted on coronal reformations. Confluence of granuloma may result in larger irregularly marginated nodules, ground-glass opacities, or consolidations (Criado et al. 2010).

There might be an overlap between irregularly thickened interlobular septa caused by lymphangitis carcinomatosa and a perilobular sarcoidosis with predominantly nodules along the interlobular septa. While lymphangitis carcinomatosa is frequently associated with pleural effusion and strong thickening of the central bronchovascular interstitium, it is never characterized by lung distortion. Sarcoidosis on the other hand can show heavy distortion and usually no pleural effusion.

Typical for a *random distribution* is its uniformity throughout the lung without a preference for certain anatomical structures. The involvement

tends to be bilateral and symmetrical. A nodular pattern with a random distribution in relation to leading structures of the secondary lobule is indicative for a disease process with hematogenous spread as seen in hematogenous spread of malignant disease, miliary tuberculosis, fungal infections, cytomegaly, or herpes virus infections.

Centrilobular nodules are limited to the centrilobular regions and are never in contact with fissures or the pleura. They either originate from the respiratory bronchioles or bronchioli terminales or from the peripheral pulmonary artery branches. The nodules have a distance of at least several millimeters from interlobular septa and fissures and 5–10 mm from the pleural surface and pleura resulting in the characteristic subpleural sparing. They present as ill-defined, centrilobular ground-glass opacities in exogenous allergic alveolitis or respiratory bronchiolitis. A bit larger nodules, mostly ill-defined or consisting of solid components with a small halo around, are caused by bronchiolitis or small foci of bronchopneumonia. In silicosis, nodules can have a centrilobular as well as subpleural distribution pattern with a predominance in the posterior aspect of the upper lobes. Typically, they are smoothly marginated. The nodules range between 2 and 5 mm in diameter and can be calcified.

A *tree-in-bud* pattern– representing small-branching opacities with nodular endings – also show a centrilobular distribution; they represent small airway disease with wall thickened and/or secretion-filled small airways.

As described earlier, maximum intensity projections are most helpful in analyzing the distribution of nodules (see Sect. 3.3).

4.3 Septal/Reticular Pattern With or Without Signs of Parenchymal Distortion

Thickening of the lung interstitium caused by fluid, fibrous tissue, or cellular infiltration usually results in an increase in reticular or linear opacities on HRCT. Interlobular septal thickening is differentiated from intralobular septal thickening, although mostly seen together.

The normal interlobular septa contain venous and lymphatic structures. They measure approximately 0.1 mm in thickness and are only occasionally or partially seen on HRCT under normal conditions. Thickening of interlobular septa results in outlining the margins of the secondary lobules in part or completely; a regular network becomes apparent, and the centrilobular arteries are easily identified as small dots in the center of the secondary lobules. For differential diagnosis it is most important whether increased reticular margins are associated with signs of parenchymal distortion (e.g., traction bronchiectasis) suggesting the diagnosis of fibrosis, or whether there are no signs of distortion as, e.g., seen in crazy paving (Fig. 13).

Any diseases causing alveolar filling-in and subsequent filling of intralobular and interlobular lymphatics will cause a pattern of *crazy paving* which describes the combination of ground-glass and reticular densities. Such conditions are seen in edema, bleeding, and pneumonic infiltrations, but also in alveolar proteinosis, storage diseases, or lymphoproliferative disorders.

When caused by fibrosis, intralobular interstitial thickening results in traction bronchiectasis and bronchiolectasis, as well as displacement of fissures. This reticular pattern of thickened intra- and interlobular septa, as well as irregular thickening of the bronchovascular interstitium (interface sign) is an important diagnostic finding in the heterogeneous group of interstitial lung diseases (ILD). The most recent 2013 classification of the American Thoracic Society (ATS) and European Respiratory Society (ERS) distinguishes usual interstitial pneumonia (UIP), the specific histopathological pattern seen in idiopathic pulmonary fibrosis (IPF), from six non-IPF subtypes: acute interstitial pneumonia (AIP), respiratory bronchiolitis interstitial lung disease (RB-ILD), desquamative interstitial pneumonia (DIP), organizing pneumonia (OP), lymphoid interstitial pneumonia (LIP), and nonspecific interstitial pneumonia (NSIP) (Walsh and Hansell 2010).

Usual interstitial pneumonia (UIP) carries a particularly poor prognosis: its 5-year survival is approximately 15–30 %. Because of prognos-

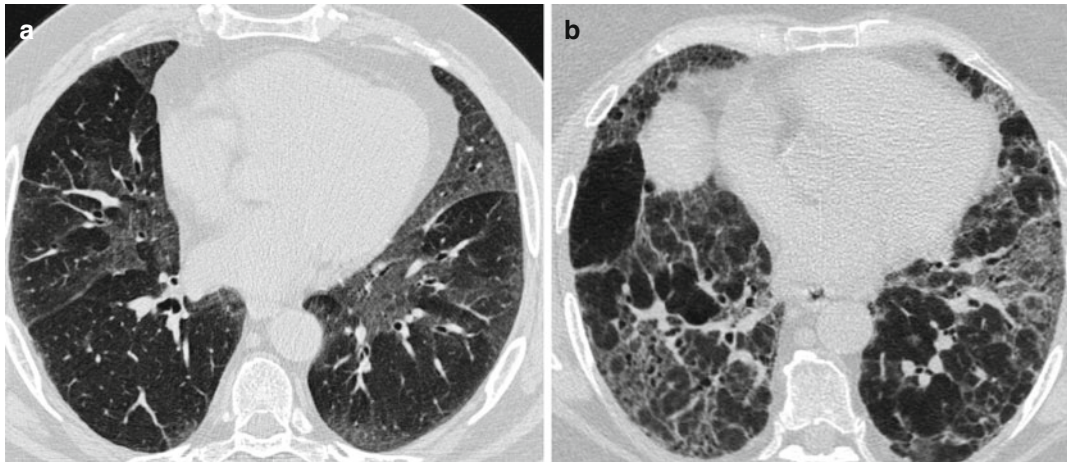

Fig. 13 1 mm axial slices in two patients with increased density in a geographic distribution: (**a**) shows no signs of distortion (desquamative interstitial pneumonia = DIP), (**b**) shows bronchiectasis and reticulation as signs of fibrosis; additionally, there are areas of air trapping (chronic exogenic allergic alveolitis)

tic and lately also therapeutic differences, UIP/IPF is separated from the remaining ILDs. The definition of IPF is a specific form of chronic, progressive fibrosing interstitial pneumonia of unknown cause that occurs primarily in older adults and is limited to the lungs and associated with the histopathologic and/or radiologic pattern of UIP. Other forms of interstitial pneumonia, including other idiopathic interstitial pneumonias and ILD associated with environmental exposure, medication, or systemic disease, must be excluded. UIP is characterized by the presence of reticular opacities associated with traction bronchiectasis. Honeycombing is critical for making a definite diagnosis following the criteria by Raghu et al. (Raghu et al. 2011) (Fig. 14). For the HRCT-based diagnosis of UIP, ground glass can be present, but is less extensive than reticulation. The distribution of UIP is characteristically predominantly basal and subpleural. Coexistent pleural abnormalities (e.g., pleural plaques, calcifications, pleural effusion) suggest an alternative etiology for the UIP pattern. Also, findings such as micronodules, air trapping, cysts, extensive ground-glass opacities, consolidation, or a peribronchovascular-predominant distribution represent findings *inconsistent* with UIP and suggest an alternative diagnosis (Fig. 15).

A UIP pattern on HRCT is highly accurate for the presence of UIP pattern on surgical lung biopsy. In the absence of honeycombing, but imaging features otherwise meeting the criteria for UIP, the HRCT findings are regarded as representing a "possible UIP," and surgical lung biopsy is necessary if a definitive diagnosis is required (Raghu et al. 2011).

Nonspecific interstitial pneumonia (NSIP) forms the second group of lung fibrosis, having a very variable clinical, radiological, and histological presentation. It may be idiopathic but is more commonly associated with collagen vascular diseases, hypersensitivity pneumonitis, drug-induced lung disease, or slowly healing DAD. The typical HRCT features are ground-glass opacities, irregular linear (reticular) opacities, and traction bronchiectasis. It has a peripheral and basal predominance, with typically (but not always present) relative sparing of the immediate subpleural space in the dorsal regions of the lower lobes. A more acute inflammatory (cellular) type of NSIP representing with predominant ground glass is differentiated from the more fibrotic type representing with reticulation and traction bronchiectasis (Fig. 16). Opposite to UIP, NSIP can also demonstrate a very patchy distribution. NSIP is typically characterized by a more uniform pattern, indicating the same stage

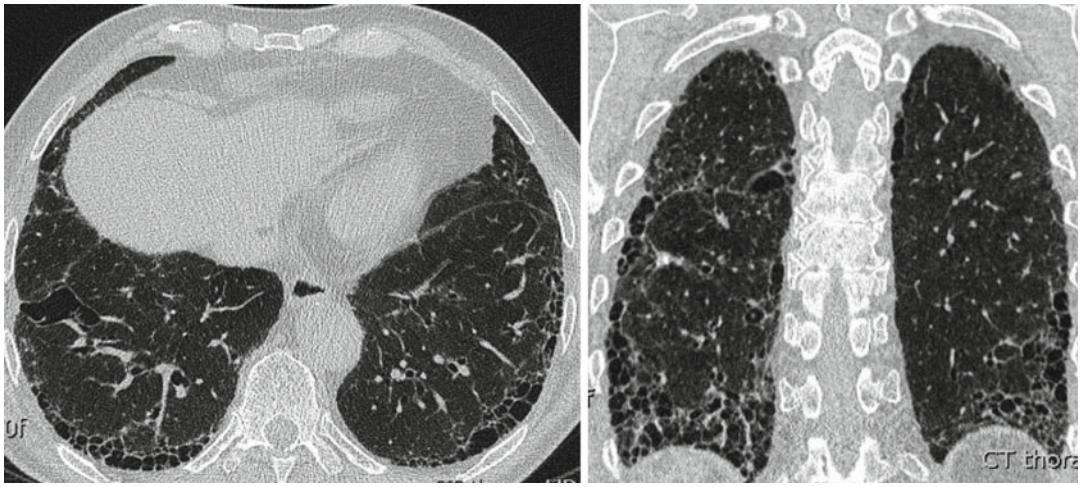

Fig. 14 Definite usual interstitial pneumonia (UIP) with honeycombing in a subpleural and mostly basal distribution. There is traction bronchiectasis and very little ground glass

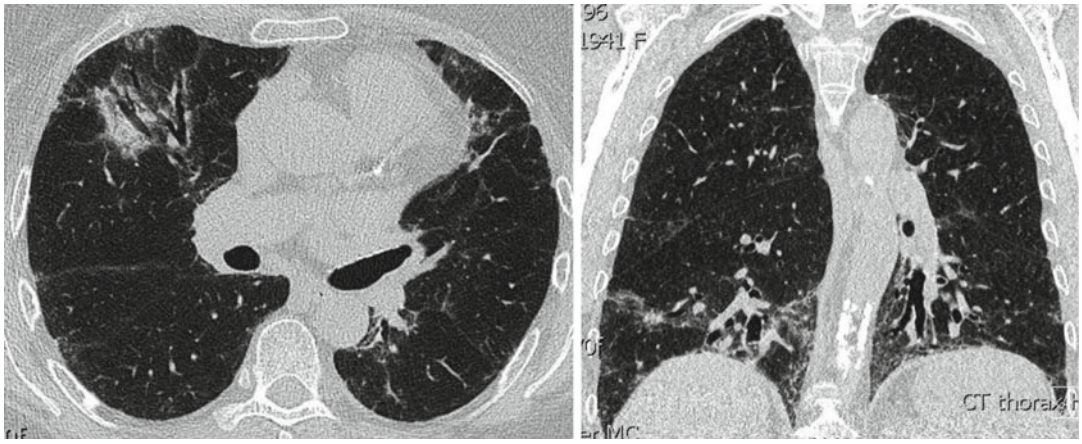

Fig. 15 Patient with fibrosis *inconsistent* with UIP through the predominant basal distribution: there is no honeycombing, but areas of ground glass and consolidations; reticulation is not predominant over ground glass

of evolution of disease, distinct from the multitemporal and morphological heterogeneity of UIP.

It has to be noted that UIP is not specific for IPF. UIP is also seen in a number of other DILD, such as asbestosis (pleural plaques and calcifications), sarcoidosis (upper lobe disease, heavy parenchymal distortion, associated nodular disease in perilymphatic distribution), or exogenic allergic alveolitis (bronchovascular-centered fibrosis, air trapping, relative sparing of the posterior costophrenic recesses).

4.4 Increased Density

Acute interstitial pneumonia (AIP) is histologically characterized by hyaline membranes within the alveoli and diffuse, active interstitial fibrosis also described as "diffuse alveolar damage" (DAD). There is clinical, pathological, and radiological overlap with ARDS, and patients often present with respiratory failure developing over days or weeks. Typical HRCT features are bilateral ground-glass opacities (patchy or diffuse) and consolidations. Focal sparing of lung lobules

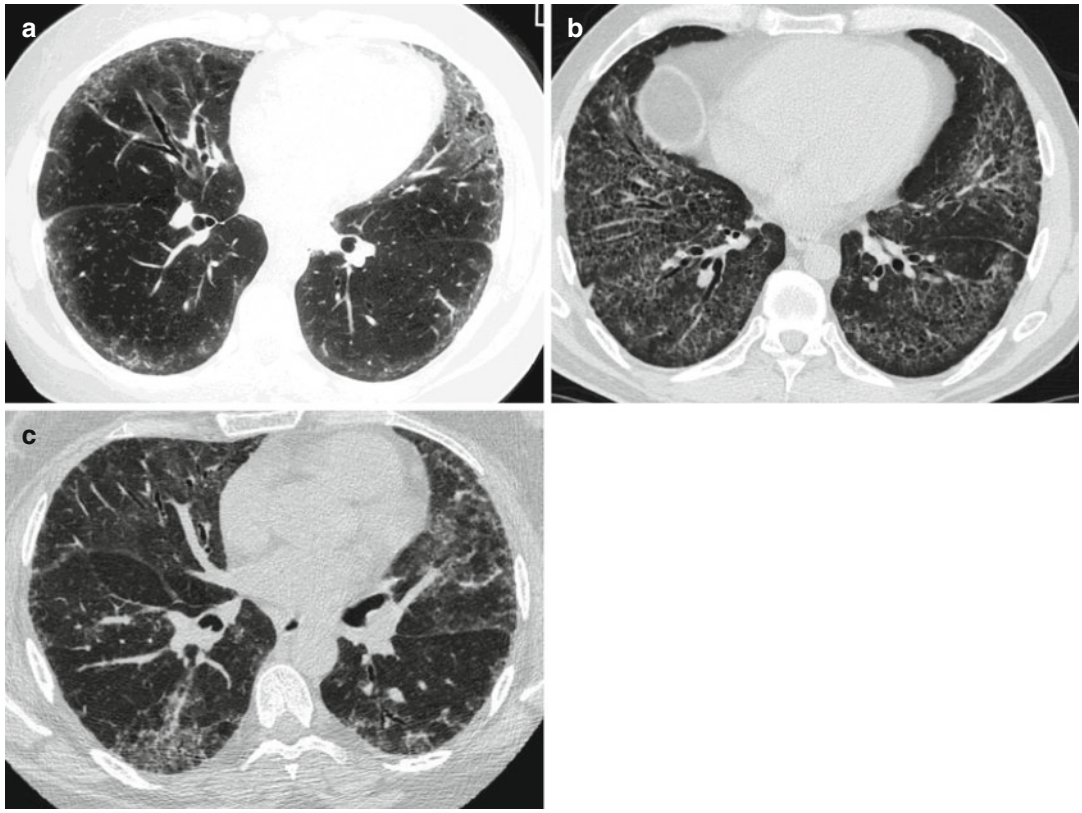

Fig. 16 The "many faces" of nonspecific interstitial pneumonia (NSIP): (**a**) subpleural bands of reticulation and ground glass (systemic sclerosis), (**b**) diffuse fine reticulation and traction bronchiectasis (systemic sclerosis), (**c**) patchy areas of ground glass and traction bronchiectasis (CREST)

frequently result in a geographic distribution. In later stages architectural distortion with traction bronchiectasis, reticulation, and even honeycombing develops.

Respiratory bronchiolitis interstitial lung disease (RB-ILD), *desquamative interstitial pneumonia (DIP)*, and, last but not least, nonspecific interstitial lung disease (NSIP) belong to the spectrum of smoking-induced lung changes. RB-ILDs consist of centrilobular acinar ground-glass nodules that may be confluent to areas of ground-glass opacities and thickening of the bronchial walls. A small percentage has a mild reticular pattern mainly in the lower lung zones. Desquamative interstitial pneumonia (DIP) is uncommon in its idiopathic form and mostly associated with smoking. HRCT features are similar to those encountered in RB-ILD, although the distribution is diffuse in DIP and more bronchiolocentric in RB-ILD. The typical HRCT feature of DIP is diffuse ground-glass opacity, sometimes in a geographic distribution; reticulation is uncommon.

Organizing pneumonia (OP) is a common reaction pattern secondary to pulmonary infection, connective tissue diseases, inflammatory bowel disease, inhalation injury, hypersensitivity pneumonitis, drug toxicity, malignancy, radiation therapy, or aspiration but can also be idiopathic. Organizing pneumonia can present with a wide variety of HRCT findings with increased density, ranging from a more nodular pattern to geographically demarcated ground-glass or focal consolidations. Suggestive for organizing pneumonia (as opposed to an infectious pneumonia) are sharply demarcated consolidations in a peripheral subpleural distribution or following the bronchovascular bundle (Fig. 17). Mostly the

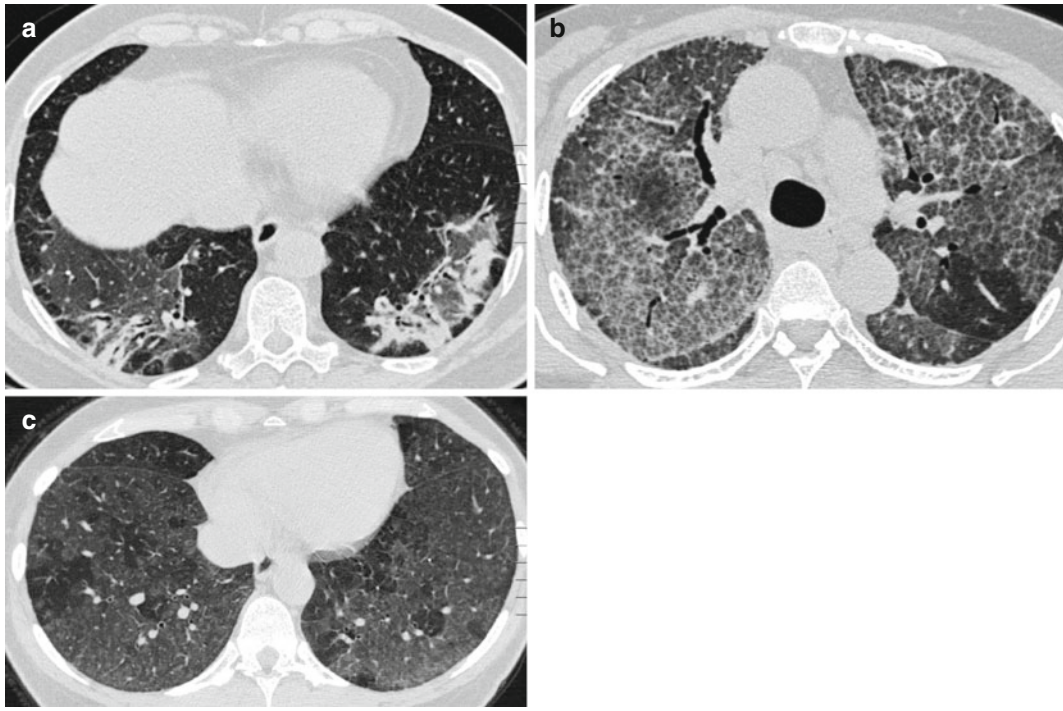

Fig. 17 Patterns with increased density: (**a**) organizing pneumonia with sharply demarcated areas of consolidations and ground glass, (**b**) crazy pacing in alveolar proteinosis, (**c**) ground glass with air trapping in subacute exogenic allergic alveolitis

areas with increased density show dilated air-filled bronchi without signs of underlying distortion. A patchy distribution is described as atoll sign, demonstrating islands with a peripheral rim-like consolidation around central areas of ground glass (reversed halo). Densities along the periphery of the secondary lobules are described as perilobular pattern.

4.5 Decreased Density/Cysts

A cystic pattern results from a heterogeneous group of diseases, all having in common the presence of focal, multifocal, or diffuse parenchymal lucencies and lung destruction. For the differential diagnosis, the presence of walls around the lucencies and the form of the lucencies (bizarre shaped or uniform round) is important.

The term "cyst" by itself is nonspecific and refers to a well-circumscribed round or irregular lesion with a visible wall. The wall is usually thin (<2–3 mm), but can have a uniform or variable thickness. Most cysts are filled with air, but can also contain liquid, semisolid, or solid material. Cysts can be very small and diffuse, but also large and confluent resulting in polygonal bizarre shapes. The presence of a definable wall demonstrated on CT differentiates cysts from emphysema.

Cysts are the leading pattern of specific lung diseases, such as Langerhans cell histiocytosis or lymphangioleiomyomatosis (LAM). Other more rare diseases with cysts are LIP and Birt-Hogg-Dube (Fig. 18).

Incidental lung cyst without other HRCT abnormalities and without a history of lung disease or signs of architectural distortion have been reported as a normal finding in elderly patients, ranging from 5 to 22 mm and located in all lobes.

In the early phase, *Langerhans cell histiocytosis (LCH)* has a typical nodular pattern with multiple, <10 mm small centrilobular nodules with irregular margins. Later these nodules increase in

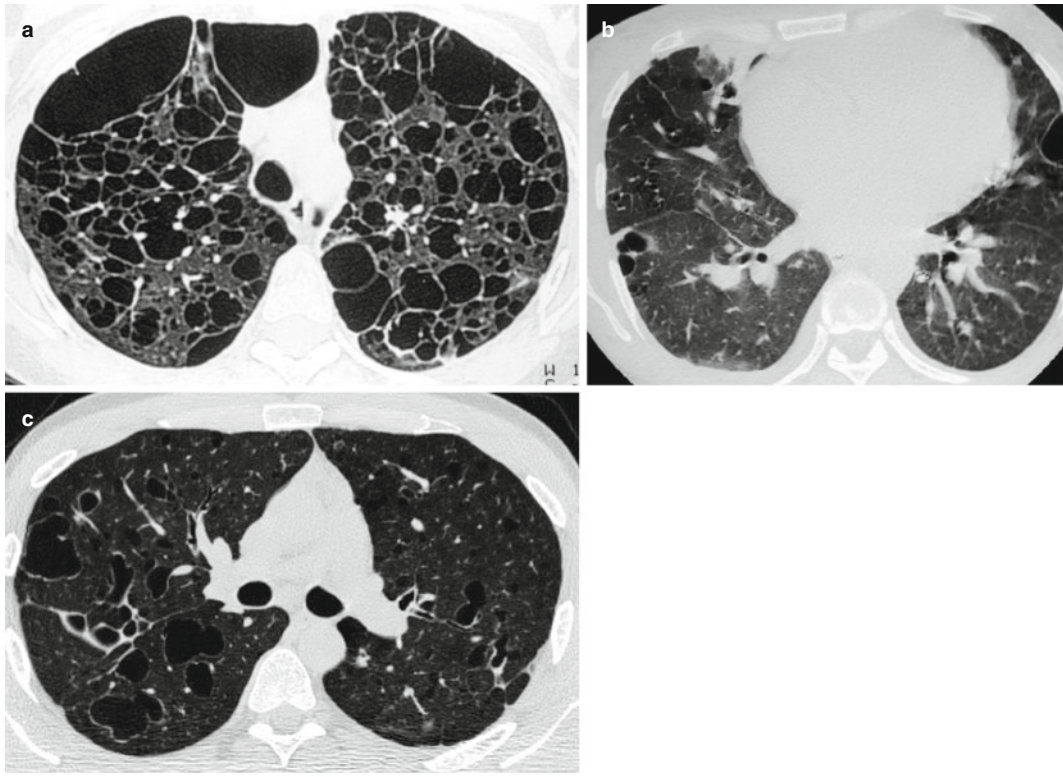

Fig. 18 Patterns with cystic parenchymal disease density: (**a**) Lymphangiomyomatosis with uniform cysts and enlarged pleural space after recurrent pneumothoraces, (**b**) diffuse ground glass and subpleural cysts in lymphocytic interstitial pneumonia (LIP), (**c**) bizarre-shaped cysts predominantly located in the upper lobes in Langerhans cell histiocytosis (LCH)

size and have a tendency to cavitate and to develop into cystic lesions with a diameter of up to 2 cm. The cysts are often confluent, have bizarre or irregular shapes, and are usually thin walled, but may be thick walled. LCH is predominantly located in the upper lobes, with sparing of the costophrenic sinus, which is better depicted on coronal reformations than on cross-sectional images. The thin walls of the cysts are prone to rupture, with an increased risk of pneumothorax. Concomitant nodules are usually irregular, measure 1–5 mm, and often have a centrilobular distribution. The interspersed pulmonary parenchyma is typically normal, without evidence of fibrosis or septal thickening.

Lymphoid interstitial pneumonia (LIP) is uncommon and considered as part of a spectrum of pulmonary lymphoproliferative disorders, ranging from benign accumulation to malignant lymphomas. Mostly it is associated with Sjögren's disease, HIV infection, or other immunological disorders. On HRCT, typical findings are sharply demarcated cysts in a subpleural distribution with intraluminal septae associated with diffuse ground glass of the lung parenchyma. Poorly defined centrilobular nodules, thickening of the bronchovascular bundles, patchy ground-glass opacities, and focal consolidations also belong to the spectrum. In cases with consolidations, a lymphoma needs to be excluded.

Lymphangioleiomyomatosis (LAM) usually occurs in young women and is frequently associated with recurrent pneumothorax and pleural effusion. The cysts are distributed bilateral diffusely throughout the lung, involving both upper and lower lobes, with also involvement of the lung bases. They are thin walled, round, and measure 0.2–5 cm. Their wall is thin, ranging from

barely visible to 4 mm in thickness. Since the thin walls of the cysts are prone to rupture, there is an increased risk of pneumothorax. Pleural effusion may also be seen. The surrounding parenchyma is typically normal. Nodules are uncommon, but may be associated with the cysts.

Sometimes it may be difficult to distinguish lymphangioleiomyomatosis and Langerhans cell histiocytosis from emphysema. A helpful finding is that the cystic spaces in LAM and LCH do not have any central nodular opacities, whereas the cystic spaces seen with centrilobular emphysema contain a small central nodular opacity representing the centrilobular artery.

Honeycomb cysts constitute the irreversible final stage of parenchymal destruction in patients with interstitial fibrosis (end-stage lung) of UIP. It is seen in IPF but also in collagen vascular diseases, asbestosis, hypersensitivity pneumonitis, or drug-related fibrosis. The cystic spaces are usually round or ovoid and measure between several millimeters and 1 cm in diameter, although more rarely they can be several centimeters in size. Within one individual, however, they are mostly uniform. They have clearly definable walls which are 1–3 mm thick. Honeycomb cysts seem to develop from alveolar disruption and massively dilated alveolar ducts and bronchioles. Honeycombing is associated with other findings of lung fibrosis, such as septal and reticular pattern, architectural distortion, and traction bronchiectasis. Most patients demonstrate several layers of irregular cystic spaces (honeycombs), which are separated from each other by irregular thick walls and intralobular septa and lines. However, note that also a singular layer of cystic spaces with thickened wall are described as honeycombing and fulfill the criteria for a definite UIP under appropriate conditions.

Though the definition of honeycombing is quite straightforward, a substantial interreader variability has been described for the diagnosis of honeycombing, which needs attention given the importance of honeycombing for the diagnosis of UIP. Even on HRCT it is not always possible to securely separate the walls of the honeycomb cysts from the thickened intralobular fibrous bands. Secondly, it is important to differentiate honeycombing from tubular bronchiectasis reaching all the way to the pleura. MinIPs have been described as helpful to differentiate between tubular bronchiectasis and focal cysts (see Sect. 3.3).

5 Summary

Continuous volumetric HRCT offers a number of advantages over discontinuous axial thin section CT slices, of which the most important ones refer to improved detection of subtle disease, better and more accurate comparability, and superior quantitative measures. A number of processing options such as MIP and MinIP ease analysis of HRCT patterns. Most recent developments of detector and reconstruction technology have made up for the disadvantage of continuous versus discontinuous data acquisition of the past, allowing for substantial dose savings. All these arguments have led to the fact that HRCT is routinely based on volumetric data acquisition. Today basically each chest CT offers the spatial resolution of a HRCT in all three dimensions, and it depends on the indication of the examination (e.g., malignancy versus diffuse parenchymal disease) whether contrast media is injected and which slice thickness and reconstruction techniques (e.g., MIP and MinIP) are applied.

References

Bankier AA, Fleischmann D, Mallek R et al (1996) Bronchial wall thickness: appropriate window settings for thin-section CT and radiologic-anatomic correlation. Radiology 199(3):831–836

Bankier AA, Schaefer-Prokop C, De Maertelaer V et al (2007) Air trapping: comparison of standard-dose and simulated low-dose thin-section CT techniques. Radiology 242(3):898–906

Bartholmai BJ, Raghunath S, Karwoski RA et al (2013) Quantitative computed tomography imaging of interstitial lung diseases. J Thorac Imaging 28(5):298–307

Beigelman-Aubry C, Hill C, Guibal A, Savatovsky J, Grenier PA (2005) Multi-detector row CT and post-processing techniques in the assessment of diffuse lung disease. Radiographics 25(6):1639–1652

Boehm T, Willmann JK, Hilfiker PR et al (2003) Thin-section CT of the lung: does electrocardiographic triggering influence diagnosis? Radiology 229(2):483–491

Christe A, Lin MC, Yen AC et al (2012) CT patterns of fungal pulmonary infections of the lung: comparison of standard-dose and simulated low-dose CT. Eur J Radiol 81(10):2860–2866

Christe A, Charimo-Torrente J, Roychoudhury K et al (2013) Accuracy of low dose computed tomography (CT) for detecting and characterizing the most common CT-Patterns of pulmonary disease. EJR 82:e142–e150

Criado E, Sánchez M, Ramírez J et al (2010) Pulmonary sarcoidosis: typical and atypical manifestations at high-resolution CT with pathologic correlation. Radiographics 30(6):1567–1586

Eibel R, Türk T, Kulinna C et al (2001a) Value of multiplanar reformations (MPR) in multi-slice spiral CT of the lung. Rofo 173(1):57–64

Eibel R, Türk TR, Kulinna C et al (2001b) Multidetector-row CT of the lungs: multiplanar reconstructions and maximum intensity projections for the detection of pulmonary nodules. Rofo 173(9):815–821

Gavelli G, Giampalma E, Cenni M et al (1998) High-resolution volumetric computerized tomography of the lung: optimization of technique and image quality as a function of its clinical-diagnostic use and dose to the patient. Radiol Med 95(4):322–328. (Italian)

Goh NS, Desai SR, Veeraraghavan S et al (2008) Interstitial lung disease in systemic sclerosis: a simple staging system. Am J Respir Crit Care Med 177(11):1248–1254

Goldin JG (2013) Computed tomography as a biomarker in clinical trials imaging. J Thorac Imaging 28(5):291–297

Gotway MB, Lee ES, Reddy GP et al (2000) Low-dose, dynamic, expiratory thin-section CT of the lungs using a spiral CT scanner. J Thorac Imaging 15(3):168–172

Hansell DM, Goldin JG, King TE Jr et al (2015) CT staging and monitoring of fibrotic interstitial lung diseases in clinical practice and treatment trials: a Position Paper from the Fleischner society. Lancet Respir Med 3(6):483–496

Kauczor HU, Wielpütz MO, Owsijewitsch M, Ley-Zaporozhan J (2011) Computed tomographic imaging of the airways in COPD and asthma. J Thorac Imaging 26(4):290–300

Kim HJ, Brown MS, Elashoff R et al (2011) Quantitative texture-based assessment of one-year changes in fibrotic reticular patterns on HRCT in scleroderma lung disease treated with oral cyclophosphamide. Eur Radiol 21(12):2455–2465

Kim SY, Diggans J, Pankratz D et al (2015) Classification of usual interstitial pneumonia in patients with interstitial lung disease: assessment of a machine learning approach using high-dimensional transcriptional data. Lancet Respir Med 3(6):473–482

Kubo T, Ohno Y, Kauczor HU, Hatabu H (2014) Radiation dose reduction in chest CT – review of available options. Eur J Radiol 83(10):1953–1961. Do

Lee KS, Boiselle PM (2010) Update on multidetector computed tomography imaging of the airways. J Thorac Imaging 25(2):112–124

Lucidarme O, Grenier PA, Cadi M et al (2000) Evaluation of air trapping at CT: comparison of continuous-versus suspended-expiration CT techniques. Radiology 216(3):768–772

Mayo JR, Webb WR, Gould R, Stein MG, Bass I, Gamsu G, Goldberg HI. (1987) High-resolution CT of the lungs: an optimal approach. Radiology 163(2):507–10

Müller NL (1991) Computed tomography in chronic interstitial lung disease. Radiol Clin North Am 29(5): 1085–93

Murata K, Khan A, Herman PG (1989) Pulmonary parenchymal disease: evaluation with high-resolution CT. Radiology 170:629–635

Nishino M, Boiselle PM, Copeland JF et al (2004) Value of volumetric data acquisition in expiratory high resolution computed tomography of the lung. J CAT 28:209–214

O'Donnell CR, Bankier AA, O'Donnell DH, Loring SH, Boiselle PM (2014) Static end-expiratory and dynamic forced expiratory tracheal collapse in COPD. Clin Radiol 69(4):357–362. doi:10.1016/j.crad.2013.11.003

Ohno Y, Takenaka D, Kanda T et al (2012) Adaptive iterative dose reduction using 3D processing for reduced- and low-dose pulmonary CT: comparison with standard-dose CT for image noise reduction and radiological findings. AJR Am J Roentgenol 199(4): W477–W485

Peloschek P, Sailer J, Weber M et al (2007) Pulmonary nodules: sensitivity of maximum intensity projection versus that of volume rendering of 3D multidetector CT data. Radiology 243(2):561–569

Pontana F, Duhamel A, Pagniez J et al (2011) Chest computed tomography using iterative reconstruction vs filtered back projection (part 2): image quality of low-dose CT examinations in 80 patients. Eur Radiol 21(3):636–643

Prakash P, Kalra MK, Ackman JB et al (2010) Diffuse lung disease: CT of the chest with adaptive statistical iterative reconstruction technique. Radiology 256(1): 261–269

Prosch H, Schaefer-Prokop CM, Eisenhuber E et al (2013) CT protocols in interstitial lung diseases – a survey among members of the European Society of Thoracic Imaging and a review of the literature. Eur Radiol 23(6):1553–1563

Raghu G, Collard HR, Egan JJ et al (2011) ATS/ERS/JRS/ALAT Committee on Idiopathic Pulmonary Fibrosis. An official ATS/ERS/JRS/ALAT statement: idiopathic pulmonary fibrosis: evidence-based guidelines for diagnosis and management. Am J Respir Crit Care Med 183(6):788–824

Remy-Jardin M, Remy J, Artaud D, Deschildre F, Duhamel A (1996) Diffuse infiltrative lung disease: clinical value of sliding-thin-slab maximum intensity projection CT scans in the detection of mild micronodular patterns. Radiology 200(2):333–339

Travis WD, Costabel U, Hansell DM, ATS/ERS Committee on idiopathic Interstitial Pneumonias et al (2013) An official American Thoracic Society/

European Respiratory Society statement: update of the international multidisciplinary classification of the idiopathic interstitial pneumonias. Am J Respir Crit Care Med 188(6):733–748

Vernhet H, Bousquet C, Vergnes C et al (1999) Contribution of high-resolution volume computed tomography (HRVCT) for the exploration of diffuse pulmonary infiltrative disorders. Rev Mal Respir 16(2):188–197. (French)

Verschakelen JA, Scheinbaum K, Bogaert J et al (1998) Expiratory CT in cigarette smokers: correlation between areas of decreased lung attenuation, pulmonary function tests and smoking history. Eur Radiol 8(8):1391–1399

Vikgren J, Johnsson AA, Flinck A et al (2008) High-resolution computed tomography with 16-row MDCT: a comparison regarding visibility and motion artifacts of dose-modulated thin slices and "step and shoot" images. Acta Radiol 49(7):755–760

Volpe J, Storto ML, Lee K, Webb WR (1997) High-resolution CT of the lung: determination of the usefulness of CT scans obtained with the patient prone based on plain radiographic findings. AJR Am J Roentgenol 169(2):369–374

Walsh SL, Hansell DM (2010) Diffuse interstitial lung disease: overlaps and uncertainties. Eur Radiol 20(8):1859–1867

Walsh SL, Nair A, Hansell DM (2013) Post-processing applications in thoracic computed tomography. Clin Radiol 68(5):433–448

Walsh SL, Wells AU, Sverzellati N et al (2014a) An integrated clinicoradiological staging system for pulmonary sarcoidosis: a case-cohort study. Lancet Respir Med 2(2):123–130

Walsh SL, Sverzellati N, Devaraj A et al (2014b) Connective tissue disease related fibrotic lung disease: high resolution computed tomographic and pulmonary function indices as prognostic determinants. Thorax 69(3):216–222

Watadani T, Sakai F, Johkoh T et al (2013) Interobserver variability in the CT assessment of honeycombing in the lungs. Radiology 266(3):936–944

Wells AU, Hirani N (2008) Interstitial lung disease guideline. Thorax 63:v1–v58

Pulmonary Infections: Imaging with CT

Catherine Beigelman-Aubry and Sabine Schmidt

Abstract

Computed tomography (CT) plays a key role in various kinds of pulmonary infections especially in immunocompromised patients, owing to its much higher sensitivity and specificity than the traditionally performed chest X-ray. CT permits the detection of the main infectious pattern and associated findings with high confidence and allows for the precise assessment of all involved structures, to potentially guide a bronchoalveolar lavage or another diagnostic procedure, and to ensure a reliable follow-up. It may be performed at a carefully chosen dose, which may nearly reach that of a chest X-ray in specific situations. The importance of post-processing tools is undeniable in some conditions, in particular for the evaluation of micronodules in the immunocompromised population. The wide spectrum of features of specific organisms according to the immune status, such as in aspergillosis or tuberculosis, must be known, as well as the potential of atypical presentations in case of *Pneumocystis jirovecii* (PCP) pneumonia when occurring in non-HIV immunocompromised patients. In all cases, underlying disorders must be considered as well as all the differential diagnoses. Overall, CT definitely helps clinicians to diagnose pulmonary infections and to make treatment decisions, especially in vulnerable patients.

Imaging plays a crucial role in the diagnosis of respiratory infections that are a source of high morbidity and mortality especially regarding the increasing number of elderly and immunocompromised patients (Franquet 2006; Herold and Sailer 2004). Despite its much greater sensitivity and specificity than plain film radiography (Heussel et al. 1999), computed tomography (CT) has not been recommended for the initial assessment in

C. Beigelman-Aubry (✉) • S. Schmidt
Diagnostic and Interventional Radiology,
University Hospital Lausanne, Lausanne, Switzerland
e-mail: Catherine.Beigelman-Aubry@chuv.ch;
Sabine.Schmidt@chuv.ch

U.J. Schoepf, F.G. Meinel (eds.), *Multidetector-Row CT of the Thorax*, Medical Radiology,
DOI 10.1007/978-3-319-30355-0_8

most cases. It must be performed when there is a high clinical suspicion of infection with normal, ambiguous, or nonspecific chest X-ray findings, especially in immunocompromised patients (Beigelman-Aubry et al. 2012), in case of atypical clinical and/or radiological presentations, or when an empyema or abscess is suspected (Stigl and Marrie 2013). CT is able to detect even subtle lesions, while demonstrating them earlier than chest X-ray, as well as associated abnormalities or underlying conditions. In addition, it may suggest alternative diagnoses, and can guide interventions to take specimens for microbiology, regardless of the applied technique, either bronchoalveolar lavage (BAL) or percutaneous, transbronchial, or transthoracic needle biopsy. CT is also the imaging modality of choice to monitor response to specific treatment. Although the major CT patterns of pneumonia may be individualized, there is no specific one caused by one particular microorganism. Moreover, multiple CT patterns frequently coexist in the same patient with pulmonary infection. In addition, the radiological appearance of the organism-specific infection can change depending on the degree of the patients' immunosuppression. The infective agents also vary with the type of immune deficiency. As the suggested diagnoses will very much depend on the individual setting, the conclusions drawn from the CT exam must always be integrated into the epidemiological, clinical data and laboratory tests and should result from a multidisciplinary approach. A first reminder of the most common types of pneumonias will be proposed before describing the technical approach and the main CT patterns encountered in routine practice.

1 Pneumonia Types

Community-acquired pneumonia (CAP), hospital-acquired pneumonia (HAP), ventilator-associated pneumonia (VAP), and healthcare-associated pneumonia (HCAP) are the main categories of pneumonias recognized by the currently accepted clinical classification of pneumonia (American Thoracic Society/Infectious Diseases Society of America 2005).

1.1 Community-Acquired Pneumonia (CAP)

Community-acquired pneumonia (CAP) is defined as an acute infection of the lung parenchyma acquired in the community, i.e., in outpatients or residents in long-term care facilities, >2 weeks before the onset of symptoms (Stigl and Marrie 2013). It can vary from a mild outpatient illness (Herold and Sailer 2004) to a more severe disease requiring hospital admission and, at times, intensive care (Niedemann 2015). The development of CAP may be related to either a defect in host defense, an exposure to an especially virulent pathogen, an overwhelming inoculum of microorganisms, or a combination of those factors (Stigl and Marrie 2013). Respiratory disorders, such as chronic obstructive pulmonary disease (COPD), cardiovascular disease, diabetes mellitus, chronic liver disease, HIV infection, and other forms of immune suppression, chronic kidney disease, old age, malignancy, any neurologic illness that predisposes to aspiration including seizures, alcoholic abuse, smoking, and splenectomy, are predisposing host conditions (Niedemann 2015). The diagnosis of CAP, usually based on the presence of cough, fever, sputum production, and/or pleuritic chest pain, is supported by infiltrates detected on the chest radiography in most cases. CT is therefore rarely required. Typical causative organisms of bacterial CAP include gram-positive bacteria such as *Streptococcus pneumoniae* (pneumococcus) that is responsible for approximately one-third of all cases of CAP, *Haemophilus influenzae*, and atypical pathogens, such as *Mycoplasma pneumoniae*, *Chlamydophila pneumoniae* (formally *Chlamydia*), and *Legionella* (Niedemann 2015). Viral agents, such as *influenza A* virus and *respiratory syncytial virus*, may also be involved, as well as fungi and parasites.

About 10–20 % of all adult patients hospitalized with CAP require admission to an intensive care unit. Severe CAP, usually defined by respiratory and/or circulatory failure, requires mechanical ventilation in 40–80 % of cases, with

concomitant septic shock in up to 50 % of cases and a high mortality rate (Stigl and Marrie 2013). Usual complications observed in severe CAP include empyema, lung abscess, pneumothorax, acute respiratory distress syndrome (ARDS), chronic respiratory failure requiring tracheostomy, major cardiac events such as acute coronary syndrome, and multisystem organ failure (Stigl and Marrie 2013).

1.2 Hospital-Acquired or Nosocomial Pneumonia (HAP), Ventilator-Associated Pneumonia (VAP), and Healthcare-Associated Pneumonia (HCAP) (American Thoracic Society/ Infectious Diseases Society of America 2005)

HAP or nosocomial pneumonia occurs 48 h or more after admission and does not appear to be incubating at the time of admission. Nosocomial pneumonia is the leading cause of death from hospital-acquired infections and most commonly affects intensive care unit (ICU) patients, particularly individuals requiring mechanical ventilation (Franquet 2008). VAP is a type of HAP that develops more than 48–72 h after endotracheal intubation. HCAP is defined as pneumonia that occurs in settings of a nonhospitalized patient with extensive healthcare contact, such as wound care, residency in a nursing home, or hemodialysis. The latter pneumonia is increasingly caused by multidrug-resistant (MDR) pathogens. Common pathogens of HAP, VAP, and HCAP are found in both the Proteobacteria and the Firmicutes phylum and include aerobic gram-negative bacilli (e.g., *Escherichia coli*, *Klebsiella pneumoniae*, *Enterobacter* spp., *Pseudomonas aeruginosa*, *Acinetobacter* spp.) and gram-positive cocci (e.g., *Staphylococcus aureus*, including methicillin-resistant *S. aureus* [MRSA], *Streptococcus* spp.) (Jones 2010). Nosocomial pneumonia due to viruses or fungi is significantly less common, except in the immunocompromised patient.

2 Technical Aspects of CT Procedures

Today, CT has to be performed on a multidetector row CT scanner acquiring around 1 mm-thick sections and using an exposure dose which needs to be carefully chosen. Low-dose (LD) CT may be used without impairing the diagnostic information of specific CT patterns, in particular in case of pulmonary fungal infections (Christe et al. 2012), and even ultralow dose (ULD) CT may be possible, according to the clinical context. Overall, the dose may be decreased depending on the size of anomalies to be detected. If they are greater than 1 cm, which is often the case for patients with cystic fibrosis and suspected of acute pulmonary infections, ULD-CT at a dose that nearly reaches that of a chest X-ray may demonstrate the abnormalities, provided that the series are reconstructed with the correct technical parameters (Fig. 1). These doses also apply to the follow-up of this young population that is exposed to frequent ionizing radiation procedures during the whole life. In other cases, LD-CTs with a CTDI of 2–3 mGy.cm in non-obese patients (Bankier and Tack 2010) are perfectly suited for the follow-up of infectious lung diseases (Fig. 2). A comparison with previous baseline examinations is always required to accurately assess the disease's evolution. Of importance, although ULD-CT with a mean radiation expose dose of 0.60 ± 0.15 mSv has been proven to provide acceptable image quality in case of pulmonary infections in febrile neutropenic patients with hematologic malignancy (Kim et al. 2014), caution must be taken due to potential pitfalls with LD-CT (Fig. 3). Multiplanar reformats with average intensity projection (AIP) post-processing of variable thickness may give rise to tomographic or chest X-ray appearance (Figs. 4 and 5) that may be compared with previous or following conventional chest X-rays. The use of maximum intensity projection (MIP) may optimize the detection of micronodules, which sometimes cannot be assessed by using thin slices alone (Fig. 6). It is also helpful to characterize micronodules as centrilobular ones with tree in bud appearance (Fig. 7), corresponding to a

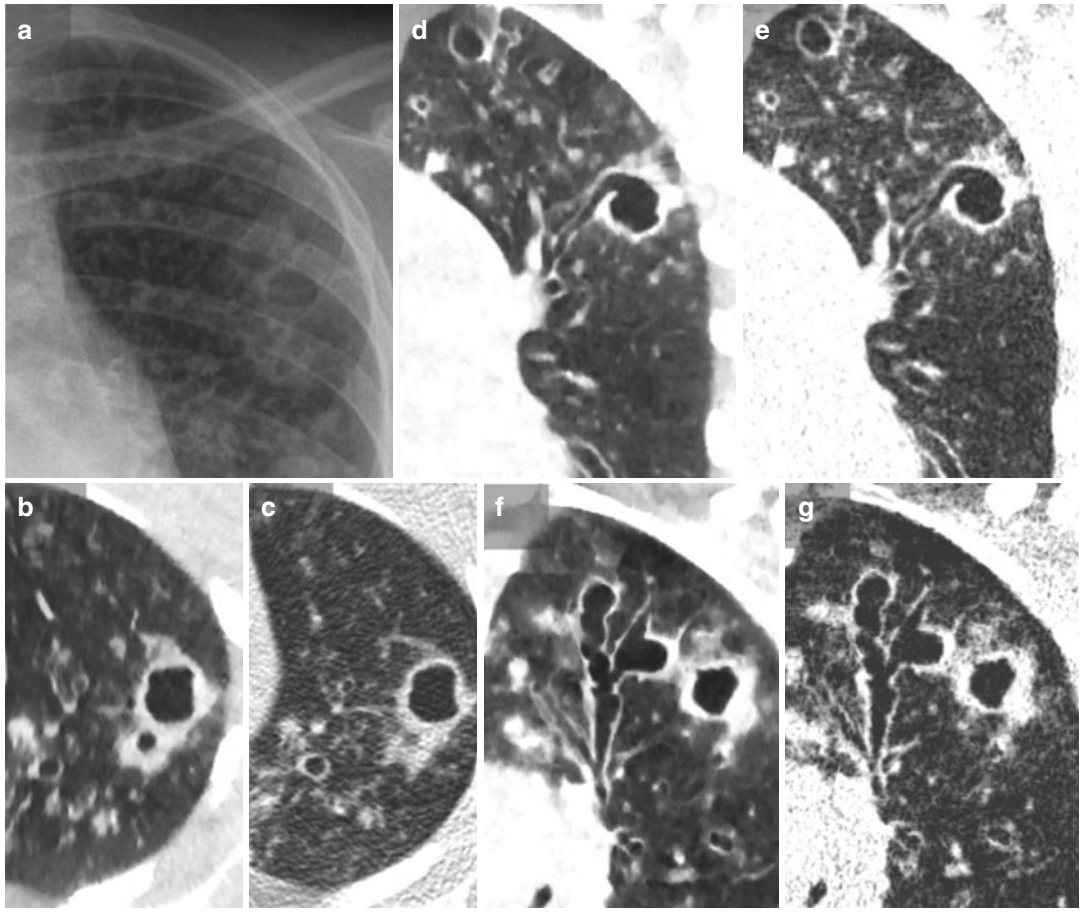

Fig. 1 Ultralow dose CT was performed because of the appearance of a cavity with an air-fluid level in the left axillary area on chest X-ray (**a**) in a 20-year-old female patient with cystic fibrosis and persistent symptoms due to *Staphylococcus aureus* and *Cepacia* infection despite antibiotic treatment. Axial sections reconstructed by using iterative reconstruction (IR) algorithm (**b**) and FBP with soft kernel and a slice thickness of 4 mm (**c**). Coronal reformatted image reconstructed by using IR (**d**, **f**) and filtered back projection (FBP) with soft kernel (e.g). The drainage bronchus of the abscess cavity (**d**, **e**) is clearly differentiated from the varicose bronchiectasis that are well assessed with a 3 mm-thick minimum intensity projection (mIP) reformat (**f**, **g**). Despite a slight distortion of the details seen on the axial image when using IR (**b**) compared with FBP (**c**), a substantial reduction of the noise is observed with IR (**d**, **f**)

bronchocentric distribution, or as ones with a random distribution as seen in miliary disease (Fig. 8) (Beigelman-Aubry et al. 2005). The use of minimum intensity projection (mIP) allows to accurately locate an abnormal area in order to guide a bronchoalveolar lavage (BAL) (Fig. 9), to differentiate bronchiectasis from a cavitary lesion (Fig. 1), to visualize the drainage bronchus in the latter situation, as well as to help to recognize a bronchopleural fistula.

CT may be performed without or with intravenous (IV) contrast, the latter especially to evaluate the necrotic component of a pneumoniae or abscesses (Fig. 9) and to optimize the differentiation from an empyema (Figs. 10 and 11). It has also been described as helpful for differentiation between a pulmonary angioinvasive mycosis and a bacterial pneumonia in high-risk hematologic patients by using volume perfusion CT (Schulze et al. 2012). IV contrast-enhanced CT is also

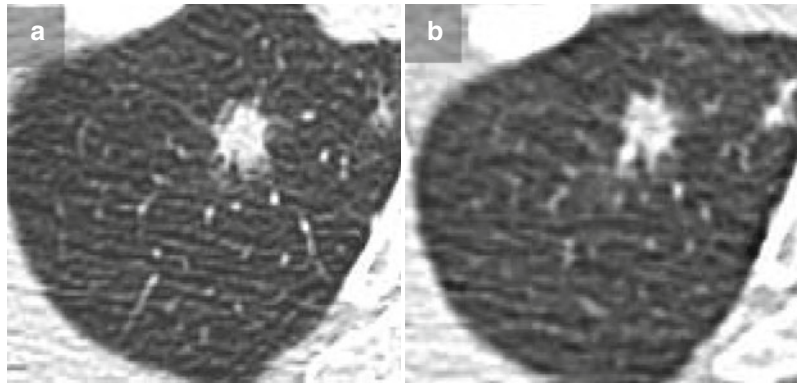

Fig. 2 Low-dose CT was performed for the follow-up of an angioinvasive aspergillosis in a 38-year-old woman with acute myeloid leukemia. The baseline CT (**a**) was performed with a CTDI of 5 and a DLP at 147 mGy.cm and the follow-up CT (**b**) with a CTDI of 2 and a DLP of 72 mGy.cm by using filter back projection reconstruction (FBP) with a soft kernel, without iterative reconstruction (IR) algorithm. Although a relative lesser image quality than the reference image, the disease's evolution may be perfectly assessed at less than half of the initial dose

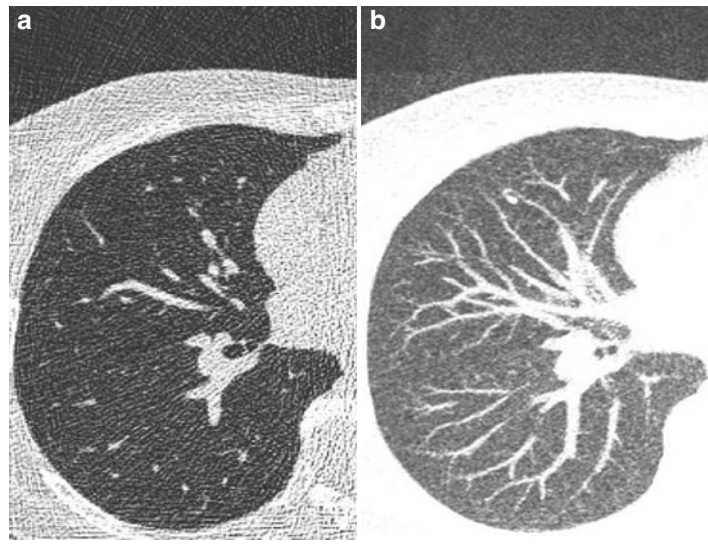

Fig. 3 Ultralow dose CT performed at 100 kV and 10 mAs corresponding to a CTDIvol of 0.4 mGy reconstructed with FBP and a lung kernel. Native thin axial section (**a**) and 10 mm-thick maximum intensity projection reformat (**b**) exhibit noise well seen outside of the chest wall. Such noise projected on the lung mimics micronodulation with random distribution that may simulate a miliary disease in a context of a febrile immunocompromised patient. Although IR is the method of reconstruction of choice with low-dose CT and available in most institutions today, such potential pitfalls with FBP and lung kernel must be known when IR is not available. This precludes the use of such doses in this setting

required in case of hemoptysis, being able to demonstrate enlarged bronchial and non-bronchial systemic arteries due to former tuberculosis or, less frequently, Rasmussen aneurysms (Fig. 12) occurring in the same situation as well as vessel involvement in case of fungal disease (Fig. 13). It may also highlight a concomitant thromboembolic disease.

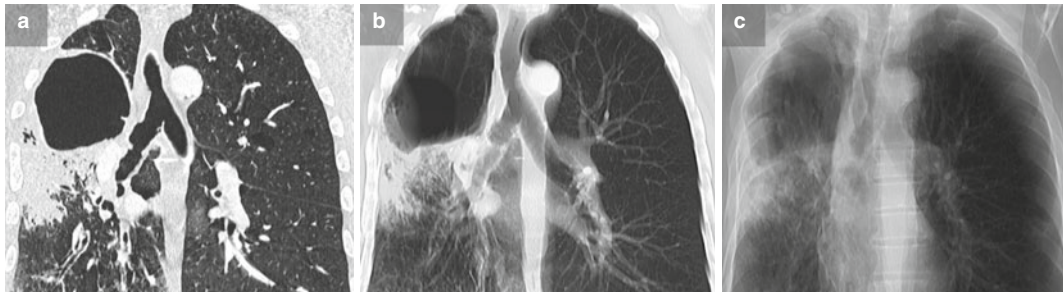

Fig. 4 Coronal reformatted images with progressive thickening of the slabs from 1 (**a**) to 30 (**b**) to 150 mm (**c**) thick slabs by using the average intensity projection (AIP) post-processing tool in a patient known for a voluminous bullae of the right apex of the lung with superimposed infectious alveolar consolidation. Note that the bullae is not easily seen on the chest X-ray rendering in (**c**), as it was the case with the conventional chest X-ray (not shown). The same limitation also occurs in case of cavitation that may be missed on conventional chest X-ray

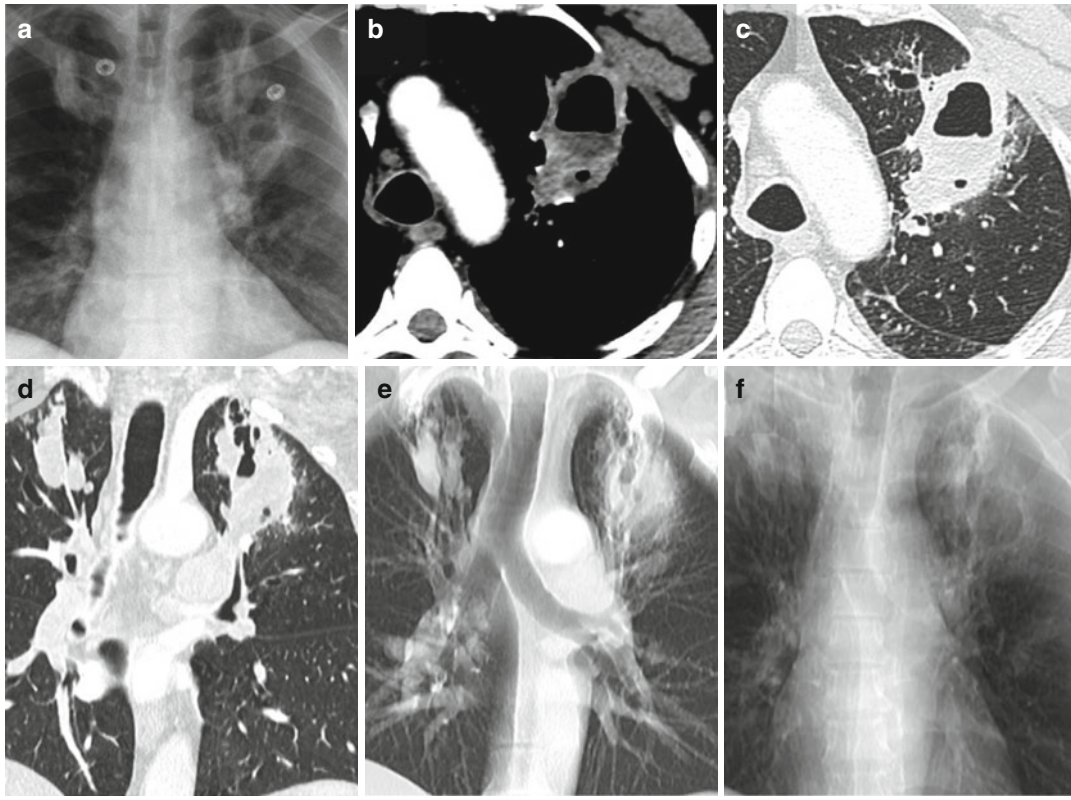

Fig. 5 A 60-year-old man suffering from bronchiectasis of unknown cause presented with fever and new respiratory symptoms related to an abscess due to a usually nosocomial germ, *Serratia marcescens* and *Cronobacter*, a gram-negative bacteria of the *Enterobacteriaceae* family. Chest X-ray (**a**) and axial CT section with IV contrast in mediastinal (**b**) and lung (**c**) windows show the abscess of the LUL with thick walls, a necrotic component and an air-fluid level. The coronal 1.5 mm (**d**), 30 mm (**e**), and 150 mm (**f**) thick AIP reformatted images allow for a better understanding of the opacities related to a bronchocele at the level of the RUL and the abscess situated close to a bronchiectatic area of the LUL

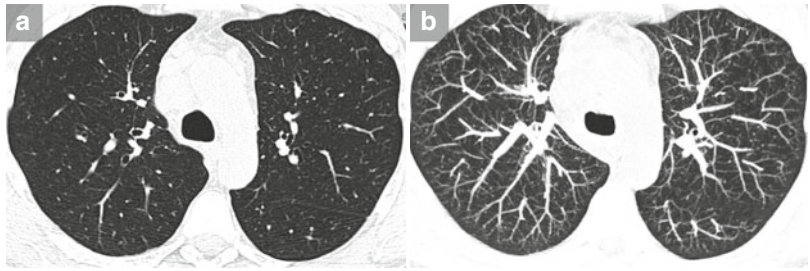

Fig. 6 16 mm-thick axial MIP image in a 58-year-old patient with Crohn disease under infliximab treatment. Although invisible on 1.25 mm-thick axial image (**a**), the MIP reformatted image (**b**) permits to detect micronodules with random distribution that were related to a miliary tuberculosis

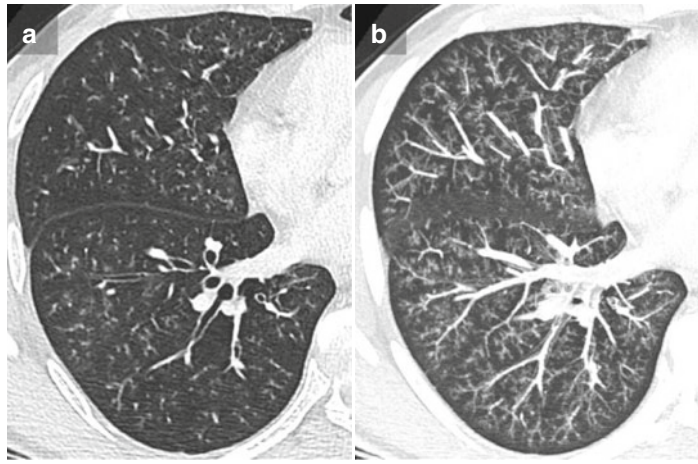

Fig. 7 Chest CT of a 36-year-old patient with ankylosing spondylarthritis treated by using anti-TNF alpha. Although numerous micronodules are visible on the thin axial section (**a**), their profusion and centrilobular distribution with tree in bud appearance related to *Mycoplasma pneumoniae* is more obvious when using 10 mm-thick MIP reformat (**b**). Note the sparing of the subpleural area typical of centrilobular distribution

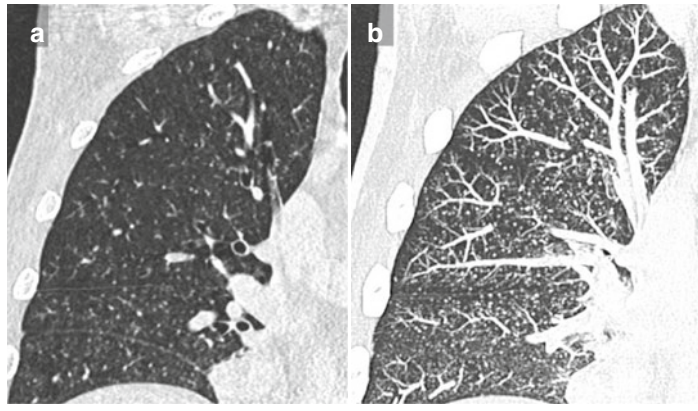

Fig. 8 Chest CT of a patient suffering from a Good's syndrome (thymoma with immunodeficiency) and miliary tuberculosis (TB). The thin coronal reformatted image (**a**) shows an apparent limited number of nodules, unlike the 10 mm-thick MIP reformat (**b**) that shows obvious micronodules with random distribution that were related to a hematogenous spread of TB

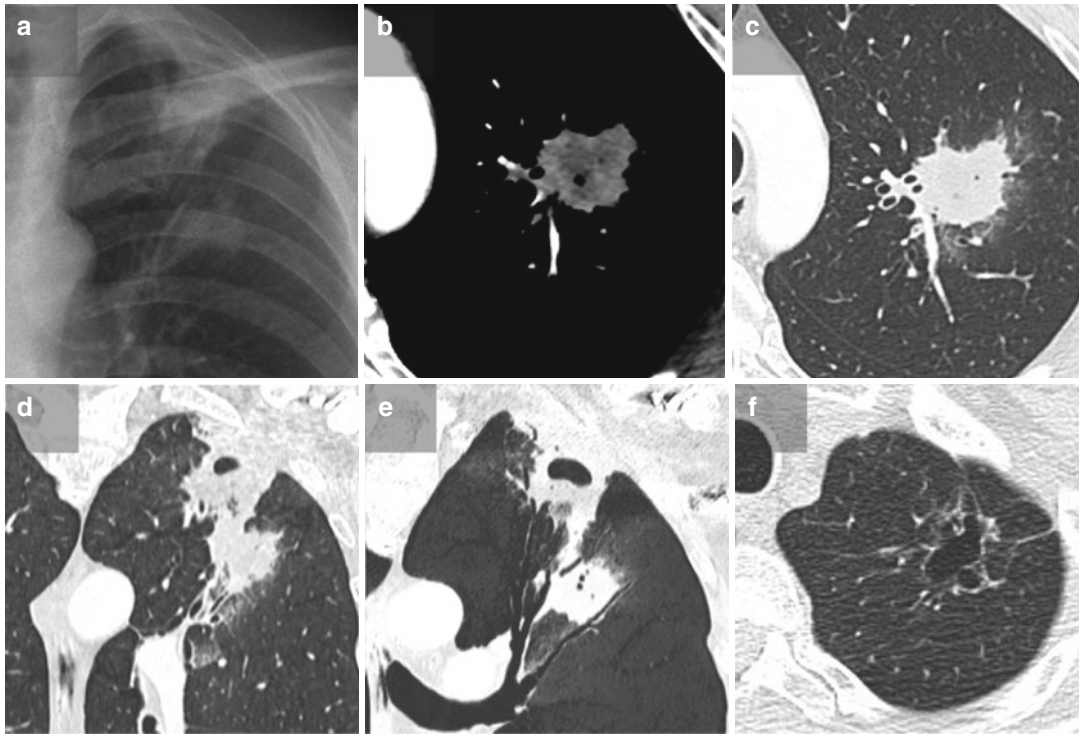

Fig. 9 Pulmonary abscess related to multisensible *Escherichia coli* in a 52-year-old male alcoholic and heavy smoker suffering from fever with respiratory symptoms resisting to first line of antibiotics. After an initial chest X-ray (**a**), a chest CT with intravenous (IV) contrast media injection was performed due to worsening of the status. It allowed for the exclusion of pulmonary embolism and demonstrated the necrotic component of a pulmonary abscess of the LUL on axial sections with mediastinal (**b**) and lung (**c**) windows. A coronal reformatted image (**d**) showed cavitation within the upper part of the lesion that was better assessed when applying 7 mm-thick mIP post-processing (**e**). The latter also allowed for demonstration of the drainage bronchus that helped the clinician to guide the BAL. A follow-up CT in axial sections (**f**) demonstrated the resolution of this lesion with a sequelae appearing as a cavity with lobulated margins with thin wall

3 Main CT Patterns

Although an overlap may be observed among the different patterns, with several patterns potentially occurring in various infectious disorders, the type of pneumonia may be suggested according to the predominant CT feature.

3.1 Alveolar Consolidation

Alveolar consolidation, which refers to an exudate or another product of disease replacing alveolar air and rendering the lung solid, appears as a homogeneous increase in pulmonary parenchymal attenuation obscuring the margins of vessels and airway walls. It may be associated with an air bronchogram, a pattern of air-filled bronchi on a background of high-attenuation airless lung (Hansell et al. 2008) that argues against the presence of a central obstructing lesion (Walker et al. 2014). Alveolar consolidation can be differentiated from atelectasis by the absence of direct and indirect signs of volume loss, such as fissural displacement, mediastinal shift, and diaphragmatic elevation. Alveolar consolidation is a major feature of infectious pneumonia as well as the predominant CT pattern of lobar pneumonia, bronchopneumonia, or diffuse alveolar consolidation.

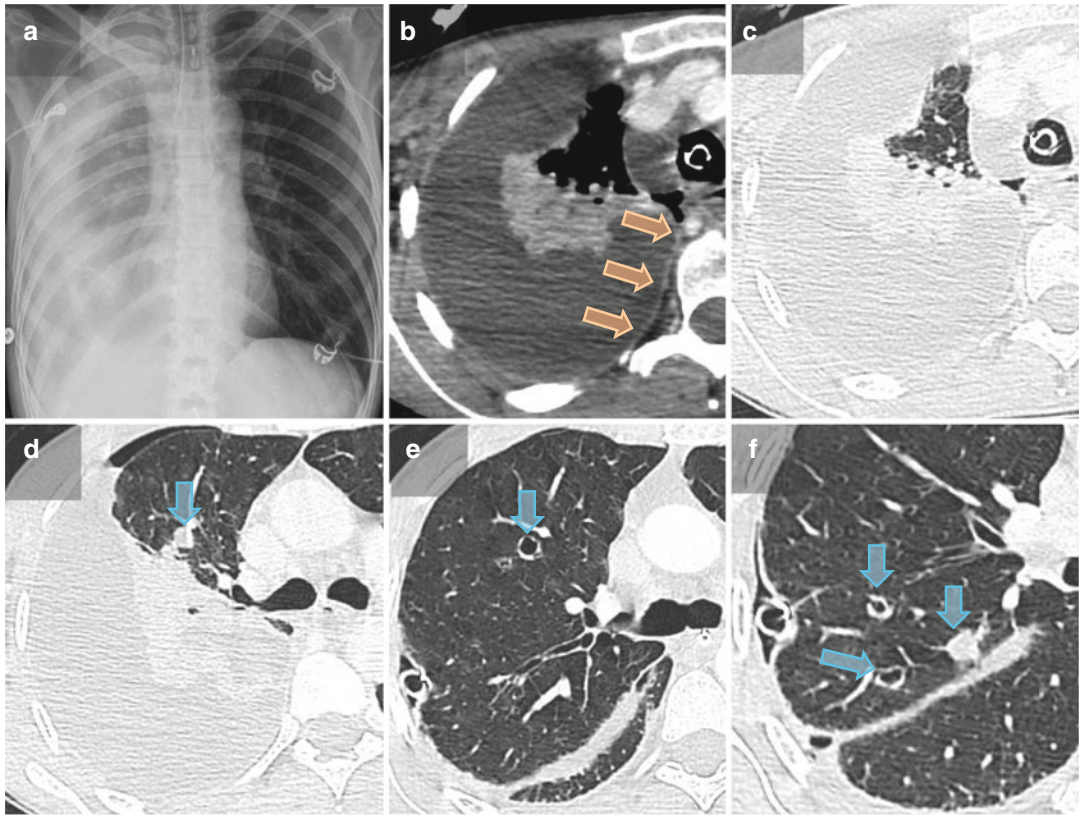

Fig. 10 Empyema with right pulmonary abscesses in a context of bronchoaspiration pneumonia due to *Streptococcus milleri* and *Fusobacterium necrophorum* in a 47-year-old patient known for previous drug abuse that was found unconscious at home. In addition to antibiotherapy, a thoracoscopy was performed with drainage of the empyema. The reference chest X-ray (**a**) shows a pleural effusion. The axial CT with IV contrast media administration in mediastinal (**b**) and lung (**c**) window at the level of the apical segment of the RUL performed at the same day confirms the pleural effusion with thin enhancement of the parietal pleura suggesting empyema with associated alveolar consolidation. An axial section in lung window at the level of the right upper lobe bronchus (**d**) of the reference CT and also a follow-up CT performed 3 days later (**e**) demonstrate the cavitation of a pulmonary abscess of the anterior segment of the RUL that appears solid in (**d**). An axial image at the level of the middle lobe (**f**) shows additional cavities and another solid nodule related to multiple abscesses

3.1.1 Lobar Pneumonia

Lobar pneumonia, characterized by an inflammatory exudate filling distal airspaces, typically begins in the lung area adjacent to the visceral pleura and spreads through the interalveolar pores of Kohn and the small airways from one segment to another (Muller 2003) respecting a centripetal pattern. Appearing as a single subpleural area of alveolar consolidation with blurred margins restricted to the area next to the fissures, it then progresses to a sublobar or lobar alveolar consolidation sharply demarcated by the interlobar fissure (Fig. 14) (Franquet 2008). An air bronchogram sign is strongly suggestive (Fig. 15) (Syrjälä et al. 1998). Ground-glass opacities adjacent to the alveolar consolidation corresponding to a partial filling of the alveoli may be observed (Fig. 16) (Tanaka et al. 1996). This aspect is the classical presentation of acute bacterial community-acquired pneumonia (CAP), mainly caused by *S. pneumoniae* (Bhalla and McLoud 1998), other agents responsible of complete lobar consolidation including *Klebsiella pneumoniae*, and other gram-negative bacilli, *L. pneumophila*, *H. influenzae*, and occasionally *M. pneumoniae* (Franquet 2008). A *P. jirovecii* infec-

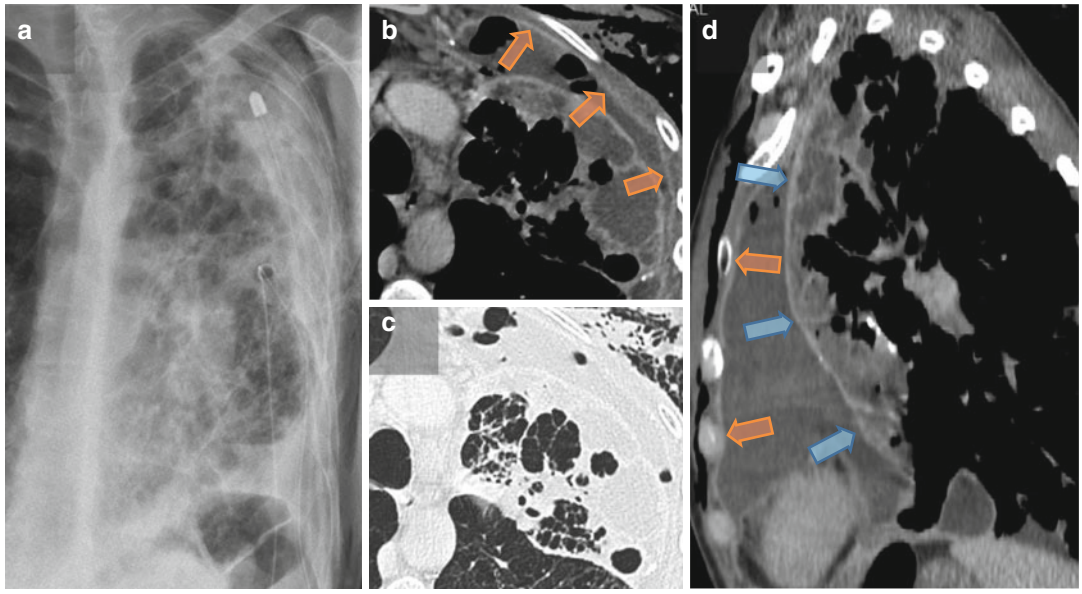

Fig. 11 A 46-year-old male drug abuser known for COPD presents with fever after bullectomy and pleurodesis performed for a spontaneous pneumothorax. Chest X-ray (**a**) and axial chest CT after IV contrast media injection in mediastinal (**b**) and lung (**c**) windows with sagittal reformat (**d**) allow for an easy differentiation between the parenchymal involvement with necrosis on an underlying bullous emphysema from empyema. The thickening of the pleura that is suggestive of empyema (*orange* and *blue arrows*) appears laterally as a continuous line internal to the ribs (*orange arrows*)

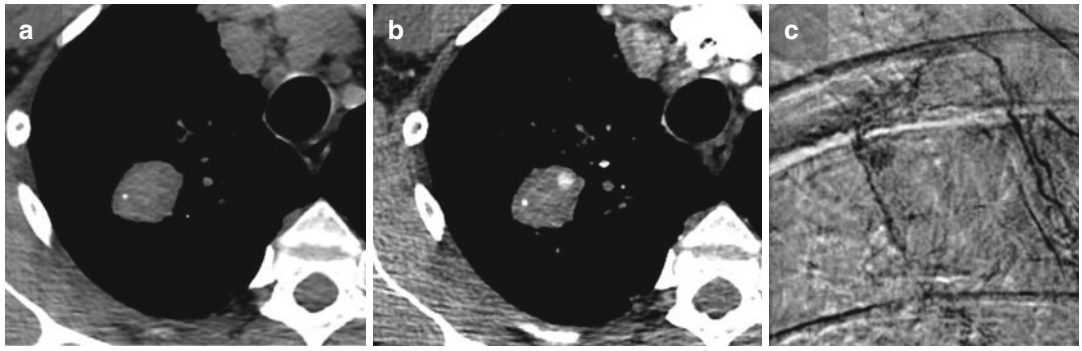

Fig. 12 Rasmussen aneurysm in a 35-year-old patient presenting hemoptysis 9 days after the initial diagnosis of TB. Axial CT without (**a**) and with IV contrast media injection (**b**) focused at the level of the RUL shows a vascular enhancement within the tuberculoma that was clearly differentiated from the calcification depicted without contrast. The selective angiogram of the right bronchial artery (**c**) shows the aneurysm that was immediately successfully embolized

tion, a fungal infection, or a mycobacteriosis has also to be considered in case of immunocompromised patients. An enlarged lobe with bulging fissures due to edematous engorgement may be observed, in particular with *K. pneumoniae* infection, with a current lower occurrence likely due to early treatment in case of suspected pneumonia (Walker et al. 2014).

The differential diagnosis includes aspiration pneumonia when the lower lung is affected, especially on the right side. Lobar or segmental consolidation may also be related to bronchial

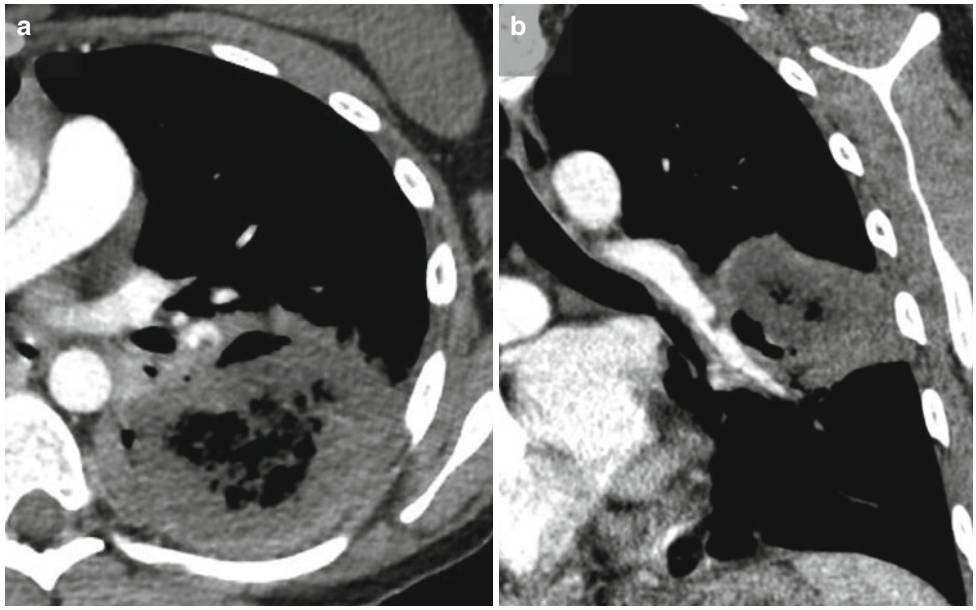

Fig. 13 Hemoptysis in the context of a mucormycosis in a 26-year-old woman suffering from acute lymphoblastic leukemia under antifungal prophylaxis. CT angiography in axial (**a**) and coronal oblique reformat (**b**) shows the vessel involvement originating from the necrotic parenchymal mass of the left lower lobe. This was confirmed after LLL lobectomy

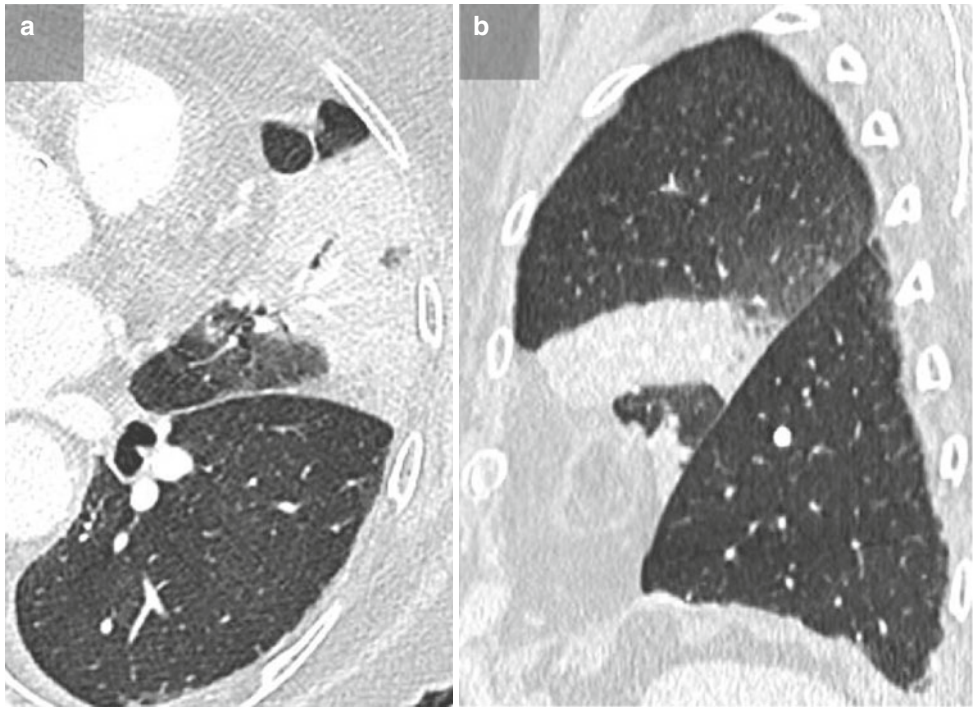

Fig. 14 Segmental pneumonia of the lingula in an 82-year-old woman. Axial CT scan focused at the level of the lower part of the LUL (**a**) and sagittal reformat (**b**) show an alveolar consolidation with a well-defined air bronchogram anterior to the great fissure

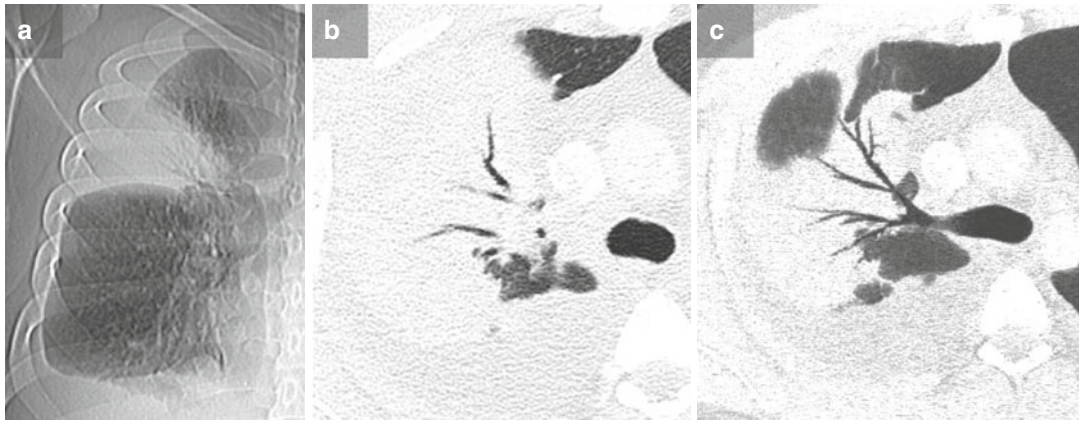

Fig. 15 Lobar pneumonia of the RUL related to *Streptococcus pneumococcus* in a 25-year-old smoker. Scout view (**a**) and axial CT image (**b**) show an alveolar consolidation with an air bronchogram. The 10 mm-thick mIP (**c**) permits to display the entire length of the bronchi from their origin within the alveolar consolidation. Although CT does not replace fiber-optic bronchoscopy, no obstructive lesion was detected by using CT

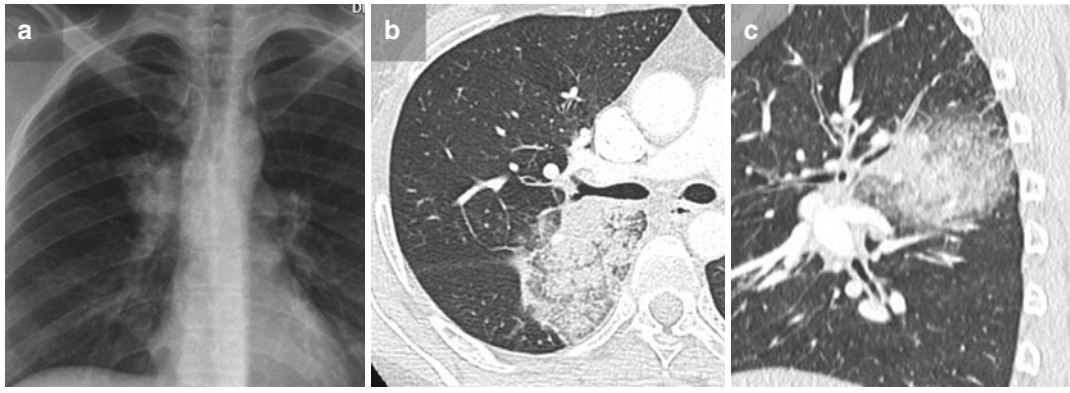

Fig. 16 Round pneumonia occurs in a 44-year-old man suddenly presenting with fever and chest pain and addressed to the emergency department. The chest X-ray (**a**) shows a right parahilar pseudo-tumoral opacity. Due to this atypical aspect, chest CT was performed on the same day. Axial CT image (**b**) and sagittal reformat (**c**) demonstrate a rounded alveolar consolidation of the posterior segment of the RUL and the apical segment of the RLL. Note the ground-glass opacity located around the alveolar consolidation reflecting the partial filling of the alveoli

obstruction, pulmonary hemorrhage, organizing pneumonia, acute fibrinous organizing pneumonia (Fig. 17), radiation pneumonitis, adenocarcinoma (Fig. 18), or lymphoma.

3.1.2 Bronchopneumonia or Lobular Pneumonia

Histologically, bronchopneumonia is characterized by a predominantly bronchiolar and peribronchiolar inflammation with a patchy distribution. Firstly, the adjacent alveoli are involved, followed by the lobules, segments, and/or lobes. An air bronchogram is usually absent. CT features include those of infectious bronchiolitis consisting of thickening of the bronchial walls, centrilobular nodules and tree-in-bud sign (Fig. 19) (see below), airspace nodules generally smaller than 1 cm in size related to the inflammatory spreading to the peribronchiolar alveoli with areas of ground-glass opacity or peribronchiolar consolidation (Fig. 20), and multifocal lobular, segmental, or lobar consolidation (Figs. 21 and 22). Bronchopneumonias are most commonly encountered in nosocomial infections and usually caused by gram-negative bacteria (GNB), especially

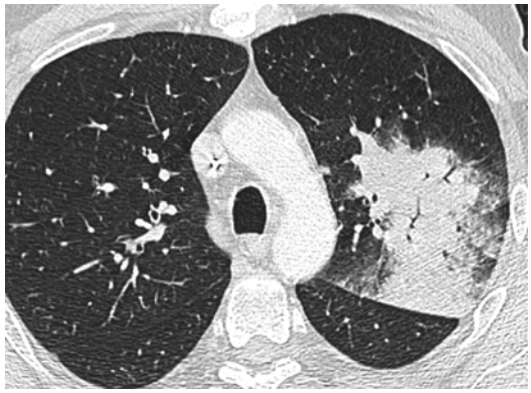

Fig. 17 Acute fibrinous organizing pneumonia (AFOP) in a 52-year-old patient suffering from plasmacytoid dendritic cells acute leukemia with febrile agranulocytosis. The noninfectious nature of the alveolar consolidation with peripheral ground-glass attenuation of the LUL was proven by a transbronchial biopsy performed under endobronchial ultrasonography (EBUS)

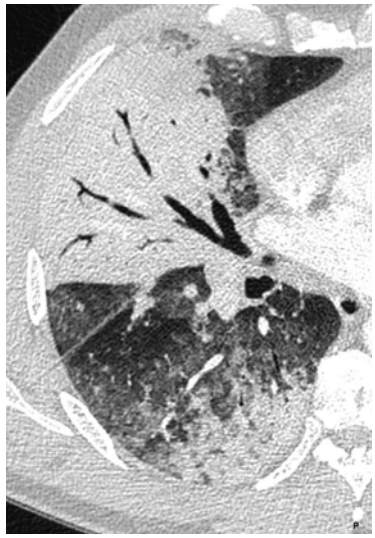

Fig. 18 Alveolar consolidation of the middle lobe related to an adenocarcinoma. The stretched appearance of the bronchi may suggest the diagnosis (Courtesy Pr Brillet, Bobigny, France)

P. aeruginosa or *E. coli*. Other commonly involved bacteria are *S. aureus* (Morikawa et al. 2012), *Haemophilus influenzae*, anaerobes, and some species of fungus, especially *Aspergillus* (Fig. 23). The latter as well as viruses (Franquet 2011) or atypical mycobacteriosis has to be considered when suggested by the individual clinical setting.

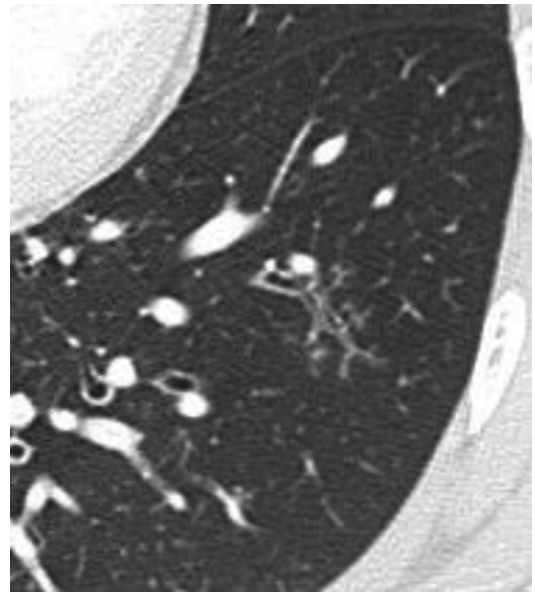

Fig. 19 Infectious bronchiolitis appears as thickening of the bronchial walls and centrilobular nodules with tree-in-bud sign

Bronchiectasis predominantly located at the level of the middle lobe and the lingula may be associated in case of *mycobacterium avium* complex (MAC) infection (Lady Windermere syndrome).

Differential diagnoses include organizing pneumonia, lymphoma, adenocarcinoma, radiation pneumonitis, acute hypereosinophilic syndrome, pulmonary alveolar proteinosis, granulomatous or inflammatory conditions, or lipoid pneumonia (Kjeldsberg et al. 2002).

3.1.3 Diffuse Alveolar Consolidation

Diffuse alveolar consolidation suggests diffuse alveolar damage (DAD), typically encountered in case of adult respiratory distress syndrome (ARDS). An air bronchogram sign is usually observed as well as small pleural effusions. *P. jirovecii* pneumonia (Festic et al. 2005) (Fig. 24) as well as uncommon, unusual, or exotic organisms can be involved. Nondependent anomalies are more related to pneumonia rather than lesions in the dependent lung (Beigelman-Aubry et al. 2012).

The differential diagnoses of infectious causes in case of diffuse involvement are pulmonary edema, noninfectious causes of DAD, and acute interstitial pneumonia.

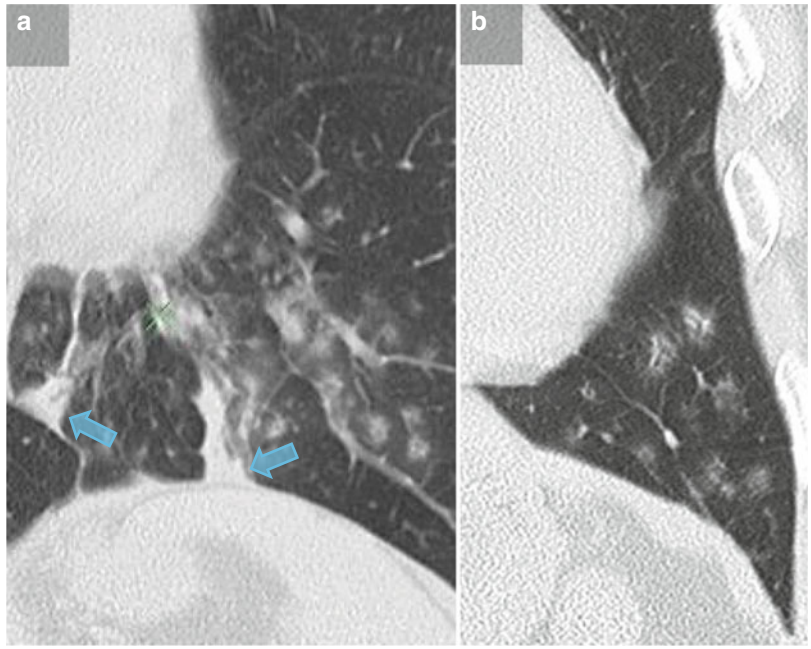

Fig. 20 Two consecutive coronal reformats in a 67-year-old man suffering from a bronchopneumonia show airspace nodules smaller than 1 cm with perinodular ground-glass opacity and patchy alveolar consolidation (*arrows*) (**a**) as well as peribronchiolar consolidation (**b**)

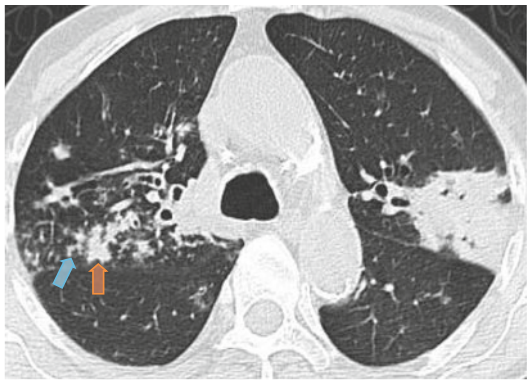

Fig. 21 Bronchopneumonia pattern appears on this axial section at the level of the upper lobes as bronchial wall thickening, centrilobular nodules with tree-in-bud sign (*blue arrow*), lobular (*orange arrow*), and segmental alveolar consolidation with multifocal and patchy involvement

3.2 Ground-Glass Opacity and Interstitial Pneumonia

Ground-glass opacity, a common but nonspecific finding, which refers to a hazy increased opacity of lung with preservation of bronchial and vascular margins (Hansell et al. 2008), is a major feature of interstitial pneumonia. Pathologically, it is characterized by a mononuclear inflammatory cellular infiltrate in the alveolar septa and the distal peribronchovascular interstitium (Muller 2003). This interstitial inflammatory reaction results from epithelial damage, with thickening of the peribronchial area and interlobular septa. Initially applied to different clinical and radiographic findings from those caused by *S. pneumoniae*, atypical pneumonia refers to an interstitial pattern that can be associated with dense consolidation.

The most common causes are viruses, *Mycoplasma pneumoniae*, *Chlamydia*, and *P. jirovecii*. In viral infections and in those caused by *M. pneumoniae*, ground-glass attenuation is associated with signs of cellular bronchiolitis and focal consolidation fitting with bronchopneumonia. When a predominant ground-glass opacity occurs in an immunocompetent patient, *respiratory syncytial virus* or varicella infection should be first considered. In immunocompromised patients, *P. jirovecii* (Thomas and Limper 2004)

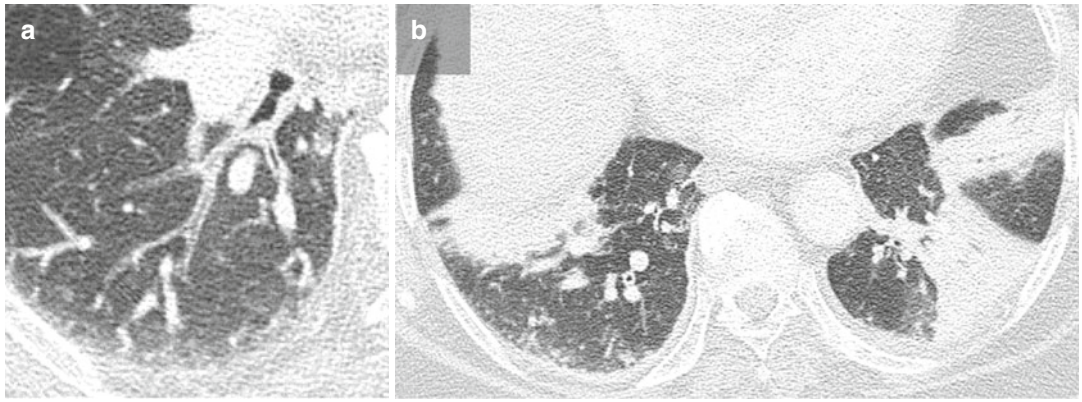

Fig. 22 CMV infection in a patient with renal graft appears as a bronchopneumonia pattern on two successive axial sections (**a**, **b**). The bronchial thickening in (**a**) is associated with bilateral segmental alveolar consolidations at the lung bases in (**b**)

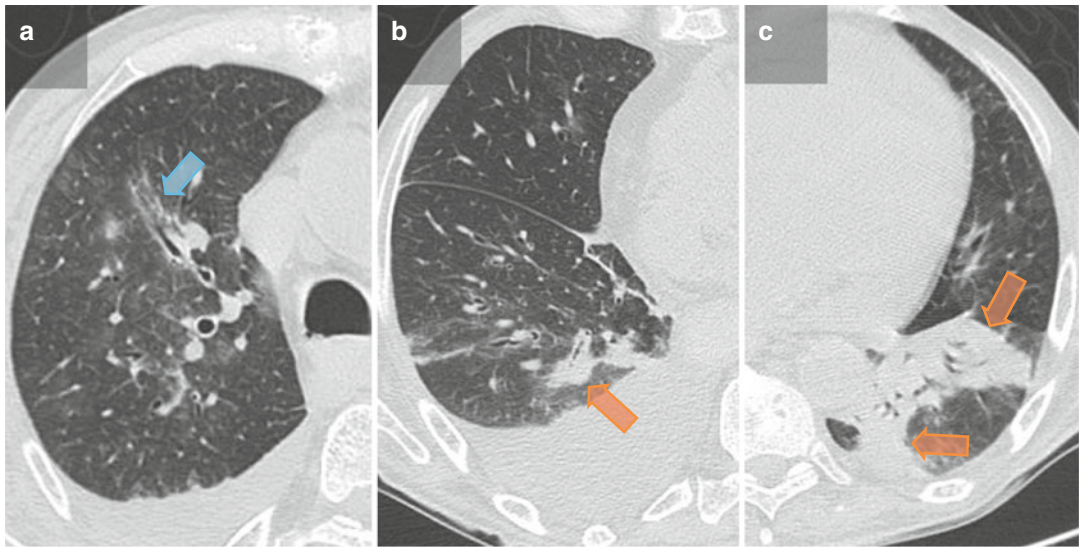

Fig. 23 Invasive airway aspergillosis. Three axial CT images show peribronchial ground-glass attenuation at the level of the RUL (*blue arrows*) with slight bronchial wall thickening and ill-defined nodules (**a**) and alveolar consolidation (*orange arrows*) in a peribronchial location at the level of the posterobasal bronchus of the RLL (**b**) and a segmental distribution in the LLL (**c**). This presentation of aspergillosis mainly concerns non-acute leukemia patients with a leukocyte count >100/mm^3

CMV (McGuinness et al. 1994) or *Mycoplasma* infection must be suggested. *P. jiroveci* infections typically present as ground-glass opacity sparing the pulmonary cortex that predominantly affects the upper region, especially in AIDS patients (Fig. 25). A crazy-paving sign, defined as a combination of ground-glass opacity and smooth interlobular septal thickening that resembles a masonry pattern used in walkways (Hansell et al. 2008), may be observed in infections, in particular with *Pneumocystis jirovecii* pneumonia and *influenza* (Walker et al. 2014). Pulmonary cysts or pneumatoceles within the same areas should suggest PCP (Fig. 26). In immunocompromised non-HIV-positive patients, features are less suggestive of the diagnosis, with rapid progression,

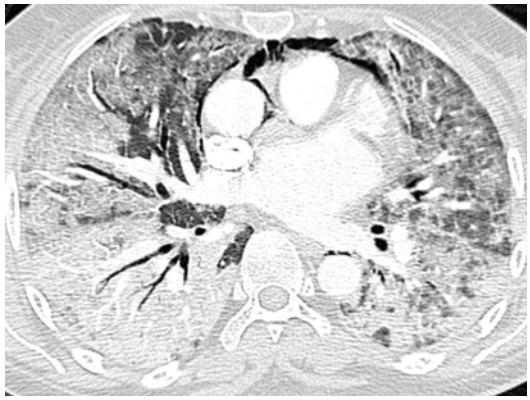

Fig. 24 Diffuse alveolar consolidation with air bronchogram and ground-glass opacity in a patient with autoimmune hepatitis treated with long-term steroids presenting with dyspnea and severe hypoxemia. This was related to a *Pneumocystis jirovecii* pneumonia. Note the pneumomediastinum in this mechanically ventilated patient staying in the intensive care unit who died from this severe infection with rapid deterioration

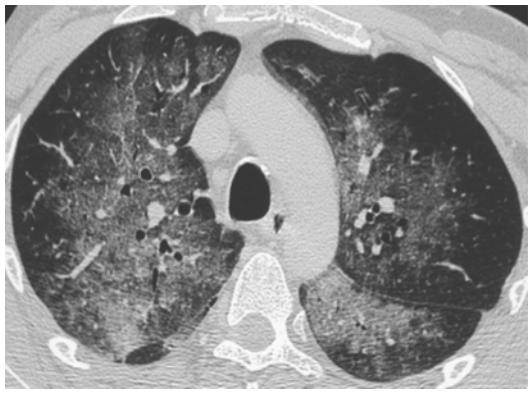

Fig. 25 *P. jirovecii* pneumonia in an AIDS patient appearing as ground-glass opacity sparing the pulmonary cortex and typically predominantly located at the upper region of the lungs

this being the result of severe or dysregulated inflammatory responses that are evoked by a relatively small number of *Pneumocystis* organisms (Chang et al. 2013; Tasaka and Tokuda 2012) (Fig. 27). In the latter category of patients, ground-glass opacities can also be caused by viral (Fig. 28) or pyogenic infection (Kang et al. 1996).

Peculiar aspects of GGO are seen with *the halo sign* (see below) and *the reversed halo sign*

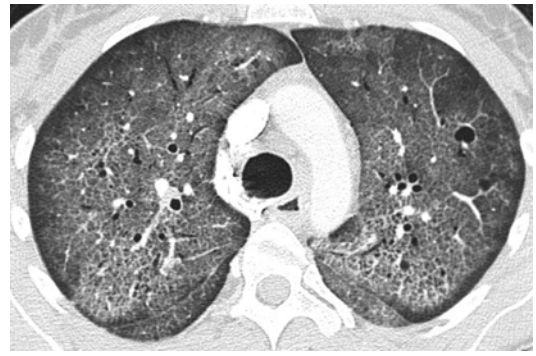

Fig. 26 PCP pneumonia in an AIDS patient presenting with cough and fever. The crazy-paving appearance associated with cysts strongly suggests the diagnosis

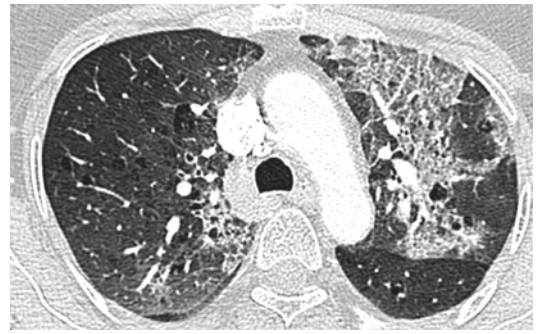

Fig. 27 PCP pneumonia in an HIV-negative patient with a history of cerebral glioblastoma treated by surgery and radiochemotherapy. Axial CT shows ground-glass opacity predominating on the *left side* without sparing of the pulmonary cortex. The rounded hypoattenuated areas mostly correspond to centrilobular emphysema and not cysts that are rare in this condition

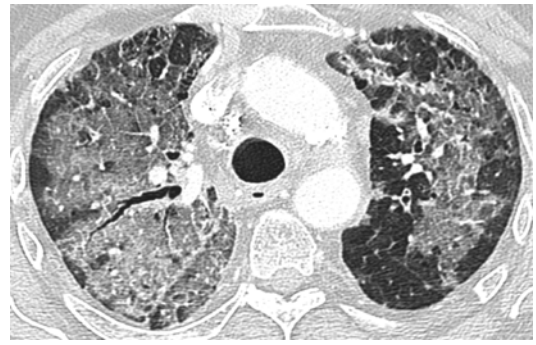

Fig. 28 Bilateral ground-glass opacity at the level of the upper lobes are related to a *Coronavirus* infection in a 72-year-old man known for a small cell carcinoma treated by radiochemotherapy

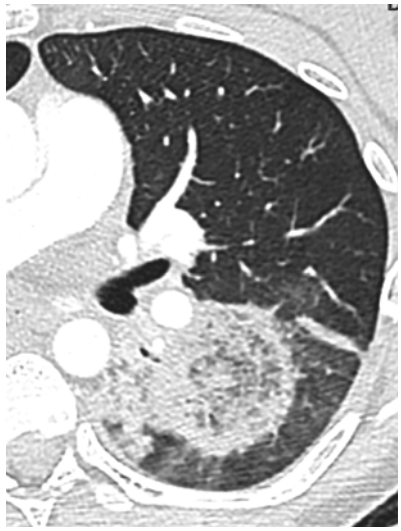

Fig. 29 Axial CT image shows a reverse halo sign in a 26-year-old woman known for an acute lymphoblastic leukemia that developed fever and cough with hemodynamic compromise despite antifungal prophylaxis. This was related to a mucormycosis (*Lichtheimia* spp) proven by transbronchial biopsy and panfungal PCR in the BAL

(RHS), defined as focal rounded area of ground-glass opacity surrounded by a crescent or complete ring of consolidation (Fig. 29) (Georgiadou et al. 2011). Histopathologically, the RHS has been associated to infarcted lung tissue, with a greater amount of hemorrhage at the periphery than at the center, with a frequent subsequent cavitation after neutropenia recovery (Wahba et al. 2008). Halo sign (HS) and RHS are highly suggestive of early infection by an angioinvasive fungus in severely immunocompromised patients. The former is most commonly associated with invasive pulmonary aspergillosis and the latter with pulmonary mucormycosis. An RHS may also be related to other infectious diseases, in particular invasive aspergillosis, tuberculosis, or paracoccidioidomycosis (Georgiadou et al. 2011).

The differential diagnosis of ground-glass attenuation is wide, especially in immunocompromised patients. It can be related to drug-induced toxicity (Fig. 30), alveolar hemorrhage, post-radic changes, pulmonary edema, organizing pneumonia, or hypersensitivity pneumonitis.

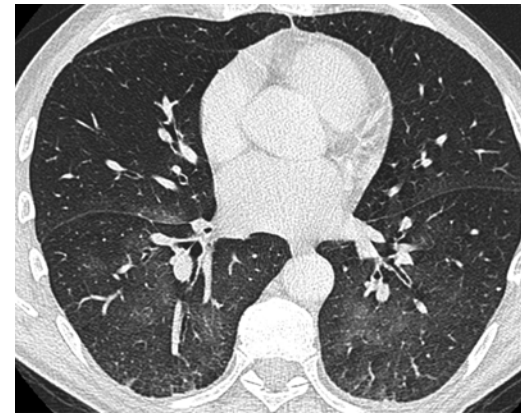

Fig. 30 Pulmonary hemorrhage in a 65-year-old woman known for an acute myeloid leukemia with thrombocytopenia appears as a perihilar ground-glass opacity predominantly located at the level of the lower lobes

An RHS may also be observed in numerous conditions including granulomatosis with polyangiitis, organizing pneumonia (Georgiadou et al. 2011), or pulmonary infarct (Fig. 31).

3.3 Nodular Pattern

3.3.1 Micronodules

Micronodules in an infectious setting, with a diameter lower than 6 mm, may appear with a centrilobular (bronchogenic) or miliary (hematogenous) distribution.

- Bronchogenic distribution presents as nonhomogeneous centrilobular micronodules that spare the subpleural space with a location at least 3 mm from the pleura and that are associated with a tree-in-bud pattern, defined as centrilobular branching structures that resemble a budding tree (Hansell et al. 2008). This presentation may be seen in bacterial, fungal, viral, mycobacterial, or mycoplasma (Fig. 7) infections. In postprimary (reactivation) tuberculosis, centrilobular micronodules and linear branching opacities have a dense attenuation and distinct margins. These features are readily associated with cavitation, predominantly localized in the apical and posterior segments of the superior lobes and the superior segment of the

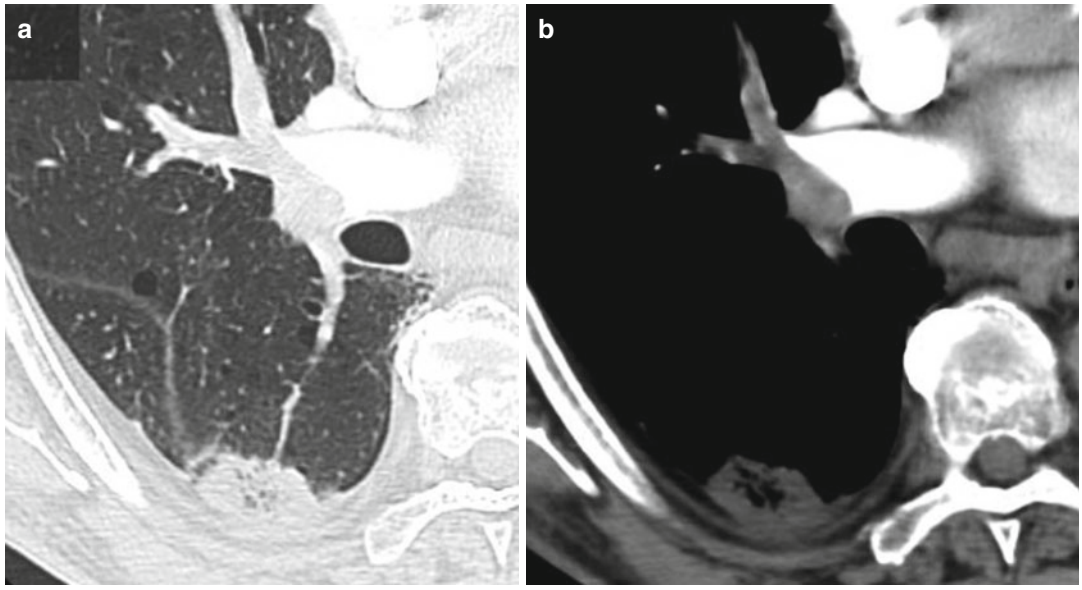

Fig. 31 Pulmonary infarct appears as a reverse halo sign in a 93-year-old patient with bilateral pulmonary emboli as nicely seen on axial CT section in lung (**a**) and mediastinal (**b**) windows

lower lobes in this setting (Fig. 32). *Aspergillus* bronchiolitis and/or bronchopneumonia must be considered in immunocompromised patients (Logan et al. 1994).

- A hematogenous miliary pattern in case of random distribution may suggest tuberculosis (Figs. 8 and 33), histoplasmosis, candidiasis, blastomycosis, or a viral cause (*CMV*, *herpes*, *varicella*) (Fig. 34), especially in immunocompromised patients.

The differential diagnosis of infectious micronodules is miliary metastatic disease in case of micronodules with a random distribution. Uncommonly, multiple centrilobular nodules may be related to vascular lesions as embolized tumor or foreign material (Walker et al. 2014). Other differential diagnoses of centrilobular nodules include hypersensitivity pneumonitis or vasculitis.

3.3.2 Nodules

Pulmonary nodules of infectious nature, sometimes cavitated, are most commonly seen in nosocomial pneumonia and in immunocompromised patients. They may be due to nocardiosis, tuberculosis, and angioinvasive aspergillosis (Althoff Souza et al. 2006) in neutropenic patients, *Cryptococcus neoformans*, *Coccidioides immitis*, *Blastomyces* sp., or atypical mycobacteriosis (Oh et al. 2000; Franquet et al. 2003). Less often, infections such as candidiasis (Fig. 35), legionella, or Q fever may be considered if suggested by the individual setting. They must be differentiated from noninfectious causes including malignancy (Fig. 36).

Nodules with a peripheral ground-glass halo refer to the *halo sign* (HS), which is a CT finding of ground-glass opacity surrounding a nodule or a mass (Hansell et al. 2008). Although inconstant, with a reported incidence of ranging from 25 to 95 % among neutropenic patients with hematological malignancies (Georgiadou et al. 2011), the HS strongly suggests an early invasive aspergillosis in patients with severe neutropenia (Fig. 37), in association with wedge-shaped areas of subpleural consolidation. Furthermore, initiation of antifungal treatment on the basis of the identification of an HS by chest CT appears associated with a significantly better response to treatment and improved survival (Greene et al. 2007). In invasive aspergillosis, these nodules typically become larger during neutrophil

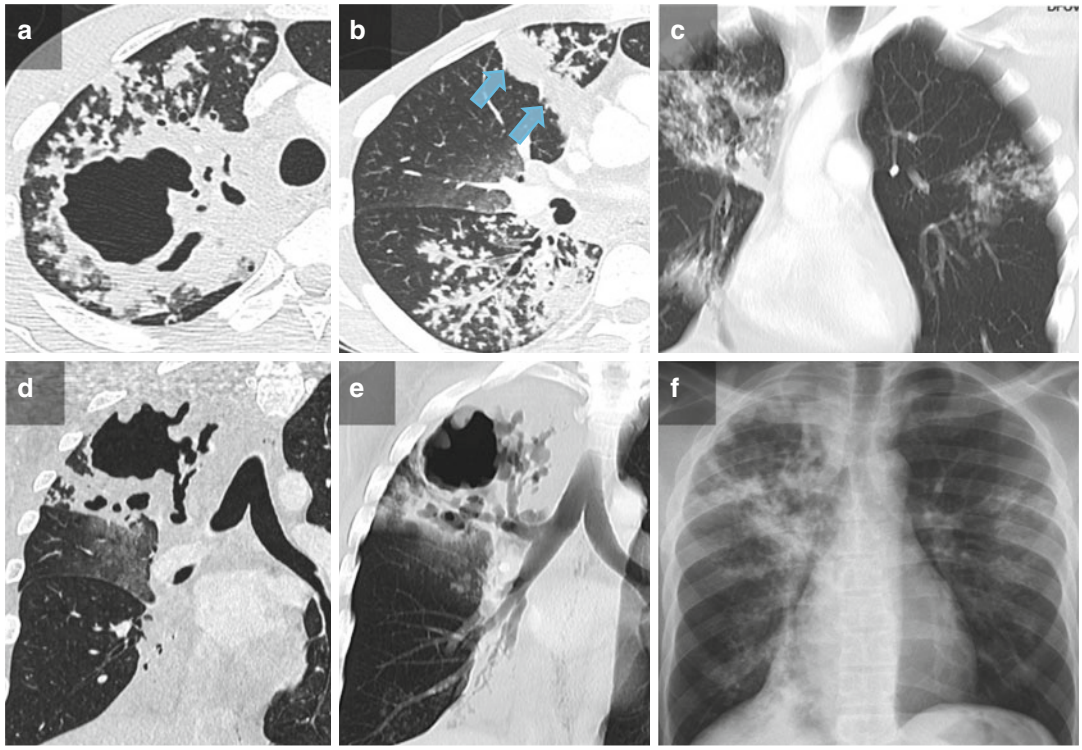

Fig. 32 Postprimary (reactivation) tuberculosis in a 37-year-old man, native of Cameroun, complaining about cough, weight loss, and night sweats for 3 months. Axial CT image at the level of the RUL (**a**) shows the typical hallmarks of reactivation TB including cavities, surrounded by thick and irregular borders, and dense centrilobular nodules with sharp margins predominantly located at the level of the apical and posterior segments of the upper lobes and the apical segment of the lower lobes. A 4 mm-thick MIP axial reformat at the level of the apical bronchus of the RLL (**b**) demonstrates typical centrilobular nodules with sparing of the subpleural space (3 mm) and lobular consolidation of the anterior segment of the RUL (*arrows*). Two consecutive coronal reformats 20 mm-thick AIP (**c**, **e**) and thin coronal slice at the level of the drainage bronchus of the largest cavity of the RUL (**d**) allow for a complete understanding of the appearance seen on chest X-ray (**f**)

engraftment (Barnes and Marr 2007) and/or during the first 10 days of therapy (Caillot et al. 2001). Histopathologically, the HS represents a focus of pulmonary infarction surrounded by alveolar hemorrhage, secondary to invasion by *Aspergillus* of small and medium-sized pulmonary vessels causing thrombosis and subsequent ischemic necrosis of the lung parenchyma (Georgiadou et al. 2011). The same appearances have been reported in numerous infectious pulmonary diseases such as observed with *Mucorales*, *Candida*, *herpes simplex virus*, *cytomegalovirus*, *varicella-zoster virus*, mycobacterial infections, bacterial pneumonia, or septic emboli (Fig. 38). The differential diagnoses of non-infectious nodules with an HS include granulomatosis with polyangiitis, cryptogenic organizing pneumonia, adenocarcinoma, angiosarcoma, Kaposi's sarcoma in association with spiculated nodules, and hemorrhagic metastases (Georgiadou et al. 2011).

Cavitated nodules can be related to septic embolism. The primary source of infection is tricuspid endocarditis, especially in intravenous illicit drug use, peripheral thrombophlebitis, venous catheter, and pacemaker wires. The mechanism includes endothelial damage combined with the formation of crumbling thrombi containing infective agents. Turbulences caused by the circulating blood detach fragments of thrombus which then migrate to the peripheral

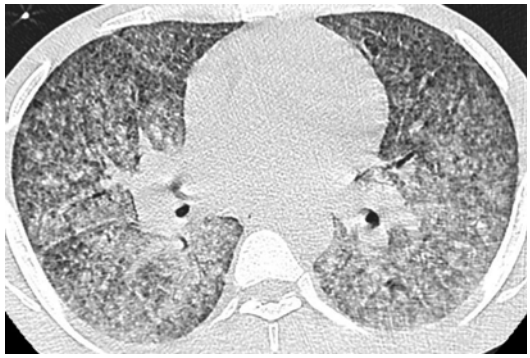

Fig. 33 Miliary tuberculosis with multisystemic involvement in an HIV-positive CDC stage three patient highly immunosuppressed with CD4 level at 64 c/mm^3. Axial CT scan shows diffuse tiny micronodules with ground-glass opacity leading to alveolar consolidation at the level of the apical segment of the RLL. Such an involvement may result in a respiratory distress syndrome (ARDS)

pulmonary arteries with consecutive obstruction. Ischemia then results in infarction and/or hemorrhage and the organisms release toxins causing parenchymal necrosis (Muller 2003). Nodules related to septic emboli are mainly peripheral and basal with blurred margins. A simultaneous appearance of solid nodules and nodules with variable size cavitations (Fig. 38) as well as subpleural wedge-shaped consolidation may be seen (Franquet 2008). The nodules often appear to have a vessel leading into them on axial views – the so-called "feeding vessel" sign – corresponding to the pulmonary vein, whereas most arteries have a lateralized trajectory around the nodule (Dodd et al. 2006) (Fig. 39).

Other causes of cavitated nodules include granulomatosis with polyangiitis and cavitated metastases.

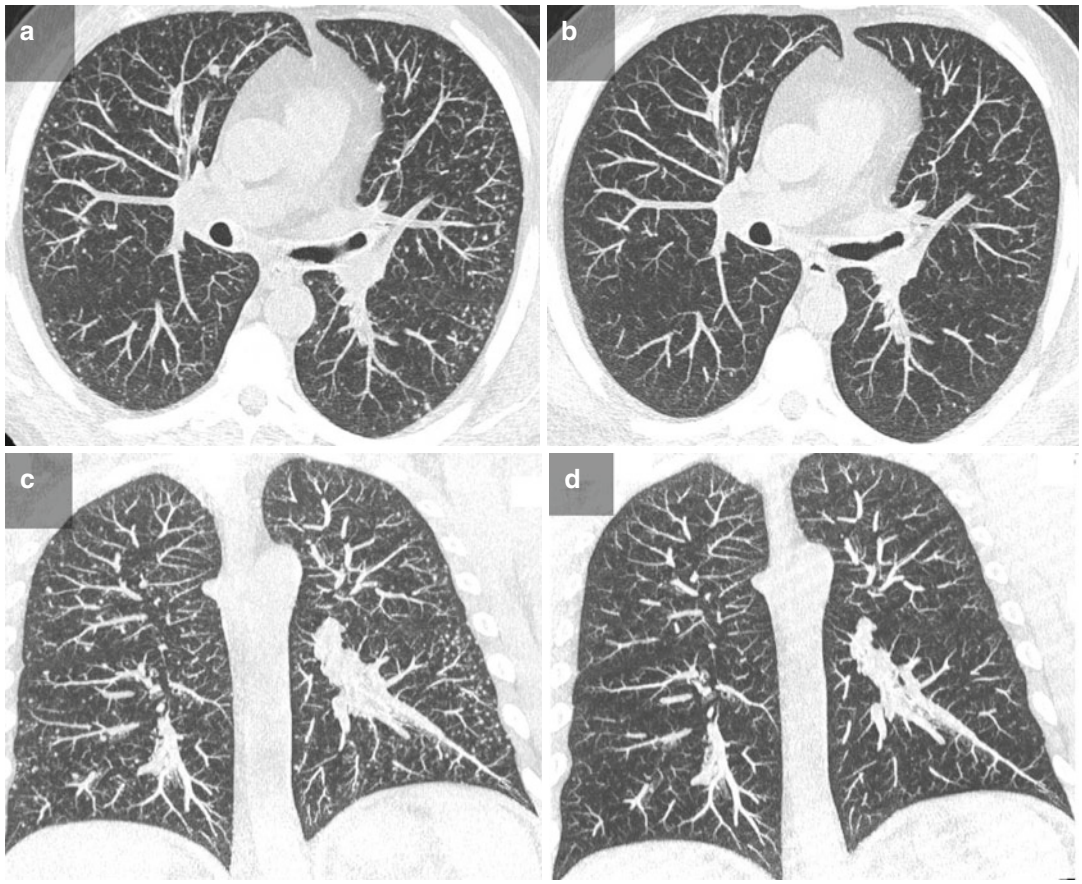

Fig. 34 A 50-year-old man developing a varicella without respiratory symptoms. Axial (**a**) and coronal (**b**) 10 mm-thick MIP images of a CT performed due to suspicion of pulmonary nodules on the chest X-ray show micronodules with random distribution that almost completely disappeared at the follow-up 3 months later (**c**, **d**)

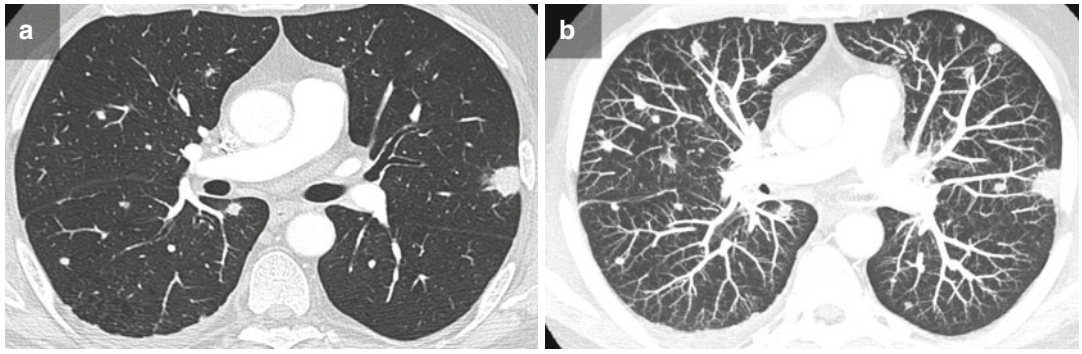

Fig. 35 Pulmonary and hepatosplenic candidiasis in a 62-year-old patient with an acute myeloid leukemia treated by chemotherapy. Axial CT image of 1 mm (**a**) and 15 mm-thick MIP (**b**) shows multiple nodules of various sizes with random distribution. The added value of MIP in the assessment of the detection and evaluation of profusion of nodules is undeniable

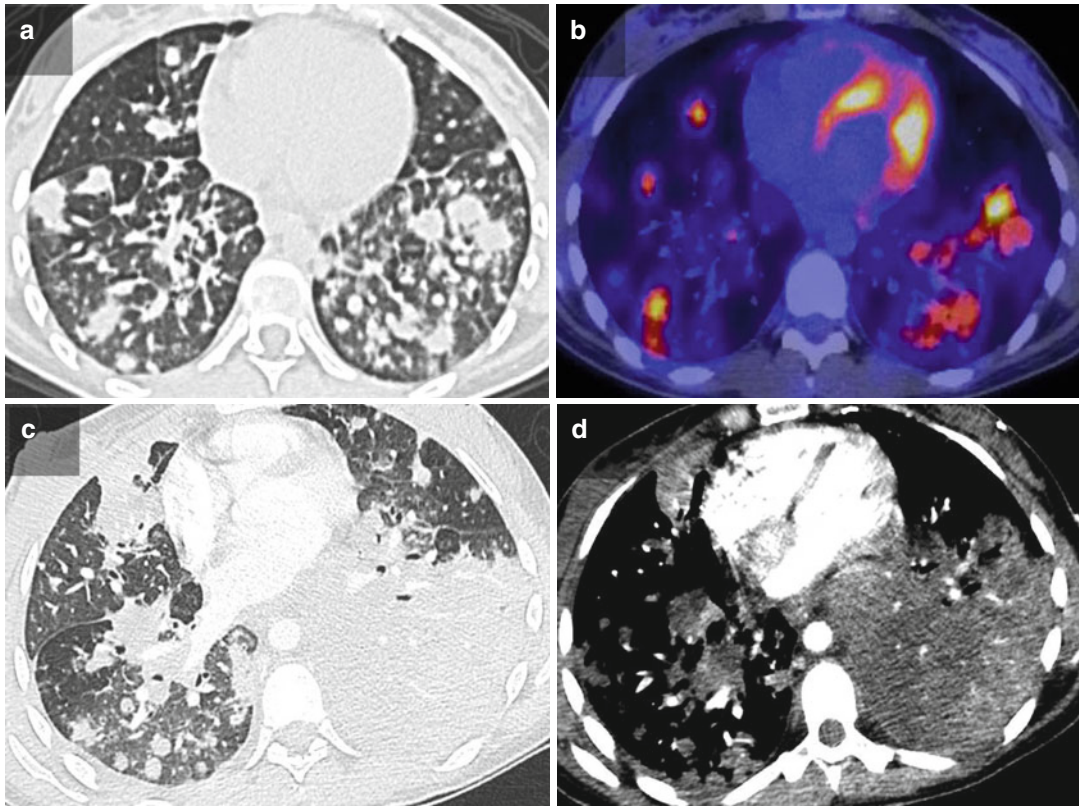

Fig. 36 A 24-year-old woman is known for a recurrence of Hodgkin's lymphoma appearing on the PET-CT (**a**, **b**) as multiple pulmonary nodules. A necrotic bronchopneumonia occurring 2 months later presents as bilateral alveolar consolidation superimposed on the preexisting nodules (**c**, **d**) that lead to a septic shock with death of the patient. This case reinforces the usefulness of evaluation of previous imaging features

3.4 Cavities

Cavities may be observed in case of necrotizing pneumonia or pulmonary gangrene, abscesses, or pneumatoceles.

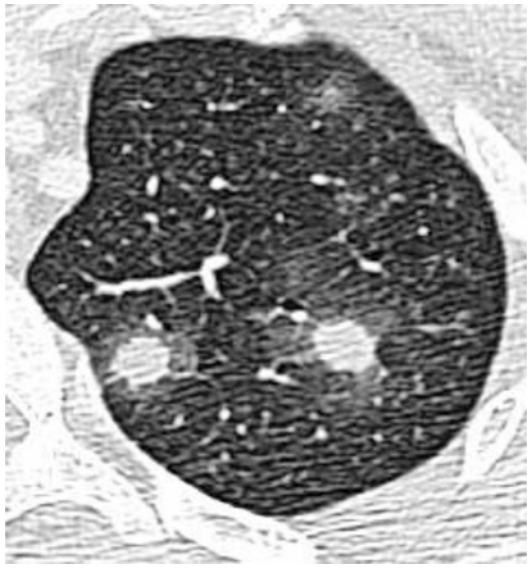

Fig. 37 Angioinvasive aspergillosis in a 27-year-old woman appears as nodules with peripheral ground-glass opacity at the apex of the LUL

3.4.1 Necrotizing Pneumonia or Pulmonary Gangrene

Necrotizing pneumonia or pulmonary gangrene presenting with hypoenhancing geographic areas of low lung attenuation and cavitation is frequently seen before frank abscess formation (Walker et al. 2014). They can be encountered in various situations such as acute CAP, pulmonary tuberculosis (Fig. 32), atypical mycobacteria (Fig. 40), anaerobic bacteria, and angioinvasive or chronic fungal infections. Unilateral or bilateral areas of consolidation, multiple expanding usually thick-walled cavities containing or not aspergillomas and concomitant pleural thickening, suggest chronic cavitary pulmonary aspergillosis. In young patients with no medical history, an infection caused by *S. aureus*, Panton-Valentine leukodicin secretor, that can be severe and rapid in onset with a poor prognosis should routinely be investigated. Bilateral consolidations of the superior lobes followed by the development of coalescent lucencies are commonly seen. An air-crescent sign may also be present (see below).

Cavitation may occur in other conditions including malignancy and lung infarction (Walker et al. 2014).

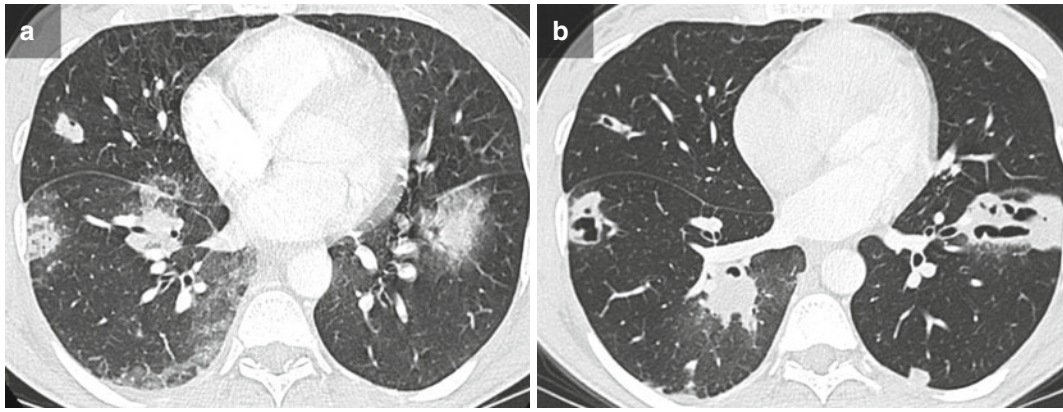

Fig. 38 Septic emboli in a 31-year-old female; HIV-negative drug abuser, known for chronic HCV and IV cocaine injections, presents with fever, shivering, and episodes of hemoptysis. Blood cultures were positive for *Staphylococcus aureus* with a 2 cm vegetation at the level of the tricuspid valve causing marked tricuspid insufficiency. Axial CT sections at baseline (**a**) and 8 days later (**b**), respectively, show multiple nodules with peripheral ground-glass opacity (**a**) that secondary cavitated. The latter is a usual finding with *Staphylococcus aureus* infection

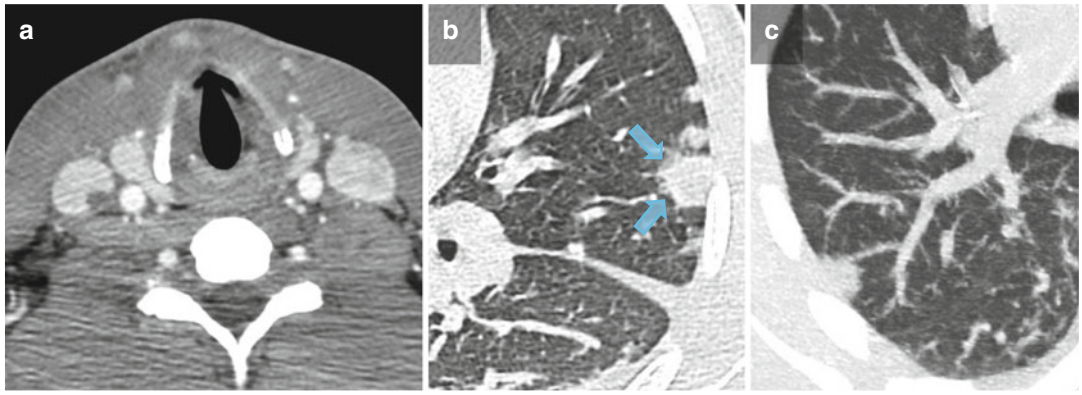

Fig. 39 Lemierre syndrome in a 21-year-old man suffering from a sore throat with jugular vein thrombosis well depicted by CT with contrast media injection (**a**) and septic embolism appearing as peripheral nodules of various sizes with wedge-shaped consolidation (*arrows*) and slight peripheral ground-glass opacity on axial CT image (**b**). The 8 mm-thick MIP image (**c**) shows the lateralized trajectory of the artery around the nodule

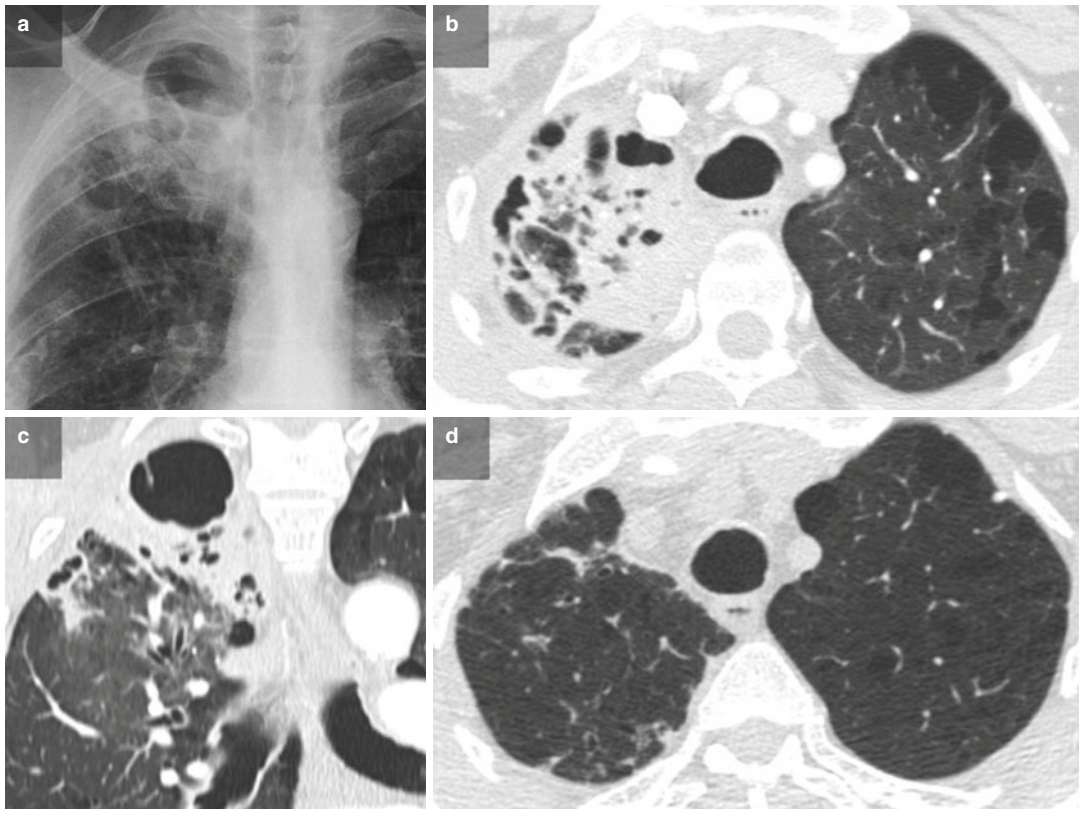

Fig. 40 *Mycobacterium xenopi* infection in a COPD patient. Chest X-ray (**a**), coronal reformat (**b**), and axial CT at the level of upper lobes (**c**) show an alveolar consolidation with cavities of various sizes that almost totally resolved on the follow-up CT performed 1 year later (**d**)

3.4.2 Pulmonary Abscess

A pulmonary abscess may be single or multiple, with a characteristic spherical shape. It measures between 2 and 6 cm in diameter, demonstrates a central hypoattenuation (Fig. 9) or cavitation representing localized necrotic cavity, contains pus, and demonstrates peripheral enhancement after intravenous contrast medium injection, without or with an air-fluid level (Fig. 5). It usually displays an acute angle when it intersects with an adjacent pleural surface. Consolidation in the adjacent parenchyma occurs in half of all cases (Muller 2003). Bronchopulmonary fistula may be observed. As the most frequent cause of lung abscess is aspiration, the most common localizations are the posterior segment of an upper lobe or the superior segment of a lower lobe (Muller 2003). Bilateral involvement that predominantly affects the lung bases with abscess formation suggests a *P. aeruginosa* infection. Infections caused by anaerobic bacteria are commonly encountered, abscesses caused by *S. aureus*, *K. pneumoniae*, and *P. aeruginosa* being associated with higher mortality (Francis et al. 2005).

3.4.3 Air-Crescent Sign

The air-crescent sign, defined as a collection of air in a crescentic shape that separates the wall of a cavity from an inner mass, firstly suggests an *Aspergillus* colonization of preexisting cavities, i.e., an aspergilloma (Fig. 41). An aspergilloma may also be manifested as an irregular spongeworks or fungal strands forming a coarse and irregular network within a cavity. An air-crescent sign also suggests the retraction of a central necrotic mass after recovery of the bone marrow in a rather late stage of angioinvasive aspergillosis (De Marie 2000) (Fig. 42). It may also occur in mucormycosis (Fig. 43), tuberculosis, granulomatosis with polyangiitis, intracavitary hemorrhage, and cavitary lung cancer (Fig. 44) (Hansell et al. 2008).

3.4.4 Septic Emboli

Septic embolism may appear as cavitated nodules (see cavitated nodules).

3.4.5 Pneumatoceles

Pneumatoceles manifest as single or multiple approximately round thin-walled and gas-filled spaces in the lung (Hansell et al. 2008) (Fig. 10). These lucencies are associated with a recent infection and usually transient, progressively increasing in size over the following days and weeks and then resolving after weeks or months. They are most likely due to bronchial drainage of necrotic parenchymal tissue, followed by a check-valve airway obstruction. They usually occur in *P. jirovecii* infections occurring in patients with acquired immune deficiency syndrome (AIDS) (Fig. 26) or in case of previous *S. aureus* pneumonia, but they can also be seen with other infections including *E. coli* and *S. pneumoniae* (Beigelman-Aubry et al. 2012).

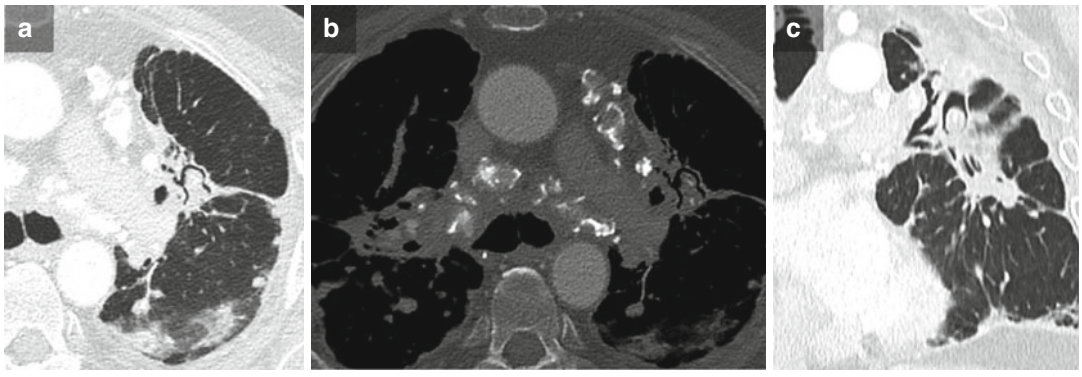

Fig. 41 Aspergilloma developing in a cavity in a 69-year-old man with a history of stage IV sarcoidosis who complained of hemoptysis. The treatment consisted of antifungal therapy and bronchial embolization followed by a left upper lobectomy. Axial CT section in lung window (**a**) at the level of the LUL shows the air-crescent sign. Axial CT section on bone window (**b**) at the same level demonstrates the calcified lymph nodes related to sarcoidosis and the slight calcifications within the aspergilloma. The coronal reformat (**c**) shows the typical dependent location of the aspergilloma within the cavity

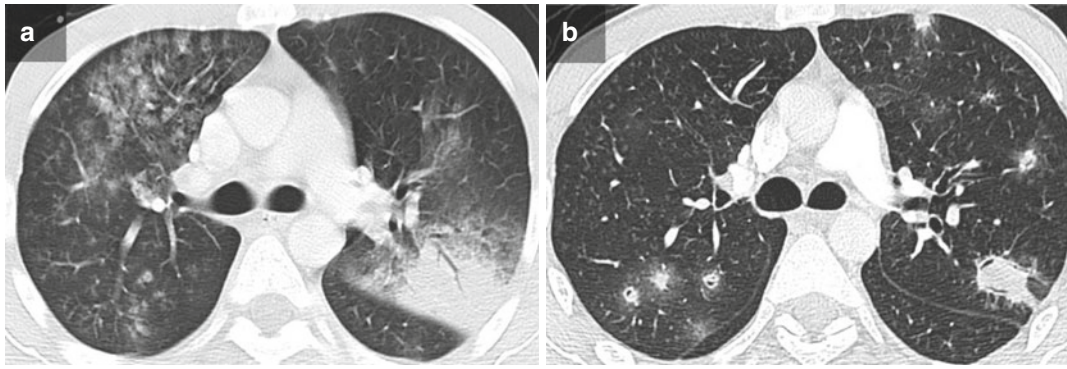

Fig. 42 Invasive aspergillosis in a 27-year-old woman with acute myeloid leukemia. Baseline CT (**a**) performed in a context of febrile agranulocytosis (**a**) with 5 mm-thick axial sections shows alveolar consolidation of the posterior segment of the upper part of the LUL with peripheral ground-glass opacity. Bronchiolo-alveolar nodules with ill borders are also seen in the RUL. On CT performed 3 weeks after (**b**), during bone marrow recovery, multiple nodules with air-crescent sign were seen, this finding suggesting a rather late stage of angioinvasive aspergillosis. Note the somewhat atypical presence of peripheral ground glass at this late stage of the disease

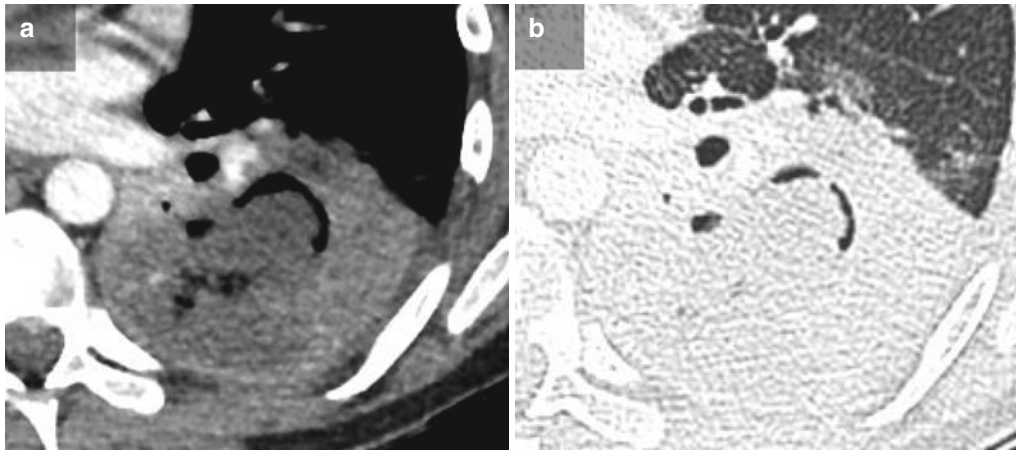

Fig. 43 Necrotizing pneumonia in a context of mucormycosis (same patient as in Fig. 13) presenting with hemoptysis 2 weeks after initial diagnosis despite adequate treatment. The retraction of the central necrotic mass of the LLL creates an air-crescent sign visible on mediastinal (**a**) and lung (**b**) windows. It had occurred at the same time as the pulmonary artery involvement

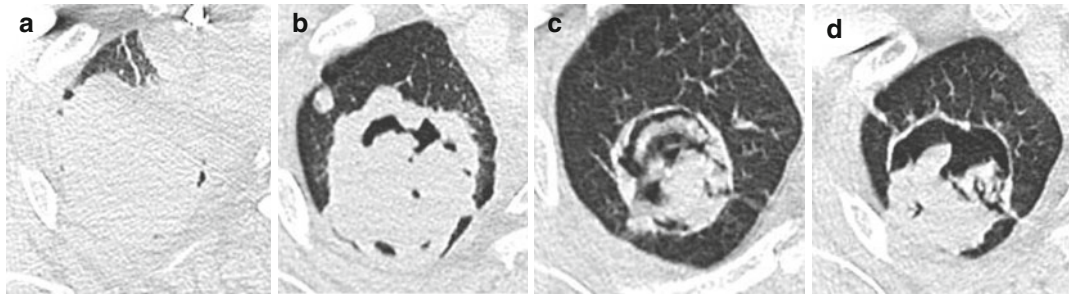

Fig. 44 Air-crescent sign caused by an invasive epidermoid carcinoma stage IIIb treated by radiochemotherapy that progressively cavitated. Axial image at baseline CT (**a**), 3 weeks (**b**) and two consecutive axial CT images performed 3 months (**c**, **d**) after beginning of the treatment. The necrotic tumor appears progressively as a pseudo-aspergilloma with an air-crescent sign

Numerous noninfectious disorders may also manifest with pneumatoceles/cysts, including cavitary metastases.

3.4.6 Meniscus, Cumbo, and Water Lily Signs

Meniscus, cumbo, and water lily signs are related to air dissecting the different layers of an echinococcal cyst secondary to bronchial erosion (Walker et al. 2014).

While a pericystic emphysema or meniscus sign refers to air between the outer pericyst and ectocyst, the cumbo sign is related to air penetrating the endocyst with an air-fluid level capped with air between pericyst and endocyst. The water lily sign relates to the ruptured hydatid cyst with the endocyst membrane floating on surface fluid (Walker et al. 2014).

3.5 Associated Abnormalities

3.5.1 Mediastinal and Hilar Abnormalities

- The most common mediastinal and hilar abnormality is *lymphadenopathy* (Fig. 45). Right paratracheal, hilar, and subcarinal regions and/or hilar lymph node enlargement with associated homolateral small focal infiltrate or parenchymal consolidation, which is commonly sublobar and subpleural in location in the middle lobe, basal segments of lower lobes, and anterior segments of upper lobes, is the usual hallmark of primary TB (Beigelman et al. 2000). Necrotic components with peripheral rim enhancement (rim sign) mainly suggest tuberculosis, but they can also correspond to fungal infection, atypical mycobacteria, histoplasmosis, metastases (Fig. 46) from head/neck and testicular malignancy, and lymphoma (Bhalla et al. 2015). Bronchonodal fistula can be observed as a complication of active pulmonary TB with TB lymphadenitis especially in the elderly. The fistulas usually involve the right lobar bronchus and the main bronchus on the left side (Park et al. 2015).
- A circumferential thickening of the *esophagus* may be related to a *cytomegalovirus* (CMV) infection, esophagitis being the second most common gastrointestinal manifestation of this organism after colitis (Wang et al. 2015), or *Candida* (Kuyumcu 2015) infection in immunocompromised patients.

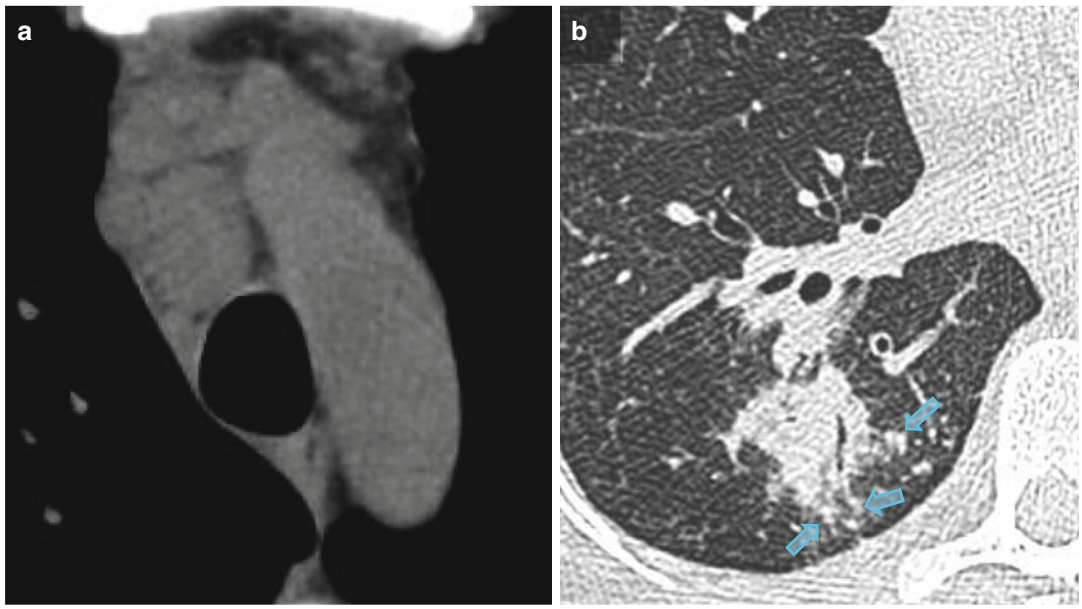

Fig. 45 Tuberculosis in a patient with a history of ulcerous colitis under anti-TNF treatment and lung graft for panlobular emphysema related to α1-antitrypsin deficiency. Axial sections in mediastinal (**a**) and lung (**b**) windows show an enlarged right paratracheal lymph node associated with a homolateral alveolar consolidation of the RLL, hallmarks of primary TB. Note the peripheral centrilobular nodules (*arrows*)

- In case of a circumferential thickening of the *trachea* or main bronchi occurring in the same context, the possibility of invasive aspergillosis of the respiratory tract should always be considered (Fig. 47) with the specific risk of tracheal rupture. Acute tuberculous tracheobronchial involvement may also be seen with circumferential narrowing associated with smooth or irregular wall thickening (Bhalla et al. 2015). Sequelar fibrotic bronchostenosis predominating on the left main bronchus and post-obstructive bronchiectasis may occur in this setting (Bhalla et al. 2015).
- Acute *infectious mediastinitis* may rarely be observed. It appears as increased soft tissue attenuation of mediastinal fat with fluid collections, air bubbles, air-fluid levels, and pneumomediastinum, with pericardial/pleural effusion. Regarding chronic or fibrosing mediastinitis, especially related to tuberculosis and fungal infections, including histoplasmosis, aspergillosis, mucormycosis, cryptococcosis, and blastomycosis, CT may display focal or diffuse involvement with calcifications as well as stenosis/obstruction of the vessels, airways, or esophagus (Akman et al. 2004).

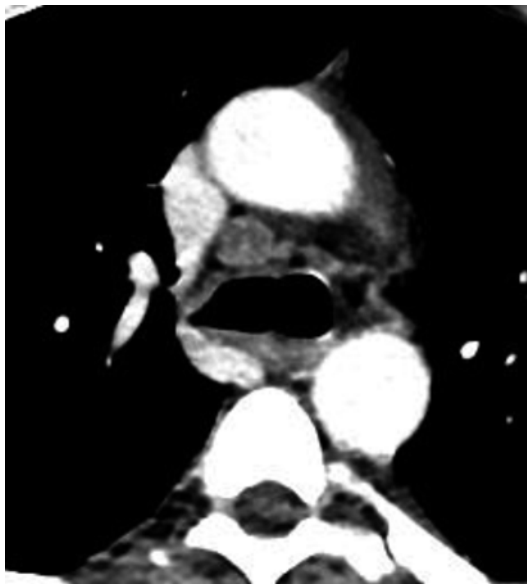

Fig. 46 Right paratracheal lymph node metastasis with necrosis and parietal enhancement in a patient treated by chemotherapy and immunotherapy in a context of a poorly differentiated carcinoma with hepatic and bone metastases

3.5.2 Pleural Abnormalities

- *Pleural effusions*, sometimes loculated, are encountered in 20–60 % of acute bacterial pneumonias. Most of the parapneumonic effusions without pleural thickening resolve under adequate medical treatment.

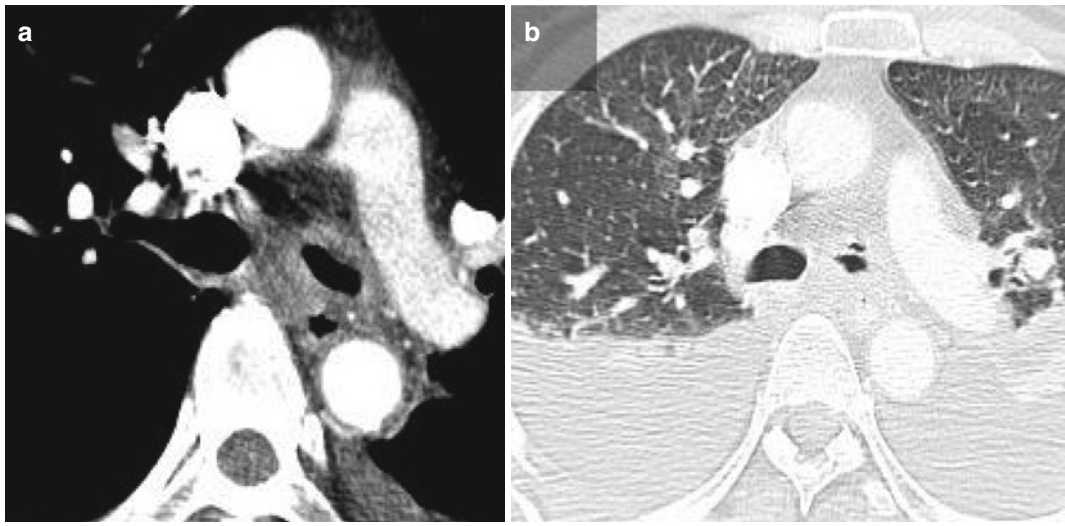

Fig. 47 Airway aspergillosis in a 74-year-old woman with lymphoma of the marginal zone complaining of cough and fever. A circumferential peribronchial thickening around the mainstem left bronchus is seen on the axial CT image with mediastinal window (**a**). Two weeks later, a worsening of the stenosis with a wall fistula is observed on the axial image with the lung window (**b**). Note the presence of a bilateral pleural effusion

- *Empyema*, which occurs in less than 5% of pulmonary infections, typically displays obtuse angles along its interface with adjacent pleura. It appears as a smooth and thin enhancement of the visceral and parietal pleura that surrounds the fluid collection and that is referred as the split pleura sign (Walker et al. 2014) (Figs. 10 and 11). It is commonly associated with a hyperattenuation of the extra-pleural fat. The pathogens traditionally involved in empyema are *S. pneumoniae*, *Streptococcus pyogenes*, and *S. aureus*. The same findings may be seen in case of TB.
- In this setting, an air-fluid level suggests a *bronchopleural fistula* (Walker et al. 2014), which is a sinus tract between a bronchus and the pleural space that most often results from a necrotizing pneumonia. CT features of bronchopleural fistula include an intrapleural airspace of various sizes, a new or changed air-fluid level, and, possibly, a fistulous communication, which may be become visible after the use of mIP post-processing. The air-fluid level within the pleura usually exhibits a length disparity when comparing posterior and lateral chest radiographs or between coronal and sagittal reformats unlike an air-fluid level associated with a pulmonary abscess typically displaying a spherical shape (Walker et al. 2014).

3.5.3 Other Features

- *Mycotic aneurysms* of pulmonary vessels may be observed in case of hemoptysis and a context of invasive fungal infections (Georgiadou et al. 2011) or tuberculosis (Fig. 12).
- *Spondylodiscitis* and/or an intramuscular *cold abscess* firstly suggests tuberculosis. A wavy periosteal reaction highly suggests thoracic actinomycosis.
- Concomitant small hypodense *lesions in the liver and/or spleen* may suggest pyogenic abscesses or fungal infections, in particular candidiasis.
- A worsening of CT findings may be encountered in case of "immune reconstitution inflammatory syndrome" *(IRIS)*. This syndrome is related to paradoxical worsening of preexisting infectious processes such as mycobacterial, viral, and *Pneumocystis jirovecii* infection following the initiation of highly active antiretroviral therapy (HAART) in HIV-infected individuals, a low CD4+ T-cell count being a major risk factor (Huis in 't Veld et al. 2012). IRIS syndrome may also be encountered in HIV-negative patients in conditions such as following corticosteroid withdrawal, discontinuation of antitumor necrosis factor-alpha therapy or recovery of neutropenia after cytotoxic chemotherapy, and engraftment of stem cell transplantation. It may be then observed in case of aspergillosis, candidiasis, and viral pneumonitis (Cheng et al. 2000).

3.6 Sequelae

Fibro-parenchymal lesions with bronchovascular distortion and bronchiectasis, thin-walled cavities, emphysema, and fibro-atelectatic bands firstly suggest prior tuberculosis with scarring (Fig. 48). Calcified mediastinal/hilar lymph nodes (Fig. 49), well-defined nodules, and pleural thickening with or without calcification (Fig. 50) are also common imaging features of healed TB. Tuberculomas and small calcified lung nodules suggest likewise prior TB infection (Bhalla et al. 2015). Calcified nodules may also be seen as sequelae of histoplasmosis or varicella infection (Chou et al. 2015) but also in other conditions like amyloidosis or metastasis, in particular from osteogenic sarcoma or medullary carcinoma of the thyroid.

Calcified peribronchial lymph nodes can erode into adjacent bronchi or cause distortion of the latter and can generate a broncholithiasis (Bhalla et al. 2015).

In conclusion, the recognition of the main CT pattern in association with the knowledge of the underlying disorders and the clinical context permits to strongly narrow the differential diagnosis. The application of a good technique is crucial for patients' management. In all cases, a multidisciplinary approach ensures the best outcome for the patient.

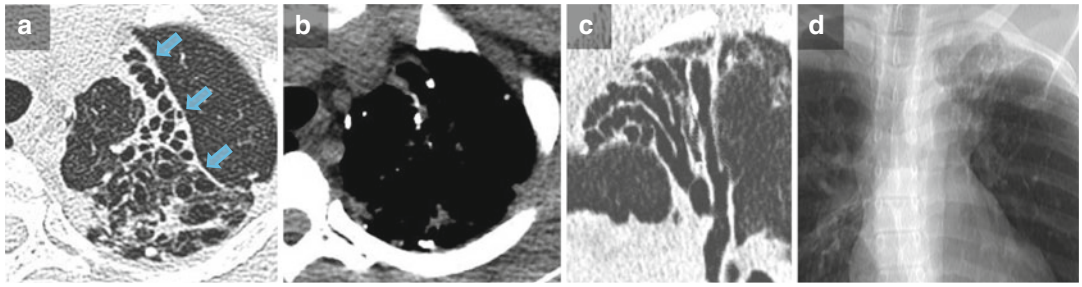

Fig. 48 Sequelae of TB in a 35-year-old woman originating from Cameroun. Axial section in parenchymal (**a**) and mediastinal windows (**b**) at the level of the upper lobes showing cicatricial collapsus of the upper part of LUL well delineated by a small accessory fissure (*arrows*) with bronchovascular distortion, bronchiectasis, thin-walled cavities, and calcified nodules. The 3 mm-thick mIP oblique reformat (**c**) allows for an overall assessment of the bronchiectasis. The coronal 150 mm-thick AIP reformat (**d**) shows the upper retraction of the left hilum

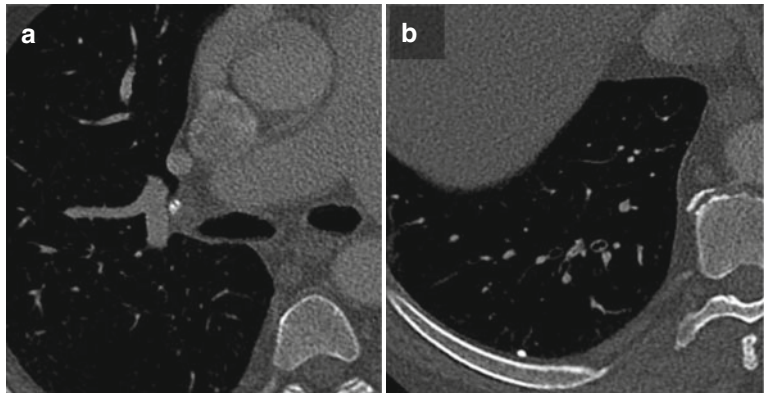

Fig. 49 Ranke complex related to scars from a previous primary TB. Axial section with the bone window at the level of the right hilum (**a**) and of the RLL (**b**) show a calcified hilar node and a calcified parenchymal nodule, respectively

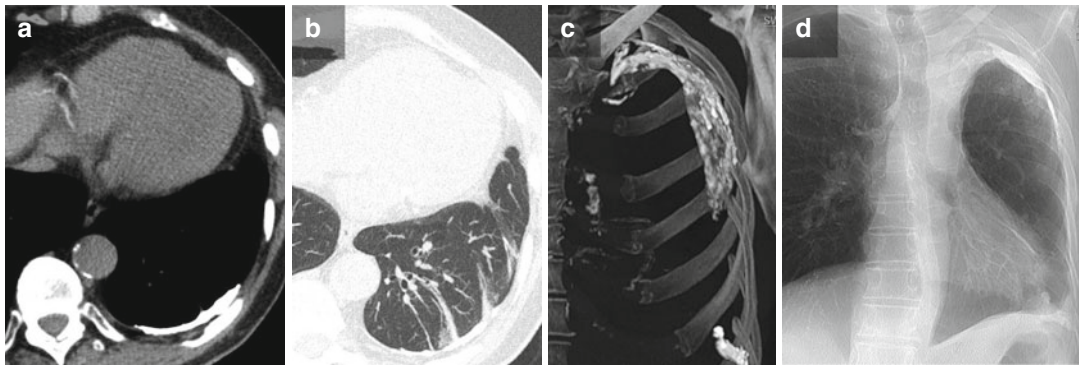

Fig. 50 A 77-year-old man with a calcified fibrothorax as a sequelae of a previous TB. Axial section in mediastinal (**a**) and lung (**b**) windows show a pleural calcification with parenchymatous bands converging toward the latter and related to fibrosis of the visceral pleura. A 70 mm-thick MIP coronal reformat in bone window (**c**) shows the upper predominance of this fibrothorax. A 180 mm-thick AIP reformat (**d**) reproducing the chest X-ray appearance shows the retraction of the left hemithorax and the blunting of the costophrenic angle, a classical finding in this setting

Acknowledgment Thanks to Pr Laurent Nicod, Pr John-David Aubert, Dr Frederic Tissot, Dr Francesco Doentz and Dr Khalid Alfudhili for their help.

References

Akman C, Kantarci F, Cetinkaya S (2004) Imaging in mediastinitis: a systematic review based on aetiology. Clin Radiol 59:573–585

Althoff Souza C, Müller NL, Marchiori E et al (2006) Pulmonary invasive aspergillosis and candidiasis in immunocompromised patients: a comparative study of the high-resolution CT findings. J Thorac Imaging 21(3):184–189

American Thoracic Society/Infectious Diseases Society of America (2005) Guidelines for the management of adults with hospital-acquired, ventilator-associated, and healthcare-associated pneumonia. Am J Respir Crit Care Med 171(4):388–416

Bankier AA, Tack D (2010) Dose reduction strategies for thoracic multidetector computed tomography background, current issues, and recommendations. J Thorac Imaging 25:278–288

Barnes PD, Marr KA (2007) Risks, diagnosis and outcomes of invasive fungal infections in haematopoietic stem cell transplant recipients. Br J Haematol 139:519–531

Beigelman C, Sellami D, Brauner M (2000) CT of parenchymal and bronchial tuberculosis. Eur Radiol 10: 699–709

Beigelman-Aubry C, Hill C, Guibal A et al (2005) Multidetector row CT and postprocessing techniques in the assessment of diffuse lung disease. Radiographics 25(6):1639–1652

Beigelman-Aubry C, Godet C, Caumes E (2012) Lung infections: the radiologist's perspective. Diagn Interv Imaging 93:431–440

Bhalla M, McLoud T (1998) Pulmonary infections in the normal host in thoracic radiology. In: Mc Loud T (ed) The requisistes. James H. Thrall Mosby: Philadelphia; pp 91–133

Bhalla AS, Goyal A, Guleria R (2015) Chest tuberculosis: radiological review and imaging recommendations. In J Radiol Imag 25(3):213–225

Caillot D, Couallier JF, Bernard A et al (2001) Increasing volume and changing characteristics of invasive pulmonary aspergillosis on sequential thoracic computed tomography scans in patients with neutropenia. J Clin Oncol 19:253–259

Chang CH, Ruan SY, Li CC, Yu CJ (2013) Non-human immunodeficiency virus Pneumocystis jirovecii pneumonia. Respirology 18(1):191–192

Cheng VCC, Yuen KY, Chan W et al (2000) Immunorestitution disease involving the innate and adaptive response. Clin Infect Dis 30:882–892

Chou CC, Shen T-C, Tu C-Y et al (2015) Calcified pulmonary nodules. Eur J Intern Med 26:e27–e28

Christe A, Lin MC, Yen AC et al (2012) CT patterns of fungal pulmonary infections of the lung: comparison of standard-dose and simulated low-dose CT. Eur J Radiol 8:2860–2866

De Marie S (2000) New developments in the diagnosis and management of invasive fungal infections. Haematologica 85:88–93

Dodd JD, Souza CA, Müller NL (2006) High-resolution MDCT of pulmonary septic embolism: evaluation of the feeding vessel sign. AJR Am J Roentgenol 187(3): 623–629

Festic E, Gajic O, Limper AH, Aksamit TR (2005) Acute respiratory failure due to pneumocystis pneumonia in patients without human immunodeficiency virus infection: outcome and associated features. Chest 128(2): 573–579

Francis JS, Doherty MC, Lopatin U et al (2005) Severe community-onset pneumonia in healthy adults caused by methicillin-resistant Staphylococcus aureus carrying the Panton-Valentine leukocidin genes. Clin Infect Dis 40(1):100–107

Franquet T (2006) High-resolution computed tomography (HRCT) of lung infections in non-AIDS immunocompromised patients. Eur Radiol 16:707–718

Franquet T (2008) Pulmonary infection in adults. In: Adam A, Dixon AK, Gillard JH, Shaefer-Prokop CM (eds) Diagnostic radiology grainger & Allison's Churchill Livingsrone. Elsevier: Edinburgh, London, New York; p 246–266

Franquet T (2011) Imaging of pulmonary viral pneumonia. Radiology 260(1):18–39

Franquet T, Müller NL, Giménez A, Martínez S, Madrid M, Domingo P (2003) Infectious pulmonary nodules in immunocompromised patients: usefulness of computed tomography in predicting their etiology. J Comput Assist Tomogr 27(4):461–468

Georgiadou SP, Sipsas NV, Marom EM et al (2011) The diagnostic value of halo and reversed halo signs for invasive mold infections in compromised hosts. Clin Infect Dis 52(9):1144–1155

Greene RE, Schlamm HT, Oestmann JW et al (2007) Imaging findings in acute invasive pulmonary aspergillosis: clinical significance of the halo sign. Clin Infect Dis 44(3):373–379

Hansell DM, Bankier AA, MacMahon H et al (2008) Fleischner Society: glossary of terms for thoracic imaging. Radiology 246:697–722

Herold CJ, Sailer JG (2004) Community-acquired and nosocomial pneumonia. Eur Radiol 14(Suppl 3):E2–E20

Heussel CP, Kauczor HU, Heussel GE et al (1999) Pneumonia in febrile neutropenic patients and in bone marrow and blood stem-cell transplant recipients: use of high-resolution computed tomography. J Clin Oncol 17:796–805

Huis in 't Veld D, Sun HY, Hung CC (2012) The immune reconstitution inflammatory syndrome related to HIV co-infections: a review. Eur J Clin Microbiol Infect Dis 31:919–927

Jones RN (2010) Microbial etiologies of hospital-acquired bacterial pneumonia and ventilator-associated bacterial pneumonia. Clin Infect Dis 51(Suppl 1):S81–S87

Kang EY, Patz EF Jr, Müller NL (1996) Cytomegalovirus pneumonia in transplant patients: CT findings. J Comput Assist Tomogr 20:295–299

Kim HJ, Park SY, Lee HY et al (2014) Ultra-low-dose chest CT in patients with neutropenic fever and hematologic malignancy: image quality and its diagnostic performance. Cancer Res Treat 46(4):393–402

Kjeldsberg KM, Oh K, Murray KA et al (2002) Radiographic approach to multifocal consolidation. Semin Ultrasound CT MR 23:288–301

Kuyumcu S (2015) Candida esophagitis mimicking esophageal malignancy on 18FDG PET/CT. Turk J Gastroenterol 26:63–64

Logan PM, Primack SL, Miller RR, Müller NL (1994) Invasive aspergillosis of the airways: radiographic, CT, and pathologic findings. Radiology 193(2):383–388

McGuinness G, Scholes JV, Garay SM et al (1994) Cytomegalovirus pneumonitis: spectrum of parenchymal CT findings with pathologic correlation in 21 AIDS patients. Radiology 192(2):451–459

Morikawa K, Okada F, Ando Y et al (2012) Methicillin-resistant Staphylococcus aureus and methicillin-susceptible S. aureus pneumonia: comparison of clinical and thin-section CT findings. Br J Radiol 85:e168–e175

Muller N (2003) Pulmonary infections in diseases of the lung. In: Muller N (ed) Radiologic and pathologic correlations. Lippincott Williams & Wilkins: Baltimore, Philadelphia; pp 17–75

Niedemann MS (2015) Community-Acquired Pneumonia. Ann Intern Med 163(7):ITC1

Oh YW, Effmann EL, Godwin JD (2000) Pulmonary infections in immunocompromised hosts: the importance of correlating the conventional radiologic appearance with the clinical setting. Radiology 217: 647–656

Park SH, Jeon KN, Park MY et al (2015) Tuberculous bronchonodal fistula in adult patients: CT findings. Jpn J Radiol 33:360–365

Schulze M, Vogel W, Spira D et al (2012) Reduced perfusion in pulmonary infiltrates of high-risk hematologic patients is a possible discriminator of pulmonary angioinvasive mycosis: a pilot volume perfusion computed tomography (VPCT) study. Acad Radiol 19(7):842–850

Stigl WI, Marrie TJ (2013) Severe community-acquired pneumonia. Crit Care Clini 29:563–601

Syrjälä H, Broas M, Suramo I, Ojala A, Lähde S (1998) High-resolution computed tomography for the diagnosis of community acquired pneumonia. Clin Infect Dis 27:358–363

Tanaka N, Matsumoto T, Kuramitsu T et al (1996) High resolution CT findings in community-acquired pneumonia. J Comput Assist Tomogr 20:600–608

Tasaka S, Tokuda H (2012) Pneumocystis jirovecii pneumonia in non-HIV-infected patients in the era of novel immunosuppressive therapies. J Infect Chemother 18(6):793–806

Thomas CF Jr, Limper AH (2004) Pneumocystis pneumonia. N Engl J Med 350(24):2487–2498

Wahba H, Truong MT, Lei X, Kontoyiannis DP, Marom EM (2008) Reversed halo sign in invasive pulmonary fungal infections. Clin Infect Dis 46: 1733–1737

Walker CM, Abbott GF, Greene RE (2014) Imaging pulmonary infection: classic signs and patterns. AJR 202:479–492

Wang HW, Kuo CJ, Lin W-R et al (2015) The clinical characteristics and manifestations of cytomegalovirus esophagitis. Dis Esophagus. pp 1–8. doi:10.1111/dote.12340

Lung Cancer Screening: Evidence, Recommendations, and Controversies

Robin Peters, Matthijs Oudkerk, and Rozemarijn Vliegenthart

Abstract

Lung cancer causes the most cancer-related deaths worldwide. The incidence of lung cancer increases with age, and the most important risk factor is smoking. Smoking prevention and cessation programs have decreased the number of lung cancer cases. The overall prognosis of lung cancer remains poor, despite advances in treatment. The purpose of lung cancer screening is detecting malignancy at an earlier and curable stage. The National Lung Screening Trial demonstrated that early detection of lung cancer with low-dose computed tomography (LDCT) decreases mortality compared with screening by chest radiography. In the United States, several organizations published guidelines, recommending implementation of lung cancer screening for high-risk patients. However, some important questions regarding LDCT screening have so far been unanswered. The awaited results of the European trials and pooling of data will be crucial in establishing recommendations regarding clinical implementation of lung cancer screening in asymptomatic high-risk persons. This review presents an overview of current evidence, recommendations, and controversies concerning lung cancer screening.

1 Introduction

Lung cancer is the most common cause of cancer-related mortality, not only in the United States and Europe but also around the world. Worldwide, there are an estimated 1.59 million lung cancer deaths annually, which is 19.4 % of the total number of cancer deaths. In 2012, lung cancer was the most commonly diagnosed cancer as well as the leading cause of cancer death in men. In women, it was the fourth most commonly

R. Peters, MD • M. Oudkerk, MD, PhD
R. Vliegenthart, MD, PhD (✉)
Department of Radiology, University of Groningen, University Medical Center Groningen,
Center for Medical Imaging – North East Netherlands,
Hanzeplein 1, 30.001, Groningen 9700RB, Netherlands
e-mail: r.vliegenthart@umcg.nl

U.J. Schoepf, F.G. Meinel (eds.), *Multidetector-Row CT of the Thorax*, Medical Radiology,
DOI 10.1007/978-3-319-30355-0_9

diagnosed cancer after breast, colon, and cervix carcinoma and the second leading cause of cancer death after breast carcinoma (Siegel et al. 2012; Jemal et al. 2011).

More than two-thirds of patients presenting with clinical symptoms of lung cancer have locally advanced or metastatic disease. Despite advances in treatment, lung cancer has a poor prognosis with an overall 5-year survival rate after diagnosis of only 16 % (Siegel et al. 2012). For comparison, 5-year survival rates for colon, breast, and prostate cancer are between 64 and 99 %. To achieve a substantial reduction in lung cancer mortality, progress in prevention, early detection, and treatment are very important.

At this moment, there are several ongoing lung cancer screening trials that investigate whether early detection of lung cancer in high-risk individuals will reduce lung cancer mortality. In 2011, the National Lung Screening Trial (NLST) was the first randomized clinical trial reporting a beneficial effect of lung cancer screening: lung cancer mortality was 20 % lower among high-risk individuals screened with low-dose computed tomography (LDCT), compared to those screened with chest radiography (National Lung Screening Trial Research Team et al. 2011). In the United States, several organizations, including the American Cancer Society and the American Lung Association, have since then published recommendations and guidelines for LDCT lung cancer screening in high-risk patients. In Europe, there are seven ongoing randomized controlled trials. Three published studies in relatively smaller cohorts found no benefit from low-dose CT screening in high-risk patients in contrast to the NLST, although individual trials may have been too low in power to detect a significant mortality reduction (Infante et al. 2009; Pastorino et al. 2012; Saghir et al. 2012). In Europe, results from large trials such as the NELSON study (see below) are awaited before advice on lung cancer screening can be given.

Major challenges in lung cancer screening are the high false-positive rate of screen tests, overdiagnosis, cumulative radiation exposure from repeated LDCT scans, and patient anxiety. Also, little is known about the cost-effectiveness of lung cancer screening.

2 Study Design of Screening Trials

Table 1 presents the study design and participant characteristics of the NLST and seven European lung cancer screening trials.

In 2002, the National Cancer Institute initiated a randomized control trial for lung cancer screening, the NLST. The NLST was designed to compare two imaging modalities to detect lung cancer: LDCT and standard chest radiography. The main aim was to determine whether screening with LDCT or standard radiography could reduce mortality from lung cancer in a high-risk population. Over 53,000 subjects were randomly assigned to undergo three annual rounds of LDCT or three annual rounds of radiography. Participants were followed for lung cancer diagnosis and mortality through December 31, 2009 (median duration of follow-up 6.5 years, with a maximum duration of 7.4 years) (National Lung Screening Trial Research Team et al. 2011). NLST involved manual measurement of the diameter of detected nodules, where nodules of 4 mm and larger were classified as positive, so as suspicious for lung cancer.

The second largest trial with finished inclusion is the Dutch-Belgian Randomized Lung Cancer Screening Trial (acronym NELSON), launched in 2003, with nearly 16,000 participants. The NELSON trial was designed to investigate whether low-dose spiral CT screening in year 1, 2, 4, and 6.5 will decrease 10-year lung cancer mortality by at least 25 % in high-risk (ex-)smokers. In contrast to the NLST, the NELSON trial compared the screen participants to a control group receiving smoking cessation advice but no screening. Participants in the screen group underwent LDCT, and depending on the screening round, blood sampling and pulmonary function testing were performed on the same day. Other aims of the trial include evaluation of the cost-effectiveness of the screening program, assessment of the optimal screening interval, and evaluation of the impact on quality of life (Van Iersel et al. 2007). In contrast to the diameter-based NLST, the NELSON trial applied three-dimensional information of lung nodules

Table 1 Study design and baseline characteristics of participant in randomized clinical trials of lung cancer screening trials using low-dose computed tomography

	NLST	NELSON	DANTE	ITALUNG	MILD	DLCST	LUSI	UKLS
Design	RCT	RCT	RCT	RCT	RCT	RCT	RCT	RCT
Recruitment period	2002–2004	2003–2006	2001–2006	2004–2006	2005–2011	2004–2006	2007-	2011-
Arms	LDCT vs. RX	LDCT vs. usual care	LDCT vs. usual care, RX at baseline in both arms	LDCT vs. usual care	LDCT vs. usual care	LDCT vs. usual care	LDCT vs. usual care	LDCT
Number of screening rounds	3	4	4	4	10/5	5	4	1
Length of screening interval (y)	1	1, 2 and 2,5	1	1	1 or 2 (randomized)	1	1	1
Total follow-up period (y)	8	10	4	4	10	10	5	1.5
Nodule measurement	Diameter	Volume and diameter	Diameter	Diameter	Volume	Volume and diameter	Volume and diameter	Volume and diameter
CT slice thickness (mm)	2–3.2	1	5	1–3	1	1–3	1	1
N participants	53,439	15,822	2,811	3,206	4,099	4,104	4,052	32,000 (planned)
Age range (y)	55–74	50–75	60–74	55–69	49–75	50–70	50–69	50–75
Mean age (y ± SD)	61 (5)	59 (6)	65 (5)	61 (4)	59 (6)	57 (5)	58 (5)	NR
Male, %	59	84	100	65	68	55	66	NR
Smoking criteria								5 % risk of developing lung cancer in 5 years (Liverpool Lung Project risk model)
Pack-years	≥30	>15	≥20	≥20	≥20	≥20	>15	
Years since quitting	≤15	≤10	<10	<10		<10[a]		

RCT randomized controlled trial, *NR* not reported, *SD* standard deviation

[a]Ex-smokers had to have quit after the age of 50 years and less than 10 years ago

(volumetry) and a short-term follow-up CT for indeterminate nodules instead of direct referral.

The other ongoing randomized control trials are the Detection and Screening of Early Lung Cancer by Novel Imaging Technology and Molecular Assays (DANTE) in Italy, the Italian Lung Cancer Computed Tomography Screening Trial (ITALUNG), the Multicentre Italian Lung Detection Trial (MILD), the Danish Lung Cancer Screening Trial (DLCST), the Lung Cancer Screening Intervention Study (LUSI) in Germany, and the UK Lung Cancer Screening trial (UKLS) in the United Kingdom (Field et al. 2013). The UKLS is the trial with the most recent start of screening.

3 Who Should Be Screened?

The purpose of a lung CT screening test is to detect lung cancer in patients before they develop symptoms. A patient with an early-stage lung cancer is eligible for resection and has a 5-year survival rate of more than 50 % (Siegel et al. 2012).

Precise identification of individuals at high risk is important to achieve the goal of a high sensitivity of diagnosed lung cancers per screened population with minimized harms and high cost-effectiveness. Tobacco use remains the dominant risk factor for development of lung cancer. Approximately 85 % of all lung cancers develop in current or former smokers (Paoletti et al. 2012). The number of cigarettes and the number of years a person has been smoking play an important role in the risk of lung cancer. Increased age is also associated with an increased risk of malignancy. Lung cancer is rare in individuals under the age of 40. Other risk factors include chronic obstructive lung disease, passive smoking, alcohol consumption, air pollution, occupational exposure to carcinogenic substances (e.g., asbestos, arsenic, cadmium), and lung cancer susceptibility genes (Molina et al. 2008).

The inclusion criteria of study participants varied between the different trials (Table 2). The NLST recruited asymptomatic men and women (55–74 years of age) who were either current

Table 2 Results of randomized clinical trials of lung cancer screening using low-dose computed tomography

	NLST	NELSON	DANTE	ITALUNG	MILD	DLCST	LUSI	UKLS
Participants in screen arm at baseline	26,309	7557	1276	1613	1190[a] 1186[b]	2052	2029	NR
Baseline test positive, %	27.3 %	2.6 %	4.8 %	4.2 %	2.2 %	8.7 %	2.6 %	NR
Baseline test indeterminate, %	X	19 %	12 %	26 %	13 %	8 %	17 %	NR
Lung cancer detection rate baseline, %	1.0 %	0.9 %	2.2 %	1.5 %	0.7 %	0.8 %	1.1 %	NR
Stage I cancer baseline, %	54.1 %	63.9 %	57 %	48 %	63 %	53 %	82 %	NR
Second round test positive, %	27.9 %	1.8 %	0.8 %	1.0 %	NR	2.3 %	1.9 %	NR
Second round test indeterminate, %	X	3.8 %	3.4 %	16 %	3 %	1.5 %	28 %	NR
Lung cancer detection rate, second round	0.6 %	0.8 %	4.7 %	0.15 %	0.8 %	0.6 %	NR	NR
Stage I cancer second round, %	63 %	73.7 %	70 %	100 %	NR	66 %	57 %	NR
Number of CT-detected lung cancers	649	209	58	22	29[a] 20[b]	69	22	NR

[a]*MILD* annual arm
[b]*MILD* biennial arm, *NR* not reported

smokers or had been smokers within the previous 15 years, with at least 30 pack-years of cigarette smoking (one pack-year = one package of 20 cigarettes daily for 1 year). Excluded were participants with a history of lung cancer, who had undergone chest CT within 18 months before enrollment, who had hemoptysis, or who had unexplained weight loss of more than 15 lb (6.8 kg) in the preceding year (National Lung Screening Trial Research Team et al. 2011).

The NELSON study recruited participants based on a questionnaire about health, smoking, cancer history, and other health factors. Eligible participants were between 50 and 75 years of age, being current or former smokers with a history of more than 15 cigarettes daily for more than 25 years or more than 10 cigarettes for more than 30 years. Persons who had a moderate or bad self-reported health; who were unable to climb two flights of stairs; had a body weight of more than 140 kg; had a history of lung cancer less than 5 years ago or ongoing treatment, current or past renal cancer, melanoma, or breast cancer; or had undergone chest CT less than 1 year prior to inclusion were not eligible to participate (Van Iersel et al. 2007).

The three Italian trials had the same smoking criteria: 20 or more pack-years and, if former smoker, quit less than 10 years before the moment of inclusion. DANTE recruited healthy male subjects, aged 60–74 years, through general practitioners, advertising leaflets, and local media (Infante et al. 2008). The MILD trial included men and women of 49 years and older without cancer in the previous 5 years, through advertisements published in the lay press and in television broadcast (Pastorino et al. 2012; Pastorino 2006). ITALUNG included patients, 55–69 years of age, of 269 general practitioners, recruited via invitation letters (Lopes Pegna et al. 2009).

The DLCST recruited by advertisements in free newspapers and magazines from 2004 to 2006. Asymptomatic current or former smokers (20 or more pack-years), male or female, aged 50–70 years, were included if they were able to walk up at least 36 stairs without stopping. Former smokers had to have quit after the age of 50 years and less than 10 years before the moment of inclusion (Pedersen et al. 2009).

In Germany, the LUSI trial included men and women in the age range of 50–69 years by questionnaire sent on the basis of population registers. The LUSI trial used the same smoking criteria as in the NELSON study (Becker et al. 2012).

A different approach for recruiting participants is used in the UKLS. This trial uses the Liverpool Lung Project risk model, a lung cancer risk prediction questionnaire, calculating the risk of developing cancer over the next 5 years in potential participants. In the UKLS, participants with at least 5 % risk of lung cancer in the next 5 years are included.

Currently, there is no consensus or clear-cut evidence for a certain definition of selection criteria. Older age and heavy smoking history are generally adopted as criteria for possible LDCT screening. Individuals outside of these demographics have not been studied in detail or have so far not shown to benefit from lung cancer screening. Nearly all randomized controlled trials used age and smoking history as inclusion criteria; only the UKLS trial used a prediction model to define the population to screen. The finalization of inclusion and the results of the UKLS are awaited for more information about this type of screen population selection (Nair and Hansell 2011).

4 Technical Parameters for Low-Dose CT for Lung Cancer Screening

In the 1960s and 1970s, several randomized controlled trials showed no survival benefit for participants screened with the use of chest radiography despite the fact that more early-stage lung cancers were found (Frost et al. 1984; Marcus et al. 2000; Bach et al. 2003; Humphrey et al. 2004). The Mayo Lung Project ($n = 10{,}933$) studied the potential of screening with chest X-ray and sputum cytology every 4 months for 6 years (Fontana et al. 1991). Marcus et al. showed no decrease in death rate from lung cancer in extended follow-up of Mayo Lung Project participants (Marcus et al. 2000). More recently, the Prostate, Lung, Colorectal, and Ovarian Cancer

Screening Trial, a large randomized study ($n = 154,942$), showed no significant decrease in lung cancer incidence or mortality in men and women screened with annual chest X-ray compared to participants receiving usual care (no screening) (Oken et al. 2011). Chest X-ray has been concluded to be ineffective for lung cancer screening. Studies in high-risk populations have shown that spiral CT screening detects more lung cancers than chest radiography (Henschke et al. 1999; Kaneko et al. 1996).

LDCT scans are obtained with the use of multi-detector CT scanners (16 or more detectors) that allow quick acquisition (in one breathhold) of thin overlapping slices. Scans for lung cancer screening are acquired in a cranio-caudal scan direction without intravenous contrast. To minimize breathing artifacts, scans are performed in inspiration after appropriate instruction by the technician. Typical technical parameters for LDCT in the NELSON trial included a tube current time product of 20–30 mAs and a pitch of 1.3. The kVp setting was dependent on the patient body weight (<50 kg, 80–90 kVp; 50–80 kg, 120 kVp; >80 kg, 140 kVp) (Xu et al. 2006; Zhao et al. 2011). In the two largest screening trials (NLST, NELSON), the mean effective dose of the lung cancer screening CT scan was 1.4 millisievert (mSv) (National Lung Screening Trial Research Team et al. 2011; Xu et al. 2006). Lower mAs and/or kVp produce increased image noise. A good balance is needed to obtain diagnostic image quality at optimally low radiation dose for participants in screening programs. Data sets were derived with a slice thickness of 1 mm reconstructed at overlapping 0.7-mm intervals in the NELSON study and 1–3.2 mm, reconstructed at 1.0–2.5 mm intervals, in the NLST trial. An advantage of European CT screening trials is that most trials have acquired isotropic image data which allowed for semiautomated volume measurements with the use of dedicated software. More detailed discussion of the CT scan protocol can be found under technical parameters in the chapter "Characterisation of lung nodules and management of the incidentally detected nodule."

5 Results

In 2011, the NLST published the mortality results in *The New England Journal of Medicine* (National Lung Screening Trial Research Team et al. 2011). NLST enrolled 53,454 persons at high risk of lung cancer. Of the participants, 98 % (52,344/53,454) received a screening examination in the first round. 26,309 subjects underwent three annual rounds of screening with LDCT, and 26,035 subjects underwent three annual rounds of standard radiography. In all three rounds, the number of participants with positive screening results was higher in the LDCT group than in the X-ray group. In the baseline screening round (T0), 27.3 % of CT screenees had a positive test result versus 9.2 % of individuals undergoing chest radiography (T1, 27.9 % versus 6.2 %; T2, 16.8 % versus 5.0 %). Of the positive test results, the large majority was false-positive: across the three rounds, the rate of false-positive test results was 96.4 % in the LDCT group and 94.5 % in the radiography group. In the first round, malignancy was confirmed in 292/26,309 participants (1.1 %) who underwent LDCT screening versus 190/26,035 (0.7 %) in the radiography group (54 % versus 37 % stage I disease and 41 % versus 59 % stage IIB–IV disease). In the LDCT group, 10.2 % of all screened participants with a negative screening result had clinically significant findings other than lung cancer; this rate was 3 % in the radiography group (National Lung Screening Trial Research Team et al. 2011). In the LDCT group, 356 lung cancer deaths occurred, and 443 participants of the radiography group died from lung cancer, corresponding to cumulative lung cancer mortality rates of 247 and 309 per 100,000 person-years, respectively. This led to a relative reduction of 20.3 % in lung cancer-specific mortality after 6.5 years of follow-up in participants screened with LDCT compared to those screened with chest X-ray. All-cause mortality (death from any cause, including lung cancer) was 6.7 % lower in subjects screened with LDCT (National Lung Screening Trial Research Team et al. 2011; Aberle et al. 2013).

First and second round results of the NELSON trial were published in 2009 (Van Klaveren et al. 2009). In total, 15,822 eligible participants were included. Of the participants, 50 % (n = 7,915) were randomized to the screen group undergoing LDCT and 50 % (n = 7,907) to the control group receiving no screening. Both groups obtained advice on smoking cessation. In the first round, 7,557 participants received LDCT screening. At baseline, 1.6 % (119/7,557) of subjects in the LDCT group had a positive test result and 79.2 % a negative result. Of the screenees, 19.2 % received an intermediate test result, with 5.3 % showing a growing nodule suspicious for malignancy at the 3-month follow-up LDCT scan. In total, 2.6 % (196/7,557) of participants had a positive screen test. After workup, 70 of these had lung cancer (false-positive rate of 64.3 %). In the lung cancer patients, 63.9 % had stage I disease. Lung cancer detection rate was 0.9 %. In the second round, 1.8 % (128) of participants had a positive screen result, with 54 subsequently proven to be lung cancer (73.7 % stage I disease). The lung cancer detection rate in the second round was 0.8 %. Sensitivity of the first and second screening round was 94.6 % and 96.4 %, respectively. The negative predictive value was 99.7 % for the first round and 99.9 % for the second round (Zhao et al. 2011). In the third round, 75 of 6,922 subjects had lung cancer with a lung cancer detection rate of 1.0 %. In the first three screening rounds, 51.2 % of the screen-detected lung cancers were adenocarcinomas, and 70.8 % was diagnosed at stage I (Horeweg et al. 2013). Follow-up of the NELSON study population is ongoing; a conclusive mortality analysis is expected 10 years after randomization.

The DLCST, initiated in 2004, randomized 4,104 current and former smokers either to annual LDCT screening for 5 years (2,052) or to no screening (2,052) (Saghir et al. 2012). The DANTE trial recruited 2,472 male subjects who were randomized to the LDCT screen group (1,276) or to the control group without screening (1,196). All subjects underwent baseline chest radiography and sputum cytology; the screening group also underwent four annual LDCTs (Infante et al. 2009). In the MILD trial, a total of 1,190 participants were randomized to annual LDCT, 1,186 to biennial LDCT, and 1,723 to usual care (Pastorino et al. 2012). The ITALUNG trial randomized 3,206 participants to four annual LDCT examinations (1,613) or usual care (1,593).

Three European trials have published their mortality results: DANTE, MILD, and DLCST. In the smaller DANTE and DLCST trials, no statistically significant difference in lung cancer mortality was observed when comparing the screen group to the control group (Infante et al. 2009; Saghir et al. 2012). The MILD study, which compared annual to biennial screening, showed that biennial screening had the same performance as no screening (Pastorino et al. 2012). These mortality results are contradictory to the larger NLST that showed a significant reduction in lung cancer mortality. Most likely this is (mainly) related to lack of power to show a significant difference in mortality in these European trials. The NELSON study will show results of lung cancer mortality in the coming year (2016). Analysis of lung cancer mortality is planned 10 years after randomization (Van Iersel et al. 2007). The NELSON results and pooled data from the European trials will provide crucial answers to quantify the effects of LDCT screening on lung cancer-specific mortality (Field et al. 2013).

More results of described randomized clinical trials of lung cancer screening using LDCT are presented in Table 2.

6 Current Recommendations in the United States

After publication of the results from the NLST, guidelines have been released in the United States by major organizations regarding lung cancer screening, namely, the National Comprehensive Cancer Network (Wood et al. 2012), the American College of Chest Physicians (Detterbeck et al. 2013), the American Society of Clinical Oncology, the American Lung Association (American Lung Association 2012), the American Association for Thoracic Surgery

(Jaklitsch et al. 2012), the American Cancer Society (Wender et al. 2013), and the US Preventive Services Task Force (Moyer and U.S. Preventive Services Task Force 2014). Most organizations recommend annual screening with LDCT for high-risk patients who match the inclusion criteria of the NLST: current or former smokers, 55–74 years of age, at least 30 pack-years, and no history of lung cancer.

In 2012, the American College of Chest Physicians and the American Society of Clinical Oncology recommended screening for lung cancer with LDCT in current or former smokers (quit within the past 15 years) aged 55–74 years with ≥ 30 pack-year smoking history. For persons younger than 55 years or older than 74 years or persons who quit smoking more than 15 years ago and for individuals with severe comorbidity, LDCT screening should not be performed according to these recommendations. Screening programs should be offered only in clinical settings similar to those in the NLST with multidisciplinary coordination. Only centers with extensive experience in image interpretation and management of findings should be offering LDCT screening (Detterbeck et al. 2013). The National Comprehensive Cancer Network has recommended LDCT screening in high-risk participants: age 55–74 years with ≥ 30 pack-year smoking history and smoking cessation <15 years or age ≥ 50 years and ≥ 20 pack-year smoking history and one additional risk factor such as cancer history, lung disease history, family history of lung cancer, or radon exposure (Wood et al. 2012). In 2013, the American Cancer Society recommended that clinicians with access to high-quality lung cancer screening and treatment centers should initiate discussion about lung cancer screening with high-risk individuals (persons aged 55–74 years with ≥ 30 pack-year smoking history and currently smoking or having quit in the past 15 years). Screening programs should be performed in experienced centers (Wender et al. 2013). In the latest guideline, the US Preventive Services Task Force has given a Grade B recommendation for annual LDCT screening for individuals aged 55–80 years at high risk of lung cancer (30 pack-year smoking history and currently smoking or having quit within the past 15 years). Interestingly, they recommend that screening should be stopped once a person has quit smoking more than 15 years or develops a health problem that substantially limits life expectancy (Moyer and U.S. Preventive Services Task Force 2014).

7 Incidental Findings

Lung cancer screening LDCT examinations are currently used for evaluation of pulmonary nodules, but these examinations can reveal additional, potentially useful diagnostic and prognostic information. In a systematic review, 14.2 % of participants in CT lung cancer screening had other findings necessitating follow-up or additional imaging (Jacobs et al. 2008). Kucharczyk et al. reported in a Canadian study a prevalence of 0.7 % of non-lung cancer findings that were potentially life-threatening (Kucharczyk et al. 2011). The NELSON trial reported 1 % clinically relevant incidental findings in CT screening. Table 3 gives an overview of unrequested information that is detectable on screening LDCT, in particular coronary artery calcifications (CAC), emphysema, airway remodeling, thoracic aortic aneurysms, and osteoporosis.

Smoking cigarettes is known to contribute to an increased risk of coronary heart disease morbidity (Iribarren 2000; Shaper et al. 2003) and mortality (Jacobs et al. 1999). Among NELSON

Table 3 Radiological findings in lung cancer CT screening

Minor abnormalities	Clinically relevant abnormalities
Aortic calcium	Lymphadenopathy
Pulmonary fibrosis	Aortic aneurysm
Pleural plaques	Aortic valve calcifications
Pleural calcifications	Coronary artery calcifications
Adrenal adenoma	Emphysema and bronchial wall remodeling
Bronchiectasis	Adrenal lesion (>10 Hounsfield unit)
	Extrathoracic tumor
	Pleural fluid
	Pneumonia
	Osteoporosis
	Bone destruction

participants, 70 % of the screened population had calcifications of the coronary arteries detected on the lung cancer screening CT (Jacobs et al. 2012). Investigators of the NELSON and the MILD studies reported that coronary calcium scores can be derived from non-ECG-gated LDCT for lung cancer screening and that results have predictive value for cardiovascular events and mortality (Jacobs et al. 2011; Sverzellati et al. 2012). Individuals with high coronary calcium scores have up to nine times higher risk to die within 2 years than those in whom no coronary calcium was detected (Jacobs et al. 2012; Jacobs et al. 2011). These high-risk asymptomatic individuals should be referred to a cardiologist for further workup and preventive treatment. Thereby, the overall survival rate due to the screening program and, thus, the screening efficiency could increase.

Besides cardiovascular disease and cancer, chronic obstructive pulmonary disease (COPD) is a major cause of death in heavy smokers. COPD is currently the third leading cause of death worldwide (World Health Organization. Updated May 2014). The prevalence of COPD is high in a lung cancer screening population. COPD is characterized by chronic airflow limitation mainly caused by emphysema, large airway disease, and small airway remodeling due to inflammation. Quantitative COPD measurements based on LDCT scans include measurement of emphysema severity, airway wall thickness, and air trapping. Participants with COPD can be identified in lung cancer screening program with accuracy of 78 %, sensitivity of 63 %, and specificity of 88 % (Mets et al. 2011). COPD can progress to advanced stages with functional disability, acute exacerbations, and death. Early detection of COPD should lead to earlier treatment that can slow down disease progression and complications.

Decreased bone density, loss of trabecular bone, and vertebral fractures are manifestations of vertebral osteoporosis. Romme et al. demonstrated that CT attenuation values in vertebral bone are highly correlated with dual energy X-ray absorptiometry values in patients with COPD (Romme et al. 2012). More recently, a high prevalence of vertebral fractures on LDCT was found in a random sample of the NELSON trial. In this subcohort, vertebral fractures and lower bone density were independently associated with all-cause mortality (Van der Aalst et al. 2010).

A calcified aortic valve is a strong predictor of aortic valve stenosis; patients with severe aortic valve calcification could benefit from referral to a cardiologist. An incidental thoracic aorta aneurysm can be detected on LDCT and lead to timely treatment.

The benefit of lung screening can be improved by evaluating additional findings. More evidence is needed about the cost-effectiveness and potential benefits when additional findings are also incorporated in the screening management.

8 Benefits and Harms of LDCT Screening

Advantages and disadvantages of lung screening should be carefully considered. An overview of potential benefits and harms is shown in Table 4. Potential benefits include mortality reduction, early detection of lung cancer, and morbidity and mortality reduction from nonmalignant disease.

The major benefit of lung cancer screening is lung cancer mortality reduction. Four screening trials (NLST, DANTE, MILD, DLCST) reported the effect of LDCT screening on lung cancer-specific mortality and all-cause mortality. The NLST demonstrated a relative reduction in lung cancer-specific mortality of 20 % in the LDCT group versus the radiography group over a

Table 4 Advantages and disadvantages of lung cancer CT screening

Advantages	Disadvantages
Decrease in lung cancer mortality Early detection of lung cancer Discouraging cigarette smoking and promoting smoking cessation Potential for reduction of morbidity and mortality from non-lung cancer diseases: COPD, coronary artery calcification, thoracic aorta aneurysm	False-positive results Overdiagnosis Cumulative radiation exposure Anxiety Complications from (unnecessary) diagnostic procedures

median follow-up of 6.5 years ($p = .004$) and showed a reduction of all-cause mortality by 6.7 %. In the smaller trials that published mortality results, no statistically significant difference in lung cancer mortality was observed comparing the screening and control arm.

Identification of patients at early-stage lung cancer can improve prognosis. Stage I cancer disease rate is high in the baseline screening round among screening trials: NLST 63 %, NELSON 64 %, DANTE 54 %, and DLCST 53 %. Stage I and II lung cancers can be treated by surgical resection, sometimes in combination with adjuvant chemotherapy. These patients have a better outcome with a 5-year survival rate of more than 52 % (Siegel et al. 2012). Advanced-stage lung cancer requires more aggressive treatment.

Promoting smoking cessation is the most cost-effective way to reduce tobacco-induced cancer. There is hope that screening for lung cancer can increase the motivation to stop smoking, especially if a participant receives an indeterminate or positive test result. In the NELSON study, 14.5 % of participants in the LDCT group stopped smoking versus 19.1 % in the control group compared to a background population smoking cessation rate of 6–7 % (Van der Aalst et al. 2010). Thus, perhaps participation in a lung cancer screening study itself can make smokers more aware of the importance to stop smoking. Other investigators argue that participants with a negative test result may believe that they will not develop lung cancer and will continue to smoke, which would be an unwanted effect of screening. However, this effect has not been proven so far.

As described above, lung cancer screening LDCT can be an opportunity to reveal additional information such as coronary artery calcification, COPD, and osteoporosis (Mets et al. 2011; Buckens et al. 2015). The cost-effectiveness of lung cancer screening could be improved by using the non-contrast LDCT scan to detect early stages of other diseases with impact on overall morbidity and mortality.

Potential harms of LDCT screening include false-positive results, overdiagnosis, radiation-induced cancers, anxiety, costs induced by screening, and additional diagnostic testing.

Overdiagnosis of lung cancer is defined as screen-detected tumors that do not affect the patient's life expectancy if left untreated. These slow-growing tumors have a benign behavior. Discrimination of these tumors from malignant ones based on imaging is difficult, leading to unnecessary diagnostic biopsy, additional surgery, or treatment for cancer (chemotherapy or radiation), as well as additional cost, anxiety, and morbidity associated with cancer treatment. In the NLST, 18 % of all detected lung cancers in the LDCT arm were indolent (Patz et al. 2014). The magnitude of overdiagnosis is currently uncertain. More data from other lung cancer screening trials is necessary.

False-positive results are suspicious findings on LDCT that do not turn out to be lung cancer. False-positive results lead to unnecessary noninvasive procedures (additional imaging: follow-up, PET/CT, radiation exposure) and invasive procedures such as percutaneous or surgical biopsy. Minimizing false-positive results is very important, not only to decrease complications from unnecessary workup but also to optimize the cost-effectiveness of screening. For this, optimization of the pulmonary nodule management protocols is essential. In the NELSON trial, in which nodule management is based on semiautomated volumetry, the number of false-positive screening tests was ten times lower compared to lung cancer screening trials based on maximal diameter. Likely, this is due to the combination of volumetry and volume-doubling time (VDT) assessment. VDT of nodules plays an essential role to assess growth, especially in individuals with indeterminate nodules of 5–10 mm in diameter (or 100–300 mm^3 in volume). Nodules with VDT greater than 600 days can be regarded as negative (benign), while VDT of <600 days necessitates at least follow-up evaluation (Horeweg et al. 2014a). Heuvelmans et al. (Heuvelmans et al. 2013) reported that all malignant fast-growing lung nodules after the short-term follow-up LDCT in the first round of the NELSON trial had a VDT of ≤ 232 days. Optimization of the VDT cutoff in screen management protocols can reduce false-positive rates even further (National Lung Screening Trial

Research Team et al. 2011; Van Klaveren et al. 2009; Heuvelmans et al. 2013).

Complications related to diagnostic procedures (percutaneous lung biopsy, transbronchial biopsy) include pneumothorax, bleeding, infection, pain, and discomfort. Percutaneous lung biopsy is complicated in 20.5 % by pneumothorax, and 3.1 % of patients require a chest drainage for pneumothorax (Richardson et al. 2002). Hemorrhage is rare. Bleeding complications present most often as hemoptysis (Richardson et al. 2002). Sometimes thoracoscopy or thoracotomy is necessary to obtain tissue, with the same potential complications of biopsy. In the NLST, 1.2 % of participants underwent an invasive procedure for a benign nodule. The NLST revealed a major complication in five per every 10,000 screenees with a benign result (National Lung Screening Trial Research Team et al. 2011).

Cost-effectiveness of lung cancer screening is a major consideration in clinical practice. In most countries, the health-care systems are under pressure due to increasing costs, so pros and cons must be carefully considered. Several factors influence the outcome of the cost-effectiveness such as costs of LDCT (interpretation, workup, treatment), stage of disease at time of diagnosis, false-positive results, health effects (quality of life impact), and workup of incidental findings. Black et al. (Black et al. 2014) estimated the cost-effectiveness in the NLST population comparing different strategies: LDCT, radiography, or no screening. Screening with LDCT was more cost-effective in certain subgroups like current smokers and older participants. Preliminary results of cost-effectiveness analyses from NLST data thus suggest that LDCT screening could be cost-effective, depending on how screening is implemented in clinical practice (Black et al. 2014; American College of Radiology website. Guidance for ACR members on lung cancer screening with CT. www.acr.org. Published 24 June 2013). The most cost-effective way to reduce lung cancer mortality remains smoking cessation. This unavoidable, important topic will be further investigated when more mortality data become available.

Exposure to ionizing radiation can induce cancer. Minimization of the radiation dose is important in screening of asymptomatic, healthy subjects. The scanning parameters should be set, keeping radiation dose as low as reasonably achievable (ALARA principle) (ICRP 1977), while pulmonary nodules can still be detected accurately. This can be reached by lowering tube currents (mAs), lowering tube voltages (kVp), using filters, and optimizing scan length (z-axis). A disadvantage of dose reduction is that small partial-solid or ground-glass nodules might be less visible. Cumulative exposure to radiation depends on participant age at the start of screening, the number of scans received, and the participants' exposure to other sources of radiation.

Receiving news that a LDCT screen for lung cancer is positive is understandably frightening. Unfortunately, this includes a large number of false-positive results leading to unnecessary anxiety. Currently, there is not much known about induced anxiety after lung cancer screening. Van den Bergh et al. (Van den Bergh et al. 2010) investigated whether health-related quality of life (HRQoL) changed over time in subjects with an indeterminate or negative screen result. They reported short-term increased lung cancer-specific distress in nearly one half of subjects awaiting screen results and in participants whom received an indeterminate screen result. After 6 months, there was no HRQoL effect in the group with an indeterminate result requiring an additional 1-year follow-up CT. So, the investigators concluded that lung cancer screening has no negative impact on HRQoL in long term (Van den Bergh et al. 2010). More studies into this topic are needed.

9 Controversy: Diameter- or Volume-Based Nodule Management

The NLST showed that LDCT screening in high-risk patients for lung cancer provided significant reduction in mortality rates, but a number of important questions have so far remained unanswered. Uncertainty still exists regarding the

optimal screen population, potential harms, optimal nodule management protocol, number of screening rounds, the effect of overdiagnosis, and the cost-effectiveness of lung cancer screening. A number of these issues were described and discussed above. In the current section, the focus is on the nodule management and, in the next, on the optimal screening interval. One of the issues in determining the optimal nodule management is the way to evaluate nodule size and detect nodule growth. The NLST, DANTE, and ITALUNG trials used nodule management solely based on manual diameter measurements (Table 1) (National Lung Screening Trial Research Team et al. 2011; Infante et al. 2008; Lopes Pegna et al. 2009), while in a number of European trials, nodule management strategy was based on nodule volume and volume-based VDT, derived from semiautomated software. Optimization of nodule management protocol is essential to reduce the number of false-positive test results in lung cancer screening.

In the NLST, using a diameter-based nodule protocol, all noncalcified nodules with long-axis diameters of 4 mm or greater in the axial plane were considered as a positive test result. The radiologist measured nodules manually with electronic calipers. A positive screening result led to a diagnostic procedure: follow-up imaging, 18 F-fluorodeoxyglucose-positron emission tomography (FDG-PET), percutaneous cytology or biopsy procedure, or diagnostic surgical biopsy. In the DANTE trial, nodules with diameter of $\geq$ 10 mm or 5–10 mm but showing spiculated margins tested positive and received workup (Infante et al. 2008).

The NELSON study was the first lung cancer screening trial in which semiautomated volumetric measurements were used for solid nodules and the solid part of partial-solid nodules. Also the LUSI and DLCST trials used volume-based nodule management for detected nodules (Pedersen et al. 2009; Becker et al. 2012). In the NELSON trial, lung nodules were classified as follows: nodules $<$50 mm^3 (corresponding to a diameter of around 4.6 mm) tested negative, nodules $>$500 mm^3 (corresponding to a diameter of around 9.8 mm) tested positive, and nodules with volume in between these cutoffs tested indeterminate. Participants with an indeterminate test result received a short-term follow-up LDCT (Fig. 1) (Van Klaveren et al. 2009). Then, nodule growth in terms of VDT was calculated according to the formula (Xu et al. 2006):

$$\text{Volume doubling time}(\text{days}) = \frac{\ln(2)\,\Delta t}{\ln(\text{V2}) - \ln(\text{V1})}$$

Δt represents time in days between scans, V1 the regular round and V2 the follow-up round (Xu et al. 2006). VDT of less than 400 days warrants additional diagnostic procedures. Participants whose nodules had a VDT of 400–600 days were indeterminate, requiring an extra follow-up CT 12 months after the regular round CT (Figs. 2 and 3). A VDT of more than 600 days was negative, i.e., no further evaluation was needed (Xu et al. 2006; Heuvelmans et al. 2013). A similar nodule management protocol to the NELSON trial was used in the UKLS (Baldwin et al. 2011). The MILD trial used also volumetry for nodule management, but different cutoff values were applied: nodules $<$60 mm^3 received a negative result and nodules $>$250 mm^3 were considered positive (Pastorino 2006).

In the NLST, the percentage of positive screen results was 27.3 % at baseline and 27.9 % in the second round, while the NELSON trial presented ten times lower positive test results (2.6 % at baseline and 1.8 % in the second round). In both trials, the negative predictive value was comparably high (NLST 99.9 % versus NELSON 99.7–99.9 %) (National Lung Screening Trial Research Team et al. 2011; Van Klaveren et al. 2009). Horeweg et al. recently published results comparing different nodule management strategies based on nodule volume and VDT versus diameter, derived from the baseline data of the NELSON study. Nodule management based on volumetric measurements and VDT had a sensitivity (90.9 %, 95 % CI: 81.2–96.1) and negative predictive value (99.9 %, 95 % CI: 99.8–100) comparable to the diameter-based protocol (92.4 %, 95 % CI: 83.1–97.1 and 99.9 %, 95 % CI:

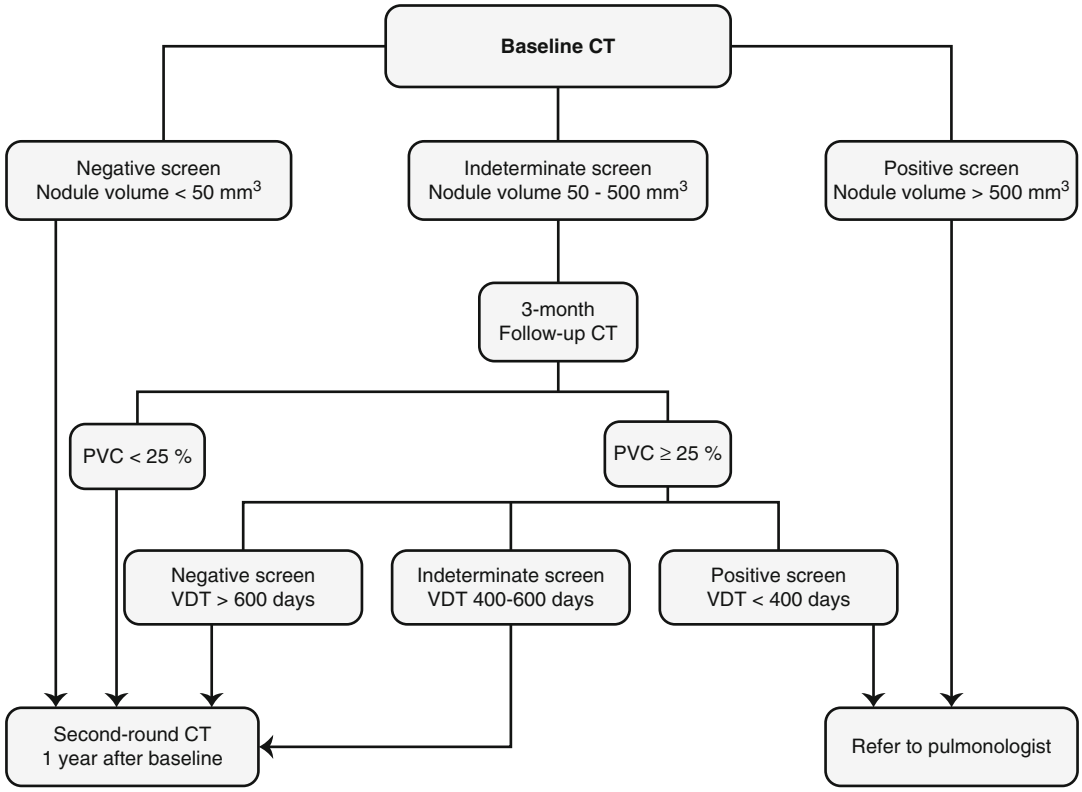

Fig. 1 Overview of the nodule management protocol of the baseline round in the NELSON trial, as example of a volumetry and VDT-based protocol

99.8–100). However, the specificity and positive predictive value were favorable for the volume-based protocol (volume protocol 94.9 %, 95 % CI: 94.4–95.4 and 14.4 %, 95 % CI: 11.3–18.1 versus diameter protocol 90.0 %, 95 % CI: 89.3–90.7 and 7.9 %, 95 % CI: 6.2–10.1) (Horeweg et al. 2014a; Heuvelmans et al. 2013). These findings suggest that nodule management based on volume is more accurate than diameter-based nodule management (Horeweg et al. 2014a).

10 Controversy: Optimal Screen Interval

Other important remaining questions are the length of the screen interval and the frequency of screening. The screen interval can influence the percentage of early-stage lung cancers in screening programs, as well as the number of interval cancers. In the NLST and most European trials, subjects were screened in three to five annual screening rounds (National Lung Screening Trial Research Team et al. 2011; Saghir et al. 2012; Infante et al. 2008; Lopes Pegna et al. 2009; Becker et al. 2012). In contrast, subjects in the NELSON trial underwent LDCT screening in year 1, 2, 4, and 6.5, so with differing screen intervals (Zhao et al. 2011). Investigators reported an increased number of interval cancers in case of prolonged screen intervals (Horeweg et al. 2014b). However, overall the number of interval cancers and the percentage of stage 1 disease lung cancer detected in the first two rounds of the NELSON trial did not differ significantly from the results in the NLST (stage I disease 62 % in NELSON versus stage I disease 59 % in NLST) (National Lung Screening Trial

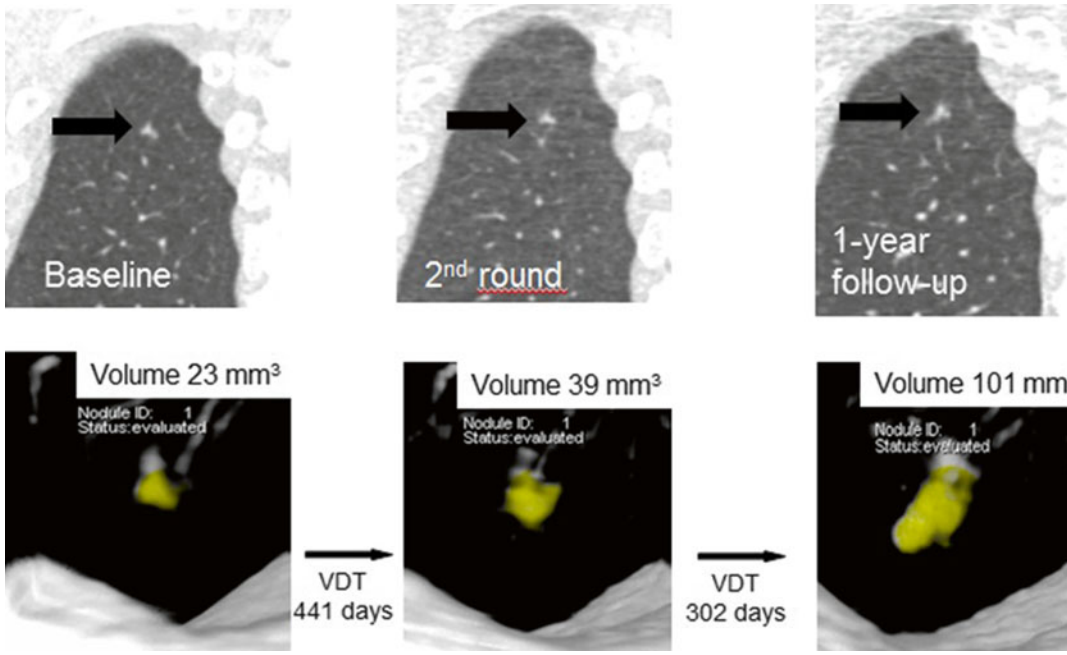

Fig. 2 Example of a growing, malignant lung nodule in a 55-year-old former smoker with 63.7 pack-years. Coronal computed tomography (*CT*) scan image (**a**) showed a lesion with a baseline volume of 23 mm^3 in the right lower lobe (*arrow*). According to the nodule management algorithm, the screen result was negative. At the regular second round screening (12 m.a.b.) (**b**), the nodule volume was 39 mm^3, and the calculated *VDT* was 441 days. Due to the *VDT* (400–600 days), the screen result was indeterminate, and a repeat *CT* at 1 year was indicated (24 m.a.b.). The follow-up *CT* 1 year later (**c**) showed a nodule volume of 101 mm^3. The *VDT* at that time was 302 days. Due to the *VDT* (<400 days), the screen result was positive, and the participant was referred to the pulmonologist. Workup revealed stage Ia adenocarcinoma. M.a.b. = months after baseline

Research Team et al. 2011). The second study that did not only use annual screening rounds was the MILD trial; participants were randomized to either no LDCT screening, annual LDCT, or biennial LDCT screening. The cumulative 5-year lung cancer incidence rate was 311 per 100,000 for no LDCT, 620 per 100,000 for annual LDCT and 457 per 100,000 for biennial LDCT. Thus, more cancers were detected in the annual screening group. However, no difference in mortality and number of interval cancers was observed between the annual and biennial screening group in the 5-year results (Pastorino et al. 2012). More data are needed to determine the optimal screening interval. Optimization of the screen interval is needed to assess the benefit-harm balance of less frequent LDCT screening.

In summary, the NLST has demonstrated a mortality benefit from lung cancer screening for high-risk participants using low-dose computed tomography. Various American societies now recommend lung cancer screening to be implemented in practice. However, there are still a number of important issues that need answering before implementation of LDCT screening in Europe.

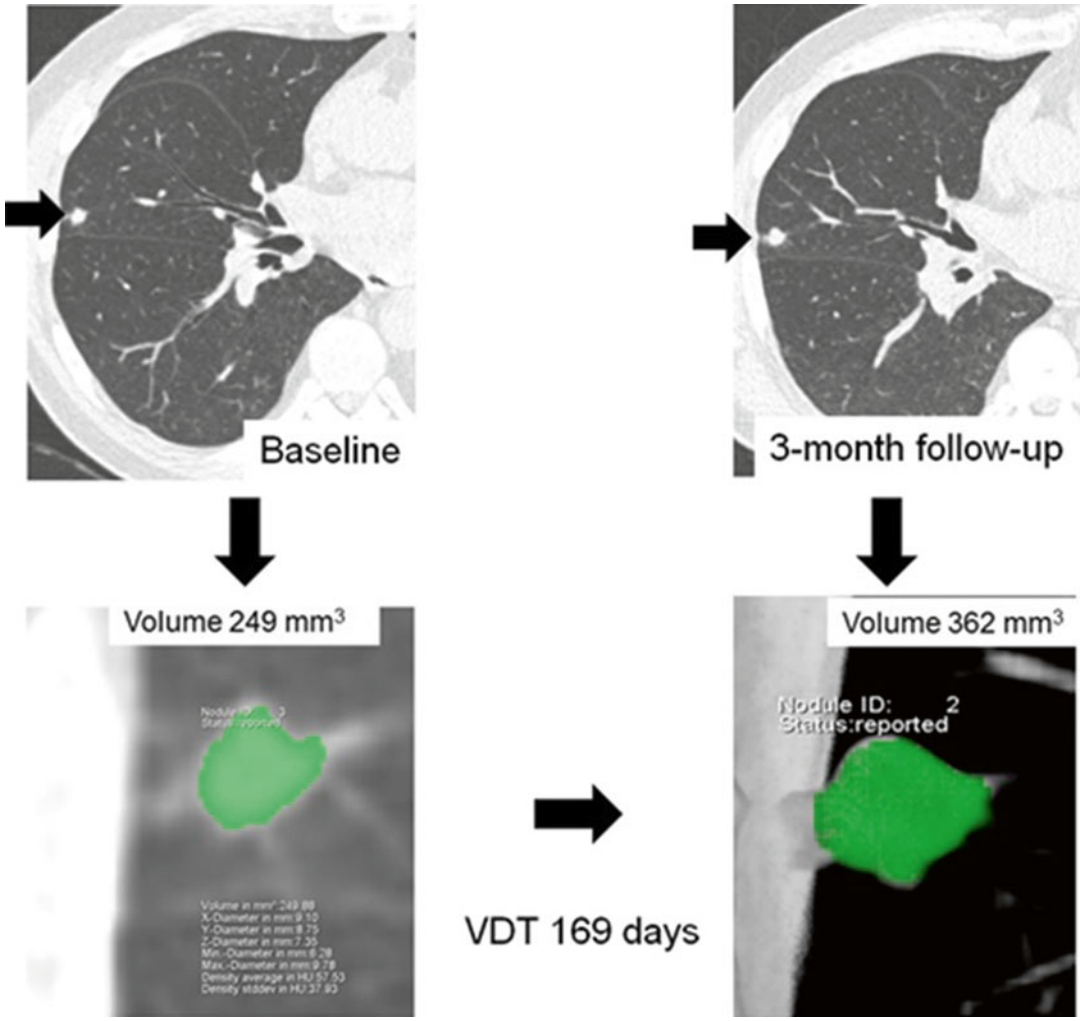

Fig. 3 Growing malignant lesion in a 72-year-old man. Axial *CT* scan shows a round nodule with a volume of 249 mm^3 in the middle lobe. Three months later, the nodule volume increased to 362 mm^3 (*VDT* = 169 days). Biopsy revealed a pT1 N0 Mx squamous cell carcinoma

References

Aberle DR, DeMello S, Berg CD et al (2013) Results of two incidence screenings in the National Lung Screening Trial. N Engl J Med 369:920–931

American College of Radiology website. Guidance for ACR members on lung cancer screening with CT. www.acr.org. Published 24 June 2013. Accessed 4 Nov 2013.

American Lung Association (2012) Providing guidance on lung cancer screening to patients and physicians (internet). American Lung Association, Chigaco

Bach P, Kelly M, Tate R, McCrory DC (2003) Screening for lung cancer: a review of the literature. Chest 123(Suppl 1):72S–82S

Baldwin DR, Duffy SW, Wald NK et al (2011) UK Lung Screen (UKLS) nodule management protocol: modelling of a single screen randomised controlled trial of low-dose CT screening for lung cancer. Thorax 66: 308–313

Becker N, Motsch E, Gross ML et al (2012) Randomized study on early detection of lung cancer with MSCT in Germany: study design and results of the first screening round. J Cancer Res Clin Oncol 138:1475–1486

Black WC, Gareen IF, Soneji SS et al (2014) Cost-effectiveness of CT screening in the National Lung Cancer Screening Trial. N Eng J Med 371:19

Buckens CF, van der Graaf Y, Verkooijen HM et al (2015) Osteoporosis markers on low-dose lung cancer screening chest computed tomography scans predict all-cause mortality. Eur Radiol 25(1):132–139

Detterbeck FC, Mazzone PJ, Naidich DP et al (2013) Screening for lung cancer: diagnosis and management of lung cancer, 3rd ed: American College of Chest Physicians evidence-based clinical practice guidelines. Chest 143(Suppl):e78S–e92S

Field JK, van Klaveren R, Pedersen JH et al (2013) European randomized lung cancer screening trials: post NLST. J Surg Oncol 108:280–286

Fontana RS, Sanderson DR, Woolner LB, Taylor WF, Miller WE, Muhm JR et al (1991) Screening for lung cancer: a critique of the Mayo Lung Project. Cancer 67(4 Suppl):1155–1164

Frost JK, Ball WC Jr, Levin ML et al (1984) Early lung cancer detection: results of the initial (prevalence) radiologic and cytologic screening in the Johns Hopkins study. Am Rev Respir Dis 130(4):549–554

Henschke CI, McCauley DI, Yankelevitz DF et al (1999) Early Lung Cancer Action Project: overall design and findings from baseline screening. Lancet 354:99–105

Heuvelmans MA, Oudkerk M, de Bock GH et al (2013) Optimisation of volume-doubling time cutoff for fast-growing lung nodules in CT lung cancer screening reduces false-positive referrals. Eur Radiol 23(7): 1836–1845

Horeweg N, van der Aalst CM, Thunnissen E et al (2013) Characteristics of lung cancers detected by computed tomography screening in the randomized NELSON trial. Am J Respir Crit Care Med 187:848–854

Horeweg N, van Rosmalen J, Heuvelmans MA et al (2014a) Lung cancer probability in patients with CT-detected pulmonary nodules: a prespecified analysis of data from the NELSON trial of low-dose CT screening. Lancet Oncol 15(12):1332–1341

Horeweg N, Th Scholten E, de Jong PA et al (2014b) Detection of lung cancer through low-dose CT screening (NELSON): a prespecified analysis of screening test performance and interval cancers. Lancet Oncol 15(12):1342–1350

Humphrey LL, Teutsch S, Johnson M, U. S. Preventive Services Task Force (2004) Lung cancer screening with sputum cytologic examination, chest radiography, and computed tomography: an update for the U.S. Preventive Services Task Force. Ann Intern Med 140(9):740–753

ICRP (1977) Recommendations of the ICRP. Ann ICRP 1:3

Infante M, Lutman FR, Cavuto S et al (2008) Lung cancer screening with spiral CT: baseline results of the randomized DANTE trial. Lung Cancer 59:355–363

Infante M, Cavuto S, Lutman FR et al (2009) A randomized study of lung cancer screening with spiral computed tomography: three-year results from the DANTE trial. Am J Respir Crit Care Med 180:445–456

Iribarren C (2000) Reexamining health effects of cigar smoking: fashionable, but may increase the risk of coronary heart disease. Eur Heart J 21:505–506

Jacobs EJ, Thun MJ, Apicella LF (1999) Cigar smoking and death from coronary heart disease in a prospective study of US men. Arch Intern Med 159:2413–2418

Jacobs PC, Mali WP, Grobbee DE, van der Graaf Y (2008) Prevalence of incidental findings in computed tomographic screening of the chest: a systematic review. J Comput Assist Tomogr 32(2):214–221

Jacobs PC, Gondrie MJ, Mali WP et al (2011) Unrequested information from routine diagnostic chest CT predicts future cardiovascular events. Eur Radiol 21(8): 1577–1585

Jacobs PC, Gondrie MJ, van der Graaf Y et al (2012) Coronary artery calcium can predict all-cause mortality and cardiovascular events on low-dose CT screening for lung cancer. AJR Am J Roentgenol 198(3):505–511

Jaklitsch MT, Jacobson FL, Austin JH et al (2012) The American Association for Thoracic Surgery guidelines for lung cancer screening using low-dose computed tomography scans for lung cancer survivors and other high-risk groups. J Thorac Cardiovasc Surg 144:33–38

Jemal A, Bray F, Center MM et al (2011) Global cancer statistics. CA Cancer J Clin 61:69–90

Kaneko M, Eguchi K, Ohmatsu H et al (1996) Peripheral lung cancer: screening and detection with low-dose spiral CT versus radiography. Radiology 201:798–802

Kucharczyk MJ, Menezes RJ, McGregor A et al (2011) Assessing the impact of incidental findings in a lung cancer screening study by using low-dose computed tomography. Can Assoc Radiol J 62:141–145

Lopes Pegna A, Picozzi G, Mascalchi M et al (2009) Design, recruitment and baseline results of the ITALUNG trial for lung cancer screening with low dose CT. Lung Cancer 64:34–40

Marcus P, Bergstralh E, Fagerstrom R et al (2000) Lung cancer mortality in Mayo Lung Project: impact of extended follow up. J Natl Cancer Inst 92:1308–1316

Mets OM, Buckens CF, Zanen P et al (2011) Identification of chronic obstructive pulmonary disease in lung cancer screening computed tomographic scans. JAMA 306(16):1775–1781

Molina JR, Yang P, Adjei AA et al (2008) Non-small cell lung cancer: epidemiology, risk factors, treatment and survivorship. Mayo Clin Proc 83(5):584–594

Moyer VA, U.S. Preventive Services Task Force (2014) Screening for lung cancer: U.S. Preventive Services Task Force recommendation statement. Ann Intern Med 160:330–338

Nair A, Hansell DM (2011) European and North American lung cancer screening experience and implications for pulmonary nodule management. Eur Radiol 21(12): 2445–2454

National Lung Screening Trial Research Team, Aberle DR, Adams AM, Berg CD et al (2011) Reduced lung-cancer mortality with low-dose computed tomographic screening. N Engl J Med 365:35–409

Oken MM, Hocking WG, Kvale PA et al (2011) Screening by chest radiograph and lung cancer mortality: the Prostate, Lung, Colorectal, and Ovarian (PLCO) randomized trial. JAMA 306:1865–1873

Paoletti L, Jardin B, Carpenter MJ, Cummings KM, Silvestri GA (2012) Current status of tobacco policy and control. J Thorac Imaging 27:213–219

Pastorino U (2006) Early detection of lung cancer. Respiration 73:5–13

Pastorino U, Rossi M, Rosato V et al (2012) Annual or biennial CT screening versus observation in heavy smokers: 5-years results of the MILD trial. Eur J Cancer Prev 21:308–315

Patz EF Jr, Pinsky P, Gatsonic C et al (2014) Overdiagnosis in low-dose computed tomography screening for lung cancer. JAMA Intern Med 174(2):269–274

Pedersen JH, Ashraf H, Dirksen A et al (2009) The Danish randomized lung cancer CT screening trial: overall design and results of the prevalence round. J Thorac Oncol 4:608–614

Richardson CM, Pointon KS, Manhire AR et al (2002) Percutaneous lung biopsies: a survey of UK practice based on 5444 biopsies. Br J Radiol 75(897): 731–735

Romme EA, Murchison JT, Phang KF et al (2012) Bone attenuation on routine chest CT correlates with bone mineral density on DXA in patients with COPD. J Bone Miner Res 27:2338–2343

Saghir Z, Dirksen A, Ashraf H et al (2012) CT screening for lung cancer brings forward early disease. The randomized Danish lung cancer screening trial: status after five annual screening rounds with low-dose CT. Thorax 67:296–301

Shaper AG, Wannamethee SG, Walker M (2003) Pipe and cigar smoking and major cardiovascular events, cancer incidence and all-cause mortality in middle-aged British men. Int J Epidemiol 32:802–808

Siegel R, Naishadham D, Jemal A (2012) Cancer statistics, 2012. CA Cancer J Clin 62:10–29

Sverzellati N, Cademartiri F, Bravi F et al (2012) Relationship and prognostic value of modified coronary artery calcium score, FEV1 and emphysema in lung cancer screening population: the MILD trial. Radiology 262(2):460–467

Van den Bergh KA, Essink-Bot ML, Borsboom GJ et al (2010) Short-term health-related quality of life consequences in a lung cancer CT screening trial (NELSON). Br J Cancer 102:27–34

Van der Aalst CM, van den Bergh KA, Willemsen MC et al (2010) Lung cancer screening and smoking abstinence: 2 year follow-up data from the Dutch-Belgian randomised controlled lung cancer screening trial. Thorax 65:711–718

Van Iersel CA, de Koning HJ, Draisma G, Mali WP, Scholten ET, Nackaerts K et al (2007) Risk-based selection from the general population in a screening trial: selection criteria, recruitment and power for the Dutch-Belgian randomized lung cancer multi-slice CT screening trial (NELSON). Int J Cancer 120(4):868–874

Van Klaveren RJ, Oudkerk M, Prokop M et al (2009) Management of lung nodules detected by volume CT scanning. N Engl J Med 361:2221–2229

Wender R, Fontham ET, Barrera E Jr et al (2013) American Cancer Society lung cancer screening guidelines. CA Cancer J Clin 63:107–117

Wood DE, Eapen GA, Ettinger DS et al (2012) Lung cancer screening. J Natl Compr Canc Netw 10(2): 240–265

World Health Organization. Updated May 2014. www.who.int/mediacentre/factsheets/fs310/en/accessed march 10, 2016

Xu DM, Gietema H, de Koning H et al (2006) Nodule management protocol of the NELSON randomised lung cancer screening trial. Lung Cancer 54(2):177–184

Zhao YR, Xie X, de Koning HJ, Mali WP, Vliegenthart R, Oudkerk M (2011) NELSON lung cancer screening study. Cancer Imaging 11:S79–S84

Computed Tomography Characterisation of Lung Nodules and Management of Incidentally Detected Nodules

Anand Devaraj, Charlie Sayer and John Field

Abstract

Pulmonary nodules are a frequently encountered incidental phenomenon on thoracic CT. This chapter will review a number of strategies that are available to help clinicians distinguish between benign and malignant nodules, including assessment of nodule size, nodule morphology, nodule density and nodule growth rate.

1 Introduction

The pulmonary nodule is defined by the Fleischner society as a rounded opacity, well or poorly defined, measuring up to 3 cm in diameter (Hansell et al. 2008). Since the advent of multidetector CT, the frequency with which pulmonary nodules are encountered as incidental findings on CT has increased substantially.

While the prevalence of pulmonary nodules has varied from approximately 27 % in the National Lung Screening Trial (NLST) (Aberle et al. 2011) to 75 % in the Pan-Canadian (PANCAN) study (McWilliams et al. 2013), on average lower rates are reported in investigations of incidental pulmonary nodules outside of lung cancer screening (Barrett et al. 2009). However, in general it is difficult to compare studies carried out in a screening setting to those from clinical practice due to methodological and demographic differences. Studies examining the rate of incidentally detected nodules have tended to rely on retrospective chart review, while in screening trials CTs are examined by thoracic radiologists with a greater emphasis on identifying nodules. Interestingly, in one study of incidental nodules, in which over 2000 thoracic CTs were re-reviewed by expert radiologists, a nodule prevalence of up to 26.5 % was reported (Gomez-Saez et al. 2014), a figure not dissimilar to findings from the NLST trial.

Given the high prevalence of nodules identified on CT, distinguishing between benign and malignant nodules becomes of paramount importance. On CT, the strategies available to achieve this are (i) evaluation of nodule size, morphology

A. Devaraj, MRCP, FRCR, MD (✉)
Department of Radiology, Royal Brompton Hospital, Sydney Street, London, UK
e-mail: a.devaraj@nhs.net

C. Sayer
Department of Radiology, Brighton and Sussex University Hospitals Trust, Eastern Road, Brighton, UK

J. Field
Department of Molecular and Clinical Cancer Medicine, The University of Liverpool, Institute of Translational Medicine, West Derby Street, Liverpool, UK

U.J. Schoepf, F.G. Meinel (eds.), *Multidetector-Row CT of the Thorax*, Medical Radiology,
DOI 10.1007/978-3-319-30355-0_10

and density and (ii) surveillance over time. This chapter will review both of these strategies as well as novel CT techniques.

2 Solid Nodules

2.1 Nodule Size as an Indicator of Malignancy

The positive relationship between nodule size and lung cancer risk has been known for some time, with an approximate 1.1 odds ratio for cancer for each 1 mm increase in nodule diameter reported in early studies (Gould et al. 2007a). A very low risk of lung cancer in very small nodules is also a long established observation. In the Mayo Lung Cancer Screening Trial of 1520 patients, lung cancer risk was 0.2 % for nodules less than 3 mm, 0.9 % for nodules between 4 and 7 mm and 18 % for nodules between 9 and 20 mm (Swensen et al. 2003).

More recently, a considerable volume of new data has emerged from two large lung cancer screening trials that have particular relevance for the management of small lung nodules. Horeweg et al. (2014) reported the 2-year outcomes in 7155 participants with and without nodules from the NELSON lung cancer screening trial. It was shown that individuals with nodules < 100 mm^3 had a 0.6 % risk for lung cancer, which was not statistically different from participants without nodules (0.4 %). The same report also confirmed the exponentially increasing risk with increasing nodule size (2.4 % for nodules between 100 mm^3 and 300 mm^3 and 16.9 % for nodules >300 mm^3).

In the NLST trial, Gierada et al. (2014) reported that the 12-month risk of lung cancer was only 0.15 % for participants with nodules < 5 mm, which was almost identical to participants without any nodules at all (0.1 %) at initial CT. By contrast, the risk for participants with nodules between 5 and 8 mm and >8 mm was 0.6 % and 9.3 %, respectively.

It is unlikely that further data in similar numbers to the NELSON and NLST trials, on the behaviour of small nodules over time will be forthcoming in the near future. Indeed, on the basis of this evidence, the British Thoracic Society in 2015 recommended that patients with incidentally detected very small nodules do not undergo follow-up CT.

2.2 Nodule Morphology

The morphology or shape of pulmonary nodules has been shown to have some influence on the likelihood of malignancy, though this characteristic does not appear to be as strong a predictor as size, growth and attenuation characteristics (see later for growth and attenuation characteristics). Diederich et al. showed that well-defined, non-lobulated nodules were more likely to show complete, rather than incomplete, resolution at follow-up in an early lung cancer screening trail (Diederich et al. 2005). In a larger study based on data from the NELSON screening trial, Xu et al. prospectively demonstrated that a solid pulmonary nodule, less than 1 cm in diameter, highly spherical, with smooth margins, was less likely to show interval growth or turn out to be malignant than one with spiculated, lobulated or irregular margins (Xu et al. 2008). However, size remained independently a much stronger predictor of malignancy. In another study, the same authors also looked at 891 subcentimetre, solid, non-calcified nodules retrospectively (Xu et al. 2009). All malignant nodules were nonspherical and unattached to vessels, pleura or fissures. At 1-year follow-up in 891 nodules, only 2 % of smooth nodules ($n = 262$) were malignant compared with 22 % of lobulated nodules ($n = 106$) and 14.5 % of spiculated nodules ($n = 68$). However, in the same study, 27 % of spherical nodules ($n = 387$) were malignant, illustrating the overlap in morphological features between benign and malignant nodules. Further data from the NLST has shown that subjectively assessed poorly defined margins or spiculation increased the odds of malignancy in a nodule by 2.8 times compared to a smooth margin (Bartholmai et al. 2015). These results were also supported in another prospective study by Harders et al. which included 213 consecutive pulmonary nodules (5–30 mm) in patient's referred for suspected lung cancer. Using the reference standard of biopsy or follow-up to 24 months of follow-up, the authors demonstrated a malignancy likelihood

ratio of 5.5 for spiculated nodules, 2.0 for lobulated nodules and 1 for smooth or polygonal nodules (Harders et al. 2011). Despite the results of these studies, it is intuitive that in small nodules, the subjective assessment of morphology is prone to both inter- and intra-observer variability and therefore only weakly predicts the chance of malignancy. In fact, in the context of lung cancer screening, descriptors of morphology may be over- or understated by the reader, to support or negate a need for recall when combined with other factors such as size, location and attenuation characteristics (Fig. 1).

To counter the subjective element, some investigators have evaluated quantitative methods to see if an improved discrimination between benign and malignant nodules can be made. Li et al. showed that a computer-aided diagnosis (CAD) using linear discrimination analysis of 56 morphological features could improve detection of malignancy amongst radiologists looking at benign and malignant lesions between 6 and 20 mm (Li et al. 2004).

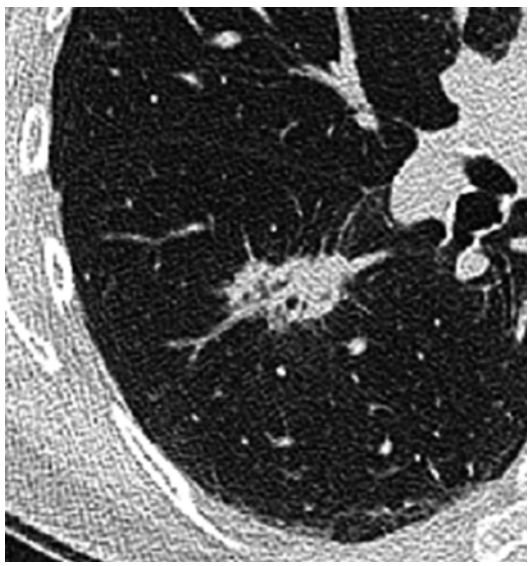

Fig. 1 CT shows a large spiculated nodule in the right lower lobe which proved to be lung adenocarcinoma. Spiculation has been shown to be more likely to be associated with malignant than benign nodules, although benign nodules can also show spiculation. However, in this example, size is the best predictor of malignancy, and the utility of nodule morphology in smaller nodules is limited

2.3 Peri-fissural Nodules and Intrapulmonary Lymph Nodes

Recognising the typical CT features of benign intrapulmonary lymph nodes is important and may help avoid unnecessary surveillance or biopsy in some patients. The morphological characteristics of benign intrapulmonary lymph nodes (IPLNs) have been described in five studies evaluating resected nodules histologically confirmed as IPLNs (Wang et al. 2013) (Shaham et al. 2010; Hyodo et al. 2004; Oshiro et al. 2002; Takenaka et al. 2013). Described features include nonspherical shape, subpleural location, size typically less than 1 cm, smooth margins and often the presence of an attached interlobular septum (Fig. 2). Two large long-term surveillance studies have also reported benign and indolent behaviour in

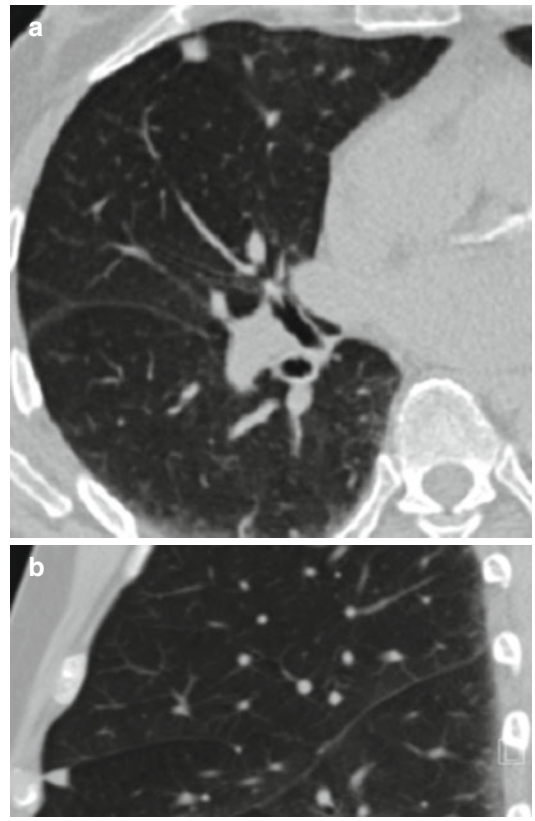

Fig. 2 (**a**) CT shows nonspherical nodule adjacent to horizontal fissure, with emerging interlobular septum. (**b**) Sagittal image confirms the peri-fissural location and triangular shape of this likely benign intrapulmonary lymph node

so-called peri-fissural nodules, which may well constitute intrapulmonary lymph nodes. De Hoop et al. (2012) and Ahn et al. (2010) both showed an absence of malignancy in fissure-attached nodules with a lentiform or triangular shape. Even in the presence of rapid growth, no malignancies were identified in peri-fissural nodules in the study by de Hoop et al. (2012). It should be noted that fissure-attached nodules with non-smooth margins or in patients with known primary malignancies should not automatically be regarded as benign.

2.4 CT Assessment of Nodule Growth Rate

Lung nodule growth is one of the most powerful markers of malignancy, though uncertainties exist regarding growth assessment: (i) there is no widely accepted definition of lung nodule growth on CT or how it should be measured; and (ii) because benign nodules also grow, capturing the rate of growth is perhaps as important as defining growth in itself.

In clinical practice, growth is often assessed by demonstrating an increase in nodule diameter measurement using electronic callipers. The screening nodule management guidelines "Lung-Rads" define growth as a diameter increase of 1.5 mm (Kazerooni et al. 2015). By contrast, others such as the NLST trial defined growth as an increase in size of 10 %, while the National Comprehensive Cancer Network screening guidelines stipulate a 2 mm increase as constituting growth (Wood et al. 2015).

Although diameter measurements of lung nodules are readily performed, they are subject to reliability issues. Revel et al. found that inter-reader variability for diameter measurements was 1.73 mm or 20 % of average diameter (Revel et al. 2004). However, when translated into volume, this variation is approximately 100 %, a substantially larger figure. Inconsistency in diameter measurement occurs because of the requirement of readers to place cursors at the edges of a lung nodule. Diameter measurements may also underestimate nodule growth because nodules are not perfect spheres and do not grow in a symmetrical fashion.

To overcome these limitations, volumetry applications have been used to determine nodule size and growth in several lung cancer screening trials (Baldwin et al. 2011; van Klaveren et al. 2009). Importantly many trials have used volumetry in conjunction with volume-doubling times (VDT), calculated using volume measurements at two time points. The volume-doubling time of lung cancer has typically been reported to be less than 400 days in clinical practice (Detterbeck and Gibson 2008) and screening studies (Henschke et al. 2012). In the NELSON lung cancer screening trial, Horeweg et al. (2014) established that 2-year lung cancer risk was 9.9 %, 4.0 % and 0.8 % in patients with VDT of <400 days, 400–600 days and >600 days, respectively (Fig. 3). It should be remembered that volumetry measurements are influenced by reconstruction and other parameters such as slice thickness and reconstruction algorithms. Hence consistency of acquisition, reconstruction and patient factors is crucial when using this software.

3 Subsolid Nodules

The term subsolid nodule (SSN) refers to a rounded area of increased attenuation less than 3 cm in diameter that is lower in density than surrounding soft tissue structures but may contain small solid elements. These nodules may also be referred to as 'pure ground-glass' or, when areas of obscuration of normal parenchymal architecture occur, 'part-solid' nodules (Lee and Lee 2011). The presence of SSN on thoracic CT is variable but not uncommon, with reported frequencies of 2–3 % in the NLST (Aberle et al. 2011) and NELSON (van Klaveren et al. 2009) trials and approximately 15 % in the PANCAN study (McWilliams et al. 2013). A significant number of subsolid nodules are transient and inflammatory, with up to 70 % of pure or part-solid GGN reported to resolve on subsequent follow-up imaging (Oh et al. 2007). However, persistent subsolid nodules are by contrast more likely to be malignant and in particular represent

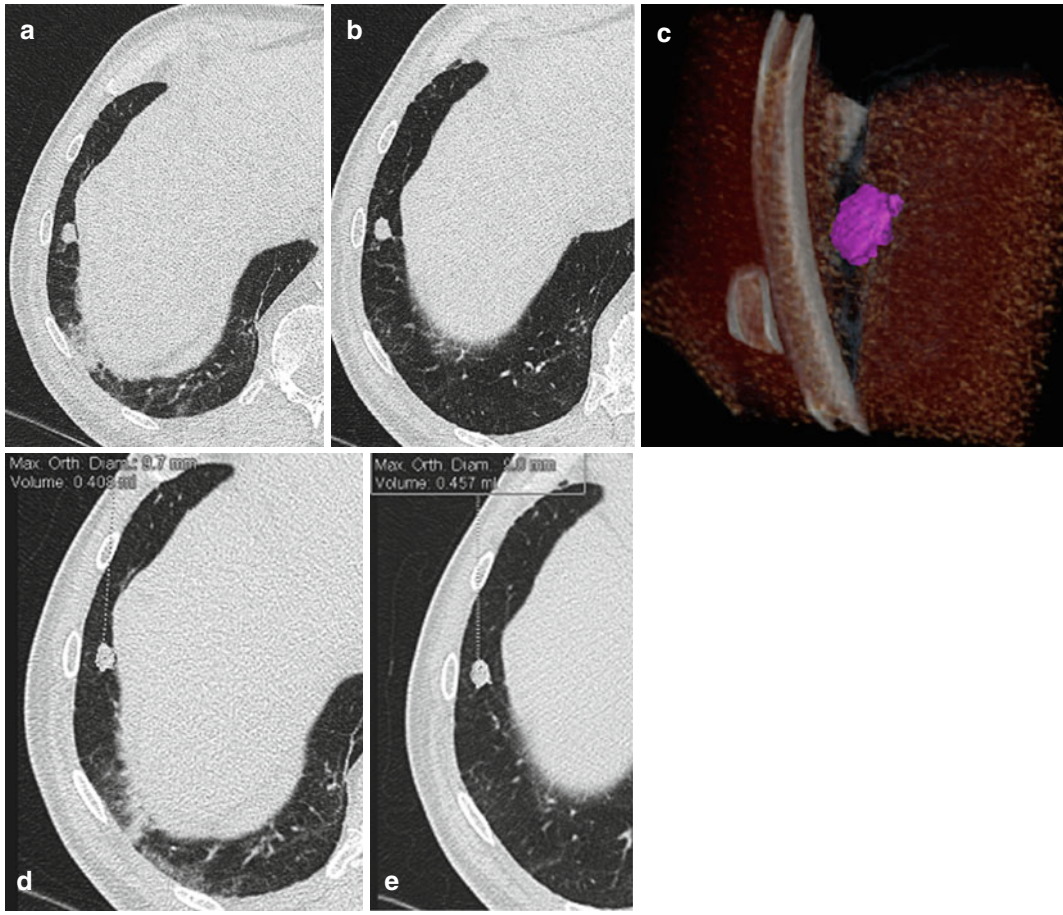

Fig. 3 CT shows nodule in the right lower lobe at baseline (**a**) and at 12 months of follow-up CT (**b**). 3D volume-rendered images (**c**) show the nodule to have been successfully segmented by nodule volumetry application. It measures 408mls (**d**) at baseline and 457mls at follow-up (**e**). This equated with a volume-doubling time of over 2000 days in keeping with a more benign rate of growth

adenocarcinoma histopathologically. The classification of adenocarcinoma led by the IASCL in 2011 introduced a number of terms including atypical adenomatous hyperplasia (AAH), adenocarcinoma in situ (AIS), minimally invasive adenocarcinoma (MIA) and invasive adenocarcinoma (Travis et al. 2011). Much work has recently been done on evaluating the relationship between the appearances of subsolid nodules and the spectrum of lung adenocarcinoma, and this has shown that CT may distinguish different subtypes even though there is considerable overlap in the CT characteristics of these lesions.

AAH and AIS are considered preinvasive lesions. AAH is usually less than 5 mm in diameter and most often of purely ground-glass composition with no obscuration of vascular or bronchiolar margins (Ishikawa et al. 2005; Kim et al. 2007). Although some studies have demonstrated that a spherical shape is more prevalent in AAH when compared to malignant lesions, this is not a reliable discriminator (Oda et al. 2008). AIS is defined as adenocarcinoma with a purely lepidic growth pattern (along alveolar structures with no stromal, vascular or pleural invasion). On CT, AIS most often manifest as a pure ground-glass nodule with or without small solid components when viewed on thin section CT, though AIS tends to be more opaque than AAH (Park et al. 2006) (Ikeda et al. 2007).

MIA is defined as a lesion with a predominant lepidic growth with <5 mm stromal invasion (Travis et al. 2011).

Much recent literature has focused on the size of the solid component on CT as a predictor of the extent of invasion, with a solid component greater than 5 mm being considered malignant unless proven otherwise. However, the solid component of a persistent SSN may represent a number of entities including alveolar collapse, inflammatory cellular infiltrate, fibrosis, non-invasive lepidic growth or invasive adenocarcinoma. For this reason, the size of the solid component on CT may be larger than any potential invasive component histologically (Naidich et al. 2013; Noguchi et al. 1995). Conversely the size of a small invasive component histologically may not be visible on CT with a spatial resolution not more than 200–300 μm. It follows therefore that there is considerable overlap between preinvasive and invasive lesions on CT. For instance, Lim et al. (2013) examined the histopathological findings in 46 large pure GGNs (>10 mm) and found that, although most represented AIS, approximately one third were invasive adenocarcinoma. In another study by Lee et al. (2013), 208 resected part-solid lesions were examined. 23 % were preinvasive, although there was a significant difference in the size of the solid component between preinvasive and invasive lesions (3.5 + −2.6 mm versus 10.2 + −5.8 mm, $p < 0.001$).

A key limitation of relying on visual assessment of part-solid nodules is the difficulty sometimes in establishing the presence or absence of a solid component (never mind the size of the solid component) (Fig. 4). Thus, using computerised texture analysis to predict invasiveness in subsolid nodules has also attracted the attention of investigators recently. Early studies suggest that invasive lesions demonstrate more density heterogeneity than preinvasive lesions (as shown by an increase in the texture parameter known as entropy) (Chae et al. 2014; Son et al. 2014).

Regardless of the degree of invasion, there is evidence from screening trials that some subsolid lesions characterised either as pure ground-glass nodules or part-solid nodules with small solid components can remain indolent over long periods of time (5–7 years), suggesting they can be managed in some scenarios with long-term CT surveillance depending on patient wishes and comorbidities (Scholten et al. 2015; Silva et al. 2012). In this setting, the development of new solid components, an increase in nodule density or an increase in the overall size of the lesion should prompt consideration of further investigation or resection. An interesting parameter, nodule mass (which is nodule volume multiplied by mean attenuation), has also been proposed as a sensitive indicator of changes in nodule characteristics (de Hoop et al. 2010).

An important technical consideration is that CT imaging of subsolid nodules must be performed with a slice thickness <3 mm to avoid partial volume effects causing ground-glass opacities to appear as solid elements (Lee et al. 2014) (Fig. 5).

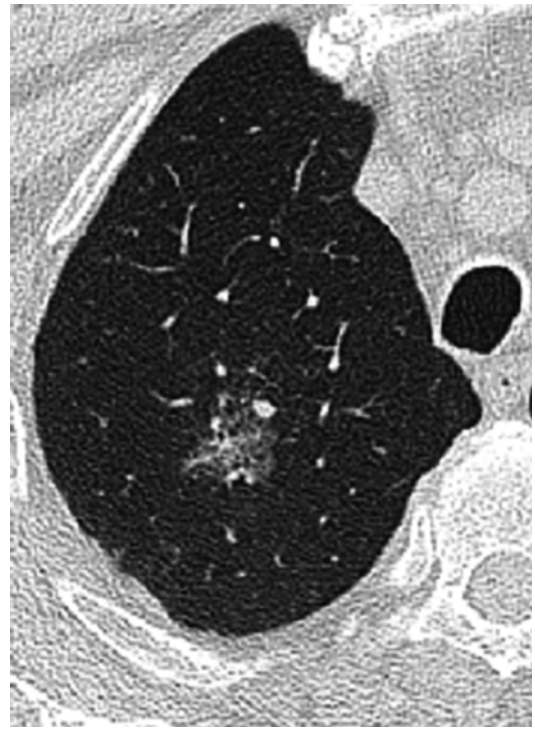

Fig. 4 CT shows amorphous subsolid nodule. This is an example of a subsolid nodule which is difficult to confidently describe as either pure ground glass or part solid. The lesion was minimally invasive adenocarcinoma on histopathology

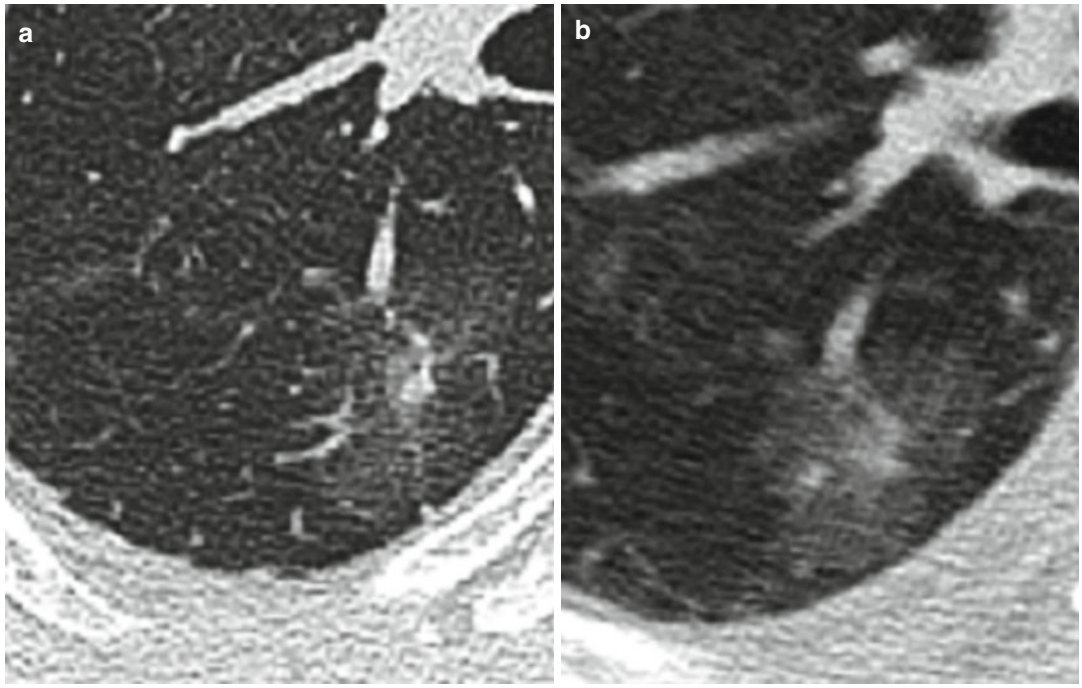

Fig. 5 (**a**) Axial thin section high-resolution CT shows part-solid nodule with small central solid component. (**b**) (Same nodule) illustrates the impact of thick section reconstruction on reliably evaluating subsolid nodules, producing blurred margins of both the solid and nonsolid component

It is also suggested that high-resolution reconstructions of 1–1.5 mm using a high-frequency algorithm are used to best identify subtle solid components in subsolid nodules.

4 Evaluating Pulmonary Nodules With Dynamic Contrast CT

The degree of enhancement of pulmonary nodules has been widely investigated as a predictor of malignancy. A growing malignant nodule needs its own blood supply which may be mediated by a release of vascular endothelial growth factor (VEGF) with a corresponding increase in microscopic vascular density (Yi et al. 2004). This feature can be exploited by measuring differences in vascularity, vessel density and blood flow patterns on CT following iodinated contrast (Ohno et al. 2014). Since the mid-1990s, several studies have focused on the Hounsfield unit (HU) cut-off value for distinguishing benign from malignant pulmonary nodules. Using a dynamic CT acquisition, usually with 1 min intervals, 15 and 20 HU have been shown to be reliable cut-offs using single-detector CT, with peak enhancement usually seen at around 2 min (Swensen et al. 1992; Swensen et al. 1995; Swensen et al. 1996; Zhang and Kono 1997; Jeong et al. 2005; Swensen et al. 2000; Yamashita et al. 1995). Swenson and co-workers found that malignant nodules showed significantly different mean peak enhancement from benign nodules (46.5 HU, range 11–100 HU versus 8 HU, range -10–94 HU); with 20 HU as a threshold, this resulted in a sensitivity of 98 % and a specificity of 73 % (Swensen et al. 1996). Interestingly, the results correlated with the degree of staining for nodule vascularity at histological analysis. A multicentre study led by the same author published in 2000 concluded that a simple approach in which the absence of significant enhancement (<15 HU) at dynamic CT is strongly predictive of benignity (sensitivity 98 %, specificity 58 %) (Swensen et al. 2000).

Since 2004, dynamic enhancement of pulmonary nodules has been evaluated with multidetector CT (Yi et al. 2004; Jeong et al. 2005) (Ohno et al. 2008). Yi et al. combined dynamic nodule contrast enhancement at 30 s intervals for 3 min using MDCT with measurement of VEGF and microvessel density. They found that a cut-off of 30 HU for net enhancement (peak attenuation in HU – pre-contrast attenuation) resulted in a sensitivity of 99 % and a specificity of 54 %. Again, expression of VEGF and microvessel density was higher in the malignant nodule group. The reason for the higher observed net enhancement values compared to earlier studies is attributed to newer CT techniques, e.g. higher volume of contrast delivery in a shorter period of time and high-speed MDCT, allowing multiple images at shorter time intervals. Other authors have described dynamic 'wash-in' and 'washout' indices on the time-attenuation curve (Jeong et al. 2005) (Ohno et al. 2013) with malignant nodules showing greater wash-in and washout. In a retrospective study of 107 nodules, a value of >25 HU during 'wash-in' (defined as the peak attenuation value in HU – non-contrast baseline value in HU) and >31 HU during absolute washout (peak attenuation value at 15 min) had the highest sensitivity, specificity and accuracy for differentiation between malignant and benign SPN. In that study, benign nodules also tended to have longer times to peak attenuation.

A few studies have evaluated dynamic first-pass perfusion of pulmonary nodules using 64 or 320 row MDCT. This can allow 'true' first-pass perfusion data to be obtained using a large-area detector that can provide continuous isotropic scanning with a reduced risk of misregistration, allowing for simultaneous qualitative and quantitative evaluation (Ohno et al. 2014). These studies resulted in an incrementally increased threshold value (likely owing to the increased speed of such systems) of 30–40 HU providing sensitivities of 86–91 % and specificities of 80–86 % for the detection of malignancy (Li et al. 2010) (Ohno et al. 2011) (Ohno et al. 2013). In one study, this technique has been shown to have a higher specificity and accuracy compared to FDG PET-CT (Ohno et al. 2013).

5 Published Guidelines for the Management of Solid and Subsolid Nodules

Lung nodule management guidelines are provided by the American College of Chest Physicians (ACCP) (in 2003, 2007 and 2013) (Gould et al. 2013; Gould et al. 2007b), by the Fleischner Society (2005 for solid nodules (MacMahon et al. 2005) and 2013 for subsolid nodules (Naidich et al. 2013)) and by the British Thoracic Society (2015) (Callister et al. 2015), and readers are directed to these individual documents for a detailed review of the specific nodule management algorithms. However, in general terms, these guidelines share a number of similarities: management recommendations are typically divided into (i) no action required or (ii) CT surveillance (with varying frequency and duration) or (iii) further investigation (e.g. PET/CT or tissue sampling). In turn these recommendations are typically based on the following parameters: (i) nodule size, (ii) nodule growth, (iii) nodule morphology and (iv) patient risk factors. While the ACCP guidelines and Fleischner guidelines for solid nodules predate much of the recent evidence discussed above, the Fleischner guidelines for subsolid nodules and the British Thoracic Society Guidelines for nodule management are able to take into account much of the recent evidence. In particular, the BTS Guidelines advocate certain policies distinct from the earlier ACCP and Fleischner guidelines. For example, a more important role for volumetry in the assessment of nodule size and growth rate and a more rigorous evaluation of patient risk factors using risk prediction tools is advocated.

References

Aberle DR, Adams AM, Berg CD, Black WC, Clapp JD, Fagerstrom RM et al (2011) Reduced lung-cancer mortality with low-dose computed tomographic screening. N Engl J Med 365(5):395–409

Ahn MI, Gleeson TG, Chan IH, McWilliams AM, Macdonald SL, Lam S et al (2010) Perifissural nodules seen at CT screening for lung cancer. Radiology 254(3):949–956

Baldwin DR, Duffy SW, Wald NJ, Page R, Hansell DM, Field JK (2011) UK Lung Screen (UKLS) nodule management protocol: modelling of a single screen randomised controlled trial of low-dose CT screening for lung cancer. Thorax 66(4):308–313

Barrett TW, Schierling M, Zhou C, Colfax JD, Russ S, Conatser P et al (2009) Prevalence of incidental findings in trauma patients detected by computed tomography imaging. Am J Emerg Med 27(4):428–435

Bartholmai BJ, Koo CW, Johnson GB, White DB, Raghunath SM, Rajagopalan S et al (2015) Pulmonary nodule characterization, including computer analysis and quantitative features. J Thorac Imaging 30(2):139–156

Callister ME, Baldwin DR, Akram A, Bardard S, Cane P, Draffan J, Franks K (2015) British thoracic society guidelines for the investigation and management of pulmonary nodules. Thorax 70 Suppl 2:ii1–ii54

Chae HD, Park CM, Park SJ, Lee SM, Kim KG, Goo JM (2014) Computerized texture analysis of persistent part-solid ground-glass nodules: differentiation of preinvasive lesions from invasive pulmonary adenocarcinomas. Radiology 273(1):285–293

de Hoop B, Gietema H, Van de Vorst S, Murphy K, van Klaveren RJ, Prokop M (2010) Pulmonary ground-glass nodules: increase in mass as an early indicator of growth. Radiology 255(1):199–206

de Hoop B, van Ginneken B, Gietema H, Prokop M (2012) Pulmonary perifissural nodules on CT scans: rapid growth is not a predictor of malignancy. Radiology 265(2):611–616

Detterbeck FC, Gibson CJ (2008) Turning gray: the natural history of lung cancer over time. J Thorac Oncol 3(7):781–792

Diederich S, Hansen J, Wormanns D (2005) Resolving small pulmonary nodules: CT features. Eur Radiol 15(10):2064–2069

Gierada DS, Pinsky P, Nath H, Chiles C, Duan F, Aberle DR (2014). Projected outcomes using different nodule sizes to define a positive CT lung cancer screening examination. J Natl Cancer Inst. 106(11):284.

Gomez-Saez N, Gonzalez-Alvarez I, Vilar J, Hernandez-Aguado I, Domingo ML, Lorente MF et al (2014) Prevalence and variables associated with solitary pulmonary nodules in a routine clinic-based population: a cross-sectional study. Eur Radiol 24(9):2174–2182

Gould MK, Ananth L, Barnett PG, Veterans Affairs SCSG (2007a) A clinical model to estimate the pretest probability of lung cancer in patients with solitary pulmonary nodules. Chest 131(2):383–388

Gould MK, Fletcher J, Iannettoni MD, Lynch WR, Midthun DE, Naidich DP et al (2007b) Evaluation of patients with pulmonary nodules: when is it lung cancer?: ACCP evidence-based clinical practice guidelines (2nd edition). Chest 132(3 Suppl):108S–130S

Gould MK, Donington J, Lynch WR, Mazzone PJ, Midthun DE, Naidich DP et al (2013) Evaluation of individuals with pulmonary nodules: when is it lung cancer? diagnosis and management of lung cancer, 3rd ed: american college of chest physicians evidence-based clinical practice guidelines. Chest 143(5 Suppl): e93S–e120S

Hansell DM, Bankier AA, MacMahon H, McLoud TC, Muller NL, Remy J (2008) Fleischner society: glossary of terms for thoracic imaging. Radiology 246(3): 697–722

Harders SW, Madsen HH, Rasmussen TR, Hager H, Rasmussen F (2011) High resolution spiral CT for determining the malignant potential of solitary pulmonary nodules: refining and testing the test. Acta Radiol 52(4):401–409

Henschke CI, Yankelevitz DF, Yip R, Reeves AP, Farooqi A, Xu D et al (2012) Lung cancers diagnosed at annual CT screening: volume doubling times. Radiology 263(2):578–583

Horeweg N, van Rosmalen J, Heuvelmans MA, van der Aalst CM, Vliegenthart R, Scholten ET et al (2014) Lung cancer probability in patients with CT-detected pulmonary nodules: a prespecified analysis of data from the NELSON trial of low-dose CT screening. Lancet Oncol 15(12):1332–1341

Hyodo T, Kanazawa S, Dendo S, Kobayashi K, Hayashi H, Kouno Y et al (2004) Intrapulmonary lymph nodes: thin-section CT findings, pathological findings, and CT differential diagnosis from pulmonary metastatic nodules. Acta Med Okayama 58(5):235–240

Ikeda K, Awai K, Mori T, Kawanaka K, Yamashita Y, Nomori H (2007) Differential diagnosis of ground-glass opacity nodules: CT number analysis by three-dimensional computerized quantification. Chest 132(3): 984–990

Ishikawa H, Koizumi N, Morita T, Tani Y, Tsuchida M, Umezu H et al (2005) Ultrasmall pulmonary opacities on multidetector-row high-resolution computed tomography: a prospective radiologic-pathologic examination. J Comput Assist Tomogr 29(5):621–625

Jeong YJ, Lee KS, Jeong SY, Chung MJ, Shim SS, Kim H et al (2005) Solitary pulmonary nodule: characterization with combined wash-in and washout features at dynamic multi-detector row CT. Radiology 237(2): 675–683

Kazerooni EA, Armstrong MR, Amorosa JK, Hernandez D, Liebscher LA, Nath H et al (2015) ACR CT accreditation program and the lung cancer screening program designation. J Am Coll Radiol 12(1):38–42

Kim HY, Shim YM, Lee KS, Han J, Yi CA, Kim YK (2007) Persistent pulmonary nodular ground-glass opacity at thin-section CT: histopathologic comparisons. Radiology 245(1):267–275

Lee HY, Lee KS (2011) Ground-glass opacity nodules histopathology, imaging evaluation, implications. J Thorac Imaging 26(2):106–118

Lee SM, Park CM, Goo JM, Lee HJ, Wi JY, Kang CH (2013) Invasive pulmonary adenocarcinomas versus preinvasive lesions appearing as ground-glass nodules: differentiation by using CT features. Radiology 268(1):265–273

Lee HY, Choi YL, Lee KS, Han J, Zo JI, Shim YM et al (2014) Pure ground-glass opacity neoplastic lung

nodules: histopathology, imaging, and management. AJR Am J Roentgenol 202(3):W224–W233

Li F, Aoyama M, Shiraishi J, Abe H, Li Q, Suzuki K et al (2004) Radiologists' performance for differentiating benign from malignant lung nodules on high-resolution CT using computer-estimated likelihood of malignancy. AJR Am J Roentgenol 183(5):1209–1215

Li Y, Yang ZG, Chen TW, Yu JQ, Sun JY, Chen HJ (2010) First-pass perfusion imaging of solitary pulmonary nodules with 64-detector row CT: comparison of perfusion parameters of malignant and benign lesions. Br J Radiol 83(993):785–790

Lim HJ, Ahn S, Lee KS, Han J, Shim YM, Woo S et al (2013) Persistent pure ground-glass opacity lung nodules >/= 10 mm in diameter at CT scan: histopathologic comparisons and prognostic implications. Chest 144(4):1291–1299

MacMahon H, Austin JH, Gamsu G, Herold CJ, Jett JR, Naidich DP et al (2005) Guidelines for management of small pulmonary nodules detected on CT scans: a statement from the fleischner society. Radiology 237(2):395–400

McWilliams A, Tammemagi MC, Mayo JR, Roberts H, Liu G, Soghrati K et al (2013) Probability of cancer in pulmonary nodules detected on first screening CT. N Engl J Med 369(10):910–919

Naidich DP, Bankier AA, MacMahon H, Schaefer-Prokop CM, Pistolesi M, Goo JM et al (2013) Recommendations for the management of subsolid pulmonary nodules detected at CT: a statement from the fleischner society. Radiology 266(1):304–317

Noguchi M, Morikawa A, Kawasaki M, Matsuno Y, Yamada T, Hirohashi S et al (1995) Small adenocarcinoma of the lung. Histologic characteristics and prognosis. Cancer 75(12):2844–2852

Oda S, Awai K, Liu D, Nakaura T, Yanaga Y, Nomori H et al (2008) Ground-glass opacities on thin-section helical CT: differentiation between bronchioloalveolar carcinoma and atypical adenomatous hyperplasia. AJR Am J Roentgenol 190(5):1363–1368

Oh JY, Kwon SY, Yoon HI, Lee SM, Yim JJ, Lee JH et al (2007) Clinical significance of a solitary ground-glass opacity (GGO) lesion of the lung detected by chest CT. Lung Cancer 55(1):67–73

Ohno Y, Koyama H, Takenaka D, Nogami M, Maniwa Y, Nishimura Y et al (2008) Dynamic MRI, dynamic multidetector-row computed tomography (MDCT), and coregistered 2-[fluorine-18]-fluoro-2-deoxy-D-glucose-positron emission tomography (FDG-PET)/CT: comparative study of capability for management of pulmonary nodules. J Magn Reson Imaging 27(6):1284–1295

Ohno Y, Koyama H, Matsumoto K, Onishi Y, Takenaka D, Fujisawa Y et al (2011) Differentiation of malignant and benign pulmonary nodules with quantitative first-pass 320-detector row perfusion CT versus FDG PET/CT. Radiology 258(2):599–609

Ohno Y, Nishio M, Koyama H, Fujisawa Y, Yoshikawa T, Matsumoto S et al (2013) Comparison of quantitatively analyzed dynamic area-detector CT using various mathematic methods with FDG PET/CT in management of solitary pulmonary nodules. AJR Am J Roentgenol 200(6):W593–W602

Ohno Y, Nishio M, Koyama H, Seki S, Tsubakimoto M, Fujisawa Y et al (2014) Solitary pulmonary nodules: comparison of dynamic first-pass contrast-enhanced perfusion area-detector CT, dynamic first-pass contrast-enhanced MR imaging, and FDG PET/CT. Radiology 132289

Oshiro Y, Kusumoto M, Moriyama N, Kaneko M, Suzuki K, Asamura H et al (2002) Intrapulmonary lymph nodes: thin-section CT features of 19 nodules. J Comput Assist Tomogr 26(4):553–557

Park CM, Goo JM, Lee HJ, Lee CH, Kim HC, Chung DH et al (2006) CT findings of atypical adenomatous hyperplasia in the lung. Korean J Radiol 7(2):80–86

Revel MP, Bissery A, Bienvenu M, Aycard L, Lefort C, Frija G (2004) Are two-dimensional CT measurements of small noncalcified pulmonary nodules reliable? Radiology 231(2):453–458

Scholten ET, de Jong PA, de Hoop B, van Klaveren R, van Amelsvoort-van de Vorst S, Oudkerk M et al (2015) Towards a close computed tomography monitoring approach for screen detected subsolid pulmonary nodules? Eur Respir J 45(3):765–773

Shaham D, Vazquez M, Bogot NR, Henschke CI, Yankelevitz DF (2010) CT features of intrapulmonary lymph nodes confirmed by cytology. Clin Imaging 34(3):185–190

Silva M, Sverzellati N, Manna C, Negrini G, Marchiano A, Zompatori M et al (2012) Long-term surveillance of ground-glass nodules: evidence from the MILD trial. J Thorac Oncol 7(10):1541–1546

Son JY, Lee HY, Lee KS, Kim JH, Han J, Jeong JY et al (2014) Quantitative CT analysis of pulmonary ground-glass opacity nodules for the distinction of invasive adenocarcinoma from pre-invasive or minimally invasive adenocarcinoma. PLoS One 9(8), e104066

Swensen SJ, Morin RL, Schueler BA, Brown LR, Cortese DA, Pairolero PC et al (1992) Solitary pulmonary nodule: CT evaluation of enhancement with iodinated contrast material--a preliminary report. Radiology 182(2):343–347

Swensen SJ, Brown LR, Colby TV, Weaver AL (1995) Pulmonary nodules: CT evaluation of enhancement with iodinated contrast material. Radiology 194(2):393–398

Swensen SJ, Brown LR, Colby TV, Weaver AL, Midthun DE (1996) Lung nodule enhancement at CT: prospective findings. Radiology 201(2):447–455

Swensen SJ, Viggiano RW, Midthun DE, Muller NL, Sherrick A, Yamashita K et al (2000) Lung nodule enhancement at CT: multicenter study. Radiology 214(1):73–80

Swensen SJ, Jett JR, Hartman TE, Midthun DE, Sloan JA, Sykes AM et al (2003) Lung cancer screening with CT: mayo clinic experience. Radiology 226(3): 756–761

Takenaka M, Uramoto H, Shimokawa H, So T, Hanagiri T, Aoki T et al (2013) Discriminative features of thin-slice computed tomography for peripheral intrapulmonary lymph nodes. Asian J Surg 36(2):69–73

Travis WD, Brambilla E, Noguchi M, Nicholson AG, Geisinger KR, Yatabe Y et al (2011) International association for the study of lung cancer/american thoracic society/european respiratory society international multidisciplinary classification of lung adenocarcinoma. J Thorac Oncol 6(2):244–285

van Klaveren RJ, Oudkerk M, Prokop M, Scholten ET, Nackaerts K, Vernhout R et al (2009) Management of lung nodules detected by volume CT scanning. N Engl J Med 361(23):2221–2229

Wang CW, Teng YH, Huang CC, Wu YC, Chao YK, Wu CT (2013) Intrapulmonary lymph nodes: computed tomography findings with histopathologic correlations. Clin Imaging 37(3):487–492

Wood DE, Kazerooni E, Baum SL, Dransfield MT, Eapen GA, Ettinger DS et al (2015) Lung cancer screening, version 1.2015: featured updates to the NCCN guidelines. J Natl Compr Canc Netw 13(1):23–34, quiz

Xu DM, van Klaveren RJ, de Bock GH, Leusveld A, Zhao Y, Wang Y et al (2008) Limited value of shape, margin and CT density in the discrimination between benign and malignant screen detected solid pulmonary nodules of the NELSON trial. Eur J Radiol 68(2): 347–352

Xu DM, van der Zaag-Loonen HJ, Oudkerk M, Wang Y, Vliegenthart R, Scholten ET et al (2009) Smooth or attached solid indeterminate nodules detected at baseline CT screening in the NELSON study: cancer risk during 1 year of follow-up. Radiology 250(1):264–272

Yamashita Y, Torashima M, Takahashi M, Mizutani H, Miyazaki K, Matsuura K et al (1995) Contrast-enhanced dynamic MR imaging of postmolar gestational trophoblastic disease. Acta Radiol 36(2): 188–192

Yi CA, Lee KS, Kim EA, Han J, Kim H, Kwon OJ et al (2004) Solitary pulmonary nodules: dynamic enhanced multi-detector row CT study and comparison with vascular endothelial growth factor and microvessel density. Radiology 233(1):191–199

Zhang M, Kono M (1997) Solitary pulmonary nodules: evaluation of blood flow patterns with dynamic CT. Radiology 205(2):471–478

Staging of Lung Cancer

James G. Ravenel

Abstract

Despite decline in smoking rates, lung cancer remains the leading cause of cancer-related deaths with an estimated 224,000 new cases in 2014 (Siegel et al., CA Cancer J Clin 64:9–29, 2014). Tobacco remains the major causative agent, and as smoking behaviors between men and women have evolved, the gap in lung cancer between males and females has narrowed (Thun and Jemal, Tob Control 15:345–347, 2006). Approximately one in four lung cancers occur in never smokers (Pallis and Syrigos, Crit Rev Oncol Hematol 88:494–503, 2013). Other environmental risks for lung cancer include radon, occupational exposure, and air pollution. In addition to the environmental risks described previously, there does appear to be a component of both hormonal and genetic susceptibility to lung cancer development (Pallis and Syrigos, Crit Rev Oncol Hematol 88:494–503, 2013; Matakidou et al., Br J Cancer 93:825–833, 2005).

Following diagnosis, it is imperative to assess prognosis, optimize treatment, as well as avoid potentially harmful of futile treatments. In order to accomplish this, one must have knowledge of the tumor stage, histology, and molecular characteristics. To a great extent, this is accomplished using CT and integrated PET/CT. Using these tools, a clinical stage can be determined, and the most appropriate site for histologic and molecular diagnosis can be identified which in turn allows for confirmation of pathological stage and planning the most appropriate treatment.

In this chapter, the role of CT in the staging and follow-up of lung cancer is discussed.

1 CT Findings of Lung Cancer

Lung cancers are grouped based on histologic subtypes with the most common histologies being adenocarcinoma, squamous cell carcinoma, large cell carcinoma (sometimes grouped

J.G. Ravenel, MD
Department of Radiology and Radiological Science,
Medical University of South Carolina,
96 Jonathan Lucas St MSC 323,
Charleston, SC 29425, USA
e-mail: ravenejg@musc.edu

U.J. Schoepf, F.G. Meinel (eds.), *Multidetector-Row CT of the Thorax*, Medical Radiology,
DOI 10.1007/978-3-319-30355-0_11

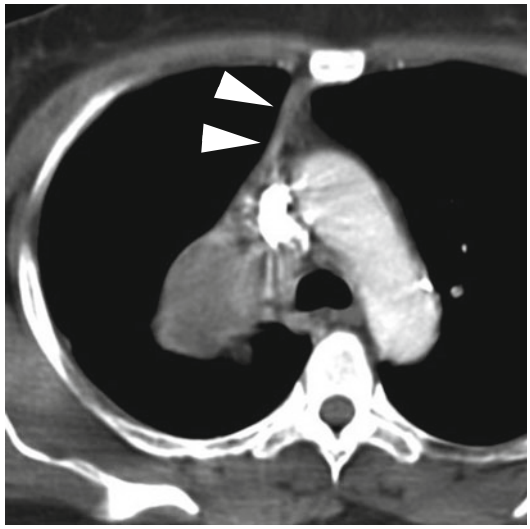

Fig. 1 Central right upper lobe neoplasm resulting in right upper lobe anterior segmental atelectasis (*arrowheads*)

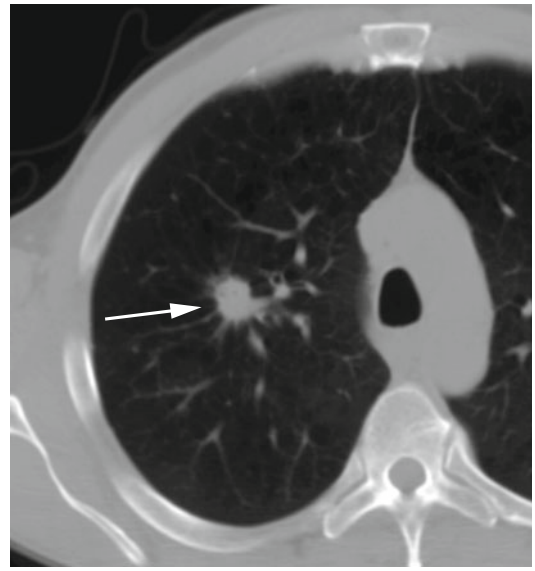

Fig. 2 Peripheral lung cancer (*arrow*)

as non-small cell carcinoma), and small cell carcinoma. In addition, molecular markers are becoming of great significance in determining whether specific targeted treatment agents are appropriate. Biopsy specimens must provide sufficient tissue to determine cancer subtype as well as stain for a battery of molecular markers.

Lung cancers may be divided loosely into central and peripheral tumors, with central lesions slightly more common. Central tumors may be more difficult to discretely measure as they can result in post-obstructive atelectasis and/or pneumonitis (Fig. 1). Clues to the presence of a central tumor when one cannot be discretely visualized include convex contour of the fissure near the hilum, volume expansion of a consolidated lobe, and visible mucus bronchograms (Woodring 1988). Peripheral lung cancers arise distal to the segmental bronchi and are often characterized as a nodule or mass with lobulated and/or spiculated borders (Fig. 2). Calcification is unusual and may result from an engulfed calcified granuloma or dystrophic calcification (Zerhouni et al. 1986). Cavitation when identified is often associated with an eccentrically thick, irregular wall.

On occasion, CT will provide clues that suggest a particular histologic subtype. For example, a cavitary lung cancer favors a diagnosis of squamous cell carcinoma (Fig. 3). Nodules that have a ground glass component are most often adenocarcinoma (Aquino et al. 2007). Moreover, the extent of ground glass opacity is generally related to the aggressiveness of the lesion. The greater the extent of ground glass opacity, the more indolent the lesion (Aoki et al. 2000, 2001; Kim et al. 2001; Kuriyama et al. 1999). When neoplastic, pure ground glass nodules are typically atypical adenomatous hyperplasia or in situ adenocarcinoma (Nakata et al. 2002).

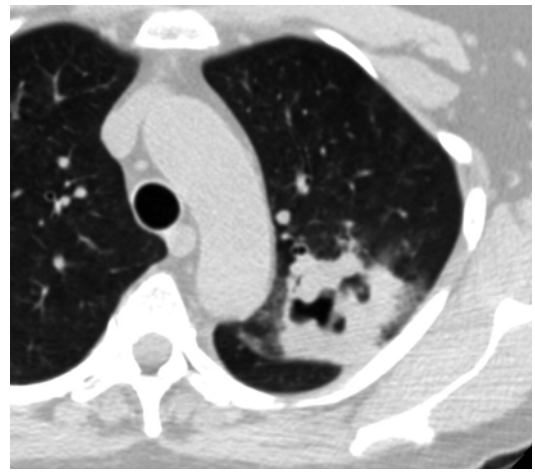

Fig. 3 Squamous cell carcinoma. Axial image reveals cavitary mass in left upper lobe

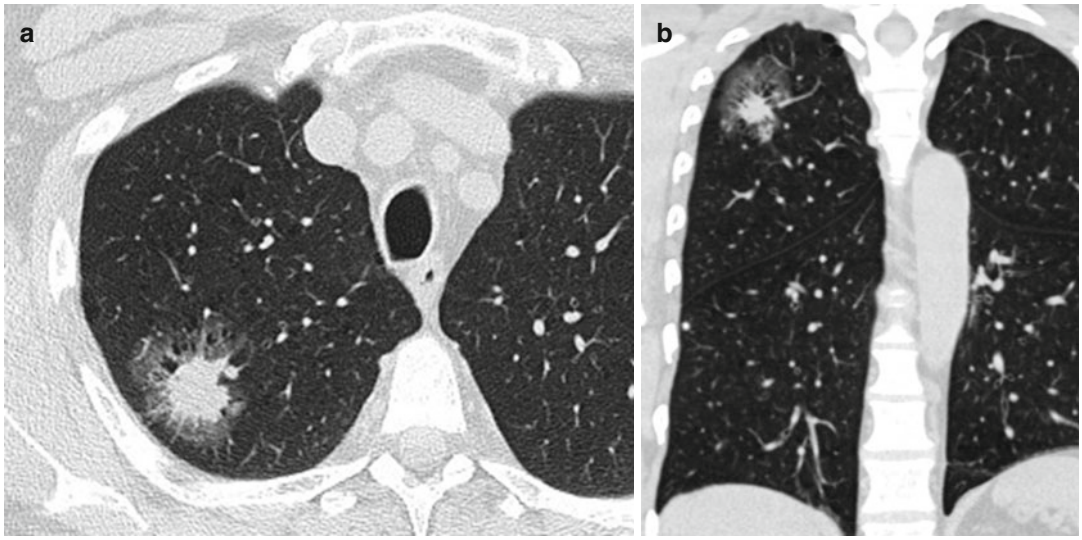

Fig. 4 Adenocarcinoma. Axial (**a**) and coronal (**b**) images of part-solid nodule with bubble-like lucencies in the ground glass component

The spectrum of low-grade adenocarcinoma is complex often requiring resection of the entire lesion to exclude an invasive component (Travis et al. 2005). When targeting lesion for biopsy, it is critical to sample the solid core which is most likely to harbor invasive tumors. Nodules may have a variety of appearances including lobulated or spiculated borders, pleural tags, air bronchograms, and internal lucencies (pseudocavitation) (Patsios et al. 2007) (Fig. 4). The ground glass opacity histologically reflects the lepidic tumor growth with or without alveolar collapse (Lee et al. 2004), while the lucencies presumably reflect either uninvolved lobules or focal air trapping with bronchiolar obstruction (Gaeta et al. 1999; Weisbrod et al. 1992). While a solid component may simply reflect alveolar collapse, it is more likely to represent areas of fibroblast proliferation or invasive adenocarcinoma (Gandara et al. 2006). On rare occasions, tumor growth may occur purely as lepidic growth and present as multifocal air-space disease (Fig. 5).

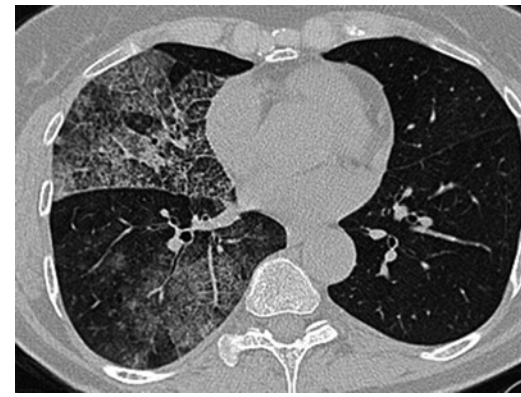

Fig. 5 Lepidic growth pattern. Axial CT image reveals mixed ground glass opacity and interlobular septal thickening in right middle and lower lobes

2 NSCLC Staging

CT is the initial means for anatomic staging including detection of mediastinal disease and limited detection of extrathoracic disease. Rather than being truly diagnostic, CT also sets the stage for determining the most appropriate sites for biopsy, preferably choosing a site that can encompass not only the diagnosis but also confirm highest stage of disease. Staging is generally completed by performing PET/CT with MR or CT of the brain when necessary.

Staging is categorized by the TNM system, which is accepted by the American Joint Committee on Cancer (AJCC) (Mountain 1997). Components of tumor staging include the primary

Table 1 Staging of lung cancer-TNM descriptors

Primary lesion
T0 – no evidence of primary tumor
Tis – carcinoma in situ
T1 – tumor < 3 cm surrounded by lung or visceral pleura without invasion proximal to lobar bronchus
1a- < 2 cm
1b- > 2–3 cm
T2 – tumors > 3 cm; any tumor invading main bronchi but >2 cm from the carina; invasion of visceral pleura; obstructive pneumonitis extending to hila but does not involve the entire lung
2a- > 3–5 cm
2b- >5–7 cm
T3 – tumor > 7 cm. Tumor of any size that directly invades chest wall, diaphragm, mediastinal pleura, or parietal pericardium; involves main bronchus within 2 cm of the carina, but does not involve the carina; or results in obstructive atelectasis or pneumonitis of the entire lung. Separate nodule (s) in same lobe
T4 – tumor invades any of the following: the mediastinum, heart great vessels, trachea, esophagus, vertebral body, or carina; malignant ipsilateral pleural or pericardial effusion; separate nodule(s) in a different ipsilateral lobe
Lymph nodes
N0 – no regional lymph node metastases
N1 – spread to ipsilateral peribronchial or hilar nodes
N2 – spread to ipsilateral mediastinal or subcarinal nodes
N3 – spread to contralateral mediastinal or hilar nodes, scalene nodes, and supraclavicular nodes
Distant disease
M0 – no distant metastases
M1 – distant metastases present
M1a – separate tumor nodule in contralateral lung, pleural nodules, and malignant pleural or pericardial effusion
M1b – all other distant metastasis

Table 2 Staging of lung cancer based on TNM classification

0 – carcinoma in situ
1A – T1N0M0
1B – T2aN0M0
2A – T2bN0M0
T1N1M0
T2aN1M0
2B – T2bN1M0
T3N0M0
3A – T3N1M0
T1-3N2M0
T4N0-1 M0
3B – T4N2M0
Any N3
4 – Any M1

lesion (T), lymph node involvement (N), and metastatic disease (M) (Tables 1 and 2).

2.1 T-Stage

T-stage is based upon size and local extension of the primary lesion. The use of intravenous (IV) contrast can be useful in showing the relationship to vascular structures but does not show clear superiority in staging (Cascade et al. 1998; Haramati et al. 1995; Patz et al. 1999). The use of IV contrast is therefore best determined based on the radiographic findings, risks of contrast administration, and preference of the interpreting physician. For all tumors, relationships to the pulmonary artery, lobar fissures, and incomplete fissures are important when considering a surgical approach (Munden et al. 2005). The CT-based findings contribute to the pretreatment clinical stage and may be modified based on pathologic findings.

T1 tumors are less than 3 cm in maximal diameter and do not invade the visceral pleura or main stem bronchi (Fig. 6). For peripheral tumors, the confirmation of the presence or absence of visceral pleura invasion is not possible radiographically without clear chest wall invasion. Fortunately, this distinction is not critical for the initial management of the patient. T1 tumors can be further divided by size into T1a (<2 cm) and T1b (≥2 cm <3 cm).

T2 tumors are greater than 3 cm and <7 cm in maximal diameter and also include tumors less than 3 cm that involve the visceral pleura or main stem bronchi greater than 2 cm from the carina (Fig. 7). T2 tumors can be further subdivided into T2a (≥3 cm <5 cm) and T2b (≥5 cm <7 cm).

T3 tumors are either ≥7 cm in maximal diameter or invade the chest wall, diaphragm, mediastinal pleura, parietal pericardium, or main bronchus within 2 cm but not involving the carina. In addition, tumors with satellite nodules

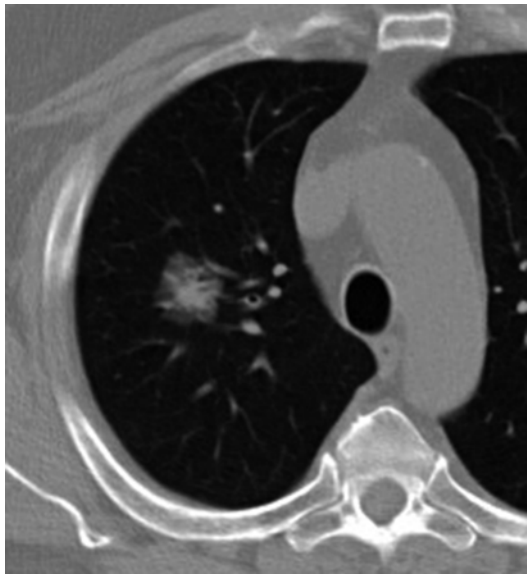

Fig. 6 T1 lung cancer. Axial CT reveals part-solid nodule measuring 1.8 cm

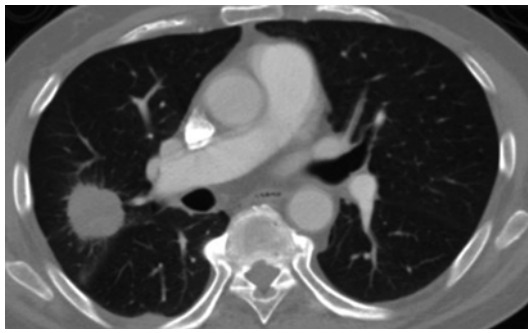

Fig. 7 T2 lung cancer. Axial CT reveals solid spiculated nodule measuring 3.5 cm

in the same tumor lobe are included as T3 tumors. Direct findings of chest wall involvement are present when bone erosion or invasion is present (Fig. 8). Other helpful findings include greater than 3 cm of contact with the pleural surface, pleural thickening, absent fat planes, and obtuse angle of tumor with the chest wall (Glazer et al. 1985a). It should be noted that localized chest pain remains a better predictor of chest wall invasion (Glazer et al. 1985a). The use of thin collimation with coronal and sagittal reformation improves the ability to reliably detect chest wall involvement (Higashino et al. 2005).

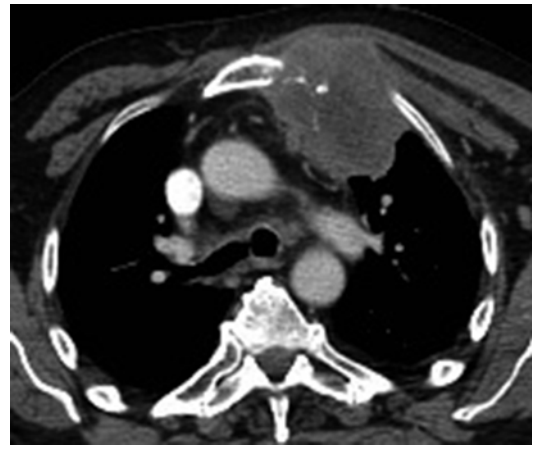

Fig. 8 T3 lung cancer. Axial contrast-enhanced CT reveals left upper lobe mass invading anterior chest wall with erosion of the sternum

T4 tumors are tumors of any size which invade vital anatomy such as the heart, great vessels, esophagus, trachea, or vertebral body (Figs. 9 and 10). Satellite suspicious nodules within the same lung but in a different lobe are also classified as T4 for staging purposes. While a T4 designation generally renders a patient inoperable, in certain circumstances, complete surgical resection may be feasible (Munden et al. 2005). These circumstances may include limited invasion of a vertebral body, the carina, and ipsilateral satellite nodules (Bruzzi et al. 2008). Surgery is contraindicated by local extension when the brachial plexus is involved above the level of T1, more than 50 % of a vertebral is invaded, or when there is invasion of the trachea or esophagus. MR is superior to CT for detection of involvement of the neural foramina, spinal canal, and brachial plexus and should be considered for superior sulcus tumors when a surgical approach is contemplated (Bruzzi et al. 2008). In cases where a tumor abuts but does not clearly invade vital structures, surgical exploration may be necessary to determine resectability.

2.2 N-Stage

N-stage is defined by the presence or absence of enlarged lymph nodes (>1 cm short axis diameter)

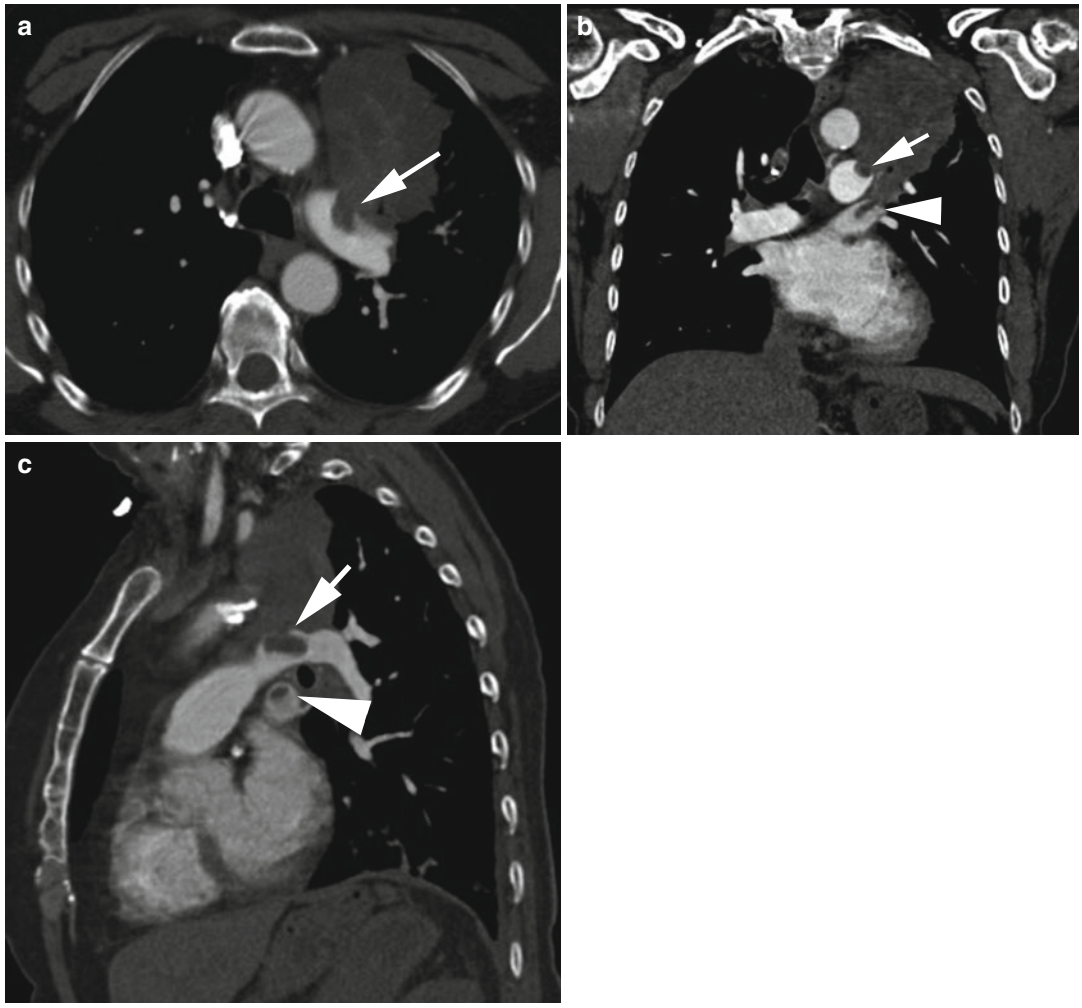

Fig. 9 T4 lung cancer. Axial (**a**), coronal (**b**), and sagittal (**c**) contrast-enhanced CT reveals left upper lobe mass with direct invasion of the left pulmonary artery (*arrow*) and tumor thrombus in the left superior pulmonary vein (*arrowhead*)

(Glazer et al. 1985b) (Fig. 11). While the individual nomenclature is defined by the IASLC lymph node map (Rusch et al. 2009), the most important determinant is the relationship to the primary tumor. N1 lymph nodes are defined as ipsilateral intrapulmonary, peribronchial, and hilar lymph nodes. N2 lymph nodes are defined as ipsilateral mediastinal nodes, including lymph nodes in the midline. N3 nodes include those contralateral to the primary tumor or involve the scalene or supraclavicular nodal stations. Abnormal lymph nodes distant to these sites are generally considered as metastatic disease (M-stage).

As size is the main criteria for malignancy, CT is relatively inaccurate for staging the mediastinum. While lymph nodes of any size may harbor malignancy, the chance that a node is malignant is clearly influenced by size. The prevalence of metastatic disease in lymph nodes is approximately 30 % for nodes 10–15 mm in size and 67 % for nodes >15 mm in size (de Langen et al. 2006). Among 43 studies conducted from 1991 to 2005, the sensitivities of CT for nodal disease ranged from 26 to 86 % and specificity ranged from 31 to 97 % with a pooled sensitivity, and specificity from a total of 5,111 patients in whom

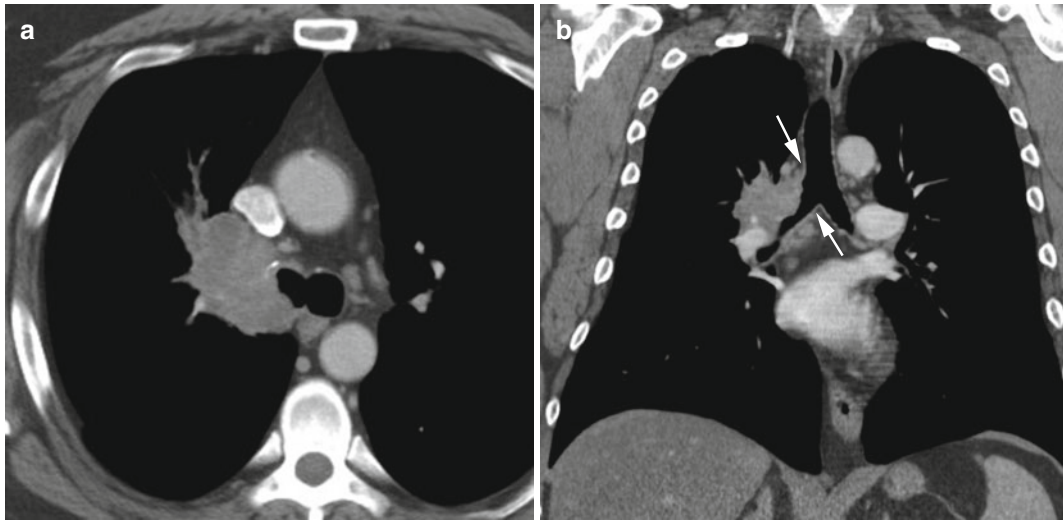

Fig. 10 T4 lung cancer. Axial (**a**) and coronal (**b**) CT reveal right hilar mass with involvement of right main bronchus, carina, and distal right tracheal sidewall (*arrows*)

prevalence of nodal disease was 28 % was 51/86 %(Silvestri et al. 2007). Thus, the presence of adenopathy should not be based on size alone, and lymph node sampling is critical to defining mediastinal adenopathy. In this regard, CT is a road map for interpreting 18 F-FDG PET studies and selection of the most appropriate pathway for biopsy.

Combining lymph node size with metabolic activity is quite helpful (Kelly et al. 2004; Gould et al. 2003). For lymph nodes greater than 1 cm, sensitivity of 18 F-FDG PET approaches 100 % but specificity decreases (~78 %), while for lymph nodes less than 1 cm, 18 F-FDG PET has a lower sensitivity (82 %) but higher specificity (93 %) (Gould et al. 2003). The likelihood of malignancy for PET-negative nodes 10–15 mm in short axis is 5 % and for nodes greater than 15 mm, 21 %. For PET-positive nodes, the likelihood of malignancy in a 10–15 mm lymph node is 62 % and 90 % when >15 mm (de Langen et al. 2006).

The site of the primary lesion can be useful in predicting the most likely site for nodal metastases. Right upper lobe tumors most often drain to right paratracheal nodes, while right middle and lower lobe tumors most frequently drain to lower right paratracheal and subcarinal nodes. Left upper lobe tends to go to the AP window and prevascular regions, while left lower tumors favor the prevascular and subcarinal stations (Cerfolio and Bryant 2006). Superior segment of the lower lobe tumors tends to have similar drainage patterns as upper lobe tumors (Watanabe et al. 2008).

2.3 M-Stage

The initial staging CT may provide insights into possible sites of metastatic disease, but this is ultimately defined by PET/CT. M-stage is defined by the absence (M0) or presence (M1) of distant metastasis and can be subdivided into M1a-malignant pleural effusion and M1b other distant metastases. In the absence of clinical signs or symptoms, the negative predictive value for metastatic disease is 95 % for the liver, brain, and adrenal gland and 90 % for the bone (Silvestri et al. 1995, 2003). This should be kept in mind when interpreting incidental findings on staging CT. When only a single site of metastatic disease is suspected, the diagnosis must be confirmed by histology regardless of CT and PET/CT results. Sites that may be assessed on the initial CT include the pleura, adrenal gland, liver, and bone.

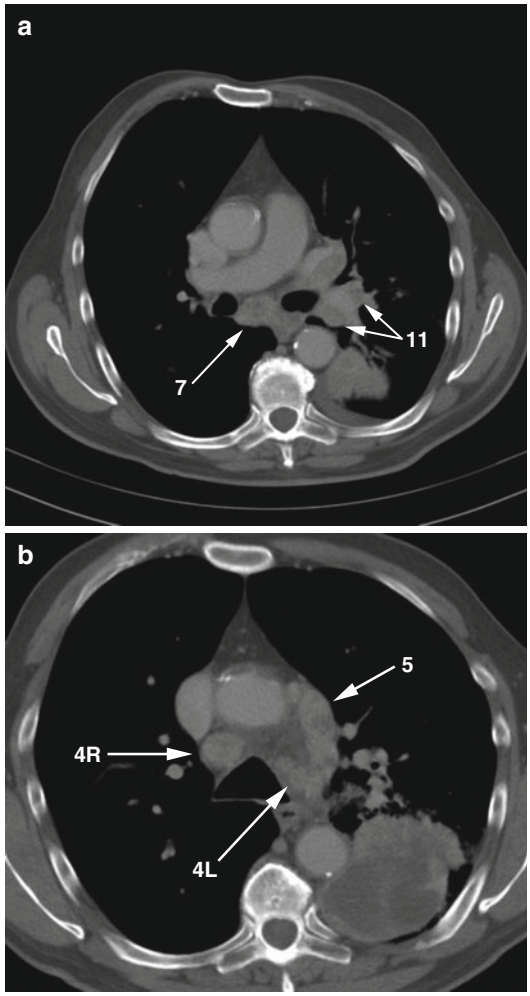

Fig. 11 Mediastinal adenopathy. Axial contrast-enhanced CT reveals left lower lobe neoplasm with N1 (11) lymph nodes, N2 (4L, 6, 7) lymph nodes, and N3 (4R) lymph nodes

2.3.1 Pleural Metastasis

Pleural effusions are not uncommon in patients with lung cancer and are not necessarily due to the presence of malignant disease in the pleural space. Malignant pleural effusions are by definition those with tumor cells in the pleural space and should be suspected with exudative effusions in the setting of lung cancer. Rarely, a transudative effusion may be malignant (3–10 %) (Heffner and Klein 2008). Alternative causes of pleural effusion in lung cancer include paramalignant effusion due to central venous or lymphatic obstruction or post-obstructive atelectasis/pneumonitis (American Thoracic Society 2000) as well as effusions unrelated to the tumor such as heart, kidney, or liver disease. CT findings that should raise suspicion for a malignant effusion include parietal pleural thickness >1 cm, circumferential pleural thickening, discrete pleural nodules, and involvement of mediastinal pleura (Heffner and Klein 2008) (Fig. 12).

2.3.2 Adrenal Metastasis

Adrenal nodules are a common incidental finding in the general population (4–10 %), and thus even in patients with lung cancer, the majority of these lesions represent benign disease (Boland et al. 2008). When the initial study is performed without intravenous contrast, a density measurement of <10 HU virtually assures the diagnosis of benign adenoma (Boland et al. 1998). Those with a density >10 HU are considered indeterminate and need to be correlated with PET/CT. Unfortunately, on contrast-enhanced CT, both benign and malignant lesions invariably exceed the threshold of 10 HU.

2.3.3 Liver Metastasis

The liver is rarely the sole site of metastatic disease at time of diagnosis, occurring in approximately 3 % of cases (Kagohashi et al. 2003), and thus the vast majority of isolated hepatic lesions detected during the evaluation of lung cancer are benign cysts or hemangiomas. In difficult cases, MR and/or biopsy should be used for confirmation.

2.3.4 Bone Metastasis

Bone metastases may appear as lytic or destructive lesions or as regional areas of sclerosis. As most patients with bone metastases have symptoms or elevated alkaline phosphatase, clinical information can be quite helpful in determining the significance of a detected bone lesion.

Review of osseous structures with "bone" window and level settings frequently allows for the detection of metastases. CT may also help limit false-positive PET/CT or bone scintigraphy studies by confirming degenerative changes or occult non-pathologic fractures.

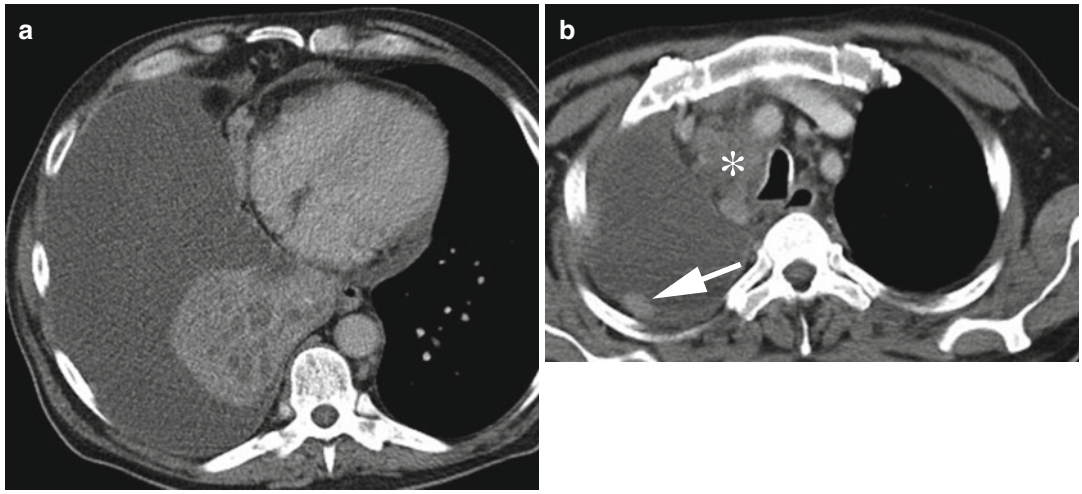

Fig. 12 Malignant effusion. Axial contrast-enhanced CT images at (**a**) lung base and (**b**) thoracic inlet reveal large right pleural effusion occupying entire right hemithorax and resulting in collapse of left lung with associated nodule along the parietal pleura (*arrow*) and mediastinal adenopathy (*)

2.3.5 Brain Metastasis

In the absence of neurological symptoms, cerebral metastases are found in less than 10 %(Cole et al. 1994; Colice et al. 1995; Ferrigno and Buccheri 1994).

Features on chest CT that suggest the need for brain imaging (preferably MR) in asymptomatic patients include T2 tumors and patients with mediastinal adenopathy (Mujoomdar et al. 2007). Adenocarcinoma and large cell carcinoma histology can also be associated with asymptomatic cerebral metastases (Mintz et al. 1984).

3 Imaging of Small Cell Lung Cancer

In the current staging paradigm, small cell carcinomas (SCLC) are staged by the same criteria as non-small cell carcinoma (Vallieres et al. 2009); however, practically speaking, the two-stage system developed by the Veterans Administration Lung Cancer Study Group (Osterlind et al. 1983) suffices since the major treatment distinction is often whether to treat with chemotherapy alone or chemotherapy along with radiation therapy. Disease that can be combined into one tolerable radiation port is usually treated with combined modalities (Stahel et al. 1989). Those with metastatic disease or disease within the thorax that is too extensive to be safely radiated are treated with chemotherapy alone. When considering surgery, decisions should be based on the TNM descriptors.

In most cases, SCLC is defined on imaging by metastatic spread. That is to say that the primary tumor itself is often a radiographically occult submucosal endobronchial lesion and the imaging appearance is the result of early lymphatic and vascular invasion resulting in extensive mediastinal adenopathy and distant metastases (Jackman and Johnson 2005). A primary tumor manifest as a solitary pulmonary nodule is an uncommon manifestation accounting for <5 % of SCLC (Kreisman et al. 1992). There are no distinct imaging features that definitively separate SCLC and other forms of lung cancer.

At diagnosis, the mediastinum is invariably involved varying in older series from 66 to 92 % of cases (Jackman and Johnson 2005; Pearlberg et al. 1988). Large mediastinal masses are often invasive, narrowing pulmonary arteries, bronchi, and systemic veins with obstruction of the superior vena cava (SVC) occurring in approximately 10 % at diagnosis (Pearlberg et al. 1988) (Figs. 13 and 14).

A majority of patients will have distant metastatic disease at presentation with up to 60 % having metastatic disease in the abdomen at the

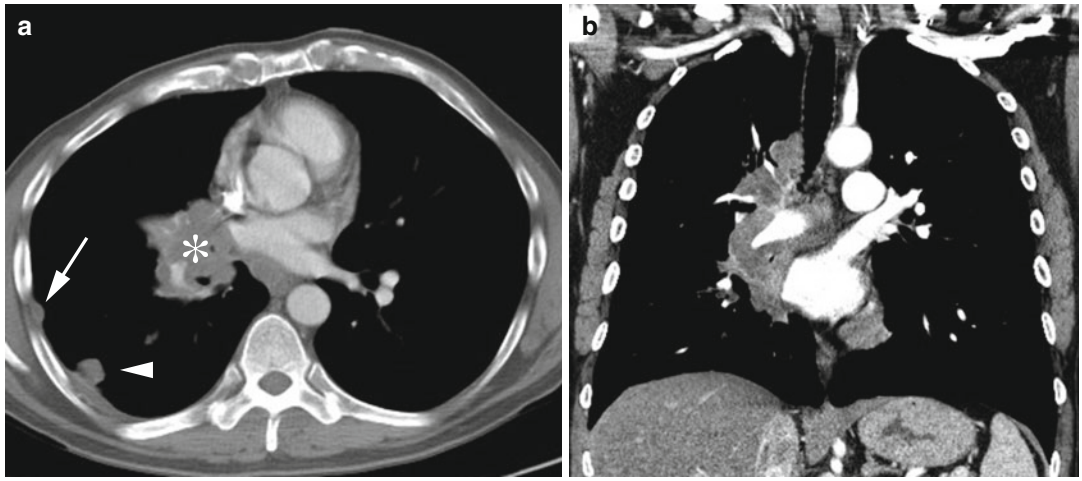

Fig. 13 Small cell carcinoma. Axial (**a**) and coronal (**b**) contrast-enhanced images reveal a large central lymph node conglomerate due to small cell carcinoma (*). Note also pleural (*arrow*) and parenchymal metastases (*arrowhead*)

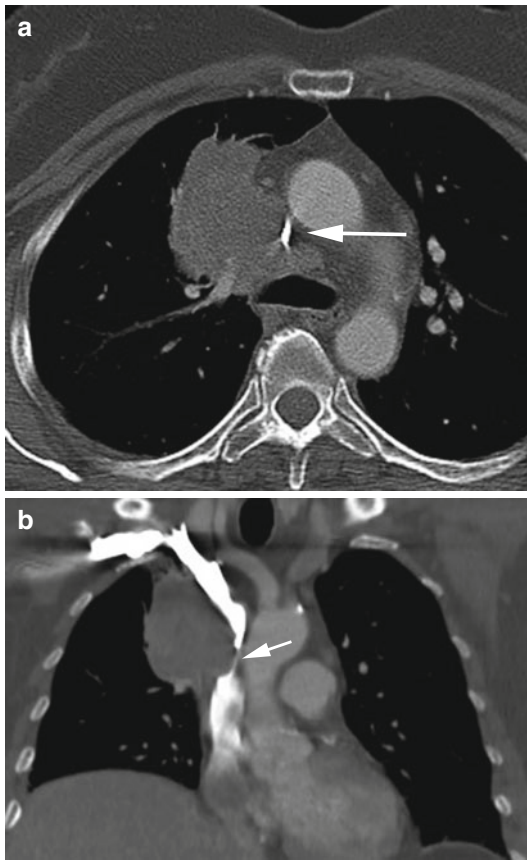

Fig. 14 Small cell carcinoma. Axial (**a**) and coronal (**b**) contrast-enhanced images reveal a paratracheal mass with slit-like appearance of superior vena cava (*arrows*)

time of diagnosis. The adrenal gland and liver are the most frequent sites of disease (Whitley and Mirvis 1989; Mirvis et al. 1987) Due to the high incidence of brain metastases, routine imaging of the brain is warranted (Simon and Turrisi 2007).

3.1 CT Perfusion

CT perfusion is based on the theory that iodine uptake over time is a surrogate for tumor vascularity. Although the evaluation of lung tumors with perfusion CT can be challenging owing to imaging time, studies can be performed over whole tumor volumes with well-coached free breathing (Fraioli et al. 2011; Tacelli et al. 2013) (Fig. 15). Parameters of blood volume and volume transfer product (a measure of permeability) can be obtained. Low blood volume and high permeability on perfusion CT correlate with a greater vascularity within a tumor (Tacelli et al. 2010). Studies have suggested that perfusion parameters in lung tumors have suggested that an increase in tumor blood volume is associated with better prognosis and that changes in permeability during therapy (decrease in permeability correlates with improved survival) can also predict outcome (Wang et al. 2009). It has been suggested that response to antiangiogenic therapy may be better detected with perfusion CT as

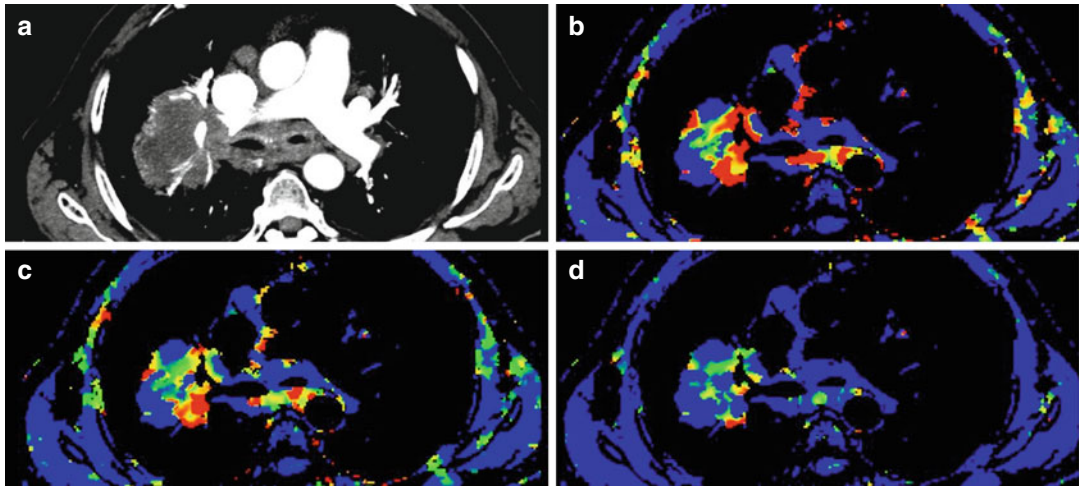

Fig. 15 CT perfusion. Axial contrast-enhanced image (**a**) with blood flow (**b**), blood volume, (**c**) and permeability (**d**) maps reveals partially necrotic right hilar mass with regional differences in blood flow, volume, and permeability. *Blue color* implies lower values for each parameter (Courtesy of Dr. Thomas Henzler, Mannheim, Germany)

perfusion changes may be more predictive than change in tumor size (Fraioli et al. 2011). In another small study, patients treated with epidermal growth factor receptor (EGFR)-targeted therapy who had a decrease in perfusion at 1 week were more likely to have a response to treatment as well as longer progression-free survival (Qiao et al. 2016). These observations await confirmation in larger multi-institutional clinical trials.

4 Follow-Up

4.1 Follow-Up Imaging for Surveillance and Recurrence

Local recurrence for non-small cell tumors after surgery occurs in 3–7 % of patients who undergo lobectomy and is more common in larger tumors (Crabtree et al. 2014; Su et al. 2014). As such more recurrences are seen in regional lymph nodes (~10 %) and distant metastatic sites (~15 %) (Crabtree et al. 2014). Locoregional recurrence rates are higher for resected small cell tumors (~35 %) (Stish et al. 2015). The presence of nodal disease in surgically treated does not appear to result in more frequent local recurrence but is associated with more frequent distant metastases (Varlotto et al. 2015). Comparatively, SBRT has a slightly higher local and regional failure rates with similar rates of distant disease (Crabtree et al. 2014; Senthi et al. 2012). For patients treated with definitive chemoradiation, most local failures occur within the radiation field rather than nodal stations not included in the radiation field (Garg et al. 2013) (Fig. 16). These findings may inform search patterns at CT when assessing for locoregional recurrence.

After definitive treatment with curative intent, follow-up takes on a lung cancer screening paradigm (Rubins et al. 2007; National Comprehensive Cancer Network 2000). Interestingly, a retrospective analysis of chest radiography and CT showed that while CT could document recurrence or second primary earlier, this did not translate into improvements in rates of treatment with curative intent or overall survival (Crabtree et al. 2015). CT also has a higher false-positive rate and lower positive predictive value which may lead to additional procedures (Hanna et al. 2014). In the absence of good evidence, most major society guidelines are developed by consensus of expert panels. Consensus is converging on using CT surveillance given the high risk of developing second primary tumors as well as disease recurrence at 6-month intervals for the first 2 years and annually after that (Rubins et al. 2007).

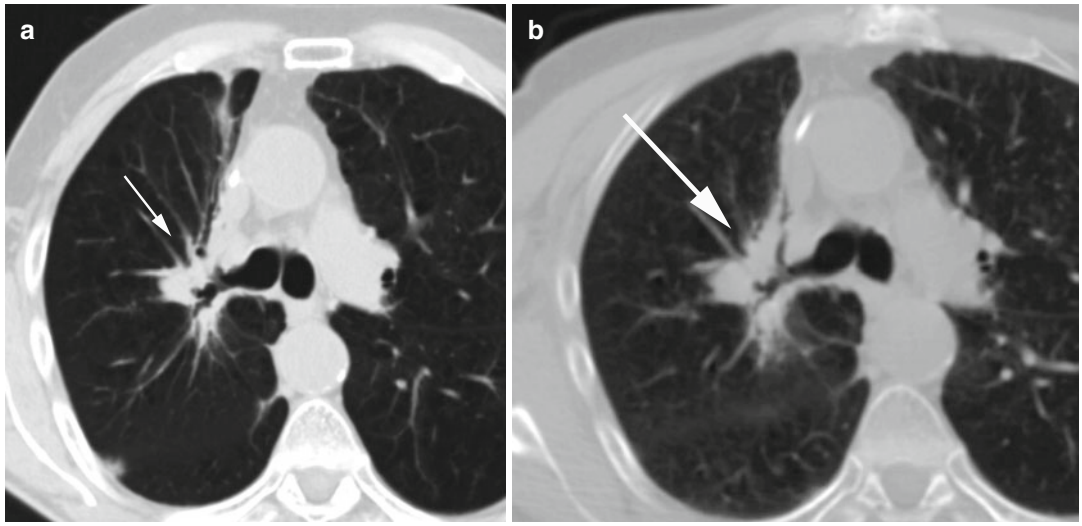

Fig. 16 In-field local recurrence. Axial CT baseline following radiation therapy (**a**) and 6 months later (**b**) show enlargement of right hilar soft tissue nodule with filling in of concave borders (*arrow*). Recurrence confirmed at bronchoscopy

4.2 Follow-Up Imaging for Treatment Response

Assessment of the change in tumor burden is an important feature of the clinical evaluation of cancer therapeutics: both tumor shrinkage (objective response) and disease progression are useful endpoints in clinical practice and trials (Eisenhauer et al. 2009). Unidimensional long-axis measurement using RECIST 1.1 is the current standard for response in most clinical trials. The most recent RECIST 1.1 criteria definitions of complete response (CR), partial response (PR), progressive disease (PD), and stable disease (SD) in target lesion and lymph nodes are summarized in Table 3.

Optimal assessment of response, however, is dependent on the reproducibility of measurements. Perhaps more important than technique, reader variability may play a greater role in accuracy of response assessment (Erasmus et al. 2003; Revel et al. 2004a). Inter- and intraobserver variations for initial tumor size are 10–15 % and 5 %, respectively (Erasmus et al. 2003) (Hopper et al. 1996), with an impact on disease progression or response to a greater degree. Using RECIST criteria, inter- and intraobserver variability for progressive disease ranged from 21 to 48 % (avg. 30 %) and 3 to 15 % (avg. 9 %), respectively. Response was affected to a lesser degree, interobserver 3–27 % (avg. 15 %) and intraobserver 0–6 % (avg. 4 %) (Erasmus et al. 2003). Thus, to the extent possible, the same scanning technique and interpreter should follow an individual case.

Table 3 Tumor response evaluation

Target lesions
Complete response (CR): disappearance of all target lesions; all pathologic lymph nodes less than 10 mm short axis
Partial response (PR): at least 30 % decrease in sum total diameters of all target lesions compared to baseline
Progressive disease (PD): at least 20 % increase in sum total diameters of all target lesions compared to smallest sum (baseline or best response) with absolute increase greater than 5 mm *OR* new metastatic lesions
Stable disease: meets neither condition for partial response or progressive disease
Nontarget lesions
Complete response: disappearance of all target lesions; all pathologic lymph nodes less than 10 mm short axis
Non-CR/non-PD: persistence of one or more nontarget lesions
Progressive disease: unequivocal progression of nontarget lesions (sufficient to warrant discontinuation of current therapy)

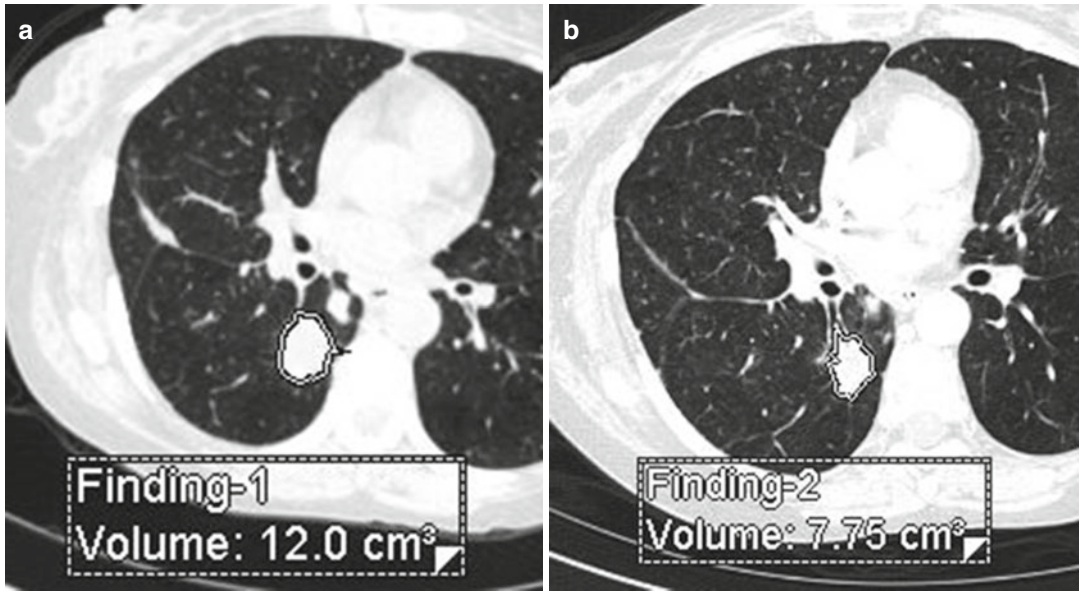

Fig. 17 CT volumetry. Axial CT images at 0 (**a**) and 3 (**b**) months. Tumor manually measured as decreasing from 2.6 cm to 2.2 cm (18 % decrease, RECIST stable disease), whereas automated volumetric analysis shows decrease from 12.0 cm^3 to 7.75 cm^3 (35 % decrease, RECIST treatment response)

Automated volumetric imaging has the potential advantage of eliminating measurement variability through improved precision (Petrou et al. 2007) (Revel et al. 2004b). Accuracy and precision can be best maintained by standardizing protocols including reconstruction interval, reconstruction kernel, and field of view (Ravenel et al. 2008). As a practical matter, patient motion, respiration, and relationship to adjacent structures further degrade the accuracy of volumetric change to a much greater extent than the precision of the technique (Gavrielides et al. 2009). Early studies comparing volumetry with RECIST have generally been favorable to volume assessment (Fig. 17) (Marten et al. 2006) (Tran et al. 2004) (Zhao et al. 2006). One important caveat is that volumetric response has not been rigorously defined. Additionally, a study evaluating two-dimensional measurements and semiautomated volume measurements on scans obtained the same day (no growth) showed similar degrees of variability (up to 20 % variance) in size across all measurements (Zhao et al. 2009). It should be noted that most studies only account for the volume of pulmonary lesions that can be adequately segmented and do not include all sites of tumor as called for by RECIST. Thus, volumetry may not be an improvement over standard two-dimensional measurements or an adequate tumor biomarker for therapeutic trials.

Regardless, all anatomic response measurements are limited in scope particularly in the setting of targeted therapies that may (1) prolong survival without change in tumor size, (2) mischaracterize increased size due to tumor bleeding or edema (response to drug) as progression, or (3) fail to characterize new tumor tissue in a complex mass (Shankar et al. 2009). As such, changes in lesion size must be correlated closely with the imaging technique, type of therapy, and clinical status of patient.

With the expanded use of immunomodulating therapies, there has been concern that response profiles may not fit those associated with cytotoxic drugs. An alternative proposed system has been termed immune RECIST (irRC) based on the observation of ipilimumab monotherapy in the treatment of metastatic melanoma (Wolchok et al. 2009). In addition to traditional responses of response and stable disease, two additional patterns of response were identified including response after initial tumor "growth" and response

despite the appearance of new metastatic lesions. To do this, the concept of total tumor burden is used so that growth of single lesions or new measurable lesions can be offset by shrinkage in other lesions. The application of irRC in lung cancer remains theoretical as traditional RECIST criteria have been used to document efficacy of the immune-modulator nivolumab in squamous cell tumors (Brahmer et al. 2015).

Conclusion

Computed tomography plays a critical role in the management of lung cancer patients as a diagnostic test, assessment of prognosis, and management tool helping to select the most appropriate site for tissue diagnosis. In concert with tumor histology, the careful evaluation of CT images, especially when correlated with physiologic information from18F-FDG PET/CT, ensures the most appropriate treatment selection.

References

American Thoracic Society (2000) Management of malignant pleural effusions. Am J Respir Crit Care Med 162:1987–2001

Aoki T, Nakata H, Watanabe H et al (2000) Evolution of peripheral lung adenocarcinomas: CT findings correlated with histology and tumor doubling time. AJR Am J Roentgenol 174:763–768

Aoki T, Tomoda Y, Watanabe H et al (2001) Peripheral lung adenocarcinoma: correlation of thin-section CT findings with histologic prognostic factors and survival. Radiology 220:803–809

Aquino SL, Halpern EF, Kuester LB, Fischman AJ (2007) FDG-PET and CT features of non-small cell lung cancer based on tumor type. Int J Mol Med 19:495–499

Boland GW, Lee MJ, Gazelle GS, Halpern EF, McNicholas MM, Mueller PR (1998) Characterization of adrenal masses using unenhanced CT: an analysis of the CT literature. AJR Am J Roentgenol 171:201–204

Boland GW, Blake MA, Hahn PF, Mayo-Smith WW (2008) Incidental adrenal lesions: principles, techniques, and algorithms for imaging characterization. Radiology 249:756–775

Brahmer J, Reckamp KL, Baas P et al (2015) Nivolumab versus docetaxel in advanced squamous-cell non-small-cell lung cancer. N Engl J Med 373:123–135

Bruzzi JF, Komaki R, Walsh GL et al (2008) Imaging of non-small cell lung cancer of the superior sulcus: part 2: initial staging and assessment of resectability and therapeutic response. Radiographics 28:561–572, a review publication of the Radiological Society of North America, Inc

Cascade PN, Gross BH, Kazerooni EA et al (1998) Variability in the detection of enlarged mediastinal lymph nodes in staging lung cancer: a comparison of contrast-enhanced and unenhanced CT. AJR Am J Roentgenol 170:927–931

Cerfolio RJ, Bryant AS (2006) Distribution and likelihood of lymph node metastasis based on the lobar location of nonsmall-cell lung cancer. Ann Thorac Surg 81: 1969–1973, discussion 73

Cole FH Jr, Thomas JE, Wilcox AB et al (1994) Cerebral imaging in the asymptomatic preoperative bronchogenic carcinoma patient : is it worthwhile? Ann Thorac Surg 57:838–840

Colice G, Birkmeyer J, Black W, Littenberg B, Silvestri G (1995) Cost-effectiveness of head CT in patients with lung cancer without clinical evidence of metastases. Chest 108:1264–1271

Crabtree TD, Puri V, Robinson C et al (2014) Analysis of first recurrence and survival in patients with stage I non-small cell lung cancer treated with surgical resection or stereotactic radiation therapy. J Thorac Cardiovasc Surg 147:1183–1191, discussion 91-2

Crabtree TD, Puri V, Chen SB et al (2015) Does the method of radiologic surveillance affect survival after resection of stage I non-small cell lung cancer? J Thorac Cardiovasc Surg 149:45–52, 3 e1-3

de Langen AJ, Raijmakers P, Riphagen I, Paul MA, Hoekstra OS (2006) The size of mediastinal lymph nodes and its relation with metastatic involvement: a meta-analysis. Eur J Cardiothorac Surg 29:26–29, official journal of the European Association for Cardiothoracic Surgery

Eisenhauer EA, Therasse P, Bogaerts J et al (2009) New response evaluation criteria in solid tumours: revised RECIST guideline (version 1.1). Eur J Cancer 45:228–247

Erasmus JJ, Gladish GW, Broemeling L et al (2003) Interobserver and intraobserver variability in measurement of non-small-cell carcinoma lung lesions: implications for assessment of tumor response. J Clin Oncol 21:2574–2582

Ferrigno D, Buccheri G (1994) Cranial computed tomography as a part of the initial staging procedures for patients with non-small cell lung cancer. Chest 106:1025–1029

Fraioli F, Anzidei M, Zaccagna F et al (2011) Whole-tumor perfusion CT in patients with advanced lung adenocarcinoma treated with conventional and antiangiogenetic chemotherapy: initial experience. Radiology 259:574–582

Gaeta M, Caruso R, Blandino A, Bartiromo G, Scribano E, Pandolfo I (1999) Radiolucencies and cavitation in bronchioloalveolar carcinoma: CT-pathologic correlation. Eur Radiol 9:55–59

Gandara DR, Aberle D, Lau D et al (2006) Radiographic imaging of bronchioloalveolar carcinoma: screening,

patterns of presentation and response assessment. J Thorac Oncol 1:S20–S26, official publication of the International Association for the Study of Lung Cancer

Garg S, Gielda BT, Turian JV et al (2013) Patterns of regional failure in stage III non-small cell lung cancer treated with neoadjuvant chemoradiation therapy and resection. Pract Radiat Oncol 3:287–293

Gavrielides MA, Kinnard LM, Myers KJ, Petrick N (2009) Noncalcified lung nodules: volumetric assessment with thoracic CT. Radiology 251:26–37

Glazer HS, Duncan-Meyer J, Aronberg DJ, Moran JF, Levitt RG, Sagel SS (1985a) Pleural and chest wall invasion in bronchogenic carcinoma: CT evaluation. Radiology 157:191–194

Glazer GM, Gross BH, Quint LE, Francis IR, Bookstein FL, Orringer MB (1985b) Normal mediastinal lymph nodes: number and size according to American Thoracic Society mapping. AJR Am J Roentgenol 144:261–265

Gould MK, Kuschner WG, Rydzak CE et al (2003) Test performance of positron emission tomography and computed tomography for mediastinal staging in patients with non-small-cell lung cancer: a meta-analysis. Ann Intern Med 139:879–892

Hanna WC, Paul NS, Darling GE et al (2014) Minimal-dose computed tomography is superior to chest x-ray for the follow-up and treatment of patients with resected lung cancer. J Thorac Cardiovasc Surg 147: 30–33

Haramati LB, Cartagena AM, Austin JH (1995) CT evaluation of mediastinal lymphadenopathy: noncontrast 5 mm vs postcontrast 10 mm sections. J Comput Assist Tomogr 19:375–378

Heffner JE, Klein JS (2008) Recent advances in the diagnosis and management of malignant pleural effusions. Mayo Clin Proc 83:235–250

Higashino T, Ohno Y, Takenaka D et al (2005) Thin-section multiplanar reformats from multidetector-row CT data: utility for assessment of regional tumor extent in non-small cell lung cancer. Eur J Radiol 56:48–55

Hopper KD, Kasales CJ, Van Slyke MA, Schwartz TA, TenHave TR, Jozefiak JA (1996) Analysis of interobserver and intraobserver variability in CT tumor measurements. AJR Am J Roentgenol 167:851–854

Jackman DM, Johnson BE (2005) Small-cell lung cancer. Lancet 366:1385–1396

Kagohashi K, Satoh H, Ishikawa H, Ohtsuka M, Sekizawa K (2003) Liver metastasis at the time of initial diagnosis of lung cancer. Med Oncol 20:25–28

Kelly RF, Tran T, Holmstrom A, Murar J, Segurola RJ Jr (2004) Accuracy and cost-effectiveness of [18F]-2-fluoro-deoxy-D-glucose-positron emission tomography scan in potentially resectable non-small cell lung cancer. Chest 125:1413–1423

Kim EA, Johkoh T, Lee KS et al (2001) Quantification of ground-glass opacity on high-resolution CT of small peripheral adenocarcinoma of the lung: pathologic and prognostic implications. AJR Am J Roentgenol 177: 1417–1422

Kreisman H, Wolkove N, Quoix E (1992) Small cell lung cancer presenting as a solitary pulmonary nodule. Chest 101:225–231

Kuriyama K, Seto M, Kasugai T et al (1999) Ground-glass opacity on thin-section CT: value in differentiating subtypes of adenocarcinoma of the lung. AJR Am J Roentgenol 173:465–469

Lee KS, Jeong YJ, Han J, Kim BT, Kim H, Kwon OJ (2004) T1 non-small cell lung cancer: imaging and histopathologic findings and their prognostic implications. Radiographics 24:1617–1636, a review publication of the Radiological Society of North America, Inc discussion 32-6

Marten K, Auer F, Schmidt S, Kohl G, Rummeny EJ, Engelke C (2006) Inadequacy of manual measurements compared to automated CT volumetry in assessment of treatment response of pulmonary metastases using RECIST criteria. Eur Radiol 16:781–790

Matakidou A, Eisen T, Houlston RS (2005) Systematic review of the relationship between family history and lung cancer risk. Br J Cancer 93:825–833

Mintz BJ, Turhim S, Alexander S et al (1984) Intracranial metastases in the initial staging of bronchogenic carcinoma. Chest 86:850–853

Mirvis SE, Whitley NO, Aisner J, Moody M, Whitacre M, Whitley JE (1987) Abdominal CT in the staging of small-cell carcinoma of the lung: incidence of metastases and effect on prognosis. AJR Am J Roentgenol 148:845–847

Mountain C (1997) Revisions in the international system for staging lung cancer. Chest 111:1710–1717

Mujoomdar A, Austin JH, Malhotra R et al (2007) Clinical predictors of metastatic disease to the brain from non-small cell lung carcinoma: primary tumor size, cell type, and lymph node metastases. Radiology 242:882–888

Munden RF, Swisher SS, Stevens CW, Stewart DJ (2005) Imaging of the patient with non-small cell lung cancer. Radiology 237:803–818

Nakata M, Saeki H, Takata I et al (2002) Focal ground-glass opacity detected by low-dose helical CT. Chest 121:1464–1467

National Comprehensive Cancer Network (2000) Practice guidelines for non-small cell lung cancer. National Comprehensive Cancer Network, Rockledge

Osterlind K, Ihde DC, Ettinger DS et al (1983) Staging and prognostic factors in small cell carcinoma of the lung. Cancer Treat Rep 67:3–9

Pallis AG, Syrigos KN (2013) Lung cancer in never smokers: disease characteristics and risk factors. Crit Rev Oncol Hematol 88:494–503

Patsios D, Roberts HC, Paul NS et al (2007) Pictorial review of the many faces of bronchioloalveolar cell carcinoma. Br J Radiol 80:1015–1023

Patz EJ, Erasmus J, McAdams H et al (1999) Lung cancer staging and management: comparison of contrast-enhanced and nonenhanced helical CT of the thorax. Radiology 212:56–60

Pearlberg JL, Sandler MA, Lewis JW Jr, Beute GH, Alpern MB (1988) Small-cell bronchogenic carcinoma: CT evaluation. AJR Am J Roentgenol 150:265–268

Petrou M, Quint LE, Nan B, Baker LH (2007) Pulmonary nodule volumetric measurement variability as a function of CT slice thickness and nodule morphology. AJR Am J Roentgenol 188:306–312

Qiao PG, Zhang HT, Zhou J, et al (2016) Early evaluation of targeted therapy effectiveness in non-small cell lung cancer by dynamic contrast-enhanced CT. Clin Transl Oncol 18:47–57

Ravenel JG, Leue WM, Nietert PJ, Miller JV, Taylor KK, Silvestri GA (2008) Pulmonary nodule volume: effects of reconstruction parameters on automated measurements--a phantom study. Radiology 247:400–408

Revel MP, Bissery A, Bienvenu M, Aycard L, Lefort C, Frija G (2004a) Are two-dimensional CT measurements of small noncalcified pulmonary nodules reliable? Radiology 231:453–458

Revel MP, Lefort C, Bissery A et al (2004b) Pulmonary nodules: preliminary experience with three-dimensional evaluation. Radiology 231:459–466

Rubins J, Unger M, Colice GL (2007) Follow-up and surveillance of the lung cancer patient following curative intent therapy: ACCP evidence-based clinical practice guideline (2nd edition). Chest 132:355S–367S

Rusch VW, Asamura H, Watanabe H, Giroux DJ, Rami-Porta R, Goldstraw P (2009) The IASLC lung cancer staging project: a proposal for a new international lymph node map in the forthcoming seventh edition of the TNM classification for lung cancer. J Thorac Oncol 4:568–577, official publication of the International Association for the Study of Lung Cancer

Senthi S, Lagerwaard FJ, Haasbeek CJ, Slotman BJ, Senan S (2012) Patterns of disease recurrence after stereotactic ablative radiotherapy for early stage non-small-cell lung cancer: a retrospective analysis. Lancet Oncol 13:802–809

Shankar LK, Van den Abbeele A, Yap J, Benjamin R, Scheutze S, Fitzgerald TJ (2009) Considerations for the use of imaging tools for phase II treatment trials in oncology. Clin Cancer Res 15:1891–1897

Siegel R, Ma J, Zou Z, Jemal A (2014) Cancer statistics, 2014. CA Cancer J Clin 64:9–29

Silvestri G, Littenberg B, Colice G (1995) The clinical evaluation for detecting metastatic lung cancer: a meta-analysis. Am J Respir Crit Care Med 152:225–230

Silvestri GA, Tanoue LT, Margolis ML, Barker J, Detterbeck F (2003) The noninvasive staging of non-small cell lung cancer: the guidelines. Chest 123: 147S–156S

Silvestri GA, Gould MK, Margolis ML et al (2007) Noninvasive staging of non-small cell lung cancer: ACCP evidenced-based clinical practice guidelines (2nd edition). Chest 132:178S–201S

Simon GR, Turrisi A (2007) Management of small cell lung cancer: ACCP evidence-based clinical practice guidelines (2nd edition). Chest 132:324S–339S

Stahel R, Ginsberg R, Havemann K et al (1989) Staging and prognostic factors in small cell lung cancer: a consensus report. Lung Cancer 5:119–126

Stish BJ, Hallemeier CL, Olivier KR, Harmsen WS, Allen MS, Garces YI (2015) Long-term outcomes and patterns of failure after surgical resection of small-cell lung cancer. Clin Lung Cancer 16:e67–e73

Su S, Scott WJ, Allen MS et al (2014) Patterns of survival and recurrence after surgical treatment of early stage non-small cell lung carcinoma in the ACOSOG Z0030 (ALLIANCE) trial. J Thorac Cardiovasc Surg 147: 747–752, Discussion 52-3

Tacelli N, Remy-Jardin M, Copin MC et al (2010) Assessment of non-small cell lung cancer perfusion: pathologic-CT correlation in 15 patients. Radiology 257:863–871

Tacelli N, Santangelo T, Scherpereel A et al (2013) Perfusion CT allows prediction of therapy response in non-small cell lung cancer treated with conventional and anti-angiogenic chemotherapy. Eur Radiol 23: 2127–2136

Thun MJ, Jemal A (2006) How much of the decrease in cancer death rates in the United States is attributable to reductions in tobacco smoking? Tob Control 15:345–347

Tran LN, Brown MS, Goldin JG et al (2004) Comparison of treatment response classifications between unidimensional, bidimensional, and volumetric measurements of metastatic lung lesions on chest computed tomography. Acad Radiol 11:1355–1360

Travis WD, Garg K, Franklin WA et al (2005) Evolving concepts in the pathology and computed tomography imaging of lung adenocarcinoma and bronchioloalveolar carcinoma. J Clin Oncol Off J Am Soc Clin Oncol 23:3279–3287

Vallieres E, Shepherd FA, Crowley J et al (2009) The IASLC Lung Cancer Staging Project: proposals regarding the relevance of TNM in the pathologic staging of small cell lung cancer in the forthcoming (seventh) edition of the TNM classification for lung cancer. J Thorac Oncol 4:1049–1059, official publication of the International Association for the Study of Lung Cancer

Varlotto JM, Yao AN, DeCamp MM et al (2015) Nodal stage of surgically resected non-small cell lung cancer and its effect on recurrence patterns and overall survival. Int J Radiat Oncol Biol Phys 91:765–773

Wang J, Wu N, Cham MD, Song Y (2009) Tumor response in patients with advanced non-small cell lung cancer: perfusion CT evaluation of chemotherapy and radiation therapy. AJR Am J Roentgenol 193:1090–1096

Watanabe S, Suzuki K, Asamura H (2008) Superior and basal segment lung cancers in the lower lobe have different lymph node metastatic pathways and prognosis. Ann Thorac Surg 85:1026–1031

Weisbrod GL, Towers MJ, Chamberlain DW, Herman SJ, Matzinger FR (1992) Thin-walled cystic lesions in bronchioalveolar carcinoma. Radiology 185:401–405

Whitley NO, Mirvis SE (1989) Abdominal CT in the staging of small cell carcinoma of the lung. Crit Rev Diagn Imaging 29:103–116

Wolchok JD, Hoos A, O'Day S et al (2009) Guidelines for the evaluation of immune therapy activity in solid tumors: immune-related response criteria. Clin Cancer Res 15:7412–7420

Woodring JH (1988) Determining the cause of pulmonary atelectasis: a comparison of plain radiography and CT. AJR Am J Roentgenol 150:757–763

Zerhouni EA, Stitik FP, Siegelman SS et al (1986) CT of the pulmonary nodule: a cooperative study. Radiology 160:319–327

Zhao B, Schwartz LH, Moskowitz CS, Ginsberg MS, Rizvi NA, Kris MG (2006) Lung cancer: computerized quantification of tumor response – initial results. Radiology 241:892–898

Zhao B, James LP, Moskowitz CS et al (2009) Evaluating variability in tumor measurements from same-day repeat CT scans of patients with non-small cell lung cancer. Radiology 252:263–272

CT Imaging of the Mediastinum

Chang Hyun Lee and Julien Dinkel

Abstract

Mediastinal lesions include various diseases such as tumors, congenital disorder, inflammatory diseases, and vascular disorders. Statistically, most mediastinal masses in adults (>60 %) comprise lymphsadenopathy, thymomas, benign cysts, and neurogenic tumors, while teratoma and granulomatous disease and other rare pathologies represent 30 % of the mediastinal tumors. Vascular disorders in the mediastinum such as aortic aneurysm comprise the remaining 10 %. A good diagnostic strategy combines classification of the mass by location, tissue density, and a probabilistic approach. This chapter discusses both common and rare diseases with specific regard to radiologic findings in the mediastinum.

1 Anatomy and Compartments of the Mediastinum

This chapter follows Fraser's mediastinal classification of anterior, middle, and posterior mediastinum based on lateral chest X-ray images (Fraser et al. 1994). The anterior mediastinum is located between the lung apex and the diaphragm, posterior to the sternum and anterior to the heart and brachiocephalic vessels. It is defined as a prevascular space and contains thymus, fat, and lymph nodes on CT or MRI. The middle mediastinum is a space containing the heart, pericardium, ascending aorta, aortic arch, brachiocephalic vessels, superior and inferior vena cava, main pulmonary artery and vein, trachea, bronchi, and lymph nodes. The posterior mediastinum contains the descending aorta, esophagus, azygos vein, autonomic nerves and ganglia, thoracic duct, lymph nodes, and fat.

C.H. Lee, MD, PhD (✉)
Department of Radiology, College of Medicine, Seoul National University, Seoul, South Korea
e-mail: changhyun.lee.snuh@gmail.com

J. Dinkel, MD, PhD
Institute for Clinical Radiology, Ludwig-Maximilians-University Hospital, Munich, Germany
e-mail: Julien.Dinkel@med.uni-muenchen.de

1.1 Anterior Mediastinal Lesions

The most common anterior mediastinal tumors are thymoma, teratoma, intrathoracic goiter, and lymphoma. Thymic carcinoma, thymolipoma, germ cell tumors except teratoma, parathyroid adenoma,

U.J. Schoepf, F.G. Meinel (eds.), *Multidetector-Row CT of the Thorax*, Medical Radiology,
DOI 10.1007/978-3-319-30355-0_12

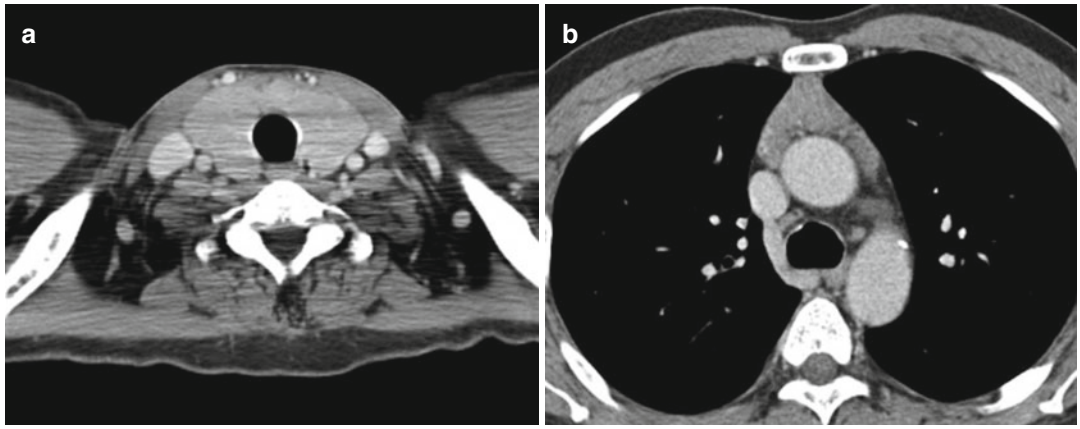

Fig. 1 A 44 year old male patient with hyperthyroidism. (**a**) There is an enlargement of the thyroid gland on contrast-enhanced CT scan. (**b**) Diffuse enlargement of the thymic tissue, thymic hyperplasia, is seen in the anterior mediastinum

thymic cyst, and lymphangioma are also anterior mediastinal tumors (Strollo et al. 1997a; Hansell et al. 2010; Tecce et al. 1994; Shahrzad et al. 2014). While lymphoma does occur in the anterior mediastinum, it arises more often in the middle mediastinum, and therefore will be mentioned in the section on the middle mediastinum.

CT generally diagnoses anterior mediastinal lesions more effectively than MR. However, thymomas with hemorrhage or inflammation are seen as a solid nodule on CT images but as cystic tumors on MRI, so MRI is superior to CT in this regard (Tomiyama et al. 2008).

1.1.1 Thymic Hyperplasia

Thymic hyperplasia is generally divided into true thymic hyperplasia and lymphoid follicular hyperplasia. True thymic hyperplasia is defined as an abnormally increased size of the thymus considering the patient's age. Rebound thymic hyperplasia, one of the typical thymic hyperplasias, occurs when the thymus gradually increases as a rebound phenomenon months after surgery or chemotherapy, after the thymus has decreased in size during the early stages of chemotherapy. Furthermore, thymic hyperplasia can be associated with a history of steroid therapy, infection, and thermal burn (Strollo et al. 1997a; Tecce et al. 1994).

Lymphoid follicular hyperplasia is defined as a histologic finding of increased size in the lymphoid element of the thymus, regardless of the entire size of the thymus. The disease can be found in 65–71 % of myasthenia gravis patients and can also be present in patients diagnosed with hyperthyroidism and acromegaly (Fig. 1) (Strollo et al. 1997a; Tecce et al. 1994). According to Nicolaou (Nicolaou et al. 1996), who analyzed 45 myasthenia gravis patients, 10 of 22 patients pathologically diagnosed with lymphoid follicular hyperplasia had CT images with normal thymus size, seven showed diffuse enlargement of the thymus, and five showed solid localized mass Also, 10 of 26 patients with normal thymus size were diagnosed with lymphoid follicular hyperplasia, and 16 showed normal histologic findings; five of 12 patients who showed local solid mass findings had lymphoid follicular hyperplasia, and the remaining seven patients were diagnosed with thymoma.

It is difficult to distinguish between thymic hyperplasia and thymic tumor on CT or conventional MR pulse sequences. Although the thymus shows normal fluorodeoxyglucose (FDG) uptake in positron emission tomography (PET), it is difficult to distinguish between thymic hyperplasia and malignant thymic tumor using PET (Ferdinand et al. 2004). MRI can identify the fine adipose tissues in normal thymus and genuine thymic hyperplasia by using chemical-shift MR, and therefore can distinguish between genuine thymic hyperplasia and thymic tumor. Thus, while thymic hyperplasia has lower signal

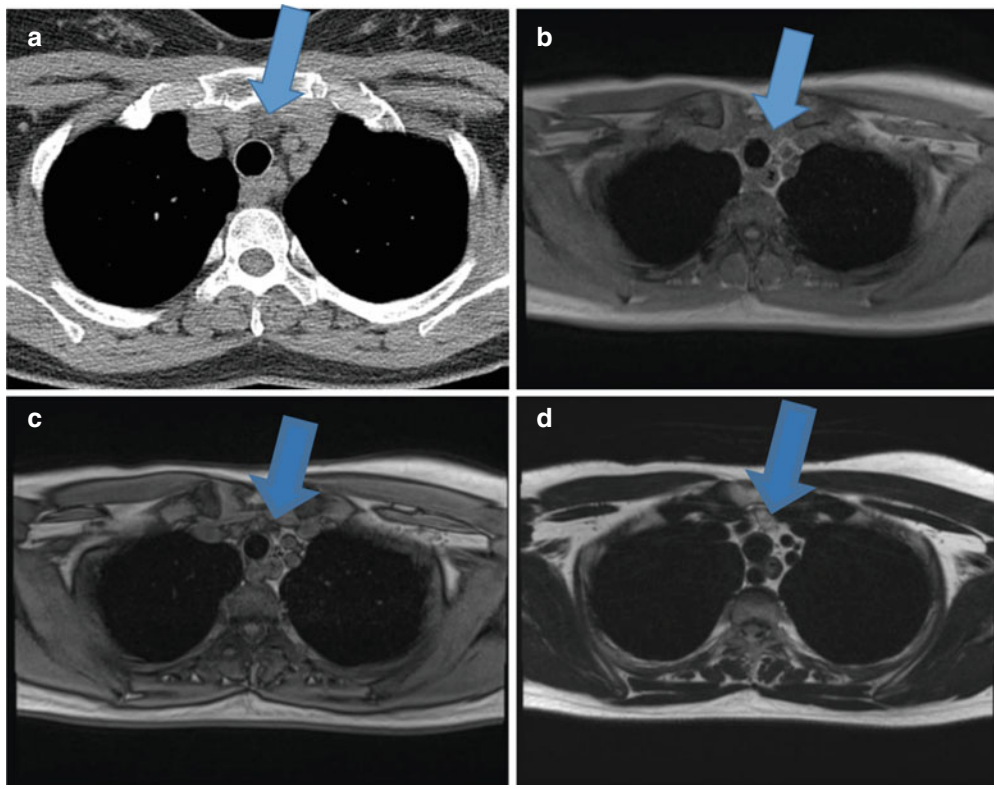

Fig. 2 (**a**) On non-contrast CT scan shows low attenuated soft tissue lesion in the anterior mediastinum (*arrow*). (**b**) There is an anterior mediastinal nodular lesion which shows iso-signal intensity on in-phase T1WI (*arrow*) and (**c**) low-signal intensity on out of phase T1WI (*blank arrow*). (**d**) On T2WI, this lesion shows high signal intensity similar to fat tissue and is confirmed as thymic hyperplasia

intensity in opposed-phase images than in in-phase images in chemical-shift MRI, thymic tumor does not have a difference in signal intensity (Fig. 2). Also, the average chemical-shift ratio, the ratio of the signal intensity of thymus and paraspinal muscles, is significantly lower in thymic hyperplasia than in thymic tumor (Inaoka et al. 2007).

1.1.2 Thymic Cyst

Thymic cysts can be divided into congenital and acquired cysts, although most are congenital. In CT, congenital thymic cysts have well-defined margins and are homogeneous unilocular cysts showing low attenuation. They have invisible thin cyst walls and no calcification (Fig. 3) (Strollo et al. 1997a; Tecce et al. 1994).

Unlike congenital cysts, acquired cysts have identifiable multilocular thick cyst walls, inflammation, or fibrous septa, and thus are also defined as multilocular thymic cysts (Suster and Rosia 1991; Choi et al. 2001). Acquired cysts are often associated with human immunodeficiency virus,

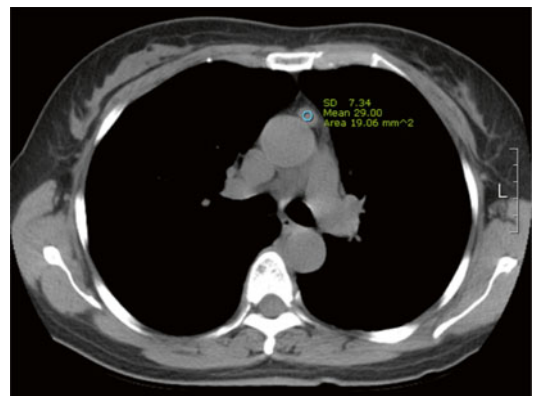

Fig. 3 A 47-year-old woman with anterior mediastinal thymic cyst, which was measured 29 HU on noncontrast-enhanced CT

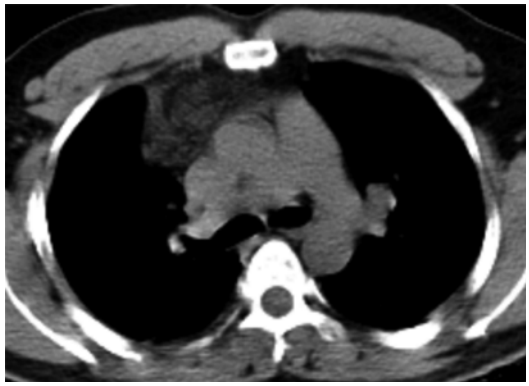

Fig. 4 A 24-year-old man with right anterior mediastinal thymolipoma. Non-contrast-enhanced chest CT shows that the mass is of fat attenuation with strands of interspersed soft tissue

systemic lupus erythematosus, or Sjögren syndrome. While similar to teratoma in having enhanced cyst walls and inner septa with calcified walls, acquired cysts do not have fatty or solid components (Choi et al. 2001).

1.1.3 Thymolipoma

Thymolipoma is a slow-growing benign thymic tumor (Fig. 4). It is commonly seen as an anterior mediastinal mass in the cardiophrenic angle. On plain radiography it appears to naturally adapt/drape the diaphragm, thus simulating cardiomegaly or diaphragm elevation, confusing its appearance with that of pleural or pericardial tumor and with atelectasis in the lower lobes (Fig. 6) (Strollo et al. 1997a; Tecce et al. 1994; Shahrzad et al. 2014; Rosado-de-Christenson et al. 1994). The shape of the mass changes with the position of the body. On chest radiography, a fat component in thymolipoma is helpful in making a diagnosis because it allows the lesion to be separated from the diaphragm. On CT, the attenuations of the soft-tissue component in the thymolipoma are similar to those of fat, and the mass effect can be seen (Rosado-de-Christenson et al. 1994). Other tumors containing fat in the anterior mediastinum are lipoma, liposarcoma, mediastinal lipomatosis, teratoma, and diaphragmatic hernia.

1.1.4 Thymic Epithelial Tumor

Thymic epithelial tumor can be sub divided into thymoma and thymic carcinoma. Whereas thymoma shows benign cytologic findings with no cytologic atypia, thymic carcinoma has highly malignant cytologic findings and potential for distant metastasis, and therefore has a poor prognosis (Nishino et al. 2006; Rosado-de-Christenson et al. 2008; Marom 2013).

The most common histologic classification is the World Health Organization (WHO) classification published in 2004. According to the WHO, thymomas are divided into five types, A, AB, B1, B2, and B3, by the shape of the epithelial cell and the ratio between the lymphocyte and the epithelial cell (Travis et al. 2004; Ströbel et al. 2005). When grouping by prognosis, types A, AB, and B1 are low-risk thymoma, B2 and B3 are high-risk thymomas, and thymic carcinomas carry the highest risk. Types A, AB, and B1 have typical organotypic, thymus-like pathology and do not have tissues outside of the thymus, but thymic carcinoma has various pathologic types (e.g., epithelial carcinoma, adenocarcinoma), and identical types of tumors may occur outside of the thymus (Sadohara et al. 2006).

CT and MR show similar accuracy when diagnosing mediastinal invasion in thymic epithelial tumors. CT can show the presence of calcification within the thymoma much better than MRI, while MRI can depict tumor capsule, intratumoral fibrous septum, and hemorrhage better than CT (Sadohara et al. 2006).

Thymoma

Thymoma is the most common primary tumor in the anterior mediastinum in patients older than 40 years, and is uncommon in persons younger than 20. Thirty-five percent of thymoma patients are also diagnosed with myasthenia gravis, while only 15 % of myasthenia patients are diagnosed with thymoma. Furthermore, thymoma is also associated with red cell hypoplasia and autoimmune disease (Strollo et al. 1997a; Tecce et al. 1994; Rosado-de-Christenson et al. 2008; Marom 2013).

The most common types are type AB and B2, each comprising 20–35 % of all thymoma types. Types A, AB, and B1, which are entirely removable by surgery, are well delineated and encapsulated (Fig. 5). High-risk thymoma types B2 and B3 often do not have surrounding capsule, invade

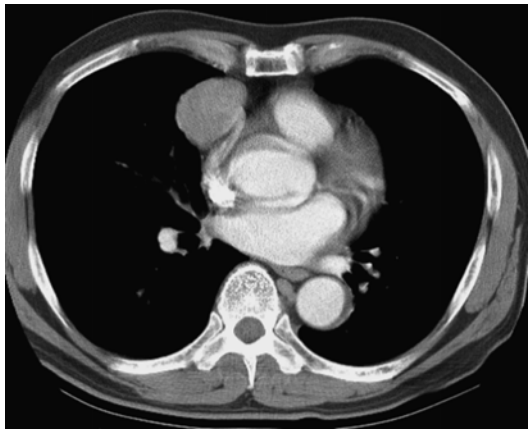

Fig. 5 A 61-year-old man with type A thymoma. On contrast-enhanced chest CT, the well-defined round mass is seen with slight enhancement in the right anterior mediastinum

nearby organs and mediastinal fat (Fig. 6), are difficult to remove by surgery, and have high chances of local recurrence and metastasis (Rosado-de-Christenson et al. 2008; Marom 2013; Jeong et al. 2004).

Most thymomas grow asymmetrically within the anterior mediastinum. Thymomas usually form in front of the aortic root, but can form anywhere from the neck to the cardiodiaphragmatic angle (Verstandig et al. 1992). They are usually seen with homogeneously enhanced soft-tissue attenuation, are oval, round, or lobulated, and have well-defined margins often with cystic change and calcification (Fig. 7). Typical septa within the tumor can also be seen (Strollo et al. 1997a; Tecce et al. 1994; Verstandig et al. 1992; Rosado-de-Christenson et al. 1992a; Suster and Rosai 1992).

The most important factor for the prognosis is the presence of local invasion. Sharp margins of the tumor and the presence of a fat plane between the tumor and the adjacent mediastinal structures suggest noninvasive tumors (Fig. 7), while findings indicating local or capsular invasion are irregular tumor margins, invasions of thoracic wall or great vessel structures, encasement of mediastinal structures, irregular interface with the lung, and compression of the vessels (Strollo et al. 1997a; Tecce et al. 1994; Sadohara et al. 2006; Rosado-de-Christenson et al. 1992a; Tomiyama et al. 2001). Pleural or pericardial nodules and thickening can also be found (Verstandig et al. 1992; Maher and Shepard 2005).

Thymic Carcinoma

Thymic carcinoma is a rare malignant tumor of the anterior mediastinum. Its clinical behavior is much more aggressive than thymoma, and most patients have local invasion within the thorax in addition to extrathoracic metastasis. Thymic carcinoma is not accompanied by myasthenia gravis or hypogammaglobulinemia.

According to the 2004 WHO classification (Travis et al. 2004), thymic carcinomas are malignant epithelial tumors because of overt cytologic atypia, almost invariable invasiveness, and lack of "organotypic" (thymus-like) features. The most common types are epithelial carcinoma and neuroendocrine carcinoma, which normally arise in middle age. Typical and atypical carcinoids arise within well-differentiated neuroendocrine carcinoma, and large and small cell neuroendocrine carcinomas originate within poorly differentiated neuroendrocrine carcinoma (Travis et al. 2004; Ströbel et al. 2005; Suster 2006).

While invasive growth into the surrounding tissues is similar to the pattern of invasive thymoma, metastasis to mediastinal lymph nodes, lung, liver, and brain occur more often and pleural implants occur less frequently than in invasive thymoma (Fig. 8) (Do et al. 1995). Thymic carcinoma tends to be larger than thymoma, and neither septa within the tumor nor nodular opacity is seen. They are often present with necrosis or cystic changes, and show irregular or lobulating contours, but calcification is rare. When presenting as large tumors, they might have already invaded the adjacent organs, accompanied with pleural and pericardial effusion, and have a poor prognosis (Fig. 9) (Strollo et al. 1997a; Tecce et al. 1994; Sadohara et al. 2006; Jeong et al. 2004; Lee et al. 1991; Tomiyama et al. 2002; Jung et al. 2001).

Differential Diagnosis of Thymic Epithelial Tumor

While the majority of CT and MR findings are limited in distinguishing the thymoma subtypes,

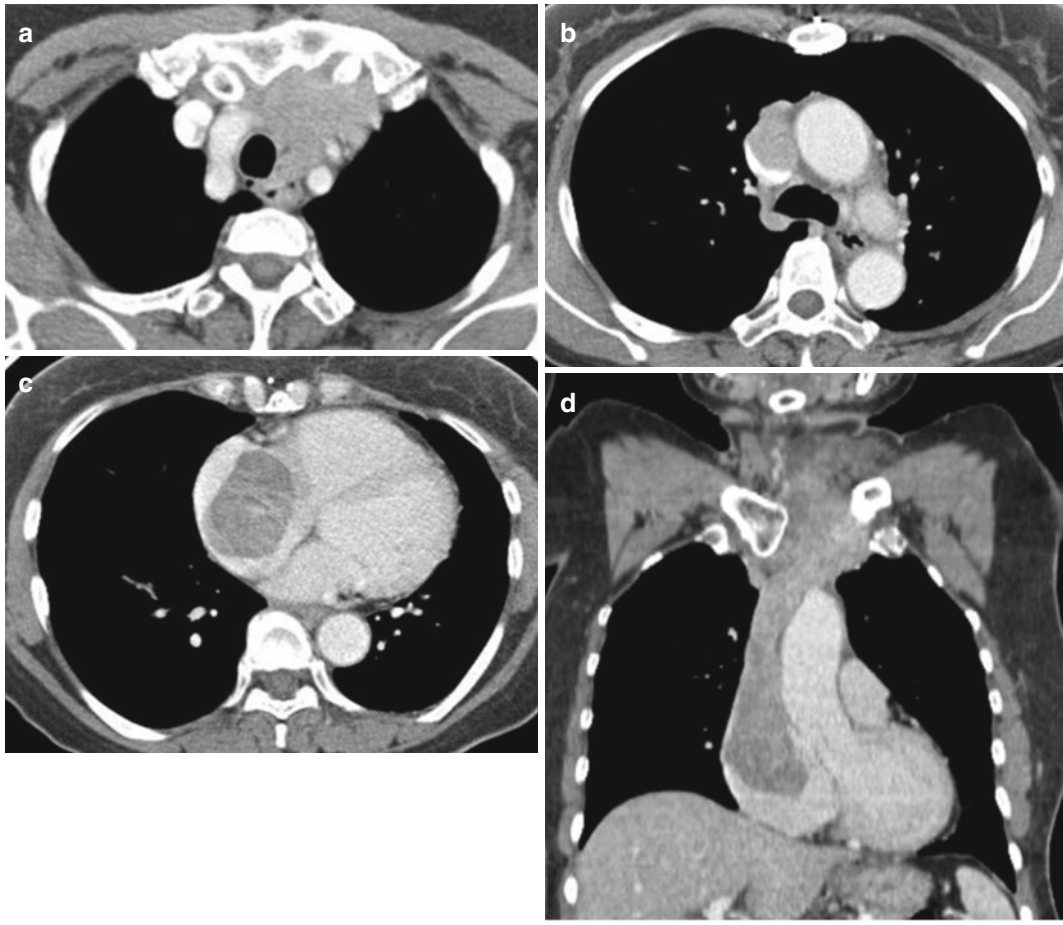

Fig. 6 A 52-year-old woman with type B3 thymoma complaining of facial edema and left arm swelling. (**a–c**) Contrast-enhanced chest CT shows that the mass invades the mediastinum, superior vena cava, and left innominate vein. (**d**) Coronal reformatted image shows the mass extending into the right atrium

some helpful points exist. Heterogeneous enhancement of the mass on CT or MRI may suggest high-risk thymoma or thymic carcinoma. Smooth margins, round shape, and relatively small size indicate type A thymoma, while unclear margins, necrotizing or cystic components, non-homogeneous enhancement, enlarged lymph nodes, and vascular invasion suggest thymic carcinoma. On MRI, smooth margins, intact capsule and diaphragm, and homogeneous enhancement strongly suggest a low-risk thymoma. Calcification suggests type B thymoma and thymic carcinoma (Sadohara et al. 2006; Jeong et al. 2004; Tomiyama et al. 2001; Tomiyama et al. 2002).

FDG-PET is helpful in distinguishing thymic epithelial tumors. The maximum standardized uptake value of thymic carcinoma is greater than that of thymoma, and the FDG uptake of thymic carcinoma was slightly more homogeneous than that of thymoma. PET is also useful for detecting lymph node metastasis (Rosado-de-Christenson et al. 2008; Saski et al. 1999; Sung et al. 2006).

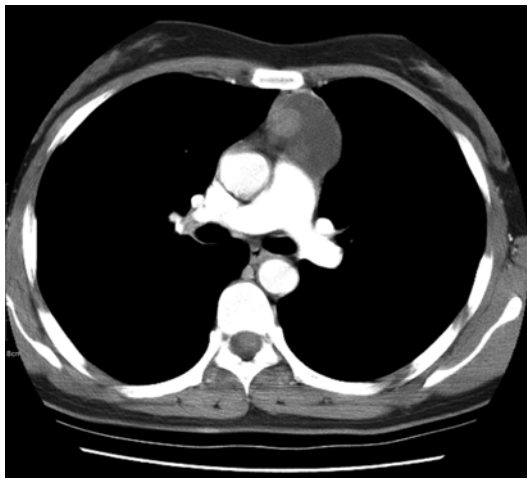

Fig. 7 A 43-year-old woman with type B1 thymoma showing cystic change. Contrast-enhanced CT shows cystic change and mural nodule in the left anterior mediastinal mass

1.1.5 Mediastinal Germ Cell Tumor

The anterior mediastinum is the most common extragonadal primary site for germ cell tumors. Germ cell tumors are generally divided into benign and malignant teratoma, seminoma, and malignant nonseminomatous tumor. Malignant nonseminomatous tumors include embryonal carcinoma, yolk sac tumor, choriocarcinoma, and mixed germ cell tumor (Travis et al. 2004). Most arise in the teens or early adulthood. Mature teratoma arises similarly regardless of gender, but 90 % of malignant lesions arise among males (Travis et al. 2004). The most common germ cell tumors are malignant cystic teratomas and the most common malignant tumors are seminoma and mixed germ cell tumors. For primary mediastinal germ cell tumors to be diagnosed, there have to be no tumors discovered in

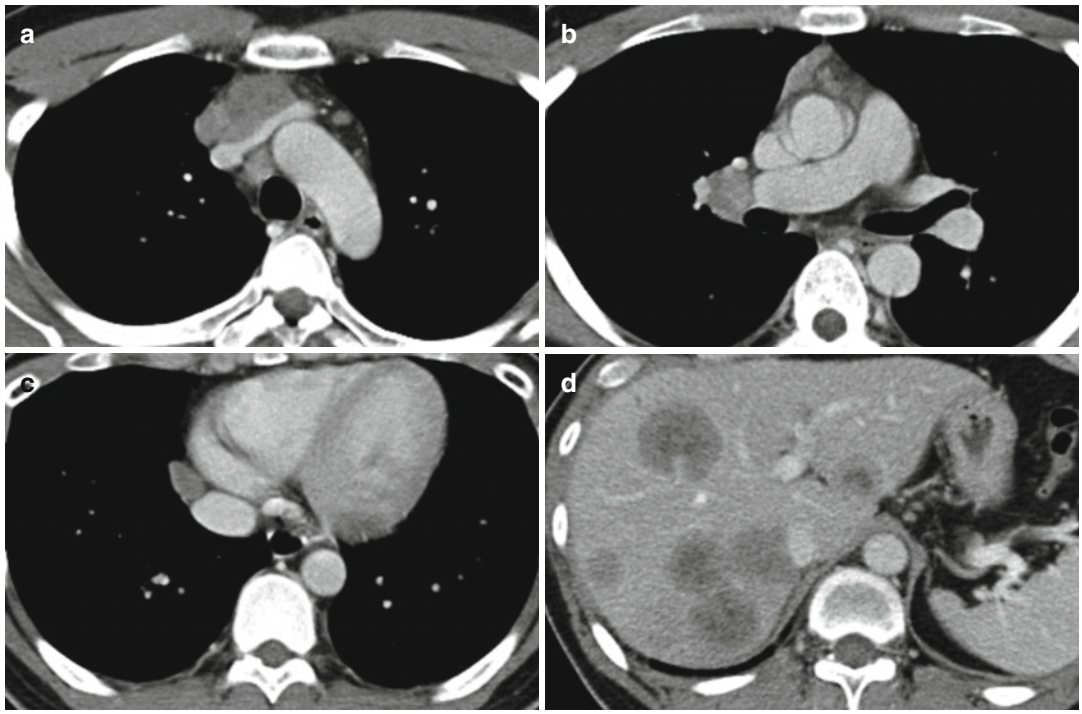

Fig. 8 A 30-year-old woman with thymic carcinoma. (**a, b**) Contrast-enhanced CT shows anterior mediastinal nodule and multiple mediastinal lymph node enlargement. (**c**) Pleural implant is also seen anterior to the inferior vena cava. (**d**) Multiple distant metastasis in the liver is noted

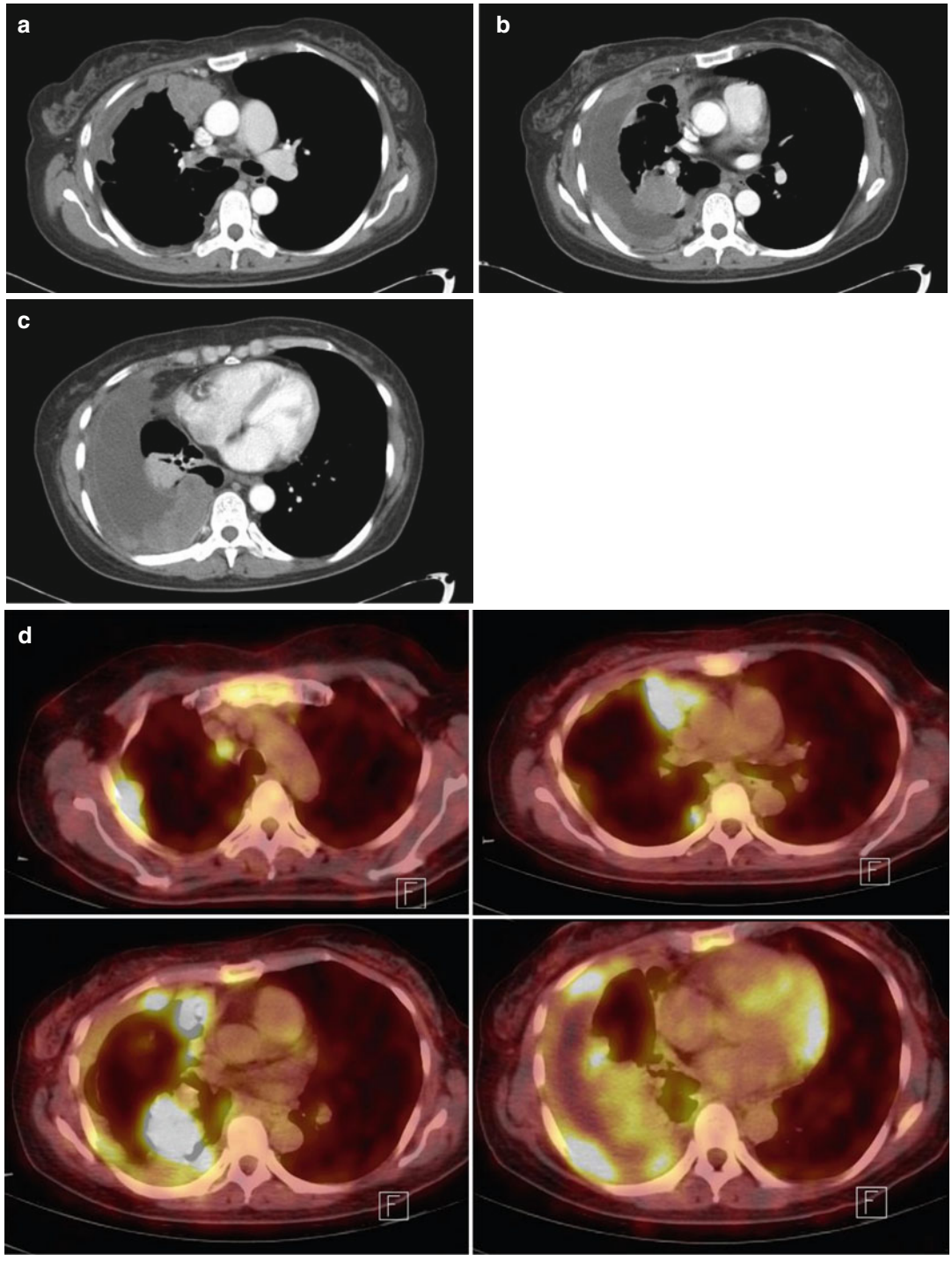

Fig. 9 A 50-year-old woman with thymic carcinoma with pleural effusion and metastasis. (**a–c**) Contrast-enhanced CT scan shows right anterior mediastinal mass with pleural metastatic nodules and right lower lobe metastatic mass. Malignant right pleural effusion is also seen. (**d**) FDG-PET CT shows increased uptake in the right anterior mediastinal mass and metastatic lesions

the testis or ovary on physical examination, ultrasonography, and MRI (Strollo et al. 1997a; Drevelegas et al. 2001). An increase in α-fetoprotein or β-human chorionic gonadotropin is seen in 80–90 % of patients with malignant germ cell tumors.

Teratoma

Teratomas derive from various types of tissues within two or more germ cell layers. They are categorized into three groups, namely mature, immature, and teratoma with additional malignant components, although most teratomas are mature (Travis et al. 2004). Mature teratomas are benign tumors made from histologically well-differentiated adult-type tissues (Fig. 10). Because of the digestive enzyme created from the tissue of teratomas, they can rupture into the bronchus, pleura, pericardium, and lung (Fig. 11). Immature teratomas are those that contain less differentiated tissue and that are similar to a developing fetus. Mature teratomas and most immature teratomas are benign. Mature teratomas occur 1.4 times more often in females than in males, while most immature teratomas occur in males. Malignant teratoma is a very rare form of teratoma that may contain somatic elements (non-germ cell) (Shahrzad et al. 2014; Travis et al. 2004).

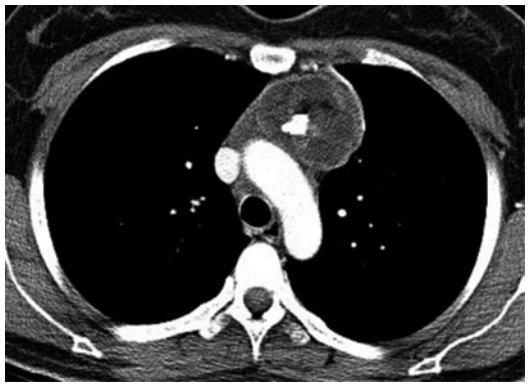

Fig. 10 A 30-year-old woman with mature teratoma. Contrast-enhanced CT shows a well-circumscribed anterior mediastinal mass that contains fat, calcification, and fluids. Note the thin uniform cyst wall

Eighty percent of mature teratomas arise in the anterior mediastinum, 3–8 % in the posterior mediastinum, 2 % in the middle mediastinum, and 13–15 % in multiple compartments (Travis et al. 2004). Mature teratomas are generally multilocular tumors with enhanced walls, and are observed along with water, fat, soft tissue, and calcification (Fig. 10) (Shahrzad et al. 2014; Drevelegas et al. 2001; Moeller et al. 1997). Cystic mature teratomas have thick cyst walls, unlike those of congenital thymic cyst. Fat or fat-fluid level is a diagnostic finding. When tera-

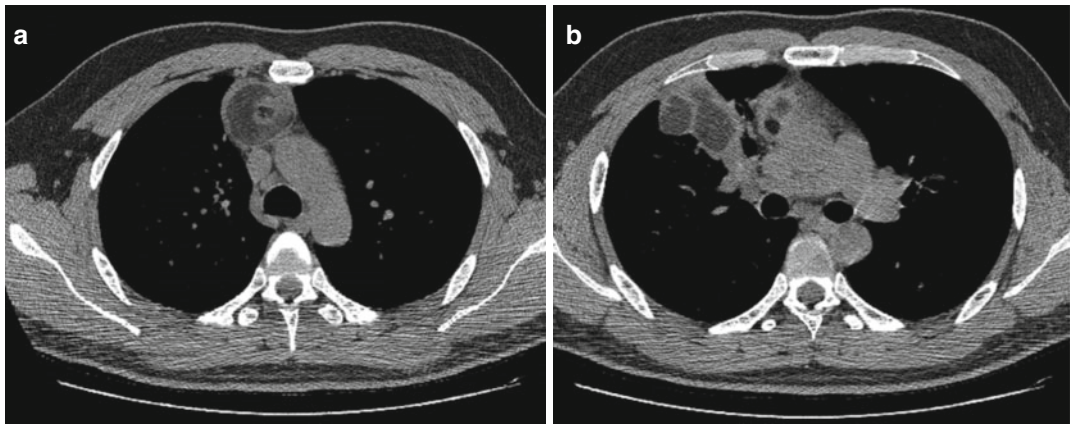

Fig. 11 A 33 year old male with mature teratoma ruptured into the right upper lobe of the lung. (**a**) Non-contrast enhanced CT shows that cystic mass in the anterior mediastinum that contains fat and fluid with thin smooth wall. (**b**) Cystic masses and consolidations are seen in the RUL suggesting rupture of the mass

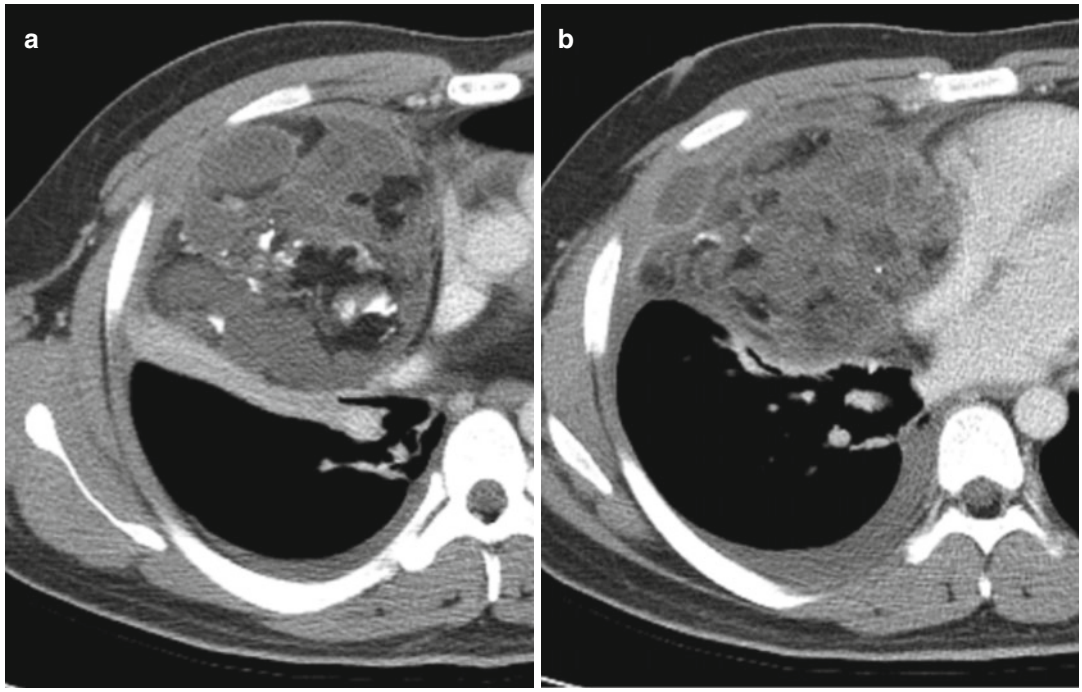

Fig. 12 A 31-year-old man with mature teratoma rupture into the right pleural space. (**a**) Contrast-enhanced CT shows fat, calcification, and fluid in the right anterior mediastinum. (**b**) Fluid and consolidation around the mass with right pleural effusion suggest teratoma rupture in the pleural space

tomas rupture, fat in the pleural effusion, or nonhomogeneous inner components, surrounding pneumonitis, and pericardial effusion may appear (Fig. 12) (Strollo et al. 1997a; Tecce et al. 1994; Drevelegas et al. 2001; Choi et al. 1998).

Seminoma

Seminona is the most common type of malignant germ cell tumor and occurs in approximately two-thirds of cases in patients in their twenties to forties. Found mostly in males, seminoma responds well to radiation therapy and general chemotherapy. While 10 % of cases show positive reaction to β-human chorionic gonadotropin, there are no cases of positive α-fetoprotein reaction. On CT, seminoma is normally a large homogeneous mass without calcification, and has cystic changes in only 25 % of the mass (Fig. 13) (Strollo et al. 1997a; Tecce et al. 1994; Drevelegas et al. 2001; Moeller et al. 1997; Rosado-de-Christenson et al. 1992). Seminoma can metastasize to local lymph node and bones, and sometimes can infiltrate into the surrounding organs.

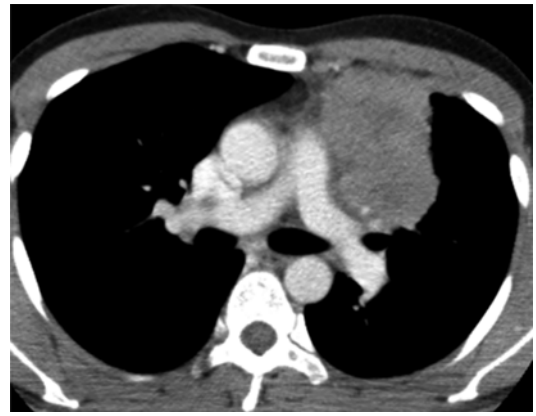

Fig. 13 A 30-year-old man with seminoma. Contrast-enhanced CT shows relatively heterogeneous enhancement of the left anterior mediastinal mass with focal low attenuation

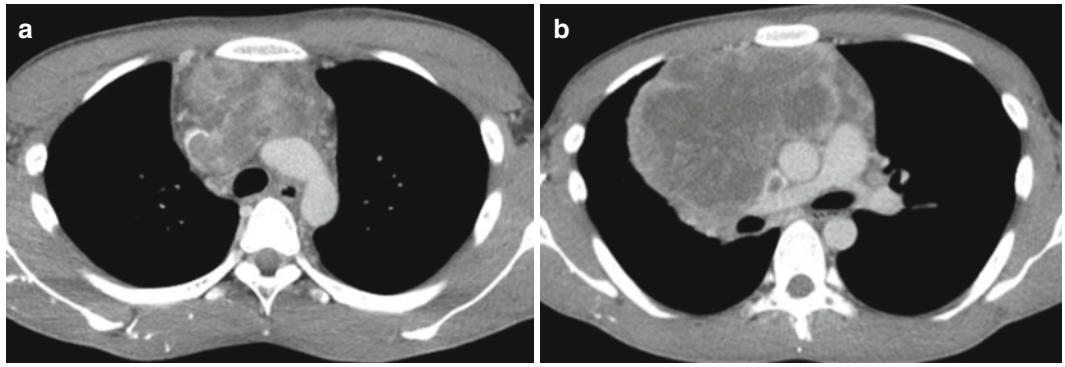

Fig. 14 A 22-year-old man with yolk sac tumor (α-fetoprotein 43,500 ng/mL). (**a**) Contrast-enhanced CT shows heterogeneous enhancement of the anterior mediastinal mass involving vessels. (**b**) Extensive necrosis or cystic portions are noted in the mass

Malignant Nonseminoma

Embryonal carcinoma, yolk sac tumor, choriocarcinoma, and mixed germ cell tumor are all types of malignant nonseminoma, which are treated with surgery and chemotherapy but have a poor prognosis. Serum markers and lactate dehydrogenase such as α-fetoprotein and β-human chorionic gonadotropin often have positive reactions, whereby α-fetoprotein is associated with yolk sac tumor components and β-human chorionic gonadotropin is associated with choriocarcinoma.

Unlike seminoma, malignant nonseminoma can often be observed with low-attenuated cysts with septa and necrosis, sometimes occupying more than 50 % of the mass (Fig. 14) (Lee et al. 1989; Rosado-de-Christenson et al. 1992). The tumor often invades surrounding structures, and calcification may exist (Drevelegas et al. 2001). Distant or local lymph node metastasis, pleural effusion, and pericardial effusion also frequently occur. Malignant germ cell tumors show necrosis and cystic changes even after treatment, and the remaining masses can be seen for years without progression.

1.1.6 Mediastinal Vascular Disorder

Hemangioma

Arising in all age groups from infancy to adulthood, hemangioma is seen as in parts of isolated or multicentric hemangiomas, for instance in cases of Osler-Weber-Rendu syndrome. Hemangioma is mostly found in the anterior superior mediastinum and is sometimes discovered in the anterior mediastinum at the level of the thymus (Fig. 15). The mass usually has a clear margin with heterogeneous attenuation and central enhancement on contrast-enhanced CT (Fig. 16) (Strollo et al. 1997a; Tecce et al. 1994; McAdams et al. 1994). Hemangiomas sometimes have irregular borders with surrounding mediastinal structures and are diffusely infiltrative, resulting in hyperplasia or erosion of the nearby ribs.

Lymphangioma

Lymphangioma is a common disease in young children, in whom 90 % of the cases are discovered before the age of 2 years. Lymphangioma is rarely seen in young adults. Cystic hygroma is a type of lymphangioma. Ninety-five percent of lymphangiomas arise from the neck or the axilla and 10 % from the upper anterior mediastinum, and others from the middle and posterior mediastinum. When discovered in adults, most cases arise in the mediastinum, and there is a possibility of recurrence of incompletely removed tumors from past childhood, but such histories are rare (Shaffer et al. 1994; Scalzetti et al. 1991).

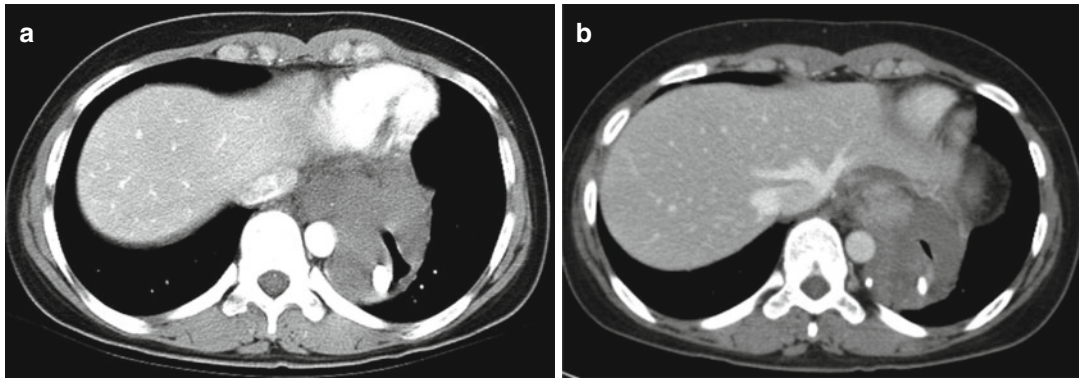

Fig. 15 A 31-year-old woman with mediastinal hemangioma. (**a**) Non-contrast-enhanced CT shows several calcifications in the mass. (**b**) After contrast enhancement, vascular pedicle to the mass is noted in the early state of enhancement

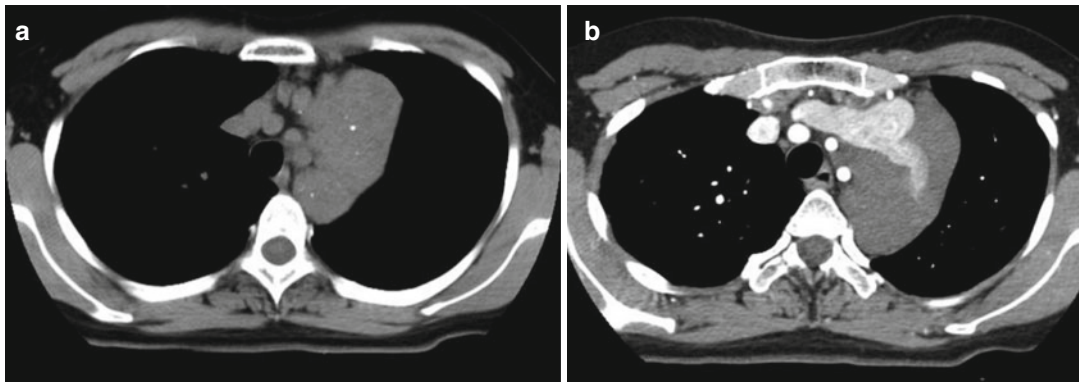

Fig. 16 A 27-year-old woman with mediastinal hemangioma. (**a**) Contrast-enhanced CT shows calcification within the posterior mediastinal mass. (**b**) Delayed enhancement is noted in the mass

Lymphangiomas typically arises in the anterior superior mediastinum and are associated with lesions near the neck or axilla. A lymphangioma is radiologically round and lobulated, with possibilities of growing into a large multilocular tumor, invading into the tissue layer, and encapsulating the mediastinal structure (Fig. 17) (Kim et al. 2003; Shaffer et al. 1994). Seen as homogeneous cystic tumors on CT, the size of the cyst can range from 1–2 mm to several centimeters and can appear as a slightly enhanced lesion. Multilocular cystic lesions with enhanced septa can be seen in one-third of lymphangiomas. Calcification is extremely rare (Shahrzad et al. 2014; Scalzetti et al. 1991; Kim et al. 2003; Charruau et al. 2000).

1.1.7 Intrathoracic Goiter

Goiters can extend from the thyroid gland into the anterior mediastinum or at times into the middle mediastinum; 75–80 % are located anterior to the trachea and 20–25 % in the posterior mediastinum. Pathologically multinodular goiters can also occur (Tecce et al. 1994).

Intrathoracic goiter is seen as an encapsulated, lobulated, and inhomogeneous mass. Diagnostic CT findings are anatomic continuity with the thyroid gland, local calcification, relatively high attenuation on the non-contrast-enhanced CT images, remarkable enhancement after bolus injection of contrast agent, and prolonged enhancement (Fig. 18) (Strollo et al. 1997a; Tecce et al. 1994; Lazer et al. 1982). Although

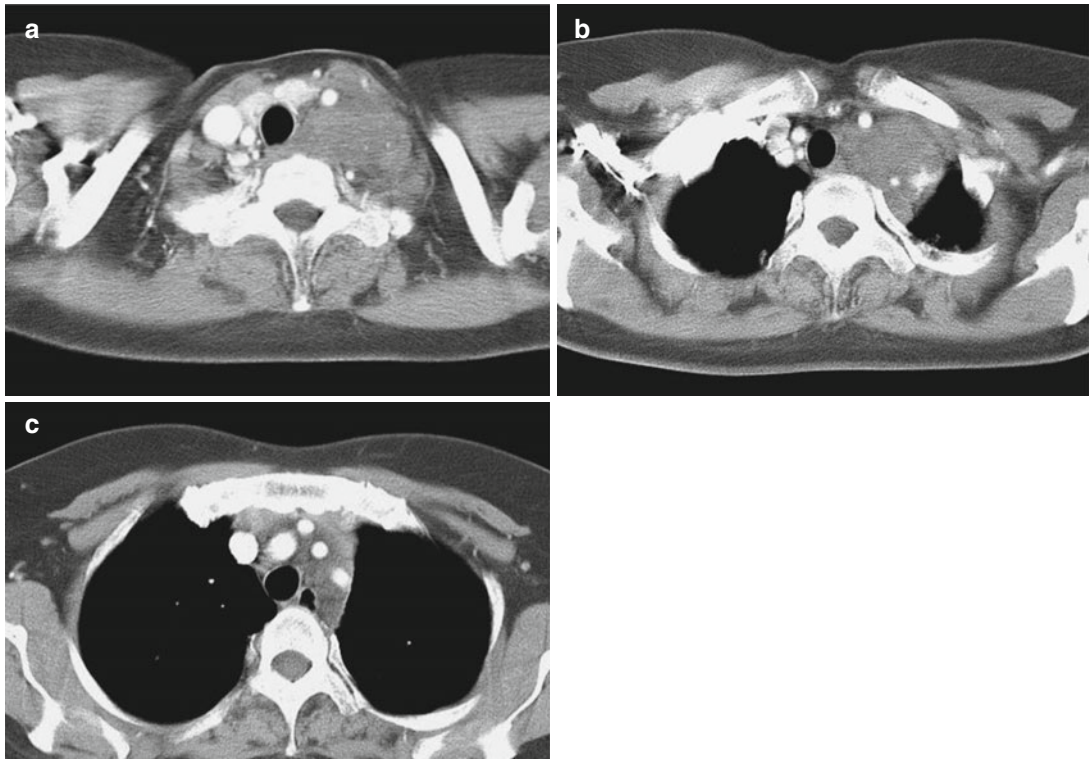

Fig. 17 A 35-year-old man with mediastinal lymphangioma. (**a**–**c**) Contrast-enhanced CT shows low-attenuated cystic masses encasing left carotid arteries and internal jugular vein in the left lower neck and mediastinum

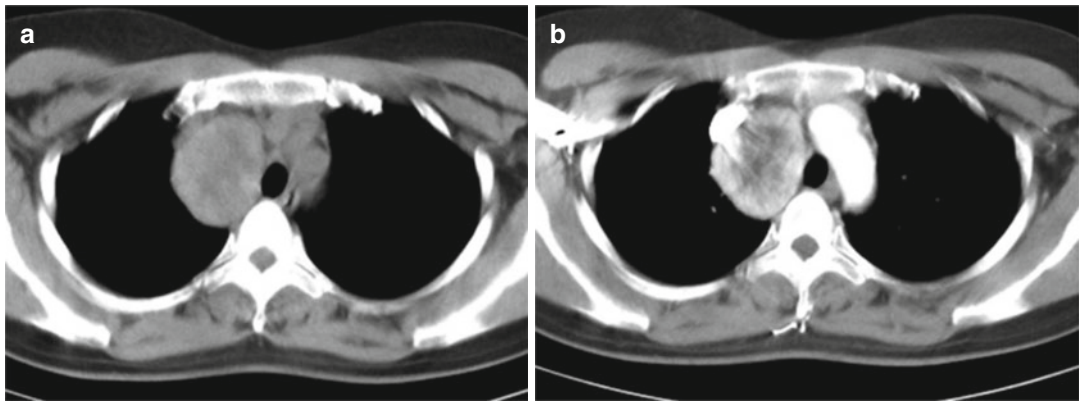

Fig. 18 A 36-year-old woman with intrathoracic goiter. (**a**) Non-contrast-enhanced CT shows relatively highly attenuated inhomogeneous mass in the right paratracheal region. (**b**) Contrast-enhanced CT shows remarkable enhancement owing to iodine content

thyroid gland and thoracic mass may appear disconnected on CT, goiters cannot be ruled out as the connection site may be extremely thin, fibrous, or contain vascular pedicles.

1.2 Middle Mediastinal Lesions

Various diseases accompanying lymphadenopathy are seen in the middle mediastinum, and lym-

Table 1 CT evaluation of lymphadenopathy in the mediastinum

A. Calcified lymph nodes
Common: infectious granulomatous disease (tuberculosis, fungus), sarcoidosis, Hodgkin disease (after radiation therapy)
Rare: *Pneumocystis jirovecii* pneumonia, metastasis (mucinous adenocarcinoma of gastrointestinal origin or osteosarcoma), amyloidosis, scleroderma, Castleman disease
B. Low-density or necrotic lymph nodes
Common: infections (tuberculosis, fungus), metastasis (lung cancer, seminoma)
Rare: Whipple disease
C. Enhancing lymph nodes
Common: metastasis (renal cell carcinoma, small cell lung cancer, papillary thyroid cancer, carcinoid), Castleman disease
Rare: Sarcoidosis, angioimmunoblastic lymphoma

Modified from Naidich et al. (1991)

phoma is one of the most common mediastinal disorders that can involve any parts of the mediastinum (Table 1) (Hansell et al. 2010). Congenital cysts also usually arise in the middle mediastinum.

1.2.1 Mediastinal Lymphoma

In both Hodgkin and non-Hodgkin disease, the most common thoracic abnormality is the enlargement of mediastinal lymph nodes. However, patients with lymph node enlargement only in the mediastinum are rare (Strollo et al. 1997).

The most common primary lymphomas are large B-cell lymphoma, precursor T-cell lymphoblastic lymphoma/leukemia, and the classic Hodgkin disease (especially nodular sclerosis) (Travis et al. 2004; Tateishi et al. 2004). Primary mediastinal large B-cell lymphoma generally occurs in the twenties to thirties and arises in females 1.5 times more than in males. Precursor T-cell lymphoblastic lymphoma arises twice as often in males and in patients in late childhood, adolescence, and early adulthood. A majority of Hodgkin disease in the mediastinum is of the nodular sclerosing type and occurs in females with a median age of 28 years (Fig. 19) (Travis et al. 2004).

Mediastinal lymphomas are commonly seen as large anterior mediastinal masses, enlarged mediastinal lymph nodes, or pleural or pericardial effusion. These three types of lymphoma may show necrosis. Forty percent of the lymphoma involves a single lymph node. PET/CT is efficient in assessing the staging and treatment response of the disorder. While it is difficult to completely differentiate Hodgkin disease from non-Hodgkin lymphoma using shape and distribution on CT, a differential diagnosis is possible by looking at the distribution of affected lymph nodes. Hodgkin disease is an asymmetric disease that usually forms in a single site and continuously spreads to the surrounding lymph nodes. By comparison, non-Hodgkin lymphoma is symmetric, assumed to arise in multiple sites, and spread in a discontinuous manner. The frequency rate of vascular invasion is 7 % in Hodgkin disease and is much greater in non-Hodgkin lymphoma, 38–62 %. The frequency rate of lung invasion is 20 % in Hodgkin disease and 6–10 % in non-Hodgkin lymphoma (Tateishi et al. 2004).

Hodgkin Disease

Hodgkin disease arises mostly in early adulthood and second most often in the fifties, and arises most frequently around the anterior mediastinal vessels and the paratracheal lymph nodes. The nodular sclerosing type is the most common form of Hodgkin disease, and may appear as a single lobulating mass or lymph node enlargements.

Mediastinal Hodgkin disease appears as round, multicentric lymph nodes, or one large soft tissue mass (nodular coalescence) (Hopper et al. 1990), or a sharply demarcated, aggressive thoracic mass. While the mass shows homogeneous soft-tissue attenuation, large tumors can appear as heterogeneous because of necrosis and hemorrhage (Fig. 20) (Tateishi et al. 2004; Strollo et al. 1997b). Mass effect in the mediastinum or invasion into the adjacent mediastinal structures can be seen. Calcification is rare before treatment. New or gradually enlarging mediastinal mass in the previously treated patients can be due to thymic cysts or thymic rebound hyperplasia rather than recurrence of lymphoma. PET/CT is useful in assessing remaining lesions or progression of the disease (Veeze-Kuijpers et al. 1989).

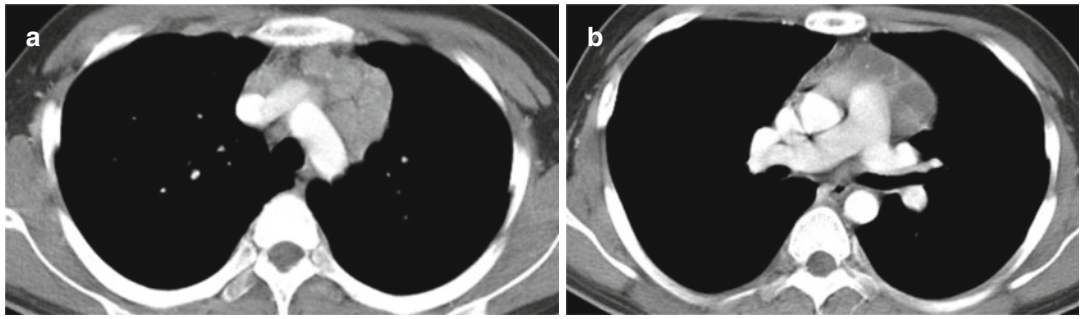

Fig. 19 A 17-year-old man with Hodgkin lymphoma (nodular sclerosing type). (**a**) Contrast-enhanced CT shows lymph node enlargements in the mediastinum. (**b**) Some of the enlarged lymph nodes are seen as low attenuation because of necrosis

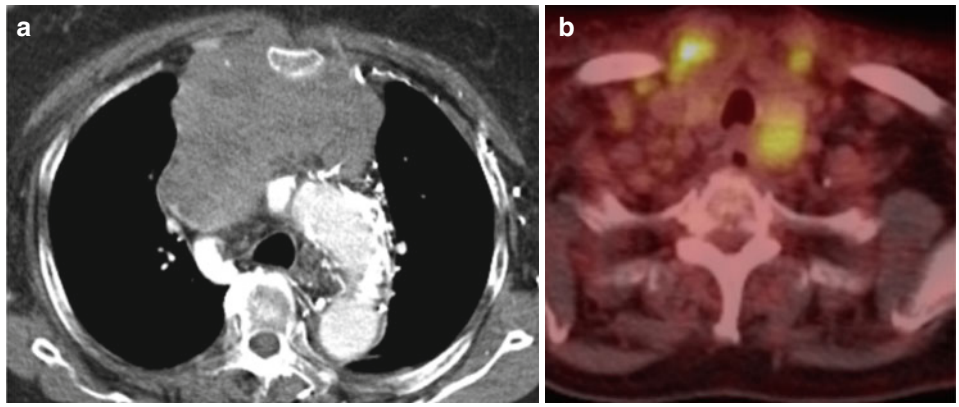

Fig. 20 A 76-year-old man with diffuse large B-cell non-Hodgkin lymphoma. (**a**) Contrast-enhanced CT shows large anterior mediastinal mass invading superior vena cava, sternum, and chest wall. (**b**) FDG-PET shows FDG uptake in several neck lymph nodes

Non-Hodgkin Lymphoma

In the thorax, non-Hodgkin lymphomas usually arise in the middle mediastinum and may also involve other parts of the mediastinum (Fig. 21). Non-Hodgkin lymphomas normally arise after the age of 2 years among children (Tateishi et al. 2004; Shaffer et al. 1996). Discontiguous or hematogenous spread is common in non-Hodgkin lymphoma. Thus other mediastinal involvement, not only in paracardiac, retrocrural lymph glands but also in extranodal lymph glands, can be seen. Calcification is rare. Non-Hodgkin lymphomas show low-attenuated mass with necrosis, and lung infiltration along the bronchovascular bundle can be found on CT in up to one-third of cases (Castellion et al. 1996).

1.2.2 Castleman Disease

Thoracic Castleman disease (or giant lymph node hyperplasia, or angiofollicular lymph node hyperplasia) occurs most frequently in the mediastinal lymph nodes but also can arise in the lung, pleura, and the thoracic wall. The disease is histologically classified into hyaline vascular type (90 %) and plasma cell type (10 %), and can arise in any age group. The hyaline vascular type normally does not have any symptoms and is incidentally found in the middle mediastinum, posterior mediastinum, and hilum as a mass (Tateishi et al. 2004). This is seen as a non-necrotizing homogeneous soft-tissue mass on CT, and has various shapes of calcifications and strong contrast enhancement (Moon et al. 1994).

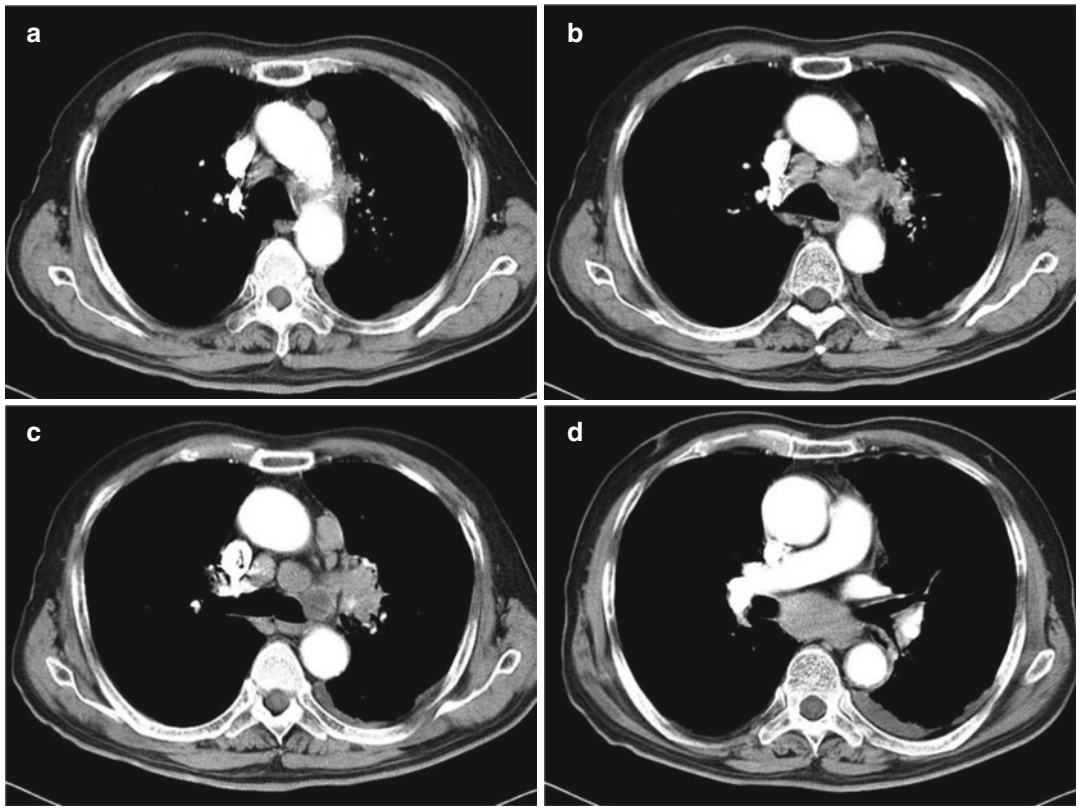

Fig. 21 A 45-year-old man with diffuse large B-cell non-Hodgkin lymphoma. (**a–d**) Multiple lymph node enlargements are seen in the mediastinum and left hilum. Small left pleural effusion and peribronchial infiltration are combined

On the other hand, the plasma cell type is often characterized by symptoms of fever, anemia, and weight loss, and is not well enhanced on CT.

The disease is clinically classified as localized type and multicentric type. Localized disease is observed in the hyaline vascular type and appears as a well-delineated mediastinal/hilar mass or an invasive mass with mediastinal lymph node involvement (Fig. 22). Typically the multicentric type is seen as a bilateral hilar and mediastinal lymph node enlargement (Fig. 23). Sometimes centrilobular nodules attributable to lymphoid interstitial pneumonia, thin-walled pulmonary cysts, bronchovascular bundle thickening, and interlobular septal thickening are found on CT. Ground-glass opacity, consolidation, and bronchiectasis are rare (Saeed-Abdul-Rahman and Al-Amri 2012; Johkoh et al. 1998). The plasma cell type is more common in multicentric disease (Strollo et al. 1997b; McAdams et al. 1998) (Fig. 24).

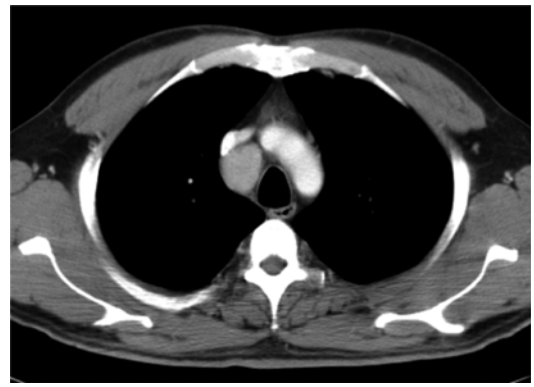

Fig. 22 A 33-year-old man with Castleman disease (hyaline vascular type). Contrast-enhanced CT shows enlarged enhancing well-defined right paratracheal mass

1.2.3 Tuberculous Lymphadenitis

Paratracheal and tracheobronchial lymph node enlargement is the most common finding in tuberculous lymphadenitis, and quite often

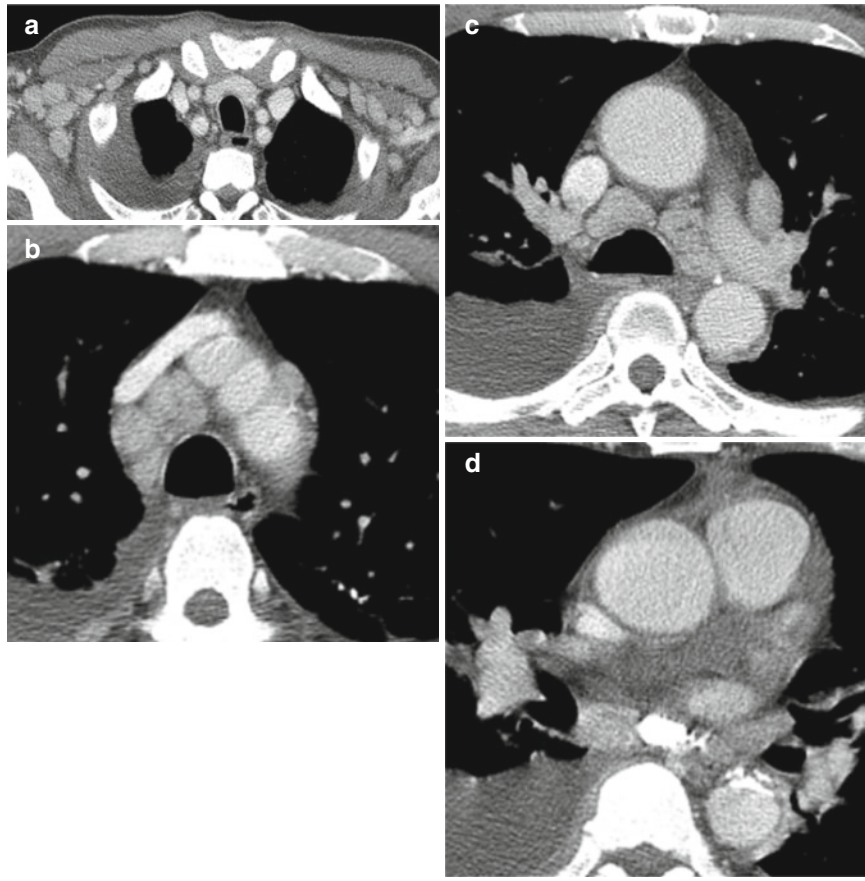

Fig. 23 A 63-year-old man with Castleman disease (plasma cell type). (**a–d**) Contrast-enhanced CT shows multiple bilateral axillary and mediastinal lymph node enlargement (multicentric form), and the lymph nodes are well enhanced

affects the subcarinal and aorticopulmonary lymph node. It tends to appear on the same side of the involved lung. Low-attenuated center from caseation necrosis and rim enhancement are characteristic radiologic findings on CT and MRI (Im et al. 1989). However, mycosis, metastasis, Kaposi sarcoma, lymphoma, and sarcoidosis can also have similar findings. Involvement with lung parenchyma is common (Lee et al. 1993).

1.2.4 Sarcoidosis

Sarcoidosis is common in the 20- to 40-year-old age group, and 80–90 % of the patients show enlarged lymph nodes, where involvement of paratracheal lymph node enlargement and

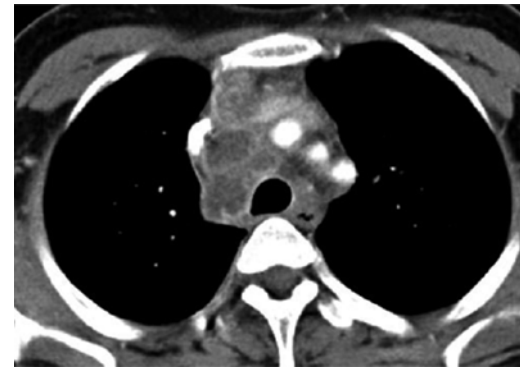

Fig. 24 A 25-year-old woman with pulmonary tuberculous lymphadenitis. Contrast-enhanced CT shows multiple lymph node enlargement with rim enhancement in the prevascular and right paratracheal region

symmetric enlargement of bilateral hilar lymph nodes are most frequent radiologic findings (Fig. 25). Symmetric enlargement of hilar lymph nodes is a significant finding in distinguishing sarcoidosis from lymphoma, tuberculosis, and metastatic disorders. Aortopulmonary lymph node and subcarinal lymph node enlargement may cause airway obstruction. Enlarged lymph nodes rarely show calcification, but eggshell-shaped calcification can be seen in chronic patients (Patil 1999; Miller et al. 1995).

1.2.5 Pericardial Cyst

Radiologically, congenital pericardial cysts are sharply marginated, round, or cystic unilocular cysts with unidentifiable thin walls. Adherence to heart, pericardium, and/or diaphragm is characteristic (Fig. 26). A connection to the pericardial cavity is occasional. Calcification of the cyst wall is rare. The site of occurrence is 70 % in the right cardiophrenic angle and 22 % in the left cardiophrenic angle. Eight percent arises in other parts of the heart, which is why pericardial cysts are

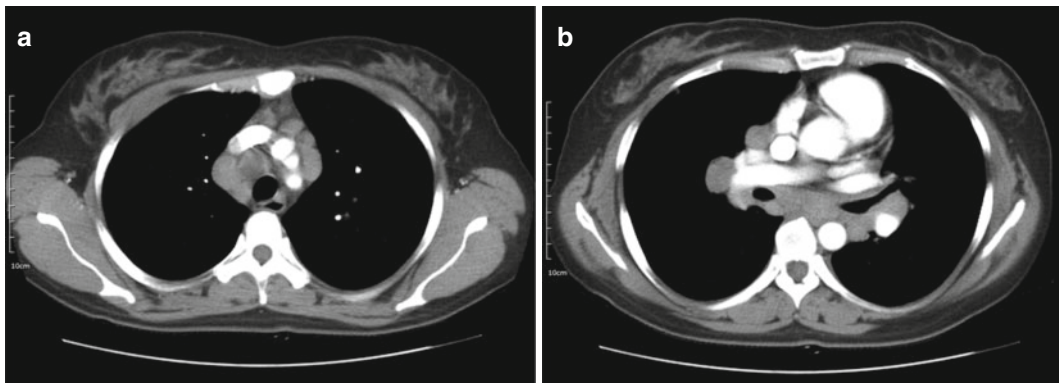

Fig. 25 A 42-year-old woman with sarcoidosis. (**a, b**) Contrast-enhanced CT shows multiple bilateral symmetric lymph node enlargement in the mediastinum

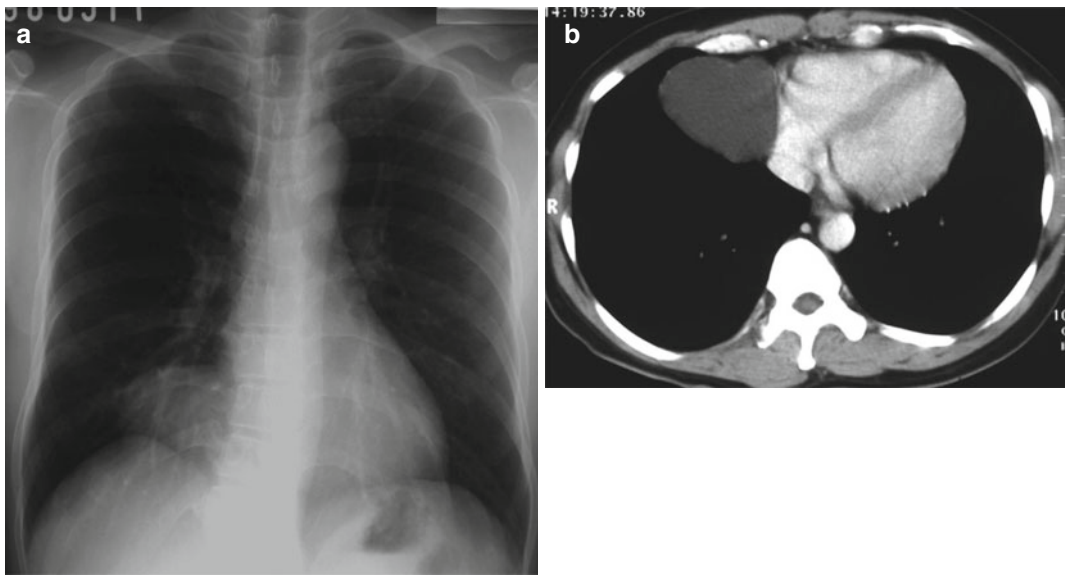

Fig. 26 Pericardial cyst. (**a**) Chest X-ray shows mass-like opacity in the right cardiophrenic angle. (**b**) Contrast-enhanced CT shows cystic mass with thin wall attached to the heart or pericardium

difficult to distinguish from bronchogenic cysts and thoracic cysts (Strollo et al. 1997; Feigin et al. 1977).

1.2.6 Acute Mediastinitis

The most common cause of acute mediastinitis is an iatrogenic esophageal perforation from gastrointestinal endoscopy or infection following surgery such as median sternotomy. The complications of esophageal perforation include esophagocutaneous fistula, esophagopleural fistula, and esophagobronchial fistula. Descending necrotizing mediastinitis, another type of acute mediastinitis, is the condition whereby oropharyngeal infection spreads into the mediastinum through the fascial plane and cervical spaces.

Enlargement of the mediastinum and increased mediastinal attenuation, pneumomediastinum, fat plane loss, and localized fluid collection or abscess formation are general radiologic findings, while unilateral or bilateral pleural effusion is also common (Fig. 27). When caused by esophageal rupture, acute mediastinitis usually shows esophageal wall thickening, air outside of the esophagus, pleural effusion, mediastinal abscess, and contrast leakage from the esophagus on CT (Akman et al. 2004; Feigin et al. 1977; Exarhos et al. 2005).

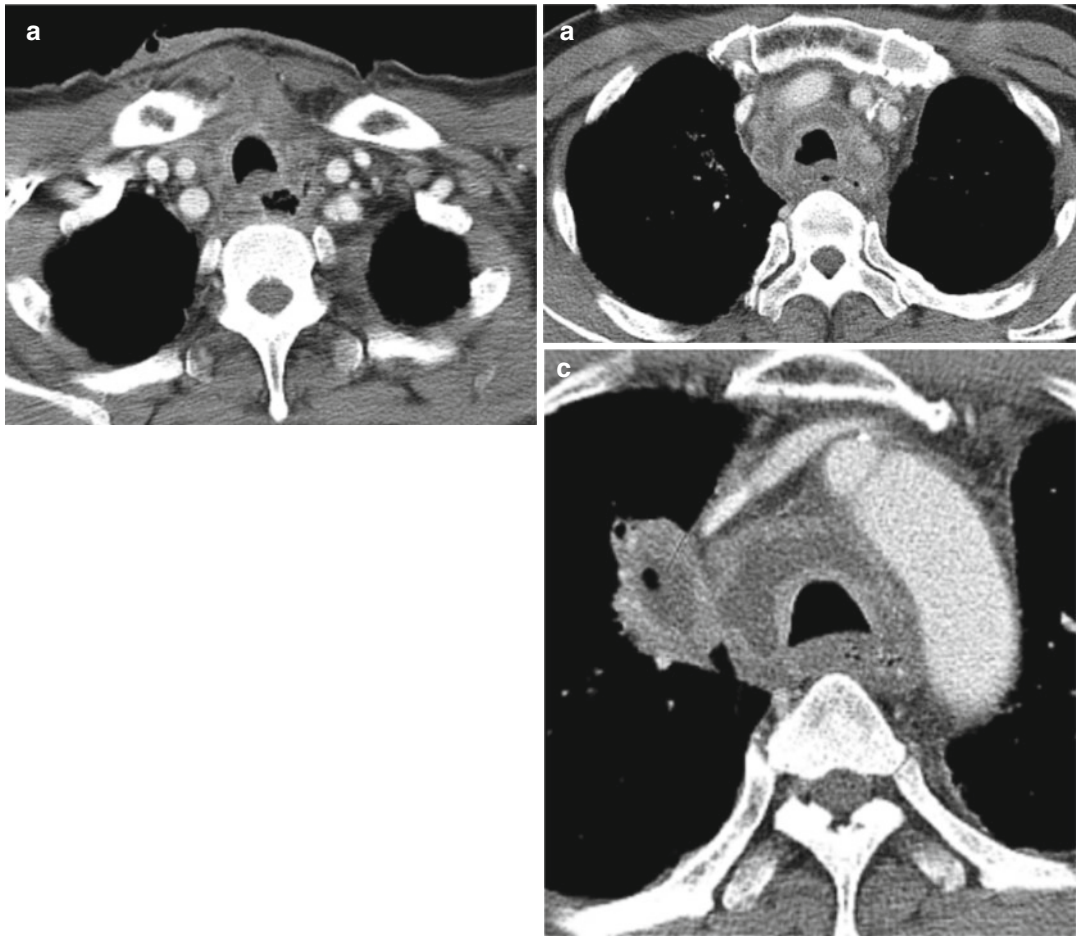

Fig. 27 A 69-year-old man with acute mediastinitis after left lower lobe lobectomy. (**a**) Contrast-enhanced CT shows fluid collections at the site of mediastinoscopy. (**b**) The abscess-like fluid collection extends into the anterior mediastinum and around the trachea. (**c**) Mediastinal abscess ruptures into the right upper lobe, and esophageal wall thickening is seen

1.2.7 Fibrosing Mediastinitis

In only 50 % of cases of fibrosing mediastinitis can a specific cause be identified, which include histoplasma or an abnormal immune reaction to tuberculosis antigen, systemic autoimmune disease, lymphoma, radiotherapy, trauma, and drugs (i.e., methysergide) (Shahrzad et al. 2014). Other cases are defined as idiopathic. When caused by infection, the main pathologic finding is a necrotizing granulomatous inflammation, whereas idiopathic fibrosing mediastinitis shows mature fibrous tissue invaded by monocytic inflammatory cells.

There are two types of CT findings: local, often with calcifications, and diffuse, without calcification (Devaraj et al. 2007; Se et al. 2001). The local type usually shows a mediastinal or hilar mass with inner calcification, esophageal compression, airway stricture, and obstruction of pulmonary trunk, pulmonary vein, or superior vena cava (Fig. 28) (McNeeley MF et al. 2012; Williams and Jones 1997). Secondary pulmonary hypertension, cor pulmonale, and refractory right heart failure due to pulmonary trunk compression can also be found (Williams and Jones 1997).

The presence of calcification is the key difference from lymphoma and metastatic carcinoma. However, the diffuse type of fibrosing mediastinitis involves mediastinum without any calcification, invades mediastinal fat planes, and either encases or infiltrates surrounding structures (Se et al. 2001). An inhomogeneous signal intensity is seen on MRI, with rather low signal intensity on T2-weighted images because of fibrosis.

1.3 Posterior Mediastinal Disorders

The posterior mediastinum can be divided into true posterior mediastinum (located between the heart and the vertebral bodies), and paravertebral area. True posterior mediastinal disorders comprise descending aortic diseases, enlarged lymph nodes, foregut cysts, thoracic goiters, and pseudocysts. Paravertebral diseases include neurogenic tumor, lymph nodes, tuberculous spondylitis, spinal injury, spinal tumor, and extramedullary hematopoiesis (Hansell et al. 2010; Woo et al. 2008). This section discusses neurogenic tumors, foregut cysts, aortic disorders, spinal injuries, and extramedullary hematopoiesis.

1.3.1 Neurogenic Tumor

The neurogenic tumor is the most common mass in the posterior mediastinum. It is located near the vertebrae, and subdivided by location of origin (peripheral nerve, sympathetic ganglia, and paraganglia). Ninety percent of the tumors in the peripheral nerve are benign and histologically classified as neurilemmoma or schwannoma, neurinoma, and neurofibroma. Malignant tumors are described as malignant tumor of nerve sheath origin. Tumors originating from the sympathetic ganglia comprise

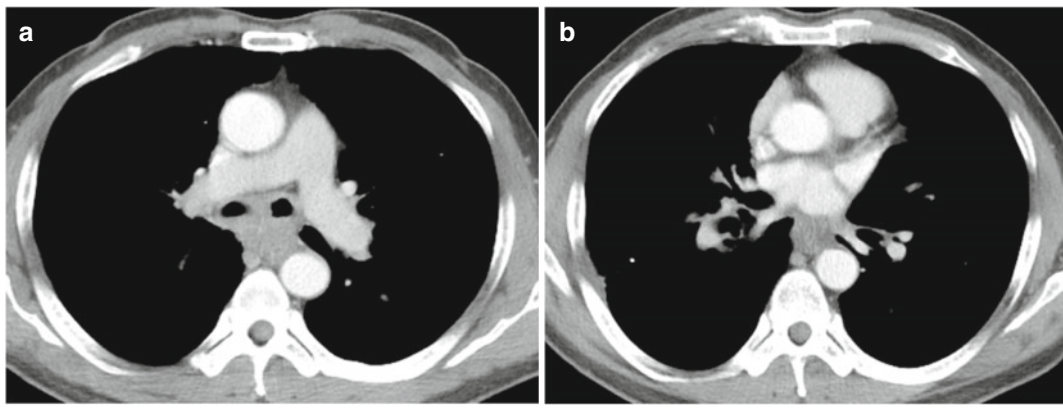

Fig. 28 A 58-year-old man with fibrosing mediastinitis. (**a**) Contrast-enhanced CT shows infiltration along the main bronchial wall and esophagus. (**b**) Esophageal narrowing attributable to diffuse esophageal wall thickening is noted

ganglioneuroma, ganglioneuroblastoma, and neuroblastoma. Paraganglioma arises from the paraganglia. The most common neurogenic tumor in adults is neurilemmoma, while sympathetic ganglia tumors are more common in children (Woo et al. 2008; Lee et al. 1999; Cohen et al. 1986; Kawashima et al. 1991; Beggs 1997).

Peripheral Nerve Sheath Tumor

Neurinoma and Neurofibromatosis

Neurinoma and neurofibroma are the most common neurogenic tumors, and are slow-growing benign tumors that often arise from the spinal roots. Radiologically, neurinoma and neurofibroma are well delineated, round, and lobulated tumors found near the vertebrae. Benign pressure erosion of the ribs, vertebrae, and neural foramen may exist. When they grow into the spinal cord they may show a dumbbell shape on CT.

Neurinomas have homogeneous iso-attenuation or slightly lower than the soft tissue on non-contrast-enhanced CT, but show homogeneous or nonhomogeneous attenuation after injection of contrast medium. The heterogeneous enhancement may be caused by the inhomogeneous distribution of high cell density (Antoni type A) and low cell density (Antoni type B) or the presence of a lipidized foamy cells and cystic xanthomatous hemorrhagic portion (Fig. 29) (Lee et al. 1999; Cohen et al. 1986). Central enhancement of the mass may be seen in the early phase of the contrast enhancement.

When there are suspicious signs of invasion into the spinal cord, MRI is recommended. On T2-weighted images, a neurofibroma has high signal intensity in the periphery and low signal intensity center showing the characteristic target sign, but can show findings similar to that of neurinoma (Tanaka et al. 2005).

A plexiform neurofibroma involves the sympathetic chain and sometime invades the vagus and phrenic nerves (Bourgouin et al. 1988). The mass is seen as peripheral diffuse spindle shape enlargement or as multiple, irregular lobulated tumors.

Usually the mass shows lower attenuation than that of the chest wall muscles before contrast enhancement, and only the peripheral regions are enhanced on postcontrast images on CT (Tanaka et al. 2005). Multiple neurofibromas or plexiform neurofibromas are diagnostic findings of neurofibromatosis (Fig. 30) (Bourgouin et al. 1988).

Malignant Tumor of Nerve Sheath Origin

Malignant tumors of nerve sheath origin are also known as malignant neurilemmomas or neurofibrosarcomas. While radiologically seen as a round, well-defined posterior mediastinal mass, the tumor can locally infiltrate mediastinal structures or chest wall. Size greater than 5 cm, especially in neurofi-

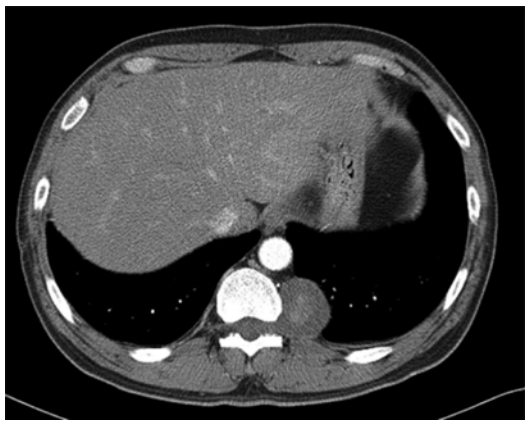

Fig. 29 A 40-year-old man with neurogenic tumor. Contrast-enhanced CT shows central enhancement of the left paravertebral mass (target sign). The mass extends into the neural foramen

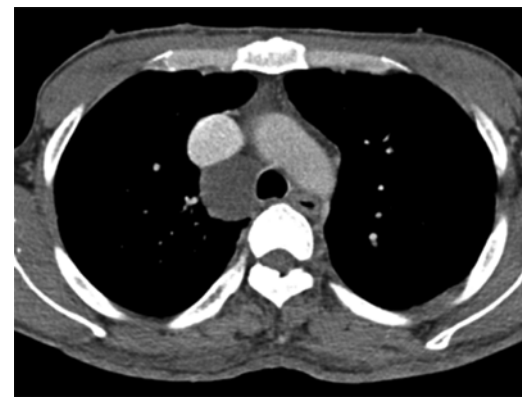

Fig. 30 A 42-year-old man with neurofibromatosis. Contrast-enhanced CT shows low-attenuated mass in the right paratracheal region and multiple subcutaneous nodules in the anterior chest wall

bromatosis patients, low attenuation within the lump, irregular borders, collapse of surrounding structures, pleural effusion or nodes, and metastatic pulmonary nodules suggest malignancy. The presence of hematogenous lung metastasis is not uncommon rare but lymph node metastases are rare (Bourgouin et al. 1988).

Sympathetic Ganglia Tumors

Sympathetic ganglia tumors include benign ganglioneuromas, malignant ganglioneuroblastomas, and malignant neuroblastomas. Ganglioneuroma usually occurs from age 3 years to young adulthood, ganglioneuroblastoma in children under 10 years, and neuroblastoma in children under 5 (Strollo et al. 1997).

On CT, while peripheral nerve tumors are usually round, sympathetic ganglia tumors are wide near the front of the spine and vertically long masses along 3–5 vertebrae. Thoracic scoliosis, spondylolisthesis, and benign pressure erosion can be seen. A dumbbell-shaped mass with the spinal canal or neural foramen extension, and calcification, may exist (Beggs 1997).

A ganglioneuroma (Fig. 31) is a well-defined mass showing homogeneous low attenuation prior to enhancement and slight enhancement after contrast enhancement, and does not metastasize. On the other hand, ganglioneuroblastomas (Ribet and Cardot 1994) and neuroblastomas (Adam and Hochholzer 1981) show irregular margins and heterogeneous attenuation. Invasion to the surrounding structures and/or metastasis to the contralateral side may occur (Strollo et al. 1997; Stark et al. 1983).

Paraganglioma

A paraganglioma, or chemodectoma, is a rare neurogenic tumor that originates from paraganglia near sympathetic ganglia and plexuses. In the chest, paraganglioma usually forms in the aortopulmonary window, the space near the heart or the pericardium, or near the vertebrae. As benign and malignant tumors have very similar histologic findings, the clinical findings (e.g., metastasis, recurrence) determine the patient's prognosis. They appear as very well enhanced soft-tissue masses on CT (Fig. 32). On MRI, T1-weighted images show low or medium signal intensity and T2-weighted images show mid-to-high or high signal intensity with heterogeneous enhancement (Sahdev et al. 2005).

Lateral Thoracic Meningocele

Lateral thoracic meningocele is a rare cystic lesion bulging through the neural foramen filled with cerebrospinal fluid (CSF). Often occurring in the thirties to forties, 75 % of such patients have neurofibromas. Radiologically a sharply marginated cystic mass near the vertebrae is depicted, and is accompanied with rib and vertebral or other skeletal abnormalities such as lumbar vertebral

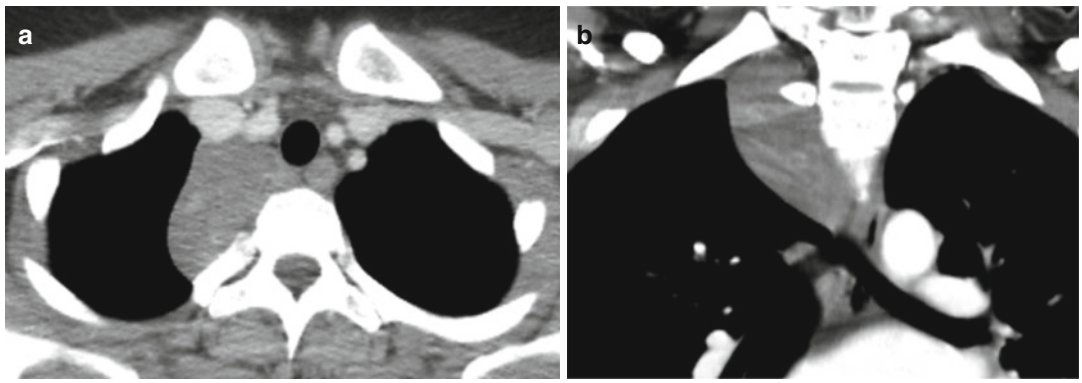

Fig. 31 A 24-year-old woman with ganglioneuroma. (**a**) Contrast-enhanced CT shows paravertebral mass in the right upper lobe. (**b**) Coronal reformatted image shows vertically long mass in the right upper paravertebral region

erosion. On CT, the connection of CSF fluid attenuation between meningocele and thecal sac is pathognomonic, but is not always found (Strollo et al. 1997).

1.3.2 Foregut Cysts

Foregut cysts comprise bronchogenic and enterogenic cysts. Enterogenic cysts include esophageal duplication cyst and neurenteric cyst (Salyer et al. 1977). Foregut cysts are aberrantly developed primitive ventral foreguts, and the enteric cysts bud in the dorsal foregut. Foregut cysts are cystic structures with inner epithelium and are distinguished by histologic findings rather than their location (Salyer et al. 1977). Foregut cysts generally are well delineated, homogeneously attenuated, thin-walled unilocular cystic mass.

Esophageal Duplication Cyst

Esophageal duplication cysts have mucous membrane and muscular layer similar to those of esophagus, stomach, or the small intestine and, unlike bronchogenic cysts, do not contain cartilage (Kuhlman et al. 1985). Appearing as cysts in or near the esophagus, most esophageal duplication cysts arise close to the esophagus particularly in the vicinity of the right lower esophagus (Strollo et al. 1997; Kuhlman et al. 1985; Kuhlman et al. 1988). They are rarely connected to the esophageal lumen or bronchus, and approximately 12 % are involved with gastrointestinal congenital disorders.

Esophageal duplication cysts seldom have calcification and have radiologic findings almost identical to those of bronchogenic cysts, the walls being slightly thicker and tending to be tubular. The cyst can be seen as an intramural or external mass on barium esophagography.

Bronchogenic Cyst

Bronchogenic cysts are typically found in characteristic locations such as the paratracheal or the subcarinal region. On CT they manifest as an oval or round mass of water attenuation, but may present soft-tissue attenuation (Fig. 33). However, they may occur within the lung parenchyma or in the pleura. They are sometimes associated with other congenital pulmonary malformations such as sequestration. Bronchogenic cysts seldom have calcifications. Their walls are almost invisible and they do not enhance after injection of contrast medium. MRI can be very useful for differentiating soft-tissue attenuating bronchogenic cysts from soft-tissue masses. They show a CSF-like hypersignal on T2-weighted sequences, and may show hypointense muscle isosignal or slightly hyperintense signal on T1-weighted images suggesting mucus and proteins within the cyst (McAdams et al. 2000).

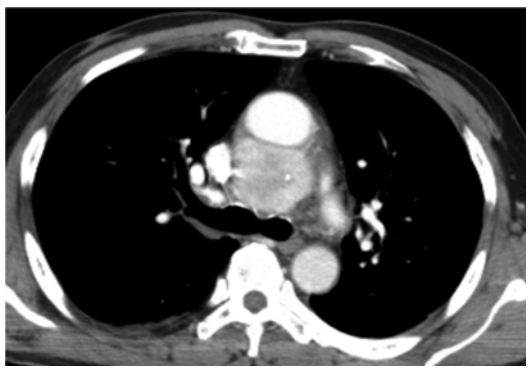

Fig. 32 A 68-year-old man with paraganglioma. Contrast-enhanced CT shows marked enhancement of the mass in the mediastinum. Small calcification is also seen in the mass

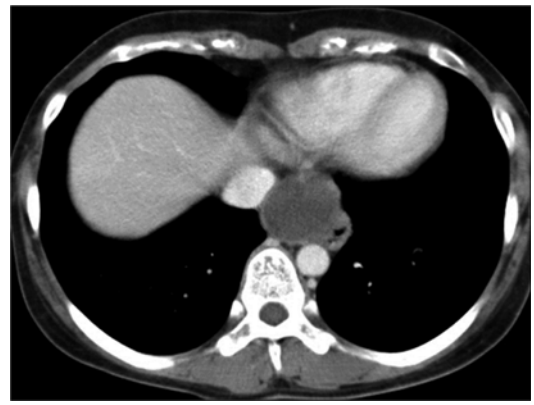

Fig. 33 A 25-year-old woman with bronchogenic cyst. Contrast-enhanced CT shows thin-walled cystic lesion in the paraesophageal region

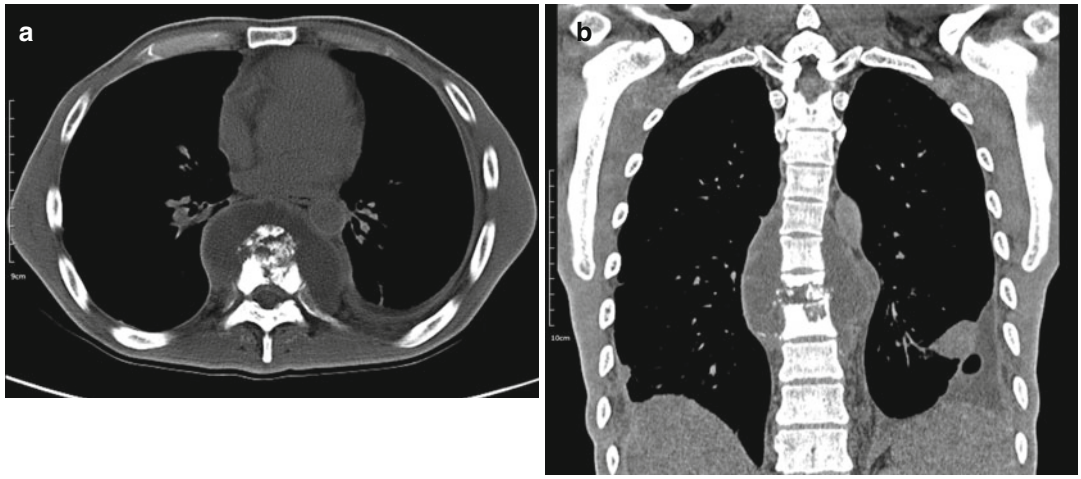

Fig. 34 A 35-year-old man with tuberculous spondylitis. (**a**) Non-contrast-enhanced CT shows osteolytic bone lesion in the thoracic spine with paravertebral abscess formation. (**b**) Coronal reformatted image shows paraspinal abscess contiguously involving several vertebral bodies and left pleural effusion

Neurenteric Cyst

The formation of neurenteric cysts is due to an endodermal diverticulum that is created when notochords are incompletely separated. They are pathologically identical to esophageal duplication cysts, and are often seen with neural and enteric tissue. They often have fibrous connections with the vertebrae or spine and are often accompanied by spine malformation, i.e., cervical and upper thoracic scoliosis, anterior spina bifida, hemivertebra, butterfly vertebra, and fusion. The accompanying spine malformation is usually located slightly above the cyst. Neurenteric cysts are mostly discovered in infants younger than 1 year.

Neurenteric cysts are seen as typically round, cystic, or lobulated fluid-attenuated lesions. Ninety percent of neurenteric cysts are located in the posterior mediastinum, especially on the right upper side of the carina away from the esophagus. Cysts are molded from adjacent structures and sometimes are connected with the meninges, and more often with a portion of the gastrointestinal tract.

1.3.3 Aortic Lesions

Aortic lesions (aortic aneurysm and dissection) are described in detail the vascular section elsewhere in this volume.

1.3.4 Infectious Spondylitis

Tuberculous spondylitis is the most common cause of infectious spondylitis. Radiologic findings include narrowed intervertebral disk space, osteolysis in the adjacent bones, contiguous involvement of two vertebral bodies, and paravertebral soft-tissue mass (Fig. 34). Active new bone formation is rare in tuberculous spondylitis, and the destruction of the anterior vertebral bodies often causes gibbus deformity.

1.3.5 Extramedullary Hematopoiesis

Extramedullary hematopoiesis occurs in cases of severe anemia when there is inadequate production or excessive destruction of blood cells. It is seen most often in cases of congenital hemolytic anemia (e.g., hereditary spherocytosis) or thalassemia. Extramedullary hematopoiesis occurs most often in the spleen and liver but can also arise in the paravertebral region.

In the chest, one or multiple lobulated masses near the lower thoracic spine is a common finding. While appearing as slightly homogeneous enhanced soft-tissue attenuation (Fig. 35), large fat tissues can sometimes be seen on CT. Medullary cavity expansion showing widening of ribs, and lace-like vertebrae can also be seen (Gerogiades et al. 2002; Gumbs et al. 1987).

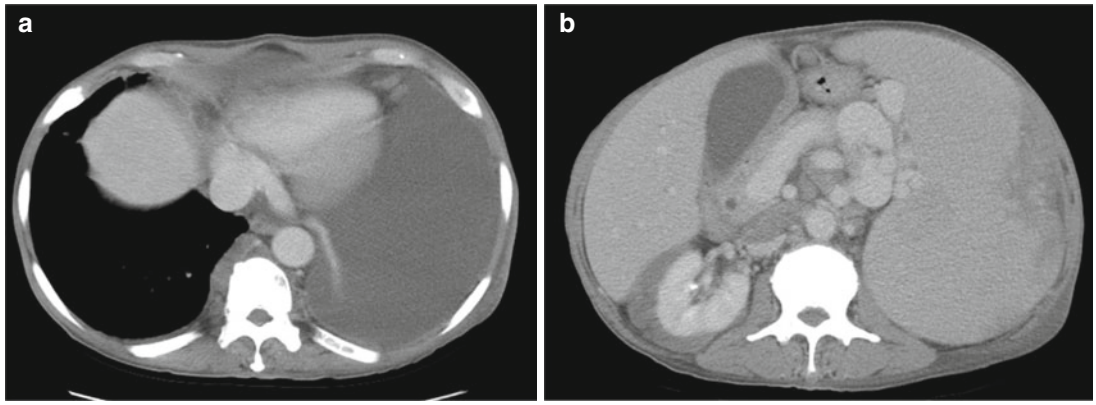

Fig. 35 A 70-year-old man with extramedullary hematopoiesis. (**a**) Contrast-enhanced CT shows paravertebral mass and left pleural effusion. (**b**) Perirenal soft tissues and splenic involvements are also noted

References

Adam A, Hochholzer L (1981) Ganglioneuroblastoma of the posterior mediastinum: a clinicopathologic review of 80 cases. Cancer 47:373–381

Akman C, Kantarci F, Cetinkaya S (2004) Imaging in mediastinitis: a systematic review based on aetiology. Clin Radiol 59:573–585

Beggs I (1997) Pictorial review: imaging of peripheral nerve tumours. Clin Radiol 52:8–17

Bourgouin PM, Shepard JO, Moore EH, McLoud TC (1988) Plexiform neurofibromatosis of the mediastinum: CT appearance. AJR Am J Roentgenol 151:461–463

Castellion RA, Hilton S, O'Brien JP, Portlock CS (1996) Non-Hodgkin lymphoma: contribution of chest CT in the initial staging evaluation. Radiology 199:129–132

Charruau L, Parrens M, Jougon J et al (2000) Mediastinal lymphangioma in indults: CT and MR imaging features. Eur Radiol 10:1310–1314

Choi SJ, Lee JK, Song KS, Lim TH (1998) Mediastinal teratoma: CT differentiation of ruptured and unruptured tumors. AJR Am J Roentgenol 171:591–594

Choi YW, McAdams HP, Jeon SC et al (2001) Idiopathic multilocular thymic cyst: CT features with clinical and histopathologic correlation. AJR Am J Roentgenol 177:881–885

Cohen LM, Schwartz AM, Rockoff SD (1986) Benign schwannomas: pathologic basis for CT inhomogeneities. AJR Am J Roentgenol 147:141–143

Devaraj A, Griffin N, Nicholson AG, Padley SPG (2007) Computed tomography findings in fibrosing mediastinitis. Clin Radiol 62:781–786

Do YS, Im JG, Lee BH et al (1995) CT findings in malignant tumors of thymic epithelium. J Comput Assist Tomogr 19:192–197

Drevelegas A, Palladas P, Scordalaki A (2001) Mediastinal germ cell tumors: a radiologic-pathologic review. Eur Radiol 11:1925–1932

Exarhos DN, Malagari K, Tsatalous EG et al (2005) Acute mediastinitis: spectrum of computed tomography findings. Eur Radiol 15:1569–1574

Feigin DS, Fenoglio JJ, McAllister HA, Madewell JE (1977) Pericardial cysts. A radiologic-pathologic correlation and review. Radiology 125:15–20

Ferdinand B, Gupta P, Kramer EL (2004) Spectrum of thymic uptake at 18F-FDG PET. Radiographics 24:1611–1616

Fraser RS, Paré JAP, Frase RG, Paré PD (1994) The normal chest. In: Fraser RS, Paré JAP, Fraser RG, Paré PD (eds) Synopsis of diseases of the chest, 2nd edn. WB Saunders, Philadelphia, pp 1–116

Georgiades CS, Neyman EG, Francis IR et al (2002) Typical and atypical presentation of extramedullary hemopoiesis. AJR Am J Roentgenol 179:1239–1243

Gumbs RV, Higginbotham-Ford EA, Teal JS et al (1987) Thoracic extramedullary hematopoiesis in sickle-cell disease. AJR Am J Roentgenol 149:889–893

Hansell DM, Lynch DA, McAdams HP, Bankier AA (2010) Imaging of diseases of the chest. Mosby Elsevier, Edinburgh

Hopper KD, Diehl LF, Cole BA et al (1990) The significance of necrotic mediastinal lymph nodes on CT in patients with newly diagnosed Hodgkin disease. AJR Am J Roentgenol 155:267–270

Im JG, Song KS, Kang HS et al (1989) Mediastinal tuberculous lymphadenitis: CT manifestations. Radiology 164:115–119

Inaoka T, Takahashi K, Mineta M et al (2007) Thymic hyperplasia and thymus gland tumors: differentiation with chemical shift MR imaging. Radiology 243:869–876

Jeong YJ, Lee KS, Kim J et al (2004) Does CT of thymic epithelial tumors enable us to differentiate histologic subtypes and predict prognosis? AJR Am J Roentgenol 183:283–289

Johkoh T, Müller NL, IChikado K et al (1998) Intrathoracic multicentric Castleman disease: CT findings in 12 patients. Radiology 209:477–481

Jung KJ, Lee KS, Han J et al (2001) Malignant thymic epithelial tumors: CT-pathologic correlation. AJR Am J Roentgenol 176:433–439

Kawashima A, Fishman EK, Kuhlman JE, Nixon MS (1991) CT of posterior mediastinal masses. Radiographics 11:1045–1067

Kim JH, Goo JM, Lee HJ et al (2003) Cystic tumors in the anterior mediastinum. Radiologic-pathological correlation. J Comput Assist Tomogr 27:714–723

Kuhlman JE, Fishman EK, Wang KP, Siegelman SS (1985) Esophageal duplication cyst: CT and transesophageal needle aspiration. AJR Am J Roentgenol 145:531–532

Kuhlman JE, Fishman EK, Wang K et al (1988) Mediastinal cysts: diagnosis by CT and needle aspiration. AJR Am J Roentgenol 150:75–78

Lazer GM, Axel L, Moss AA (1982) CT diagnosis of mediastinal thyroid. AJR Am J Roentgenol 138: 495–498

Lee KS, Im JG, Han CH et al (1989) Malignant primary germ cell tumors of the mediastinum: CT features. AJR Am J Roentgenol 153:947–951

Lee JD, Choe KO, Kim SJ et al (1991) CT findings in primary thymic carcinoma. J Comput Assist Tomogr 15:429–433

Lee KS, Song KS, Lim TH et al (1993) Adult-onset pulmonary tuberculosis: findings on chest radiographs and CT scans. AJR Am J Roentgenol 160:753–758

Lee JY, Lee KS, Han J et al (1999) Spectrum of neurogenic tumors in the thorax: CT and pathologic findings. J Comput Assist Tomogr 23:399–406

Maher MM, Shepard JA (2005) Imaging of thymoma. Semin Thorac Cardiovasc Surg 17:12–19

Marom EM (2013) Advances in thymoma imaging. J Thorac Imaging 28:69–83

McAdams HP, Rosado-de-Christenson ML, Moran CA (1994) Mediastinal hemangioma: radiographic and CT features in 14 patients. Radiology 193:399–402

McAdams HP, Rosado-de-Christenson M, Fishback NF, Templeton PA (1998) Castleman disease of the thorax: radiologic features with clinical and histopathologic correlation. Radiology 209:221–228

McAdams HP, Kirejczyk WM, Rosado-de-Christenson ML, Matsumomo S (2000) Bronchogenic cyst: imaging features with clinical and histopathologic correlation. Radiology 217:441–446

McNeeley MF, Chung JH, Bhalla S, Godwin JD (2012) Imaging of Granulomatous Fibrosing Mediastinitis. AJR Am J Roentgenol 199:319–327

Miller BH, Rosado-de-Christenson ML, McAdams HP, Fishback NF (1995) Thoracic sarcoidosis: radiologic-pathologic correlation. Radiographics 15:421–437

Moeller KH, Rosado-de-Christenson ML, Templeton PA (1997) Mediastinal mature teratoma: imaging features. AJR Am J Roentgenol 169:985–990

Moon WK, Im JG, Kim JS et al (1994) Mediastinal Castleman disease: CT findings. J Comput Assist Tomogr 18:43–46

Naidich DP, Zerhouni EA, Siegelman SS et al (1991) CT and MR of the thorax, 2nd edn. Raven Press, New York, 69

Nicolaou S, Müller NL, Li DK, Oger JJ (1996) Thymus in myasthenia gravis: comparison of CT and pathologic findings and clinical outcome after thymectomy. Radiology 201:471–474

Nishino M, Ashiku SK, Kocher ON et al (2006) The thymus: a comprehensive review. Radiographics 26:355–348

Patil SN, Levin DL (1999) Distribution of thoracic lymphadenopathy in sarcoidosis using computed tomography. J Thorac Imaging 14:114–117

Ribet ME, Cardot GR (1994) Neurogenic tumors of the thorax. Ann Thorac Surg 58:1091–1095

Rosado-de-Christenson ML, Galobardes J, Moran CA (1992a) Thymoma: radiologic-pathologic correlation. Radiographics 12:151–168

Rosado-de-Christenson ML, Templeton PA, Moran CA (1992b) From the archives of the AFIP. Mediastinal germ cell tumors: radiologic and pathologic correlation. Radiographics 12:1013–1030

Rosado-de-Christenson ML, Pugatch RD, Moran CA, Galobardes J (1994) Hymolipoma: analysis of 27 cases. Radiology 193:121–126

Rosado-de-Christenson ML, Strollo DC, Marom EM (2008) Imaging of thymic epithelial neoplasms. Hematol Oncol Clin North Am 22:409–431

Sadohara J, Fujimoto K, Müller NL et al (2006) Thymic epithelial rumors; comparison of CT and MR imaging findings of low-risk thymomas, high-risk thymomas, and thymic carcinomas. Eur J Radiol 60:70–79

Saeed-Abdul-Rahman I, Al-Amri AM (2012) Castleman disease. Korean J Hematol 47:163–167

Sahdev A, Sohaib A, Monson JP et al (2005) CT and MR imaging of unusual locations of extra-adrenal paragangliomas (pheochromocytomas). Eur Radiol 15:85–92

Sakurai K, Hara M, Ozawa Y et al (2008) Thoracic hemangiomas: imaging via CT, MR and PEt along with pathologic correlation. J Thorac Imaging 23:114–120

Salyer DC, Salyer WR, Eggleston JC (1977) Benign developmental cysts of the mediastinum. Arch Pathol Lab Med 101:136–139

Saski M, Kuwabara Y, Ichiya Y et al (1999) Differential diagnosis of thymic tumors using a combination of 11C-methionine PET and FDG PET. J Nucl Med 40:1595–1601

Scalzetti EM, Heitzman ER, Groskin SA et al (1991) Developmental lymphatic disorders of the thorax. Radiographics 11:1069–1085

Se R, McAdams HP, Rasado-de-Cristenson ML et al (2001) Fibrosing mediastinitis. Radiographics 21:737–757

Shaffer K, Rosado-de-Cristenson ML, Patz EF Jr et al (1994) Thoracic lymphangioma in adults: CT and MR imaging features. AJR Am J Roentgenol 162:283–289

Shaffer K, Smith D, Kirn D et al (1996) Primary mediastinal large-B-cell-lymphoma: radiological findings at presentation. AJR Am J Roentgenol 167:425–430

Shahrzad M, Le TS, Silva M et al (2014) Anterior mediastinal masses. AJR Am J Roentgenol 203:W128–W138

Stark DD, Moss AA, Brasch RC et al (1983) Neuroblastoma: diagnostic imaging and staging. Radiology 148:101–105

Ströbel P, Marx A, Zettl A, Müller-Hermelink HK (2005) Thymoma and thymic carcinoma: an update of the WHO classification 2004. Surg Today 35:805–811

Strollo DC, Rosado de Cristenson ML, Jett JR (1997a) Primary mediastinal tumors. Part 1: tumors of the anterior mediastinum. Chest 112:511–522

Strollo DC, Rosado-de-Christenson ML, Jett JR (1997b) Primary mediastinal tumors: part II. Tumors of the middle and posterior mediastinum. Chest 112:1344–1357

Sung YM, Lee KS, Kim CT et al (2006) 18F-FDG PET/CT of thymic epithelial tumors: usefulness for distinguishing and staging tumor subgroups. J Nucl Med 47:1628–1634

Suster S (2006) Thymic carcinoma: update of current diagnostic criteria and histologic types. Semin Diagn Pathol 22:198–212

Suster S, Rosai J (1992) Cystic thymomas. A clinicopathologic study of ten cases. Cancer 69:92–97

Suster S, Rosia J (1991) Multilocular thymic cyst: an acquired reactive process. Study of 18 cases. Am J Surg Pathol 15:388–398

Tanaka O, Kiryu T, Hirose Y et al (2005) Neurogenic tumors of the mediastinum and chest wall: MR imaging appearance. J Thorac Imaging 20:316–320

Tateishi U, Müller NL, Johkoh T et al (2004) Primary mediastinal lymphoma: characteristic features of the various histological subtypes of CT. J Comput Assist Tomogr 28:782–789

Tecce PM, Fishman EK, Kuhlman JE (1994) CT evaluation of the anterior mediastinum: spectrum of disease. Radiographics 14:973–990

Tomiyama N, Müller NL, Ellis SJ et al (2001) Invasive and noninvasive thymoma: distinctive CT features. J Comput Assist Tomogr 25:388–393

Tomiyama N, Johkoh T, Mihara N et al (2002) Using the world health organization classification of thymic epithelial neoplasms to describe CT findings. AJR Am J Roentgenol 179:881–886

Tomiyama N, Honda O, Tsubamoto M et al (2008) Anterior mediastinal tumors: diagnostic accuracy of CT and MRI. Eur J Radiol 69:280–288

Travis WD, Brambilla E, HK M –H et al (2004) Pathology and genetics of tumours of the lung, pleura, thymus, and heart. World health organization classification of tumours. IARC Press, Lyon

Veeze-Kuijpers B, Van Andel JG, Stiegelis WF, Boldwijn JK (1989) Benign thymic cyst following mantle radiotherapy for Hodgkin's disease. Clin Radiol 38: 289–290

Verstandig AG, Epstein DM, Miller WT Jr et al (1992) Thymoma—report of 71 cases and a review. Crit Rev Diagn Imaging 33:201–230

Williams SM, Jones ET (1997) General case of the day. Fibrosing mediastinitis. Radiographics 17: 1324–1327

Woo OH, Yong HS, Shin BK et al (2008) Wide spectrum of thoracic neurogenic tumours: a pictorial review of CT and pathological findings. Br J Radiol 81:668–676

Zyalk CM, Standen JR, Barnes GR, Zyalk CJ (2000) Pneumomediastinum revisited. Radiographics 20: 1043–1057

PET/CT of Lung Cancer

Victor H. Gerbaudo and Camilo A. Garcia

Abstract

Tumors are highly heterogeneous entities, both morphologically and functionally. This heterogeneity applies to the primary tumor and to systemic metastasis. The tumoral molecular profile not only can change and evolve over time across different pathophysiological states but is also capable of dynamically activating its inherent capacity of acquiring resistance to different treatments. Metabolic and molecular imaging techniques such as positron emission tomography (PET) are capable of interrogating in vivo, in one imaging session, several of the abovementioned processes, highlighting some of the heterogeneous signatures of the lung cancer cell phenotype by using specific positron-emitting radiopharmaceuticals. Several of these PET-based molecular probes are available today to noninvasively interrogate glycolytic activity, cellular proliferation, hypoxia, amino acid transport, receptor expression, and apoptosis, among other processes. 18F-Fluorodeoxyglucose (FDG) is a glucose analogue that is widely used clinically to evaluate regional glucose metabolism in several cancer types. FDG-PET yields functional information based on altered tissue metabolism and is useful for both diagnosing and staging cancer. The basis for the use of PET with FDG is the increased glucose consumption by cancer cells compared to normal tissues. In addition, alterations in tissue metabolism that generally precede changes in tumor size are also reflected

V.H. Gerbaudo (✉)
Division of Nuclear Medicine and Molecular Imaging, Brigham and Women's Hospital, Harvard Medical School, 75 Francis Street, Boston, MA 02492, USA
e-mail: gerbaudo@bwh.harvard.edu

C.A. Garcia
Service de Médecine Nucléaire, Université Libre de Bruxelles, Institut Jules Bordet, Bv. de Waterloo 121, Brussels 1000, Belgium
e-mail: camilo.garcia@bordet.be

U.J. Schoepf, F.G. Meinel (eds.), *Multidetector-Row CT of the Thorax*, Medical Radiology,
DOI 10.1007/978-3-319-30355-0_13

by this technique. FDG-PET/CT imaging is a superior clinical tool to accurately assess lung cancer's anatomometabolic phenotype. This molecular imaging technique contributes to the diagnosis and initial staging of lung cancer patients by: (a) improving the characterization of the benign or malignant nature of indeterminate solitary pulmonary nodules; (b) complementing conventional imaging techniques to assess primary tumor extent; (c) assessing lymph node status; and (d) detecting systemic disease. FDG-PET/CT also plays an integral role in the subsequent treatment strategy of lung cancer patients. In this context, PET is used to assess the morphologic-metabolic phenotype of tumoral response to cytotoxic and cytostatic cancer therapies, as well as to radiotherapy, and to detect and characterize locorregional and systemic relapse after treatment. PET/CT imaging without a doubt is here to stay as a highly sensitive molecular imaging pearl that provides anatomo-biological and functional insight into the heterogeneous phenotype of lung neoplasia.

1 Pathophysiological Basis of PET/CT Imaging in Oncology

Modern oncology relies on characterizing malignancies by interrogating cell biology and genetic information intrinsic to the carcinogenesis process and that drive the ability of cancer cells to proliferate, degree of cellular differentiation, expression of receptors, antigen expression, gene mutations, cellular metabolic state, expression of oncogenes and antioncogenes, tumor aggressiveness, as well as cellular chemosensitivity and radiosensitivity, among others. To make matters even more complicated, tumors are highly heterogeneous entities, both morphologically and functionally. This heterogeneity is present in the primary tumor and in its systemic metastasis (Vogelstein et al. 2013). The tumoral molecular profile not only can change and evolve over time across different pathophysiological states but is also capable of dynamically activating its inherent capacity of acquiring resistance to different treatments (Aparicio and Caldas 2013). Owing to this spatiotemporal tumoral heterogeneity, cancer cells from different sites in the same patient at different time points may yield different results when attempting to characterize their corresponding phenotype and genotype.

Abnormally high glucose consumption is another prominent characteristic of neoplastic cells, as elegantly described in Otto Warburg's seminal observations (Warburg et al. 1927; Warburg 1956). Warburg taught us that cancer cells utilize glucose anaerobically leading to the production of lactic acid in non-hypoxic tissues, rather than relying on the efficiency of the tricarboxylic acid cycle of oxidative phosphorylation to produce ATP in the mitochondria. The Warburg effect can be summarized as a shift from cellular ATP generation through oxidative phosphorylation to ATP generation through glycolysis, even under normal oxygen conditions (Cairns et al. 2011). Increased glucose consumption by cancer cells is also associated with overexpression and activity of glucose transporters, the activity of hexokinase isoform II, and hypoxia selection and adaptation (Merrall et al. 1993).

Metabolic and molecular imaging techniques such as positron emission tomography (PET) are capable of interrogating in vivo, in one imaging session, several of the abovementioned processes, highlighting some of the heterogeneous signatures of the cancer cell phenotype by using specific positron-emitting radiopharmaceuticals. Several of these PET-based molecular probes are available today to noninvasively interrogate glycolytic activity, cellular proliferation, hypoxia, amino acid

transport, receptor expression, and apoptosis, among other processes (Garcia et al. 2012).

^{18}F-Fluorodeoxyglucose (FDG) is a glucose analogue that is widely used clinically to evaluate regional glucose metabolism in several cancer types. FDG-PET yields functional information based on altered tissue metabolism and is useful for both diagnosing and staging cancer. The basis for the use of PET with FDG is the increased glucose consumption by cancer cells compared to normal tissues. In addition, alterations in tissue metabolism that generally precede changes in tumor size are also reflected by this technique. The degree of FDG uptake in a given lesion is a function of the number of viable tumor cells, the malignant histologic type, the degree of anaplasia and proliferative activity, the presence of inflammatory cells, and, last but not least, lesion size. All these factors contribute to the ability of PET to differentiate malignant from benign processes. These and other characteristics and attributes have brought FDG-PET to become an integral and almost indispensable technique used in the management of lung cancer patients as it will be discussed in the pages that follow.

2 The Role of FDG-PET and PET/CT in the Initial Treatment Strategy of Lung Cancer Patients

FDG-PET provides molecular imaging access to the pathobiology of neoplasia in vivo in one imaging session. PET/CT in particular couples anatomical and functional imaging information in order to more accurately characterize tumor invasion and metastasis in cancer patients. PET imaging's success in today's clinical practice is based on its capacity to study tumoral biological behavior in vivo without relying solely on lesion size, density, and shape. Information on lesion morphology provided by CT is related to its biological significance in the PET images, allowing for greater confidence during the interpretation of the images, when compared to either modality alone.

At the time of this writing, it is well accepted worldwide that FDG-PET/CT imaging is a superior clinical tool to accurately assess lung cancer's anatomo-metabolic phenotype. This molecular imaging technique contributes to the diagnosis and initial staging of lung cancer patients by (a) improving the characterization of the benign or malignant nature of indeterminate solitary pulmonary nodules and guiding biopsy to metabolically active heterogeneous lesions minimizing sampling errors; (b) complementing conventional imaging techniques to assess primary tumor extent (T status) by capitalizing on the power of fused anatomo-metabolic images, overcoming the limitations of either modality alone; (c) assessing lymph node status; and (d) detecting systemic disease.

The most important prognostic factors in the lung cancer patient are the extent of disease at presentation and nodal status, and therefore, accurate disease staging is essential to direct treatment strategy. The standard workup of patients with lung cancer calls for a complete history and physical examination, followed by imaging studies. The main role of imaging is to locate and define tumoral extent, both in the thorax and systemically to minimize further unnecessary invasive staging. Various imaging modalities are used to stage lung cancer with their well-known advantages and limitations. Conventional imaging modalities have already been described elsewhere in this book; this chapter centers on the role of FDG-PET/CT-based molecular imaging in lung cancer.

2.1 The Indeterminate Solitary Pulmonary Nodule

Most solitary pulmonary nodules (SPNs) are incidentally discovered during a routine physical exam or a screening test in patients at risk. It is a relatively common finding in daily clinical practice. The prevalence of cancer in lung nodules varies according to the population studied and depends on the age group, smoking history, exposure to toxic materials (i.e., asbestos), previous history of cancer, and geographical location where patients reside (e.g., areas with high prevalence of fungal infections and granulomatous

diseases). Solitary lung nodules can represent malignancies such as non-small cell lung cancer (NSCLC) with a predominance of adenocarcinoma over squamous cell carcinomas, small cell lung cancer, carcinoid tumors, as well as metastatic lesions arising from primary tumors in other organs. The most common benign etiologies include old sequelae from noninfectious granulomas, infections, and benign tumors. For these reasons, a Bayesian approach to the characterization of SPN is necessary and must include the information provided by FDG-PET/CT. In fact, likelihood ratios (LRs) from FDG-PET/CT for overall prevalence of malignancy in SPN have been published and are higher with an abnormal PET scan when compared to most clinical and radiologically derived LRs.

According to several meta-analyses, the sensitivity and specificity of FDG-PET to characterize an SPN as malignant are greater than 95 % and 73 %, respectively (Gould et al. 2001; Gambhir et al. 2001; Cronin et al. 2008). Concurrently, FDG-PET has a high negative predictive value to exclude cancer, especially if the size of the SPN in CT is less than 15 mm. Focal hypermetabolism in an SPN on FDG-PET, especially in a small lesion, is considered to have a high probability of cancer (Bryant and Cerfolio 2006) (Fig. 1).

Several teams have compared the diagnostic performance to characterize an SPN as malignant using CT, FDG-PET, and FDG-PET/CT. Systematically FDG-PET has better accuracy than CT, and hybrid images with PET/CT are more accurate than FDG-PET alone to diagnose a malignant SPN (Christensen et al. 2006; Yi et al. 2006; Jeong et al. 2008; Fletcher et al. 2008a; Divisi et al. 2010).

Some investigators postulate the use of a fixed SUV cutoff, while others recommend using visual/qualitative characterization of the lesion in PET (Nomori et al. 2005; Hamberg et al. 1994; Grgic et al. 2010). Lowe and colleagues (1998) studied eighty-nine patients with indeterminate SPNs with FDG-PET. Sixty SPNs were malignant and twenty-nine were benign. Using an SUVavg cutoff of 2.5, PET had an overall sensitivity of 92 % and specificity of 90 % for the detection of malignant nodules. In contrast, using SUVmax, Bryant and coworkers found in a surgical series of 585 patients that 24 % of cancerous pulmonary nodules had an SUVmax lower than 2.5. These included 11 cases of bronchioloalveolar carcinomas, 4 carcinoids, and 2 metastases from renal cell carcinoma (Bryant and Cerfolio 2006). The very fact that a lesion observed in the images has been confirmed as lung cancer does not mean that it will be FDG avid. It should be kept in mind that some primary lung malignancies such as adenocarcinomas in situ (former bronchioloalveolar carcinomas), carcinoids, and even some well-differentiated adenocarcinomas may not be as metabolically active as one would expect, yielding false-negative PET findings (Higashi et al. 1998; Erasmus et al. 1998) (Fig. 2). In addition, it is common knowledge that the SUV is a function of histologic type, cellular density, aggressive behavior, and technical factors such as equipment used (dedicated PET versus PET/CT), image reconstruction, injected FDG activity, and time between FDG injection and image acquisition. Nowadays, in the absence of strict FDG-PET/CT imaging standardization across PET centers, the use of a fixed SUV value is not recommended to characterize an SPN as benign or malignant.

Although lesions with very low FDG uptake may be benign, false-negative findings may be related to lesion size, lesion biology, and respiratory motion. Characterizing SPNs smaller than 1 cm in diameter is not an easy task. For the most part these small nodules are benign, with some reports claiming a 4 % chance of being malignant if they are located in a different lobe (Kim et al. 2002), while others have found that 18–25 % may be malignant regardless of their location (Chalmers and Best 1991; Yuan et al. 2003).

Modern PET cameras have a spatial resolution of approximately 5–8 mm. If the lesion in question is below this size, their volumes will be "diluted" in a larger one corresponding to the resolution limit of the PET scanner. This is known as the "partial volume effect." In general, it is considered that any lesion size smaller than twice the spatial resolution of the system at full width half maximum will be affected by the partial volume effect. This in turn results in underestimation of the recovered counts from the lesion, resulting in

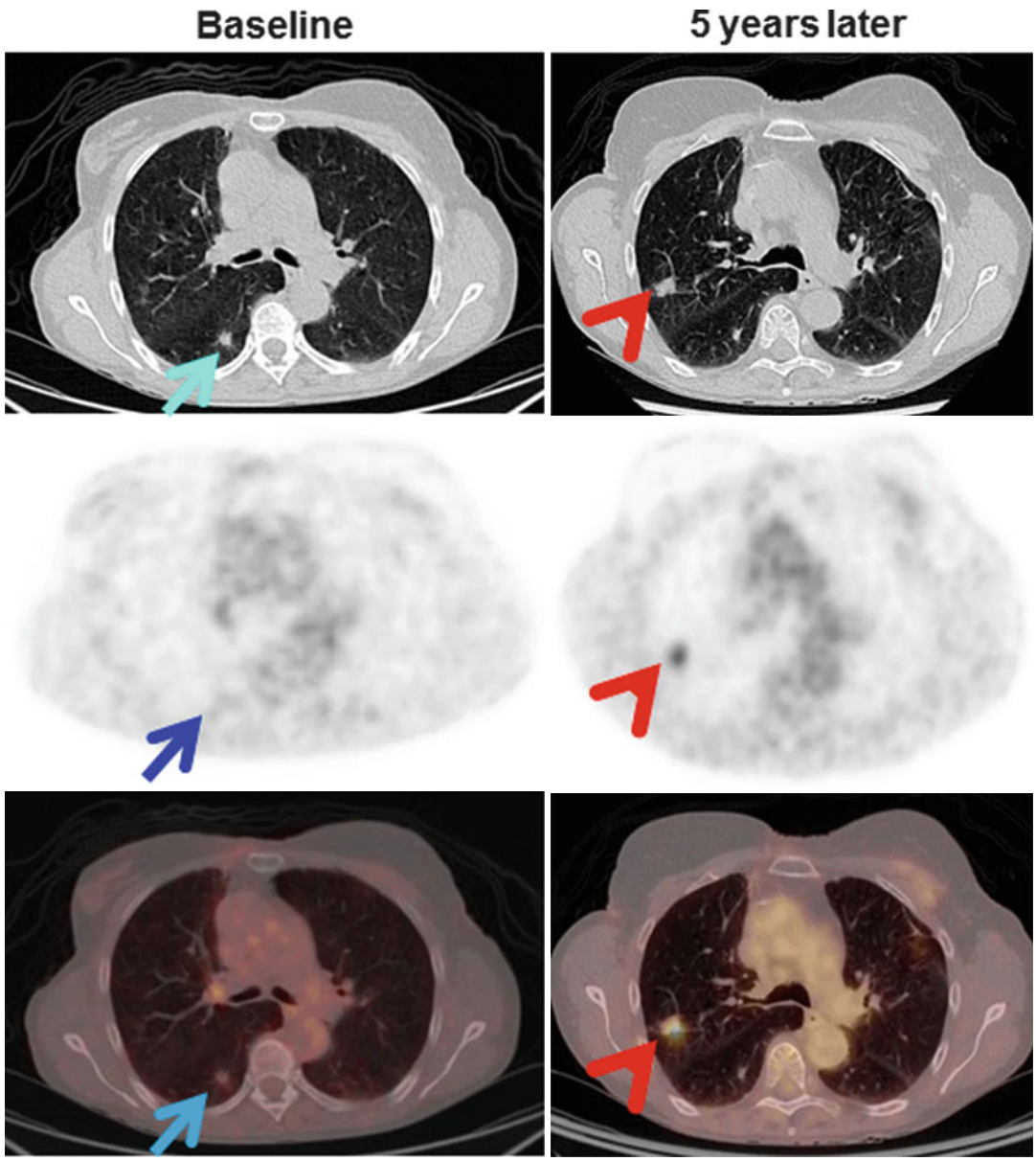

Fig. 1 FDG-PET/CT images of a 65-year-old female, heavy smoker, acquired at baseline showing a 9 mm SPN in the apical segment of the inferior right pulmonary lobe that was non-FDG avid (*blue arrows*). FDG-PET/CT images from the same patient obtained 5 years later showed a decrease in size as well as metabolic stability in the previously described SPN. However, a new nodule (13 mm) is observed in the posterior segment of the superior right lobe, which is FDG avid (SUV max 4.6) (*red arrowhead*). Histopathology confirmed an adenocarcinoma

an erroneously lower SUV. Caution should be exercised when attempting to characterize SPNs smaller than 8 mm in diameter with PET.

On the other side of the spectrum, false-positive results may be found in patients with highly FDG-avid infectious and/or inflammatory processes such as active tuberculosis, sarcoidosis, and fungal infections (e.g., histoplasmosis, coccidioidomycosis, aspergillosis, etc.) (Jones et al. 1991; Wachsmann and Gerbaudo 2014; Alavi

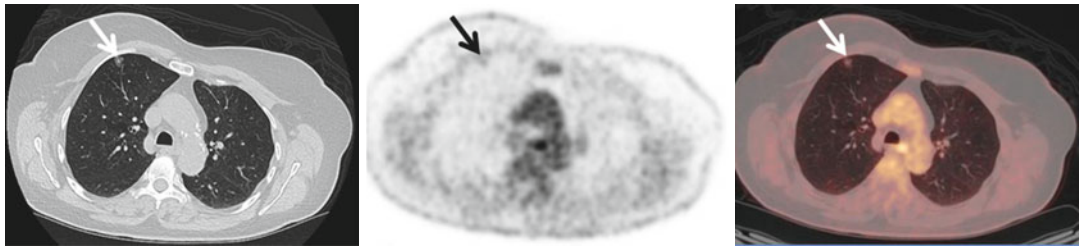

Fig. 2 FDG-PET/CT images for initial treatment strategy of a 69-year-old female smoker. Axial slices: (**a**) CT, (**b**) FDG-PET, and (**c**) fused PET/CT show a 1.2 cm, ground glass opacity with a dense central component in the anterior segment of the superior right lobe (*arrow* on **a**). PET and fused images show very low (lower than mediastinal blood pool activity) FDG uptake in the SPN. Histopathology diagnosis: 6 mm lepidic predominant adenocarcinoma in situ

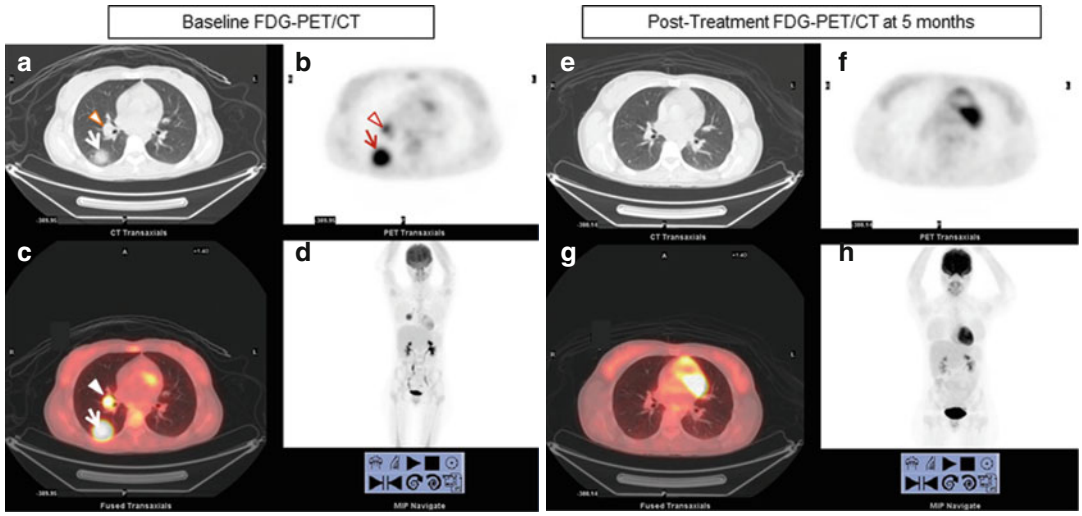

Fig. 3 *Baseline FDG-PET/CT in a 29-year-old female:* Axial (**a**) CT, (**b**) FDG-PET, (**c**) fused PET/CT slices, and (**d**) MIP image show an indeterminate, 2.8×2.8 cm, intensely FDG-avid soft tissue lesion (*arrow*) in the inferior lobe of the right lung posteriorly. There are right hilar and right peribronchial lymph nodes that are highly FDG avid (*arrowhead*). The anatomo-metabolic pattern of the lesion was highly concerning for a fungal infection. Transthoracic CT-guided biopsy of the lung lesion was nondiagnostic and the patient was subsequently started on empiric treatment with voriconazole and Levaquin. *FDG-PET/CT obtained 5 months later*, (**e**) CT, (**f**) FDG-PET, (**g**) fused PET/CT slices, and (**h**) MIP image, showed complete resolution of the previously noted right lower lobe lesion and associated lymphadenopathy. There was minimal soft tissue within the anterior mediastinum consistent with thymus

et al. 2002) (Figs. 3 and 4). This is because GLUT1 and GLUT3 transporters are overexpressed and active, especially in the acute phase of inflammation. Furthermore, FDG uptake is not uncommon in granulation tissue and in activated macrophages and neutrophils. Therefore, the recommendation is that FDG-positive nodules should always be evaluated histopathologically.

In summary, the diagnostic workup and management of patients with SPNs should rely on clinical history coupled with the complementary information arising from PET and CT in the context of the patient's clinical pretest probability of malignancy. In patients with a negative PET and with low probability of having cancer, observation is certainly optimal. When the CT shows an indeterminate pattern, then an FDG-PET is indicated, followed by surgery if the lesion is FDG avid and there is no other evidence of secondarism. On the other hand, needle biopsy is indicated if

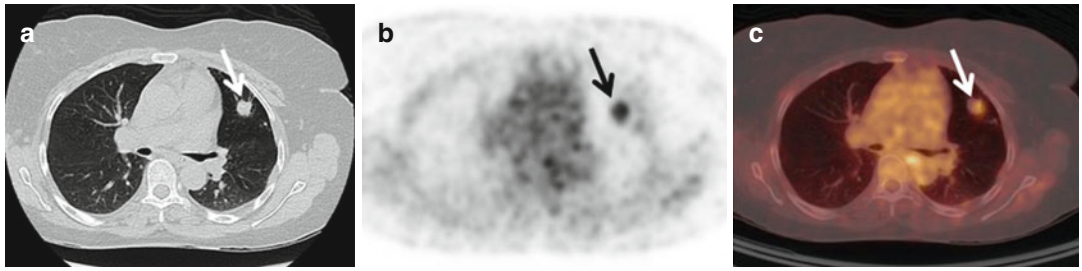

Fig. 4 Initial staging FDG-PET/CT of a 49-year-old female, HIV positive. Axial (**a**) CT, (**b**) FDG-PET, and (**c**) fused FDG-PET/CT slices show a 1.3 cm, FDG-avid SPN (SUVmax = 3.8, with higher metabolic activity than the mediastinal blood pool) in the anterior segment of the left inferior pulmonary lobe (*arrows*). Histopathologic diagnosis: tuberculosis

the PET is negative, but suspicion persists (Gould et al. 2003a). The Society of Nuclear Medicine and Molecular Imaging recommends that FDG-PET should be used (Fletcher et al. 2008b) (1) to detect potential malignant lesions early in the course of the disease, (2) to exclude the possibility of malignancy in indeterminate lesions in low-risk patients, and (3) to improve health-care outcomes by avoiding futile surgeries in low-risk patients and enabling curative surgeries in high-risk patients.

2.2 T Status

Accurate staging of disease extent in patients with lung cancer is necessary to determine if the disease is operable or not and, if it is, to determine which surgical technique is the most appropriate (e.g., pneumonectomy versus lobectomy). Furthermore, precise tumor delineation is a must for accurate radiation treatment planning. CT is the modality of choice to accurately characterize lesion size and its relationship to neighboring structures. FDG images alone, on the other hand, lack the necessary spatial resolution to properly assess disease extent and therefore lesion resectability status. The main limitation is the lack of fine detail in the metabolic images, which are unable to distinguish direct invasion of mediastinal structures (inoperable disease) from contiguity of tumor with the mediastinum (operable disease).

New-generation hybrid scanners were introduced to the clinical setting approximately in the year 2000. As experience was gained with the use of these systems, the medical community learned that the whole is certainly more than the sum of its parts. Numerous publications to this date have confirmed that most of the time the information provided by the fused anatomo-metabolic images overcomes the limitations of either modality alone. In one of the first publications on the topic, Lardinois et al. (2003) showed that FDG-PET/CT imaging adds value to assess T status and increases the diagnostic accuracy to stage lung cancer when compared to either modality alone. The investigators compared the role of PET/CT versus PET and CT alone to assess TNM status in 50 patients with proven or suspected NSCLC. PET/CT was superior to PET and CT alone to assess the correct T stage (88 % of the patients compared to 40 % and 58 %, respectively). As expected, PET/CT improved the detection of disease affecting the chest wall and invading the mediastinum and more accurately assessed N and M status in their patient population. Antoch and colleagues (2003) published very similar results the same year. The peer-reviewed publications that followed further confirmed that PET/CT is the technique of choice to define the extent of invasion more accurately, to detect the presence of additional pulmonary nodules, and to differentiate tumor from atelectasis (Gerbaudo and Julius 2007), the latter having a significant impact in radiation therapy planning, where PET-derived information has been shown to change the radiation field in approximately 30 % of cases (Dizendorf et al. 2003).

2.3 N Status

At the time of this writing, it is well accepted that PET/CT plays a very important role staging the mediastinum of lung cancer patients, serving as a complementary modality to mediastinoscopy. Its most salient advantage is the fact that FDG-PET imaging does not rely on nodal size to characterize metastatic nodes. This molecular imaging technique interrogates the metabolic behavior of lesions to characterize the presence of malignancy. To this end, pattern and intensity of uptake are used to exclude tumor involvement in large lymph nodes and to detect tumor in those that might be considered normal based on size criteria alone. PET interrogates the entire mediastinum, with most publications reporting an average change in the N stage in approximately 20 % of lung cancer patients (Figs. 5 and 6).

One of the initial publications on this topic was that of Gould et al. (2003b). The investigators conducted a meta-analysis of 39 studies with a total of 1,959 patients comparing the usefulness of PET and CT to stage the mediastinum. The authors reported a median sensitivity and specificity of 61 % and 79 %, respectively, for CT, compared to 85 % and 90 %, respectively, for PET. The authors underscored the fact that PET was more sensitive at the expense of lower specificity when enlarged lymph nodes were found in CT. The same year Toloza and colleagues (2003) reviewed the literature addressing the performance of CT, PET, and EUS to stage the mediastinum in lung cancer patients. Their findings were similar to those of Gould et al., with PET imaging being superior for detecting N disease, with a sensitivity of 84 % and a specificity of 89 %, compared to 57 % and 82 %, respectively, for CT, and 78 % and 71 %, respectively, for EUS.

The evidence accrued throughout the past decade has taught the molecular imaging practitioner that when centering specifically on the detection of micrometastases in extrapleural mediastinal nodes, the negative predictive value (NPV) of PET is far from perfect. The American College of Surgeons Oncology Group Z0050 trial, comparing CT, PET, and mediastinoscopy in 303 patients with potentially resectable NSCLC, confirmed the limitations of PET to detect microscopic N2 metastases. While PET was superior to CT for the detection of N1, N2, and N3 disease, PET's sensitivity to detect N2 metastases was 61 % with a less than perfect NPV of 87 % (Reed et al. 2003). The authors concluded that mediastinal staging always should be done with more than one staging modality and

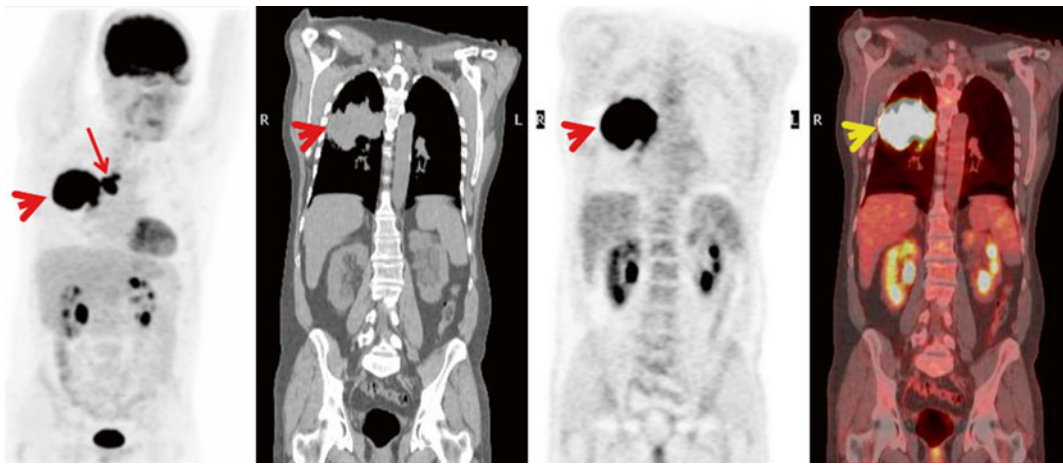

Fig. 5 Initial staging FDG-PET MIP and coronal CT, PET, and PET/CT images of a 62-year-old male with a history of pathologically confirmed NSCLC. There is intense FDG activity within a large right lung mass (*arrowhead*). Intense radiotracer uptake is also evident in ipsilateral hilar and mediastinal lymph nodes (*arrow*), consistent with stage IIIA disease

that a negative and a positive mediastinum in PET should be confirmed by mediastinoscopy in patients that are considered surgical candidates.

Furthermore, false-negative nodes harboring micrometastases are not uncommon in PET images of patients with early-stage lung cancer. In a prospective study of 150 patients to evaluate the accuracy of FDG-PET/CT for the preoperative diagnosis of N disease in stage T1 NSCLC, Kim and colleagues (2006) reported a sensitivity of 42 % on a per-nodal-station basis and 47 % on a per-patient basis. While the specificity and PPV were both 100 %, the NPV was 94 % on a per-nodal-station and 87 % on a per-patient basis.

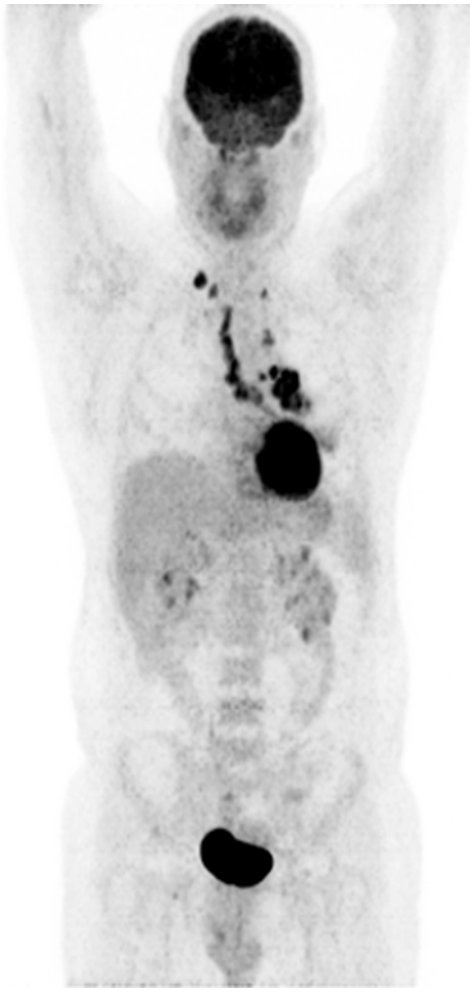

Fig. 6 Initial staging FDG-PET MIP image of a 53-year-old male smoker with a history of pathologically confirmed lung adenocarcinoma. There is intense FDG activity within a 4.5 cm left hilar and paramediastinal mass. Intense radiotracer uptake is also noted in numerous ipsilateral and contralateral hilar and mediastinal lymph nodes, consistent with stage IIIB disease

In stage II and III lung cancer, the NPV of FDG-PET tends to be low when the primary is centrally located, when the size of the nodal metastatic deposits is small, and when the primary tumor's avidity for the radiopharmaceutical is low (Vansteenkiste 2005).

In summary, the literature shows approximately a 10 % to 38 % incidence of metastatic pathologically confirmed N2 disease in PET-negative patients. Therefore, the consensus is that mediastinoscopy is clinically indicated in all cases that are potentially operable. On the other hand, it should be kept in mind that not all hot nodes are metastatic, because reactive nodes can be FDG avid as well. Therefore, nodal sampling is also indicated to prevent patients from being excluded from surgical treatment due to false-positive findings.

A meta-analysis by de Langen and colleagues (2006) looked at the relationship between node size and the probability of malignancy. When non-FDG-avid nodes were 10–15 mm on CT, the post-test probability of disease affecting N2 nodes was only 5 %, and therefore, surgery could be performed without mediastinoscopy. When PET-negative nodes measured ≥16 mm on CT, the post-test probability of malignancy increased to 21 %, indicating that in this cohort thoracotomy should be preceded by mediastinoscopy.

Despite PET's limited performance in the setting of micrometastatic N2 disease, recent reports revealed that the accuracy of nodal staging seems to improve with the use of combined PET/CT imaging. This hybrid technique allows for more precise localization of extrapleural nodal metastasis by pinpointing the exact anatomical location of single, small nodes, as well as supraclavicular and infraclavicular nodes, with an accuracy of 93 %, versus 89 % for PET alone and 63 % for CT alone (Antoch et al. 2003). The results of a randomized clinical trial of 189 operable lung cancer patients, whose N status was defined by mediastinoscopy and/or endoscopic ultrasound with fine needle aspiration, confirmed that FDG-PET/CT

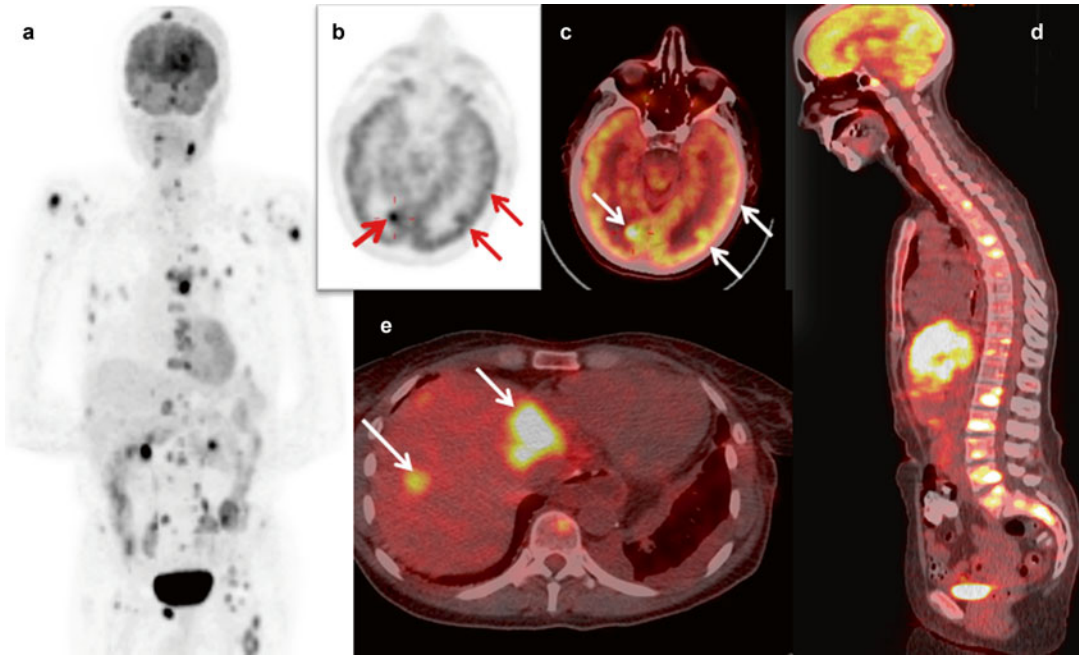

Fig. 7 Systemic metastases from lung cancer: (**a**) FDG-PET MIP image shows multiple systemic metastases with different intensities of FDG uptake; (**b**) axial FDG brain slice and (**c**) corresponding fused PET/CT image of the brain show hypermetabolic cerebral metastases (*arrows*); (**d**) sagittal fused PET/CT image shows multiple highly FDG-avid metastases in the axial skeleton; and (**e**) axial fused PET/CT shows two hypermetabolic liver metastases (*arrows*)

performed before mediastinoscopy increased the accuracy of N staging to 95 % from 85 % in those that did not undergo PET imaging prior to mediastinoscopy (Fischer et al. 2011).

2.4 M Status

The frequency of occult metastasis from adenocarcinomas is approximately 67 %, followed by 21 % from squamous cell carcinomas and 12 % from large cell tumors (Sider and Horejs 1988). While systemic metastases from lung cancer can affect every organ in the body, the most common sites include the skeleton, liver, adrenal glands, and brain.

As of today the consensus is that FDG-PET and PET/CT are the most sensitive imaging techniques for the detection of extracerebral metastasis from lung cancer (Fig. 7). Among the most significant contributions of PET/CT to M staging is its ability to detect extrathoracic lesions more accurately while assessing in parallel the clinical significance of an abnormal focus by localizing it to a specific anatomical structure and therefore characterizing its physiologic or pathologic nature. This increases the confidence of image interpretation. Hellwig and colleagues (2001) conducted a review of the literature from 1985 to 1999 on FDG-PET for the evaluation of lung cancer for the third German Consensus Conference on PET in Oncology. The results of 4 studies with 336 patients revealed that FDG-PET had a sensitivity of 94 %, a specificity of 97 %, and an accuracy of 96 % for the detection of systemic metastasis. In 7 studies with 581 patients, unexpected extrathoracic metastases were found in 12 % of the patients, and in 8 studies with 695 patients, PET changed therapeutic management in 18 % of the cases. Lastly, in 3 studies with 263 patients, the sensitivity, specificity, and accuracy of FDG-PET for the detection of adrenal metastasis were 96 %, 99 %, and 98 %, respectively (Fig. 8).

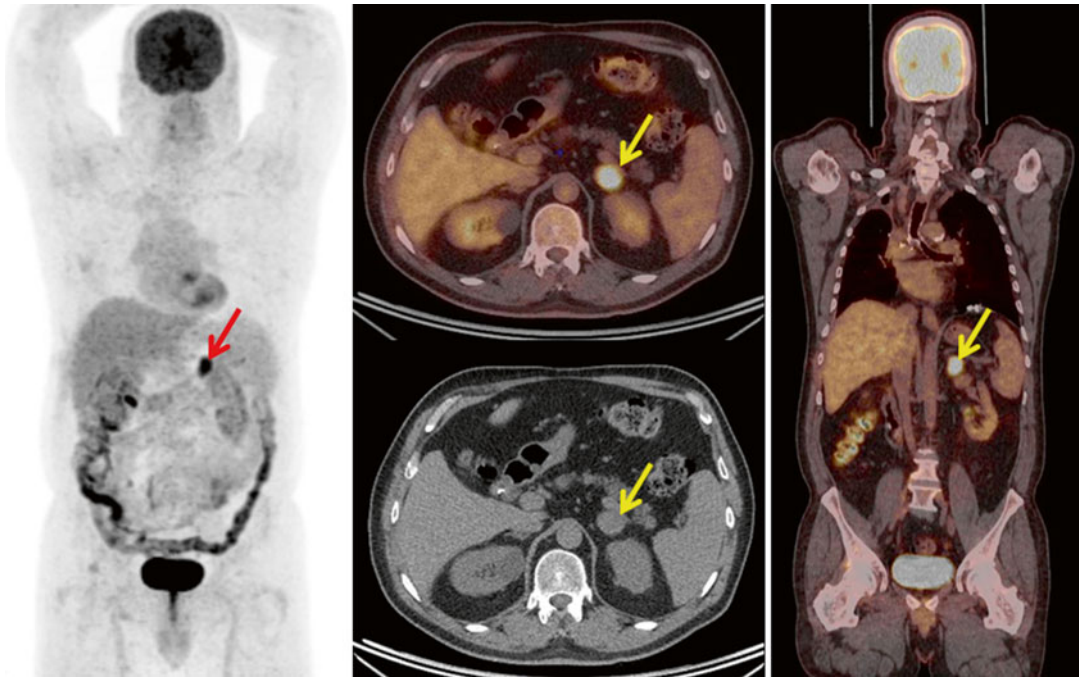

Fig. 8 A 67-year-old male, former smoker, was treated for a 4.5 cm hypermetabolic large cell carcinoma in the upper right pulmonary lobe with 10 negative lymph nodes (images not shown). Stage at presentation: pT2aN0. FDG-PET/CT images acquired 6 months later detected recurrent disease evidenced by a hypermetabolic left adrenal mass (*arrows*). Histopathologic diagnosis: large cell carcinoma metastasis

While FDG-PET's sensitivity to detect osteoblastic lesions is less than ideal, due to their low cell density and therefore low glycolytic activity, it has similar sensitivity (90–92 %) and higher specificity (98–99 %) than bone scintigraphy for the detection of osteoclastic bone metastasis (Cook et al. 1998), and it is superior for the evaluation of bone marrow metastasis for which bone scans are insensitive (Ak et al. 2010).

FDG-PET has higher sensitivity, specificity, and accuracy than CT, to detect liver metastasis. Moreover, FDG-PET adds new information in approximately 24 % of the cases (Hustinx et al. 1998). On the other hand, the diagnostic accuracy of PET is limited to detect brain metastasis due to high FDG uptake in the gray matter (sensitivity ~60 %). Alternatively, MRI is the modality of choice to assess the central nervous system in stage II and above, as well as in symptomatic patients.

MacManus et al. reported that the incidence of occult metastasis increases with stage, ranging from 7.5 % when the clinical stage is I to approximately 24 % in stage III patients (MacManus et al. 2001).

However, to be remembered is that not all extrathoracic FDG-avid lesions found in lung cancer patients are malignant. To this end, the American College of Surgeons Oncology Group Z0050 trial showed that while PET detected unsuspected metastatic disease in 6.3 % of patients, there was a 6.6 % incidence of extrathoracic false-positive PET findings subsequently shown to be benign. The investigators righteously recommended that when PET detects metastatic disease, especially when dealing with a single focus, further confirmatory evaluation is indicated (Reed et al. 2003).

The above results were corroborated two years later by Lardinois and coworkers (2005). Their study evaluated prospectively 350 patients and PET showed extrapulmonary FDG-avid lesions in 71 of them. Thirty-seven out of 69 lesions that were biopsied were confirmed to be metastasis, while 32 were not. Of the latter, 6 lesions consisted

of unsuspected second primaries or recurrence, and the remaining 26 lesions were benign or inflammatory. Once again these results further support the need to biopsy extrathoracic lesions if their malignant nature could alter patient management.

In summary, when FDG-PET is used for initial staging of newly diagnosed lung cancer, the data shows that it has a significant impact on the management of more than 35 % of the patients. Changes in management affect both the selection of the treatment modality (e.g., surgery to radiotherapy) and the treatment intent (e.g., curative to palliative) (Hicks et al. 2001a; Gregory et al. 2012). Last but not least, while the pre-PET stage remains significantly associated with survival, the post-PET stage provides better prognostic stratification (Gregory et al. 2012).

3 The Role of FDG-PET and PET/CT in the Subsequent Treatment Strategy of Lung Cancer Patients

FDG-PET/CT also plays an integral role in the subsequent treatment strategy of lung cancer patients. PET is used for the assessment of the morphologic-metabolic phenotype of tumoral response to cytotoxic and cytostatic cancer therapies, as well as to radiotherapy, and to detect and characterize locoregional and systemic relapse after treatment.

3.1 Monitoring Response to Therapy and Assessment of Tumor Relapse

Treatment options are based on the stage and the histologic type of lung cancer. Surgery is the treatment of choice for NSCLC, and depending on the extent of disease at presentation, treatment may include chemotherapy in the neoadjuvant and adjuvant settings, 3D conformal radiation therapy and stereotactic body radiation, or radiofrequency ablation, and in advanced-stage disease, cytotoxic drugs may be combined with cytostatic agents such as erlotinib or gefitinib (tyrosine kinase inhibitors), bevacizumab [a monoclonal antibody anti-vascular endothelial growth factor (VEGF)], crizotinib, and others.

Survival improves in early-stage disease when platinum-based chemotherapy is given following surgical resection. When the disease is more advanced (stage IIIA and IIIB), treatment decisions are for the most part multidisciplinary and addressed on a patient-by-patient basis. Options include surgery and combination of chemotherapy and radiotherapy in the neoadjuvant and adjuvant settings to reduce tumor bulk and to eliminate micrometastatic disease. Systemic disease (stage IV) can be treated with chemotherapy and radiation, as well as with surgical resection of solitary metastasis when feasible.

Small cell lung cancer (SCLC) on the other hand is treated with chemotherapy alone or combined with radiation. Leveraging on the high radiosensitivity of SCLC, treatment for patients with limited disease at presentation is based on chemotherapy given with concurrent consolidative radiation treatment of the thorax and prophylactic cranial irradiation (PCI). In fact, concurrent chemoradiotherapy has been shown to prolong survival in this patient cohort. Others with limited disease may be treated with surgery plus chemotherapy in the adjuvant setting (Jackman and Johnson 2005; Simon et al. 2007). In extensive-stage disease, usually characterized by the presence of metastasis at presentation, the treatment of choice is chemotherapy. On the other hand, radiation therapy may be used to treat brain and osseous metastases. Prophylactic cranial irradiation may sometimes be offered to those that respond well to chemotherapy in an attempt to prevent recurrence in the brain.

Treatment options for recurrent NSCLC include chemotherapy for local relapse, radiation therapy for metastases, and brachytherapy for endobronchial disease in patients that cannot tolerate additional external radiation. It is uncommon to treat recurrent solitary metastasis surgically. The treatment of a locally recurrent NSCLC follows the same guidelines as for primary tumor stages I through III. If surgery was

the primary line of treatment, radiation therapy is used. If relapse manifests as distant metastases, patients are treated with palliative intent.

When using conventional imaging techniques, it is often very difficult to differentiate recurrent disease from postsurgical and/or radiotoxicity-induced changes in lung cancer patients. On the other hand, PET very accurately detects and stages recurrent disease after surgery, chemotherapy, and radiotherapy, earlier than other imaging modalities. Although false-positive findings have been reported, for the most part the power of PET in this setting relies on the metabolic phenotype of relapse, which in turn is usually not affected by the postsurgical landscape or by therapy-induced necrosis or fibrosis. Published sensitivities and specificities range from 90 to 100 % and 62 to 92 %, respectively, for PET, compared to 72 % and 95 %, respectively, for CT (Inoue et al. 1995; Patz et al. 1994; Bury et al. 1999; Hicks et al. 2001b; Higashi et al. 2002; Singnurkar et al. 2011; Shiono et al. 2011; Hellwig et al. 2006).

Kanzaki and colleagues (2010) reported their findings on 241 stage I and II patients treated with curative surgery for NSCLC more than 6 months before FDG-PET/CT. A final diagnosis of recurrence was confirmed by histopathology or by clinical and imaging follow-up. FDG-PET/CT's sensitivity, specificity, accuracy, and positive and negative predictive values to detect recurrence were 97 %, 96 %, 96 %, 81 %, and 99 %, respectively. It correctly diagnosed recurrence in 34 of 35 patients, with true negative findings in 198 of 206 patients who had no evidence of recurrence. Only eight patients had false-positive studies associated with postoperative changes.

Hellwig et al. showed that FDG-PET imaging improves the detection of recurrent disease and found a significantly higher mean SUV in recurrent tumors (10.6 ± 5.1) compared to postsurgical inflammation (SUV 2.1 ± 0.6). Most importantly, the authors indicated that SUV in recurrent lung cancer has prognostic value and that the images provide the necessary information to accurately individualize those patients in whom additional treatment will be of benefit (Hellwig et al. 2006). Lower FDG uptake in recurrent lesions of patients that subsequently were treated with surgery was a significant predictor of longer median overall survival in their study.

FDG-PET imaging does not rely on changes in lesion size and shape to characterize response to treatment or lack thereof, and most importantly the nature of the molecular information in the images is not confounded by therapy-induced necrosis or fibrosis. Following radiotherapy, the radiation-induced mass-like pattern of fibrosis limits the accuracy of CT to identify recurrent disease. FDG-PET imaging, on the other hand, is helpful to differentiate viable tumor from fibrosis early after treatment. PET has a high negative predictive value in this setting, with indeterminate changes on CT with low FDG uptake (SUVmax <5) having a low probability of recurrence (Huang et al. 2012).

FDG uptake in radiation-induced inflammation is always a concern, and therefore, the recommendation has always been to image patients 3–4 months after radiotherapy. However, Hicks and colleagues recently confirmed that radiation-induced inflammation after radical radiotherapy does not confound the assessment of therapeutic response by FDG-PET acquired at a median of 70 days after completion of treatment (Hicks et al. 2004). In fact, the authors showed that increased FDG uptake in normal tissues due to radiotoxicity was associated with complete or partial tumor response on PET and CT.

3.2 Monitoring Response to Cytotoxic Cancer Therapy

FDG-PET's superior accuracy to predict tumoral response to chemotherapy rests on the very fact that changes in lesion morphology are often preceded by moleculo-metabolic response to treatment (Vansteenkiste et al. 2004). Despite the lack of consensus on the timing of the PET acquisition during and after therapy, and on the criteria to define PET response to lung cancer treatment, in the majority of the cases, FDG-PET predicts response earlier than CT, with outcomes being prognosticated as early as after one or two courses of neoadjuvant chemotherapy (Weber et al. 2003; Cerfolio et al. 2004) (Fig. 9).

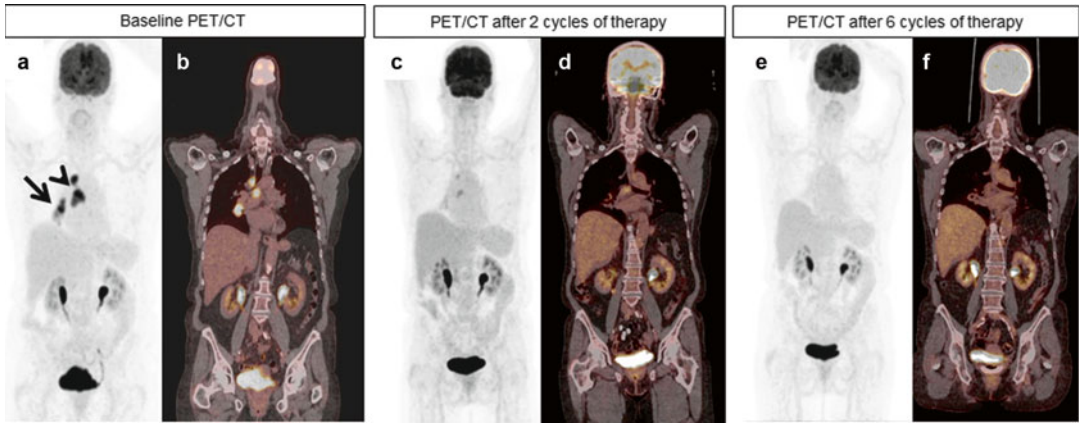

Fig. 9 A 76-year-old female, former smoker, that stopped 16 years ago, now with pathologically confirmed squamous cell lung carcinoma. *Baseline* (**a**) coronal FDG-PET and (**b**) fused FDG-PET/CT images reveal a heterogeneously FDG-avid, 2.4 cm inferior right pulmonary lobe lesion (*arrow*) and hypermetabolic lymph nodes in positions 10R, 7, and 4R (*arrowhead*), consistent with stage IIIA disease. (**c**) Coronal FDG and (**d**) fused PET/CT images *after 2 cycles of cisplatin + vinorelbine* demonstrate a significant decrease in uptake in all lesions, consistent with early response to treatment. (**e**) Coronal FDG and (**f**) fused PET/CT images *after 6 cycles of chemotherapy and 65 Gy of radiation* show complete disappearance of lesion uptake, consistent with complete response to treatment

Weber et al. (2003) showed that in 57 stage IIIB or IV NSCLC patients studied with FDG-PET before and after the first cycle of therapy, a reduction in tumor FDG uptake of more than 20 % after one cycle of platinum-based chemotherapy correlated well with the final outcome. Median progression-free survival was 163 days in responders, versus 54 days in those that did not. Furthermore, overall survival was significantly longer for metabolic responders compared to nonresponders, 252 days versus 151 days, respectively. Similar findings were reported by Vansteenkiste et al. (2004) using PET after three cycles of platinum-based neoadjuvant chemotherapy in patients with stage IIIA-N2 NSCLC. The investigators found that a reduction in FDG uptake in the primary tumor exceeding 50 %, or clearance of nodal uptake, was consistent with significantly longer survival. Two years later Hoekstra et al. (2005) reported similar results from a prospective study of 47 patients with stage IIIA-N2 potentially resectable NSCLC. A reduction of 35 % in FDG uptake in the primary tumor after one cycle of induction therapy was significantly consistent with prolonged overall survival.

Dooms and colleagues (2008) recently shared their results of an FDG-PET study to evaluate the prognostic value of tumor response after completion of induction chemotherapy in 30 patients with stage IIIA-N2 NSCLC. The investigators showed that after treatment completion, the group of patients in whom there was disappearance or persistent minor FDG uptake in mediastinal nodes, coupled with a decrease in SUVmax in the primary tumor of more than 60 %, had a significantly longer 5-year overall survival (62 %) and benefited from surgery. On the other hand, patients with persistent major mediastinal disease had a poor prognosis (5-year overall survival rate: 0 %), and the authors recommended that this cohort should not be considered for surgery.

To the best of our knowledge, there is only one study to date suggesting that anatomical response but not metabolic response to chemotherapy is predictive of survival of NSCLC patients (Tanvetyanon et al. 2008), and it still remains unclear why.

In some cases tumoral response to treatment may be mixed. While some lesions respond favorably, others do not, and new lesions may appear as well (Fig. 10). As discussed previously

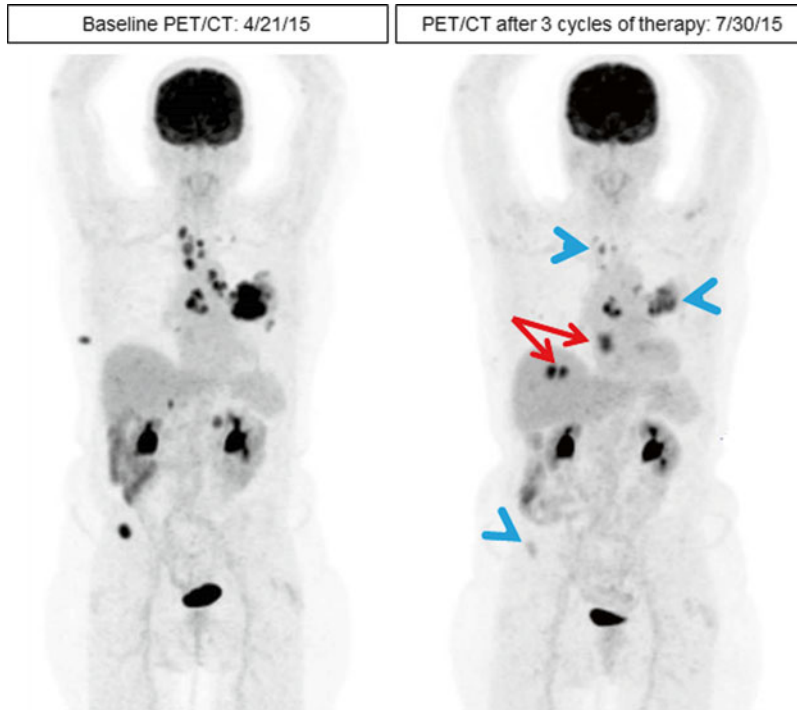

Fig. 10 An 83-year-old female, occasional smoker, that stopped 25 years ago, with pathologically confirmed lung adenocarcinoma, TTF1 positive and negative for EGFR and ALK. Coronal FDG-PET images acquired at baseline and after 3 cycles of carboplatin plus vinorelbine show the characteristic pattern of mixed response to treatment. New lesions in the liver and pericardium are evident in the post-therapeutic image (*red arrows*), while other lesions show partial (*blue arrowheads*) and complete response

in this chapter, the molecular profile of tumors is a dynamic process that can change and evolve over time and over different pathophysiological conditions. This change can drive the selection of resistant clones during treatment. In our opinion, the anatomo-metabolic criteria used to assess tumor response to therapy need to be adapted, especially when evaluating response in the multi-metastatic patient, in order to better guide clinical oncologists as to when to continue with the same drug, when to add a supplementary chemotherapeutic, or when treatment should be stopped.

3.3 Monitoring Response to Cytostatic Cancer Therapy

In today's practice of lung oncology, molecular mapping of the different tumor subtypes has greatly changed clinical practice. In fact, molecular biology of lung cancer is now integrated to daily clinical management due to the availability of therapies that are directed toward specific molecular targets. These targeted therapies block biological key pathways in the lung cancer cell and are less toxic to normal tissues (Lindeman et al. 2013).

More than a decade ago, the demonstration of growth inhibition after treatment of lung tumors with tyrosine kinase inhibitors (TKIs) that express somatic mutations of the epidermal growth factor receptor (EGFR) gene has revolutionized the treatment of this malignancy (Paez et al. 2004).

This discovery was the starting point for intensive research in lung cancer in order to identify other drivers of oncogenic mutations as therapeutic targets. This wave of enthusiasm was augmented with the identification of a fusion gene comprising portions of the echinoderm

microtubule-associated protein-like 4 (EML4) gene and the anaplastic lymphoma kinase (ALK) gene in NSCLC cells, predicting a very high response rate to crizotinib, a TKI that inhibits the c-MET and ALK (Soda et al. 2007).

The increased use of these targeted therapies creates new challenges in the follow-up and treatment assessment of patients with lung cancer. Morphologic criteria like WHO or Response Evaluation Criteria in Solid Tumors (RECIST) mainly address response to cytotoxic chemotherapy. Targeted therapies, which are usually more cytostatic than cytolytic, changed completely the follow-up paradigm for lung cancer patients. Much remains to be learned about the relevance of morphologic criteria to assess response in patients treated with these drugs, because tumor shrinkage is not always related to treatment efficacy.

Molecular imaging has been proposed as an appropriate tool that could provide relevant and useful information on the effect of targeted therapies in lung cancer patients treated with cytostatic drugs. In fact, there already is emerging evidence that FDG-PET/CT might be a better early predictor of lung cancer response to tyrosine kinase inhibitors (TKIs) like erlotinib and gefitinib (Sunaga et al. 2008; Takahashi et al. 2012; Benz et al. 2011).

In the USA, erlotinib is approved as frontline therapy in patients with inoperable NSCLC harboring EGFR-activating mutations and after failure of previous chemotherapy. In addition, it can be used as maintenance therapy in patients with metastatic NSCLC whose disease hasn't progressed after four cycles of platinum-based first-line chemotherapy.

Effective treatment with cytostatic agents (e.g., TKIs) halts tumor cell proliferation resulting in disease stability and may not necessarily induce fast and early tumor size reduction. Therefore, the use of CT-based RECIST or WHO criteria, to assess response in this scenario, may lead to underestimation of the efficacy of these drugs. Preliminary publications on the use of molecular imaging with FDG-PET/CT are starting to show its superiority to predict early response to TKIs. A reduction in FDG tumor uptake observed at 2 days (Sunaga et al. 2008; Takahashi et al. 2012) and 2 weeks (Benz et al. 2011; Hachemi et al. 2014) after treatment with erlotinib or gefitinib predicts tumoral response earlier as confirmed by CT performed at 6 weeks. In contrast, SUVmax increases significantly at 2 days and at 2 weeks in patients with progressive disease.

So far, we have observed that when patients are classified as nonresponders by FDG-PET, they remain as such on CT later on, and the opposite also holds true. The greatest benefit is that if metabolic response to TKIs is not evident early after the commencement of treatment, the patients may be spared the toxicity of futile treatment.

There is also preliminary evidence that FDG-PET patterns of response to cytostatic agents have better prognostic value in terms of PFS and OS compared to conventional imaging modalities (Takahashi et al. 2012; Benz et al. 2011; Hachemi et al. 2014). While reported delta changes in tumoral FDG uptake between the baseline and posttreatment scan range from 15 % to approximately 30 % in responders, the magnitude of a "significant" change in uptake after treatment remains to be defined. Therefore, randomized controlled trials are needed to reproduce these promising preliminary results arising from single-center studies and to standardize the PET-based response criteria to cytostatic drugs.

In summary, while both PET- and CT-based responses to therapy are associated with longer survival, PET-based response on its own is a superior prognosticator. A better outcome for the patient is usually consistent with larger and earlier reductions in tumor FDG uptake after the start of cytotoxic and/or cytostatic cancer therapy.

4 FDG-PET as a Biomarker of Prognosis in Lung Cancer

4.1 Intensity of Tumoral FDG Uptake

FDG uptake in cancer in general, and in primary lung lesions in particular, is a function of the number of cancer cells, degree of cellular

differentiation, proliferative capacity, and expression and activity of GLUT receptors, all of which have been correlated with poor outcome. The study of the prognostic value of FDG uptake in lung tumors is of utmost importance, because its main purpose rests on identifying those patients that are at high risk of fast disease progression or even recurrent disease, regardless of the clinical stage at diagnosis. This information could help personalize treatment to potentially decide if postsurgical adjuvant chemotherapy would be of benefit for patients that have early-stage disease but highly FDG-avid tumors.

Time and experience have taught us that highly metabolic tumors tend to be more aggressive and responsible for a poor clinical course compared to those with lower FDG uptake. For the most part this statement holds true across different stages and histologic types of lung cancer; however, as of today an optimal SUV cutoff value remains to be defined. Different investigators have used a wide range of primary tumor SUVmax values (2.5 to 20) to stratify for survival of lung cancer patients reaching similar conclusions as discussed below.

One of the first studies interrogating the prognostic value of FDG-PET in lung cancer is the one from Ahuja et al. (1998) published in 1998. In this 155-patient study, univariate analysis showed that those with a primary tumor SUV >10 had a significantly shorter overall survival of 11.4 months, compared to 24.6 months for patients whose lesions had an SUV <10. When factoring in lesion size, patients with primary lesions >3 cm and an SUV > 10 had the worst prognosis (median survival of 5.7 months). Furthermore, the lesion SUV remained as an independent predictor of survival in multivariate analysis.

The results of a study of 315 patients published by Cerfolio and colleagues (2005) concurred with the preceding study results, showing that an SUV > 10 in the primary tumor was an independent predictor of progression-free survival, stage, and tumor differentiation. This study was quite interesting in that the investigators analyzed disease-free survival based on high and low SUVs within each stage (I through III). The conclusion was that those patients with a higher primary tumor SUV within the same stage are more likely to have progression of their disease and a shorter overall survival. The SUV was also an independent predictor of nodal and distant metastases in their patient population.

Ohtsuka and investigators (2006) evaluated the prognostic value of FDG-PET in terms of progression-free survival in 98 patients with pathologic stage I lung adenocarcinomas (63 stage IA and 35 stage IB) that were treated surgically. The study showed that recurrence was more common in those patients with a tumor SUVmax≥3 and with a moderately or poorly differentiated histologic grade. The investigators concluded that the intensity of lesion uptake in early-stage patients could be used to determine who will benefit from adjuvant chemotherapy after surgery.

Nair and coworkers (2010) studied the association of tumor metabolic activity with overall survival in 75 patients with stage IA NSCLC treated surgically. Patients had a significantly shorter survival when their tumors were more FDG avid, and this was true when the SUVmax was analyzed as a continuous variable or dichotomized at a value of 5 or 10. Interestingly, the adjusted hazard of death was 20 % higher with each unit increment in the SUVmax, and it was 3 times higher when the tumor SUVmax >5. In addition, tumor SUV values were significantly higher in patients with lesions of squamous histology, in whom, surprisingly, the survival was shorter than in patients with adenocarcinomas.

The prognostic value of tumor FDG uptake has also been studied preoperatively in patients with node-negative, pure, and mixed bronchioloalveolar carcinomas (BACs, now called adenocarcinoma in situ) that have been resected completely (Raz et al. 2006). The study consisted of 36 patients, of which 17 had FDG-avid lesions and 19 did not, with both groups receiving similar treatment. The FDG-avid group (SUV ≥ 2.5) had a significantly shorter 3-year survival of 49 % compared to 95 % in those patients whose tumors had an SUV < 2.5. The message conveyed by the

results of this interesting single-institution study is that the intensity of FDG uptake in node-negative adenocarcinomas in situ (former BAC) might be a good surrogate marker to identify a subpopulation of patients that have a higher risk of death and who will benefit from more aggressive therapy after surgery.

The association between tumor SUV in FDG-PET and survival of stage III patients with NSCLC was recently evaluated in the prospective National Cancer Institute-funded American College of Radiology Imaging Network/Radiation Therapy Oncology Group cooperative group trial (ACRIN 6668/RTOG 0235) (Machtay et al. 2013). Patients underwent FDG-PET at baseline and 14 weeks after concurrent platinum-based chemoradiotherapy without surgery. A total of 226 patients were evaluable for pretreatment SUV and 173 for posttreatment analyses. Interestingly, the results showed that while posttreatment SUVpeak and SUVmax were associated with survival (hazard ratio, 1.087; 95 % CI, 1.014 to 1.166; $P = 0.02$), pretreatment values were not.

Despite the fact that an optimal SUV cutoff value remains to be defined, it is safe to consider that high SUV values are consistently associated with aggressive phenotypes and poor prognosis across different stages of the disease and histologic types of lung cancer (Paesmans et al. 2010).

4.2 Metabolic Tumor Volumes

Tumor burden, in terms of morphologic tumor bulk, is known to have prognostic value in different human neoplasias, including lung cancer. Recent evidence supports the use of PET-derived metabolic tumor volumes as biomarkers of prognosis in lung cancer patients (Larson et al. 1999; Lee et al. 2007; Dehing-Oberije et al. 2008). The study of metabolic volumes was conducted to evaluate other PET-derived indices of metabolic activity that could be more reliable than the SUV alone. The reason being is that SUV as a single measure of metabolic activity might not be fully reflective of the entire metabolic tumor burden.

Metabolic tumor volumes are estimated from the PET images by using semiautomatic tumor contouring software that uses a predefined SUV value as the threshold to segment metabolic tumoral boundaries. After the threshold is defined, the software generates 3D tumor regions from which measures of the total tumor metabolic volume (MTV), maximum standardized uptake value (SUVmax), and mean SUV of the entire tumor (SUVavg) are obtained. In some cases, manual adjustments of the estimated tumor boundaries are necessary to avoid overestimation of the metabolic tumor volume. Then, total lesion glycolysis (TLG) is estimated by multiplying the SUVavg by the MTV (Barbone et al. 2015).

The prognostic value of TLG is expected to be superior to SUV alone, because TLG combines the metabolic volume of the whole tumor with its degree of metabolic activity. In other words, it represents the total volume of metabolically active tumor.

Studies investigating the prognostic value of MTV and TLG have done so by evaluating these indices at the primary tumor level and by estimating the patients' whole-body tumor burden by adding the total lesion glycolysis (TLG_{WB}) indices together or the metabolic tumor volume (MTV_{WB}) of all lesions (T, N, and M) in the body.

In summary, preliminary evidence arising from studies evaluating both the primary lesion and the whole-body-based metabolic tumor burden shows that these indices have independent and significant prognostic value in patients with early- and advanced-stage lung cancer (Park et al. 2015; Zhang et al. 2013; Liao et al. 2012). In addition, study results suggest that PET-derived indices of metabolic volume are better prognostic measures than SUVmax and SUVmean.

A second analysis of the ACRIN 6668/RTOG 0235 trial data published in early 2015 was conducted to evaluate pretreatment PET-based tumoral volumetric parameters as predictors of survival (Ohri et al. 2015). Survival data was available for 214 patients. The results of multivariable analysis found MTV to be an independent predictor of overall survival (HR = 1.04 per 10 cm^3 increase, 95 % CI = 1.03 to 1.06, $P < 0.001$). In addition, high metabolic volumes were also

associated with increased risk of locoregional failure at baseline (HR = 1.16 per 10 cm^3 increase, 95 % CI = 1.08 to 1.23, $P < 0.001$) and at 6 months. The investigators concluded that pretreatment MTV is an accurate predictor of clinical outcomes in NSCLC patients after chemoradiotherapy.

Large-scale prospective multicenter studies are needed to confirm not only these promising results regarding the prediction of outcomes but also to ascertain the added value of volumetric indices to further stratify lung cancer patients within each stage of the disease. This should prove to be an important contribution to directing optimal personalized treatment choices for these patients. Last but not least, these trials should confirm if in fact MTV and TLG are superior to SUV alone in this respect and how they should be incorporated into daily clinical practice.

4.3 Patterns of Intratumoral Metabolic Heterogeneity

There is emerging promising data showing that PET-derived measures of tumor heterogeneity estimated through texture analysis might prove to be accurate prognostic indicators in non-small cell lung cancer patients.

As discussed previously, intratumoral heterogeneity is highly correlated with substandard response to treatment and poor progression-free and overall survival. Therefore, it will be of great clinical benefit if an imaging-based method capable of interrogating neoplastic lesion heterogeneity is incorporated into daily imaging practice. In this manner, personalized selection of more aggressive therapy could be accomplished for patients with "textural-based patterns of poor prognosis." Multiple texture parameters are being studied and tested to characterize the degree of tumoral heterogeneity, and these include intensity, uniformity, entropy, contrast, energy, homogeneity, dissimilarity, and correlation (Davnall et al. 2012; van Gómez et al. 2014). These parameters seem to be more robust and applicable to larger tumors, due to the inability of PET to accurately characterize tracer distribution within small lesions, because of its limited spatial resolution.

Pretreatment PET-derived textural features of lung cancer heterogeneity have been found to correlate with metabolic parameters such as SUVmax, SUVmean, metabolic tumor volume (MTV), and total lesion glycolysis (TLG), as well as pathologic stage and prognosis (van Gómez et al. 2014; Orlhac et al. 2014; Cook et al. 2013).

First-order and high-order textural features on FDG-PET images of NSCLC patients have also been studied as predictors of response and survival in patients treated with erlotinib (Cook et al. 2015). This prospective single-center study included 47 NSCLC patients who underwent FDG-PET/CT at baseline and 6 weeks after treatment with erlotinib. Response was assessed using RECIST on CT images obtained at 12 weeks. Favorable response to erlotinib was associated with reduced heterogeneity, and the percentage change in first-order entropy was independently associated with treatment response. On the other hand, high-order contrast at 6 weeks and percentage change in first-order entropy were found to be independent predictors of survival.

No consensus has been reached yet on which is in fact the best parameter, and the reproducibility of texture analysis calculations has to be studied widely as well. While these "new metabolic" parameters seem very promising, prospective, randomized trials are needed to define with certainty if they should be included in daily clinical PET/CT practice and to fully understand their predictive and prognostic strength.

5 The Role of FDG-PET/CT in Small Cell Lung Cancer (SCLC) Patients

SCLCs account for 15–20 % of all cases of lung cancer and are associated with cigarette smoking. It is considered a neuroendocrine tumor known to cause paraneoplastic syndromes in patients. It presents as a central tumor that arises from the main or lobar bronchi, with hilar or perihilar lesions, which infiltrate peribronchially and may cause obstruction of the airways. Systemic metastases are common early in the disease process. In

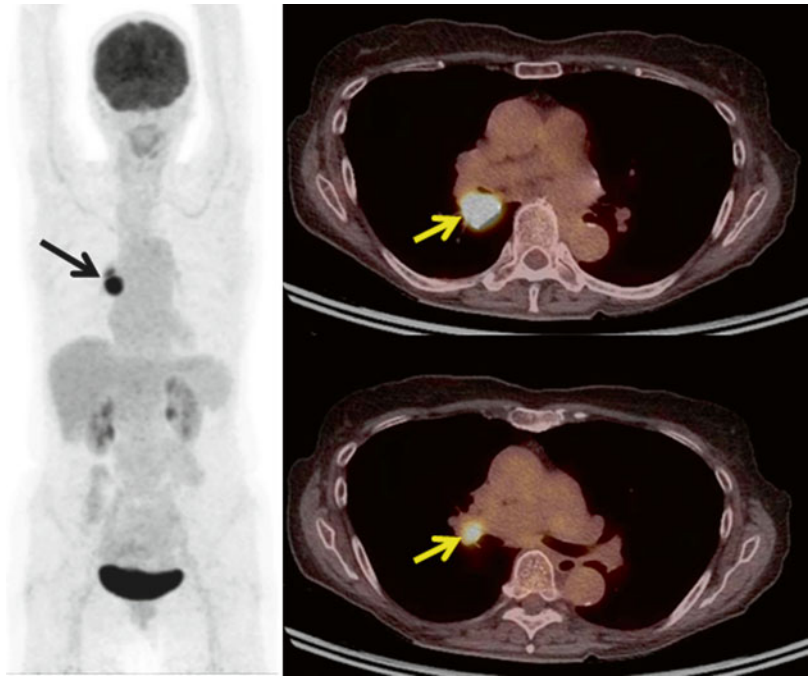

Fig. 11 FDG-PET/CT of a 67-year-old female with stage IIA small cell lung carcinoma (SCLC) obtained for initial staging. The images show one of the classic presentations of limited-stage disease in SCLC, with the typical pulmonary hilar mass which is highly FDG avid (SUVmax: 15.2 in this case) (*arrows* in MIP and axial images)

1950, the Veterans Administration Lung Study Group classified SCLC into limited-stage disease affecting one hemithorax and its corresponding lymph nodes and into extensive-stage disease, consistent with disease invading beyond. In 1989, the IASLC updated the limited disease classification to include tumors in one hemithorax and metastasis in ipsilateral hilar, contralateral mediastinal, and ipsilateral and contralateral supraclavicular nodes. Limited disease also includes ipsilateral pleural effusions without other concurrent extrathoracic systemic disease. Recently the IASLC determined that the revised 2010 TNM staging system should now be applied to SCLC as well.

There isn't reliable evidence yet to support the use of FDG-PET for the diagnosis and staging of SCLC. The number of studies is limited, with a small number of patients. These small studies found that adding PET to conventional staging results in a change in patient management ranging from 9 to 30 % (Kamel et al. 2003; Bradley et al. 2004; Shen et al. 2002; Azad et al. 2010) and that PET may influence clinical stage migration by detecting systemic disease. In up to 33 % of cases, FDG-PET upstages the disease from limited to extensive, while it downstages it in approximately 17 % of patients (Figs. 11 and 12).

Fischer and colleagues (2006) evaluated the role of FDG-PET/CT to monitor response to SCLC therapy. The investigators observed a significant difference in relative change in tumor FDG avidity and volume between responding and nonresponding patients. However, they stressed the fact that they could not find a significant difference between qualitative and semiquantitative analysis of the PET images when attempting to assess response. The message was that although response evaluation to treatment is possible with PET/CT, it is uncertain if the technique adds additional information to the one already provided by conventional imaging modalities.

FDG uptake in SCLC lesions has been shown to have prognostic value. Lee et al. (2009) imaged 76 consecutive patients with pathologically proven SCLC using FDG-PET to study the prognostic value of pretreatment tumoral uptake. A high tumoral SUVmax was associated with poor survival, with the intensity of tumor uptake

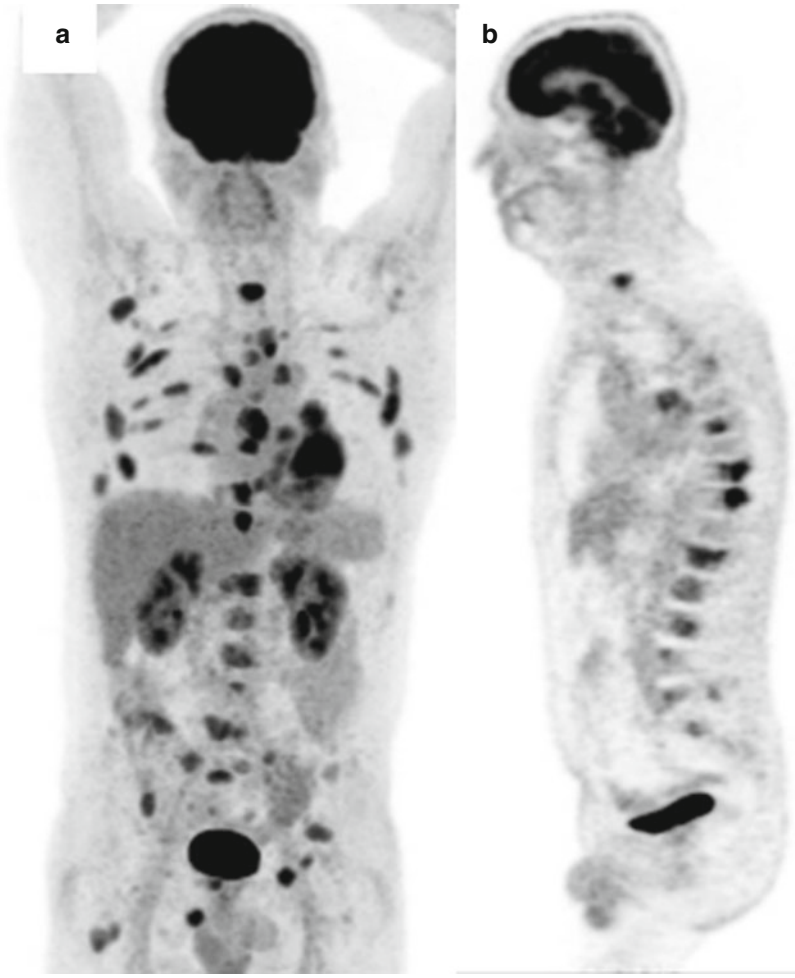

Fig. 12 Extensive-stage SCLC. (**a**) Coronal and (**b**) sagittal FDG-PET images illustrate the PET pattern of metastatic small cell lung cancer. Large, hypermetabolic left pulmonary hilar lesion (SUV max = 11.8) with concomitant metastatic disease affecting lymph nodes and bone. Although not shown in this image, brain metastases are also frequent

identifying prognostic subgroups in patients with extensive and limited disease.

Conclusion

PET/CT imaging without a doubt is here to stay as a highly sensitive molecular imaging pearl that provides anatomo-biological and functional insight into the heterogeneous phenotype of lung neoplasia. This pathophysiological imaging technique plays a decisive, cost-efficient, and unique role in the personalized care of lung cancer patients, from diagnosis to aiding in the selection of the most appropriate treatment algorithm and from the early monitoring of response to cytotoxic and cytostatic therapies to the characterization of tumor relapse and accurate prognostication.

References

Vogelstein B, Papadopoulos N, Velculescu VE, Zhou S, Diaz LA Jr, Kinzler KW (2013) Cancer genome landscapes. Science 339(6127):1546–1558

Aparicio S, Caldas C (2013) The implications of clonal genome evolution for cancer medicine. N Engl J Med 368(9):842–851

Warburg O, Wind F, Negelein E (1927) The metabolism of tumours in the body. J Gen Physiol 8(6):519–530

Warburg O (1956) On respiratory impairment in cancer cells. Science 124(3215):269–270

Cairns RA, Harris IS, Mak TW (2011) Regulation of cancer cell metabolism. Nat Rev Cancer 11(2):85–95

Merrall NW, Plevin R, Gould GW (1993) Growth factors, mitogens, oncogenes and the regulation of glucose transport. Cell Signal 5:667–675

Garcia C, Gebhart G, Flamen P (2012) New PET imaging agents in the management of solid cancers. Curr Opin Oncol 24:748–755

Gould MK, Maclean CC, Kuschner WG, Rydzak CE, Owens DK (2001) Accuracy of positron emission tomography for diagnosis of pulmonary nodules and mass lesions: a meta-analysis. JAMA 287:914–924

Gambhir SS, Czernin J, Schwimmer J, Silverman DH, Coleman RE, Phelps ME (2001) A tabulated summary of the FDG PET literature. J Nucl Med 42:1S–93S

Cronin P, Dwamena B, Kelly AM, Carlos RC (2008) Solitary pulmonary nodules: meta-analytic comparison of cross-sectional imaging modalities for diagnosis of malignancy. Radiology 246:772–782

Bryant AS, Cerfolio RJ (2006) The maximum standardized uptake values on integrated FDG-PET/CT is useful in differentiating benign from malignant pulmonary nodules. Ann Thorac Surg 82:1016–1020

Christensen JA, Nathan MA, Mullan BP, Hartman TE, Swensen SJ, Lowe VJ (2006) Characterization of the solitary pulmonary nodule: 18F-FDG PET versus nodule-enhancement CT. AJR Am J Roentgenol 187(5):1361–1367

Yi CA, Lee KS, Kim BT, Choi JY, Kwon OJ, Kim H et al (2006) Tissue characterization of solitary pulmonary nodule: comparative study between helical dynamic CT and integrated PET/CT. J Nucl Med 47(3):443–450

Jeong SY, Lee KS, Shin KM, Bae YA, Kim BT, Choe BK et al (2008) Efficacy of PET/CT in the characterization of solid or partly solid solitary pulmonary nodules. Lung Cancer 61(2):186–194

Fletcher JW, Kymes SM, Gould M, Alazraki N, Coleman RE, Lowe VJ, Marn C, Segall G, Thet LA, Lee K, VA SNAP Cooperative Studies Group (2008a) A comparison of the diagnostic accuracy of 18F-FDG PET and CT in the characterization of solitary pulmonary nodules. J Nucl Med 49:179–185

Divisi D, Di Tommaso S, Di Leonardo G, Brianzoni E, De Vico A, Crisci R (2010) 18-fluorine fluorodeoxyglucose positron emission tomography with computerized tomography versus computerized tomography alone for the management of solitary lung nodules with diameters inferior to 1.5 cm. Thorac Cardiovasc Surg 58(7):422–426

Nomori H, Watanabe K, Ohtsuka T, Naruke T, Suemasu K, Uno K (2005) Visual and semiquantitative analyses for F-18 fluorodeoxyglucose PET scanning in pulmonary nodules 1 cm to 3 cm in size. Ann Thorac Surg 79:984–988

Hamberg LM, Hunter GJ, Alpert NM, Choi NC, Babich JW, Fischman AJ (1994) The dose uptake ratio as an index of glucose metabolism: useful parameter or oversimplification? J Nucl Med 35(8):1308–1312

Grgic A, Yüksel Y, Gröschel A, Schäfers HJ, Sybrecht GW, Kirsch CM, Hellwig D (2010) Risk stratification of solitary pulmonary nodules by means of PET using (18)F-fluorodeoxyglucose and SUV quantification. Eur J Nucl Med Mol Imaging 37(6):1087–1094

Lowe VJ, Fletcher JW, Gobar L, Lawson M, Kirchner P, Valk P, Karis J, Hubner K, Delbeke D, Heiberg EV, Patz EF, Coleman RE (1998) Prospective investigation of positron emission tomography in lung nodules. J Clin Oncol 16:1075–1084

Higashi K, Ueda Y, Seki H et al (1998) Fluorine-18-FDG PET imaging is negative in bronchioloalveolar lung carcinoma. J Nucl Med 39:1016–1020

Erasmus JJ, McAdams HP, Patz EF Jr, Coleman RE, Ahuja V, Goodman PC (1998) Evaluation of primary pulmonary carcinoid tumors using FDG PET. AJR Am J Roentgenol 170:1369–1373

Kim YH, Lee KS, Primack SL, Kim H, Kwon OJ, Kim TS, Kim EA, Kim J, Shim YM (2002) Small pulmonary nodules on CT accompanying surgically resectable lung cancer: likelihood of malignancy. J Thorac Imaging 17:40–46

Chalmers N, Best JJ (1991) The significance of pulmonary nodules detected by CT but not by chest radiography in tumor staging. Clin Radiol 44:410–412

Yuan Y, Matsumoto T, Hiyama A, Miura G, Tanaka N, Emoto T, Kawamura T, Matsunaga N (2003) The probability of malignancy in small pulmonary nodules coexisting with potentially operable lung cancer detected by CT. Eur Radiol 13:2447–2453

Jones HA, Clark RJ, Rhodes CG, Schofield JB, Krausz T, Haslett C (1991) Positron emission tomography of 18FDG uptake in localized pulmonary inflammation. Acta Radiol Suppl 376:148

Wachsmann J, Gerbaudo VH (2014) Thorax: normal and benign pathologic patterns in FDG-PET/CT imaging. PET Clin 9(2):147–168

Alavi A, Gupta N, Alberini JL, Hickeson M, Adam LE, Bhargava P, Zhuang H (2002) Positron emission tomography imaging in nonmalignant thoracic disorders. Semin Nucl Med 32(4):293–321

Gould MK, Sanders GD, Barnett PG, Rydzak CE, Maclean CC, McClellan MB, Owens DK (2003a) Cost-effectiveness of alternative management strategies for patients with solitary pulmonary nodules. Ann Intern Med 138(9):724–735

Fletcher JW, Djulbegovic B, Soares HP, Siegel BA, Lowe VJ, Lyman GH, Coleman RE, Wahl R, Paschold JC, Avril N, Einhorn LH, Suh WW, Samson D, Delbeke D, Gorman M, Shields AF (2008b) Recommendations on the use of 18F-FDG PET in oncology. J Nucl Med 49(3):480–508

Lardinois D, Weder W, Hany TF, Kamel EM, Korom S, Seifert B, von Schulthess GK, Steinert HC (2003) Staging of non–small-cell lung cancer with integrated positron emission tomography and computed tomography. N Engl J Med 348:2500–2507

Antoch G, Stattaus J, Nemat AT, Marnitz S, Beyer T, Kuehl H, Bockisch A, Debatin JF, Freudenberg LS (2003) Non-small cell lung cancer: dual-modality PET/CT in preoperative staging. Radiology 229(2):526–533

Gerbaudo VH, Julius B (2007) Anatomo-metabolic characteristics of atelectasis in F-18 FDG-PET/CT imaging. Eur J Radiol 64(3):401–405

Dizendorf EV, Baumert BG, von Schulthess GK et al (2003) Impact of whole-body 18E-EDG PET on staging and managing patients for radiation therapy. J Nucl Med 44:24–29

Gould MK, Kuschner WG, Rydzak CE, Maclean CC, Demas AN, Shigemitsu H, Chan JK, Owens DK (2003b) Test performance of positron emission tomography and computed tomography for mediastinal staging in patients with non-small-cell lung cancer: a meta-analysis. Ann Intern Med 139:879–892

Toloza EM, Harpole L, McCrory DC (2003) Noninvasive staging of non-small cell lungcancer: a review of the current evidence. Chest 123(1 Suppl):137S–146S

Reed CE, Harpole DH, Posther KE, Woolson SL, Downey RJ, Meyers BF, Heelan RT, Macapinlac HA, Jung SH, Silvestri GA, Siegel BA, Rusch VW, American College of Surgeons Oncology Group Z0050 trial (2003) Results of the American College of Surgeons Oncology Group Z0050 trial: the utility of positron emission tomography in staging potentially operable non-small cell lung cancer. J Thorac Cardiovasc Surg 126(6):1943–1951

Kim BT, Lee KS, Shim SS, Choi JY, Kwon OJ, Kim H, Shim YM, Kim J, Kim S (2006) Stage T1 non-small cell lung cancer: preoperative mediastinal nodal staging with integrated FDG PET/CT--a prospective study. Radiology 241(2):501–509

Vansteenkiste JF (2005) FDG-PET for lymph node staging in NSCLC: a major step forward, but beware of the pitfalls. Lung Cancer 47(2):151–153

de Langen AJ, Raijmakers P, Riphagen I, Paul MA, Hoekstra OS (2006) The size of mediastinal lymph nodes and its relation with metastatic involvement: a meta-analysis. Eur J Cardiothorac Surg 29(1):26–29

Fischer BM, Mortensen J, Hansen H, Vilmann P, Larsen SS, Loft A, Bertelsen AK, Ravn J, Clementsen P, Høegholm A, Larsen KR, Dirksen A, Skov BG, Krasnik M, Højgaard L, Lassen U (2011) Multimodality approach to mediastinal staging in non-small cell lung cancer. Faults and benefits of PET-CT: a randomised trial. Thorax 66(4):294–300

Sider L, Horejs D (1988) Frequency of extrathoracic metastases from bronchogenic carcinoma in patients with normal-sized hilar and mediastinal lymph nodes on CT. AJR Am J Roentgenol 151(5):893–895

Hellwig D, Ukena D, Paulsen F, Bamberg M, Kirsch CM, Onko-PET der Deutschen Gesellschaft fur Nuklearmedizin (2001) Meta-analysis of the efficacy of positron emission tomography with F-18-fluorodeoxyglucose in lung tumors. Basis for discussion of the German Consensus Conference on PET in Oncology 2000. Pneumologie 55(8):367–377

Cook GJ, Houston S, Rubens R, Maisey MN, Fogelman I (1998) Detection of bone metastases in breast cancer by 18FDG PET: differing metabolic activity in osteoblastic and osteolytic lesions. J Clin Oncol 16(10):3375–3379

Ak I, Sivrikoz MC, Entok E, Vardareli E (2010) Discordant findings in patients with non-small-cell lung cancer: absolutely normal bone scans versus disseminated bone metastases on positron-emission tomography/computed tomography. Eur J Cardiothorac Surg 37(4):792–796

Hustinx R, Paulus P, Jacquet N, Jerusalem G, Bury T, Rigo P (1998) Clinical evaluation of whole-body 18F-fluorodeoxyglucose positron emission tomography in the detection of liver metastases. Ann Oncol 9(4):397–401

MacManus MP, Hicks RJ, Matthews JP, Hogg A, McKenzie AF, Wirth A, Ware RE, Ball DL (2001) High rate of detection of unsuspected distant metastases by pet in apparent stage III non-small-cell lung cancer: implications for radical radiation therapy. Int J Radiat Oncol Biol Phys 50(2):287–293

Lardinois D, Weder W, Roudas M, von Schulthess GK, Tutic M, Moch H, Stahel RA, Steinert HC (2005) Etiology of solitary extrapulmonary positron emission tomography and computed tomography findings in patients with lung cancer. J Clin Oncol 23:6846–6853

Hicks RJ, Kalff V, MacManus MP, Ware RE, Hogg A, McKenzie AF, Matthews JP, Ball DL (2001a) (18) F-FDG PET provides high-impact and powerful prognostic stratification in staging newly diagnosed non-small cell lung cancer. J Nucl Med 42(11):1596–1604

Gregory DL, Hicks RJ, Hogg A, Binns DS, Shum PL, Milner A, Link E, Ball DL, Mac Manus MP (2012) Effect of PET/CT on management of patients with non-small cell lung cancer: results of a prospective study with 5-year survival data. J Nucl Med 53(7):1007–1015

Jackman DM, Johnson BE (2005) Small-cell lung cancer. Lancet 366(9494):1385–1396

Simon GR, Turrisi A, American College of Chest Physicians (2007) Management of small cell lung cancer: ACCP evidence-based clinical practice guidelines (2nd edition). Chest 132(3 Suppl):324S–339S

Inoue T, Kim EE, Komaki R, Wong FC, Bassa P, Wong WH, Yang DJ, Endo K, Podoloff DA (1995) Detecting recurrent or residual lung cancer with FDG-PET. J Nucl Med 36(5):788–793

Patz EF Jr, Lowe VJ, Hoffman JM, Paine SS, Harris LK, Goodman PC (1994) Persistent or recurrent bronchogenic carcinoma: detection with PET and 2-[F-18]-2-deoxy-D-glucose. Radiology 191(2):379–382

Bury T, Corhay JL, Duysinx B, Daenen F, Ghaye B, Barthelemy N, Rigo P, Bartsch P (1999) Value of FDG-PET in detecting residual or recurrent nonsmall cell lung cancer. Eur Respir J 14(6):1376–1380

Hicks RJ, Kalff V, MacManus MP, Ware RE, McKenzie AF, Matthews JP, Ball DL (2001b) The utility of (18) F-FDG PET for suspected recurrent non-small cell lung cancer after potentially curative therapy: impact on management and prognostic stratification. J Nucl Med 42(11):1605–1613

Higashi K, Ueda Y, Arisaka Y, Sakuma T, Nambu Y, Oguchi M, Seki H, Taki S, Tonami H, Yamamoto I (2002) 18F-FDG uptake as a biologic prognostic factor for recurrence in patients with surgically resected non-small cell lung cancer. J Nucl Med 43(1):39–45

Singnurkar A, Solomon SB, Gönen M, Larson SM, Schöder H (2011) 18F-FDG PET/CT for the prediction and detection of local recurrence after radiofrequency ablation of malignant lung lesions. J Nucl Med 52(1):106

Shiono S, Abiko M, Sato T (2011) Positron emission tomography/computed tomography and lymphovascular invasion predict recurrence in stage I lung cancers. J Thorac Oncol 6(1):43–47

Hellwig D, Gröschel A, Graeter TP, Hellwig AP, Nestle U, Schäfers HJ, Sybrecht GW, Kirsch CM (2006) Diagnostic performance and prognostic impact of FDG-PET in suspected recurrence of surgically treated non-small cell lung cancer. Eur J Nucl Med Mol Imaging 33(1):13–21

Kanzaki R, Higashiyama M, Maeda J, Okami J, Hosoki T, Hasegawa Y, Takami M, Kodama K (2010) Clinical value of F18-fluorodeoxyglucose positron emission tomography-computed tomography in patients with non-small cell lung cancer after potentially curative surgery: experience with 241 patients. Interact Cardiovasc Thorac Surg 10(6):1009–1014

Huang K, Dahele M, Senan S, Guckenberger M, Rodrigues GB, Ward A, Boldt RG, Palma DA (2012) Radiographic changes after lung stereotactic ablative radiotherapy (SABR)--can we distinguish recurrence from fibrosis? A systematic review of the literature. Radiother Oncol 102(3):335–342

Hicks RJ, Mac Manus MP, Matthews JP, Hogg A, Binns D, Rischin D, Ball DL, Peters LJ (2004) Early FDG-PET imaging after radical radiotherapy for non-small-cell lung cancer: inflammatory changes in normal tissues correlate with tumor response and do not confound therapeutic response evaluation. Int J Radiat Oncol Biol Phys 60(2):412–418

Vansteenkiste J, Fischer BM, Dooms C, Mortensen J (2004) Positron-emission tomography in prognostic and therapeutic assessment of lung cancer: systematic review. Lancet Oncol 5:531–540

Weber WA, Petersen V, Schmidt B, Tyndale-Hines L, Link T, Peschel C, Schwaiger M (2003) Positron emission tomography in non-small-cell lung cancer: prediction of response to chemotherapy by quantitative assessment of glucose use. J Clin Oncol 21:2651–2657

Cerfolio RJ, Bryant AS, Winokur TS, Ohja B, Bartolucci AA (2004) Repeat 18F- FDG-PET after neoadjuvant therapy is a predictor of pathologic response in patients with non-small cell lung cancer. Ann Thorac Surg 78:1903–1909

Hoekstra CJ, Stroobants SG, Smit EF, Vansteenkiste J, van Tinteren H, Postmus PE, Golding RP, Biesma B, Schramel FJ, van Zandwijk N, Lammertsma AA, Hoekstra OS (2005) Prognostic relevance of response evaluation using [18F]-2-fluoro-2-deoxy-D-glucose positron emission tomography in patients with locally advanced non-small-cell lung cancer. J Clin Oncol 23(33):8362–8370

Dooms C, Verbeken E, Stroobants S, Nackaerts K, De Leyn P, Vansteenkiste J (2008) Prognostic stratification of stage IIIA-N2 non-small-cell lung cancer after induction chemotherapy: a model based on the combination of morphometric-pathologic response in mediastinal nodes and primary tumor response on serial 18-fluoro-2-deoxy-glucose positron emission tomography. J Clin Oncol 26(7):1128–1134

Tanvetyanon T, Eikman EA, Sommers E, Robinson L, Boulware D, Bepler G (2008) Computed tomography response, but not positron emission tomography scan response, predicts survival after neoadjuvant chemotherapy for resectable non-small-cell lung cancer. J Clin Oncol 26(28):4610–4616

Lindeman NI, Cagle PT, Beasley MB, Chitale DA, Dacic S, Giaccone G, Jenkins RB, Kwiatkowski DJ, Saldivar JS, Squire J, Thunnissen E, Ladanyi M (2013) Molecular testing guideline for selection of lung cancer patients for EGFR and ALK tyrosine kinase inhibitors: guideline from the College of American Pathologists, International Association for the Study of Lung Cancer, and Association for Molecular Pathology. J Thorac Oncol 8(7):823–859

Paez JG, Jänne PA, Lee JC, Tracy S, Greulich H, Gabriel S, Herman P, Kaye FJ, Lindeman N, Boggon TJ, Naoki K, Sasaki H, Fujii Y, Eck MJ, Sellers WR, Johnson BE, Meyerson M (2004) EGFR mutations in lung cancer: correlation with clinical response to gefitinib therapy. Science 304(5676):1497–1500

Soda M, Choi YL, Enomoto M, Takada S, Yamashita Y, Ishikawa S, Fujiwara S, Watanabe H, Kurashina K, Hatanaka H, Bando M, Ohno S, Ishikawa Y, Aburatani H, Niki T, Sohara Y, Sugiyama Y, Mano H (2007) Identification of the transforming EML4-ALK fusion gene in non-small-cell lung cancer. Nature 448(7153):561–566

Sunaga N, Oriuchi N, Kaira K, Yanagitani N, Tomizawa Y, Hisada T, Ishizuka T, Endo K, Mori M (2008) Usefulness of FDG-PET for early prediction of the response to gefitinib in non-small cell lung cancer. Lung Cancer 59(2):203–210

Takahashi R, Hirata H, Tachibana I, Shimosegawa E, Inoue A, Nagatomo I, Takeda Y, Kida H, Goya S, Kijima T, Yoshida M, Kumagai T, Kumanogoh A, Okumura M, Hatazawa J, Kawase I (2012) Early [18F] fluorodeoxyglucose positron emission tomography at two days of gefitinib treatment predicts clinical outcome in patients with adenocarcinoma of the lung. Clin Cancer Res 18(1):220–228

Benz MR, Herrmann K, Walter F, Garon EB, Reckamp KL, Figlin R, Phelps ME, Weber WA, Czernin J, Allen-Auerbach MS (2011) (18)F-FDG PET/CT for

monitoring treatment responses to the epidermal growth factor receptor inhibitor erlotinib. J Nucl Med 52(11):1684–1689

Hachemi M, Couturier O, Vervueren L, Fosse P, Lacœuille F, Urban T, Hureaux J (2014) [18F]FDG positron emission tomography within two weeks of starting erlotinib therapy can predict response in non-small cell lung cancer patients. PLoS One 9(2):e87629

Ahuja V, Coleman RE, Herndon J, Patz EF Jr (1998) The prognostic significance of fluorodeoxyglucose positron emission tomography imaging for patients with nonsmall cell lung carcinoma. Cancer 83(5):918–924

Cerfolio RJ, Bryant AS, Ohja B, Bartolucci AA (2005) The maximum standardized uptake values on positron emission tomography of a non-small cell lung cancer predict stage, recurrence, and survival. J Thorac Cardiovasc Surg 130(1):151–159

Ohtsuka T, Nomori H, Watanabe K, Kaji M, Naruke T, Suemasu K, Uno K (2006) Prognostic significance of [(18)F]fluorodeoxyglucose uptake on positron emission tomography in patients with pathologic stage I lung adenocarcinoma. Cancer 107(10):2468–2473

Nair VS, Barnett PG, Ananth L, Gould MK, Veterans Affairs Solitary Nodule Accuracy Project Cooperative Studies Group (2010) PET scan 18F-fluorodeoxyglucose uptake and prognosis in patients with resected clinical stage IA non-small cell lung cancer. Chest 137(5):1150–1156

Raz DJ, Odisho AY, Franc BL, Jablons DM (2006) Tumor fluoro-2-deoxy-D-glucose avidity on positron emission tomographic scan predicts mortality in patients with early-stage pure and mixed bronchioloalveolar carcinoma. J Thorac Cardiovasc Surg 132(5):1189–1195

Machtay M, Duan F, Siegel BA, Snyder BS, Gorelick JJ, Reddin JS, Munden R, Johnson DW, Wilf LH, DeNittis A, Sherwin N, Cho KH, Kim SK, Videtic G, Neumann DR, Komaki R, Macapinlac H, Bradley JD, Alavi A (2013) Prediction of survival by [18F]fluorodeoxyglucose positron emission tomography in patients with locally advanced non-small-cell lung cancer undergoing definitive chemoradiation therapy: results of the ACRIN 6668/RTOG 0235 trial. J Clin Oncol 31(30):3823–3830

Paesmans M, Berghmans T, Dusart M, Garcia C, Hossein-Foucher C, Lafitte JJ, Mascaux C, Meert AP, Roelandts M, Scherpereel A, Terrones Munoz V, Sculier JP (2010) Primary tumor standardized uptake value measured on fluorodeoxyglucose positron emission tomography is of prognostic value for survival in non-small cell lung cancer: update of a systematic review and meta-analysis by the European Lung Cancer Working Party for the International Association for the Study of Lung Cancer Staging Project. J Thorac Oncol 5(5):612–619

Larson SM, Erdi Y, Akhurst T, Mazumdar M, Macapinlac HA, Finn RD, Casilla C, Fazzari M, Srivastava N, Yeung HW, Humm JL, Guillem J, Downey R, Karpeh M, Cohen AE, Ginsberg R (1999) Tumor Treatment Response Based on Visual and Quantitative Changesin Global Tumor Glycolysis Using PET-FDG Imaging. The Visual Response Score and the Change in Total Lesion Glycolysis. Clin Positron Imaging 2(3):159–171

Lee P, Weerasuriya DK, Lavori PW, Quon A, Hara W, Maxim PG, Le QT, Wakelee HA, Donington JS, Graves EE, Loo BW Jr (2007) Metabolic tumor burden predicts for disease progression and death in lung cancer. Int J Radiat Oncol Biol Phys 69(2):328–333

Dehing-Oberije C, De Ruysscher D, van der Weide H, Hochstenbag M, Bootsma G, Geraedts W, Pitz C, Simons J, Teule J, Rahmy A, Thimister P, Steck H, Lambin P (2008) Tumor volume combined with number of positive lymph node stations is a more important prognostic factor than TNM stage for survival of non-small-cell lung cancer patients treated with (chemo)radiotherapy. Int J Radiat Oncol Biol Phys 70(4):1039–1044

Barbone D, Follo C, Echeverry M, Gerbaudo VH, Klabatsa A, Bueno R, Felley-Bosco E, Broaddus VC. (2015) Autophagy correlates with the therapeutic responsiveness of malignant pleural mesothelioma in 3D models. PLOS One (in press)

Park SY, Cho A, Yu WS, Lee CY, Lee JG, Kim DJ, Chung KY (2015) Prognostic value of total lesion glycolysis by 18F-FDG PET/CT in surgically resected stage IA non-small cell lung cancer. J Nucl Med 56(1):45–49

Zhang H, Wroblewski K, Liao S, Kampalath R, Penney BC, Zhang Y, Pu Y (2013) Prognostic value of metabolic tumor burden from (18)F-FDG PET in surgical patients with non-small-cell lung cancer. Acad Radiol 20(1):32–40

Liao S, Penney BC, Zhang H, Suzuki K, Pu Y (2012) Prognostic value of the quantitative metabolic volumetric measurement on 18F-FDG PET/CT in Stage IV nonsurgical small-cell lung cancer. Acad Radiol 19(1):69–77

Ohri N, Duan F, Machtay M, Gorelick JJ, Snyder BS, Alavi A, Siegel BA, Johnson DW, Bradley JD, DeNittis A, Werner-Wasik M (2015) Pretreatment FDG-PET metrics in stage III non-small cell lung cancer: ACRIN 6668/RTOG 0235. J Natl Cancer Inst 107(4), pii: djv004

Davnall F, Yip CS, Ljungqvist G, Selmi M, Ng F, Sanghera B, Ganeshan B, Miles KA, Cook GJ, Goh V (2012) Assessment of tumor heterogeneity: an emerging imaging tool for clinical practice? Insights Imaging 3(6):573–589

van Gómez LO, García Vicente AM, Honguero Martínez AF, Soriano Castrejón AM, Jiménez Londoño GA, Udias JM, León AP (2014) Heterogeneity in [18F] fluorodeoxyglucose positron emission tomography/computed tomography ofnon-small cell lung carcinoma and its relationship to metabolic parameters and pathologic staging. Mol Imaging 13:1–12

Orlhac F, Soussan M, Maisonobe JA, Garcia CA, Vanderlinden B, Buvat I (2014) Tumor texture analysis in 18F-FDG PET: relationships between texture parameters, histogram indices, standardized uptake values, metabolic volumes, and total lesion glycolysis. J Nucl Med 55(3):414–422

Cook GJ, Yip C, Siddique M, Goh V, Chicklore S, Roy A, Marsden P, Ahmad S, Landau D (2013) Are pretreatment 18F-FDG PET tumor textural features in non-small cell lung cancer associated with response and survival after chemoradiotherapy? J Nucl Med 54(1):19–26

Cook GJ, O'Brien ME, Siddique M, Chicklore S, Loi HY, Sharma B, Punwani R, Bassett P, Goh V, Chua S (2015) Non-Small Cell Lung Cancer Treated with Erlotinib:Heterogeneity of (18)F-FDG Uptake at PET-Association with Treatment Response and Prognosis. Radiology 276(3):883–93, 141309

Kamel EM, Zwahlen D, Wyss MT, Stumpe KD, von Schulthess GK, Steinert HC (2003) Whole-body (18) F-FDG PET improves the management of patients with small cell lung cancer. J Nucl Med 44:1911–1917

Bradley JD, Dehdashti F, Mintun MA, Govindan R, Trinkaus K, Siegel BA (2004) Positron emission tomography in limited-stage small-cell lung cancer: a prospective study. J Clin Oncol 22:3248–3254

Shen YY, Shiau YC, Wang JJ, Ho ST, Kao CH (2002) Whole-body 18F-2 deoxyglucose positron emission tomography in primary staging small cell lung cancer. Anticancer Res 22:1257–1264

Azad A, Chionh F, Scott AM, Lee ST, Berlangieri SU, White S et al (2010) High impact of 18F-FDG-PET on management and prognostic stratification of newly diagnosed small cell lung cancer. Mol Imaging Biol 12:443–451

Fischer BM, Mortensen J, Langer SW, Loft A, Berthelsen AK, Daugaard G, Lassen U, Hansen HH (2006) PET/CT imaging in response evaluation of patients with small cell lung cancer. Lung Cancer 54(1):41–49

Lee YJ, Cho A, Cho BC, Yun M, Kim SK, Chang J, Moon JW, Park IK, Choi HJ, Kim JH (2009) High tumor metabolic activity as measured by fluorodeoxyglucose positron emission tomography is associated with poor prognosis in limitedand extensive stage small-cell lung cancer. Clin Cancer Res 15(7):2426–2432

CT of Pulmonary Thromboembolic Disease

Chandra Bortolotto, Suonita Khung, Julien Pagniez, Jacques Remy, and Martine Remy-Jardin

Abstract

This chapter highlights new areas of interest in the management of patients with acute thromboembolic disease with the objective of emphasizing new options applicable in daily practice.

Key Points

- CT is no longer exclusively dedicated to the diagnosis of PE, but also participates in the prognostic approach of this disease.
- The major determinant of patient's outcome is the presence of right ventricular dysfunction, easily accessible on transverse imaging.
- The estimation of the clot burden could be replaced by the analysis of the extent of perfusion impairment on dual-energy CT examinations.
- Early risk stratification now tends to consider four categories of PE patients with different therapeutic options. Radiologists can provide clinicians with relevant information from chest CT angiographic examination regarding this stratification.
- Spectral imaging could represent a new standard for routine CT diagnosis of PE using low-concentrated contrast agents.

1 Introduction

Multidetector row computed tomographic angiography (CTA) has become the first-line modality for imaging the pulmonary vasculature in patients with suspected acute pulmonary embolism (PE) (Remy-Jardin et al. 2007). This disease is the third most common acute cardiovascular disease after myocardial infarction and stroke in the Unites States and results in many deaths each year. These data fully justify a

C. Bortolotto, MD • S. Khung, MD
J. Pagniez, MD • J. Remy, MD
Department of Thoracic Imaging, Hospital Calmette (EA 2694), University of Lille Nord de France, Lille F-59000, France

M. Remy-Jardin, MD, PhD (✉)
Department of Thoracic Imaging, Hospital Calmette, Boulevard Jules Leclercq, Lille 59037, France
e-mail: martine.remy@chru-lille.fr

U.J. Schoepf, F.G. Meinel (eds.), *Multidetector-Row CT of the Thorax*, Medical Radiology,
DOI 10.1007/978-3-319-30355-0_14

regular update of the radiologists' role in the management of patients suspected of acute pulmonary embolism. Some aspects are currently well established such as the CT features of endovascular clots whose description has not changed over time. However, their detection has greatly benefited from the improvement of cross-sectional imaging that has almost completely suppressed technically related artifacts. Some clinically relevant aspects have to be considered by radiologists in their CT reports owing to their impact in early risk stratification. The purpose of this chapter is to provide an insight into new options applicable in the daily practice in the clinical context of acute pulmonary embolism.

2 New Options in the Diagnostic Approach

2.1 Clinical Decision Support

Over the last decade, numerous articles have underlined the increase in CT examinations indicated for clinical suspicion of PE. In a recent study, Mamlouk et al. reported that of 2003 patients referred for diagnostic CT angiography, 1806 (90.16 %) had negative results (Mamlouk et al. 2010). These authors stated that a CT angiogram positive for pulmonary embolism was extremely unlikely (0.95 % chance) if patients had none of the studied thromboembolic risk factors, raising questions on the appropriate indication of the CT examination. As recently underlined, the number of CT examinations can be reduced with more appropriate use of CT angiography for PE. Clinicians can utilize risk factor assessment to help decide when to request CT angiograms for patients who are suspected of having a PE; age and immobilization are the risk factors of most concern for a CT angiogram positive for PE. Another option has been proposed to increase the appropriateness of imaging in patients suspected of PE. Raja et al. reported their experience with a computerized clinical decision support (CDS) on the use and yield of CT pulmonary angiography in the emergency department (Raja et al. 2012). At each stage of the proposed decision tree, clinicians could either cancel the imaging or ignore the advice. The implementation of evidence-based CDS was found to be associated with a significant decrease in the use and significant increase in the yield of CT pulmonary angiography for the evaluation of acute PE in the emergency department during a 2-year period.

2.2 Optimization of the Radiation Dose

In parallel to these efforts to decrease the number of unnecessary examinations, the radiological community is directly involved in the optimization of the radiation dose delivered to patients. As recently underlined in a panel discussion (Araoz et al. 2012), the radiation risk from pulmonary CT angiography (CTA) is strongly dependent on age, sex, and pulmonary CTA acquisition parameters (Woo et al. 2012). The radiological community demonstrated the usefulness of several practical methods, the most frequently employed relying on individual adjustment of milliamperage to patient weight, alone or in association with automated tube current modulation systems. This approach achieves an average dose reduction of 20 % (Kubo et al. 2008; Christner et al. 2010). However, because dose and radiation exposure vary approximately with the square of voltage in the setting of a constant tube current, lowering the kilovoltage has a greater effect on patient dose than reducing the tube current (Matsuoka et al. 2009). The current trend is to perform chest CT examinations with a kilovoltage adapted to the patient's body weight which has a greater effect on patient dose than reducing the tube current (Table 1) (Fig. 1). This approach was investigated in several studies in adult populations, from which several conclusions were drawn (Sigal-Cinqualbre et al. 2004; Schueller-Weidekamm et al. 2006; Szucs-Farkas et al. 2008; Gorgos et al. 2009). First, substantial dose reduction can be achieved with low-voltage protocols for pulmonary CT angiography in adult patients, with an average dose reduction of 40 % when lowering the setting from 120 to 80 kVp. Second, by lowering the tube voltage, we improve vascular

Table 1 Selection of kilovoltage and milliamperage according to the patient's body weight in routine clinical practice

(a) Scanning parameters for CT examinations reconstructed with filtered back projection

Patient's weight (kg)	Kilovoltage	Reference (mAs)
<50 kg	80 kV	120 mAs
50–80 kg	100 kV	90 mAs
81–100 kg	120 kV	90 mAs
≥100 kg	140 kV	90–140 mAs

(b) Scanning parameters for low-kilovoltage examinations reconstructed with raw-data-based iterative reconstructions

Patient's weight (kg)	Kilovoltage	Reference (mAs)
<50 kg	80 kV	120 mAs
50–80 kg	100 kV	65 mAs
81–100 kg	100 kV	90 mAs
≥100 kg	120 kV	90–140 mAs

From de Broucker et al. 2012
Abbreviations: *kg* kilogram, *kV* kilovoltage, *mAs* milliampere-second

enhancement, as the attenuation of iodinated contrast media increases at low tube voltage. This was found to improve the analyzability of central and peripheral pulmonary arteries, even when reducing the volume of contrast material (Szucs-Farkas et al. 2011). However, radiologists may be reluctant to apply low-kVp protocols in daily clinical routine because of the lack of standardized guidelines not only for the tube potential selection but also for the adjustment of the tube current to avoid grainy images. This difficulty can be overcome by the use of automated systems which can determine the most appropriate kV settings in relation to the patient's attenuation (Niemann et al. 2013). Lastly, the availability of iterative reconstructions offers a unique means to combine dose reduction (up to 50 %; averaged DLP less than 80 mGy.cm), excellent vascular enhancement, and better image quality than that obtained at standard dose (Pontana et al. 2013; Kaul et al. 2014; McLaughlin et al. 2014). With such possibilities of dose reduction, it is no longer necessary to try to save dose by reducing the scan length. Important additional or alternative diagnosis may be excluded from the limited imaging volume and therefore go undetected.

2.3 Optimization of the Iodine Load

2.3.1 Low Contrast Medium Volume

Although iodinated contrast medium is relatively safe, some adverse reactions such as contrast-induced nephropathy may occur. The risk of developing contrast-induced nephrotoxicity is increased with higher doses of iodinated contrast medium. Subsequently, one can decrease the risks by reducing the volume of highly concentrated contrast agents administered during a chest CT angiographic examination. This approach can be facilitated when combining low tube voltage and high-pitch techniques together with iterative reconstruction (Sodickson and Weiss 2012; Lu et al. 2014). The volumes administered varied between 50 and 20 mL of contrast material.

2.3.2 Low-Concentrated Contrast Agents

With the advent of fast CT scanning modes, administration of contrast media with high iodine concentration (i.e., 300 to 370 mg of iodine per milliliter) has become routine clinical practice to maximize the arterial enhancement of systemic and pulmonary arterial circulation. However, the inflow of highly concentrated contrast material to systemic veins can generate streak artifacts between the concentrated agent and the surrounding structures that may obscure mediastinal and pathological hilar and right upper lobe pulmonary arterial abnormalities. Moreover, the application of CTPA is limited in patients with impaired renal function because of the risk of developing contrast medium-induced nephropathy. Many patients at risk of developing pulmonary embolism are elderly and have comorbid conditions that increase the risk for renal injury. Therefore, it could be interesting to perform chest CT angiographic examinations with reduced iodine load. To date, this approach has not been found to be clinically acceptable owing to the poor level of arterial enhancement on images acquired at high kilovoltages. This limitation has recently been overcome by acquiring data sets with dual-energy CT. This new scanning mode offers the possibility of generating virtual

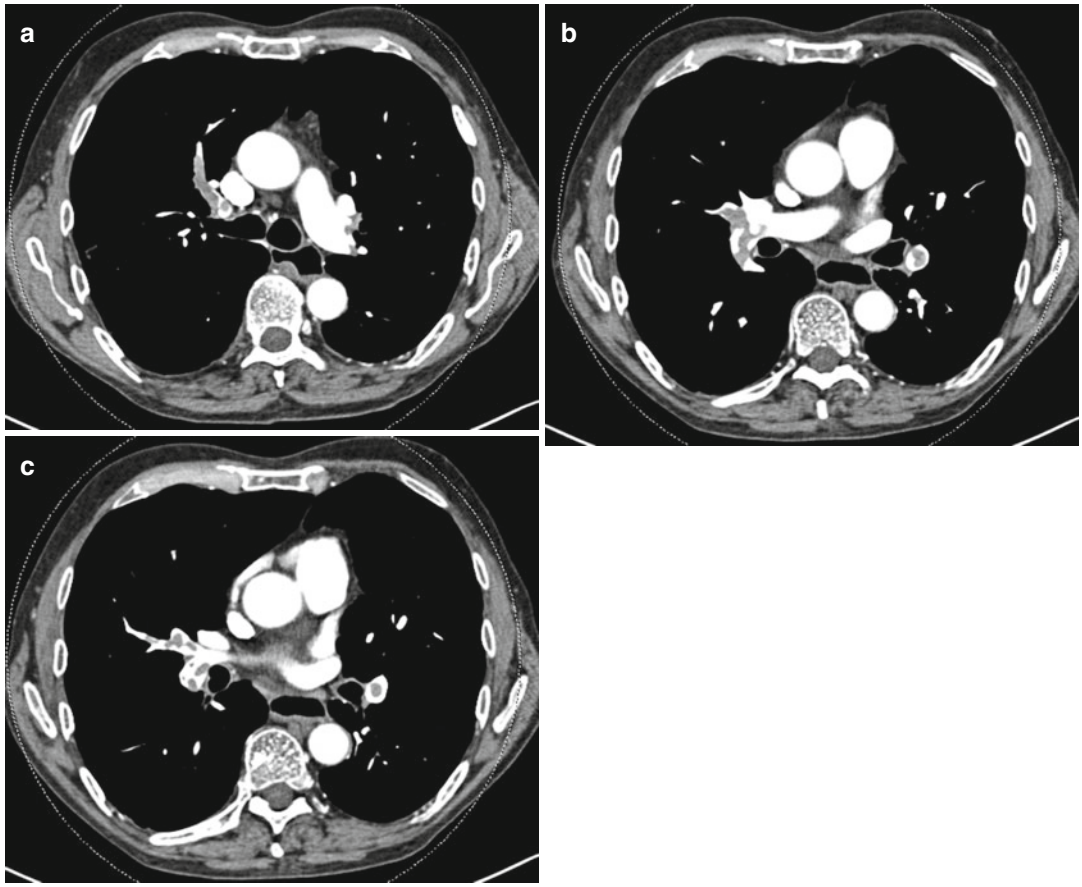

Fig. 1 Chest CT angiography obtained in a 72-year-old male patient suspected of acute pulmonary embolism (182 cm; 69 kg). The examination was obtained with dual-source, single energy with a high-pitch mode at 100 kVp and 90 ref mAs (35 % iodinated contrast agent; flow rate: 4 mL/s). The dose-length product was 115 mGy. cm. The images (**a**, **b**, **c**) were reconstructed with raw-data-based iterative reconstruction (Note the sharp delineation of the numerous endoluminal clots identified on both sides)

monochromatic spectral (VMS) imaging with a wide range of energy levels accessible from a single data set. Using single-source, dual-energy CT, Yuan et al. were the first authors to demonstrate that these acquisitions facilitated iodine load reduction at CT pulmonary angiography (Yuan et al. 2012). Delesalle et al. investigated the energy levels providing optimal imaging of the thoracic circulation using dual-source, dual-energy CT angiography with reduced iodine load (Delesalle et al. 2013). These authors found that the use of low-concentration contrast media enabled suppression of streak artifacts around systemic veins on high-energy images while providing satisfactory central arterial enhancement on low-energy images. The additional advantage of this scanning mode was the considerable reduction in the amount of iodine administered to patients (Fig. 2). These preliminary studies confirm that dual-energy CT has the potential to represent a new option for greater use of low-concentration contrast agents for chest CT examinations in routine clinical practice.

2.4 Current Role of CAD Systems

Whereas the diagnosis of acute PE remains based on the visual depiction of endoluminal filling defects, identification of peripheral clots remains

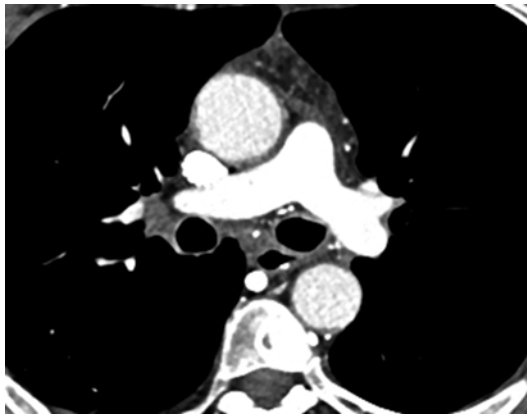

Fig. 2 Chest CT angiography obtained in a 52-year-old male patient (178 cm; 71 kg). The examination was acquired with dual-source, dual energy after administration of a low-concentrated contrast agent (i.e., 170 mg I/mL). This CT section illustrates the excellent quality of attenuation within pulmonary arteries on this image generated from both tubes (Note the presence of dilated systemic veins secondary to the presence of superior vena cava syndrome)

a difficult task, and more than 30 % can be missed on initial review (Ritchie et al. 2007). This limitation can be solved by the use of computer-aided diagnostic (CAD) systems which have been developed to aid radiologists with the depiction of endovascular clots that require careful analysis of hundreds of pulmonary vascular branches. Used as a second reader, these systems can help detect small clots initially missed (Wittenberg et al. 2010; Lee et al. 2011), increasing reader sensitivity for the detection of peripheral emboli (Dewailly et al. 2010; Wittenberg et al. 2012). In addition, the high negative predictive value of these tools is helpful to reassure inexperienced readers (Blackmon et al. 2013). However, these results are obtained at the expense of an increased reading time due to the presence of numerous false-negative and false-positive findings, as recently demonstrated by Wittenberg et al. (Wittenberg et al. 2012). These authors also demonstrated a strong association between CT image quality and the number of false-positive findings indicated by the CAD system (Wittenberg et al. 2011) which is a current limitation of CAD in clinical practice.

3 New Options in the Prognostic Assessment

3.1 Clot Burden

The degree of vascular obstruction on CT images can be estimated with semiquantitative scores such as those described by Quanadli et al. (2001) and Mastora et al. (2003). More recently, quantitative estimates of blood clot volume have also been introduced (Furlan et al. 2011). Whereas clot burden indexes have been proposed as predictive biomarkers for short-term mortality in patients with acute PE (Engelke et al. 2006; Ghaye et al. 2006), other studies have reported no significant association between mortality and these indexes (Furlan et al. 2011; Araoz et al. 2003; Pech et al. 2007). This controversy may be explained by the fact that these studies did not systematically correlate their results with the presence of a preexisting pulmonary disease. Whereas an isolated subsegmental clot may have no clinical consequence in an otherwise healthy patient, the same clot may lead to respiratory failure in a patient with poor respiratory condition due to previously altered pulmonary perfusion. Therefore, it appears interesting to switch from a clot burden estimate to an analysis of the extent of perfusion impairment as currently possible on perfusion images generated from dual-energy acquisitions (Chae et al. 2010; Bauer et al. 2011; Thieme et al. 2012). New scores have thus been defined, grading the degree of perfusion defect per lobe (Chae et al. 2010; Thieme et al. 2012), estimating the volume of perfusion defects relatively to the total lung volume (Bauer et al. 2011). Good correlations were found between perfusion impairment and CT features of right ventricular dysfunction, suggesting that perfusion defects could be a predictor of patient outcome. To our knowledge, a single study used a model adjusted for age, gender, and prior history of COPD and heart failure (Thieme et al. 2012). Good correlations were found between the proposed dual-energy-based PE score and a number of parameters of PE severity. These authors concluded that this approach was easier and faster to perform than the traditional CT scoring methods for vascular obstruction with better prognostic implications.

3.2 Right Ventricular Dysfunction

As previously underlined, the presence of right ventricular dysfunction in hemodynamically stable patients is the major determinant of patient's outcome. Recent updates in the literature should help radiologists gather accurate information. Regarding the CT features of right ventricular dysfunction, the description published by Reid and Murchison in 1998 remains of major clinical usefulness (Reid and Murchison 1998) (Table 2). In the list of CT features of right ventricular dysfunction, the RV/LV diameter ratio is the most important parameter to consider, as recently confirmed by Becattini et al. in a meta-analysis (Becattini et al. 2014).

Table 2 CT features of right ventricular dysfunction

1 Main indicators of right ventricular dysfunction
Dilatation of the right ventricle
Interventricular septal shift *(displaced to the left)*
Compression of the left ventricle
2 Secondary effects of right ventricular dilatation and dyskinesia
Tricuspid regurgitation
Right atrial enlargement
Reflux of contrast material within the inferior vena cava and hepatic veins
Dilatation of the coronary sinus, superior vena cava, and azygos vein

From Reid and Murchison 1998

Several practical approaches have been proposed to determine the RV/LV diameter ratio, including measurements on transverse CT sections, short-axis images, and four-chamber views of the cardiac cavities. Kamel et al. were the first authors to suggest that measurements of ventricular diameters on transverse CT sections were accurate enough to estimate the RV/LV ratio (Kamel et al. 2008). This has been recently confirmed by Lu et al. (2012) who have reported that the axial RV/LV diameter ratio is no less accurate than the reformatted four-chamber RV/LV diameter ratio for predicting 30-day mortality after PE (Fig. 3). A step further in the simplification of the estimation of the RV/LV diameter ratio has been proposed by Kumamaru et al. (2012). These authors have recently demonstrated that complex measurements of RV/LV diameter ratios can be replaced by subjective determination of right ventricular enlargement. When the right ventricle appeared larger than the left ventricle, it provided prognostic information that did not significantly differ from that

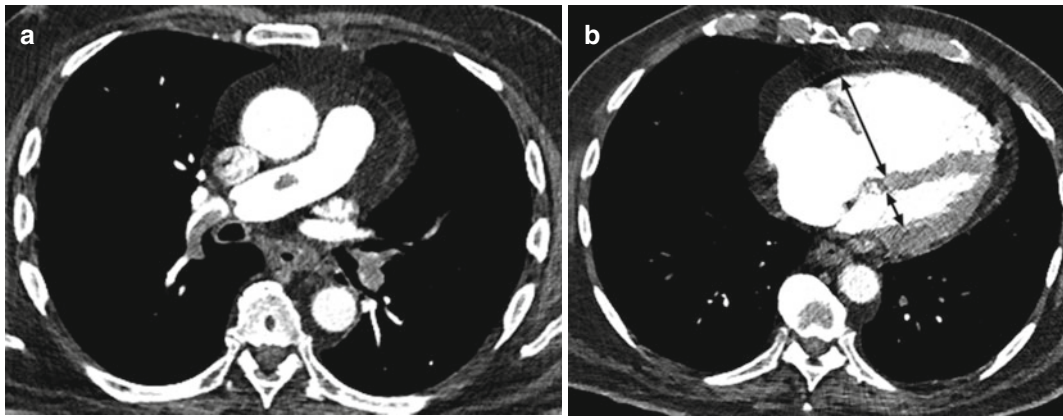

Fig. 3 Chest CT angiography obtained in a 70-year-old male patient (171 cm; 79 kg), admitted for massive acute pulmonary embolism at the emergency department. The examination was obtained at 120 kVp and 90 mAs with single-source, standard-dose CT (35 % iodinated contrast agent; flow rate: 4 mL/s). The dose-length product was 158 mGy.cm. (**a**) Transverse CT section obtained at the level of the right bronchus intermedius showing complete filling defects within left pulmonary arteries and partial filling defects within right pulmonary arteries. (**b**) Transverse CT section obtained at the level of cardiac cavities showing an RV/LV ratio greater than 1, suggestive of right ventricular dysfunction

of more traditional, quantitative RV/LV diameter ratios. The authors concluded that a right ventricle that appears larger than the left ventricle should be reported by the radiologist and interpolated into clinical risk stratification. This information can be reinforced when a prior CT examination negative for PE indications is available. In such circumstances, Lu et al. have shown that the interval increase in four-chamber RV/LV diameter ratio is more accurate than the diameter ratio of the CT examination with positive findings for PE alone for mortality prediction after acute PE (Lu et al. 2012). Kim et al. have recently completed the list of conventional chest CT-derived hemodynamic findings with the left-bulging atrial septum, an abnormal sign indicating hemodynamic overloading of the right heart (Kim et al. 2014).

3.3 Perfusion Imaging

An alternative to CAD for the detection of small-sized clots can theoretically be found with dual-energy CT which can provide perfusion imaging in addition to cross-sectional imaging of the pulmonary circulation (Fig. 4). As demonstrated in an experimental study by Zhang et al. (2009), abnormal pulmonary blood distribution shown at dual-source CT improves detection of acute PE, particularly by emphasizing the presence of subsegmental pulmonary iodine mapping defects. However, acute PE cannot be assessed on the sole finding of perfusion defects, even if observed as triangular-shaped defects known to be suggestive of acute PE. In a recent study, Pontana et al. demonstrated that small-airways disease could lead to similar filling defects, depicted in 30 % of COPD patients (Pontana et al. 2012). Moreover, the presence of an underlying lung disease altering lung perfusion makes it more difficult to detect PE-related filling defects. Therefore, CT detection of small-sized clots remains a difficult task. In daily practice, this does not represent a major clinical limitation except for the subset of patients with isolated subsegmental PE in whom cross-sectional imaging may fail to depict them.

4 The Radiologist's Report: Which Information Is Particularly Relevant for Clinicians?

The various mortality rates reported among studies illustrate the heterogeneous clinical and prognostic spectrum in acute PE (Table 3). This situation has raised debates on the most appropriate therapeutic options for the various PE-related

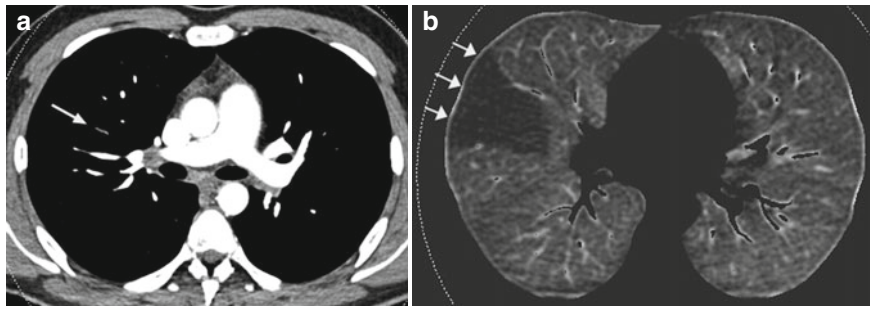

Fig. 4 Dual-energy chest CT angiography obtained in a 19-year-old male suspected of acute pulmonary embolism (183 cm; 87 kg). The examination was obtained with dual-source, dual-energy CT (tube A, 80 kV; tube B, 140 kVp; 35 % iodinated contrast agent; flow rate, 4 mL/s). The dose-length product was 325 mGy.cm. (**a**) Presence of a small-sized, peripheral clot in a subsegmental pulmonary artery of the axillary area (*arrow*). (**b**) Whereas the small clot is difficult to visualize, the corresponding perfusion defect (*arrows*) is easily depicted

Table 3 Risk stratification of patients with acute PE: standard approaches and new horizons

1. High-risk PE (i.e., "massive acute PE")
(a) PE-associated arterial hypotension or shock at the time of presentation
(b) Short-term mortality of at least 15 %
(c) Consensus on thrombolytic therapy
2. Intermediate-risk PE (i.e., "submassive acute PE")
(a) Hemodynamic stability but presence of right ventricular dysfunction at the time of presentation
(b) Mortality risk similar to that of massive PE
(c) Thrombolytic therapy or anticoagulation alone?
3. Low-risk PE (*new category upon discussion – from Lankeit and Konstantinides* 2012)
(a) Possible criteria for early discharge and home treatment:
(i) Absence of overt right heart failure
(ii) Absence of right ventricular dysfunction
(iii) Absence of serious comorbidity
(iv) Low risk of early recurrence
(v) Exclusion of a patent foramen ovale
(b) Outpatient treatment (*awaiting for results of ongoing trials*)
No-risk PE (*new category upon discussion – from Stein et al.* 2012)
(a) Criteria for considering to withhold treatment:
(i) Good pulmonary-respiratory reserve
(ii) No evidence of deep venous thrombosis with serial leg tests
(iii) Transient major risk factor for PE that is no longer present
(iv) No history of central venous catheterization or atrial fibrillation
(v) Patient's willingness to return for serial venous ultrasound
(b) Full patients' information

Table 4 New messages for radiologists

Some clots may not require anticoagulant therapy
Selected patients might be treated as outpatients
Some stable patients might receive thrombolytic therapy

risk categories. Regarding the prognostic parameters, it is well established that the hemodynamic status at the time of presentation has the strongest prognostic implication for short-term mortality. Therefore, the highest risk is that of "massive acute PE," characterized by the presence of PE-associated arterial hypotension or shock. Accounting for 5 % of all cases of PE, consensus guidelines recommend treatment with thrombolysis. These patients are not referred to the CT room. In the remaining majority of PE patients who present without hypotension, there is a subgroup of patients with "submassive acute PE," characterized by the presence of right ventricular dysfunction at the time of diagnosis. These patients are considered as having a higher risk of clinical deterioration than those with preserved systemic arterial blood pressure and normal right ventricular function. They correspond to the "intermediate-risk" category. Current debates question the recommendations for thrombolytic therapy in this subset of patients (Todd and Tapson 2009; Piazza and Goldhaber 2010; Jimenez et al. 2013). It was only recently that improved risk assessment strategies permitted advances in the identification of another category, i.e., the "low-risk PE." The current state of knowledge of this category has been recently summarized by Lankeit and Konstantinides (2012). Patients presenting without hemodynamic instability and without elevated biomarker levels or imaging findings indicating right ventricular dysfunction or myocardial injury may constitute this low-risk group (Torbicki et al. 2008). In this category, selected patients might be considered for early discharge and treatment at home. Lastly, the high quality of chest CT examinations currently achievable enables depiction of small-sized pulmonary embolism, sometimes incidentally diagnosed, which could represent a "no-risk category." These situations have raised debates in the literature on the clinical significance of such clots, described as "isolated subsegmental PE," comprising a spectrum ranging from a single subsegmental clot to multiple clots exclusively confined to the subsegmental arterial bed. Eyer et al. were the first authors to report the clinicians' decision to withhold anticoagulation in this category of patients, without adverse effects of this clinical decision (Eyer et al. 2005). Later, Anderson et al. suggested that some pulmonary emboli detected by CT might be clinically unimportant, the equivalent of deep vein

thrombosis isolated to the calf veins that might not require anticoagulant therapy (Anderson et al. 2007). In a recent review article, Stein et al. summarized the conditions which should be fulfilled for such therapeutic decisions (Stein et al. 2012). From this description of current trends in PE risk stratification (Table 4), one can deduce that the radiologist's report should provide clinicians with relevant information for early risk stratification. Consequently, particular attention should be directed toward analysis of the amount and location of clots in the pulmonary arterial tree, description of cardiac cavity morphology with special attention to CT features suggestive of right ventricular dysfunction, as well as abnormalities suggesting preexisting pulmonary and/or cardiac disease.

5 Pulmonary Embolism from Pregnancy to Young Adults

5.1 Pulmonary Embolism in Pregnancy

To prepare the mother for the blood losses associated with delivery, a state of hypercoagulability develops during pregnancy, which explains the increased risk for venous thromboembolism reported during pregnancy. Because clinical symptoms are nonspecific, reliable diagnostic tests are needed, but the most adapted diagnostic strategy remained a matter of discussion until the publication of clinical practice guidelines in 2011 (Leung et al. 2011). A multidisciplinary panel developed evidence-based guidelines using the Grading of Recommendations, Assessment, Development, and Evaluation (GRADE) system. Strong recommendations were made for three specific scenarios: (a) performance of chest radiography as the first radiation-associated procedure, (b) use of lung scintigraphy as the preferred test in the setting of a normal chest radiograph, and (c) performance of CT pulmonary angiography rather than digital subtraction angiography in a pregnant woman with a nondiagnostic ventilation-perfusion result. In addition to general recommendations for radiation dose savings for the fetus and the maternal breast, the scanning protocol for a chest CT pulmonary angiography in a pregnant patient should be adapted to the hemodynamic effects of pregnancy. These effects combine an increase in cardiac output, heart rate, and plasma volume leading to dilution of the contrast bolus (Ridge et al. 2011). Moreover, suboptimal opacification can also be due to the increased venous return of nonopacified blood to the right atrium during inspiration. Consequently, several technical adjustments have been proposed, including the use of automated bolus triggering, a high contrast medium flow rate, a high concentration of contrast medium, and acquisition during quiet or suspended respiration rather than at deep inspiration (Schaefer-Prokop and Prokop 2008; Miller et al. 2011) (Fig. 5). Regarding potential harmful effects of a chest CT examination to the fetus, it is important to be aware that the radiation dose delivered is in the range of that absorbed by the fetus from naturally occurring background radiation during the 9-month gestational period. In a series of 343 neonates exposed to an iodinated contrast agent at various stages of gestation, all had a normal thyroxine level at birth. In the 85 neonates tested for thyroid-stimulating hormone, only one (with comorbid conditions) had a transiently abnormal level that reverted to normal by day 6 (Bourjeily et al. 2010). From this study, it was concluded that a single, high-dose in utero exposure to water-soluble, low-osmolar iodinated intravenous products, such as iohexol, is unlikely to have a clinically important effect on thyroid function at birth.

5.2 Pulmonary Embolism in Children

As recently reported by Lee et al. (2012a), the incidence of PE ranges from 0.73 to 4.2 % in the pediatric population with concerns about potential overutilization of CT pulmonary angiography in children suspected of having PE. From their study, it was concluded that risk factor assessment should be a primary tool for guiding when to perform CT pulmonary angiography in this

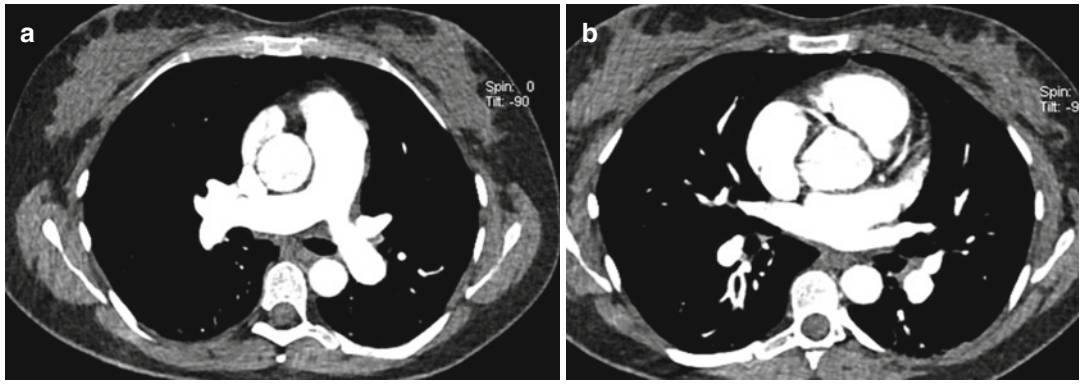

Fig. 5 Chest CT angiography obtained in a 38-year-old pregnant patient at 27 weeks' gestation (165 cm; 76 kg). The examination was obtained at 100 kVP and 66 ref mAs (30 % iodinated contrast agent; 4 mL/s). The dose-length product was 83 mGy.cm. Images were reconstructed with raw-data-based iterative reconstruction. Transverse CT section obtained at the level of the pulmonary trunk (**a**) and cardiac cavities (**b**) illustrating the excellent level of vascular enhancement achievable over the entire thorax at low kVp

population. With such an approach, CT pulmonary angiography can be targeted more appropriately, with the potentials to substantially reduce costs and radiation exposure. Five independent risk factors were found to be significantly associated with a positive CT pulmonary angiography result, namely, immobilization, hypercoagulable state, excess estrogen state, indwelling central venous line, and prior PE and/or deep venous thrombosis. Lastly, they observed that the D-dimer test was of little value in screening for PE among children with a high clinical probability of PE. From the same group, it appears that similar conclusions can be drawn in older children and young adults (Lee et al. 2012b).

Conclusion

CT pulmonary angiography is a well-recognized diagnostic tool but is also a unique means of providing prognostic information from the same examination as that used for diagnostic purposes. Radiologists should be aware of current trends in the management of patients with acute PE as this knowledge has direct influence on the content of their daily reports. RV function and information on the likelihood of an underlying cardiopulmonary disease are of the utmost importance for risk stratification. Lastly, CT is a rapidly evolving technology and radiologists should regularly adapt their single-energy scanning protocols and consider new options with dual-energy CT whenever available.

References

Remy-Jardin M, Pistolesi M, Goodman LR, Gefter WB, Gottschalk A, Mayo JR, Sostman HD (2007) Management of suspected acute pulmonary embolism in the era of CT angiography: a statement from the Fleischner Society. Radiology 245:315–29

Mamlouk MD, vanSonnenberg E, Gosalia R et al (2010) Pulmonary embolism at CT angiography: implications for appropriateness, cost and radiation exposure in 2003 patients. Radiology 256:625–632

Raja AS, Ip IK, Prevedello LM et al (2012) Effect of computerized clinical decision support on the use and yield of CT pulmonary angiography in the emergency department. Radiology 262:468–474

Araoz PA, Haramati LB, Mayo JR, Mortani Barbosa EJ Jr, Rybicki FJ, Colletti PM (2012) Panel discussion: pulmonary embolism imaging and outcomes. AJR 198:1313–1319

Woo JKH, Chiu RYW, Thakur Y, Mayo JR (2012) Risk-benefit analysis of pulmonary CT angiography in patients with suspected pulmonary embolus. AJR 198:1332–1339

Kubo T, Lin PJP, Stiller W, Takahashi M, Kauczor HU, Ohno Y, Hatabu H (2008) Radiation dose reduction in chest CT: a review. AJR 190:335–343

Christner JA, Zavaletta VA, Eusemann CD, Walz-Flannigan AI, McCollough CH (2010) Dose reduction

in helical CT: dynamically adjustable z-axis X-ray beam collimation. AJR 194:W49–55
Matsuoka S, Hunsaker AR, Gill RR et al (2009) Vascular enhancement and image quality of MDCT pulmonary angiography in 400 cases: comparison of standard and low kilovoltage settings. AJR 192:1651–1656
Sigal-Cinqualbre AB, Hennequin R, Abada HT, Chen X, Paul JF (2004) Low-kilovoltage multi-detector row chest CT in adults: feasibility and effect on image quality and iodine dose. Radiology 231:169–174
Schueller-Weidekamm C, Schaefer-Prokop CM, Weber M, Herold CJ, Prokop M (2006) CT angiography of pulmonary arteries to detect pulmonary embolism: improvement of vascular enhancement with low kilovoltage settings. Radiology 241:899–907
Szucs-Farkas Z, Kurmann L, Strautz T, Patak MA, Vock P, Schindera ST (2008) Patient exposure and image quality of low-dose pulmonary computed tomography angiography: comparison of 100- and 80 kVp protocols. Invest Radiol 43:871–876
Gorgos A, Remy-Jardin M, Duhamel A, Faivre JB, Tacelli N, Delannoy V, Remy J (2009) Evaluation of peripheral pulmonary arteries at 80 kV and 140 kV: dual-energy computed tomography assessment in 51 patients. J Comput Assist Tomogr 33:981–986
Szucs-Farkas Z, Schibler F, Cullmann J et al (2011) Diagnostic accuracy of pulmonary CT angiography at low tube voltage: intraindividual comparison of a normal-dose protocol at 120 kVp and a low-dose protocol at 80 kVp using reduced amount of contrast medium in a simulation study. AJR 197:W852–W859
Niemann T, Simon H, Faivre JB, Yasunaga K, Bendaoud S, Simeone A, Remy J, Duhamel A, Flohr T, Remy-Jardin M (2013) Clinical evaluation of automatic tube voltage selection in chest CT angiography. Eur Radiol 23:2643–2651
Pontana F, Pagniez J, Duhamel A et al (2013) Reduced-dose low-voltage chest CT angiography with sinogram-affirmed iterative reconstruction versus standard-dose filtered back projection. Radiology 267:609–618
Kaul D, Grupp U, Kahn J, Ghadjar P, Wiener E, Hamm B, Streitparth F (2014) Reducing radiation dose in the diagnosis of pulmonary embolism using adaptive statistical iterative reconstruction and lower tube potential in computed tomography. Eur Radiol 24:2685–2692
McLaughlin PD, Liang T, Homiedan M, Louis LJ, O'Connel TW, Krzymyk K, Nicolaou S, Mayo MR (2014) High pitch, low voltage dual source CT pulmonary angiography: assessment of image quality and diagnostic acceptability with hybrid iterative reconstruction. Emerg Radiol. [Epub ahead of print]
Sodickson A, Weiss M (2012) Effect of patient size on radiation dose reduction and image quality in low-kVp CT pulmonary angiography performed with reduced IV contrast dose. Emerg Radiol 19:437–445
Lu GM, Luo S, Meinel FG, McQuiston AD, Zhou CS et al (2014) High-pitch computed tomography pulmonary angiography with iterative reconstruction at 80 kVp and 20 mL contrast agent volume. Eur Radiol 24:3260–3268
Yuan R, Shuman WP, Earls JP, Hague CJ, Mumtaz HA, Scott-Moncrieff A, Ellis JD, Mayo JR, Leipsic JA (2012) Reduced iodine load at CT pulmonary angiography with dual-energy monochromatic imaging: comparison with standard CT pulmonary angiography--a prospective randomized trial. Radiology 262:290–297
Delesalle MA, Pontana F, Duhamel A, Faivre JB, Flohr T, Tacelli N, Remy J, Remy-Jardin M (2013) Spectral optimization of chest CT angiography with reduced iodine load: experience in 80 patients evaluated with dual-source, dual-energy CT. Radiology 267:256–266
Ritchie G, McGurk S, Mc Creath C, Graham C, Murchison JT (2007) Prospective evaluation of unsuspected pulmonary embolism on contrast multidetector CT (MDCT) scanning. Thorax 62:536–540
Wittenberg R, Peters JF, Sonnemans JJ, Prokop M, Schaefer-Prokop C (2010) Computer-assisted detection of pulmonary embolism: evaluation of pulmonary CT angiograms performed in an on-call setting. Eur Radiol 20:801–806
Lee CW, Seo JB, Song JW et al (2011) Evaluation of computer-aided detection and dual-energy software in detection of peripheral pulmonary embolism on dual-energy pulmonary CT angiography. Eur Radiol 21:54–62
Dewailly M, Remy-jardin M, Duhamel A et al (2010) Computer-aided detection of acute pulmonary embolism with 64-slice multidetector row computed tomography: impact of the scanning conditions and overall image quality in the detection of peripheral clots. J Comput Assist Tomogr 34:23–30
Wittenberg R, Berger FH, Peters JF et al (2012) Acute pulmonary embolism: effect of a computer-assisted detection prototype on diagnosis – An observer study. Radiology 262:305–313
Blackmon KN, Florin C, Bogoni L, McCain JW, Koonce JD, Bastarrika G, Thilo C, Costello P, Salganicoff M, Schoepf UJ (2013) Computer-aided detection of pulmonary embolism at CT pulmonary angiography: can it improve performance of inexperienced readers? Eur Radiol 21:1214–1223
Wittenberg R, Peters JF, Sonnemans JJ et al (2011) Impact of image quality on the performance of computer-aided detection of pulmonary embolism. AJR 196:95–101
Quanadli SD, EI Hajjam M, Vieillard-Baron A, Joseph T, Mesurolle B, Oliva VL, Barré O, Bruckert F, Dubourg O, Lacombe B (2001) New CT index to quantify arterial obstruction in pulmonary embolism : comparison with angiographic index and echocardiography. AJR 176:1415–1420
Mastora I, Remy-Jardin M, Masson P, Galland E, Delannoy V, Bauchart JJ, Remy J (2003) Severity of acute pulmonary embolism : evaluation of a new spiral CT angiographic score in correlation with echocardiographic data. Eur Radiol 13:29–35
Furlan A, Patil A, Park B et al (2011) Accuracy and reproducibility of blood clot burden quantification with pulmonary CT angiography. AJR 196:516–523
Engelke C, Rummeny EJ, Marten K (2006) Acute pulmonary embolism on MDCT of the chest: prediction of

cor pulmonale and short-term patient survival from morphologic embolus burden. AJR 186:1265–1271
Ghaye B, Ghuysen A, Willems V, Lambermont B, Gerard P, D'Orio V, Gevenois PA, Dondelinger RF (2006) Severe pulmonary embolism: pulmonary artery clot load scores and cardiovascular parameters as predictors of mortality. Radiology 239:884–891
Araoz PA, Gotway MB, Trowbridge RL, Bailey RA, Auerbach AD, Reddy GP, Dawn SK, Webb WR, Higgins CB (2003) Helical CT pulmonary angiography predictors of in-hospital morbidity and mortality in patients with acute pulmonary embolism. J Thorac Imaging 18:207–216
Pech M, Wieners G, Dul P, Fischbach F, Dudeck O, Lopez Hänninen E, Ricke J (2007) Computed tomography pulmonary embolism index for the assessment of survival in patients with pulmonary embolism. Eur Radiol 17:1954–1959
Chae EJ, Seo JB, Jang MY et al (2010) Dual-energy CT for assessment of the severity of acute pulmonary embolism: pulmonary perfusion defect score compared with CT angiographic obstruction score and right ventricular/left ventricular diameter ratio. AJR 194:604–610
Bauer RW, Frellesen C, Renker M et al (2011) Dual energy CT pulmonary blood volume assessment in acute pulmonary embolism – correlation with D-dimer level, right heart strain and clinical outcome. Eur Radiol 21:1914–1921
Thieme SF, Ashoori N, Bamberg F et al (2012) Severity assessment of pulmonary embolism using dual energy CT – correlation of a perfusion defect score with clinical and morphological parameters of blood oxygenation and right ventricular failure. Eur Radiol 22:269–278
Reid JH, Murchison JT (1998) Acute right ventricular dilatation: a new helical CT sign of massive pulmonary embolism. Clin Radiol 53:694–698
Becattini C, Agnelli G, Germini F, Vedovati MC (2014) Computed tomography to assess risk of death in acute pulmonary embolism: a meta-analysis. Eur Respir J 43:1678–1690
Kamel EM, Schmidt S, Doenz F, Adler-Etechami G, Schnyder P, Quanadli SD (2008) Computed tomographic angiography in acute pulmonary embolism: do we need multiplanar reconstructions to evaluate the right ventricular dysfunction? J Comput Assist Tomogr 32:438–443
Lu MT, Demehri S, Cai T, Parast L, Hunsaker AR, Goldhaber SZ, Rybicki FJ (2012) Axial and reformatted four-chamber right ventricle-to-left ventricle diameter ratios on pulmonary CT angiography as predictors of death after acute pulmonary embolism. AJR 198:1353–1360
Kumamaru KK, Hunsaker AR, Bedayat A, Soga S, Signorelli J, Adams K, Wake N, Lu MT, Rybicki FJ (2012) Subjective assessment of right ventricle enlargement from computed tomography pulmonary angiography images. Int J Cardiovasc Imaging 28:965–973
Kim MJ, Jung HO, Jung JI, Kim KJ, Jeon DS, Youn HJ (2014) CT-derived atrial and ventricular septal signs for risk stratification of patients with acute pulmonary embolism: clinical associations of CT-derived signs for prediction of short-term mortality. Int J Cardiovasc Imaging 30:25–32
Zhang LJ, Zhao YE, Wu SY et al (2009) Pulmonary embolism detection with dual-energy : experimental study of dual-source CT in rabbits. Radiology 252: 61–70
Pontana F, Chalayer C, Faivre JB, Murphy C, Remy-Jardin M, Remy J. Pseudo-embolic perfusion defects in COPD: evaluation with dual-energy CT angiography (DECT) in 170 patients. Abstract B 0272, Eur Cong Radiol 2012, SS504 – CTTA – Dual energy and dose reduction
Todd JL, Tapson VF (2009) Thrombolytic therapy for acute pulmonary embolism : a critical appraisal. Chest 135:1321–1329
Piazza G, Goldhaber SZ (2010) Management of submassive pulmonary embolism. Circulation 122:1124–1129
Jimenez D, Billello KL, Murin S (2013) Point/Counterpoint editorials. Should systemic lytic therapy be used for submassive pulmonary embolism ? Yes. Chest 143:296–9
Lankeit M, Konstantinides S (2012) Is it time for home treatment of pulmonary embolism ? Eur Respir J 40:742–749
Torbicki A, Perrier A, Konstantinides SV et al (2008) Guidelines on the diagnosis and management of acute pulmonary embolism: The Task force for the diagnosis and management of acute pulmonary embolism of the European Society of Cardiology (ESC). Eur Heart J 29:2276–2315
Eyer BA, Goodman LR, Washington L (2005) Clinicians' response to radiologists' reports of isolated subsegmental pulmonary embolism or inconclusive interpretation of pulmonary embolism using MDCT. AJR 184:623–628
Anderson DR, Kahn SR, Rodgers MA et al (2007) Computed tomographic pulmonary angiography vs ventilation-perfusion lung scanning in patients with suspected pulmonary embolism. JAMA 298:2743–2753
Stein PD, Goodman LR, Hull RD et al (2012) Diagnosis and management of isolated subsegmental pulmonary embolism: review and assessment of the options. Clin Appl Thromb Hemost 18:20–26
Leung AN, Bull TM, Jaeschke R et al (2011) An official American Thoracic Society/Society of Thoracic radiology clinical practice guideline: evaluation of suspected pulmonary embolism in pregnancy. Am J Respir Crit Care Med 184:1200–1208
Ridge CA, Mhuircheartaigh JN, Dodd JD, Skehan SJ (2011) Pulmonary CT angiography protocol adapted to the hemodynamic effects of pregnancy. AJR 197:1058–1063
Schaefer-Prokop C, Prokop M (2008) CTPA for the diagnosis of acute pulmonary embolism during pregnancy. Eur Radiol 18:2705–2708

Miller MA, Chalhoub M, Bourjeily G (2011) Peripartum pulmonary embolism. Clin Chest Med 32:147–164

Bourjeily G, Chalhoub M, Phornphutkul C, Alleyne TC, Woodfield CA, Chen KK (2010) Neonatal thyroid function: effect of a single exposure to iodinated contrast medium in utero. Radiology 256:744–750

Lee EY, Tse SKS, Zurakowski D, Johnson VM, Lee NJ, Tracy DA, Boiselle PM (2012a) Children suspected of having pulmonary embolism: multidetector CT pulmonary angiography – Thromboembolic risk factors and implications for appropriate use. Radiology 262:242–251

Lee EY, Neuman MI, Lee NJ, Johnson VM, Zurakowski D, Tracy DA, Boiselle PM (2012b) Pulmonary embolism detected by pulmonary MDCT angiography in older children and young adults: risk factor assessment. AJR 198:1431–1437

de Broucker T, Pontana F, Santangelo T, Faivre JB, Tacelli N, Delannoy-Deken V, Duhamel A, Remy J, Rémy-Jardin M (2012) Single- and dual-source chest CT protocols: levels of radiation dose in routine clinical practice. Diagn Interv Imaging 93:852–858

Dual-Energy CT of the Thorax

Felix G. Meinel, Long Jiang Zhang,
and U. Joseph Schoepf

Abstract

In dual-energy CT, two CT datasets are acquired at different photon energy spectra. Because chemical elements vary in their attenuation properties at different photon energies, this allows to analyze the chemical composition of the imaged tissues and to extract or suppress individual chemical components. Dual-energy CT of the thorax makes use of this possibility in a variety of ways. The iodine distribution within the pulmonary parenchyma can be visualized to assess pulmonary perfusion. Inhaled noble gasses such as xenon and krypton are employed to image pulmonary ventilation. Iodine uptake of lung nodules has been investigated as a tool to distinguish between benign and malignant lesions and to assess tumor vascularity. Dual-energy CT myocardial perfusion imaging can visualize myocardial perfusion defects by displaying the iodine distribution within the myocardium. Dual-energy CT datasets also enable specific post-processing tools such as virtual non-contrast images, virtual non-calcium images, and virtual extrapolation to lower or higher photon energies, which have found promising applications for imaging the pulmonary vasculature, the aorta, and the spine. This chapter briefly reviews key technical aspects of dual-energy CT before discussing various established and investigational thoracic applications.

F.G. Meinel (✉)
Institute for Clinical Radiology, Ludwig-Maximilians-University Hospital, Munich, Germany
e-mail: felix.meinel@med.uni-muenchen.de

L.J. Zhang
Department of Medical Imaging, Jinling Hospital, Medical School of Nanjing University, Nanjing, Jiangsu Province, China

U.J. Schoepf
Department of Radiology and Radiological Science, Medical University of South Carolina, Charleston, SC, USA

1 Introduction

Dual-energy CT became commercially available in 2006, 2 years after the first edition of this book was published. Since then, it has seen immense technical development and refinement and has been the focus of numerous preclinical and clinical studies. Considering the prime role CT plays in thoracic imaging, it comes as no surprise that

U.J. Schoepf, F.G. Meinel (eds.), *Multidetector-Row CT of the Thorax*, Medical Radiology,
DOI 10.1007/978-3-319-30355-0_15

thoracic pathologies are also among the most well-investigated and promising applications of dual-energy CT. Dual-energy CT reveals photon energy-dependent differences in X-ray attenuation. In some applications, this is used to analyze the chemical composition of tissues and thus gain insights into pathology. In others, it allows to improve image characteristics or obtain functional information on perfusion or ventilation.

2 Technical Aspects

2.1 Physical Principle

Image contrast in CT is the result of differences in X-ray attenuation within the body. In the clinically relevant energy range, X-ray attenuation occurs primarily as a result of photoelectric absorption and Compton scattering. The probability of photoelectric absorption is strongly increased at low photon energies and in tissues rich in atoms with high atomic numbers. By acquiring datasets at two different spectra with different mean photon energies, dual-energy CT is sensitive to the chemical composition of tissues. The attenuation difference between the data acquired at low and high photon energy will be relatively small for human soft tissues composed of atoms with relative low atomic numbers (such as hydrogen, carbon, oxygen, nitrogen) and greater when heavier atoms (such as calcium, iodine, or xenon) are present intrinsically or as contrast media. This information about the composition of tissues allows generating images that isolate or suppress specific chemical components. This is typically done using a three-material decomposition algorithm, which analyzes each image voxel as being composed of three base materials that are chosen depending on the clinical application. For example, for dual-energy CT pulmonary perfusion imaging, each voxel is assumed to be composed of air, soft tissue, and iodine. The algorithm uses the attenuation difference between both spectra to compute the relative contribution of each of these materials to the X-ray attenuation. The iodine distribution in the pulmonary parenchyma can thus be extracted, visualized, and quantified.

2.2 Technical Implementations

The most basic approach to dual-energy CT imaging is to perform two subsequent image acquisitions at different tube voltages. However, due to the temporal delay between both acquisitions, this approach is prone to motion artifacts, particularly in the thorax. It is also not useful for contrast-enhanced applications, since the contrast distribution will have changed in the interval between both acquisitions. For thoracic applications, simultaneous or near-simultaneous acquisition of both datasets is required. To achieve this, different technological solutions have been developed by the various CT vendors. In *dual-source CT*, two X-ray tubes are mounted on a single gantry in a roughly 90° angle to each other, each with a corresponding detector on the opposite side of the gantry. The tubes are operated simultaneously with different tube voltages. In *rapid kilovoltage switching*, a single X-ray tube is used and the tube voltage is rapidly switched back and forth between the low- and high-energy settings. CT systems with *dual-layer detector* technology use a single tube operated at constant tube voltage but feature a detector composed of two layers with the top layer predominantly absorbing lower-energy photons and the bottom layer mainly absorbing higher-energy photons. The most recently introduced concept is *split filter* dual-energy CT, in which one half of the cone beam of a single X-ray source is directed through a tin filter and the other half through a gold filter, thus hardening or softening the energy spectrum, respectively.

2.3 Acquisition Protocols

In terms of image acquisition, dual-energy CT of the thorax does not require any major changes to clinical workflow compared to conventional single-energy CT. The requirements for patient preparation, the duration of the image acquisition, and the contrast administration protocols are often very similar to single-energy CT. One exception to this rule is the more technically challenging dual-energy CT pulmonary ventila-

tion imaging, which uses inhaled contrast agents. In dual-energy CT of the thorax, 80 and 140 kVp have most commonly been used as low- and high-energy spectra. However, more recent CT systems have brought greater flexibility in this regard with the lower-energy spectrum ranging from 70 to 100 kVp and the higher-energy spectrum from 140 to 150 kVp. Some CT systems use tin filters to remove lower-energy photons from the higher-energy spectrum and thus decrease the overlap in photon energies between both spectra. Due to the recency of these options, there is no consensus as to the optimal spectral combination for specific dual-energy applications in the thorax, and it is probably best to follow manufacturers' recommendations. Specific acquisition protocols for the most important clinical applications are described in the pertinent paragraphs below.

2.4 Image Reconstruction

2.4.1 Basic Image Reconstructions

As a first step, the information obtained at each of the two energy spectra is reconstructed as separate image series. Some vendors recommend specific dual-energy reconstruction kernels to accurately preserve measured density values and thus allow quantitative applications of dual-energy CT. In addition, a weighted average series is typically reconstructed by blending equal or weighted contributions from low- and high-energy datasets. For example, the 140 kVp dataset may contribute 70 % and the 80 kVp dataset 30 % to the image characteristics. The image characteristics of this weighted average series are intended to be similar to a standard, single-energy acquisition at 120 kVp. This series is often used for the standard morphological evaluation of the examination.

2.4.2 Material-specific Reconstructions

Based on material decomposition algorithms, color-coded parametric images can be reconstructed to visualize the distribution of specific materials. Iodine distribution maps capture the distribution of the iodinated contrast agent and are thus used to visualize the perfusion of the pulmonary parenchyma, lung nodules and tumors, or the myocardium. These iodine distribution maps can be viewed in isolation or as overlay images, in which the distribution of iodine is color coded and superimposed on anatomical gray-scale images. Similarly, the distribution of inhaled contrast agents (xenon or krypton) can be analyzed and displayed. Conversely, the contribution of specific materials to the X-ray attenuation can be virtually subtracted from the image. This allows creating virtual non-contrast (iodine-subtracted) images or virtual non-calcium images.

2.4.3 Virtual Monoenergetic Imaging

The spectral information contained in dual-energy datasets allows creating virtual monoenergetic images. These images simulate the appearance that would have resulted if the CT had been acquired with monochromatic X-rays of a specific photon energy. By extrapolation, these virtual monoenergetic images can also be created for photon energies that are lower than the mean photon energy of the low-energy spectrum or higher than the mean photon energy of the high-energy spectrum. Extrapolation to lower photon energies is frequently used to enhance iodine attenuation, since iodine attenuation sharply increases with photon energies approaching its k-edge.

2.4.4 Nonlinear Blending

Standard (weighted) average images are reconstructed with linear blending functions, i.e., the relative contributions from the low- and high-energy datasets are equal for each voxel. The goal of nonlinear blending techniques is to combine the high iodine contrast at low photon energies with the low image noise that is seen with higher photon energies. For this purpose, nonlinear blending functions are used in which the relative contributions from the low- and high-energy datasets are different for each voxel depending on its CT density (Holmes et al. 2008). In regions with high iodine attenuation, the information from the low-energy dataset will be given greater

weight to achieve high image contrast, while in regions with low attenuation information from the high-energy spectrum will be predominantly used to limit image noise.

2.5 Radiation Dose Considerations

Most reports on the effective radiation dose of dual-energy CT pulmonary angiography or dual-energy contrast-enhanced chest CT fall in the 2.5–5 mSv range (Pontana et al. 2008; Zhang et al. 2013a, b; Meinel et al. 2013a). Older publications have often reported that dual-energy CT of the thorax does not increase the effective radiation dose compared to standard single-energy chest CT at 120 kVp. More recent publications, however, conclude that the radiation dose associated with dual-energy CT in clinical practice may be as much as threefold the dose of single-energy CT (de Broucker et al. 2012; Remy-Jardin et al. 2014). This discrepancy can easily be explained by the substantial dose reduction that has occurred with lowering tube potential in single-energy CT. This is particularly true for CT pulmonary angiography, which is now commonly performed at 80-100 kV in suitable patients. Similarly, high-pitch helical acquisition has been established as a very dose-efficient acquisition strategy for coronary CT angiography and other thoracic applications in single-energy, dual-source CT. Evidently, dual-energy CT is incommensurable with both low kV and high-pitch acquisition and thus deprives patients who are suitable for these techniques of their dose reduction potential.

A fair comparison of radiation dose in single- and dual-energy chest CT should acknowledge that dual-energy CT can provide valuable additional information compared to single-energy CT. In some clinical scenarios, this information may obviate the need for additional functional imaging examinations such as nuclear perfusion studies of the lungs or the myocardium and thus decrease the patient's cumulative radiation exposure. Nevertheless, the higher radiation dose associated with dual-energy chest CT compared to dose-efficient single-energy protocols suggests that it is probably not justified to routinely acquire chest CT in dual-energy mode in all patients. Dual-energy CT should be performed in cases in which additional diagnostic clues with a potential consequence for patient management can reasonably be expected from dual-energy data.

3 Clinical Applications

3.1 CT Pulmonary Angiography

3.1.1 Image Optimization Using Monoenergetic Extrapolation and Nonlinear Blending

Unsatisfactory contrast enhancement of the pulmonary vasculature is not uncommon in CT pulmonary angiography and can hamper the accurate detection of pulmonary emboli. It can be due to suboptimal contrast administration protocols, problems with the timing of the scan relative to the contrast bolus, variations in patients' circulatory physiology, or inflow of non-opacified blood from the inferior vena cava during deep inspiration. If CT pulmonary angiography is acquired in dual-energy mode, the spectral information can be used to improve intravascular contrast and thus salvage an examination that would otherwise be non-diagnostic. In the most simple approach, this can be done by reconstructing and evaluating the lower-energy (typically 80 kVp) dataset separately. Since iodine attenuation sharply increases with lower photon energies, intravascular iodine attenuation is substantially higher in the lower-energy dataset compared to the higher-energy or weighted average dataset. However, image noise in the lower-energy dataset is also substantial. A more sophisticated approach to improve intravascular contrast in dual-energy CT pulmonary angiography is virtual monoenergetic extrapolation, i.e., images are virtually made to appear as if they had been acquired with a specific, relatively low photon energy (Fig. 1). Typically, images reconstructed at virtual photon energies in the range of 60 to 70 keV will show optimal contrast-to-noise ratio

for the detection of pulmonary emboli. Recently, more advanced algorithms have been developed, which use nonlinear image-blending techniques to combine the high intravascular iodine attenuation at low virtual photon energies with the low image noise characteristics at high virtual photon energies and thus further optimize contrast-to-noise characteristics (Fig. 1).

In a significant percentage of examinations with unsatisfactory contrast enhancement, these tools can restore diagnostic image quality to exclude or confirm pulmonary embolism. This is particularly true in examinations that are borderline or partially diagnostic, i.e., when intravascular attenuation at routine reconstructions is just below the diagnostic level or diagnostic in the

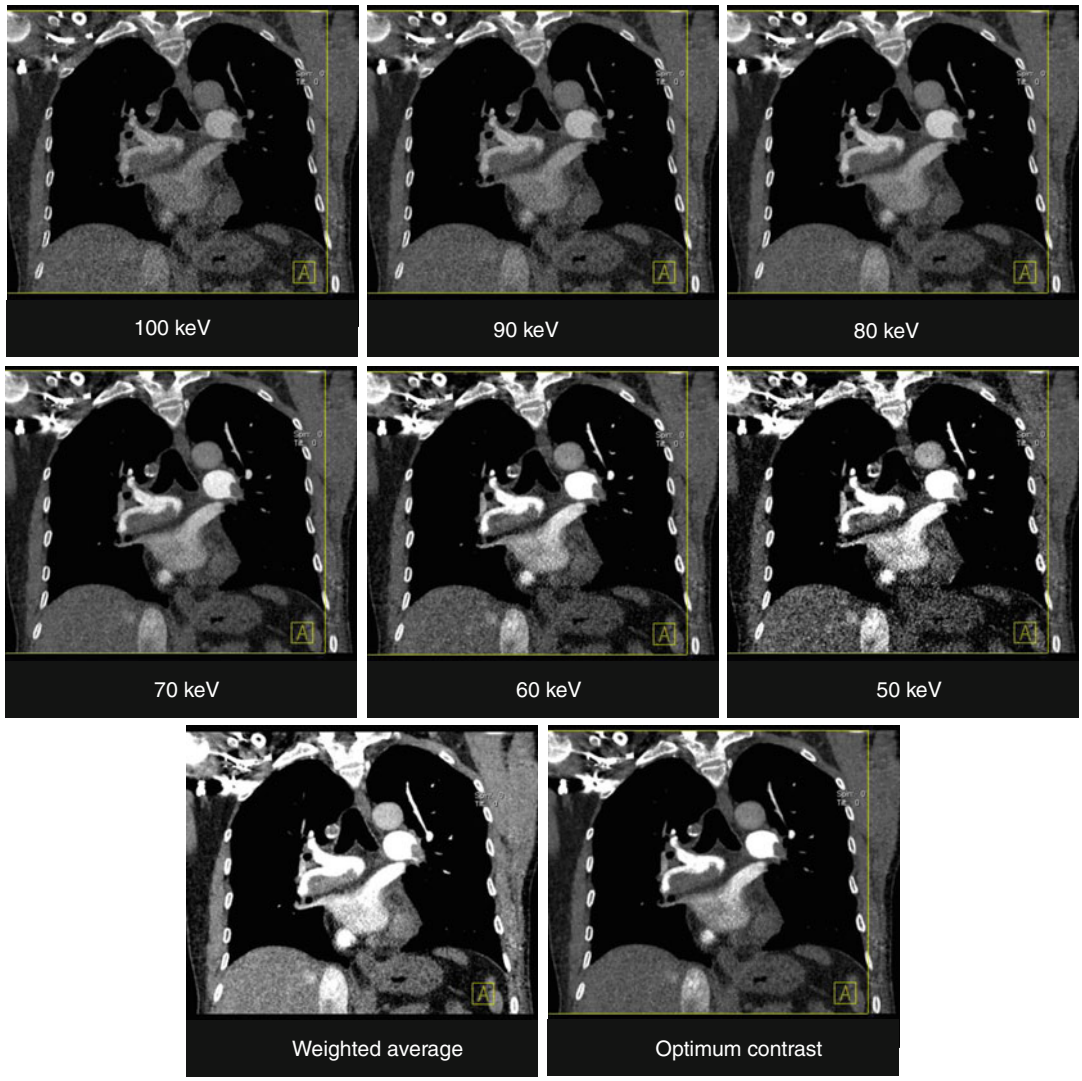

Fig. 1 Dual-energy CT pulmonary angiography in a 48-year-old male patient with pulmonary embolism. Filling defects in both main pulmonary arteries are noted. Virtual monochromatic images extrapolated to photon energies ranging from 100 to 50 keV are shown (**a**–**f**). The weighted average image (**g**) is generated by blending equal (or weighted) contributions of the lower- and higher-energy datasets. The optimum contrast images (**h**) are based on a nonlinear blending algorithm combining the high iodine attenuation at lower photon energies with the low image noise at high photon energies

central pulmonary arteries but just not sufficient peripherally. Clearly, all these tools require at least a certain concentration of iodine in the pulmonary vasculature. They cannot salvage cases of complete absence or interruption of contrast material in the pulmonary arteries such as occasionally seen due to inflow of non-opacified blood from the inferior vena cava during deep inspiration.

Increasing intravascular attenuation can also be used to decrease the amount of contrast agent required for CT pulmonary angiography. In one study, reducing iodine load by 35 % and reconstructing virtual monoenergetic images at 60 keV resulted in comparable image quality to standard single-energy CT pulmonary angiography at 120 kVp (Delesalle et al. 2013). This approach may be of value in patients with renal insufficiency in whom contrast-induced nephropathy is a concern. Arguably, a reduction in the required amount of contrast agent can also be achieved by simply lowering tube potential to 100 or 80 kV in single-energy CT. The potential advantage of dual-energy acquisition with monoenergetic extrapolation is that it allows viewing images at various photon energies. While 60-70 keV may be the optimal setting for evaluating the pulmonary arteries, higher photon energies (e.g., 100 keV) may be useful to decrease streak artifacts from dense contrast material in the superior vena cava or brachiocephalic vein and examine these vessels and their surrounding structures (Delesalle et al. 2013). Extrapolation to higher photon energies (in the range of 100-120 keV) is also useful to reduce artifacts from metallic implants (Fig. 2) (Meinel et al. 2012).

3.2 Pulmonary Perfusion Imaging

Dual-energy CT pulmonary angiography can be used to capture the distribution of the iodinated contrast agent in the pulmonary microcirculation at one time point during its inflow. Although not a true measurement of pulmonary perfusion, the distribution of iodine in the pulmonary capillary bed is considered a surrogate of pulmonary perfusion, and this technique is hence referred to as dual-energy CT pulmonary perfusion imaging. The accuracy of the technique has been validated against nuclear techniques of pulmonary perfusion imaging (Thieme et al. 2008, 2012) and dynamic CT measurements of pulmonary perfusion (Fuld et al. 2013).

3.2.1 Acquisition Technique

The optimal combination of spectra depends on the available CT system. The combination of 80 and 140 kVp has been standard for some time. With newer generations of dual-source CT scanners, combinations of 100 and 140 kVp or 90 and 150 kVp have been suggested. These systems use a tin filter to harden the higher-energy spectrum and thus decrease the overlap in photon energies between both spectra. Recommendations for the specific acquisition parameters for each CT system can be found in the literature (Lu et al. 2012). Either a test bolus or a bolus-tracking technique can be used to trigger image acquisition. A relatively long delay (5-7 s) ensures that the contrast material has reached the pulmonary capillary system. An iodine delivery rate of approximately 1.6 g I/s has been reported to result in optimal image quality in both morphological image series and perfusion maps (Nance et al. 2012). Residual concentrated contrast material in the superior vena cava can cause substantial beam hardening artifacts, which can interfere with the assessment of iodine distribution maps. These artifacts can be avoided by a triphasic injection protocol in which the undiluted contrast is followed by 30 mL of a saline/contrast mixture followed by a 50 mL chaser of pure saline (Kerl et al. 2011). For the same reason, image acquisition in caudocranial direction is preferred to minimize residual contrast material in the superior vena cava.

3.2.2 Image Interpretation

Iodine distribution maps are visually evaluated for perfusion defects or pathological perfusion patterns. Occasionally, it can be challenging to distinguish true perfusion defects from artifacts and perfusion defects related to thromboembolic disease from defects caused by other causes (Kang et al. 2010; Kim et al. 2012a). To avoid misinterpretation, dual-energy iodine distribution

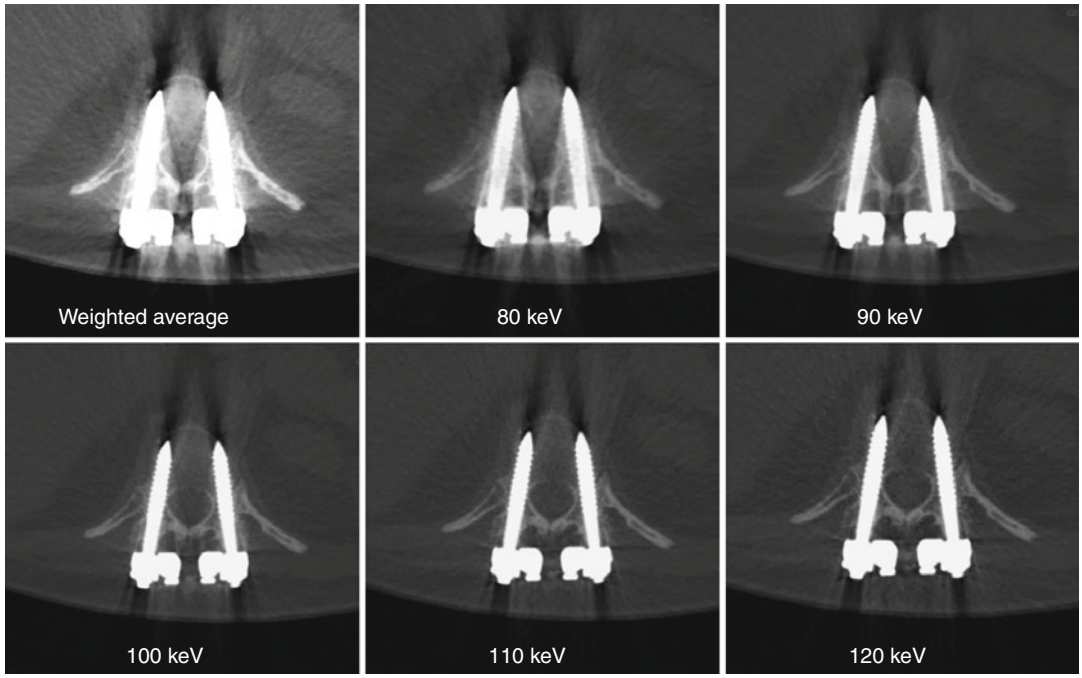

Fig. 2 Dual-energy CT without intravenous contrast in a 61-year-old female patient who had been treated with spinal fusion surgery (vertebra T12 to L2). The transverse weighted average image on the T12 level (**a**) shows substantial streak artifacts from the metal implant. Monoenergetic extrapolation to higher photon energies (**b**–**f**) substantially reduces the metal artifacts and allows for precise assessment of the pedicle screws and the surrounding bone

maps should be viewed side-by-side with morphological image reconstructions of the pulmonary parenchyma and vasculature. Since the pulmonary "perfusion" maps in dual-energy CT really represent a single snapshot of the iodine distribution in the pulmonary microcirculation, they are subject to various technical and physiological influences. The contrast delivery protocol, the timing of the scan relative to the contrast bolus, and a patient's individual anatomy and physiology can affect pulmonary iodine content. Rarefaction of the pulmonary microcirculation occurs with normal aging, leading to reductions in pulmonary iodine concentration in dual-energy CT with advancing age (Meinel et al. 2013b). It is further important to bear in mind the role of the systemic circulation (Remy-Jardin et al. 2014). Since the CT acquisition is timed for peak enhancement in the pulmonary arteries and capillaries, it does not accurately account for the contributions of systemic collaterals to the pulmonary circulation, which can be substantial in conditions such as chronic pulmonary embolism. Although dual-energy pulmonary perfusion maps are primarily evaluated visually, studies have used dual-energy CT to automatically quantify pulmonary perfused blood volume (Nagayama et al. 2013; Meinel et al. 2013a, c, 2014; Sueyoshi et al. 2011).

3.2.3 Clinical Applications

Dual-energy CT pulmonary perfusion imaging has been chiefly investigated for the diagnosis and assessment of pulmonary embolism, but it has also been used in patients with chronic thromboembolic pulmonary hypertension (Dournes et al. 2013; Nakazawa et al. 2011), pulmonary emphysema (Lee et al. 2012), pulmonary artery agenesis (Johnson et al. 2009), and Takayasu's arteritis (Zhang and Lu 2012).

3.2.4 Acute Pulmonary Embolism

The typical findings in dual-energy CT pulmonary perfusion imaging of acute pulmonary

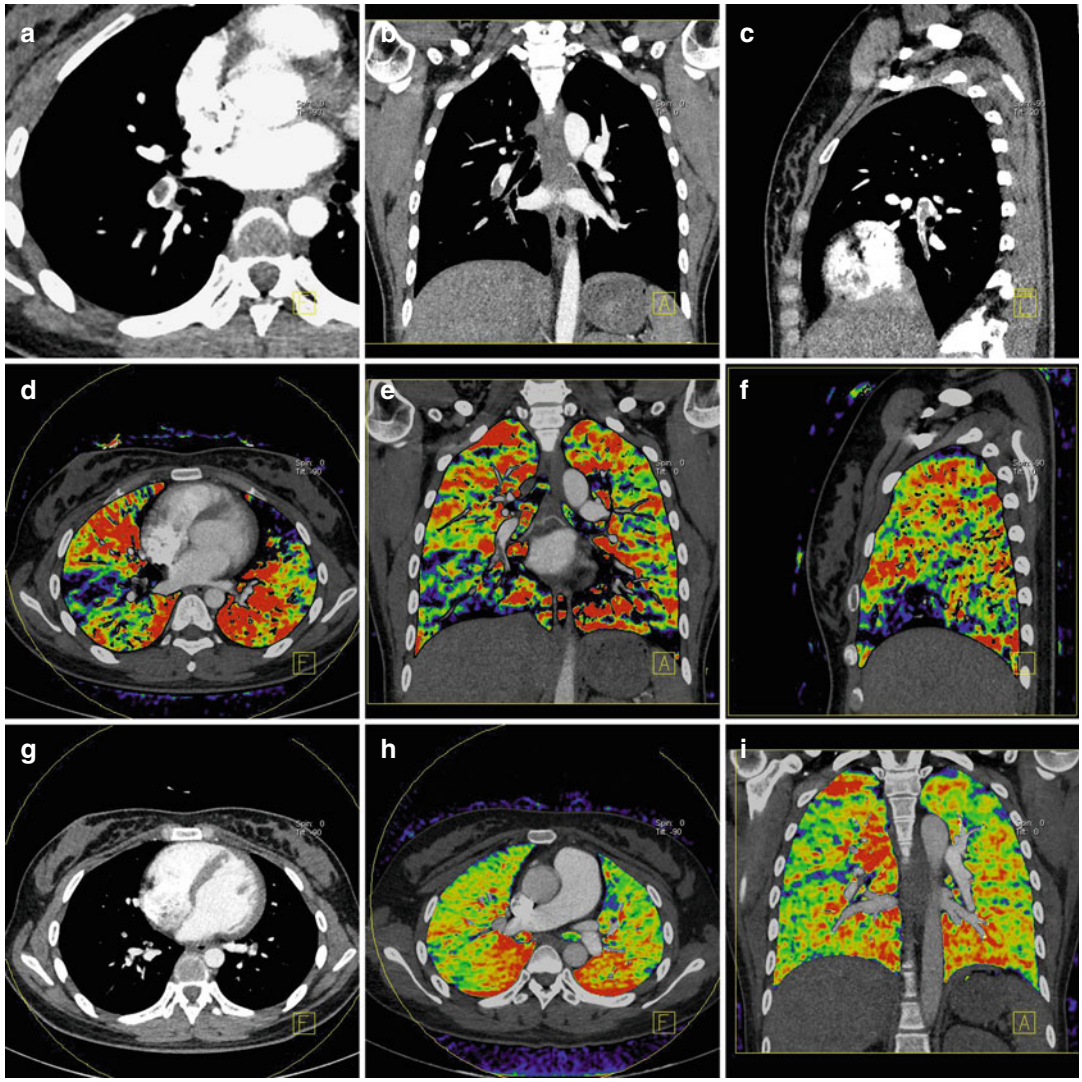

Fig. 3 Dual-energy CT pulmonary angiography in a 24-year-old female patient with nephrotic syndrome and pulmonary embolism. Weighted average images (**a**–**c**) demonstrate a filling defect in the right inferior pulmonary artery. Iodine overlay images (**d**–**f**) show a corresponding perfusion defect in the right lower lobe. The ratio of right to left ventricular diameter is normal, indicating absence of right ventricular dysfunction (**g**). The follow-up examination 2 months after anticoagulant therapy shows resolution of thrombus and normal homogeneous perfusion to both lungs (**h**–**i**)

embolism are wedge-shaped perfusion defects with a subsegmental or segmental distribution for peripheral emboli and larger perfusion defects for more centrally located occlusive thrombi (Figs. 3, 4, 5, 6, and 7). Two potential clinical benefits of using dual-energy CT perfusion imaging in acute pulmonary embolism have been suggested. One potential benefit is that dual-energy CT perfusion imaging may increase the sensitivity of CT for the detection of subsegmental emboli, the other is severity assessment and risk stratification in pulmonary embolism. Indeed, subsegmental pulmonary emboli can be too small to be visualized on CT pulmonary angiography but manifest as peripheral perfusion defects on dual-energy CT perfusion images. There is some evidence indicating that evaluating dual-energy pulmonary perfusion maps together with CT pulmonary

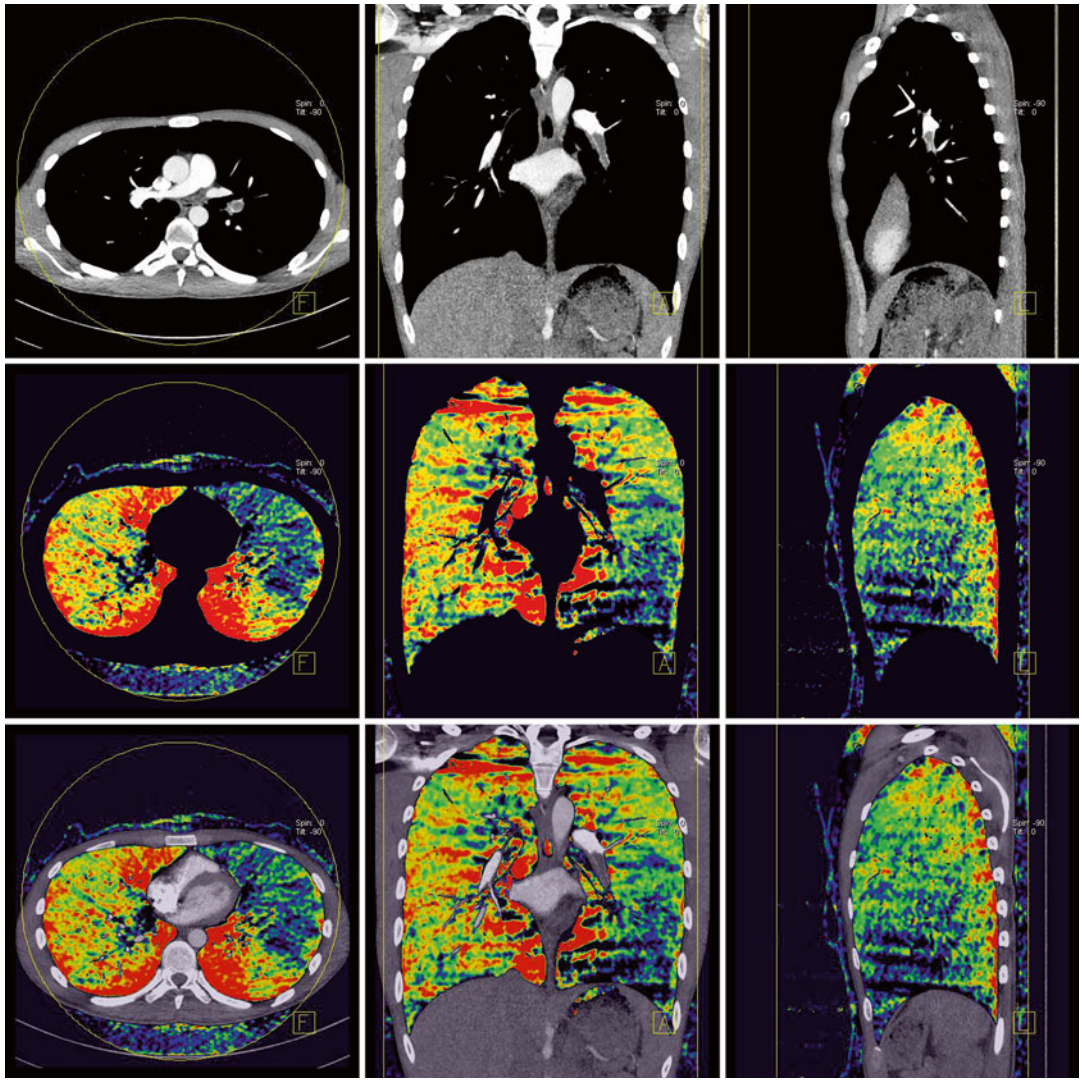

Fig. 4 Dual-energy CT pulmonary angiography in a 28-year-old male patient with pulmonary embolism. Weighted average images (**a**–**c**) demonstrate a filling defect in the left inferior pulmonary artery. Color-coded iodine distribution maps (**d**–**f**) as well as iodine overlay images (**g**–**i**) reveal a large corresponding perfusion defect in the left lower lobe

angiography reconstructions increases readers' sensitivity for small peripheral pulmonary emboli compared to reading CT angiography reconstructions alone (Zhang et al. 2009; Lee et al. 2011). Others have questioned the value of dual-energy CT for improving the accuracy of pulmonary emboli detection arguing that perfusion defects with an embolic pattern can be difficult to identify in patients with preexisting respiratory disease and that in particular small airway disease can mimic embolic perfusion defects (Remy-Jardin et al. 2014). In times of growing concern about potential overdiagnosis or overtreatment of small pulmonary emboli, it is also not evident whether ever-increasing sensitivity for small, peripheral emboli provides clinical benefit. The second proposed clinical use – severity assessment and risk stratification – therefore appears more attractive. In retrospective studies, the degree of perfusion impairment in acute pulmonary embolism has

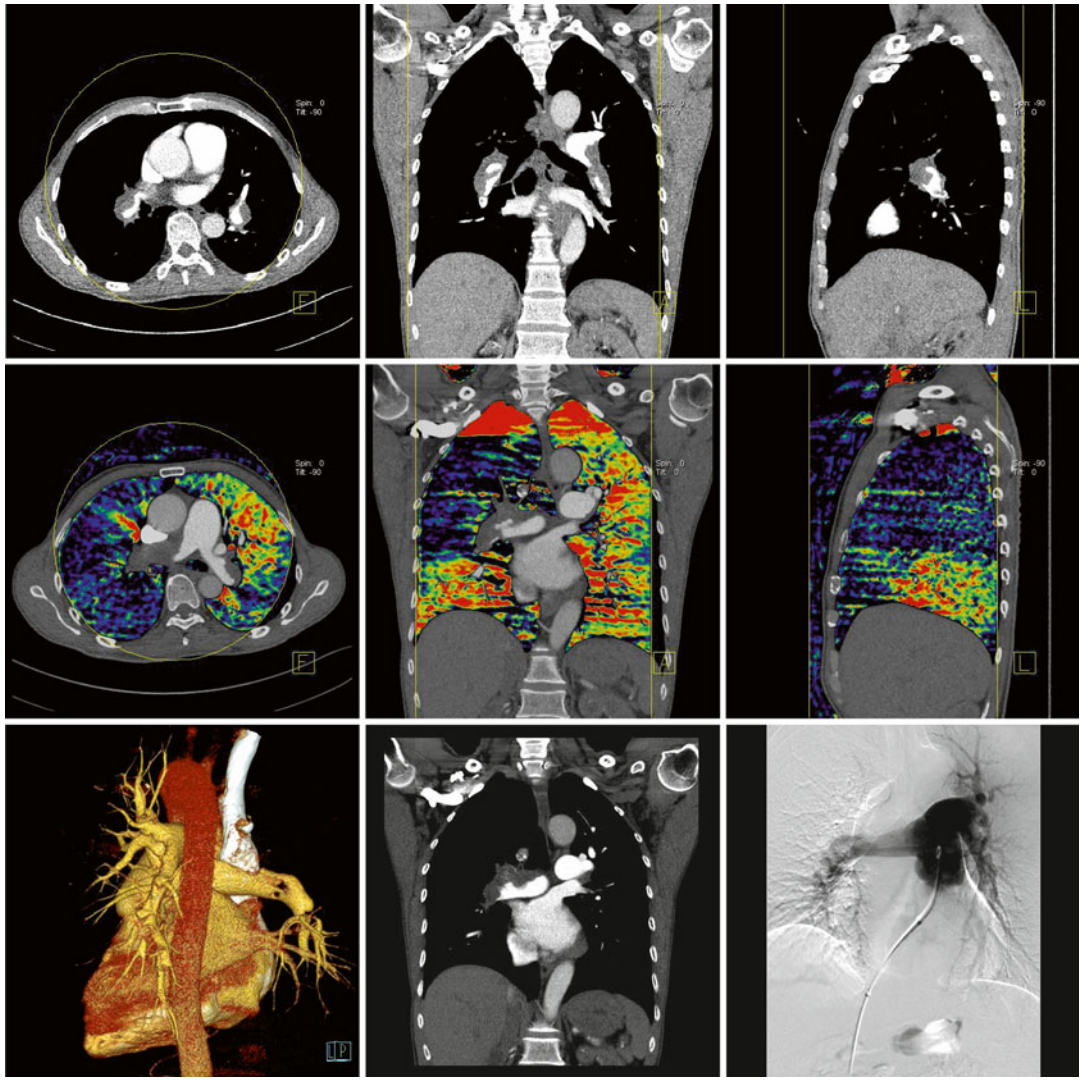

Fig. 5 Dual-energy CT pulmonary angiography in a 56-year-old male patient with pulmonary embolism. Weighted average images (**a**–**c**) demonstrate multiple filling defects in the pulmonary vasculature bilaterally including a large central thrombus in the right main pulmonary artery with complete obstruction of the upper and middle right pulmonary arteries. Color-coded iodine overlay images (**d**–**f**) reveal severely decreased perfusion to large parts of the right lung, particularly the upper and middle lobe. Smaller perfusion defects are also present in the right lower lobe and the left lung. Three-dimensional volume-rendered image (**g**) and optimum contrast image (**h**) again demonstrate complete obstruction and absence of contrast material in the upper and middle right pulmonary arteries. These findings were confirmed by invasive digital subtraction pulmonary angiography (**i**)

been reported to correlate with established markers of pulmonary embolism severity and an adverse clinical course (Meinel et al. 2013a).

An alternative strategy of using dual-energy CT in pulmonary embolism is to analyze the iodine concentration inside the pulmonary arteries. Their iodine content is color coded and thus used to enhance the conspicuity of pulmonary emboli in the pulmonary arteries. Figures 6 and 7 show examples of this technique, which has been reported to improve the detection of peripheral pulmonary emboli (Tang et al. 2013).

3.2.5 Chronic Pulmonary Embolism

Imaging plays an important role in patients with newly diagnosed pulmonary hypertension in

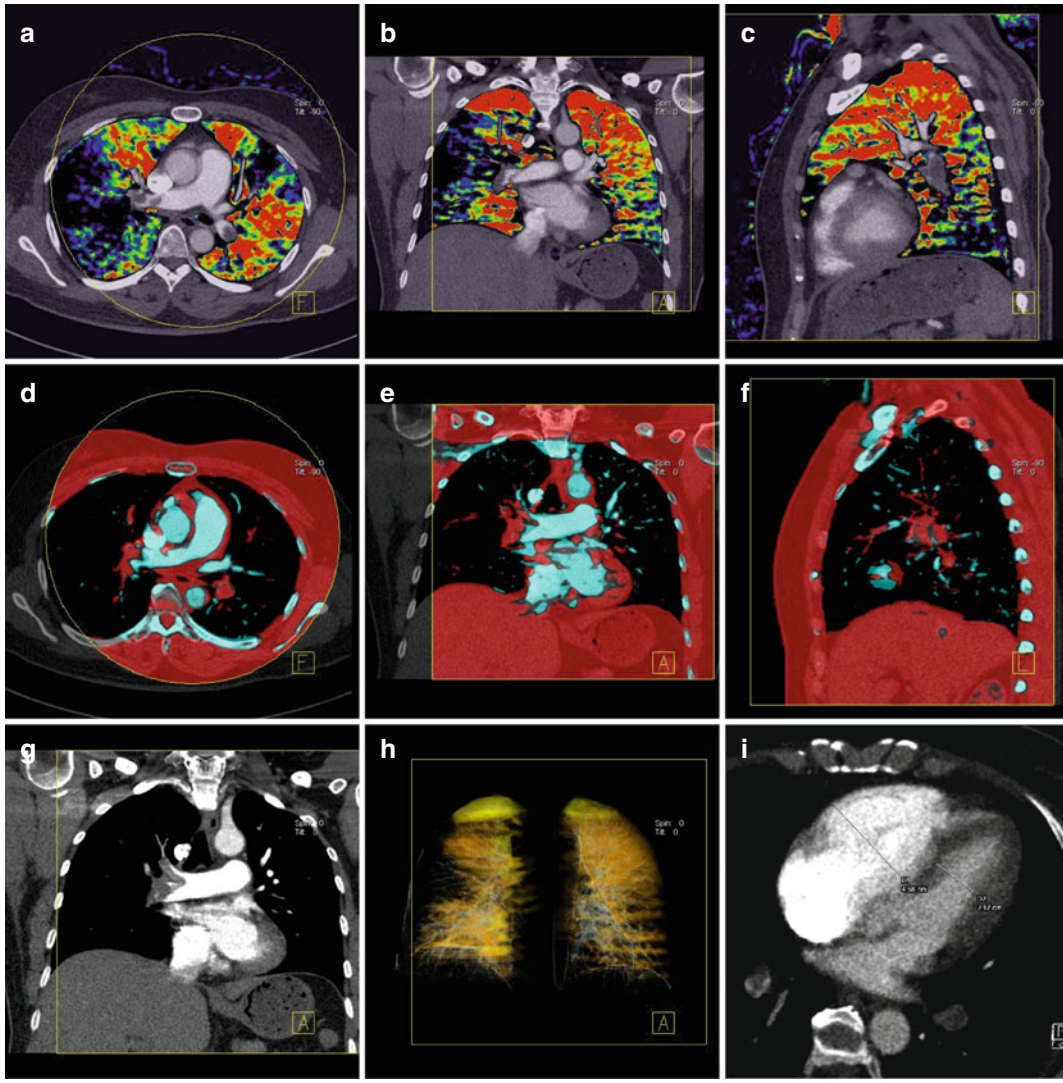

Fig. 6 Dual-energy CT pulmonary angiography in a 46-year-old female patient with recent immobilization due to a lower leg fracture and new-onset chest pain. Color-coded iodine overlay images (**a**–**c**) demonstrate multiple filling defects in the pulmonary vasculature bilaterally and corresponding perfusion defects in both lungs consistent with pulmonary embolism. The "lung vessels" application (**d**–**f**) automatically detects vessels with significantly decreased iodine concentration as affected by pulmonary emboli; these are color coded in red. Optimum contrast reconstruction (**g**) is used to enhance intravascular iodine attenuation while keeping image noise low. Volume-rendered display of pulmonary iodine distribution (**h**) again demonstrates bilateral perfusion defects. There is evidence of right ventricular dysfunction with a markedly increased ratio of right to left ventricular diameter (**i**)

whom a chronic thromboembolic etiology is suspected. Nuclear ventilation/perfusion imaging is standard in the workup of these patients. Visualization of peripheral perfusion defects with ventilation/perfusion mismatch confirms chronic pulmonary embolism, whereas a negative ventilation/perfusion study virtually rules out this diagnosis. Most patients also undergo chest CT to rule out acute or acute-on-chronic pulmonary embolism, to visualize the distribution of embolic material, and to assess associated vascular and parenchymal changes. Performing dual-energy CT in these patients is a promising approach as it provides perfusion images in addition to the anatomical information of standard CT. While the perfusion irregularities in chronic

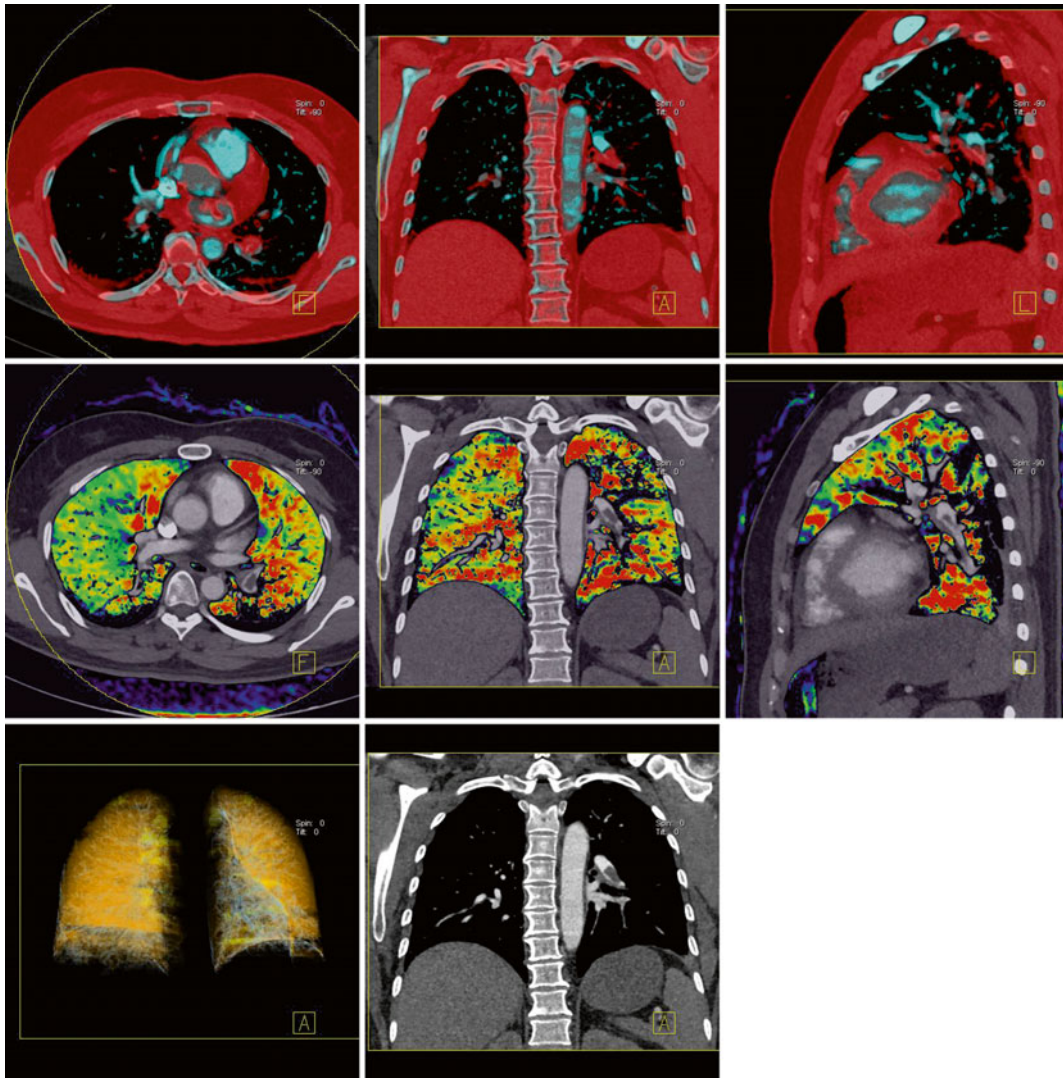

Fig. 7 Dual-energy CT pulmonary angiography in the same patient shown in Fig. 6 repeated 12 days after thrombolytic therapy. Lung vessel images (**a**–**c**) and optimum contrast image (**h**) demonstrate partial resolution of the thrombi. Residual thrombotic material is noted particularly in the left-sided pulmonary vasculature. Iodine overlay images (**d**–**f**) and volume-rendered display of pulmonary iodine distribution (**g**) demonstrate near-normalization of pulmonary perfusion, although some smaller left-sided perfusion defects remain

thromboembolic disease can often be appreciated as ground-glass opacities in a mosaic attenuation pattern on standard CT, this finding can be subtle and difficult to distinguish from ground-glass opacities from other causes (Remy-Jardin et al. 2014). Dual-energy CT pulmonary perfusion maps clearly demonstrate the perfusion inhomogeneities and peripheral perfusion defects in chronic thromboembolic pulmonary hypertension (Fig. 8). The degree of perfusion impairment seen on dual-energy CT has been reported to correlate with the degree of vascular obstruction and functional impairment in chronic pulmonary embolism (Meinel et al. 2014; Renard et al. 2011).

3.2.6 Pulmonary Emphysema

The functional consequences of COPD and emphysema are determined by parenchymal destruction as well as impairment of pulmonary perfusion and

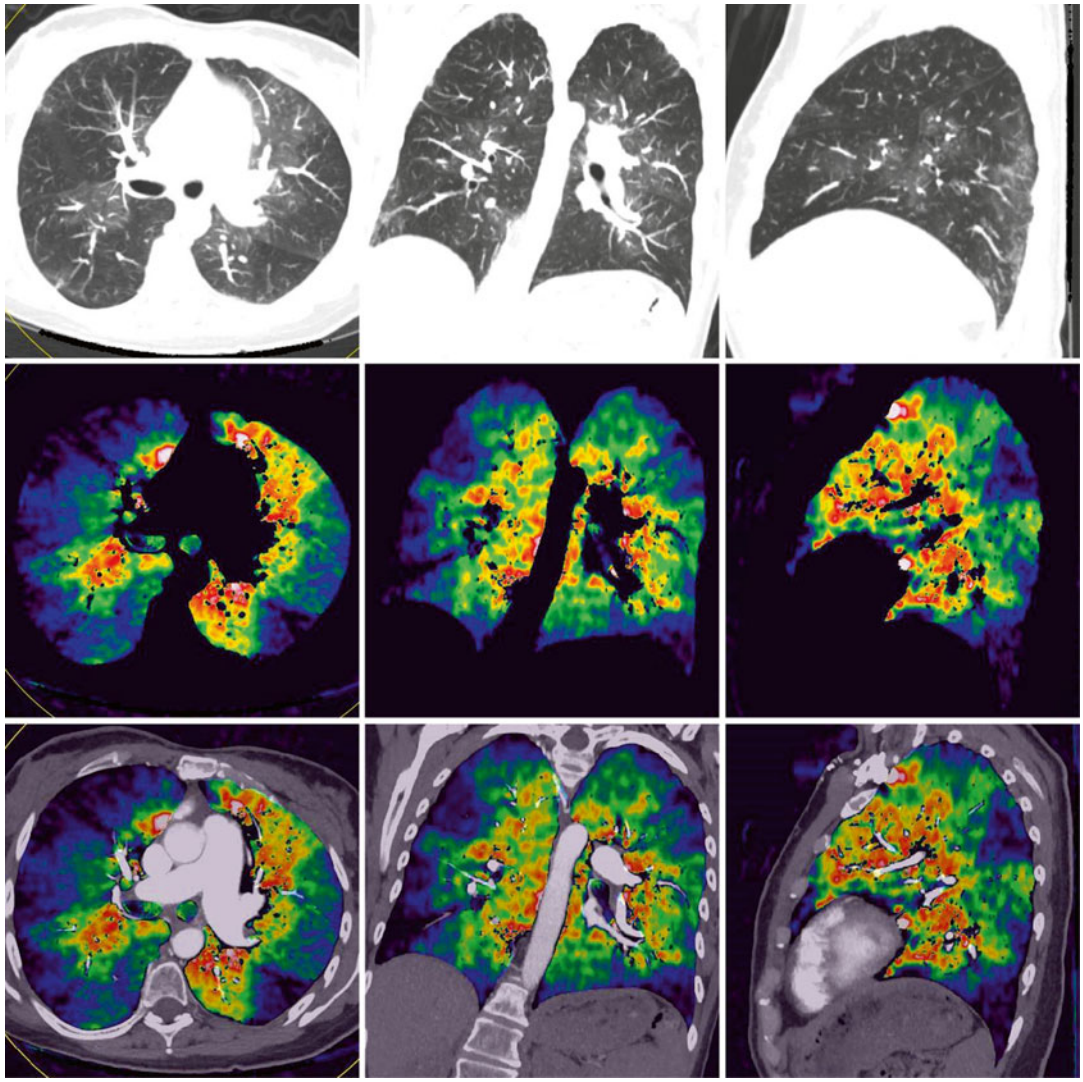

Fig. 8 Dual-energy CT pulmonary angiography in a 44-year-old female patient with chronic thromboembolic pulmonary hypertension. The weighted average images displayed in a lung window (**a**–**c**) demonstrate enlargement of central pulmonary arteries with irregular tapering of distal pulmonary arteries and a mosaic perfusion pattern. Color-coded iodine distribution maps (**d**–**f**) as well as iodine overlay images (**g**–**i**) demonstrate extensive perfusion defects in the periphery of the lung, many of them with a classic wedge-shaped configuration

ventilation. Single-energy CT imaging in pulmonary emphysema can assess the degree, pattern, and distribution of parenchymal changes. Although changes in pulmonary perfusion are closely connected to parenchymal destruction, they are also influenced by pulmonary vascular remodeling, a hallmark of smoking-related lung disease (Remy-Jardin et al. 2014). Assessing pulmonary perfusion in emphysema is particularly relevant in patients considered for surgical or endoscopic treatment. Several studies have investigated the relationship between pulmonary perfusion at dual-energy CT, parenchymal destruction, and functional parameters and suggested that dual-energy CT pulmonary perfusion imaging can play a role in the severity assessment and functional characterization of pulmonary emphysema (Fig. 9) (Meinel et al. 2013c; Lee et al. 2012; Pansini et al. 2009).

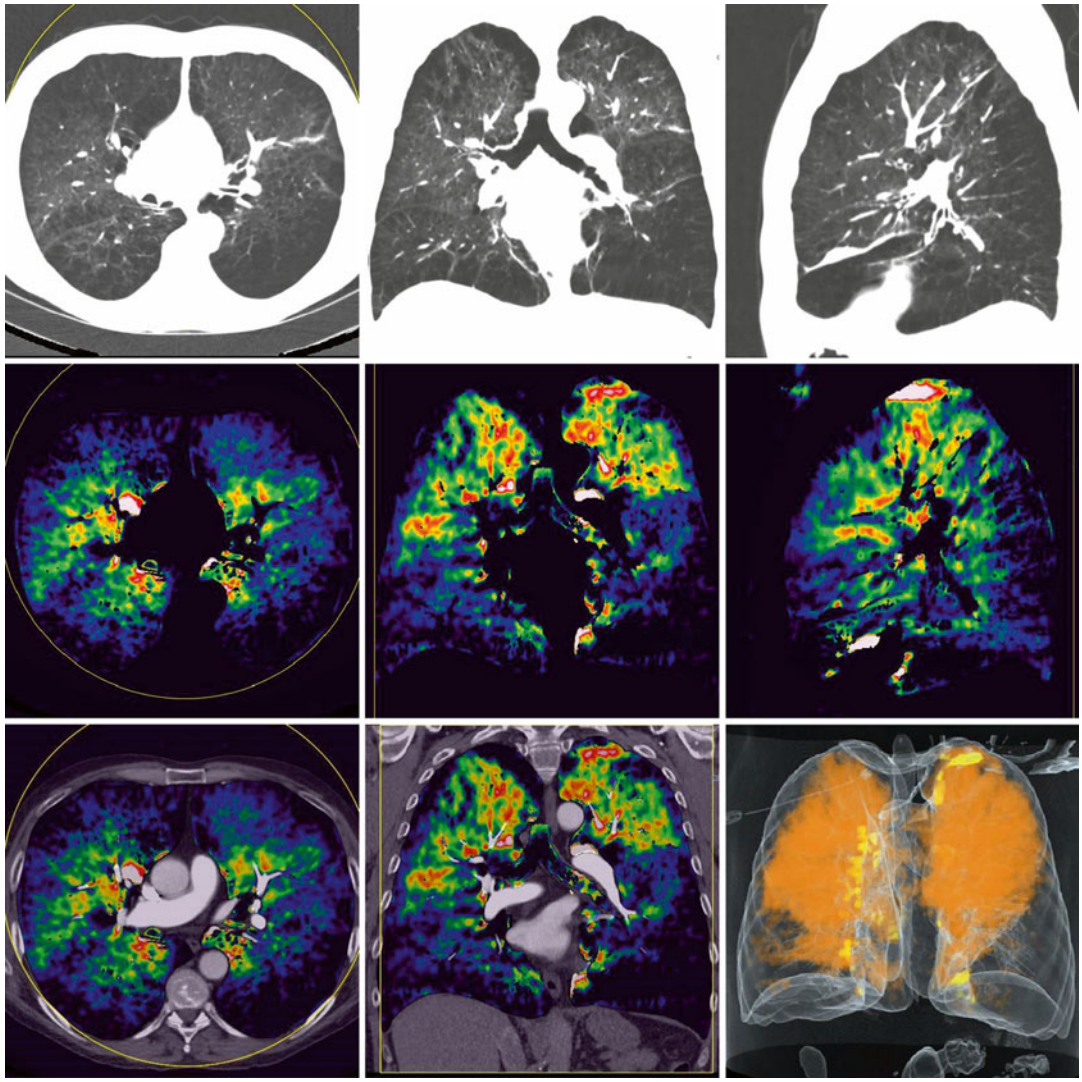

Fig. 9 Dual-energy CT pulmonary angiography in a 55-year-old male patient with chronic obstructive pulmonary disease and severe pulmonary emphysema. The weighted average images in a lung window (**a**–**c**) demonstrate advanced parenchymal destruction, particularly in the lower lobes and the periphery of the upper lobes. Bronchial wall thickening is also noted. Color-coded iodine distribution maps (**d**–**f**), iodine overlay images (**g**–**h**), and the 3D volume-rendered image (**i**) reveal the abnormal distribution of pulmonary perfusion in this patient

3.3 Pulmonary Ventilation Imaging

3.3.1 Acquisition Technique

Dual-energy CT ventilation imaging uses xenon or krypton, both noble gasses with relatively high atomic numbers, as inhalative contrast agents. These are mixed with oxygen and applied to the patients via a ventilation mask. When a sufficient end-expiratory concentration of xenon or krypton is reached, concentrated oxygen is administered for wash-out. Various acquisition protocols have been described in the literature (Kong et al. 2014). Dynamic acquisition protocols consist in repeated CT acquisitions during the wash-in and wash-out phase. Static acquisition protocols

acquire a CT scan at a single time point, typically at the end of the wash-in phase.

3.3.2 Applications

Pulmonary functions tests are widely used in clinical routine to assess respiratory function. Not accessible to pulmonary function is the regional distribution of ventilation within the lung. Dual-energy CT ventilation imaging has the unique ability to visualize the regional distribution of ventilation in exact co-registration with information on morphological changes of the airways and pulmonary parenchyma. Dual-energy CT ventilation imaging has been applied in mechanically ventilated ICU patients (Thieme et al. 2010; Hoegl et al. 2013) and in various pulmonary diseases such as COPD (Park et al. 2010; Hachulla et al. 2012), asthma (Chae et al. 2010a; Goo and Yu 2011; Park et al. 2012; Kim et al. 2012b), bronchiolitis obliterans (Goo et al. 2010), bronchial atresia (Goo et al. 2008, 2011), and pulmonary embolism (Zhang et al. 2012, 2013b). Most of these studies have shown that pathological ventilation patterns observed on xenon or krypton distribution maps correlated well with the morphological changes of the pulmonary parenchyma and airways and pulmonary function tests. In a few cases, an incremental value of CT ventilation was reported such as the assessment of collateral ventilation in patients with bronchial atresia or obstruction (Kong et al. 2014). Combined ventilation/perfusion dual-energy CT has been successfully performed using intravenous iodine and inhaled xenon as contrast agents and has been able to visualize ventilation/perfusion mismatch in pulmonary embolism (Fig. 10) (Zhang et al. 2012, 2013b).

As of today, dual-energy CT ventilation imaging has remained a research tool. The main obstacle to clinical implementation is the sophisticated nature of the procedure that requires close monitoring of the patient's vital signs and respiratory gas concentrations. Also, a considerable percentage of patients experience transient but significant side effects with xenon inhalation including headache, nausea, vomiting, and respiratory depression (Park et al. 2010; Goo et al. 2010; Remy-Jardin et al. 2010). Krypton has been suggested as a potentially safer alternative, but experience with krypton as an inhalative contrast agent is very limited (Hachulla et al. 2012).

3.4 Assessment of Lung Nodules and Thoracic Malignancies

3.4.1 Acquisition Technique

When dual-energy chest CT is performed for the assessment of lung nodules, masses, or lymph nodes, the examination is typically acquired in a delayed phase to ensure adequate contrast enhancement of these structures. In the delayed phase, there is minimal enhancement of the pulmonary parenchyma. Therefore, a dual-energy CT pulmonary angiography needs to be acquired before the delayed phase if pulmonary perfusion should also be assessed.

3.4.2 Characterization of Pulmonary Nodules/Masses as Benign or Malignant

The assessment and management of pulmonary nodules on single-energy CT is discussed in depth in a previous chapter of this book. The iodine uptake of pulmonary nodules in dual-energy CT has been considered a surrogate for the vascularity of a lesion and explored as a tool to differentiate benign from malignant pulmonary nodules (Zhang et al. 2013a). A few pilot studies have found differences in the degree and pattern of iodine uptake between malignant and benign pulmonary nodules, both solid (Chae et al. 2008; Hou et al. 2014) and subsolid (Kawai et al. 2011). However, there can be a significant overlap between the iodine uptake of infectious and neoplastic pulmonary lesions. Based on the published literature and our own experience, the degree and pattern of iodine uptake in dual-energy CT is not a reliable indicator to distinguish benign from malignant lesions. Examples of malignant and benign pulmonary masses imaged with dual-energy CT are shown in Figs. 11, 12, 13, 14, 15, 16, and 17. The presence of certain patterns of calcification (such as homogeneous, laminated, or popcorn calcifications) can suggest a benign entity. Occasionally, virtual

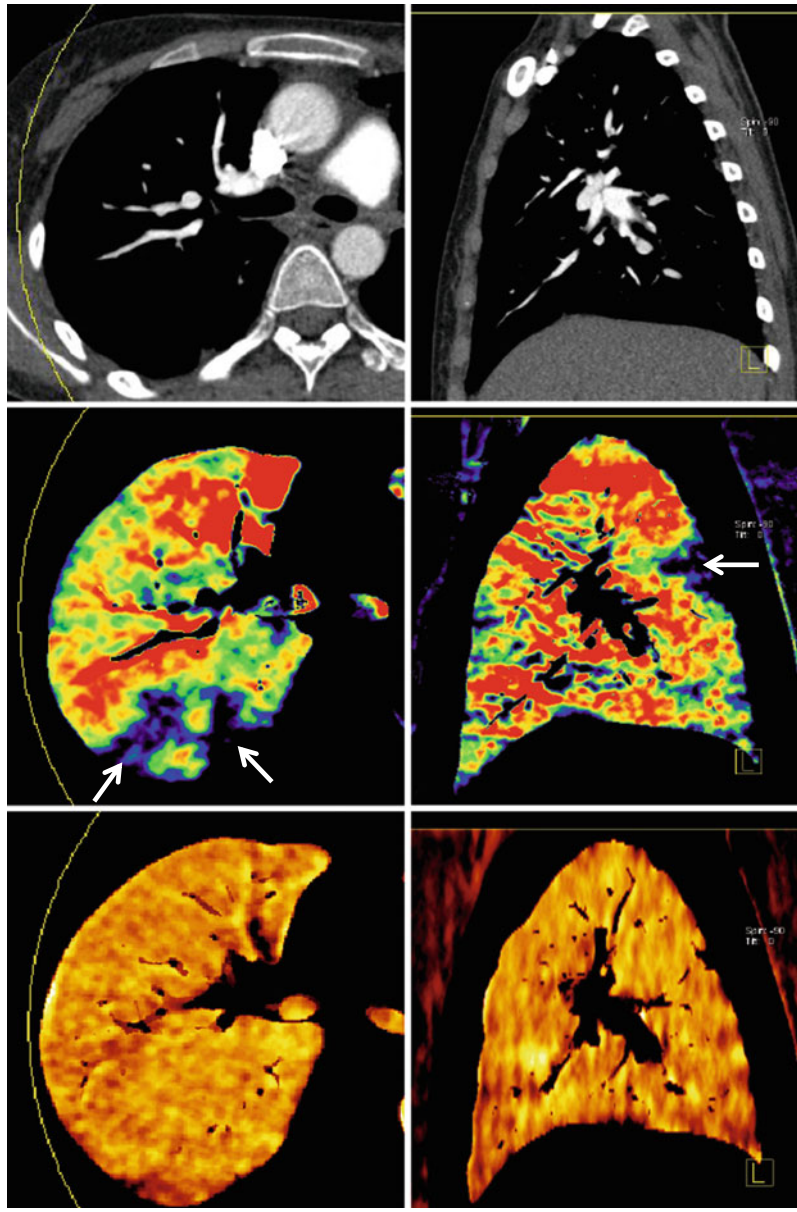

Fig. 10 Dual-energy CT pulmonary angiography and dual-energy CT pulmonary ventilation imaging in a 19-year-old female patient with nephrotic syndrome and pulmonary embolism. No pulmonary emboli are detected in weighted average CT reconstructions (**a**, **b**). Dual-energy iodine distribution maps (**c**, **d**) visualize several wedge-shaped peripheral perfusion defects (*arrows*) consistent with subsegmental pulmonary emboli. Xenon distribution maps (**e**, **f**) show preserved ventilation in these areas making this an example of ventilation/perfusion mismatch in pulmonary embolism

non-contrast images reconstructed from dual-energy CT can be useful to confirm the presence and pattern of calcification and distinguish calcium from iodine enhancement (Fig. 17) (Chae et al. 2010b).

3.4.3 Lung Cancer: Assessment of Tumor Perfusion, Therapy Response, and Nodal Staging

In patients with a confirmed diagnosis of lung cancer, the potential utility of dual-energy CT

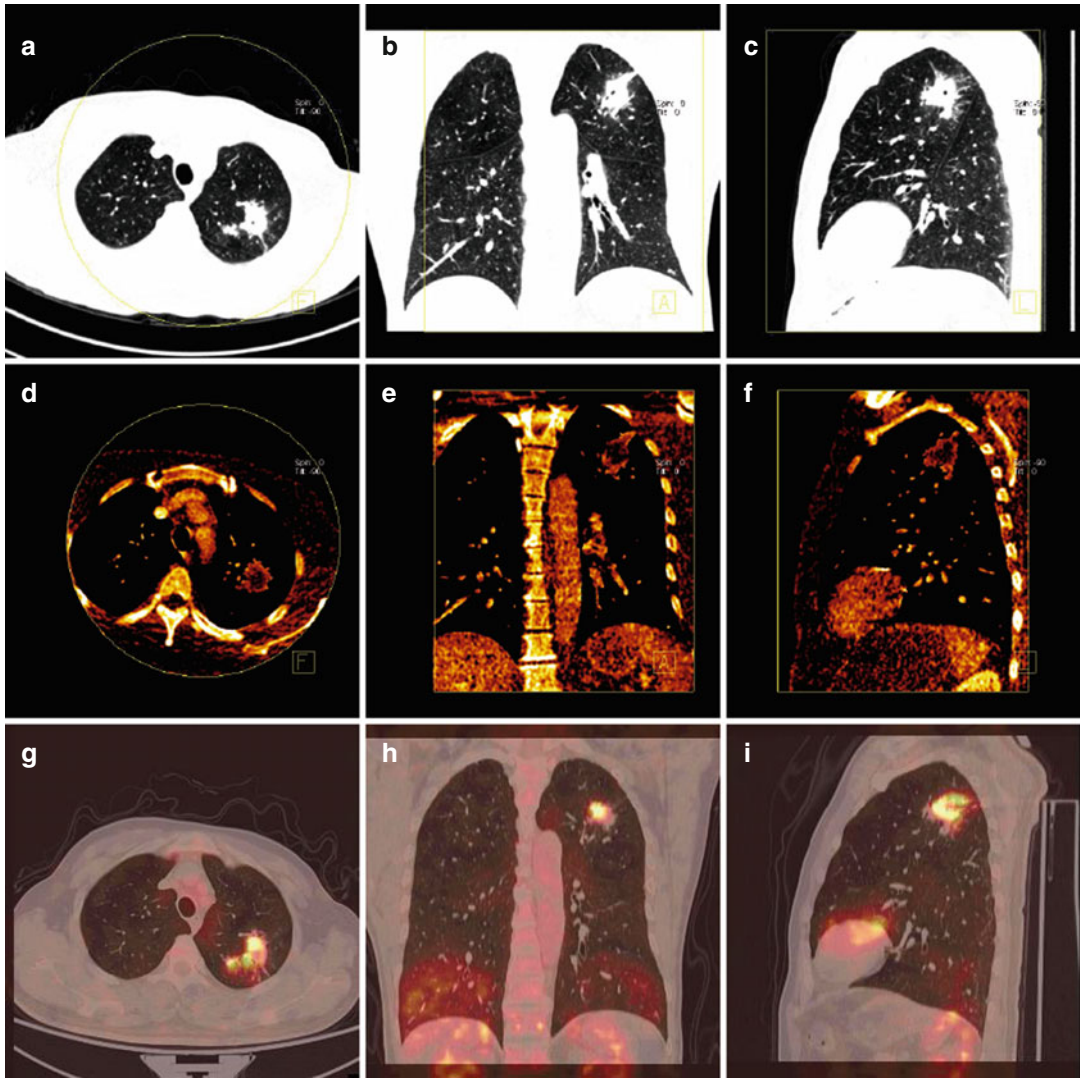

Fig. 11 Dual-energy CT in a 52-year-old male patient with an incidentally detected pulmonary mass. Weighted average images in the lung window (**a**–**c**) depict a mass with irregular, spiculated margins in the left upper lobe. Iodine distribution maps in the delayed phase (**d**–**f**) indicate strong peripheral perfusion of the mass. PET-CT (**g**–**i**) demonstrates high glucose metabolism of the lesion, particularly in its periphery. The lesion was found to represent tuberculosis on histopathology

could be to assess tumor vascularity, vitality, and therapy response or to use iodine uptake in lymph nodes to determine nodal metastatic involvement. The iodine uptake of non-small cell lung cancer as determined by dual-energy CT has been reported to correlate with metabolic activity on FDG-PET (Schmid-Bindert et al. 2012). In a small pilot study in patients with non-small cell lung cancer treated with the anti-angiogenic agent bevacizumab, iodine uptake at dual-energy CT has been used to assess therapy response and to discriminate between contrast enhancement and intra-tumor hemorrhage (Kim et al. 2012c). Another study retrospectively analyzed the iodine uptake of mediastinal lymph nodes in patients with non-small cell lung cancer on arterial and venous phase dual-energy CT and reported that the arterial enhancement fraction was higher in

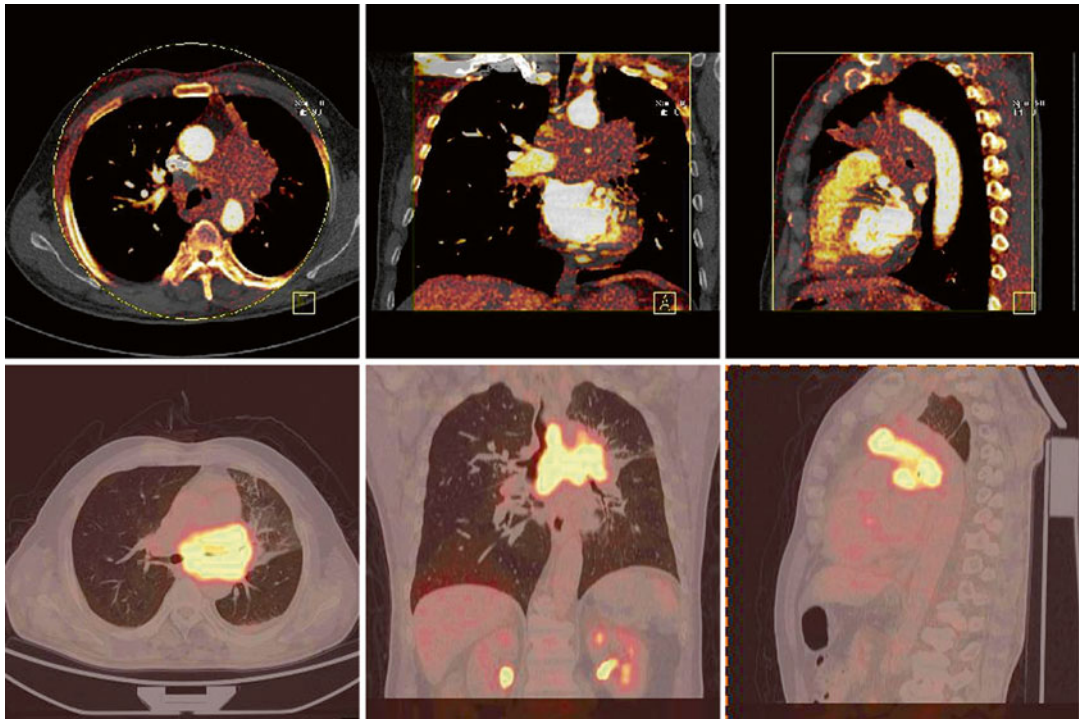

Fig. 12 Dual-energy CT in a 61-year-old male patient with poorly differentiated squamous cell lung cancer. Iodine overlay images from arterial phase dual-energy CT (**a**–**c**) demonstrate a large, centrally located mass with homogeneous iodine uptake. Corresponding PET/CT images (**d**–**f**) demonstrate high glucose metabolism

pathologically enlarged lymph nodes and decreased in nodes that shrank under chemotherapy (Baxa et al. 2014).

3.4.4 Lung Cancer: Assessment of Pulmonary Perfusion and/or Ventilation

In patients with lung cancer amenable to surgical resection, preoperative estimation of postoperative pulmonary function is important to determine whether the patient can safely undergo the surgery. This is particularly critical in the large number of patients with coexisting chronic obstructive pulmonary disease and/or pulmonary emphysema. Prediction is commonly based on pulmonary function tests, occasionally supplemented by nuclear lung perfusion imaging. One investigation has used preoperative dual-energy CT to predict postoperative pulmonary perfusion and ventilation (Chae et al. 2013). The authors reported that dual-energy CT was superior to scintigraphy for predicting postoperative lung function, depicting perfusion and ventilation defects, and assessing collateral ventilation.

3.5 Myocardial Perfusion Imaging

3.5.1 Acquisition Technique

The concept and techniques of CT myocardial perfusion imaging are introduced in detail in the chapter "CT Imaging of Ischemic Heart Disease" of this volume. One of the approaches to CT myocardial perfusion imaging is to perform a single CT acquisition capturing the contrast distribution in the myocardium during the inflow of contrast agent into the myocardium. This technique is often referred to as "static" or "snapshot" CT myocardial perfusion imaging. Images are usually acquired during stress and at rest. The stress acquisition is acquired after administration of a pharmacological stress agent such as adenos-

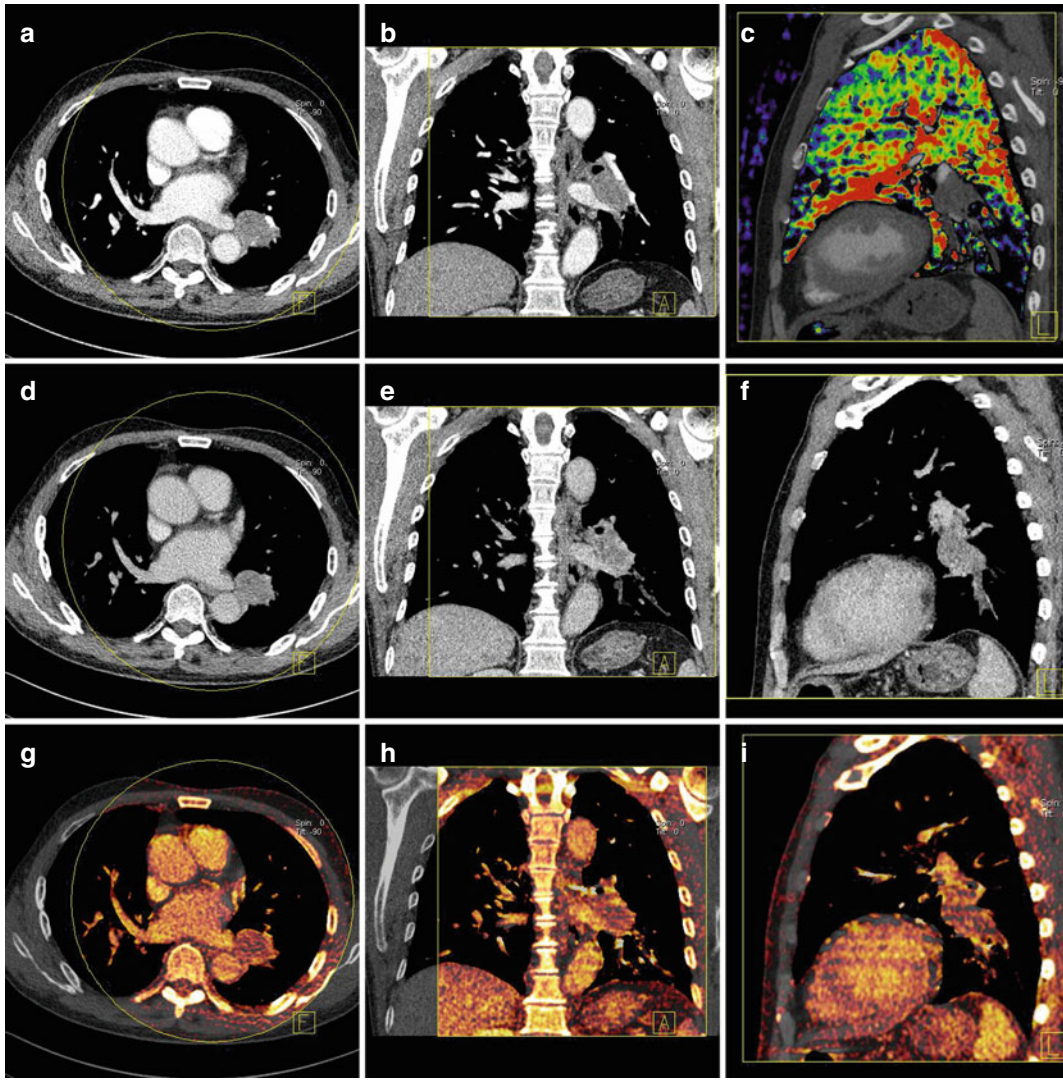

Fig. 13 Dual-energy CT with arterial and delayed phase acquisitions in a 64-year-old male patient 4 years after resection of a carcinoma of the right upper lung. Average weighted images in the arterial (**a**–**b**) and delayed phase (**d**–**f**) demonstrate a centrally located mass in the left lower lobe infiltrating the left inferior pulmonary artery. Obstruction of the artery is confirmed by the visualization of a perfusion defect in the left lower lobe on the iodine overlay image (**c**). Iodine overlay images in the delayed phase (**g**–**i**) demonstrate strong, fairly homogeneous iodine uptake in the lesion, which proved to be metastasis from the lung cancer resected 4 years ago

ine or regadenoson. The rest and stress images are then reviewed for perfusion defects in the left ventricular myocardium which appear as areas of decreased myocardial attenuation and can indicate ischemia or infarction depending on whether they are only present at stress or persist at rest. Occasionally, an additional delayed acquisition is performed to detect late enhancement in infarcted myocardium.

Static CT myocardial perfusion imaging can be performed in dual-energy mode. Dual-energy acquisition has the advantage that the iodine distribution in the left ventricular myocardium can be directly visualized and displayed, leading some researchers to conclude that perfusion defects can be more easily recognized on dual-energy compared to single-energy static myocardial perfusion imaging (Fig. 18) (Arnoldi et al.

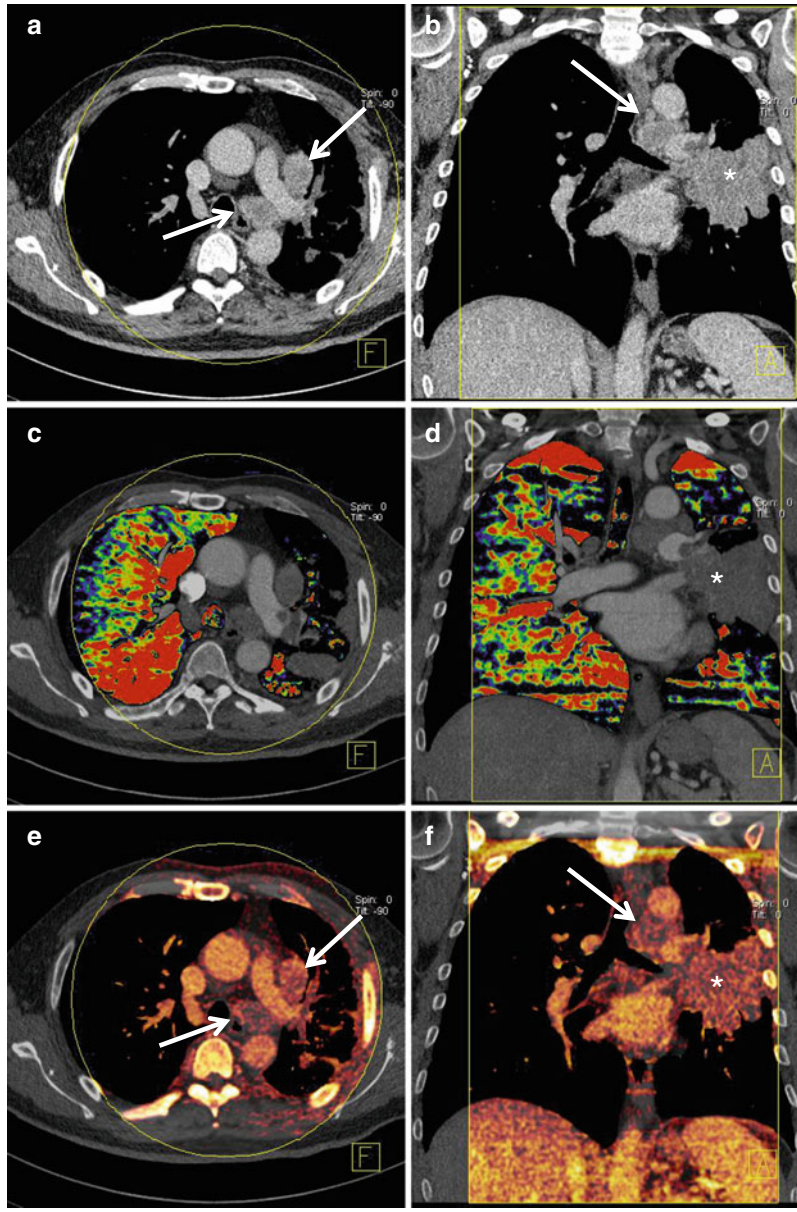

Fig. 14 Dual-energy CT with arterial and delayed phase acquisitions in a 56-year-old male patient with squamous cell lung cancer. Weighted average images in the delayed phase (**a**, **b**) demonstrate a centrally located left-sided pulmonary mass (*asterisk*) infiltrating the left main pulmonary artery. Mediastinal lymph node metastasis is also noted (*arrows*). Iodine overlay images in the arterial phase (**c**, **d**) indicate markedly reduced perfusion to the left lung due to obstruction of the left main pulmonary artery. Iodine overlay images in the delayed phase (**e**, **f**) demonstrate strong, relatively homogeneous iodine uptake in the pulmonary mass. The mediastinal lymph node metastases show strong peripheral iodine uptake with reduced uptake in their hypodense centers consistent with central necrosis

2011; Vliegenthart et al. 2012; Varga-Szemes et al. 2015). Another potential advantage of dual-energy acquisition is that it allows to accurately measure the iodine concentration in the myocardium (Koonce et al. 2014) and thus perform an objective, quantitative analysis of myocardial enhancement in addition to the visual evaluation for perfusion defects.

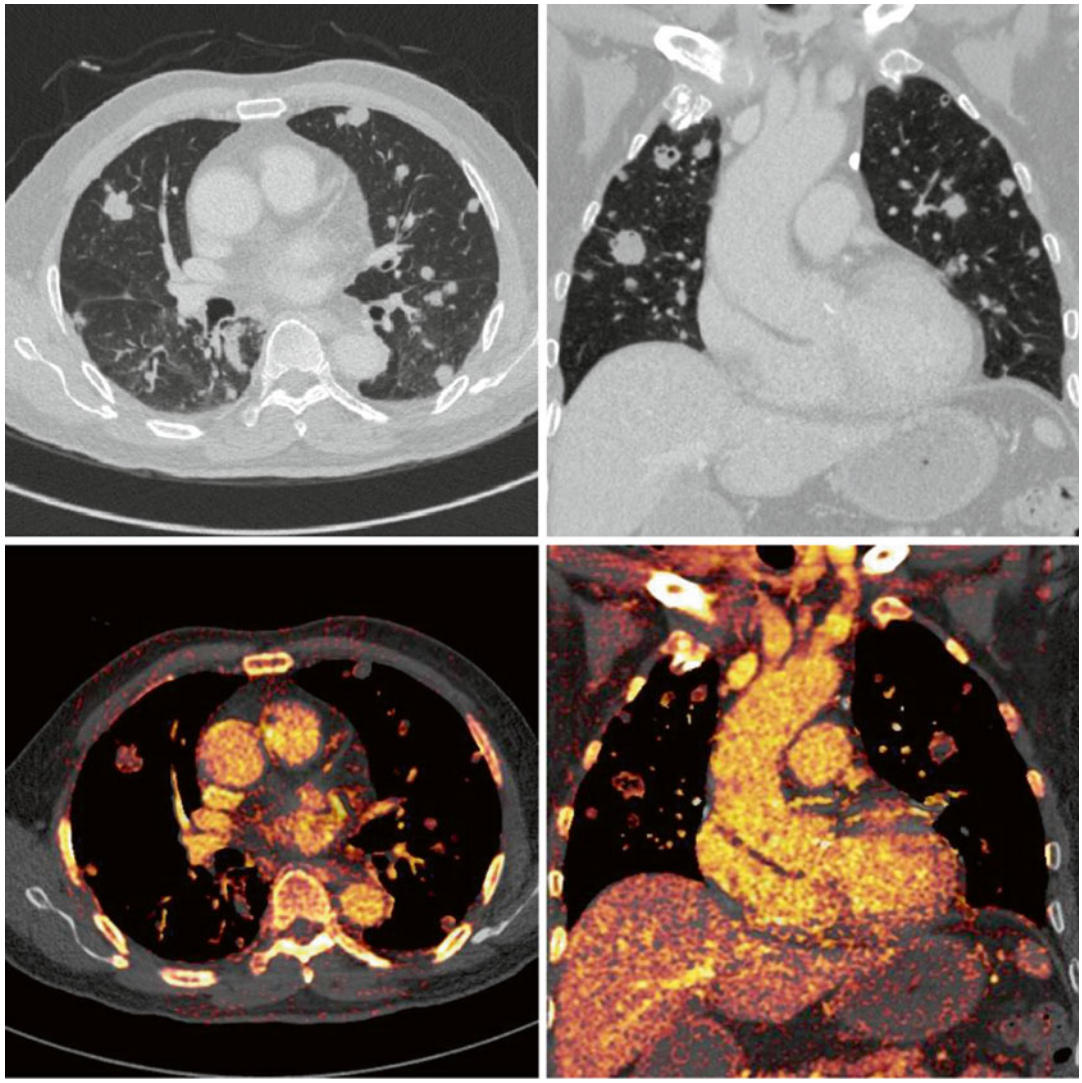

Fig. 15 Dual-energy CT in an 84-year-old male patient with rectal cancer and pulmonary metastases. Weighted average images in the lung window (**a**, **b**) demonstrate multiple intrapulmonary nodules, some of which appear cavitated. Iodine overlay images (**c**, **d**) indicate marked iodine uptake of the lesions with peripheral, rim-like uptake of the larger nodules

3.5.2 Application in Ischemic Heart Disease

The potential value of CT myocardial perfusion imaging is to detect or exclude myocardial ischemia, particularly in patients with an intermediate stenosis on coronary CT angiography or those where heavy calcifications or smaller stents preclude an accurate, noninvasive assessment of coronary artery patency. Thus, the promise of adding stress CT myocardial perfusion imaging to coronary CT angiography is to improve the specificity of CT for detecting hemodynamically significant stenosis, i.e., stenosis causing ischemia. A number of studies have evaluated dual-energy CT myocardial perfusion using SPECT, cardiac MRI, or catheter angiography as the reference standard (Varga-Szemes et al. 2015). Overall, these studies have reported good accuracy compared to the reference modalities, and most have shown an increase in specificity compared to coronary CT

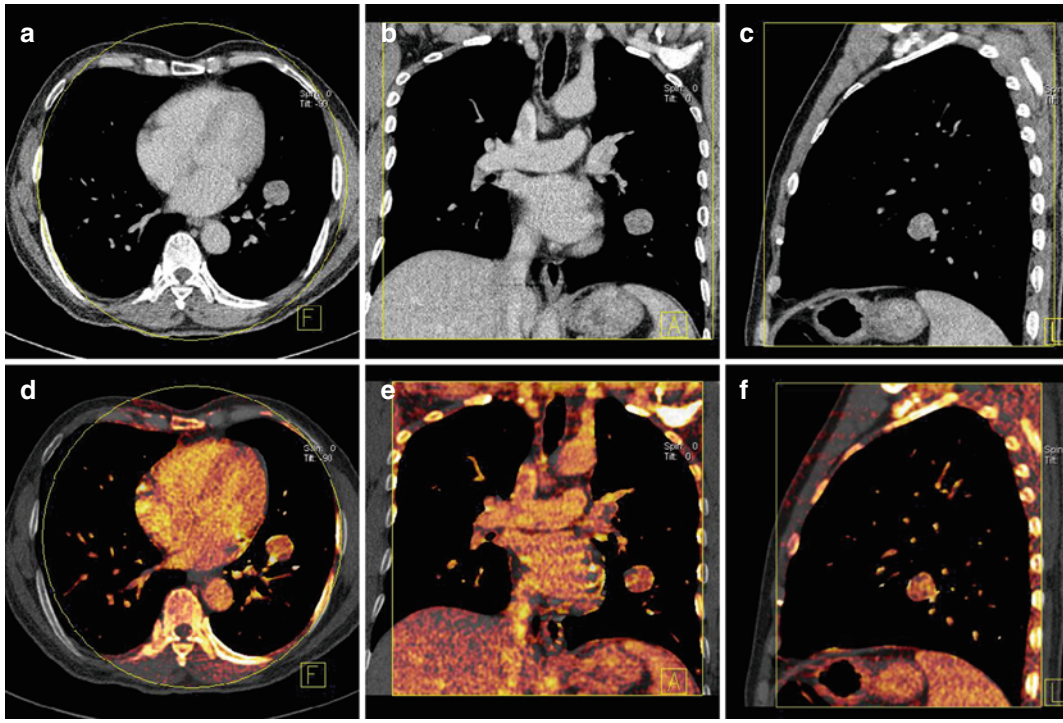

Fig. 16 Delayed phase dual-energy CT in a 49-year-old male patient with a known history of intracranial solitary fibrous tumors. Weighted average images (**a**–**c**) demonstrate a round, sharply demarcated mass in the left lower lobe adjacent to the oblique fissure. Iodine overlay images (**d**–**f**) indicate strong, homogeneous perfusion of the mass. CT-guided needle biopsy was performed, and the mass was found to represent a solitary fibrous tumor. The term solitary fibrous tumor denotes a rare group of mesenchymal tumors. Although typically benign, cases of malignant behavior including local recurrence and distant metastasis have been documented

angiography alone for the detection of hemodynamically significant stenosis.

Dual-energy CT myocardial perfusion imaging is struggling with a number of limitations that equally apply to single-energy static myocardial perfusion imaging and have so far precluded the technique from broad clinical acceptance. Beam hardening and other artifacts are common and are often very difficult to distinguish from true perfusion defects, which potentially causes false-positive results. Contrast-to-noise ratio for myocardial enhancement can be low, particularly for late enhancement imaging. Because a single time point is acquired, timing of the scan relative to the contrast bolus is critical, and perfusion defects can be missed due to suboptimal timing. The existing studies are limited to relatively small, single-center studies. Larger studies with a rigorous image analysis by blinded core labs are required to establish the clinical value of dual-energy CT myocardial perfusion imaging.

3.6 Aortic Imaging

3.6.1 Image Optimization Using Monoenergetic Extrapolation and Nonlinear Blending

In some clinical scenarios, it can be advantageous to perform CT angiography of the aorta in dual-energy mode. In patients with renal insufficiency, it may be desirable to restrict the administered amount of contrast media as much as possible. In these patients, it is reasonable to perform dual-energy CT angiography of the aorta using a small amount of contrast material and then perform virtual monochromatic extrapolation to lower photon energies to enhance intravascular iodine

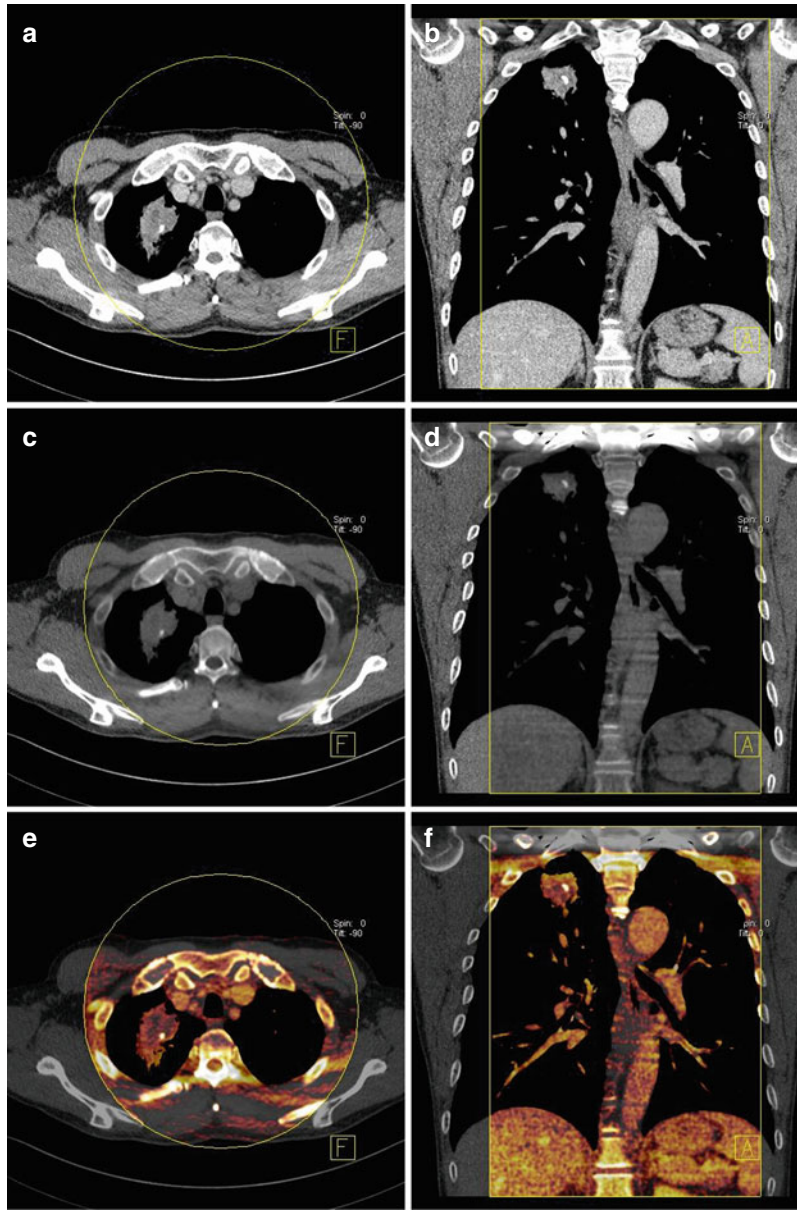

Fig. 17 Delayed phase dual-energy CT in a 63-year-old male patient with adenocarcinoma of the lung. Weighted average images (**a**, **b**) demonstrate an irregular shaped mass in the right upper lobe. There is a small hyperdensity within the mass. Virtual non-contrast images (**c**, **d**) confirm that the hyperdensity represents calcification. Iodine overlay images (**e**, **f**) show strong iodine uptake in the periphery of the mass and reduced uptake in its center

attenuation. Nonlinear blending techniques can further enhance contrast-to-noise characteristics.

3.6.2 Virtual Non-contrast Imaging

Another potential advantage of dual-energy CT angiography of the aorta is that it allows reconstructing virtual non-contrast images that may obviate the need for a non-contrast acquisition. Non-contrast acquisitions of the aorta are most relevant in two specific clinical scenarios: In suspected acute aortic syndrome, a non-contrast acquisition is strongly recommended for the

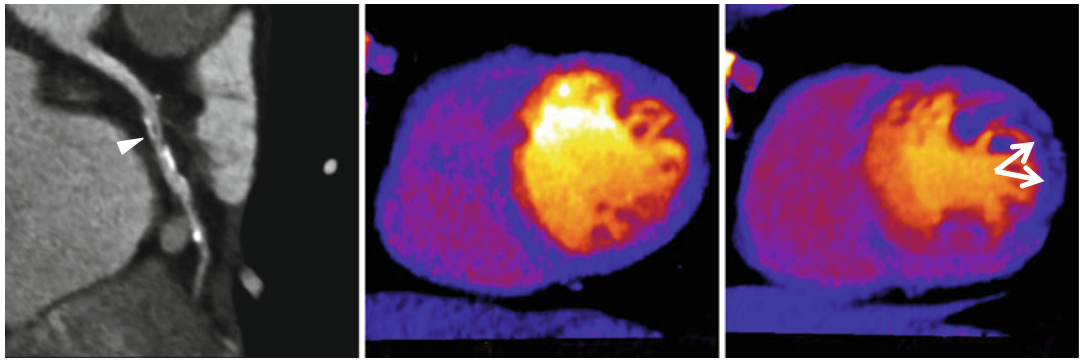

Fig. 18 Dual-energy coronary CT angiography and myocardial perfusion imaging in a 72-year-old male patient with multiple cardiovascular risk factors presenting with chest pain suggestive for ischemic heart disease. The curved multiplanar reformatted view of the left circumflex artery (**a**) demonstrates mixed plaque with intermediate to severe stenosis (*arrowhead*). In the dual-energy myocardial iodine distribution map at rest (**b**), no perfusion defects are visualized. The iodine distribution map at stress (**c**) demonstrates a well-demarcated area of decreased myocardial iodine content (*arrows*) in the lateral wall of the left ventricle consistent with ischemia (Reprinted with permission from the American Journal of Roentgenology (Varga-Szemes et al. 2015))

detection of intramural hematoma, which can be subtle and very difficult to detect on contrast-enhanced series. Non-contrast acquisitions are also recommended as part of the CT follow-up protocol in patients after endovascular repair of aortic aneurysm or dissection. In these patients, the non-contrast images are occasionally necessary to differentiate between calcifications within the aneurysm sac and iodine indicating the presence of an endoleak (Fig. 19). If dual-energy virtual non-contrast reconstructions could replace non-contrast acquisitions in these scenarios, the overall radiation exposure could be substantially reduced. For the follow-up of patients after endovascular repair of aortic aneurysm or dissection, there is good evidence that the true non-enhanced acquisitions can be safely replaced by virtual non-contrast reconstructions without compromising the diagnostic accuracy for endoleak detection (Flors et al. 2014; Sommer et al. 2010). To the best of our knowledge, no study so far has investigated the accuracy of virtual non-contrast images for the detection of aortic intramural hematoma. As long as no such evidence exists, we would recommend acquiring a true non-contrast series in patients with suspected acute aortic syndrome.

3.7 Spine Imaging

3.7.1 Detection of Bone Marrow Edema

The spectral information of dual-energy CT datasets can be used to identify and virtually subtract calcium thus generating virtual non-calcium images. This post-processing method has been found useful to evaluate for bone marrow edema, which would normally be obscured by the high attenuation of calcium. Vertebral fractures are a common incidental finding on chest CT. In this setting, dual-energy virtual non-calcium images can be evaluated for the presence of bone marrow edema indicating recent fracture. In one prospective study including more than 100 thoracic and lumbar vertebral compression fractures, the authors used a cutoff value of -80 HU to distinguish between edematous and non-edematous vertebrae and found high diagnostic accuracy particularly in those vertebrae without substantial sclerosis or air inclusions (Wang et al. 2013).

3.7.2 Determination of Bone Mineral Density

The ability to identify calcium in dual-energy CT by means of material decomposition has also

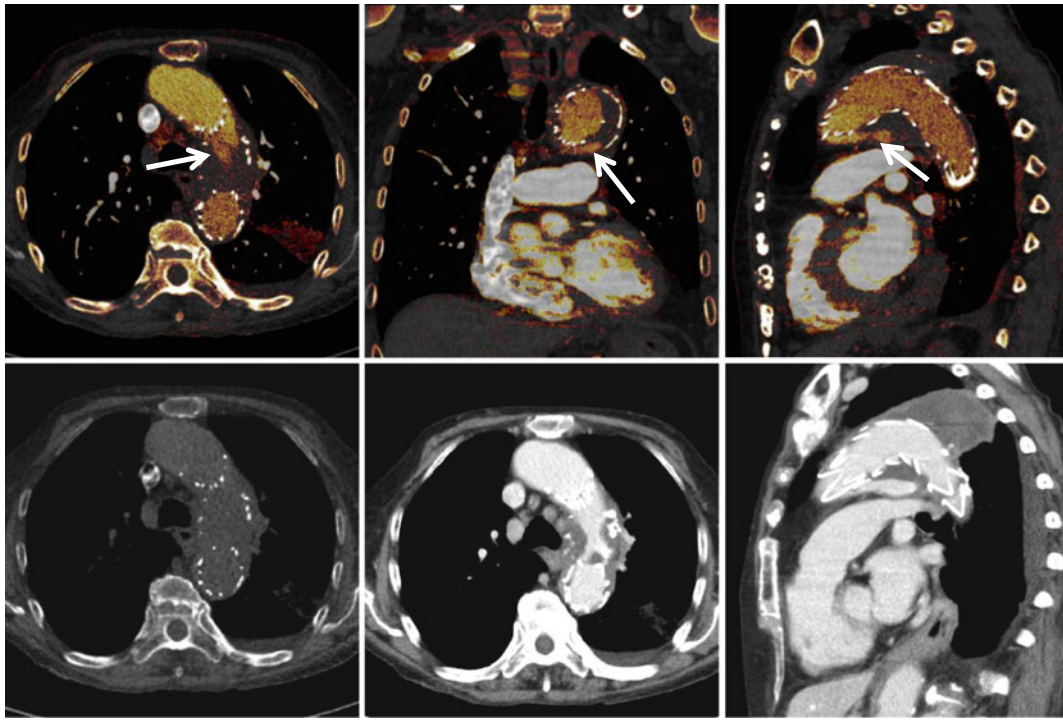

Fig. 19 Dual-energy CT angiography in a 78-year-old female patient 2 months after endovascular repair of a thoracic aortic aneurysm. Arterial phase iodine overlay images (**a**–**c**) demonstrate contrast agent leaking into the aneurysm sac at the proximal end of the stent graft, consistent with a type 1a endoleak (*arrows*). Virtual non-contrast image (**d**) shows correct subtraction of iodine including the endoleak. Venous phase images (**e**, **f**) show progressive accumulation of contrast agent in the aneurysm sac outside the stent graft, confirming the endoleak

been exploited to quantify the calcium concentration in the trabeculous part of vertebra and thus determine bone mineral density (Wichmann et al. 2014). The advantage of this approach over standard quantitative CT for the assessment of bone mineral density is that dual energy can directly quantify calcium concentration without a calibration phantom. Therefore, this evaluation can be employed retrospectively on dual-energy CT datasets performed for another indication.

Conclusions

Dual-energy CT has found numerous promising applications in the thorax (Table 1). The most robust and well-established applications are monoenergetic extrapolation and nonlinear blending techniques to enhance iodine attenuation and improve contrast-to-noise

Table 1 Applications of dual-energy CT in the thorax

Pulmonary angiography
Image optimization using monoenergetic extrapolation and nonlinear blending
Pulmonary perfusion imaging
Pulmonary ventilation imaging
Oncologic imaging
Lung nodule characterization
Assessment of tumor perfusion, therapy response, and nodal staging in lung cancer
Myocardial perfusion imaging
Aortic Imaging
Virtual Non-Contrast Imaging
Image optimization using monoenergetic extrapolation and nonlinear blending
Spine imaging
Detection of bone marrow edema in vertebral fractures
Assessment of bone mineral density

characteristics or reduce artifacts. These algorithms are manageable to use and can easily be integrated into the clinical workflow. There is also ample clinical experience with dual-energy CT pulmonary perfusion imaging demonstrating that it can reliably visualize pulmonary perfusion in a variety of pulmonary conditions, although its interpretation requires some caution and experience. As of today, most other thoracic applications of dual-energy CT are still investigational. More research and clinical experience will show whether they offer true clinical value.

References

Arnoldi E, Lee YS, Ruzsics B et al (2011) CT detection of myocardial blood volume deficits: dual-energy CT compared with single-energy CT spectra. J Cardiovasc Comput Tomogr 5:421–429

Baxa J, Vondrakova A, Matouskova T et al (2014) Dual-phase dual-energy CT in patients with lung cancer: assessment of the additional value of iodine quantification in lymph node therapy response. Eur Radiol 24:1981–1988

Chae EJ, Song JW, Seo JB, Krauss B, Jang YM, Song KS (2008) Clinical utility of dual-energy CT in the evaluation of solitary pulmonary nodules: initial experience. Radiology 249:671–681

Chae EJ, Seo JB, Lee J et al (2010a) Xenon ventilation imaging using dual-energy computed tomography in asthmatics: initial experience. Invest Radiol 45:354–361

Chae EJ, Song JW, Krauss B et al (2010b) Dual-energy computed tomography characterization of solitary pulmonary nodules. J Thorac Imaging 25:301–310

Chae EJ, Kim N, Seo JB et al (2013) Prediction of postoperative lung function in patients undergoing lung resection: dual-energy perfusion computed tomography versus perfusion scintigraphy. Invest Radiol 48:622–627

de Broucker T, Pontana F, Santangelo T et al (2012) Single- and dual-source chest CT protocols: levels of radiation dose in routine clinical practice. Diagn Interv Imaging 93:852–858

Delesalle MA, Pontana F, Duhamel A et al (2013) Spectral optimization of chest CT angiography with reduced iodine load: experience in 80 patients evaluated with dual-source, dual-energy CT. Radiology 267:256–266

Dournes G, Verdier D, Montaudon M et al (2013) Dual-energy CT perfusion and angiography in chronic thromboembolic pulmonary hypertension: diagnostic accuracy and concordance with radionuclide scintigraphy. Eur Radiol. doi:10.1007/s00330-013-2975-y

Flors L, Leiva-Salinas C, Norton PT, Patrie JT, Hagspiel KD (2014) Imaging follow-up of endovascular repair of type B aortic dissection with dual-source, dual-energy CT and late delayed-phase scans. J Vasc Interv Radiol 25:435–442

Fuld MK, Halaweish AF, Haynes SE, Divekar AA, Guo J, Hoffman EA (2013) Pulmonary perfused blood volume with dual-energy CT as surrogate for pulmonary perfusion assessed with dynamic multidetector CT. Radiology 267:747–756

Goo HW, Yu J (2011) Redistributed regional ventilation after the administration of a bronchodilator demonstrated on xenon-inhaled dual-energy CT in a patient with asthma. Korean J Radiol 12:386–389

Goo HW, Chae EJ, Seo JB, Hong SJ (2008) Xenon ventilation CT using a dual-source dual-energy technique: dynamic ventilation abnormality in a child with bronchial atresia. Pediatr Radiol 38:1113–1116

Goo HW, Yang DH, Hong SJ et al (2010) Xenon ventilation CT using dual-source and dual-energy technique in children with bronchiolitis obliterans: correlation of xenon and CT density values with pulmonary function test results. Pediatr Radiol 40:1490–1497

Goo HW, Yang DH, Kim N, Park SI, Kim DK, Kim EA (2011) Collateral ventilation to congenital hyperlucent lung lesions assessed on xenon-enhanced dynamic dual-energy CT: an initial experience. Korean J Radiol 12:25–33

Hachulla AL, Pontana F, Wemeau-Stervinou L et al (2012) Krypton ventilation imaging using dual-energy CT in chronic obstructive pulmonary disease patients: initial experience. Radiology 263:253–259

Hoegl S, Meinel FG, Thieme SF et al (2013) Worsening respiratory function in mechanically ventilated intensive care patients: feasibility and value of xenon-enhanced dual energy CT. Eur J Radiol 82:557–562

Holmes DR 3rd, Fletcher JG, Apel A et al (2008) Evaluation of non-linear blending in dual-energy computed tomography. Eur J Radiol 68:409–413

Hou WS, Wu HW, Yin Y, Cheng JJ, Zhang Q, Xu JR (2014) Differentiation of lung cancers from inflammatory masses with dual-energy spectral CT imaging. Acad Radiol. doi:10.1016/j.acra.2014.10.004

Johnson TR, Thieme SF, Deutsch MA et al (2009) Images in cardiovascular medicine: unilateral pulmonary artery agenesis: noninvasive diagnosis with dual-source computed tomography. Circulation 119:1158–1160

Kang MJ, Park CM, Lee CH, Goo JM, Lee HJ (2010) Focal iodine defects on color-coded iodine perfusion maps of dual-energy pulmonary CT angiography images: a potential diagnostic pitfall. AJR Am J Roentgenol 195:W325–W330

Kawai T, Shibamoto Y, Hara M, Arakawa T, Nagai K, Ohashi K (2011) Can dual-energy CT evaluate contrast enhancement of ground-glass attenuation? Phantom and preliminary clinical studies. Acad Radiol 18:682–689

Kerl JM, Bauer RW, Renker M et al (2011) Triphasic contrast injection improves evaluation of dual energy lung perfusion in pulmonary CT angiography. Eur J Radiol 80:e483–e487

Kim BH, Seo JB, Chae EJ, Lee HJ, Hwang HJ, Lim C (2012a) Analysis of perfusion defects by causes other

than acute pulmonary thromboembolism on contrast-enhanced dual-energy CT in consecutive 537 patients. Eur J Radiol 81:e647–e652

Kim WW, Lee CH, Goo JM et al (2012b) Xenon-enhanced dual-energy CT of patients with asthma: dynamic ventilation changes after methacholine and salbutamol inhalation. AJR Am J Roentgenol 199:975–981

Kim YN, Lee HY, Lee KS et al (2012c) Dual-energy CT in patients treated with anti-angiogenic agents for non-small cell lung cancer: new method of monitoring tumor response? Korean J Radiol 13:702–710

Kong X, Sheng HX, Lu GM et al (2014) Xenon-enhanced dual-energy CT lung ventilation Imaging: techniques and clinical applications. AJR Am J Roentgenol 202:309–317

Koonce JD, Vliegenthart R, Schoepf UJ et al (2014) Accuracy of dual-energy computed tomography for the measurement of iodine concentration using cardiac CT protocols: validation in a phantom model. Eur Radiol 24:512–518

Lee CW, Seo JB, Song JW et al (2011) Evaluation of computer-aided detection and dual energy software in detection of peripheral pulmonary embolism on dual-energy pulmonary CT angiography. Eur Radiol 21:54–62

Lee CW, Seo JB, Lee Y et al (2012) A pilot trial on pulmonary emphysema quantification and perfusion mapping in a single-step using contrast-enhanced dual-energy computed tomography. Invest Radiol 47:92–97

Lu GM, Zhao Y, Zhang LJ, Schoepf UJ (2012) Dual-energy CT of the lung. AJR Am J Roentgenol 199:S40–S53

Meinel FG, Bischoff B, Zhang Q, Bamberg F, Reiser MF, Johnson TR (2012) Metal artifact reduction by dual-energy computed tomography using energetic extrapolation: a systematically optimized protocol. Invest Radiol 47:406–414

Meinel FG, Graef A, Bamberg F et al (2013a) Effectiveness of automated quantification of pulmonary perfused blood volume using dual-energy CTPA for the severity assessment of acute pulmonary embolism. Invest Radiol 48:563–569

Meinel FG, Graef A, Sommer WH, Thierfelder KM, Reiser MF, Johnson TR (2013b) Influence of vascular enhancement, age and gender on pulmonary perfused blood volume quantified by dual-energy-CTPA. Eur J Radiol 82:1565–1570

Meinel FG, Graef A, Thieme SF et al (2013c) Assessing pulmonary perfusion in emphysema: automated quantification of perfused blood volume in dual-energy CTPA. Invest Radiol 48:79–85

Meinel FG, Graef A, Thierfelder KM et al (2014) Automated quantification of pulmonary perfused blood volume by dual-energy CTPA in chronic thromboembolic pulmonary hypertension. Rofo 186:151–156

Nagayama H, Sueyoshi E, Hayashida T, Ashizawa K, Sakamoto I, Uetani M (2013) Quantification of lung perfusion blood volume (lung PBV) by dual-energy CT in pulmonary embolism before and after treatment: preliminary results. Clin Imaging 37:493–497

Nakazawa T, Watanabe Y, Hori Y et al (2011) Lung perfused blood volume images with dual-energy computed tomography for chronic thromboembolic pulmonary hypertension: correlation to scintigraphy with single-photon emission computed tomography. J Comput Assist Tomogr 35:590–595

Nance JW Jr, Henzler T, Meyer M et al (2012) Optimization of contrast material delivery for dual-energy computed tomography pulmonary angiography in patients with suspected pulmonary embolism. Invest Radiol 47:78–84

Pansini V, Remy-Jardin M, Faivre JB et al (2009) Assessment of lobar perfusion in smokers according to the presence and severity of emphysema: preliminary experience with dual-energy CT angiography. Eur Radiol 19:2834–2843

Park EA, Goo JM, Park SJ et al (2010) Chronic obstructive pulmonary disease: quantitative and visual ventilation pattern analysis at xenon ventilation CT performed by using a dual-energy technique. Radiology 256:985–997

Park SJ, Lee CH, Goo JM et al (2012) Quantitative analysis of dynamic airway changes after methacholine and salbutamol inhalation on xenon-enhanced chest CT. Eur Radiol 22:2441–2450

Pontana F, Faivre JB, Remy-Jardin M et al (2008) Lung perfusion with dual-energy multidetector-row CT (MDCT): feasibility for the evaluation of acute pulmonary embolism in 117 consecutive patients. Acad Radiol 15:1494–1504

Remy-Jardin M, Faivre JB, Pontana F et al (2010) Thoracic applications of dual energy. Radiol Clin North Am 48:193–205

Remy-Jardin M, Faivre JB, Pontana F, Molinari F, Tacelli N, Remy J (2014) Thoracic applications of dual energy. Semin Respir Crit Care Med 35:64–73

Renard B, Remy-Jardin M, Santangelo T et al (2011) Dual-energy CT angiography of chronic thromboembolic disease: can it help recognize links between the severity of pulmonary arterial obstruction and perfusion defects? Eur J Radiol 79:467–472

Schmid-Bindert G, Henzler T, Chu TQ et al (2012) Functional imaging of lung cancer using dual energy CT: how does iodine related attenuation correlate with standardized uptake value of 18FDG-PET-CT? Eur Radiol 22:93–103

Sommer WH, Graser A, Becker CR et al (2010) Image quality of virtual noncontrast images derived from dual-energy CT angiography after endovascular aneurysm repair. J Vasc Interv Radiol 21:315–321

Sueyoshi E, Tsutsui S, Hayashida T, Ashizawa K, Sakamoto I, Uetani M (2011) Quantification of lung perfusion blood volume (lung PBV) by dual-energy CT in patients with and without pulmonary embolism: preliminary results. Eur J Radiol 80:e505–e509

Tang CX, Zhang LJ, Han ZH et al (2013) Dual-energy CT based vascular iodine analysis improves sensitivity for peripheral pulmonary artery thrombus detection: an

experimental study in canines. Eur J Radiol. doi:10.1016/j.ejrad.2013.06.021

Thieme SF, Becker CR, Hacker M, Nikolaou K, Reiser MF, Johnson TR (2008) Dual energy CT for the assessment of lung perfusion--correlation to scintigraphy. Eur J Radiol 68:369–374

Thieme SF, Hoegl S, Nikolaou K et al (2010) Pulmonary ventilation and perfusion imaging with dual-energy CT. Eur Radiol 20:2882–2889

Thieme SF, Graute V, Nikolaou K et al (2012) Dual Energy CT lung perfusion imaging – correlation with SPECT/CT. Eur J Radiol 81:360–365

Varga-Szemes A, Meinel FG, De Cecco CN, Fuller SR, Bayer RR 2nd, Schoepf UJ (2015) CT myocardial perfusion imaging. AJR Am J Roentgenol 204:487–497

Vliegenthart R, Pelgrim GJ, Ebersberger U, Rowe GW, Oudkerk M, Schoepf UJ (2012) Dual-energy CT of the heart. AJR Am J Roentgenol 199:S54–S63

Wang CK, Tsai JM, Chuang MT, Wang MT, Huang KY, Lin RM (2013) Bone marrow edema in vertebral compression fractures: detection with dual-energy CT. Radiology 269:525–533

Wichmann JL, Booz C, Wesarg S et al (2014) Dual-energy CT-based phantomless in vivo three-dimensional bone mineral density assessment of the lumbar spine. Radiology 271:778–784

Zhang LJ, Lu GM (2012) Takayasu's arteritis involving the pulmonary arteries: evaluation by quantitative dual-energy computed tomographic pulmonary angiography. Eur Heart J 33:928

Zhang LJ, Zhao YE, Wu SY et al (2009) Pulmonary embolism detection with dual-energy CT: experimental study of dual-source CT in rabbits. Radiology 252:61–70

Zhang LJ, Zhou CS, Lu GM (2012) Dual energy computed tomography demonstrated lung ventilation/perfusion mismatch in a 19 year-old patient with pulmonary embolism. Circulation 126:2441–2443

Zhang LJ, Yang GF, Wu SY, Xu J, Lu GM, Schoepf UJ (2013a) Dual-energy CT imaging of thoracic malignancies. Cancer Imaging 13:81–91

Zhang LJ, Zhou CS, Schoepf UJ et al (2013b) Dual-energy CT lung ventilation/perfusion imaging for diagnosing pulmonary embolism. Eur Radiol 23:2666–2675

CT Angiography of the Thoracic Aorta

Geoffrey D. Rubin

Abstract

CT angiography is the primary tool for thoracic aortic assessment. It offers the knowledgeable interpreter the ability to assess the aortic lumen, wall, and branches in a broad spectrum of aortic abnormalities, to plan and evaluate surgical and transluminal aortic treatment, and to assess the relationships between aortic abnormalities and adjacent pulmonary, mediastinal, and chest wall structures (Rubin et al. 2014). Technical developments that have emerged over the past 10 years have allowed reliable cardiac imaging, which, while treated comprehensively in separate chapters, is highly relevant to thoracic aortic assessment owing to the importance of cardiac analysis in the setting of aortic disease. The goal of this chapter is to review the technical factors that must be considered when acquiring and interpreting thoracic aortic CT angiograms as well as the range of abnormalities for which CTA can be valuable.

1 CT Technique

Since publication of the first edition of this book, CT has undergone extensive technical enhancements that have improved the quality and expanded the applicability of thoracic CT angiography. These include the widespread availability and routine use of ≥64 detector rows, faster gantry rotation, multiple x-ray sources, iterative reconstruction, and multispectral or dual-energy imaging (Rubin et al. 2014). The details of these technologies are covered in other portions of this book, but in brief, they have resulted in substantial improvements in image quality, reduced radiation exposure, and reduced iodinated contrast medium requirements since the first edition in the early 2000s. Despite these tremendous gains, the basic technique for performing thoracic aortic CTA is unchanged.

The first step in performing thoracic aortic CTA is to determine the anatomic coverage required to assess the clinical question. At a minimum, the initiation point of the CT scan should be at the base of the neck so that the proximal aspect of the common carotid and vertebral arteries is included within the CT scan. Inferiorly, coverage should extend to include the origin of the celiac axis. The inclusion of the supra-aortic branches is

G.D. Rubin, MD, MBA, FACR
Department of Radiology, Duke University School of Medicine, Durham, NC, USA
e-mail: grubin@duke.edu

U.J. Schoepf, F.G. Meinel (eds.), *Multidetector-Row CT of the Thorax*, Medical Radiology,
DOI 10.1007/978-3-319-30355-0_16

important when lesions involving the aortic arch extend into these brachiocephalic branches, which commonly occurs in the setting of both aneurysmal disease and aortic dissection. The purpose of including the celiac origin is that lesions of the distal thoracic aorta can be accurately localized relative to this anatomic landmark, which can greatly facilitate planning of endovascular and open repair. There may be some instances when additional anatomic coverage is necessary. For example, in the setting of acute aortic dissection, frequent imaging through the abdomen and pelvis is necessary due to signs and symptoms of diminished blood flow to the abdominal viscera or lower extremity. Similarly, some disease processes may warrant inclusion of portions of the upper extremities particularly when assessing for sources of embolization to the hands. Finally, occasionally a greater degree of anatomic coverage to include the entirety of the carotid arterial circulation may be warranted, particularly in the setting of assessment of large vessel artertitis and aortic dissection associated with symptoms of cerebral ischemia.

1.1 Unenhanced Scans

Defining the scan acquisition range is often accomplished using an anteroposterior scout radiographic projection. Nevertheless, there are several reasons why acquiring unenhanced CT sections prior to performing the CT angiogram is valuable. The principal reason for a preliminary unenhanced scan is concern for intramural or periaortic blood. Unenhanced scans are also useful for mapping mural calcium and differentiating it from iodine enhancement. Dual-energy techniques have been proposed for the identification of intramural hemorrhage or mural calcium and their separation from iodinated contrast material enhancement. While this strategy may one day prove valuable for simplifying CT acquisitions and eliminated an unenhanced scan, data published to date suggest that dual-energy CT approaches are not yet sufficiently sensitive for the detection of intramural hemorrhage and that unenhanced scans remain the standard for detecting extraluminal blood (Lemos et al. 2014).

Another reason to obtain unenhanced images is to assure that the full extent of aortic abnormality is included in the CT angiogram. This of course necessitates that the abnormality is visible on the unenhanced scans. An example of this principle would be the assessment of an incidental abdominal aorta for aneurysmal disease in the setting of thoracic aortic aneurysm. The acquisition of unenhanced scans will increase the radiation exposure associated with the examination and should be factored into the decision for additional scans or for extending the scan range. One can reasonably argue that adjacent anatomical territories can be imaged using the CTA acquisition without a preliminary assessment of unenhanced images. The decision to obtain unenhanced images to assure that the coverage of the CTA is sufficiently comprehensive ultimately will depend upon patient specific factors and local CT practice.

1.2 Contrast Material

CT angiography depends upon an effectively sized and timed iodinated contrast medium injection. The iodine dose should be sufficient to assure adequate aortic enhancement and will depend upon the duration of the CT scan, the patient's physiology, and their size. While it is appealing to set a specific enhancement target, the ideal degree of aortic enhancement will vary with the size of the patient. Because the clarity of arterial depiction relates to the ratio of contrast to noise, the increased image noise encountered with larger subjects typically requires greater aortic enhancement.

Prior to performing the CT angiogram, the iodinated contrast administration protocol must be determined. As a general rule, we do not perform CT angiography at a flow rate less than 3 ml/s and for thoracic aortic CT angiograms. Larger patients may require injection rates of up to 6 ml/s. The duration of the bolus should be equivalent to the duration of the CT scan plus 8 s, and therefore the volume of contrast required is determined by multiplying this calculated bolus duration by the flow rate. We have found that a volume of at least 75 ml of iodinated contrast medium (≥350 mg of iodine/ml) is necessary for reliable opacification, although recent studies of iterative reconstruction coupled with low peak kilovoltage suggest that lower iodine dosing is

feasible (Zhang et al. 2015). This volume of contrast medium at the recommended flow rate is readily delivered through a 20-gauge antecubital intravenous catheter. Because highly attenuative undiluted contrast medium within the in-flowing veins can obscure adjacent structures, we prefer to perform thoracic aortic CT angiography through a right antecubital venous source to avoid opacification of the left brachiocephalic vein, which can substantially obscure the origins of the brachiocephalic, left common carotid, and left subclavian arteries. A saline flush of 30–50 ml is also helpful to maximize arterial opacification and reduce perivenous artifact.

Another critical step in optimizing contrast medium delivery is the determination of the scan delay time following initiation of the contrast medium bolus. In the past, we relied upon a preliminary injection of 15 mL of iodinated contrast medium coupled with serial CT sections acquired within the proximal descending aorta to obtain a time-attenuation curve. We selected the time from the initiation of the injection to the peak of this curve plus 8 s as the scan delay for the CT angiogram. The availability of automated scan-triggering capabilities on the CT scanner has led us to abandon this approach. We have found this direct method of visualizing aortic enhancement to be the most reliable method for achieving consistently high-quality CT angiograms (Fig. 1). A much deeper treatment of the topic of contrast material dosing and deliver can be found in Chapter 3.

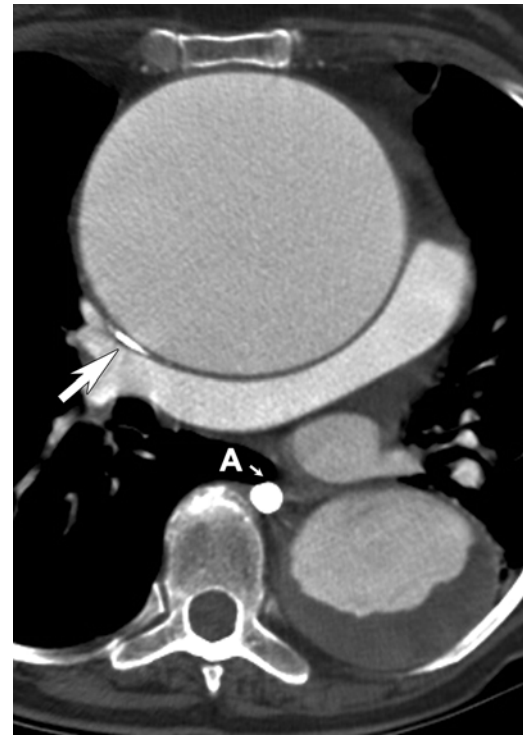

Fig. 1 Transverse CT section demonstrates 11 cm ascending aortic aneurysm compressing the superior vena cava (*arrow*). Redirection of flow down the azygos vein (A) will delay the arrival of the contrast medium into the heart, which occurs through lumbar veins that drain into the renal veins and inferior vena cava. While bolus monitoring allowed this scan to be triggered 32 s after the initiation of the right antecubital intravenous injection, slow flow through a capacious ascending aorta results in a lesser degree of enhancement within a descending aortic aneurysm

1.3 CTA Acquisition

Most thoracic CT angiograms are acquired with a continuous spiral acquisition using the fastest gantry rotation available. The pitch of the scan will vary with the CT scanner configuration as discussed in Chapter 4. For scanners with detector widths of ≥280 mm, a single or two contiguous acquisitions with the table stationary may be preferred.

Because the aorta undergoes both translation and expansion with each cardiac systole, blurring and misregistration artifacts are commonly observed at the aortic root and in the ascending aorta. The magnitude of these artifacts diminishes with wider detectors and higher temporal resolution scans; however, electrocardiographic (ECG) gating is required to eliminate them completely. Key considerations for their use in thoracic aortic CT angiography related to concerns over radiation exposure and the importance of high-quality images during only a portion or the entirety of the cardiac period. These issues will drive decisions for prospective triggering or retrospective gating as well as the use of x-ray tube current pulsing for retrospectively gated scans. These methods are described fully in Chapter 4.

The CT angiogram should be performed within a single breath-hold. If breath-holding is not possible due to mechanical ventilation of the patient or extreme dyspnea, then attempts should be made to avoid sudden gasps for air by

allowing the patient to breathe quietly throughout the acquisition rather than attempting a breath-hold that cannot be completed.

For the vast majority of CT angiograms, an arterial phase acquisition is sufficient; however, for the assessment of stent-graft repair of aortic aneurysm, delayed views can be very important to assess for endoleak (Rozenblit et al. 2003; Hiatt and Rubin 2004). We typically acquire these views 70 s after the initiation of the arterial phase acquisition and limit the scan coverage to the region of the stent graft.

1.4 Reconstruction

Thoracic aortic CT angiography should be reconstructed with a nominal section thickness of 1.5 mm or less (Fig. 2). The decision to use submillimeter section thickness depends upon the application and size of the patient, but for many applications, 1–1.5 mm thick sections are sufficient. Applications that might benefit from submillimeter section thickness include assessments where small vessels such as intercostal arteries and other chest wall arteries are important to assess. The ability to improve the assessment of smaller arteries using submillimeter sections should be considered within the context of noise and other artifacts that worsen with thin-section reconstruction.

The reconstruction field of view should be minimized to only include the relevant arterial anatomy and typically ranges between 25 and 30 cm. When reconstructing with filtered back projection, we usually use a soft or standard reconstruction algorithm for CT angiograms as these reconstruction algorithms minimize noise in the data, which

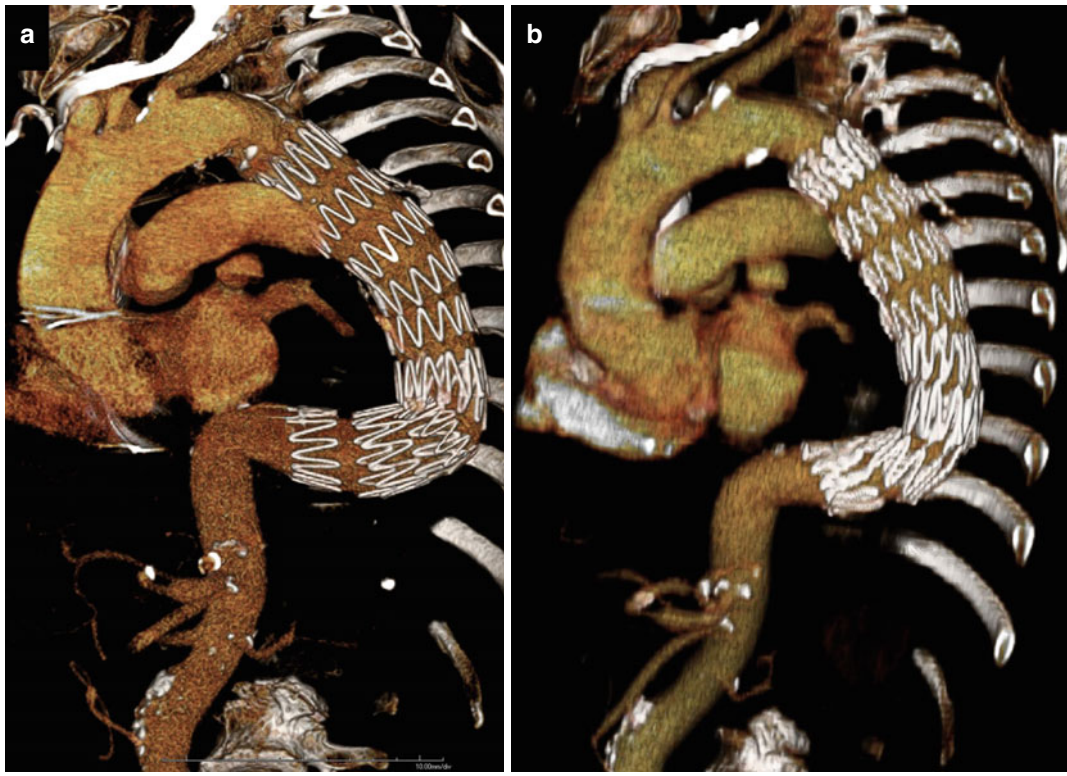

Fig. 2 Key to the effective interpretation of CT angiograms is an ability to reformat and rendering them through any orientation while preserving a high degree of clarity. This begins with thin (≤1.5 mm thick) CT sections (**a**). Renderings derived from thicker sections, in this case 3 mm, will suffer from image degradation and will have limited clinical value (**b**)

greatly facilitate the creation of 3D views. Because of the benefits toward reducing noise in reconstructed images, iterative reconstruction has replaced filtered back projection as the primary reconstruction technique for CT scanning (Zhang et al. 2015; Willemink et al. 2013; Hansen et al. 2014). The rapid evolution of these methods together with the unique qualities of different manufacturers' implementations makes it difficult to offer specific recommendations on optimizing iterative reconstruction for thoracic CT angiography. Iterative reconstruction in thoracic CT is discussed in greater detail in Chapter 2.

The interpretation of thoracic aortic CT angiograms is greatly facilitated by the use of a workstation to perform and flexibly migrate between viewing primary transverse reconstructions and alternative reformations and renderings. When viewing cross sections reconstructed from CT angiograms, substantial variations in the degree of aortic enhancement require customization of window width and level settings. It is important to adjust the display setting to ensure that the aortic lumen does not appear to be white to facilitate discrimination of luminal enhancement from mural calcifications.

1.5 Image Display and Rendering

Transverse sections viewed in a stacked mode are the mainstay of thoracic CTA interpretation; however, we find the use of curved planar reformations and volume renderings to be particularly useful for assessing the thoracic aorta. Curved planar reformations allow visualization of the entirety of the thoracic aorta in a single image. The resulting image is a cross section that conforms to the median centerline of the aortic lumen, and thus the wall of the aorta is visible together with the lumen and its contents. The relationship of intimal flaps, mural thrombus, atheroma, or hematoma to branch ostia can be well depicted relative to the flow lumen and branch ostia, and the interior of stents or stent grafts can be assessed for stenosis from neointima or for branch origin stenosis due to overlying graft material (Raman et al. 2002).

Of particular utility are orthogonal reformations created perpendicular to the aortic centerline. These cross sections provide a basis for characterizing the size of the aortic lumen and outer wall free from elongation manifest in cross sections that are not perpendicular to the central axis of the vessel (Rubin et al. 1998; Rudarakanchana et al. 2014). While this statement should be uniformly true for assessing the aortic lumen, there are circumstances where a centerline derived from the luminal counter does not specifically conform to the central axis of the outer wall of the aorta. These circumstances typically occur in regions with asymmetries in wall thickening. In these instances, the obliquity of automatically calculated "orthogonal cross sections" may require adjustment.

Volume renderings are most useful for displaying surface properties of the aorta and for contextualizing the aorta and its branches with adjacent structures. There are many different versions and interfaces for VR, but the general approach is that all voxel values are assigned an opacity level that varies from total transparency to total opacity. This opacity function can be applied to the histogram of voxel values as a whole or to regions of the histogram that are classified as specific tissue types. With the latter approach, rectangular or trapezoidal regions are selected that correspond to the range of attenuation values for a structure. Volume renderings can provide excellent summarizing presentations of complex pathology for both referring physicians and for the patient (Fishman et al. 2006).

Maximum intensity projections while a common tool for many thoracic CT applications are not particularly useful when assessing the thoracic aorta. Aortic branch ostia are often obscured overlapping aortic lumen, and details in the wall of the aorta are not displayed effectively on maximum intensity projections (Fig. 3).

1.6 Common Artifacts in Thoracic Aortic CTA

Two artifacts result in the majority of interpretative limitations of thoracic aortic CTA: perivenous

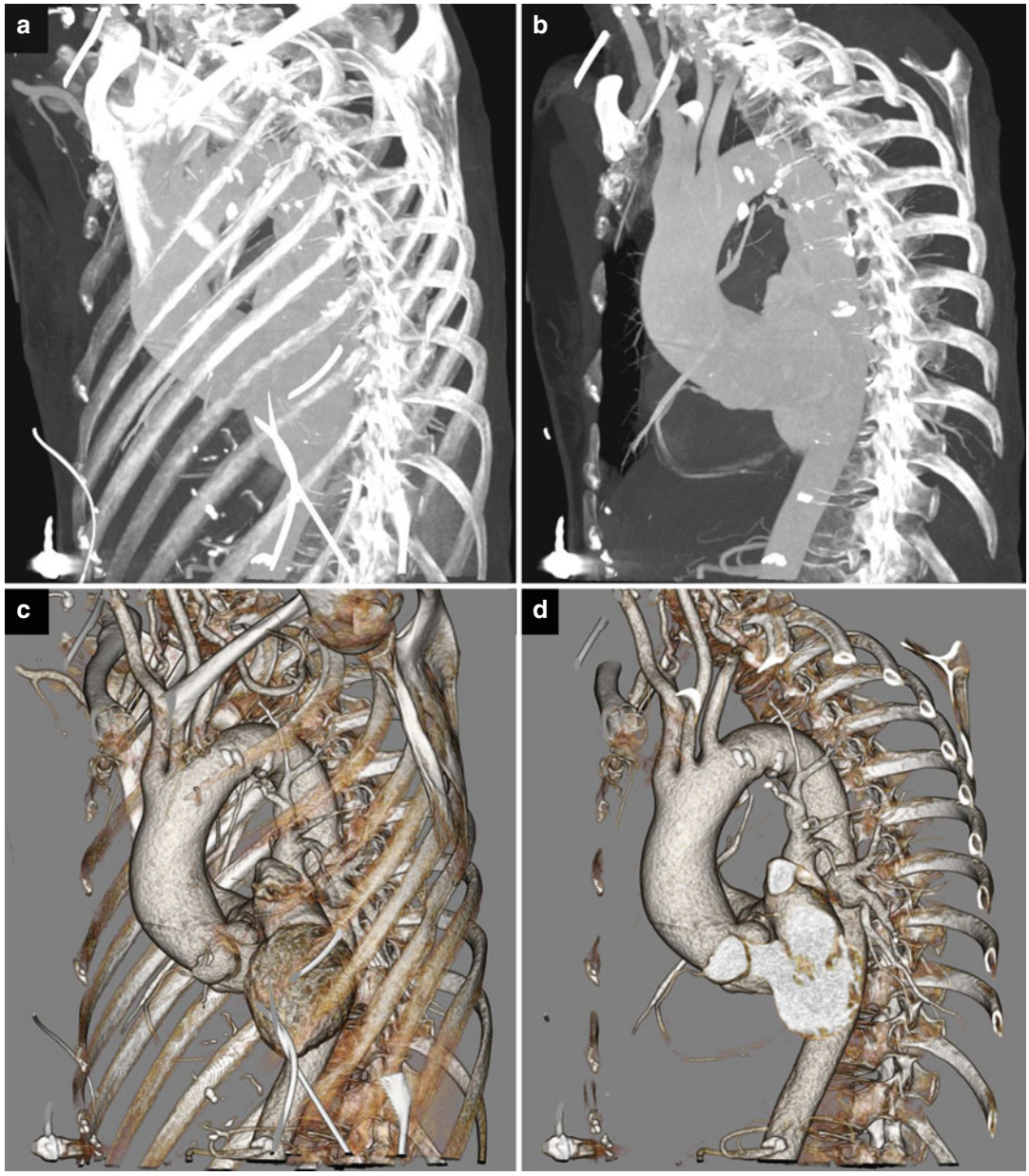

Fig. 3 (**a**) Left posterior oblique maximum intensity projection of the full imaging volume from a thoracic aortic CT angiogram shows how the chest wall, particularly the ribs, obscures underlying detail. (**b**) Reducing the volume to an 8-cm thick slab centered upon the aorta eliminated the overlying chest wall, but the heart and descending aorta and the origins of the brachiocephalic and left common carotid arteries merge into a single indistinguishable region. (**c**) Volume rendering of the full CT volume from the same view as in (**a**) provides greater context for the rendered anatomy. Because structures closer to the viewpoint prevent visualization of structures deeper in the volume, the right ribs do not interfere with ascending aortic visualization. (**d**) Volume rendering of the same slab as in (**b**) shows how restriction of the rendering to structures contained within a slab eliminated overlying chest wall structures, but also reveals the origins of the brachiocephalic and left common carotid arteries with greater clarity than seen with the maximum intensity projection

streaks and arterial pulsation. Both of these artifacts tend to have their greatest influence on the visualization of the ascending aorta and therefore are particularly important to bear in mind when assessing patients suspected of aortic dissection.

Perivenous streaks are likely caused by a combination of beam hardening and motion caused by transmitted pulsation in veins carrying undiluted contrast medium to the heart. Strategies designed to minimize this artifact include the use of dilute contrast medium solutions (Rubin et al. 1996), caudal to cranial scan direction, and femoral venous access. In practice, perivenous streaks are rarely confused with intimal dissection in the ascending aorta as their orientation typically varies from section to section and they typically extend beyond the confines of the aortic wall. The most problematic region for perivenous artifacts is the origin of the supra-aortic branches adjacent to an opacified left brachiocephalic vein. Perivenous streaks in this region can mask extension of intimal flaps into these branches as well as occlusive disease caused by atherosclerotic plaque at their origins.

Arterial pulsation has been recognized as a cause of false-positive aortic dissection on CT angiograms. Pulsation artifacts are substantially reduced with increasing table speed and eliminated with electrocardiographic triggering or gating.

2 Acute Aortic Syndromes

The accurate detection and evaluation of acute aortic syndrome is one of the radiologist's most important and immediately impactful opportunities to improve human health. Acute aortic syndrome is often a clinical emergency and a situation that demands accurate radiologic diagnosis and intervention to provide lifesaving care. The diagnosis of acute aortic syndrome has evolved significantly over the last two decades, evolving from an arteriographic diagnosis to a diagnosis based upon multi-detector CT angiography and, to a limited extent, MRI. With the advent of these new techniques for diagnosis, investigators have revisited the questions and pathologies surrounding acute aortic syndromes.

2.1 Anatomic and Pathological Considerations

Acute aortic syndromes are principally diseases of the aortic wall. As a result, it is useful to understand some fundamental pathological features of the aortic wall in order to categorize the acute aortic syndromes.

The aorta is composed of three layers. From inner to outer, they are the intima, media, and adventitia. The intima is made up of a single layer of flattened epithelial cells with a supporting layer of elastin-rich collagen, fibroblasts, and myointimal cells. The latter myointimal cells tend to accumulate lipid with aging, resulting in intimal thickening which is the earliest sign of atherosclerosis. The majority of the aortic wall thickness is composed of the media which itself is broad and elastic with concentric fenestrated sheets of elastin, collagen, and sparsely distributed smooth muscle fibers. The predominance of elastin arrayed as elastic lamina is a reflection of the fact that the aorta and the pulmonary arteries are considered to be the only elastic arteries of the body. Because the aorta and the pulmonary arteries receive the entirety of the cardiac output, they undergo substantial deformation in order to accommodate large volume changes with each cardiac contraction. The remaining arteries of the body are considered muscular arteries with a paucity of elastin and predominance of smooth muscle, allowing for the body to regulate regional blood flow. The boundary between the intima and media is not readily defined, and the division between the intima and media is defined histologically at the internal elastic lamina, which represents the innermost of the many elastic lamellae within the aortic media. The adventitia lacks elastic lamellae and is predominantly composed of loose connective tissue and blood vessels or vasa vasorum.

Anatomically, the aorta can be divided longitudinally into five zones—the aortic root, ascending thoracic aorta, aortic arch, descending

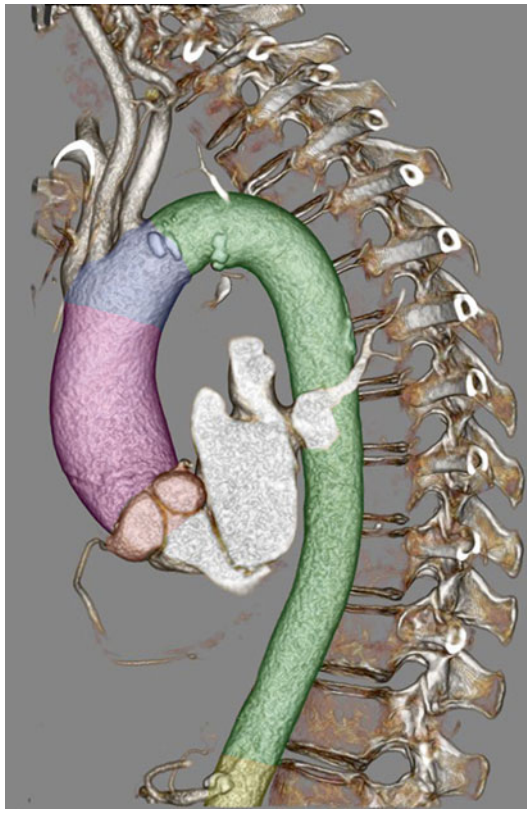

Fig. 4 Left posterior oblique volume rendering showing the locations of the aortic root (*red*), ascending aorta (*purple*), aortic arch (*blue*), descending aorta (*green*), and abdominal aorta (*yellow*). Aortic dissection is considered to be type B if it does not involve the ascending aorta, and therefore, while typically originating in the descending aorta, it can originate from or extend proximally to the aortic arch

thoracic aorta, and abdominal aorta (Fig. 4). Acute aortic syndromes can involve any of these five anatomic zones; however, they only rarely originate within the abdominal aorta. An important principle in the management of acute aortic syndromes is the classification of lesions into Stanford type A or type B. Type A lesions, defined as those involving the ascending aorta or aortic root, are considered lesions that demand urgent surgical intervention with replacement of the diseased ascending aortic segment. The rationale for this urgent intervention is a high risk of aortic rupture, which can lead to pericardial tamponade or frank exsanguination (Fig. 5). Type B lesions do not involve the ascending aorta and as a result can occur within the aortic arch or the descending thoracic aorta. If there is evidence for active aortic rupture, then these patients too should be referred for urgent surgical intervention; however, in the absence of active bleeding, they are typically managed with blood pressure reduction and regular monitoring to assess the evolution of aortic dimension and disease extension.

2.2 Definitions and Classifications

Collectively, acute aortic syndromes represent life-threatening conditions that are associated with a high risk of aortic rupture and sudden death (Vilacosta and Román 2001). The typical presentation is the sudden onset of chest pain, which may be accompanied by signs or symptoms of hypoperfusion or ischemia to distal organs, extremities, or brain.

Traditionally, acute aortic syndromes are categorized as aortic dissection, intramural hematoma, and penetrating atherosclerotic ulcer. There are two limitations to this traditional classification. One concerns the omission of a rupturing true aortic aneurysm, as the nature of the presentation and the severity of the event are similar to that of the other acute aortic syndromes. The other limitation is that IMH, defined as a stagnant intramural collection of blood, can be observed in the setting of AD, PAU, and rupturing aortic aneurysm. As such, it is a feature or characteristic associated with any of the acute aortic syndromes, reflecting degradation of the aortic wall as a harbinger of impending aortic rupture.

In consideration of these two points, a new classification scheme has been proposed based upon the primary location of the lesion within the aortic wall (Fleischmann et al. 2008). In this new classification scheme, there are three pathological entities: AD, PAU, and rupturing aortic aneurism. These three entities are differentiated by the fact that AD principally involves the aortic media, PAU originates within the aortic intima, and aortic aneurysm is a disease of all three layers. The presence of IMH is an observation or epiphenomenon to be applied to any of these three fundamental pathologies. In the setting of an isolated IMH without PAU, "noncommunicating

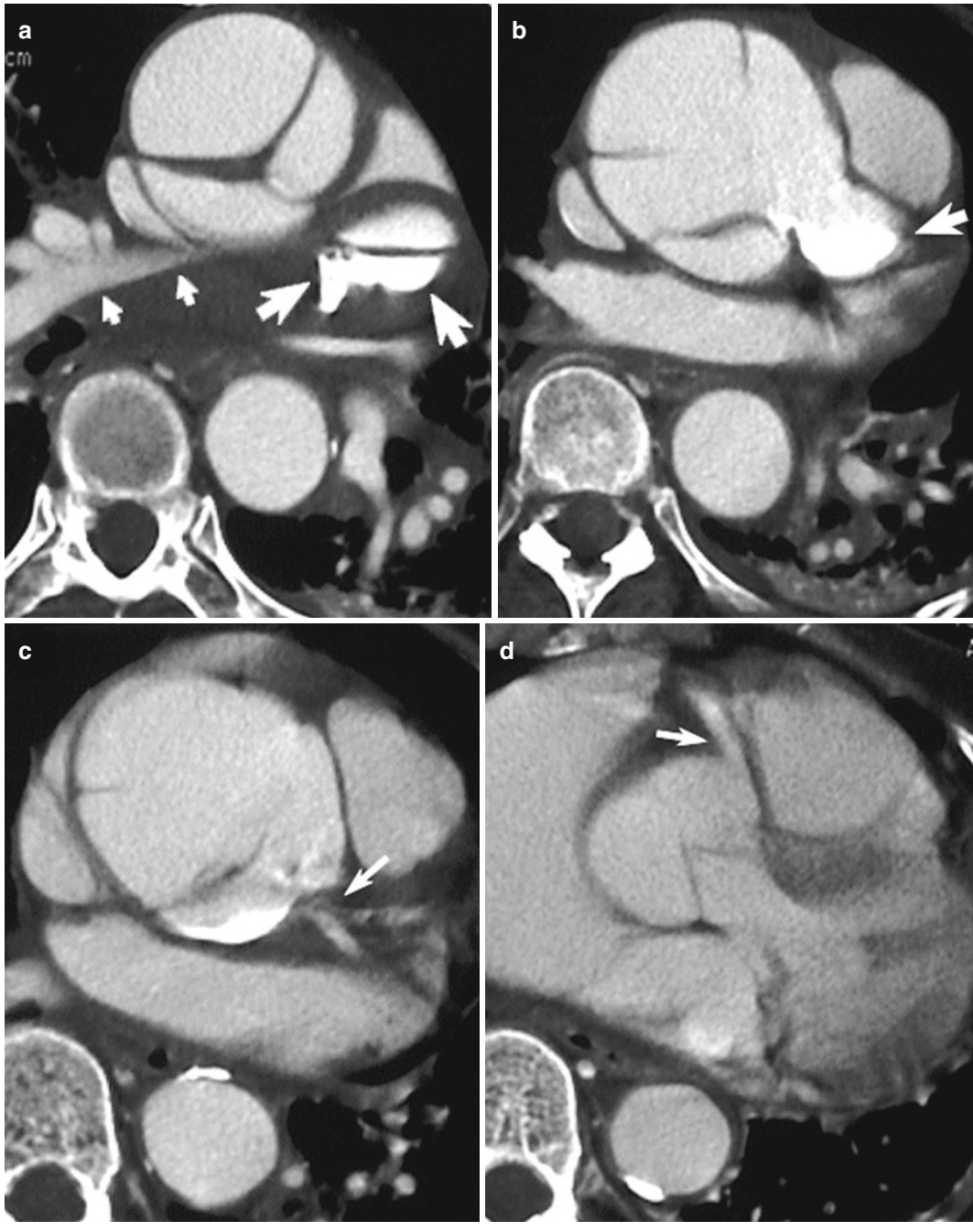

Fig. 5 (**a**, **b**) Transverse CT sections in a patient with acute chest pain demonstrate a type A aortic dissection with posteromedial rupture of the proximal ascending aorta and active extravasation of arterial contrast medium into the mediastinum through a pseudoaneurysm (*larger arrows*). A mediastinal hematoma is resulting in substantial right pulmonary arterial compression (*small arrows*). (**c**) The original left main coronary artery could be visualized one section below this image, which demonstrates the proximal left anterior descending and circumflex coronary arteries (*arrow*) originated immediately below the pseudoaneurysm from the left sinus of Valsalva. (**d**) The right coronary artery origin is clearly uninvolved as is the aortic valve

dissection" has been proposed as a descriptor, although most people will associate the term "IMH" with this lesion.

2.3 Aortic Dissection

Aortic dissection (AD) is characterized by a separation of the aortic media, creating an intimal medial complex, which separates from the remaining aortic wall. Blood flowing between the intimal medial complex or flap and the remaining wall is considered to be within a false lumen, whereas blood flow bounded by the intima is considered to be within a true lumen. Multiple communication points can be observed between the true and false lumen. The proximal most communication is considered to be the "entry tear" with the remaining points of communication considered to be "exit tears," implying flow directionality from true to false lumen and from false to true lumen, respectively. The actual incidence of AD is difficult to define, since AD involving the ascending aorta is often a fatal disease and patients frequently die prior to hospitalization. Likewise, AD is sometimes misdiagnosed on initial presentation, and these patients are also at risk for death outside of the hospital. Nevertheless, various population-based studies suggest that the incidence of AD ranges from 2 to 4 case per 100,000 patients (Hiratzka et al. 2010).

CT is an excellent tool for visualizing the origin and extent of the flap, including proximal extension into the root of the aorta, where electrocardiographically gated acquisitions facilitate intracoronary extension and extension to the aortic valve annulus. Differential flow in the true and false lumina can result in the spurious appearance of a thrombosed false lumen when scan delay is based upon a timing study directed to the true lumen of the aorta. In the setting of suspected aortic dissection, bolus timing should be performed just below the aortic arch, where transverse cross sections of the distal ascending and proximal descending aorta can be evaluated. A region of interest is placed in both the true and the false lumen and two curves are generated. A delay time that assures some false luminal opacification is selected and the bolus duration then extended by the number of seconds between the true luminal peak and the selected delay time. This assures true and false luminal opacification for the duration of the CT acquisition. When considering alternative visualization techniques in the setting of aortic dissection, it should not be surprising that MIPs are limited, as they will not demonstrate the intimal flap unless it is oriented perpendicular to the MIP. Curved planar reconstructions can be very useful for displaying the flap within the center of the vessel, while shaded surface displays depict the interface of the intimal flap with the aortic wall.

Clinically relevant aortic branch involvement may involve branches to the head and neck or intra-abdominal where mesenteric ischemia, renal insufficiency, and lower extremity claudication indicate involvement of mesenteric, renal, and iliac arteries, respectively. This latter condition of aortic branch occlusion due to either collapse of the flap over the branch origins or collapse of the true lumen within the aorta proximal to the occlusion results in the restriction of blood flow to aortic branches originating from the true lumen (Fig. 6).

Fig. 6 An uncommon complication of type A dissection results from mobilization and intussusception of the entire intimomedial complex with associated occlusion of aortic arch branches. This 48-year-old hypertensive man was found unconscious with a head CT that revealed diffuse cerebral edema. (**a**) Coronal oblique and (**b**) transverse CT sections show a focal intimomedial flap in the posterior sinus of Valsalva. Aside from enlargement of the ascending aorta (**c**), the mid-ascending aorta shows minimal abnormality. The true lumen is collapsed within the descending aorta (*arrows*). (**d**) A large mass of intimomedial complex (IMC) is seen in the aortic arch. (**e**) The proximal left common carotid and subclavian arteries (x) are completely occluded. A linear filling defect within the brachiocephalic artery indicates extension of the dissection. (**f**) The relationship of the IMC (*black arrows*) with the occluded left common carotid (*large white arrow*) and subclavian (*small white arrow*) arteries is seen best with an oblique sagittal reformation

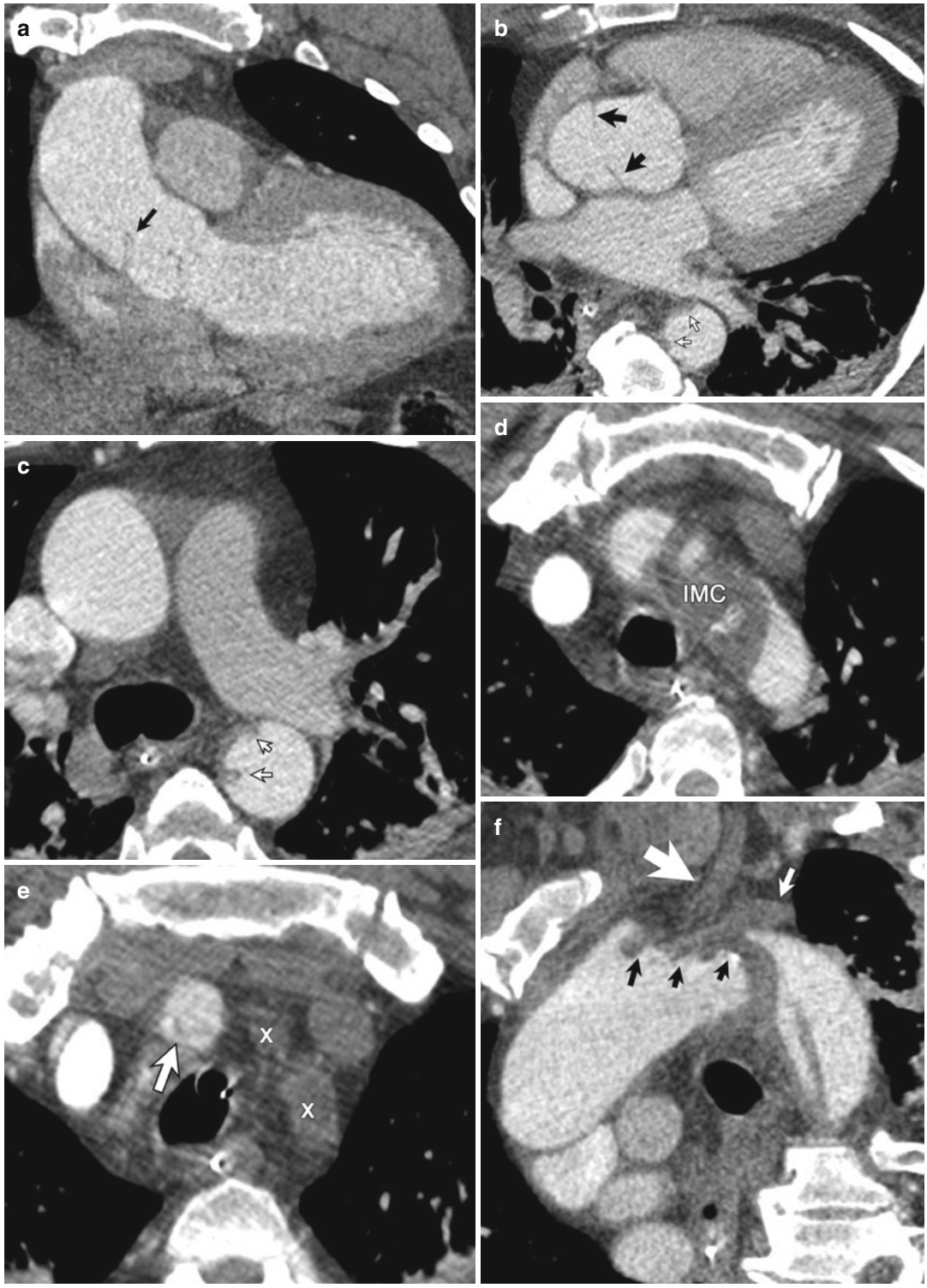
a
b
c
d
IMC
e
X
X
f

2.4 Intramural Hematoma

Intramural hematoma (IMH) is an entity that was first described approximately 25 years ago as a stagnant collection of blood within the aortic wall (Evangelista et al. 2005). The common association of IMH with pathologically detected intimal defects led to the hypothesis that most are sequelae of penetrating atherosclerotic ulcer. An alternative cause of IMH, typically invoked in the absence of an intimal defect, is rupture of the vasa vasorum. This hypothetical cause of IMH has never been definitively proven. IMH is treated similar to dissections in terms of initial diagnosis as well as clinical management. While most IMH occur in the descending thoracic aorta (Fig. 7), in-hospital mortality is greatest for those with type A lesions. The imaging features vary depending on the amount of blood accumulated in the wall of the aorta, but typically the normal wall measures less than 3 mm in thickness. The natural history of IMH is variable and characterized by small clinical series only. Roughly 15–20 % of them will progress to aortic dissection (Fig. 8); 20 % will die during their index hospital admission predominately from aortic rupture. The remainder will resolve with subsequent dissection or aneurysm developing in approximately 10 % (Evangelista et al. 2005). The mortality for patients with IMH involving the ascending aorta is similar to that of classic dissection, and therefore these patients are treated as though they have a classic AD with emergent surgery. On the other hand, IMH involving the descending thoracic aorta can be followed, given appropriate therapy for hypertension.

2.5 Penetrating Atherosclerotic Ulcer

Penetrating atherosclerotic ulcer (PAU) is a condition that originates with atherosclerotic plaque involvement of the aorta, primarily the descending thoracic aorta. As the plaque evolves, the ulceration "penetrates" through the internal elastic lamina into the media of the aortic wall. Overtime the PAU may extend through all three layers of the aortic wall to form a false or pseudoaneurysm. A finding of PAU does not necessarily imply the existence of an acute aortic syndrome. Signs of IMH or extravasation indicate acuity.

3 Acute Aortic Trauma

Aortic injury is an important source of mortality for patients with blunt chest trauma. The most common cause of aortic injury is motor vehicle collision. Three trends in the diagnosis and management of blunt aortic trauma over the past 15 years are worth emphasizing. Diagnosis is now accomplished using CT angiography as opposed to catheter-based aortography; an increasing incidence and decreasing mortality of aortic injury following chest trauma appear to relate to an increase in imaging accompanied by the diagnosis of milder forms of aortic injury; and treatment has shifted from open to endovascular repair (de Mestral et al. 2013). These changes have been accompanied by a statement by the Society for Vascular Surgery supporting initial nonoperative management for intimal tears and endovascular repair reserved for injuries that progress (Lee et al. 2011).

Effective diagnosis and characterization of blunt aortic injury do not require special imaging techniques beyond proper CT angiography with thin-section reconstruction (Fig. 9). Positions of relative aortic immobility are particularly susceptible to aortic injury from blunt trauma. The interpreter should scrutinize the region of the aortic isthmus. Owing to its tether to the pulmonary artery via the ligamentum arteriosum, it is the most common location where aortic injury is encountered at CT angiography. Other key locations are the aortic root and the aorta at the aortic hiatus of the diaphragm. While a common site of acute aortic injury, aortic root injury is rarely encountered at CT angiography due to its high mortality in the immediate post-injury period.

The spectrum of direct aortic observations encountered in acute aortic injury includes isolated intimal tears, intimal tear with pseudoaneurysm, and intraluminal thrombus (Ait Ali Yahia

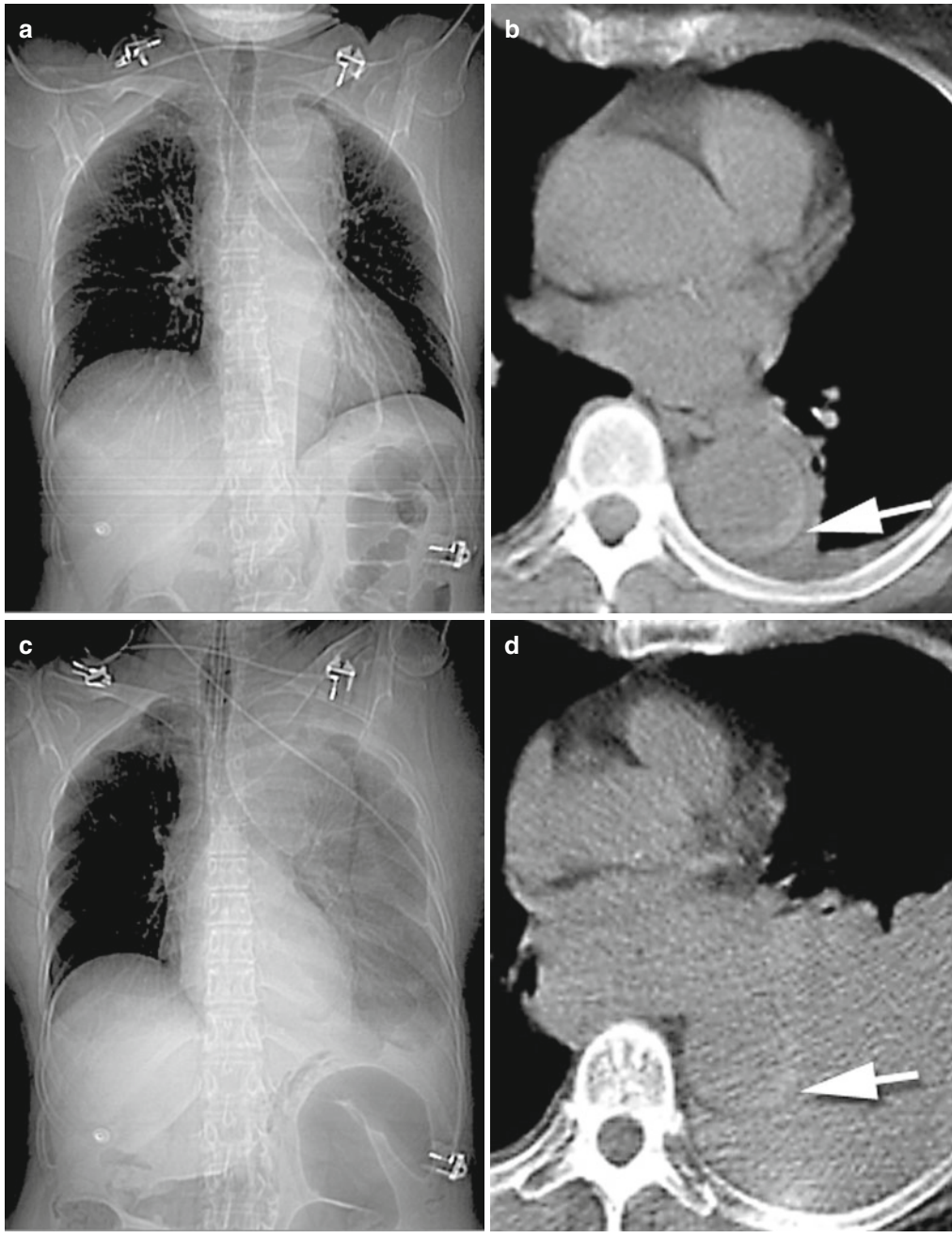

Fig. 7 (**a**) Frontal projectional radiograph of the chest demonstrates a widened aortic arch in a patient with acute chest pain. (**b**) Unenhanced transverse CT section obtained in anticipation of performing a CT angiogram demonstrates a high-attenuation crescent within the posterior wall of the descending aorta (*arrow*). A small left pleural effusion is present. This high-attenuation crescent is pathognomonic for an intramural hematoma. Prior to performing the ensuing CT angiogram, the patient became acutely hemodynamically unstable on the CT table necessitating cardiopulmonary resuscitation. (**c**) 45 min after the initial acquisition, (**a**, **b**) the patient was stabilized hemodynamically. A repeat frontal projectional radiograph demonstrates that the left hemothorax is now filled with fluid. (**d**) Transverse CT section at this time demonstrates a large left pleural effusion, which was subsequently demonstrated to represent blood due to acute rupture of the aorta at the site of the intramural hematoma. The high-attenuation crescent within the aorta wall, which is now displaced anteriorly, compared to the earlier cross section, is still visible

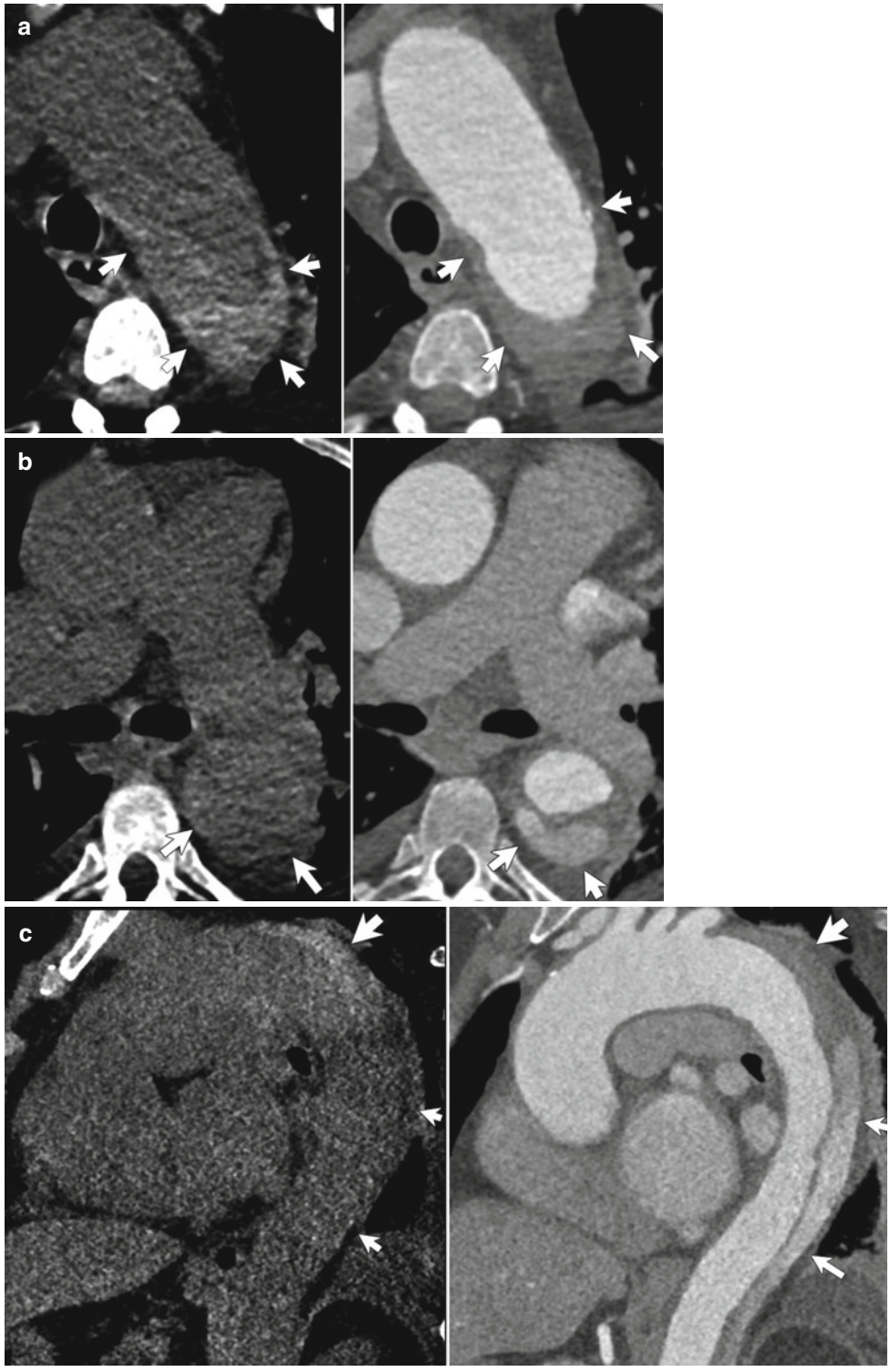

Fig. 8 Intramural hematoma associated with aortic dissection. (**a**) Transverse pre- (*left*) and post-contrast material-enhanced (*right*) CT sections through the aortic arch demonstrate high-attenuation blood within the aortic wall (*arrows*). (**b**) Several centimeters inferior, contrast material enhances a false lumen (*arrow*), which is isoattenuative with respect to the true lumen. (**c**) Oblique sagittal reformations show the relationship between the high-attenuation thrombosed false lumen (*wide arrow*) and the lower attenuation patent region of the false lumen (*small arrows*)

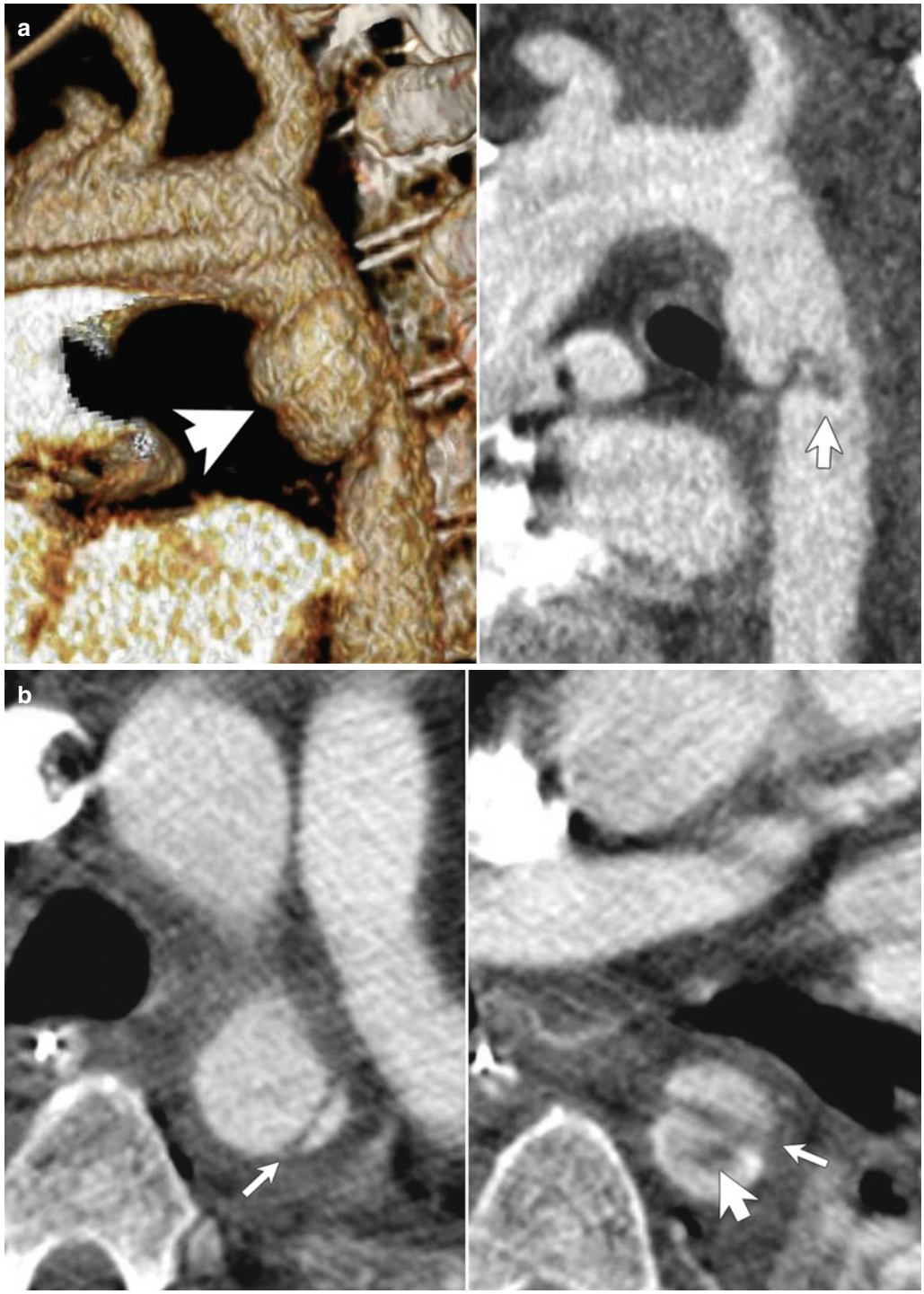

Fig. 9 CT angiogram following high-speed motor vehicle collision. (**a**) Volume rendering (*left*) and curved planar reformation (*right*) demonstrate a pseudoaneurysm at the aortic isthmus, near the expected location of the ligamentum arteriosum. The curved reformation reveals a linear filling defect corresponding to a posttraumatic intimomedial flap. (**b**) Transverse CT sections immediately below the aortic arch (*left*) and 2 cm distal (*right*) illustrate the intimomedial flap (*thin arrow*) and a rounded filling defect in the true lumen corresponding to a small thrombus at the tip of the flap (*wide arrow*)

et al. 2015). These may be associated with mediastinal hemorrhage and fractures of the rib, vertebra, and sternum.

3.1 Thoracic Aortic Aneurysm

CTA is a useful tool for diagnosing thoracic aortic aneurysms, determining their extent, and predicting appropriate management. While the diagnosis of aortic aneurysms is readily made from transverse sections, an assessment of the extent of the lesion, particularly when the brachiocephalic branches are involved, is facilitated by an assessment of curved planar reformations and volume renderings.

In general thoracic aortic aneurysms greater than 5 cm are at an increased risk for rupture. Although thoracic aortic aneurysm expands at a slower rate than abdominal aortic aneurysms, surgical repair is contemplated when thoracic aneurysms reach a diameter of 5–6 cm. CT angiography can facilitate surgical planning by delineating the extent of the aneurysm and the involvement of aortic branches (Hiratzka et al. 2010).

Because of the tortuosity and curvature of the thoracic aorta, aneurysm sizing is performed most accurately when double-oblique reformations are generated perpendicular to the aortic flow lumen. The challenge of such an approach is that data concerning the risk of aneurysm rupture and expansion rate are based upon measurements made from transverse sections, where true diameters can be overestimated. Further the measurement technique must be reproducible to assess the rate of aneurysm expansion on sequential studies.

The most geometrically robust measure of aneurysm size, however, is not the determination of true aortic diameters or even cross-sectional area, but aneurysm volume. Currently this approach has substantial drawbacks. While the volumetric data of CT should be excellent for determining aneurysm volume, patent, thrombosed, and atheromatous elements of the aorta must be segmented accurately from the adjacent structures to make this determination. The only technique available to perform this is painstaking manual segmentation performed by drawing regions of interest around the aorta on each cross section. Further, to date aneurysm expansion has been studied primarily in terms of radial expansion of the aorta. While aneurysm volume determination is an attractive measure of aneurysm growth based upon theoretical considerations, data concerning the risk of aneurysm rupture and guidelines for intervention are based upon traditional transverse diameter measurements (Masuda et al. 1992).

3.2 Endovascular Repair of TAA

Aortic endografting or stent grafting has become an important alternative to open surgical repair of the thoracic aortic aneurysms (Greenberg et al. 2008; Coady et al. 2010). Critical to successful endografting is the presence of a relatively normal aortic segment for proximal and distal fixation of the endograft that does not result in occlusion of critical aortic branches. As a result, aneurysms isolated to the descending thoracic aorta are most amenable to endografting. In the setting where there is an adequate proximal neck distal to the left subclavian artery and an adequate distal neck proximal to the celiac axis, intercostal arteries are the only significant aortic branches that will be covered, occluding their ostia. The significance of endografting over intercostal artery ostia is diminished when the branches are already occluded by luminal thrombus within the aneurysm. When intercostal arteries in the lower thoracic spine are occluded, there is risk of interrupting blood supply to the anterior spinal artery via the artery of Adamkiewicz. Predicting the risk of spinal cord ischemia based upon preoperative anatomy can be challenging and relates not only to the number and extent of patent intercostal arteries preoperatively but also the possibility of collateralization from lumbar arteries. Nevertheless, the likelihood of spinal cord ischemia following thoracic aortic repair has been shown to have greatest association with the extent of aortic coverage by the endograft (Bisdas et al. 2015).

When the aneurysm begins in the aortic arch or the ascending aorta, the use of simple stent grafts is more limited. When descending thoracic

aortic aneurysms extend into the aortic arch, a common intervention to provide a greater opportunity for proximal stent-graft fixation is to transpose the left subclavian artery onto the left common carotid artery at the base of the neck (Peterson et al. 2006). Following this limited open surgical procedure, coil embolization of the proximal left subclavian artery is performed, and an aortic stent graft can then be placed over the occluded left subclavian artery origin. The rationale for coil embolizing the left subclavian artery after performing the bypass is to prevent retrograde flow from the left subclavian artery via the left common carotid artery into the aneurysm sac and resulting in persistent aneurysm pressurization. Recently, branched endografts have been introduced as a means of treating aortic arch aneurysms (Cires et al. 2011; Andersen et al. 2013). Further sophistication and creativity in managing complex thoracic aortic aneurysms have resulted from the development of hybrid techniques that combine traditional open bypass grafting to relocate aortic branch origins away from aortic aneurysms, allowing the secondary deployment of an endograft proximally across the aortic arch and into the ascending aorta. A detailed review of the broad spectrum of endograft approaches including fenestration, branching, chimneys, and snorkels is beyond the scope of this chapter, but the interested reader is referred to the attached references (Tsilimparis et al. 2013; Cariati et al. 2014).

Variants of descending thoracic aortic aneurysm that involve the abdominal aorta are called thoracoabdominal aneurysm and have been classified by Crawford et al. (1978). The approach to managing thoracoabdominal aneurysms is dependent upon its proximal and distal extent. With greater extension of thoracic aortic aneurysms into the abdominal aorta, involvement of the celiac axis, superior mesenteric artery, and renal arteries can be seen. When the distal neck of a thoracoabdominal aortic aneurysm extends below the celiac axis origin, the native ostia of these key aortic branches would need to be covered if endografting is determined to be the primary means of isolating the aneurysm. In this setting, hybrid repairs are often executed using an open approach into the retroperitoneum to transpose key abdominal aortic branches followed by thoracic aortic endografting (Patel et al. 2010; Nordon et al. 2009). These hybrid approaches often involve suturing fabric grafts to the distal abdominal aorta or common iliac artery and positioning that graft proximally to anastomose with the celiac, superior mesenteric, and/or renal arteries. Once this proximal abdominal aortic branch transposition has been executed and the proximal course of the native vessels oversewn, endografting can be performed with distal extension of the endograft into the abdominal aorta (Fig. 10). While frequently complex to execute, these hybrid procedures are associated with substantially less morbidity and mortality to the patient, as they avoid the performance of a thoracotomy together with retroperitoneal access to the abdominal aorta which are required to manage the aneurysm using traditional surgical methods.

When undertaking endograft repair of the aorta, the CT angiogram becomes a critical tool in the planning of the procedure. Planning consists of two primary components: sizing of the endograft and assessing the access route for deployment.

Because endografts are manufactured with specific diameters and lengths, determining the appropriate endograft diameter at the proximal and distal necks, predicting the course of the endograft as it passes through the aorta, and ascertaining the anticipated length required of the final device are key to a durable repair of the thoracic aortic aneurysm. If the diameter of the endograft is undersized, then there will be insufficient sealing at the proximal or distal neck, resulting in perigraft flow or type I endoleak with associated instability of device fixation and pressurization of the aneurysm sac. If an oversized device is selected, it will not expand fully, and pleating of the device at the fixation points can similarly limit the effectiveness of fixation and sealing. Measurement of the aortic dimensions in the anticipated location for proximal and distal fixation and sealing should be performed using oblique cross sections through the aorta that are perpendicular to the flow lumen. Commercially

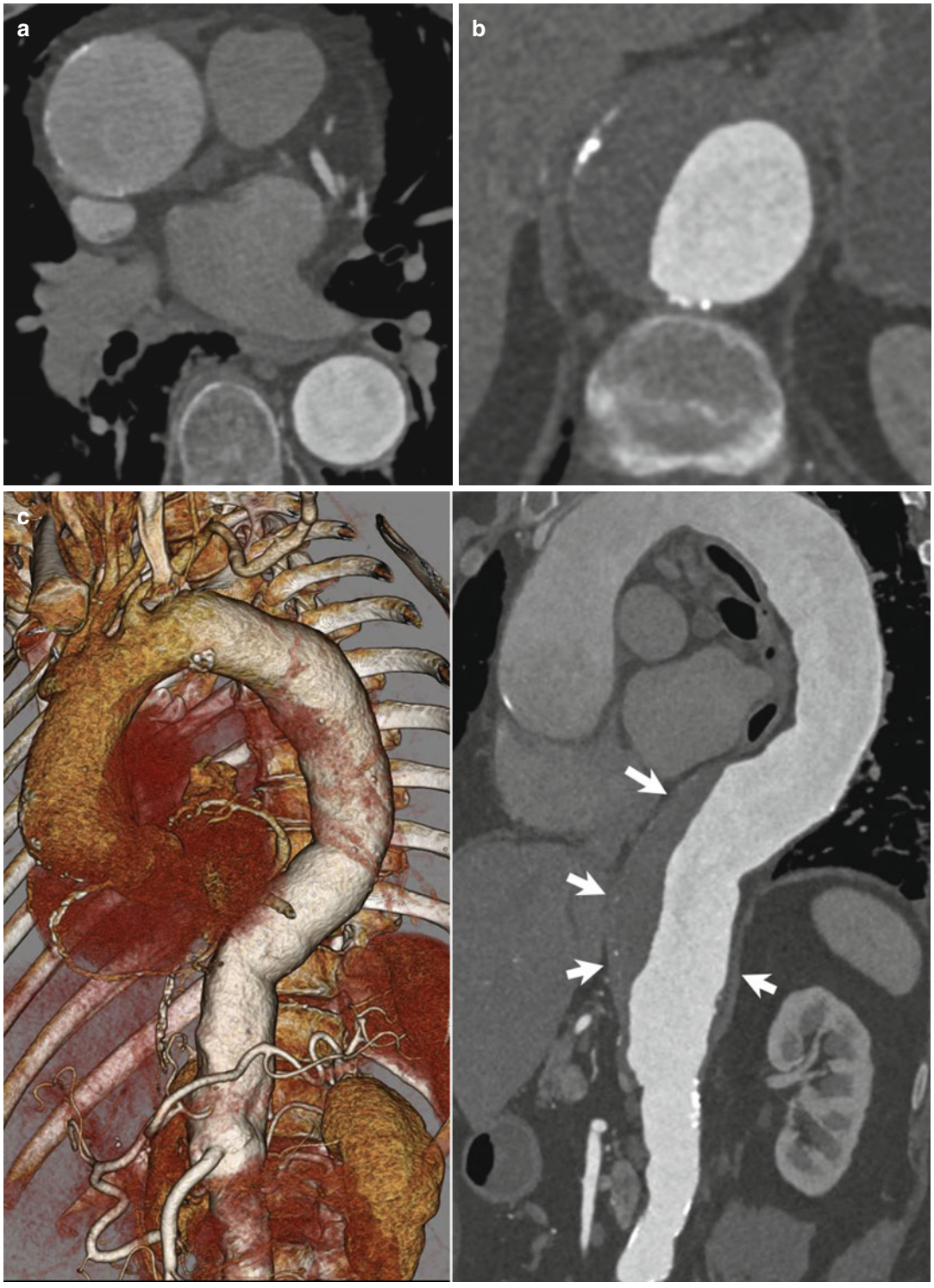
a
b
c

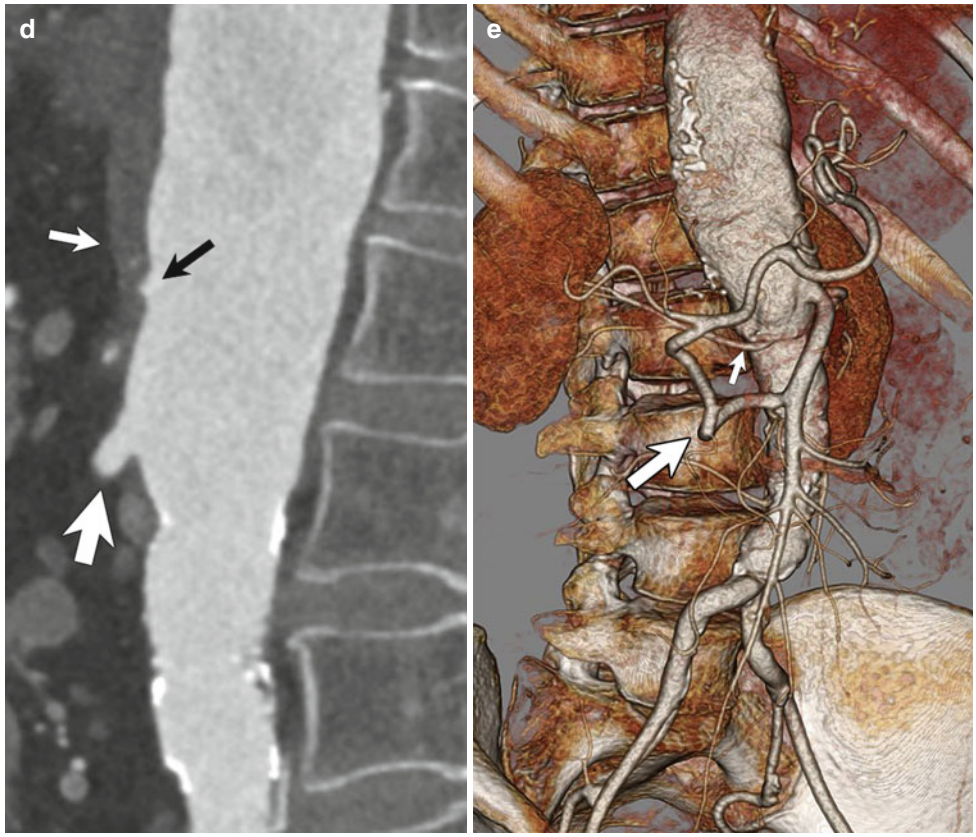

Fig. 10 (continued)

Fig. 10 Hybrid repair of ascending and thoracoabdominal aortic aneurysms. Transverse CT sections of (**a**) 5.5 cm ascending, 4.5 cm descending, and (**b**) 5 cm supraceliac aortic aneurysms are shown preoperatively. (**c**) Volume rendering (*left*) and curved planar reformation (*right*) provide an overview of the diffusely aneurysmal aorta with substantial luminal thrombus (*arrows*) extending from the distal descending to the juxtarenal abdominal aorta. (**d**) Sagittal reformation of the upper abdominal aorta demonstrates luminal thrombus (*thin white arrow*) extending over and occluding the origin of the celiac axis (*black arrow*) and terminating above a patent superior mesenteric artery (*wide white arrow*). (**e**) Enlarged gastroduodenal and inferior pancreaticoduodenal arteries (*large arrow*) accommodate the presumably long-standing celiac occlusion, perfusing the celiac territory via retrograde supply from the superior mesenteric artery. The right renal artery (*small arrow*) originates from the inferior aspect of the thoracoabdominal aortic aneurysm. (**f**) The final aortic repair aorta was performed in three stages over 3 weeks. (**g**) Through a median sternotomy, an ascending aortic interposition graft was anastomosed to the aorta proximally at the sinotubular junction with a beveled distal anastomosis to the aortic arch in what is termed a "hemiarch repair" (*green*). (**h**) Via retroperitoneal access, the second stage of the repair began with a side-to-side anastomosis of the midportion of a tubular graft to the left common iliac artery, marked with a metallic ring. The direction of blood flow into this primary conduit is indicated (*long*, *thin black arrow*). The right renal artery was detached from the aorta and anastomosed to the end of a jump graft that anastomosed to the main conduit (*large black arrow*). Large metal clips mark the proximal end of the conduit. (**i**) Direct anastomosis of the superior mesenteric artery to the proximal end of the conduit (*wide arrow*) and a jump graft from the conduit to the right renal artery (*small arrow*) are visible on a right anterior oblique volume rendering. (**j**) The distal end of the conduit (*arrows*), which is partially thrombosed post-repair, was tunneled to the left inferior flank where metallic clips mark its terminus. The final stage of the procedure involved access of the distal conduit through a low flank incision, clearance of thrombus from the conduit, and delivery of multiple stent-graft bodies proximally into the descending thoracic and abdominal aorta following the path indicated with the *long white arrow* in (**h**) and passing retrograde through the metallic ring at the ilio-conduit anastomosis. Debranching the abdominal aorta and reconstitution of blood flow from the left common iliac artery via the conduit allowed isolation of the entirety of the thoracoabdominal aortic aneurysm with the stent grafts.

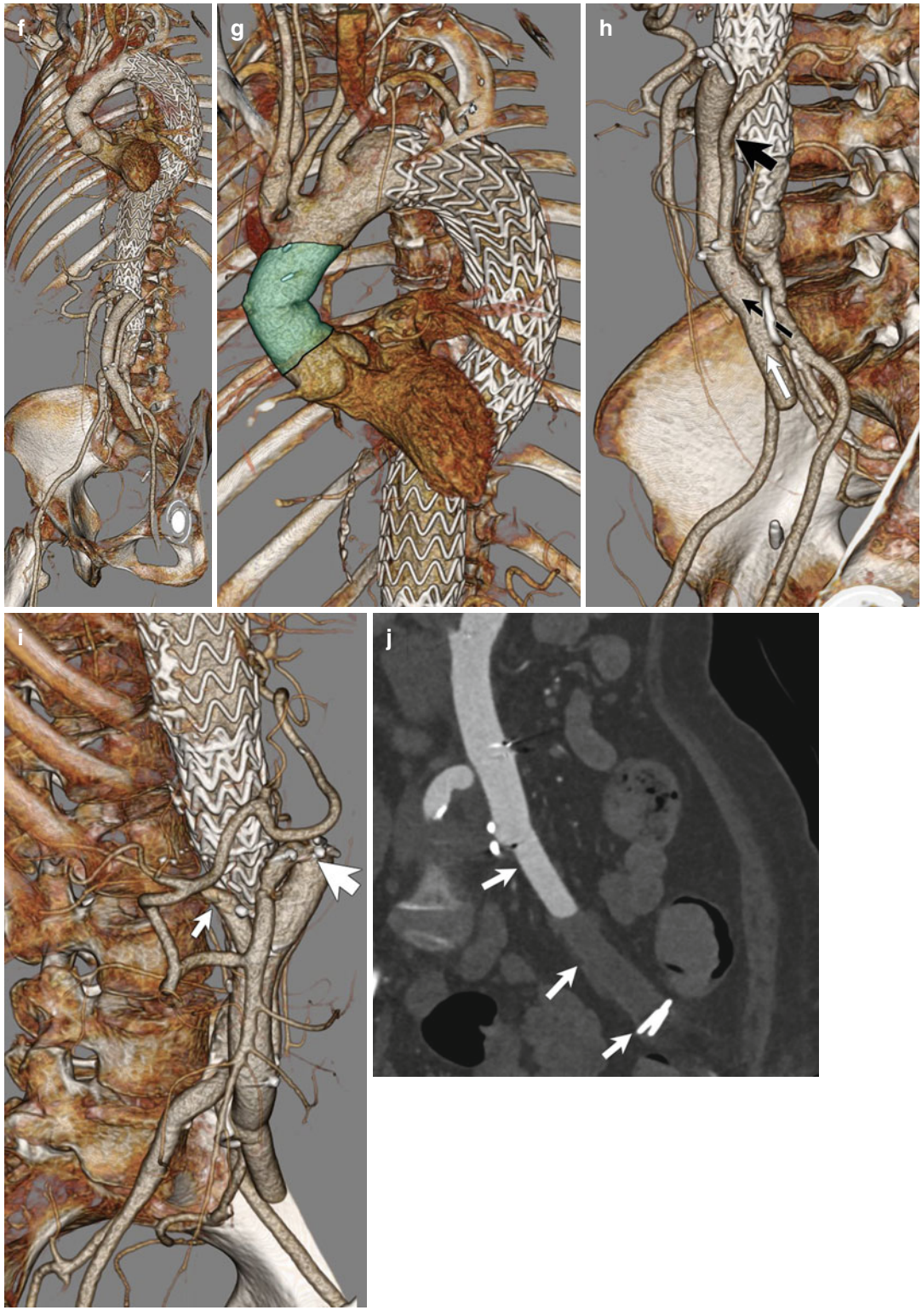

Fig. 10 (continued)

available endograft planning tools are commonplace on clinical advanced image processing workstations. These tools begin with the extraction of the median centerline of the aorta and subsequent calculation of orthogonal cross sections.

Once the proximal and distal fixation zones are identified on the CT angiogram, the length of the endograft can be predicted. A first-order approximation of this length can be derived by measuring the distance along the median centerline from proximal to distal fixation points; however, more sophisticated techniques that predict the actual course of the endograft through large aortic aneurysms have been shown to be more accurate at predicting final endograft length. The importance of accurate prediction of endograft length is diminished when multiple endograft segments are to be deployed and dynamic adjustment of the final endograft complex length can be performed by adjusting the degree of overlap between the individual endograft segments at the time of deployment.

In addition to sizing the endograft, CT angiography is critical in assessing the delivery route for the endograft. As a result, pre-deployment CT angiography in the setting of thoracic aortic aneurysm should always extend to involve the abdomen and pelvis to the bifurcation of the femoral artery. This latter landmark is readily identified from a scout radiograph at the lesser trochanter of the femur. Depending upon the device to be deployed, the size and tortuosity of the iliac arteries can be important barriers to the preferred transfemoral approach for stent-graft introduction into the arterial system. An additional relative contraindication relates to the amount of calcification present within the iliac arteries as well. Further, in the setting of thoracic aortic aneurysm, many patients will have significant abdominal aortoiliac atherosclerotic disease, and thus assessment for atheromatous plaque and focal arterial stenosis is important to avoid complication at the time of stent-graft delivery. Tortuosity of iliac arteries has been documented to influence the likelihood of injury to the iliac arteries during delivery of aortic endografts, resulting in post-procedural intimomedial dissection of the iliac arteries. In the setting of iliac arteries that are too small, too torturous, or too diseased to serve as a conduit for delivery for the aortic stent graft, surgeons may elect to insert the thoracic aortic stent graft directly into the distal abdominal aorta. This is typically performed through a segment of fabric graft, which is sutured to the distal abdominal aorta and passed superficially for access at the time of stent-graft delivery. Following successful deployment of the stent graft, this graft is oversewn; however, patent remnants can remain post-procedure.

3.3 Assessment Following Thoracic Aortic Aneurysm Repair

In the immediate postsurgical period, numerous complications can arise from traditional open and endograft repair of the thoracic aorta. It is important to be attentive to these complications and their appearances.

One of the first elements of assessing the postoperative aorta is to identify the nature of the procedure performed. While the metallic components of an endograft are easily identified using effective image window leveling to assure that the metal of the endograft can be discriminated from enhancing contrast within the aortic lumen, the identification of fabric graft material can be more challenging (Fig. 11). Virtually all fabric grafts are hyper-dense relative to the native aortic wall; however, this hyper-density is subtle, typically ranging from 10 to 30 HU. The acquisition of unenhanced CT sections is valuable for recognizing this graft signature. If unenhanced sections are not available, then graft material can also be recognized by its consistent circular cross section, which is often best appreciated upon volume renderings. Once the extent of the graft material is identified, the proximal and distal anastomosis should be examined carefully for the possibility of anastomotic dehiscence. Pseudoaneurysms resulting from graft dehiscence are critical findings that require

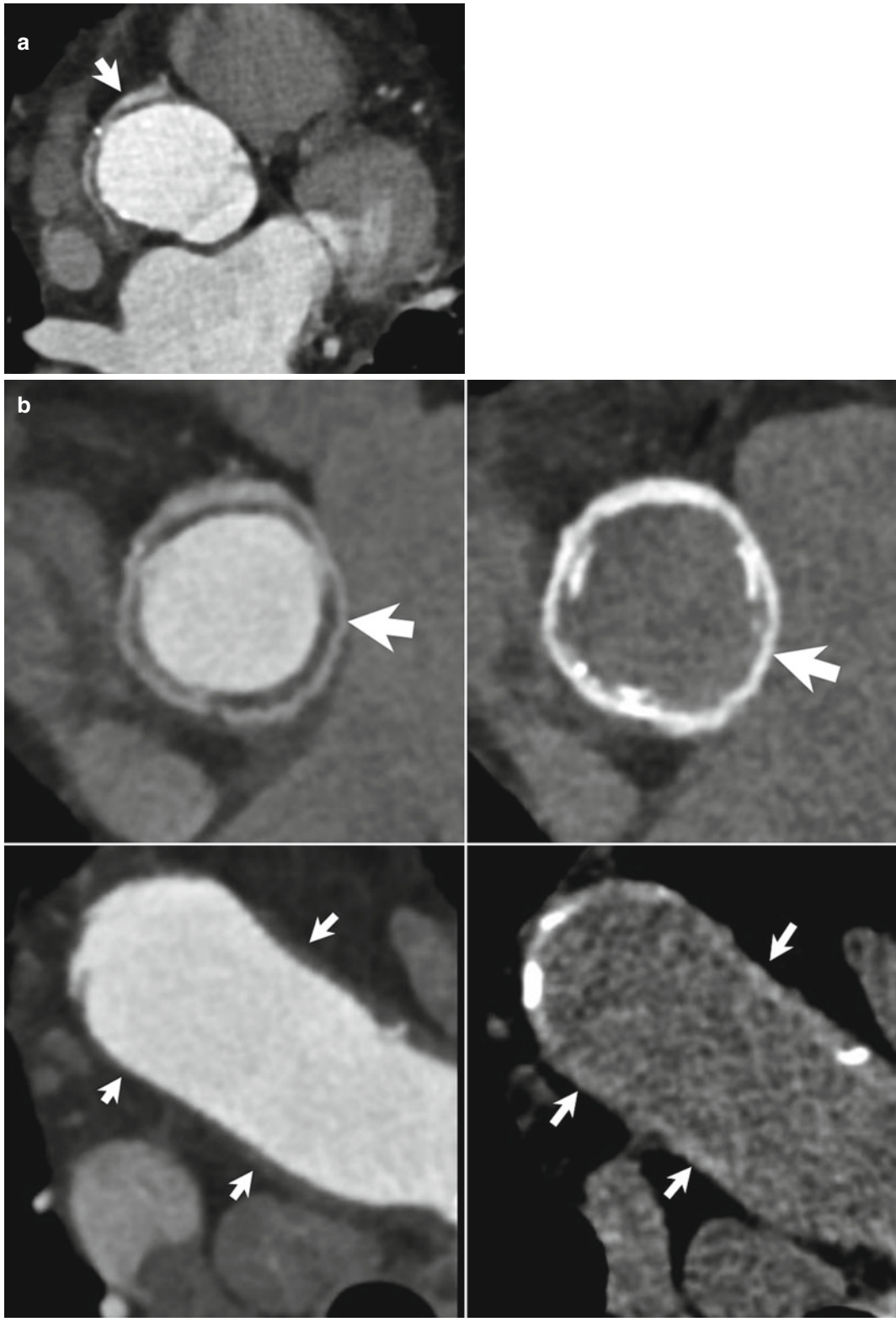
a
b

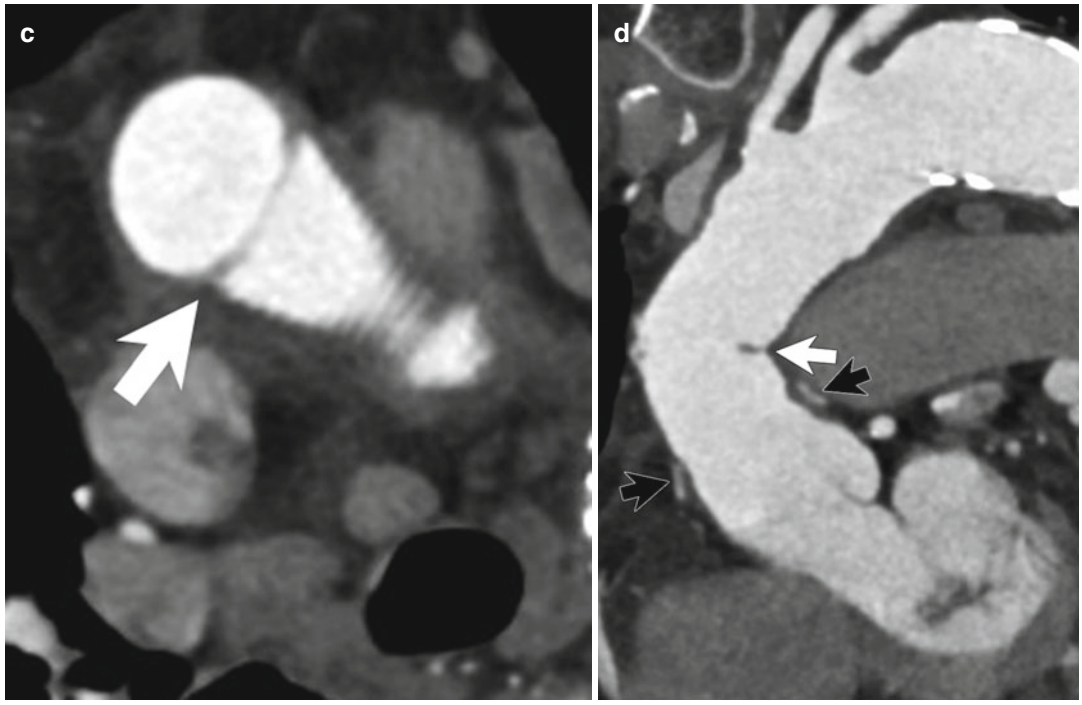

Fig. 11 (continued)

Fig. 11 CT appearance of unsupported interposition grafts. (**a**) Transverse CT section post-contrast medium enhancement through the aortic root demonstrates a high attenuation structure lateral to the aortic wall (*arrow*). (**b**) Oblique reformations at the level of the sinotubular junction (post-contrast medium enhancement on left and pre-contrast medium enhancement on right) reveal that the high attenuation crescent indicated in (**a**) is a high-attenuation circular ring, which corresponds to felt incorporated into the proximal anastomosis of an ascending aortic interposition graft (*large arrows*). At the level of the proximal aortic arch (*bottom row*) the graft material cannot be discriminated from the aortic luminal on the contrast material enhanced view (*left*). The unenhanced view (*right*) reveals subtle high attenuation thickening corresponding to the graft material without felt (*small arrows*). (**c**) A linear filling defect within a graft segment (*arrow*) can be confused for an intimomedial flap; however, it simply represents fold or pleat in the graft and is of no clinical concern. (**d**) When viewed longitudinally, the graft is recognized by its constant cross section, where a graft fold (*white arrow*) is easier to recognize. The felt ring shown in (**a**, **b**) is shown in cross section (*black arrows*). (**e**) Volume rendering can provide the easiest means of recognizing graft material owing to its signature cylindrical shape. The image on the left was created using the default volume rendering settings and shows the graft with the fold (*white arrow*). The felt is barely visible (*black arrow*). Fine-tuning the volume rendering parameters or opacity transfer functions provides an image (*right*) that better depicts the graft and the felt ring. By shifting the opacity curves to encompass lower attenuation values, the left brachiocephalic vein (*LBCV*) becomes visible, obscuring the origins of the aortic arch branches. The two images underscore the tradeoffs that should be considered when optimizing volume renderings and the fact that sometimes two different renderings are needed to fully convey key information within the CT angiogram

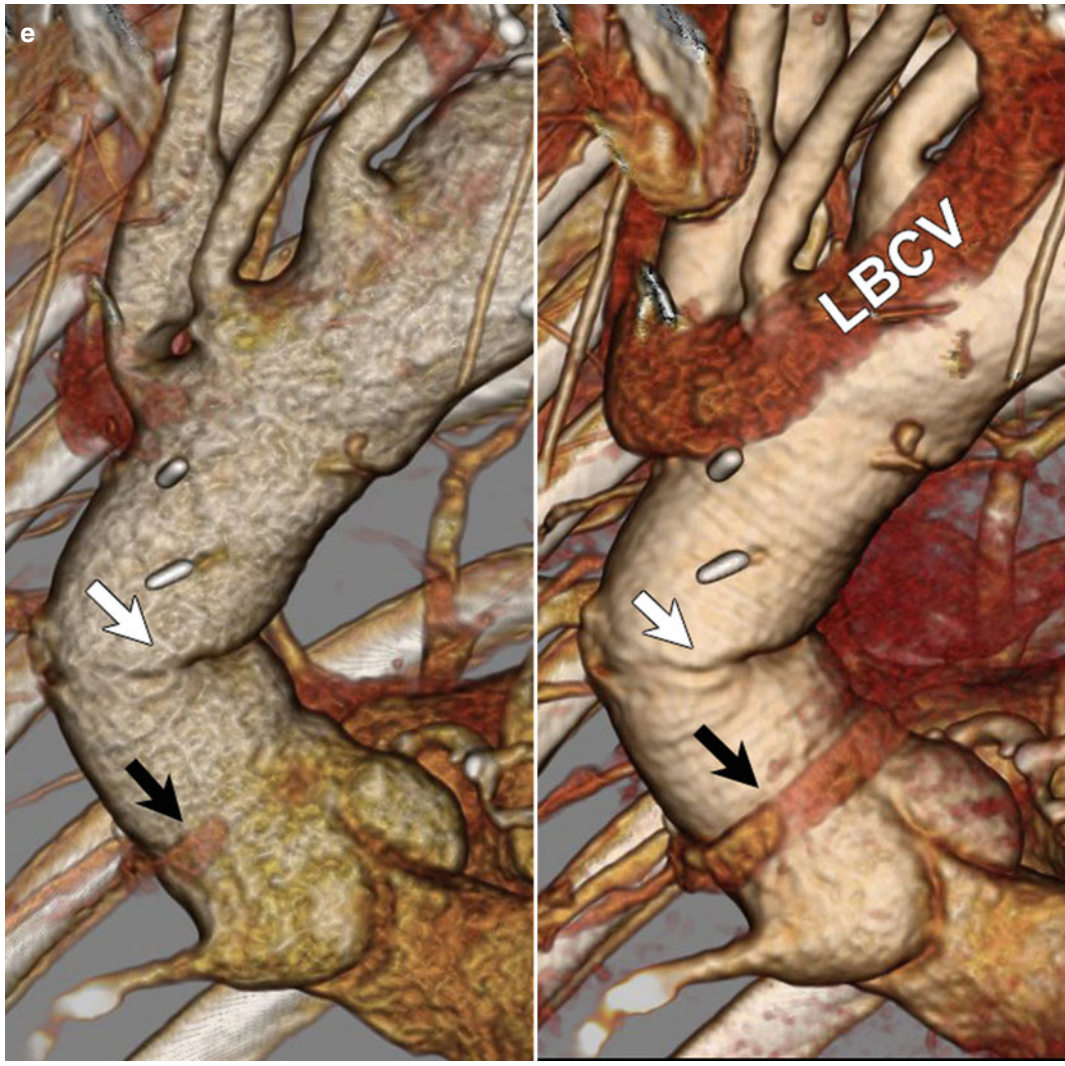

Fig. 11 (continued)

urgent repair. When assessing following ascending aortic repair, particularly for proximal graft extent into the aortic root, a retrospectively gated acquisition can be critical to attaining a sufficiently clear depiction of the structures of the root to identify pseudoaneurysms, the status of implanted coronary arterial origins onto the graft material, and the relationship of the aortic graft to aortic root structures.

A common characteristic of fabric grafts within the thoracic aorta is that they can develop folds or pleats in regions of curvature. These should not be a cause for alarm; however, when not successfully recognized, they can be misinterpreted as regions of aortic dissection. Curve reformations and volume renderings through the region can be very helpful in depicting the characteristic appearance of a graft fold.

When assessing aortic endograft repair in the acute period, attention should be placed both on the region of the endograft itself and the entirety of the delivery route. Complications

occurring along the delivery route include intimal injury to the delivery vessels as well as secondary occlusion. In the presence of atheroma and intraluminal thrombus along the delivery route, the risk of atheroembolism occurring during the deployment is raised. Examination of the abdominal viscera, particularly the kidneys and spleen, should be used to identify infarcts as a telltale sign of atheroembolism. Hematoma and pseudoaneurysm formation can be seen at the site of entry for endograft delivery either in the region of the femoral arteries or more proximally depending upon the site of arterial access.

When examining the endograft itself, it is important to determine that it is positioned to allow successful sealing both proximally and distally. Because endograft components can migrate or be primarily maldeployed, attention to their location and configuration is necessary to avoid complications due to endograft migration and potential injury or occlusion of the aorta or its branches. In the acute post-procedural period, first 30 days, the presence of endoleak can be over 50 %. Endoleak is defined as contrast opacification within the aneurysm sac following isolation of the aneurysm wall by an endograft. Endoleaks have been classified into five primary categories based upon their cause (Veith et al. 2002; Cao et al. 2010).

Type I endoleaks occur at endograft attachment sites with a type 1A endoleak corresponding to proximal attachment site and type 1B corresponding to distal attachment site perigraft flow. The visualization of a flow channel opacified by iodinated contrast between the endograft and the aortic wall at the seal zone indicates an unstable repair and should be urgently communicated with strong consideration for reintervention.

Type II endoleaks, which are the most common type of endoleak, occur due to filling from patent side branches. These endoleaks rarely require direct intervention and can be followed over time and associated with changes in aneurysm sac size. The decision to intervene on a type II endoleak is usually made when there is aneurysm enlargement associated with the type II endoleak.

A type III endoleak represents transgraft flow and most commonly occurs at junction zones of individual endograft components; however, it may also be seen due to tears or holes developing within the fabric of the endograft. Similar to the type I endoleaks, the likelihood of serious complication, particularly from aneurysm rupture makes type III endoleak an urgent condition for secondary repair.

Type IV endoleaks are transient phenomenon relating either to sequestration of contrast material delivered to the aneurysm sac at the time of stent-graft deployment or transmission of iodinated contrast through the wall of porous endograft material in the immediate post-procedural period. They do not represent clinically significant findings. The interpreter of CT angiograms should simply be aware of their existence so that a type IV endoleak is not misinterpreted as a more serious condition.

Finally, type V endoleaks are also called "endotension" and correspond to persistent elevated pressures within the isolated aneurysm sac in the absence of a demonstrable endoleak. While some of these cases are due to the development of serous collections within the sac, over time, some of them correspond to type II or type III endoleaks that are not successfully diagnosed on the CT angiogram, often due to flawed CT acquisition or image display strategies.

Maximizing the likelihood of endoleak detection on CT angiograms necessitates dedicated CT acquisition technique that includes a delayed phase acquisition in addition to the arterial phase acquisition. A delayed phase is typically acquired between 30 and 60 s after the arterial phase acquisition and has been shown to facilitate detection of endoleaks that are not visualized on the arterial phase (Rozenblit et al. 2003; Golzarian et al. 2013). The majority of these endoleaks will be type II endoleaks that experience delayed filling due to collateral supply from aortic side branches and the added time required for

contrast material to flow through those collateral pathways. Another important step in assuring that endoleaks are detected is the use of narrow image display windows and lower levels that are typically employed for CT angiography to assure that subtle degrees of enhancement within the aneurysm sac are visualized.

Surveillance of the aorta following repair may be performed on a routine basis following aortic stent grafting or based upon a change in the patient's status. In addition to the aforementioned abnormalities that can be seen during the acute phase, following the passage of time, the size of the aortic aneurysm should be assessed. After endografting, aneurysms may shrink; however, many stabilize in size and do not change. Growth in the aneurysm both in diameter and length is a cause for concern and may require further intervention. It is also important to assess the position of endografts on serial exams to assure that device is not migrating. Over time, the relatively normal regions of stent-graft fixation and sealing can enlarge, resulting in a once stable fixation becoming unstable. Migration of five millimeters or greater indicates instability of the device and secondary intervention should be considered. Finally, over time, endografts can degrade resulting in tears to the fabric or fractures of the metallic elements. When this occurs, the structural competence of the endograft is compromised which can cause secondary dislodgment and migration as well Type III endoleak formation. Detection of metallic fractures as well as breakages in the suture material fixing metallic elements to the fabric graft is best performed with volume rendering dedicated to the visualization of the endograft components.

3.4 Congenital Anomalies

Congenital anomalies of the thoracic aorta and aberrant branches of the descending aorta such as vascular rings, aberrant supra-aortic branching (Fig. 12), coarctation, and enlarged bronchial arteries or major arteriopulmonary communicating arteries are easily diagnosed and characterized with CT. The simultaneous visualization of the airways complements vascular visualization by allowing a direct determination of the specific structures responsible for tracheobronchial narrowing and the presence of aberrant airways. Aortic stenosis secondary to coarctation is clearly demonstrated, and the conduits for collateral blood flow via intercostal arteries, internal mammary arteries, and lateral thoracic arteries can be visualized as well (Karaosmanoglu et al. 2015) (Fig. 13).

3.5 Summary

With progressive improvements in CT technology and minimally invasive thoracic aortic therapies, CT angiography has become the first-line imaging modality for virtually all thoracic aortic abnormalities. As new technologies of iterative reconstruction and multispectral imaging mature, the technique will continue to improve by requiring less radiation and providing greater tissue characterization.

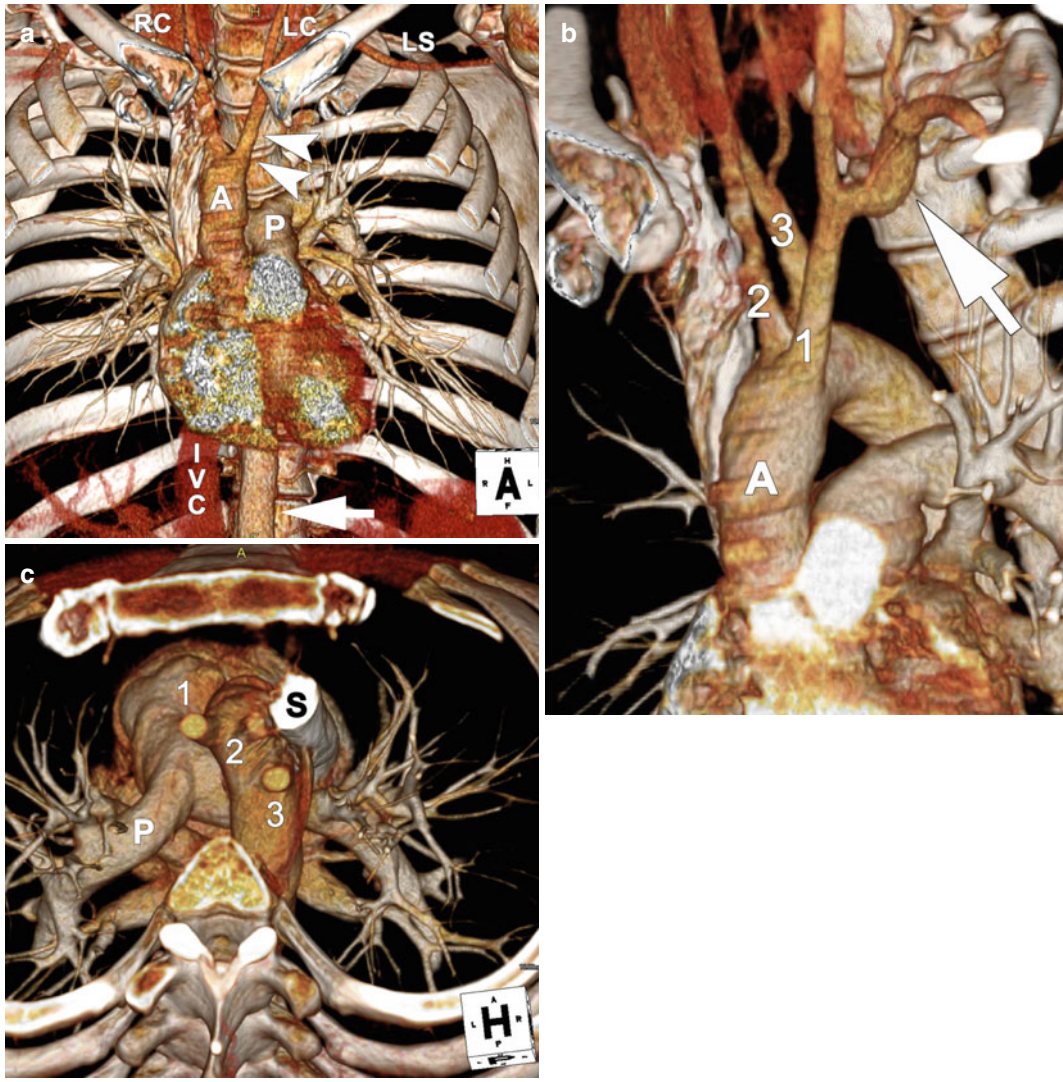

Fig. 12 Right-sided aortic arch with mirror image branching pattern. An incidental finding in a 23-year-old male evaluated for chest pain. No other congenital heart disease (CHD) was found by CT, physical exam, or echocardiography. Most (>95 %) patients with this anatomy have coexistent CHD. (**a**) Frontal volume rendering shows the aortic arch (A) and descending thoracic aorta (*arrow*) to be to the right of the spine. The first branch from the arch is the left innominate artery (*arrowheads*), consistent with mirror image anatomy. *LS* left subclavian artery, *LC* left common carotid artery, *RC* right common carotid artery, *P* pulmonary trunk, *IVC* inferior vena cava. (**b**) Left anterior oblique volume rendering shows the left innominate artery as the first branch arising from the right aortic arch (*1*). The right common carotid arises second (*2*), followed by the right subclavian artery (*3*), which is not aberrant. An aneurysm of the left subclavian artery is present (*arrow*). (**c**) Cranial volume rendering shows origins of the left innominate (*1*), right common carotid (*2*), and right subclavian (*3*) arteries without retro-esophageal component. *S* superior vena cava, *P* left main pulmonary artery (Figure created by Richard L. Hallett, MD)

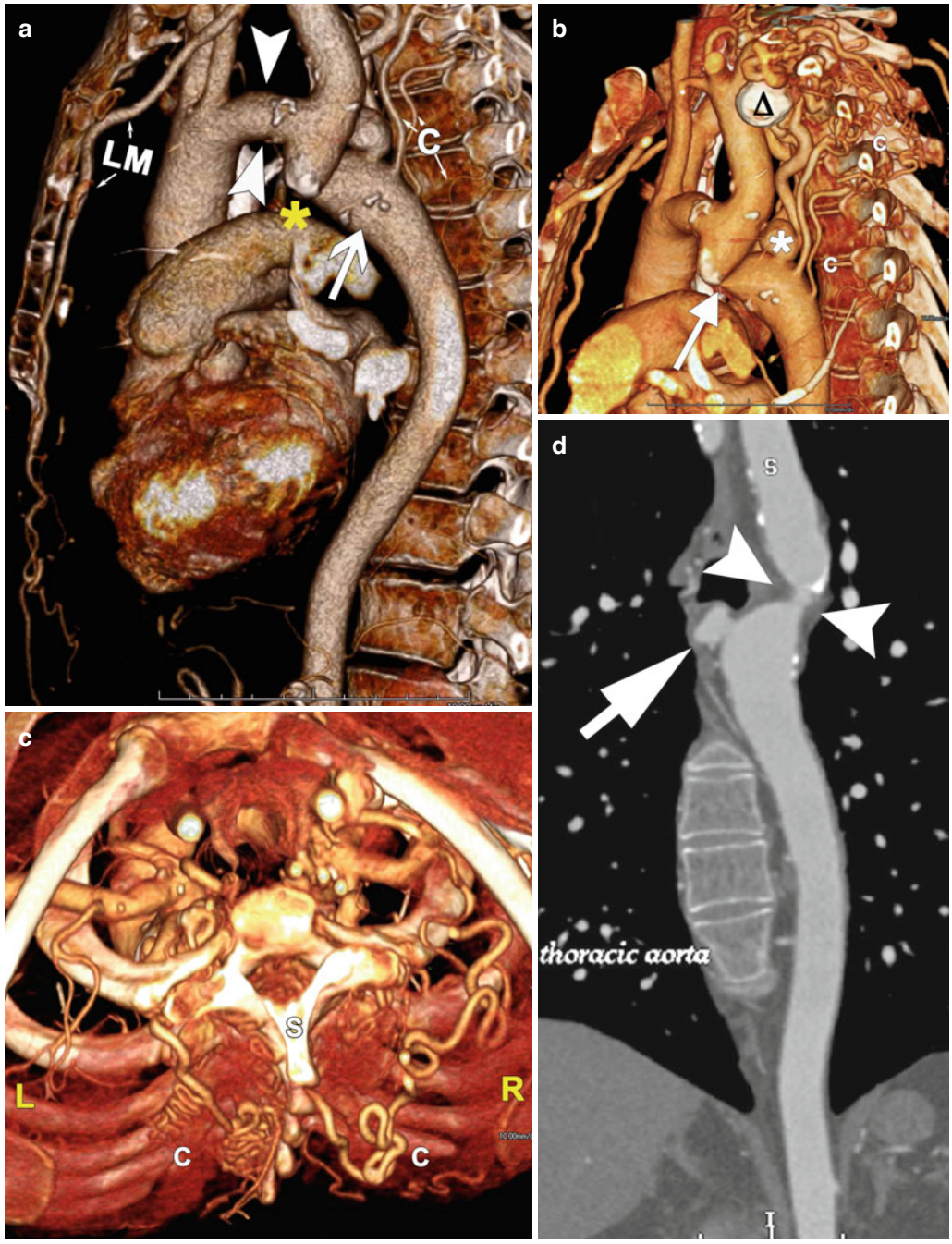

Fig. 13 Adult presentation of aortic coarctation. A 74-year-old female with pulse deficit in left upper extremity. (**a**) Sagittal volume rendering demonstrates a focal juxtaductal coarctation, with stenosis immediately distal to a calcified ductal remnant (*) with tubular hypoplasia of the aortic arch (*arrowheads*). There are large intercostal and costocervical collaterals (*C*), as well as hypertrophy of the left internal mammary artery (*LM*). Note foci of calcified atherosclerotic plaque along the aorta (*large arrow*). (**b**) Left posterior oblique volume rendering better demonstrates the extensive intercostal and costocervical collateral arteries (*C*). Aneurysms of intercostal (*) and costocervical (Δ) collaterals are present. The point of maximal stenosis is also well depicted (*arrow*). (**c**) Cranial volume rendering demonstrates numerous collaterals in the soft tissues of the upper back (*C*), which communicate from right (*R*) to left (*L*). *S* spinous process of first cervical vertebrae. (**d**) Curved planar reformation of the descending thoracic aorta demonstrates severe stenosis at the coarctation (*arrowheads*). A portion of an aneurysm at the origin of an intercostal collateral is also visible (*arrow*) (Figure created by Richard L. Hallett, MD)

References

Ait Ali Yahia D, Bouvier A, Nedelcu C et al (2015) Imaging of thoracic aortic injury. Diagn Interv Imaging 96:79–88

Andersen ND, Williams JB, Hanna JM, Shah AA, McCann RL, Hughes GC (2013) Results with an algorithmic approach to hybrid repair of the aortic arch. J Vasc Surg 57:655–667

Bisdas T, Panuccio G, Sugimoto M, Torsello G, Austermann M (2015) Risk factors for spinal cord ischemia after endovascular repair of thoracoabdominal aortic aneurysms. J Vasc Surg 61:1408–1416

Cao P, De Rango P, Verzini F, Parlani G (2010) Endoleak after endovascular aortic repair: classification, diagnosis and management following endovascular thoracic and abdominal aortic repair. J Cardiovasc Surg 51:53–69

Cariati M, Mingazzini P, Dallatana R, Rossi UG, Settembrini A, Santuari D (2014) Endovascular treatment of a symptomatic thoracoabdominal aortic aneurysm by Chimney and Periscope techniques for total visceral and renal artery revascularization. Cardiovasc Interv Radiol Springer US 37:251–256

Cires G, Noll RE Jr, Albuquerque FC Jr, Tonnessen BH, Sternbergh WC III (2011) Endovascular debranching of the aortic arch during thoracic endograft repair. J Vasc Surg 53:1485–1491

Coady MA, Ikonomidis JS, Cheung AT et al (2010) Surgical management of descending thoracic aortic disease: open and endovascular approaches a scientific statement from the American Heart Association. Circulation Lippincott Williams & Wilkins 121:2780–2804

Crawford ES, Snyder DM, Cho GC, Roehm JOF, Jr (1978) Progress in treatment of thoracoabdominal and abdominal aortic aneurysms involving celiac, superior mesenteric, and renal arteries. Ann Surg. Lippincott, Williams, and Wilkins. 188:404

de Mestral C, Dueck A, Sharma SS et al (2013) Evolution of the incidence, management, and mortality of blunt thoracic aortic injury: a population-based analysis. J Am Coll Surg 216:1110–1115

Evangelista A, Mukherjee D, Mehta RH et al (2005) Acute intramural hematoma of the aorta: a mystery in evolution. Circulation 111(8):1063–1070

Fishman EK, Ney DR, Heath DG, Corl FM, Horton KM, Johnson PT (2006) Volume rendering versus maximum intensity projection in CT angiography: what works best, when, and why. Radiographics Radiological Society of North America 26:905–922

Fleischmann D, Mitchell RS, Miller DC (2008) Acute aortic syndromes: new insights from electrocardiographically gated computed tomography. Semin Thorac Cardiovasc Surg 20:340–347

Golzarian J, Dussaussois L, Abada HT, et al (2013) Helical CT of aorta after endoluminal stent-graft therapy: value of biphasic acquisition. AJR Am J Roentgenol 171:329–331

Greenberg RK, Lu Q, Roselli EE et al (2008) Contemporary analysis of descending thoracic and thoracoabdominal aneurysm repair: a comparison of endovascular and open techniques. Circulation Lippincott Williams & Wilkins 118:808–817

Hansen NJ, Kaza RK, Maturen KE, Liu PS, Platt JF (2014) Evaluation of low-dose CT angiography with model-based iterative reconstruction after endovascular aneurysm repair of a thoracic or abdominal aortic aneurysm. AJR Am J Roentgenol 202:648–655

Hiatt MD, Rubin GD (2004) Surveillance for endoleaks: how to detect all of them. Semin Vasc Surg 17(4): 268–78

Hiratzka LF, Bakris GL, Beckman JA, et al. 2010 ACCF/AHA/AATS/ACR/ASA/SCA/SCAI/SIR/STS/SVM guidelines for the diagnosis and management of patients with Thoracic Aortic Disease: a report of the American College of Cardiology Foundation/American Heart Association Task Force on Practice Guidelines, American Association for Thoracic Surgery, American College of Radiology, American Stroke Association, Society of Cardiovascular Anesthesiologists, Society for Cardiovascular Angiography and Interventions, Society of Interventional Radiology, Society of Thoracic Surgeons, and Society for Vascular Medicine (2010) Circulation e266–e369

Karaosmanoglu AD, Khawaja RD, Onur MR, Kalra MK (2015) CT and MRI of aortic coarctation: pre- and postsurgical findings. AJR Am J Roentgenol 204:W224–W233

Lee WA, Matsumura JS, Mitchell RS et al (2011) Endovascular repair of traumatic thoracic aortic injury: clinical practice guidelines of the Society for vascular surgery. J Vasc Surg 53:187–192

Lemos AA, Pezzullo JC, Fasani P et al (2014) Can the unenhanced phase be eliminated from dual-phase CT angiography for chest pain? Implications for diagnostic accuracy in acute aortic intramural hematoma. AJR Am J Roentgenol 203:1171–1180

Masuda Y, Takanashi K, Takasu J, Morooka N, Inagaki Y (1992) Expansion rate of thoracic aortic aneurysms and influencing factors. Chest 102:461–466

Nordon IM, Hinchliffe RJ, Holt PJ, Loftus IM, Thompson MM (2009) Modern treatment of juxtarenal abdominal aortic aneurysms with fenestrated endografting and open repair – a systematic review. Eur J Vasc Endovasc Surg 38:35–41

Patel HJ, Upchurch GR Jr, Eliason JL et al (2010) Hybrid debranching with endovascular repair for thoracoabdominal aneurysms: a comparison with open repair. Ann Thorac Surg 89:1475–1481

Peterson BG, Eskandari MK, Gleason TG, Morasch MD (2006) Utility of left subclavian artery revascularization in association with endoluminal repair of acute and chronic thoracic aortic pathology. J Vasc Surg 43:433–439

Raman R, Napel S, Beaulieu CF, Bain ES, Jeffrey RB, Rubin GD (2002) Automated generation of curved planar reformations from volume data: method and evaluation. Radiology 223:275–280

Rozenblit AM, Patlas M, Rosenbaum AT et al (2003) Detection of endoleaks after endovascular repair of abdominal aortic aneurysm: value of unenhanced and delayed helical CT acquisitions. Radiology 227:426–433

Rubin GD, Lane MJ, Bloch DA, Leung AN, Stark P (1996) Optimization of thoracic spiral CT: effects of iodinated contrast medium concentration. Radiology 201:785–791

Rubin GD, Paik DS, Johnston PC, Napel S (1998) Measurement of the aorta and its branches with helical CT. Radiology 206:823–829

Rubin GD, Leipsic J, Joseph Schoepf U, Fleischmann D, Napel S (2014) CT angiography after 20 years: a transformation in cardiovascular disease characterization continues to advance. Radiology 271:633–652

Rudarakanchana N, Bicknell CD, Cheshire NJ et al (2014) Variation in maximum diameter measurements of descending thoracic aortic aneurysms using unformatted planes versus images corrected to aortic centerline. Eur J Vasc Endovasc Surg 47:19–26

Tsilimparis N, Perez S, Dayama A, Ricotta JJ II (2013) Endovascular repair with fenestrated-branched stent grafts improves 30-day outcomes for complex aortic aneurysms compared with open repair. Ann Vasc Surg 27:267–273

Veith FJ, Baum RA, Ohki T et al (2002) Nature and significance of endoleaks and endotension: summary of opinions expressed at an international conference. J Vasc Surg 35:1029–1035

Vilacosta I, Román JA (2001) Acute aortic syndrome. Heart 85:365–368

Willemink MJ, Leiner T, Jong PA et al (2013) Iterative reconstruction techniques for computed tomography part 2: initial results in dose reduction and image quality. Eur Radiol Springer-Verlag 23:1632–1642

Zhang LJ, Zhao YE, Schoepf UJ et al (2015) Seventy-peak kilovoltage high-pitch thoracic aortic CT angiography without ECG gating: evaluation of image quality and radiation dose. Acad Radiol 22:890–897

CT Imaging of Ischemic Heart Disease

Julian L. Wichmann, Stefanie Mangold, U. Joseph Schoepf, Stephen R. Fuller, and Felix G. Meinel

Abstract

This book chapter provides an overview of the most important established and evolving applications of CT imaging in patients with known or suspected ischemic heart disease. We place a special emphasis on technical innovations including state-of-the-art acquisition techniques for coronary CT angiography (CCTA) as well as investigational techniques of CT myocardial perfusion imaging (CTMPI) and CT-derived fractional flow reserve (CT-FFR). Coronary artery calcium scoring is a useful tool with a well-established prognostic value for risk stratification in asymptomatic, intermediate-risk patients. The primary indication for CCTA is to exclude potentially obstructive coronary artery disease in symptomatic patients with a low to intermediate pretest probability of CAD. State-of-the-art acquisition protocols have substantially reduced the radiation exposure and contrast volume required for CCTA. CT myocardial perfusion imaging and CT-FFR are two different approaches to assess the hemodynamic significance of coronary lesions. The clinical role of these novel techniques in guiding the management of patients with ischemic heart disease remains to be determined.

J.L. Wichmann, MD (✉)
Department of Radiology and Radiological Science, Medical University of South Carolina, Charleston, SC, USA

Department of Diagnostic and Interventional Radiology, University Hospital Frankfurt, Frankfurt, Germany
e-mail: docwichmann@gmail.com

S. Mangold, MD
Department of Radiology and Radiological Science, Medical University of South Carolina, Charleston, SC, USA

Department of Diagnostic and Interventional Radiology, University Hospital of Tuebingen, Tuebingen, Germany
e-mail: stefanie.mangold@med.uni-tuebingen.de

U.J. Schoepf, MD • S.R. Fuller, BS
Department of Radiology and Radiological Science, Medical University of South Carolina, Charleston, SC, USA
e-mail: schoepf@musc.edu; fullerst@musc.edu

F.G. Meinel, MD
Institute for Clinical Radiology, Ludwig-Maximilians-University Hospital, Munich, Germany
e-mail: felix.meinel@med.lmu.de

U.J. Schoepf, F.G. Meinel (eds.), *Multidetector-Row CT of the Thorax*, Medical Radiology,
DOI 10.1007/978-3-319-30355-0_17

1 Introduction

Coronary artery disease (CAD) remains the leading cause of death in most industrialized nations throughout the world (Yusuf et al. 2001). CAD is defined as narrowing or occlusion of coronary arteries, most commonly caused by atherosclerosis, leading to an inadequate oxygen supply of the myocardium. Over the last decades, CT has evolved into a very versatile tool for imaging ischemic heart disease. In asymptomatic patients at risk for CAD, CT coronary artery calcium scoring is frequently used to more precisely estimate a patient's risk for adverse cardiac events and thus guide risk factor modification. Coronary CT angiography (CCTA) has evolved into a routinely used modality which allows for noninvasive diagnosis or exclusion of CAD in patients with symptoms concerning for myocardial ischemia. Several studies have shown a consistently high sensitivity of approximately 95 % and a specificity of approximately 90 % for the detection of anatomically significant CAD. Therefore, it has been incorporated into most guidelines as a first-line noninvasive imaging modality to detect and especially rule out CAD. However, the specificity of CCTA for functionally relevant stenosis (i.e., stenosis causing myocardial ischemia) is rather low. Therefore, evolving CT techniques aim at assessing the hemodynamic significance of coronary artery lesions either by directly visualizing myocardial perfusion (CT myocardial perfusion imaging) or by computational fluid dynamics based on CCTA datasets (CT fractional flow reserve).

2 Coronary Artery Calcium Scoring

2.1 Appropriate Use

Coronary calcifications are a marker of the overall burden of coronary atherosclerosis. Coronary artery calcium scoring by CT is a useful imaging test for improving coronary risk assessment in asymptomatic patients with an intermediate cardiovascular risk. Current guidelines and appropriate use criteria consider coronary artery calcium scoring appropriate in patients with clinical risk factors suggesting an intermediate (10–20 %) 10-year risk of hard cardiac events and potentially appropriate in patients with a low to intermediate (6–10 %) risk (Greenland et al. 2010; Alani and Budoff 2014). The results of coronary artery calcium scoring can reclassify some of these patients into a lower or higher risk group and thus guide more aggressive or more lenient lifestyle modification and pharmacological therapy of cardiovascular risk factors. Patients with a low (<6 %) 10-year risk for cardiac events should not undergo coronary artery calcium scoring as there is no evidence that these patients benefit. Similarly, coronary artery calcium scoring is generally not considered an appropriate test in symptomatic patients with chronic or acute symptoms concerning for ischemic heart disease (Wolk et al. 2013).

2.2 Imaging Technique

Although first introduced on electron-beam CT systems, coronary artery calcium scoring is now performed with multi-detector CT as a prospectively ECG-triggered, low-dose, non-contrast CT acquisition of the heart. The examination is acquired at 120 kV since lower kV settings would overestimate calcium scores. The typical effective radiation dose associated with coronary artery calcium scoring is 0.5–1.5 mSv. Relatively thick (2.5–3 mm) axial slices are reconstructed using filtered back projection. The use of iterative reconstruction is generally discouraged as it may underestimate calcium scores. Semiautomated coronary calcium scoring is then performed on dedicated post-processing workstations (Fig. 1). The Agatston score is most commonly used and calculated by multiplying the area of a lesion by a weighting factor that depends on the maximum CT density in the lesion and then adding the scores for all calcified lesions in the coronary arteries (defined as lesions ≥1 mm in size with a density ≥130 HU). The volume score and the calcium mass score have been suggested as potentially more reproducible approaches to quantifying coronary artery calcium but remain less commonly used.

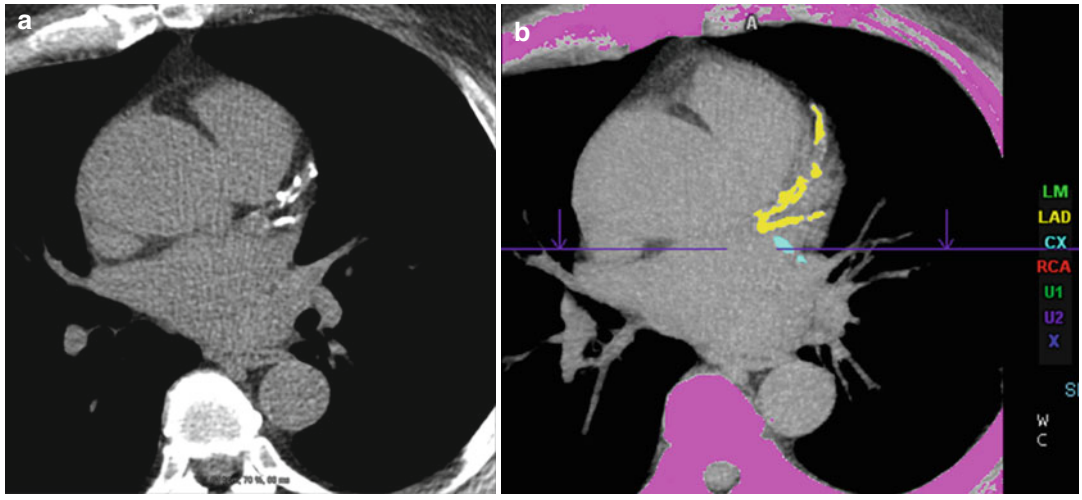

c

Artery	Lesions	Volume [mm3]	Equiv. mass [mg]	Score
LM	0	0.0	0.0	0.0
LAD	7	835.6	165.85	1041.3
CX	2	710.3	144.49	874.3
RCA	12	960.6	191.89	1106.4
Total	**21**	**2506.6**	**502.23**	**3022.0**

Fig. 1 Images from a 71-year-old male patient with a body mass index of 32.1 kg/m^2 with visible extensive calcifications of the left anterior descending (*LAD*, *yellow*) and circumflex (*CX*, turquoise) coronary arteries seen on calcium scoring CT. Figures show CT images (**a**), view in dedicated post-processing software (**b**), and corresponding calculated results (**c**)

2.3 Prognostic Value

Several, large prospective trials have conclusively demonstrated that coronary artery calcium scoring has incremental prognostic value beyond clinical risk factors for the risk stratification of asymptomatic individuals. A pooled analysis of six major studies encompassing more than 27,000 patients demonstrated that patients with no detectable coronary artery calcium (calcium score of 0) have a very low (0.4 %) risk of cardiac death or myocardial infarction during the next 3–5 years (Greenland et al. 2007). The presence of any detectable calcium (calcium score >0) inferred a 4.3-fold risk increase with relative risks (compared to a zero calcium score) of 1.9 for scores 1–112, 4.3 for scores 100–400, 7.2 for scores 400–999, and 10.8 for scores >1000 (Greenland et al. 2007). Two more recent studies have evaluated the prognostic value of coronary artery calcium scoring for all-cause mortality in more than 44,000 and 25,000 asymptomatic individuals, respectively (Alani and Budoff 2014). During a mean follow-up period of 5.6–6.8 years, both studies demonstrated a low (≈0.5 %) rate of all-cause mortality in patients with a calcium score of 0. The risk for all-cause mortality increased with increasing calcium score. The relative risk (compared to a calcium score of 0) was 12.5 in patients with a calcium score of >1000.

3 Coronary CT Angiography

3.1 Appropriate Use

CCTA is considered an appropriate test for the initial evaluation of patients with stable chest pain and an intermediate CAD likelihood, especially in the setting of an uninterpretable ECG or

inability to exercise (Wolk et al. 2013; Meinel et al. 2015). In symptomatic patients with a high pretest probability of CAD, CCTA may be an appropriate initial test as an alternative to invasive coronary angiography and/or functional testing (Wolk et al. 2013). In patients with a low pretest probability of CAD, CCTA is typically only considered appropriate in the setting of an uninterpretable ECG or inability to exercise (Wolk et al. 2013). In patients with stable chest pain and prior testing for suspected CAD, CCTA is an appropriate next diagnostic step for abnormal or equivocal findings at stress imaging or exercise ECG and may be appropriate in the setting of abnormal, potentially ischemic findings at rest ECG (Wolk et al. 2013). CCTA has an emerging role in triaging patients with acute chest pain in the emergency department, since three recent prospective studies have demonstrated that this strategy allows for an expedited, safe discharge of patients with a normal CCTA (Meinel et al. 2015). The role of CT imaging in acute chest pain is discussed in depth in a dedicated chapter of this book. It is further appropriate to use CCTA to exclude an ischemic etiology in newly diagnosed heart failure or new onset cardiac arrhythmias including ventricular tachycardia, ventricular fibrillation, or frequent premature ventricular contractions (Meinel et al. 2015). Further indications are the preoperative evaluation of patients undergoing non-coronary surgery and assessment of coronary anomalies.

In asymptomatic individuals, CCTA does not provide a clinically meaningful improvement in risk prediction compared to calcium scoring (Cho et al. 2012). Performing CCTA in asymptomatic individuals for the purpose of screening or risk stratification is therefore generally considered inappropriate due to the lack of a clear benefit/risk advantage (Earls et al. 2014). CCTA is also rarely appropriate in asymptomatic patients with known coronary artery disease and prior coronary revascularization. CCTA may be an option in the evaluation of patients with prior revascularization who experience recurrent symptoms, although invasive coronary angiography and/or functional tests are typically more appropriate in this setting (Wolk et al. 2013).

3.2 Imaging Technique

CCTA has seen rapid advances in imaging capabilities over the past decade. Due to the implementation of several major technical improvements, CCTA is capable of producing high-resolution images of the coronary arteries with simultaneous substantial reduction of radiation exposure (Schuhbaeck et al. 2013) (Fig. 2).

Patient preparation is key to achieving good image quality in CCTA. In particular, image quality in CCTA strongly depends on heart rate. It is recommended to lower the heart rate to a target of <60 bpm in all patients with a baseline heart rate above 60 bpm except those with contraindications to beta-blockers (such as asthma, severe COPD, hypotension, acute cardiac failure, or allergy to beta-blockers). Both oral regimens (typically 100 mg metoprolol PO 1 h prior to CT scan) and intravenous regimens (typically 5 mg metoprolol IV on arrival at CT, repeat injections of 2.5–5 mg metoprolol every 5 min as needed up to a total dose of 20–30 mg) are com-

Fig. 2 Image shows advanced virtual rendering technique reconstruction (Cinematic Rendering, Siemens) of a coronary CT angiography scan in a 54-year-old male patient with suspected coronary artery disease

monly used and have been demonstrated to be very safe (Mahabadi et al. 2010). However, many patients referred for cardiac CT have a history of hypertension or arrhythmia and are already medicated with beta-blockers. Additional beta-blockers may not be effective in reducing heart rate in these patients, and the ideal heart rate of <60 bpm is often not achievable. Furthermore, sublingual application of 1–2 sprays (0.4–0.8 mg) of nitroglycerin 5–7 min prior to the CT scan can improve visualization of coronary arteries by providing coronary artery dilatation and preventing coronary vasospasm. However, contraindications exist including concurrent medication with other vasodilators (e.g., sildenafil). Some authors have argued that newer scanner technologies with faster image acquisition and improved temporal resolution have made such premedications less important in clinical routine (Morsbach et al. 2014), but they are still clearly recommended.

After careful patient preparation, it is crucial to choose the most suitable method of ECG synchronization of the individual patient. This choice will chiefly depend on the clinical indication as well as the patient's age, weight, heart rate, and rhythm. The traditional retrospective ECG-gating mode acquires a spiral CT scan of the heart at low pitch such that image data at each point of the cardiac cycle is acquired for each portion of the heart along the z-axis. This method allows for robust CCTA acquisition even in patients with severe arrhythmia and simultaneously provides quantitative and qualitative functional analysis (e.g., depiction of wall motion abnormalities or determination of ejection fraction) since scan data is acquired throughout the entire cardiac cycle. However, only data from the cardiac phase with the least motion (usually the end-diastolic or end-systolic phase) is used for CCTA image reconstruction. This implies that a substantial amount of unnecessary data is acquired that does not contribute to the reconstruction images. Accordingly, retrospectively ECG-gated CCTA is associated with a relatively high effective radiation dose on the order of 12–20 mSv. This dose can be somewhat lowered by ECG-dependent dose current modulation, i.e., by substantially reducing tube current during cardiac phases that are unlikely to be used for CCTA image reconstruction. However, the indications for retrospectively ECG-gated CCTA are decreasing due to more robust and dose-efficient CCTA techniques and the use of alternative modalities for functional evaluation that are not associated with ionizing radiation.

Prospective ECG triggering is a dose-efficient CCTA acquisition technique in which the x-ray tube is activated only during a prespecified phase within the cardiac cycle which is expected to show minimal coronary motion. An end-diastolic image acquisition (around 70 % the R-R' interval) typically minimizes motion artifacts in patients with a relatively low heart rate (<70 bpm), whereas an end-systolic acquisition window (around 30–35 % of the R-R' interval) is most robust in patients with higher heart rates (>70 bpm). This technique has allowed for substantial dose reductions in CCTA with typical effective radiation doses on the order of 3–4 mSv (Earls et al. 2008; Menke et al. 2013). Prospectively ECG-triggered CCTA acquisition can be successfully employed even in most patients with substantial heart rate variability or arrhythmias. In such patients, it is often useful to use a fixed trigger delay (e.g., 300 ms after the R wave) rather than percentages of the R-R' interval. Recently, new padding techniques for prospectively gated acquisition which allow for more flexibility in image reconstruction and functional analysis have also been introduced and have shown promising results (Takx et al. 2012). Taken together, prospective ECG triggering is a robust and dose-efficient acquisition technique and should be the default protocol for CCTA in most patients.

The most advanced CT systems also allow "single heartbeat" CCTA in selected patients. This can either be achieved by using broad detectors (as in 320-detector row CT), which are able to capture the entire heart with a single gantry position, or with dual-source CT systems, which allow for the depiction of the entire heart within the diastolic phase of one heartbeat by using a prospectively ECG-triggered high-pitch spiral

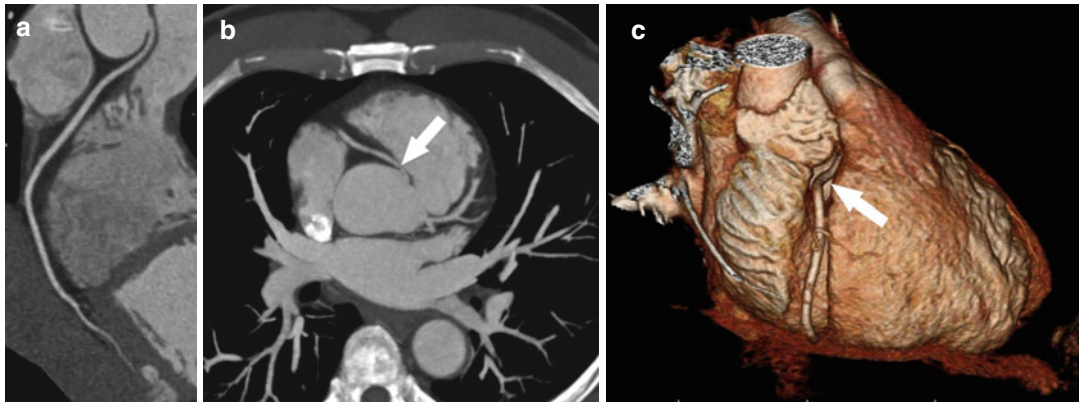

Fig. 3 Images of a 50-year-old male patient who underwent prospectively ECG-gated coronary CT angiography. There is no evidence of coronary atherosclerosis. However, curved multiplanar reformats (**a**), maximum intensity projections (**b**), and volume rendering technique images (**c**) show a coronary anomaly with the right coronary artery arising from the left coronary cusp (*arrow*) and taking an inter-arterial, partially intramural proximal course

acquisition. In suitable patients, this approach reduces the effective radiation dose to <1 mSv (Achenbach et al. 2010). However, this acquisition mode requires a regular and low heart rate (<60 beats/min) and is also problematic in heavier patients.

3.3 Image Reconstruction and Post-processing

Image reconstruction and post-processing play a crucial role in cardiac CT. CCTA images are typically reconstructed in thin (0.6–075 mm) axial slices using a smooth vascular reconstruction kernel. The use of sharper kernels can improve the evaluation of patients with severe calcifications or implanted coronary stents (Renker et al. 2011a; b). Furthermore, curved multiplanar reconstructions created by dedicated post-processing software are helpful for visualization of coronary anatomy and can help characterize stenosis and luminal obstruction. It should be noted that severity of coronary artery stenosis is usually slightly overestimated on CCTA compared to invasive catheter angiography (Doh et al. 2014). Three-dimensional virtual rendering is especially useful for visualization of coronary artery bypass grafts and coronary anomalies.

3.4 Techniques for Reduction of Radiation Exposure

Due to technical advances in CT technology, multiple approaches to decrease overall effective dose levels in cardiac imaging have been implemented. Especially for CCTA, the average radiation exposure has been reduced considerably over the last decade. While the effective radiation dose from 64-slice retrospectively ECG-gated coronary CT typically ranges from 8 to 25 mSv, newer technologies and imaging protocols allow image acquisition with <5 mSv in most patients and with <1 mSv in selected patients (Fig. 3).

Dose-efficient methods of ECG synchronization are now available on all state-of-the-art CT systems. Prospectively ECG-triggered sequential acquisition should be the default acquisition protocol for most patients undergoing CCTA and limits the effective dose to 3–4 mSv. Prospectively ECG-triggered high-pitch spiral image acquisition, which is available on second- and third-generation dual-source CT systems, can reduce effective dose below 1 mSv but is limited to patients with regular and relatively low heart rates <60 bpm (Achenbach et al. 2010) (Fig. 4).

Another widely available dose-saving strategy in CCTA is the use of automated software algorithms to select the most dose-efficient tube voltage for an individual patient (Ghoshhajra et al.

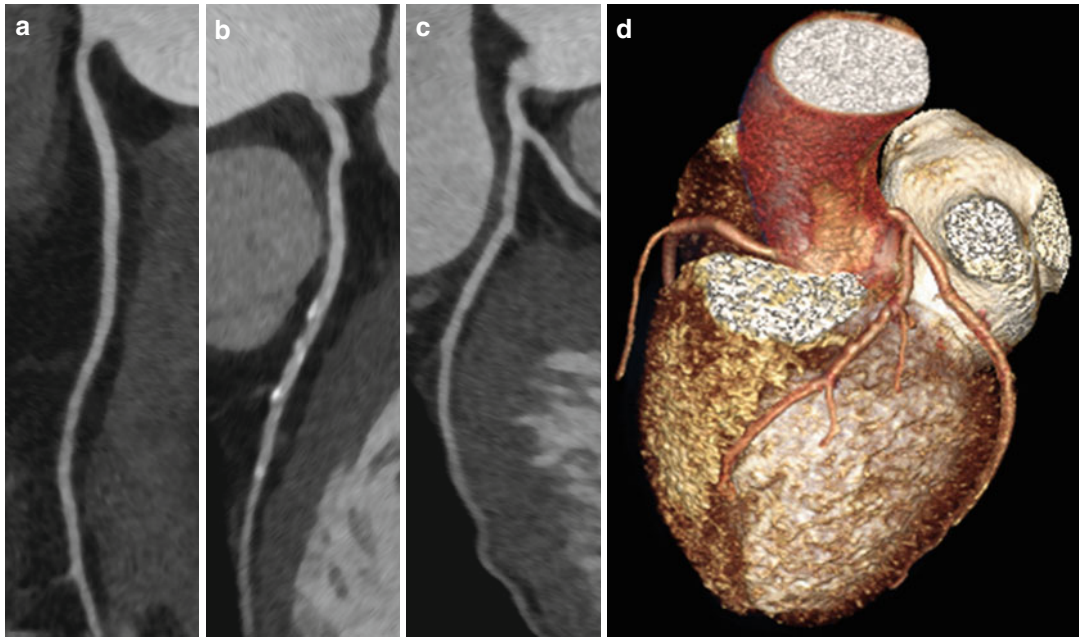

Fig. 4 Coronary CT angiography images of a 60-year-old woman (BMI 28.9 kg/m^2) with suspected coronary artery disease. Images were obtained using a prospectively ECG-triggered high-pitch protocol with a decreased tube voltage of 70 kVp resulting in an effective radiation dose of 0.9 mSv. Images show curved multiplanar reformats of the right coronary artery (**a**), left anterior descending artery with mild atherosclerotic changes (**b**), and left circumflex artery (**c**) and a volume rendering technique of the heart (**d**). No hemodynamically significant coronary artery stenosis was observed

2013; Leipsic et al. 2011; Krazinski et al. 2014). Since lowering tube voltage in suitable patients reduces radiation dose while increasing contrast attenuation, this approach has shown additional potential for reducing radiation exposure in CCTA while maintaining image quality (Layritz et al. 2013). These algorithms are typically used in conjunction with algorithms that modulate tube current along the z-axis tailored to the patient's attenuation profile. Layritz et al. demonstrated that attenuation-based selections of tube voltage and current are superior to BMI-based selection rules in CCTA (Layritz et al. 2013). Such technique is also helpful in defining suitable acquisition parameters in obese patients (Fig. 5).

Furthermore, the implementation and further development of iterative reconstruction algorithms have proven to allow a further reduction of radiation dose since they mitigate the increased image noise seen with lower dose. In an intraindividual comparison, Yin and colleagues demonstrated non-inferior image quality and diagnostic accuracy of CCTA acquired at 50 % reduced dose reconstructed with iterative reconstruction (Yin et al. 2013). Similarly, the PROTECTION V study recently demonstrated that iterative reconstruction allows for reducing dose by 30 % with no decrease in image quality and no increase in downstream testing (Deseive et al. 2015).

Several examples from the literature demonstrate how far radiation dose can be reduced if all available techniques for dose reduction are used in combination. These extreme examples show that – in selected patients – the radiation dose of CCTA can be reduced to values below 0.1 mSv when using high-pitch spiral acquisition at 80 kVp and raw data-based iterative reconstruction or to below 0.2 mSv when using a prospectively ECG-triggered high-pitch CCTA protocol at 70 kVp and iterative reconstruction while maintaining diagnostic imaging quality (Schuhbaeck et al. 2013; Zhang et al. 2014a).

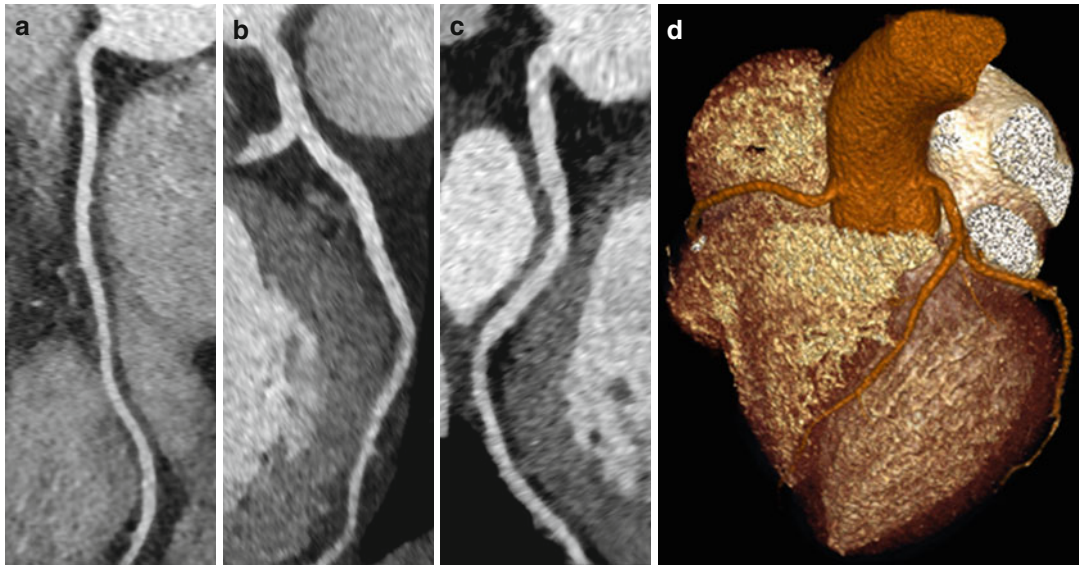

Fig. 5 Coronary CT angiography images of a 68-year-old obese female patient with a BMI of 47.2 kg/m^2. Suspected coronary artery disease was ruled out with diagnostic image quality despite the large body habitus. Images show curved multiplanar reformats of the right coronary artery (**a**), left anterior descending artery (**b**), and left circumflex artery (**c**) and a volume rendering technique of the heart (**d**)

3.5 Techniques for Reduction of Contrast Medium Volume

The risk of contrast-induced nephropathy from intravenous contrast agent has been disputed and is probably much lower than historically thought (Meinel et al. 2014a). Nevertheless, due to increased attention toward the risk of contrast-induced nephropathy, the development of CCTA protocols with low volumes of contrast agent constitutes an important aspect of current research. With the introduction of CT technologies with substantially decreased acquisition time, the duration of the contrast agent administration can be markedly shortened, simultaneously allowing for the reduction of contrast agent dose. Furthermore, lower tube voltage protocols enhance iodine attenuation and thus enable the use of lower amounts of contrast agent especially when combined with iterative reconstruction algorithms (Zhang et al. 2014a, b).

Zhang et al. investigated a prospectively ECG-triggered high-pitch CCTA protocol at 70 kV and 30 mL of contrast agent (370 mg iodine/ml) and found no significant differences regarding image quality compared to 80 and 100 kV protocols with 60 ml contrast agent in a patient population with a body mass index of less than 23 kg/m^2 (Zhang et al. 2014b). However, there are many factors influencing the arterial enhancement such as different iodine concentrations of the available contrast agents, scan duration, tube settings, and especially bodyweight which emphasize the need to tailor CCTA protocols on a per-patient basis (Alkadhi et al. 2008).

3.6 Diagnostic Accuracy

A large body of literature has investigated the accuracy of CCTA for detecting anatomically significant stenosis (commonly defined as ≥50 % reduction in luminal diameter) with invasive angiography as the reference standard (Meinel et al. 2015). Across all published meta-analyses on the accuracy of CCTA using at least 64-slice MDCT systems, the median sensitivity on a per-patient level was 97.8 % with 89.6 % specificity (Menke et al. 2013). This high sensitivity translates into a negative predictive value of 95–100 %.

A CCTA with fully diagnostic image quality that demonstrates no significant stenosis can thus exclude obstructive CAD with a high degree of certainty. These accuracy data chiefly originate from retrospectively ECG-gated CCTA and 64-slice MDCT. Several recent studies have evaluated the accuracy of CCTA using more dose-efficient techniques and more advanced CT systems. Two meta-analyses specifically analyzed studies on prospectively ECG-triggered CCTA and demonstrated a pooled sensitivity of 99–100 % and specificity of 89–91 % on a per-patient level (Menke et al. 2013; von Ballmoos et al. 2011). Other meta-analyses have investigated the diagnostic accuracy of CCTA with specific state-of-the-art CT systems. For 320-slice CCTA, a pooled per-patient sensitivity of 93 % and specificity of 86 % were reported, translating into a negative predictive value of 90 % (Li et al. 2013). For dual-source CT, pooled sensitivity was 98–99 % and specificity was 88–89 % with a negative predictive value of 98–99 % (Salavati et al. 2012; Li et al. 2014). Based on these results, it is reasonable to conclude that the accuracy of CCTA with state-of-the-art equipment and reduced-dose acquisition techniques is at least equivalent to retrospectively ECG-gated CCTA with 64-slice CT (Fig. 6).

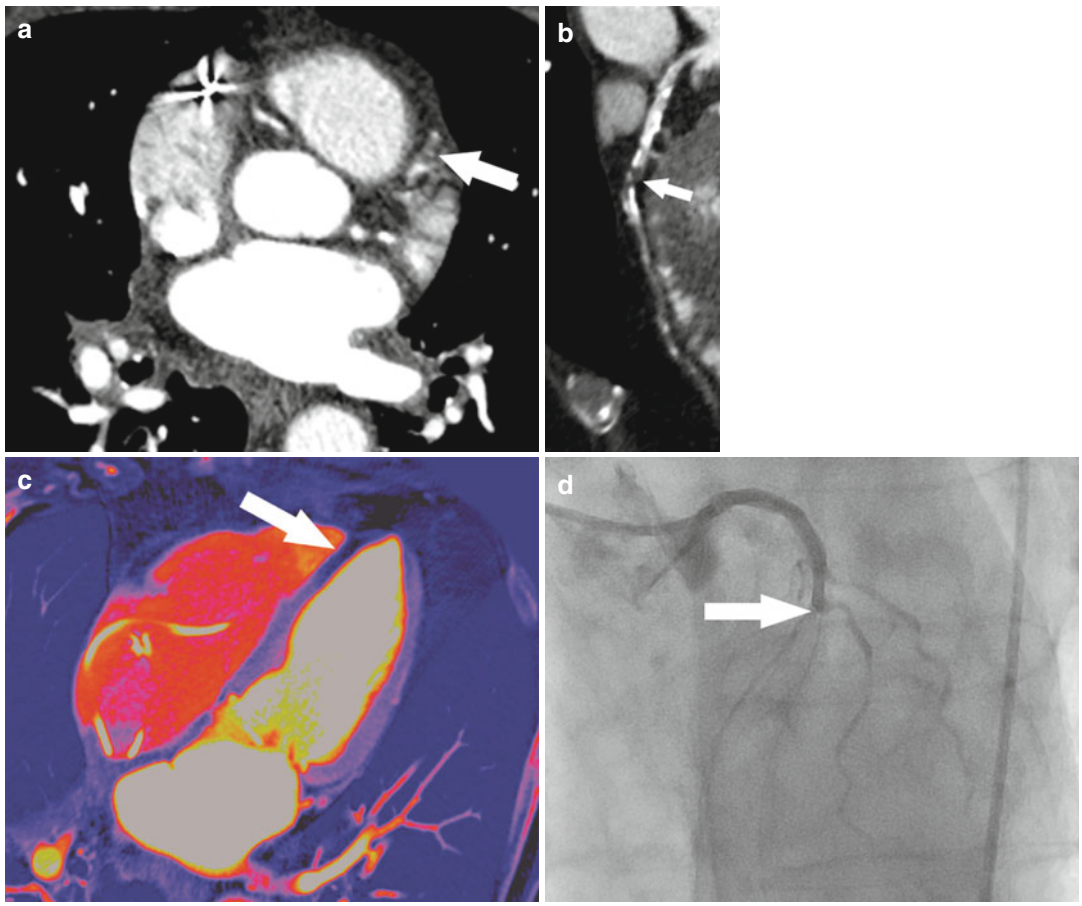

Fig. 6 Images of an 80-year-old male patient referred by the emergency department with acute chest pain and inconclusive electrocardiographic findings and lab results who underwent dual-energy coronary CT angiography. Axial images (**a**) demonstrate a complete occlusion of the left anterior descending artery (*arrow*), and curved multiplanar reconstructions (**b**) show diffuse calcified plaque. Dual-energy perfusion images (**c**) show a perfusion deficit (*arrow*) in the corresponding vessel territory. Invasive coronary angiography (**d**) confirmed the total occlusion of the left anterior descending artery (*arrow*) (Reprinted with permission from Wichmann et al. (2015))

3.7 Prognostic Value

In a meta-analysis analyzing 11 studies including a total of more than 7,000 mostly symptomatic patients with suspected CAD, the presence of any >50 % stenosis at CCTA was associated with a ten-fold higher risk for cardiovascular events during a median follow-up of 20 months. The finding of any evidence of CAD inferred a 4.5-fold risk, and each coronary segment involved increased the risk for adverse outcomes by 23 % (Bamberg et al. 2011a). A more recent analysis of more than 17,000 patients – the majority with chronic chest pain – showed that the number of proximal segments with mixed or calcified plaques and the number of proximal segments with ≥50 % stenosis were the CCTA parameters with the strongest predictive value for all-cause mortality at a median follow-up of 2.3 years (Hadamitzky et al. 2013a). Evidence on the more long-term prognostic value of CCTA is beginning to accumulate. Hadamitzky and colleagues followed more than 1,500 patients for a median of 5.6 years and found annual major adverse cardiac event (MACE) rates of 0.2 % for patients with no CAD and 1.1 % in patients with obstructive CAD (Hadamitzky et al. 2013b). Another study reported on 218 patients followed for a median of 6.9 years and recorded annual MACE rates of 0.3 %, 2.7 %, and 6.0 % in patients with normal CCTA, non-obstructive and obstructive CAD, respectively (Dougoud et al. 2014). In summary, the available evidence suggests that the presence of any CAD, obstructive CAD, and the burden of atherosclerotic changes at CCTA are strong predictors for cardiac outcomes in patients with chronic chest pain. A CCTA study negative for any evidence of CAD infers an excellent prognosis for at least 5 years.

4 CT Myocardial Perfusion Imaging

While CCTA has been established as a noninvasive modality to reliably rule out CAD, it still suffers from a moderate specificity to detect flow-limiting coronary stenosis (Gaemperli et al. 2008). This can be partly explained by the metabolism of the heart. Under resting conditions, approximately 80 % of the oxygen available in the coronary blood flow (CBF) is extracted by the myocardium (Strauer 1979). Since a coronary stenosis leads to a pressure drop across the stenosis, the distal coronary arterioles have to decrease the focal pressure by dilation to increase the intravascular blood volume. This coronary flow reserve is however limited and becomes exhausted under resting conditions if approximately >85 % stenosis is present and under pharmacological stress conditions with approximately >50 % stenosis (Strauer 1979; Heusch 2010). However, the degree of diameter stenosis is known to be a poor marker for hemodynamically significant stenosis. While most lesions with a luminal narrowing of <30–50 % on CT do not cause ischemia and most lesions with a luminal narrowing of >75–80 % do, there is considerable uncertainty regarding the hemodynamic relevance of stenoses in the intermediate range. The location, length, and geometrical configuration of a stenosis can all be factors influencing the hemodynamic significance of the lesion, which is therefore not accurately assessed by the degree of diameter stenosis alone.

To noninvasively assess the hemodynamic relevance of detected coronary stenosis, nuclear stress testing or – less commonly – MRI is often performed (Wagner et al. 2003). These techniques can have a negative impact on clinical workflow since additional examinations have to be scheduled and certain contraindications exist especially for MRI. Thus, a main goal of cardiac CT research has been the development of CTMPI techniques to provide a comprehensive anatomical and functional assessment of coronary artery stenosis (Pelgrim et al. 2015). Initial attempts to visualize myocardial perfusion using CT have been made in the late 1970s (Adams et al. 1976), but although multiple major technical advances were achieved, CTMPI still remains a research topic and has not translated into clinical routine. However, technical innovations have led to several recent studies which demonstrated a high diagnostic accuracy for CTMPI compared to established imaging modalities to assess myocardial perfusion and viability.

4.1 Technical Considerations

Time of CT Acquisition Available CTMPI protocols differ in regard to the timing of image acquisition. Static CTMPI techniques acquire a single "snapshot" of the blood distribution within the myocardium. This should be performed during the early moment of first-pass distribution, while contrast material is mostly intravascular (Heusch 2010). Dynamic CTMPI techniques consist in repeated acquisitions during the first-pass inflow and distribution of contrast medium into the myocardium. Some authors have advocated the additional acquisition of a delayed phase in order to visualize late iodine enhancement in the infarcted myocardium and thus determine myocardial viability. However, the signal-to-noise ratio of late enhancement CT imaging is often quite poor, and the value of this technique has been questioned (Meinel et al. 2014b).

Pharmacological Stress Agents Imaging of myocardial perfusion can be performed either under resting conditions, after administration of pharmacological stress agents, or both (Heusch 2010). Stress-only protocols are commonly used in order to limit radiation dose. Combined stress/rest acquisition protocols are necessary if perfusion defects need to be classified as reversible at rest or fixed. Different pharmacological stress agents have been suggested for CTMPI. Adenosine is most commonly used and administered in a continuous infusion with a dose of 140 μg/kg/min for at least 2 min to induce an increase in the heart rate of 10–20 beats above the resting heart rate (Varga-Szemes et al. 2015). Regadenoson is an alternative vasodilator drug that requires only a single bolus injection and has been suggested to have fewer systemic side effects. However, side effects and potentially serious complications have been reported with both agents.

Temporal Resolution Since pharmacological stress agents cause a substantial increase in heart rate, imaging under these conditions is more prone to motion artifacts and thus impaired image quality. This has a direct impact on the delineation of the subendocardial layers which are more sensitive to myocardial ischemia. Temporal resolution has been a major limitation of CTMPI since development of initial concepts. Recently introduced scanner generations provide a high enough temporal resolution for motion artifact CTMPI and especially dynamic acquisition which requires fast and repetitive scanning of the myocardium to visualize temporal changes in contrast distribution (Meyer et al. 2014).

Radiation Exposure Recent innovations in CT technology have substantially decreased the average exposure to ionizing radiation during CCTA. In contrast, CTMPI can be expected to result in substantially higher radiation doses during a comprehensive cardiac CT examination. While innovations to decrease dose for CTMPI can be expected within the near future, simple changes in the acquisition protocol which are already present in modern low-dose CCTA protocols can also be used applied to CTMPI. In that regard, modification of the tube voltage remains the main principle. A general limitation of CT is the relatively poor contrast resolution when imaging the soft tissue. This is also true for imaging of the heart since differences between the normal and hypoperfused myocardium usually do not exceed 50 Hounsfield units. By lowering the tube voltage closer to the k-edge of iodine, attenuation of the contrast-perfused soft tissue substantially increases. Simultaneously, significant reductions in radiation exposure can be achieved this way (Yoneyama et al. 2012). While prior scanner generations were limited regarding lowest tube voltage settings and accompanying increased image noise, newest scanners allow for image acquisition at values as low as 70 kV and have substantially reduced image noise at these levels (Meyer et al. 2014). Although these techniques should not be applied in obese patients due to a limited penetration depth of the x-ray photons, low-tube-voltage acquisition can be routinely applied in slim patients to reduce radiation exposure (Yoneyama et al. 2012).

4.2 Imaging Technique

Depending on the used CT system and physician preference, CTMPI can be performed using two completely different approaches, either static or dynamic mode.

Static CTMPI The basic principle of static acquisition is to capture a snapshot of the iodine distribution within the myocardium during the first-pass inflow of contrast medium into the myocardium. The advantage of this technique is the relatively straightforward acquisition which can be performed with most scanners and the lower radiation dose compared with dynamic CTMPI. In addition, static acquisition can also be performed in dual-energy mode which allows for optimized iodine quantification and calculation of color-coded iodine distribution maps which some authors have found superior for the detection of ischemia compared to standard grayscale static CTMPI datasets (Meinel et al. 2014b). In static CTMPI, assessment of myocardial perfusion is based on visual evaluation and measuring the attenuation of the ischemic area and comparing it to the remote – supposedly healthy – myocardium or normalizing it to the left ventricular blood pool. Since static CTMPI is performed during a single scan, this examination is highly dependent on timing and correct administration of the contrast material bolus. Therefore, optimal peak enhancement may be missed due to variations in perfusion during the examination or improper planning of the scan. Strongest contrast between the ischemic and normal myocardium is also dependent on the contrast material injection rate as well as cardiac function, rhythm, and output.

Dynamic CTMPI Dynamic CTMPI techniques consist in repeated acquisitions during the first-pass inflow and distribution of contrast medium into the myocardium. Thus, dynamic CTMPI is more independent of technical influences which might compromise optimal myocardial enhancement and therefore more robust in clinical routine (Meinel et al. 2014c). This technique requires a correction algorithm to mitigate respiratory motion artifacts. Dynamic CTMPI allows for the quantification of myocardial blood flow (MBF) and other perfusion parameters instead of relying on relative differences in attenuation (Fig. 7). Depending on the CT system, image acquisition

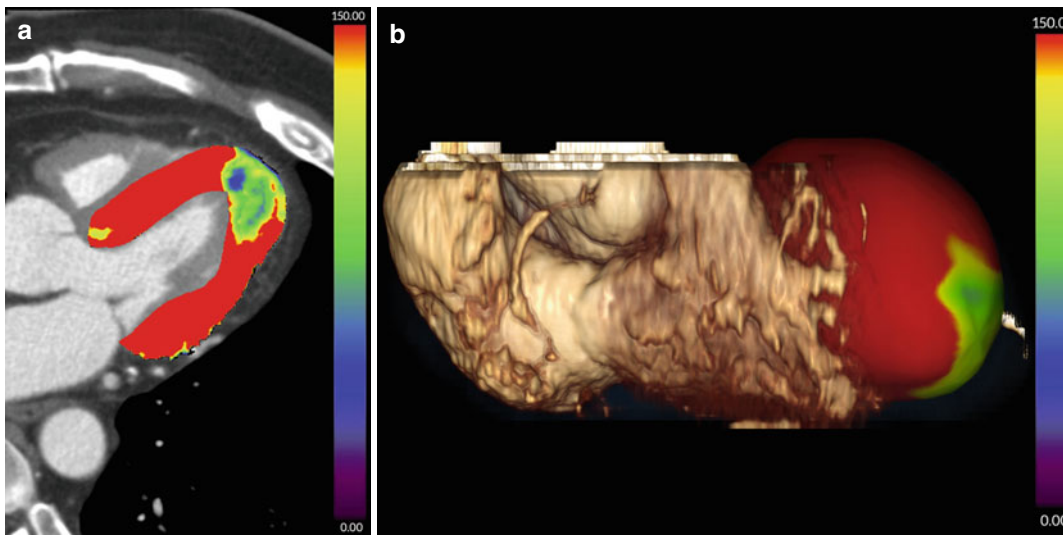

Fig. 7 Images from CT myocardial perfusion imaging in a 60-year-old man with suspected coronary artery disease show a focal, sharply demarcated perfusion deficit at the cardiac apex corresponding to a stenosis of the left anterior descending coronary artery. Decreased myocardial blood flow is indicated on the axial reformat (**a**) and the volume rendering technique image (**b**) in *green*

can be performed with the table in stationary position or in a shuttle mode technique with the table alternating quickly between two positions to cover the entire myocardium.

A major disadvantage of dynamic CTMPI is the higher radiation dose compared to static acquisition due to the multiple image acquisitions. The effective doses reported in the literature are on the order of 18 mSv for combined rest and stress CTMPI protocols and on the order of 9–10 mSv for a stress-only CTMPI protocol (Varga-Szemes et al. 2015). Nevertheless, the general principles for radiation dose reduction in cardiac CT can also be applied to dynamic CTMPI. Automatic tube current modulation during dual-source dynamic CTMPI has already been demonstrated to reduce radiation dose by approximately one third down to 7.7 mSv (Kim et al. 2013). Tube voltage can also be decreased as previously described. The expected decrease in image quality can be compensated by applying iterative reconstruction algorithms (Gramer et al. 2012).

4.3 Diagnostic Accuracy

A substantial body of literature on the diagnostic accuracy of both static and dynamic CTMPI techniques exists using established techniques such as SPECT, MR myocardial perfusion imaging, and invasive catheter angiography with or without fractional flow reserve measurements as reference standards (Varga-Szemes et al. 2015). However, experience is still limited to mostly smaller single-center studies.

Static CTMPI In a direct comparison with invasive coronary angiography and SPECT, static stress CTMPI has been shown to add incremental value to purely anatomical evaluation of CCTA in the detection of obstructive coronary lesions with increased sensitivity (91 % vs. 83 %), specificity (91 % vs. 71 %), PPV (86 % vs. 66 %), and NPV (93 % vs. 87 %), respectively (Rocha-Filho et al. 2010). Magalhaes et al. demonstrated that static stress CTMPI may improve the diagnostic accuracy of CCTA to detect in-stent restenosis which may be missed on anatomical datasets due to blooming artifacts (Magalhaes et al. 2011). Reports from the recently completed CORE320 (Combined Coronary Atherosclerosis and Myocardial Perfusion Evaluation Using 320-Detector Row CT) trial found that the combination of CCTA and CTMPI helped to correctly identify patients with flow-limiting obstructive coronary stenosis with a matching perfusion defect on SPECT/MRI. Rochitte et al. reported an AUC of 0.87 (95 % confidence interval, 0.84–0.91) to identify patients with or without hemodynamically significant CAD (Rochitte et al. 2014). George et al. reported a higher diagnostic performance of CTMPI compared to SPECT for the detection of anatomical CAD (stenosis ≥50 %) (George et al. 2014). Rybicki et al. reported a mean radiation dose for combined CTA and CTMPI in patients of the CORE320 trial of 8.6 mSv, which was significantly lower than the average dose of SPECT (10.5 mSv) or invasive diagnostic catheter angiography (11.6 mSv), further encouraging the implementation of combined CCTA and CTMPI in clinical routine (Rybicki et al. 2015).

Dynamic CTMPI A high diagnostic accuracy has also been reported for dynamic CTMPI which in addition allows for the calculation of MBF thresholds to detect perfusion deficits. Bamberg et al. initially analyzed 33 patients with a MBF cutoff value of 75 mL/100 mL/min and reported that CTMPI helped to increase the PPV for the detection of hemodynamically significant coronary artery stenosis detected via CCTA from 49 to 78 % (Bamberg et al. 2011b). Rossi et al. also found that the MBF index performed better than visual analysis of CCTA in the identification of hemodynamically relevant coronary stenosis (AUC, 0.95 vs. 0.85) (Rossi et al. 2014). In a recent meta-analysis, Pelgrim et al. reported a segment-based sensitivity and specificity for dynamic stress CTMPI compared to stress SPECT of 77 % and 89 %, respectively (Pelgrim et al. 2015). Dynamic CTMPI can also be used to quantify global myocardial perfusion parameters (Meinel et al. 2014c). Nevertheless, future

large-scale multicenter studies are necessary to establish standardized evaluation techniques and MBF thresholds for dynamic CTMPI and assess its diagnostic accuracy.

5 CT Fractional Flow Reserve

Most of the recent technological innovations in cardiac CT are driven by an increasing effort to provide a comprehensive evaluation of the coronary artery and myocardial disease during a single examination. While CCTA has a very high sensitivity for the detection of severe coronary artery stenosis, its specificity for functionally relevant stenosis (i.e., stenosis causing myocardial ischemia) is rather low. This is particularly true for intermediate lesions (50–75 % luminal stenosis). This is not necessarily a limitation of CT technology per se but rather the nature of these lesions since approximately only half of such intermediate lesions cause ischemia, while the other half does not impair coronary blood flow. Thus, the hemodynamic significance of such lesions cannot be reliably assessed with established CT techniques.

Since this is a limitation of all anatomical imaging techniques, during invasive coronary angiography an additional pressure wire is inserted and advanced over the stenosis in question. The fractional flow reserve (FFR) is measured as the ratio between the coronary pressure distal to the stenosis divided by the pressure proximal to the lesion (commonly measured within the ascending aorta) during pharmacologically induced hyperemia. Invasive assessment of FFR has been established as the gold standard for evaluation of lesion-specific hemodynamic significance. FFR values below 0.8 or 0.75 have been confirmed in large-scale studies as thresholds to detect relevant ischemia and necessity for revascularization.

Recently, the intriguing concept of FFR has also been applied to CT technology. Using dedicated post-processing algorithms, CT-based FFR values can be obtained from routinely performed CCTA examinations (Fig. 8). Interestingly, CT-FFR has shown good agreement with invasive FFR measurements in multiple large-scale studies although no pharmacological stress agents are administered during CT.

5.1 Technical Considerations

The basic principle for CT-FFR is based on sophisticated calculations comprising computational fluid dynamic algorithms to model fluid flow. These techniques are established in industrial engineering to predict flow properties in pipe and wind canal design. These algorithms were first translated into modeling of lesion-specific coronary flow as a dedicated off-site service ("FFR_{CT}," Heartflow, Inc., Redwood City, CA). This service provides a color-coded three-dimensional visualization of blood flow in the major epicardial vessels with accompanying segmental FFR_{CT} values. Several multicenter studies reported that this technique shows a very good agreement with invasively obtained FFR values and can therefore be used as an additional evaluation technique especially in lesions with intermediate stenosis and uncertain hemodynamic significance.

Since it would be desirable to perform post-processing on-site to save time in clinical workflows, a different approach for CT-derived FFR assessment has been recently introduced ("cFFR," Siemens Healthcare, Forchheim, Germany) (Renker et al. 2014a). By employing reduced-order and full-order models for rapid calculation of coronary artery tree models, this noninvasive technique can be used on a standard dedicated workstation to obtain lesion-specific assessment via FFR values (Baumann et al. 2014; Renker et al. 2014b).

5.2 Diagnostic Accuracy

Multiple large-scale prospective studies have confirmed the diagnostic performance of the FFR_{CT} approach (Heartflow, Inc.) compared to invasive FFR measurements. In the single-center DISCOVER-FLOW (Diagnosis of Ischemia-Causing Stenoses Obtained Via Noninvasive

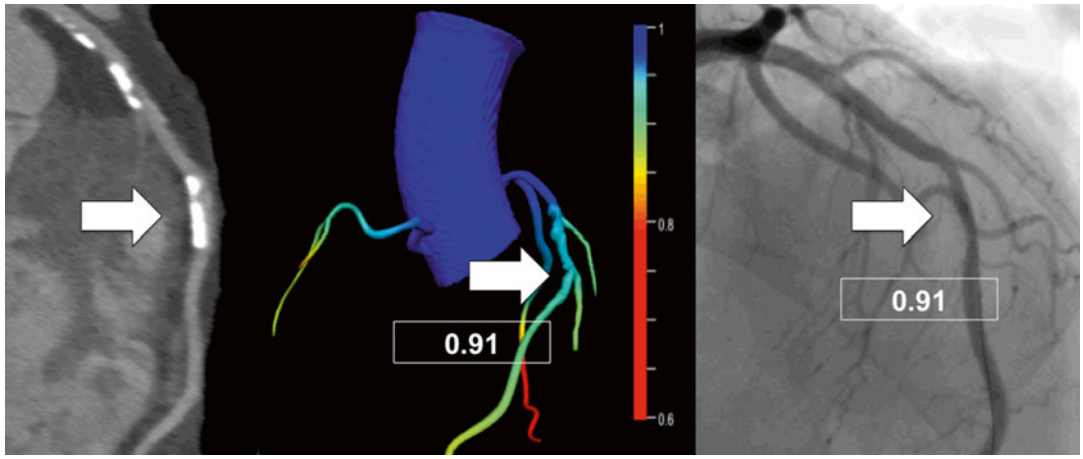

Fig. 8 Images of a 67-year-old male patient who underwent coronary CT angiography. An extensive mostly calcified plaque in the left anterior descending coronary artery can be seen. Using dedicated on-site postprocessing, CT fractional flow reserve (FFR) was computed and visualized in a color-coded three-dimensional model. The FFR value of the stenosis was calculated as 0.91 based on the CT datasets, indicating a nonsignificant lesion (a FFR value ≤0.80 is commonly considered hemodynamically significant). Subsequent invasive coronary angiography confirmed the presence of the stenosis and nonsignificant FFR value using catheter-based FFR measurements

Fractional Flow Reserve) trial with 103 patients, FFR_{CT} demonstrated 81 % accuracy, 93 % sensitivity, 82 % specificity, 85 % positive predictive value (PPV), and 91 % negative predictive value (NPV) on a per-patient basis compared to invasive FFR measurements (Koo et al. 2011). When compared to conventional assessment of CCTA datasets, FFR_{CT} resulted in a higher accuracy for detecting ischemia-causing coronary lesions (0.90 vs. 0.75, $P = 0.001$).

The DeFACTO (Determination of Fractional Flow Reserve by Anatomic Computed Tomographic Angiography) study explored the diagnostic performance of FFR_{CT} in a multicenter setting with 252 patients. On a per-patient basis, the diagnostic accuracy to detect hemodynamically significant coronary artery stenosis was significantly higher for FFR_{CT} compared to visual assessment of CCTA datasets (sensitivity, 90 % vs. 84 %; specificity, 54 % vs. 42 %; PPV, 67 % vs. 61 %; NPV, 84 % vs. 72 %) (Min et al. 2012). FFR_{CT} (AUC, 0.81; 95 % CI, 0.75–0.86; $P < 0.001$) also showed a higher diagnostic power for the detection of obstructive CAD compared to CCTA (AUC, 0.68; 95 % CI, 0.62–0.74). Remarkably, a substantially increased sensitivity for the detection of significant stenosis specifically in intermediate-grade lesions (30–70 % luminal degree of obstruction) was observed for FFR_{CT} (82 % vs. 37 %) compared to CCTA with similar specificity (66 % vs. 66 %).

In the similarly large multicenter prospective NXT (Analysis of Coronary Blood Flow Using CT Angiography: Next Steps) trial, Norgaard et al. also observed a superior diagnostic performance of FFR_{CT} compared to visual CCTA analysis on a per-patient analysis (AUC, 0.90 vs. 0.81) for the detection of obstructive CAD (Norgaard et al. 2014). In this study, FFR_{CT} was particularly helpful for reclassifying lesions with false-positive (67 %) findings on CCTA compared to invasive FFR measurements.

Experience with the novel on-site cFFR algorithm is currently scarce and limited to single-center studies. Renker et al. reported a significantly higher diagnostic accuracy for evaluation of significant coronary stenosis (AUC, 0.92 vs. 0.72) on a per-lesion basis compared to CCTA in 53 patients (Renker et al. 2014b). Calculation of cFFR required 37.5 ± 13.8 min on average. Baumann et al. investigated the same on-site technique in 28 patients and reported an

average necessary calculation time of 51.9 ± 9.0 min and a relatively strong correlation between cFFR and invasive FFR values (Pearson's correlation coefficient $r = 0.74$) (Baumann et al. 2014). Additional large-scale multicenter studies are required to further validate this technique for clinical practice.

5.3 Future Perspectives

CT-FFR is one of the most promising innovations in the field of cardiovascular imaging. In accordance with CCTA and CTMPI, a comprehensive assessment of coronary artery stenosis and hemodynamic significance of detect lesions may be provided in the future. Since CT-FFR is based on standard CCTA datasets, no additional radiation exposure is required. However, future studies are required to confirm the diagnostic accuracy and impact on clinical outcome of this technique. Auxiliary applications of CT-FFR algorithms may be the pre-procedural virtual planning of coronary stent or bypass graft placement to assess and visualize the impact of expected changes in coronary flow (Kim et al. 2014).

6 Summary

CT is evolving into an ever more versatile tool for the evaluation of patients with suspected or known coronary artery disease. Coronary artery calcium scoring consists in a low-dose, non-contrast CT scan and provides important prognostic information that helps refine risk stratification in asymptomatic patients at intermediate risk for cardiac events. In symptomatic patients with a low to intermediate pretest probability of CAD, CCTA is an appropriate option to rule out or confirm potentially obstructive CAD. The indications for CCTA should be informed by available guidelines and appropriate use criteria. In recent years, the acquisition techniques for CCTA have constantly evolved toward reducing radiation exposure and contrast media volume. CT myocardial perfusion imaging and CT-FFR are novel, investigational techniques that can improve the specificity of CCTA for hemodynamically relevant stenosis either by directly visualizing myocardial perfusion or by extracting functional information from CCTA datasets using computational fluid dynamics. It seems likely that both of these techniques will be valuable in specific clinical scenarios. CT-FFR appears particularly attractive in cases where CCTA allows good anatomical evaluation of the coronary vasculature and shows an intermediate stenosis with unclear hemodynamic significance. CT myocardial perfusion imaging could be useful in patients in whom heavy coronary calcifications or smaller stents preclude the anatomical visualization of the coronary lumen. However, more research is needed to establish the appropriate clinical role of these techniques.

References

Achenbach S, Marwan M, Ropers D et al (2010) Coronary computed tomography angiography with a consistent dose below 1 mSv using prospectively electrocardiogram-triggered high-pitch spiral acquisition. Eur Heart J 31(3):340–346

Adams DF, Hessel SJ, Judy PF, Stein JA, Abrams HL (1976) Computed tomography of the normal and infarcted myocardium. AJR Am J Roentgenol 126(4):786–791

Alani A, Budoff MJ (2014) Coronary calcium scoring and computed tomography angiography: current indications, future applications. Coron Artery Dis 25(6):529–539

Alkadhi H, Stolzmann P, Scheffel H et al (2008) Radiation dose of cardiac dual-source CT: the effect of tailoring the protocol to patient-specific parameters. Eur J Radiol 68(3):385–391

Bamberg F, Sommer WH, Hoffmann V et al (2011a) Meta-analysis and systematic review of the long-term predictive value of assessment of coronary atherosclerosis by contrast-enhanced coronary computed tomography angiography. J Am Coll Cardiol 57(24):2426–2436

Bamberg F, Becker A, Schwarz F et al (2011b) Detection of hemodynamically significant coronary artery stenosis: incremental diagnostic value of dynamic CT-based myocardial perfusion imaging. Radiology 260(3):689–698

Baumann S, Wang R, Schoepf UJ et al (2014) Coronary CT angiography-derived fractional flow reserve correlated with invasive fractional flow reserve measurements – initial experience with a novel physician-driven algorithm. Eur Radiol 25(4):1201–1207

Cho I, Chang HJ, Sung JM et al (2012) Coronary computed tomographic angiography and risk of all-cause mortality and nonfatal myocardial infarction in subjects without chest pain syndrome from the CONFIRM Registry (coronary CT angiography evaluation for clinical outcomes: an international multicenter registry). Circulation 126(3):304–313

Deseive S, Chen MY, Korosoglou G et al (2015) Prospective randomized trial on radiation dose estimates of CT angiography applying iterative image reconstruction: the PROTECTION V Study. JACC Cardiovasc Imaging 8(8):888–896

Doh JH, Koo BK, Nam CW, et al. Diagnostic value of coronary CT angiography in comparison with invasive coronary angiography and intravascular ultrasound in patients with intermediate coronary artery stenosis: results from the prospective multicentre FIGURE-OUT (Functional Imaging criteria for GUiding REview of invasive coronary angiOgraphy, intravascular Ultrasound, and coronary computed Tomographic angiography) study (2014) Eur Heart J Cardiovasc Imaging 15(8):870–877

Dougoud S, Fuchs TA, Stehli J et al (2014) Prognostic value of coronary CT angiography on long-term follow-up of 6.9 years. Int J Cardiovasc Imaging 30(5):969–976

Earls JP, Berman EL, Urban BA et al (2008) Prospectively gated transverse coronary CT angiography versus retrospectively gated helical technique: improved image quality and reduced radiation dose. Radiology 246(3):742–753

Earls JP, Woodard PK, Abbara S et al (2014) ACR appropriateness criteria asymptomatic patient at risk for coronary artery disease. J Am Coll Radiol 11(1):12–19

Gaemperli O, Schepis T, Valenta I et al (2008) Functionally relevant coronary artery disease: comparison of 64-section CT angiography with myocardial perfusion SPECT. Radiology 248(2):414–423

George RT, Mehra VC, Chen MY et al (2014) Myocardial CT perfusion imaging and SPECT for the diagnosis of coronary artery disease: a head-to-head comparison from the CORE320 multicenter diagnostic performance study. Radiology 272(2):407–416

Ghoshhajra BB, Engel LC, Karolyi M et al (2013) Cardiac computed tomography angiography with automatic tube potential selection: effects on radiation dose and image quality. J Thorac Imaging 28(1):40–48

Gramer BM, Muenzel D, Leber V et al (2012) Impact of iterative reconstruction on CNR and SNR in dynamic myocardial perfusion imaging in an animal model. Eur Radiol 22(12):2654–2661

Greenland P, Bonow RO, Brundage BH, et al. ACCF/AHA 2007 clinical expert consensus document on coronary artery calcium scoring by computed tomography in global cardiovascular risk assessment and in evaluation of patients with chest pain: a report of the American College of Cardiology Foundation Clinical Expert Consensus Task Force (ACCF/AHA Writing Committee to Update the 2000 Expert Consensus Document on Electron Beam Computed Tomography) developed in collaboration with the Society of Atherosclerosis Imaging and Prevention and the Society of Cardiovascular Computed Tomography (2007) J Am Coll Cardiol 49(3):378–402

Greenland P, Alpert JS, Beller GA et al (2010) 2010 ACCF/AHA guideline for assessment of cardiovascular risk in asymptomatic adults: a report of the American College of Cardiology Foundation/American Heart Association Task Force on Practice Guidelines. Circulation 122(25):e584–e636

Hadamitzky M, Achenbach S, Al-Mallah M et al (2013a) Optimized prognostic score for coronary computed tomographic angiography: results from the CONFIRM registry (COronary CT Angiography EvaluatioN For Clinical Outcomes: An InteRnational Multicenter Registry). J Am Coll Cardiol 62(5):468–476

Hadamitzky M, Taubert S, Deseive S et al (2013b) Prognostic value of coronary computed tomography angiography during 5 years of follow-up in patients with suspected coronary artery disease. Eur Heart J 34(42):3277–3285

Heusch G (2010) Adenosine and maximum coronary vasodilation in humans: myth and misconceptions in the assessment of coronary reserve. Basic Res Cardiol 105(1):1–5

Kim SM, Kim YN, Choe YH (2013) Adenosine-stress dynamic myocardial perfusion imaging using 128-slice dual-source CT: optimization of the CT protocol to reduce the radiation dose. Int J Cardiovasc Imaging 29(4):875–884

Kim KH, Doh JH, Koo BK et al (2014) A novel noninvasive technology for treatment planning using virtual coronary stenting and computed tomography-derived computed fractional flow reserve. JACC Cardiovasc Interv 7(1):72–78

Koo BK, Erglis A, Doh JH et al (2011) Diagnosis of ischemia-causing coronary stenoses by noninvasive fractional flow reserve computed from coronary computed tomographic angiograms. Results from the prospective multicenter DISCOVER-FLOW (Diagnosis of Ischemia-Causing Stenoses Obtained Via Noninvasive Fractional Flow Reserve) study. J Am Coll Cardiol 58(19):1989–1997

Krazinski AW, Meinel FG, Schoepf UJ et al (2014) Reduced radiation dose and improved image quality at cardiovascular CT angiography by automated attenuation-based tube voltage selection: intra-individual comparison. Eur Radiol 24(11):2677–2684

Layritz C, Muschiol G, Flohr T et al (2013) Automated attenuation-based selection of tube voltage and tube current for coronary CT angiography: reduction of radiation exposure versus a BMI-based strategy with an expert investigator. J Cardiovasc Comput Tomogr 7(5):303–310

Leipsic J, LaBounty TM, Mancini GB et al (2011) A prospective randomized controlled trial to assess the diagnostic performance of reduced tube voltage for coronary CT angiography. AJR Am J Roentgenol 196(4):801–806

Li S, Ni Q, Wu H et al (2013) Diagnostic accuracy of 320-slice computed tomography angiography for detection of coronary artery stenosis: meta-analysis. Int J Cardiol 168(3):2699–2705

Li M, Zhang GM, Zhao JS et al (2014) Diagnostic performance of dual-source CT coronary angiography with and without heart rate control: systematic review and meta-analysis. Clin Radiol 69(2):163–171

Magalhaes TA, Cury RC, Pereira AC et al (2011) Additional value of dipyridamole stress myocardial perfusion by 64-row computed tomography in patients with coronary stents. J Cardiovasc Comput Tomogr 5(6):449–458

Mahabadi AA, Achenbach S, Burgstahler C et al (2010) Safety, efficacy, and indications of beta-adrenergic receptor blockade to reduce heart rate prior to coronary CT angiography. Radiology 257(3):614–623

Meinel FG, De Cecco CN, Schoepf UJ, Katzberg R (2014a) Contrast-induced acute kidney injury: definition, epidemiology, and outcome. Biomed Res Int 2014:859328

Meinel FG, De Cecco CN, Schoepf UJ et al (2014b) First-arterial-pass dual-energy CT for assessment of myocardial blood supply: do we need rest, stress, and delayed acquisition? Comparison with SPECT. Radiology 270(3):708–716

Meinel FG, Ebersberger U, Schoepf UJ et al (2014c) Global quantification of left ventricular myocardial perfusion at dynamic CT: feasibility in a multicenter patient population. AJR Am J Roentgenol 203(2):W174–W180

Meinel FG, Bayer RR 2nd, Zwerner PL, De Cecco CN, Schoepf UJ, Bamberg F (2015) Coronary computed tomographic angiography in clinical practice: state of the art. Radiol Clin North Am 53(2):287–296

Menke J, Unterberg-Buchwald C, Staab W, Sohns JM, Seif Amir Hosseini A, Schwarz A (2013) Head-to-head comparison of prospectively triggered vs retrospectively gated coronary computed tomography angiography: meta-analysis of diagnostic accuracy, image quality, and radiation dose. Am Heart J 165(2):154–63.e3

Meyer M, Haubenreisser H, Schoepf UJ et al (2014) Closing in on the K edge: coronary CT angiography at 100, 80, and 70 kV-initial comparison of a second-versus a third-generation dual-source CT system. Radiology 273(2):373–382

Min JK, Leipsic J, Pencina MJ et al (2012) Diagnostic accuracy of fractional flow reserve from anatomic CT angiography. JAMA 308(12):1237–1245

Morsbach F, Gordic S, Desbiolles L et al (2014) Performance of turbo high-pitch dual-source CT for coronary CT angiography: first ex vivo and patient experience. Eur Radiol 24(8):1889–1895

Norgaard BL, Leipsic J, Gaur S et al (2014) Diagnostic performance of noninvasive fractional flow reserve derived from coronary computed tomography angiography in suspected coronary artery disease: the NXT trial (Analysis of Coronary Blood Flow Using CT Angiography: Next Steps). J Am Coll Cardiol 63(12):1145–1155

Pelgrim GJ, Dorrius M, Xie X et al (2015) The dream of a one-stop-shop: meta-analysis on myocardial perfusion CT. Eur J Radiol 84(12):2411–2420

Renker M, Nance JW Jr, Schoepf UJ et al (2011a) Evaluation of heavily calcified vessels with coronary CT angiography: comparison of iterative and filtered back projection image reconstruction. Radiology 260(2):390–399

Renker M, Ramachandra A, Schoepf UJ et al (2011b) Iterative image reconstruction techniques: applications for cardiac CT. J Cardiovasc Comput Tomogr 5(4):225–230

Renker M, Wang R, Schoepf UJ, Spearman JV, Baumann S (2014a) A novel approach for fractional flow reserve derivation from coronary computed tomographic angiography. Coron Artery Dis 26(3):279–280

Renker M, Schoepf UJ, Wang R et al (2014b) Comparison of diagnostic value of a novel noninvasive coronary computed tomography angiography method versus standard coronary angiography for assessing fractional flow reserve. Am J Cardiol 114(9):1303–1308

Rocha-Filho JA, Blankstein R, Shturman LD et al (2010) Incremental value of adenosine-induced stress myocardial perfusion imaging with dual-source CT at cardiac CT angiography. Radiology 254(2):410–419

Rochitte CE, George RT, Chen MY et al (2014) Computed tomography angiography and perfusion to assess coronary artery stenosis causing perfusion defects by single photon emission computed tomography: the CORE320 study. Eur Heart J 35(17):1120–1130

Rossi A, Dharampal A, Wragg A et al (2014) Diagnostic performance of hyperaemic myocardial blood flow index obtained by dynamic computed tomography: does it predict functionally significant coronary lesions? Eur Heart J Cardiovasc Imaging 15(1):85–94

Rybicki FJ, Mather RT, Kumamaru KK et al (2015) Comprehensive assessment of radiation dose estimates for the CORE320 study. AJR Am J Roentgenol 204(1):W27–W36

Salavati A, Radmanesh F, Heidari K, Dwamena BA, Kelly AM, Cronin P (2012) Dual-source computed tomography angiography for diagnosis and assessment of coronary artery disease: systematic review and meta-analysis. J Cardiovasc Comput Tomogr 6(2):78–90

Schuhbaeck A, Achenbach S, Layritz C et al (2013) Image quality of ultra-low radiation exposure coronary CT angiography with an effective dose <0.1 mSv using high-pitch spiral acquisition and raw data-based iterative reconstruction. Eur Radiol 23(3):597–606

Strauer BE (1979) Myocardial oxygen consumption in chronic heart disease: role of wall stress, hypertrophy and coronary reserve. Am J Cardiol 44(4):730–740

Takx RA, Moscariello A, Schoepf UJ et al (2012) Quantification of left and right ventricular function and myocardial mass: comparison of low-radiation dose 2nd generation dual-source CT and cardiac MRI. Eur J Radiol 81(4):e598–e604

Varga-Szemes A, Meinel FG, De Cecco CN, Fuller SR, Bayer RR 2nd, Schoepf UJ (2015) CT myocardial perfusion imaging. AJR Am J Roentgenol 204(3):487–497

von Ballmoos MW, Haring B, Juillerat P, Alkadhi H (2011) Meta-analysis: diagnostic performance of low-radiation-dose coronary computed tomography angiography. Ann Intern Med 154(6):413–420

Wagner A, Mahrholdt H, Holly TA et al (2003) Contrast-enhanced MRI and routine single photon emission computed tomography (SPECT) perfusion imaging for detection of subendocardial myocardial infarcts: an imaging study. Lancet 361(9355):374–379

Wichmann JL, Hu X, Engler A et al (2015) Dose levels and image quality of second-generation 128-slice dual-source coronary CT angiography in clinical routine. Radiol Med 120(12):1112–1121

Wolk MJ, Bailey SR, Doherty JU, et al. ACCF/AHA/ASE/ASNC/HFSA/HRS/SCAI/SCCT/SCMR/STS 2013 multimodality appropriate use criteria for the detection and risk assessment of stable ischemic heart disease: a report of the American College of Cardiology Foundation Appropriate Use Criteria Task Force, American Heart Association, American Society of Echocardiography, American Society of Nuclear Cardiology, Heart Failure Society of America, Heart Rhythm Society, Society for Cardiovascular Angiography and Interventions, Society of Cardiovascular Computed Tomography, Society for Cardiovascular Magnetic Resonance, and Society of Thoracic Surgeons (2014) J Am Coll Cardiol 63(4):380–406

Yin WH, Lu B, Li N et al (2013) Iterative reconstruction to preserve image quality and diagnostic accuracy at reduced radiation dose in coronary CT angiography: an intraindividual comparison. JACC Cardiovasc Imaging 6(12):1239–1249

Yoneyama K, Vavere AL, Cerci R et al (2012) Influence of image acquisition settings on radiation dose and image quality in coronary angiography by 320-detector volume computed tomography: the CORE320 pilot experience. Heart Int 7(2):e11

Yusuf S, Reddy S, Ounpuu S, Anand S (2001) Global burden of cardiovascular diseases: Part II: variations in cardiovascular disease by specific ethnic groups and geographic regions and prevention strategies. Circulation 104(23):2855–2864

Zhang LJ, Qi L, Wang J et al (2014a) Feasibility of prospectively ECG-triggered high-pitch coronary CT angiography with 30 mL iodinated contrast agent at 70 kVp: initial experience. Eur Radiol 24(7):1537–1546

Zhang LJ, Qi L, De Cecco CN et al (2014b) High-pitch coronary CT angiography at 70 kVp with low contrast medium volume: comparison of 80 and 100 kVp high-pitch protocols. Medicine (Baltimore) 93(22):e92

Comprehensive CT Imaging in Acute Chest Pain

Amelia M. Wnorowski and Ethan J. Halpern

Abstract

Triple rule-out (TRO) CT simultaneously evaluates the coronary arteries, aorta and pulmonary arteries for the patient presenting with acute chest pain in the emergency department. Compared to dedicated coronary CT angiography (cCTA), TRO CT requires slightly more intravenous contrast and a higher radiation dose. Appropriate patient selection is essential. TRO CT is most appropriate for patients at low to intermediate risk for acute coronary syndrome and in whom alternative diagnoses, such as pulmonary embolism or acute aortic pathology, are being considered. Adequate patient selection, preparation, premedication, and monitoring ensure a high-quality diagnostic study. The major differences between TRO CT and dedicated cCTA are scan length and injection technique. Compared to cCTA, where images are obtained between the carina and diaphragm, TRO CT must include the entire thoracic aorta and the pulmonary arteries. Injection protocols are tailored to provide high levels of arterial enhancement in the left- (coronary arteries and aorta) and right-sided circulations (pulmonary arteries). Different strategies may be employed to limit radiation exposure, including electrocardiogram (ECG) tube current modulation and prospective ECG gating. When performed with careful attention to technique, TRO CT provides high-quality diagnostic opacification of the coronary arteries, aorta and pulmonary arteries equal to that of dedicated CT angiography. A negative study allows for the safe and rapid discharge from the emergency department and a reduction in subsequent testing.

A.M. Wnorowski (✉) • E.J. Halpern
Department of Radiology, Thomas Jefferson University, Philadelphia, PA, USA
e-mail: Amelia.Wnorowski@jefferson.edu; Ethan.Halpern@jefferson.edu

U.J. Schoepf, F.G. Meinel (eds.), *Multidetector-Row CT of the Thorax*, Medical Radiology,
DOI 10.1007/978-3-319-30355-0_18

1 Introduction to Triple Rule-Out CT

Acute chest pain is a common presenting complaint in the emergency department in the United States, accounting for 5.5 million visits in 2007–2008 or 9 % of all emergency department visits (Bhuiya et al. 2010). Acute coronary syndrome (ACS) is a serious cause of acute chest pain with high morbidity and mortality, as well as an estimated annual cost of $150 billion (Kolansky 2009). Approximately 3–33 % of patients with ACS die from their ACS, and up to 30 % of discharged ACS patients are rehospitalized within 6 months (Kolansky 2009; Ropp et al. 2015). Morbidity and mortality are reduced with accurate and rapid diagnosis. However, ACS accounts for a minority of acute chest pain visits, only 13 % in 2007–2008 (Bhuiya et al. 2010). Patient presentation is often not straightforward, and various other diagnoses are often considered. The workup of acute chest pain can be expensive and time consuming and may include electrocardiogram (ECG) evaluation, laboratory tests, diagnostic imaging studies, and observation or hospital admission. The goal of diagnostic imaging is to triage patients in the emergency department and allow for safe and rapid discharge directly from the emergency department after life-threatening conditions have been excluded. The use of advanced diagnostic imaging for acute chest pain evaluation increased from 3.4 % of all emergency department visits in 1999–2000 to 15.9 % in 2007–2008 (Bhuiya et al. 2010).

Triple rule-out (TRO) CT is an attractive option for acute chest pain assessment, simultaneously examining the coronaries, aorta, and pulmonary arteries as well as the adjacent extravascular structures (Fig. 1). TRO CT excludes the potentially fatal diagnoses of pulmonary embolism and aortic dissection, along with ACS. When used in the appropriate patient population, TRO CT can be safe, efficient, and cost-effective. When performed with appropriate technique, TRO CT image quality is equivalent to dedicated coronary CT angiography (cCTA) for evaluation of the coronary arteries but with greater enhancement of the distal thoracic aorta and adequate enhancement of the pulmonary arteries for diagnosis of pulmonary embolism (Halpern et al. 2009; Shapiro et al. 2009; Rahmani et al. 2009; Johnson et al. 2007; Litmanovich et al. 2008). Note that comprehensive cardiac CT imaging may include perfusion imaging or CT fractional flow reserve calculation, but these topics are covered in other chapters of this text.

Multiple studies have been performed comparing dedicated cCTA to invasive coronary angiography, demonstrating a high negative predictive value of 83–99 % (Budoff et al. 2008; Miller et al. 2008; Meijboom et al. 2008). As discussed in other chapters, dedicated cCTA may be superior to myocardial perfusion imaging in the acute chest pain setting, (Gallagher et al. 2007) with decreased time to diagnosis, with decreased cost for the acute care episode, and without increase in major cardiac adverse events (Goldstein et al. 2011). The main limitation of cCTA in the acute setting is the relatively low specificity, as patients with intermediate severity lesions often require further physiological testing to confirm presence of clinically significant disease (Goldstein et al. 2007; Chen et al. 2012). The major strength of cCTA is in its high negative predictive value in low- to intermediate-risk patients, allowing for the safe, rapid discharge of these patients directly from the emergency department after a negative evaluation (Goldstein et al. 2007; Hoffmann et al. 2012; Litt et al. 2012; Chang et al. 2008a, b). Patients discharged after a negative cCTA have very low risk of adverse cardiovascular events at 1–2 years (Rubinshtein et al. 2007; Hollander et al. 2009; Schlett et al. 2011). In patients admitted for further workup, cCTA results in decreased length of stay compared to standard evaluation. Although cCTA reduces repeat evaluations for recurrent chest pain, (Goldstein et al. 2007) at least one study links cCTA to increased downstream testing and higher radiation exposure (Hoffmann et al. 2012).

In contrast to dedicated cCTA, TRO CT simultaneously evaluates the pulmonary arteries, entire thoracic aorta, and additional portions of the adjacent lung zones. TRO CT can be helpful to evaluate patients with acute chest pain in whom additional diagnoses other than ACS are

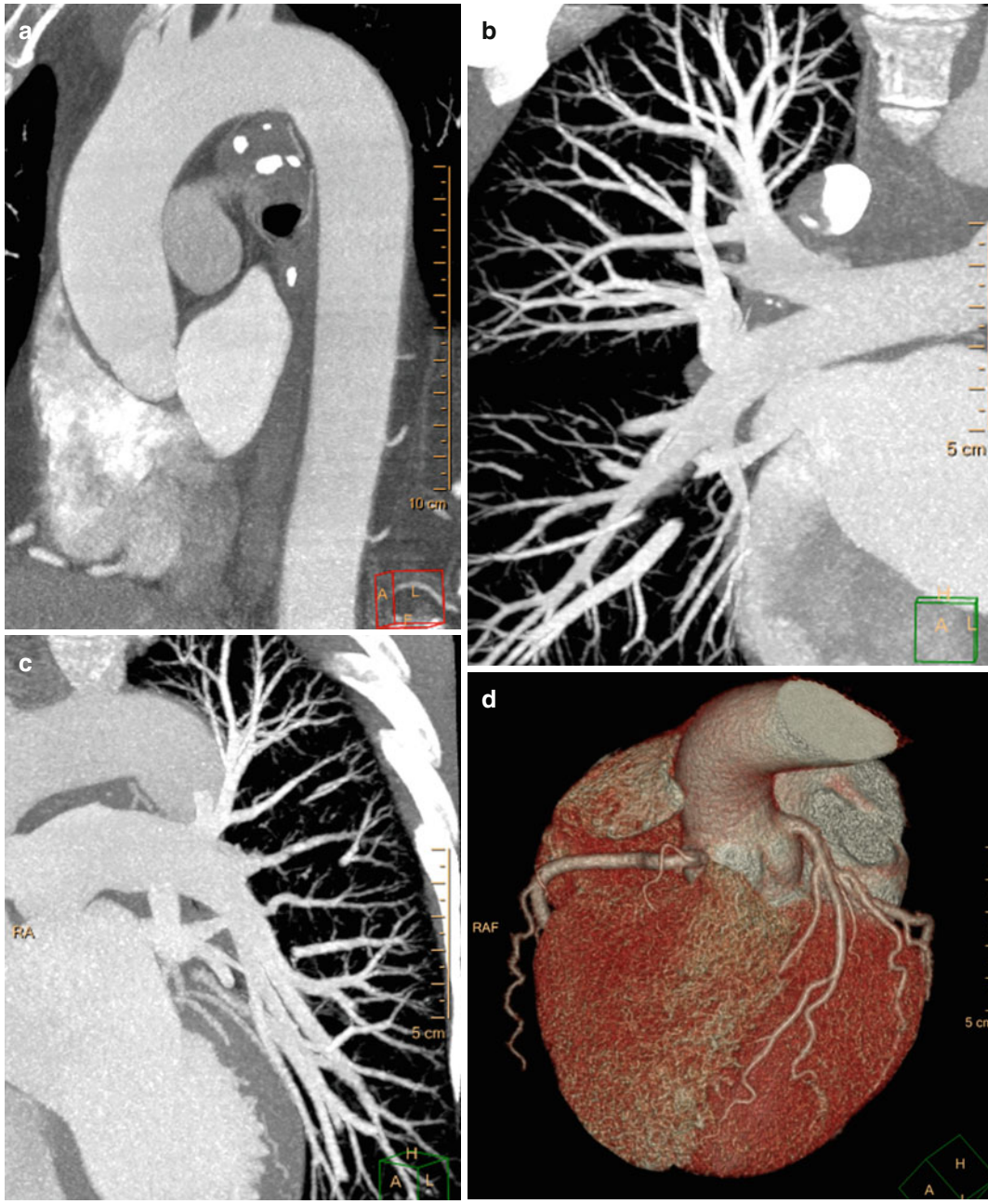

Fig. 1 Images from a normal TRO CT. Oblique sagittal slab maximum intensity projection (MIP) image of the thoracic aorta (**a**) and coronal slab MIP images of the right (**b**) and left (**c**) pulmonary arteries show normal vascular opacification without acute aortic pathology or pulmonary embolism. Both right- and left-sided circulations are opacified adequately. The scan length includes the aortic arch (**a**) allowing for complete evaluation of the thoracic aorta. Note adequate opacification to the level of the subsegmental pulmonary artery branches (**b**, **c**). Volume-rendered images of the coronary arteries (**d**, **e**) demonstrate opacification of all coronary arteries without stenosis or segmental occlusion. Slab MIP images allow evaluation of each vessel individually to exclude disease (**f** left anterior descending (LAD)

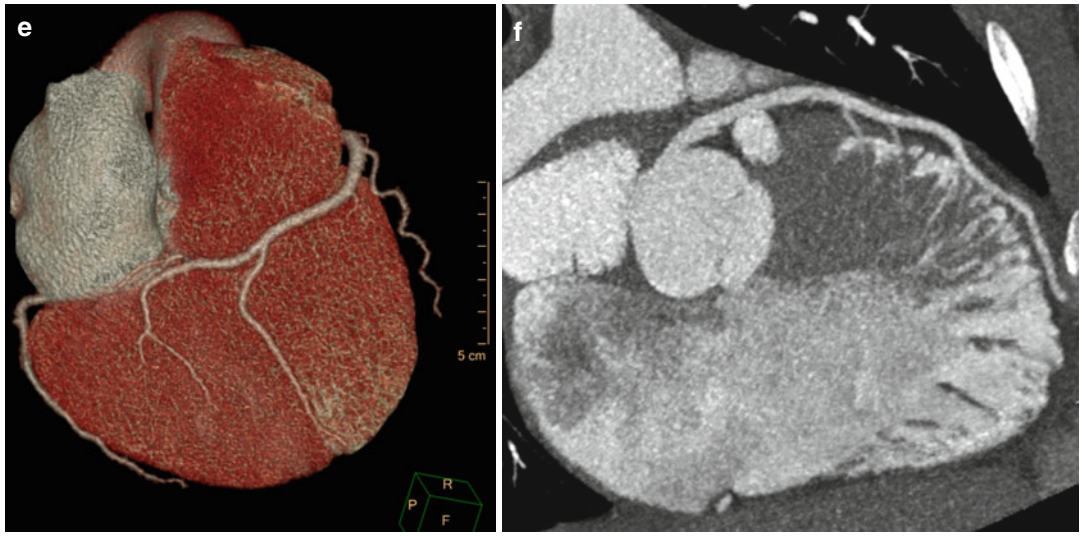

Fig. 1 (continued)

considered. Because the image quality of TRO CT is equivalent to dedicated cCTA (Halpern et al. 2009; Shapiro et al. 2009; Rahmani et al. 2009; Johnson et al. 2007; Litmanovich et al. 2008), we expect the same diagnostic accuracy and negative predictive value for TRO CT as cCTA with respect to coronary artery evaluation. Published reports suggest that TRO CT has a sensitivity of 94.3 % and specificity of 97.4 % for the diagnosis of coronary disease (Ayaram et al. 2013) with a negative predictive value similar to dedicated cCTA of 99 % (Takakuwa and Halpern 2008), allowing for safe discharge of patients with negative evaluations (Gruettner et al. 2013). Unlike cCTA, there are only a few studies directly comparing TRO CT to invasive coronary angiography. These demonstrate 100 % sensitivity and negative predictive value for coronary disease (Johnson et al. 2008) and high agreement with invasive coronary angiography (Litmanovich et al. 2008). TRO CT reduces length of hospitalization and cost compared to invasive coronary angiography (Savino et al. 2006). Compared to nuclear stress imaging, TRO CT results in decreased length of stay and mean imaging time but with higher mean imaging cost related to the higher charge for TRO CT as compared with dedicated cCTA (Takakuwa et al. 2011).

The main advantage of TRO CT over cCTA is in the evaluation of noncoronary diagnoses (Figs. 2, 3, and 4). In a previous study at our institution, TRO CT identified a noncoronary diagnosis to explain the presenting complaint in 11 % of patients and eliminated the need for further diagnostic testing in over 75 % of patients (Takakuwa and Halpern 2008). A more recent review of our 9-year experience performing TRO CT demonstrated a significant noncoronary diagnosis that may explain the chest pain presentation in 8.9 % of patients. These most commonly included pulmonary embolism, aortic aneurysm, and other aortic pathology. Approximately one third of noncoronary diagnoses would not have been identified on a dedicated cCTA (Wnorowski and Halpern 2016) because of unopacified right-sided circulation or limited z-axis coverage in cCTA (Figs. 5 and 6).

The relatively low prevalence of pulmonary embolism and aortic dissection in the TRO CT population has largely precluded calculation of sensitivity for these conditions (Ayaram et al. 2013). Diagnostic accuracy of dedicated CT angiography for acute aortic dissection (Willoteaux et al. 2004; Yoshida et al. 2003; Hamada et al. 1992; Shiga et al. 2006; Sebastia et al. 1999) and pulmonary embolism (Quiroz et al. 2005; Ghanima et al. 2005; Prologo et al.

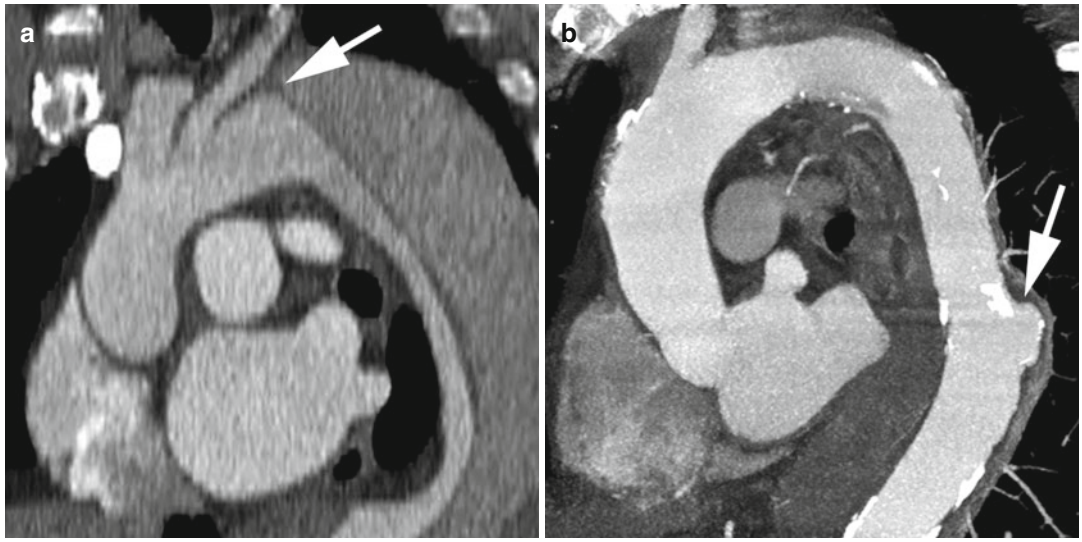

Fig. 2 Acute aortic pathology. Oblique sagittal slab MIP image from TRO CT (**a**) demonstrates a type B aortic dissection extending from the distal aortic arch (*arrow*) to the descending aorta. Inclusion of the aortic arch in the scan length of TRO CT allows for more complete evaluation in cases of aortic dissection. Oblique sagittal slab MIP image from TRO CT in a second patient (**b**) shows diffuse atherosclerotic changes with a penetrating ulcer of the mid descending thoracic aorta (*arrow*)

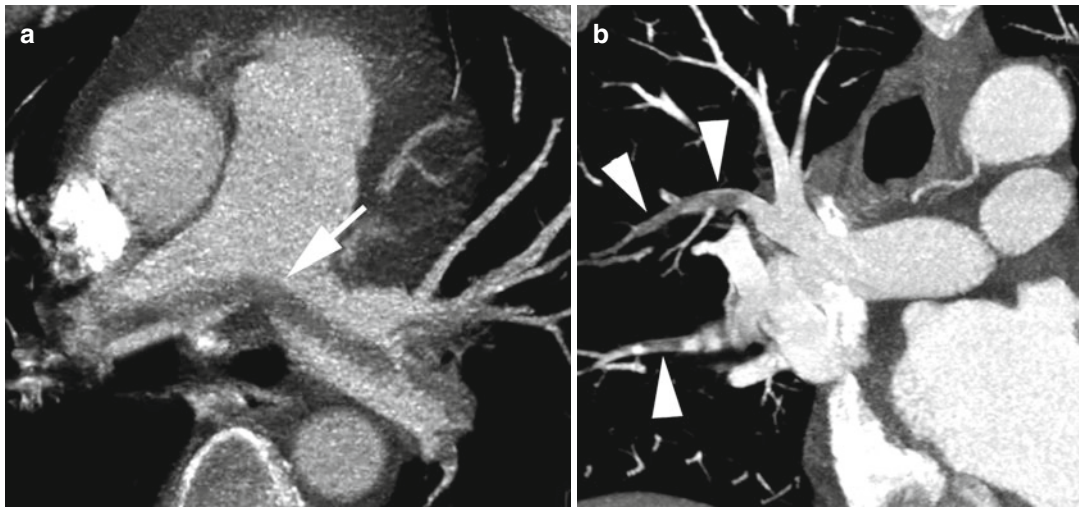

Fig. 3 Acute pulmonary embolism. Axial slab MIP image (**a**) demonstrates a central filling defect (*arrow*) spanning the right and left main pulmonary arteries, consistent with an acute saddle pulmonary embolus. Oblique coronal slab MIP image (**b**) in a second patient shows acute pulmonary emboli within right upper and middle lobe segmental and subsegmental pulmonary artery branches (*arrowheads*)

2004; Ghaye et al. 2002) has been well established. As there is no difference in vascular enhancement and image quality in properly performed TRO CT compared to dedicated CT angiography, we can expect similar diagnostic accuracy. The high quality that is routinely obtained for aortic and pulmonary evaluation with our TRO CT studies is illustrated in the previous figures (Figs. 2, 3, 5, and 6). Overall sensitivity, specificity, and positive and negative

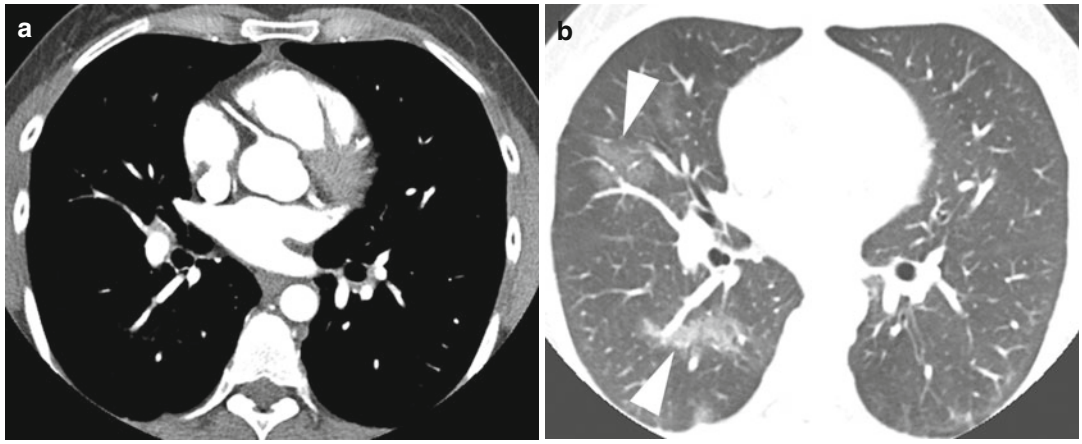

Fig. 4 Pneumonia. Axial CT image from a TRO CT in a soft tissue window (**a**) in a patient presenting with acute chest pain shows normal coronary arteries. The same axial CT image displayed in a lung window (**b**) demonstrates multifocal pneumonia with airspace opacities in the right middle and lower lobes (*arrowheads*)

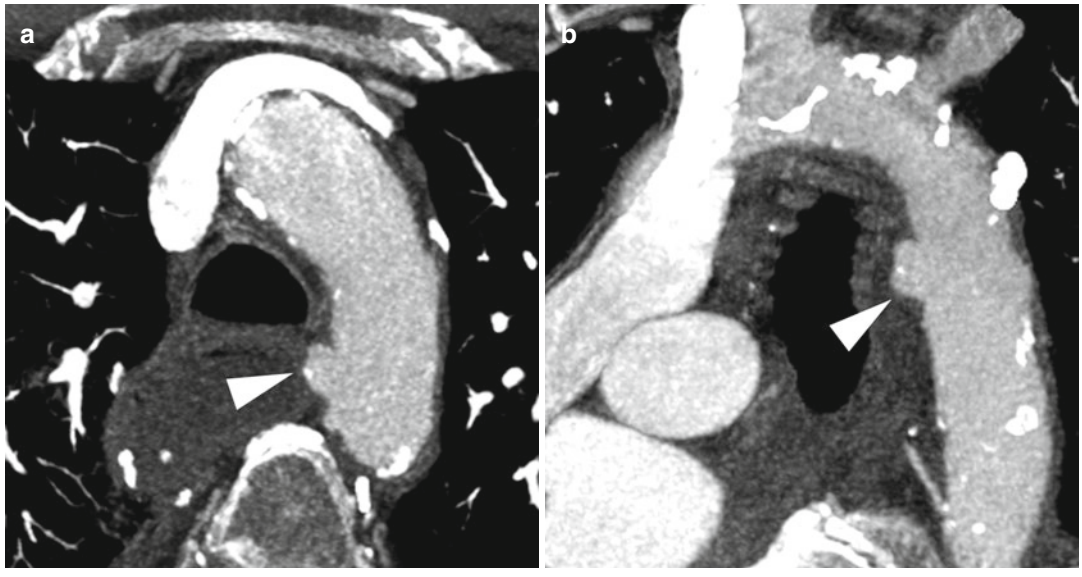

Fig. 5 Penetrating aortic ulcer of the distal aortic arch. Axial (**a**) and oblique sagittal (**b**) slab MIP images demonstrate diffuse atherosclerotic changes of the thoracic aorta with a penetrating ulcer of the distal aortic arch (*arrowheads*). This ulcer would not have been included within the typical z-axis coverage of a dedicated coronary CTA (cCTA)

predictive value of TRO CT for the diagnosis of all vascular pathology is 100 %, 98 %, 95 %, and 100 %, respectively (Schertler et al. 2009). Other authors who have evaluated patients presenting with suspected pulmonary embolism have also demonstrated a significant number of non-pulmonary embolism diagnoses that were well evaluated with TRO CT (Schertler et al. 2009).

In summary, TRO CT provides a single imaging study to evaluate major vascular pathology in the aorta, pulmonary arteries, and coronary circulation. Evaluation with either cCTA or TRO CT reduces total healthcare costs as compared to standard of care evaluation with a nuclear stress study (Henzler et al. 2013). Although there is data suggesting TRO CT to be equivalent to

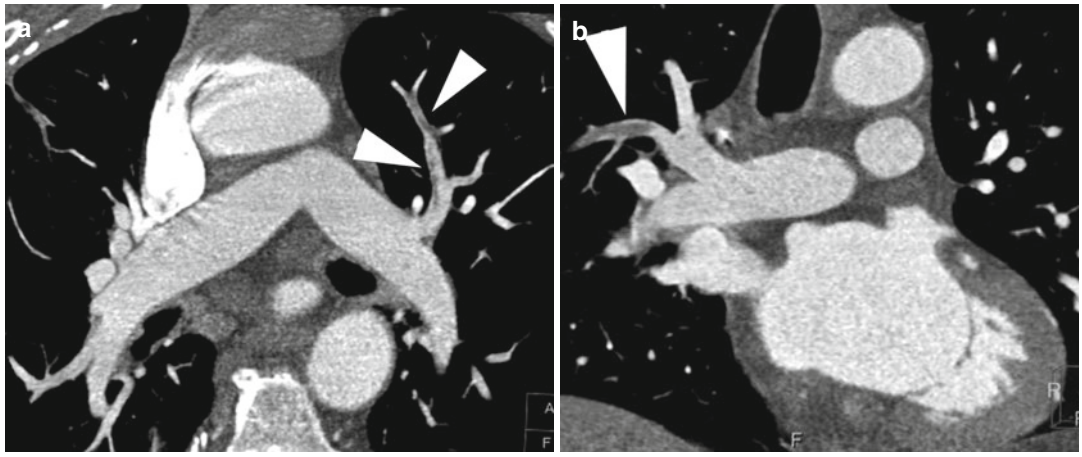

Fig. 6 Isolated acute upper lobe pulmonary emboli. Axial slab MIP image (**a**) from a TRO CT demonstrates an isolated left upper lobe pulmonary embolus extending into an anterior segmental branch (*arrowheads*). Oblique coronal slab MIP image (**b**) in a second patient shows an isolated right upper lobe pulmonary embolus involving a segmental branch (*arrowhead*). Opacification of right-sided circulation and extended z-axis coverage allow for identification of pulmonary emboli that would not be diagnosed on dedicated cCTA. Because of decreased z-axis coverage, isolated upper lobe pulmonary emboli would likely be missed even if dedicated cCTA opacified both right- and left-sided circulations, especially in the case of isolated upper lobe segmental branch emboli (**b**)

dedicated coronary, aortic, or pulmonary CTA, several studies have failed to demonstrate superior clinical outcomes with TRO CT, such as improved diagnostic yield, decreased length of stay, reduced diagnostic time, reduced adverse events, or diminished downstream resource use (Rogers et al. 2011; Madder et al. 2011). The major objections to TRO CT as compared to dedicated CT angiography are higher radiation dose and increased iodinated contrast exposure, (Ayaram et al. 2013) making appropriate patient selection for this protocol of utmost importance.

2 Patient Selection

Appropriate patient selection is crucial to the diagnostic accuracy and effective application of TRO CT. The ideal patient for TRO CT presents to the emergency department with acute chest pain where an alternative diagnosis to ACS, such as pulmonary embolism or acute aortic syndrome, is a real diagnostic concern in addition to the possibility of ACS. Some centers limit TRO CT to patients with a positive d-dimer in whom pulmonary embolism needs to be excluded (Gruettner et al. 2013). At our institution, positive d-dimer, while often a factor in the decision to order a TRO CT, is not a requirement. If the suspected diagnosis is truly limited to ACS, cCTA is more appropriate because of decreased radiation dose and iodinated contrast load. Similarly, if pulmonary embolism or acute aortic syndrome is the only diagnosis considered, dedicated CT angiography of the pulmonary arteries or aorta may be preferred, as there is no justification for the additional premedication, radiation dose, and interpretation time that is required for cCTA.

Importantly, TRO CT, like cCTA, is most effective in patients at low to intermediate risk for ACS, which ensures a high negative predictive value. A high negative predictive value is critical for safe discharge of patients from the emergency department after a negative evaluation. Therefore, patients with few risk factors, negative initial cardiac biomarkers (myoglobin and troponin I), and normal or nonspecific ECG are most appropriate. Patients with positive biomarkers or dynamic ECG changes are considered high risk and are more appropriate for cardiac catheterization. Some patients may have

low-level cardiac biomarkers, but the diagnosis of ACS is not certain, and other diagnoses are still being considered. In this population, TRO CT is appropriate.

There is reduced diagnostic accuracy of cCTA or TRO CT in high-risk patients or patients with known coronary artery disease for several reasons. First, high calcified plaque burden limits coronary evaluation and often leads to overestimation of disease burden due to blooming artifact. Extensive coronary calcifications are more likely in older patients with more coronary risk factors (Wexler et al. 1996). Patients with elevated calcium scores (>400–1000) are more likely to have indeterminate results (Hecht and Bhatti 2008), and the performance of calcium scoring may be considered prior to the study to determine if a patient is an appropriate candidate for cCTA or TRO CT. Second, the presence of coronary stents limits coronary evaluation due to resultant artifact, increasing the probability of indeterminate results. TRO CT is not recommended in these patient populations. Similarly, TRO CT is of limited utility in patients with a history of coronary artery bypass grafting because of the heavily calcified native vessels. Lastly, high-risk patients are more likely to have evidence of coronary disease which will require additional physiological evaluation, such as with stress testing and/or cardiac catheterization with evaluation of fractional flow reserve.

Patients selected for TRO CT must be able to tolerate the CT and cooperate with breathing instructions. Cardiac rate and rhythm must be compatible with ECG gating to ensure adequate image quality. The preferred heart rate is sinus bradycardia. While abnormal cardiac rate or rhythm is not an absolute contraindication, it can make obtaining diagnostic quality images challenging. New CT technology with increased temporal resolution has reduced the impact of arrhythmias on image quality. Ultimately, the decision of whether to proceed depends on the severity of the arrhythmia and the capability of the CT scanner. Lastly, the patient must be able to receive intravenous iodinated contrast. Patients with contrast allergy or renal impairment may not be appropriate candidates for TRO CT.

3 Patient Preparation

Careful attention to patient preparation increases the likelihood of an efficient and high-quality diagnostic study. Although frequently not possible in the emergency population, it is ideal to withhold cardiac stimulants, including caffeine, in order to reduce ectopy. Patients must have adequate intravenous access (18–20 gauge) in a large vein, such as the antecubital fossa. The intravenous line should be tested with rapid saline injection to ensure no extravasation or pain at the site. Pain with injection can affect the patient's heart rate during the study, impacting image quality. In order to avoid compression of the subclavian vein during contrast injection and to facilitate a tight contrast bolus, the arm with the intravenous line should not be held in full abduction above the patient's head. We have found it helpful to position the arm directly anterior to the patient, resting on the CT gantry. Correct placement of ECG leads is needed to identify clear R waves. Leads should be positioned above and below the level of the scan to reduce streak artifact. The leads should be tested during table motion to ensure they do not detach when the table moves for the scan. Lastly, a 15 s breath-hold should be practiced with the patient. The patient should be instructed to take in a slow, small breath, as a large breath will increase the amount of unopacified blood drawn into the right heart from the inferior vena cava and result in suboptimal pulmonary arterial opacification (Wittram and Yoo 2007).

4 Patient Monitoring and Medication Administration

Patients must have vital signs monitored (heart rate and blood pressure) before, during, and after administration of medications that impact the cardiovascular system. A baseline blood pressure and heart rate determines if medications are needed or can be safely administered. Sinus bradycardia at 50–60 beats per minute is ideal (Ferencik et al. 2006). A regular heart rate and

rhythm optimizes image quality and reduces radiation dose. Heart rate can be reduced with beta-blocker administration. Beta-blocker administration is generally very safe but may be contraindicated in patients with asthma, acute congestive heart failure, severe cardiomyopathy, hypotension, or recent cocaine use. Oral beta-blockers may be administered in the emergency department at least 1 h prior to the study. However, intravenous administration upon arrival to the CT suite may be needed if the heart rate is not adequately controlled with oral agents or if oral agents have not been administered. Intravenous beta-blockers may be administered while the patient is on the CT table, during performance of the scout topogram and during bolus tracking setup without a substantial increase in overall scan time. Intravenous metoprolol, what is primarily used at our institution, has an onset of action within minutes. Dose is determined by baseline heart rate; 2.5 mg intravenous metoprolol is given for a heart rate of 60–65 beats per minute, and 5 mg is given for higher heart rates. An additional 5 mg may be administered every 3–5 min until the target heart rate is achieved. Attention to blood pressure is necessary during titration. No further dose should be administered if systolic blood pressure falls below 100 mmHg. Our maximum dose of metoprolol is 30 mg. However, patients with no response after 10–20 mg are unlikely to respond with any further increased dose. In the setting of acute pulmonary embolism with tachycardia, beta-blocker administration is unlikely to result in adequate heart rate control; when pulmonary embolism is strongly suspected but a TRO CT is requested, we tend to limit the dose of metoprolol to 10 mg.

Sublingual nitroglycerin is administered prior to TRO CT for coronary vasodilation, which may improve diagnostic accuracy (Chun et al. 2008). Up to 800 mcg of sublingual nitroglycerin is administered 2–3 min prior to the scan as long as systolic blood pressure is greater than 100 mmHg. Nitroglycerin can usually be safely administered with beta-blockers, but blood pressure should be carefully monitored. Beta-blockers may actually be helpful in reducing the reflex tachycardia that may be seen after nitroglycerin administration. Contraindications to nitroglycerin administration include hypovolemia, idiopathic hypertrophic subaortic stenosis, severe aortic stenosis, and recent use of a phosphodiesterase inhibitor.

5 TRO CT Technique

5.1 CT Hardware

The advent of multi-slice, helical CT technology and ECG gating has facilitated the development of cardiac imaging with high temporal and spatial resolution. TRO CT has larger anatomic coverage compared to dedicated cCTA and thus requires at least 64 detector rows to cover the entire scan length in a single breath-hold. Today, scans may be performed more quickly and with decreased motion artifact using 256- or 320-slice scanners or high-pitch scan techniques.

5.2 Scanning Technique

The standard technique for TRO CT discussed in this section is based upon a helical, low-pitch (0.2–0.3) acquisition. The reader should be aware that with recent advances in helical CT technology, high-pitch subsecond CTA of the chest may alter the scan protocol, as will the use of prospective ECG gating with axial "step-and-shoot" technology (see below).

The major differences between TRO CT and dedicated cCTA are scan length and injection technique. Compared to cCTA, where images are obtained between the carina and diaphragm, TRO CT must include the entire thoracic aorta and the pulmonary arteries (with the exception of the small upper lobe pulmonary arteries above the aortic arch – see below). The scan is started approximately 1–2 cm above the level of the aortic arch, which is usually at the level of the inferior margins of the clavicular heads on the scout topogram. Although it is relatively uncommon to have isolated pulmonary embolism or aortic pathology outside the z-axis coverage of dedicated cCTA (Lee et al. 2011), limiting the scan length to the level of the heart alone will not

definitively exclude life-threatening pathology in the aorta and pulmonary arteries (Figs. 5 and 6). In the review of almost 1200 cases in our 9-year experience of TRO CT, approximately one third of all noncoronary diagnoses would likely have been missed on a dedicated cCTA study due to unopacified right-sided circulation or limited z-axis coverage (manuscript in preparation). Furthermore, even if dedicated cCTA opacified both the right and left circulations, we found four cases of isolated segmental upper lobe pulmonary emboli that would not have been included in the z-axis coverage of the dedicated cCTA (Fig. 6). At our institution, the lung apices above the level of the aortic arch are not included in order to reduce radiation exposure. Excluding the lung apices above the arch decreases scan length by 4–5 cm, thus reducing radiation dose by 15–20 %. We are comfortable excluding the extreme lung apex from the scan, as the subsegmental pulmonary arteries at this level are generally not adequately opacified to identify embolic disease by CTA and because isolated subsegmental pulmonary embolism above the level of the aortic arch is extremely uncommon (Oser et al. 1996). With low-pitch TRO CT acquisition, it may be helpful to monitor the scan in real time and to terminate the scan as soon as the base of the heart is reached. This method may decrease scan length by 1.5–2 cm, further decreasing radiation dose by approximately 7–10 %.

The patient is positioned so that the heart is in the center of the gantry, as spatial resolution is highest at the center of the gantry due to the geometry of the x-ray beam. Using a conventional low-pitch ECG-gated helical scan, images are acquired in a cranial-to-caudal direction. The cranial-to-caudal scan direction adds a few seconds between the initiation of breath-hold and the cardiac portion of the scan. This delay provides for greater reduction and stability of the heart rate, which generally occur approximately 5–15 s after initiation of breath-hold. Furthermore, a cranial-to-caudal scan direction images the upper pulmonary artery branches prior to the heart, which is a reasonable approach as pulmonary opacification is achieved prior to coronary opacification since blood must first pass through the right-sided circulation prior to arriving on the left. Proponents of a caudal-to-cranial scan direction argue that scanning at the lung bases first results in decreased respiratory motion artifact at the lung bases (Wittram 2007); we have not found respiratory motion to be a major issue in our studies.

TRO CT is typically performed with a mean effective tube current of 600 mAs/slice and tube voltage of 100 kVp. Heavier patients may necessitate an increase in tube current (800–1000 mA) and/or voltage (120–140 kVp) to maintain diagnostic quality. Smaller patients may require less tube current. The vast majority of our studies are performed with a helical scan acquisition, and most often tube current modulation is employed to reduce radiation dose. An additional technique to reduce radiation dose is prospective ECG gating using the "step-and-shoot" axial mode. This technique may be employed only in patients with stable heart rates as any arrhythmia will substantially degrade image quality. Prospective ECG gating can decrease radiation dose by approximately 80 % relative to a retrospectively gated helical study without dose modulation. It is important to understand that prospective ECG gating does not obtain images throughout the entire cardiac cycle and therefore does not provide information about cardiac function and regional wall motion. Nonetheless, we often employ prospective ECG gating with an axial technique in younger female patients where there is greater concern about radiation exposure.

5.3 Injection Technique

Injection technique is another major difference between cCTA and TRO CT. Contrast injection in cCTA aims to completely opacify the left-sided circulation (coronary arteries and left heart) while minimizing right-sided enhancement to decrease potential artifact. Dedicated cCTA technique does not adequately opacify the pulmonary arteries for evaluation of pulmonary embolism (Dodd et al. 2008). In contrast, the goal of TRO CT is to obtain high-contrast opacification of both the right- (pulmonary arteries) and left-sided (coronary arteries

and aorta) circulations. Typical enhancement is greater than 200 Hounsfield units in the pulmonary arteries and greater than 300 Hounsfield units in the coronary arteries and aorta. This is accomplished by adjusting the volume, rate, and timing of contrast injection to extend the contrast bolus to opacify the right-sided circulation. However, it is important not to have too much contrast in the superior vena cava as streak artifact degrades image quality. TRO CT necessitates more contrast material than cCTA, approximately 95 mL compared to 60–70 mL. A carefully tailored injection technique with less than 100 mL of iodinated contrast material can adequately opacify all three vascular beds.

There are several different injection strategies that may be employed. We employ a biphasic injection protocol as we have found more homogenous enhancement with such a technique. With a biphasic protocol, the first phase opacifies the left-sided circulation (coronaries and aorta), and the second phase opacifies the right-sided circulation (pulmonary arteries). Our typical protocol is 60 mL of I-350 mg/mL, followed by 60 mL dilute contrast (30 mL I-350 mg/mL and 30 mL saline). The second phase of contrast administration opacifies the right-sided circulation adequately for diagnosis of pulmonary embolism, but because it is diluted with saline, it does not result in streak artifact in the superior vena cava. The entire injection is administered at 5.5 mL/s. This rapid flow rate is maintained throughout the injection to minimize the effect of unopacified venous return through the inferior vena cava. Heating the contrast to 37° prior to administration, which decreases the viscosity, may facilitate the rapid flow rate (Cademartiri et al. 2005). The volume and rate in this biphasic protocol are optimized for a 14–15 scan time.

Rarely there may be a need for an extended TRO CT protocol of greater than 14–15 s, most likely when using an older 16 slice system with a tall patient. The biphasic technique described above can be adjusted to 80 mL I-350 mg/mL, followed by 70 mL dilute contrast (35 mL I-350 mg/mL and 35 mL saline), and the injection rate may be slowed to 5.0 mL/s (Halpern et al. 2009). This protocol is adequate for an 18–20 s scan time. As compared to cCTA studies, we do not use a saline flush for TRO CT because the saline flush may result in complete washout of contrast from the right-sided circulation, leading to nondiagnostic evaluation of the pulmonary arteries. Imaging is initiated by bolus tracking and is triggered off of the left atrium, which opacifies 2–3 s earlier than the descending aorta. If the scan is started 5 s after contrast enters the left atrium, the coronary arteries and aorta will be in the plateau phase of peak enhancement.

Other variations in injection technique have been described. One example of a triphasic technique uses undiluted contrast material (I-320 mg/mL) with a flow rate of 5 mL/s for the first phase, followed by 3 mL/s for the second phase and a saline flush for the third phase (Vrachliotis et al. 2007; Haidary et al. 2007). Even though the contrast is not diluted, the reduced flow rate in the second phase reduces the streak artifact in the superior vena cava. However, we have found that a faster flow rate of diluted contrast for the second phase is preferred as it results in less unopacified blood return from the inferior vena cava. When using a high-pitch acquisition, scan time is reduced, allowing for a potential reduction in the amount of contrast. For example, a total of 90 mL I-370 mg/mL with a flow rate of 6 mL/s may be used with automated bolus tracking and scan initiation 5 s after opacification of the ascending aorta (Bamberg et al. 2012).

6 Image Interpretation

Interpretation of images from a TRO CT requires evaluation of the coronary arteries, aorta, pulmonary arteries, and adjacent lung and soft tissues. Evaluation of the coronary arteries is no different from a cCTA examination. Evaluation of the coronaries is performed on 0.6–0.8 mm axial images with 5 mm slab maximum intensity projection (MIP) reconstructions. These may be reconstructed in real time during interpretation. Cardiac post-processing software with vessel tracking may be helpful for problem solving, especially in the case of diseased vessels. Each segment of each coronary artery should be

examined in multiple projections. At our institution, ACS is ruled out if there are normal coronaries (Fig. 1) or lesions with less than 25 % stenosis (Fig. 7). A stenosis of less than 50 % is unlikely to be related to chest pain symptoms and generally allows for expedited discharge with outpatient follow-up for management of coronary disease (Fig. 8). However, a stenosis of greater than 70 % or a segmental occlusion (Fig. 9) raises suspicion for ACS. Moderate lesions with narrowing in the range of 50–70 % (Fig. 10) often require additional evaluation, such as with physiologic stress testing or invasive angiography. If retrospective ECG gating is employed, multiphase

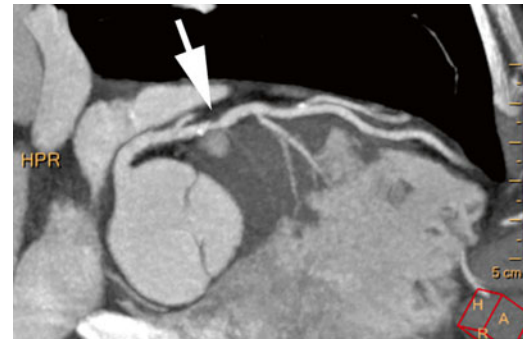

Fig. 7 LAD lesion with less than 25 % stenosis. Slab MIP image of the LAD from a TRO CT demonstrates minimal atherosclerotic disease with less than 25 % stenosis at the site of noncalcified plaque (*arrow*)

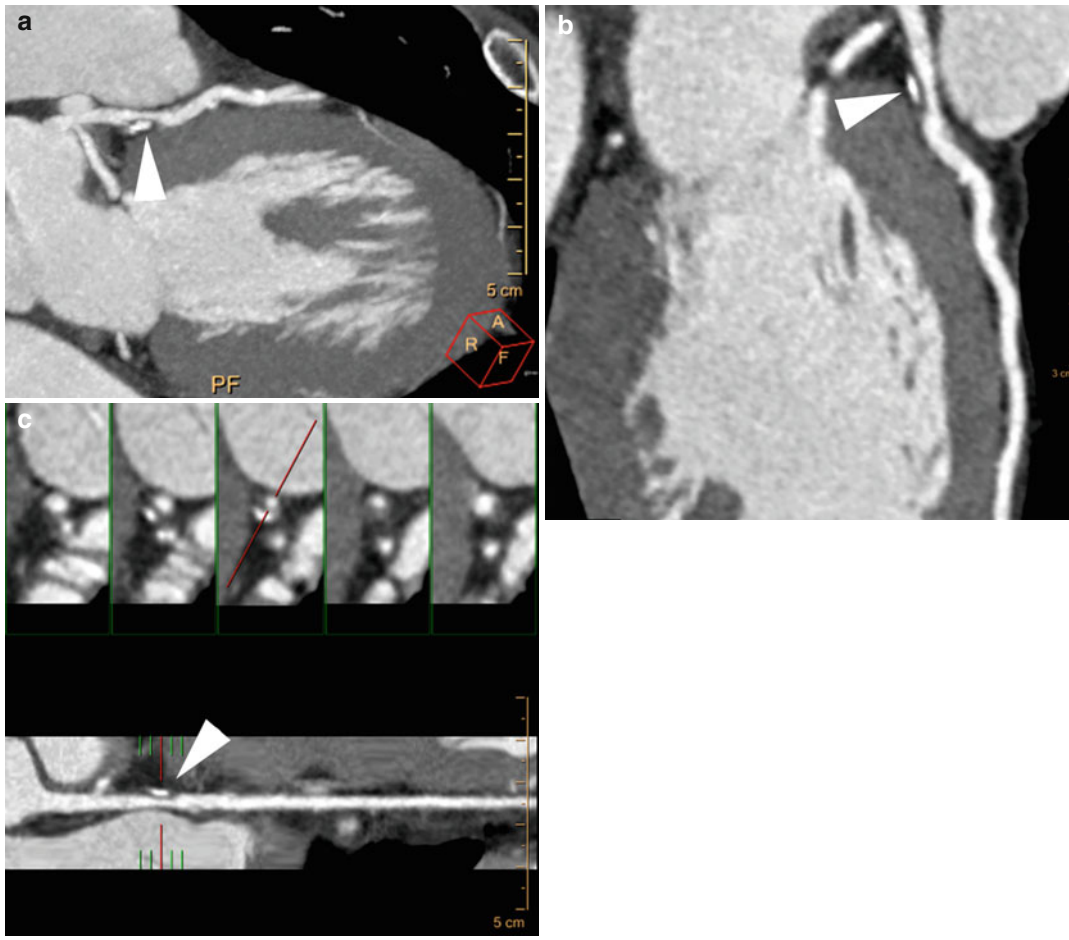

Fig. 8 LAD lesion with less than 50 % stenosis. Images from TRO CT demonstrate a mixed calcified and noncalcified plaque in the proximal LAD (*arrowheads*) resulting in less than 50 % stenosis. Slab MIP image along the long axis of the left ventricle (**a**), curved MIP image (**b**) and straightened MIP image (**c**)

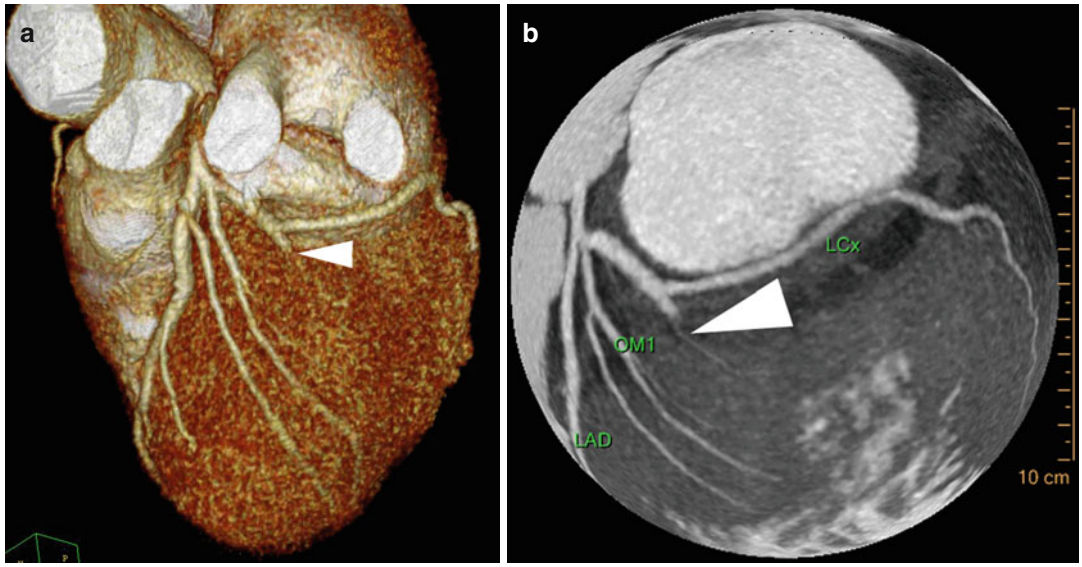

Fig. 9 Segmental occlusion of the second obtuse marginal branch (OM2) is the etiology of ACS in this patient who presented with chest pain, negative troponins, and a normal ECG. Volume-rendered image (**a**) and globe MIP image (**b**) from TRO CT demonstrate segmental occlusion of OM2 (*arrowheads*), raising suspicion for ACS. This patient proceeded to make positive cardiac enzymes a few hours after the TRO CT study

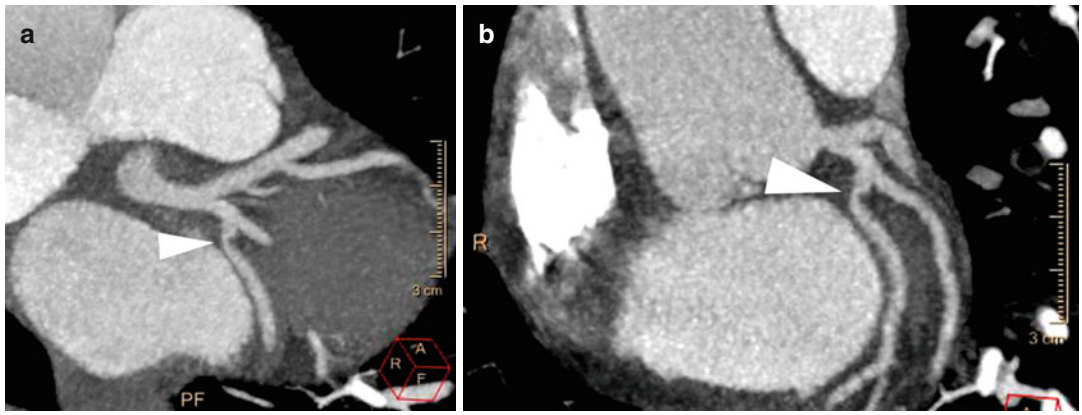

Fig. 10 Moderate LCx lesion with 50–70 % stenosis. Two slab MIP images (**a**, **b**) from TRO CT show noncalcified plaque in the proximal LCx (*arrowheads*) with 50–70 % stenosis

reconstruction at 10 % increments throughout the cardiac cycle can be performed for functional assessment. Wall motion is assessed in standard echocardiogram projections, and regional wall motion abnormalities are correlated with anatomic data to confirm physiologic significance of any stenoses.

Up to one in six patients without coronary abnormalities are diagnosed with noncoronary findings that can explain the presenting chest pain (Onuma et al. 2006). Noncoronary diagnoses include aortic and pulmonary arterial pathology, pneumonia, valvular disease including endocarditis, pericardial effusion, lung or mediastinal masses, pneumothorax, osseous lesions, esophageal pathology, and upper abdominal pathology. In our patient population, the most frequent diagnoses seen that could explain the presenting complaint are pulmonary embolism and pneumonia. Aortic dissection is rarely

encountered. It is also common to identify incidental noncoronary findings that are significant, but may not explain the presenting complaint (Gil et al. 2007). Many of these findings may require immediate action, further evaluation, or continued follow-up. In our population, the most common incidental lesions encountered are lung nodules or masses, abdominal lesions, lymphadenopathy, and additional cardiac findings such as valvular disease, shunt lesions, or wall motion abnormalities. Noncoronary structures are best evaluated using 3–5 mm thick axial images. Thinner sections can be evaluated if abnormalities are noted on the thicker slices.

7 Patient Disposition

A negative TRO study frequently obviates the need for further workup in the emergency department and allows for direct discharge. The majority of these patients do not require additional testing (Takakuwa and Halpern 2008). If a study is positive for a coronary lesion, the patient is triaged appropriately for admission or observation for further workup depending on the severity of the lesion and the clinical scenario. Any noncoronary finding that may explain the patient's presentation is managed appropriately. Any incidental finding requiring additional evaluation is communicated to the emergency department to ensure proper follow-up is obtained after discharge.

8 Radiation Dose Considerations

A limitation of a TRO CT protocol compared to cCTA is the higher effective radiation dose, which is directly proportional to scan length. TRO CT may have increased radiation dose by up to 50 % relative to dedicated cCTA (Gallagher and Raff 2008). Furthermore, patients with indeterminate results or intermediate severity disease may require additional evaluation with myocardial perfusion imaging or invasive angiography, which leads to an even larger combined total radiation dose. As discussed earlier, tube current modulation and prospective ECG gating can significantly reduce radiation dose. Tube current modulation automatically lowers the tube current of a helical acquisition during phases of the cardiac cycle that are less useful for diagnosis, typically systole. Alternatively, prospective ECG gating is an axial acquisition limited to diastole which may further reduce radiation dose. However, prospective ECG gating can only be used in patients with stable heart rates and does not allow for functional assessment. Additionally, in smaller patients, tube voltage can be reduced, and, as dual-source CT technology is becoming increasingly available, high-pitch helical scanning may allow for adequate quality TRO CT at a fraction of the dose (<2 mSv) (Kligerman and White 2014). Finally, new model-based iterative reconstruction techniques are constantly improving; model-based iterative reconstruction can provide high-quality images with reduced radiation exposure to the patient (Halpern et al. 2014).

In our initial experience with TRO CT, the mean effective dose for a helical scan at 120 kVp without tube current modulation was typically as high as 18 mSv and was reduced to 8.75 mSv with tube current modulation (Takakuwa et al. 2009). Prospective ECG gating at 120 kVp generally reduces effective radiation dose even further to 4–5 mSv. Reducing tube voltage to 100 kVp and lowering tube current, we now often obtain prospective ECG-gated studies with doses of 2–3 mSv. One study of 256-slice TRO CT using prospective ECG gating with step-and-shoot mode documented a mean effective dose of 6.5 mSv for females, compared to 3.8 mSv for males (Perisinakis et al. 2012). This resulted in mean lifetime attributable risk of radiation-induced cancer of 41 per 10^5 female and 17 per 10^5 male patients and increased intrinsic risk of lung or breast cancer less than 0.5 % and 0.1 %, respectively. Following the principle of ALARA (as low as reasonably achievable), imaging should only be obtained when clinically appropriate, especially in highly radiosensitive populations, such as young females. TRO CT remains most appropriate in a population where there is strong consideration of alternative diagnoses in addition to ACS.

Conclusions

TRO CT is a useful technique to triage patients presenting to the emergency department with low to moderate risk of ACS and in whom alternative diagnoses, such as pulmonary embolism or aortic dissection, are also being considered. An optimized study requires careful attention to appropriate patient selection, patient preparation, and injection/scanning technique. Major objections to TRO CT as compared to dedicated cCTA are the higher radiation exposure and increased iodinated contrast dose related to the longer scan length. New CT technologies, including tube current modulation, prospective ECG gating, high-pitch helical acquisition, and model-based iterative reconstruction, have decreased radiation and contrast dose such that these issues will be less of a concern in the near future. When performed correctly, TRO CT provides high-quality diagnostic opacification of the coronary arteries, aorta, and pulmonary arteries and also allows for evaluation of adjacent extravascular pathology. A negative study allows for the safe and rapid discharge from the emergency department and a reduction in subsequent testing.

References

Ayaram D, Bellolio MF, Murad MH et al (2013) Triple rule-out computed tomographic angiography for chest pain: a diagnostic systematic review and meta-analysis. Acad Emerg Med 20:861–871

Bamberg F, Marcus R, Sommer W et al (2012) Diagnostic image quality of a comprehensive high-pitch dual-spiral cardiothoracic CT protocol in patients with undifferentiated acute chest pain. Eur J Radiol 81:3697–3702

Bhuiya FA, Pitts SR, McCaig LF (2010) Emergency department visits for chest pain and abdominal pain: United States, 1999–2008. NCHS Data Brief 43:1–8

Budoff MJ, Dowe D, Jollis JG et al (2008) Diagnostic performance of 64-multidetector row coronary computed tomographic angiography for evaluation of coronary artery stenosis in individuals without known coronary artery disease: results from the prospective multicenter ACCURACY (Assessment by Coronary Computed Tomographic Angiography of Individuals Undergoing Invasive Coronary Angiography) trial. J Am Coll Cardiol 52:1724–1732

Cademartiri F, Mollet NR, van der Lugt A et al (2005) Intravenous contrast material administration at helical 16-detector row CT coronary angiography: effect of iodine concentration on vascular attenuation. Radiology 236:661–665

Chang SA, Choi SI, Choi EK et al (2008a) Usefulness of 64-slice multidetector computed tomography as an initial diagnostic approach in patients with acute chest pain. Am Heart J 156:375–383

Chang AM, Shofer FS, Weiner MG et al (2008b) Actual financial comparison of four strategies to evaluate patients with potential acute coronary syndromes. Acad Emerg Med 15:649–655

Chen ML, Mo YH, Wang YC et al (2012) 64-slice CT angiography for the detection of functionally significant coronary stenoses: comparison with stress myocardial perfusion imaging. Br J Radiol 85:368–376

Chun EJ, Lee W, Choi YH et al (2008) Effects of nitroglycerin on the diagnostic accuracy of electrocardiogram-gated coronary computed tomography angiography. J Comput Assist Tomogr 32:86–92

Dodd JD, Kalva S, Pena A et al (2008) Emergency cardiac CT for suspected acute coronary syndrome: qualitative and quantitative assessment of coronary, pulmonary and aortic image quality. AJR Am J Roentgenol 191:870–877

Ferencik M, Nomura CH, Maurovich-Horvat P et al (2006) Quantitative parameters of image quality in 64-slice computed tomography angiography of the coronary arteries. Eur J Radiol 57:373–379

Gallagher MJ, Raff GL (2008) Use of multislice CT for the evaluation of emergency room patients with chest pain: the so-called "triple rule-out". Catheter Cardiovasc Interv 71:92–99

Gallagher MJ, Ross MA, Raff GL, Goldstein JA, O'Neill WW, O'Neil B (2007) The diagnostic accuracy of 64-slice computed tomography coronary angiography compared with stress nuclear imaging in emergency department low-risk chest pain patients. Ann Emerg Med 49:125–136

Ghanima W, Almaas V, Aballi S et al (2005) Management of suspected pulmonary embolism (PE) by D-dimer and multi-slice computed tomography in outpatients: an outcome study. J Thromb Haemost 3:1926–1932

Ghaye B, Remy J, Remy-Jardin M (2002) Non-traumatic thoracic emergencies: CT diagnosis of acute pulmonary embolism: the first 10 years. Eur Radiol 12: 1886–1905

Gil BN, Ran K, Tamar G, Shmuell F, Eli A (2007) Prevalence of significant noncardiac findings on coronary multidetector computed tomography angiography in asymptomatic patients. J Comput Assist Tomogr 31:1–4

Goldstein JA, Gallagher MJ, O'Neill WW, Ross MA, O'Neil BJ, Raff GL (2007) A randomized controlled trial of multi-slice coronary computed tomography for evaluation of acute chest pain. J Am Coll Cardiol 49:863–871

Goldstein JA, Chinnaiyan KM, Abidov A et al (2011) The CT-STAT (Coronary Computed Tomographic Angiography for Systematic Triage of Acute Chest Pain Patients to Treatment) trial. J Am Coll Cardiol 58:1414–1422

Gruettner J, Fink C, Walter T et al (2013) Coronary computed tomography and triple rule out CT in patients with acute chest pain and an intermediate cardiac risk profile. Part 1: impact on patient management. Eur J Radiol 82:100–105

Haidary A, Bis K, Vrachliotis T, Kosuri R, Balasubramaniam M (2007) Enhancement performance of a 64-slice triple rule-out protocol vs 16-slice and 10-slice multidetector CT-angiography protocols for evaluation of aortic and pulmonary vasculature. J Comput Assist Tomogr 31:917–923

Halpern EJ, Levin DC, Zhang S, Takakuwa KM (2009) Comparison of image quality and arterial enhancement with a dedicated coronary CTA protocol versus a triple rule-out coronary CTA protocol. Acad Radiol 16:1039–1048

Halpern EJ, Gingold EL, WHite H, Read K (2014) Evaluation of coronary artery image quality with knowledge-based iterative model reconstruction. Acad Radiol 21:805–811

Hamada S, Takamiya M, Kimura K, Imakita S, Nakajima N, Naito H (1992) Type A aortic dissection: evaluation with ultrafast CT. Radiology 183:155–158

Hecht HS, Bhatti T (2008) How much calcium is too much calcium for coronary computerized tomographic angiography? J Cardiovasc Comput Tomogr 2:183–187

Henzler T, Gruettner J, Meyer M et al (2013) Coronary computed tomography and triple rule out CT in patients with acute chest pain and an intermediate cardiac risk for acute coronary syndrome: part 2: economic aspects. Eur J Radiol 82:106–111

Hoffmann U, Truong QA, Schoenfeld DA et al (2012) Coronary CT angiography versus standard evaluation in acute chest pain. N Engl J Med 367:299–308

Hollander JE, Chang AM, Shofer FS et al (2009) One-year outcomes following coronary computerized tomographic angiography for evaluation of emergency department patients with potential acute coronary syndrome. Acad Emerg Med 16:693–698

Johnson TR, Nikolaou K, Wintersperger BJ et al (2007) ECG-gated 64-MDCT angiography in the differential diagnosis of acute chest pain. AJR Am J Roentgenol 188:76–82

Johnson TR, Nikolaou K, Becker A et al (2008) Dual-source CT for chest pain assessment. Eur J Radiol 18:773–780

Kligerman SJ, White CS (2014) Image quality and feasibility of an ultralow-dose high-pitch helical triple-rule-out computed tomography angiography acquired in the caudocranial direction. J Thorac Imaging 29:50–59

Kolansky DM (2009) Acute coronary syndromes: morbidity, mortality, and pharmacoeconomic burden. Am J Manag Care 15:S36–S41

Lee HY, Song IS, Yoo SM et al (2011) Rarity of isolated pulmonary embolism and acute aortic syndrome occurring outside of the field of view of dedicated coronary CT angiography. Acta Radiol 52:378–384

Litmanovich D, Zamboni GA, Hauser TH, Lin PJ, Clouse ME, Raptopoulos V (2008) ECG-gated chest CT angiography with 64-MDCT and tri-phasic IV contrast administration regimen in patients with acute non-specific chest pain. Eur Radiol 18:308–317

Litt HI, Gatsonis C, Snyder B et al (2012) CT angiography for safe discharge of patients with possible acute coronary syndromes. N Engl J Med 366:1393–1403

Madder RD, Raff GL, Hickman L et al (2011) Comparative diagnostic yield and 3-month outcomes of "triple rule-out" and standard protocol coronary CT angiography in the evaluation of acute chest pain. J Cardiovasc Comput Tomogr 5:165–171

Meijboom WB, Meijs MF, Schuijf JD et al (2008) Diagnostic accuracy of 64-slice computed tomography coronary angiography: a prospective, multicenter, multivendor study. J Am Coll Cardiol 52:2135–2144

Miller JM, Rochitte CE, Dewey M et al (2008) Diagnostic performance of coronary angiography by 64-row CT. N Engl J Med 359:2324–2336

Onuma Y, Tanabe K, Nakazawa G et al (2006) Noncardiac findings in cardiac imaging with multidetector computed tomography. J Am Coll Cardiol 48:402–406

Oser RF, Zuckerman DA, Gutierrez FR, Brink JA (1996) Anatomic distribution of pulmonary emboli at pulmonary angiography: implications for cross-sectional imaging. Radiology 199:31–35

Perisinakis K, Seimenis I, Tzedakis A, Papadakis AE, Damilakis J (2012) Triple-rule-out computed tomography angiography with 256-slice computed tomography scanners: patient-specific assessment of radiation burden and associated cancer risk. Invest Radiol 47:109–115

Prologo JD, Gilkeson RC, Diaz M, Asaad J (2004) CT pulmonary angiography: a comparative analysis of the utilization patterns in emergency department and hospitalized patients between 1998 and 2003. AJR Am J Roentgenol 183:1093–1096

Quiroz R, Kucher N, Zou KH et al (2005) Clinical validity of a negative computed tomography scan in patients with suspected pulmonary embolism: a systematic review. JAMA 293:2012–2017

Rahmani N, Jeudy J, White CS (2009) Triple rule-out and dedicated coronary artery CTA: comparison of coronary artery image quality. Acad Radiol 16:604–609

Rogers IS, Banerji D, Siegel EL et al (2011) Usefulness of comprehensive cardiothoracic computed tomography in the evaluation of acute undifferentiated chest discomfort in the emergency department (CAPTURE). Am J Cardiol 107:643–650

Ropp A, Lin CT, White CS (2015) Coronary computed tomography angiography for the assessment of acute chest pain in the emergency department: evidence, guidelines, and tips for implementation. J Thorac Imaging

Rubinshtein R, Halon DA, Gaspar T et al (2007) Impact of 64-slice cardiac computed tomographic angiography on clinical decision-making in emergency department patients with chest pain of possible myocardial ischemic origin. Am J Cardiol 100:1522–1526

Savino G, Herzog C, Costello P, Schoepf UJ (2006) 64 slice cardiovascular CT in the emergency department: concepts and first experiences. Radiol Med 111:481–496

Schertler T, Frauenfelder T, Stolzmann P et al (2009) Triple rule-out CT in patients with suspicion of acute pulmonary embolism: findings and accuracy. Acad Radiol 16:708–717

Schlett CL, Banerji D, Siegel E et al (2011) Prognostic value of CT angiography for major adverse cardiac events in patients with acute chest pain from the emergency department: 2-year outcomes of the ROMICAT trial. JACC Cardiovasc Imaging 4:481–491

Sebastia C, Pallisa E, Quiroga S, Alvarez-Castells A, Dominguez R, Evangelista A (1999) Aortic dissection: diagnosis and follow-up with helical CT. Radiographics 19:45–60; quiz 149–150

Shapiro MD, Dodd JD, Kalva S et al (2009) A comprehensive electrocardiogram-gated 64-slice multidetector computed tomography imaging protocol to visualize the coronary arteries, thoracic aorta, and pulmonary vasculature in a single breath hold. J Comput Assist Tomogr 33:225–232

Shiga T, Wajima Z, Apfel CC, Inoue T, Ohe Y (2006) Diagnostic accuracy of transesophageal echocardiography, helical computed tomography, and magnetic resonance imaging for suspected thoracic aortic dissection: systematic review and meta-analysis. Arch Intern Med 166:1350–1356

Takakuwa KM, Halpern EJ (2008) Evaluation of a "triple rule-out" coronary CT angiography protocol: use of 64-Section CT in low-to-moderate risk emergency department patients suspected of having acute coronary syndrome. Radiology 248:438–446

Takakuwa KM, Halpern EJ, Gingold EL, Levin DC, Shofer FS (2009) Radiation dose in a "triple rule-out" coronary CT angiography protocol of emergency department patients using 64-MDCT: the impact of ECG-based tube current modulation on age, sex, and body mass index. AJR Am J Roentgenol 192:866–872

Takakuwa KM, Halpern EJ, Shofer FS (2011) A time and imaging cost analysis of low-risk ED observation patients: a conservative 64-section computed tomography coronary angiography "triple rule-out" compared to nuclear stress test strategy. Am J Emerg Med 29:187–195

Vrachliotis TG, Bis KG, Haidary A et al (2007) Atypical chest pain: coronary, aortic, and pulmonary vasculature enhancement at biphasic single-injection 64-section CT angiography. Radiology 243:368–376

Wexler L, Brundage B, Crouse J et al (1996) Coronary artery calcification: pathophysiology, epidemiology, imaging methods, and clinical implications. A statement for health professionals from the American Heart Association. Writing Group. Circulation 94:1175–1192

Willoteaux S, Lions C, Gaxotte V, Negaiwi Z, Beregi JP (2004) Imaging of aortic dissection by helical computed tomography (CT). Eur Radiol 14:1999–2008

Wittram C (2007) How I, do it: CT pulmonary angiography. AJR Am J Roentgenol 188:1255–1261

Wittram C, Yoo AJ (2007) Transient interruption of contrast on CT pulmonary angiography: proof of mechanism. J Thorac Imaging 22:125–129

Wnorowski AM, Halpern EJ (2016) Diagnostic Yield of Triple-Rule-Out CT in an Emergency Setting. AJR Am J Roentgenol. W1–W7. [Epub ahead of print]

Yoshida S, Akiba H, Tamakawa M et al (2003) Thoracic involvement of type A aortic dissection and intramural hematoma: diagnostic accuracy–comparison of emergency helical CT and surgical findings. Radiology 228:430–435

CT Imaging of the Heart-Lung Axis

Edwin J.R. van Beek and Saeed Mirsadraee

Abstract

The traditional split reporting of chest and cardiac imaging investigations is increasingly being recognised as outdated. Patients present with similar symptoms, often have overlapping risk factors, and may be referred through different specialities. Ultimately, there is a direct link between heart and lung function and therefore it is important to recognise the comorbidities and ensure that patients are approached holistically.

This chapter will go into some detail highlighting the overlaps between pulmonary and cardiac disorders, and how they may affect the imaging findings.

1 Introduction

Traditionally, the evaluation of chest disorders was largely confined to two different radiological sub-specialities: cardiac imaging and chest imaging. However, as the imaging technologies improved, it became increasingly feasible to investigate both the lungs and the heart and great vessels in a single-step investigation. As a result, it became obvious that lung diseases, pulmonary vascular diseases and the heart are intricately linked and that they have an immense propensity to act in synchronous development of disease states. This is easily understood given the mutual dependence of their functioning, while many of the diseases affecting the organ systems have a common aetiology, with smoking a primary factor in contracting many of these diseases.

This chapter aims to discuss the interdependence of diseases across the spectrum of lung parenchyma, pulmonary vascular and coronary disease states and the role that imaging can play in diagnosis and management. It will focus on smoking-related lung disease in particular.

E.J.R. van Beek, MD, PhD, FRCR, FRCPE (✉)
S. Mirsadraee, MD, PhD, FRCR, FRCPE
Clinical Research Imaging Centre, University of Edinburgh, Edinburgh, Scotland, UK

Clinical Research Imaging Centre, The Queen's Medical Research Institute, 47 Little France Crescent, Edinburgh EH16 4TJ, UK
e-mail: edwin-vanbeek@ed.ac.uk; saeed.mirsadraee@ed.ac.uk

U.J. Schoepf, F.G. Meinel (eds.), *Multidetector-Row CT of the Thorax*, Medical Radiology,
DOI 10.1007/978-3-319-30355-0_19

2 Evidence of Comorbidity

The effects of smoking have far-reaching consequences for the body, and it is clear that there is a common aetiology for smoking-related lung diseases (as a result of combustible gases) and atherosclerosis (as a result of toxic substances being absorbed through the lung vasculature) as well as a link to a range of other diseases (The health consequences of smoking: 50 years of progress: a report of the Surgeon General 2014). Thus, around half a million deaths per year are directly attributed to smoking in the USA alone (The health consequences of smoking: 50 years of progress: a report of the Surgeon General 2014). However, in spite of linking 21 diseases to the effects of smoking, the two- to threefold increase in mortality among current smokers is still not fully explained (Carter et al. 2015). Thus, it is rapidly becoming clear that the situation of smoking-related diseases is much more complex and mechanisms of interactions are only partially understood. Nevertheless, there are particular relationships between chronic obstructive pulmonary diseases and heart diseases, both involving the right and the left heart, and between chronic obstructive pulmonary diseases and the pulmonary vasculature, which in itself has a direct impact on right ventricular function.

3 Pulmonary Vascular Diseases and Right Heart Effects

Pulmonary hypertension is defined by a mean pulmonary artery pressure >25 mmHg at rest, measured during right heart catheterisation (Hoeper et al. 2013). Pulmonary hypertension can develop both acutely (mostly in a situation of significant obstructing pulmonary embolism) or more chronic in the form of chronic thromboembolic pulmonary hypertension or due to underlying lung and cardiac diseases (Simonneau et al. 2013). Pulmonary hypertension is a progressive disorder with a poor long-term prognosis, which exerts its main effects through increased load on the right ventricle. The right ventricle will adapt through increased contractility, development of right ventricular hypertrophy to maintain output, but ultimately, it will fail (Vonk-Noordegraaf et al. 2013).

If the onset of pulmonary hypertension is acute, the right ventricular stress can be seen as enlargement of the right ventricle and right atrium, backflow of contrast into the inferior vena cava and hepatic veins (Fig. 1) and bowing of the interventricular septum into the left ventricular cavity (Fig. 2). In the case of acute pulmonary embolism, as the thrombus resolves, the pulmonary artery pressure normalises, and the right ventricular pressure will recover (Fig. 3).

However, in a significant proportion of patients, particularly those with large pulmonary embolism, the pressure does not normalise and the pulmonary hypertension becomes chronic in around 3 % of patients following a significant acute event (Pengo et al. 2004). In chronic forms of pulmonary hypertension, the right ventricular hypertrophy and enlargement of the pulmonary arteries will be the main features (Fig. 4).

Given the relatively frequent occurrence of chronic thromboembolic pulmonary hypertension following acute (large) pulmonary embolism, it has been suggested that such high-risk patients should have follow-up investigations (Pengo et al. 2004). A variety of options are in existence to perform such follow-up investigations, including perfusion scintigraphy (Brandjes

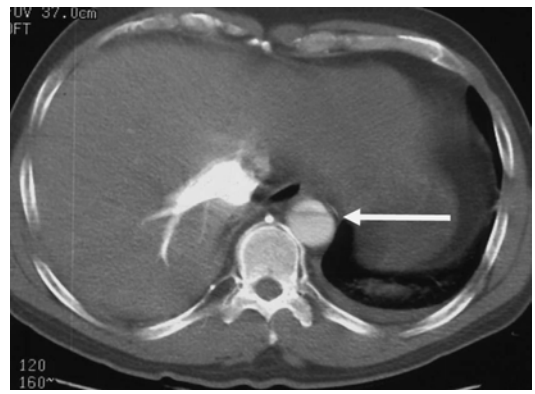

Fig. 1 Patient with suspected pulmonary embolism. Contrast reflux into the inferior vena cava and hepatic veins due to raised right atrial and ventricular pressure. Note: incidental finding of a chronic aorta dissection (*arrow*)

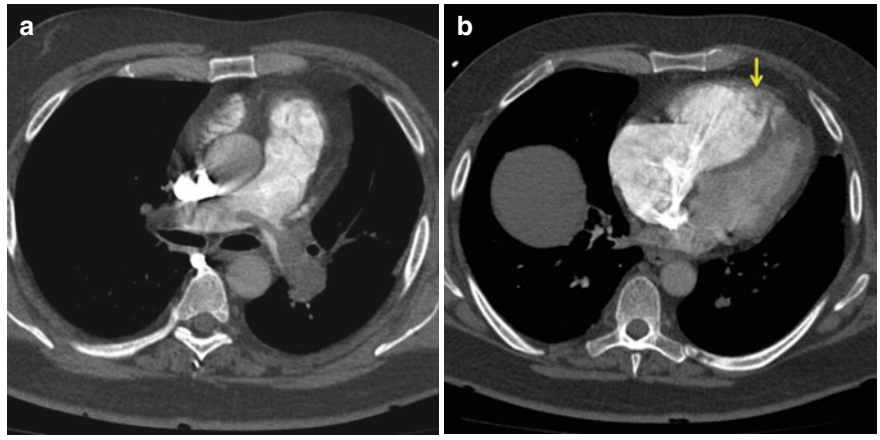

Fig. 2 CT pulmonary angiography demonstrated saddle embolus (**a**) with near occlusion of both pulmonary arteries and dilatation of the main pulmonary artery. Image (**b**) shows right cardiac dilatation and systolic bowing of the septum to the *left* indicating right heart strain. Note residual thrombus in the apex of the right ventricle (*arrow*)

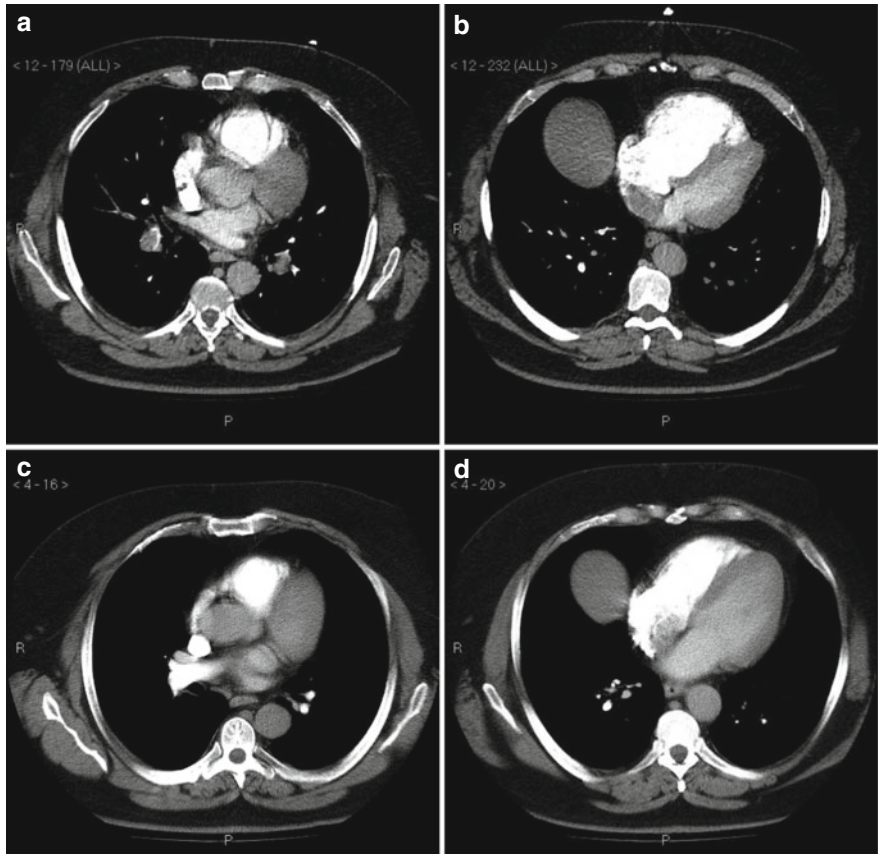

Fig. 3 Patient with massive pulmonary embolism (**a**) and evidence of right heart strain (**b**). Two days following treatment with fibrinolytics, the central emboli resolved (**c**) and the heart strain also normalised (**d**)

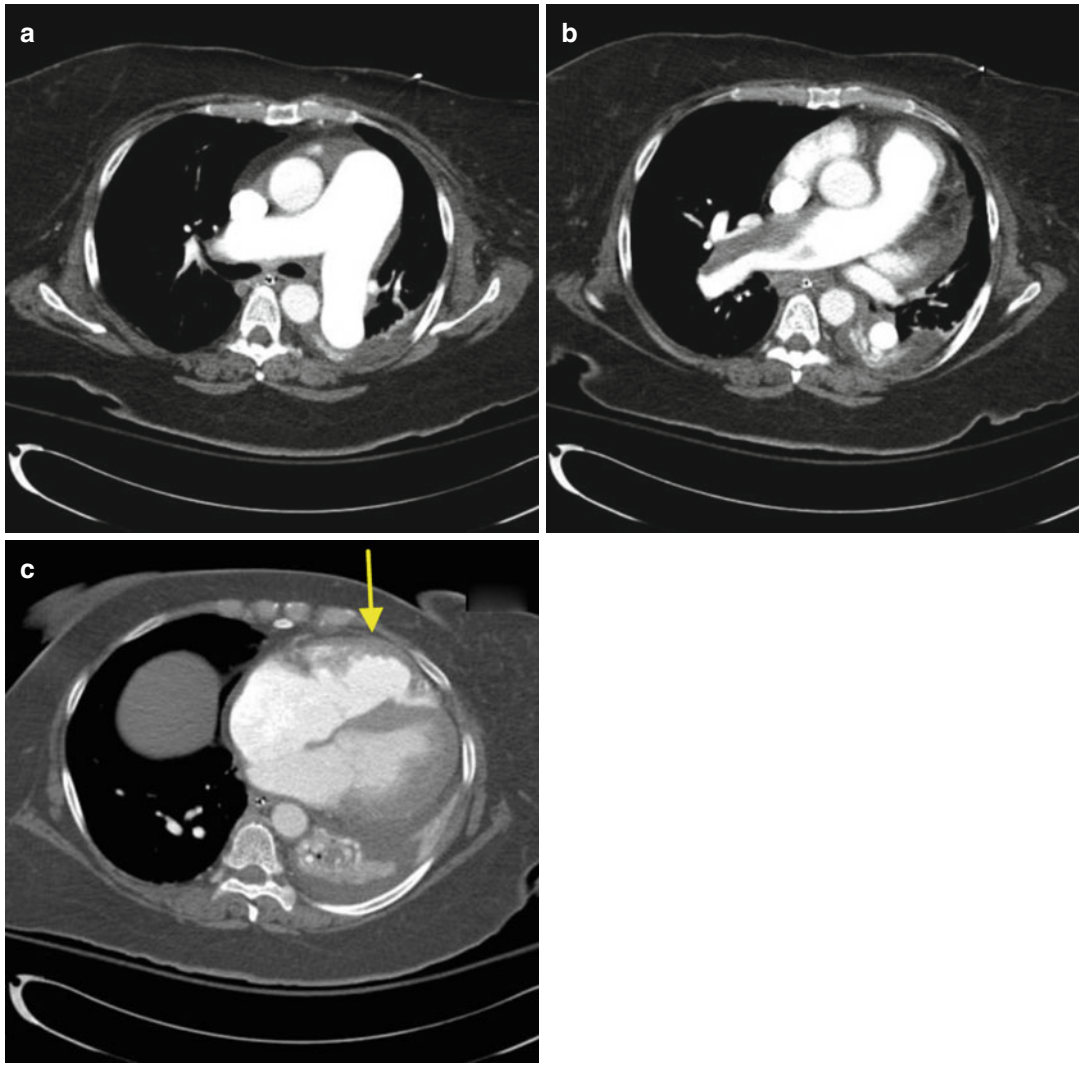

Fig. 4 Patient with chronic thromboembolic pulmonary hypertension. Notice the enlarged pulmonary artery compared to the ascending aorta (**a**), the mural thrombus in the right main pulmonary artery (**b**) and the right ventricular enlargement and right ventricular hypertrophy (**c**, *arrow*)

et al. 1992; Bajc et al. 2014), MRI methods (Ley et al. 2010) and CT methods (Thieme et al. 2012; Ameli-Renani et al. 2014; Hoey et al. 2011). Although the vast majority of patients demonstrate complete resolution of initial pulmonary embolism, a significant number of patients do not normalise and will ultimately develop the hallmarks of thromboembolic pulmonary hypertension, including endothelialised thrombus in the main vessels, webs and right ventricular remodelling (Fig. 4). In addition, even with morphological resolution, the functional effects at microvasculature level may still be relevant, and these changes would require more advanced imaging than simple CT pulmonary angiography, such as dual-energy CT which may demonstrate blood volume defects in the iodine distribution map or dynamic contrast-enhanced CT studies which may demonstrate true perfusion changes and delayed perfusion through the bronchial circulation (Fig. 5).

Patients with primary pulmonary hypertension will not exhibit any thrombus but will show signs of right heart strain and abnormal inhomogeneous attenuation (so-called mosaic attenuation) in an inspiratory CT scan (Fig. 6). Apart

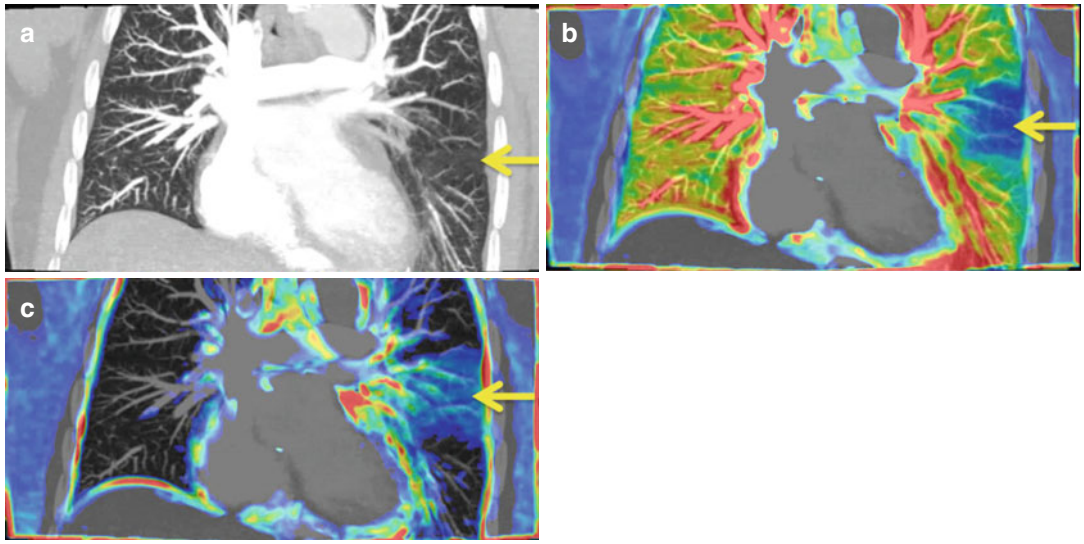

Fig. 5 Delayed perfusion following an episode of recent pulmonary embolism. Pixels are colour coded in the parametric maps according to the degree of perfusion (from high to low perfusion values: red, yellow, green, blue/black). Maximum-intensity projection (**a**) shows lack of pulmonary artery branch enhancement while vein branches are enhancing. Dual-phase perfusion analysis shows lack of perfusion from pulmonary artery in the left upper lobe (*arrow*; image **b**), but perfusion from other sources (*arrow*; image **c**). The time delay between **b** and **c** was approximately 4 s

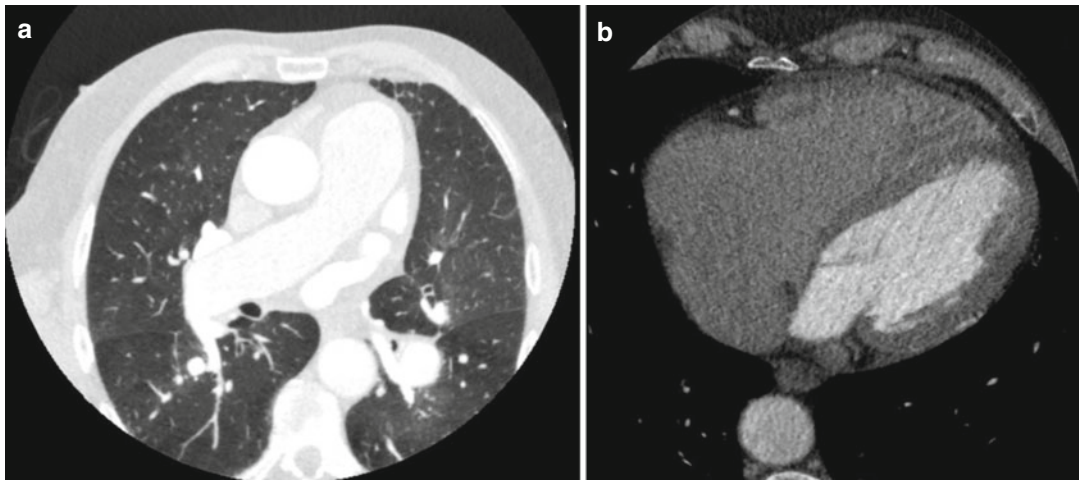

Fig. 6 Primary pulmonary hypertension. This patient was investigated for exertional dyspnoea. Gated cardiac CT demonstrated minimal coronary artery disease. Image (**a**) shows pulmonary artery dilatation and mosaic perfusion, and image (**b**) shows right heart dilatation and septal straightening, all supporting diagnosis of primary pulmonary hypertension

from the idiopathic form of pulmonary hypertension, there are many other causes for this vascular disease, including sarcoidosis (Fig. 7), iatrogenic following radiation therapy (Fig. 8) and with interstitial pulmonary fibrosis (Fig. 9) (Simonneau et al. 2013).

4 Lung Diseases and Right Heart Effects

Most chronic lung diseases result in obliteration of the pulmonary vascular bed through parenchymal destruction and air trapping. The most

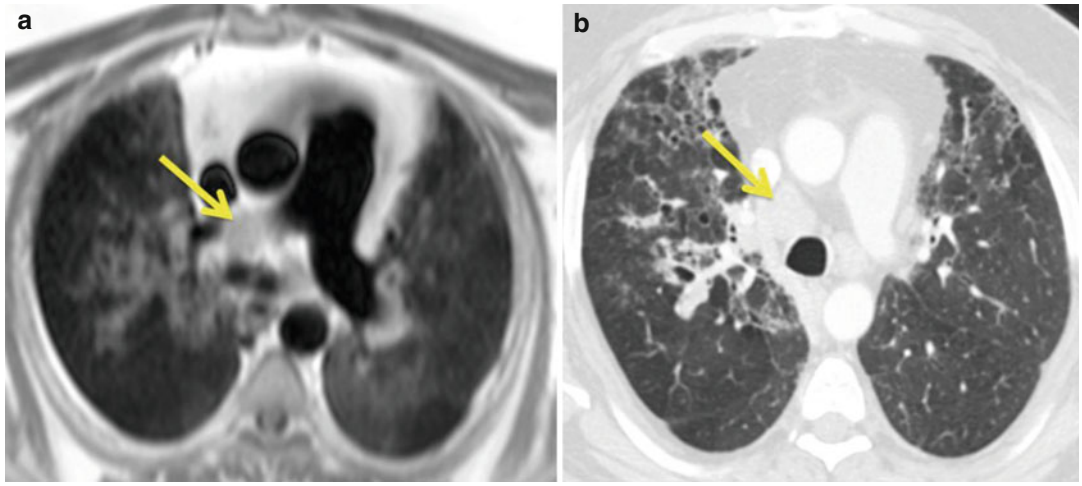

Fig. 7 Pulmonary hypertension in a patient with sarcoidosis. 54-year-old man with shortness. HASTE cardiac MRI (**a**) demonstrated mediastinal lymphadenopathy (*arrow*) and parenchymal thickening. CT (**b**) confirmed findings of the MRI and better demonstrated traction bronchiectasis supporting a diagnosis of pulmonary sarcoidosis. Dilatation of pulmonary artery (33 mm) indicated pulmonary hypertension. *HASTE* half-Fourier acquisition single-shot turbo

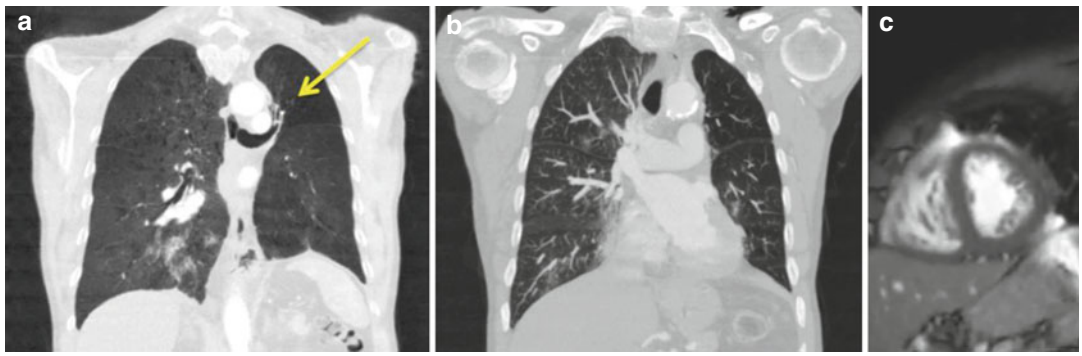

Fig. 8 Pulmonary hypertension post-radiotherapy. Regional radiotherapy in this patient resulted in left upper lobe bronchiolar stenosis (**a**; *arrow*). This patient suffered from secondary pulmonary hypertension. Note paucity of left upper lobe vessels on the maximum-intensity projection (**b**) and septal straightening secondary to right heart strain on accompanying cardiac MRI study (**c**)

important example of this effect can be seen in patients with chronic obstructive pulmonary disease (COPD). Prior to the lung destruction, smoking leads to a significant inflammatory response in the lungs. A study using CT in follow-up of smokers demonstrated that smokers with ground glass nodules progressed to parenchymal destruction and emphysema faster than those without these changes or those that stopped smoking (Remy-Jardin et al. 2002). This is in direct competition with the hypoxic vasorestrictive response (actually overriding it) and leads to inhomogeneous perfusion which can be demonstrated using dynamic contrast-enhanced CT, as shown in a study comparing healthy nonsmokers, healthy smokers and smokers with early COPD (Alford et al. 2010). In another study of severe emphysema, it was demonstrated that there is a direct inverse correlation between the total cross-sectional area of small pulmonary vessels as assessed by CT and the severity of pulmonary hypertension, suggesting that it is the loss of lung parenchyma and vascular bed that is the main driver for pul-

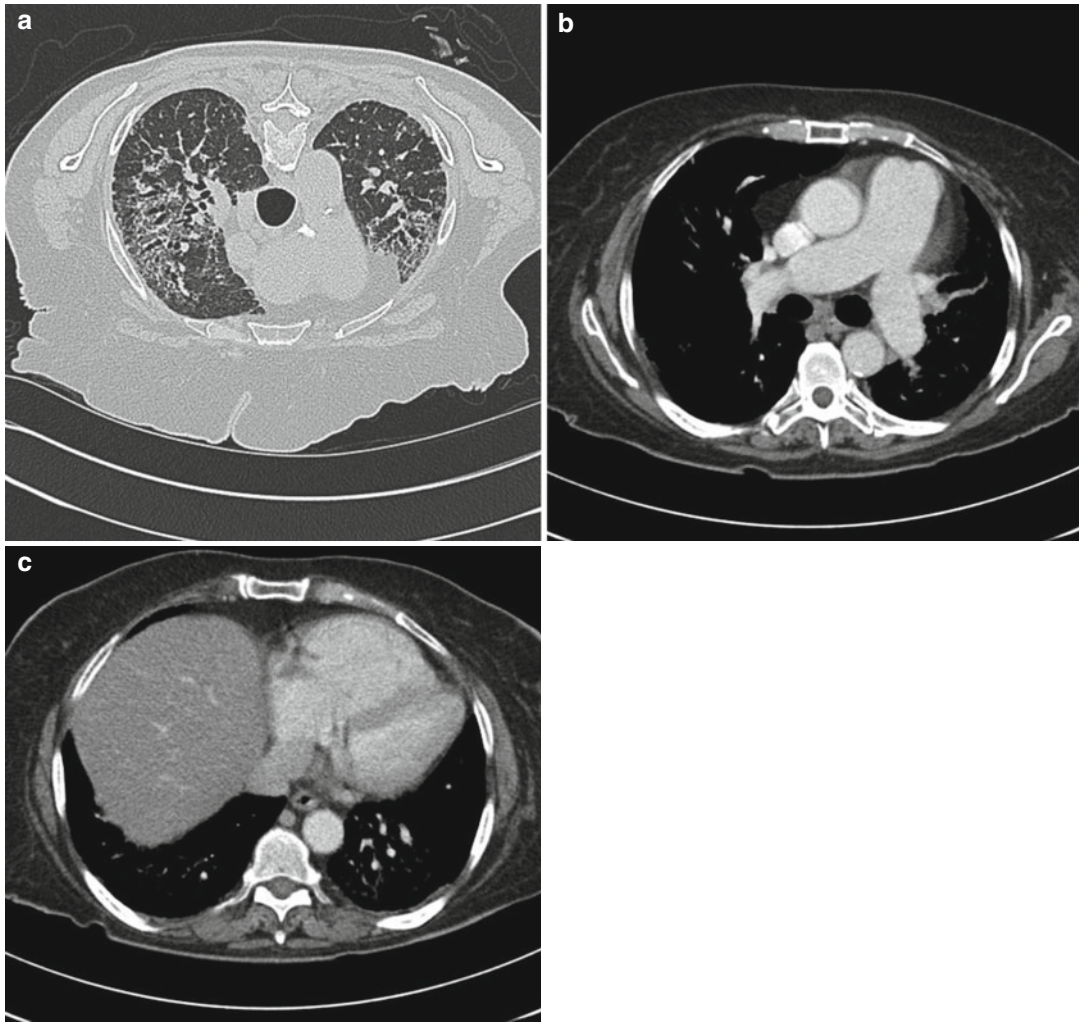

Fig. 9 Pulmonary hypertension in patient with idiopathic pulmonary fibrosis (prone CT, panel **a**). The pulmonary artery is clearly enlarged (**b**) and the right ventricle is dilated with interventricular septal deviation (**c**)

monary hypertension (Matsuoka et al. 2010). This was further demonstrated in a large cohort study of smoking-related COPD, which demonstrated the combined changes as distal pruning of the small blood vessels (0.5 mm^2) in combination with a loss of tissue in excess of the vasculature (Estépar et al. 2013). It was the magnitude of these changes that predicted the clinical severity of disease. In another study, right ventricular volumes were lower without significant alterations in right ventricular mass and ejection fraction in contemporary COPD, and this reduction was directly related to the extent of emphysema as measured on CT (Kawut et al. 2014). Eventually, all these changes will result in perfusion abnormalities (Fig. 10).

In spite of these changes, the actual reserve that is built within the pulmonary vascular bed is quite astonishing. As a result, most patients with COPD will develop mild to moderate pulmonary hypertension, with around 5 % of patients developing severe pulmonary hypertension (Minai et al. 2010). Furthermore, progression of pulmonary hypertension in COPD patients who do not require oxygen therapy is slow at a rate of pressure increase of 0.4 mmHg/year (Kessler et al. 2001).

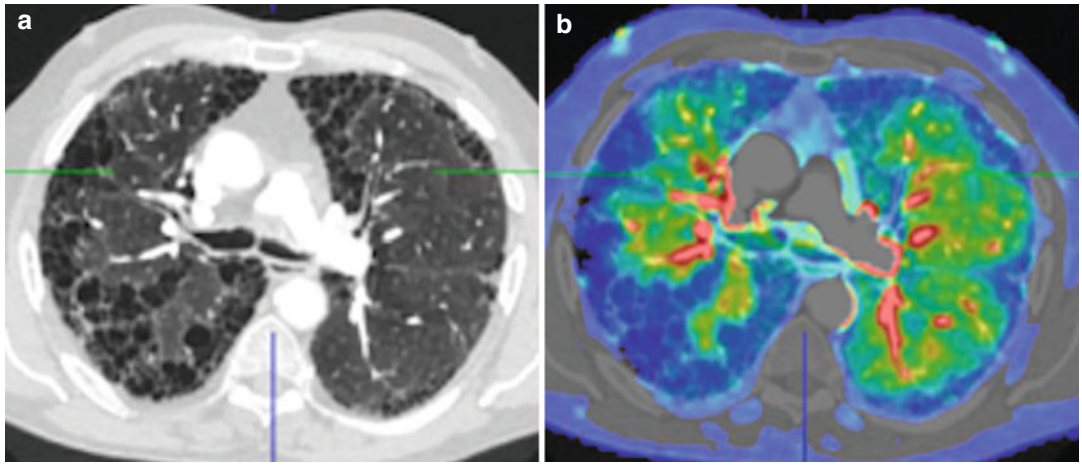

Fig. 10 Perfusion abnormality in emphysema. Image (**a**) shows sub-pleural emphysema. Dynamic perfusion CT demonstrated reduced pulmonary blood flow in areas with emphysema (**b**). Pixels are colour coded in the parametric maps according to the degree of perfusion (from high to low perfusion values: red, yellow, green, blue/black)

Further influences need to be considered, particularly the effects of vascular dysfunction due to responses to cigarette smoke, such as vasoconstriction, vascular remodelling, intima and muscular changes of the vessel wall (Barbera 2013). Some of these changes may offer a mechanism for intervention, such as vascular dysfunction due to a redox imbalance, which may be corrected using antioxidant therapies (Ives et al. 2014).

More recently, it was shown that it is not just the vascular changes that correlate with pulmonary hypertension in COPD (Dournes et al. 2015). Airway remodelling is a distinctly different phenotype from emphysema and likely results in the "blue bloater" clinical patient, who will exhibit chronic hypoxaemia and therefore will more likely develop pulmonary hypertension compared to the patients with emphysema.

Finally, it should be pointed out that patients with COPD are at increased risk of developing other complications, including pulmonary embolism, which will further compromise the pulmonary vascular bed (Chen et al. 2014).

CT measures are very capable of determining the status of COPD patients, both by offering phenotype analysis and by performing measurements on both native and contrast-enhanced studies. Relatively easy measurements, which should be performed in any CT examination, include quantification of emphysema at a cut-off of −950 HU or −910 HU and measurement of cross-sectional diameter of the pulmonary artery in relation to the ascending aorta. In a recent large cohort study, it was shown that patients with COPD exhibited signs of pulmonary hypertension as demonstrated by enlargement of the central pulmonary arteries compared to nonsmoking controls (Wells et al. 2012). Another study demonstrated that a pulmonary artery that was greater than the corresponding aorta (ratio >1) was an independent predictor for mortality in patients with COPD (Shin et al. 2014).

The management of patients with moderate to severe COPD in relation to pulmonary hypertension is rather disappointing. Treatment with a pulmonary vascular dilator agent (sildenafil) in ten patients with COPD without pulmonary hypertension did not improve outcomes and in fact worsened gas exchange and quality of life (Lederer et al. 2012). A randomised double-blind multicentre study in 120 patients with moderate to severe COPD using tadalafil also did not improve exercise capacity or quality of life despite exerting pulmonary vasodilatation (Goudie et al. 2014).

5 Lung Diseases and Atherosclerosis

Smoking clearly has an extensive effect on the body and particularly affects the pulmonary and circulatory system. Therefore, it should come as no surprise that there is a close correlation between smoking-related lung disease and atherosclerosis and a recent systematic review found that there was sufficient evidence to state that there is an increased risk for ischaemic and non-ischaemic cardiovascular disease in COPD and that this risk has a direct correlation with the severity of emphysema (Müllerova et al. 2013).

There are several perceived mechanisms that underpin this notion. In one small study, systemic elastin degradation products were increased in patients with COPD compared to nonsmokers, suggesting systemic enzymatic effects that affect arterial stiffness and lung parenchymal destruction (McAllister et al. 2007; Maclay et al. 2012). In a larger cohort, poor clinical outcomes in COPD could be traced to comorbidities of heart disease, hypertension and diabetes in association with increased systemic inflammation (Miller et al. 2013).

A cohort study in screening for coronary artery disease found that the brachial artery diameter is directly correlated with right ventricular dysfunction, thus linking systemic and pulmonary circulatory effects (Dibble et al. 2012). In the same cohort, it was also demonstrated that carotid intima thickness was greater and brachial-ankle index was decreased in smokers with airflow obstruction (Barr et al. 2012).

Other studies have pointed to a possible link between coronary artery disease and COPD. A Swedish study in a general population showed that COPD was independently associated with ischaemic heart disease, while the reverse independent association was also present (Eriksson et al. 2013). Studies in Canadian cohorts have similarly pointed to the prognostic influence of comorbid cardiovascular disease in patients with COPD (Alhaj et al. 2008; Curkendall et al. 2006a, b).

The association of COPD with coronary artery calcification as a sign of coronary atherosclerosis has been found in a number of studies using different methodologies. In a study using an ordinal scoring system of non-gated non-contrast chest CT scans showed that coronary artery severity and emphysema severity were related and strongly as well as independently associated with prognosis in patients with moderate to severe COPD (O'Hare et al. 2014). Another cross-sectional study revealed a number of associations of COPD, including higher coronary artery calcium score, increased prevalence of hypertension or ischaemic heart disease and higher arterial stiffness (Eriksson et al. 2013). Coronary artery calcium score, thoracic aorta calcium score and extent of emphysema as shown on CT all were predictors of all-cause mortality (Romme et al. 2013).

A larger study, which included 672 subjects with COPD, 199 normal smokers and 71 non-smokers also revealed a direct relationship between coronary artery calcium score and extent of COPD and clinical outcomes such as reduced exercise capacity and increased mortality (Williams et al. 2014).

Contrary to the above studies, the MESA lung study showed that an obstructive pattern of spirometry and emphysema was independently associated with subclinical atherosclerosis in the carotid arteries, but they weren't independently related to coronary artery calcium (Barr et al. 2012).

Coronary artery disease in severe COPD is often underdiagnosed, as shown in a study in patients referred for lung transplantation (Reed et al. 2012). Coronary artery disease was shown by invasive coronary angiography in 60 % of patients, while 16 % of patients had severe coronary artery disease and 9 % of patients had occult severe coronary artery disease (Reed et al. 2012).

The relationship between COPD and heart disease is not isolated to coronary atherosclerosis and ischaemic heart disease. There are also effects on the conductivity of the heart, leading to an increase in atrial arrhythmias (both atrial fibrillation and atrial flutter) as well as ventricular tachycardias (Konecny et al. 2014). In addition, there are significant compounding effects on both right and left ventricular filling, which is impaired due to the hyperinflation that results from air trapping in severe emphysema (Barr et al. 2010; Watz et al. 2010).

Apart from COPD, we need to realise that other lung diseases are commonly part of a systemic spectrum. A recent study demonstrated asymptomatic coronary artery disease was present in a quarter of patients investigated for idiopathic pulmonary fibrosis (Cassagnes et al. 2015). Other diseases associated with combined pulmonary and cardiac disease, such as systemic sclerosis (Condcliffe et al. 2011) and sarcoidosis (Seeger et al. 2013), tend to have an impact on all affected organs.

6 What Has CT to Offer?

There is a range of CT methodologies available in standard clinical practice, and the types of investigations are affected by scanner type, availability of ECG gating (either routine or as a special application) and the utility of post-processing tools (Rahagi et al. 2014).

The increasing capabilities of advanced CT scanners, including faster rotation speeds, high-pitch mode and higher spatial and temporal resolution, allow for more detailed and comprehensive imaging even without the need for ECG gating (Cassagnes et al. 2015; Remy-Jardin et al. 2010). The advent of ECG gating and state-of-the-art CT scanner faster rotation speed, high spatial and temporal resolution, high-pitch mode, shorter acquisition time and dedicated cardiac reconstruction algorithms has opened new possibilities for chest imaging, integrating cardiac morphologic and even functional information within a diagnostic chest CT scan. The contrast administration protocol has an important role, as it is important to ensure both the pulmonary and systemic circulation are adequately opacified (Fig. 11).

In addition, it needs to be remembered that patients will be referred from a host of sources and that the clinical details given will influence the choice of examination. For example, a patient from a chest clinic with dyspnoea and obstructive pulmonary function tests will normally undergo a non-contrast-enhanced CT chest examination (with or without expiratory series to assess for air trapping), whereas a suspicion for pulmonary hypertension will yield a contrast-enhanced CT pulmonary angiogram without ECG gating. In contrast, patients referred for CT coronary angiography for indeterminate chest pain will have a limited chest examination (although it is now accepted that a full field-of-view reconstruction is vital to detect other pathology in the scanned volume) (Mirsadraee and van Beek 2014). Thus, a patient with an acute myocardial infarction may present as "suspected pulmonary embolism" (Fig. 12). Similarly, a patient may present with cardiac complaints, in whom a lung cancer is extending into the pericardium of the heart (Fig. 13) or in whom metastases to the heart are present (Fig. 14). Alternatively, patients may present with dyspnoea, in whom the underlying cause is cardiac disease, such as cardiomyopathy (Fig. 15).

Thus, there is a new focus to try and introduce a comprehensive single examination of the

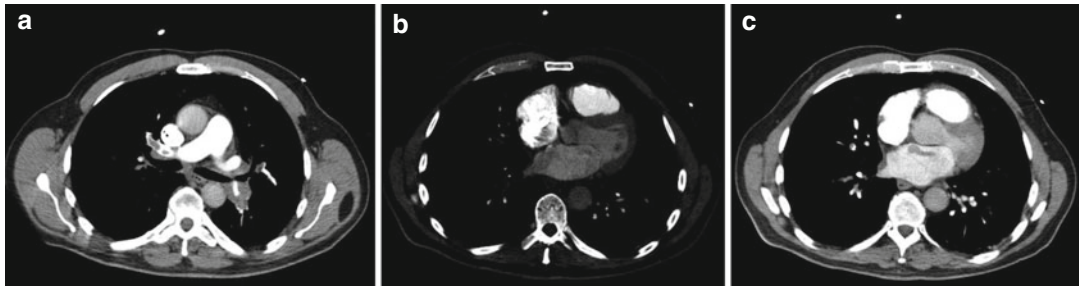

Fig. 11 Patient with bilateral central pulmonary embolism (**a**) with clot demonstrated in the right atrium (**b**) on CT pulmonary angiogram. On the delayed scan, contrast has entered the left cardiac chambers, which confirm a thrombus through a patent foramen ovale from the right to the left atrium (**c**)

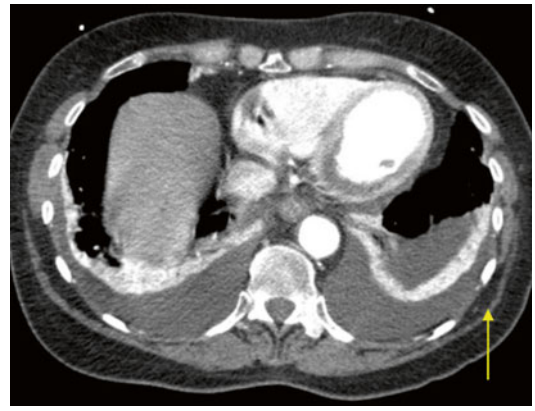

Fig. 12 Patient presenting with suspected acute pulmonary embolism. There are bilateral pleural effusions with dependent lung collapse and a rim of non-enhancing myocardium (*arrow*). Patient was diagnosed with acute myocardial infarction and congestive heart failure

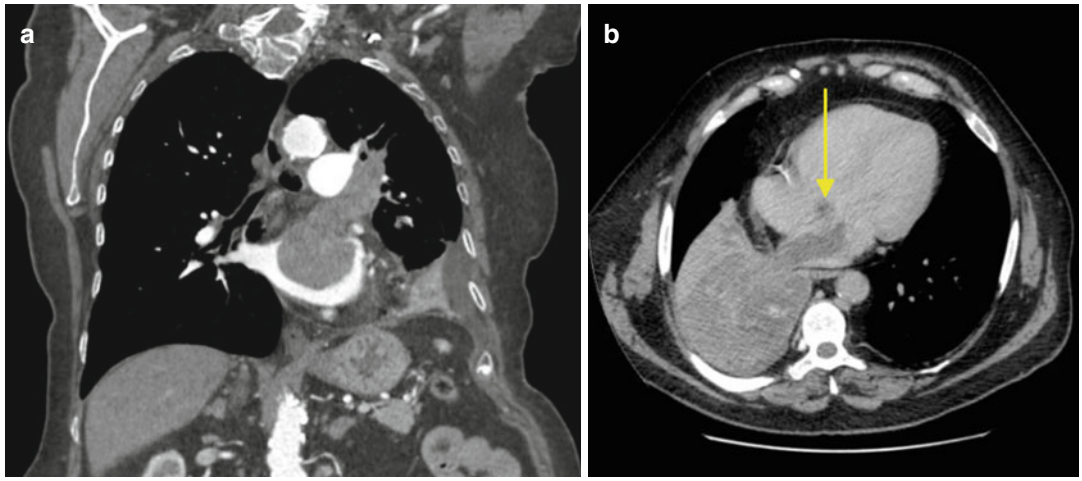

Fig. 13 Left upper lobe bronchial carcinoma with direct extension from the left upper pulmonary vein into the left atrium (**a**) and another patient with bronchial carcinoma extension into the left atrium and through the patent foramen ovale (*arrow*; **b**)

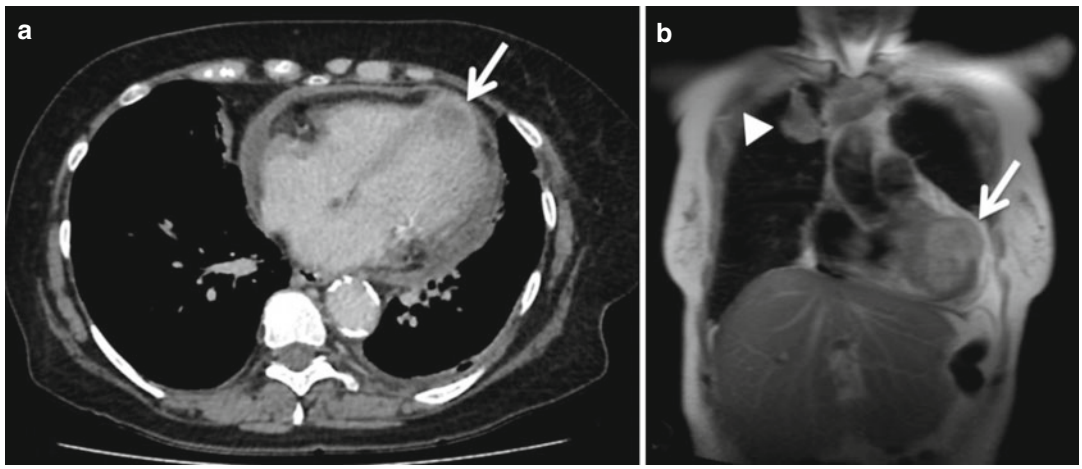

Fig. 14 Lung cancer with myocardial metastasis. *Arrow* shows anteroseptal metastatic mass on contrast-enhanced CT (**a**) and contrast-enhanced HASTE cardiac MRI. *Arrowhead* (**b**) shows the primary mass in the right upper lobe

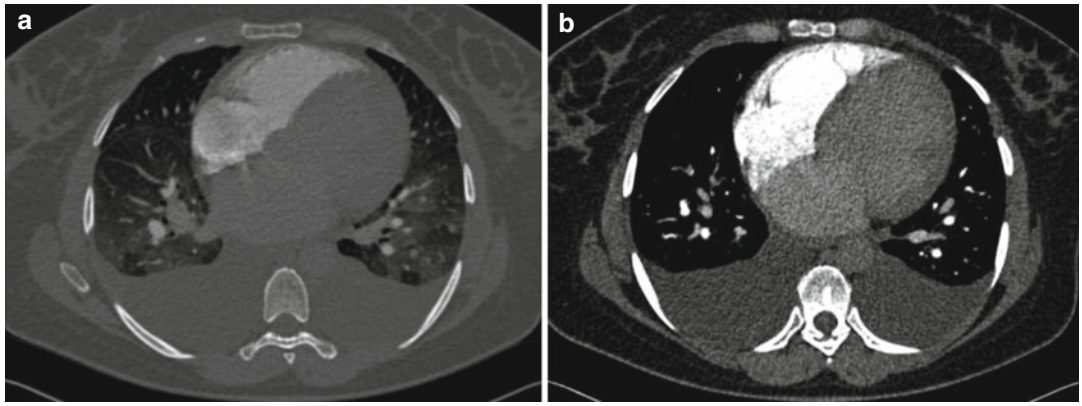

Fig. 15 Pregnant woman with dilated cardiomyopathy presenting with dyspnea. The CT demonstrates mosaic attenuation due to postcapillary pulmonary hypertension with pulmonary oedema and bilateral pleual effusions (**a**), and a dilated left ventricle (**b**)

chest, although this would require ECG gating for some CT systems, as well as different contrast injection techniques to cope with the different time delays for sufficient opacification of both the pulmonary arterial system and the left heart and coronary arterial tree (Marano et al. 2015).

Aside from the pros and cons of comprehensive CT, there is a need for assessment that includes a semi-quantitative or quantitative assessment of a variety of findings. Coronary artery calcification can be scored on an ordinal scale, giving insight into extent of coronary atherosclerosis (O'Hare et al. 2014). This needs to be put into the context of the age and gender of the patient, similar to formal coronary artery calcium scoring on ECG-gated CT (Agatston et al. 1990; McClelland et al. 2006).

Emphysema extent can be determined using formal post-processing software tools, which can also assess airway wall thickness, for instance. However, visual scoring will also enable assessment of extent of emphysema (COPDGene CT Workshop Group et al. 2012). The pulmonary artery/aortic root ratio can be easily measured on either non-contrast or contrast-enhanced CT scans (Wells et al. 2012).

Apart from these morphological assessment capabilities, CT is increasingly able to assess functional characteristics of cardiothoracic diseases. The application of dual-energy contrast-enhanced CT can yield a pulmonary blood volume map, giving an indirect measure of pulmonary perfusion (Thieme et al. 2012; Ameli-Renani et al. 2014; Hoey et al. 2011). The use of larger-volume CT scanners allows volumetric dynamic assessment of contrast-enhanced CT, thus giving quantifiable time curves of contrast enhancement, which can be used to calculate true perfusion and offers insight into the pulmonary and bronchial circulation (Figs. 5 and 10), with the latter increasingly important in patients with pulmonary hypertension either with or without pulmonary arterial obstruction (Sun et al. 2013; Mirsadraee et al. 2015).

7 Concluding Remarks

The capability of CT to perform a rapid holistic investigation of the cardiothoracic systems has made significant strides over the past decade. This has resulted in the ability to assess the mutual dependencies of pulmonary and cardiac diseases. This is particularly relevant in smoking-related lung disease and in various types of pulmonary hypertension. This field is quite rapidly under development, and it is very likely that a combined morphologic and functional assessment, with quantifiable biomarkers of disease,

will soon become available as part of the routine workup of these patients.

References

Agatston AS, Janowithz WR, Hildner FJ et al (1990) Quantification of coronary artery calcium using ultrafast computed tomography. J Am Coll Cardiol 15:827–832

Alford SK, van Beek EJ, McLennan G, Hoffman EA (2010) Heterogeneity of pulmonary perfusion as a mechanistic image-based phenotype in emphysema susceptible smokers. Proc Natl Acad Sci U S A 107:7485–7487

Alhaj EK, Alhaj NE, Bergmann SR et al (2008) Coronary artery calcification and emphysema. Can J Cardiol 24:369–372

Ameli-Renani S, Rahman F, Nair A et al (2014) Dual-energy CT for imaging of pulmonary hypertension: challenges and opportunities. Radiographics 34:1769–1790

Bajc M, Maffioli L, Miniati M (2014) Good clinical practice in pulmonary embolism diagnosis: where do we stand today? Eur J Nucl Med Mol Imaging 41:333–336

Barbera JA (2013) Mechanisms of development of chronic obstructive pulmonary disease-associated pulmonary hypertension. Pulm Circ 3:160–164

Barr RG, Bluemke DA, Ahmed FS et al (2010) Percent emphysema, airflow obstruction and impaired left ventricular filling. N Engl J Med 362:217–227

Barr RG, Ahmed FS, Carr JJ et al (2012) Subclinical atherosclerosis, airflow obstruction and emphysema: the MESA Lung Study. Eur Respir J 39:846–854

Brandjes DP, Heijboer H, Büller HR, de Rijk M, Jagt H, ten Cate JW (1992) Acenocoumarol and heparin compared with acenocoumarol alone in the initial treatment of proximal-vein thrombosis. N Engl J Med 327:1485–1489

Carter BD, Abnet CC, Feskanich D et al (2015) Smoking and mortality – beyond established causes. N Engl J Med 372:631–640

Cassagnes L, Gaillard V, Monge E et al (2015) Prevalence of asymptomatic coronary disease in fibrosing idiopathic interstitial pneumonias. Eur J Radiol 84:163–171

Chen WJ, Lin CC, Lin CY et al (2014) Pulmonary embolism in chronic obstructive pulmonary disease – a population based cohort study. COPD 11:438–443

Condcliffe R, Radon M, Hurdman J et al (2011) CT pulmonary angiography combined with echocardiography in suspected systemic sclerosis-associated pulmonary arterial hypertension. Rheumatology 50: 1480–1486

COPDGene CT Workshop Group, Barr RG, Berkowitz EA, Bigazzi F et al (2012) A combined pulmonary-radiology workshop for visual evaluation of COPD: study design, chest CT findings and concordance with quantitative evaluation. COPD 9:151–158

Curkendall SM, Lanes S, de Luise C et al (2006a) Chronic obstructive pulmonary disease severity and cardiovascular outcomes. Eur J Epidemiol 21:803–813

Curkendall SM, de Luise C, Jones JK et al (2006b) Cardiovascular disease in patients with chronic obstructive pulmonary disease, Saskatchewan Canada cardiovascular disease in COPD patients. Ann Epidemiol 16:63–70

Dibble CT, Shimbo D, Barr RG et al (2012) Brachial artery diameter and the right ventricle: the Multi-Ethnic Study of Atherosclerosis-right ventricle study. Chest 142:1399–1405

Dournes G, Laurent F, Coste F et al (2015) Computed tomographic measurement of airway remodelling and emphysema in advanced chronic obstructive pulmonary disease. Am J Respir Crit Care Med 191:63–70

Eriksson B, Lindberg A, Müllerova H, Rönmark E, Lundbäck B (2013) Association of heart diseases with COPD and restrictive lung function – results from a population survey. Respir Med 107:98–106

Estépar RS, Kinney GL, Black-Shinn JL et al (2013) Computed tomographic measures of pulmonary vascular morphology in smokers and their clinical implications. Am J Respir Crit Care Med 188:231–239

Goudie AR, Liworth BJ, Hopkinson PJ, Wei L, Struthers AD (2014) Tadalafil in patients with chronic obstructive pulmonary disease: a randomised, double-blind, parallel-group, placebo-controlled trials. Lancet Respir Med 2:293–300

Hoeper MM, Bogaard HJ, Condliffe R et al (2013) Definitions and diagnosis of pulmonary hypertension. J Am Coll Cardiol 25(Suppl D):42–50

Hoey ET, Mirsadraee S, Pepke-Zaba J et al (2011) Dual-energy CT angiography for assessment of regional pulmonary perfusion in patients with chronic thromboembolic pulmonary hypertension: initial experience. Am J Roentgenol 196:524–532

Ives SJ, Haris RA, Witman MA et al (2014) Vascular dysfunction and chronic obstructive pulmonary disease – the role of redox balance. Hypertension 63:459–467

Kawut SM, Poor HD, Parikh MA et al (2014) Cor pulmonale parvus in chronic obstructive pulmonary disease and emphysema. The MESA COPD study. J Am Coll Cardiol 64:2000–2009

Kessler R, Faller M, Weitzenblum E et al (2001) "Natural history" of pulmonary hypertension in a series of 131 patients with chronic obstructive lung disease. Am J Respir Crit Care Med 164:219–224

Konecny T, Park JY, Somers KR et al (2014) Relation of chronic pulmonary disease to atrial and ventricular arrhythmias. Am J Cardiol 114:272–277

Lederer DJ, Bartels MN, Schluger N et al (2012) Sildenafil for chronic obstructive pulmonary disease: a randomized crossover trial. COPD 9:268–275

Ley S, Grünig E, Kiely DG, van Beek E, Wild J (2010) Computed tomography and magnetic resonance imaging of pulmonary hypertension: pulmonary vessels

and right ventricle. J Magn Reson Imaging 32:1313–1320
Maclay JD, McAllister DA, Rabinovich R et al (2012) Systemic elastin degradation in chronic obstructive pulmonary disease. Thorax 67:606–612
Marano R, Pirro F, Silvestri V et al (2015) Comprehensive CT cardiothoracic imaging: a new challenge for chest imaging. Chest 147:538–551
Matsuoka S, Washko GR, Yamashiro T et al (2010) Pulmonary hypertension and computed tomography measurement of small pulmonary vessels in severe emphysema. Am J Respir Crit Care Med 181: 218–225
McAllister DA, Maclay JD, Mills NL et al (2007) Arterial stiffness is independently associated with emphysema severity in patients with chronic obstructive pulmonary disease. Am J Respir Crit Care Med 176: 1208–1214
McClelland RL, Chung H, Detrano R et al (2006) Distribution of coronary artery calcium by race, gender, and age: results from the Multi-Ethnic Study of Atherosclerosis (MESA). Circulation 113:30–37
Miller J, Edwards LD, Agust A et al (2013) Comorbidity, systemic inflammation and outcomes in the ECLIPSE cohort. Respir Med 107:1376–1384
Minai OA, Chaouat A, Adnot S (2010) Pulmonary hypertension in COPD: epidemiology, significance, and management: pulmonary vascular disease: the global perspective. Chest 137(Suppl 6):39S–51S
Mirsadraee S, van Beek EJ (2014) Cross-sectional cardiac imaging: prevalence and significance of extracardiac findings. J Thorac Imaging 29:92–97
Mirsadraee S, Weir NW, Connolly S et al (2015) Feasibility of radiation dose reduction using AIDR-3D in dynamic pulmonary CT perfusion. Clin Radiol 70(8):844–851
Müllerova H, Agusti A, Erqou S, Mapel DW (2013) Cardiovascular comorbidity in COPD. Systematic literature review. Chest 144:1163–1178
O'Hare PE, Ayres JF, O'Rourke RL et al (2014) Coronary artery calcification on computed tomography correlates with mortality in chronic obstructive pulmonary disease. J Comput Assist Tomogr 38:753–759
Pengo V, Lensing AW, Prins MH et al (2004) Incidence of chronic thromboembolic pulmonary hypertension after pulmonary embolism. N Engl J Med 350:2257–2264
Rahagi FN, van Beek EJ, Washko GR (2014) Cardiopulmonary coupling in chronic obstructive pulmonary disease. The role of imaging. J Thorac Imaging 29:80–91
Reed RM, Eberlein M, Girgis RE et al (2012) Coronary artery disease in under-diagnosed and under-treated in advanced lung disease. Am J Med 125:1228
Remy-Jardin M, Edme JL, Boulenguez C, Remy J, Mastora I, Sobaszek A (2002) Longitudinal follow-up study of smoker's lung with thin section CT in correlation with pulmonary function tests. Radiology 222:261–270
Remy-Jardin M, Faivre JB, Santangelo T, Tacelli N, Remy J (2010) Imaging the heart-lung relationships during a chest computed tomography examination: is electrocardiographic gating the only option? J Thorac Imaging 25:239–246
Romme EA, McAllister DA, Murchison JT et al (2013) Associations between COPD related manifestations: a cross-sectional study. Respir Res 14:129
Seeger W, Adir Y, Barbera JA et al (2013) Pulmonary hypertension in chronic lung diseases. J Am Coll Cardiol 62(Suppl D):109–116
Shin S, King CS, Brown AW et al (2014) Pulmonary artery size as a predictor of pulmonary hypertension and outcomes in patients with chronic obstructive pulmonary disease. Respir Med 108:1626–1632
Simonneau G, Garzoulis MA, Adatia I et al (2013) Updated clinical classification of pulmonary hypertension. J Am Coll Cardiol 25(Suppl D):34–41
Sun H, Gao F, Li N, Liu C (2013) An evaluation of the feasibility of assessment of volume perfusion for the whole lung by 128-slice spiral CT. Acta Radiol 54:921–927
The health consequences of smoking: 50 years of progress: a report of the Surgeon General. Atlanta: Department of Health and Human Services, Centers for Disease Control and Prevention, National Center for Chronic Disease Prevention and Health Promotion, Office on Smoking and Health (2014) http://www.surgeongeneral.gov/library/reports/50-years-of-progress/#fullreport
Thieme SF, Ashoori N, Bamberg F et al (2012) Severity assessment of pulmonary embolism using dual energy CT: correlation of a pulmonary perfusion defect score with clinical and morphological parameters of blood oxygenation and right ventricular failure. Eur Radiol 22(2):269–278
Vonk-Noordegraaf A, Haddad F, Chin KM et al (2013) Right heart adaptation to pulmonary arterial hypertension. Physiology and pathobiology. J Am Coll Cardiol 25(Suppl D):22–33
Watz H, Waschki B, Meyer T et al (2010) Decreasing cardiac chamber sizes and associated heart dysfunction in COPD: role of hyperinflation. Chest 138:32–38
Wells JM, Washko GR, Han MK et al (2012) Pulmonary arterial enlargement and acute exacerbations of COPD. N Engl J Med 367:913–921
Williams MC, Murchison JT, Edwards LD et al (2014) Coronary artery calcification in increased in patients with COPD and associated with increased morbidity and mortality. Thorax 69:718–723

Anomalies and Malformations of the Pulmonary Circulation

Carlos S. Restrepo, Rashmi Katre, and Amy Mumbower

Abstract

Congenital anomalies of the pulmonary circulation can be seen as isolated anomalies or as part of more complex malformations affecting numerous organs and systems, in particular the lungs, heart, and great vessels. These malformations may affect the pulmonary arteries, pulmonary veins, the aorta, and the intrathoracic systemic veins. With its superb spatial and temporal resolution, contrast-enhanced multidetector CT has become the imaging modality of choice for the evaluation of these entities, allowing imaging of the heart, vasculature, and lungs in one single examination.

1 Introduction

Congenital anomalies of the pulmonary circulation can be seen as isolated anomalies or as part of more complex malformations affecting numerous organs and systems, in particular the lungs, heart, and the great vessels. These malformations may affect the pulmonary arteries, pulmonary veins, the aorta, and the intrathoracic systemic veins. With its superb spatial and temporal resolution, contrast-enhanced multidetector CT has become the imaging modality of choice for the evaluation of these entities, allowing imaging of the heart, vasculature, and lungs in one single examination.

C.S. Restrepo, MD (✉) • R. Katre, MD
A. Mumbower, MD
Department of Radiology, The University of Texas Health Science Center at San Antonio, San Antonio, TX, USA
e-mail: RestrepoC@UTHSCSA.edu; Katre@UTHSCSA.edu; Mumbower@UTHSCSA.edu

2 Congenital Anomalies of the Pulmonary Arteries

There are four pulmonary artery congenital abnormalities that can be seen as isolated anomalies or associated with other cardiovascular and tracheobronchial anomalies: (1) congenital interruption of the pulmonary artery, (2) peripheral pulmonary artery stenosis, (3) idiopathic aneurysm of the pulmonary artery, and (4) aberrant origin of the left pulmonary artery. Conotruncal abnormalities (tetralogy of Fallot, transposition of the great arteries, interrupted aortic arch, aortopulmonary window) comprise a diverse group of complex congenital heart defects affecting the great vessels, and outflow tracts of the heart

U.J. Schoepf, F.G. Meinel (eds.), *Multidetector-Row CT of the Thorax*, Medical Radiology,
DOI 10.1007/978-3-319-30355-0_20

(embryonic conus arteriosus and truncus arteriosus) are more in the realm of congenital cardiac pathology and will not be discussed here.

3 Congenital Interruption of the Pulmonary Artery

Unilateral absence of a pulmonary artery may be seen associated with congenital heart disease, such as septal defects, truncus arteriosus, and tetralogy of Fallot, or as an isolated anomaly. This condition was previously known as congenital absence of the pulmonary artery, but the term "interruption" is preferred, since only the mediastinal segment of the right or left pulmonary artery is absent, whereas the more peripheral intrapulmonary network is present. The affected lung receives oxygenated blood and vascular supply through collateral systemic arteries such as the bronchial arteries, intercostal arteries, internal mammary artery, and a patent ductus arteriosus. The interrupted pulmonary artery usually lies on the opposite side of the aortic arch (Figs. 1 and 2). The right pulmonary artery is more commonly affected in the isolated form, with congenital absence or interruption of the left more often seen in patients with other congenital anomalies like tetralogy of Fallot (Davis 2000). Women are affected more often than men (3:2), with those patients with associated congenital heart disease manifesting earlier in life. A patent ductus arteriosus is commonly present ipsilateral to the absent pulmonary artery (Apostolopouou et al. 2002). Patients with the isolated form usually present with nonspecific clinical manifestations such as dyspnea (40 %), recurrent pulmonary infection (37 %), or hemoptysis (20 %), and nearly half of affected patients (44 %) will have arterial pulmonary hypertension (Harjel et al. 2002). It has been postulated that a unilateral interruption of the pulmonary artery results from the proximal sixth aortic arch in the embryo which gives rise to the extraparenchymal pulmonary artery with persistent connection of the intrapulmonary arteries to the distal sixth aortic arch which originates the ductus arteriosus (Apostolopouou et al. 2002). On imaging exams the affected lung is usually smaller, which is evidenced by shifting of the heart and mediastinum, and elevation of the hemidiaphragm to the affected side (Fig. 3). There is complete absence of the mediastinal segment of the pulmonary artery with a smaller ipsilateral hilum and a prominent contralateral hilum

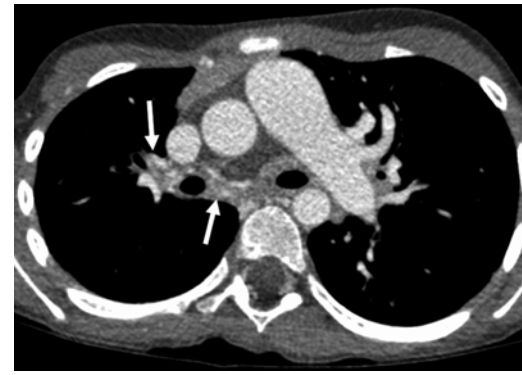

Fig. 1 Interrupted right pulmonary artery in an 11-year-old female with a normal left-side aortic arch. Contrast-enhanced CT shows only a left pulmonary artery arising from the pulmonary trunk and slightly prominent bronchial arteries in the right hilum (*arrows*)

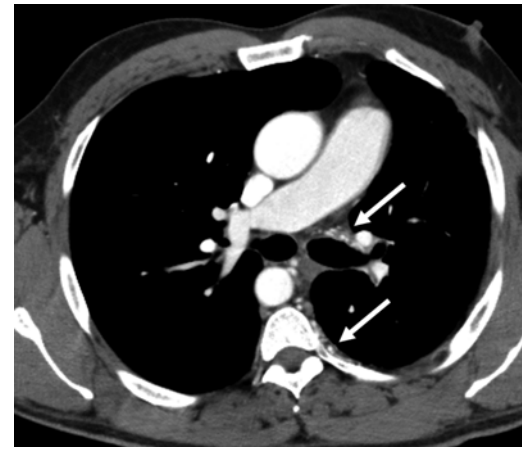

Fig. 2 Congenital interruption of the left pulmonary artery in a 48-year-old male with right-side aortic arch. Contrast-enhanced CT shows absence of the left pulmonary artery, a right-side descending thoracic aorta, and prominent systemic arterial circulation in the left hilum, mediastinum, and left-side chest wall (*arrows*)

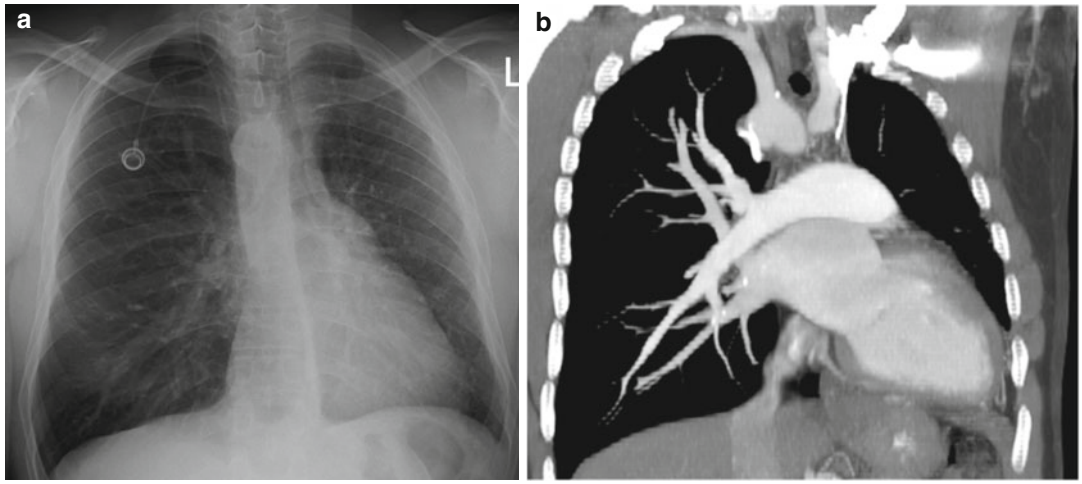

Fig. 3 Left-side cardiac and mediastinal shifting in a patient with congenital interruption of the left-side pulmonary artery. (**a**) Chest X-ray shows a right-side aortic arch and diminished volume in the left hemithorax. (**b**) Contrast-enhanced CT, MIP coronal reconstruction reveals a mildly enlarged single right pulmonary artery with leftward deviation of the heart with a smaller left hemithorax

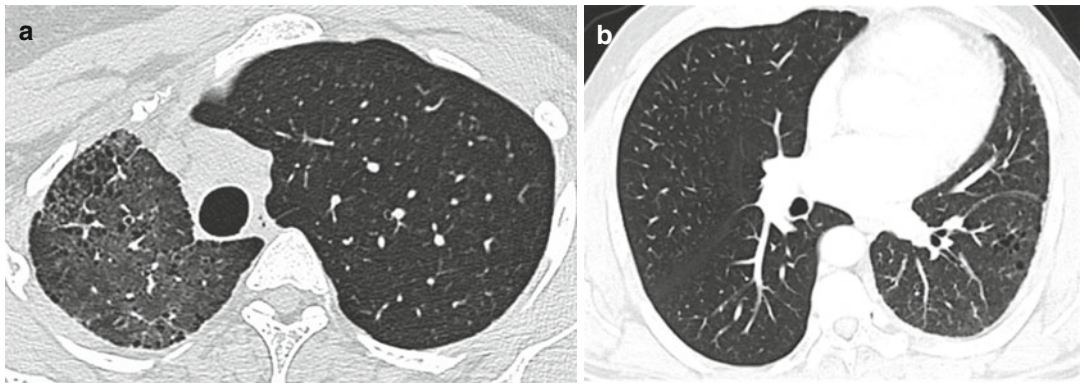

Fig. 4 (**a**) High-resolution CT in a female patient with congenital interruption of the right pulmonary artery. Axial image at the level of the upper lobes demonstrates numerous cysts in the right lung. (**b**) Lung window axial image at the level of the lower lobes in a patient with congenital interruption of the left pulmonary artery shows small pulmonary cysts in the left lung

which receives the entire output of the right ventricle and pulmonary trunk. The extrapleural space is prominent, and collateral circulation may be also appreciated in the chest wall. On high-resolution CT, the affected lung demonstrates reticular opacities, septal thickening, cystic lung changes/honeycombing, and bronchial dilation similar to interstitial pulmonary fibrosis (Fig. 4) (Ryu et al. 2004; Sakai et al. 2002).

4 Peripheral Pulmonary Artery Stenosis

Pulmonary artery stenosis is commonly associated with other complex congenital heart diseases, in particular tetralogy of Fallot, transposition of the great vessels, atrial septal defect, and ventricular septal defect. Isolated congenital peripheral pulmonary stenosis or pulmonary branch stenosis is less common. Three conditions classically associated with peripheral pulmonary artery stenosis are in utero exposure to rubella virus (post-rubella or maternal rubella syndrome), Noonan's syndrome, and Williams' syndrome. More recently Alagille's syndrome, cutis laxa syndrome, and Ehlers-Danlos syndrome have also been reported to be also associated with congenital pulmonary artery branch stenosis (Kamath et al. 2004; Wahab et al. 2003). Rarely, it can present as an idiopathic isolated condition in the adult not associated with any systemic condition or known syndrome (Kreutzer et al. 1996; Shaj et al. 2000). Depending on the degree and extension of stenosis, affected patients may be asymptomatic or present with arterial pulmonary hypertension. Physical signs and symptoms may include dyspnea, fatigue, chest pain, palpitations, right ventricular heart failure, hepatomegaly, and peripheral edema. The morphology of peripheral pulmonary artery stenosis is quite variable and can present as single narrowing of the pulmonary trunk, right or left pulmonary artery (type I), bifurcation of the pulmonary trunk extending to the proximal right or left pulmonary arteries (type II), multiple peripheral pulmonary arteries without abnormality of the central vasculature (type III), or a combination of involvement of the central and peripheral vessels (type IV) (Gray et al. 1963). Differential diagnosis includes changes from systemic vasculitis such as Behçet's disease or Takayasu's arteritis (Toledano et al. 2011). In cases of vasculitis, there is associated abnormal thickening of the arterial walls, not encountered in congenital causes (Fig. 5).

5 Idiopathic Aneurysm of the Main Pulmonary Artery

Idiopathic dilation of the main pulmonary artery or pulmonary trunk with or without the central pulmonary arteries is defined as an abnormal dilation that occurs in the absence of a preexistent cardiac or pulmonary disease such as pulmonic valve stenosis, pulmonary arterial hypertension, syphilis, or connective tissue disor-

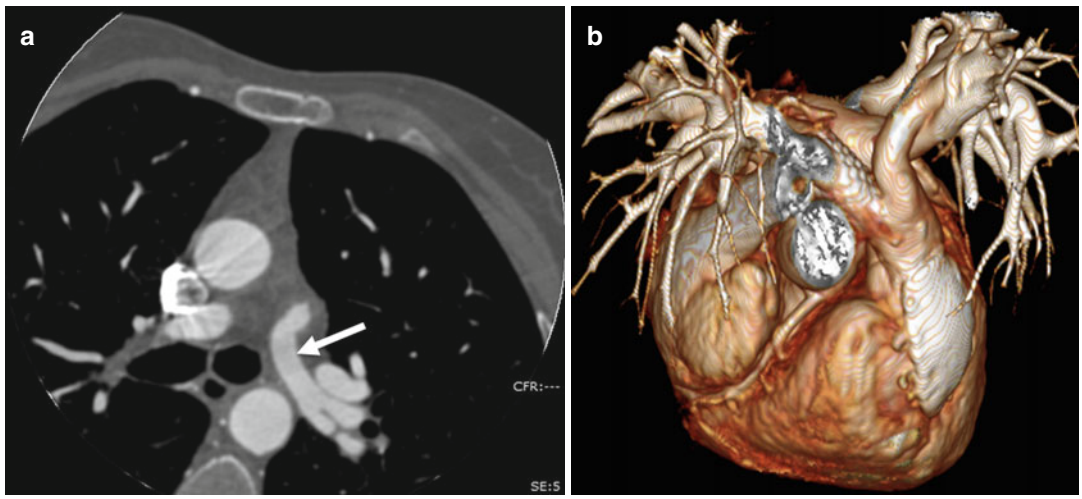

Fig. 5 Branch pulmonary artery stenosis in a female patient with maternal rubella syndrome. (**a**) Contrast-enhanced axial CT. (**b**) Volume-rendered 3-D reconstruction. CT demonstrates a long segment stenosis of the left pulmonary artery

der. Idiopathic pulmonary artery aneurysms are rare, typically asymptomatic and incidentally encountered. Little is known about the natural history of this condition, and reported outcomes range from asymptomatic cases to rupture and sudden death (van Rens et al. 2000; Nair and Cobanoglu 2001; Seguchi et al. 2011; Andrews et al. 1993). These aneurysms can grow very large, up to 12 cm in diameter, producing mass effect on adjacent structures such as the trachea or laryngeal nerve. Cystic medial degeneration of the arterial wall is the most common pathologic abnormality reported (Deb et al. 2005). The diagnosis of this condition is established by exclusion of diseases that induce enlargement of the pulmonary arteries. The following diagnostic criteria have been proposed: (1) simple dilatation of the pulmonary trunk, (2) absence of intra- or extracardiac shunt, (3) absence of chronic cardiopulmonary disease, (4) absence of arterial wall disease, and (5) normal pressure in the right ventricle and pulmonary artery (Niida et al. 2011). Even though the pulmonary arterial system is a low pressure entity, surgery is advocated for aneurysms with a diameter of 6 cm or greater to prevent potential complications, such as rupture, dissection, and cardiac death, and is also recommended in patients experiencing symptoms such as tracheobronchial compression or chest pain (Fig. 6) (Kharge et al. 2013).

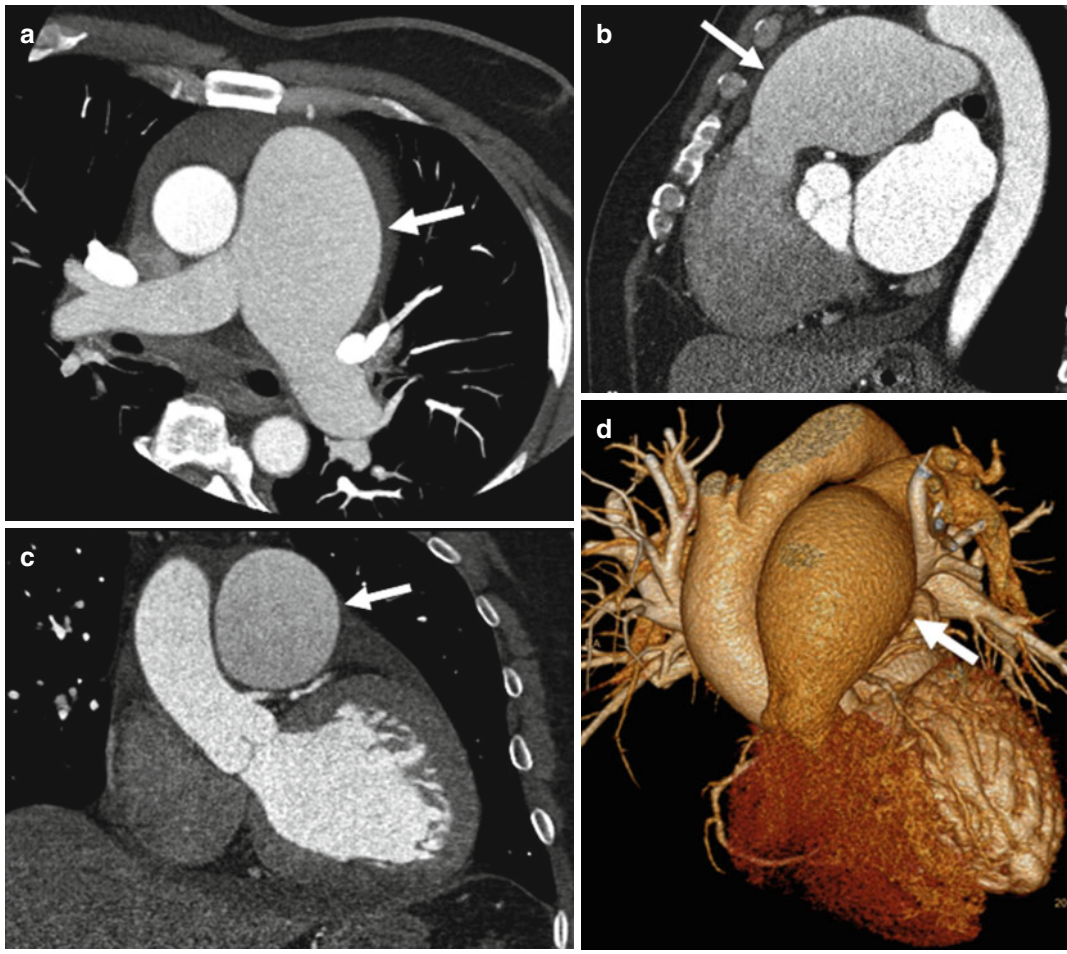

Fig. 6 Idiopathic aneurysm of the main pulmonary artery. (**a**–**d**) Contrast-enhanced cardiac-gated CT with axial, sagittal, coronal, and 3-D reconstruction. There is a large aneurysmal dilation of the pulmonary trunk and to a lesser extent of the central pulmonary arteries in this patient with no evidence of cardiopulmonary disease, systemic, or known arterial wall disorder (*arrows*)

6 Aberrant Origin of the Left Pulmonary Artery (Pulmonary Artery Sling)

This rare condition is characterized by an abnormal origin of the left pulmonary artery from the posterior aspect of the right pulmonary artery to the right of the trachea and immediately above the right mainstem bronchus with a course between the trachea and the esophagus on its way to the left pulmonary hilum (Fig. 7). The exact prevalence of this condition is not known, but is considered a rare anomaly with a male to female ratio of 3:2. The majority of patients are symptomatic during the first year of life (90 %), mainly with respiratory symptoms to include stridor, wheezing, and recurrent respiratory infection. Tracheobronchial anomalies are common (40 %), including tracheal stenosis, abnormal branching pattern with the right tracheal bronchus, and complete cartilaginous tracheal rings, an association known as the "ring-sling" complex (Berdon et al. 1984). Underdevelopment of the right lung presenting as either agenesis or hypoplasia can be seen in up to 22 % of cases (Chen et al. 2007). Major cardiovascular anomalies including atrial septal defect, ventricular septal defect, patent ductus arteriosus, aortic coarctation, and tetralogy of Fallot are found in 30 % of affected patients (Gikonyo et al. 1989). Occasionally asymptomatic individuals are diagnosed later in life (Collins et al. 2008). Cross-sectional imaging, in particular multidetector CT, offers accurate anatomic information on both the vascular and tracheobronchial abnormalities of these patients, allowing appropriate surgical planning (Fig. 8) (Chen et al. 2007; Lee et al. 2001; Kagadis et al. 2007).

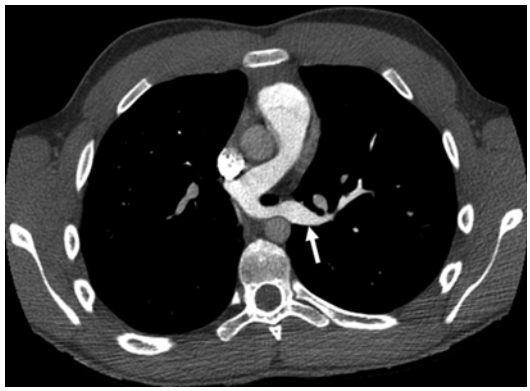

Fig. 7 Pulmonary artery sling in a young adult female patient. Contrast-enhanced CT, axial image at the level of the pulmonary trunk demonstrates aberrant origin of the left pulmonary artery from the right pulmonary artery, with the aberrant artery passing between the trachea and the esophagus (*arrow*)

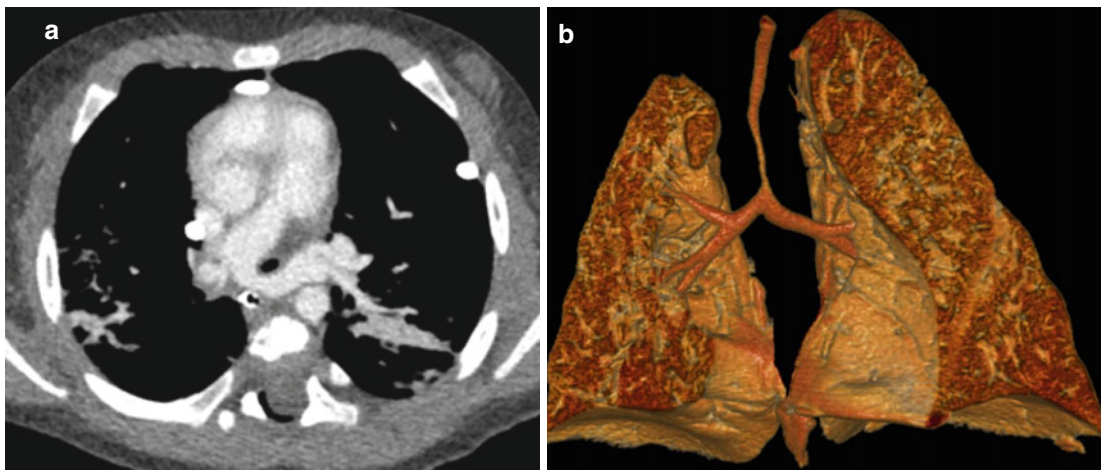

Fig. 8 Pulmonary artery sling in a four-month-old male with history of recurrent respiratory symptoms. (**a**) Cardiac CT axial image depicts the abnormal origin of the left pulmonary artery from the right. (**b**) Volume-rendered 3-D reconstruction demonstrates a long segment tracheal stenosis

7 Developmental Anomalies of Pulmonary Veins

Developmental pulmonary venous anomalies are predominantly comprised of anomalous venous connections which result in an extracardiac left-to-right shunt, as pulmonary venous blood flows directly into the right side of the heart or into the systemic veins. In partial anomalous pulmonary venous return (PAPVR), up to three pulmonary veins drain into the systemic circulation, while in total anomalous pulmonary venous return (TAPVR), all four pulmonary veins drain into the systemic circulation. To be compatible with life, TAPVR requires a right-to-left shunt via a cardiac septal defect or a patent ductus arteriosus. TAPVR has been classified into four groups: supracardiac, cardiac and infracadraiac, and mixed. Pathogenesis of this entity is closely related to the complex embryology.

8 Embryology

Three basic systems of venous drainage, the cardinal, umbilicovitelline, and omphalomesenteric systems, are seen in a developing embryo. The cardinal veins eventually differentiate into the superior vena cava (SVC) and coronary sinus, whereas the umbilicovitelline system develops into the inferior vena cava (IVC), ductus venosus, and portal vein. The common pulmonary vein (CPV) develops from the primordial left atrium and extends toward the lung buds. At approximately day 28 of gestation, the CPV joins the pulmonary portion of the splanchnic plexus, allowing flow of pulmonary blood into the heart. Over time, obliteration of pulmonary-splanchnic connections occurs with incorporation of CPV into the left atrial wall, leaving four independent pulmonary veins directly entering the left atrium. Early atresia or malposition of the CPV results in anomalous pulmonary venous return, with one or more pulmonary veins draining into the systemic venous circulation. Persistence of the cardinal veins and umbilicovitelline veins results in TAPVR (Total Anomalous Pulmonary Venous Return). It is hypothesized that "unroofing" of the right superior pulmonary vein into the SVC during development produces a combination of anomalous return and a distinct type of atrial septal defect, the sinus venosus atrial septal defect (SVASD). Failure of resorption of membrane between the CPV and primordial left atrium results in cor triatriatum (Katre et al. 2012).

9 Partial Anomalous Pulmonary Venous Return

Classically, a partial anomalous pulmonary venous connection has been described as presenting in childhood, most frequently on the right side and associated with SVASD. The overall incidence of PAPVR is approximately 0.5 % (Van Meter et al. 1990; Posniak et al. 1993; Dillon and Camputaro 1993). Significant variation is seen in the epidemiology of PAPVR in pediatric and adult populations. In pediatric patients who are symptomatic, the diagnosis is usually made earlier secondary to significant hemodynamic changes, while the condition remains undiagnosed until the adulthood in asymptomatic patients. In adults, frequently PAPVR is an incidental finding and only a few adult patients present with symptoms (Ho et al. 2009; Oliver et al. 2002). In pediatric studies (<18 years old), PAPVR has been reported to be twice as common in males as females and more frequently arises from the right (90 %) more often than the left upper lobe (LUL) (10 %). In addition, right upper lobe (RUL) PAPVR is associated with an SVASD in 80–90 % which is located high and posterior in the septum near the SVC orifice, while ostium secundum atrial septal defect (OSASD) is seen in 10–15 % of cases (Davia et al. 1973). PAPVR is more often hemodynamically significant when associated with congenital heart disease or scimitar syndrome. The "scimitar syndrome" is a complex form of PAPVR in which the anomalous pulmonary veins may drain into the supra- or infradiaphragmatic IVC or rarely into the hepatic or portal veins. It is also known as "hypogenetic lung syndrome" or "venolobar syndrome" to emphasize that this anomaly is not simply a variant of pulmonary venous return, but it is rather more extensive mal-

formation. Scimitar syndrome is essentially an anomaly of the right lung. The anomalous right pulmonary vein commonly drains the entire right lung but rarely may drain only the middle and lower lobes and usually descends in a cephalad-to-caudal direction toward the diaphragm with a crescentic shape. The radiographic appearance of this anomalous vein resembles a "curved Turkish sword" or "scimitar," from which the name has been derived (Vida et al. 2010; Gudjonsson and Brown 2006). Cardiopulmonary signs and symptoms depend upon the hemodynamic changes secondary to a left-to-right shunt and volume of the shunted blood, as well as whether PAPVR is associated with an atrial septal defect (ASD) or other congenital heart diseases. The volume of the shunt is calculated as a ratio between pulmonary blood flow (Qp) and systemic blood flow (Qs), at a given point of time. If the volume of the shunt is significant, that is, if the Qp:Qs is more than 1.5–1.7, surgical intervention is usually needed to prevent development of pulmonary hypertension (Greene and Miller 1986). Commonly encountered signs and symptoms include dyspnea, orthopnea, fatigue, chest pain, palpitations, tachycardia, and peripheral edema. Electrocardiographic abnormalities include abnormal P wave, nonspecific ST segment changes, left axis deviation, right axis deviation, sinus tachycardia, sinus bradycardia, and other arrhythmias.

10 Imaging Findings

Left upper lobe PAPVR is characterized by an aberrant draining vein which usually conducts blood cranially from the left upper lobe to the left innominate vein which eventually drains into the normally positioned superior vena cava on the right side of the aortic arch. This vein is called the "vertical vein," which is visualized as an anomalous vascular structure in the left paraaortic region or prevascular space where only mediastinal fat is normally present. A similar finding is observed in patients with persistent left-sided SVC (PLSVC); however a few differences exist between the vertical vein and PLSVC. In PLSVC, an aberrant vein usually conducts blood caudally from the left subclavian and jugular veins to the right atrium via the coronary sinus. In LUL PAPVR, a normal to large left innominate vein is seen in the expected position (Adler and Silverman 1973; Oropeza et al. 1970). However in PLSVC, left innominate vein is often absent or small in caliber. In PLSVC, up to 20 % of cases left innominate vein can be of normal size (Winter 1954). Therefore, although the absence of a left innominate vein is a reliable indicator of PLSVC, visualization of this vein does not aid in differentiation. The coronary sinus appears normal in LUL PAPVR but is usually enlarged in left-sided SVC, as it receives the blood flow from the left subclavian and jugular veins. Another differentiating point is the number of veins anterior to the left mainstem bronchus. Normally, only one vessel, which is the left superior pulmonary vein, is present in this location. In PLSVC, two vessels are present anterior to the left mainstem bronchus, specifically the left superior pulmonary vein and the more medially located left superior vena cava. In LUL PAPVR, no vessel is present in this location (Fig. 9).

Right upper lobe PAPVR is frequently more severe and diagnosed early in the pediatric population. It tends to be associated with other congenital malformations including a distinct type of ASD called as sinus venosus type ASD which is seen along the most posterior and superior aspect of the interatrial septum, usually at the level of SVC (Haramati et al. 2003). This is thought to be due to "unroofing" of the right superior pulmonary vein and the SVC during development. Anomalous right upper lobe pulmonary vein may connect to the superior vena cava, azygos vein, or right atrium directly (Herlong et al. 2000). This can be a subtle finding on CT, and unless anatomy of the region is closely scrutinized, this anomaly may remain undetected (Fig. 10).

The "scimitar syndrome" is commonly associated with right lung hypoplasia, dextroposition of the heart, hypoplasia of the right pulmonary artery, systemic arterial blood supply to the right lower lung from the branches of infradiaphragmatic aorta, lung sequestration, and sinus venosus or septum secundum atrial septal defects. The right lung may have abnormal lobation (fre-

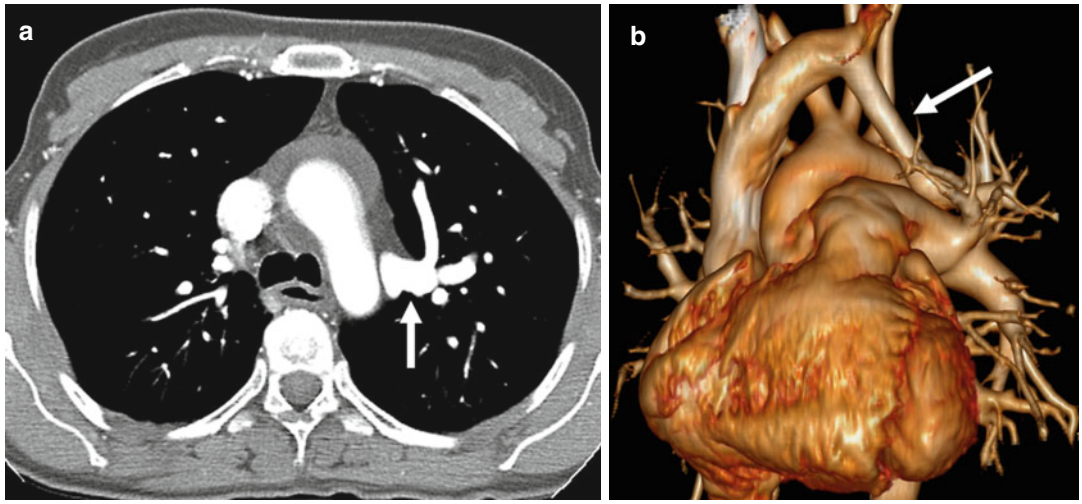

Fig. 9 Left upper lobe partial anomalous pulmonary venous return. (**a**) Contrast-enhanced CT, axial image at the level of the aortic arch. (**b**) CT and volume-rendered 3-D reconstruction. Images show an abnormal left upper lobe pulmonary vein draining to a left-side vertical vein (*arrow*)

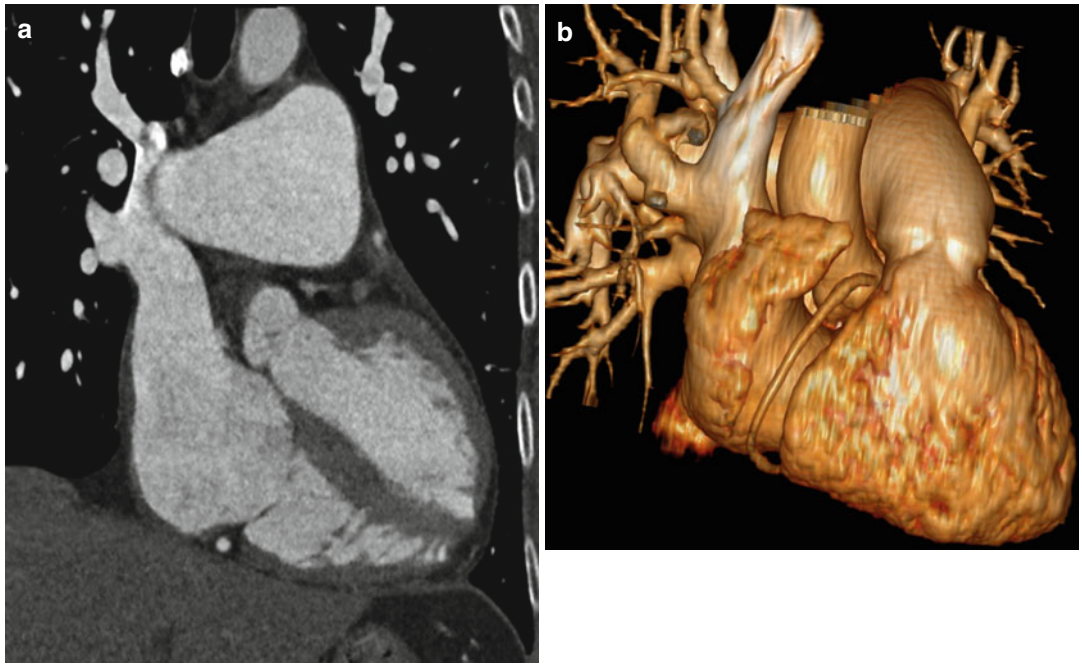

Fig. 10 Right upper lobe partial anomalous pulmonary venous return. (**a**) Contrast-enhanced CT with coronal reconstruction. (**b**) Volume-rendered 3-D reconstruction. There is abnormal drainage of the right upper lobe pulmonary veins to the distal superior vena cava

quently only two lobes) with a bronchial branching pattern that mimics the left lung (Gudjonsson and Brown 2006; Korkmaz et al. 2011; Konen et al. 2003). In most patients, right pulmonary hypoplasia causes a marked mediastinal shift and cardiac dextroposition. In severe cases, the entire

heart can be seen in the right hemithorax. Systemic arterial flow to the hypoplastic right lung originates directly from the upper segment of the abdominal aorta, and it is more common in the infantile form than in the adult form. A small pulmonary artery may also be present. Associated cardiac anomalies such as hypoplastic left heart, coarctation of the aorta, patent ductus arteriosus, tetralogy of Fallot, and persistent left superior vena cava can be seen. Overall, 19–31 % of patients with scimitar syndrome have associated cardiac anomalies (Fig. 11) (Alsoufi et al. 2007).

"Pseudoscimitar syndrome" or a "meandering right pulmonary vein" (MRPV), the entity described by Goodman and colleagues, is closely related to scimitar syndrome in which an anomalous right pulmonary vein courses circuitously through the right lung, seen as scimitar sign on the chest radiograph, and drains into the left atrium rather than into the IVC or systemic circulation. MRPV can occur with or without other features of the classic scimitar syndrome. While most cases involve the right pulmonary veins, cases of anomalous

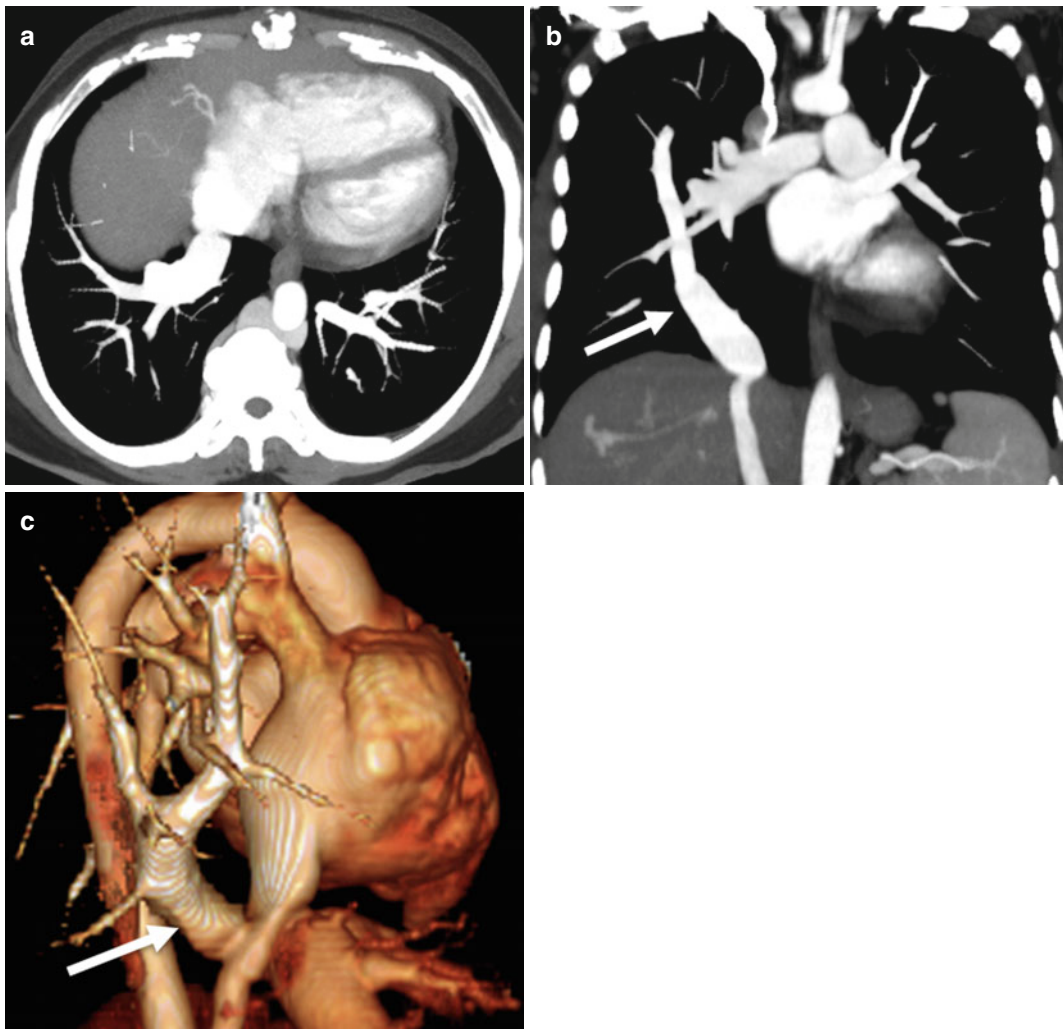

Fig. 11 Scimitar syndrome. (**a**) Contrast-enhanced CT, axial MIP. (**b**) Coronal MIP. (**c**) Volume-rendered 3-D reconstruction. There is a large anomalous vein (*arrows*) collecting the entire venous drainage of the right lung draining to the suprahepatic inferior vena cava immediately above the diaphragm

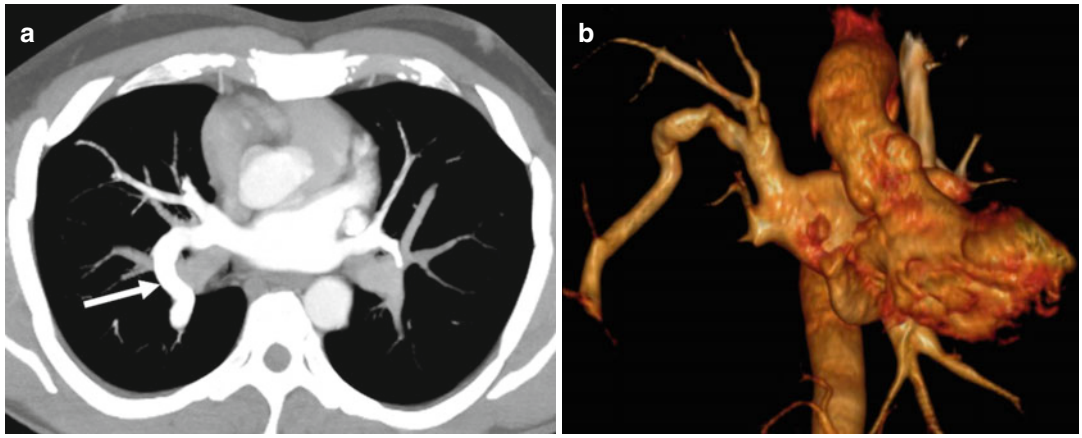

Fig. 12 Pseudoscimitar. (**a**, **b**) Contrast-enhanced CT, axial MIP, and volume-rendered 3-D reconstruction. There is an elongated and tortuous pulmonary vein in the right mid lung that terminates normally in the left atrium (*arrow*)

right and left pulmonary veins have been described (Goodman et al. 1972; Collins et al. 1982). The scimitar sign is not always present. It is important to distinguish between scimitar syndrome and MRPV. Scimitar syndrome results in a left-to-right shunt, which can lead to cyanosis and may require surgical correction. Consequently the patients are often symptomatic and present at a young age. In contrast, there is no left-to-right shunt in MRPV. In addition, some of the reported cases of meandering pulmonary veins connect to the left atrium and IVC simultaneously, also called as scimitar variant (Takeda et al. 1994). Contrast-enhanced multidetector computed tomography (MDCT) is the modality of choice for diagnosis of anomalous pulmonary venous connections, considered as "one stop shop" imaging. It allows rapid acquisition of data with high spatial resolution and wide anatomic coverage with a high sensitivity and specificity that approaches 100 % (Fig. 12) (Kim et al. 2000).

11 Cor Triatriatum

Cor triatriatum (CTT) is a rare congenital heart anomaly (0.1 %) in which left atrium is divided into two distinct anterior and posterior chambers by a fibromuscular membrane. Failure of resorption of a membrane between common pulmonary vein and primordial left atrium results in this anomaly. The posterior chamber receives blood flow from the pulmonary veins, whereas the anterior chamber delivers blood to the mitral valve. The location of the atrial membrane differentiates cor triatriatum from a supravalvular mitral ring. CTT is differentiated from supravalvular mitral ring by the position of the left atrial appendage (LAA). In CTT, the LAA is part of the anterior (mitral valve) atrial chamber, whereas the LAA is part of the posterior (pulmonary vein) atrial chamber in patient with a supravalvular ring (Bezgin et al. 2014). Although symptoms are usually encountered in infancy, this entity may rarely present in adulthood when the membrane contains multiple fenestrations. The most common presenting symptoms in adults are dyspnea, hemoptysis, and orthopnea, which mimic mitral stenosis at presentation (Su et al. 2008). Cor triatriatum is frequently associated with other cardiovascular abnormalities. In adults, the most common associated abnormalities are atrial secundum septal defect, mitral regurgitation, and the presence of PLSVC. Diagnosis is usually established by echocardiography; however MDCT or MRI is more specific in evaluating the size and number of fenestrations and to find associated congenital cardiovascular anomalies (Fig. 13).

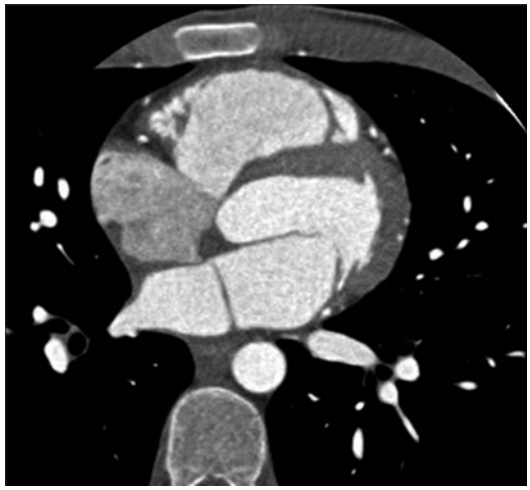

Fig. 13 Cor triatriatum in a 24-year-old male. Contrast-enhanced CT shows a thin membrane dividing the left atrium in two distinct chambers

12 Total Anomalous Pulmonary Venous Connection

Total anomalous pulmonary venous connection is a rare form of congenital heart disease accounting for 1.5–3 % of congenital heart diseases in which all pulmonary veins connect to the systemic veins, right atrium, coronary sinus, or IVC. Depending on the drainage site of the pulmonary veins, the defect may be divided into the following four types: supracardiac (50 %), intracardiac (25 %), infracardiac (20 %), and mixed type (5 %). This condition is a cause of neonatal cyanosis. Approximately 1/3 of patients with TAPVC have other associated cardiac lesions including single ventricle, atrioventricular septal defect, transposition of the great arteries, hypoplastic left heart syndrome, or patent ductus arteriosus. Type 1 TAPVC (supracardiac connection) is the most common subtype in which connection to the left innominate vein is found (Karamlou et al. 2007). Other less common supracardiac venous connections include SVC and azygos veins. Anomalous connection to the right superior vena cava is much less frequent, but when present it is often associated with heterotaxy syndrome (polysplenia/asplenia, Ivemark syndrome). Pulmonary venous obstruction (PVO) is less common in this type. On chest radiograph, the classic "snowman" or "figure of 8" appearance is seen secondary to widening of the mediastinum due to dilated SVC and innominate vein. But this diagnostic cardiac configuration might not manifest during neonatal and infantile periods until there is a physiological decrease in pulmonary vascular resistance type 2 TAPVC (cardiac connection) in which all four pulmonary veins connect at the level of the coronary sinus or in the posterior wall of right atrium near the midatrial septum (Shen et al. 2013). The anomalous veins may connect via a short channel or multiple openings to the right atrium. The coronary sinus ostium is markedly enlarged although normal in position. The infracardiac type, type 3, is the most common type of pulmonary venous obstruction, and this obstruction results in severe pulmonary congestion and pulmonary hypertension. The obstruction is either within the anomalous connecting vein or at its connection to the systemic circulation. The pulmonary veins from both sides converge behind the left atrium and form a common vertical descending vein, which courses anterior to the esophagus and traverses the diaphragm at the esophageal hiatus. This vertical descending vein may join the portal venous system (80–90 %, in which case obstruction is almost always present since the blood passes through the hepatic sinusoids), either at the splenic or splenic-superior mesenteric venous confluence (Shen et al. 2013). Occasionally, the vertical vein may connect directly to the ductus venosus, hepatic veins, or inferior vena cava. Chest radiograph typically demonstrates passive vascular engorgement or pulmonary edema or both and absence of cardiomegaly. The last subtype is the mixed pattern representing about 2–10 % of cases. In this form, pulmonary veins drain to at least two different locations, including a brachiocephalic vein, SVC, azygos vein, coronary sinus, right atrium, or below the diaphragm. The most common pattern of mixed obstruction is drainage of a vertical vein to the left innominate vein and drainage of the right lung either via the right atrium or the coronary sinus. This pattern of anomalous venous connection is generally associated with other major cardiac lesions. Transthoracic echocardiography is the first-line

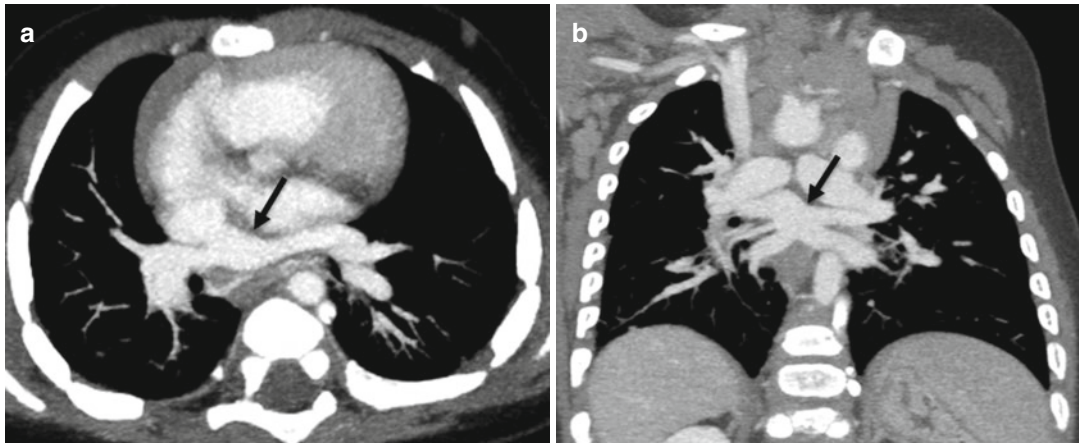

Fig. 14 Total anomalous pulmonary venous return in a seven-month-old boy. (**a**) Contrast-enhanced CT, axial MIP. (**b**) Coronal reconstruction. All bilateral pulmonary veins are seen draining into the posterior aspect of the right atrium (*arrows*)

study for assessing children with suspected TAPVC. However, cross-sectional imaging is most useful in evaluation of patients with mixed TAPVC and PAPVC. Detailed 3-D and volume-rendered capacity of MDCT and MRI are a unique contribution to both diagnosis and treatment (Fig. 14).

13 Pulmonary Arteriovenous Malformation

Pulmonary arteriovenous malformation (PAVM) is defined as a direct communication between a peripheral pulmonary artery and a peripheral pulmonary vein without an intervening capillary bed. This is probably the most common anomaly of the pulmonary vasculature and commonly associated with hereditary hemorrhagic telangiectasia (HHT) or Osler-Weber-Rendu disease (80 %), an autosomal dominant hereditary condition with variable penetrance, clinically characterized by epistaxis (80 %), mucocutaneous telangiectasia (70 %), and visceral arteriovenous malformations (20–50 %). All patients with possible or confirmed HHT and family members should be screened for PAVM, since pulmonary arteriovenous anomalies are so frequent in this population (45 %), with 60 % of affected individuals having multiple lesions (Gossage and Kanj 1998; Khurshid and Downie 2002; Jaskolka et al. 2004). Contrast echocardiography is commonly used as the first imaging modality of choice for screening, but CT is considered the gold standard for the diagnosis of this condition. Current technology with MDCT allows detection of small PAVM even on non-contrast examination (Faugham et al. 2009). On CT, PAVM appears as dilated feeding and draining intrapulmonary vessels which present as irregular tubular densities in communication with "nodules" or serpiginous masses, more commonly seen in the lower lobes. Smaller lesions are better appreciated on thick slab images or maximum intensity projection (MIP) with multiplanar reconstruction. As for other vascular pathologies, contrast-enhanced CT can better demonstrate the vascular nature of this condition, but contrast is not always required (Fig. 15).

13.1 Systemic Venous Anomalies

As opposed to pulmonary venous abnormalities, systemic venous anomalies are typically incidental findings. The incidence of systemic venous anomalies of the thorax is quite rare, but these anomalies are more frequently encountered in patients with congenital heart disease (CHD) as opposed to the general population. These anoma-

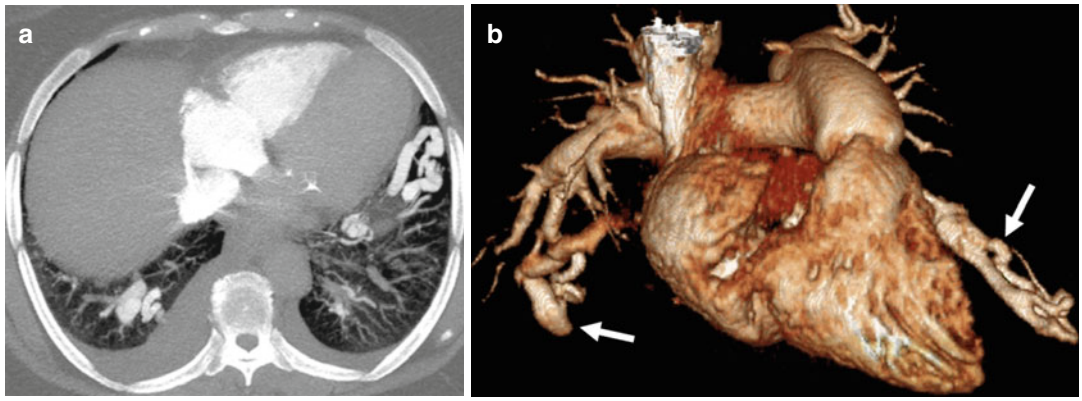

Fig. 15 Bilateral pulmonary arteriovenous malformations in a patient with HHT. (**a**) Contrast-enhanced CT, axial MIP. (**b**) Volume-rendered 3-D reconstruction. Dilated and tortuous vessels with abnormal communication between arteries and veins are appreciated in the bilateral lower lobes (*arrows*), as well as bilateral pleural effusions

lies can be especially important in patients with CHD with regard to selection of a surgical approach and also have implications relative to the venous cannulation for cardiac bypass during surgery; thus they should be purposely sought for in these patients (Corno et al. 2013). These systemic venous anomalies in the thorax are the result of complex variations in the persistence and/or regression of segments of three sets of veins during the first 2 months of fetal development including the umbilical, vitelline, and cardinal systems. Anomalies most frequently encountered include those related to the superior vena cava (SVC) and azygos system although left brachiocephalic vein and intrathoracic IVC anomalies are also encountered (Webb et al. 1982).

13.2 SVC Anomalies

13.2.1 Left-Sided SVC/Double SVC

In normal cases, the right anterior and common cardinal veins form a right-sided SVC, and the left anterior cardinal vein regresses. If there is persistence of both anterior cardinal veins, a double SVC is encountered, and if the right anterior cardinal vein regresses, a left-sided SVC will be the only large vessel draining into the right side of the heart (Webb et al. 1982; Demos et al. 2004).

Persistent LSVC is the most common variant of systemic venous drainage which is discovered as an incidental finding in 0.3–0.5 % of the normal population and seen in up to 4–5 % of patients with congenital heart disease (Webb et al. 1982; Lawler et al. 2002; Godwin and Chen 1986; Biffi et al. 2001; Piciucchi et al. 2014). In the vast majority of cases (82–90 %), the left SVC is a component of a duplicated system (double SVC). Sixty-five percent of these cases will have absence of the left brachiocephalic vein (LBCV). The right and left SVC will lie in the same relative position on either side of the mediastinum and be similar in caliber, as opposed to cases with persistence of the LBCV, where the right SVC will typically be larger than the left (Webb et al. 1982; Godwin and Chen 1986). As an isolated anomaly in the absence of CHD, the left SVC will almost always drain through the oblique vein of Marshall which extends behind the left atrium, into the coronary sinus and then into the right atrium (Lawler et al. 2002). In these cases, the coronary sinus is typically enlarged, and if encountered during contrast-enhanced CT, the vessel may be densely opacified if IV contrast is injected into the left arm (Demos et al. 2004). PLSVC is readily recognized on CT and MR of

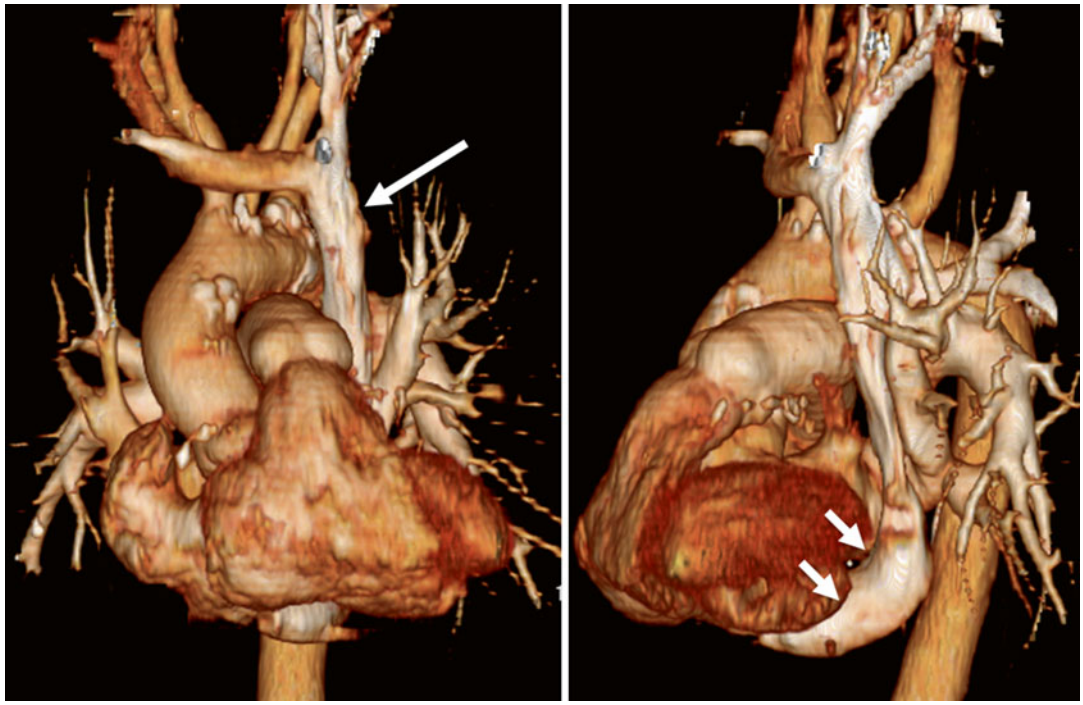

Fig. 16 Left-side superior vena cava. Volume-rendered 3-D reconstructions show a single left-side superior vena cava (*long arrow*) ending in a dilated coronary sinus (*short arrows*)

the chest and may be seen, often retrospectively, as focal widening of the mediastinum on chest X-ray along the superior mediastinal border. However, this anomaly is most often recognized on chest X-ray when the vessel is traversed by an indwelling catheter (Fig. 16). In patients with a solitary left SVC, the condition can simulate an abnormal aorta, although this vascular variant is not clinically significant unless there is narrowing of the ostium of the coronary sinus, which can lead to difficulties placing IV lines and pacemaker/defibrillator leads (Demos et al. 2004; Lawler et al. 2002; Biffi et al. 2001). Additionally, atresia of the coronary sinus may be encountered in these patients. Although occluded, the coronary sinus, by way of collateral vessels, still receives the total venous output of the coronary veins. The coronary venous drainage to the heart, however, is then retrograde through the left SVC to the LBCV. If this is unrecognized, ligation of the LSVC as part of a cardiac surgical procedure has led to acute coronary venous hypertension and myocardial ischemia. Drainage of a PLSVC into the left atrium instead of the CS is rarely encountered and occurs in association with many types of CHD, but is rare if the heart is normal (Fig. 17) (Demos et al. 2004).

13.2.2 Right-Sided SVC

Isolated anomalies of a right-sided SVC are rare. The vessel may insert low into the right atrium, may drain into the left atrium, or may be aneurysmal, typically congenital in nature (Demos et al. 2004).

13.3 Azygos System Anomalies

The azygos system consists of paired paravertebral venous structures in the posterior thorax including the azygos and hemiazygos veins with the intercostal and mediastinal tributaries draining into the azygos, hemiazygos, and accessory hemiazygos veins. The azygos vein originates at the junction of the right ascending lumbar and subcostal veins, enters the chest at the aortic hiatus,

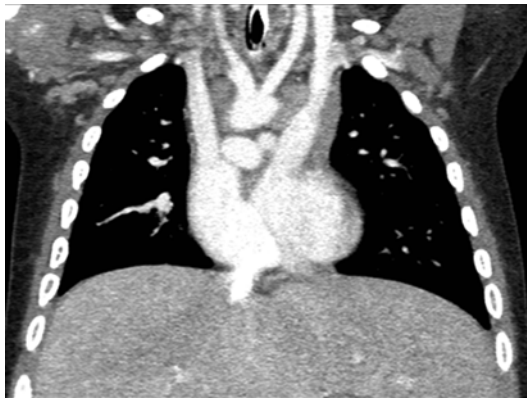

Fig. 17 Left superior vena cava draining into the left atrium in a patient with a duplicated vena cava. Contrast-enhanced CT, coronal reconstruction shows the right superior vena cava terminating in the right atrium and the left superior vena cava terminating in the left atrium

and ascends along the right anterolateral surface of the thoracic vertebrae. At T5–T6, the vessel arches anteriorly, just cephalad to the right mainstem bronchus, and drains into the SVC, or rarely the right brachiocephalic vein (BCV), right subclavian vein (SCV), intrapericardial SVC, or right atrium. Similar to the azygos vein, the hemiazygos vein originates at the junction of the left ascending lumbar and left subcostal veins and often receives tributaries from the left renal vein and IVC. The right superior intercostal vein drains the right second through fourth intercostal spaces and joins the azygos just proximal to the arch. The hemiazygos ascends along the left anterolateral aspect of the thoracic vertebral column and at T8–T9 and crosses dorsal to the descending thoracic aorta to join the azygos vein. From this point, the accessory hemiazygos vein extends further cephalad in the left paravertebral location and may communicate with the azygos vein at different levels. The left superior intercostal vein drains the left second through fourth intercostal spaces and communicates with the accessory hemiazygos in 75 % of patients, then arches ventrally adjacent to the aortic arch and drains into the left BCV. This can be seen on frontal CXR en face, known as the aortic nipple (Demos et al. 2004).

The right and left supreme intercostal veins drain the first intercostal spaces and usually empty into the left BCV, although they may communicate with the corresponding superior intercostal veins.

The embryology of the azygos-hemiazygos venous system is not entirely clear. The azygos venous system develops on the basis of multiple transformations of the subcardinal veins with the azygos vein considered to derive from the upper right supracardinal vein, the arch from the upper segment of right posterior cardinal vein, and the hemiazygos from the upper left supracardinal vein (Piciucchi et al. 2014). The left superior intercostal vein and accessory hemiazygos vein are derived from the left posterior cardinal vein, and this vein simultaneously forms the upper part of the azygos vein. The part connecting the azygos to the hemiazygos vein is the remainder of the anastomosis between the left and right posterior cardinal veins.

13.4 Anomalies

13.4.1 Absent Azygos Vein

Total absence of the azygos vein occurs rarely when the right cranial aspect of the supracardinal vein fails to develop. Drainage of the right and left intercostal vein in this case happens through hemiazygos and accessory hemiazygos veins where the accessory hemiazygos vein converges with the left BCV through the left supreme intercostal vein. Resultant/expected enlargement of the hemiazygos, accessory hemiazygos, and left superior intercostal veins will be seen in these patients with no clinical symptoms encountered (Demos et al. 2004).

13.4.2 Azygos/Hemiazygos Lobe

Anomalous course of the azygos vein in the right lung apex gives rise to azygos lobe in 0.4–1 % of the population, encountered on about 0.4 % of chest radiographs and 1 % of anatomic specimens. It occurs when the right posterior cardinal vein, one of the precursors of the azygos vein,

fails to migrate over the apex of the lung and penetrates it instead, carrying along pleural layers that entrap a portion of the right upper lobe (Demos et al. 2004; Mata et al. 1991; Kim et al. 1995). This anomaly is readily identifiable on imaging studies, typically plain radiographs and CT, as the abnormally located vessel indents the lung and overlying visceral and parietal pleural layers, resulting in four layers of pleura that form a "mesentery-like" structure, the meso-azygos, which contains the azygos vein, seen coursing through the right upper lobe, located more cephalad than normal. The enclosed lung between the fissure and the mediastinum is not an independent segment as its bronchial and arterial supplies arise from the apical or posterior segments of the right upper lobe (Mata et al. 1991). The fissure is visible as a fine line with right convexity on chest X-ray with the azygos vein visible as a tear-shaped opacity in the lowermost part of the fissure. The azygos arch is not visible at its usual location at the right tracheobronchial angle (Kim et al. 1995). Much less commonly seen is a left azygos or hemiazygos lobe caused by malpositioned left superior intercostal vein draining into the left BCV (Fig. 18).

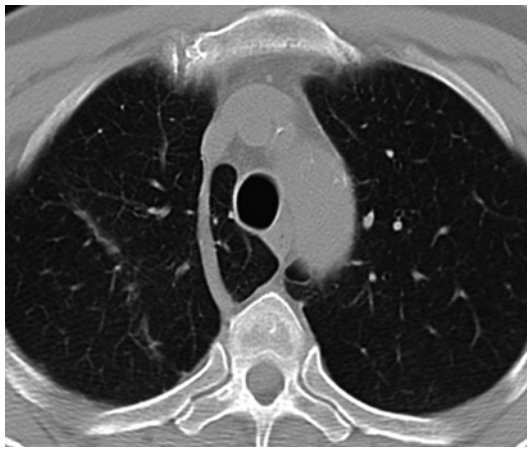

Fig. 18 Azygos fissure in the right upper lobe. The azygos vein is seen as a linear or tubular density in the right upper lobe lateral to the trachea

13.4.3 Azygos and Hemiazygos Continuation of the IVC

Embryogenesis of the IVC is one of the most complicated sequences as several vessels must develop and regress in turn for it to form normally. In utero, the vessels that form the azygos and hemiazygos veins normally communicate with the suprarenal IVC, but this communication breaks down in the typical scenario. If it does not, azygos or hemiazygos continuation of the IVC is said to be present. These lesions may be isolated or associated with other congenital anomalies. The incidence in patients with CHD is 0.2–1.3 % (Demos et al. 2004).

13.4.4 Azygos Continuation

Azygos continuation of the IVC (ACIVC) is a sporadic congenital anomaly characterized by agenesis of the hepatic tract of the IVC and posterior redirection of blood through the enlarged azygos vein that courses the right edge of the spine and drains into the SVC. This anomaly is common in patients with polysplenia (left isomerism) and rarely seen in patients with asplenia (right isomerism). Other associated anomalies include abnormal abdominal situs and left or duplicated IVC. At imaging, dilation of the azygos vein, azygos arch, and SVC is seen secondary to increased flow, and the hepatic veins drain into the right atrium via a suprahepatic IVC. The hepatic segment of the IVC is absent or hypoplastic, and this condition must be documented to exclude other causes of an enlarged azygos vein. Azygos continuation has also been reported in association with azygos lobe (Fig. 19) (Demos et al. 2004).

13.4.5 Hemiazygos Continuation

Hemiazygos continuation of the IVC (HAIVC) is an even rarer anomaly where the large venous blood vessel courses the left side of the spine. In some cases, the enlarged HV drains into the SVC. Hemiazygos continuation of a left-sided IVC has several variations including three possible routes for blood in the hemiazygos vein to reach the right atrium. Most commonly, the hemiazygos vein drains into the azygos vein at T8–T9 (in this case the findings at more cephalad levels are simi-

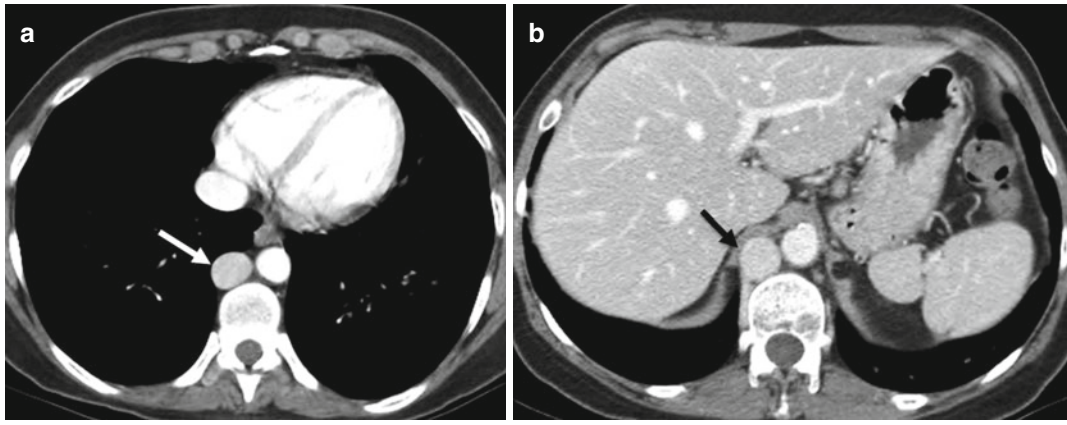

Fig. 19 Azygos continuation of the inferior vena cava. Contrast-enhanced CT axial images in the chest (**a**) and abdomen (**b**) show the dilated azygos vein to the right of the aorta and anterior to the spine (*arrows*). Note the absence of the intrahepatic segment of the IVC in the upper abdomen

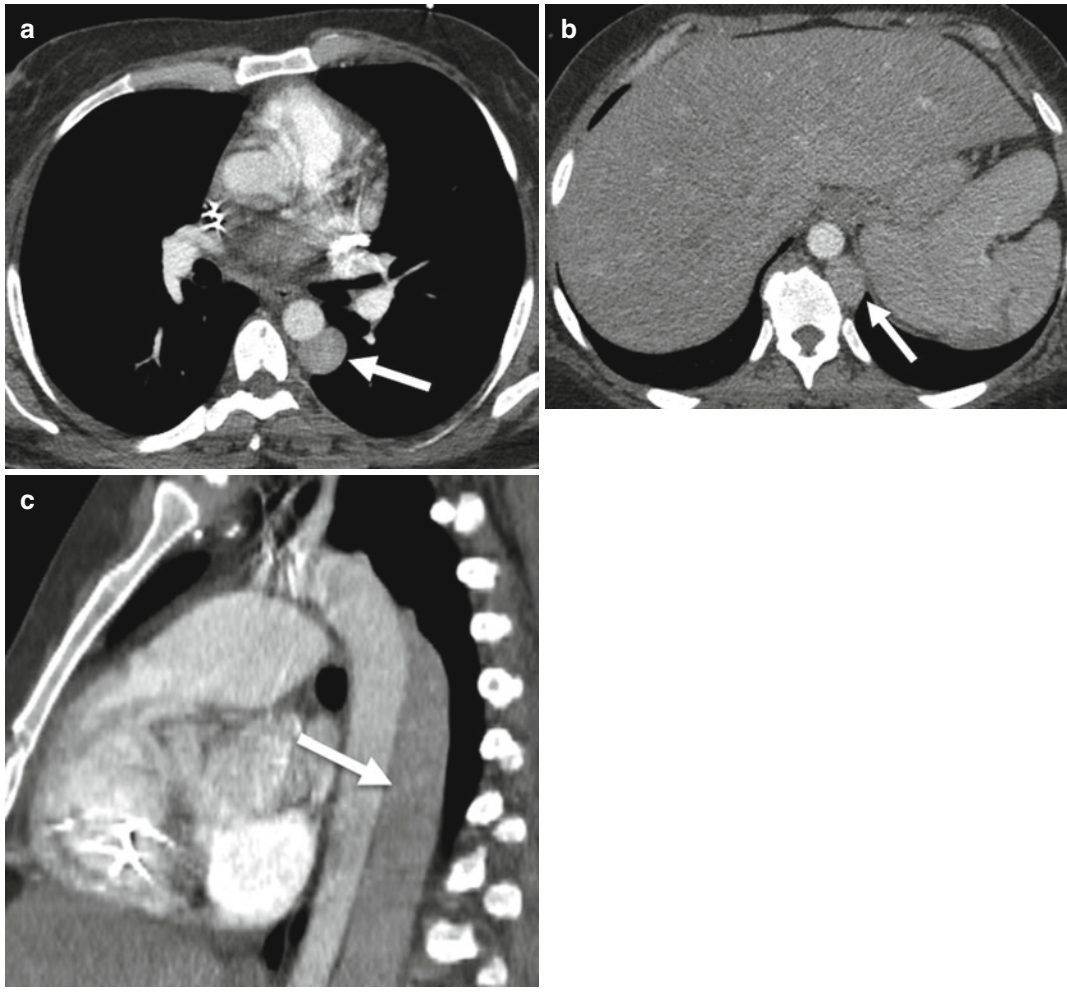

Fig. 20 Intrahepatic interruption of the inferior vena cava with hemiazygos continuation. (**a**, **b**) Contrast-enhanced CT axial images at the level of the lower thoracic region and upper abdomen demonstrate a dilated hemiazygos vein posterolateral to the descending aorta (*arrows*). (**c**) Left sagittal reconstruction shows the hemiazygos vein behind the descending thoracic aorta

lar to azygos continuation with enlargement of the distal azygos, and hemiazygos vein is also enlarged). Second, a persistent LSVC with blood flowing from the hemiazygos into the accessory hemiazygos vein and left SVC and then into the coronary sinus, all of which are dilated, and finally may see hemiazygos vein drain into the accessory hemiazygos vein, left superior intercostal vein, and left BCV into a normal right SVC (Fig. 20) (Demos et al. 2004; Kim et al. 1995; Bass et al. 2000).

References

Adler SC, Silverman JF (1973) Anomalous venous drainage of the left upper lobe. A radiographic diagnosis. Radiology 108:563–565

Alsoufi B, Cai S, Van Arsdell GS et al (2007) Outcomes after surgical treatment of children with partial anomalous pulmonary venous connection. Ann Thorac Surg 84:2020–2026

Andrews R, Colloby P, Heubner PJB (1993) Pulmonary artery dissection in a patient with idiopathic dilatation of the pulmonary artery: a rare cause of sudden cardiac death. Br Heart J 69:268–269

Apostolopouou SC, Kelekis NL, Brountzos EN et al (2002) "Absent" pulmonary artery in one adult and five pediatric patients: imaging, embryology and therapeutic implications. AJR Am J Roentgenol 179:1253–1260

Bass JE, Redwine MD, Kramer LA et al (2000) Spectrum of congenital anomalies of the inferior vena cava: cross sectional imaging findings. Radiographics 20:639–652

Berdon WE, Baker DH, Wung J-T et al (1984) Complete cartilage-ring tracheal stenosis associated with anomalous left pulmonary artery: the ring-sling complex. Radiology 152:57–64

Bezgin T et al (2014) Multimodality imaging of cor triatriatum sinister in an octogenerian. Echocardiography 31:E254–E256

Biffi M, Boriani G, Frabett L et al (2001) Left superior vena cava persistence in patients undergoing pacemaker or cardioverter-defibrillator implantation – a 10 year experience. Chest 120:139–144

Chen S-J, Lee W-J, Lin M-T et al (2007) Left pulmonary artery sling-complex: computed tomography and hypothesis of embryogenesis. Ann Thorac Surg 84:1645–1650

Collins DR, Shea PM, Vieweg WV (1982) Idiopathic prominence of pulmonary veins on chest x-ray. Angiology 33:613–616

Collins RT II, Weinberg PW, Ewing S, Fogel M (2008) Pulmonary artery sling in an asymptomatic 15-year-old boy. Circulation 117:2403–2406

Corno A, Alahdal SA, Das KM et al (2013) Systemic venous anomalies in the Middle East. Front Pediatr 1:1

Davia JE, Cheitlin MD, Bedynek JL (1973) Sinus venosus atrial septal defect: analysis of fifty cases. Am Heart J 85:177–185

Davis SD (2000) Case 28: proximal interruption of the right pulmonary artery. Radiology 217:437–440

Deb SJ, Zehr KJ, Shields RC (2005) Idiopathic pulmonary artery aneurysm. Ann Thorac Surg 80:1500–1502

Demos TC, Posniak HV, Pierce KL et al (2004) Venous anomalies of the thorax, a pictorial review. AJR Am J Roentgenol 182:1139–1150

Dillon EH, Camputaro C (1993) Partial anomalous pulmonary venous drainage of the left upper lobe vs duplication of the superior vena cava: distinction based on CT findings. AJR Am J Roentgenol 160:375–379

Faugham ME, Granton JT, Young LH (2009) The pulmonary vascular complications of hereditary haemorrhagic telangiectasia. Eur Respir J 33:1186–1194

Gikonyo BM, Jue KL, Edwards JE (1989) Pulmonary vascular sling: report of seven cases and review of the literature. Pediatr Cardiol 10:81–89

Godwin JD, Chen JTT (1986) Thoracic venous anatomy. AJR Am J Roentgenol 147:674–684

Goodman LR, Jamshidi A, Hipona FA (1972) Meandering right pulmonary vein simulating the Scimitar syndrome. Chest 62:510–512

Gossage JR, Kanj G (1998) Pulmonary arteriovenous malformations. A state of the art review. Am J Respir Crit Care Med 158:643–661

Gray BB, Franch RH, Shuford WH, Rogers JV (1963) The roentgenologic features of single and multiple coarctations of the pulmonary artery and branches. Am J Roentgenol Radium Ther Nucl Med 90:599–613

Greene R, Miller SW (1986) Cross-sectional imaging of silent pulmonary venous anomalies. Radiology 159:279–281

Gudjonsson U, Brown JW (2006). Scimitar syndrome. Semin Thorac cardiovasc Surg; Pediatr Card Surg Annual 9(1):56–62

Haramati LB, Moche IE, Rivera VT et al (2003) Computed tomography of partial anomalous pulmonary venous connection in adults. J Comput Assist Tomogr 27:743–749

Harjel ADJT, Blom NA, Ottenkamp J (2002) Isolated unilateral absence of a pulmonary artery. Chest 122:1471–1477

Herlong JR, Jaggers JJ, Ungerleider RM (2000) Congenital Heart Surgery Nomenclature and Database Project: pulmonary venous anomalies. Ann Thorac Surg 69:S56–S69

Ho ML, Bhalla S, Bierhals A, Gutierrez F (2009) MDCT of partial anomalous pulmonary venous return (PAPVR) in adults. J Thorac Imaging 24:89–95

Jaskolka J, Wu L, Chan RP, Faughan ME (2004) Imaging of hereditary hemorrhagic telangiectasia. AJR Am J Roentgenol 183:307–314

Kagadis GC, Panagiotopoulou EC, Priftis KN et al (2007) Preoperative evaluation of the trachea in a child with pulmonary artery sling using 3-dimensional computed tomographic imaging and virtual bronchoscopy. J Pediatr Surg 42:E9–E13

Kamath BM, Spinner NB, Emerick KM et al (2004) Vascular anomalies in Alagille syndrome: a significant cause of morbidity and mortality. Circulation 109:1354–1358

Karamlou T, Gurofsky R, Al Sukhni E et al (2007) Factors associated with mortality and reoperation in 377 children with total anomalous pulmonary venous connection. Circulation 115:1591–1598

Katre R, Burns S, Murillo H et al (2012) Anomalous pulmonary venous connections. Semin Ultrasound CT MR 33:485–499

Kharge J, Singh AP, Raghu TR et al (2013) Idiopathic dilatation of the pulmonary artery-a case report. Echocardiography 30:E265–E268

Khurshid I, Downie GH (2002) Pulmonary arteriovenous malformation. Postgrad Med J 78:191–197

Kim HJ, Ahn IO, Park ED (1995) Azygos continuation of a left inferior vena cava draining into a right atrium via persistent left superior vena cava: demonstration by helical computed tomography. Cardiovasc Intervent Radiol 18:65–67

Kim TH, Kim YM, Suh CH, Cho DJ et al (2000) Helical CT angiography and three-dimensional reconstruction of total anomalous pulmonary venous connections in neonates and infants. AJR Am J Roentgenol 175:1381–1386

Konen E, Raviv-Zilka L, Cohen RA et al (2003) Congenital pulmonary venolobar syndrome: spectrum of helical CT findings with emphasis on computerized reformatting. Radiographics 23:1175–1184

Korkmaz AA, Yildiz CE, Onan B et al (2011) Scimitar syndrome: a complex for of anomalous pulmonary venous return. J Card Surg 26:529–534

Kreutzer J, Landzberg MJ, Preminger TJ et al (1996) Isolated peripheral pulmonary artery stenosis in the adult. Circulation 93:1417–1423

Lawler LP, Cor FM, Fishman EK (2002) Multi-detector row and volume-rendered CT of the normal and accessory flow pathways of the thoracic systemic and pulmonary veins. Radiographics 22:S45–S60

Lee K-H, Yoon C-S, Choe KO et al (2001) Use of imaging for assessing anatomical relationship of tracheobronchial anomalies associated with left pulmonary artery sling. Pediatr Radiol 31:269–278

Mata J, Caceres J, Alegret X et al (1991) Imaging of the azygos lobe: normal anatomy and variations. AJR Am J Roentgenol 156:931–937

Nair KKS, Cobanoglu AM (2001) Idiopathic main pulmonary artery aneurysm. Ann Thorac Surg 71:1688–1690

Niida T, Kitai T, Isoda K et al (2011) A case of idiopathic dilatation of the pulmonary artery with mild subvalvular pulmonary stenosis revealed by cardiovascular magnetic resonance. J Cardiol Cases 3:e53–e56

Oliver JM, Gallego P, Gonzalez A, Dominguez FJ, Aroca A, Mesa JM (2002) Sinus venosus syndrome: atrial septal defect or anomalous venous connection? A multiplane transesophageal approach. Heart 88:634–638

Oropeza G, Hernandez FA, Callard GM, Jude JR (1970) Anomalous pulmonary venous drainage of the left upper lobe. Ann Thorac Surg 9:180–185

Piciucchi S, Barone D, Sanna S et al (2014) The azygos vein pathway; an overview from anatomical variations to pathological changes. Insight Imaging 5:619–628

Posniak HV, Dudiak CM, Olson MC (1993) Computed tomography diagnosis of partial anomalous pulmonary venous drainage. Cardiovasc Intervent Radiol 16:319–320

Ryu DS, Spirn PW, Trotman-Dickenson B et al (2004) HRCT findings of proximal interruption of the right pulmonary artery. J Thorac Imaging 19:171–175

Sakai S, Muruyama S, Soeda H et al (2002) Unilateral proximal interruption of the pulmonary artery in adults: CT findings in eight patients. J Comput Assist Tomogr 26:777–783

Seguchi M, Wada H, Sakakura K et al (2011) Idiopathic pulmonary artery aneurysm. Circulation 124:e369–e370

Shaj R, Cestone P, Mueller C (2000) Congenital multiple peripheral pulmonary artery stenosis (pulmonary branch stenosis). AJR Am J Roentgenol 175:856–857

Shen Q et al (2013) Role of plain radiography and CT angiography in the evaluation of obstructed total anomalous pulmonary venous connection. Pediatr Radiol 43:827–835

Su CS, Tsai IC, Lin WW et al (2008) Usefulness of multidetector-row computed tomography in evaluating adult cor triatriatum. Tex Heart Inst J 35:349–351

Takeda S, Imachi T, Arimitsu K et al (1994) Two cases of scimitar variant. Chest 105:292–293

Toledano K, Guralnik L, Lorber A et al (2011) Pulmonary arteries involvement in Takayasu's arteritis: two cases and literature review. Semin Arthritis Rheum 41:461–470

Van Meter C Jr, LeBlanc JG, Culpepper WS 3rd, Ochsner JL (1990) Partial anomalous pulmonary venous return. Circulation 82:IV195–IV198

van Rens MTM, Westermann CJJ, Postmus PE, Schramel FMNH (2000) Untreated idiopathic aneurysm of the pulmonary artery. Respir Med 94:404–405

Vida VL, Padalino MA, Boccuzzo G et al (2010) Scimitar syndrome: a European Congenital Heart Surgeons Association (ECHSA) multicentric study. Circulation 122:1159–1166

Wahab AA, Janahi IA, Eltohami A, Zeid A et al (2003) A new type of Ehlers-Danlos syndrome associated with tortuous systemic arteries in a large kindred from Qatar. Acta Paediatr 92:456–462

Webb WR, Gamsu G, Speckman JM et al (1982) Computed tomographic demonstration of mediastinal venous anomalies. AJR Am J Roentgenol 139:157–161

Winter FS (1954) Persistent left superior vena cava; survey of world literature and report of thirty additional cases. Angiology 5:90–132

Workflow Design for CT of the Thorax

Matthew K. Fuld and Juan Carlos Ramirez-Giraldo

Abstract

CT technology continues to evolve at a high rate providing higher dose efficiency, faster scanning speeds, and improved image quality. As such, one can argue that CT technology already provides adequate image quality for most diagnostic tasks in areas such as thoracic CT. Moreover, the acquisition time of many examinations, such as those of the thorax, can be well below one second, thus addressing major issues such as motion artifacts. However, the management of a patient within a typical radiology department or imaging center implies other workflow aspects that go beyond just the CT scan itself. Aspects that impact the workflow can be associated with each individual patient, the CT technologists and nurses, or radiologists and referring physicians. Hence, an important question arises such as how to address consistency in CT scanning in the era of personalized medicine? With the substantial increase in imaging data generated per examination, which can well exceed 1000 images per study in daily practice, another issue of concern is how quickly exams can be read after CT acquisition is complete, with data transfer speeds being a major limiting factor for the radiologists and referring physicians. Hence, we must endeavor to determine whether there are smarter ways to analyze or preprocess this information such that we can reduce the time required for interpretation by radiologists in order to reach a diagnosis. Or at the very least can we utilize these new workflow tools to improve accuracy? The answer to this question is heavily associated with the design of new workflows.

1 Introduction

CT technology continues to evolve at a high rate providing higher dose efficiency, faster scanning speeds, and improved image quality. As such, one can argue that CT technology already provides adequate image quality for most diagnostic

M.K. Fuld (✉) • J.C. Ramirez-Giraldo
Diagnostic Imaging, Computed Tomography, Collaborations, Siemens Medical Solutions, Inc., 40 Liberty Blvd, Malvern, PA 19355, USA
e-mail: matthew.fuld@siemens.com; juancarlos.ramirezgiraldo@siemens.com

U.J. Schoepf, F.G. Meinel (eds.), *Multidetector-Row CT of the Thorax*, Medical Radiology,
DOI 10.1007/978-3-319-30355-0_21

tasks in areas such as thoracic CT. Moreover, the acquisition time of many examinations, such as those of the thorax, can be well below one second, thus addressing major issues such as motion artifacts. However, the management of a patient within a typical radiology department or imaging center implies other workflow aspects that go beyond just the CT scan itself. Aspects that impact the workflow can be associated with each individual patient, the CT technologists and nurses, or radiologists and referring physicians. Hence, an important question arises such as how to address consistency in CT scanning in the era of personalized medicine? With the substantial increase in imaging data generated per examination, which can well exceed 1000 images per study in daily practice, another issue of concern is how quickly exams can be read after CT acquisition is complete, with data transfer speeds being a major limiting factor for the radiologists and referring physicians. Hence, we must endeavor to determine whether there are smarter ways to analyze or preprocess this information such that wemiku can reduce the time required for interpretation by radiologists in order to reach a diagnosis. Or at the very least can we utilize these new workflow tools to improve accuracy? The answer to this question is heavily associated with the design of new workflows.

In thoracic CT, some of these new developments have a broad range of applications, whereas others strive for better acquisition and quantitation and are focused on specific diseases (i.e., lung cancer screening or emphysema). In addition, the advent of reimbursement for lung cancer screening in the USA has added a level of complexity in pre- and post-scan patient management that was previously only seen in mammography. Hence, in the era of personalized medicine, automation and new technologies have a significant impact on scan protocol design and optimization as well as greatly impacting postacquisition workflows.

Due to the recognized importance of workflows, most major manufacturers of CT scanners and vendors of post-processing software solutions continue to develop applications addressing these specific needs. For simplicity, in this chapter most of the examples provided are associated with a single CT manufacturer (Siemens Healthcare), although the reader is reminded that several other workflow solutions and approaches from other manufacturers do exist. Nonetheless, every effort was made to write this chapter from a vendor-neutral perspective and provide recommendations which will be, for the most part, applicable regardless of the tools available at a given institution.

2 Automation of CT Image Acquisition: Patient Personalization

Due to the high spatial and temporal resolution, CT is the modality of choice for many thoracic applications. These applications range from detection of solid and/or sub-solid nodules in lung cancer screening to the measurement of function with ventilation and perfusion studies. Each of these applications yields their own challenges, but the common denominator is motion. The National Lung Screening Trial (NLST) has shown that successful lung cancer screening can be accomplished using four-slice scanners (NLST Research Team 2011), but scanning with four-slice scanners also translates into motion artifacts due on the long scan times. Fortunately, most providers are currently using 16-slice or greater scanners for their thoracic-imaging work. Table 1 provides an overview of the specifications of existing mid-range to high-end CT scanners from major manufacturers.

As exemplified in Chap. 1 (*CT Acquisition chapter by Thomas Flohr*), in an effort to reduce radiation dose, accelerate data acquisition, and maintain image quality, modern CT scanners continue to add new advanced features. This translates in an increasing number of variables which have to be considered when building CT acquisition protocols.

For thoracic CT examination protocols, the following scan parameters are considered of importance:

Table 1 Specifications of mid-range and high-end CT scanners from major manufacturers as of October 2015

Scanners[a]	Collimation [mm]	Fastest rotation [s]	Temporal resolution [ms]	Iterative reconstruction	Automated exposure control
High end					
Aquilion ONE (Toshiba)	320×0.5	0.275	150	AIR3D	SureExposure3D
iCT (Philips)	256×0.6	0.25	150	IMR	Z-DOM and D-DOM
Revolution (GE)	256×0.625	0.28	140	ASIR-V, VEO	SmartmA
Somatom Force (Siemens)	192×0.6	0.25	65	ADMIRE	CARE Dose4D
Mid range					
Aquilion PRIME (Toshiba)	80×0.6	0.35	175	AIR3D	SureExposure3D
Brilliance CT (Philips)	64×0.625	0.4	210	IMR	Z-DOM and D-DOM
LightSpeed VCT (GE)	64×0.625	0.35	200	ASIR	SmartmA
Somatom Definition AS 64 (Siemens)	64×0.6	0.28	150	ADMIRE[b], SAFIRE	CARE Dose4D
Somatom Perspective (Siemens)	64×0.6	0.48	195[b]	SAFIRE	CARE Dose4D

It is common now for mid-range systems to have at least 64 slices allowing for the acquisition of thorax exams much more quickly than in the past

[a]Scanners listed in alphabetical order

[b]Requires special hardware/software

Collimation: determines the beam width and the minimum reconstruction slice thickness. For most thoracic applications, it is desired to use the widest collimation available as the beam width contributes to scan acquisition speed, at the same time offering the ability to reconstruct with high spatial resolution in the transaxial range by allowing reconstruction of thinnest slices.

Rotation time: in general, fastest rotation times of the scanners are desired to avoid motion artifacts (e.g., chest CT examination), but also for specific applications such as gated cardiac CT acquisitions where temporal resolution plays a vital role to determine image quality.

Scan acquisition speed: depends on variables including the pitch, collimation, and rotation time. Increases in pitch, wider collimation, and reduction in reduction times all lead to a proportional increases in scan speed.

Radiation exposure: is primarily determined by the kilovoltage and tube current-time product combination. Automatic and/or adjustments according to patient size are required.

Image reconstruction technique: will primarily determine trade-off of image noise and spatial resolution, especially when using routine FBP kernels. With iterative reconstruction in most instances, the user predetermines a desired spatial resolution and then applies iterative reconstruction to reduce image noise while retaining spatial resolution.

Scan range: in conjunction with other acquisition settings, will determine what can be visualized as well as the overall radiation dose. Having precise and consistent control over what areas are exposed limits radiation dose and ensures acquisition of the right anatomical areas.

As of today, most of the mid-range and high-end scanners from various vendors integrate more advanced image reconstruction techniques that include iterative methods into their workflows. The integration of iterative reconstruction capabilities expands beyond the traditional filtered back-projection (FBP). The most relevant benefit of iterative reconstruction is that it can reduce image noise which in most cases can be translated to dose reduction and/or improvement of image quality. Some of the most cutting-edge iterative reconstruction methods also include an advanced modeling of the physics of the CT acquisition (detector size, scanner geometry, etc.), such that it can also help decreasing image artifacts and improving spatial resolution (Ramirez-Giraldo et al. 2014; Solomon and Samei 2014; Newell et al. 2015; Solomon et al. 2015).

A well-established dose reduction feature, which is now fundamental in the data acquisition workflow of modern CT scanners, is the automatic exposure control (AEC) of the tube current. The AEC adapts the overall current exposure to a patient according to its size and anatomy, or more specifically the patient's x-ray attenuation. The AEC technology is currently a standard feature in all CT scanners (NEMA 2015). The main benefit of AEC from a workflow perspective is that it obviates the need to use complex, often manual, lookup tables or multiple protocols to accommodate different patient sizes or age groups.

Tube potential adjustments are another strategy that can be used to better individualize the CT scan. Newer CT scanner models offer a wider range of tube potential values, typically between 80 to 140 kV, with some manufacturers now offering even lower values such as 70 kV and up to 150 kV (Gordic et al. 2014). Reducing the tube potential has shown tremendous potential to reduce dose and improve quality (Sigal-Cinqualbre et al. 2004). However, manual adjustments of the tube potential are challenging since other parameters of the scan have to be considered such as tube current and scan speed, in addition to considering patient size and type of examination. To make this adjustments easier to integrate in routine workflows, some manufacturers have started to offer specific technologies in which the scanner automatically selects the tube potential (CARE kV™, Siemens Healthcare). The automatic selection is based on patient size and also according to the use (or not) of iodinated contrast agent (Fig. 1). Scientific publications in a wide range of thoracic applications in adult and pediatrics (Mayer et al. 2014; Siegel et al. 2013) have shown that automated tube potential selection technology can reduce dose while at the same time maintaining or improving image quality. Most recently, other manufacturers have introduced technologies also attempting to automate the tube potential selection (kV Assist™, GE Healthcare).

In 2013, the National Electrical Manufacturers Association (NEMA) released a set of standards (XR-29) which have become a commonplace in CT scanners by all manufacturers (NEMA 2015). These technologies are integrated into the work-

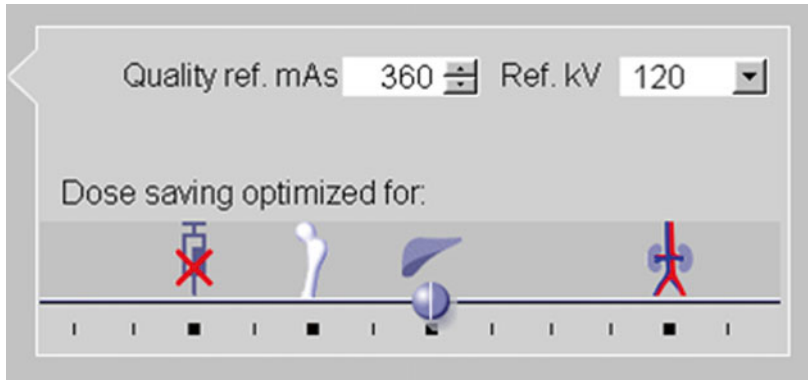

Fig. 1 Example screenshot of an automated tube potential selection technology. Example illustrating the setup and optimization based on CT application and iodinated contrast usage. Example taken is based on a technology called CARE kV™ (Siemens Healthcare)

flow of CT scanning and have an impact in radiation dose management. In the one hand, they define dose check features which provide automatic notifications to the user when a threshold dose (e.g., based $CTDI_{vol}$ or DLP values) has been reached when using a given protocol or can also output an alert when a global threshold value has been reached, in which case the user will have to write down the reason for the excess. Another aspect of the standard is the definition of standard DICOM structured reports to capture post-exam information regarding the radiation exposure such that it can be included in the patient records. These standardized DICOM reports provide relevant source which can be used by dose-tracking software tools (such as Radimetrics, DoseWatch, or Team Play), allowing these to record radiation exposures within an institution or group of institutions. Other two components of the XR-29 standard include the availability of specific protocols for pediatric and adult patients and the availability of AEC systems within CT scanners.

2.1 Special Topics in Thoracic Acquisition

State-of-the-art CT systems offer special acquisition protocols for thoracic application. Some of the existing approaches include faster acquisition modes by either using wide-beam collimation systems which can cover a range of up to 16 cm with only one gantry rotation (Khan et al. 2011) or by using a dual-source high-pitch CT acquisition mode with pitch values up to 3.4 and covering a range of up to 73.7 cm in less than 1 s. To ease integration of these acquisition modes into the workflows, manufacturers provide users with default protocols.

Most recently, a special low-dose acquisition mode based on additional tube filtration has been introduced. To facilitate the workflow and the use of this protocol, the users only have to select if they want to operate at 100 or 150 kVp, and the scanner will automatically place a flat filter made of tin right in front of the x-ray tubes (inside the gantry). This technology has been shown to provide a more efficient performance in unenhanced CT examinations when compared to routine kV imaging, particularly by requiring less radiation dose to achieve high image quality for discriminating soft tissues and air. Various publications have already shown the successful use of this technology for applications such as low-dose chest CT, as needed for lung cancer screening programs (Haubenreisser et al. 2015; Gordic et al. 2014; Newell et al. 2015).

In the last 10 years, the CT field has begun moving beyond traditional CT acquisitions of a solely Hounsfield Unit (HU) Unit attenuation-based approach and has begun to explore multi-energy imaging in the clinical routine. The most widespread adoption of this principle is dual-energy CT (DECT), which consists of acquiring volumetric data at two different spectra, providing not only anatomical information but also material-specific information. The main technological approaches to DECT acquisition which are currently commercially available include the dual-source CT, fast kV switching, dual-layer detectors, split-filter technology (e.g., Twin Beam™), and consecutive CT scans (McCollough et al. 2015; Johnson 2012). Comprehensive description of strengths and weaknesses of the various approaches is discussed elsewhere (McCollough et al. 2015).

Workflow aspects associated with DECT include the data acquisition and the data post-processing. For data acquisition, platforms such as the dual-source CT facilitate the user to personalize the examination to patient size, by offering choices in the pair of energies used in the exam (Krauss et al. 2015). In addition, dual-source platforms provide compatibility with automatic exposure control and provide additional x-ray tube filtration such that there is no radiation dose penalty (Schenzle et al. 2010).

3 Automation of Image Acquisition: Protocol Design, Tools for Technologists

In modern CT scanners, the users will find predetermined scan protocols for various adult and pediatric applications (NEMA 2013). These default protocols are provided by the manufacturers, although they can be improved or customized

by individual institutions. Predefined scan protocols are critical for workflow, as it is not practical to manually change all parameters for all patients. Independent efforts to describe CT-imaging protocols across manufacturers for thoracic (and other) indications have been proposed by several organizations including the American Association of Physicists in Medicine (AAPM 2015).

In general, for routine use, the available thoracic CT protocols should predetermine acquisition parameters which prioritize fast acquisition speed while optimizing radiation exposure with tools such as AEC and automatic tube potential selection when available. The purpose of this thoracic protocol setup is to achieve CT image data free from motion artifacts, using the right radiation dose and achieving diagnostic image quality.

Appropriate workflow tools for acquisition and image generation are crucial to maintaining consistency in the operation of CT. As an example, consider the x-ray CT localizers (aka topogram, scout, or scanigram depending on manufacturer). The CT localizers are typically used to aid in the centering of the patients in the CT table, to define the CT scan range, and also as input for the AEC. Newer technologies such as FAST Planning (Siemens Healthcare) facilitate the automatic recognition of scan (and reconstruction) ranges according to predefined anatomical locations. With such automation, there is an increased consistency across operators, as defined anatomical landmarks are used rather than solely relying on operator experience. Importantly, such automation can also help in avoiding cutoffs of relevant anatomy and can also aid in preventing unnecessary overradiation.

Another important aspect that contributes to consistency between CT technologists in the operation of the CT scanner is associated with how to resolve scan parameter conflicts which arise when scanning challenging patients (e.g., obese patients). Typical conflicts include the scanner needing to reach a higher tube current than is technically feasible considering the finite power capacity of an x-ray tube at certain tube voltage settings. One vendor solution to automatically solve this problem is illustrated in Fig. 2, with a technology called FAST Adjust™. This software will automatically adapt the technical parameters to resolve the conflict. For instance, FAST Adjust will automatically suggest an increase to the pitch and/or rotation time to allow for the necessary dose to be delivered, hence reaching the prescribed image quality. If the conflict cannot be resolved by increasing the scan time alone, the maximum mAs for the scan will be reduced. Alternatively, for thoracic applications where acquisition speed is important, the operator can also use the FAST Adjust to speed up the acquisition, while the scan-

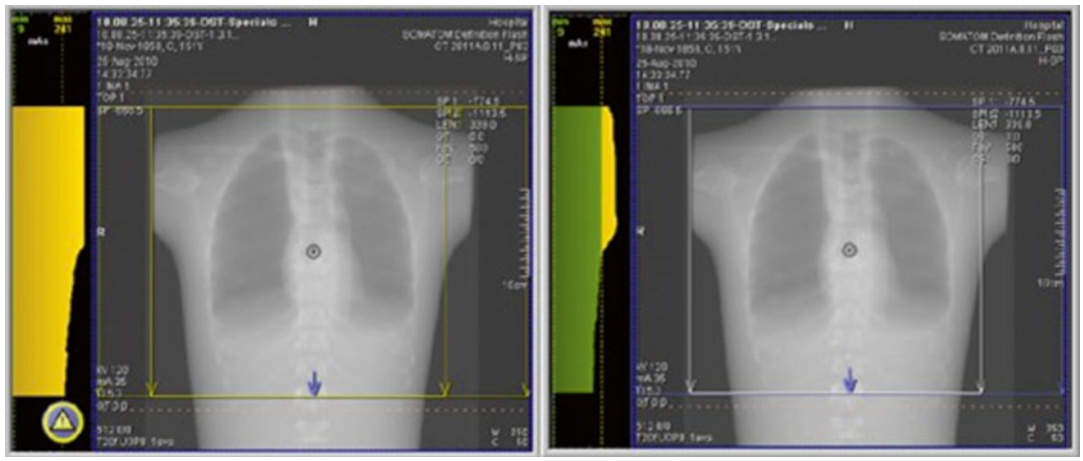

Fig. 2 Example software solution to automatically resolve scan parameter conflicts, which can occur when imaging challenging cases such as scanning very large patients. The solution illustrated by the screenshots is called FAST Adjust (Siemens Healthcare). The software indicates (*yellow curves*) user of parameter conflicts and offers a "FAST Adjust" button which automatically adjusts parameters according to user preconfigurations. Typical adjusted parameters include scan speed-related parameters (e.g., pitch and rotation time) as well as dose-related parameters such as the mAs

ner will automatically adjust acquisition parameters accordingly while keeping exposure and image quality the same. For most protocols, there are pre-configured limits for how much the scan time and maximum mAs will be adapted, while the user can customize the values if needed.

Another important source of "inconsistencies" in scanning by CT technologies is the cardiac CT examinations. Cardiac scanning is among the most complex scan acquisition modes for a novice CT technologist or even experienced ones that do not have opportunity to perform gated cardiac exams often. A solution to ease the workflow of this complex examination is the *FAST Cardio Wizard* (Siemens Healthcare). This special mode integrates into the cardiac scan protocol providing a step-by-step guide to the cardiac scanning. The user is aided in the selection of scan protocol (e.g., prospective vs. retrospective mode), as well as setting up cardiac phases of interest and selection of an appropriate ECG-based tube current modulation alternative.

3.1 Protocol Management

A typical radiology department will have several CT acquisition protocols which are predefined across their scanner fleet. With the increased importance of optimization and consistency of the CT techniques, it is desirable that scan protocols are protected and not arbitrarily adjusted by unauthorized users. Currently, some manufacturers provide software solutions which only allow authorized users, using a password, to modify or create CT scan protocols.

Another tool, which is helpful for (lead/manager) CT technologists in protocol management, is the Scan Protocol Assistant (Fig. 3). The Scan Protocol Assistant can facilitate adaptation of

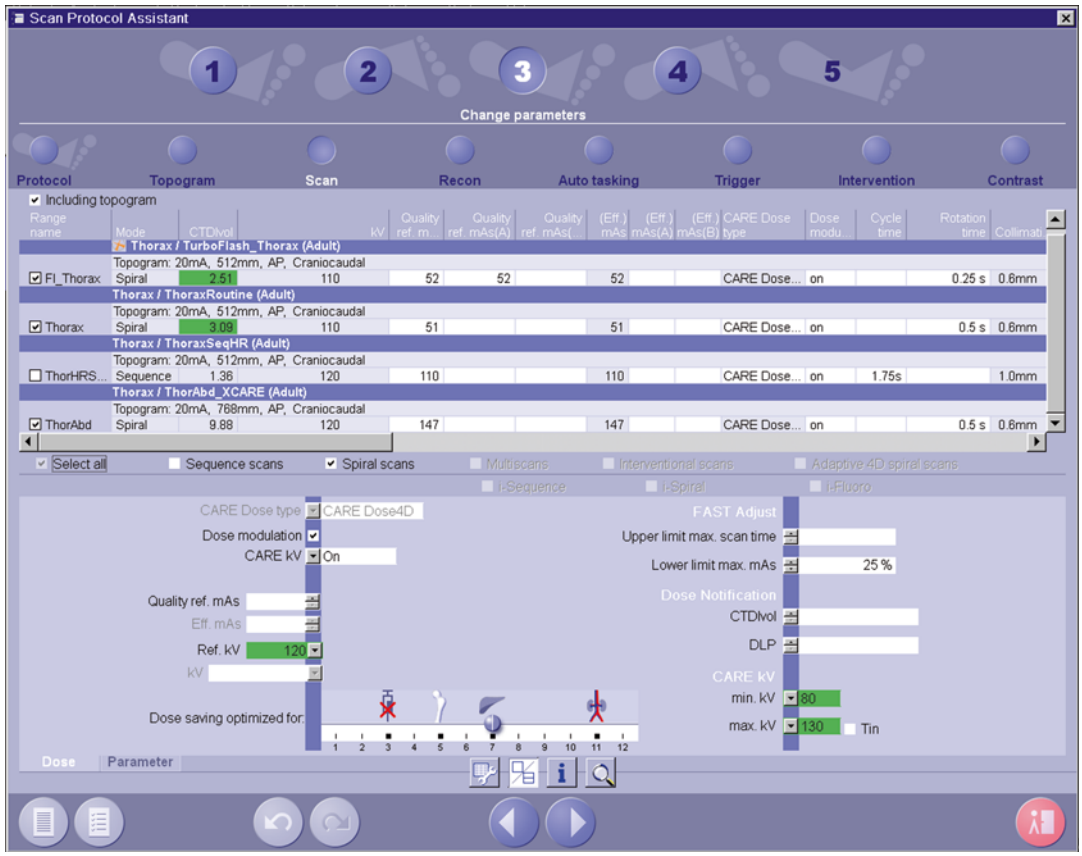

Fig. 3 Example of a Scan Protocol Assistant solution (Siemens Healthcare). This tool allows the user to quickly customize one or more scan protocols by manipulating acquisition and/or reconstruction parameters

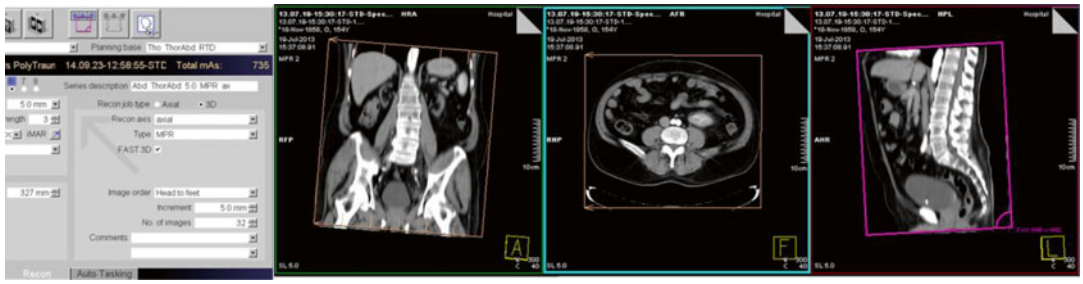

Fig. 4 Automatic alignment of MPRs reconstruction according to the orientation of the patient using FAST 3D Align. Left image indicates how it is activated in the scanner software (checkbox), and right images provide an example of how the tool centers each plane according to the actual location of patient anatomy

scan parameters for several protocols simultaneously, hence saving time and promoting standardization across protocols. For instance, changes in slice thickness, reconstruction kernel, can be determined for various protocols at the same time.

Radiology departments are facing financial pressures from recent changes in healthcare reimbursement yielding an environment in which scanners are no longer renewed for the state-of-the-art systems every few years, but instead on an 8–10-year time frame. In addition, when combined with recent healthcare consolidation, radiology departments are facing with more frequency a heterogeneous scanner fleet from various manufacturers, but also departments must optimally operate older and newer scanners together. These issues present challenges for protocol management and optimization at the enterprise level. While individual scanner technologies have come a long way for individual patient and scanner personalization, the field still does not yet have a solution for enterprise management of scan protocols, e.g., a centralized location from which one can administer the protocols of the entire scanner fleet at the institution and with an approach that is mindful of the several technologies available across the different scanners.

4 Image Post-Processing: Scanner-Based Automation

In addition to traditional generation of axial images, the integration of direct 3D multiplanar reconstructions (MPRs) at the scanner console constitutes an important workflow step in modern operation of a CT. Coronal, sagittal, and oblique reconstruction can be reconstructed at the scanner and hence can be directly transferred to PACS without the need of any intermediary software. Likewise, for cardiac application, relevant cardiac planes (i.e., horizontal long-axis, vertical long-axis, and short-axis) can also be generated in the scanner console. Another example of an advanced technology is the recently introduced FAST 3D Align (Siemens Healthcare). The FAST 3D Align provides automatic centering and aligning of a scanned volume (Fig. 4). As a result, three 3D recon segments (coronal, sagittal, axial) are calculated and contain the complete aligned body region (e.g., without black images). The alignment algorithm detects the boundaries and the centerline of the dataset directly from the real-time (preview) reconstruction. The 3D recon segments are displayed with the reconstruction axis aligned to the patient's anatomy. Because of the automatic alignment of FOV including adjustments and reconstruction of standard views, this facilitates minimal interaction from the user but consistency in the presentation when transferring the data to PACS.

Another customized solution to facilitate reconstructions, in this case contextualized to spine scans in thoracic region (or other anatomical regions), is a technology called FAST Spine. This tool facilitates an anatomically aligned preparation of the reconstructions with minimal user interaction (Fig. 5). The tool is also able to label spine vertebrae automatically within a predefined scan range.

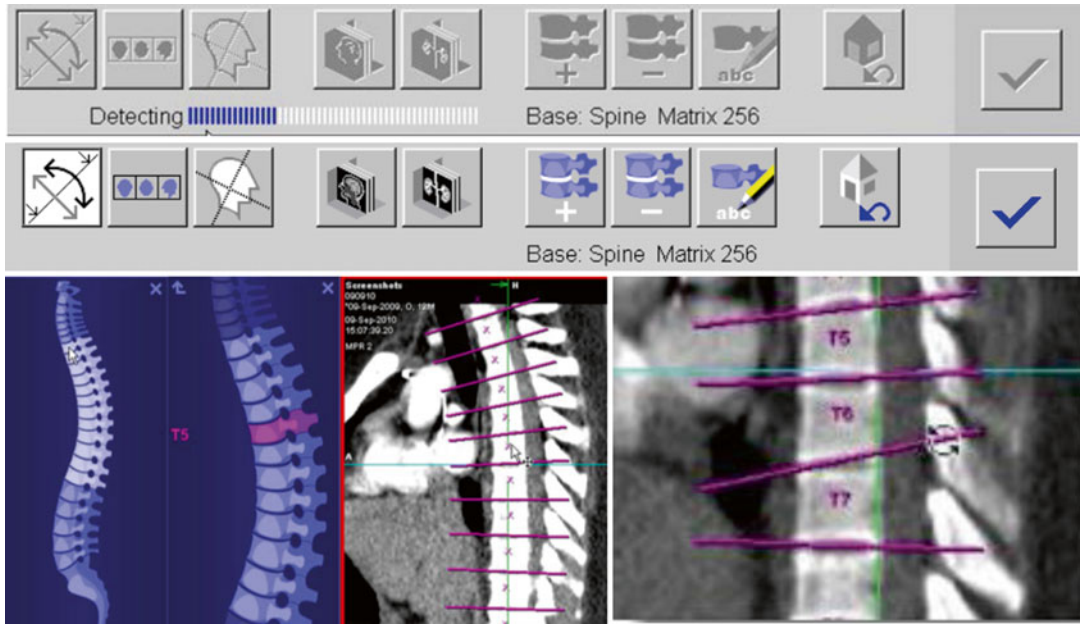

Fig. 5 Illustration of the workflow of a software solution used to automatically set up spine reconstructions with corresponding labeling. Example corresponds to a software tool called FAST Spine (Siemens Healthcare). The software requires minimal user interaction as most steps are automated. Users can edit results (e.g., labels) as needed

4.1 Dual-Energy CT

Dual-energy CT is an acquisition technique that is gaining in adoption in routine clinical practice thus workflow solutions for handling dual-energy CT data are required. All vendors that offer dual-energy-capable scanners either offer alternatives at the scanner console level and/or permit export of the data to specialized workstations or thin clients for post-processing of dual-energy data. To ease workflow, vendors such as GE and Siemens offer the possibility to directly transfer to PACS dual-energy post-processed images such as virtual monoenergetic (or monochromatic) reconstructions which are generated at the scanner console. This workflow allows interpreting radiologists to read dual-energy images in PACS without necessarily using additional post-processing software. Recent noise-optimized monoenergetic imaging (Monoenergetic Plus, Siemens) has allowed to further enhance the capabilities of this technique, improving visualization in applications such as CT angiography and contrast-enhanced examinations (Grant et al. 2014). Virtual Monoenergetic Plus datasets offer better iodine visualization compared to standard linear blending and can be used to reduce artifacts cause by beam hardening associated with metal (ECG leads, valves, etc.) or high concentrations of iodine and other similar high-density materials. In addition, iodine maps and virtual non-contrast images can be calculated on the scanner and directly sent to PACS (Fig. 6).

Siemens FAST DE Results also allows protocols to be customized to the needs of the institution. Different datasets with different kernels and slice thicknesses can be calculated and automatically sent to PACS and/or thin-client solutions. This limits the amount of data being reconstructed and sent over the network allowing for a streamlined workflow.

5 Image Post-Processing: Workstation/Thin-Client Solutions

Modern PACS offer a considerable number of features for measurements and visualization beyond archiving and accessibility to image data.

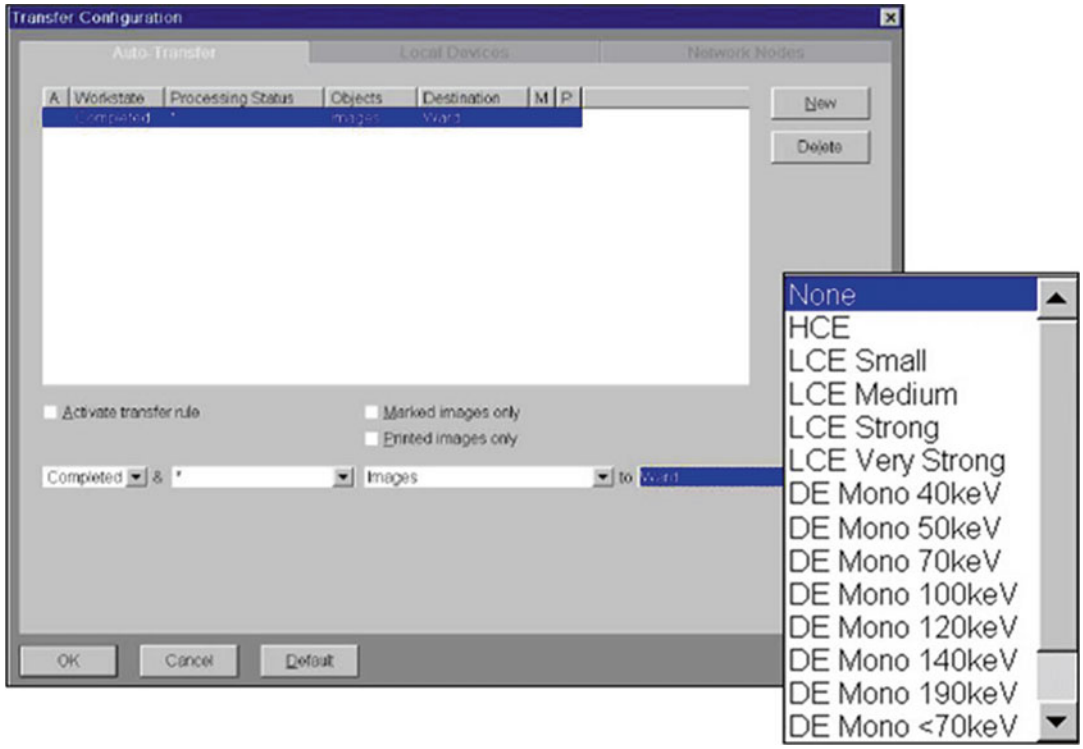

Fig. 6 PACS-ready workflow solution for DECT. Images such as virtual monoenergetic, iodine maps, and VNC images can be automatically reconstructed on the scanner and send directly to PACS without user interaction required. Sample screenshot of configuration and reconstruction options for FAST DE Results (Siemens Healthcare)

Increasingly thin-client solutions are replacing stand-alone workstations for the purpose to offer advanced 3D visualization as well as providing application-specific solutions. Moreover, to facilitate workflow in a busy radiology department, thin-client solutions can connect directly to PACS so that a radiologist can, on demand, access the 3D visualization or other advanced post-processing software only for those patients in which it can be needed or desired. Common visualization capabilities offered by thin clients include 3D reconstructions as well as customized application-specific solutions such as oncology follow-ups (e.g., RECIST measurements), TAVR planning, and others.

With the advent of CT into the clinical routine, imaging data could now be acquired in 3D volumetric form. Despite this fact, most radiologists today still routinely read CT axial and in some cases MPR reformatted 2D images in coronal or sagittal planes. This is partly due to limitations in standard reading workflow and the capability of PACS systems until recent years. Recent trainees have grown up in a culture of computed and advanced graphics and have an appetite for advanced visualization. Advances in computer processing power along with new GPU based solutions and advanced 3D algorithm development have led to real-time 3D visualization (Johnson et al. 1996; Lawler et al. 2001) Lessons learned from the evolution of computer gaming and the film industry have led to even more advanced photo-realistic 3D volume rendering technology (VRT) (Cinematic Rendering, *syngo*. via Frontier, Siemens Healthcare) as portrayed in Fig. 7. Technology such as these incorporates data-driven body models for visualization and can create ultrarealistic images of the patient's disease useful for ultrarealistic texture mapping, highlighting disease and pathology, enabling real-time augmentation and guidance. These advanced visualizations can also be very powerful when combined as a prerequisite for advanced

3D printing, an expanding field used for surgical planning (Rengier et al. 2010), teaching, and eventually organ replacement (Mannoor et al. 2013). Advanced visualization is a powerful new tool that supports decision-making and treatment selection.

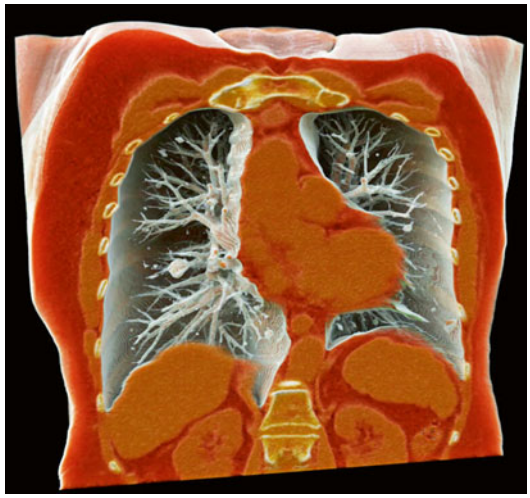

Fig. 7 A photo-realistic VRT of the thorax using a prototype advanced simulation and rendering techniques (Cinematic Rendering, *syngo*.via Frontier, Siemens Healthcare). Notice how the lesion in the lung stands out and is easily identified

The examination of thoracic bone structure looking for lesion fractures is a time-consuming and often overlooked task for chest radiologists. Hence, when someone is scanned for non-trauma purposes, this can be easily overlooked in a fast-paced department. An example workflow solution to aid with the reading of these cases is a rib-unfolding application (*syngo*.via CT Bone Reading, Siemens Healthcare) that can display the ribs unfolded for easier and quicker inspection for fractures or lesions (Fig. 8).

Some of the challenges to routine use of advanced 3D visualization and other advanced post-processing techniques are that the tasks can be time intensive while at the same time are often not reimbursed. Hence, it is not feasible for a radiologist to routinely use these tools while at the same time reading sufficient cases throughout the day. As a result, many institutions are creating specialized laboratories (e.g., 3D labs) which can take care of advanced visualization and post-

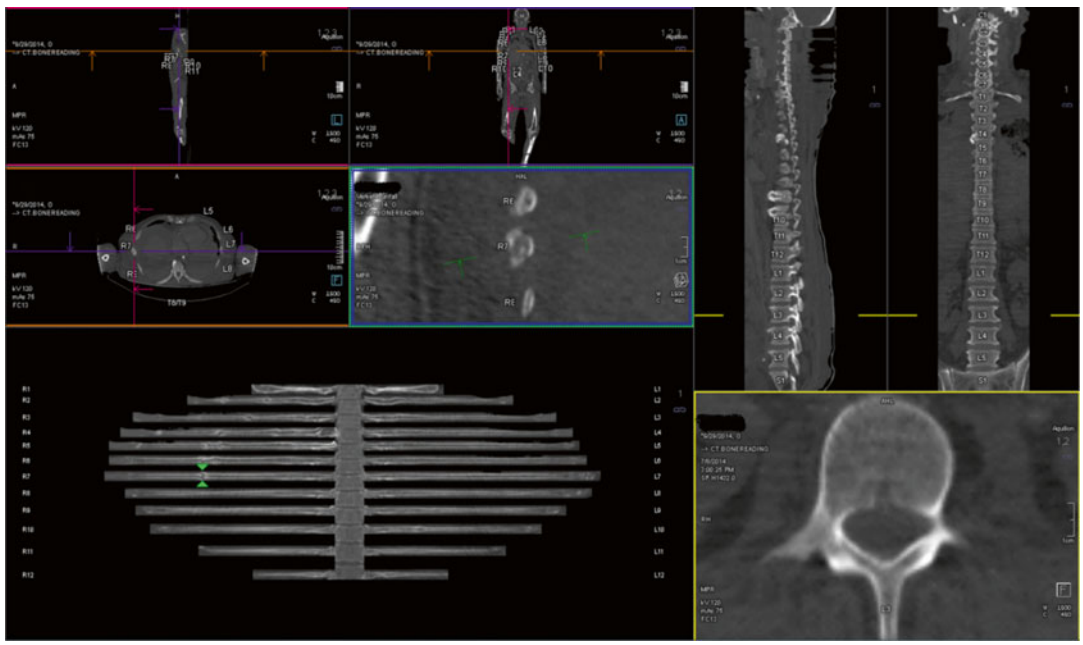

Fig. 8 An example of the *syngo*. CT Bone Reading workflow (Siemens Healthcare) in which the rib cage is unfolded and flattened from a volumetric dataset of the thorax allowing for the fast examination for fractures or lesions present without the need for scrolling through every axial image

processing. However, even under this model, data needs to be transferred from the equipment to the "3D-Lab" and then back to PACS when ordered, yet again creating constraints in time as well as cost due to the personnel needed. In response to this, recent workflow solutions have attempted to substantially reduce the time for the radiologists (or 3D lab technologists) to process data or, in other cases, to fully automate the tasks. These approaches can save time and money.

Two examples of full automation are the "Rapid Results" technology from Siemens. In the one hand, the LungCAD application can trigger automatically the creation and archiving of result series. There is even no need to open the workflow in the thin client. As such, the software (in this case *syngo*.via LungCAD) works as a node that calculates the results and then sends the results automatically to PACS. Then, the radiologist will only need to load the case on PACS where he can simultaneously read the CAD series which is already available at the same time.

A second example of fully automated workflow is the rapid results for dual-energy CT post-processing. Datasets can be sent directly from the scanner console (automatically or pushed by the CT technologists) to the server (e.g., s*yngo*.via), and when the data arrives, the software will automatically trigger automated processing which can be pre-configured in the thin client. After the data has been generated, it can be automatically sent to PACS. Example series which can be set up include monoenergetic images, automated bone removal, virtual non-contrast images, and lung PVB, among several others.

Other workflows are designed to be semiautomated, as not all the steps can be fully automated, and often time need to be revised by the radiologists or physician. In other cases, consistency regardless of operator is required, such as the stent planning. An example solution of this is *syngo*. CT Rapid Stent Planning from Siemens (Fig. 9), in which it is possible to create automatic completion of manufacturer-specific graft order forms. Preprocedural planning for the treatment of abdominal or thoracic aortic aneurysms requires a precise assessment of several anatomical parameters. Numerous vendors offer various stent grafts, each of which requires its own set of measurements. Manually completing graft order forms may be

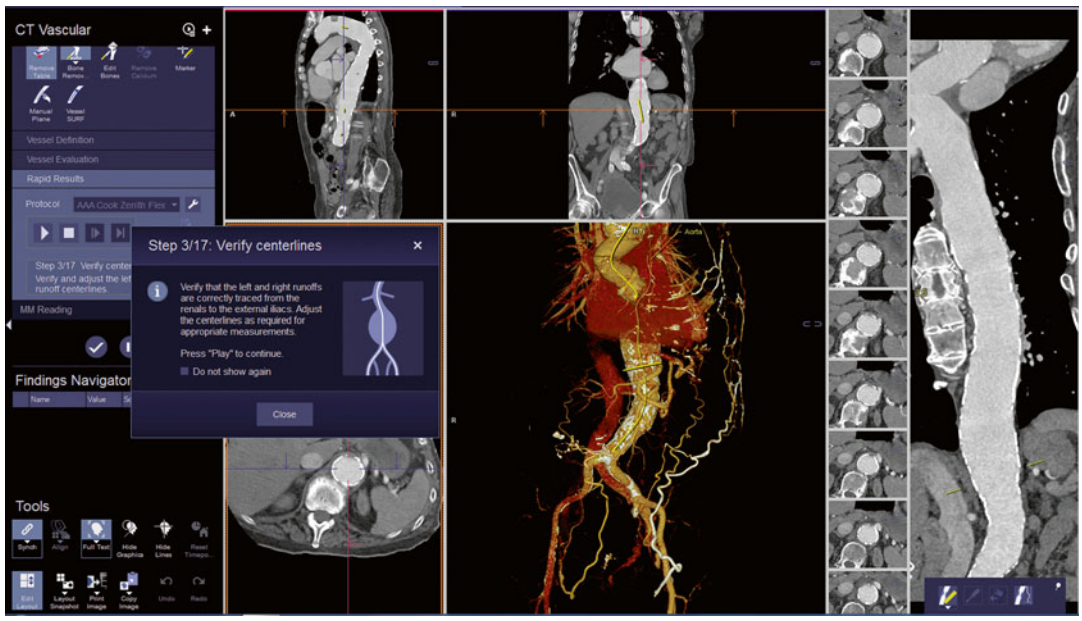

Fig. 9 Screenshot of a fully automated workflow for stent planning using Rapid Results (*RR*) technology in *syngo*.via (Siemens Healthcare). This technology introduces automatic completion of manufacturer-specific stent order forms. Protocols guide the user through all length and diameter measurements which are then automatically stored in the corresponding order form

tedious and time consuming. So, it is possible to automatically complete manufacturer-specific stent order forms, while the software provides protocols that guide the user through all length and diameter measurements which are then automatically stored in the corresponding order form.

6 Quantitative Imaging

The concept of precision/personalized medicine is one in which we do not only tailor the imaging acquisition to each patient, as described above and elsewhere, but it also comprises the motivation to drive treatment decisions based on quantitative information rather than qualitative judgment alone. The high spatial and temporal resolution of CT is an enabling technology in this pursuit, but it does not come without additional challenges, especially to workflow.

Unfortunately, with our current schemas for quantitative imaging, not all measurements can be obtained from a single reconstructed dataset. In fact, in order to get a full coverage of quantitative measurements, one might need to identify and save multiple image reconstructions of the same anatomy that are used for different purposes. In addition to reconstruction kernel, the slice thickness and slice spacing of datasets are also important factors in the performance of measurement algorithms. Sometimes measurement algorithms are tuned for specific kernels for a computer that may be different than those used for visual reading. For example, a computer algorithm can detect subtle textural features imperceptible to the human eye that can lead to improved detection and classification of disease (Raman et al. 2015; Xu et al. 2006). This then necessitates the reconstruction at minimum high-resolution thin slice data that can be later down sampled. Unfortunately, this is a conflict with the general reading paradigm in which radiologist tries to minimize the number of slices a radiologist must examine in order to maintain efficiency. In addition, these various datasets must be placed into long-term image storage for follow-up analysis and retrospective research studies. This creates strain on IT infrastructure that may not be designed to handle many thousands of images for each patient exam.

Furthermore, as image reconstruction techniques and kernels vary between manufacturers, it can sometimes be a challenge to perform multi-institutional analysis and may require additional reconstructions to match an industry standard. Societies such as the Quantitative Imaging Biomarkers Alliance (QIBA) have ongoing efforts to standardize image acquisition and analysis. An example of this effort is the committee focused on lung density as an imaging biomarker. This committee has recently been tasked with dealing with the variability in HU values between different manufacturers and scanners (QIBA; Sieren et al. 2012).

7 Workflow Example: Lung Cancer Screening

With the announcement of the measureable benefit of screening for lung cancer with low-dose MDCT from the National Lung Screening Trial (NLST) and subsequent favorable rulings to provide insurance coverage of lung cancer screening including coverage for Medicare beneficiaries, the likelihood of early detection of lung cancer has become a possibility. The NLST demonstrated that annual lung cancer screening with computed tomography for high-risk populations/patients contributes to a 20% reduction in mortality (NLST 2011). Prior to the successful start of any lung cancer screening program at any institution, it is necessary to recognize and properly prepare for the considerable workflow challenges to the standard radiology clinic workflow. This means preparing for the clinical aspects such as the need for nurse navigators and smoking cessation programs, discussed elsewhere, while also identifying and obtaining the necessary imaging and workflow tools.

A critical element for a successful LCS program is the ability to identify patients that meet the necessary criteria, bring them into your program, and appropriately follow them over time. In research studies in the past, this was done with basic systems such as Microsoft Excel workbooks and was successful due to the limited number of patients. With some estimates indicating

approximately 8 million people in the USA eligible for LCS, these basic solutions will not adequately scale for most practices. Thus working with existing tools in the EMR, configuring to streamline the process, or obtaining a dedicated LCS patient management system (Fig. 10), similar to those for mammography, is required in order to meet the higher demand.

Guidelines for appropriate image acquisition for LCS are available from a number of guidance organizations such as AAPM, CMS, and NLST (AAPM 2015; CMS 2015; NLST 2015) and utilize the latest in automation tools discussed above. The specific parameters are discussed in more detail elsewhere in this book.

After setting up the appropriate image acquisition, the reading workflow must also be addressed. Due to the estimated number of patients that a fully operation LCS program could theoretically encompass, the reading workflow must be optimized. Beyond reading with standard axial, multiplanar reformats and 3D views, computer-aided detection (CAD) tools (e.g., Siemens LungCAD) should allow for improved efficiency and sensitivity (Zhao et al. 2012). CAD tools quickly highlight areas of interest of suspected nodules to the radiologist and depending on their clearance can be used either as a second reader or more streamlined concurrent reading approaches in which the non-annotated and annotated datasets are linked together in PACS for faster reading.

Another rapidly evolving concept in radiology is structured reporting. Reports will no longer be limited to plain text descriptions from the radiologist, but they will also include codes from sources such as RadLex. This new schema provides a common pool of shorthand codes that can be used to improved report reliability and improve efficiency. With structured reporting data, advanced data analytic topics can be pursued to evaluate site performance or patient compliance

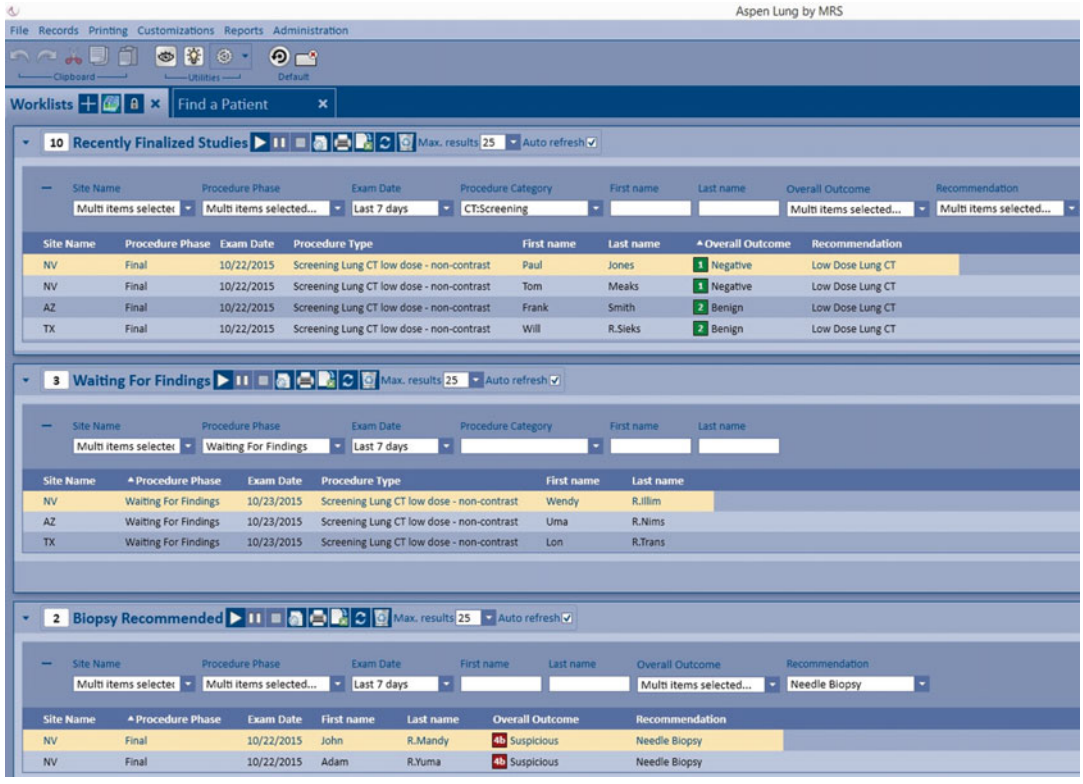

Fig. 10 Screenshot of the Aspen Lung software from MRS for LCS patient management and tracking

or to even look at diseases on a large scale and perhaps identify links that would otherwise be missed. For LCS, a schema similar to that in mammography has been developed by the ACR called Lung-RADS, and it provides recommendations for patient management based on specific factors (ACR 2014; McKee et al. 2015).

Once the results are sent back into the patient management system, a report is sent to the referring physicians with the appropriate guidance for follow-up; patients are then either sent for an intervention or placed back into the queue for additional screening at a later date. With the approval of LCS from CMS, certain requirements are placed on a site in order to receive reimbursement. One of these requirements is to submit structured patient information to a CMS-approved registry that will allow CMS to track performance of LCS on a large scale and enable the streamlining of eligibility criteria in the future. Patient management systems can provide the necessary tools to extract information from the medical record, radiology, and dose reports and automatically send them to the appropriate registry, thus streamlining the process for the radiologist.

References

American Association of Physicists in Medicine (AAPM). Standardized protocols for CT Imaging. Available at http://www.aapm.org/pubs/CTProtocols. Accessed 30 Oct 2015

American College of Radiology (ACR). Lung CT screening reporting and data system (lung-RADS). Available at: http://www.acr.org/Quality-Safety/Resources/LungRADS. Accessed 31 July 2014

Centers for Medicare and Medicaid Services (CMS) (2015) Available at https://www.cms.gov/medicare-coverage-database/details/nca-decision-memo.aspx?NCAId=274

Gordic S, Morsbach F, Schmidt B, Allmendinger T, Flohr T, Husarik D, Baumueller S et al (2014) Ultralow-dose chest computed tomography for pulmonary nodule detection: first performance evaluation of single energy scanning with spectral shaping. Invest Radiol 49(7):465–473

Grant KL, Flohr TG, Krauss B, Sedlmair M, Thomas C, Schmidt B (2014) Assessment of an advanced image-based technique to calculate virtual monoenergetic computed tomographic images from a dual-energy examination to improve contrast-to-noise ratio in examinations using iodinated contrast media. Invest Radiol 49(9):586–592

Haubenreisser H, Meyer M, Sudarski S, Allmendinger T, Schoenberg SO, Henzler T (2015) Unenhanced third-generation dual-source chest CT using a tin filter for spectral shaping at 100kVp. Eur J Radiol 84:1608–1613

Johnson TRC (2012) Dual-energy CT: general principles. Am J Roentgenol 199(5 Supplement):S3–S8

Johnson PT, Heath DG, Bliss DF, Cabral B, Fishman EK (1996) Three-dimensional CT: real-time interactive volume rendering. AJR Am J Roentgenol 167(3):581–583

Khan A, Khosa F, Nasir K, Yassin A, Clouse ME (2011) Comparison of radiation dose and image quality: 320-MDCT versus 64-MDCT coronary angiography. AJR Am J Roentgenol 197(1):163

Krauss B, Grant KL, Schmidt BT, Flohr TG (2015) The Importance of Spectral Separation: An Assessment of Dual-Energy Spectral Separation for Quantitative Ability and Dose Efficiency. Invest Radiol 50(2):114–118

Lawler LP, Fishman EK (2001) Multi–detector row CT of thoracic disease with emphasis on 3D volume rendering and CT angiography. Radiographics 21(5):1257–1273

Mannoor MS, Jiang Z, James T, Kong YL, Malatesta KA, Soboyejo WO, Verma N, Gracias DH, McAlpine MC (2013) 3D printed bionic ears. Nano Lett 13(6):2634–2639

Mayer C, Meyer M, Fink C, Schmidt B, Sedlmair M, Schoenberg SO, Henzler T (2014) Potential for radiation dose savings in abdominal and chest CT using automatic tube voltage selection in combination with automatic tube current modulation. Am J Roentgenol 203(2):292–299

McCollough C, Leng S, Yu L, Fletcher JG (2015) Dual- and multi-energy computed tomography: principles, technical approaches, and clinical applications. Radiology 276(3):637

McKee BJ, Regis SM, McKee AB, Flacke S, Wald C (2015) Performance of ACR Lung-RADS in a clinical CT lung screening program. J Am Coll Radiol 12(3):273–276

National Lung Screening Trial Protocols (NLST) via ACRIN (9/26/2015) Available at https://www.acrin.org/Portals/0/Protocols/6654/forms/qcforms/CT_Technique_Chart.pdf

National Lung Screening Trial Research Team (2011) Reduced lung-cancer mortality with low-dose computed tomographic screening. N Engl J Med 365(5):395

NEMA. XR 29–2013. Standards for optimization and dose management. Available at https://www.nema.org/Standards/Pages/Standard-Attributes-on-CT-Equipment-Related-to-Dose-Optimization-and-Management.aspx. Accessed 30 Oct 2015

Newell JD Jr, Fuld MK, Allmendinger T, Sieren JP, Chan KS, Guo J, Hoffman EA (2015) Very low-dose (0.15 mGy) chest CT protocols using the COPDGene 2 test object and a third-generation dual-source CT scanner with corresponding third-generation iterative reconstruction software. Invest Radiol 50(1):40

Quantitative Imaging Biomarkers Alliance (QIBA). Available at http://qibawiki.rsna.org/index.php?title=Lung_Density_Biomarker_Ctte

Raman SP, Schroeder JL, Huang P, Chen Y, Coquia SF, Kawamoto S, Fishman EK (2015) Preliminary data using computed tomography texture analysis for the classification of hypervascular liver lesions: generation of a predictive model on the basis of quantitative spatial frequency measurements – a work in progress. J Comput Assist Tomogr 39(3):383–395

Ramirez-Giraldo JC, Primak AN, Grant K, Schmidt B, Fuld MK (2014) Radiation dose optimization technologies in multidetector computed tomography: a review. Med Phys 2(2):420–430

Rengier F, Mehndiratta A, von Tengg-Kobligk H, Zechmann CM, Unterhinninghofen R, Kauczor HU, Giesel FL (2010) 3D printing based on imaging data: review of medical applications. Int J Comput Assist Radiol Surg 5(4):335–341

Schenzle JC, Sommer WH, Neumaier K, Michalski G, Lechel U, Nikolaou K, Becker CR, Reiser MF, Johnson TRC (2010) Dual energy CT of the chest: how about the dose? Invest Radiol 45(6):347–353

Siegel MJ, Hildebolt C, Bradley D (2013) Effects of automated kilovoltage selection technology on contrast-enhanced pediatric CT and CT angiography. Radiology 268(2):538–547

Sieren JP, Newell JD, Judy PF, Lynch DA, Chan KS, Guo J, Hoffman EA (2012) Reference standard and statistical model for intersite and temporal comparisons of CT attenuation in a multicenter quantitative lung study. Med Phys 39(9):5757–5767

Sigal-Cinqualbre AB, Hennequin R, Abada HT, Chen X, Paul J-F (2004) Low-kilovoltage multi-row chest CT in adults: feasibility and effect on image quality and iodine dose. Radiology 231:169–174

Solomon J, Samei E (2014) Quantum noise properties of CT images with anatomical textured backgrounds across reconstruction algorithms: FBP and SAFIRE. Med Phys 41(9):091908

Solomon J, Mileto A, Ramirez-Giraldo JC, Samei E (2015) Diagnostic performance of an advanced modeled iterative reconstruction algorithm for low-contrast detectability with a third-generation dual-source multidetector CT scanner: potential for radiation dose reduction in a multireader study. Radiology 275:142005

Xu Y, Sonka M, McLennan G, Guo J, Hoffman EA (2006) MDCT-based 3-D texture classification of emphysema and early smoking related lung pathologies. IEEE Trans Med Imaging 25(4):464–475

Zhao Y, de Bock GH, Vliegenthart R, van Klaveren RJ, Wang Y, Bogoni L, de Jong PA, Mali WP, van Ooijen PM, Oudkerk M (2012) Performance of computer-aided detection of pulmonary nodules in low-dose CT: comparison with double reading by nodule volume. Eur Radiol 22(10):2076–2084

Computer-Aided Diagnosis and Quantification in Chest CT

Jin Mo Goo

Abstract

With the advances of CT and computer technology, various applications for computer-aided diagnosis (CAD) and quantification have been developed to enhance the performance of radiologists. CAD provides tools to detect more nodules, to determine nodule malignancy by characterizing and measuring nodules, and to match nodules in follow-up studies. These applications will play an important role in the nodule management for lung cancer screening with low-dose CT. Parenchymal and airway lesions in chronic obstructive lung disease and diffuse interstitial lung disease can be characterized and quantified semiautomatically and this information can be used in phenotyping of disease, in explaining functional changes, and in clinical trials. However, users need to understand the limitations and measurement variability of these approaches.

1 Introduction

CT plays a critical role in morphologic analyses of various pulmonary diseases which have been traditionally based on visual and qualitative assessment. With the advances of CT and digital technology, numerous post-processing techniques are now being applied in lesion detection, characterization, and quantification as well as three-dimensional visualization. These can be attributed to isotropic imaging of CT and easy access to digital images with the advent of picture archiving and communication systems (PACS). These valuable data provided by computer applications can enhance radiologists' performance, but the current status is far from fully automated diagnosis by computer technology. Therefore, the basic concept of computer-aided diagnosis (CAD) is to provide a computer output as a "second opinion" to assist radiologists' image interpretations (Doi et al. 1992).

CAD and quantification have been under active research in many pulmonary diseases, but this chapter will mainly focus on the applications in the evaluation of lung nodule, chronic obstructive lung disease (COPD), and diffuse interstitial lung disease (DILD).

J.M. Goo, MD, PhD
Department of Radiology, Seoul National University Hospital, 101 Daehak-ro, Jongno-gu, Seoul 03080, South Korea
e-mail: jmgoo@snu.ac.kr

U.J. Schoepf, F.G. Meinel (eds.), *Multidetector-Row CT of the Thorax*, Medical Radiology,
DOI 10.1007/978-3-319-30355-0_22

2 Basic Technologic Architectures of CAD

As detailed technologic description of CAD is beyond the scope of this chapter, only basic architectures of CAD will be introduced here, which share some approaches in the evaluation of lung nodule, COPD, and DILD.

2.1 Segmentation of the Lung

The first step for lung CAD is the segmentation of the lung from other structures such as the chest wall and the mediastinum. If the lungs exhibit minimal or no pathologic conditions, this process is relatively easy compared to the segmentation of other organs such as the liver because the attenuation value of the lung is quite different from the surrounding structures. However, when a pathologic condition such as fibrosis or pleural effusion is present, the segmentation of the lung fails to perform efficiently. As no single segmentation method can achieve an optimal performance for all disease conditions at the moment, specialized methods are applied for particular disease subsets. Recent methods can also permit segmentation of lobes to compute lobar volume and parenchymal abnormalities such as areas of low attenuation (Fig. 1).

2.2 Detection of the Region of Interests

After segmenting the lung, the region of interests (ROIs) are identified, which is dependent on target of lesions: lung nodule, low attenuated pixels in the lung, airways, and typical patterns of interstitial lung disease (ILD) such as areas of ground-glass opacity (GGO), reticular opacity, nodular opacities, honeycombing, and consolidation.

The initial nodule candidates can be identified by applying a gray-level thresholding technique or shape filters to CT images. In dealing with DILD, the areas of specific patterns on CT are usually identified by machine learning-based methods. In this method, the abnormalities are predicted on the basis of the features extracted from the data.

2.3 Feature Analysis and Reduction of False-Positives

A number of image features on ROIs such as morphology (size, circularity, etc.), gray level, and texture are quantified, and false-positive findings are removed by classifiers. Linear discriminant analysis, rule-based classifier, and artificial neural network are examples of feature-based

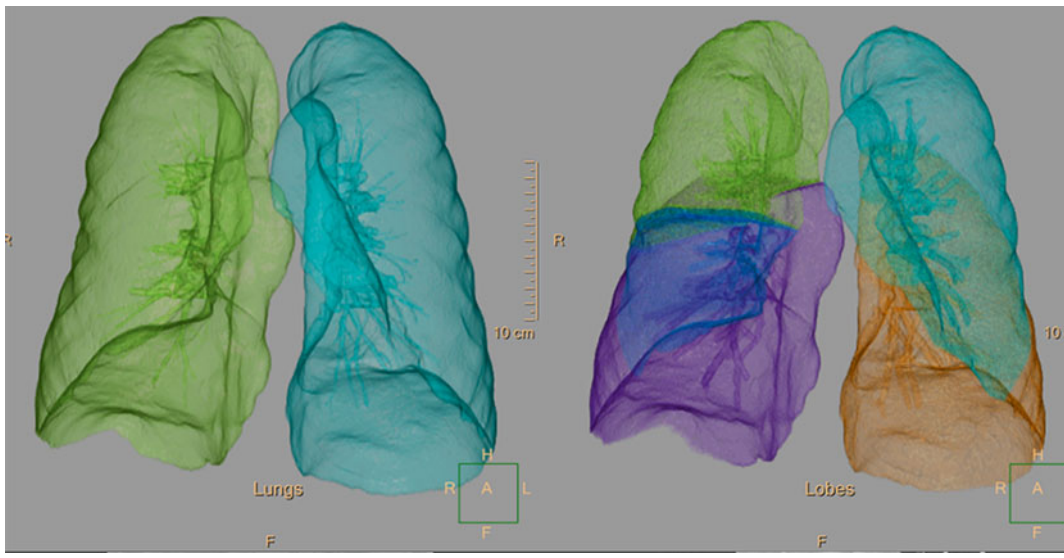

Fig. 1 Segmentation results of the lung (*left*) and each lobe of the lung (*right*)

classifiers. A classifier is trained with sets of input features and corrects class labels.

2.4 Quantification and Characterization

After segmenting ROIs from the background, various features of ROIs such as volume (Fig. 2), mass, and texture can be calculated by using the number of voxels, attenuation of voxels, and a relationship with surrounding voxels.

3 Lung Nodule

With the introduction of multidetector CT (MDCT), radiologists need to interpret a large number of CT images that require additional time and effort. Low-dose CT has been reported as an effective modality for lung cancer screening but the interpretation of low-dose CT for screening is typically a repetitive and burdensome task. As many nodules detected on screening CT are false-positives for malignancy, characterization of nodules to determine malignancy is crucial. Size, shape, and volume-doubling time of nodules are well-established indicators of nodule malignancy. However, there is considerable variability in visual assessment and manual measurement in the management of nodules. Therefore, CAD can be used in the detection, measurement, and monitoring of nodules in lung cancer screening and has been employed in some clinical trials (van Klaveren et al. 2009).

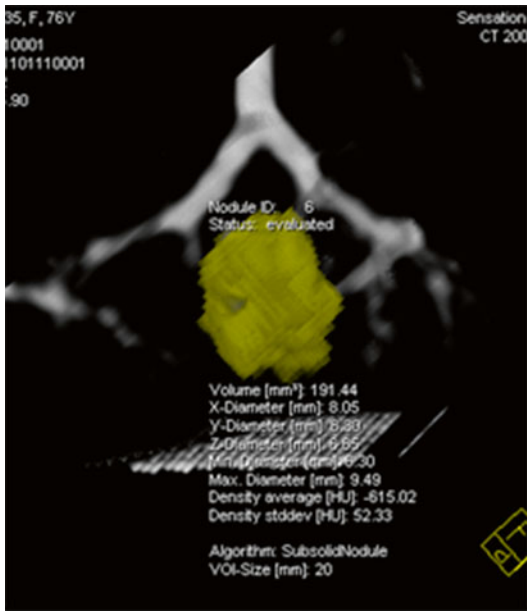

Fig. 2 Segmentation of GGN shows various measures of volume, diameter, and density

3.1 Detection

3.1.1 Performance of CAD

Many studies have shown that CAD could improve radiologists' performance in detecting lung nodules but reported performance of CAD systems is variable (Goo 2011). In addition to the CAD performance itself, the results of CAD performance can be affected by the reference standard and the characteristics of evaluated datasets. The Lung Image Database Consortium (LIDC) has shown that substantial variability exists across experienced radiologists in the task of lung nodule identification (Armato et al. 2004). In this study, the mean radiologist nodule detection sensitivities ranged from 51.0 to 83.2 % with mean false-positive rates from 0.33 to 1.39 per case by applying different reference standards. To overcome this limitation in comparing CAD algorithms, a comparative study where many CAD systems are applied to the same dataset has been performed (van Ginneken et al. 2010). When a database of same 50 CT scans from a lung cancer screening trial was tested, six algorithms showed sensitivities ranging from 24.6 to 71.2 % at a false-positive rate of 2 per case and sensitivities ranging from 12.7 to 57.0 % at a false-positive rate of 0.5 per case. Interesting suggestion of this study is that the combination of six algorithms is able to achieve a sensitivity of 79.2 % at a false-positive rate of 2 per case and a sensitivity of 63.8 % at a false-positive rate of 0.5 per case which are far superior to the sensitivity of each algorithm.

The value of CAD in improving radiologists' detection performance is attributed to the fact that a CAD system performs nodule detection task differently than radiologists do. Several studies have shown that a CAD system was good

at detecting isolated and small nodules, while radiologists are good at detecting attached and relatively larger nodules (Lee et al. 2004; Marten et al. 2005). This complementary role of a human reader and CAD in detecting lung nodules may be translated into better combined performance of readers with CAD than that of a double reading. Rubin et al. showed that the sensitivity of a reader with CAD at a false-positive rate of three can be substantially higher that with a double reading (Rubin et al. 2005). In another study, when the performance of CAD was compared with that of doubling reading with a total of 400 low-dose CT, the sensitivity of nodule detection was 78.1 % for double reading and 96.7 % for CAD (Zhao et al. 2012). In this study, 21.9 % of 151 findings that needed further evaluation were missed by readers and detected by CAD only.

The early CAD programs only targeted the detection of solid nodules, but with the increase of clinical significance of subsolid nodules, many CAD programs are now equipped with the capability to detect subsolid nodules. An initial study by Kim et al. which employed texture features and Gaussian curve fitting features showed a sensitivity of 94.3 % and a positive predictive value of 29.1 % at ROI-based analysis (Kim et al. 2005). In a study by Yanagawa et al., the figure-of-merit values with CAD did not show significant differences in detecting pure ground-glass nodule (GGN) or part-solid nodules while they showed significant improvement in detecting overall and solid nodules (Yanagawa et al. 2009). These results may be caused by poor sensitivity of CAD system (21 %) compared with that of readers (60–80 %). When a CAD system with better sensitivities (95 % for part-solid nodules and 71 % for pure GGNs) was used, readers' sensitivities were significantly increased in detecting part-solid nodules from 81 to 97 % and in detecting pure GGNs from 69 to 82 % (Godoy et al. 2013).

3.1.2 Reading Mode of CAD

According to the timing of viewing the CAD results, the reading mode of CAD can be divided into first reader, concurrent reader, and second reader. In a first-reader mode, readers review the CAD-detected nodules only. As the sensitivity of CAD is not good enough at the moment, readers may miss many significant nodules, and therefore this approach is not accepted. In a concurrent-reader mode, readers assess CT images and identify nodules while the CAD results are being displayed. This approach can be time efficient, but some nodules can be missed especially when readers are dependent on CAD results. Currently, second-reader mode is the accepted approach where readers review the CAD results after readers initially read CT images without CAD results.

Two studies have compared concurrent-reader mode and second-reader mode in the usage of CAD. In a study by Beyer et al. (2007), the sensitivity in detecting nodules above 4 mm was 68 % without CAD, 68 % with CAD as a concurrent reader, and 75 % with CAD as a second reader. In terms of reading time, concurrent reading (274 s) was significantly better than reading without CAD (294 s) and using CAD as a second reader (337 s). In a study by Matsumoto et al. (2013), the detection performance was not significantly different between the concurrent-reader mode and second-reader mode (figure of merit, 0.70 and 0.72), while reading time was significantly shorter with the concurrent-reader mode (132 s) than with second-reader mode (210 s).

3.2 Nodule Volumetry

Doubling time has been used in predicting nodule malignancy, but in dealing with subcentimeter nodules detected on CT scans, manual measurements can show considerable measurement variability. After the introduction by Yankelevitz et al. who showed all five malignant nodules out of 13 nodules had doubling time less 177 days (Yankelevitz et al. 2000), the computer-aided volumetry has become an important tool in nodule management (Fig. 3).

3.2.1 Measurement Variability

At an early study, the measurement error of volumetry was reported to be as small as 3 % when evaluated with a phantom (Yankelevitz et al. 2000). Subsequent studies have shown that various

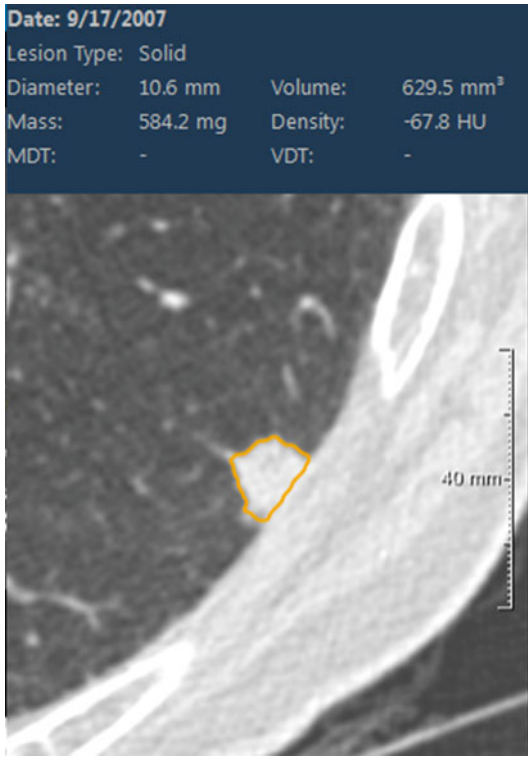

Fig. 3 Segmentation result of pleural-attached nodule showing volume of a nodule

factors can affect the measurement of nodule volume: the size and characteristics of nodules, the scan and reconstruction factors of the CT examinations, and the patient-related factors such as the respiratory status (Goo 2011; Goo et al. 2005, 2006) (Fig. 4). Volume measurements of smaller nodules, nodules attached to surrounding structures, and those with thicker CT section thickness may result in larger errors. When six software packages were compared in the evaluation of solid nodule volume, adequate segmentation determined by visual assessment could be achieved in 71–86 % of nodules, and systematic volume differences were present in 11 out of 15 comparisons (de Hoop et al. 2009). Therefore, for nodule volumetry, obtaining CT scans with thin volumetric data is essential and same software package should be used in the evaluation of interval change of nodule volume. To exclude the erroneous segmentation of nodules, readers always need to review the segmentation results as well.

As the establishment of ground truth of nodule volume in in vivo study is not feasible, the reproducibility in measuring nodule volume is more important than accuracy in determining the growth of a nodule. To evaluate the measurement variability, a same-day repeat CT protocol has been employed. After the initial study by Wormanns et al. which showed that the 95 % limits of agreement between the repeat CT scans were −20 to 22 % (Wormanns et al. 2004), many studies have shown that these limits can be up to 26 % (Goo 2011). Based on this results, the growth of a nodule in the NELSON (Nederlands-Leuvens Longkanker Screenings Onderzoek) trial was defined as an increase in nodule volume of at least 25 % between the two scans. Therefore, the measurement difference up to this threshold can be regarded as measurement error, while the measurement difference greater than this threshold can be true change between two CT scans.

3.3 Quantification of Subsolid Nodule

Due to the low contrast to the lung of subsolid nodules compared with solid nodule, segmentation of subsolid nodule is a difficult task. When a measurement error was estimated with simulated GGNs of various attenuation values, the average of the relative volume measurement error ranged from 51.1 to 85.2 % for 3 mm GGNs and from −4.1 to 7.1 % for 5 mm GGNs (Oda et al. 2010).

In addition to increased size of volume, subsolid nodules may show other growth patterns. They can show increase in attenuation, newly appeared or increased solid component, or decrease in overall size with increased solid component. To reflect these growth patterns, a measure of mass has been devised which can be calculated by multiplying nodule volume with nodule attenuation (Fig. 5). In a study by de Hoop et al., mass showed less variability and less mean time, required in determining growth than diameter or volume, which indicates that mass measurements can enable the detection of growth of subsolid nodules earlier than volume or diameter measurements (de Hoop et al. 2010). When the

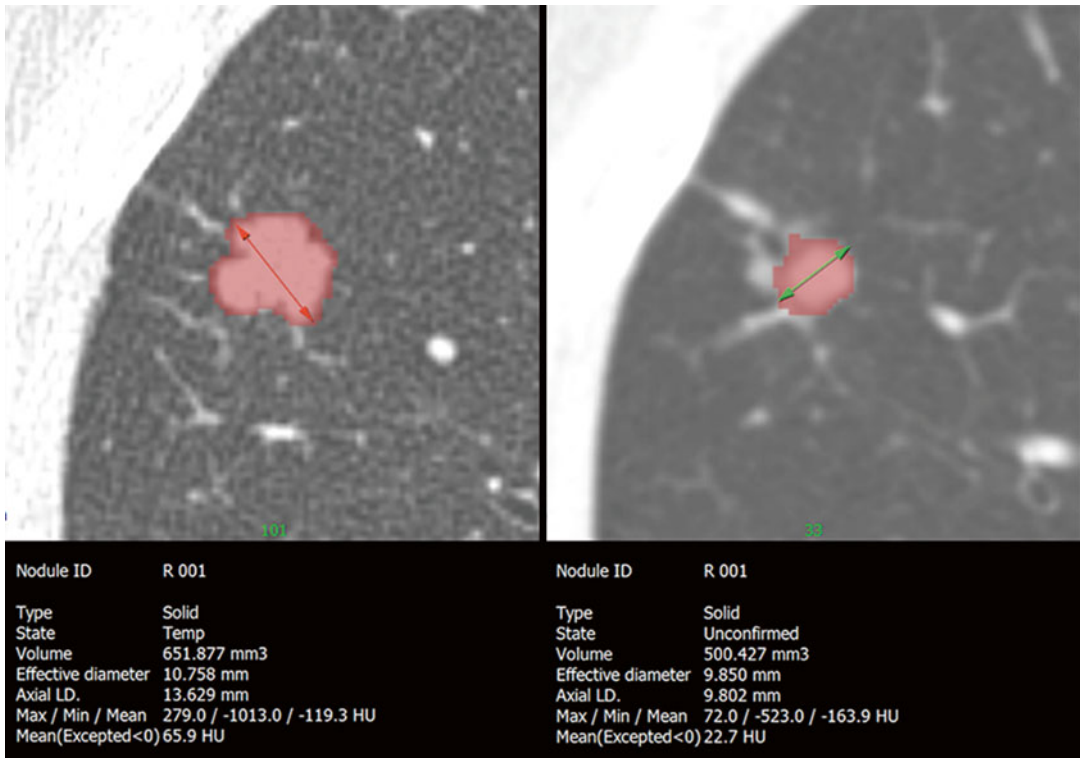

Fig. 4 CT scans of 1 mm section thickness (*left*) and 3 mm section thickness (*right*) obtained from the same raw CT data result in 26 % difference in nodule volume measurements

interscan variability of volume and mass measurement of GGN was assessed with a same-day repeat CT study, they were reported to be up to 19 % (Kim et al. 2013).

In the staging of lung adenocarcinoma, it has been suggested that the size T factor should be adjusted only to the invasive component pathologically in invasive tumors with lepidic areas. In a CT-pathology correlation study, the size of the solid component in subsolid nodules on CT has a significant correlation with the invasive component of lung adenocarcinoma on pathology (Lee et al. 2014). In an attempt to segment the solid component in subsolid nodules, a threshold of −300 HU demonstrated a good sensitivity (90 %) and specificity (88 %) (Scholten et al. 2015) (Fig. 6).

3.4 Nodule Characterization

The likelihood of nodule malignancy has been determined by experienced radiologists' visual assessment mainly based on morphology and internal composition of a nodule. Various nodule features can be quantitated according to the shape of the nodule such as sphericity and the internal configuration of the nodule such as mean attenuation or homogeneity. CAD output generated with this process may be used in determining nodule malignancy. In a study by Awai et al., the use of CAD output generated from 56 morphologic features and two clinical datasets improved the diagnostic performance of residents for the assessment of nodule malignancy while it did not improve that of radiologists (Awai et al. 2006). Texture analysis, which uses attenuation values of each voxel and their distribution within target lesions, can also provide a quantitative imaging analysis tool (Fig. 7). This approach has been applied to categorize lung adenocarcinoma manifested as subsolid nodules. In a study by Chae et al., higher kurtosis and smaller mass are significant predictors of preinvasive lesions from invasive adenocarcinomas (Chae et al. 2014).

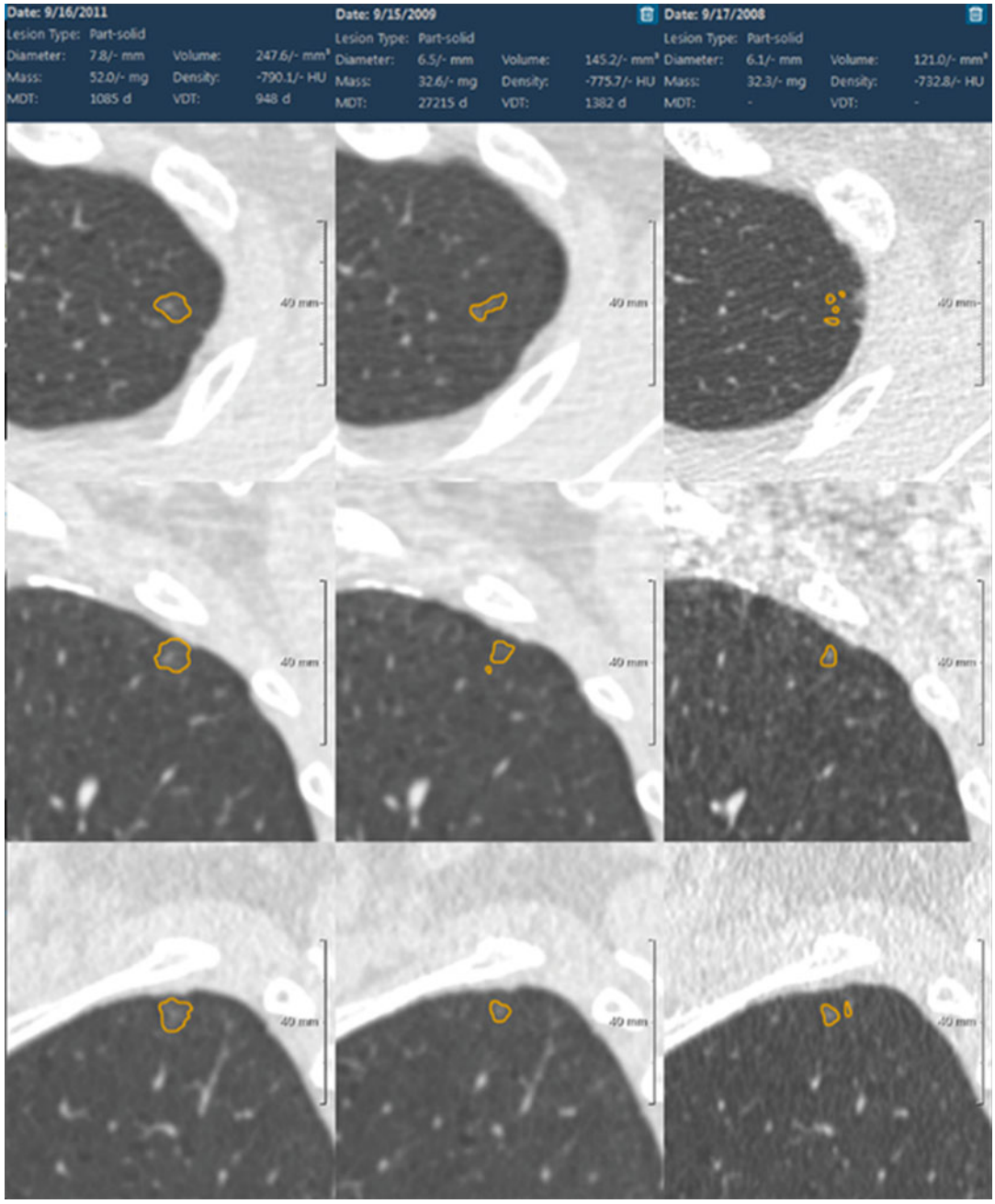

Fig. 5 Serial CT scans of a subsolid nodule show increase in diameter, volume, and mass of subsolid nodule

Similar attempt to differentiate invasive adenocarcinoma from preinvasive or minimally invasive adenocarcinoma showed that the 75th percentile CT attenuation value and entropy are predictors for invasive adenocarcinoma (Son et al. 2014).

3.5 Nodule Matching in Follow-Up CT

Evaluating changes of nodules between a former CT scan and a current follow-up CT scan is a routine clinical task, which is typically performed by

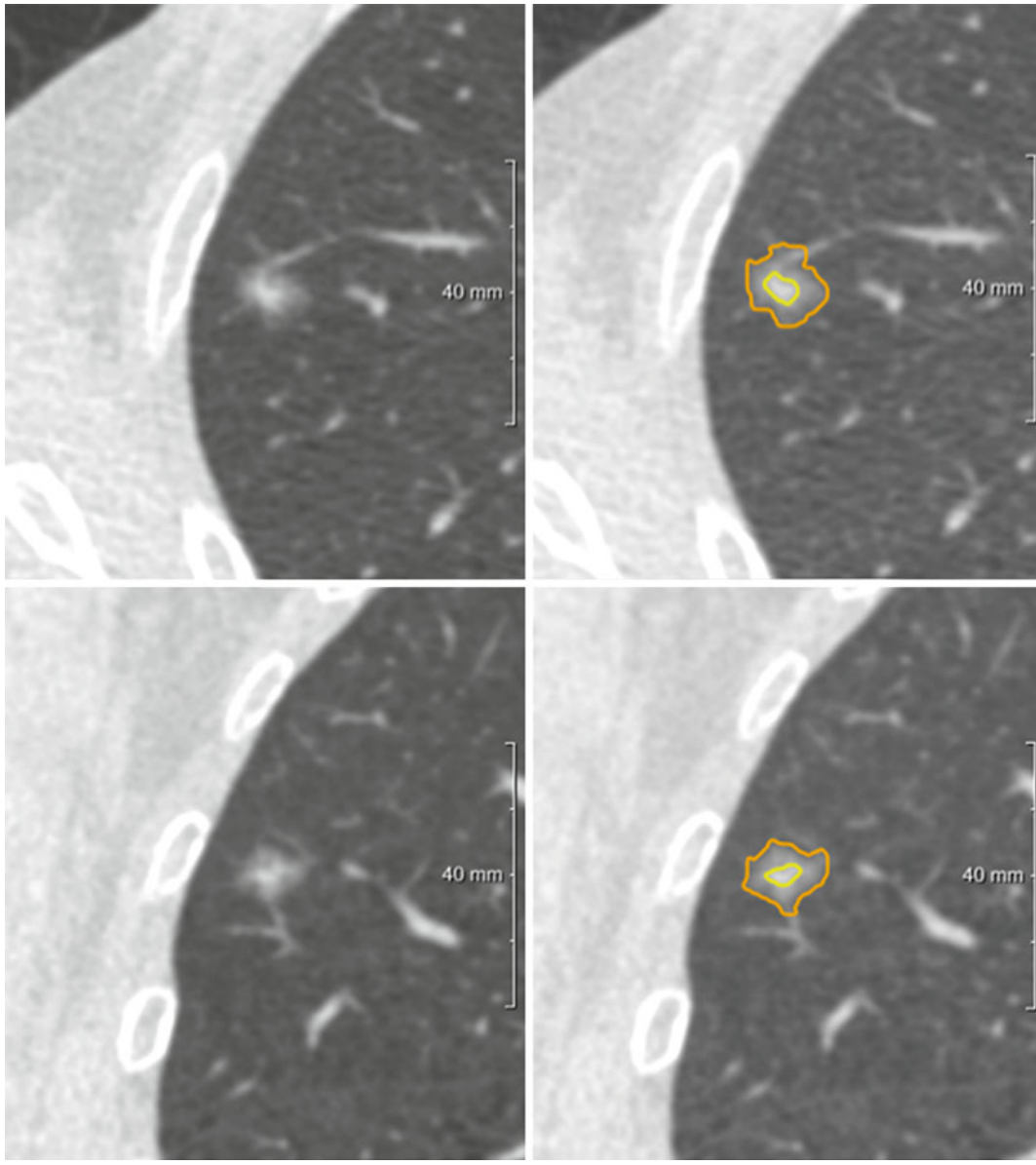

Fig. 6 Axial (*upper*) and coronal (*lower*) CT scans of a part-solid nodule (*left*) and its segmentation results (*right*) separating GGO component from solid component

manual matching of two CT scans requiring large efforts and time. Registration techniques can be applied to improve work efficiency in this task. When two serial CT scans with a 5-mm section thickness in patients with metastatic lung nodules were evaluated, the overall matching rate was 67 % (Lee et al. 2007). Higher matching rate (82 %) could be achieved on CT scans with a relatively unchanged lung configuration than on CT scans with substantial interval changes (29 %). As the change of lung configuration is small in lung screening settings, the matching rates on screening CT were reported to be 91–93 % (Beigelman-Aubry et al. 2007; Tao et al. 2009).

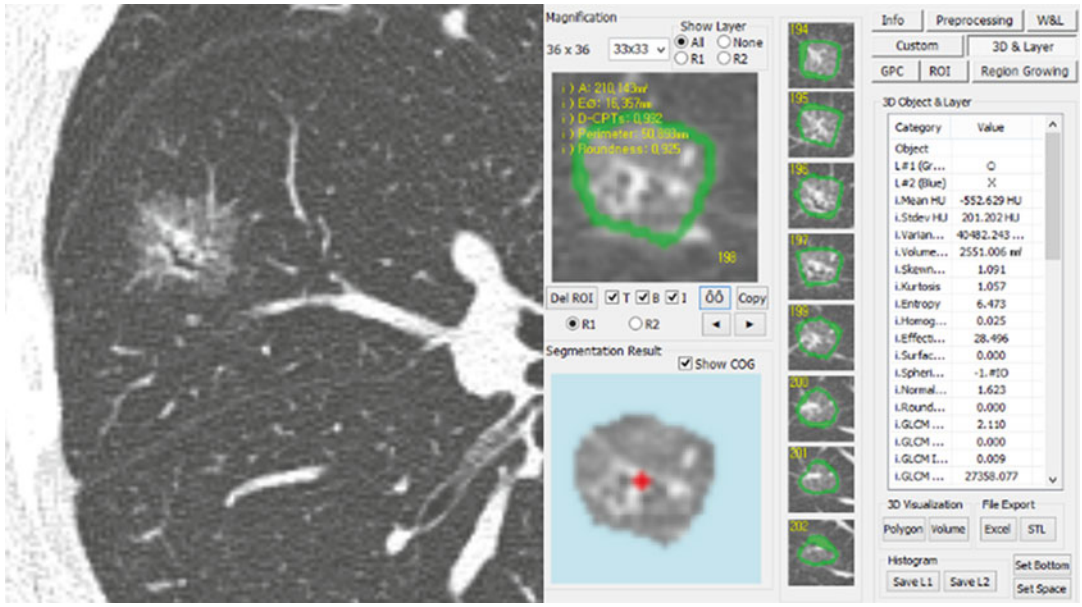

Fig. 7 Texture analysis of subsolid nodule. After segmenting a nodule, various texture features can be calculated as shown in the *right side* table (Courtesy of Park CM, Seoul National University Hospital, Seoul, Korea)

3.6 Role of CAD in Nodule Management

Nodule management in a screening setting usually starts with the assessment to determine the presence or absence of a nodule, the size of nodule, and the attenuation of a nodule whether it is solid, part solid, or pure GGN. Although this looks like a simple approach, considerable variability has been reported among readers. In a study by Jeon et al., the agreement for the positivity of the screening results and follow-up recommendations could be improved from moderate (multirater kappa value, 0.53–0.54) at initial reading to good (multirater kappa value, 0.66–0.67) after reviewing CAD results (Jeon et al. 2012). CAD can be helpful in the classification of lung nodules according to the nodule attenuation. Pairwise agreements for the differentiation between solid nodule, part-solid nodule, and pure GGN were similar between CAD and each of the reader (kappa value, 0.54–0.72) and between readers (kappa value, 0.56–0.81) (Jacobs et al. 2015). The nodule volumetry can also play an important role in lung cancer screening. In the NELSON trial, the nodule volumetry and estimated volume-doubling time proved to be an effective tool to limit the number of follow-up CT examinations and the overuse of invasive procedures (van Klaveren et al. 2009) (Fig. 8).

4 Chronic Obstructive Lung Diseases

COPD is currently the third most common cause of death in the United States, and mortality from COPD has increased progressively over the last 10 years. As COPD is defined as a disease characterized by persistent airflow limitation caused by the combination of parenchymal destruction (emphysema) and remodeling of the small airways, its diagnosis is made with spirometry. Although pulmonary function tests (PFTs) are reproducible tests and a mainstay in the evaluation of COPD, they represent global measurements of lung function of airways that contribute unequally to airflow. With similar levels of functional impairment, the morphologic manifestations of COPD vary widely. CT can help

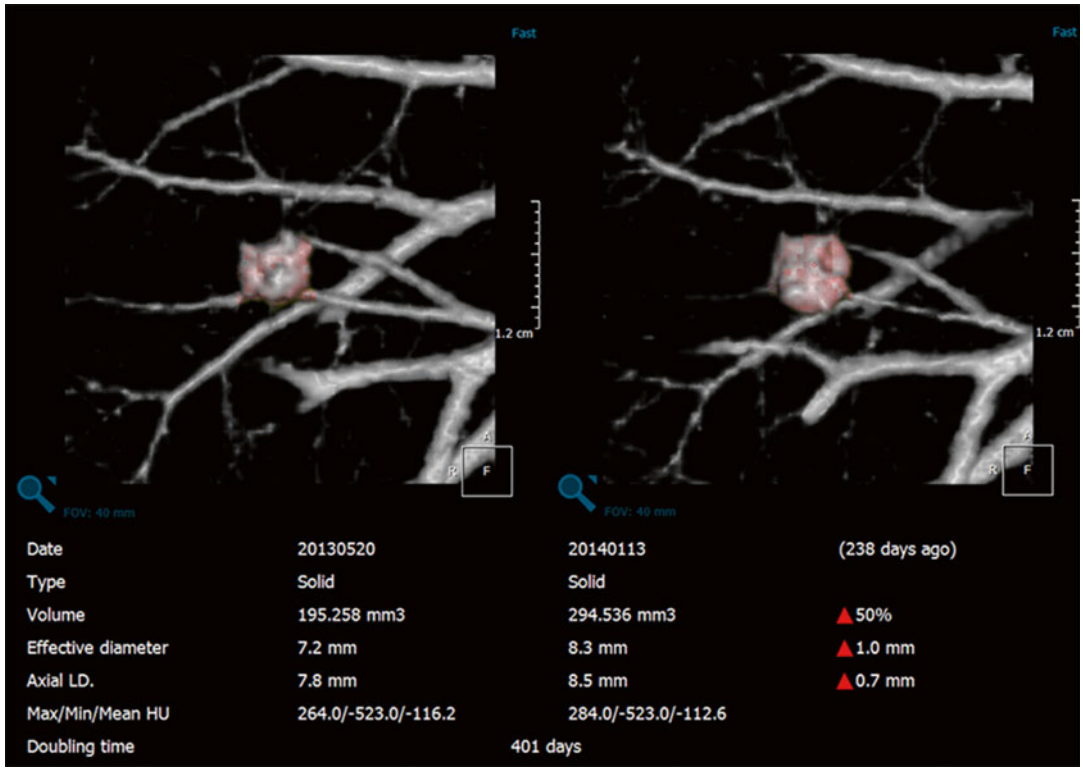

Fig. 8 CT scans obtained at an interval of 238 days shows a growth of a nodule with volume-doubling time of 401 days. This nodule turned out to be lung adenocarcinoma

understanding the heterogeneity of COPD by subphenotyping it into emphysema, large airway abnormality, and small airway obstruction.

Conventional CT analyses of COPD consist of visual assessment to determine the presence, characteristics, and extent of emphysema, airway wall thickening, and air trapping. With the vigorous investigations using quantitative CT, chest CT has become an established modality in quantifying emphysema and measuring various airway dimensions and degree of air trapping.

4.1 Quantification of Emphysema

Emphysema, which is an abnormal permanent enlargement of airspaces distal to the terminal bronchioles accompanied by destruction of alveolar walls, results in replacing the normal lung parenchyma with air-containing spaces. Therefore, areas of emphysema appear as hypoattenuated areas on CT.

Densitometric analysis for the quantification of emphysema was first introduced by Müller et al. (1988), which is based on a frequency distribution curve of voxels in the lung parenchyma according to CT attenuation coefficients (Yoon et al. 2013) (Fig. 9). Through a series of correlation studies between CT measurements and histology, threshold values representing areas of emphysema have been suggested. Although CT thresholds set at −960 HU or 970 HU showed the highest correlation with histologic emphysema (Madani et al. 2006), the threshold of −950 HU is more commonly used in the interests of balancing sensitivity and specificity (Heussel et al. 2009; Coxson et al. 2013; Regan et al. 2010) (Fig. 10). This measure is usually expressed as emphysema index, percentage of low attenuation area (%LAA), or relative area (RA) of the lung. The size and number of LAA clusters can be

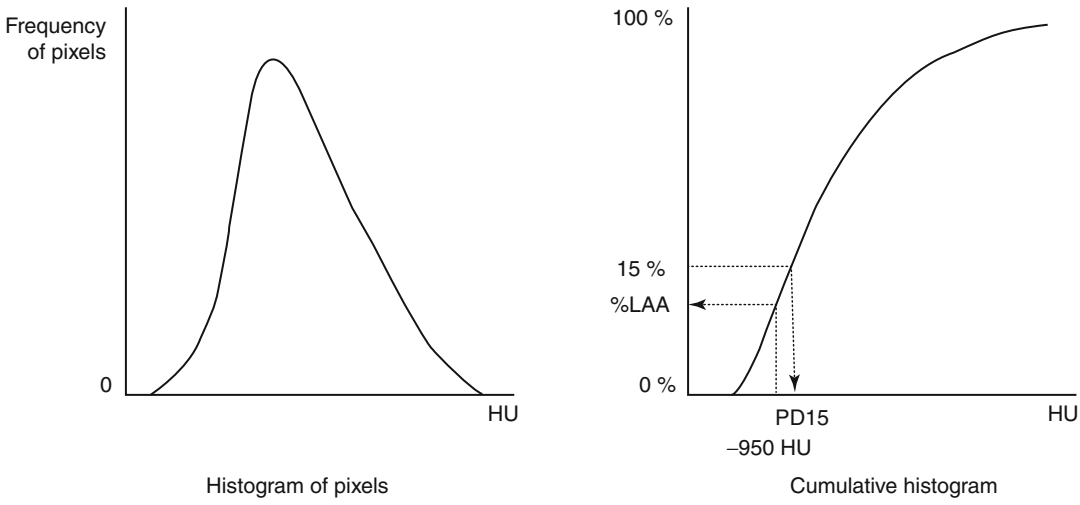

Fig. 9 After segmenting the lung, all the pixels can be plotted according to the attenuation of the pixels resulting in a histogram of pixels. This can be converted to a cumulative histogram, which can be used to calculate %LAA for a specific threshold or a percentile density corresponding to a specific percentile of the lung

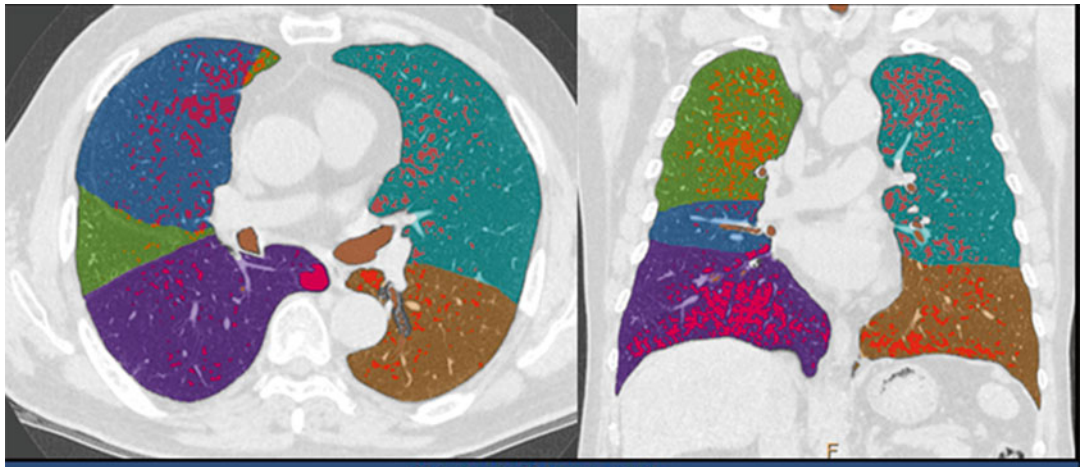

Volumetric Measurements			
	Volumetric Measurements		
	Threshold = -950 HU		
	Emphysema Volume(cc)	Total Volume(cc)	Emphysema Ratio(%)
Both Lungs	624.3	5606.8	11.1
Right Lung	351.2	2904.4	12.1
Right Upper Lobe (RUL)	73.5	1060.1	6.9
Right Middle Lobe (RML)	66.7	408.9	16.3
Right Lower Lobe (RLL)	211	1435.4	14.7
Left Lung	273.1	2702.3	10.1
Left Upper Lobe (LUL)	131.1	1345.8	9.7
Left Lower Lobe (LLL)	142	1356.5	10.5

Fig. 10 Lobe-based analysis of LAA showing color overlay with red color using a threshold of –950HU. The table shows the volume of LAA (emphysema volume) and the proportion of LAA to the lung volume (emphysema ratio)

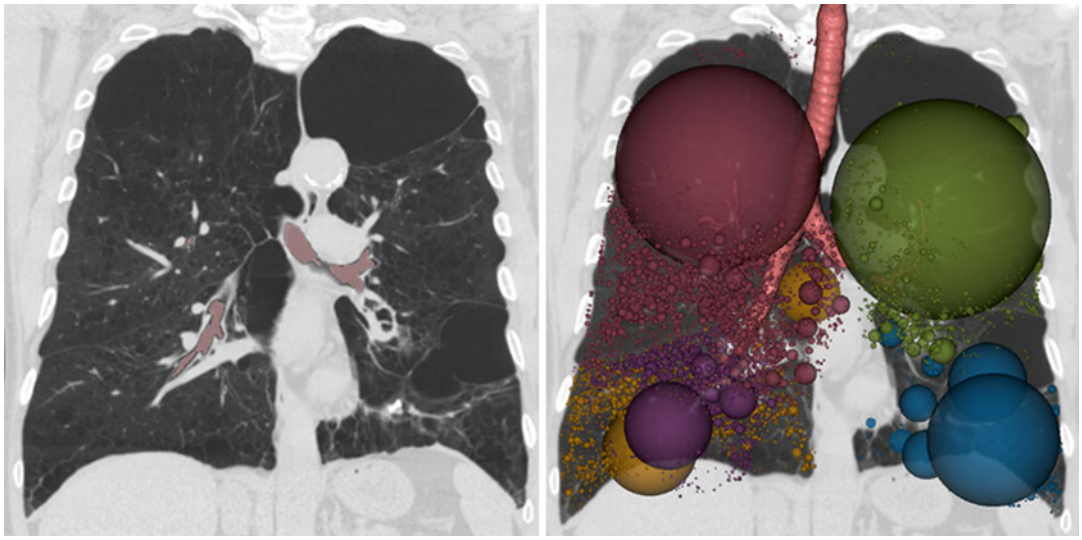

Fig. 11 Coronal CT (*left*) showing extensive emphysema and 3-D representation (*right*) for an index of the size of the low-attenuation clusters (Courtesy of Jin GY, Chonbuk National University Hospital, Jeonju, Korea)

calculated by grouping adjacent low-attenuation voxels together (Fig. 11). With progression of disease, the LAA clusters decrease in number but increase in size, which can be expressed as a fractal dimension, defined as the slope of the cumulative frequency-size distribution of the %LAA (Mishima et al. 1999). Another approach to emphysema quantification is the percentile density method to determine the CT attenuation at a given percentile along the histogram, and the 15th percentile (PD15) is a frequently used point (Fig. 9). A higher PD15 value indicates less emphysema (Heussel et al. 2009; Coxson et al. 2013). The percentile density method approach is reported to be more robust for longitudinal evaluation of emphysema and less sensitive to changes in lung volume (Dirksen 2008).

There are many factors that can affect the quantification of emphysema: lung volume, CT parameters, and status of smoking. When CT scans obtained at 100, 90, 80, 70, and 50% of vital capacity were evaluated, the %LAA at vital capacity lower than 100% decreased significantly from that at 100% vital capacity even though the difference was as small as 2–3% between 100% vital capacity and 90% vital capacity (Madani et al. 2010). Therefore, in CT scanning for emphysema quantification, careful coaching of respiratory maneuver to patients is essential. Correction for lung volume can also be employed to reduce the variability in longitudinal studies (Stoel et al. 2008; Park et al. 2012). As for CT parameters, section thickness, tube currents, and reconstruction algorithms can affect the quantification. The %LAA can decrease with increasing slice thickness and increasing tube current (Madani et al. 2007). Because the edge-enhancing reconstruction algorithms result in increased %LAA due to increased noise (Boedeker et al. 2004), a standard or smooth reconstruction algorithm is recommended in the emphysema quantification. By applying iterative reconstruction algorithms, the %LAA decreases compared with CT using filtered back projection (Choo et al. 2014). Therefore, standardization of CT parameters and maintaining the same technique are crucial in longitudinal studies. The relationship between the smoking status and %LAA is somewhat paradoxical: lower %LAA in current smokers than in former smokers and increased %LAA after smoking cessation (Grydeland et al. 2009; Ashraf et al. 2011). The potential explanation for these phenomena is that the increase of inflammatory cells in the lung can be caused by smoking and results in increased lung attenuation.

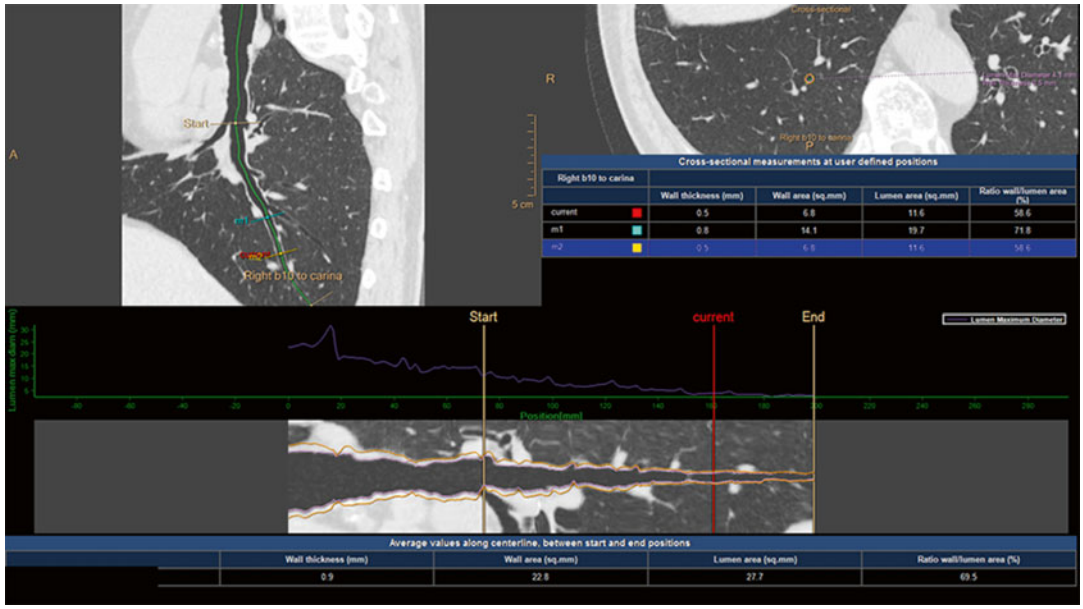

Fig. 12 Curved planar reformation of the bronchial pathway to the right lower lobe (*upper left and bottom*) and orthogonal cross section of the subsubsegmental bronchus in the right lower lobe (*upper right*) show various metrics of airway dimensions

The clinical value of CT quantification of emphysema is that it has close relationship with PFT (Kinsella et al. 1990; Park et al. 1999). Although CT scan in the evaluation of emphysema is usually obtained at inspiration, the %LAA at expiration better reflects PFT than that at inspiration (Kauczor et al. 2002). In addition to the cross-sectional study, CT is now being used for longitudinal studies (Coxson et al. 2013; Regan et al. 2010). In one cohort study which evaluated a longitudinal change over 3 years in 1928 patients with COPD, the annual decline of PD15 was more rapid in women than men and in current smokers than in former smokers, while baseline age, smoking history, airflow limitation, and exacerbation history had no effect (Coxson et al. 2013).

4.2 Measurement of Large Airways

Airway wall remodeling occurs in patients with COPD, and airflow obstruction can be caused by airway wall thickening. These changes on large airways can be seen on CT scan but visual assessment of airway wall thickening is quite subjective. With the increase use of thin-section volumetric chest CT, obtaining various metrics of airway dimensions has become more feasible. Airway luminal area, wall thickness or area, and wall area percent can be calculated to the level of 5th or 6th branches of airways. To produce these measures, after segmenting the airways, a short-axis image is reconstructed in a plane perpendicular to the long axis of the selected airways (Fig. 12). Pi10 is devised to report the summary measures of airways, which is the square root of the wall area of a hypothetical bronchus of internal perimeter 10 mm. This is calculated from the linear regression by plotting the square root of the airway wall area against the internal perimeter of all measured airways (Fig. 13).

Nakano et al. showed that the airway wall area measured at the apical bronchus has an inverse relationship with FEV_1 (Nakano et al. 2000), and subsequent studies on the measurement of airways reported similar results (Berger et al. 2005; Hasegawa et al. 2006). The correlation between

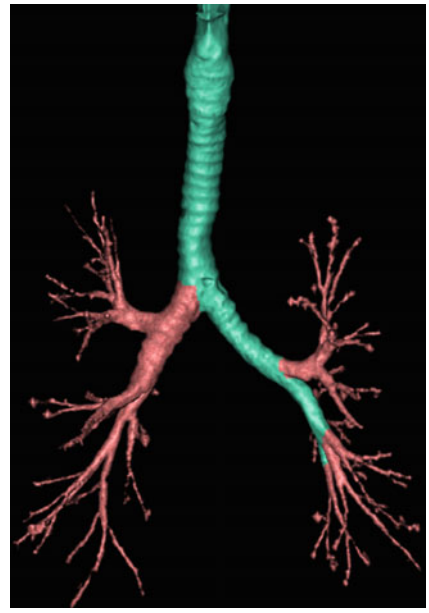

	Average inner Area (mm^2)	Average inner perimeter (mm)	Luminal eccentricity	Average wall thickness (mm)	Wall area (mm^2)	Wall area%
Trachea	280.00	60.15	0.79	2.74	191.02	40.54
LMB	110.06	38.01	0.95	1.89	82.34	42.81
LLB6	77.17	31.92	0.80	1.69	62.55	44.77
LLB	61.96	28.24	0.88	1.75	58.58	48.60
LB10	71.90	32.65	0.56	1.67	46.41	37.21

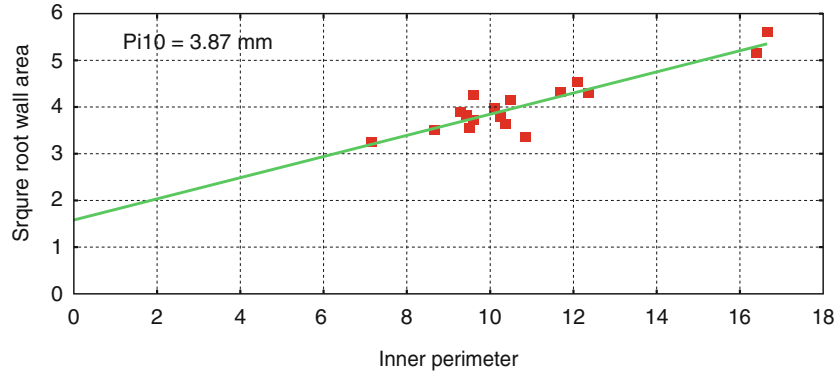

Fig. 13 Three-dimensional display of the airway with various metrics of airways. A graph at the *bottom* shows how Pi10 was plotted (Courtesy of Jin GY, Chonbuk National University Hospital, Jeonju, Korea)

the airway wall area and airflow limitation tended to be stronger at more distal generations of the bronchi (Hasegawa et al. 2006), and airway wall thickness was larger in smokers with COPD than in smokers or nonsmokers without COPD (Berger et al. 2005). Although the direct measurement of small airways is not feasible or shows large errors, as there is a significant association between the dimensions of the small and large airways, the measurement of the large airways on CT may be used in estimating the changes in the small airways (Nakano et al. 2005).

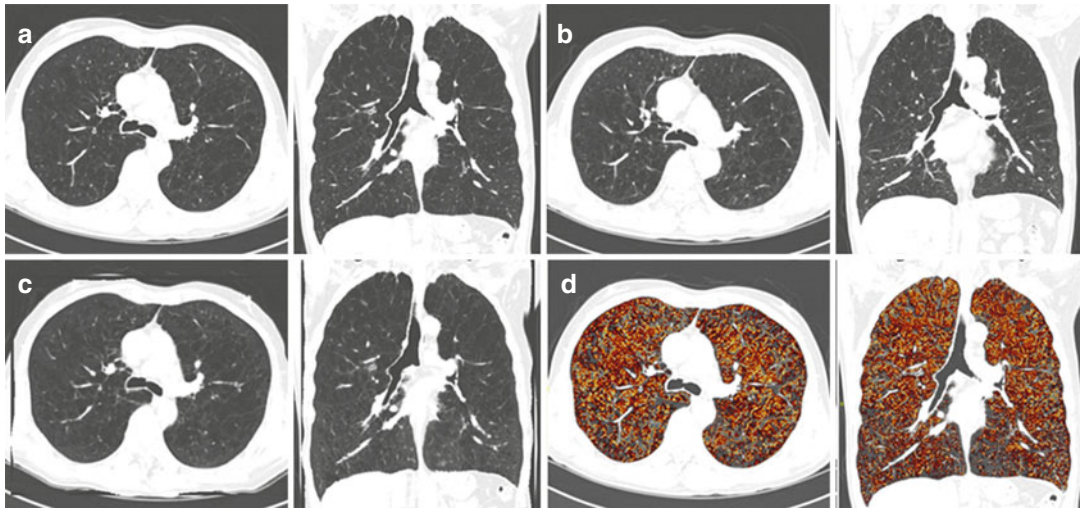

Fig. 14 CT scans obtained at inspiration (**a**) and at expiration (**b**) are used to generate deformed expiration CT images (**c**) with registration techniques. By subtraction of inspiratory CT and deformed expiratory CT, an air-trapping subtraction map (**d**) can be generated (Courtesy of Seo JB, Asan Medical Center, Seoul, Korea)

4.3 Assessment of Small Airway Disease

Small airways are airways with a diameter of 2 mm or less and the main sites of airflow obstruction in COPD. If we consider measurement errors, direct measurement of the wall or lumen of these airways is beyond the range of spatial resolution of current chest CT. Therefore, visual assessment of small airways on CT is based on the indirect findings of air trapping on expiratory CT scan obtained at functional residual capacity or at residual volume. On the other hand, a quantitative analysis of air trapping is challenging, and attenuation-based techniques similar to the quantification of emphysema have been proposed by applying a threshold of −856 or 850 HU at expiratory CT (Regan et al. 2010). The %LAA at expiration shows high correlations with the FEV_1/FVC and with the predicted FEV_1. By combining information of %LAA at inspiration and expiration, COPD subjects may be categorized into predominant emphysema, mixed emphysema and air trapping, and predominant air trapping. Other quantitative approaches for air trapping include the lung volume or attenuation ratio of inspiratory to expiratory CT and the relative volume change of voxels between inspiratory to expiratory CT with attenuation values between −860 HU and −950 HU. The drawback of an attenuation-based technique is that emphysema as well as small airway disease contributes to %LAA of specific thresholds. To overcome this limitation, Galbán et al. proposed a parametric response map which is generated with a voxel-by-voxel co-registration of inspiratory and expiratory CT scans (Galban et al. 2012). Deformable registration is used to spatially align the expiratory scan to the inspiratory scan (Fig. 14) and then classification of voxels in the map into areas of normal parenchyma, small airway disease, and emphysema. This map provides information on the local distribution and extent of COPD phenotypes of small airway disease and emphysema as well as global measures.

5 Diffuse Interstitial Lung Diseases

Impairment of pulmonary function expressed as reduced DLCO and FVC levels is consistently associated with increased mortality in patients with DILD. Although changes in FVC are the most widely used endpoint in drug trials, because of its poor sensitivity to change, it is hard to interpret marginal changes of 5–10 % in an individual (Hansell et al. 2015). Meanwhile,

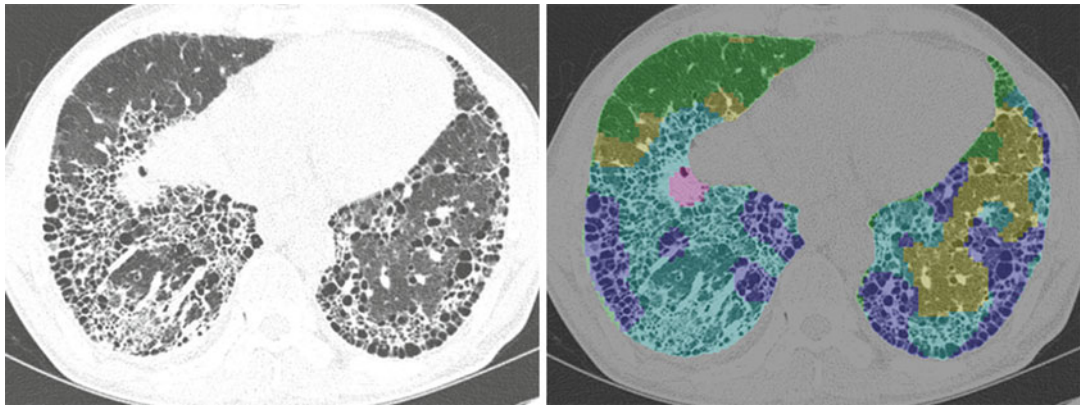

Fig. 15 Transverse CT scan (*left*) and texture-based quantification map (*right*) in a patient with IPF show the areas of different regional patterns expressed as different color overlay on the map: normal (*green*); ground-glass opacity (*yellow*); reticular opacity (*cyan*); consolidation (*pink*); honeycombing (*violet*) (Courtesy of Seo JB, Asan Medical Center, Seoul, Korea)

thin-section CT has been an essential component in making a diagnosis of DILD, but optimal use of CT in monitoring diffuse lung disease was not established. With the recent approval of new drugs by the US Food and Drug Administration for the treatment of idiopathic pulmonary fibrosis (IPF), the quantification of the extent of DILD on CT has become a more important issue (Hansell et al. 2015). In the clinical trials, CT may provide an effective endpoint in addition to PFTs and other biomarkers. Methods to assess disease extent on CT are being investigated from simple visual estimates to sophisticated software quantification. In the past, high-resolution CT scan was obtained with a limited number of thin sections at specific intervals with skipped volume. This approach was employed initially due to limited CT performance, but this technique can be used to reduce radiation exposure to patients. As this non-contiguous imaging is problematic in monitoring disease extent in serial CT scans, contiguous volumetric acquisition of CT is now recommended.

CT findings related with fibrotic interstitial lung diseases are ground-glass opacity, reticular opacity, traction bronchiectasis, and honeycombing. The extent of fibrosis on CT in patients with IPF was reported to be an important predictor of mortality (Lynch et al. 2005). Semiquantitative visual estimation of disease extent has been performed typically on several sections of thin-section CT. However, even among thoracic radiologists, there is considerable variability in defining the presence or absence of these findings (Watadani et al. 2013). Interobserver variability is inevitable in this visual assessment but can be reduced by reader training with standard image references.

5.1 Semiautomated Analysis

A texture-based adaptive multiple feature method was developed to evaluate the lung parenchyma on thin-section CT and showed overall accuracy of 81 % in differentiating four groups of normal subjects and those with emphysema, IPF, or sarcoidosis (Uppaluri et al. 1999). In a study which evaluated the feasibility of automated quantification of regional disease patterns on CT, after training the CAD system by the use of typical ROIs representing patterns of normal, GGO, reticular opacity, honeycombing, emphysema, and consolidation, the overall accuracy of the system in classifying each disease pattern was 89 % (Park et al. 2009) (Fig. 15). When similar approach was employed in evaluating short-term changes in patients with IPF, interval changes in volume of reticular opacity,

total volume of interstitial abnormalities, and % total interstitial abnormalities were predictive of survival after a median follow-up of 2.4 years (Maldonado et al. 2014). This CAD output may be used to generate a composite score which incorporates elements from clinical, radiological, and physiological assessments to predict patients' outcome more effectively than using a single test.

6 Perspective

With the continuous improvement of computer technology, image analyses in future radiology will be more quantitative and more objective using extracted features from images. Although many studies have shown advantages of CAD systems in improving radiologists' performance, the CAD is not widely used as a component of routine clinical practice. While undoubtedly multifactorial, in addition to much room for improvement of CAD performance, a major contributing reason is workflow issue which can be enhanced by seamless incorporation of a CAD system into a PACS environment. Protocol-based sending of CT images to CAD server, preprocessing and generation of CAD results before clinical reading, and robust, easy-to-use manual modification tools for CAD results are a few examples to enhance workflow in the use of CAD. We may use CAD programs consisting of several CAD algorithms targeting different disease entities. For example, a CAD program for low-dose CT scan used in lung cancer screening can be equipped with modules for a lung nodule, COPD, and calcium scoring. By combining the CAD results with the clinical data, prediction models and decision-assistant tools will be available.

To compare CAD results in longitudinal examinations, at the moment it is essential to obtain CT images with the same CT scanner and the same scanning protocol and to analyze with the same version of a CAD program. However, this can be performed only in an ideal research setting and it cannot be applied in daily clinical practice. There can be several measures to reduce measurement variability obtained at non-ideal situations. The use of standardized protocols helps to allow multicenter studies. The vendor should discuss with researchers how the CT outputs across CT vendors can be minimized. Compensation or prediction methods for measurement variability according to various factors may help in comparing quantitative measures obtained in different settings.

References

Armato SG 3rd, McLennan G, McNitt-Gray MF et al (2004) Lung image database consortium: developing a resource for the medical imaging research community. Radiology 232:739–748

Ashraf H, Lo P, Shaker SB et al (2011) Short-term effect of changes in smoking behaviour on emphysema quantification by CT. Thorax 66:55–60

Awai K, Murao K, Ozawa A et al (2006) Pulmonary nodules: estimation of malignancy at thin-section helical CT – effect of computer-aided diagnosis on performance of radiologists. Radiology 239:276–284

Beigelman-Aubry C, Raffy P, Yang W, Castellino RA, Grenier PA (2007) Computer-aided detection of solid lung nodules on follow-up MDCT screening: evaluation of detection, tracking, and reading time. AJR Am J Roentgenol 189:948–955

Berger P, Perot V, Desbarats P, Tunon-de-Lara JM, Marthan R, Laurent F (2005) Airway wall thickness in cigarette smokers: quantitative thin-section CT assessment. Radiology 235:1055–1064

Beyer F, Zierott L, Fallenberg EM et al (2007) Comparison of sensitivity and reading time for the use of computer-aided detection (CAD) of pulmonary nodules at MDCT as concurrent or second reader. Eur Radiol 17:2941–2947

Boedeker KL, McNitt-Gray MF, Rogers SR et al (2004) Emphysema: effect of reconstruction algorithm on CT imaging measures. Radiology 232:295–301

Chae HD, Park CM, Park SJ, Lee SM, Kim KG, Goo JM (2014) Computerized texture analysis of persistent part-solid ground-glass nodules: differentiation of preinvasive lesions from invasive pulmonary adenocarcinomas. Radiology 273:285–293

Choo JY, Goo JM, Lee CH, Park CM, Park SJ, Shim MS (2014) Quantitative analysis of emphysema and airway measurements according to iterative reconstruction algorithms: comparison of filtered back projection, adaptive statistical iterative reconstruction and model-based iterative reconstruction. Eur Radiol 24:799–806

Coxson HO, Dirksen A, Edwards LD et al (2013) The presence and progression of emphysema in COPD as determined by CT scanning and biomarker expression: a prospective analysis from the ECLIPSE study. Lancet Respir Med 1:129–136

de Hoop B, Gietema H, van Ginneken B, Zanen P, Groenewegen G, Prokop M (2009) A comparison of six software packages for evaluation of solid lung nodules using semi-automated volumetry: what is the minimum increase in size to detect growth in repeated CT examinations. Eur Radiol 19:800–808

de Hoop B, Gietema H, van de Vorst S, Murphy K, van Klaveren RJ, Prokop M (2010) Pulmonary ground-glass nodules: increase in mass as an early indicator of growth. Radiology 255:199–206

Dirksen A (2008) Monitoring the progress of emphysema by repeat computed tomography scans with focus on noise reduction. Proc Am Thorac Soc 5:925–928

Doi K, Giger ML, MacMahon H et al (1992) Computer-aided diagnosis: development of automated schemes for quantitative analysis of radiographic images. Semin Ultrasound CT MR 13:140–152

Galban CJ, Han MK, Boes JL et al (2012) Computed tomography-based biomarker provides unique signature for diagnosis of COPD phenotypes and disease progression. Nat Med 18:1711–1715

Godoy MC, Kim TJ, White CS et al (2013) Benefit of computer-aided detection analysis for the detection of subsolid and solid lung nodules on thin- and thick-section CT. AJR Am J Roentgenol 200:74–83

Goo JM (2011) A computer-aided diagnosis for evaluating lung nodules on chest CT: the current status and perspective. Korean J Radiol 12:145–155

Goo JM, Tongdee T, Tongdee R, Yeo K, Hildebolt CF, Bae KT (2005) Volumetric measurement of synthetic lung nodules with multi-detector row CT: effect of various image reconstruction parameters and segmentation thresholds on measurement accuracy. Radiology 235:850–856

Goo JM, Kim KG, Gierada DS, Castro M, Bae KT (2006) Volumetric measurements of lung nodules with multi-detector row CT: effect of changes in lung volume. Korean J Radiol 7:243–248

Grydeland TB, Dirksen A, Coxson HO et al (2009) Quantitative computed tomography: emphysema and airway wall thickness by sex, age and smoking. Eur Respir J 34:858–865

Hansell DM, Goldin JG, King TE Jr, Lynch DA, Richeldi L, Wells AU (2015) CT staging and monitoring of fibrotic interstitial lung diseases in clinical practice and treatment trials: a Position Paper from the Fleischner society. Lancet Respir Med 3:483–496

Hasegawa M, Nasuhara Y, Onodera Y et al (2006) Airflow limitation and airway dimensions in chronic obstructive pulmonary disease. Am J Respir Crit Care Med 173:1309–1315

Heussel CP, Herth FJ, Kappes J et al (2009) Fully automatic quantitative assessment of emphysema in computed tomography: comparison with pulmonary function testing and normal values. Eur Radiol 19:2391–2402

Jacobs C, van Rikxoort EM, Scholten ET et al (2015) Solid, part-solid, or non-solid?: classification of pulmonary nodules in low-dose chest computed tomography by a computer-aided diagnosis system. Invest Radiol 50:168–173

Jeon KN, Goo JM, Lee CH et al (2012) Computer-aided nodule detection and volumetry to reduce variability between radiologists in the interpretation of lung nodules at low-dose screening computed tomography. Invest Radiol 47:457–461

Kauczor HU, Hast J, Heussel CP, Schlegel J, Mildenberger P, Thelen M (2002) CT attenuation of paired HRCT scans obtained at full inspiratory/expiratory position: comparison with pulmonary function tests. Eur Radiol 12:2757–2763

Kim KG, Goo JM, Kim JH et al (2005) Computer-aided diagnosis of localized ground-glass opacity in the lung at CT: initial experience. Radiology 237:657–661

Kim H, Park CM, Woo S et al (2013) Pure and part-solid pulmonary ground-glass nodules: measurement variability of volume and mass in nodules with a solid portion less than or equal to 5 mm. Radiology 269:585–593

Kinsella M, Muller NL, Abboud RT, Morrison NJ, DyBuncio A (1990) Quantitation of emphysema by computed tomography using a "density mask" program and correlation with pulmonary function tests. Chest 97:315–321

Lee JW, Goo JM, Lee HJ, Kim JH, Kim S, Kim YT (2004) The potential contribution of a computer-aided detection system for lung nodule detection in multidetector row computed tomography. Invest Radiol 39:649–655

Lee KW, Kim M, Gierada DS, Bae KT (2007) Performance of a computer-aided program for automated matching of metastatic pulmonary nodules detected on follow-up chest CT. AJR Am J Roentgenol 189:1077–1081

Lee KH, Goo JM, Park SJ et al (2014) Correlation between the size of the solid component on thin-section CT and the invasive component on pathology in small lung adenocarcinomas manifesting as ground-glass nodules. J Thorac Oncol 9:74–82

Lynch DA, Godwin JD, Safrin S et al (2005) High-resolution computed tomography in idiopathic pulmonary fibrosis: diagnosis and prognosis. Am J Respir Crit Care Med 172:488–493

Madani A, Zanen J, de Maertelaer V, Gevenois PA (2006) Pulmonary emphysema: objective quantification at multi-detector row CT – comparison with macroscopic and microscopic morphometry. Radiology 238:1036–1043

Madani A, De Maertelaer V, Zanen J, Gevenois PA (2007) Pulmonary emphysema: radiation dose and section thickness at multidetector CT quantification – comparison with macroscopic and microscopic morphometry. Radiology 243:250–257

Madani A, Van Muylem A, Gevenois PA (2010) Pulmonary emphysema: effect of lung volume on objective quantification at thin-section CT. Radiology 257:260–268

Maldonado F, Moua T, Rajagopalan S et al (2014) Automated quantification of radiological patterns predicts survival in idiopathic pulmonary fibrosis. Eur Respir J 43:204–212

Marten K, Engelke C, Seyfarth T, Grillhosl A, Obenauer S, Rummeny EJ (2005) Computer-aided detection of pulmonary nodules: influence of nodule characteristics on detection performance. Clin Radiol 60:196–206

Matsumoto S, Ohno Y, Aoki T et al (2013) Computer-aided detection of lung nodules on multidetector CT in concurrent-reader and second-reader modes: a comparative study. Eur J Radiol 82:1332–1337

Mishima M, Hirai T, Itoh H et al (1999) Complexity of terminal airspace geometry assessed by lung computed tomography in normal subjects and patients with chronic obstructive pulmonary disease. Proc Natl Acad Sci U S A 96:8829–8834

Muller NL, Staples CA, Miller RR, Abboud RT (1988) "Density mask". An objective method to quantitate emphysema using computed tomography. Chest 94:782–787

Nakano Y, Muro S, Sakai H et al (2000) Computed tomographic measurements of airway dimensions and emphysema in smokers. Correlation with lung function. Am J Respir Crit Care Med 162:1102–1108

Nakano Y, Wong JC, de Jong PA et al (2005) The prediction of small airway dimensions using computed tomography. Am J Respir Crit Care Med 171:142–146

Oda S, Awai K, Murao K et al (2010) Computer-aided volumetry of pulmonary nodules exhibiting ground-glass opacity at MDCT. AJR Am J Roentgenol 194:398–406

Park KJ, Bergin CJ, Clausen JL (1999) Quantitation of emphysema with three-dimensional CT densitometry: comparison with two-dimensional analysis, visual emphysema scores, and pulmonary function test results. Radiology 211:541–547

Park SO, Seo JB, Kim N et al (2009) Feasibility of automated quantification of regional disease patterns depicted on high-resolution computed tomography in patients with various diffuse lung diseases. Korean J Radiol 10:455–463

Park SJ, Lee CH, Goo JM, Heo CY, Kim JH (2012) Interscan repeatability of CT-based lung densitometry in the surveillance of emphysema in a lung cancer screening setting. Eur J Radiol 81:e554–e560

Regan EA, Hokanson JE, Murphy JR et al (2010) Genetic epidemiology of COPD (COPDGene) study design. COPD 7:32–43

Rubin GD, Lyo JK, Paik DS et al (2005) Pulmonary nodules on multi-detector row CT scans: performance comparison of radiologists and computer-aided detection. Radiology 234:274–283

Scholten ET, Jacobs C, van Ginneken B et al (2015) Detection and quantification of the solid component in pulmonary subsolid nodules by semiautomatic segmentation. Eur Radiol 25:488–496

Son JY, Lee HY, Lee KS et al (2014) Quantitative CT analysis of pulmonary ground-glass opacity nodules for the distinction of invasive adenocarcinoma from pre-invasive or minimally invasive adenocarcinoma. PLoS One 9, e104066

Stoel BC, Putter H, Bakker ME et al (2008) Volume correction in computed tomography densitometry for follow-up studies on pulmonary emphysema. Proc Am Thorac Soc 5:919–924

Tao C, Gierada DS, Zhu F, Pilgram TK, Wang JH, Bae KT (2009) Automated matching of pulmonary nodules: evaluation in serial screening chest CT. AJR Am J Roentgenol 192:624–628

Uppaluri R, Hoffman EA, Sonka M, Hunninghake GW, McLennan G (1999) Interstitial lung disease: a quantitative study using the adaptive multiple feature method. Am J Respir Crit Care Med 159:519–525

van Ginneken B, Armato SG 3rd, de Hoop B et al (2010) Comparing and combining algorithms for computer-aided detection of pulmonary nodules in computed tomography scans: the ANODE09 study. Med Image Anal 14:707–722

van Klaveren RJ, Oudkerk M, Prokop M et al (2009) Management of lung nodules detected by volume CT scanning. N Engl J Med 361:2221–2229

Watadani T, Sakai F, Johkoh T et al (2013) Interobserver variability in the CT assessment of honeycombing in the lungs. Radiology 266:936–944

Wormanns D, Kohl G, Klotz E et al (2004) Volumetric measurements of pulmonary nodules at multi-row detector CT: in vivo reproducibility. Eur Radiol 14:86–92

Yanagawa M, Honda O, Yoshida S et al (2009) Commercially available computer-aided detection system for pulmonary nodules on thin-section images using 64 detectors-row CT: preliminary study of 48 cases. Acad Radiol 16:924–933

Yankelevitz DF, Reeves AP, Kostis WJ, Zhao B, Henschke CI (2000) Small pulmonary nodules: volumetrically determined growth rates based on CT evaluation. Radiology 217:251–256

Yoon SH, Goo JM, Goo HW (2013) Quantitative thoracic CT techniques in adults: can they be applied in the pediatric population? Pediatr Radiol 43:308–314

Zhao Y, de Bock GH, Vliegenthart R et al (2012) Performance of computer-aided detection of pulmonary nodules in low-dose CT: comparison with double reading by nodule volume. Eur Radiol 22:2076–2084

Computed Tomography of the Pediatric Chest

Shannon G. Farmakis and Marilyn J. Siegel

Abstract

Advances in multidetector computed tomography (CT) technology have revolutionized thoracic imaging in children. Faster scanning times, increased anatomic coverage, and high quality reconstructions have enabled CT to become a valuable tool in the evaluation of thoracic diseases. CT images are helpful in detecting, characterizing and determining the extent of abnormalities in the lungs, mediastinum, vasculature, chest wall and peridiaphragmatic regions. The information provided by these techniques can directly affect the treatment or aid in determining the prognosis of a patient.

This chapter highlights the diagnostic applications of CT in a wide variety of thoracic disease processes in children. General guidelines to aid in performing the CT examination also will be provided.

1 Introduction

The introduction of CT into clinical radiology has dramatically improved the diagnosis of thoracic diseases in children. This chapter addresses the areas in which multislice CT has already proved of value in the pediatric chest. The technical factors for optimizing the CT examination also are reviewed.

S.G. Farmakis, MD
St. Louis University School of Medicine,
SSM Health Cardinal Glennon Children's Hospital,
Saint Louis, MO 63104-1095, USA
e-mail: Farmakis@slu.edu

M.J. Siegel, MD (✉)
Mallinckrodt Institute of Radiology, Washington University School of Medicine,
510 South Kingshighway Blvd,
St Louis, MO 63110, USA
e-mail: siegelm@mir.wustl.edu

2 Patient Preparation

Pediatric patients have several inherent problems that are not present in adults, in particular, patient motion, small body size, and lack of perivisceral fat. These problems can be minimized or eliminated by the appropriate use of sedation and intravenous contrast medium.

2.1 Sedation

As the speed of CT increases, the need for sedation in the pediatric age group decreases (Pappas

U.J. Schoepf, F.G. Meinel (eds.), *Multidetector-Row CT of the Thorax*, Medical Radiology,
DOI 10.1007/978-3-319-30355-0_23

et al. 2000). Although the frequency has diminished, sedation has not been eliminated. Sedation will likely still be required for some infants and children 5 years of age and younger to prevent motion artifacts during scanning. Children older than 5 years of age generally will cooperate after verbal reassurance and explanation of the procedure and will not need immobilization or sedation. It also helps to ensure that the patient is comfortable, free of pain, and has an empty bladder.

Standards of care for sedation are based on recommendations from the Committee on Drugs, American Academy of Pediatrics (AAP) (Coté and Wilson 2006) and the American Society of Anesthesiologists (ASA) Task Force (Apfelbaum et al. 2012). Sedation for imaging examinations is nearly always conscious sedation. Conscious sedation is defined as a minimally depressed level of consciousness that retains the patient's abilities to maintain a patent airway, independently and continuously, and respond appropriately to physical stimulation and/or verbal command.

Sedative agents that are used for healthy infants and children include intravenous (IV) infusion of pentobarbital, propofol, and dexmedetomidine (Coté and Wilson 2006). Oral chloral hydrate has been a common sedative in children younger than 18 months. Midazolam can also be given for minimal sedation and anxiolysis. General anesthesia is used when a pediatric patient has comorbidities that are contraindications to conscious or moderate sedation. Prior to sedation, children should be nothing by os (NPO) for at least 4–6 h prior to the examination, depending on patient age.

Regardless of the choice of drug, the use of parenteral sedation requires personnel experienced in maintaining adequate cardiorespiratory support during and after the examination. Intravenous access must be continuously maintained, and continuous monitoring of vital signs must be performed and recorded. Patients should return to their baseline status with intact protective reflexes prior to discharge. The caregivers should be given verbal and written discharge instructions prior to leaving the recovery area with a contact phone number if questions arise.

3 Intravenous Contrast Medium

3.1 Power Injectors

Scanning after intravenous administration of iodinated contrast material is helpful to confirm a lesion thought to be of vascular origin or to establish its relationship to vascular structures, in addition to improving differentiation between normal and pathologic parenchyma. If intravenous contrast material is to be administered, it is helpful to have an intravenous line in place when the child arrives in the radiology department. This reduces patient agitation that otherwise would be associated with a venipuncture performed just prior to administration of contrast material. The largest gauge cannula that can be placed is recommended.

Contrast medium may be administered by hand injection or a mechanical injector. Hand injections are used when the intravenous access is via a peripheral vein placed in the dorsum of the hand or foot. Power injectors are used when a cannula, ranging in size from 18 to 24 gauge, can be placed in an antecubital vein (Amaral et al. 2006; Kaste and Young 1995; Plumb and Murphy 2011; Rigsby et al. 2007). The rate of injection and the pounds per square inch (psi) should be adjusted for the IV gauge. The following are rough published guidelines for rates and psi based on IV gauge: 22 gauge 1.5–3 ml/s 150 psi, 20 gauge 3–5 ml/s 300 psi, 18 gauge 4–6 ml/s 300 psi (Rigsby et al. 2007). A 22-gauge IV or larger is preferred, but safe injection through a 24 gauge is reported for neonates at low flow rates of 1–1.5 ml/s and psi below 100 and provided that there is proper intravascular positioning of the access line, verified by the unimpeded return of blood and the unimpeded delivery of a saline flush (Kaste and Young 1995; Plumb and Murphy 2011; Rigsby et al. 2007). Manual or power injection of central lines is generally only utilized in situations where there is no other peripheral IV access available, and it has been reported to be safe if pressure-limited injection is employed (Rigsby et al. 2007). The benefit of power injection is the uniformity of contrast delivery which allows for optimized enhancement. The complication rates for manual and power injections are similar (<0.4 %),

provided that the catheter is positioned properly and functions well (Kaste and Young 1995).

3.2 Contrast Volume and Scan Acquisition Protocols

The total contrast volume used is typically 1–2 ml/kg until the adult size and contrast rates are achieved. In general, a 20–30 s delay is sufficient for routine chest CT examinations (i.e., tumor staging, evaluation of a mediastinal or pulmonary mass, and trauma) (Siegel 2008a). The shorter delays (20 s) are used in neonates and infants (under 2 years of age), who have higher cardiac output, with longer delay times used in older children and adolescents.

For CT angiography (i.e., evaluation of cardiovascular anomalies, pulmonary sequestration, arteriovenous malformation, and hypogenetic lung), either automated bolus tracking or a fixed delay time can be used. The automated bolus-tracking method allows continuous monitoring of the attenuation within a large target vessel (e.g., aorta or pulmonary artery) by the use of a series of low-dose axial images. Once a predetermined threshold is reached, the low-dose scanning is terminated and the diagnostic examination is automatically initiated. A fixed default delay is the alternative and can be programmed in case the desired threshold is not achieved with automated tracking. In the latter setting, a 12–15 s scan delay after the start of the contrast administration usually produces excellent vascular enhancement.

Because of the additional radiation exposure, unenhanced scans are generally not obtained routinely prior to contrast administration. They are indicated when assessing stents or surgical conduits. In this assessment, they help to identify perigraft calcifications which can mimic a leak on contrast-enhanced scans.

4 Patient-Specific Radiation Reduction Techniques

Radiation dose from CT remains a major concern because of the potential carcinogenic effects of ionizing radiation. Minimizing radiation dose is particularly important in children because they are more sensitive to radiation than adults and on average live longer after receiving radiation doses from medical procedures. Therefore, careful selection of scan parameters is mandatory to optimize image quality while generating images with the least radiation exposure. The pertinent parameters that need to be selected prior to imaging are tube current (milliamperage, mAs) and voltage (kilovoltage, kVp), pitch, scan length, and slice collimation (Lambert et al. 2014; McCollough et al. 2006; McNitt-Gray 2002; Nelson 2014). These acquisition parameters have a direct impact on image quality and on the radiation dose. Iterative reconstruction is also used to reduce dose and improve image quality.

4.1 Milliamperage

The tube current determines the number of x-rays produced. The relationship between the tube current and the radiation dose is linear, thus, increasing the tube current by 50% will result in a 50% higher dose (McCollough et al. 2006; McNitt-Gray 2002). The lowest possible tube current should be used and should be selected by automated tube current modulation (automated exposure control [AEC]), which modulates mAs in relation to the patient body size and tissue attenuation based on the localizer radiographic (scout) image (Siegel et al. 2004; Lee et al. 2008; Singh et al. 2011). The mAs increases in areas with the greater tissue attenuation (e.g., shoulders and hips) and decreases in areas with less attenuation (e.g., thorax and abdomen), resulting in an overall radiation dose reduction when compared with examination where dose modulation is fixed. AEC reduces radiation dose by up to 40–50% (Siegel et al. 2004; Lee et al. 2008; Singh et al. 2011).

4.2 Kilovoltage

The tube potential determines the x-ray photon energy. Radiation dose is approximately proportional to the square of the percentage change in kVp, all other parameters being fixed. With a constant tube current, decreasing kVp from 120 to

100 can reduce radiation dose by 33%, and decreasing the kVp from 120 to 80 can result in up to a 65% dose reduction (McCollough et al. 2006; McNitt-Gray 2002; Nelson 2014; Siegel et al. 2004, 2013a, b; Lee et al. 2008; Yu et al. 2010).

Automated tube potential selection automatically calculates the optimal combination of kVp and mAs for each patient depending on the clinical task (CT angiography, contrast-enhanced CT, noncontrast CT) and the patient's body habitus based on the localizer radiograph image. The effect is the desired image quality at the lowest dose. Only 1 kVp is selected for the entire examination. For CT angiography, automated tube potential technology can reduce scanner output by nearly 50% compared with standard 120 kVp protocols (Siegel et al. 2013a). If automated technology is not available, kVp settings can be selected manually from weight-based charts (Nievelson et al. 2010).

4.3 Pitch

The scan pitch is the ratio of the table feed per table gantry rotation divided by the beam width. When the table moves the same distance as the beam width, the pitch is equal to one. The dose is inversely proportional to the pitch, so a pitch less than one means that the beam overlaps previously radiated tissue with each rotation and the dose increases. A pitch greater than one means that the dose will decrease, but some tissue may be imaged incompletely, potentially reducing image quality or introducing gaps where anatomy is incompletely visualized.

In single-source CT, the maximum pitch is limited to 1.5. The latest generation of CT technology using dual-source technology permits scanning at very high pitch values, up to 3.4 with minimal if any data loss. The high-pitch mode enables gapless volume data acquisition and has been demonstrated to reduce acquisition time for the chest CT and sedation time. In routine chest CT and chest CT angiography excluding the coronary arteries, a pitch of 1.2 with a single-source CT scanner and a pitch of 3.0 with a dual-source CT scanner have been shown to provide diagnostic CT scans and decrease image artifacts and sedation (Lell et al. 2010). A pitch of 3.4 is reserved for coronary artery CT angiography.

4.4 Scan Length

Since the CT radiation dose is directly proportional to the scan length when all other acquisition parameters are similar, it is essential that the scan length be minimized to include only the area of interest. The typical scan length for pediatric chest CT extends from just above the thoracic inlet to just below the lung bases. The patient should be centered in the middle of the CT gantry. Off-centering also leads to decreased image quality with increased image noise (Li et al. 2007).

4.5 Slice Collimation

The collimation determines the nominal or effective section thickness, which can be changed after scanning is completed provided that the raw data have been saved. A collimation $\leq$10 mm (usually 0.6–0.75 mm) is routinely used for thoracic imaging. If evaluation of small intracardiac structures or the coronary arteries is needed, thinner collimation should be used.

4.6 Iterative Reconstruction

Traditional CT reconstruction is based on filtered back projection. In iterative reconstruction, the reference mAs or noise is decreased and then information acquired during the scan is incorporated into repeated reconstruction steps to produce an image with less noise and better image quality compared with filtered back projection. The use of iterative reconstruction results in improved image quality with lower radiation doses (Singh et al. 2012; Karmazyn et al. 2014).

4.7 Other Dose-Reduction Strategies

4.7.1 Breast Shielding

Although breast shields can reduce dose, they are associated with a high frequency of artifacts. Recently, the American Association of Physicists

in Medicine issued a statement that automated tube current modulation is as effective as breast shielding in lower breast exposure and is associated with fewer artifacts and is preferred over breast shields (American Association of Physicists in Medicine 2012). Organ-based tube current modulation is another alternative to decrease tube current over radiation-sensitive areas.

4.7.2 Scan Phases

Multiphase scans significantly increase the dose. The use of multiphase CT scanning in children should be limited to absolute necessity.

5 Reconstruction Techniques

A standard reconstruction algorithm usually suffices for routine CT examinations and CT angiograms, while a high-resolution (bone) algorithm is best for examinations of the airway and diffuse lung disease.

Multiplanar reformations and 3D volume renderings are useful in the assessment of the mediastinal great vessels and central airways (Boiselle et al. 2002; Cody 2002; Siegel 2003). A more detailed discussion of multiplanar reformation and three-dimensional reconstruction techniques can be found elsewhere in this textbook.

6 Thoracic Applications

The cross-sectional and 3D CT images are helpful in detecting or clarifying abnormalities in the lungs, mediastinum, vessels, airway pleura, and chest wall. The information provided by these techniques can directly affect treatment or aid in determining the prognosis of a patient.

The common clinical applications for CT of the pediatric chest are (a) congenital lung anomalies, (b) mediastinal mass, (c) lung masses including metastases, (d) cardiovascular anomalies, (e) airway disorders, (f) diffuse lung disease, (g) complication pulmonary infections, and (h) complex chest wall abnormalities.

7 Congenital Lung Anomalies (Protocols 1 and 2)

Congenital pulmonary masses can be classified into two major categories: those with normal arterial supply and venous drainage and those with anomalous vasculature (Biyyam et al. 2010; Daltro et al. 2002; Lee et al. 2011; Siegel 2008b).

Protocol 1

Indication	Standard lung/mediastinum (Oncologic staging, detection of metastases, characterization of mediastinal or pulmonary mass, evaluation of trauma)
Extent	Lung apices to caudal bases
mAs and kVp	Lowest possible
Collimation	0.6–1.0 cm
Pitch	1.2–3.0
Reconstruction interval	5×5, 3×3 mm
IV Contrast	Nonionic 280–320 mg iodine/ml
Contrast volume	2 ml/kg (maximum of 4 ml/kg or125 ml, whichever is lower)
Contrast injection rate	Hand injection: rapid-push bolus Power injector: 22 gauge 1.5–3 ml/s 150 psi 20 gauge 3–5 ml/s 300 psi 18 gauge 4–6 ml/s 300 psi[a]
Scan delay	20–30 s
Miscellaneous	1. Breath-hold if possible. If the child is sedated or uncooperative, CT scans are obtained at quiet breathing 2. Contrast medium used at the discretion of radiologist in the evaluation of metastases. Routinely given for evaluation of mediastinal and pulmonary masses and trauma 3. Use a standard reconstruction algorithm 4. Multiplanar reconstructions should be performed

[a]References Kaste and Young (1995), Plumb and Murphy (2011), Rigsby et al. (2007)

7.1 Anomalies with Normal Vasculature

Congenital lobar overinflation, cystic pulmonary airway malformation, bronchogenic cyst, and bronchial atresia/hypoplasia are anomalies resulting

Protocol 2

Indication	CT angiography (Mediastinal vascular anomalies, sequestration, arteriovenous malformation, aneurysm, postoperative shunts)
Extent	Lung apices to caudal bases
mAs and kVp	Lowest possible
Collimation	0.6–1.0 cm
Pitch	1.2–3.0
Reconstruction interval	5×5 mm, 1×2 mm
IV contrast	Nonionic 280–320 mg iodine/ml
Contrast volume	2 ml/kg (maximum of 4 ml/kg or150 ml, whichever is lower)
Contrast injection rate	Hand injection: rapid-push bolus Power injector: 22 gauge 1.5-3 ml/s 150 psi 20 gauge 3–5 ml/s 300 psi 18 gauge 4–6 ml/s 300 psi[a]
Scan delay	Automated bolus tracking
Miscellaneous	1. Breath-hold if possible. If the child is sedated or uncooperative, CT scans are obtained at quiet breathing 2. If sequestration is suspected, scanning should extend through the upper abdominal aorta 3. Precontrast images are not needed for most examinations, but they are used in the evaluation of endovascular stents 4. Use standard reconstruction algorithm 5. Multiplanar and 3D reconstructions should be performed

[a]References Kaste and Young (1995), Plumb and Murphy (2011), Rigsby et al. (2007)

from abnormal bronchial development. The role of CT is to confirm the diagnosis and to determine the extent of abnormality in patients in whom surgery is contemplated.

7.1.1 Congenital Lobar Overinflation

Congenital lobar overinflation is characterized by hyperinflation of a lobe. The affected patient usually presents in the first 6 months of life with respiratory distress. CT shows a hyperinflated lobe with attenuated vascularity, compression of ipsilateral adjacent lobes, and mediastinal shift to the opposite side (Fig. 1). The left upper lobe is involved in about 45 % of cases, the right middle lobe in 30 %, the right upper lobe in 20 %, and two lobes in 5 % of cases (Biyyam et al. 2010; Daltro et al. 2002; Lee et al. 2011; Siegel 2008b).

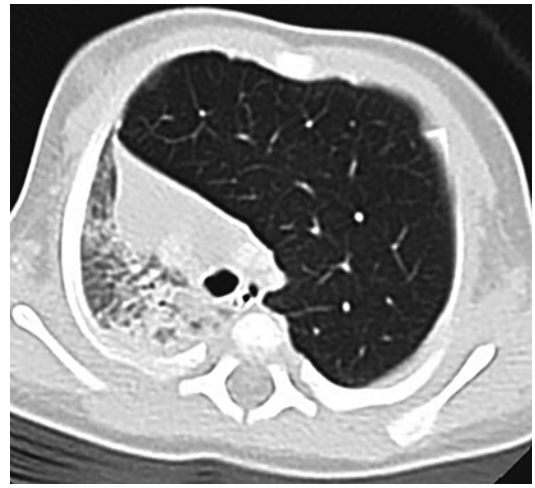

Fig. 1 Congenital lobar overinflation. Axial image in lung windows shows hyperinflation of the left upper lobe with mediastinal shift to the right resulting in right lung atelectasis. The vessels in the overinflated region are attenuated

7.1.2 Cystic Pulmonary Airway Malformation

Cystic pulmonary airway malformation (CPAM) is a hamartomatous lesion of the lung classified by the size of the cyst and the mucosal lining of the cyst (Stocker 2009). In the current expanded Stocker classification, CPAMs include five types: 0–4. In types 1–4, the clinical presentation is neonatal respiratory distress. Type 0 is the rarest form and it is virtually always lethal, with patients dying in utero or at birth. Type 0 CPAM arises from the trachea or bronchus. Cysts are small. Type 1 is the most common, accounting for 60–70 % of cases, and it arises from distal bronchus or proximal bronchiole. It is characterized by multiple cysts, measuring 3–10 cm (Fig. 2). Type 2 accounts for 15–20 % of cases and arises from terminal bronchioles. It is composed of smaller cysts, measuring 0.5–2 cm in size (Fig. 3). Type 3 accounts for 5–10 % of cases and it arises from acinar tissue. It is composed of cysts that are so small (<0.5 cm)

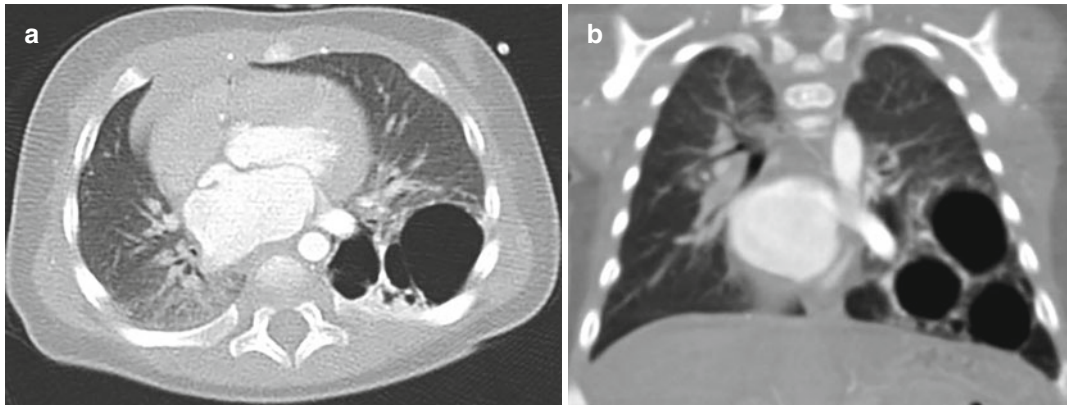

Fig. 2 Cystic pulmonary airway malformation. Type I lesion in a newborn girl. (**a**) Axial and (**b**) coronal contrast-enhanced images. An air-filled, thin-walled multicystic mass with several cysts over 3 cm in diameter is present in the left lower lobe. There is mediastinal shift to the right

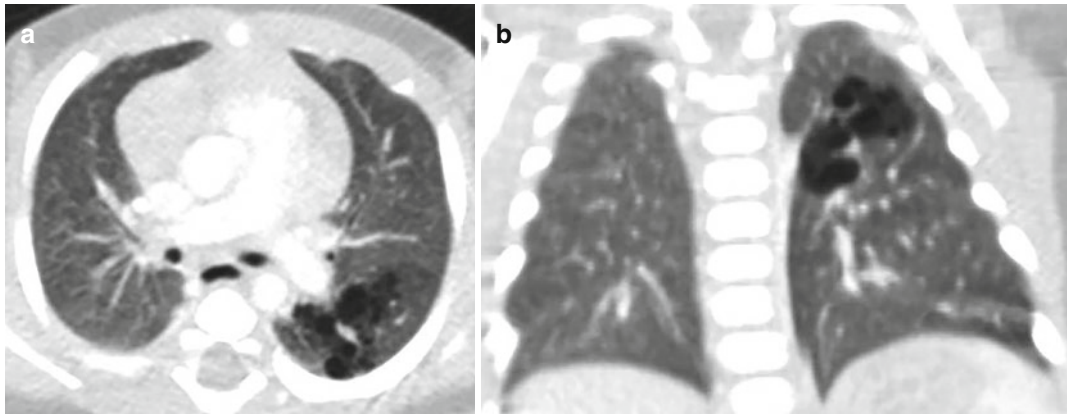

Fig. 3 Cystic pulmonary airway malformation. Type II malformation. (**a**) Axial and (**b**) coronal images show a complex mass with multiple, small cysts (<2 cm in diameter) in the left upper lobe

that they appear solid on CT. Type 4 CPAM accounts for 5–15 % of cases and it has an alveolar/distal acinar origin. This CPAM contains cysts as large as 10 cm, and it has been associated with tension pneumothorax and malignancy, specifically pleuropulmonary blastoma. Types 2 and 3 CPAMs have an increased incidence of other congenital anomalies, such as tracheoesophageal fistula, renal agenesis, intestinal atresia, diaphragmatic hernia, and cardiac anomalies, including truncus arteriosus and tetralogy of Fallot. In all types, associated findings include mediastinal shift to the contralateral side and hypoplasia of the ipsilateral lung. Cystic airway malformation can occur in association with sequestration.

7.1.3 Segmental Bronchial Atresia

Bronchial atresia results from abnormal development of a segmental or subsegmental bronchus that fails to communicate with the central airways (Gipson et al. 2009). CT features of bronchial atresia include a round, ovoid or branching density near the hilum, representing mucoid impaction just beyond the atretic bronchus, and overaerated lung distal to the atresia (Fig. 4). The absence of feeding or draining vessels helps to exclude a vascular lesion. Since the majority of patients are asymptomatic, treatment is unnecessary. Surgical excision may be indicated in patients with recurrent infection or respiratory compromise.

7.1.4 Bronchogenic Cyst

Bronchogenic cysts may be intrapulmonary or mediastinal (Biyyam et al. 2010; Daltro et al. 2002; Lee et al. 2011; Siegel 2008b). The lesions may be asymptomatic or become clinically apparent when there is superimposed infection or compression of the tracheobronchial tree. On CT, pulmonary bronchogenic cysts are typically well-defined masses with smooth walls and attenuation equal to that of water, reflecting the presence of serous fluid. The attenuation increases and approximates that of soft tissue when the contents are viscous or mucoid. The cyst may contain air or an air-fluid level if there is superimposed infection (Fig. 5). Cysts complicated by infection also may show wall enhancement.

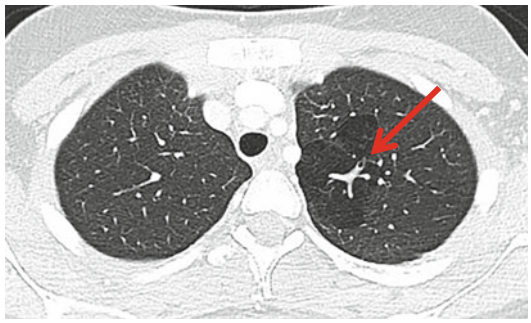

Fig. 4 Segmental bronchial atresia. A fifteen-year-old girl with incidental finding on a routine CT acquired after motor vehicle crash. The hyperinflated lung (due to collateral air drift) surrounds a dilated, mucus-filled bronchus (*arrow*) in the superior segment of the left upper lobe

7.1.5 Pulmonary Agenesis and Hypoplasia

Pulmonary agenesis refers to the absence of the lung tissue. Patients can present with respiratory distress immediately after delivery or they may be asymptomatic and the diagnosis made incidentally on imaging examinations obtained for other reasons. CT shows the absence of the lung and bronchus, an absent or rudimentary pulmonary artery, and shift of mediastinal structures to the affected side (Fig. 6).

Pulmonary hypoplasia refers to a decreased amount of lung tissue. Patients may have mild respiratory distress or no symptoms at all. In comparison to the agenetic lung, CT shows some aerated lung but it is smaller than the normal lung. The bronchus and pulmonary artery are small and there is some mediastinal shift (Fig. 7) (Biyyam et al. 2010; Daltro et al. 2002; Lee et al. 2011; Siegel 2008b).

7.2 Anomalies with Abnormal Vasculature

7.2.1 Bronchopulmonary Sequestration

Bronchopulmonary sequestration is a congenital mass of pulmonary tissue that has no normal

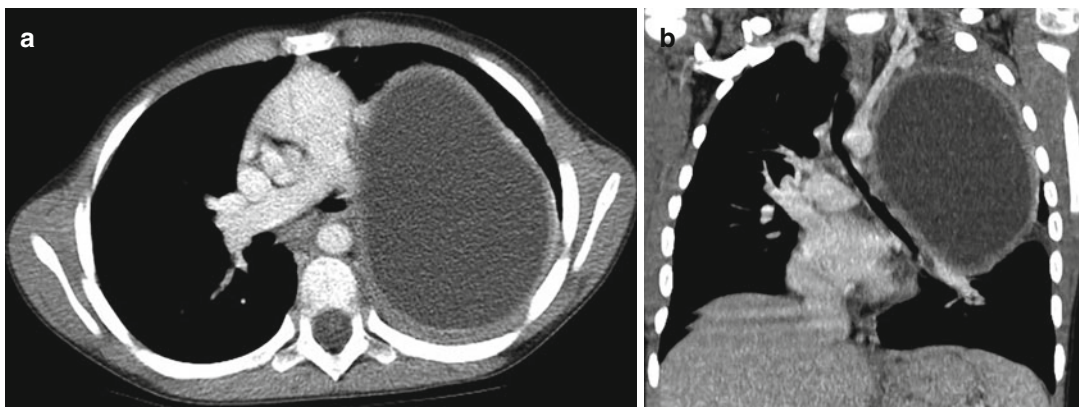

Fig. 5 Congenital bronchogenic cyst. (**a**) Axial- and (**b**) coronal-reformatted CT scans show a thin-walled, fluid-filled cyst in the left upper lobe

connection with the tracheobronchial tree and is supplied by an anomalous artery, usually arising from the aorta. When the sequestered lung is confined within the normal visceral pleura and has venous drainage to the pulmonary veins, it is termed "intralobar." The sequestered lung is termed "extralobar" when it has its own pleura and venous drainage to systemic veins. Patients with intralobar sequestrations usually present in childhood or later in life with signs of chronic or recurrent segmental or subsegmental pneumonitis, especially at a lung base. By comparison, extralobar sequestrations are often found incidentally on in utero sonography or in childhood or later in life on chest radiographs performed for other clinical indications. In the neonate, large ones may cause respiratory distress or present as abdominal masses.

CT scanning after an injection of contrast material demonstrates opacification of the anomalous vessel immediately following peak aortic enhancement (Biyyam et al. 2010; Daltro et al. 2002; Lee et al. 2011; Siegel 2008b; Ko et al. 2000) (Figs. 8 and 9). Intralobar sequestration is usually supplied by a branch of the thoracic aorta. In extralobar sequestration, the arterial supply is often from the thoracoabdominal aorta or upper abdominal aorta, but it may be from splenic, gastric, or celiac arteries.

Typically, sequestrations appear as solid soft tissue masses with varying amounts of internal enhancement. Intralobar sequestration can show cystic changes due to superimposed infection, and in both types, there may be cystic components if there is an associated cystic pulmonary airway malformation.

7.2.2 Hypogenetic Lung Syndrome

Hypogenetic lung, also known as venolobar or scimitar syndrome, refers to the combination of a small lung, which is nearly always on the right, and anomalous pulmonary venous return, usually to the inferior vena cava (Konen et al. 2003). Other findings include a corresponding small pulmonary artery and ipsilateral mediastinal displacement. The anomalous return is usually into the inferior vena cava, although it may enter the suprahepatic portion of the inferior vena cava, the hepatic veins, portal veins, azygos vein, or right atrium. Associated anomalies include systemic

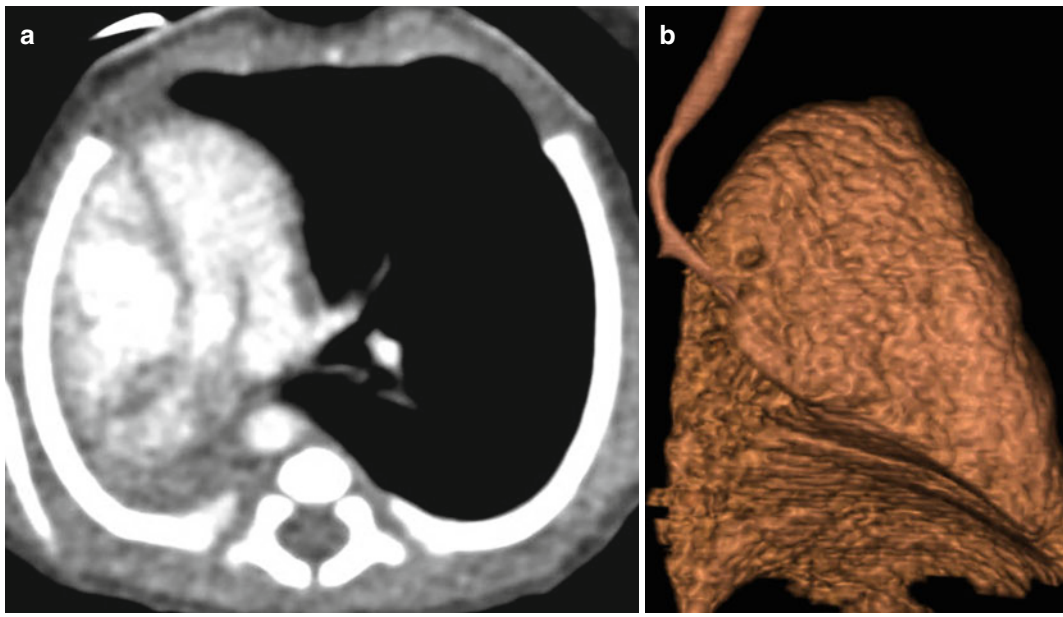

Fig. 6 Pulmonary agenesis. (**a**) Axial image in a neonate show the absence of the right lung with rightward shift of the heart and mediastinal structures. The right main bronchus and pulmonary artery are absent. (**b**) 3D volume rendering show the absence of the right main stem bronchus and right lung

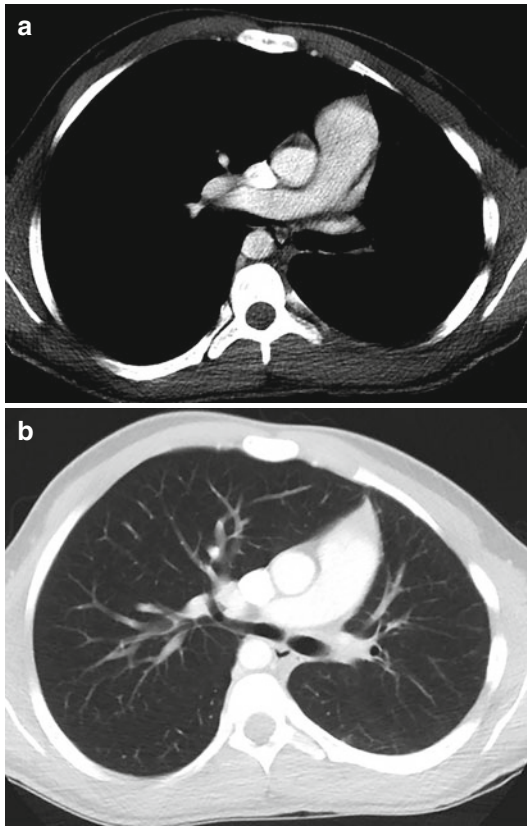

Fig. 7 Pulmonary hypoplasia. (**a**) Axial contrast-enhanced image shows the absence of the left pulmonary artery. This patient also has a right aortic arch. (**b**) Axial image in lung windows shows a small left lung. The left main bronchus is normal size

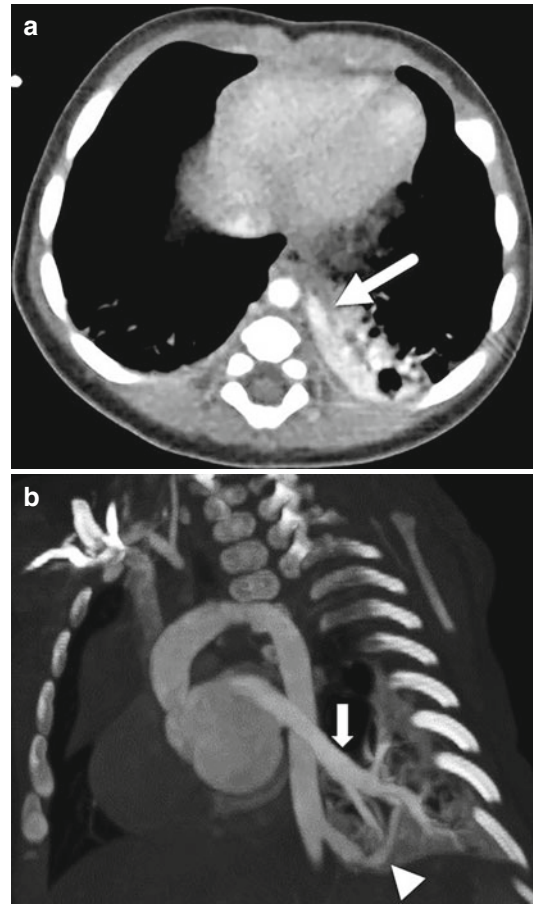

Fig. 8 Intralobar pulmonary sequestration. (**a**) Axial contrast-enhanced CT shows a feeding artery (*arrow*) extending into an area of consolidation in the left lower lobe. (**b**) Oblique maximum intensity projection image shows the feeding artery arising from the thoracic aorta (*arrowhead*). Venous drainage (*straight arrow*) is through a pulmonary vein

arterial supply to the hypogenetic lung and horseshoe lung. Horseshoe lung is a rare anomaly in which the posterobasal segments of both lungs are fused behind the pericardial sac (Fig. 10).

7.2.3 Pulmonary Arteriovenous Malformation (AVM)

Pulmonary AVM is characterized by a direct communication between a pulmonary artery and vein without an intervening capillary bed. At CT, AVMs appear as rounded or lobular masses with rapid enhancement and washout after intravenous contrast medium administration (Hoffman et al. 2000; Lacombe et al. 2013) (Fig. 11). Axial images can establish the diagnosis, but 3D reconstructions are of value in demonstrating the precise anatomy of the malformation, including the number of feeding arteries and draining veins, which is critical information for treatment planning (Lacombe et al. 2013). This anomaly can occur in isolation or with Rendu-Osler-Weber disease.

8 Mediastinal Mass Evaluation (Protocol 1)

Indications for CT and MRI of the mediastinum include (a) characterization of mediastinal widening or evaluation of a mass suspected or

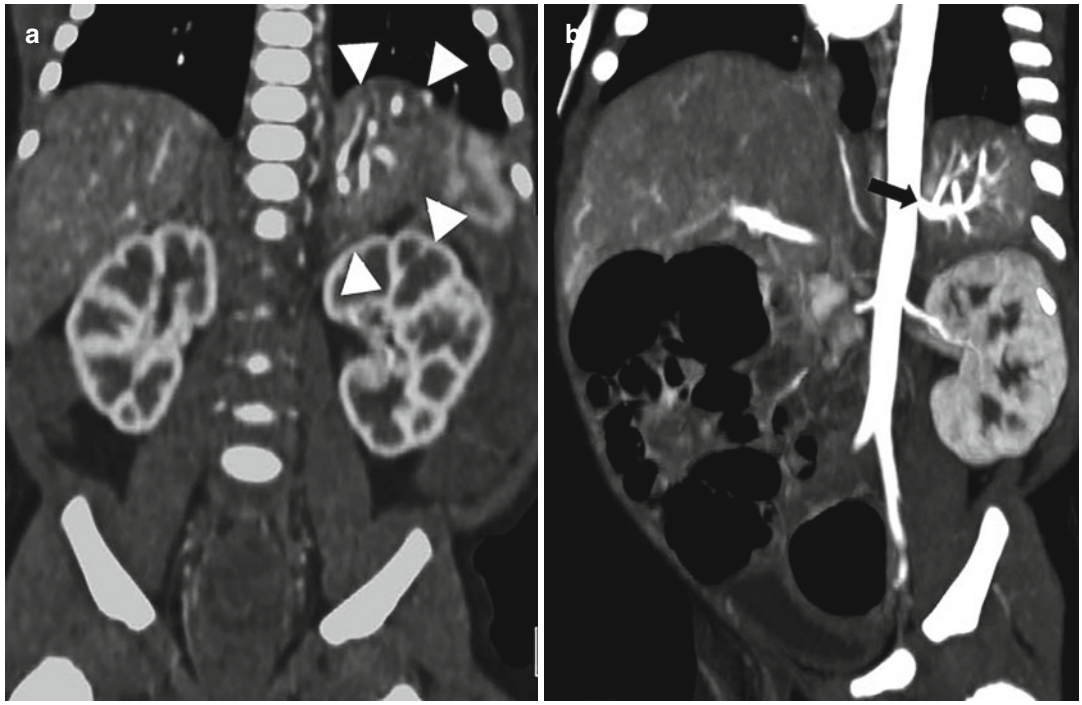

Fig. 9 Extralobar sequestration. Neonate with a left upper quadrant mass on an in utero ultrasound. A neuroblastoma was suspected and an abdominal CT was performed after birth to further characterize the abnormality. (**a**) Coronal CT image shows a mass (*arrowheads*) in the left lower lobe. (**b**) Oblique coronal image shows an artery (*arrow*) arising from the abdominal aorta which supplies the mass. Venous drainage (not shown) was into a systemic vein

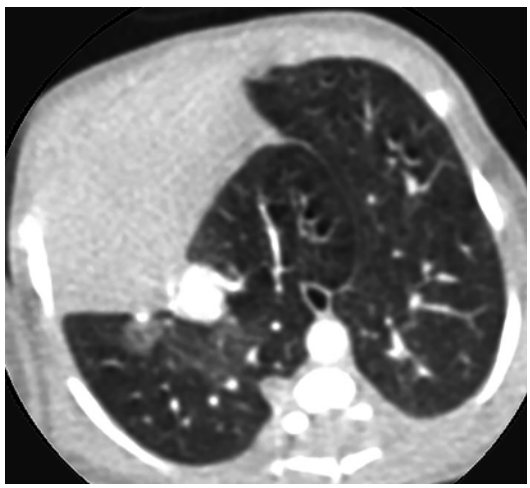

Fig. 10 Scimitar syndrome with horseshoe lung. Axial CT image shoes fusion of the posterior aspects of both lower lobes behind the pericardial sac. This patient also has a small right lung and rightward shift of the heart. Abnormal venous drainage (not shown) was seen at a more caudal image

detected on chest radiography; (b) determination of the extent of a proven mediastinal tumor; (c) detection of mediastinal involvement in children who have an underlying disease that may be associated with a mediastinal mass, but who have a normal chest radiograph; and (d) assessment of the response of a mediastinal mass to therapy.

8.1 Normal Anatomy

8.1.1 Normal Thymus

In the pediatric population, the normal thymus is seen in virtually every patient. Recognition of the various appearances of the normal thymus is important if errors in diagnosis are to be avoided (Nassseri and Effechari 2010; Nishino et al. 2006; Siegel 1993, 2008c). In patients under 5 years of age, the thymus usually has a quadrilateral shape with convex or straight lateral margins. Later in the first decade, the thymus is triangular

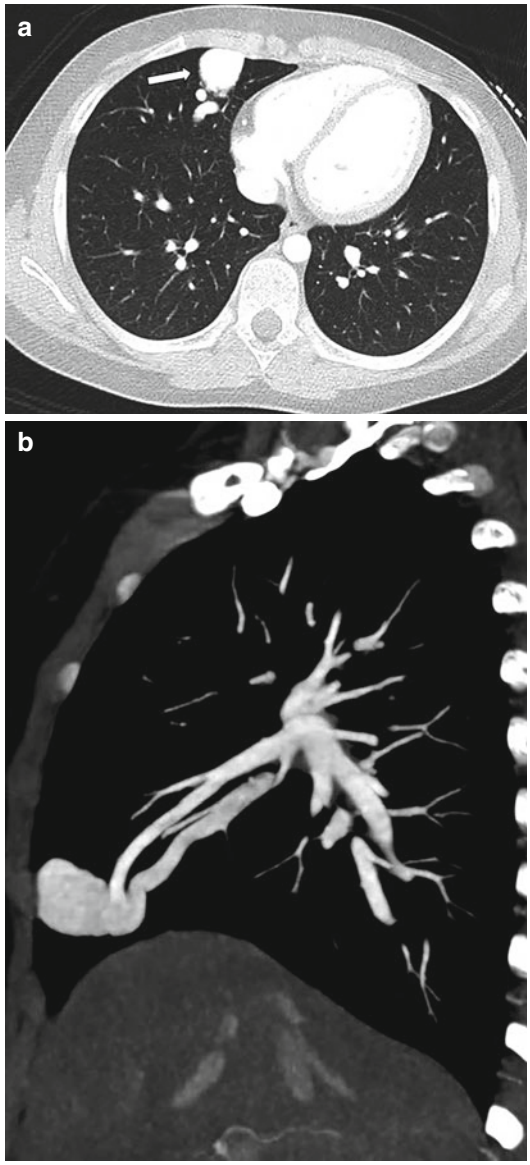

Fig. 11 Pulmonary arteriovenous malformation. (**a**) CT scan in lung windows shows a well-circumscribed, enhancing nodule (*arrow*) in the right middle lobe. Adjacent tubular structures represent vessels. (**b**) Contrast-enhanced sagittal-reformatted maximum intensity projection image shows the feeding artery arising from the right middle lobe artery and draining vein arising from the inferior pulmonary vein

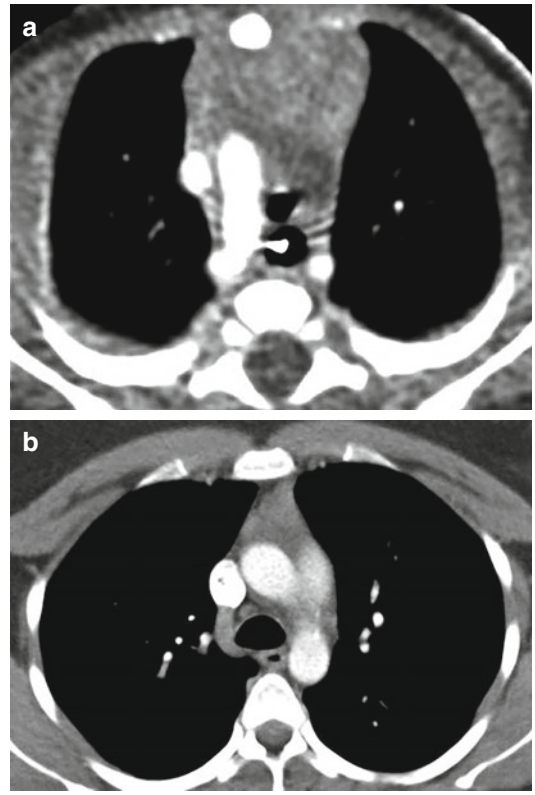

Fig. 12 Normal thymus. (**a**) Neonate. The thymus has a quadrilateral shape with convex lateral contours. This patient also has a right aortic arch. (**b**) Adolescent. The thymus has a triangular shape with straight borders. Note that the normal thymus does not compress adjacent vasculature

or arrowhead-shaped with straight or concave margins, and by 15 years of age, it is triangular in nearly all individuals (Fig. 12). In general, in the first two decades of life, the thymus abuts the sternum, separating the two lungs. A distinct anterior junction line between the lungs is usually not seen until the third decade of life. In prepubertal children and most adolescents, the thymus is homogeneous with an attenuation value equal to that of chest wall musculature. In some adolescents, it is heterogeneous, containing low-density areas of fat deposition.

Thymic lobar thickness (the largest dimension perpendicular to the long axis of the lobe) correlates inversely with advancing age, decreasing from 1.50 ± 0.46 cm for the 0–10 year age group to 1.05 ± 0.36 cm for patients between 10 and 20 years of age (Siegel 1993, 2008c).

Cervical extension of the thymus is a normal finding and is most frequent in very young children, but it can be seen in older children and

adolescents (Costa et al. 2010). Occasionally, the thymus also extends into the posterior thorax. Criteria for differentiating the normal cervical or posterior extension of the thymus from a pathologic mass are direct continuity of the cervical or posterior extension with the thymic tissue in the anterior mediastinum, an attenuation value similar to that of normal thymic tissue, and the lack of compression of adjacent mediastinal vessels or the tracheobronchial tree.

8.1.2 Azygoesophageal Recess

The configuration of the azygoesophageal recess varies with patient age. The contour of the recess is convex laterally in children under 6 years of age, straight in children between 5 and 12 years of age, and concave in adolescents or young adults (Miller et al. 1993). Recognition of the normal dextroconvex appearance in young children is important, so that it is not mistaken for lymphadenopathy.

8.2 Anterior Mediastinal Masses

Lymphoma, thymic hyperplasia, teratoma, and lymphangioma are the most common anterior mediastinal masses in children (Siegel 2008c). Rare causes of anterior mediastinal masses in children include thymoma, an enlarged thyroid, thymolipoma, lipoblastoma, and thymic cysts. These are covered elsewhere in this book.

8.2.1 Lymphoma

Lymphoma is the most common cause of an anterior mediastinal mass, with Hodgkin disease occurring 3–4 times more frequently than non-Hodgkin lymphoma (Gross and Perkins 2011; Metzger et al. 2011). Approximately 65 % of pediatric patients with Hodgkin disease have intrathoracic involvement at clinical presentation, and 90 % of the chest involvement is mediastinal. In contradistinction, about 40 % of pediatric patients with non-Hodgkin lymphoma have chest disease at diagnosis, and only 50 % of this disease involves the mediastinum.

Lymphomatous involvement in the anterior mediastinum can appear as lymphadenopathy or infiltration and enlargement of the thymus. At CT, the enlarged thymus has a quadrilateral shape with convex, lobular lateral borders (Nassseri and Effechari 2010; Nishino et al. 2006; Siegel 2008c; Siegel 1993; Franco et al. 2005; Lee 2009; McCarville 2010; Toma et al. 2007) (Fig. 13). The attenuation of the lymphomatous organ is equal to that of soft tissue. Lymph node enlargement varies from mildly enlarged nodes in a single area to large conglomerate soft tissue masses. Typically, the enlarged nodes have well-defined margins and show little enhancement after intravenous administration of contrast medium. Additional findings include hilar lymph node enlargement, airway narrowing, and compression of vascular structures.

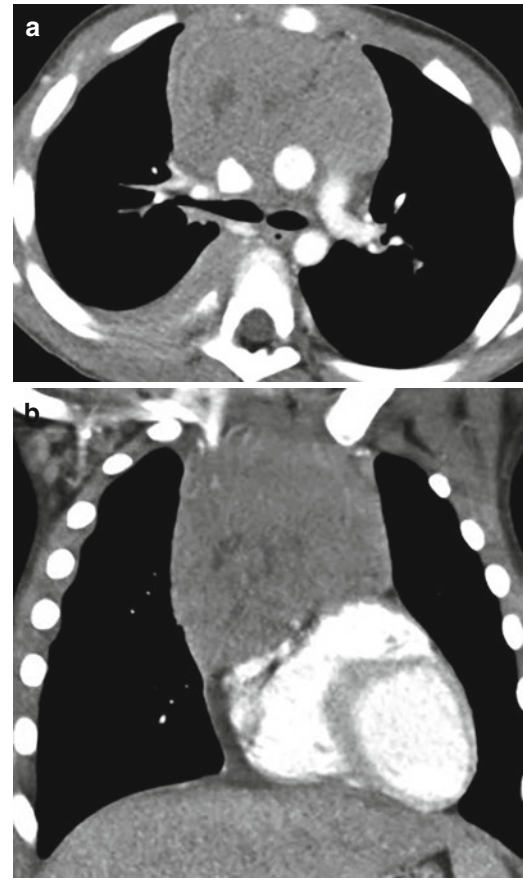

Fig. 13 T-cell lymphoblastic lymphoma. (**a**) Axial and (**b**) coronal images show a large heterogeneous mass that infiltrates and replaces the thymus, displacing the vasculature posteriorly and causing mass effect on the atria. Also seen is a small right pleural effusion

8.2.2 Thymic Hyperplasia

In childhood, thymic hyperplasia is most often "rebound" hyperplasia associated with chemotherapy. The mechanism of hyperplasia in these cases is believed to be initial depletion of lymphocytes from the cortical portion of the gland due to high serum levels of glucocorticoids, followed by repopulation of the cortical lymphocytes when the cortisone levels return to normal. Rare causes of hyperplasia include myasthenia gravis, red cell aplasia, and hyperthyroidism.

On CT, hyperplasia appears as diffuse enlargement of the thymus with preservation of the normal triangular shape (Nassseri and Effechari 2010; Nishino et al. 2006; Siegel 1993, 2008c) (Fig. 14). The attenuation value of the hyperplastic thymus is similar to that of the normal organ. It is the absence of other active disease and a gradual decrease in size of the thymus on serial CT scans that support the diagnosis of rebound hyperplasia as the cause of thymic enlargement.

8.2.3 Teratoma

Teratoma is the second most common cause of an anterior mediastinal mass in children after lymphoma, and >90% are benign. They are derived from one or more of the three embryonic germ cell layers and usually arise in the thymus. On CT, benign teratomas are well-defined, thick-walled, predominantly cystic (fluid-filled) masses containing a variable admixture of tissues: calcium, fat, and soft tissue (Barksdale and Obokhare 2009; Quillin and Siegel 1992) (Fig. 15). A fat-fluid level occasionally can be seen within these tumors.

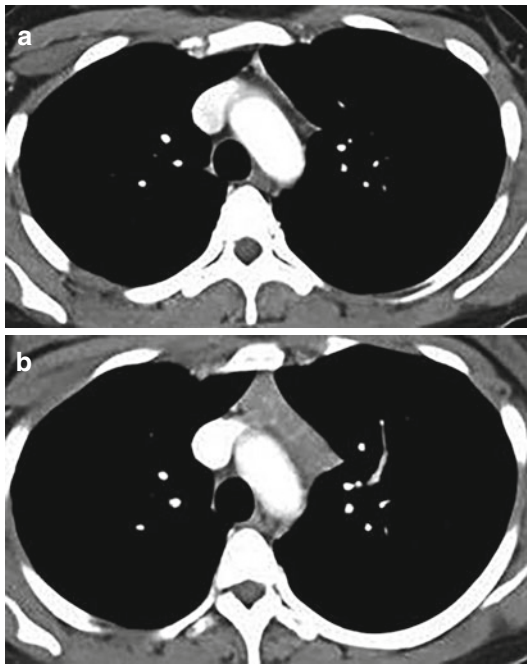

Fig. 14 Thymic hyperplasia. (**a**) Axial image in a young female with an ovarian tumor shows a normal thymus. (**b**) Axial image following chemotherapy shows that the thymus has doubled in size consistent with rebound hyperplasia

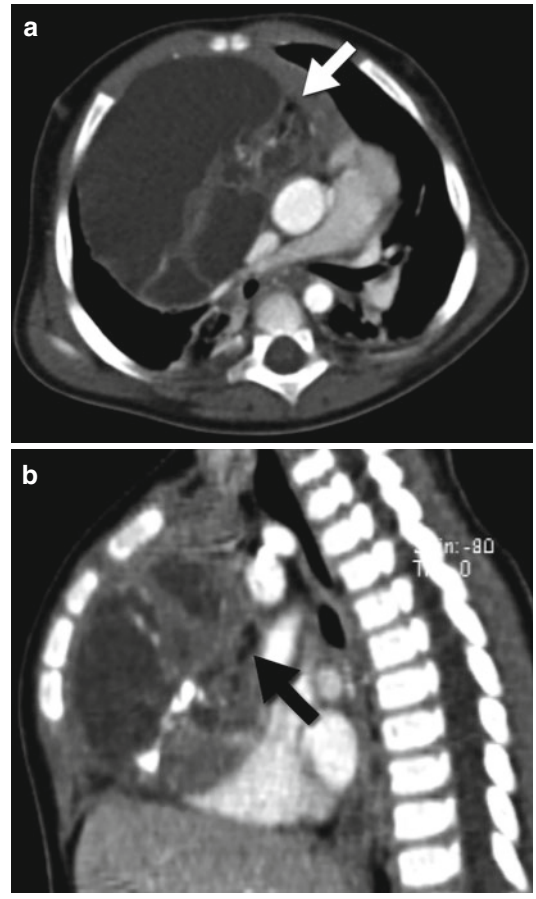

Fig. 15 Benign teratoma. (**a**) Axial and (**b**) sagittal images in a 7-month-old boy show a large predominantly cystic anterior mediastinal mass with scattered solid components and fat (*arrows*)

8.2.4 Lymphangioma

Lymphangiomas, also referred to as cystic hygromas, are developmental tumors of the lymphatic system and are almost always inferior extensions of cervical hygromas. Approximately, 90 % are found by 2 years of age. Isolated mediastinal lymphangiomas are very uncommon, but can occur (Siegel 2008c). The CT appearance is that of a thin-walled, multiloculated mass of near-water attenuation value (Fig. 16). The surrounding fascial planes are obliterated if the tumor infiltrates the adjacent soft tissues. Hemorrhage can increase the CT attenuation value.

8.2.5 Rare Anterior Mediastinal Masses

Malignant teratoma, malignant nonteratomatous germ cell tumors, including seminoma, embryonal cell carcinoma, choriocarcinoma and endodermal sinus tumor, thymic carcinoma, thymic carcinoid, thymoma, and Langerhans cell histiocytosis, are rare in the anterior mediastinum (Siegel 2008c; Crawley and Guillerman 2010). These tumors typically are poorly defined, heterogeneous, soft tissue density masses containing some low-density areas of necrosis and occasionally calcifications (Figs. 17 and 18) (Siegel 2008c). Local infiltration into the adjacent mediastinum with encasement or invasion of mediastinal vessels or airways also occurs.

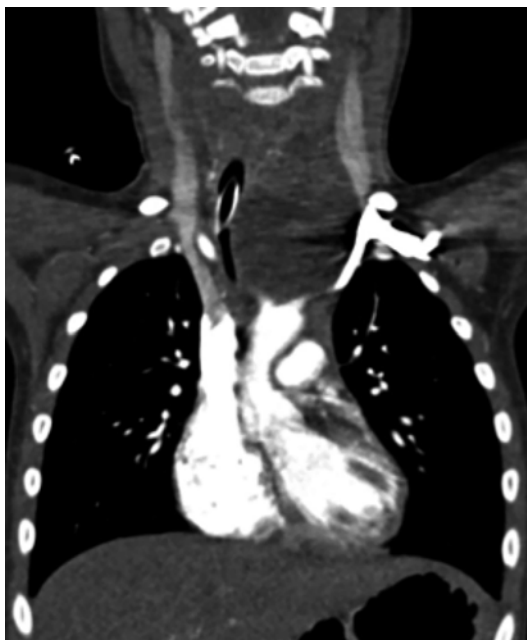

Fig. 16 Lymphangioma. Coronal image shows a low-attenuating mass extending from the left side of the neck into the mediastinum and displacing the trachea to the right

8.3 Middle Mediastinal Masses

Middle mediastinal masses are usually foregut duplication cysts or lymphadenopathy (Siegel 2008c).

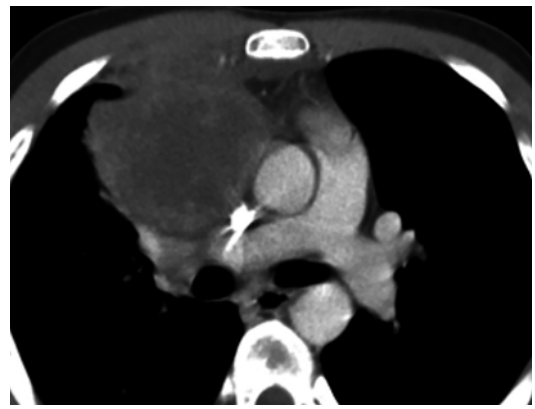

Fig. 17 Malignant teratoma. Axial CT shows a large anterior mediastinal soft tissue mass displacing great vessels to the left and posteriorly

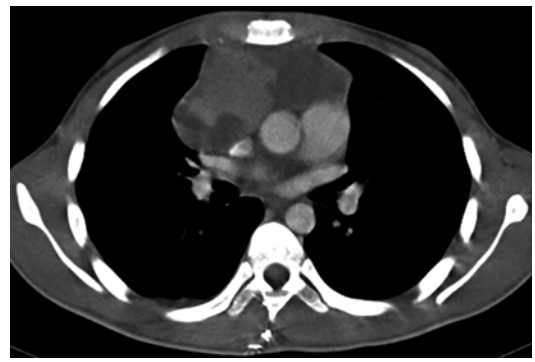

Fig. 18 Malignant thymoma. Axial image in a 16-year-old male shows a heterogeneous predominantly solid anterior mediastinal mass

8.3.1 Bronchopulmonary Foregut Cysts

Bronchopulmonary foregut cysts include bronchogenic and enteric cysts (McAdams et al. 2000). Bronchogenic cysts are lined by respiratory epithelium, and most are located in the subcarinal or right paratracheal regions. Enteric cysts, also known as esophageal duplications, are lined by gastrointestinal mucosa and usually are located close to or within the esophageal wall.

CT findings of foregut cysts include a nonenhancing round or tubular mass with well-defined margins and thin or imperceptible walls (Fig. 19). The cyst contents usually are homogeneous and of near-water attenuation, reflecting their serous nature. The attenuation values increase if the contents contain proteinaceous fluid, hemorrhage, mucus, or calcium.

8.3.2 Lymphadenopathy

Lymph node enlargement, as a cause of a middle mediastinal mass, is usually caused by lymphoma or granulomatous disease. On CT, adenopathy can appear as discrete soft tissue masses or as a single soft tissue mass with ill-defined margins. Calcification within lymph nodes suggests old granulomatous disease, such as histoplasmosis or tuberculosis. Low-attenuation areas suggest tuberculosis. Mediastinal nodes involved by granulomatous disease usually undergo spontaneous regression, frequently with resultant calcification. In some cases, healing occurs with extensive fibrosis, resulting in airway or vascular (e.g., superior vena cava) obstruction (Fig. 20).

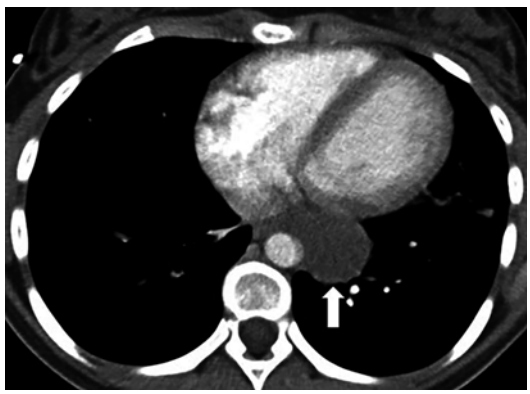

Fig. 19 Foregut cyst. Contrast-enhanced axial CT image shows a well-defined homogeneous low-attenuation mass (*arrow*) with an imperceptible wall adjacent to the esophagus, consistent with an enteric cyst

8.4 Posterior Mediastinal Masses

8.4.1 Neurogenic Tumors

Posterior mediastinal masses are of neural origin in approximately 95 % of cases and may arise from sympathetic ganglion cells (neuroblastoma, ganglioneuroblastoma, or ganglioneuroma) or from nerve sheaths (neurofibroma or schwannoma).

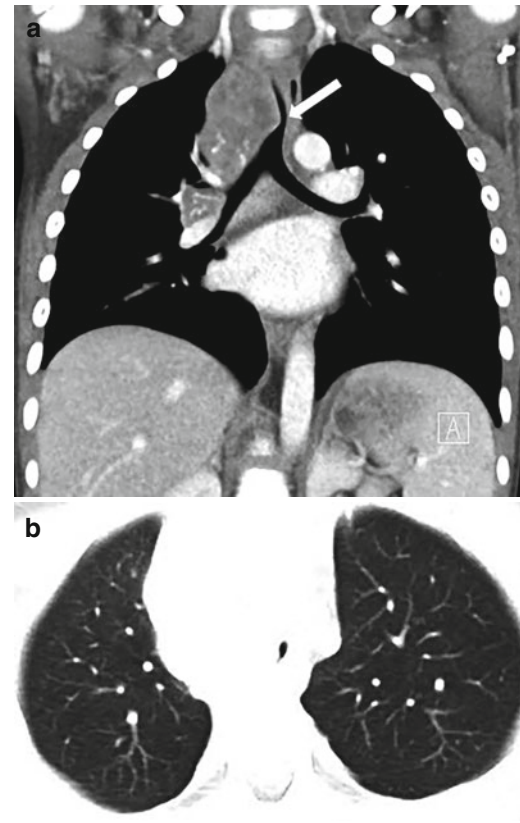

Fig. 20 Mediastinal fibrosis. (**a**) Coronal contrast-enhanced CT image shows right paratracheal, hilar, and subcarinal adenopathy with scattered calcifications in this patient with a history of histoplasmosis. The mass compresses and displaces the trachea (*arrow*) to the left. (**b**) Axial CT image in lung windows shows the markedly reduced caliber of the trachea

On CT, ganglion cell tumors appear as fusiform or elongated paraspinal masses, extending over the length of several vertebral bodies (Lonergan et al. 2002). They are of soft tissue attenuation and contain calcifications in up to 50 % of cases (Fig. 21). Nerve root tumors tend to be smaller, spherical, and occur near the junction of a vertebral body with an adjacent rib (Fig. 22).

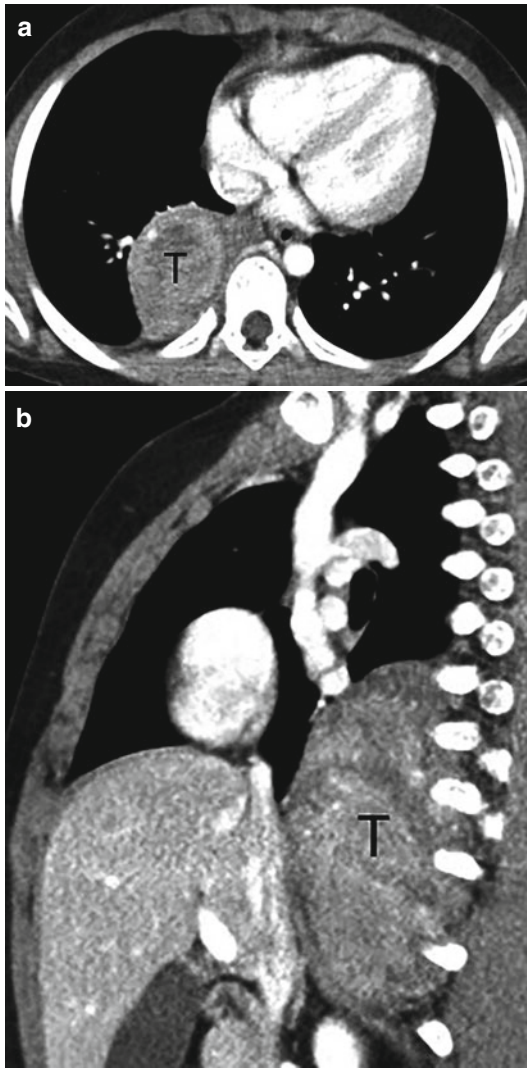

Fig. 21 Posterior mediastinal mass, ganglioneuroblastoma. (**a**) Axial contrast-enhanced CT image through the lower chest shows a large heterogeneously enhancing soft tissue tumor (*T*) with scattered calcification in the right paraspinal region. (**b**) Sagittal CT image shows the tumor (*T*) extending into the intercostal spaces at multiple levels and splaying the ribs

Both types of tumors may cause pressure erosion of a rib. Because of their origin from neural tissue, neurogenic tumors have a tendency to invade the spinal canal. Intraspinal extension is extradural in location, displacing and occasionally compressing the cord. Identification of intraspinal invasion is important because affected patients may require laminectomy prior to tumor debulking.

Rarer causes of posterior mediastinal masses include neurenteric cyst, lateral meningocele, hemangioma, and extralobar sequestration. Neurenteric cysts and lateral meningoceles demonstrate water attenuation on CT. The former are associated with a midline defect in one or more vertebral bodies. Hemangioma typically is a highly vascular paraspinal mass. Sequestration sometimes appears as a paraspinal rather than intraparenchymal mass. Identification of an anomalous feeding artery or vein can confirm the diagnosis.

9 Pulmonary Neoplasms

Most primary lung neoplasms in children are benign and include inflammatory pseudotumor, papilloma, and hamartoma (Siegel 2008b; Dishop and Kuruvilla 2008; McCarville et al. 2006; McCahon 2006).

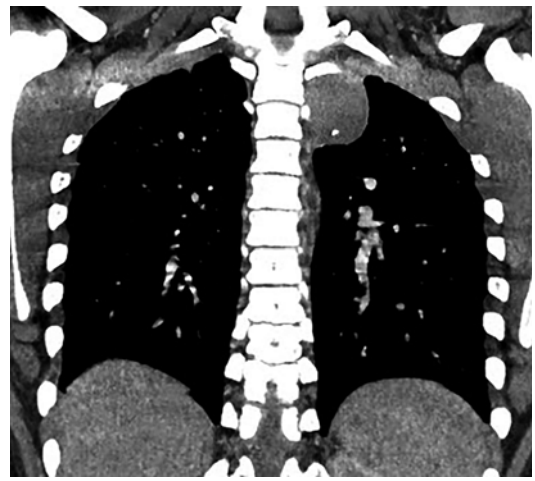

Fig. 22 Granular cell tumor. Coronal image in a 16-year-old boy shows a well-circumscribed, left paraspinal soft tissue mass with punctate calcification

9.1 Benign Pulmonary Neoplasms

Inflammatory pseudotumor, also called plasma cell granuloma, is a benign process most often involving the lung and orbit but found in anywhere in the body (Patnana et al. 2012). The cause is unknown, but it is thought to be a reparative inflammatory process to infection, trauma, or underlying low-grade malignancy. It consists of spindle cells, inflammatory cells (plasma cells and lymphocytes), and fibrous tissue. Patients may be asymptomatic with the lesion discovered incidentally on imaging, but more often they present with cough, chest pain, dyspnea, hemoptysis, and/or fever. On CT, plasma cell granuloma usually appears as a single, circumscribed, round or oval, soft tissue attenuation mass with lower-lobe predominance. Cavitation due to tumor necrosis can occur (Fig. 23). Calcifications may be fine, coarse, or densely clustered. Although histologically benign, this lesion can grow aggressively and encase bronchi or invade mediastinal structures, the chest wall, or diaphragm (Patnana et al. 2012). The CT features are not pathognomonic, and tissue sampling is necessary for diagnosis.

Laryngotracheal papilloma is a benign neoplasm that occurs in the airway of infants and children, caused by infection with human papillomavirus. It arises in the larynx and can extend into the bronchi and lungs. At CT, papillomas appear as round solitary or cystic nodules (Fig. 24). The cystic nodules may enlarge and form large cavities with thick or thin walls. The combination of an intraluminal airway mass and a pulmonary nodule or cavity is virtually diagnostic of laryngotracheal papillomatosis. Malignant transformation into squamous cell carcinoma occurs in 2–3 % of cases, usually affecting older children or adolescents, necessitating serial CT studies for surveillance (Frauenfelder et al. 2005).

Pulmonary hamartoma contains cartilage, fat, and fibrous tissue. The CT appearance is a smooth or slightly lobulated pulmonary nodule or mass, usually located in the periphery of the lung. Fat or calcification may be seen and are considered diagnostic.

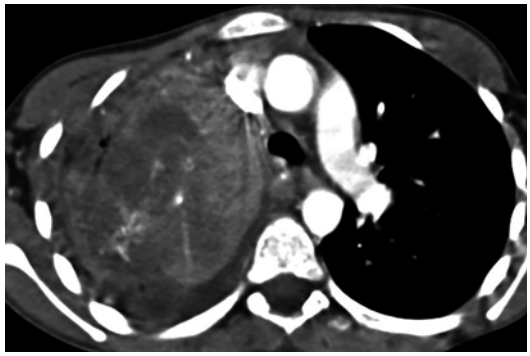

Fig. 23 Plasma cell granuloma (inflammatory pseudotumor). An eight-year-old boy with cough and fever. Axial image shows a large soft tissue mass with calcifications and areas of necrosis in the right upper lobe. The mass invades the pleura

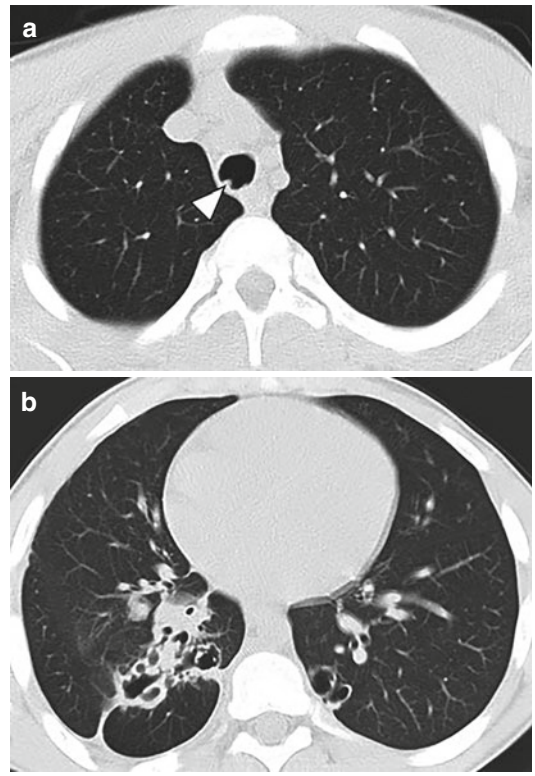

Fig. 24 Laryngotracheal papillomatosis: A 12-year-old boy with recurrent dyspnea. (**a**) Small polypoid mass (*arrowhead*) is seen within the trachea. (**b**) Axial image through the lower lobes show thick-walled cysts as a result of disseminated papillomatosis

9.2 Malignant Pulmonary Neoplasms

Bronchial adenoma encompasses carcinoid tumor, mucoepidermoid tumor, and adenoid cystic carcinoma. Carcinoid tumors, which are low-grade neuroendocrine cancers, account for the majority of bronchial adenomas (Chong et al. 2006). CT findings include an intra- and/or extrabronchial soft tissue attenuation mass, air trapping, atelectasis or obstructive pneumonitis in the subtended lung, and stippled calcification (Fig. 25).

Pleuropulmonary blastoma (also known as pulmonary blastoma) is a malignant neoplasm that occurs in young children, usually less than 5 years of age (Herman and Siegel 2008; Naffaa and Donnelly 2005; Papaioannou et al. 2009). The tumor can arise from the lung, pleura, or both. Three types are recognized. Type 1 is an entirely cystic lesion, type 2 is mixed cystic and solid, and type 3 is entirely solid. It is believed that these three types are a continuum and that the type 1 lesion progresses to type 2 and type 3 as the cysts are replaced by solid malignant tissue. On CT, the tumor can appear as a solid, cystic, or complex mass and can mimic cystic pulmonary airway malformation (Fig. 26). Associated findings include pleural effusion and contralateral mediastinal shift. The prognosis of pleuropulmonary blastoma is best in type 1; overall 5-year survival is approximately 45 % (Herman and Siegel 2008; Naffaa and Donnelly 2005; Papaioannou et al. 2009).

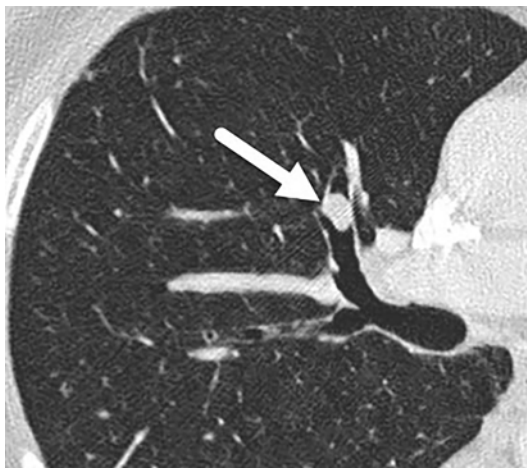

Fig. 25 Bronchial carcinoid. Axial image shows a mass (*arrow*) arising in the bronchus intermedius which partially obstructs the lumen

9.3 Metastases

Malignancies with a high propensity for lung dissemination include Wilms tumor, osteogenic sarcoma, and rhabdomyosarcoma. Demonstration of one or more pulmonary nodules or documentation of additional nodules in a patient with an apparent solitary metastasis for whom surgery is

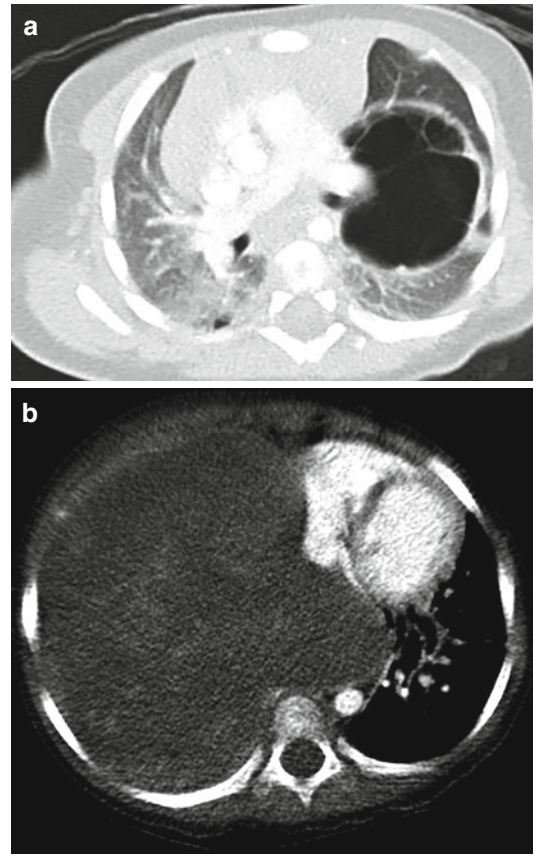

Fig. 26 Pleuropulmonary blastoma. (**a**) Type 1 lesion: Axial image in lung windows shows a cystic mass with internal septations occupying the majority of the left upper lobe. (**b**) Type 3 lesion: Axial image shows a solid mass that replaces most of the right lung. In both patients, there is mediastinal shift to the right

planned may be critical to treatment planning. In the first instance, such detection may lead to additional treatment (surgery, chemotherapy, or radiation), whereas in the latter setting, demonstration of several metastatic nodules may negate surgical plans.

9.4 Other Focal Lung Nodules

Other causes of nodular lung lesions besides metastases include granuloma, opportunistic infections, lymphoproliferative disorders, intrapulmonary lymph node, and some of the congenital anomalies including bronchial atresia and arteriovenous malformation.

10 Vascular Anomalies (CT Angiography) (Protocol 2)

Abnormalities of the aorta and its branches and of the superior or inferior vena cava can cause a mass or mediastinal widening on plain chest radiography. CT is usually the next study of choice to confirm the diagnosis and characterize the vascular anomalies (Hernanz-Schulman 2005; Lee et al. 2004; Siegel 2008d, 2011a; Siegel et al. 2009).

10.1 Left Aortic Arch with Aberrant Right Subclavian Artery

The left aortic arch with an aberrant right subclavian artery is the most common congenital abnormality of the aortic arch vessels (Hernanz-Schulman 2005; Lee et al. 2004; Siegel 2008d, 2011a; Siegel et al. 2009). This anomaly is usually asymptomatic and found incidentally on imaging examinations. However, if the aberrant subclavian artery is ectatic, it may compress the esophagus resulting in dysphagia (dysphagia lusoria). In this anomaly, the proximal to distal order of branching is as follows: right common carotid, left common carotid, left subclavian, and then the aberrant right subclavian artery (Fig. 27).

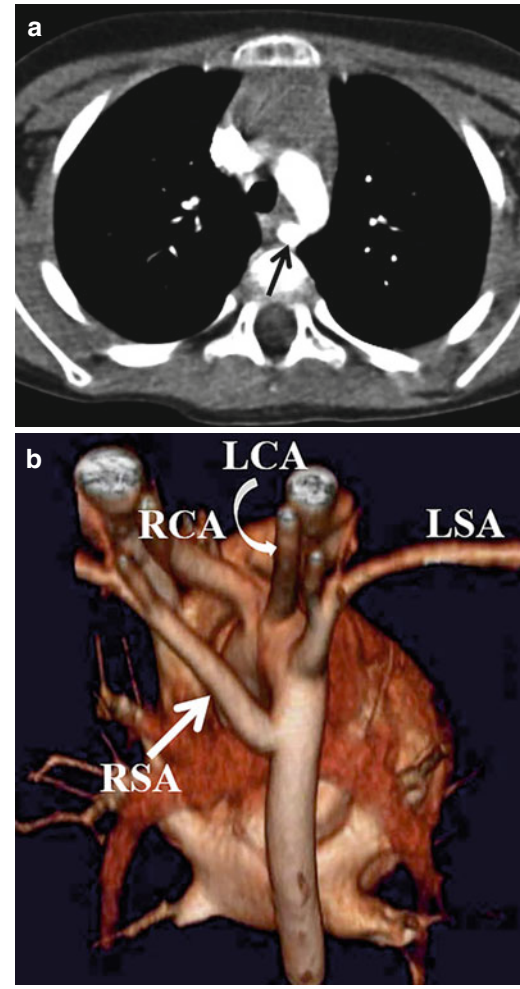

Fig. 27 Left arch with aberrant right subclavian artery. A 4-year-old girl. Upper gastrointestinal series showed extrinsic compression of esophagus. (**a**) Axial contrast-enhanced image demonstrates the right subclavian artery (*arrow*) arising from the left aortic arch and coursing posteriorly. (**b**) 3D image shows typical branching pattern: right common carotid artery (*RCA*), left common carotid artery (*LCA*), left subclavian artery (*LSA*), and the anomalous right subclavian artery (*RSA*)

10.2 Aortic Arch Anomalies

Aortic arch anomalies can produce vascular rings that surround the trachea and esophagus. The primary symptomatology relates to the structures that they encircle and can include dysphagia, odynophagia, wheezing, and shortness of breath with and without exertion.

10.2.1 Vascular Rings

The double arch and the right arch with aberrant left subclavian artery are the most common vascular rings (Hernanz-Schulman 2005; Lee et al. 2004; Siegel 2008d, 2011a; Siegel et al. 2009). In double aortic arch, there are two aortic arches, both of which arise from a single ascending aorta. Each arch gives rise to a subclavian and carotid artery, before uniting to form a single descending aorta, which is usually left-sided. The right arch tends to be higher and larger than the left (Fig. 28). The two components of the arch encircle the trachea and esophagus, resulting in airway compromise or dysphagia. Both aortic arches usually are patent, but occasionally one arch, usually the left, may be hypoplastic or atretic with a fibrous band completing the vascular ring. Double arches with hypoplastic or atretic components can still compress the esophagus and trachea and be symptomatic.

Right aortic arches are classified into two major subtypes: the right arch with an aberrant left subclavian artery and the right arch with mirror-imaging branching (Knight and Edwards 1974). In the former anomaly, the great arteries arise from proximal to distal in the following order: left common carotid artery, right common carotid artery, right subclavian artery, and left subclavian artery. The vascular ring is completed by the ligamentum arteriosum. Patients can be symptomatic because the trachea and esophagus are encircled by mediastinal vessel or because the descending aorta compresses the trachea. On CT, the aberrant left subclavian artery is seen as the last branch vessel to arise from the right aortic arch; it can be dilated at its origin forming a diverticulum of Kommerell (Fig. 29).

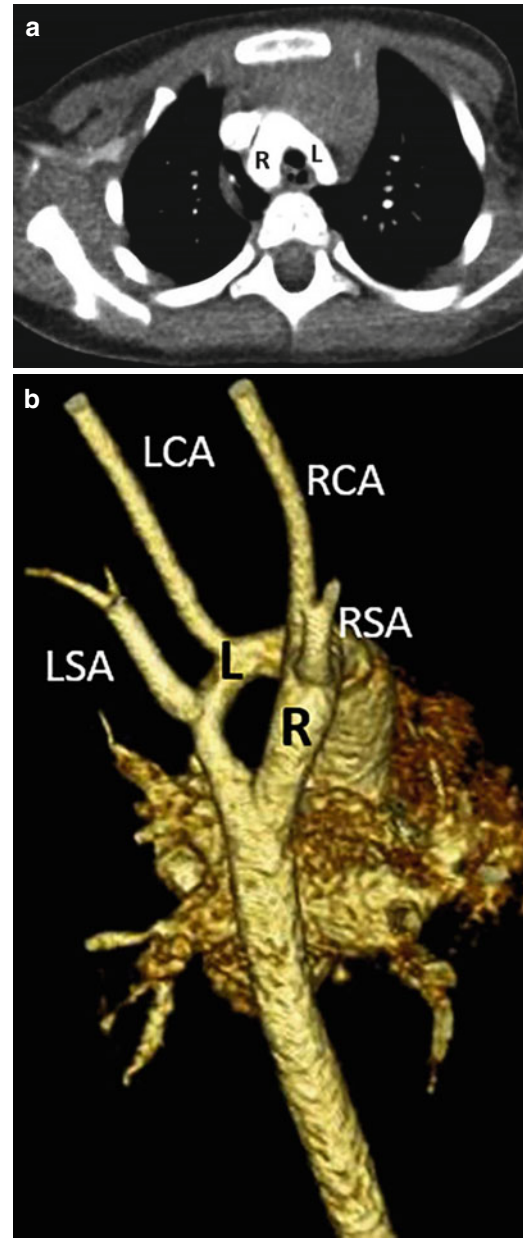

Fig. 28 Double aortic arch. (**a**) Axial contrast-enhanced CT demonstrates two aortic arches. The right arch is larger than the left (**b**): 3D reconstruction shows each aortic arch giving rise to a common carotid and subclavian artery. *R* right aortic arch, *L* left aortic arch, *LSA* left subclavian artery, *LCA* left common carotid artery, *RCA* right common carotid artery, *RSA* right subclavian artery

10.2.2 Right Arch with Mirror-Imaging Branching

A right aortic arch with mirror-imaging branching has a high incidence of congenital heart disease, but stridor and dysphagia are usually absent because there is no structure posterior to the trachea or the esophagus. The aortic arch branch arteries arise from the right arch in the following order from proximal to distal: left innominate artery, right common carotid artery, and right subclavian artery (Fig. 30). The aorta usually descends on the right.

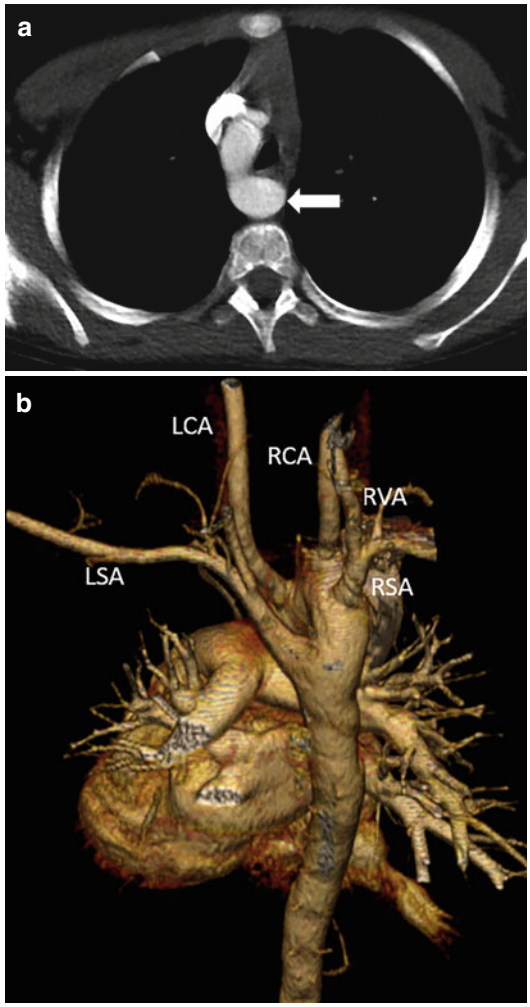

Fig. 29 (**a**) Right aortic arch with aberrant left subclavian artery. (**a**) Axial contrast-enhanced image demonstrates the left subclavian artery (*arrow*) arising from the right aortic arch and coursing posterior to the trachea and esophagus. (**b**) 3D image shows typical branching pattern; left carotid artery (*LCA*), right common carotid artery (*RCA*), right subclavian artery (*RSA*), and the left subclavian artery (*LSA*) as the last branch off the aorta. The right subclavian artery gives rise to the right vertebral artery (*RVA*)

10.2.3 Aortic Aneurysms

Aortic aneurysms are rare in children. When they occur, they are usually associated with predisposing conditions, such as Turner syndrome, aortic coarctation, Marfan syndrome, Ehlers-Danlos syndrome, Kawasaki disease, prior surgery, or trauma. Most aneurysms are fusiform in configuration. They may be focal or diffuse.

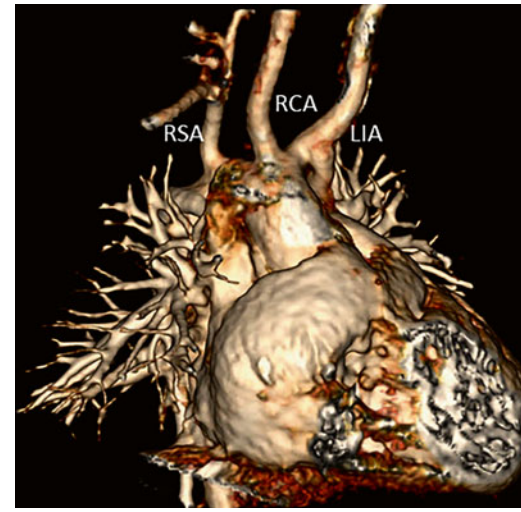

Fig. 30 Right arch with mirror-image branching. 3D reconstruction in a 6-month-old girl with tetralogy of Fallot. The right arch gives rise to the left innominate artery (LIA), right common carotid artery (*RCA*), and right subclavian artery (*RSA*) in descending order

10.2.4 Aortic Coarctation

Coarctation of the aorta is a congenital narrowing at the junction of the aortic arch and proximal descending aorta in the region of the ligamentum ductus arteriosus and inferior to the left subclavian artery (Siegel 2008e, 2011b) The two basic types of coarctation are preductal (infantile) and postductal (adult). In the preductal form, the coarctation is associated with tubular hypoplasia of the transverse arch. The ductus arteriosus is usually patent and supplies blood to the descending aorta from the pulmonary artery (Fig. 31).

The postductal form, coarctation produces a focal shelf-like indentation of the posterior aortic wall caudal to the origin of the left subclavian artery. The aortic arch is usually of normal diameter, and collateral vessel formation is common (Fig. 32). Inferior notching of the third to sixth ribs by dilated intercostal arteries is another characteristic-imaging finding.

10.3 Systemic Veins

Systemic venous anomalies comprise abnormalities characterized by abnormal connection or

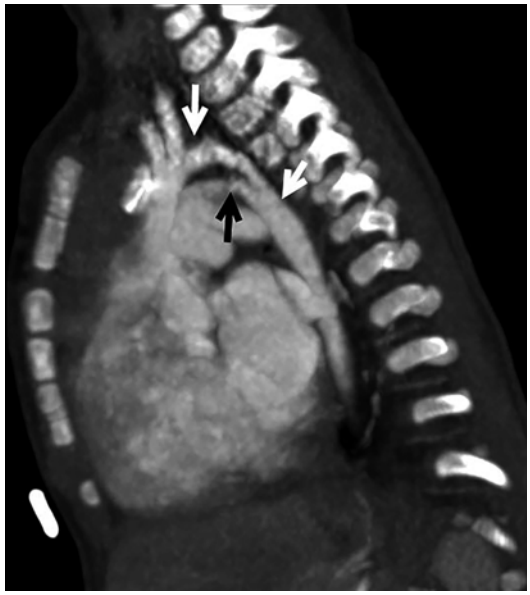

Fig. 31 Preductal aortic coarctation. Sagittal maximum intensity projection image shows long segment narrowing in the aortic arch (*white arrows*). Note also the patent ductus arteriosus (*black arrow*) which is typical of preductal coarctation

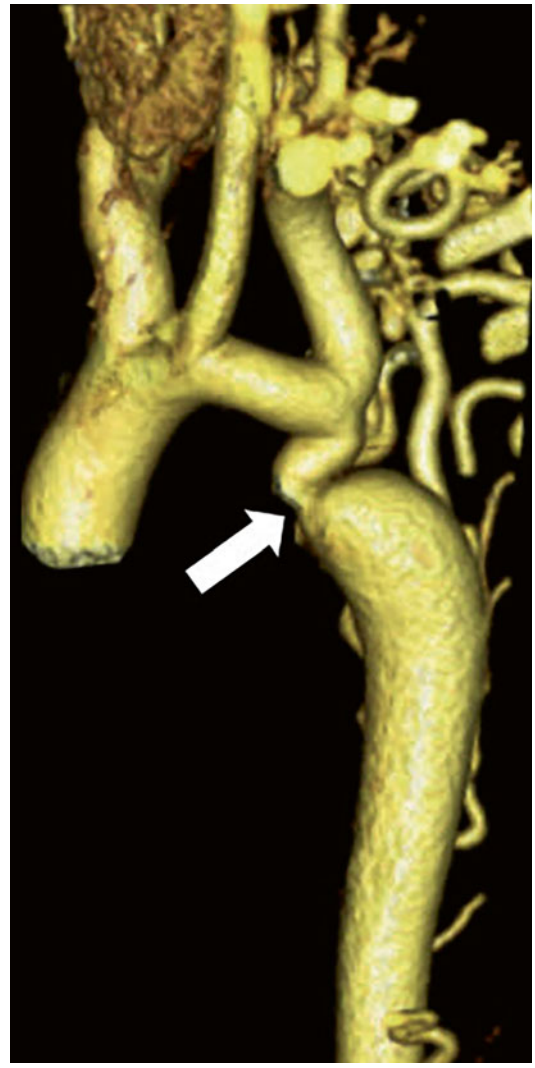

Fig. 32 Postductal aortic coarctation. 3D volume-rendered image shows a focal area of narrowing (*arrow*) in the proximal descending aorta (juxtaductal) just below the left subclavian artery. The collateral intercostal arteries are dilated and tortuous

drainage of systemic veins (Siegel 2008d; Siegel et al. 2009; Demos et al. 2004). The two major anomalies are persistent left superior vena cava and azygos continuation of the inferior vena cava (IVC). A persistent left superior vena cava can occur in the general population, but it is more likely to occur in patients with congenital heart disease (Fig. 33). The left superior vena cava lies lateral to the aortic arch. As it courses inferiorly, it passes lateral to the main pulmonary artery and anterior to the left hilum to enter the coronary sinus that wraps around the bottom of the left atrium.

Azygos continuation of the IVC, also termed the absence of the hepatic segment of the IVC with azygos continuation, results from in utero interruption of the intrahepatic IVC. The suprarenal and intrahepatic portions of the IVC are absent. Blood from the lower half of the body returns to the heart via the azygos and hemiazygos veins. Azygos continuation may be associated with congenital heart disease and asplenia or polysplenia, but it is often an isolated finding. CT findings are dilatation of the azygos arch, azygos vein, and superior vena cava caudal to the azygos junction; enlargement of the azygos and hemiazygos veins in the paraspinal and retrocrural areas; and the absence of the suprarenal and intrahepatic portions of the inferior vena cava (Fig. 34).

10.4 Pulmonary Arteries and Vein

10.4.1 Pulmonary Artery Sling

In the pulmonary sling, the left pulmonary artery originates from the right pulmonary

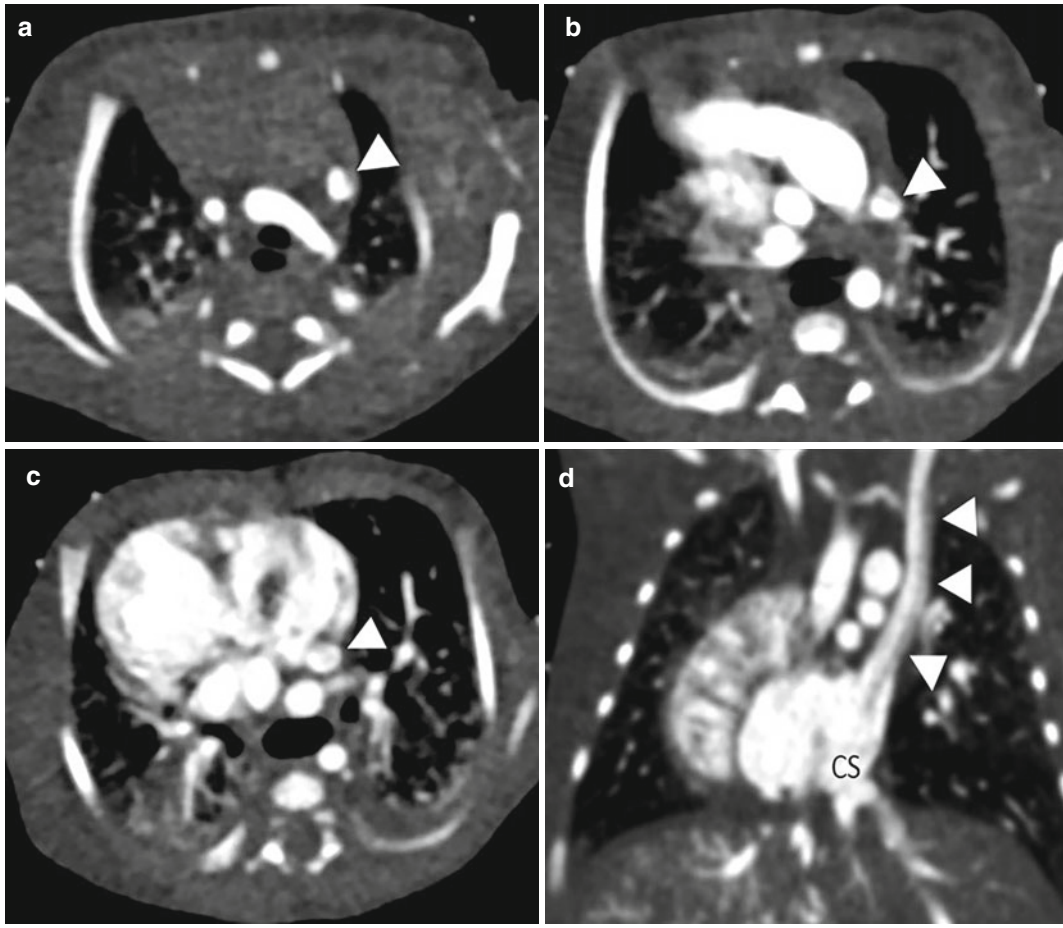

Fig. 33 Persistent left superior vena cava (SVC). (**a**–**c**) Axial CT images in a 3-day-old boy with heterotaxy syndrome show a vessel (*arrowheads*) to the left of the aortic arch, pulmonary artery, and left hilum. (**d**) Coronal image shows the left SVC (*arrowheads*) draining into the coronary sinus (*CS*)

artery and crosses the mediastinum, extending between the trachea and esophagus to reach the left hilum (Siegel 2008d, 2011a; Siegel et al. 2009) (Fig. 35). The left pulmonary artery thus forms a sling around the distal trachea and the proximal right main bronchus. This anomaly may be symptomatic because of the compressive effect of the artery on the airway and/or associated tracheal or bronchial stenosis due to cartilaginous rings, but it may also be asymptomatic and detected incidentally on imaging studies (Berdon et al. 1984). Contrast-enhanced CT can simultaneously show the abnormal left pulmonary artery and any associated tracheobronchial narrowing.

10.4.2 Pulmonary Veins

Partial anomalous return is the most common abnormality of the pulmonary veins. The anomalous connection causes a left-to-right shunt and can result in pulmonary hypertension. When the anomalous drainage is associated with right lung and pulmonary artery hypoplasia, it is termed hypogenetic lung or scimitar syndrome.

The anomalous left superior pulmonary vein drains into the left brachiocephalic vein, producing a vertical vein that courses lateral to the aortic arch and aortopulmonary window. The anomalous right inferior pulmonary vein usually drains into the IVC or occasionally into the portal or hepatic veins. The anomalous right superior pul-

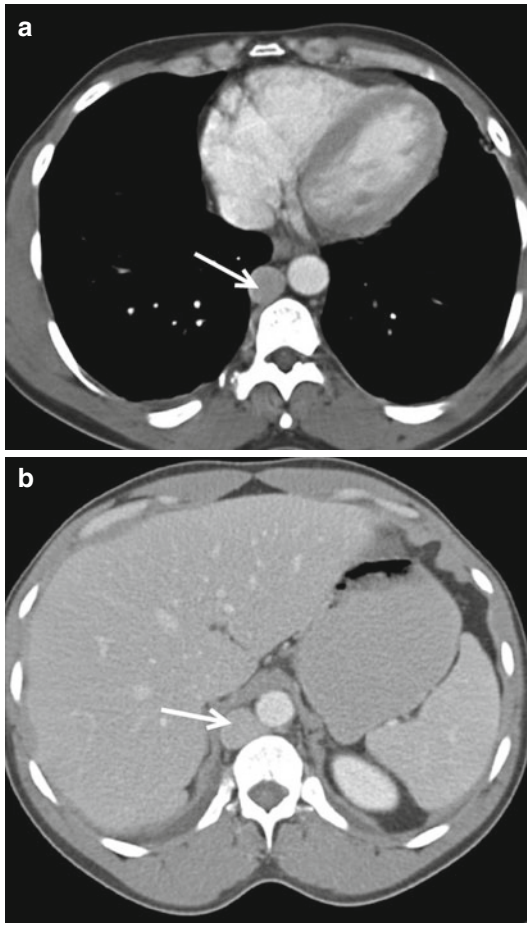

Fig. 34 Interrupted IVC with azygos continuation. (**a**) Axial CT image in an 18 year old male demonstrates a dilated azygos vein (*arrows*) through which the venous return from the lower body is returned to the heart. (**b**) Axial image of the upper abdomen in another patient shows a dilated azygos vein and absence of the intrahepatic vena cava

monary vein drains into the superior vena caval-right atrial junction and is commonly associated with a sinus venosus atrial septal defect (Fig. 36).

11 Evaluation of the Airway (Protocol 3)

11.1 Central Airway Disease

Intravenous contrast material is not needed for evaluation of airway stenosis or tracheobronchomalacia, but it is indicated in the evaluation of extrinsic causes of airway disease, such as the vascular anomalies or neoplasms. A 0.6-mm collimation and a pitch >1 suffice.

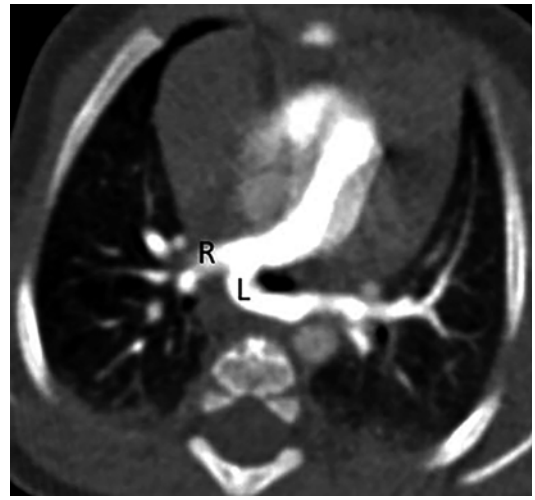

Fig. 35 Pulmonary sling. Axial image shows the left pulmonary artery (*L*) arising from the right pulmonary artery (*R*). The left pulmonary artery then crosses posterior to the trachea to reach the left hilum

Axial images are indispensable for assessing extraluminal disease, including the lung parenchyma and mediastinal structures. Multiplanar and external volume-rendered images can improve the assessment of subtle airway stenosis, the craniocaudal extent of airway narrowing, the anatomy of complex relationships, and stent localization, including malposition, migration, and fracture (Siegel 2003; Lee and Siegel 2008). They also are useful for displaying the craniocaudal extent of airway collapse in patients with tracheal or bronchial malacia (Baroni et al. 2005; Boiselle et al. 2003).

Virtual 3D bronchoscopic images, although not necessary for diagnosis, offer the benefit of viewing the airway distal to a high-grade stenosis or large obstructing neoplasm, areas which otherwise can be difficult to visualize by conventional bronchoscopy (Sorantin et al. 2002). Other applications for virtual bronchoscopy include localizing foreign bodies and determining sites for performing transbronchial needle aspirations and biopsies.

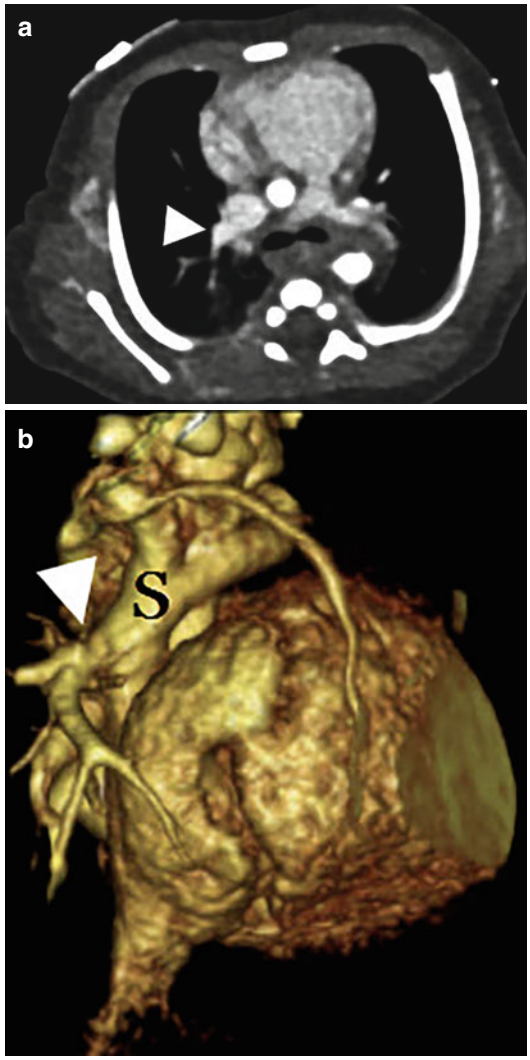

Fig. 36 Partial anomalous venous return. (**a**) Axial CT scan at the level of the hila shows the anomalous pulmonary vein (*arrowhead*) draining the right upper lobe. (**b**) 3D volume-rendered image shows the anomalous vessel (*arrowhead*) entering the superior vena cava (*S*)

Protocol 3

Indication	Tracheobronchial tree (Congenital anomalies; stricture, tracheomalacia, tumor)
Extent	Vocal cords to mainstem bronchi, just below carina
mAs and kVp	Lowest possible
Collimation	0.6–1.0 cm
Pitch	1.2–3.0
Reconstruction interval	5×5 mm, 1×2 mm
Patient instructions	Suspended inspiration
Contrast type	None
Comments	1. Aim for a single breath-hold 2. If small airway obstruction or tracheomalacia is suspected, obtain scans in inspiration and expiration 3. If child sedated or uncooperative, CT scans obtained at quiet breathing 4. Use high-spatial resolution reconstruction (bone) algorithm 5. Multiplanar and 3D reconstructions should be performed

11.1.1 Clinical Applications

Asthma and acute bronchiolitis are common diseases of the trachea and main bronchi, but they rarely require imaging other than chest radiographs (Brody 2008). The frequent indications prompting CT of the airway are evaluation of (a) congenital tracheobronchial anomalies, (b) tracheal narrowing, and (c) tracheal and bronchial malacia. By comparison with adults, tracheobronchial neoplasia is a rare indication for CT in children (Siegel 2008b).

The most common congenital tracheobronchial anomalies are the tracheal and cardiac bronchi (Ghaye et al. 2001). The ectopic tracheal or pig bronchus arises from the right lateral wall of the trachea, rather than from the right main bronchus, usually within 2 cm of the carina (Fig. 37). The accessory cardiac bronchus arises from the inferior medial wall of the right main or intermediate bronchus, and it may be blind-ending, or it may ventilate a hypoplastic lobule. Most anomalous bronchi are asymptomatic and discovered during evaluation of other clinical symptoms or signs. However, both types of bronchi may serve as reservoirs for infectious organisms leading to recurrent pneumonia.

Tracheal narrowing can be due to intrinsic strictures or extrinsic masses or vascular rings (see above discussions). Tracheal strictures can be congenital or the sequel of intubation, tracheostomy placement, or surgical anastomoses. In the evaluation of tracheal stenosis, external 3D renderings offer complementary information to axial imaging by providing

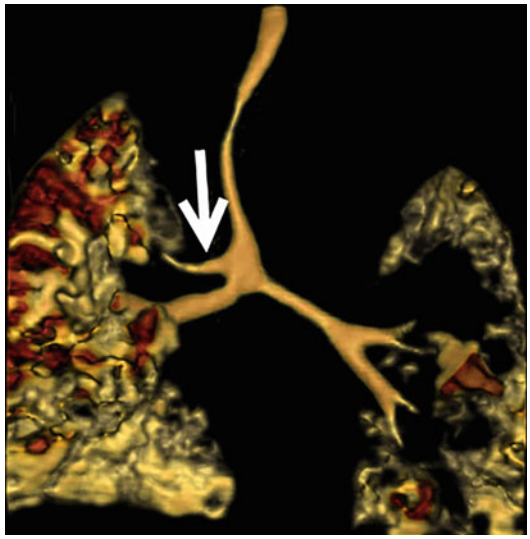

Fig. 37 Tracheal bronchus. 3D volume-rendered image shows a bronchus (*arrow*) rising from the right lateral wall of the trachea just above the carina. The bronchus supplies the right upper lobe

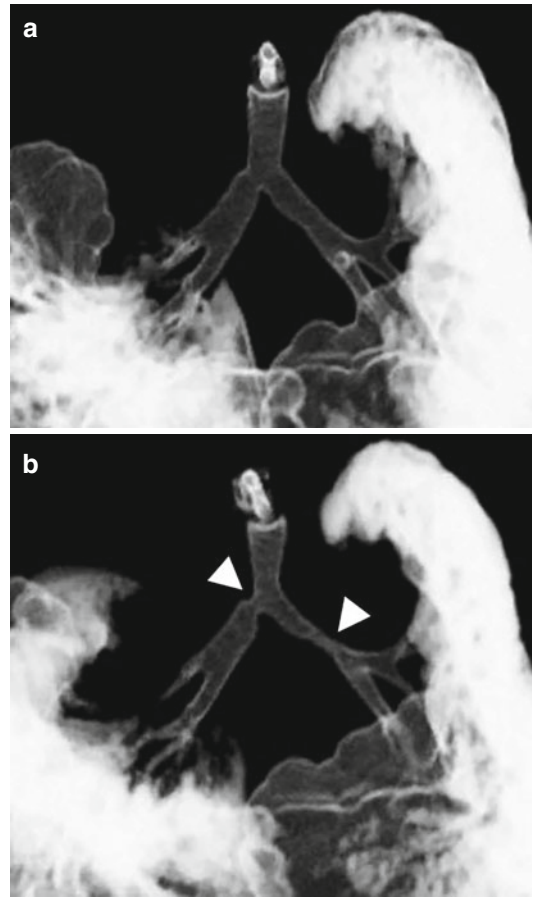

Fig. 38 Tracheomalacia. A 3-month-old girl with noisy breathing. (**a**) 3D bronchographic reconstruction at inspiration shows normal distal trachea and main bronchi. (**b**) 3D reconstruction at expiration shows at least 50 % collapse of the origin of the right main bronchus and the distal left main bronchus (*arrowheads*)

more precise evaluation of shape, length, and degree of stenosis.

Tracheobronchomalacia refers to an abnormal weakness of the tracheal walls and supporting tissues, resulting in luminal collapse during expiration (Cardin et al. 2005). The term bronchomalacia refers to weakness and exaggerated collapse of one or both main bronchi. The common symptoms include stridor, cough, wheezing, cyanosis, and recurrent pulmonary infection. When tracheobronchomalacia is suspected, scans are acquired at both end-inspiration and end-expiration and then reformatted in coronal and sagittal planes (Baroni et al. 2005; Boiselle et al. 2003; Sorantin et al. 2002). This technique is limited to cooperative patients or to patients who are on assisted ventilation. Sensitivity can be increased with dynamic-forced exhalation (Boiselle et al. 2009). The diagnosis of tracheobronchomalacia is made by CT when there is 50 % or greater reduction in transluminal diameter during expiration (Fig. 38).

An occasional indication for airway CT is foreign body aspiration (Haliloglu et al. 2003; Kosucu et al. 2004). Vegetarian matter is the most common aspirated airway foreign body, accounting for up to 95 % of cases. The remaining foreign bodies are plastic matter or metals. Relatively small foreign bodies lodge in the bronchi, usually the right main bronchus. Larger foreign bodies may become lodged in the laryngeal airway or trachea. Bronchoscopy is the standard for diagnosis. CT can be helpful to confirm the presence and location of the foreign body prior to bronchoscopy (Haliloglu et al. 2003; Kosucu et al. 2004).

11.2 Peripheral Airway Disease

Bronchiolitis obliterans is the most common peripheral airway disease in children. It is

characterized by inflammation and fibrosis of the submucosal and peribronchial tissues of the terminal and respiratory bronchioles, leading to airway narrowing and obliteration (Lau et al. 1998; Siegel et al. 2001). Bronchiolitis obliterans can be idiopathic or it can follow a variety of different insults, including viral or bacterial infections, toxic fume inhalation, collagen vascular diseases, and bone marrow and lung or heart-lung transplants. CT findings include a pattern of mosaic attenuation, due to air trapping and reflex vasoconstriction, and bronchiectasis (Fig. 39) (Brody 2008; Lau et al. 1998; Siegel et al. 2001). The mosaic attenuation manifests as areas of decreased attenuation alternating with areas of relatively increased attenuation. Air trapping is best demonstrated on expiratory scans (Siegel et al. 2001).

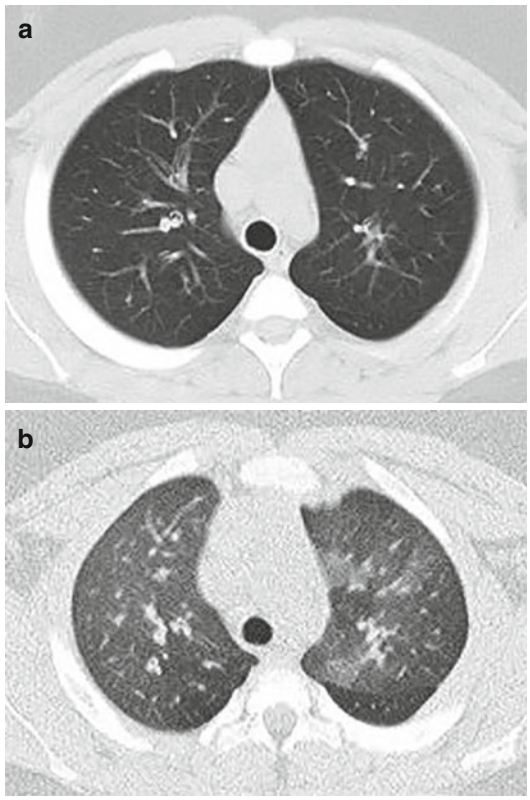

Fig. 39 Bronchiolitis obliterans in a 9-year-old girl after bilateral lung transplantation. (**a**) Axial section through the upper lungs at inspiration shows a mosaic pattern with areas of high and low attenuation. (**b**) Scan during expiration shows that the low-attenuation areas increase in size consistent with air trapping secondary to small airway obstruction. The normal nonobstructed areas increase in attenuation

12 Diffuse Interstitial Lung Disease (Protocol 4)

Chest radiography remains the initial imaging study for evaluation of suspected diffuse parenchymal lung disease. CT, however, can be useful to better define and characterize an abnormality suspected on conventional chest radiography, especially when the CT examination is performed with high-resolution technique using narrow (1 mm) collimation at 1–2 cm intervals and a high-spatial frequency reconstruction algorithm. In most instances, axial images suffice for diagnosis. Multiplanar and 3D maximum intensity projection (MIP) images can help to characterize some diffuse lung diseases. MIP images can increase small nodule detection and help in characterizing the location of centrilobular and peribronchovascular nodules.

The indications for high-resolution CT of the lung parenchyma in children include (a) detection of disease in children who are at increased risk for lung disease (e.g., immunocompromised

Protocol 4

Indication	Combined chest/high-resolution (CT) (Diffuse interstitial lung disease)
Extent	Lung apices to caudal bases
mAs and kVp	Lowest possible
Collimation	1 mm
Pitch	1.2–3.0
Reconstruction interval	5×5 mm, 1×2 mm
Patient instructions	Suspended inspiration
IV Contrast	None
Miscellaneous	1. Aim for a single breath-hold 2. Expiration imaging can be useful to evaluate suspected areas of air trapping 3. If child sedated or uncooperative, CT scans obtained at quiet breathing 4. Multiplanar reconstructions should be performed

patients) and who have respiratory symptoms but a normal chest radiograph; (b) determination of the extent, distribution, and character of diffuse lung diseases seen on chest radiography; (c) localization of the abnormal lung for biopsy; and (d) assessment of the response to treatment.

Diffuse lung disease in children is classified into two main categories: (a) those that are unique in infancy and (b) those that are nonspecific and occur in children and adolescents (Kurland et al. 2013; Das et al. 2011).

12.1 Unique Disorders of Infancy

The disorders of infancy include prematurity-related chronic lung disease (bronchopulmonary dysplasia), surfactant dysfunction disorders (associated with mutations in the genes encoding surfactant proteins B or C, the ATP-binding cassette transporter A3 gene, or thyroid transcription factor 1), neuroendocrine cell hyperplasia, and pulmonary interstitial glycogenosis (Aukland et al. 2006; Gower and Nogee 2011; Newman et al. 2001; Brody et al. 2010; Lanfranchi et al. 2010; Castillo et al. 2010). Affected infants typically present with dyspnea, tachypnea, crackles, and/or hypoxemia.

The diagnosis of chronic neonatal lung disease of prematurity or bronchopulmonary dysplasia can be established on the basis of clinical history of prematurity and CT findings, which include hyperinflation, patchy low-attenuation areas, and coarse linear opacities radiating from the lung periphery to the hilar areas (parenchymal bands) (Siegel 2008b; Aukland et al. 2006) (Fig. 40). Unlike the other lung disorders of infancy, ground-glass opacity is not a finding of lung disease of prematurity.

CT and clinical findings in the other disorders of infancy are nonspecific and overlap, and biopsy and/or lavage is required to obtain a definitive diagnosis (Gower and Nogee 2011; Newman et al. 2001; Brody et al. 2010; Lanfranchi et al. 2010; Castillo et al. 2010). CT findings include ground-glass opacity and interlobular septal thickening, sometimes resulting in a crazy paving pattern, cystic areas, and coarse linear opacities (Figs. 41 and 42).

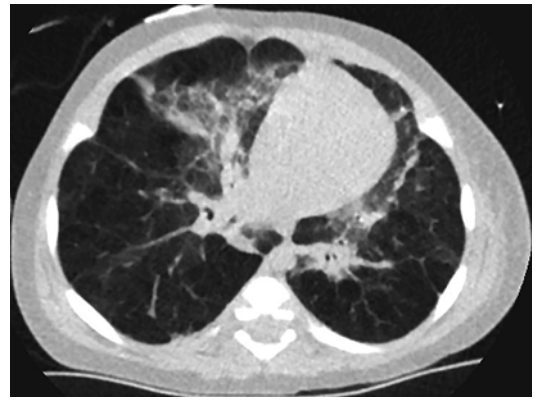

Fig. 40 Bronchopulmonary dysplasia. CT scan demonstrates areas of low attenuation and linear opacities radiating from the lung periphery to the hilum. Atelectasis is also seen in the right middle lobe and lingua

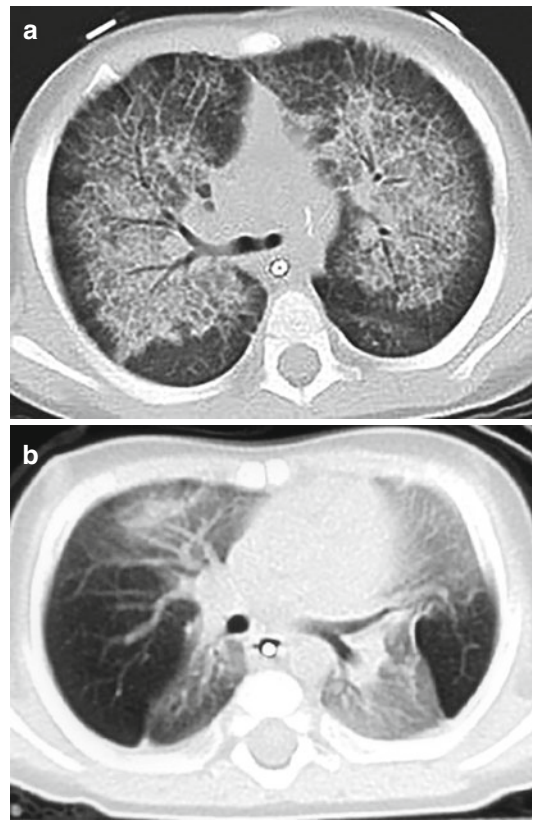

Fig. 41 Surfactant deficiency lung disease. (**a**) A 3-month-old boy. Axial image demonstrates thickened interlobular septa with regions of ground glass, creating a crazy paving pattern. (**b**) Axial image in a 5-month-old boy shows ground-glass opacity in the upper and lower lobes

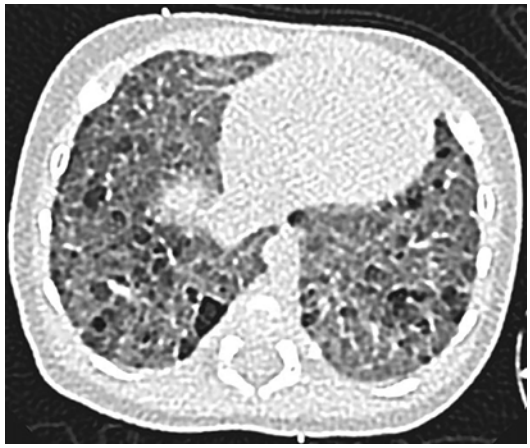

Fig. 42 Pulmonary interstitial glycogenosis. Axial image in a 1-month-old boy demonstrates diffuse ground-glass opacities, coarse linear opacities, and cystic areas

12.2 Disorders Not Specific to Infancy

Some forms of childhood diffuse interstitial lung disease are similar to disorders occurring in adults (Garcia-Pena et al. 2011; Vrielynck et al. 2008). This category comprises (a) disorders occurring in the normal host (infectious and postinfectious processes, disorders related to environmental agents including hypersensitivity pneumonitis and toxic inhalation, aspiration syndromes, and eosinophilic pneumonia), (b) disorders of the immunocompromised host (opportunistic infections, rejection syndromes), (c) disorders related to systemic disease processes (cystic fibrosis, connective tissue, metabolic and storage diseases, sarcoidosis, Langerhans cell histiocytosis, Wegener granulomatosis), and (d) disorders with vascular features (pulmonary veno-occlusive disorders). Of these diseases, cystic fibrosis is the most common chronic lung disease in children and will be discussed herein. The other lung diseases are more common in adults and are covered elsewhere in this textbook.

Cystic fibrosis, a multisystem, autosomal recessive disorder, is the most common life-limiting genetic disorder in the United States. The CT findings include bronchiectasis, peribronchial wall thickening, centrilobular nodular and tree-in-bud opacities (representing mucus plugging), mosaic attenuation, and air trapping on expiration scans (Fig. 43). Hilar and mediastinal lymph node enlargement also may be seen, due to chronic infection. The disease has a predilection for the upper lobes, although all lobes are involved. Systemic CT-scoring systems have been devised to evaluate the severity of cystic fibrosis and patient response to therapeutic regimens, but these have not gained widespread use (Calder et al. 2014).

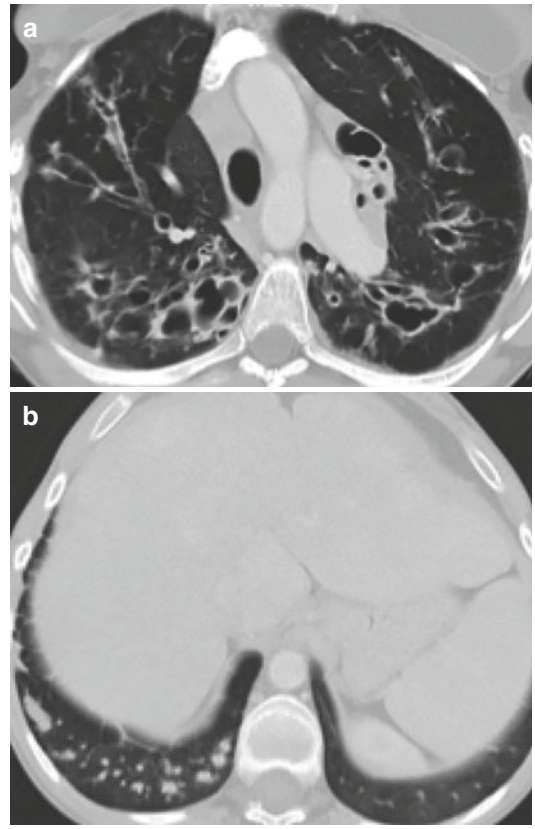

Fig. 43 Cystic fibrosis. (**a**) Axial CT image shows bronchiectasis and bronchial wall thickening. (**b**) CT image at the lung bases shows centrilobular nodules representing mucus plugging

13 Pulmonary Infections

Conventional chest radiography remains the imaging technique to exclude or confirm a clinically suspected pulmonary infection, to evaluate

for the presence of parapneumonic effusion, and to assess the response to treatment. In patients who do not respond to appropriate therapy, CT is useful to assess suspected complications, including abscess, lung necrosis (i.e., necrotizing pneumonia), and empyema (Calder and Owens 2009).

13.1 Bacterial Pneumonitis

CT of uncomplicated bacterial pneumonia demonstrates segmental or multifocal consolidation with air bronchograms, typical of air-space disease. The infected lung parenchyma usually enhances following administration of intravenous contrast medium. Centrilobular nodules, tree-in-bud, and pleural effusion also may be noted.

Complications of bacterial infection include abscess formation, cavitary necrosis, and empyema. These usually are sequelae of *Staphylococcus aureus* or anaerobic *Streptococcus* infection. On CT, abscesses have thick, irregular walls and may contain an air-fluid level if they develop a communication with the bronchus (Fig. 44). Necrotizing pneumonia manifests as cavitary lesions without well-defined walls or enhancing margins within an area of consolidation in conjunction with decreased parenchymal enhancement after administration of intravenous contrast medium (Fig. 45). Necrotizing pneumonia is important to recognize, because most children with this finding need to be hospitalized and require a longer course of antibiotic therapy than do children with uncomplicated pneumonia. Empyema is characterized by pleural fluid, pleural thickening, and enhancement of the visceral and parietal pleura (see Fig. 45). Frequently, there is associated edema/inflammation of the extrapleural tissues.

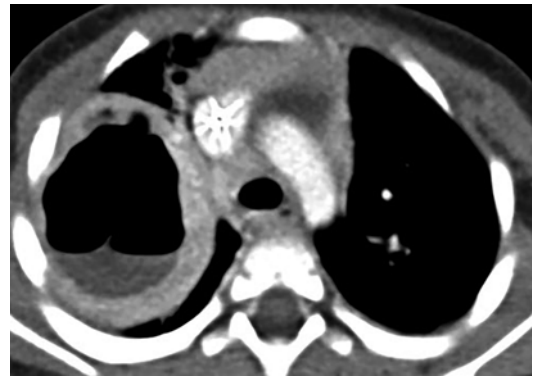

Fig. 44 Lung abscess. Axial contrast-enhanced image shows a large fluid collection with a thickened enhancing wall in the right upper lobe. The presence of an internal air-fluid level indicates a bronchial communication

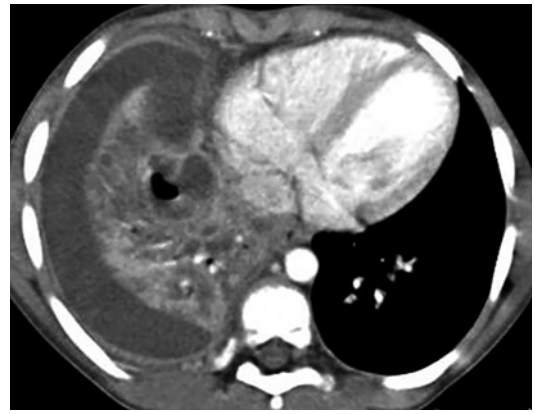

Fig. 45 Necrotizing pneumonia. Axial contrast-enhanced image in a 6-year-old girl demonstrates areas of hypoattenuation and heterogeneous enhancement in the right lower lobe consistent with a necrotizing pneumonia. There is also a large loculated pleural effusion with pleural enhancement consistent with an empyema

13.2 Mycobacterial Infection

Most children with tuberculosis have primary disease, referring to a clinical infection that follows the first exposure to the organism. CT findings are parenchymal consolidation accompanied by hilar or mediastinal lymph node enlargement, particularly the right paratracheal nodes and, in some cases, pleural effusion (Andronikou et al. 2004). The involved lymph nodes commonly show low-attenuation centers, representing areas of necrosis (Fig. 46). Calcification may develop over time. Postprimary or reactivation TB results from reactivation of latent infection. The characteristic CT findings are upper lobe consolidation with cavitation, without adenopathy and effusions.

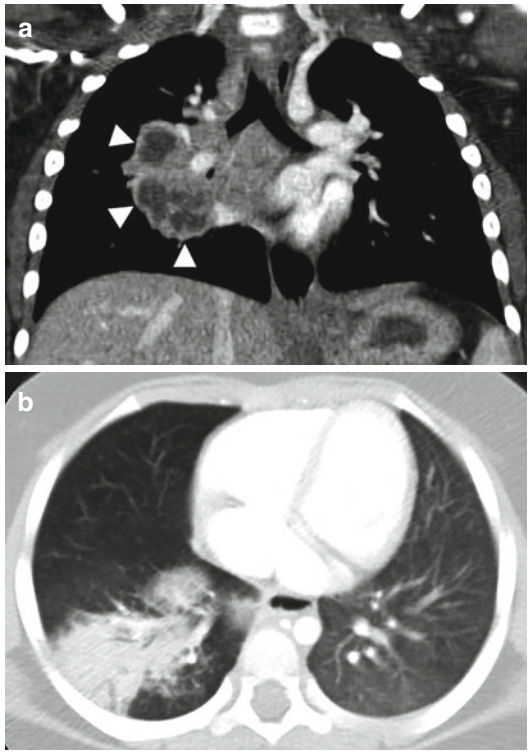

Fig. 46 Primary tuberculosis. A 4-year-old girl with cough and abnormal chest radiograph. (**a**) Coronal contrast-enhanced image shows enlarged right hilar and subcarinal lymph nodes with central areas of low attenuation (*arrowheads*). (**b**) Axial image in lung windows shows the adjacent consolidation in the right lower lobe

13.3 Immunocompromised Host

CT features of aspergillus infection, acquired immunodeficiency syndrome (AIDS), pneumocystis carinii pneumonia (PCP), and cytomegalovirus pneumonia are similar in children and adults and are covered elsewhere in this book.

14 Chest Wall

The chest wall is composed of the osseous skeleton and associated musculature and soft tissues. Any of these structures may be involved by tumor, infection, or trauma. Sonography is usually the initial examination for characterization of soft tissue chest wall masses. MRI is the imaging study for evaluating the extent of large soft tissue lesions. MRI also has become the primary imaging technique for evaluating osseous lesions seen or suspected on plain radiographs. However, CT with its greater spatial resolution can be useful for detecting contiguous bone involvement, which can be important in surgical planning (Baez and Lee 2013).

14.1 Soft Tissue Tumors

Soft tissue tumors of the chest wall in children are generally benign. Lymphangiomas and hemangiomas, and lipomas, some of which have both intrathoracic and extra-thoracic components, are the most common benign tumors. Rhabdomyosarcoma (Fig. 47) is the more common malignant soft tissue tumor (Siegel 2008b; Baez and Lee 2013). Rarer malignancies include synovial sarcoma, fibrosarcoma, neurofibrosarcoma, malignant fibrous histiocytoma, leiomyosarcoma, alveolar soft part sarcoma, and liposarcoma (Siegel 2008b; Baez and Lee 2013).

In some benign soft tissue tumors, CT can provide a specific diagnosis on the basis of attenuation values or morphology. Lymphangiomas appear as diffuse or focal masses of near-water attenuation (Fig. 48); septations are common. Hemangiomas are vascular masses with internal septations; they enhance after contrast administration (Fig. 49). Round calcifications representing phleboliths also may be seen. Lipomas are reliably diagnosed on CT by their characteristic fat attenuation values. Unfortunately, most benign and malignant soft tissue neoplasms have nonspecific features and are seen as masses with an attenuation value equal to or slightly lower than that of normal muscle, with or without pleural or rib involvement. Tissue sampling is needed for definitive diagnosis.

14.2 Osseous Lesions

Osseous chest wall masses are more likely to be malignant than benign. Benign lesions include

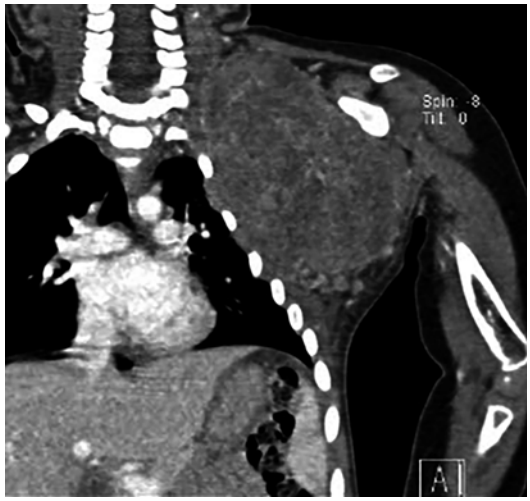

Fig. 47 Malignant soft tissue chest wall tumor, rhabdomyosarcoma. A 1-year-old boy with a left axillary mass. CT documents a soft tissue mass in the left chest wall

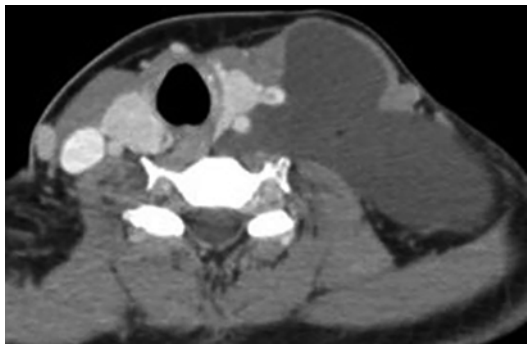

Fig. 48 Cystic hygroma. Axial image shows a low-attenuation mass in the left cervical region which extends into the axilla and chest wall

mesenchymal hamartoma, osteochondroma, and normal variations in bone or cartilage development, including prominent convexity or asymmetry of anterior rib or costal cartilage and pectus excavatum. The common malignant lesions are metastatic neuroblastoma, leukemia, lymphoma, Langerhans cell histiocytosis, Ewing sarcoma, and osteosarcoma (Siegel 2008b; Baez and Lee 2013). Benign anterior chest wall lesions are usually palpable and asymptomatic, whereas aggressive lesions are often associated with pain and/or tenderness. CT findings of osseous chest wall lesions include bone destruction or expansion, an associated soft tissue mass, and pleural effusion.

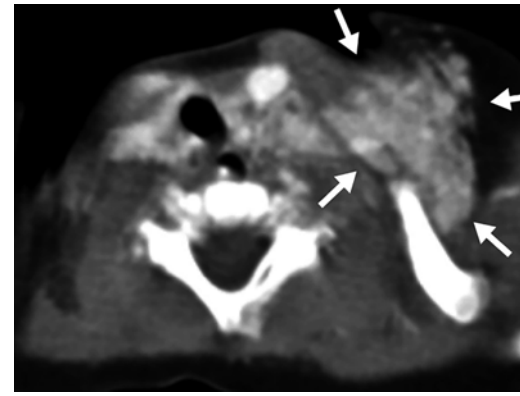

Fig. 49 Chest wall hemangioma. Axial image shows an enhancing mass (*arrows*) with septations, reflecting the presence of vascular channels

In some benign osseous tumors, CT can provide a specific diagnosis on the basis of morphology. Mesenchymal hamartoma, which is an expansile overgrowth of normal skeletal elements, presents at birth or early infancy as hard immobile subcutaneous masses. At CT, it is an expansile mass that involves one or more adjacent ribs producing an extrapleural mass, which is partially calcified or ossified and contains cystic spaces (Fig. 50) (Groom et al. 2001; Herman 2009). Osteochondroma can be sessile or pedunculated on the basis of its attachment to the bone (Fig. 51). CT can show the characteristic continuity of the parent cortex and medullary cavity with the osteochondroma. CT findings of normal variants include pectus excavatum in which the sternum indents into the thoracic cavity. Cardiovascular structures can be displaced into the left hemithorax (Fig. 52). Pectus carinatum is a deformity of the chest wall secondary to overgrowth of cartilage resulting in protrusion of the sternum. Both pectus deformities can cause respiratory abnormalities related to restriction in chest wall motion.

CT findings of malignant osseous chest wall lesions include bone destruction or expansion, pleural effusion, and an associated soft tissue mass (Fig. 53). A specific diagnosis requires tissue sampling.

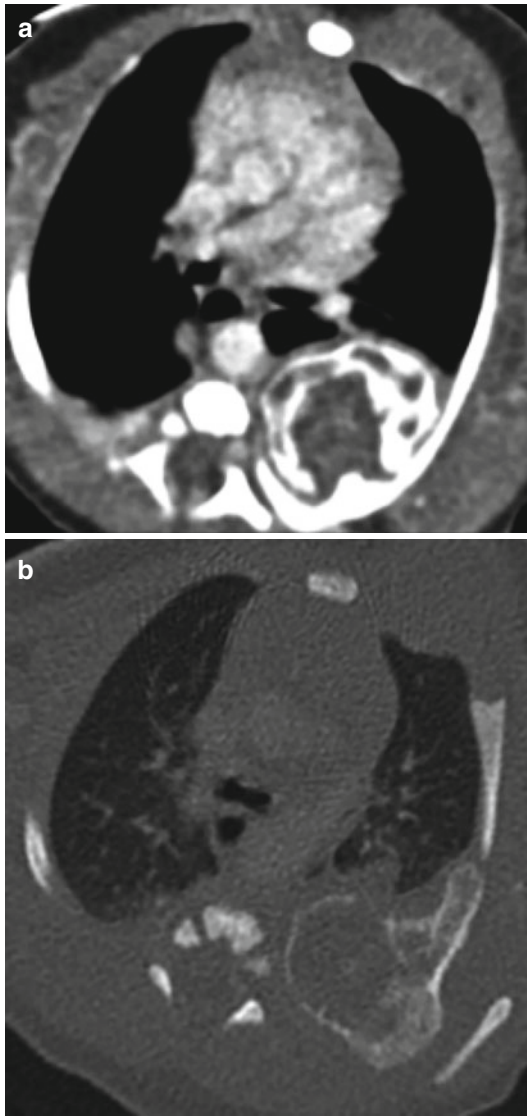

Fig. 50 Chest wall, mesenchymal hamartoma. Newborn girl with a palpable chest wall mass. (**a**) CT demonstrates a large partially calcified cystic mass. (**b**) CT at bone windows shows that the underlying rib is deformed and expanded

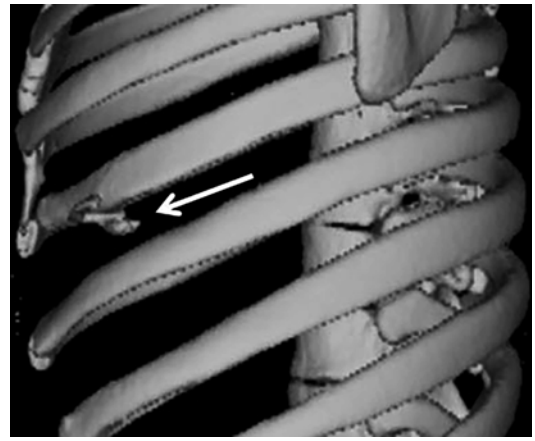

Fig. 51 Osteochondroma. 3D volume rendering shows an exostosis (*arrow*) arising from the inferior margin of a left lower rib

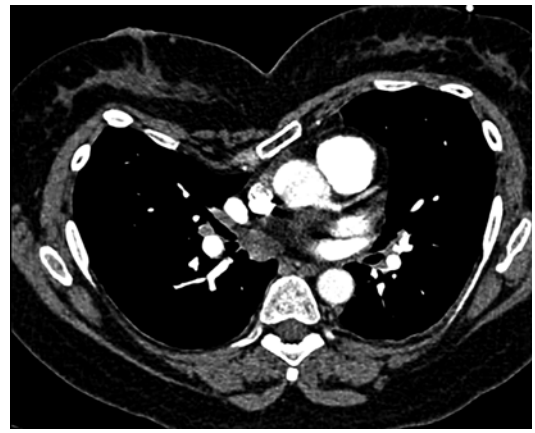

Fig. 52 Pectus excavatum. Axial image in an 18-year-old girl with shortness of breath demonstrates posterior indentation of the sternum causing mass effect on vascular structures

14.3 Chest Wall Infection

Pyogenic chest wall infections usually occur as a result of spread of osteomyelitis from pleural, parenchymal, or mediastinal infections. Common causative organism is *Staphylococcus aureus*; CT not only can demonstrate bone destruction, but it also can show subcutaneous abscess formation, pleural space fluid collections, skin fistulae, and areas of the lung (Fig. 54) (Chelli Bouaziz et al. 2009).

Chronic recurrent multifocal osteomyelitis (CRMO) is an idiopathic (possibly autoimmune) inflammatory disorder of the bone seen primarily in children and adolescents. It is characterized by multifocal nonpyogenic inflammatory bone lesions (Khanna et al. 2009). Most patients present with a single symptomatic site, but other sites of disease become apparent at imaging or during

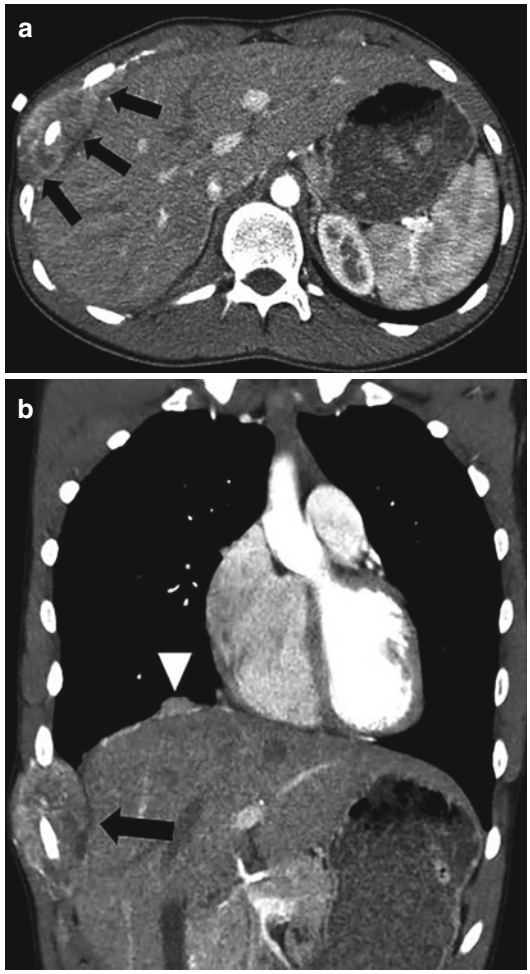

Fig. 53 Malignant osseous chest wall tumor, Ewing sarcoma. (**a**) Axial CT documents a soft tissue mass (*arrows*) arising from a lower right rib and extending into the chest wall. (**b**) Coronal image shows the mass and a pleural metastasis (*arrowhead*)

clinical follow-up. Laboratory findings are nonspecific, with the most common findings being mildly elevated erythrocyte sedimentation rate and C-reactive protein level with a normal white blood cell count. At histologic evaluation, CRMO bone lesions show nonspecific inflammatory changes with granulocytic infiltration. CRMO is unique in its tendency to involve the clavicle—an uncommon site for hematogenous osteomyelitis. CT findings include lytic bone destruction and periosteal reaction, with sclerosis developing over time, resulting in progressive hyperostosis and sclerosis (Khanna et al. 2009). Abscess

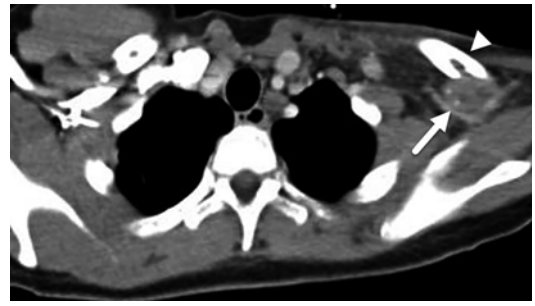

Fig. 54 Acute osteomyelitis. Axial image shows lytic changes in the distal left clavicle (*arrowhead*). There is a small adjacent fluid collection (*arrow*) consistent with an abscess

formation, soft tissue edema, and sequestrum are rare, and their presence makes the diagnosis of infectious osteomyelitis more likely than CRMO (Khanna et al. 2009).

15 Summary

In summary, CT is an important noninvasive tool for imaging the pediatric thorax. The clear delineation of anatomy, the high levels of contrast enhancement, and the continued refinement of 3D techniques have increased the applications of CT in chest imaging. Despite the obvious impact that CT has already had on thoracic imaging, it cannot be overstated that attention must be paid to patient preparation and radiation doses.

References

Amaral JG, Traubici J, BenDavid G, Reintamm G, Daneman A et al (2006) Safety of power injector use in children as measured by incidence of extravasation. AJR Am J Roentgenol 187:580–583

American Association of Physicists in Medicine. AAPM position statement on the use of bismuth shielding for the purpose of dose reduction in CT scanning. American Association of Physicists in Medicine website. www.aapm.org/org/policies/details. Published February 7, 2012

Andronikou S, Joseph E, Lucas S et al (2004) CT scanning for the detection of tuberculous mediastinal and hilar lymphadenopathy in children. Pediatr Radiol 34:232–236

Apfelbaum JL, Connis RT, Nickinovich DG et al (2012) Practice advisory for preanesthesia evaluation: an updated report by the American Society of Anesthesiologists Task Force on Preanesthesia Evaluation. Committee on Standards and Practice Parameters. Anesthesiology 116:522–538

Aukland SM, Halvorsen T, Fosse KR et al (2006) High-resolution CT of the chest in children and young adults who were born prematurely: findings in a population-based study. AJR Am J Roentgenol 187:1012–1018

Baez JC, Lee EY, Restrepo R, Eisenberg RL (2013) Chest wall lesions in children. AJR Am J Roentgenol 200:W402–W419

Barksdale EM Jr, Obokhare I (2009) Teratomas in infants and children. Curr Opin Pediatr 21:344–349

Baroni RH, Feller-Kopman D, Nishino M et al (2005) Tracheobronchomalacia: methods for evaluation of central airway collapse. Radiology 235:635–641

Berdon WE, Baker DH, Wung JT et al (1984) Complete cartilage-ring tracheal stenosis associated with anomalous left pulmonary artery: the ring-sling complex. Radiology 152:57–64

Biyyam DR, Chapman T, Ferfuson MR et al (2010) Congenital lung abnormalities: embryologic features, prenatal diagnosis, and postnatal radiologic-pathologic correlation. Radiographics 30:1721–1738

Boiselle PM, Reynolds KF, Ernst A (2002) Multiplanar and three-dimensional imaging of the central airways with multidetector CT. AJR Am J Roentgenol 179:301–308

Boiselle PM, Feller-Kopman D, Ashiku S et al (2003) Tracheobronchomalacia. Evolving role of dynamic multislice helical CT. Radilol Clin North Am 41:626–636

Boiselle PM et al (2009) Tracheal collapsibility in healthy volunteers during forced expiration: assessment with multidetector CT. Radiology 252:255–262

Brody AS (2008) Computed tomography of pediatric small airways disease. In: Boiselle PM, Lynch DA (eds) CT of the airways. Humana Press, Totowa, pp 381–404

Brody AS, Guillerman RP, Hay TC et al (2010) Neuroendocrine cell hyperplasia of infancy: diagnosis with high-resolution CT. AJR Am J Roentgenol 194:238–244

Calder A, Owens C (2009) Imaging of parapneumonic pleural effusions and empyema. Pediatr Radiol 39:527–537

Calder AD, Bush A, Brody AS, Owens CM (2014) Scoring of chest CT in children with cystic fibrosis: state of the art. Pediatr Radiol 44:1496–1506

Cardin K, Boiselle PM, Walz D, Ernst A (2005) Tracheomalacia and tracheobronchomalacia in children and adults: an in-depth review of a common disorder. Chest 127:984–1005

Castillo M, Vade A, Lim-Dunham JE et al (2010) Pulmonary interstitial glycogenosis in the setting of lung growth abnormality: radiographic and pathologic correlation. Pediatr Radiol 40:1562–1565

Chelli Bouaziz M, Jelassi H, Chaabane S et al (2009) Imaging of chest wall infections. Skeletal Radiol 38:1127–1135

Chong S, Lee KS, Chung MJ et al (2006) Neuroendocrine tumors of the lung: clinical, pathologic, and imaging findings. Radiographics 26:41–57

Cody DD (2002) Image processing in CT. Radiographics 2:1255–1268

Costa NS, Laor T, Donnelly LF (2010) Superior cervical extension of the thymus: a normal finding that should not be mistaken for a mass. Radiology 256:238–242

Coté CJ, Wilson S (2006) American academy of pediatrics, guidelines for monitoring and management of pediatric patients during and after sedation for diagnostic and therapeutic procedures: an update. Pediatrics 118:2587–2602

Crawley AJ, Guillerman RP (2010) Langerhans cell histiocytosis with intrathymic calcifications and cavitation. Pediatr Radiol 40(Suppl 1):S62

Daltro P, Fricke B, Kuroki I et al (2002) CT of congenital lung lesions in pediatric patients. AJR Am J Roentgenol 183:1497–1506

Das S, Langston C, Fan LL (2011) Interstitial lung disease in children. Curr Opin Pediatr 23:325–331

Demos TC, Posniak HV, Pierce KL et al (2004) Venous anomalies of the thorax. Am J Roentgenol 182: 1139–1150

Dishop MK, Kuruvilla S (2008) Primary and metastatic lung tumors in the pediatric population: a review and 25-year experience at a large children's hospital. Arch Pathol Lab Med 132:1079–103C

Franco A, Mody NS, Meza M (2005) Imaging evaluation of pediatric mediastinal masses. Radiol Clin North Am 43:325–339

Frauenfelder T, Marincek B, Wildermuth S (2005) Pulmonary spread of recurrent respiratory papillomatosis with malignant transformation: CT findings and airflow simulation. Eur J Radiol 56:11–16

Garcia-Pena P, Boixadera H, Barber I et al (2011) Thoracic findings of systemic diseases at high-resolution CT in children. Radiographics 31:465–482

Ghaye B, Szapiro D, Fanchamps J-M, Dondelinger RF (2001) Congenital bronchial abnormalities revisited. Radiographics 21:105–119

Gipson MG, Cummings KW, Hurth KM (2009) Bronchial atresia. Radiographics 29:1531–1535

Gower WA, Nogee LM (2011) Surfactant dysfunction. Paediatr Respir Rev 12:223–229

Groom KR, Murphey MD, Lonergan GJ et al (2001) Mesenchymal hamartoma of the chest wall: radiologic manifestations with emphasis on cross-sectional imaging and histopathologic comparison. Radiology 222:205–211

Gross TG, Perkins SL (2011) Malignant non-Hodgkin lymphoma in children. In: Pizzo PA, Poplack DG (eds) Principles and practice of pediatric oncology, 6th edn. Lippincott Williams & Wilkins, Philadelphia, pp 663–682

Haliloglu M, Cifici AO, Oto A et al (2003) CT virtual bronchoscopy in the evaluation of children with suspected foreign body aspiration. Eur J Radiol 48:188–192

Herman T, Siegel MJ (2008) Neonatal pleuropulmonary blastoma type I. J Perinatol 28:82–84
Herman T, Siegel MJ (2009) Chest wall mesenchymal hamartoma. J Perinatol 29:462–463
Hernanz-Schulman M (2005) Vascular rings: a practical approach to imaging diagnosis. Pediatr Radiol 35:961–979
Hoffman LV, Kuszyk BS, Mitchell SE et al (2000) Angioarchitecture of pulmonary AVM malformation characterization using volume-rendered 3D CT angiography. Cardiovasc Intervent Radiol 23:165
Karmazyn B, Liang Y, Al H et al (2014) Optimization of hybrid iterative reconstruction level in pediatric body CT. AJR Am J Roentgenol 202:426–431
Kaste SC, Young CW (1995) Safe use of power injectors with central and peripheral venous access devices for pediatric CT. Pediatr Radiol 26:499–501
Khanna G, Sato TSP, Ferguson P (2009) Imaging of chronic recurrent multifocal osteomyelitis. Radiographics 29:1159–1177
Knight L, Edwards JE (1974) Right aortic arch. Types and associated cardiac anomalies. Circulation 50:1047–1051
Ko SF, Ng SH, Lee TY et al (2000) Noninvasive imaging of bronchopulmonary sequestration. AJR Am J Roentgenol 175:1005–1012
Konen E, Raviv-Zilka L, Cohen RA et al (2003) Congenital pulmonary venolobar syndrome: Spectrum of helical CT findings with emphasis on computerized reformatting. Radiographics 23:1175–1184
Kosucu P, Ahmetoglu A, Koramaz I et al (2004) Low-dose MDCT and virtual bronchoscopy in pediatric patients with foreign body aspiration. AJR Am J Roentgenol 183:1171–1777
Kurland G, Deterding RR, Hagood JS et al (2013) An official American Thoracic Society clinical practice guideline: classification, evaluation, and management of childhood interstitial lung disease in infancy. Am J Respir Crit Care Med 188:376
Lacombe P, Lacout A, Marcy P-Y et al (2013) Diagnosis and treatment of pulmonary arteriovenous malformations in hereditary hemorrhagic telangiectasia: an overview. Diagn Interv Imaging 94:835–848
Lambert J, MacKenzie JD, Cody DD, Gould R (2014) Techniques and tactics for optimizing CT dose in adults and children: state of the art and future advances. J Am Coll Radiol 11:262–266
Lanfranchi M, Allbery SM, Wheelock L et al (2010) Pulmonary interstitial glycogenosis. Pediatr Radiol 40:361–365
Lau DM, Siegel MJ, Hildebolt CF, Cohen AH (1998) Bronchiolitis obliterans syndrome: thin-section CT diagnosis of obstructive changes in infants and young children after lung transplantation. Radiology 208:783–788
Lee EY (2009) Evaluation of non-vascular mediastinal masses in infants and children: an evidence based practical approach. Pediatr Radiol 39(Suppl 2):S184–S190
Lee EY, Siegel MJ (2008) Pediatric airway disorders: large airways. In: Boiselle PM, Lynch DA (eds) CT of the airways. Humana Press, Totowa, pp 351–380
Lee EY, Siegel MJ, Hildebolt CF et al (2004) MDCT evaluation of thoracic aortic anomalies in pediatric patients and young adults: comparison of axial, multiplanar and 3D images. AJR Am J Roentgenol 182:777–784
Lee CH, Goo JM, Lee HJ et al (2008) Radiation dose modulation techniques in the multidetector CT era: from basics to practice. Radiographics 28:1451–1459
Lee EY, Boiselle PM, Cleveland RH (2011) Multidetector CT evaluation of congenital lung anomalies. Radiol Clin North Am 49:921–948
Lell MM, May M, Deak P et al (2010) High pitch spiral computed tomography: effect on image quality and radiation dose in pediatric chest computed tomography. Invest Radiol 45:64–71
Li J, Udayasankar UK, Toth TL et al (2007) Automatic patient centering for MDCT: effect on radiation dose. AJR Am J Roentgenol 188:547–552
Lonergan GJ, Schwab CM, Suarez ES et al (2002) Neuroblastoma, ganglioneuroblastoma, and ganglioneuroma: radiologic-pathologic correlation. Radiographics 22:911–934
McAdams HP, Kirejczyk WM, Posado-de-Christenson ML et al (2000) Bronchogenic cyst: imaging features with clinical and histopathologic correlation. Radiology 217:441–446
McCahon E (2006) Lung tumours in children. Paediatr Respir Rev 7:191–196
McCarville MB (2010) Malignant pulmonary and mediastinal tumors in children: differential diagnoses. Cancer Imaging 10:S35–S41
McCarville MB, Lederman HM, Santana VM et al (2006) Distinguishing benign from malignant pulmonary nodules with helical chest CT in children with malignant solid tumors. Radiology 239:514–520
McCollough CH, Bruesewitz MR, Kofler JM Jr (2006) CT dose reduction and dose management tools: overview of available options. Radiographics 26:503–512
McNitt-Gray MF (2002) AAPM/RSNA physics tutorial for residents: topics in CT—radiation dose in CT. Radiographics 22:154–155
Metzger M, Krasin MJ, Hudson MM, Onciu M (2011) Hodgkin lymphoma. In: Pizzo PA, Poplack DG (eds) Principles and practice of pediatric oncology, 6th edn. Lippincott Williams & Wilkins, Philadelphia, pp 638–662
Miller FH, Fitzgerald SW, Donaldson JS (1993) CT of the azygoesophageal recess in infants and children. Radiographics 13:623–634
Naffaa LN, Donnelly LF (2005) Imaging findings in pleuropulmonary blastoma. Pediatr Radiol 35:387–391
Nassseri F, Effechari F (2010) Clinical and radiologic review of the normal and abnormal thymus: pearls and pitfalls. Radiographics 30:413–428
Nelson TR (2014) Practical strategies to reduce pediatric CT radiation dose. J Am Coll Radiol 11:292–299
Newman B, Kuhn JP, Kramer SS et al (2001) Congenital surfactant protein B deficiency—emphasis on imaging. Pediatr Radiol 31:327–331

Nievelson RAJ, van Dam IM, van der Molen AJ (2010) Multidetector CT in children: current concepts and dose reduction strategies. Pediatr Radiol 40:1324–1344

Nishino M, Ashiku SK, Kocher ON et al (2006) The thymus: a comprehensive review. Radiographics 26:333–348

Papaioannou G, Sebire NJ, McHugh K (2009) Imaging of the unusual pediatric 'blastomas'. Cancer Imaging 9:1–11

Pappas JN, Donnelly LF, Frush DP (2000) Reduced frequency of sedation of young children using new multislice helical CT. Radiology 215:897–899

Patnana M, Sevrukov AB, Elsayes KM et al (2012) Inflammatory pseudotumor: the great mimicker. AJR Am J Roentgenol 198:W217–W227

Plumb AA, Murphy G (2011) The use of central venous catheters for intravenous contrast injection for CT examinations. Br J Radiol 84:197–203

Quillin SP, Siegel MJ (1992) CT features of benign and malignant teratomas in children. J Comput Assist Tomogr 16:722–726

Rigsby CK, Gasber E, Seshadri R et al (2007) Safety and efficacy of pressure-limited power injection of iodinated contrast medium through central lines in children. AJR Am J Roentgenol 188:726–732

Siegel MJ (1993) Diseases of the thymus in children and adolescents. Postgrad Radiol 13:106–132

Siegel MJ (2003) Multiplanar and three-dimensional row CT of thoracic vessels and airways in the pediatric population. Radiology 229:641–650

Siegel MJ (2008a) Techniques. In: Siegel MJ (ed) Pediatric body CT, 2nd edn. Lippincott Williams & Wilkins, Philadelphia, pp 1–32

Siegel MJ (2008b) Lung, pleural and chest wall. In: Siegel MJ (ed) Pediatric body CT, 2nd edn. Lippincott Williams & Wilkins, Philadelphia, pp 69–120

Siegel MJ (2008c) Mediastinum. In: Siegel MJ (ed) Pediatric body CT, 2nd edn. Lippincott Williams & Wilkins, Philadelphia, pp 3–67

Siegel MJ (2008d) Great vessels. In: Siegel MJ (ed) Pediatric body CT, 2nd edn. Lippincott Williams & Wilkins, Philadelphia, pp 121–144

Siegel MJ (2008e) Heart. In: Siegel MJ (ed) Pediatric body CT, 2nd edn. Lippincott Williams & Wilkins, Philadelphia, pp 145–175

Siegel MJ (2011a) Vascular rings and slings. In: Ho VB, Reddy GP (eds) Cardiovascular imaging. Saunders/Elsevier, St. Louis, pp 542–548

Siegel MJ (2011b) Coarctation of the aorta. In: Ho V, Reddy G (eds) Cardiovascular imaging: expert radiology series. Elsevier, Philadelphia, pp 535–541

Siegel MJ, Bhallah S, Gutierrez F, Sweet S (2001) Post-lung transplantation bronchiolitis obliterans: usefulness of expiratory thin-section CT for diagnosis. Radiology 220:455–462

Siegel MJ, Schmidt B, Bradley D et al (2004) Radiation dose and image quality in pediatric CT: effect of technical factors and phantom size and shape. Radiology 233:515–522

Siegel MJ, Earls JP, Chan F (2009) Thoracic vascular anomalies. In: Rubin GD, Rofsky NM (eds) CT and MR angiography: comprehensive vascular assessment. Wolters Kluwer Health/Lippincott Williams & Wilkins, Philadelphia, pp 543–595

Siegel MJ, Hildebolt C, Bradley D (2013a) Effects of Automated kilovoltage selection technology in contrast-enhanced pediatric computed tomography and angiography. Radiology 268:538–547

Siegel MJ, Ramierez-Giraldo JC, Hildebolt C et al (2013b) Automated low-kilovoltage selection in pediatric CT angiography: phantom study evaluating effects on radiation dose and image quality. Invest Radiol 48:584–589

Singh A, Kalra MK, Thrall JH et al (2011) Automatic exposure control in CT: applications and limitations. J Am Coll Radiol 8:446–449

Singh S, Kalra M, Shenoy-Bhangle AS et al (2012) Radiation dose reduction with hybrid iterative reconstruction for pediatric CT. Radiology 263:527–546

Sorantin E, Geiger B, Lindbichler F, Eber E, Schimpi G et al (2002) CT-based virtual tracheobronchoscopy in children—comparison with axial CT and multiplanar reconstruction: preliminary results. Pediatr Radiol 32:8–15

Stocker JT (2009) Cystic lung diseases in infants and children. Fetal Pediatr Pathol 28:155–184

Toma P, Granata C, Rossi A et al (2007) Multimodality imaging of Hodgkin disease and non-Hodgkin lymphoma in children. Radiographics 27:1335–1354

Vrielynck S, Mamou-Mani T, Emond S et al (2008) Diagnostic value of high-resolution CT in the evaluation of chronic infiltrative lung disease in children. AJR Am J Roentgenol 191:914–920

Yu L, Li H, Fletcher JG et al (2010) Automatic selection of tube potential for radiation dose reduction in CT: a general strategy. Med Phys 37:234–243

MDCT of the Chest Wall

Beth A. Ripley, Tatiana Kelil, Yolonda L. Colson, and Ritu R. Gill

Abstract

Muti-row-detector CT (MDCT) is the primary modality for evaluation of both congenital and acquired chest wall disorders. Imaging data from MDCT examinations provide anatomical detail and delineate relationships between adjacent structures. Three-dimensional reconstructions from the raw data can be used to enhance visualization of complex three-dimensional (3D) anatomy and for volumetric quantification to aid in surgical planning. This chapter illustrates the technical and practical considerations of utilizing MDCT in the evaluation of chest wall lesions, tumors, infections, and trauma and highlights MDCT advances in surgical planning, including 4D imaging and three-dimensional modeling and printing.

1 Introduction

The chest wall is the rigid outer covering of the upper body, composed primarily of bones and muscles; it protects vital structures such as the heart, lungs, and mediastinal vascular structures and provides scaffolding for the muscles of respiration. The components of the chest wall include the bony skeleton, muscles, neurovascular structures, and the breasts. Pleurae and diaphragm are in close apposition with the chest wall and are often included in the evaluation of the chest wall even though technically they are not part of the chest wall. CT is the modality of choice for the evaluation of the chest wall due to its wide availability, relative low cost, superb efficiency, and ability to simultaneously image the upper abdomen, lungs, and mediastinal structures (Watt

Electronic supplementary material The online version of this chapter (doi:10.1007/978-3-319-30355-0_24) contains supplementary material, which is available to authorized users.

B.A. Ripley, MD, PhD • T. Kelil, MD
R.R. Gill, MD, MPH (✉)
Department of Radiology, Brigham and Women's Hospital and Harvard Medical School,
75 Francis Street, Boston, MA 02215, USA
e-mail: rgill@partners.org

Y.L. Colson, MD, PhD
Division of Thoracic Surgery, Brigham and Women's Hospital and Harvard Medical School,
75 Francis Street, Boston, MA 02215, USA

U.J. Schoepf, F.G. Meinel (eds.), *Multidetector-Row CT of the Thorax*, Medical Radiology,
DOI 10.1007/978-3-319-30355-0_24

2002). The imaging characteristics of most chest wall pathologies including infection and tumors tend to overlap, with very few lesions having classic diagnostic features; tissue sampling is relatively easy when compared with lung biopsies and helps confirm the pathology (Watt 2002).

Multidetector CT (MDCT) is the newest iteration in a series of technical innovations over the past 35 years. MDCT replaced the linear array of detector elements in conventional CT scanners with a two-dimensional (2D) array, allowing acquisition of data from multiple slices in the z-axis simultaneously; this faster acquisition decreases respiratory motion artifacts and improves image quality. MDCT acquisitions also allow for application of advanced three-dimensional (3D) post-processing techniques, which may be invaluable in assessing the extent, location, and degree of invasion of critical structures by tumor, as well as volumetric tumor quantification for surgical planning. *Multiplanar reformations* (*MPR*) are particularly useful when the lesion is supraclavicular or oriented parallel to the ribs (Tateishi et al. 2003).

Some authors consider MRI to be the imaging modality of choice for evaluation of chest wall lesions (Tateishi et al. 2003). MRI provides superior contrast resolution in comparison to CT, and it is more accurate in evaluating invasion of the chest wall, diaphragm, heart, vessels, airways, and bone marrow by tumor or infection. It is also superior to CT in the evaluation of trans-compartmental lesions and neurovascular involvement (Mullan et al. 2011). The main strengths of CT over MRI with respect to chest wall masses are its ability to evaluate calcification within lesions and its ability to characterize the extent of osseous involvement, especially with respect to assessing cortical integrity of the bone (Watt 2002; Weyant and Flores 2004). Furthermore, the superior spatial resolution of CT, the ability to acquire data in seconds, and the capability of fast volumetric acquisition which can then be reformatted in multiple planes and reconstructive algorithms are all clear benefits of CT over magnetic resonance imaging (MRI).

A potential drawback of CT is that it exposes the patient to ionizing radiation, which may be a relative contraindication in young patients and pregnant women – especially those who are expected to incur high cumulative radiation doses from serial imaging. Another potential drawback is the concern for nephrotoxicity with iodinated contrast, although this association has recently been called into question (McDonald et al. 2013). Intravenous (IV) contrast is vital in assessing subtle involvement of the chest wall by pleural pathology and also in cases of primary chest wall infections and tumors (Raj et al. 2011). Imaging during the late venous or tissue parenchymal phase (20–60 s after peripheral venous injection) is ideal to delineate the pleura from the adjacent lung and chest wall (Helm et al. 2010; Heffner et al. 2010). Dynamic contrast-enhanced (perfusion) CT to assess blood flow dynamics and capillary permeability is being investigated in some oncologic practices but still confined mainly to the research arena (Gill et al. 2009). Dual-energy CT has a limited role in the evaluation of chest wall pathologies.

2 MDCT Protocol for Chest Evaluation

Our MDCT protocol for the evaluation of chest wall pathologies is performed with a Sensation 64-MDCT scanner (Siemens Medical Solutions) and includes imaging during suspended end-inspiration. Before scanning, initial scout topographic images are obtained to determine the area of coverage. Scanning is performed in a craniocaudal dimension using 120 kVp, 0.6-mm collimation, high-speed mode, a pitch equivalent of 1.5, slice interval of 1.25 mm, and slice thickness of 0.75 mm. Fifty-five milliliters of contrast material (Ultravist 370 [iopromide]), Bayer HealthCare [formerly Schering] is administered IV at 4 mL/s using an automated power injector when indicated. Post-processing of the imaging data is performed using a dedicated workstation (Voxar, Barco) by experienced technicians in our 3D laboratory under the

supervision of a radiologist. For chest wall pathologies, volume-rendered and maximum intensity projections (MIPs) are most helpful; surface-shaded displays (SSD) and multi-planar reformats (MPR) can also be reconstructed.

3 Four-Dimensional (4D) CT of the Chest Wall

A four-dimensional computed tomography (4DCT) scan is a temporal scan acquired across the respiratory cycle during free breathing. A sixteen-centimeter length of the chest (determined by the CT detector width) is imaged repeatedly over the course of a respiratory cycle, then the patient is moved to the next position in the z-axis and the process is repeated. Image data sets can then be viewed as temporal stacks at each given stationary location or can be reprocessed into traditional z-axis data sets by using respiratory gating to bin data into different time points in the respiratory cycle (Bernatowicz et al. 2015).

4D CT allows visualization of lung mechanics and depiction of how these mechanics change the shape and location of structures within the chest. This is of particular importance in radiation oncology, since the motion of radiotherapy targets needs to be accounted for (Biederer et al. 2010). Targets may move more or less than predicted across individuals and have even been shown to move paradoxically. Respiratory motion can also deform tumor volume in conventional 3D CT scans (Fredberg Persson et al. 2011). Finally, irregular breathing motion can introduce image artifacts such as truncation and duplication of structures because of mismatches in the respiratory cycle (Bernatowicz et al. 2015). 4D imaging therefore allows for more accurate planning of patient-specific safety margins (Biederer et al. 2010).

Conventional 4D imaging utilizes axial slice acquisition or helical acquisition over multiple respiratory cycles, with binning of the data based on respiratory cycle (Coolens et al. 2012). One potential issue with 4D imaging is radiation dose. Because multiple image acquisitions are made at each given z position, the dose can quickly escalate. Some traditional dose reduction techniques such as decreasing the kV may not be practical since radiation planning is based on a given kV. Other strategies, however, include decreasing the z-axis coverage, decreasing the mA, and increasing the speed of the gantry. These are at the cost of coverage in the first and decreased signal to noise for the latter two.

We acquire 4D chest wall images on the dynamic volume CT (Toshiba Aquilion ONE, Ottawar japan) that comprises a conventional gantry aperture of 70 cm and a 70KW X-ray tube with an opposing solid-state detector. The detector is 16 cm in width along the rotational axis of the gantry and consists of 896 elements, which are read at 900–3600 times per rotation, depending on the gantry revolution time. Revolution times can be varied between 350 ms and 3 s for 360 data acquisition. A maximum of 320 slices for 640 slices with 50 % overlap can be acquired with each gantry rotation. The helical mode is performed with 64-detector row CT. The images generated are displayed on the monitor in the form of preliminary reconstructions in real time. In a second computational step, the image data is reconstructed as a volume set with variable slice thickness. MPR can be automatically generated in 3 planes. The scanner can be operated at 32-, 16-, and 4-detector row mode.

4 Chest Wall Pathologies

4.1 Congenital and Developmental Anomalies

Congenital chest wall anomalies are briefly summarized in Table 1 (Jeung et al. 1999). Radiographs followed by CT scan are commonly indicated for evaluation of these disorders. These are most commonly seen in the pediatric age groups, mainly because of their ability to affect quality of life in the younger population. In adults these are most commonly seen because of cosmetic defect.

Table 1 Congenital chest wall anomalies

Pectus excavatum (funnel chest)	Inward bowing of the sternum secondary to misdirected growth of the lower costal cartilages Measured using the Haller or pectus index on CT imaging calculated by dividing the transverse diameter of the chest by the AP diameter of the chest; normal value is approximately 2.56, and a value greater than 3.25 often requires surgical correction
Pectus carinatum (pigeon breast)	Outward bowing of the sternum causing a pigeon-like appearance of the chest Sometimes isolated, commonly seen in patients with congenital heart disease
Cervical rib	Supernumerary ribs articulating with the lowest cervical vertebra The true second rib articulates with the sternomanubrial joint Asymptomatic in 90 % of cases, but may be associated with thoracic outlet syndrome or Paget-Schroetter syndrome – dedicated vascular imaging with multiplanar reformatted images may be useful
Cleidocranial dysostosis	Defective development of many bones (pubic bones, long bones, vertebrae) including the clavicles, which are variably hypoplastic
Poland syndrome	Complete or partial absence of the pectoralis major Associated with ipsilateral syndactyly, rib hypoplasia, and aplasia of the ipsilateral breast or nipple

Pectus excavatum is the most common congenital abnormality of the chest wall, representing about 90 % of all cases (Brochhausen et al. 2012). With this deformity, the sternum and the 3rd to 7th costal cartilages are posteriorly displaced relative to the anterior chest wall (Brochhausen et al. 2012). The posterior displacement of the sternum causes a decrease in the prevertebral space, leading to leftward displacement of the heart. This leads to the classic radiographic finding of absence of the right heart border. Pectus excavatum rarely has associated symptoms and does not appear to routinely affect the function of the inner organs. When symptomatic, the most common symptoms are chest pain, dyspnea on exertion, respiratory infections, palpitations, or heart murmurs (Brochhausen et al. 2012). However, it does cause significant cosmetic deformity, and for this reason, it is often surgically corrected. CT is helpful in presurgical planning and also in understanding the degree of the deformity (Jeung et al. 1999). Serial CT scans after a Nuss procedure is usually acquired prior to removal of the metallic rod used for correcting the deformity (Fig. 1).

In contrast to pectus excavatum, pectus carinatum (also known as pigeon breast deformity) is caused by outward displacement of the sternum, which is shifted anteriorly. Although it can occur in isolation, it is often seen in patients with cyanotic congenital heart disease (Jeung et al. 1999). This type of deformity is not associated with any medically significant issues and therefore is generally not repaired (Fig. 2).

A cervical rib is a supernumerary rib that arises from the C7 vertebra. While asymptomatic 90 % of the time, it can result in compression of the arteries. Symptoms include pain and weakness of the arm on the affected side, hand swelling, and differences in pulse which are positional (Jeung et al. 1999). Cleidocranial dysostosis is a syndrome in which there is incomplete ossification of the clavicles, which may be absent or hypoplastic (Jeung et al. 1999). Of note, the earliest bones to ossify are the ones that are affected, with the clavicle being the first bone to ossify (Singh 2014). The jaw, skull, and long bones can be affected, with persistent patency of calvarial sutures, supernumerary teeth, and short stature. Poland syndrome is a congenital abnormality in which there is unilateral absence of the pectoralis major, serratus anterior, and external oblique muscles, with ipsilateral thoracic and upper extremity defects including sternal and hand deformities and rib hypoplasia (Cingel et al. 2013) (Fig. 3). In women, there is often aplasia of

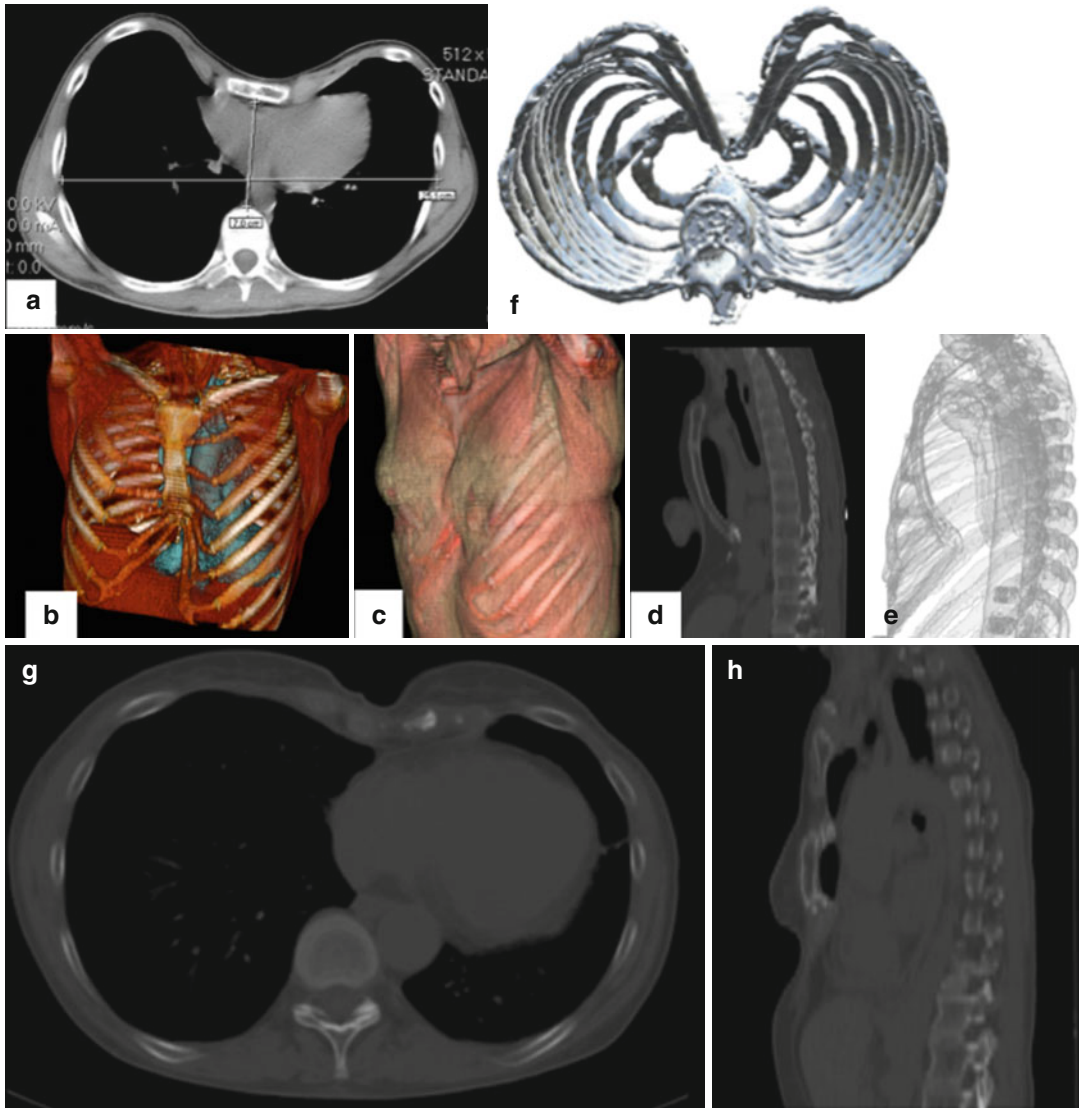

Fig. 1 (**a**) Posterior displacement of the sternum relative to the anterior ribs leads to a decrease in the prevertebral space, leading to leftward displacement of the heart. (**b**) The left lung is smaller as a result. (**c**) 3D rendering demonstrates posterior displacement of the sternum to greater effect. (**d**, **e**) 3D rendering of sagittal view highlights the decreased pre-vertebral distance (*double-headed black arrow*). (**f**) 3D printed model of the pectus. (**g**, **h**) Axial and sagittal images showing improved anteroposterior diameter post correction of the pectus by Nus procedure. (**i**, **j**) Volume-rendered images showing improved deformity of the chest wall

the breast on the affected side. For unknown reasons, the right side of the body is affected about 75 % of the time. There is debate about the underlying etiology, but a plausible explanation is that it is secondary to a vascular insult involving the subclavian arteries, the vertebral arteries, and/or branch vessels (Cingel et al. 2013).

5 Chest Wall Trauma

Chest radiography is an excellent first-line screening tool for rapid assessment of thoracic injury given its accessibility. It can readily detect tension pneumothorax, hemithorax, and flail chest (Peters et al. 2010). However, chest

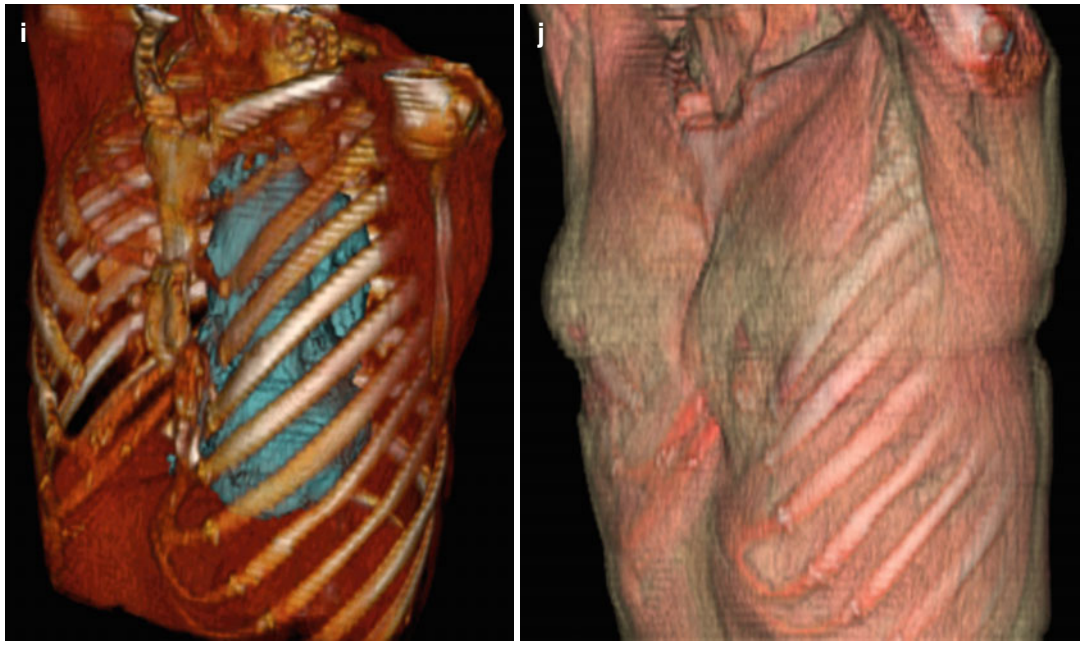

Fig. 1 continued

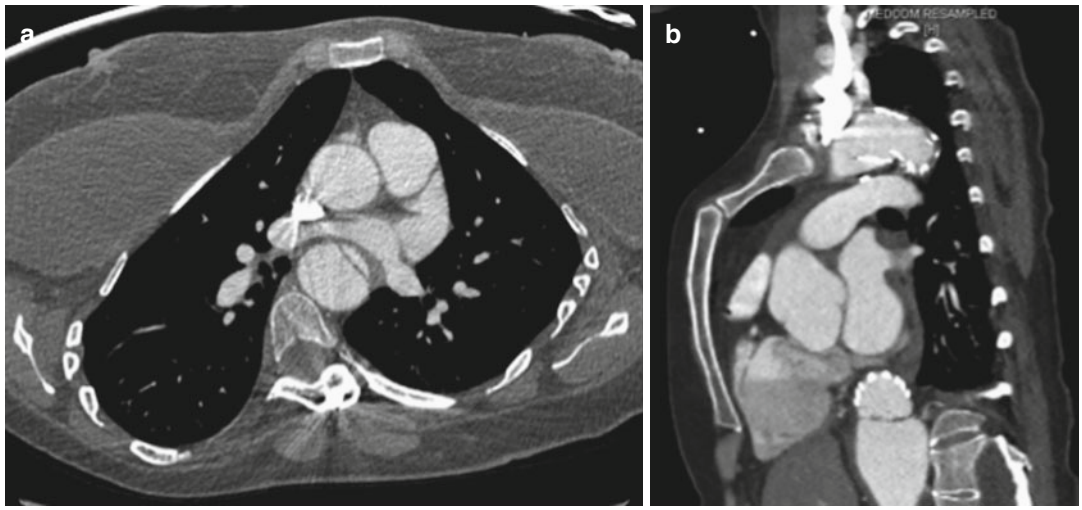

Fig. 2 (**a**, **b**) Axial and sagittal CT image showing pectus carinatum deformity of the chest. The anteroposterior diameter of the chest is increased

radiography alone is unlikely to be sufficient in the workup of trauma, given its high false-negative rate (up to 48 % in one study) (Exadaktylos et al. 2001). Up to 50 % of patients with a high-speed mechanism of injury and a normal chest radiograph are subsequently found to have injuries on chest CT (Exadaktylos et al. 2001; Omert et al. 2001), and these findings often change clinical management (Grieser et al. 2001). 3D reconstructions can help illustrate

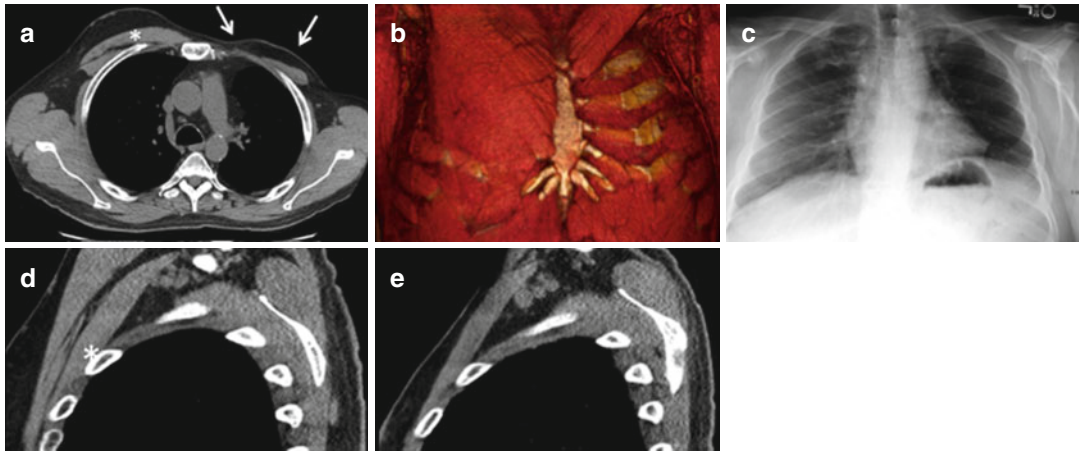

Fig. 3 (**a**) Axial non-contrast CT demonstrates absence of the pectoralis major muscle on the left (*white arrows*). The right pectoralis muscle is marked with an asterisk (*). (**b**) 3D volume-rendered image demonstrates absence of the pectoralis major on the right. (**c**) Chest X-ray is notable for relative lucency of the left lung compared to the right, which results from decreased attenuation in the absence of the left pectoralis major muscle. This appearance can be mistaken for an abnormally opacified right lung and is a known pitfall in patients with Poland syndrome. (**d**) Sagittal CT through the patient's right chest demonstrates normal pectoralis major muscle (*). (**e**) Sagittal CT through the patient's left chest demonstrates absence of the pectoralis major muscle

the course of the bullet in gunshot wounds and the trajectory of the bullet can be visualized. This technique is also being used in virtual autopsy (Fig. 4).

5.1 Rib Fractures

Rib fractures are common with thoracic trauma, occurring in 39 % of cases in one series of 1417 patients (Sirmali et al. 2003). Rib fractures are indicators of severe trauma, and the number of rib fractures may be predictive of mortality (Peters et al. 2010; Sirmali et al. 2003). The number and extent of ribs that are fractured may also help indicate the severity of the trauma (Sirmali et al. 2003). While the 4th to 9th ribs are most likely to be fractured, fracture of the 1st to 3rd ribs should raise suspicion for high-velocity trauma and underscores the need for thorough evaluation of the rest of the thorax, including the aorta and great vessels (Sirmali et al. 2003; Kaewlai et al. 2008). Fractures of the tenth through twelfth ribs should prompt evaluation of the liver, kidneys, and spleen (Sirmali et al. 2003; Kaewlai et al. 2008). Hospitalization should be considered in patients with multiple fractures. 3D reconstruction of the chest wall can help plan the internal fixing of the displaced ribs (Fig. 5).

5.2 Flail Chest

Multiple definitions exist for the term "flail chest." A common definition is fracture of three or more contiguous ribs, with each rib broken in two or more places (segmental fracture) (Kaewlai et al. 2008; Athanassiadi et al. 2010). Flail chest usually involves the anterior or anterolateral mid to lower ribs (Peters et al. 2010).

Flail chest has been shown to result in significant morbidity and mortality (Raj et al. 2011). Compromised, sometimes paradoxical respiratory excursion in flail chest can decrease effective ventilation and vital capacity (Athanassiadi et al. 2010). Some patients may require mechanical ventilation and surgical fixation (Sirmali et al. 2003). Thin-section CT with multiplanar

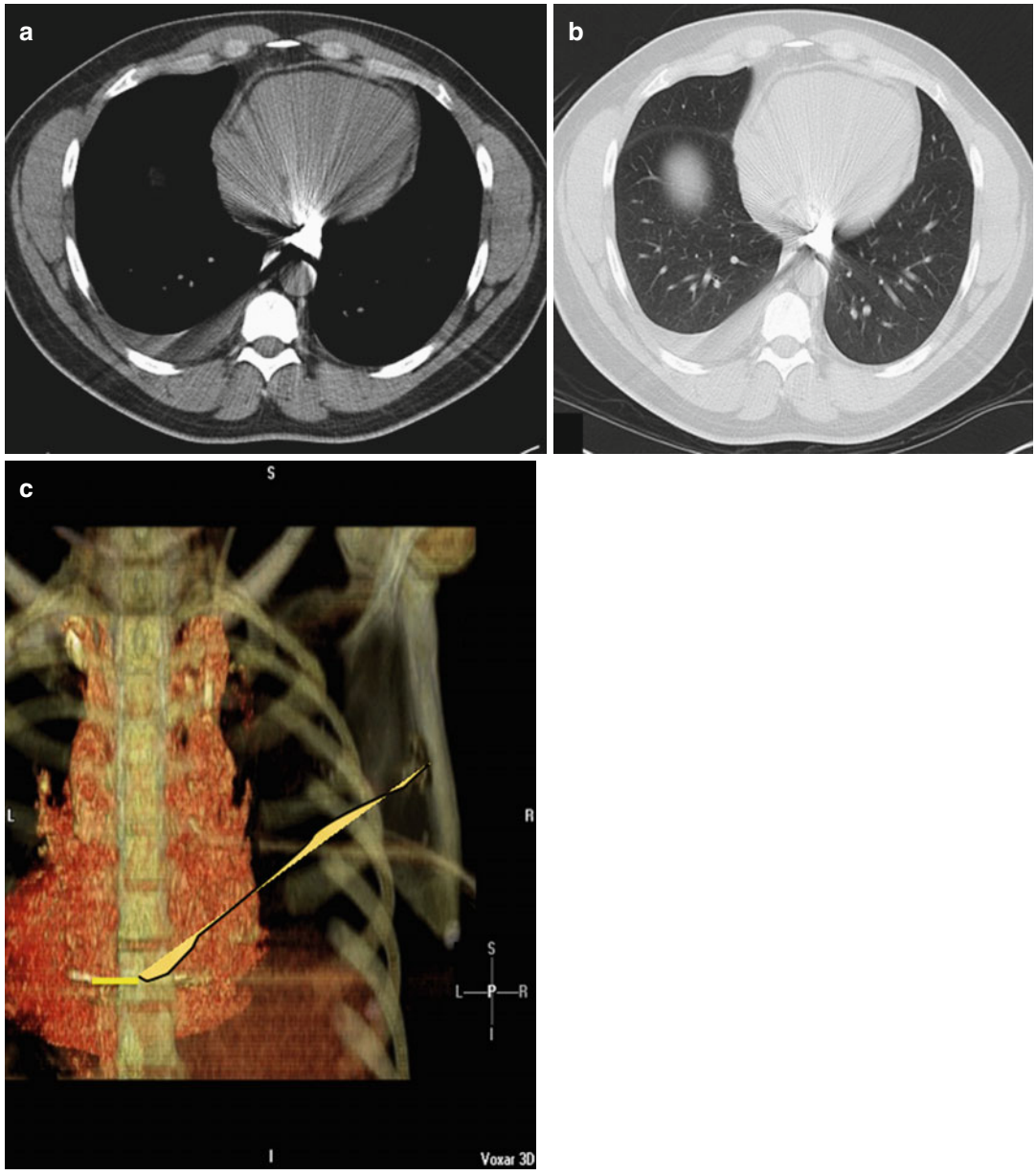

Fig. 4 (**a**, **b**) Axial CT images of a patient with a gunshot wound in the right shoulder and right pleural effusion, and the bullet is on the left of the aorta. (**c**) Volume-rendered image showing the trajectory of the bullet as it went through the scapula and hit the spine and got deflected to land in between the esophagus and aorta

reformatted images is often helpful in evaluating the "flail segment" prior to surgery (Athanassiadi et al. 2010). CT is also useful in detecting underlying pulmonary contusions, which occur in roughly 80 % of patients with a flail chest and are a significant contributing factor in respiratory failure (Athanassiadi et al. 2010). 4D CT can be helpful in cases of flail chest and can help illustrate the abnormal chest wall motion

Movies 2, 3, and 4.

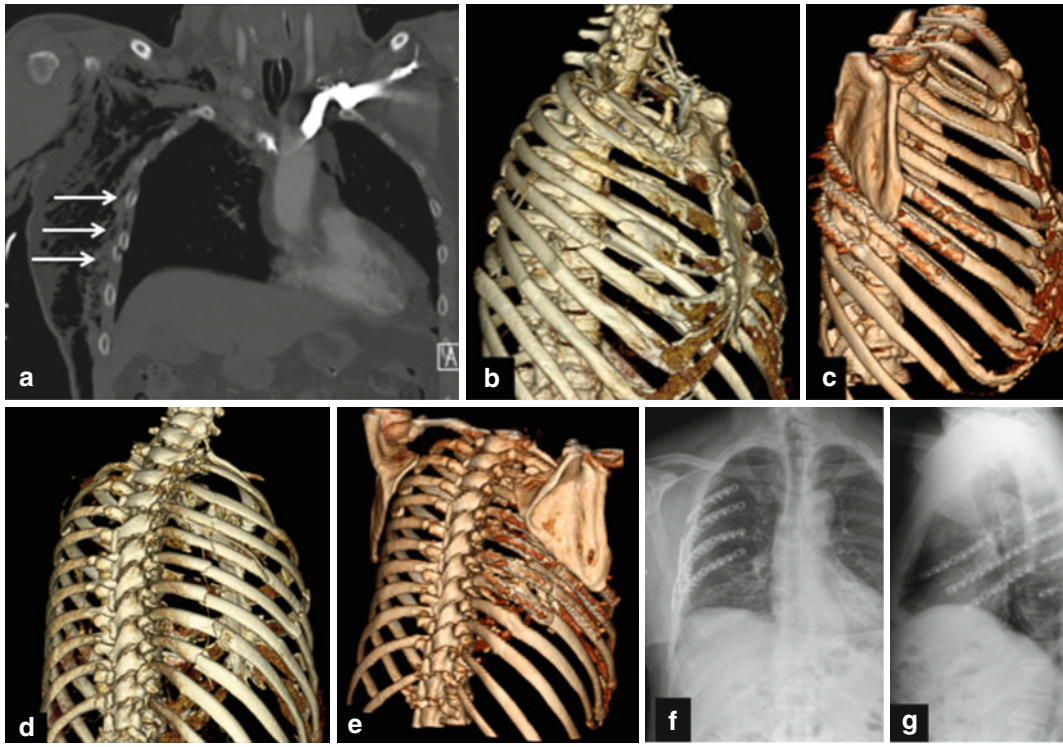

Fig. 5 (**a**) Coronal CT image showing multiple displaced right-sided rib fractures (*arrows*). (**b**, **d**) Volume-rendered images showing the displacement of the ribs and the extent of the fractures and used for surgical planning. (**c**, **e**) Post-rib plating volume-rendered images showing optimal internal fixing of the ribs. (**f**, **g**) PA and lateral radiographs of the chest showing good lung expansion post-optimal placement of internal fixation plates

5.3 Sternal Fracture

Sternal fracture is uncommon, occurring in 3–8 % of cases of thoracic trauma, and suggests high-velocity trauma (Peters et al. 2010). It is more apparent on lateral than frontal radiographs. The mechanism is often direct frontal impact, such as from a steering wheel (Peters et al. 2010). The presence of an anterior mediastinal hematoma is a secondary sign (Figure 6). Costochondral separation may occur in younger patients. Like fracture of the upper ribs, sternal fracture should prompt close inspection of the critical intrathoracic structures, especially the aorta (Raj et al. 2011) (Fig. 6).

5.4 Thoracic Spine Fracture

Thoracic spine injuries are much more readily detectable by CT than plain radiographs. On the frontal chest radiograph, inference of thoracic spinal fracture may be made by the presence of signs of associated hematoma (lifting of the paraspinal lines, apical pleural cap), decreased vertebral body height, lateral offset of the vertebral bodies, increased interpediculate and interspinous distances, and rib disarticulation. Posterior mediastinal or paravertebral hematoma is an ancillary finding on CT.

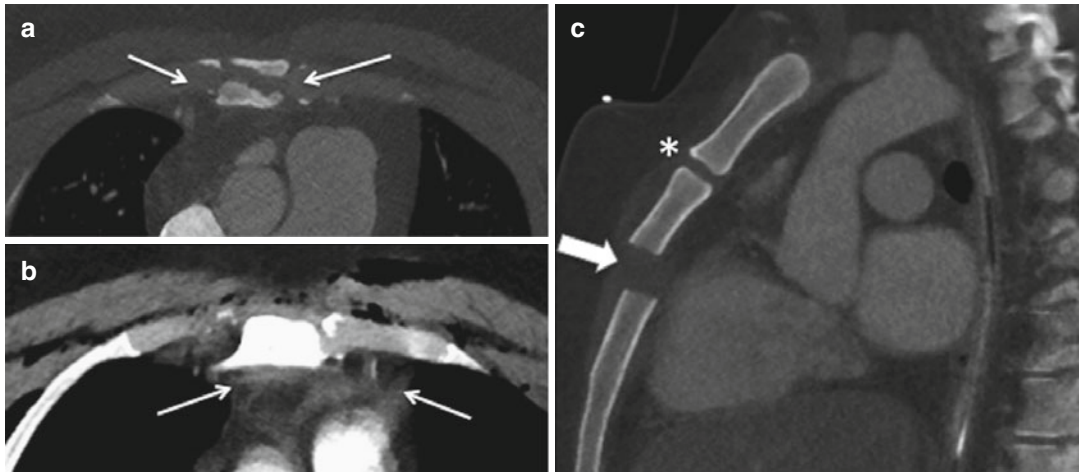

Fig. 6 (**a**) Axial CT in bone algorithm demonstrates fracture through the sternum (*arrows*). (**b**) Associated mediastinal hematoma (*arrows*) is demonstrated in soft tissue algorithm. (**c**) The sternal fracture (*arrow*) is demonstrated clearly in sagittal plane. * marks the sternomanubrial joint space

5.5 Diaphragmatic Trauma

Diaphragmatic rupture is associated with blunt abdominal trauma in 0.8–8 % cases and can go undiagnosed in 7–66 % patients at the time of initial presentation (Kaewlai et al. 2008; Desir and Ghaye 2012). The mechanism of injury is secondary to high-velocity frontal or lateral impacts, from a motor vehicle accident that can cause a sudden increase in intra-abdominal pressure. The majority of the cases are missed at initial examination due to the presence of multiple concurrent injuries resulting in broken ribs, pneumothorax, hemithorax, and splenic and liver lacerations, and in most cases, the baseline appearance of the diaphragm is not known. Complications such as ischemic bowel injury and incarceration can occur. Multiplanar reformats in coronal and sagittal planes are very helpful in ruling in or out diaphragmatic rupture.

Diaphragmatic defects tend to be smaller in penetrating trauma as compared with blunt trauma. The left diaphragm is more commonly involved due to multiple factors such as congenital weakness at the junction of the lumbar and costal diaphragm, the presence of the esophageal hiatus, and the protection offered by the liver on the right side (Fig. 7).

MDCT is considered as the gold standard for the evaluation of diaphragmatic injury. Multiplanar reformats are very helpful in illustrating the extent and degree of injury and can also help in surgical planning. Multiple signs suggestive of diaphragmatic injury have been reported in the literature and are summarized in Table 2. These comprise direct signs that help identify the diaphragmatic defect and indirect signs in which there is supportive evidence in favor of loss of the diaphragmatic plane with herniation of abdominal contents into the chest.

6 Infections of the Chest Wall

Primary chest wall infection is rare and may be underestimated by physical examination, especially in immunocompromised patients. Risk factors include diabetes mellitus, immunocompromised state, trauma, and surgical instrumentation (Bouaziz et al. 2009). Chest wall infections are potentially life-threatening if not treated early, and therefore a prompt diagnosis is important. Tuberculosis and fungal infections are most commonly seen in immune-compromised hosts and may be resistant to treatment.

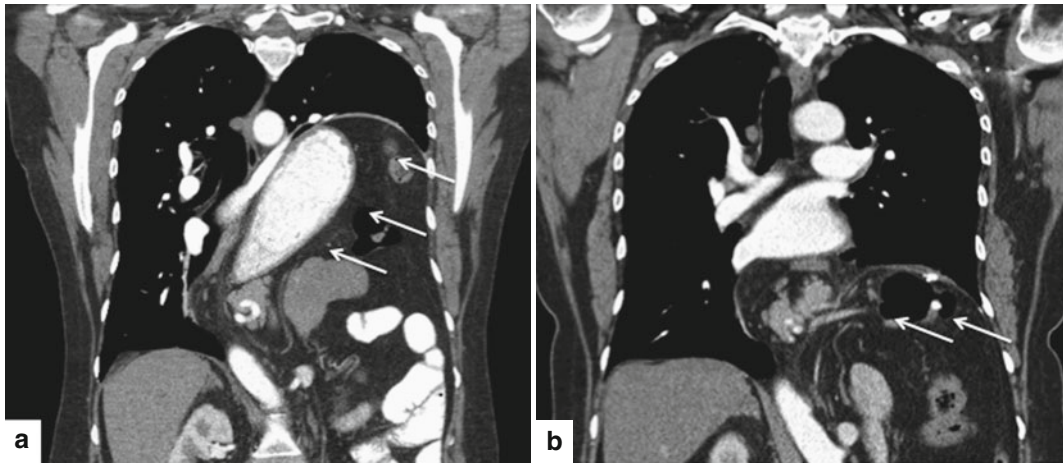

Fig. 7 Coronal CT images (**a**) showing left diaphragmatic rupture (*white arrows*) depicting displacement of the fat and bowel into the chest. (**b**) post repair of the diaphragm (*white arrows*) the bowel is below the repaired diaphragm

Table 2 Signs of diaphragmatic rupture Athanassiadi et al. 2010

"Direct" CT signs:		
CT sign:	**Findings:**	**Potential mimics:**
Segmental diaphragmatic defect	Abrupt, focal loss of continuity of the diaphragm The edge of the defect may appear thickened due to edema or hemorrhage Sagittal and coronal MPR is helpful	Normal variant in the uninjured population
Dangling diaphragm	Free edge of torn diaphragm visible as curvilinear soft tissue structure perpendicular to the chest wall	
Absent diaphragm	At fat or air interfaces where clear visualization is expected Usually associated with a large hernia	FP where the diaphragm apposes fluid or soft tissue
"Indirect" CT signs		
Collar sign (variants are the "hump" and "band" signs)	Waist-like narrowing of herniated intra-abdominal structures May appear as focal, subtle indentation of the involved organ(s) MPR is helpful	Traumatic hepatic fracture or normal diaphragmatic slips may produce FP Also seen in congenital or traumatic acquired hernias
Herniated viscera	Abdominal contents in the thorax	Also seen in congenital or a traumatic acquired hernias
Loss of border between the thorax and abdomen	Pneumothorax, hemothrorax, pneumoperitoneum, and hemoperitoneum	

In chest wall infection, ultrasound, CT, and MRI are complementary modalities: CT is preferred for evaluating bone destruction, while MR is the modality of choice for specific assessment of the soft tissues and can discern infected and necrotic debris from adjacent inflammation. Multiplanar reformatted images in both modalities add valuable information about extent of infection and interspace communication within loculated collections, and aid in surgical planning.

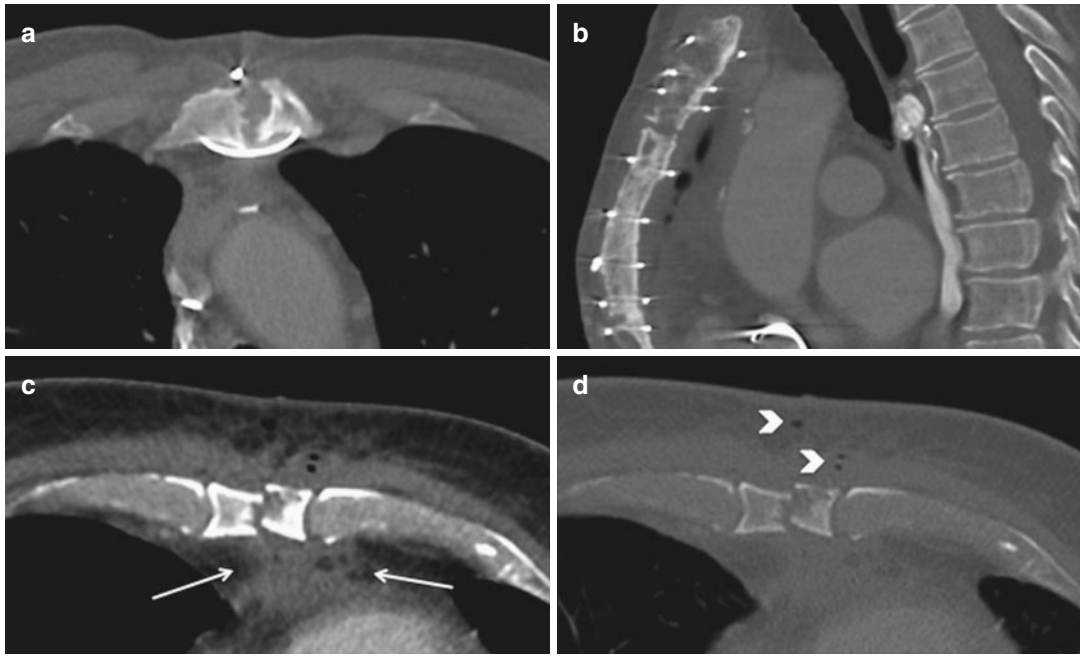

Fig. 8 Patient post-cardiac surgery with increasing white count and persistent pain in the sternum after 12 months post-sternotomy. (**a**) Axial CT and (**b**) coronal CT images showing resorption of the sternal bones and mottled appearance of the sternum, consistent with sternal osteomyelitis. (**c**) Axial CT image showing a retrosternal collection (*white arrows*). (**d**) (*arrow heads*) pockets of gas suggestive of infection

6.1 Sternal Infections

Sternal osteomyelitis is an infrequent but potentially life-threatening complication of sternotomy. It presents with draining sinus tracts from a closed sternum and can occur months or even years after sternotomy (Toccoa et al. 2013). While traditionally the treatment is excision of the infected sternum, sternal wires, and surrounding costal cartilage, newer more conservative treatments center on antibiotic regimens to clear infection, with surgery reserved for nonresponders (Toccoa et al. 2013). CT is useful in ruling out deep-space infections and in presurgical planning (Fig. 8).

6.2 Osteomyelitis

Osteomyelitis is most commonly due to contiguous spread of pulmonary infection (tuberculosis, fungal infection) or empyema (termed "empyema necessitatis" when it extends through the parietal pleura into surrounding structures such as the chest wall). Overall, *Staphylococcus aureus* and *Pseudomonas aeruginosa* are the most common causal organisms in chest wall osteomyelitis. Bone destruction is generally not evident by radiography for 1–2 weeks – CT and MRI are capable of identifying commonly associated soft tissue masses, effacement of deep soft tissue planes, and periosteal elevation much earlier (Jeung et al. 1999).

MRI is highly sensitive and specific and thus considered the modality of choice for osteomyelitis involving the thoracic bones. Typical MRI findings include hypointensity against the high background signal of fat on T1-weighted images without fat suppression, corresponding to high-signal edema on fluid-sensitive sequences, and focal enhancement. Intravenous drug use, immunosuppression, and chronic renal failure predispose to sternoclavicular osteomyelitis (Jeung et al. 1999). Subclavian venous catheter-associated infection by *S. aureus* is a common scenario in this type of infection, with

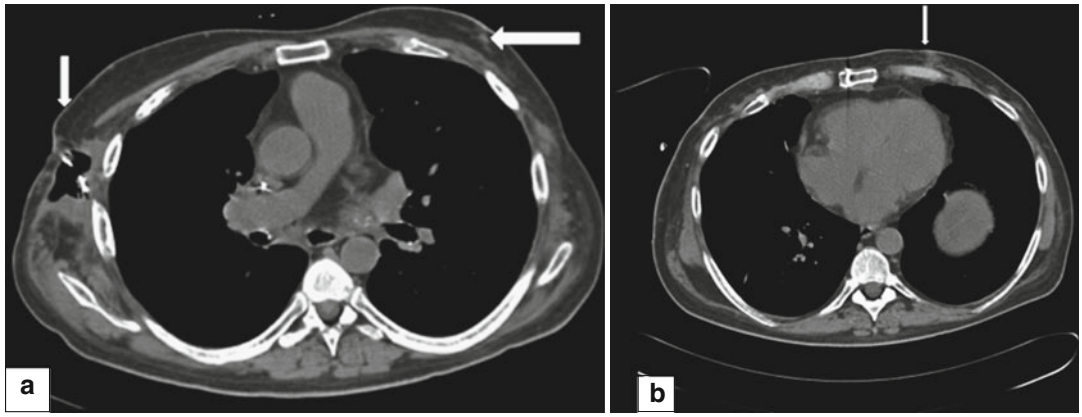

Fig. 9 (**a**, **b**) Axial CT images of a patient post-lung transplant who has multiple mycobacterial abscesses in the chest wall (*arrows*)

standard treatment being removal of the infected catheter and IV antibiotics. Surgical resection is reserved for cases in which infection is shown to extend beyond the joint on imaging.

6.3 Chest Wall Abscesses

Chest wall abscesses can be easily missed on CT scan due to low signal to noise ratio in evaluating chest wall musculature. MRI is superior to CT in evaluating chest wall abscesses; these tend to have low signal intensity on T1-weighted images and high signal intensity on STIR and T2-weighted images, with rim enhancement on post-contrast fat-saturated T1-weighted images. T1-weighted sequences are key for anatomic assessment due to their superior spatial resolution, while STIR and T2-weighted images add contrast resolution that is helpful for assessing abscess extent and location. CT is more sensitive for detecting gas and calcification and superior to MRI in distinguishing substances that cause susceptibility artifact (e.g., calcium, gas, blood products, and metallic surgical materials).

Non-pyogenic infection of the chest wall is more unusual. *Mycobacterium tuberculosis* rarely involves the chest wall. Hematogenous seeding is more common than contiguous spread. Chest wall abscess and sinus tracts are seen in about 25 % of cases. Destructive chest wall masses with calcification and rim enhancement on CT are typical (Jeung et al. 1999).

Actinomycosis is a rare infection that affects immunocompetent patients; it is more often seen in patients with respiratory ailments such as emphysema, bronchitis, and bronchiectasis. It starts as pneumonia and then *Actinomyces israelii*, along with *Nocardia asteroides*, will start within the lung parenchyma and then extend into the pleura, cause an empyema, and continue on into the surrounding soft tissues or bone. There are bacterial species that infect the chest wall by tracking through the tissue planes, separating the chest wall from the pleural space (empyema necessitans). On cross-sectional imaging, findings include soft tissue thickening and nonspecific inflammatory changes, fluid collections, draining sinus tracts, wavy periostitis, and rib destruction (Jeung et al. 1999; Kanne et al. 2011). *Aspergillus fumigatus* is a fungus species that produces multiple pulmonary manifestations. Chest wall invasion may occur, with osteolysis and fistula formation (Jeung et al. 1999) (Fig. 9).

SAPHO syndrome is composed of a constellation of radiological, pathological, and clinical characteristics, previously referred to as chronic recurrent osteomyelitis (CRMO). The syndrome includes synovitis, acne, pustulosis, hyperostosis, and osteitis. In 60–90 % of cases, it involves the

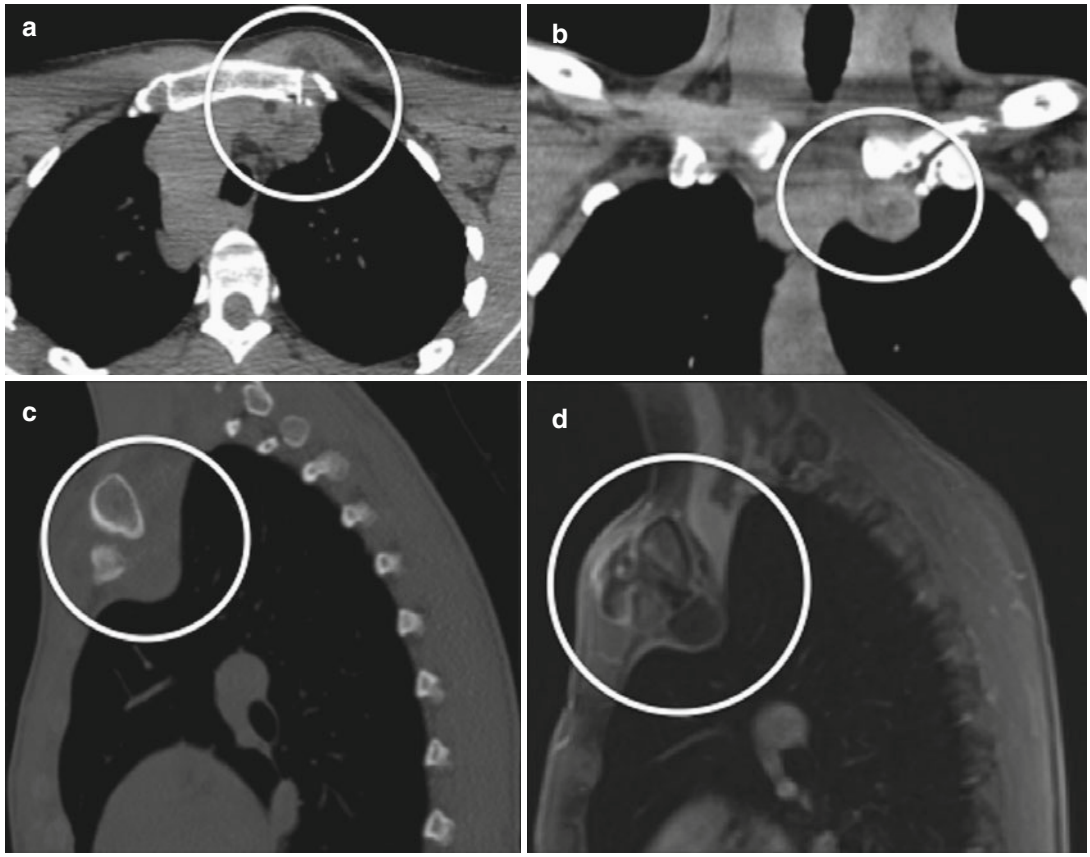

Fig. 10 A 37-year-old woman presenting with chest wall swelling and tenderness. (**a**) Axial CT images showing a mixed fat and soft tissue attenuation lesion centered at the sternoclavicular joint. (**b**) Coronal and (**c**) sagittal images of the abnormality centered at the joint with evidence of sclerosis involving the bones. (**d**) Sagittal MR post-contrast VIBE image showing fat and fluid with enhancement involving the joint. Biopsy showing chronic inflammation consistent with SAPHO syndrome. *Circle* highlights the abnormality

sternoclavicular joint, presenting as non-pyogenic inflammation of the joint. CT and MRI are often needed in conjunction to characterize the soft tissue mass and joint swelling associated with this condition. MR is superior to CT for evaluating the joint and marrow (Figs. 1 and 10).

6.4 Chest Wall Masses

Several benign processes may simulate malignancy; for example, a subacute or old rib fracture may mimic a chondroid lesion or expansile neoplasm. Also, nonmalignant rib erosions may occur with benign processes such as granulomatous disease, radiation osteitis, and fibrous dysplasia.

6.5 Lesions of Bone and Cartilaginous Origin

Benign lesions of the bone and cartilage that occur in the chest wall include fibrous dysplasia, enchondroma, osteochondroma, chondroblastoma, aneurysmal bone cyst, and giant cell tumor (Jeung et al. 1999) (Fig. 11).

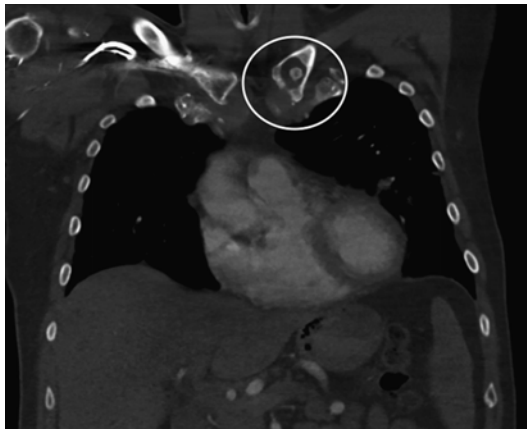

Fig. 11 Coronal CT image showing an enchondroma in the left clavicular head. *Circle* highlights the abnormality

6.6 Tumors of Adipocyte Origin

Lipomas are the most common chest wall soft tissue tumors and also the most common benign chest wall mass (Jeung et al. 1999). They are most frequently found in patients over 50 years of age and are more common in obese patients. Chest wall lipomas tend to be deep-seated, involving deep muscular and intermuscular layers, and less well circumscribed than lipomas elsewhere. In two-thirds of cases, lipomas are composed solely of adipose tissue, but non-adipose tissue such as connective tissue septa and calcifications are present in the remainder.

On CT, lipomas are circumscribed fat attenuation lesions that lack enhancement. On MRI, lipomas follow fat signal intensity on all sequences, with suppression on fat-saturated sequences including STIR. There may be sparse, fibrous septae that demonstrate low signal intensity on T1- and T2-weighted images and faint enhancement (thick, irregular, avidly enhancing septa or avidly enhancing nodules are concerning for malignancy) (Jeung et al. 1999; Kanne et al. 2011). Chemical shift artifact at interfaces with more fluid-rich tissues is characteristic. A rare variant is spindle cell lipoma, which arises in the subcutaneous tissues of the neck or shoulder in middle-aged to elderly men, appearing as a 3–5 cm mass that is heterogeneous on both T1- and T2-weighted sequences (Jeung et al. 1999). Evaluation of extent, local infiltration, and relationship with neurovascular structures by MRI is essential for surgical planning.

7 Vascular and Lymphatic Lesions

The term "hemangioma" encompasses many entities that can be classified according to the predominant vessel type – arteriovenous, capillary, and mixed vascular, cavernous (composed of dilated, tortuous, thin-walled vessels), and venous. Many lesions include nonvascular tissues including fat, smooth muscle, thrombus, fibrous tissue, and hemosiderin. Phleboliths are most commonly seen in cavernous hemangiomas but may be seen in other lesions (Nam et al. 2011).

Hemangiomas are rare in the chest wall and may be found in the synovium or musculature. These lesions usually present in the pediatric population. On CT, most cavernous hemangiomas appear as heterogeneously attenuating soft tissue masses. The heterogeneity is due to the presence of fat (which may represent a substantial portion of the lesion) and vascular or fibrous components. Background attenuation is similar to the skeletal muscle (Nam et al. 2011). Slow-flowing blood in dilated vessels leads to the characteristic MRI appearance of poorly defined curvilinear structures that are low in signal on T1-weighted sequences, with high intensity on T2-weighted images. Enhancement is marked (Nam et al. 2011). Muscle atrophy may be observed with intramuscular hemangiomas. As they are elsewhere, arteriovenous malformations (AVMs) of the chest wall are characterized by tubular flow voids (Figs. 12 and 13).

Glomus tumors most often present as painful solitary masses in adult patients. Less commonly, tumors are multiple and asymptomatic, and rarely, glomus tumors are malignant. The neoplastic cells that compose glomus tumors resemble smooth muscle cells of the normal glomus body. Lesions are often intramuscular. The typical appearance on CT is a soft tissue mass with adja-

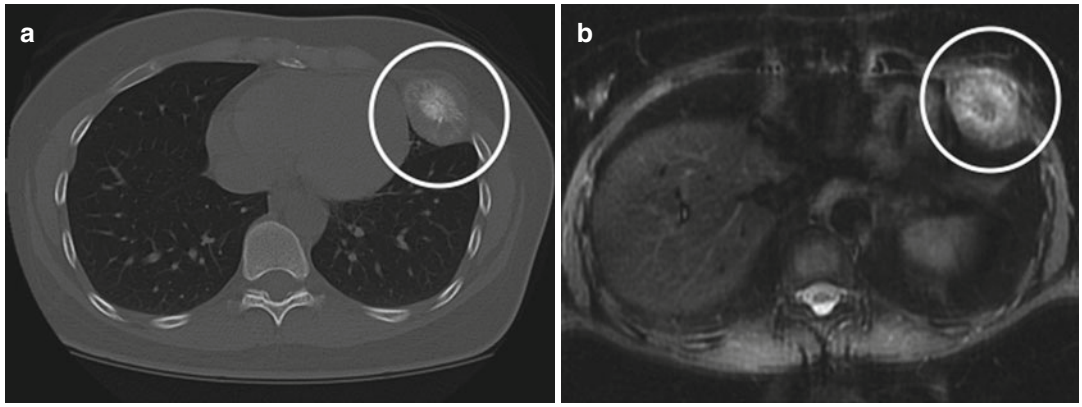

Fig. 12 (**a**) Axial CT and (**b**) axial MR image showing an expansile lesion in the anterior aspect of the 4th left rib with a radial spoke-like appearance consistent with a hemangioma. *Circle* highlights the lesion

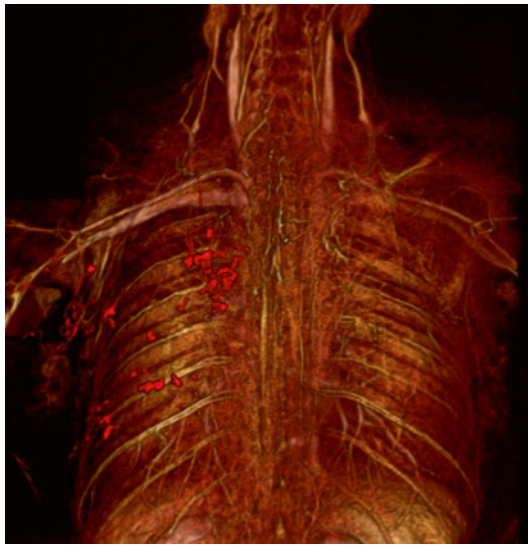

Fig. 13 Volume-rendered image showing a slow-flow AVM of the chest wall. The extent and course as seen on the reformat will serve as a roadmap for embolization

cent osseous erosion. On MRI, the mass displaces major vessels and is surrounded by tortuous vessels arising from a vascular pedicle. Heterogeneous signal intensity and sharp interfaces with adjacent tissues after IV contrast administration are typical features (Tateishi et al. 2003).

Lymphangiomas are uncommon hamartomatous lesions comprised of dilated lymphatic vessels; they most often present in early childhood as a neck mass that extends into the chest wall or axilla (Nam et al. 2011). Lesions are commonly present at the cervicothoracic junction in children and in the mediastinum in adults (probably because they are occult on physical exam) (Jeung et al. 1999; Nam et al. 2011). The constituent lymphatic channels are sequestered from the lymphatic system. MRI is the preferred imaging modality, as CT appearance is nonspecific. Lymphangiomas follow simple fluid signal on all sequences, with thin peripheral and septal enhancement (Tateishi et al. 2003).

8 Peripheral Nerve and Nerve Sheath Tumors

Spinal nerve roots, intercostal nerves, and distal brachial plexus branches may give rise to neurogenic chest wall tumors. The appearance of these tumors in the chest wall is similar to their appearance in other locations. There is overlap in the imaging appearances of neurofibroma and schwannoma, but the imaging features discussed below are often helpful in distinguishing them from one another.

Schwannomas are benign nerve sheath tumors that arise from spinal nerve roots or intercostal nerves. They tend to be slow growing and are most commonly seen in young to middle-aged adult patients. While small lesions are well circumscribed, larger lesions may be more lobulated. Scalloping rather than erosion of adjacent bones is

typical. The usual CT appearance of schwannoma is a homogeneous mass that is iso- or slightly hypoattenuating to the muscle. A less common appearance is a cyst with fibrous walls, containing smaller nodules. Schwannomas tend to be isointense on T1-weighted and markedly hyperintense on T2-weighted images, with avid enhancement. Tumors may demonstrate the "fascicular sign," with heterogeneous low signal intensity in a ring-like pattern. The nerve of origin may be identifiable. Degeneration, manifested as myxoid cystic change, hemorrhage, calcification, and fibrosis, if present, is more common in schwannomas than in neurofibromas. Biopsy is painful due to intrinsic innervation (Tateishi et al. 2003).

Neurofibromas may occur in isolation or in neurofibromatosis type 1. Most affected patients present between the ages of 20 and 40. Typically, neurofibromas originate from spinal nerve roots and may be "localized" (most common), "diffuse," or "plexiform." Plexiform tumors involve long segments of nerves or multiple nerve branches. Like other slow-growing peripheral nervous tumors, they tend to remodel without eroding bone, for instance, expanding neural foramina when they arise from spinal nerve roots. Malignant degeneration occurs rarely but is more common in cases of neurofibromatosis type 1. Malignant degeneration may be suspected in cases of rapid growth (Nam et al. 2011). The CT appearance of neurofibroma is a low-attenuation, heterogeneously enhancing lesion. On T2-weighted and post-gadolinium T1-weighted images, a "target" appearance is typical – the center of the lesion is composed of fibrous stroma, which is hypointense on T2-weighted images and demonstrates enhancement, and the periphery is composed of myxoid material which does not enhance significantly.

Ganglioneuromas and paragangliomas arise from sympathetic nervous elements. Ganglioneuromas appear as sharply marginated, homogeneous or heterogeneous paravertebral masses that may be calcified. Curvilinear bands (fibrous tissue) that are hypointense on both T1- and T2-weighted images may give these lesions a whorled or septated appearance. Paragangliomas are more commonly right-sided paravertebral masses that occur in adolescents and young adults. They tend to be homogeneous and avidly enhancing on cross-sectional imaging (Nam et al. 2011).

8.1 Fibroblastic-Myofibroblastic Tumors

Elastofibroma dorsi is a relatively common muscular pseudotumor that occurs characteristically at the inferior angle of the scapula. These tumors are much more common in women and tend to occur in middle-aged to elderly patients. These lesions are often asymptomatic and are commonly bilateral. These lesions share attenuation and intensity characteristics with muscle on CT and MRI, respectively, with interspersed fat giving a "layered" appearance (Nam et al. 2011). With typical imaging characteristics, biopsy may be avoided (Tateishi et al. 2003; Nam et al. 2011).

Fibromatosis, also known as desmoid tumor, is a benign, true neoplasm composed of fibroblasts and collagenous matrix that arises from connective tissue or posttraumatic or surgical scars. Typically, fibromatosis is infiltrative and locally aggressive. Attenuation and enhancement characteristics are variable at CT. The typical MRI appearance is a heterogeneous lesion that enhances moderately to avidly and contains bundles of collagen that are hypointense on T2-weighted images and do not enhance (O'Sullivan et al. 2007a). Recurrence is common after surgical resection (Fig. 14).

9 Malignant Chest Wall Masses

More than half of malignant chest wall masses are metastatic lesions or locally invasive breast, lung, or pleural tumors. Metastatic lesions are uncommon and are usually seen in the setting of widespread metastatic disease (Tateishi et al. 2003; Nam et al. 2011). The most common primary chest wall malignancies are sarcomas; approximately half originate from the soft tissues and half are of cartilaginous or bony origin.

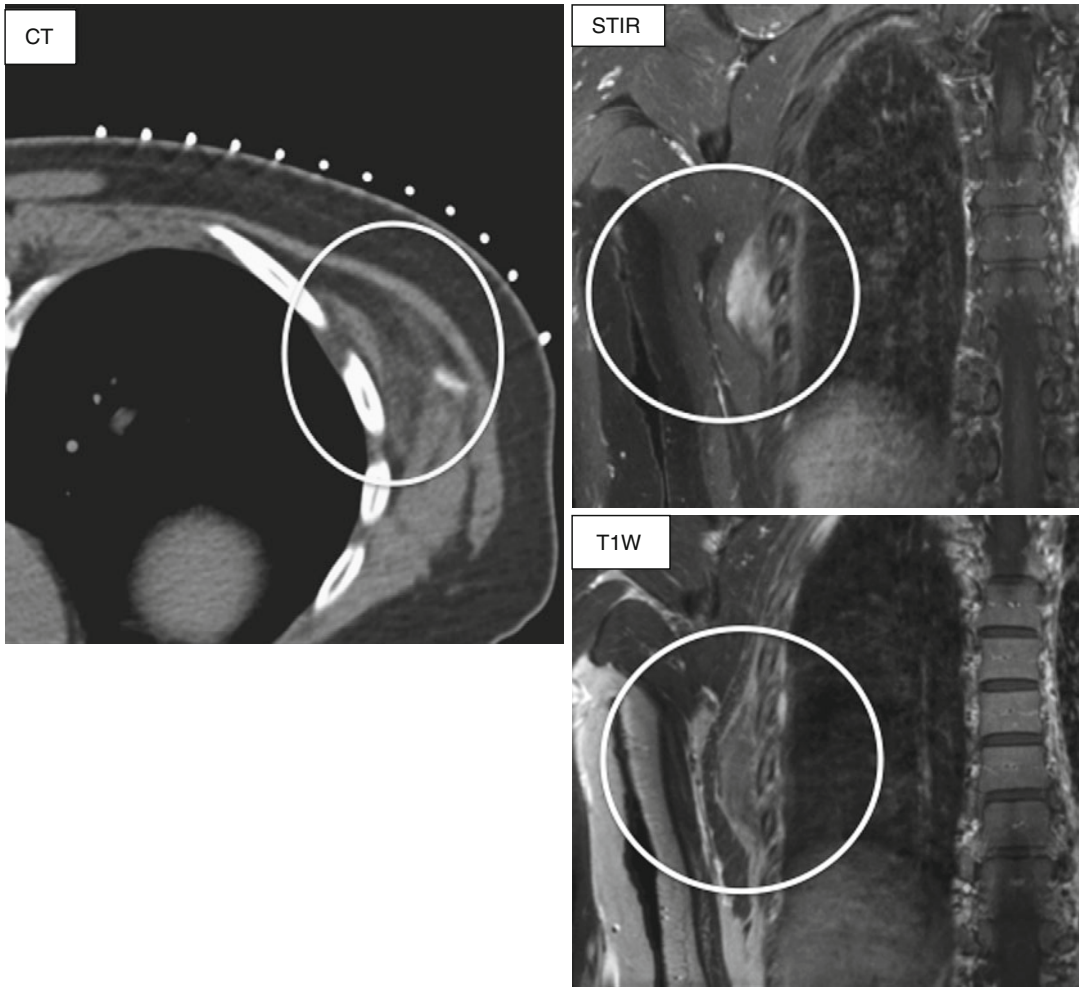

Fig. 14 (**a**) Axial CT image of a fat-containing lesion in the right subscapular region. (**b**, **c**) T1W and T2W images confirming it to be an elastofibroma. *Circle* highlights the abnormality

10 Sarcomas

Chondrosarcomas are the most common primary chest wall malignancy. These tumors are most often anteriorly located, arising from the costochondral junctions or the sternum. Up to 20% arise from the ribs themselves. In about 10% of cases, chondrosarcoma occurs due to malignant transformation of benign lesions such as enchondromas. Typically, chondrosarcomas are irregularly shaped, with bone destruction and variable calcification. Chondroid mineralization in a "ring and arc" configuration is characteristic and is best demonstrated by contrast-enhanced CT. On MRI, chondrosarcomas are lobulated, heterogeneously enhancing masses that are isointense to muscle on T1-weighted sequences and iso- or hyperintense relative to fat on T2-weighted images. These tumors tend to be slow growing with tendency to metastasize later in life (Figs. 15 and 16).

Osteosarcomas are rare in the thorax and are most often found in the ribs, scapula, and clavicle in young adult patients. Metastatic involvement of the lungs and lymph nodes is more common with chest wall osteosarcoma than with peripheral osteosarcoma. On CT, there is varied calcification that is greatest centrally and

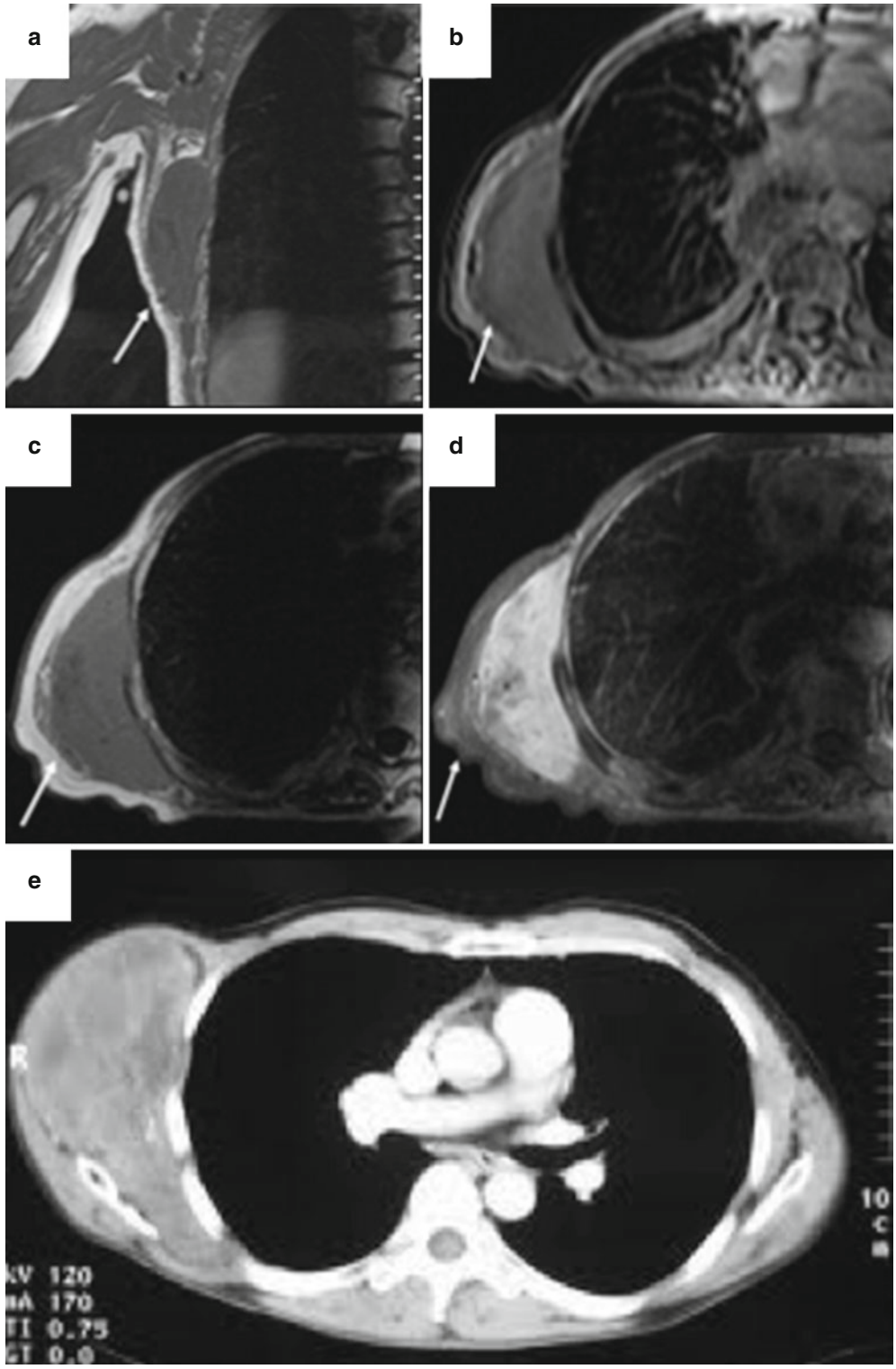

Fig. 15 (**a**) Coronal T1W image of the right chest wall showing a 5 cm mass (*arrow*) isointense to adjacent muscles on axial (**b**) T1W and (**c**) T2W images and shows (**d**) intense enhancement post-gadolinium. (**e**) Axial CT image showing a large homogenous mass in the right chest wall biopsy proven to be desmoid

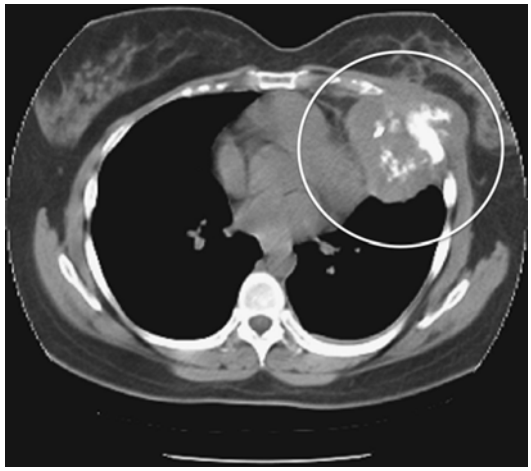

Fig. 16 Axial CT image showing a large mass arising from the anterolateral aspect of the 5th rib on the left with *rings* and arcs appearance characteristic of a chondrosarcoma

decreases toward the periphery. T1-weighted images show the lesion to be hyperintense relative to muscle, and T2-weighted images demonstrate high signal intensity. Enhancement is heterogeneous.

Liposarcomas are classified by the WHO into five groups based on histological composition, well-differentiated (most common), dedifferentiated, myxoid, pleomorphic, and mixed. Approximately 50–75 % of a typical well-differentiated liposarcoma is fat. Features that favor well-differentiated liposarcoma over lipoma on MRI include septa greater than 2 mm thick and nodular non-adipose components; however, in 4–9 % of cases, well-differentiated liposarcoma and lipoma may be indistinguishable. Other histologic types of liposarcoma contain less fat (usually <25 % by volume). Pleomorphic liposarcoma may be totally devoid of fat (Nam et al. 2011; O'Sullivan et al. 2007b).

Undifferentiated pleomorphic sarcoma (UPS) rarely involves the chest wall and is indistinguishable from other sarcomas. Ewing's sarcoma is a small round blue cell tumor of soft tissue origin that most commonly presents in adolescent boys as a painful, rapidly enlarging mass. Masses are usually solitary and most commonly occur in the ribs, scapulae, clavicles, or sternum. On CT, Ewing's sarcoma usually appears as a large, poorly defined, heterogeneous mass that may contain calcification. MRI findings are similar in Ewing's and non-Ewing's sarcomas (Fig. 17).

Both lytic and sclerotic metastases can involve the chest wall bones. The pleural metastases tend to have similar characteristics to the primary tumor (Figs. 18, 19, and 20).

11 Nonsarcomatous Primary Chest Wall Malignancy

Askin's tumor is an uncommon primitive neuroectodermal tumor that is histologically similar to rhabdomyosarcoma, neuroblastoma, Ewing's sarcoma, lymphoma, and small cell osteosarcoma. Askin's tumors generally arise in the chest wall or in a paravertebral location in young adults. CT and MRI show a mass that causes erosion of associated ribs or vertebral bodies. On MRI, the tumor is heterogeneous due to focal hemorrhage and tumor necrosis, hyperintense to muscle on T1-weighted images and hyperintense on T2-weighted images.

Uncommon primary tumors that may affect the chest wall include chondroblastomas, osteoblastomas, melanomas, lymphomas, rhabdomyosarcomas, and lymphangiosarcomas.

11.1 Pancoast Tumors

Lung tumors originating in the superior sulcus are referred to as Pancoast tumors; these tumors often cause destruction of the bones and structures in the thoracic inlet, including the brachial plexus and cervical sympathetic ganglion (Panagopoulos et al. 2014; Detterbeck 1997). Patients often present with classic symptoms of Horner's syndrome (miosis, enophthalmos, ptosis, and anhidrosis), atrophy of hand muscles,

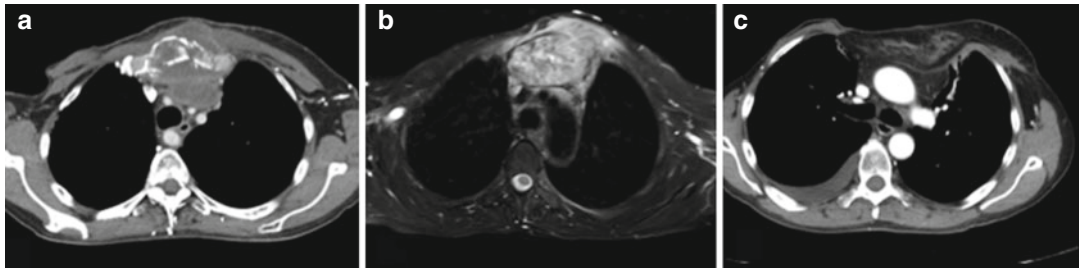

Fig. 17 (**a**) Axial CT image showing a large soft tissue mass in the anterior chest wall invading the mediastinum, in a patient previously radiated after double mastectomy for breast cancer. (**b**) MRI is done for surgical planning. (**c**) Post-resection axial CT of the chest wall with an omental flap

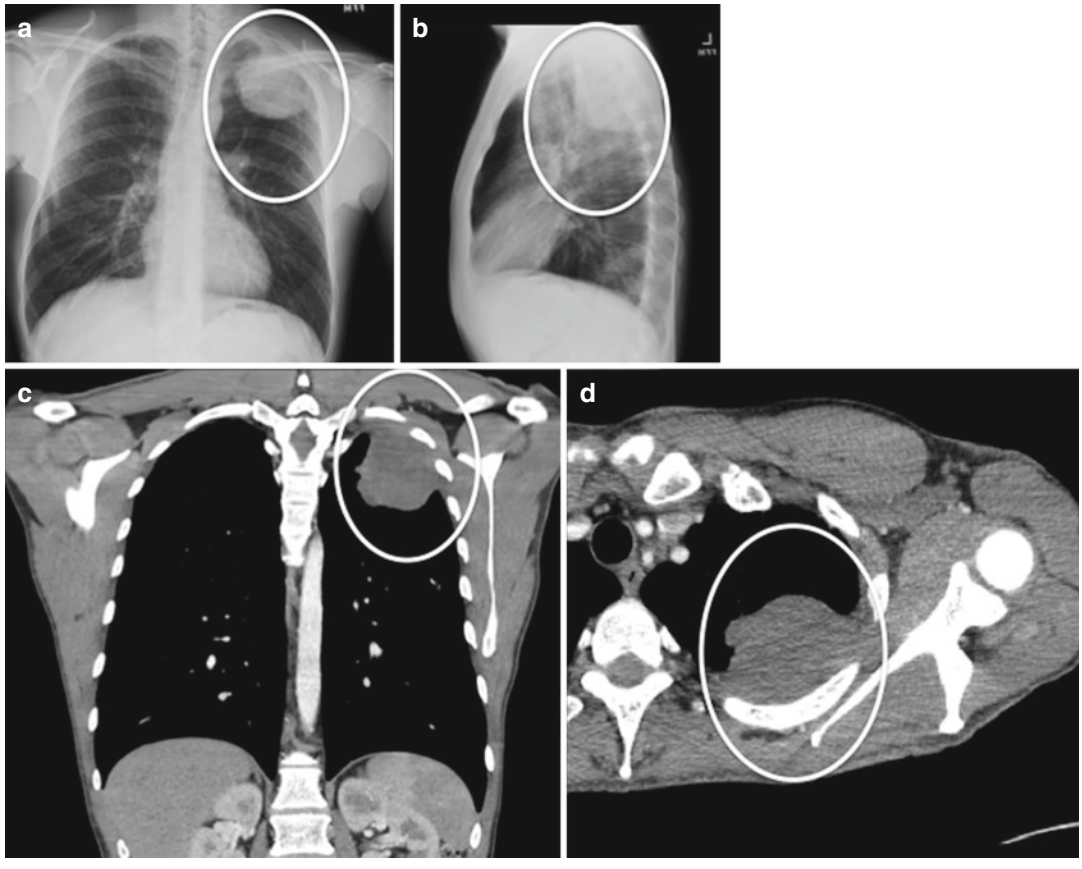

Fig. 18 (**a**, **b**) Chest PA and lateral views showing a large left apical mass. (**c**) Coronal and (**d**) axial CT images showing a large soft tissue mass in the left apex; biopsy proven to be an undifferentiated sarcoma in a patient known to have eosinophilic granuloma. *Circle* highlights the abnormality

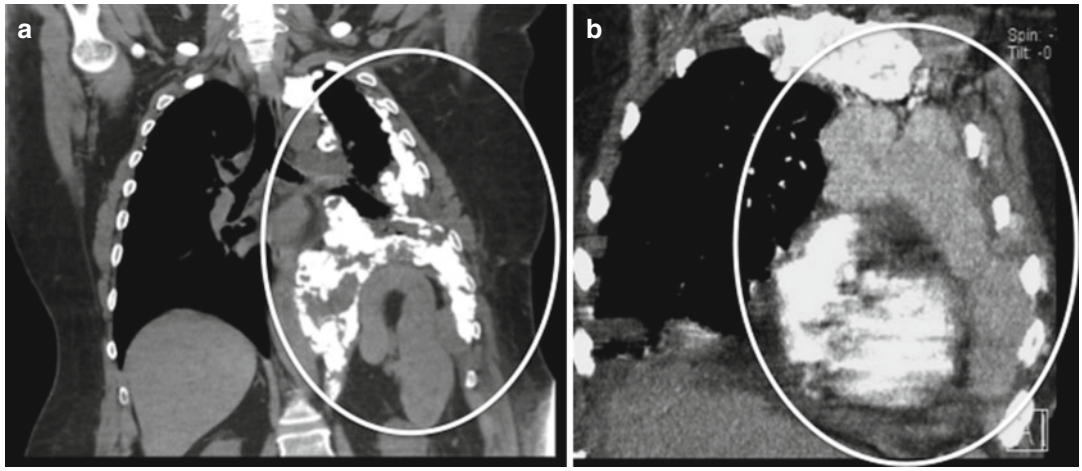

Fig. 19 Coronal images of two patients with pleural metastases. (**a**) Osteosarcoma. (**b**) Thymoma. The metastases have imaging characteristics similar to primary tumor. *Circle* highlights the tumor

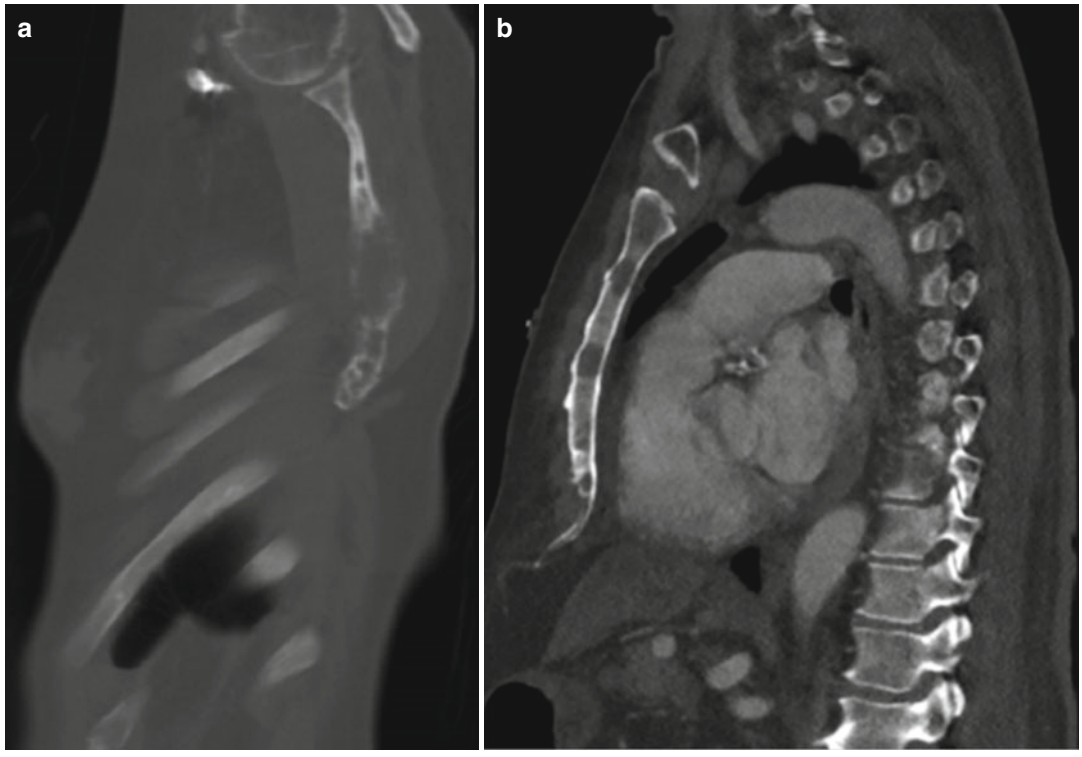

Fig. 20 Sagittal (**a**) in bone windows and (**b**) in soft tissue windows showing multiple lytic metastases from colon cancer involving the scapula and the sternum

severe shoulder pain radiating to the axilla and scapula, and compression of blood vessels. The majority of these tumors tend to be squamous cell carcinomas or adenocarcinomas and only about 3–5 % are small cell carcinomas (Panagopoulos et al. 2014). Preoperative workup includes a multimodality approach with CT being the primary modality for characterization of extent and bony involvement. These tumors tend to involve the first three ribs and vertebral bodies. MR is most helpful in evaluating for brachial plexus involvement and in also determining extent of marrow involvement by the tumor. Contraindications to resection include involvement of more than 50 % of vertebral bodies, brachial plexus invasion, or presence of distal metastatic disease.

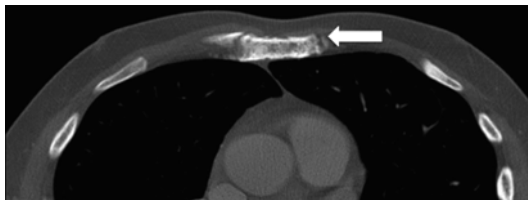

Fig. 21 Sclerotic metastatic lesions replace the sternum in this patient with malignant melanoma (*arrow*)

Volume-rendered 3D reformats and 3D-printed models generated from CT scans can help guide the surgeon and plan the surgical approach. The treatment generally involves preoperative radiation therapy followed by surgical resection (Figs. 21 and 22).

12 Chest Wall Interventions

Chest wall lesions are relatively easy to biopsy, and most interventions can be performed with ultrasound guidance. Chest wall masses are generally biopsied using 18-gauge core biopsy needles. When getting tissue for genomic characterization, it is preferable to get it from a soft tissue lesion or other sites from within the lungs rather than the bone, as decalcifying the bone can denature the DNA (Hours 2012). Catheter drainage can be performed for chest wall collections and abscesses. Ablation using radiofrequency, cryoablation, and microwave can be utilized to treat chest wall and pleural tumors. These procedures are usually performed under CT fluoroscopy (Palussière et al. 2012). Ablative therapies can be used both for treatment and palliation and treatment of pain (Figs. 23, 24, 25, and 26).

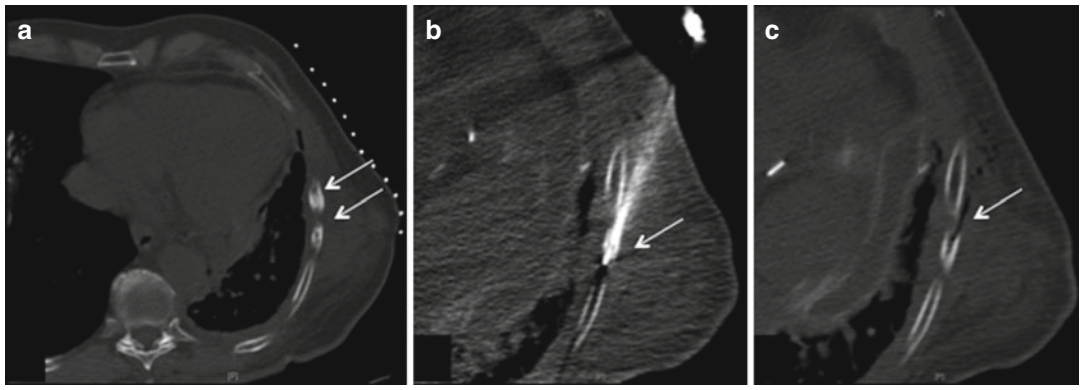

Fig. 22 Axial CT images showing (**a**) sclerotic metastases from a lung cancer (*double white arrows*) and (**b**) bone biopsy with a biopsy needle (*arrow*). (**c**) Post-procedure axial image showing the track (*arrow*) of the needle

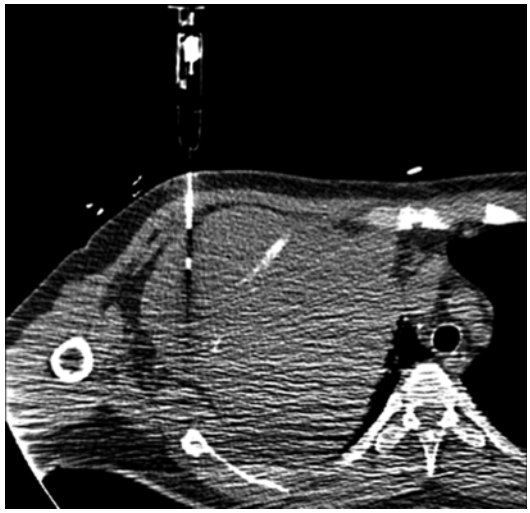

Fig. 23 CT-guided core biopsy of a soft tissue sarcoma with an 18-gauge Temno biopsy system

13 3D Printing of the Chest Wall

13.1 Technical Aspects

Medical 3D printing is a technique wherein digital 2D image data sets are converted into graspable 3D models. 3D models allow physicians and patients to interact with data in a tactile manner and, when created to scale, allow for more intuitive assessment of the size and interrelationship of important structures. Models of patient-specific anatomy can be used for education, presurgical planning, and implantable device design (Rengier et al. 2010). Multiple additional uses will likely be envisioned as the technology becomes more widespread.

Optimized image acquisition is an important first step in creating a quality 3D-printed model. Ideally, planning for a 3D model would begin before image acquisition, with the surgeon and radiologist working together to plan a protocol that would include the necessary patient anatomy, orientation (e.g., arms up or down, prone vs. supine) and timing necessary (e.g., during inspiration vs. expiration). Maximizing contrast between the anatomy of interest and surrounding structures is another important element of protocol design and will aid in subsequent post-processing steps. After data is acquired, it is important to reconstruct the raw data into high-resolution data sets with isotropic voxels and thin slices (ideally less than 1.0 mm) (Rengier et al. 2010) which will maximize the accuracy of the model and minimize stair-step effect in the model surface.

Processing of reconstructed thin slice data sets begins with segmentation of images, which is the selection of a subset of pixels within the data set that correspond to a structure of interest. Segmentation can be accomplished by manual selection of pixels or by methods such as thresholding or region growing from a seed point. Next, these pixels must be assembled into an object with a continuous surface that has a definable inside and outside. This is accomplished via software that describes the surface of the data set using a meshwork of interposed triangles. These triangulated surface models can be further post-processed and refined to ensure successful printing using computer-aided design (CAD) software. Small gaps in the model that lead to confusion over what is defined as inside versus outside or thin overhanging edges that are beyond the capability of the printer (non-manifold edges) may result in print failure. These need to be addressed within the CAD program. Finally, the model is exported in a file format that is readable by 3D printers. The most well-known file type is the STL file, which stands for Stereolithography Tesselation Language. It is also referred to as a Standard Triangle Language file. This universal file type is recognized by all current 3D-printing machines.

The actual physical process of printing is achieved by laying down sequential layers of material that form the model, hence the terminology "additive manufacturing." There are several types of 3D printers and hundreds of different materials, with new materials being created weekly and dozens of new printing methodologies likely being envisioned and created over the next several years (Figs. 27, 28, 29, and 30).

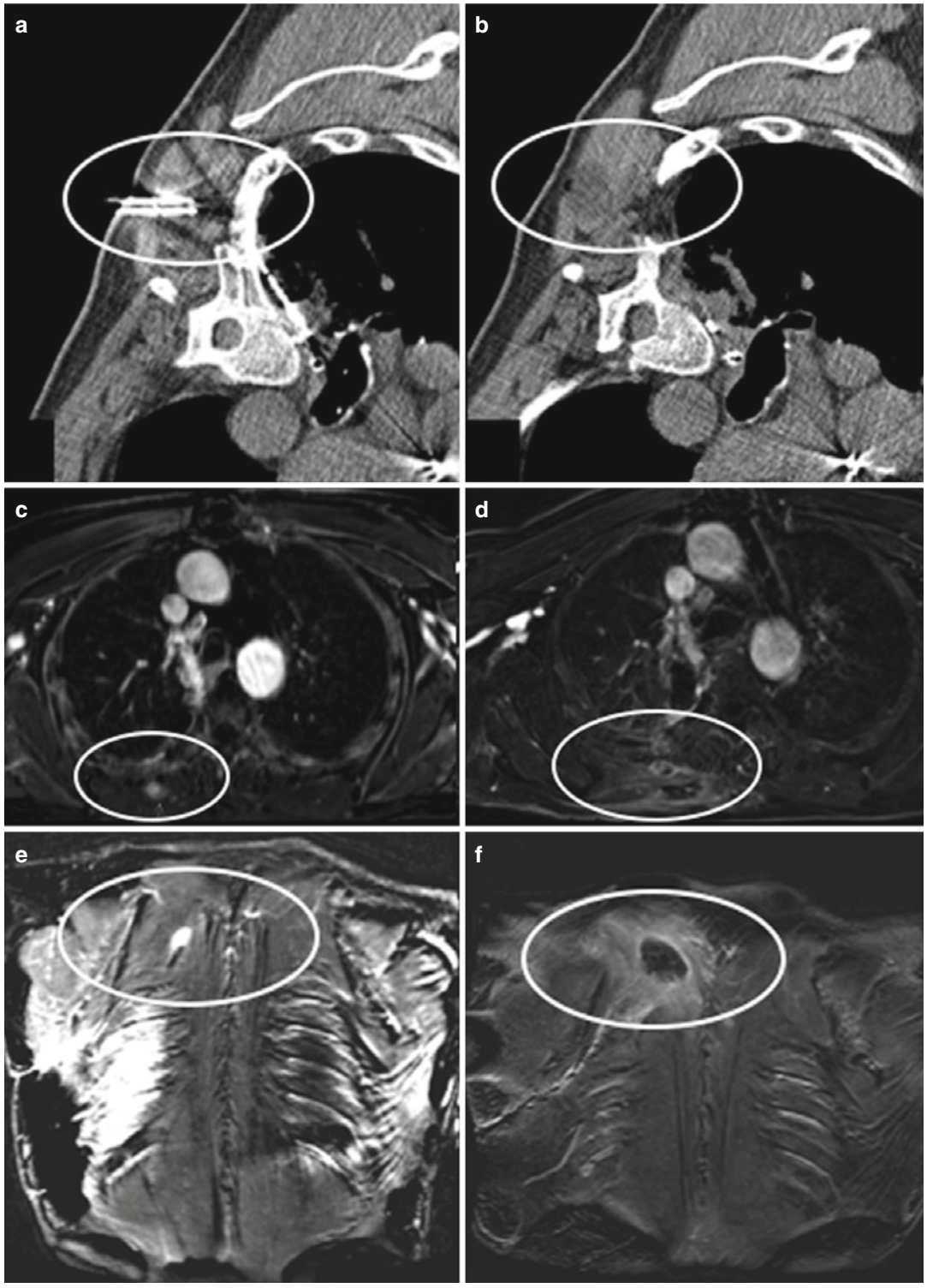

Fig. 24 Axial (**a**) CT image of mesothelioma metastases in the chest wall being cryoablated. (**b**) Post-ablation "ice ball". (**c**, **e**) Pretreatment axial VIBE image showing enhancing mass. (**d**, **f**) Good post-ablation response. *Circle* highlights the tumor

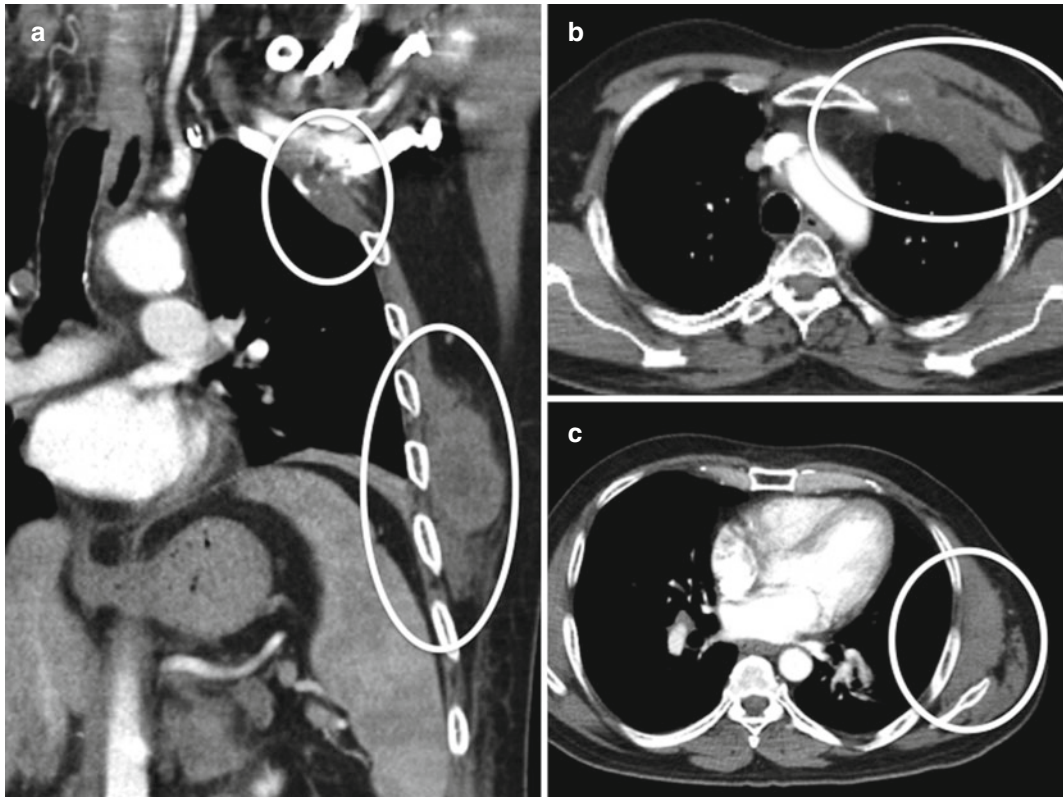

Fig. 25 Bone biopsies are problematic due to denaturation of DNA during decalcification process. The left lateral chest wall lesion is more suitable for genomic profiling than the left anterior rib metastases. Decalcification of bone metastases renders the tissue suboptimal for evaluation. (**a**) Coronal (**b**, **c**) showing two musculoskeletal metastases from lung cancer. The left lateral chest wall lesion (**c**) is more likely to yield better-quality tissue for genomic evaluation. *Circle* highlights the tumors

14 3D Printing for Surgical Planning and Bioprosthetics: Future Considerations

The utility of 3D models for chest wall tumor resection and chest wall reconstruction planning is just now being explored but will likely prove to be great. Being able to better understand a patient's complex anatomy prior to surgery and anticipate potential challenges preoperatively is one anticipated benefit. This may be of particular help in cases where there are complex 3D anatomical relationships between chest wall tumors and adjacent blood vessels and nerves, which are hard to fully appreciate in 2D. Pancoast tumors are an example of the type of case that could benefit from 3D printing. A 3D model of a Pancoast tumor was used for presurgical planning at Mayo Clinic in Rochester, Minnesota, and aided in planning a minimally invasive approach. The model additionally aided in informed consent conversations with the patient and allowed physicians to explain why sacrifice of the T1 nerve root was necessary in a particular case. The figure demonstrates a case of Pancoast tumor from Brigham and Women's Hospital.

Another potential benefit of 3D printing is the ability to design custom implants for chest wall deformities, whether resulting from congenital abnormalities, surgical resection, or trauma. En

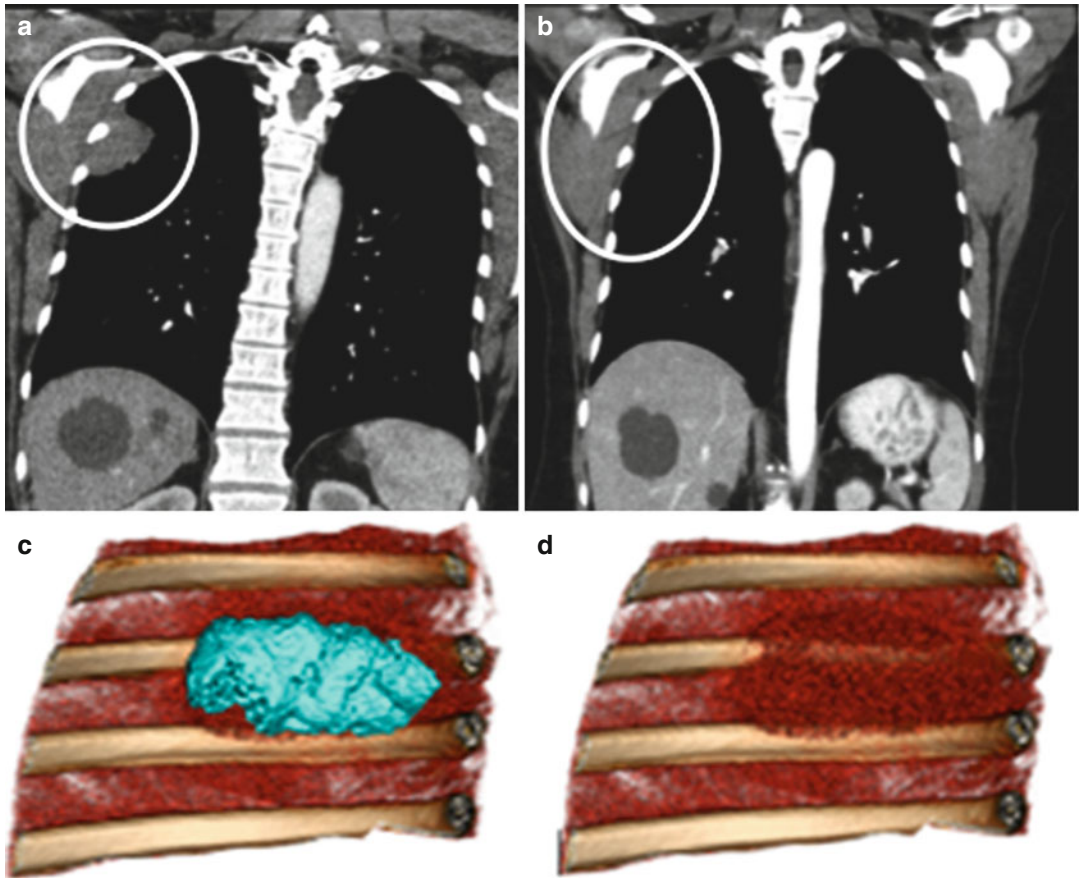

Fig. 26 Coronal images (**a**) pretreatment and (**b**) post-radiotherapy showing a soft tissue sarcoma arising from the right lateral ribs (2, 3, and 4). The tumor had a complete response to radiation. (**c**, **d**) Volume-rendered images of the tumor. *Circle* highlights the lesion

bloc resection of chest wall tumors is the standard of care but can lead to significant functional and cosmetic deformity (Thomas and Brouchet 2010). Large defects can negatively impact respiratory mechanics, put the patient at risk for lung herniation, lead to shrinkage of the operated hemithorax, and leave underlying mediastinal structures vulnerable to injury (Thomas and Brouchet 2010). Reconstructing the defect at the same time as the resection improves outcomes, most notably decreasing the chance for infection. Existing strategies include use of preformed implants versus intraoperative fabrication of an implant. These strategies can lead to improper fit or increased operative times and potential damage to tissue from the intraoperative molding of the implant, respectively (Kim et al. 2012).

Being able to preoperatively design an implant using a 3D-printed patient-specific model is one potential way to improve aesthetic outcomes and decrease operative time, with precedent for this in maxillofacial (Azuma et al. 2014; Singare et al. 2008; Cohen et al. 2009; Klammert et al. 2010) and cranioplasty (Jaberi et al. 2013) surgeries. 3D-printed models of the planned resection and surrounding chest could be created from preoperative data sets or, for patients who have already undergone resection, could be created by creating a mirror image of the contralateral chest wall. These could be used to guide appropriate

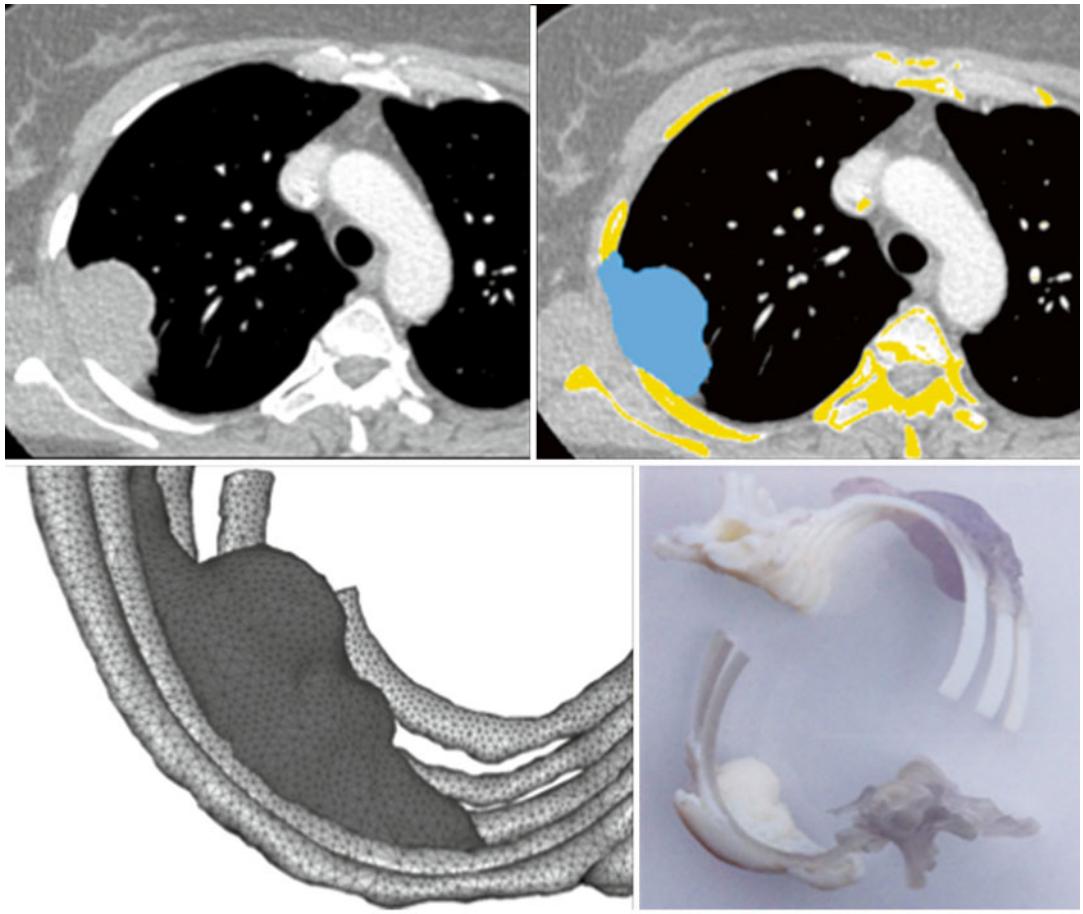

Fig. 27 Steps involved in converting a CT image to a 3D printed model

shaping and sizing of existing implant strategies, which include synthetic meshes, bone substitutes, osteosynthesis systems, and plastic and metal prostheses (Thomas and Brouchet 2010).

Alternately, a patient-specific implant could be 3D printed and directly implanted into the patient. Determining appropriate 3D-printable materials and obtaining FDA clearance are some of the challenges to overcome. Ideal characteristics of material used for an implant include biocompatibility, ability to hold appropriate shape and offer mechanical protection to the underlying tissues, osteogenic potential, and compatibility with imaging techniques (Jaberi et al. 2013) Polymethylmethacrylate (PMMA) is an inert material that is often added between layers of mesh during conventional chest wall reconstruction to provide additional rigidity. This material is easily shaped and performs with comparable complication rates to autogenous bone (Jaberi et al. 2013). PMMA (polymethylmethacrylate) is available for 3D printing but has some associated challenges, including its fast cooling, propensity to develop bubbles within the printed structure, and brittle nature when created as filament. There are potential issues with shrinkage relative to the planned model, and 3D-printed PMMA has decreased tensile strength, elongation, and modu-

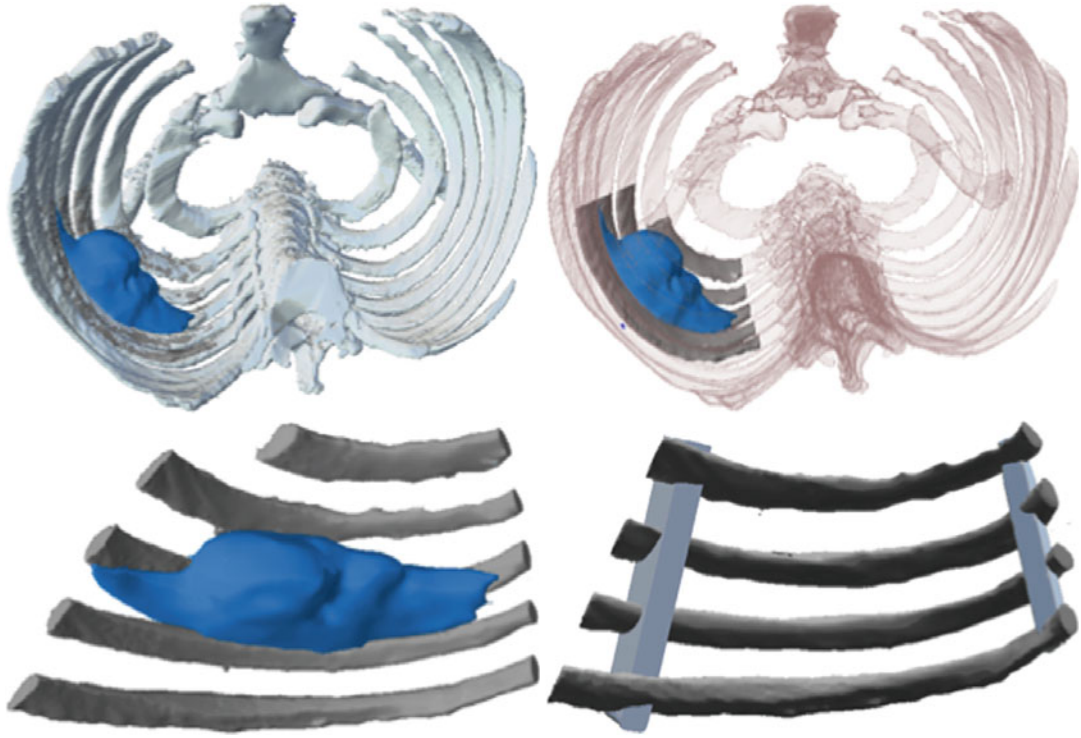

Fig. 28 Workflow to create a 3D-printed model of the sarcoma

lus of elasticity compared to traditionally fabricated PMMA parts (Polzin et al. 2013). Improvements in printer head resolution and decreased size of PMMA granules may help to address some of these issues (Polzin et al. 2013).

Titanium is biologically inert and corrosion resistant and has the highest strength/weight ratio than any metal (Thomas and Brouchet 2010), making it another excellent choice for implants. Titanium parts can be printed using various 3D-printing techniques including selective laser melting (SLM), electron beam melting (EBM), and laser-engineered net shaping (LENS) (El-Hajje et al. 2014). These techniques use high heat to melt titanium that starts in powder form. These printers are extremely expensive, limiting accessibility. However, alternate techniques using inkjet 3D printing produce titanium parts at lower price points with the trade-off of slightly less precision (El-Hajje et al. 2014).

2013 marked the first FDA-approved 3D-printed polymer implant – OsteoFab (Oxford Performance Materials, USA), customized cranioplasty implants made from the company's PEKK (polyetherketoneketone) polymer compounds.

In summary MDCT has a very important role in diagnosis and management of congenital and acquired chest wall pathologies. 3D and 4D reconstructions can help illustrate the pathology and physiology of the chest wall and help plan management strategies. The 3D reconstructions can be used for 3D printing for surgical planning and also for educational purposes. Technological advances allow for 3D printing in bio-implantable materials.

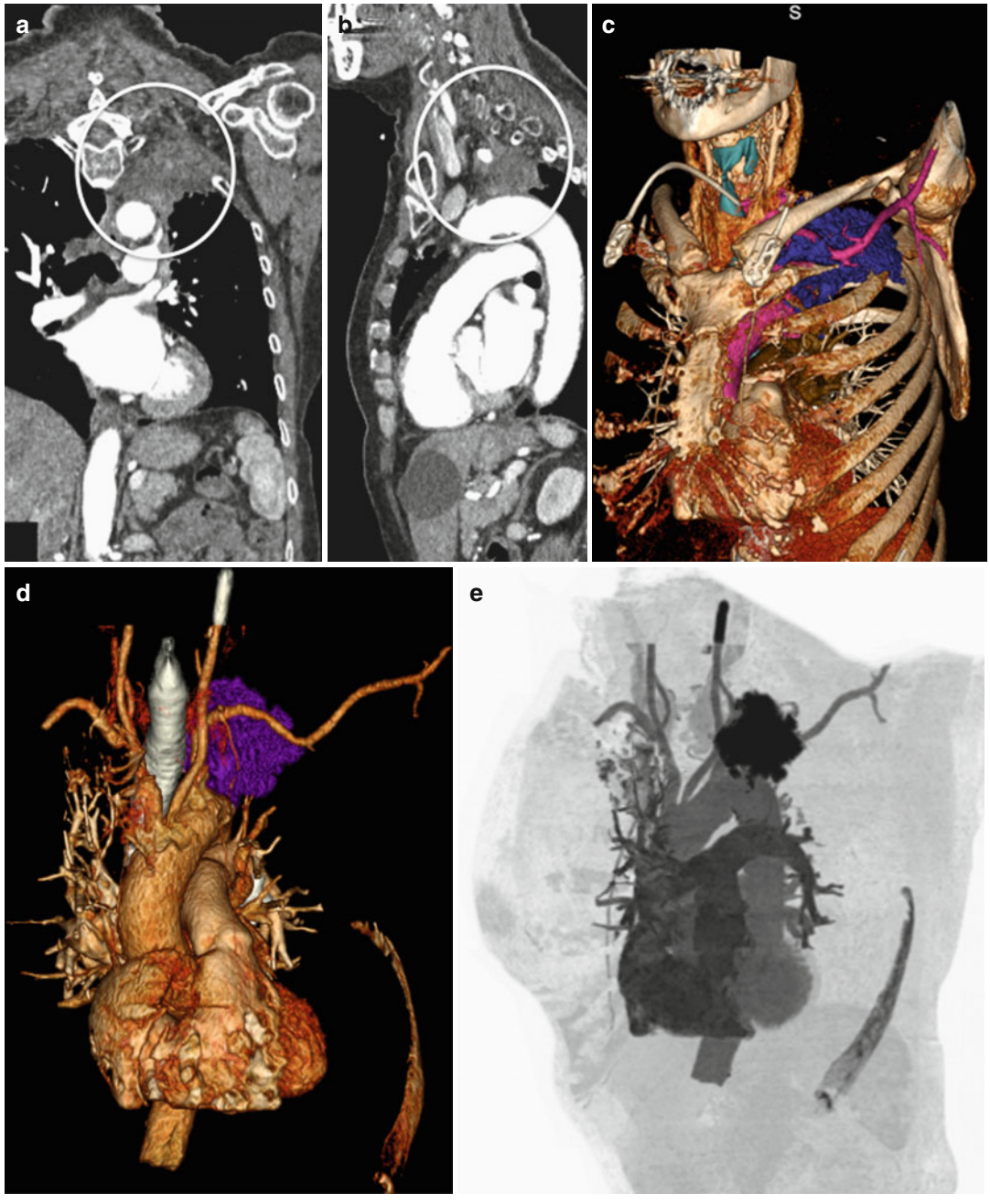

Fig. 29 (**a**) Coronal image of a left apical Pancoast tumor. (**b**) Sagittal image. (**c**) Volume-rendered images showing a left apical (**d**, **e**) showing the Pancoast tumor and its relationship to the arteries and veins and the brachial plexus. 3D models are very useful for surgical planning. *Circle* highlights the tumor

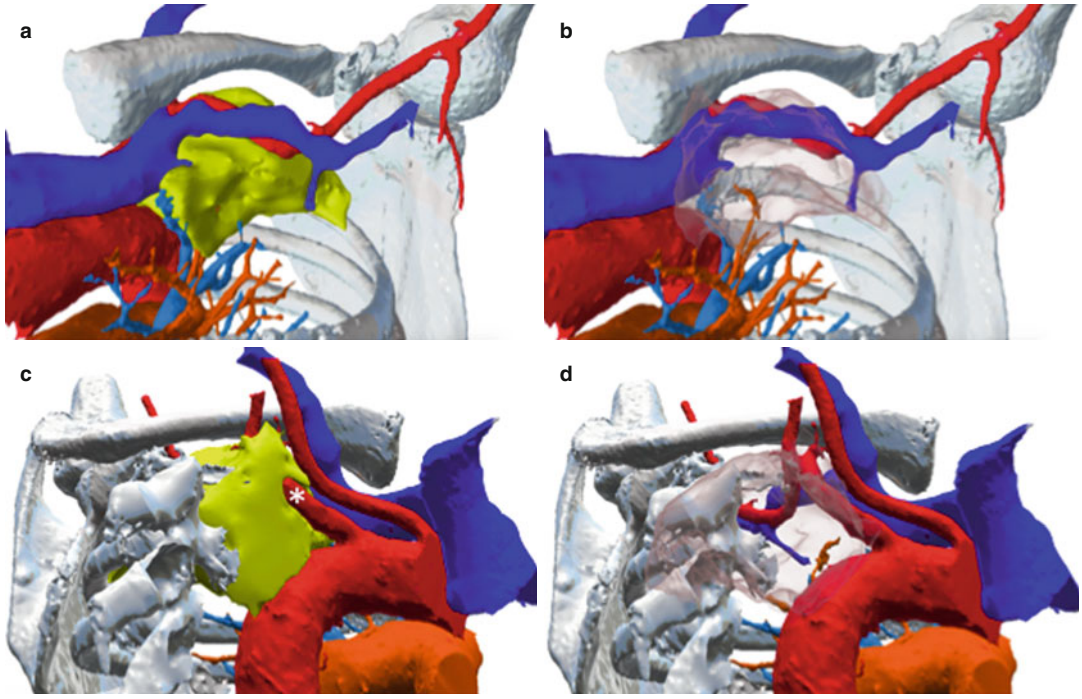

Fig. 30 (**a**) 3D surface model of a Pancoast tumor created for 3D printing demonstrates the close relationship of the subclavian artery (*red*) and subclavian vein (*blue*) with the tumor (*yellow*). (**b**). The tumor is lucent in this image, allowing visualization of the pulmonary arteries (*orange*) and veins (*light blue*) that are surrounded by the tumor. (**c**) Parasagittal view of the model demonstrates that the tumor encases a portion of the left subclavian artery (*). The right brachiocephalic artery is not included in this model. (**d**) The tumor is rendered lucent in this image to allow better visualization of the relationship of the tumor with surrounding structures

References

Athanassiadi K, Theakos N, Kalantzi N, Gerazounis M (2010) Prognostic factors in flail-chest patients. Eur J Cardiothorac Surg 38(4):466–471. doi:10.1016/j.ejcts.2010.02.034

Azuma M, Yanagawa T, Kanno NI et al (2014) Mandibular reconstruction using plates prebent to fit rapid prototyping 3-dimensional printing models ameliorates contour deformity. Head Face Med 23;10(1), p 45.

Bernatowicz K, Keall P, Mishra P, Knopf A, Lomax A, Kipritidis J (2015) Quantifying the impact of respiratory-gated 4D CT acquisition on thoracic image quality: a digital phantom study. Med Phys 42(1): 324–334. doi:10.1118/1.4903936

Biederer J, Hintze C, Fabel M, Dinkel J (2010) Magnetic resonance imaging and computed tomography of respiratory mechanics. J Magn Reson Imaging 32(6):1388–1397. doi:10.1002/jmri.22386

Bouaziz M, Helmi J, Skander C, Ladeb M, Miled-Mrad K (2009) Imaging of chest wall infections. Skeletal Radiol 38:1127–1135

Brochhausen C, Turial S, Müller FKP et al (2012) Pectus excavatum: history, hypotheses and treatment options. Interact Cardiovasc Thorac Surg 14(6):801–806. doi:10.1093/icvts/ivs045

Cingel V, Bohac M, Mestanova V, Zabojnikova L, Varga I (2013) Poland syndrome: from embryological basis to plastic surgery. Surg Radiol Anat 35(8):639–646. doi:10.1007/s00276-013-1083-7

Cohen A, Laviv A, Berman P, Nashef R, Abu-Tair J (2009) Mandibular reconstruction using stereolithographic 3-dimensional printing modeling technology. Oral Surg Oral Med Oral Pathol Oral Radiol Endod 108(5):661–666. doi:10.1016/j.tripleo.2009.05.023

Coolens C, Bracken J, Driscoll B, Hope A, Jaffray D (2012) Dynamic volume vs respiratory correlated 4DCT for motion assessment in radiation therapy simulation. Med Phys 39(5):2669. doi:10.1118/1.4704498

Desir A, Ghaye B (2012) CT of blunt diaphragmatic rupture. Radiographics 32(2):477–498. doi:10.1148/rg.322115082

Detterbeck FC (1997) Pancoast (superior sulcus) tumors. Ann Thorac Surg 63(6):1810–1818. doi:10.1016/S0003-4975(97)00360-3

El-Hajje A, Kolos EC, Wang JK et al (2014) Physical and mechanical characterisation of 3D-printed porous titanium for biomedical applications. J Mater Sci Mater Med 25:2471–2480. doi:10.1007/s10856-014-5277-2

Exadaktylos AK, Sclabas G, Schmid SW, Schaller B, Zimmermann H (2001) Do we really need routine computed tomographic scanning in the primary evaluation of blunt chest trauma in patients with "normal" chest radiograph? J Trauma 51(6):1173–1176

Fredberg Persson G, Nygaard DE, Af Rosenschöld PM et al (2011) Artifacts in conventional computed tomography (CT) and free breathing four-dimensional CT induce uncertainty in gross tumor volume determination. Int J Radiat Oncol Biol Phys 80(5):1573–1580. doi:10.1016/j.ijrobp.2010.10.036

Gill RR, Gerbaudo VH, Sugarbaker DJ, Hatabu H (2009) Current trends in radiologic management of malignant pleural mesothelioma. Semin Thorac Cardiovasc Surg 21:111–120. doi:10.1053/j.semtcvs.2009.06.011

Grieser T, Buhne KH, Hauser H, Bohndorf K (2001) Significance of findings of chest X-rays and thoracic CT routinely performed at the emergency unit: 102 patients with multiple trauma. A prospective study. Rofo 173(1):44–51. doi:10.1055/s-2001-10225

Heffner JE, Klein JS, Hampson C (2010) Diagnostic utility and clinical application of imaging for pleural space infections. Chest 137(2):467–479

Helm EJ, Matin TN, Gleeson FV (2010) Imaging of the pleura. J Magn Reson Imaging 32:1275–1286

Hours H (2012) ASCO Annual Meeting Chicago, Illinois Chicago, Illinois Certificate of Participation Ritu Gill Brigham and Womens Hosp/Dana Farber Cancer 2012 ASCO Annual Meeting 2012:25–26

Jaberi J, Gambrell K, Tiwana P, Madden C, Finn R (2013) Long-term clinical outcome analysis of poly-methylmethacrylate cranioplasty for large skull defects. J Oral Maxillofac Surg 71(2):e81–e88. doi:10.1016/j.joms.2012.09.023

Jeung MY, Gangi A, Gasser B et al (1999) Imaging of chest wall disorders. Radiographics 19(3):617–637. doi:10.1148/radiographics.19.3.g99ma02617

Kaewlai R, Avery LL, Asrani AV, Novelline RA (2008) Multidetector CT of blunt thoracic trauma. Radiographics 28(6):1555–1570. doi:10.1148/rg.286085510

Kanne JP, Yandow DR, Mohammed TLH, Meyer CA (2011) CT findings of pulmonary nocardiosis. Am J Roentgenol 197(2):266–272. doi:10.2214/AJR.10.6208

Kim BJ, Hong KS, Park KJ, Park DH, Chung YG, Kang SH (2012) Customized cranioplasty implants using three-dimensional printers and polymethyl-methacrylate casting. J Korean Neurosurg Soc 52(6):541–546. doi:10.3340/jkns.2012.52.6.541

Klammert U, Gbureck U, Vorndran E, Rödiger J, Meyer-Marcotty P, Kübler AC (2010) 3D powder printed calcium phosphate implants for reconstruction of cranial and maxillofacial defects. J Craniomaxillofac Surg 38(8):565–570. doi:10.1016/j.jcms.2010.01.009

McDonald RJ, McDonald JS, Bida JP et al (2013) Intravenous contrast material-induced nephropathy: causal or coincident phenomenon? Radiology 267(1):106–118. doi:10.1148/radiol.12121823

Mullan CP, Madan R, Trotman-Dickenson B, Qian X, Jacobson FL, Hunsaker A (2011) Radiology of chest wall masses. Am J Roentgenol 197(3):460–470. doi:10.2214/AJR.10.7259

Nam SJ, Kim S, Lim BJ et al (2011) Imaging of primary chest wall tumors with radiologic-pathologic correlation. Radiographics 31(3):749–770

O'Sullivan P, O'Dwyer H, Flint J, Munk PL, Muller N (2007a) Soft tissue tumours and mass-like lesions of the chest wall: a pictorial review of CT and MR findings. Br J Radiol 80(955):574–580. doi:10.1259/bjr/16591964

O'Sullivan P, O'Dwyer H, Flint J, Munk PL, Muller NL (2007b) Malignant chest wall neoplasms of bone and cartilage: a pictorial review of CT and MR findings. Br J Radiol 80(956):678–684. doi:10.1259/bjr/82228585

Omert L, Yeaney WW, Protetch J (2001) Efficacy of thoracic computerized tomography in blunt chest trauma. Am Surg 67(7):660–664

Palussière J, Henriques C, Mauriac L et al (2012) Radiofrequency ablation as a substitute for surgery in elderly patients with nonresected breast cancer: pilot study with long-term outcomes. Radiology 264(2):597–605. doi:10.1148/radiol.12111303

Panagopoulos N, Leivaditis V, Koletsis E et al (2014) Pancoast tumors: characteristics and preoperative assessment. J Thorac Dis 6(Suppl 1):S108–S115. doi:10.3978/j.issn.2072-1439.2013.12.29

Peters S, Nicolas V, Heyer CM (2010) Multidetector computed tomography-spectrum of blunt chest wall and lung injuries in polytraumatized patients. Clin Radiol 65(4):333–338. doi:10.1016/j.crad.2009.12.008

Polzin C, Spath S, Seitz H (2013) Characterization and evaluation of a PMMA-based 3D printing process. Rapid Prototyp J 19(1):37–43

Raj V, Kirke R, Bankart MJ, Entwisle JJ (2011) Multidetector CT imaging of pleura: comparison of two contrast infusion protocols. Br J Radiol 84(1005):796–799. doi:10.1259/bjr/55980445

Rengier F, Mehndiratta A, Von Tengg-Kobligk H et al (2010) 3D printing based on imaging data: review of medical applications. Int J Comput Assist Radiol Surg 5(4):335–341. doi:10.1007/s11548-010-0476-x

Singare S, Liu Y, Li D, Lu B, Wang J, He S (2008) Individually prefabricated prosthesis for maxilla reconstruction. J Prosthodont 17(2):135–140. doi:10.1111/j.1532-849X.2007.00266.x

Singh S (2014) Cleidocranial dysplasia: a case report illustrating diagnostic clinical and radiological findings. J Clin Diagn Res 8(6):20–22. doi:10.7860/JCDR/2014/9085.4499

Sirmali M, Türüt H, Topçu S et al (2003) A comprehensive analysis of traumatic rib fractures: morbidity, mortality and management. Eur J Cardiothorac Surg 24(1):133–138. doi:10.1016/S1010-7940(03)00256-2

Tateishi U, Gladish GW, Kusumoto M et al (2003) Chest wall tumors: radiologic findings and pathologic corre-

lation: part 1. Benign tumors. Radiographics 23(6):1477–1490. doi:10.1148/rg.236015526
Thomas PA, Brouchet L (2010) Prosthetic reconstruction of the chest wall. Thorac Surg Clin 20(4):551–558. doi:10.1016/j.thorsurg.2010.06.006
Toccoa MP, Ballardini M, Masala M, Perozzi A (2013) Post-sternotomy chronic osteomyelitis: is sternal resection always necessary? Eur J Cardiothorac Surg 43(4):715–721. doi:10.1093/ejcts/ezs449
Watt AJB (2002) Chest wall lesions. Paediatr Respir Rev 3(4):328–338. doi:10.1016/S1526-0542(02)00270-1
Weyant MJ, Flores RM (2004) Imaging of pleural and chest wall tumors. Thorac Surg Clin 14:15–23. doi:10.1016/S1547-4127(04)00033-7

MDCT of Chest Trauma

Lucas L. Geyer and Ulrich Linsenmaier

Abstract

In the industrialized countries, chest trauma is the third most common cause of relevant injuries in trauma patients and is associated with significant morbidity and mortality. As the clinical presentation of patients with thoracic injuries ranges from minor symptoms to hemodynamical instability, radiological imaging plays a pivotal role in the diagnosis and management of these patients. In recent years, multi-detector computed tomography (MDCT) has emerged as the most important imaging modality in trauma patients. Substantial technical developments have continuously improved the diagnostic performance of MDCT resulting in a considerably better outcome of trauma patients. From a radiologist's point of view, knowledge of the mechanisms of injury, recognition of CT findings of the spectrum of thoracic injuries, and awareness of coexisting injuries to other systems are essential to provide an adequate assessment of chest trauma. This chapter (1) summarizes the basic principles of adult chest trauma, (2) reviews recent advances in CT technology that enable comprehensive trauma imaging, and (3) discusses the typical imaging findings of chest trauma.

Abbreviations

AAI	Acute aortic injury
ARDS	Acute respiratory distress syndrome
CM	Contrast medium
CT	Computed tomography
CTA	CT angiography
CXR	Chest radiography
EVAR	Endovascular repair
HU	Hounsfield units
IMH	Intramural hematoma
MDCT	Multi-detector computed tomography

L.L. Geyer, MD (✉)
Institute for Clinical Radiology, LMU Ludwig-Maximilians-University Hospital Munich, Munich, Germany
e-mail: Lucas.Geyer@med.lmu.de;

U. Linsenmaier, MD, PhD
Institute for Diagnostic and Interventional Radiology, HELIOS Kliniken München WEST & HELIOS Kliniken München Perlach and Klinikum Augustinum München, Munich, Germany
e-mail: Ulrich.Linsenmaier@helios-kliniken.de

U.J. Schoepf, F.G. Meinel (eds.), *Multidetector-Row CT of the Thorax*, Medical Radiology,
DOI 10.1007/978-3-319-30355-0_25

MPR	Multiplanar reformation
MVA	Motor vehicle accident
TLICS	Thoracolumbar Injury Classification and Severity Score
VRT	Volume rendering technique
WBCT	Whole-body computed tomography

1 Introduction

Traumatic injuries rank among the leading causes of death worldwide and are the leading cause of death in the population under 45 years in the industrialized countries (Lopez et al. 2006). The thorax is the third most common injured body region, following the head and the extremities (Kaewlai et al. 2008). Although the majority of injuries are minor, approximately one-third of the patients require hospital admission (Feliciano and Rozycki 1999; Westaby and Brayley 1990). More important, chest trauma has a high primary mortality rate of 20–25 % and is a relevant contributing factor in another 50 % of all trauma-related deaths and of multiple trauma as well (Scaglione et al. 2008).

2 Biomechanics of Chest Trauma

Blunt trauma is the major cause of thoracic injuries, whereas penetrating trauma, e.g., stabbing or gunshot, accounts for 4–15 % only with remarkable regional and geographic differences in incidence (Shanmuganathan and Matsumoto 2006). Most blunt thoracic injuries are due to motor vehicle accidents (MVA, 63–78 %), followed by falls from heights or blows from blunt objects in the context of work-related and sports accidents (Mayberry 2000). In blunt trauma, three main patterns of biomechanics can be distinguished that may help recognize the full extent of injury (Scaglione et al. 2008): First, a *direct impact* results typically in minor injuries affecting the soft tissue. It is occasionally associated with simple osseous injuries of the chest wall. Rarely, the force is transmitted along its trajectory vector to deeper structures causing severe injuries of the lung or mediastinal organs. Second, in *thoracic compression*, the underlying force causes primarily a deformation of the thoracic ring. This mechanism leads to contusions, lacerations, or ruptures of thoracic or abdominal organs by both its direct impact and indirectly due to sudden increased pressure (e.g., diaphragmatic injuries). Third, *deceleration injuries* are caused by shear forces that occur abruptly with a maximum effect at anatomical fixation points (e.g., ligamentous attachments) and deceleration forces being applied on moving inner thoracic organs. This type is the most lethal mechanism as it is responsible for major aortic and airway injuries. A combination, in particular of compression and deceleration injuries, is possible.

3 Imaging Approach in Trauma

After introduction of CT in clinical medicine in the 1980s and 1990s, trauma imaging was initially restricted to focused computed tomography (CT) examinations of single body parts because of relatively slow scan speed, restricted volume coverage, limited availability, and missing of whole-body scan algorithms. Helical scan techniques facilitated shorter examination times of larger volumes, offering the possibility of multiphasic CT imaging of more than one body region. However, those improvements were gained at the expense of a low spatial and temporary resolution with thick-slice image acquisition of usually 5–10 mm, resulting in multiplanar reformations (MPR) of limited diagnostic value. Only the introduction of multi-detector CT (MDCT) delivered significant advantages, starting with the introduction of four-row MDCT in the late 1990s. Dramatically improved temporal and spatial resolution allowed for substantial reduction of motion artifacts and thinner slice collimation offering high-quality MPR and three-dimensional (3D) visualization due to nearly isotropic voxels (Dawson and Lees 2001; Linsenmaier et al. 2002; Kloppel et al. 2002; Philipp et al. 2003). Technical developments, such as high-speed imaging and

submillimeter isotropic data acquisition over lengths of up to 2000 mm facilitated by MDCT systems with at least 64 rows or dual-source configuration, have enforced the unquestionable role of MDCT as the most important and central modality in trauma imaging. Data that have shown that the use of standardized whole-body CT (WBCT) reduces mortality substantially have clearly influenced this progression. At the same time, the limited value of conventional radiography became clearly visible with the use of MDCT (Huber-Wagner et al. 2009; Kanz et al. 2010; Healy et al. 2014; Van Vugt et al. 2013).

Consequently, MDCT imaging plays an essential role in diagnostic workup of chest trauma. Nevertheless, in minor chest trauma, chest radiography (CXR) is still routinely performed at hospital admission in most trauma centers. Besides the detection of various relevant thoracic injuries, such as pneumothorax, hemothorax, or musculoskeletal injury, CXR serves as a quick screening tool for major findings such as tension pneumothorax, hemothorax, and aortic injury and for verification of correct placement of lines and tubes (Kaewlai et al. 2008). Today, however, advanced MDCT is considered the reference standard in trauma imaging due to its higher sensitivity and diagnostic accuracy (Exadaktylos et al. 2001; Trupka et al. 1997; Geyer et al. 2013; Traub et al. 2007). Therefore, the use of MDCT in major chest or multiple trauma is mandatory. In particular after high-energy trauma, CXR is insufficient to rule out all significant thoracic injuries, while the additional information provided by MDCT leads to alterations in patient management in 5–20 % of cases (Omert et al. 2001). According to the American College of Radiology Appropriateness Criteria, the use of MDCT should be strongly considered in chest trauma in patients with (a) high-energy mechanism, (b) abnormal CXR, (c) altered mental status, (d) distracting injuries, or (e) clinically suspected thoracic or spinal injury (Chung et al. 2014).

Regardless whether the chest is part of a WBCT examination or the only body region of interest, MDCT imaging of the chest should be performed after application of intravenous contrast medium (CM) (Dreizin and Munera 2012; Linsenmaier et al. 2014). Bolus tracking in the ascending aorta ensures optimal thoracic imaging in an arterial phase. Modern MDCT systems with at least 64 detector rows offer high-resolution (submillimeter isotropic voxels) examination of the entire chest within 1–5 s using high-pitch protocols. The combination of an increased pitch factor and a primary collimation of 2.5 mm is only recommended if 16-row MDCT systems are being used. ECG-synchronization techniques are not required for initial assessment of the thorax, but could be useful for follow-up in selective cases when a motion-free visualization of the heart or aortic root is desired.

4 Injuries of the Chest Wall

4.1 Rib Fractures

Rib fractures are the most common type of injury after blunt chest trauma and occur in about 50 % of the patients (Kaewlai et al. 2008). Different patterns of rib fractures can be detected depending on the mechanism of trauma; a single rib fracture is due to a focal impact and is usually not significant. In opposite, an areal impact causes deformation of the entire rib cage. Then, ribs typically fracture in two places due to the circular configuration of the thoracic cage. In addition to bony fractures, also fractures of the costal cartilage as well as costosternal or costovertebral displacements can occur. A flail chest is defined by more than two consecutive rib fractures in two or more locations resulting in mechanical inability of ventilation and paradoxic breathing (Dehghan et al. 2014). The ribs four through nine are most commonly fractured. Although the first three and lower two ribs are rarely affected, their injuries indicate severe trauma as they are often associated with coexisting injuries of the adjacent organs (e.g., the subclavian artery, brachial plexus, spleen, liver, kidneys) (Kessel et al. 2014). In imaging, a fracture appears as a sharp-edged line and cortical discontinuity with or without displacement of the fragments. In minor trauma (Table 1), CXR may usually be sufficient for clinically important decisions (Chung et al.

Table 1 Indicators of minor chest trauma

Parameter
Normal mental status
Normal clinical examination
Normal chest radiograph

Note: If all three parameters are normal, further evaluation by chest CT might not be necessary because of a low probability of significant thoracic injuries. Inclusion or exclusion of CT in this setting should be site- and/or case-specific (Chung et al. 2014)

2014). However, CT is indicated if an underlying visceral injury is suspected. Please note that rib fractures are rare findings in children due to high plasticity and, therefore, indicate a significant trauma frequently associated with extrathoracic injuries (Kessel et al. 2014).

Standard MPRs help to identify rib fractures in coronal and sagittal views, sometimes complemented by 3D volume rendering technique (VRT) as well (Fig. 1). Even if single rib fractures are of minor clinical importance, in legal medicine, forensic issues, or non-accidental trauma, their complete identification is crucial.

4.2 Fractures of the Scapula, Sternum, and Sternoclavicular Dislocation

These injuries are rare but may indicate high-energy chest trauma (Kaewlai et al. 2008). Typical trauma mechanisms and associated injuries are summarized in Table 2. On the one hand, their occurrence should raise suspicion for serious thoracic injuries (Fig. 1). On the other hand, they are prone to be overlooked because of severe, coexisting injuries ("distracting injuries"). In contrast to CXR, MDCT with MPR and 3D visualization has the highest diagnostic accuracy (Fig. 2) (Kim et al. 2012).

4.3 Spinal Fractures

Spinal injuries are frequently detected in trauma patients. Nearly 50 % of all vertebral injuries affect the thoracolumbar spine with an incidence of about 4–5 %. Approximately 15 % of the patients have fractures at multiple levels. Nineteen to 50 % of these patients sustain additional neurologic symptoms due to spinal cord injury (Sixta et al. 2012). As spinal cord injuries and their treatment have a major impact on a patient's life and on the healthcare system, all chest trauma patients have to be evaluated for possible spinal fractures. Ideally, the spine can be assessed within minutes after the trauma patient's admission into the emergency department. The accurate, clinical assessment of trauma patients, however, is frequently hampered by concomitant circumstances (uncooperative, obtunded, or unstable patients). Therefore, optimal imaging of the spine must be rapid and deliver reliable results (Wintermark et al. 2003). The superiority of MDCT over CXR for the identification of thoracolumbar spine fractures has been demonstrated in several studies (Fig. 3) (Wintermark et al. 2003; Antevil et al. 2006; Brown et al. 2005). MDCT using MPR and 3D visualization methods reveals up to 50 % more thoracolumbar spine fractures despite normal CXR (Wintermark et al. 2003). Consequently, MDCT is considered the imaging method of choice for evaluating patients with highly suspected spine trauma (Daffner and Hackney 2007). CXR is widely replaced and reserved for evaluating patients in whom suspicion of injury is low (Daffner and Hackney 2007). In major or multiple traumas, reformatted images from WBCT data set can be used for safe assessment of the spinal column (Berry et al. 2005). In addition to the reliable detection of spinal injuries, MDCT plays a major role for guiding clinical management. If MDCT shows no abnormalities, thoracolumbar spine fractures are considered as ruled out. In case of injury, MDCT contributes substantially to the assessment of the mechanical stability which determines further treatment. In this context, injury morphology is one key aspect besides the integrity of the posterior ligamentous complex and the neurologic status of the patient (Khurana et al. 2013). The Thoracolumbar Injury Classification and Severity Score (TLICS) was developed by the Spine Trauma Study Group and comprises all three components (Vaccaro et al. 2005). The TLICS is the most recent classification and scoring system of thoracolumbar

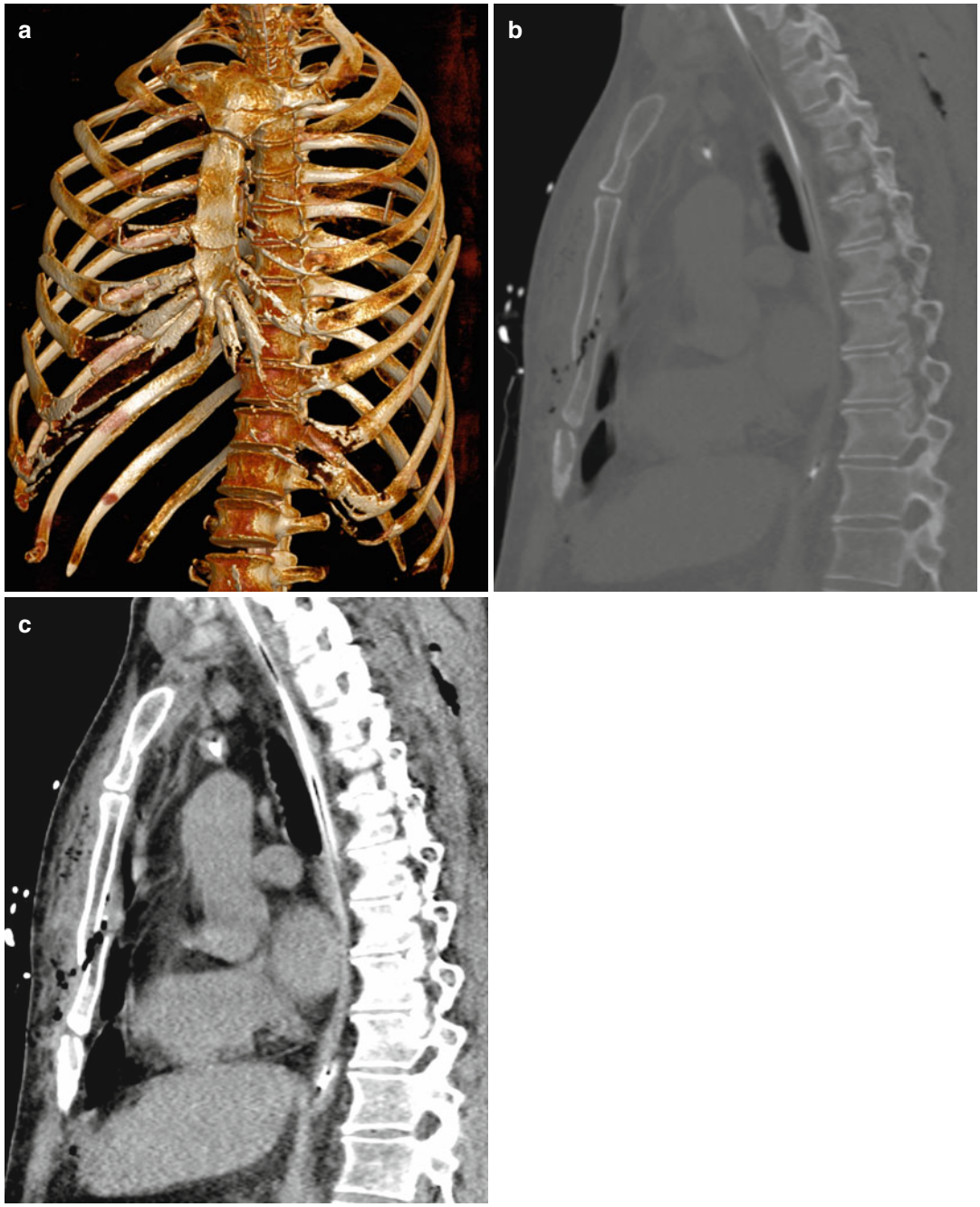

Fig. 1 MDCT of severe chest trauma showing injuries of the chest wall. (**a**) 3D VRT visualizes a flail chest with multiple bilateral rib fractures and fractures of the manubrium and body of the sternum. (**b**) The sternal fractures are also well depicted on sagittal MPR views in a bone window. (**c**) A peristernal hematoma and small free-air collections are identified in a soft-tissue window

spine injuries in order to help guiding decisions about surgical management. Details of the injury morphology are summarized in Table 3. Besides soft kernel CT reconstruction and MPR, an additional high-resolution reconstruction using thin-slice axial reformats (1.0–2.5 mm) is even improving the sensitivity of MDCT in detecting subtle osseous injuries.

Table 2 Rare chest wall injuries

Description	Typical trauma mechanism	Associated injuries
Scapular fracture	MVA, fall from great heights	Pneumo-/hemothorax, pulmonary/spinal injuries
Sternal fracture	MVA ("steering wheel injury")	Retrosternal hematoma (!), aortic/cardiac/spinal injuries
Sternoclavicular dislocation	MVA ("seat belt injury")	Upper rib fractures, vascular/tracheal/esophageal injuries

Note: *MVA* motor vehicle accident

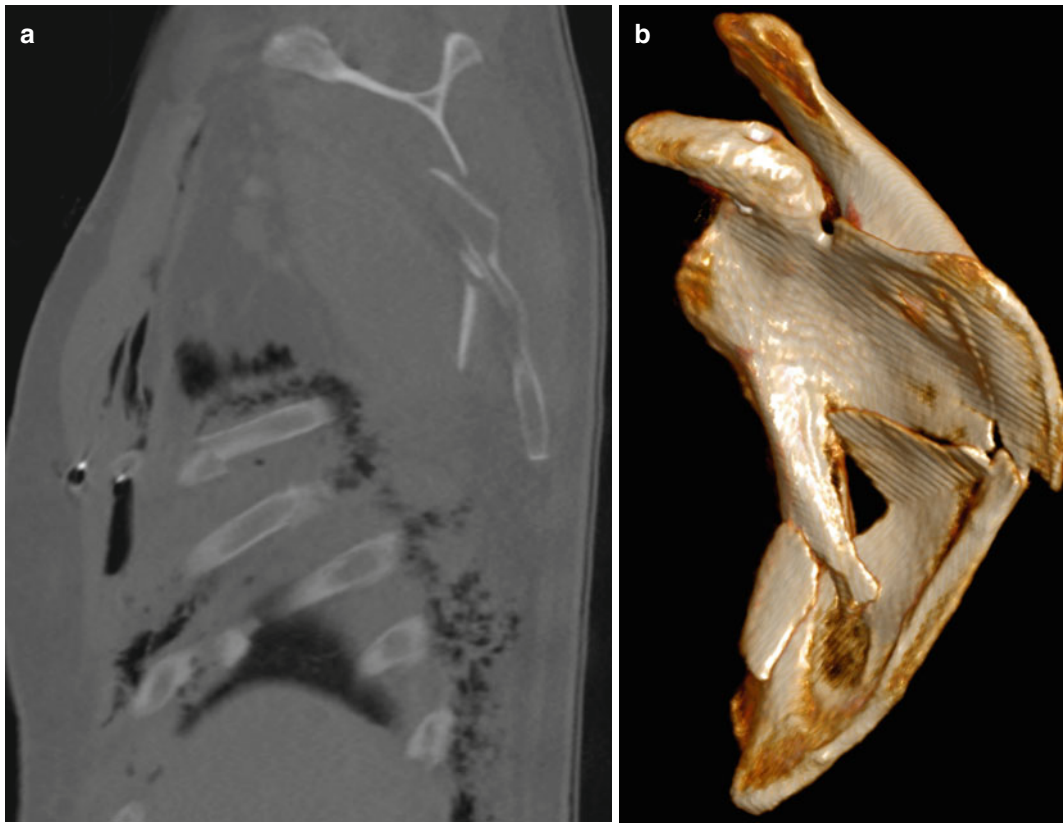

Fig. 2 (**a**) Chest trauma on WBCT: Displaced fracture of the scapula is identified on sagittal views in addition to multiple rib fractures causing extensive subcutaneous emphysema and a pneumothorax (not depicted). The pneumothorax has already been drained by a chest tube. (**b**) 3D VRT calculated from WBCT data visualizes the complex fracture of the scapular body entirely

5 Injuries of the Pleural Space

5.1 Pneumothorax

A pneumothorax is an abnormal air collection in the pleural space due to aeropleural fistulas following blunt or penetrating trauma. It is seen in 15–40 % of all patients with chest trauma (Kaewlai et al. 2008; Miller 2006; Lomoschitz et al. 2003). Bronchopleural fistulas are more common than pleurocutaneous fistulas. Abnormal chest compression can lead to sudden increase of the intra-alveolar pressure resulting in rupture of pulmonary alveoli and visceral pleura. In addition, sharp rib fragments can lacerate the lung or pleura and, therefore, cause a pneumothorax. Pleurocutaneous fistulas are less common and usually caused by penetrating trauma leading to

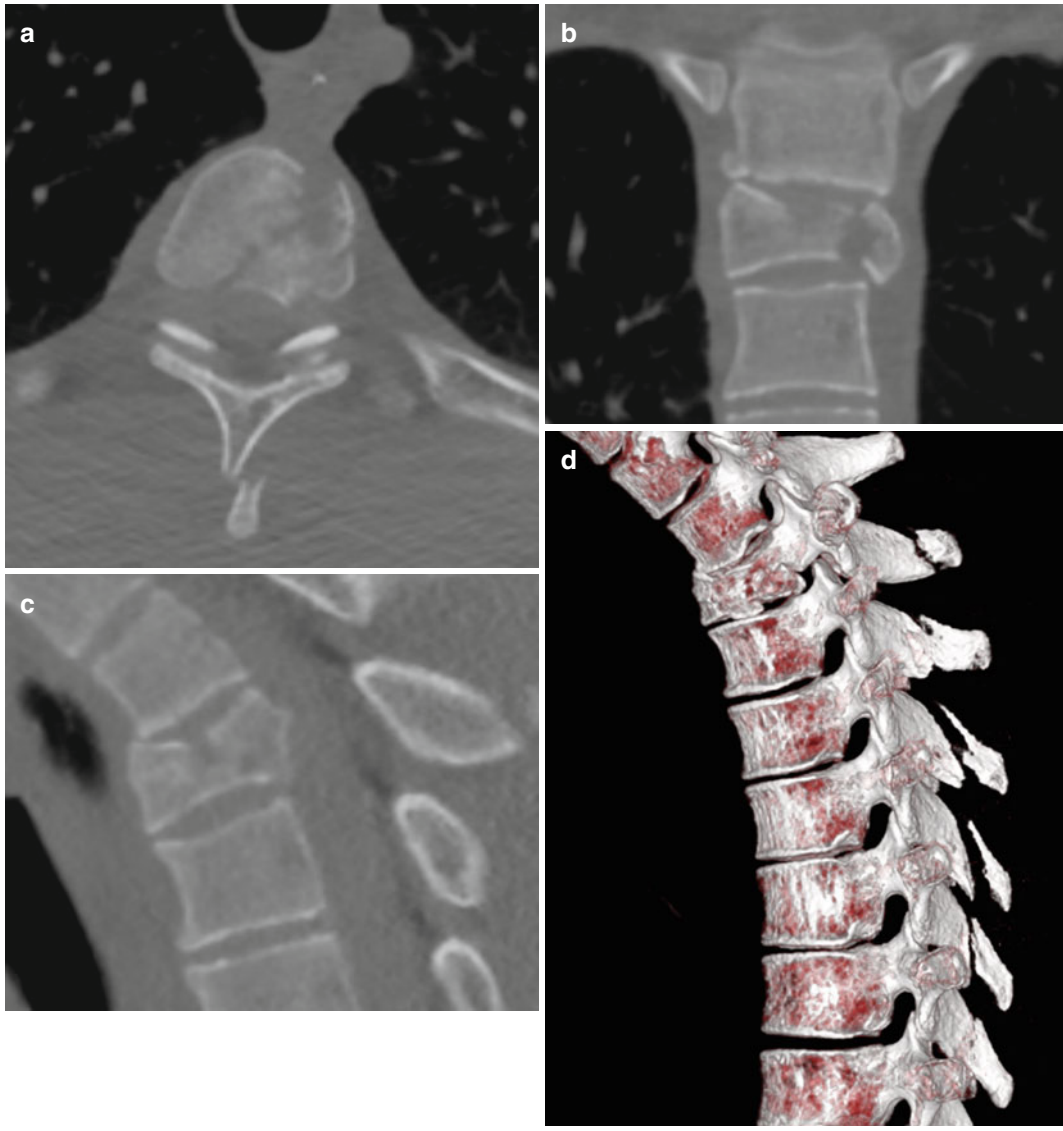

Fig. 3 (**a**–**c**) Thoracic spine trauma on MDCT: Unstable burst fracture of the third thoracic vertebra (T3) with intraspinal protrusion of the posterior vertebral wall demonstrated on axial, sagittal, and coronal views. In addition, coexisting fractures of the spinous process of T3 and the inferior endplate of T2 are shown on the axial (**a**) and coronal (**b**) image, respectively. (**d**) 3D VRT visualizes the T3-vertebral fracture as well as fractures of the spinous processes T3–T8

an air leakage directly through the chest wall (Sharma and Jindal 2008). In most cases, the pleural tear seals because of retraction and atelectasis of the lung. In contrast, a valvular opening mechanism of the injured pleura provokes a tension pneumothorax with an open valve during inspiration and a closed valve during expiration leading to a continuous increase of pressure and mediastinal shift. Although a tension pneumothorax is a clinical diagnosis, CXR and MDCT can visualize the expansive effect toward the contralateral side: The increasing pressure in the pleural space causes a progressive atelectasis of the lung, mediastinal shift, and deviation of the mediastinal vessels leading to a critical hemodynamic impairment. Therefore, a tension pneumo-

Table 3 Injury morphology of spinal fractures

Morphology	Description	Main mechanism	Findings
Compression	Loss of vertebral body height or disruption of the vertebral endplate	Axial loading or lateral flexion	Anterior compression fracture ("wedge") Lateral compression fracture Burst fracture
Translation or rotation	Horizontal displacement or rotation of one vertebral body with respect to another	Torsional or shear forces	Rotation of the spinal processes Uni-/bilateral facet fracture-dislocation Vertebral subluxation
Distraction	Anatomic dissociation along the vertical axis	Hyperextension/flexion	Dissociation of the anterior/posterior ligaments or osseous elements or a combination of both

Note: In addition to morphology, the Thoracolumbar Injury Classification and Severity Score (TLICS) developed by the Spine Trauma Study Group is based on the integrity of the posterior ligamentous complex and the neurologic status of the patient (Khurana et al. 2013)

thorax is an acute life-threatening condition and requires immediate decompression (Nelson et al. 2013).

Concerning imaging, the detectability of a pneumothorax on CXR depends on patient's positioning and the size of the pneumothorax. Particularly, a small air collection on the anterobasal pleural space might be easily overlooked on supine CXR (Sangster et al. 2007). Several studies have demonstrated the superior sensitivity of MDCT in detecting pneumothoraces (Trupka et al. 1997; Ball et al. 2005a, b; Bridges et al. 1993). Whereas the incidence of occult pneumothoraces is between 2 and 15 % in all patients after blunt trauma (Moore et al. 2011), its frequency can dramatically rise up to 76 % in severely injured patients (Ball et al. 2005b, 2009). MDCT offers a reliable detection of a pneumothorax and associated injuries, such as rib fractures or soft-tissue emphysema. The clinical management, however, is not standardized and depends on clinical symptoms and setting (Sharma and Jindal 2008). Even a small pneumothorax might become clinically relevant if the patient is placed on mechanical ventilation.

As many chest tubes nowadays are placed on the scene or during the preclinical treatment, an immediate position control by MDCT after the admission should be intended to allow for repositioning or additional test tube placement if needed. In this context, chest tube placement can immediately be performed in the CT suite, and also interventional CT guidance has been used. Repetitive low-dose scans can control the definitive result by assessing the extent of the remaining pneumothorax as well as sufficient drainage of concomitant pleural effusions.

5.2 Hemothorax

Approximately 50 % of major chest trauma patients present with a pleural effusion – typically a hemothorax (Miller 2006; Shanmuganathan and Mirvis 1999). Blood in the pleural cavity originates from injuries of intercostal, pulmonary, mediastinal, or diaphragmatic vessels. Venous bleeding is usually self-limiting, whereas an arterial source (e.g., intercostal, subclavian, internal mammary arteries) leads to a rapidly progressive hemothorax with the risk of a mediastinal shift and substantial blood loss (Shanmuganathan and Mirvis 1999). The detectability of pleural effusions on CXR depends on patient's positioning and fluid volume, e.g., the minimum detectable volume on supine CXR is about 200–300 mL (Blackmore et al. 1996). In contrast, MDCT has a high sensitivity for the detection of even smaller hemothoraces. In addition, MDCT offers the measurement of Hounsfield units (HU), which can be used to specify the origin of the pleural effusion. Typically, liquid blood has between 30 HU and 45 HU and clotted blood measures between 50 HU and 90 HU, depending on the degree of coagulation

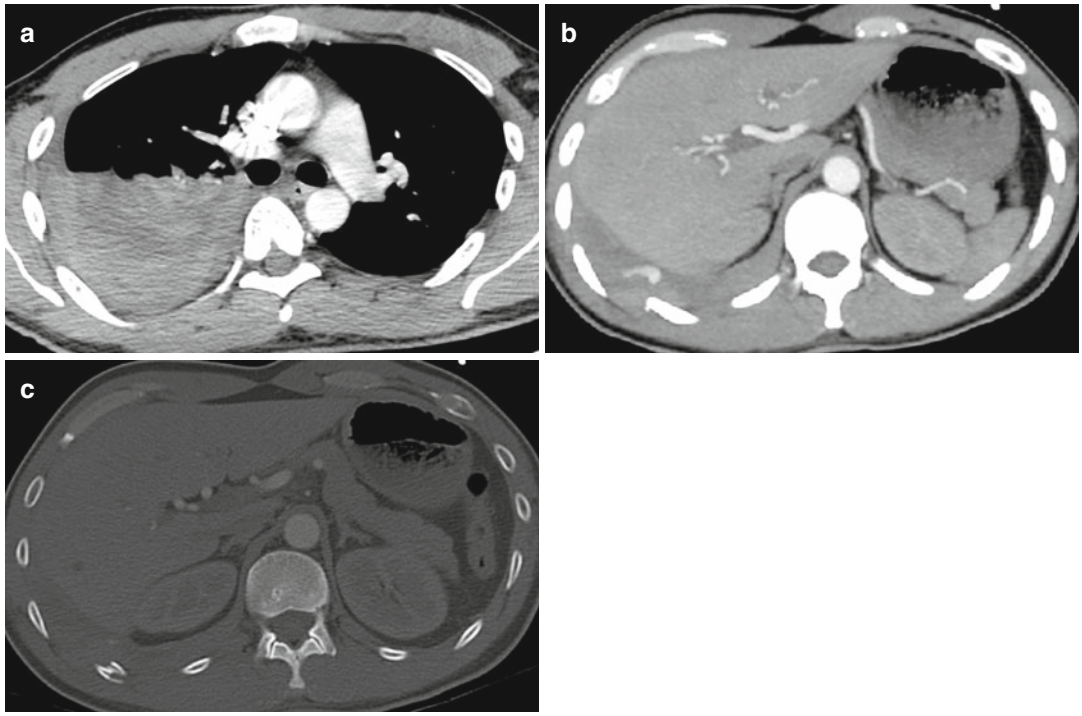

Fig. 4 (**a**) Chest trauma on WBCT: Right-sided hemothorax was suspected due to pleural effusion with a mean HU value of 61 after chest trauma caused by fall from a height of 3 m. (**b**) Active bleeding with CM extravasation due to an injury of an intercostal artery in the right basal thorax was identified as a source of bleeding on arterial 10-mm maximum intensity projections. (**c**) In addition, a displaced fracture of the adjacent rib was found on axial bone window reconstructions

(Oikonomou and Prassopoulos 2011). Thus, a hemothorax can be differentiated from serous effusion with less than 15 HU (Miller 2006; Shanmuganathan and Mirvis 1999). Moreover, CT angiography (CTA) with MPR depicts an active bleeding site as a focus of CM extravasation in arterial phase and progression on delayed images (Fig. 4) (Miller 2006; Uyeda et al. 2010).

6 Injuries of the Lung

6.1 Lung Contusion

Lung contusions due to blunt chest trauma have a prevalence of 17–70 % (Kaewlai et al. 2008). Pathophysiologically, lung contusion consists of interstitial and/or intraalveolar blood and fluid accumulations due to damage to the pulmonary capillaries. It is usually caused by a direct blunt trauma. Shock wave injuries due to explosions or high-energy penetrating trauma are less common. In young patients, pulmonary contusions can exist without injuries of the thoracic wall due to the higher plasticity of the chest (Nakayama et al. 1989). Areas of lung contusion appear as patchy, confluent ground glass opacities with ill-defined borders within the pulmonary parenchyma (Fig. 5). Areas of consolidation indicate more severe injuries. The distribution is non-segmental. However, it is important for emergency radiologists to describe the extent of contusions and the number of involved lung segments. Air bronchograms might be obscured by endoluminal obstruction caused by blood or secretions. Furthermore, a subpleural sparing of 1–2 mm might be seen, in particular in children (Donnelly and Klosterman 1997). Mostly, the location indicates the impact side (coup lesion) adjacent to solid structures, such as the vertebrae, ribs, liver, and heart.

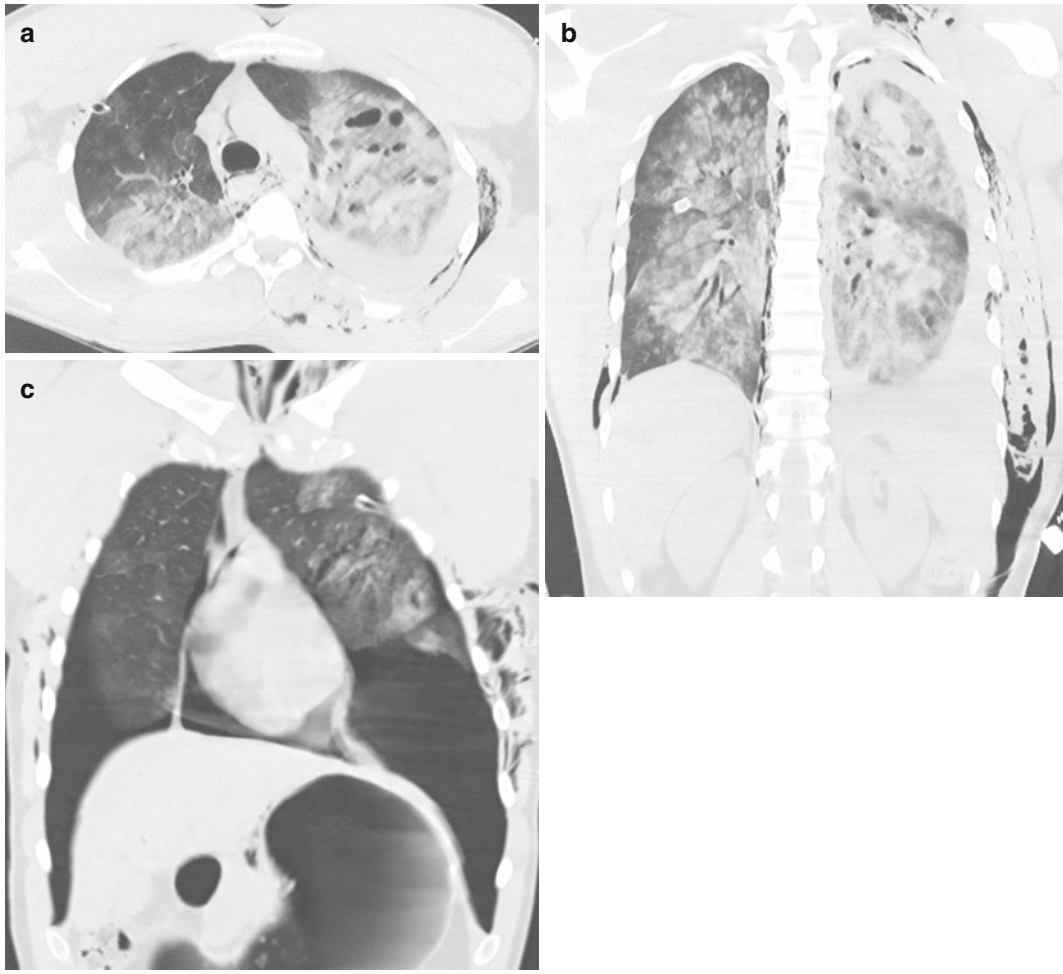

Fig. 5 (**a**–**c**) MDCT showing serious chest trauma with complex injuries of the lung, pleural space, and mediastinum. On both sides, severe pulmonary contusions are shown as patchy, confluent ground glass opacities with ill-defined borders. In addition, all types of lung lacerations (hematocele, pneumocele, hematopneumocele) are depicted as oval- or round-shaped, solid, cystic, or mixed lesions within areas of pulmonary contusions. A right-sided pneumothorax and left-sided pneumohemothorax have already been treated by chest tubes. Free-air collections result in a pneumomediastinum and extensive subcutaneous emphysema that extends along the chest wall into the cervical soft tissue

A contrecoup lesion at the opposite side is less common. MDCT is more sensitive and often reveals lung contusions immediately after trauma, whereas CXR might be normal within the first 6 h (Kaewlai et al. 2008; Schild et al. 1989). Lung contusions have their peak appearance after 6–48 h, begin resolving within 2–4 days, and are usually vanished after 3–14 days (Kaewlai et al. 2008; Wanek and Mayberry 2004). Afterward, persisting airspace opacities suggest complications such as pneumonia due to superinfection, aspiration, or acute respiratory distress syndrome (ARDS). In spite of improvements in treatment and diagnostics, lung contusions remain a critical predictor of the development of pneumonia and ARDS (Miller et al. 2001; Wang et al. 2011; Strumwasser et al. 2011) and are still associated with a high mortality rate of 10–25 % (Miller et al. 2001; Hoff et al. 1994).

6.2 Lung Laceration

Additionally to pulmonary contusions, signs of lung laceration can be found if shear forces caused parenchymal disruption (Wagner et al. 1988). The

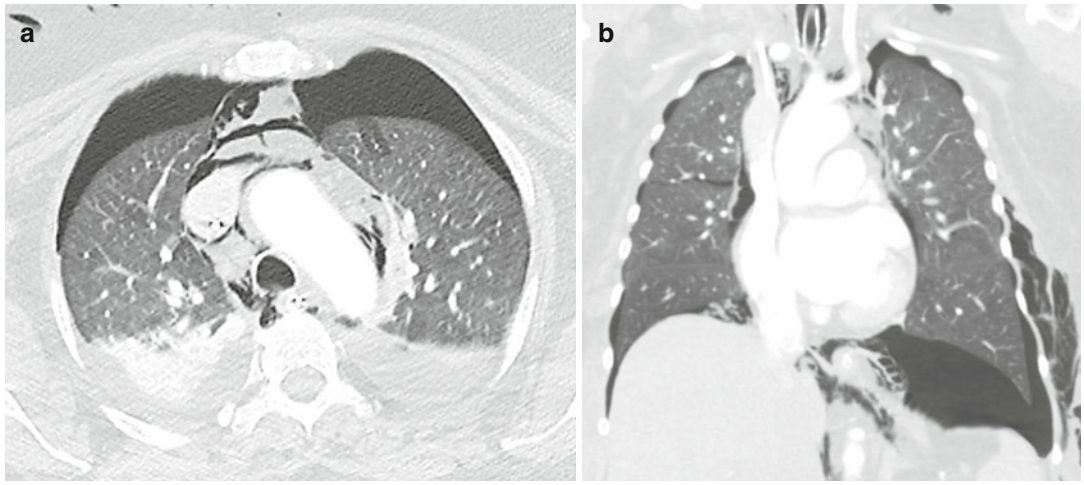

Fig. 6 (**a**) Tracheobronchial injury on WBCT: Tracheal rupture was found as vertically orientated disruption at the right-sided junction of the cartilaginous and membranous portion. (**a**, **b**) This rare type of injury is typically located close to the carina and associated with various pathological free-air collections within the mediastinum (pneumomediastinum) and can be accompanied by a bilateral pneumothorax as well as soft-tissue emphysema. In addition, bilateral hemothoraces and a right-sided atelectasis are displayed in this patient

resulting cavity can be filled with blood (hematocele), air (pneumocele), or both (hematopneumocele) (Fig. 5). A hematocele (or pulmonary hematoma) appears as an oval-shaped, sharply delineated, solid opacification. As a hematocele usually disappears within a few weeks, it can be characterized as a vanishing tumor. A pneumocele is a traumatic lung cyst. It is a unilocular, oval-shaped, well-demarcated air collection. A hematopneumocele shows an air-fluid level. The number and size are variable from a solitary lesion to various lacerations ("Swiss cheese" appearance) (Mirvis 2005). Within the first 2–3 days, a lung laceration might be obscured on CXR by the surrounding pulmonary contusions (Kaewlai et al. 2008). Lung lacerations heal more slowly than contusions and usually dissolve within several months due to resorption.

6.3 Tracheobronchial Injuries

Tracheobronchial tears or ruptures are rare but potentially lethal injuries that indicate severe chest trauma. Thirty percent to 80 % of all patients die prior to hospital admission due to respiratory insufficiency or critical coexisting injuries. The estimated incidence among trauma patients with chest and neck injuries is about 0.5–2 %. Severe associated injuries occur in 40–100 % of the patients (Prokakis et al. 2014). Airway trauma may result from directly penetrating trauma, shear forces at specific anchor points, compression between the spine and the sternum, or sudden increased intrathoracic pressure against a closed glottis. The maximum momentum takes effect about 2 cm proximal and distal to the carina (Kiser et al. 2001). Bronchial injuries are more common than lacerations of the trachea. The former are typically parallel to the bronchial cartilage, whereas the latter are typically vertically orientated at the junction of the cartilaginous and membranous portion (Fig. 6) (Chen et al. 2001). With MPR and 3D techniques by MDCT, the tracheal injury can be detected in 71–94 % of the patients (Chen et al. 2001; Scaglione et al. 2006). It typically appears as small air collections which can be found in the target area. Also, overdistension or herniation of an endotracheal balloon might indicate the location of the injury in intubated patients (Rollins and Tocino 1987). A mediastinal emphysema and tension- or therapy-resistant pneumothorax might indicate a tracheobronchial injury (Wan et al. 1997). A complete transection of a bronchus leads to a dropping down of the ipsilateral lung

into the most dependent portion of the thoracic cavity ("fallen lung" sign) (Wintermark et al. 2001). Although direct and indirect signs of tracheobronchial lacerations can be visualized by MDCT, a bronchoscopy is required to confirm the diagnosis (Prokakis et al. 2014).

7 Injuries of the Mediastinum

7.1 Pneumo-/Hemomediastinum

A pneumomediastinum is an abnormal air accumulation within the mediastinal soft tissue. It is most frequently due to ruptured alveoli of the lung with a retrograde expansion along the interstitial tissue into the mediastinum (Macklin effect) (Wintermark et al. 1999). Besides that, the reader has to exclude mediastinal sources, such as ruptures within the tracheobronchial system or the esophagus or descending air along the cervical soft tissue caused by mid-face fractures. Hematoma within the mediastinum is an indicator of severe chest trauma and often due to vascular injuries of the brachiocephalic vessels or the aorta.

7.2 Aortic Injuries

Traumatic acute aortic injury (AAI) represents the most lethal condition among chest injuries and is associated with a high mortality. About 80–90 % of all cases are estimated to die immediately, and only 10–20 % survive the first hour of whom 49–99 % die within the first 24 h (Parmley et al. 1958; Williams et al. 1994). Isolated AAI is rare, and substantial injuries of the head, thorax, and abdomen coexist in the majority of cases (Steenburg et al. 2008). However, it is estimated that 60–80 % of patients will survive if AAI is diagnosed promptly and proper therapy is initiated immediately (Steenburg et al. 2008).

MVA with speeds greater than 50 km/h or substantial car deformity accounts for the majority of causes (76 %), followed by falls from heights and crush injuries (Williams et al. 1994; Richens et al. 2002). The exact mechanism of trauma is complex and presumably a combination of different hypothesized mechanisms: abrupt deceleration causing torsion and shearing forces, hydrostatic forces ("water-hammer effect") through direct compression resulting in a peaking intravascular pressure above 2000 mmHg, and the "osseous pinch" between the sternum and the spine (Steenburg et al. 2008). Typically, a sudden deceleration causes an aortic wall injury at the insertion of the arterial ligament in about 90 % of the cases. Furthermore, an injury of the ascending aorta is usually caused by a direct impact due to fractures of the sternum or the first two ribs. The extent and morphology of AAI range from intimal and/or medial hemorrhage, intramural hematoma, pseudoaneurysms, to contained or free bleedings due to complete transection. Most AAI are transverse tears, can be segmental (55 %) or circumferential (45 %), and may be partial (65 %) or transmural (35 %). Longitudinal, spiral, or irregular lesions are rare (Parmley et al. 1958; Feczko et al. 1992; Ben-Menachem 1993).

Approximately 90 % of blunt traumatic AAI occur on the anteromedial aspect of the aortic isthmus (Feczko et al. 1992; Ben-Menachem 1993; Creasy et al. 1997). Seven to eight percent are located in the aortic root and are often associated with aortic valve, cardiac injury, or a hemopericardium with cardiac tamponade (Symbas et al. 1998; Sun et al. 2013). Nearly 2 % of blunt traumatic injuries affect the descending aorta occur at the level of the diaphragm, of which 10 % are associated simultaneously with diaphragmatic ruptures (Chughtai et al. 2007).

CTA is the imaging modality of choice. Whereas CM extravasation and an intimal flap are direct signs of AAI, periaortic or intramural hematomas can serve as indirect indicators. A transmural rupture of all three layers of the aortic wall leads almost always to on-site death of the patient. However, a sleeve of subadventitial CM accumulation might be found at the isthmus. The surrounding periaortic soft tissue may tamponade the bleeding temporarily. A careful inspection of the diameter of the aortic wall and its integrity is recommended. In any case of unclear findings or motion and pulsation image artifacts, an immedi-

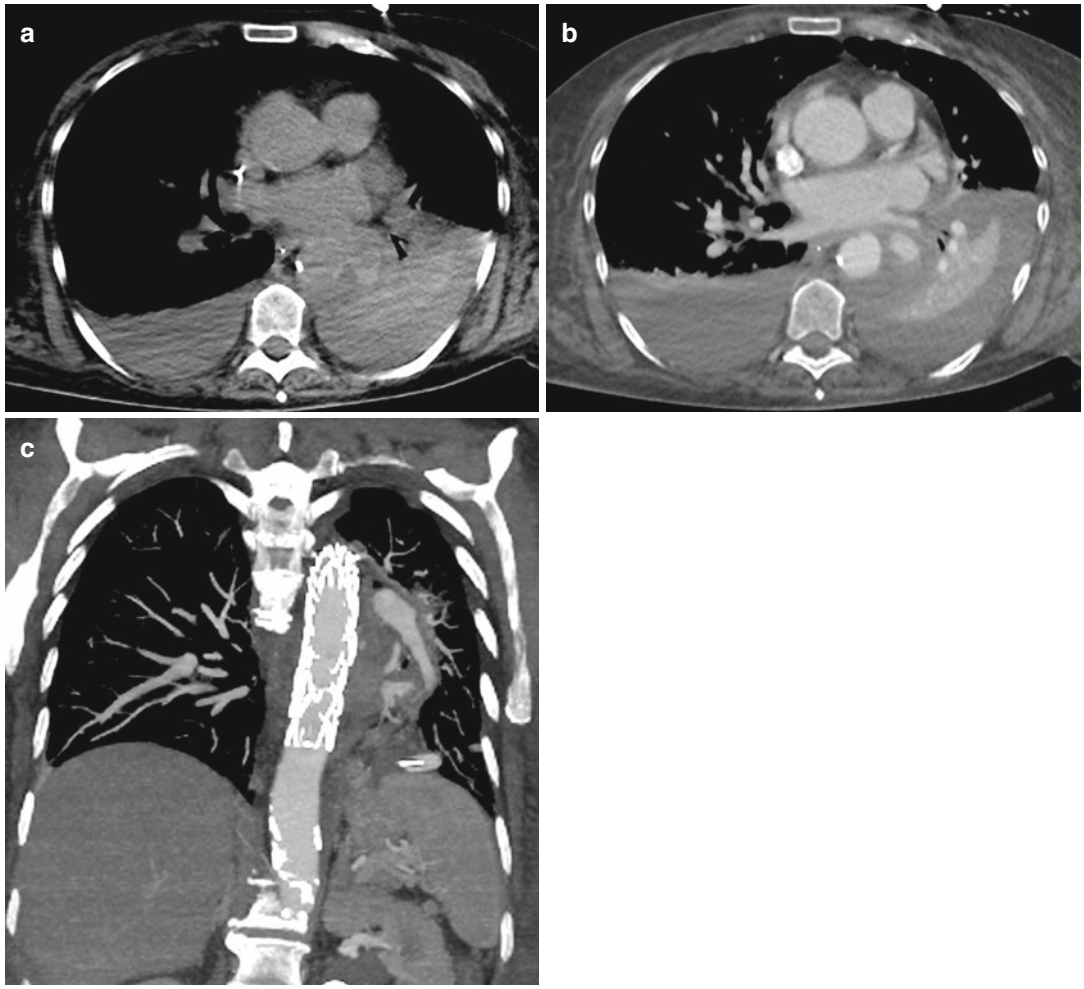

Fig. 7 (**a**) Acute aortic injury (AAI) on MDCT: Rupture of the descending aorta is suspected in non-contrast axial images due to an irregular hyperdense formation (=blood collection) within abnormal periaortic thickening. (**b**) Arterial CT angiography confirms a partial disruption with contained rupture by illustrating CM extravasation into a periaortic hematoma and bleeding to the left pleural space. Besides the hemomediastinum, a bilateral hemothorax with a left-sided atelectasis is shown. (**c**) MDCT after EVAR: Coronal maximum intensity projection of the follow-up MDCT study after endovascular repair

ate follow-up CT scan is indicated including ECG synchronization, which can significantly improve diagnosis, especially in the ascending aorta. A rapidly growing mediastinal hemorrhage can lead to left apical extrapleural capping. In addition, it may rupture into the left-sided pleural cavity, resulting in a hemothorax. A partial rupture is defined by an intact adventitia. In these cases, the arterial blood pressure or blood from intramural vasa vasorum can form a pseudoaneurysm which appears as a saccular outpouching separated from the aortic lumen by a collar. The false aneurysm is frequently associated with a hemomediastinum (Alkadhi et al. 2004). A partial rupture or tear can be treated by surgical or endovascular repair (EVAR), and early and comprehensive MDCT diagnosis are crucial in these cases (Fig. 7) (Challoumas and Dimitrakakis 2014). Aortic dissections are infrequently found in the setting of blunt thoracic trauma and account for approximately 11–12 % of patients with aortic trauma (Fisher and Hadlock 1981; Perchinsky

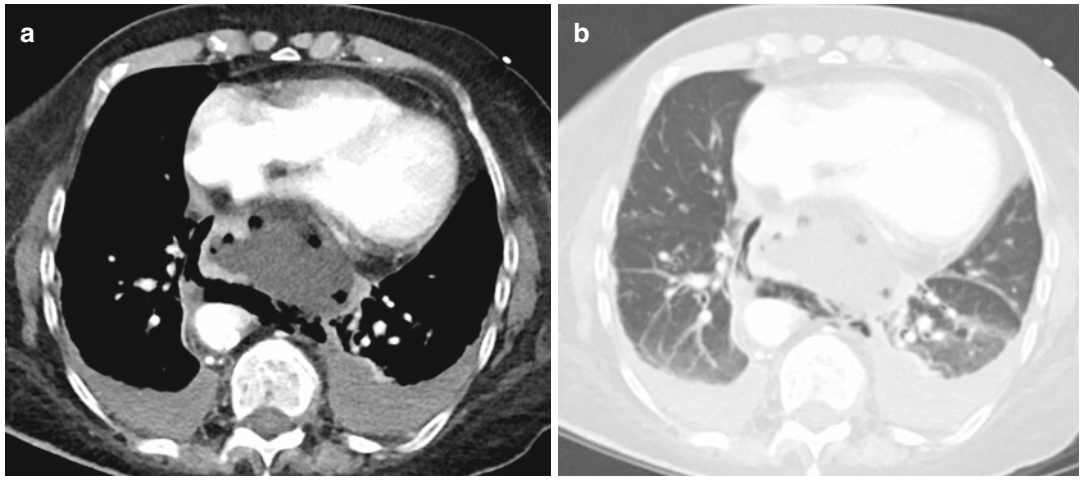

Fig. 8 (**a**, **b**) MDCT of esophageal injury: Extensive esophageal rupture results in discontinuity of the left lateral esophageal wall and extravasation of endoluminal fluid into the mediastinum. Also, a pneumomediastinum due to this type of injury can be identified. Furthermore, bilateral pleural effusions are found

et al. 1998). CTA shows the intimal flap as a key sign of the dissection and has a diagnostic accuracy for the detection of dissections of 100 % (Yoshida et al. 2003). With use of high-resolution MDCT, the occurrence of acute intramural hematoma (IMH) has been increasingly reported. In these cases, a hematoma within the media layer – most likely due to rupture of the vasa vasorum – can be found as circular wall thickening. IMH is typically hyperdense at non-contrast MDCT and hypodense at CTA. However, the use of non-enhanced CT scans in this emergency setting is questionable and controversial (Chao et al. 2009). Patients with IMH are at risk for acute aortic rupture or acute aortic dissection. Injuries of thoracic aortic branches are rare, but potentially fatal. However, branch vessel injury should be carefully excluded in the presence of hemomediastinum without direct signs of AAI (Mirvis 2006).

With the use of MDCT and MPR, the role of conventional angiography for the detection of traumatic thoracic AAI has been diminished. The sensitivity, specificity, and accuracy for detection of blunt traumatic AAI by MDCT have been reported to be 96 %, 99 %, and 99 %, respectively. At MDCT, an unremarkable mediastinum without mediastinal hematoma and normal visualization of the aorta and periaortic fat tissue has a negative predictive value 100 % for AAI (Steenburg and Ravenel 2008; Mirvis et al. 1998; Patel et al. 1998; Gavant 1999; Wintermark et al. 2002). Regarding the detection of IMH, MDCT has also been reported to have a sensitivity and negative predictive value of 100 % (Dyer et al. 1999, 2000).

7.3 Esophageal Injuries

A blunt trauma (e.g., blow to the neck or a burst-type force) leading to esophageal tears or rupture is extremely rare. Most injuries of the esophagus result from penetrating trauma (Kaewlai et al. 2008). Although esophagoscopy is required to prove the diagnosis, MDCT may show indirect findings of perforation (Fig. 8): pneumomediastinum, leakage of intraluminal fluid, or orally administered CM (Young et al. 2008).

7.4 Cardiac Injuries

Injuries of the heart are rare, but are among the most lethal injuries in chest trauma. They typically result from penetrating or high-energy blunt trauma, mainly MVA (Turan et al. 2010). The heterogeneous spectrum of entities comprises myocardial contusion, cardiac chamber rupture, as well as injuries of the valves, pericardial tears, and coronary

injuries (Kulshrestha et al. 1990). The diagnosis of cardiac injuries is substantially based on suggestive clinical, electrocardiographic, and laboratory findings. With the advent of MDCT, however, the visualization of cardiac injury has dramatically improved and facilitates the identification of these rare but potentially lethal injuries even if non-ECG-synchronized MDCT is used (Co et al. 2011).

8 Injuries of the Diaphragm

Tears or ruptures of the diaphragm are rare injuries and indicate severe chest trauma. The prevalence is about 0.16–10 % in blunt or penetrating trauma patients (Panda et al. 2014; Shanmuganathan et al. 2000). A sudden elevation of the intra-abdominal or intrathoracic pressure causes typically a tear at the posterolateral part of the diaphragm. The mortality is ranging between 5.5 and 51 % due to frequently associated injuries or complications (Sliker 2006). As the liver protects the right-sided diaphragm, diaphragmatic injury is frequently found on the left side. In most cases, coexisting thoracic injuries, e.g., fractures of the lower ribs, hemothorax, and lung contusion, can be found. However, there is also a high rate of coexisting abdominal (spleen, liver) or pelvic injuries (Kearney et al. 1989). In 7–66 % of cases, blunt diaphragmatic rupture may be initially missed either because of distracting injuries or the absence of clinical symptoms. The diagnosis is often not made before complications occur (Desir and Ghaye 2012). Regarding CT technique, the diagnostic quality of MPR was mostly insufficient for diagnosis until the early 2000s and the introduction of 16-row MDCT. The diagnostic performance has dramatically improved by the advent of high-resolution MDCT with high-quality MPR (sensitivity, 71–90 %; specificity, 98–100 %) even compared to non-helical CT (sensitivity, 0–66 %; specificity, 76–99 %) (Desir and Ghaye 2012). MDCT findings can be categorized as direct signs of diaphragmatic injury, indirect signs, and uncer-

Table 4 Common MDCT findings indicating diaphragmatic injury

Finding	Sensitivity (%)	Specificity (%)
Direct signs		
Segmental diaphragmatic defect	17–80	90–100
Dangling diaphragm sign	54	98
Absent diaphragm	18–43	91
Indirect signs		
Intrathoracic herniation of viscera	50–95	98–100
Collar sign	16–63	98–100
Hump sign	50–83	n/a
Band sign	33–42	n/a
Dependent viscera sign	54–90	98–100
Sinus cutoff sign	n/a	n/a
Segmental non-visualization of the diaphragm (e.g., abdominal viscera adjacent to thoracic structures) and contiguous injury on either side of the diaphragm (e.g., hemothorax and hemoperitoneum)	20–60[a]	95–100[a]
Uncertain signs		
Thickening of the diaphragm	56–75	95
Diaphragmatic/peridiaphragmatic contrast medium extravasation	0–12	93–98
Hypoenhanced diaphragm	n/a	n/a
Fractured rib	n/a	n/a

Modified from Desir and Ghaye (2012)
Note: *n/a* not available
[a]Diagnostic performance increases when other signs are present, e.g., hemothorax and hemoperitoneum

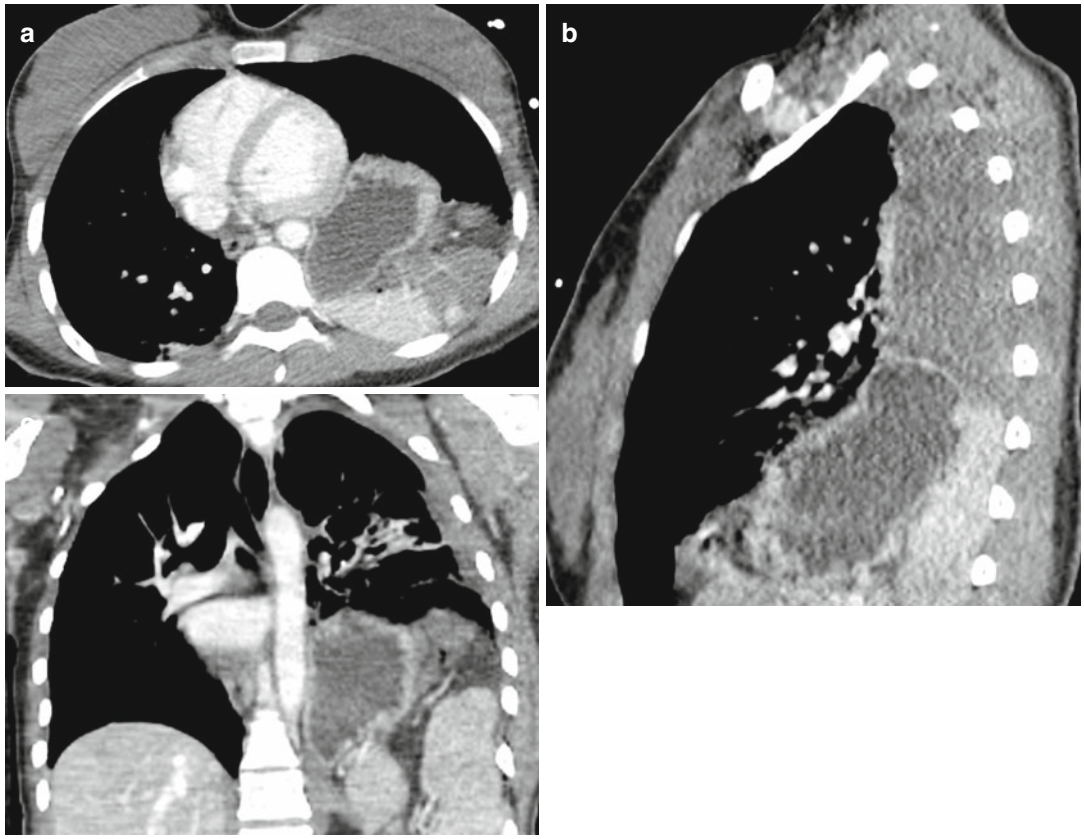

Fig. 9 (**a**–**c**) Chest trauma on WBCT: Left-sided diaphragmatic rupture is diagnosed with an absent diaphragm (direct sign) and intrathoracic herniation of spleen, stomach, and colon (indirect sign) on all three views. The "dependent viscera sign" (indirect sign) is seen on axial and sagittal views. In addition, the spleen shows a large area of decreased attenuation indicating splenic injury. The sagittal view depicts a coexisting pleural effusion

tain signs. Direct signs typically demonstrate the discontinuity of the disrupted diaphragm. Indirect signs can be further subcategorized as findings representing herniation of viscera into the thoracic cavity and findings related to the loss of delimitation between the thorax and abdomen (Desir and Ghaye 2012). An overview of typical MDCT findings and their diagnostic performance is given in Table 4. The most commonly reported signs are the "collar sign," which represents a waist-like constriction of the herniated abdominal organs by the partially ruptured diaphragm, and the "dependent viscera sign," which appears if the abdominal viscera lie against the posterior chest wall obliterating the posterior costophrenic recess (Fig. 9). Incomplete disruptions are even more difficult to diagnose and can easily be missed on initial evaluation (Bergin et al. 2001; Murray et al. 1996).

References

Alkadhi H, Wildermuth S, Desbiolles L et al (2004) Vascular emergencies of the thorax after blunt and iatrogenic trauma: multi-detector row CT and three-dimensional imaging. Radiographics 24(5):1239–1255. doi:10.1148/rg.245035728

Antevil JL, Sise MJ, Sack DI, Kidder B, Hopper A, Brown CV (2006) Spiral computed tomography for the initial evaluation of spine trauma: a new standard of care? J Trauma 61(2):382–387. doi:10.1097/01.ta.0000226154.38852.e6

Ball CG, Kirkpatrick AW, Laupland KB et al (2005a) Factors related to the failure of radiographic recognition of occult posttraumatic pneumothoraces. Am J Surg 189(5):541–546. doi:10.1016/j.amjsurg.2005.01.018; discussion 546

Ball CG, Kirkpatrick AW, Laupland KB et al (2005b) Incidence, risk factors, and outcomes for occult pneumothoraces in victims of major trauma. J Trauma 59(4):917–924; discussion 924–915

Ball CG, Ranson K, Dente CJ et al (2009) Clinical predictors of occult pneumothoraces in severely injured blunt polytrauma patients: a prospective observational study. Injury 40(1):44–47. doi:10.1016/j.injury.2008.07.015

Ben-Menachem Y (1993) Rupture of the thoracic aorta by broadside impacts in road traffic and other collisions: further angiographic observations and preliminary autopsy findings. J Trauma 35(3):363–367

Bergin D, Ennis R, Keogh C, Fenlon HM, Murray JG (2001) The "dependent viscera" sign in CT diagnosis of blunt traumatic diaphragmatic rupture. AJR Am J Roentgenol 177(5):1137–1140. doi:10.2214/ajr.177.5.1771137

Berry GE, Adams S, Harris MB et al (2005) Are plain radiographs of the spine necessary during evaluation after blunt trauma? Accuracy of screening torso computed tomography in thoracic/lumbar spine fracture diagnosis. J Trauma 59(6):1410–1413; discussion 1413

Blackmore CC, Black WC, Dallas RV, Crow HC (1996) Pleural fluid volume estimation: a chest radiograph prediction rule. Acad Radiol 3(2):103–109

Bridges KG, Welch G, Silver M, Schinco MA, Esposito B (1993) CT detection of occult pneumothorax in multiple trauma patients. J Emerg Med 11(2):179–186

Brown CV, Antevil JL, Sise MJ, Sack DI (2005) Spiral computed tomography for the diagnosis of cervical, thoracic, and lumbar spine fractures: its time has come. J Trauma 58(5):890–895; discussion 895–896

Challoumas D, Dimitrakakis G (2014) Advances in the treatment of blunt thoracic aortic injuries. Injury. doi:10.1016/j.injury.2014.10.065

Chao CP, Walker TG, Kalva SP (2009) Natural history and CT appearances of aortic intramural hematoma. Radiographics 29(3):791–804. doi:10.1148/rg.293085122

Chen JD, Shanmuganathan K, Mirvis SE, Killeen KL, Dutton RP (2001) Using CT to diagnose tracheal rupture. AJR Am J Roentgenol 176(5):1273–1280. doi:10.2214/ajr.176.5.1761273

Chughtai TS, Sharkey P, Brenneman F, Rizoli S (2007) Blunt diaphragmatic rupture mandates a search for blunt aortic injury: an update. Ann Thorac Surg 83(3):1234–1235. doi:10.1016/j.athoracsur.2006.09.060

Chung JH, Cox CW, Mohammed TL et al (2014) ACR appropriateness criteria blunt chest trauma. J Am Coll Radiol 11(4):345–351. doi:10.1016/j.jacr.2013.12.019

Co SJ, Yong-Hing CJ, Galea-Soler S et al (2011) Role of imaging in penetrating and blunt traumatic injury to the heart. Radiographics 31(4):E101–E115. doi:10.1148/rg.314095177

Creasy JD, Chiles C, Routh WD, Dyer RB (1997) Overview of traumatic injury of the thoracic aorta. Radiographics 17(1):27–45. doi:10.1148/radiographics.17.1.9017797

Daffner RH, Hackney DB (2007) ACR Appropriateness Criteria on suspected spine trauma. J Am Coll Radiol 4(11):762–775. doi:10.1016/j.jacr.2007.08.006

Dawson P, Lees WR (2001) Multi-slice technology in computed tomography. Clin Radiol 56(4):302–309. doi:10.1053/crad.2000.0651

Dehghan N, de Mestral C, McKee MD, Schemitsch EH, Nathens A (2014) Flail chest injuries: a review of outcomes and treatment practices from the National Trauma Data Bank. J Trauma Acute Care Surg 76(2):462–468. doi:10.1097/ta.0000000000000086

Desir A, Ghaye B (2012) CT of blunt diaphragmatic rupture. Radiographics 32(2):477–498. doi:10.1148/rg.322115082

Donnelly LF, Klosterman LA (1997) Subpleural sparing: a CT finding of lung contusion in children. Radiology 204(2):385–387. doi:10.1148/radiology.204.2. 9240524

Dreizin D, Munera F (2012) Blunt polytrauma: evaluation with 64-section whole-body CT angiography. Radiographics 32(3):609–631. doi:10.1148/rg.323115099

Dyer DS, Moore EE, Mestek MF et al (1999) Can chest CT be used to exclude aortic injury? Radiology 213(1):195–202. doi:10.1148/radiology.213.1.r99oc49195

Dyer DS, Moore EE, Ilke DN et al (2000) Thoracic aortic injury: how predictive is mechanism and is chest computed tomography a reliable screening tool? A prospective study of 1,561 patients. J Trauma 48(4):673–682; discussion 682–673

Exadaktylos AK, Sclabas G, Schmid SW, Schaller B, Zimmermann H (2001) Do we really need routine computed tomographic scanning in the primary evaluation of blunt chest trauma in patients with "normal" chest radiograph? J Trauma 51(6):1173–1176

Feczko JD, Lynch L, Pless JE, Clark MA, McClain J, Hawley DA (1992) An autopsy case review of 142 nonpenetrating (blunt) injuries of the aorta. J Trauma 33(6):846–849

Feliciano DV, Rozycki GS (1999) Advances in the diagnosis and treatment of thoracic trauma. Surg Clin North Am 79(6):1417–1429

Fisher RG, Hadlock F (1981) Laceration of the thoracic aorta and brachiocephalic arteries by blunt trauma. Report of 54 cases and review of the literature. Radiol Clin North Am 19(1):91–110

Gavant ML (1999) Helical CT grading of traumatic aortic injuries. Impact on clinical guidelines for medical and surgical management. Radiol Clin North Am 37(3):553–574, vi

Geyer LL, Koerner M, Wirth S, Mueck FG, Reiser MF, Linsenmaier U (2013) Polytrauma: optimal imaging and evaluation algorithm. Semin Musculoskelet Radiol 17(4):371–379. doi:10.1055/s-0033-1356466

Healy DA, Hegarty A, Feeley I, Clarke-Moloney M, Grace PA, Walsh SR (2014) Systematic review and meta-analysis of routine total body CT compared with selective CT in trauma patients. Emerg Med J 31(2):101–108. doi:10.1136/emermed-2012-201892

Hoff SJ, Shotts SD, Eddy VA, Morris JA Jr (1994) Outcome of isolated pulmonary contusion in blunt trauma patients. Am Surg 60(2):138–142

Huber-Wagner S, Lefering R, Qvick LM et al (2009) Effect of whole-body CT during trauma resuscitation on survival: a retrospective, multicentre study. Lancet 373(9673):1455–1461. doi:10.1016/S0140-6736(09)60232-4

Junewick JJ, Borders HL, Davis AT (2014) Pediatric thoracic spine injuries: a single-institution experience. AJR Am J Roentgenol 203(3):649–655. doi:10.2214/ajr.13.12143

Kaewlai R, Avery LL, Asrani AV, Novelline RA (2008) Multidetector CT of blunt thoracic trauma. Radiographics 28(6):1555–1570. doi:10.1148/rg.286085510

Kanz KG, Paul AO, Lefering R et al (2010) Trauma management incorporating focused assessment with computed tomography in trauma (FACTT) – potential effect on survival. J Trauma Manag Outcomes 4:4. doi:10.1186/1752-2897-4-4

Kearney PA, Rouhana SW, Burney RE (1989) Blunt rupture of the diaphragm: mechanism, diagnosis, and treatment. Ann Emerg Med 18(12):1326–1330

Kessel B, Dagan J, Swaid F et al (2014) Rib fractures: comparison of associated injuries between pediatric and adult population. Am J Surg 208(5):831–834. doi:10.1016/j.amjsurg.2013.10.033

Khurana B, Sheehan SE, Sodickson A, Bono CM, Harris MB (2013) Traumatic thoracolumbar spine injuries: what the spine surgeon wants to know. Radiographics 33(7):2031–2046. doi:10.1148/rg.337135018

Kim EY, Yang HJ, Sung YM, Hwang KH, Kim JH, Kim HS (2012) Sternal fracture in the emergency department: diagnostic value of multidetector CT with sagittal and coronal reconstruction images. Eur J Radiol 81(5):e708–e711. doi:10.1016/j.ejrad.2011.05.029

Kiser AC, O'Brien SM, Detterbeck FC (2001) Blunt tracheobronchial injuries: treatment and outcomes. Ann Thorac Surg 71(6):2059–2065

Kloppel R, Schreiter D, Dietrich J, Josten C, Kahn T (2002) Early clinical management after polytrauma with 1 and 4 slice spiral CT. Radiologe 42(7):541–546

Kulshrestha P, Das B, Iyer KS et al (1990) Cardiac injuries--a clinical and autopsy profile. J Trauma 30(2):203–207

Linsenmaier U, Kanz KG, Rieger J, Rock C, Pfeifer KJ, Reiser M (2002) Structured radiologic diagnosis in polytrauma. Radiologe 42(7):533–540

Linsenmaier U, Geyer LL, Korner M, Reiser M, Wirth S (2014) Importance of multidetector CT imaging in multiple trauma. Radiologe 54(9):861–871. doi:10.1007/s00117-013-2634-y

Lomoschitz FM, Eisenhuber E, Linnau KF, Peloschek P, Schoder M, Bankier AA (2003) Imaging of chest trauma: radiological patterns of injury and diagnostic algorithms. Eur J Radiol 48(1):61–70

Lopez AD, Mathers CD, Ezzati M, Jamison DT, Murray CJ (2006) Global and regional burden of disease and risk factors, 2001: systematic analysis of population health data. Lancet 367(9524):1747–1757. doi:10.1016/S0140-6736(06)68770-9

Mayberry JC (2000) Imaging in thoracic trauma: the trauma surgeon's perspective. J Thorac Imaging 15(2):76–86

Miller LA (2006) Chest wall, lung, and pleural space trauma. Radiol Clin North Am 44(2):213–224. doi:10.1016/j.rcl.2005.10.006, viii

Miller PR, Croce MA, Bee TK et al (2001) ARDS after pulmonary contusion: accurate measurement of contusion volume identifies high-risk patients. J Trauma 51(2):223–228; discussion 229–230

Mirvis SE (2005) Imaging of acute thoracic injury: the advent of MDCT screening. Semin Ultrasound CT MR 26(5):305–331

Mirvis SE (2006) Thoracic vascular injury. Radiol Clin North Am 44(2):181–197. doi:10.1016/j.rcl.2005.10.007, vii

Mirvis SE, Shanmuganathan K, Buell J, Rodriguez A (1998) Use of spiral computed tomography for the assessment of blunt trauma patients with potential aortic injury. J Trauma 45(5):922–930

Moore FO, Goslar PW, Coimbra R et al (2011) Blunt traumatic occult pneumothorax: is observation safe?--results of a prospective, AAST multicenter study. J Trauma 70(5):1019–1023. doi:10.1097/TA.0b013e318213f727; discussion 1023–1015

Murray JG, Caoili E, Gruden JF, Evans SJ, Halvorsen RA Jr, Mackersie RC (1996) Acute rupture of the diaphragm due to blunt trauma: diagnostic sensitivity and specificity of CT. AJR Am J Roentgenol 166(5):1035–1039. doi:10.2214/ajr.166.5.8615237

Nakayama DK, Ramenofsky ML, Rowe MI (1989) Chest injuries in childhood. Ann Surg 210(6):770–775

Nelson D, Porta C, Satterly S et al (2013) Physiology and cardiovascular effect of severe tension pneumothorax in a porcine model. J Surg Res 184(1):450–457. doi:10.1016/j.jss.2013.05.057

Oikonomou A, Prassopoulos P (2011) CT imaging of blunt chest trauma. Insights Imaging 2(3):281–295. doi:10.1007/s13244-011-0072-9

Omert L, Yeaney WW, Protetch J (2001) Efficacy of thoracic computerized tomography in blunt chest trauma. Am Surg 67(7):660–664

Panda A, Kumar A, Gamanagatti S, Patil A, Kumar S, Gupta A (2014) Traumatic diaphragmatic injury: a review of CT signs and the difference between blunt and penetrating injury. Diagn Interv Radiol 20(2):121–128. doi:10.5152/dir.2013.13248

Parmley LF, Mattingly TW, Manion WC, Jahnke EJ Jr (1958) Nonpenetrating traumatic injury of the aorta. Circulation 17(6):1086–1101

Patel NH, Stephens KE Jr, Mirvis SE, Shanmuganathan K, Mann FA (1998) Imaging of acute thoracic aortic injury due to blunt trauma: a review. Radiology 209(2):335–348. doi:10.1148/radiology.209.2.9807557

Perchinsky M, Gin K, Mayo JR (1998) Trauma-associated dissection of the thoracic aorta. J Trauma 45(3):626–629

Philipp MO, Kubin K, Hormann M, Metz VM (2003) Radiological emergency room management with emphasis on multidetector-row CT. Eur J Radiol 48(1):2–4

Prokakis C, Koletsis EN, Dedeilias P, Fligou F, Filos K, Dougenis D (2014) Airway trauma: a review on epidemiology, mechanisms of injury, diagnosis and treatment. J Cardiothorac Surg 9:117. doi:10.1186/1749-8090-9-117

Richens D, Field M, Neale M, Oakley C (2002) The mechanism of injury in blunt traumatic rupture of the aorta. Eur J Cardiothorac Surg 21(2):288–293

Rollins RJ, Tocino I (1987) Early radiographic signs of tracheal rupture. AJR Am J Roentgenol 148(4):695–698. doi:10.2214/ajr.148.4.695

Sangster GP, Gonzalez-Beicos A, Carbo AI et al (2007) Blunt traumatic injuries of the lung parenchyma, pleura, thoracic wall, and intrathoracic airways: multidetector computer tomography imaging findings. Emerg Radiol 14(5):297–310. doi:10.1007/s10140-007-0651-8

Scaglione M, Romano S, Pinto A, Sparano A, Scialpi M, Rotondo A (2006) Acute tracheobronchial injuries: impact of imaging on diagnosis and management implications. Eur J Radiol 59(3):336–343. doi:10.1016/j.ejrad.2006.04.026

Scaglione M, Pinto A, Pedrosa I, Sparano A, Romano L (2008) Multi-detector row computed tomography and blunt chest trauma. Eur J Radiol 65(3):377–388. doi:10.1016/j.ejrad.2007.09.023

Schild HH, Strunk H, Weber W et al (1989) Pulmonary contusion: CT vs plain radiograms. J Comput Assist Tomogr 13(3):417–420

Shanmuganathan K, Matsumoto J (2006) Imaging of penetrating chest trauma. Radiol Clin North Am 44(2):225–238. doi:10.1016/j.rcl.2005.10.002, viii

Shanmuganathan K, Mirvis SE (1999) Imaging diagnosis of nonaortic thoracic injury. Radiol Clin North Am 37(3):533–551, vi

Shanmuganathan K, Killeen K, Mirvis SE, White CS (2000) Imaging of diaphragmatic injuries. J Thorac Imaging 15(2):104–111

Sharma A, Jindal P (2008) Principles of diagnosis and management of traumatic pneumothorax. J Emerg Trauma Shock 1(1):34–41. doi:10.4103/0974-2700.41789

Sixta S, Moore FO, Ditillo MF et al (2012) Screening for thoracolumbar spinal injuries in blunt trauma: an Eastern Association for the Surgery of Trauma practice management guideline. J Trauma Acute Care Surg 73(5 Suppl 4):S326–S332. doi:10.1097/TA.0b013e31827559b8

Sliker CW (2006) Imaging of diaphragm injuries. Radiol Clin North Am 44(2):199–211. doi:10.1016/j.rcl.2005.10.003, vii

Steenburg SD, Ravenel JG (2008) Acute traumatic thoracic aortic injuries: experience with 64-MDCT. AJR Am J Roentgenol 191(5):1564–1569. doi:10.2214/AJR.07.3349

Steenburg SD, Ravenel JG, Ikonomidis JS, Schonholz C, Reeves S (2008) Acute traumatic aortic injury: imaging evaluation and management. Radiology 248(3):748–762. doi:10.1148/radiol.2483071416

Strumwasser A, Chu E, Yeung L, Miraflor E, Sadjadi J, Victorino GP (2011) A novel CT volume index score correlates with outcomes in polytrauma patients with pulmonary contusion. J Surg Res 170(2):280–285. doi:10.1016/j.jss.2011.03.022

Sun X, Hong J, Lowery R et al (2013) Ascending aortic injuries following blunt trauma. J Card Surg 28(6):749–755. doi:10.1111/jocs.12237

Symbas PJ, Horsley WS, Symbas PN (1998) Rupture of the ascending aorta caused by blunt trauma. Ann Thorac Surg 66(1):113–117

Traub M, Stevenson M, McEvoy S et al (2007) The use of chest computed tomography versus chest X-ray in patients with major blunt trauma. Injury 38(1):43–47. doi:10.1016/j.injury.2006.07.006

Trupka A, Waydhas C, Hallfeldt KK, Nast-Kolb D, Pfeifer KJ, Schweiberer L (1997) Value of thoracic computed tomography in the first assessment of severely injured patients with blunt chest trauma: results of a prospective study. J Trauma 43(3):405–411; discussion 411–402

Turan AA, Karayel FA, Akyildiz E et al (2010) Cardiac injuries caused by blunt trauma: an autopsy based assessment of the injury pattern. J Forensic Sci 55(1):82–84. doi:10.1111/j.1556-4029.2009.01207.x

Uyeda JW, Anderson SW, Sakai O, Soto JA (2010) CT angiography in trauma. Radiol Clin North Am 48(2):423–438. doi:10.1016/j.rcl.2010.02.003, ix–x

Vaccaro AR, Lehman RA Jr, Hurlbert RJ et al (2005) A new classification of thoracolumbar injuries: the importance of injury morphology, the integrity of the posterior ligamentous complex, and neurologic status. Spine 30(20):2325–2333

Van Vugt R, Keus F, Kool D, Deunk J, Edwards M (2013) Selective computed tomography (CT) versus routine thoracoabdominal CT for high-energy blunt-trauma patients. Cochrane Database Syst Rev (12):CD009743. doi:10.1002/14651858.CD009743.pub2

Wagner RB, Crawford WO Jr, Schimpf PP (1988) Classification of parenchymal injuries of the lung. Radiology 167(1):77–82. doi:10.1148/radiology.167.1.3347751

Wan YL, Tsai KT, Yeow KM, Tan CF, Wong HF (1997) CT findings of bronchial transection. Am J Emerg Med 15(2):176–177

Wanek S, Mayberry JC (2004) Blunt thoracic trauma: flail chest, pulmonary contusion, and blast injury. Crit Care Clin 20(1):71–81

Wang S, Ruan Z, Zhang J, Jin W (2011) The value of pulmonary contusion volume measurement with three-dimensional computed tomography in predicting acute respiratory distress syndrome development. Ann Thorac Surg 92(6):1977–1983. doi:10.1016/j.athoracsur.2011.05.020

Westaby S, Brayley N (1990) ABC of major trauma. Thoracic trauma--I. BMJ 300(6740):1639–1643

Williams JS, Graff JA, Uku JM, Steinig JP (1994) Aortic injury in vehicular trauma. Ann Thorac Surg 57(3):726–730

Wintermark M, Wicky S, Schnyder P, Capasso P (1999) Blunt traumatic pneumomediastinum: using CT to reveal the Macklin effect. AJR Am J Roentgenol 172(1):129–130. doi:10.2214/ajr.172.1.9888752

Wintermark M, Schnyder P, Wicky S (2001) Blunt traumatic rupture of a mainstem bronchus: spiral CT demonstration of the "fallen lung" sign. Eur Radiol 11(3):409–411. doi:10.1007/s003300000581

Wintermark M, Wicky S, Schnyder P (2002) Imaging of acute traumatic injuries of the thoracic aorta. Eur Radiol 12(2):431–442. doi:10.1007/s003300100971

Wintermark M, Mouhsine E, Theumann N et al (2003) Thoracolumbar spine fractures in patients who have sustained severe trauma: depiction with multi-detector row CT. Radiology 227(3):681–689. doi:10.1148/radiol.2273020592

Yoshida S, Akiba H, Tamakawa M et al (2003) Thoracic involvement of type A aortic dissection and intramural hematoma: diagnostic accuracy--comparison of emergency helical CT and surgical findings. Radiology 228(2):430–435. doi:10.1148/radiol.2282012162

Young CA, Menias CO, Bhalla S, Prasad SR (2008) CT features of esophageal emergencies. Radiographics 28(6):1541–1553. doi:10.1148/rg.286085520

CT-Guided Intervention in the Thorax

Stephen B. Solomon and Carole A. Ridge

Abstract

Percutaneous intervention in the thorax has been performed using radiologic guidance since 1966 when Dahlgren and colleagues described fluoroscopic needle biopsy in the lung (Dahlgren Scand J Respir Dis 47(3):187–194, 1966). With the advent of CT, percutaneous access to smaller lesions in more challenging locations became possible (vanSonnenberg et al. Radiology 167(2):457–461, 1988). CT allows for determination of an optimal cutaneous entry point in such a way as to avoid transgression of sensitive structures with greater accuracy and control than conventional fluoroscopy (Ghaye and Dondelinger Eur Respir J 17(3):507–528, 2001). CT-guided thoracic intervention has since grown to comprise pleural and mediastinal drainage, thermal ablation, mediastinal biopsy and drainage, and tumor localization to enable radiation therapy and surgical resection. This chapter describes the pre-procedure planning, techniques, outcomes, and complications of contemporary CT-guided thoracic intervention.

1 Introduction

Percutaneous intervention in the thorax has been performed using radiologic guidance since 1966 when Dahlgren and colleagues described fluoroscopic needle biopsy in the lung (Dahlgren 1966). With the advent of CT, percutaneous access to smaller lesions in more challenging locations became possible (vanSonnenberg et al. 1988). CT allows for determination of an optimal cutaneous entry point in such a way as to avoid transgression of sensitive structures with greater accuracy and control than conventional fluoroscopy (Ghaye and Dondelinger 2001). CT-guided thoracic intervention has since grown to comprise pleural and mediastinal drainage, thermal ablation, mediastinal biopsy and drainage, and tumor localization to enable radiation therapy and surgical resection. This chapter describes the pre-procedure plan-

S.B. Solomon (✉)
Department of Radiology, Memorial Sloan Kettering Cancer Center, 1275 York Avenue, New York, NY 10065, USA
e-mail: solomons@mskcc.org

C.A. Ridge
Department of Radiology, Mater Misericordiae University Hospital, Eccles Street, Dublin, Ireland
e-mail: cridge@mater.ie

U.J. Schoepf, F.G. Meinel (eds.), *Multidetector-Row CT of the Thorax*, Medical Radiology,
DOI 10.1007/978-3-319-30355-0_26

ning, techniques, outcomes, and complications of contemporary CT-guided thoracic intervention.

2 Patient Preparation

A clinical history including the indication for the procedure and current medications is needed prior to procedure scheduling, ideally in an outpatient clinic. Temporary discontinuation of anticoagulants such as Coumadin, heparin, and aspirin may be necessary according to hospital protocol (Birchard 2011). Recent platelet count, prothrombin time, and partial thromboplastin time with international normalization ratio are routinely obtained within 30 days of the procedure in our institutions. If conscious sedation is required, the patient should fast 6–8 h prior to the procedure, and an intravenous cannula should be inserted. Prior imaging should be reviewed to plan the appropriate patient position, skin entry site, and length of biopsy needle.

3 Image Acquisition

Safe and consistent image acquisition techniques are central to every CT-guided procedure. The key aim of image acquisition is to achieve (1) adequate image quality, (2) as low a radiation dose as possible both patient and operator protection, (3) accurate device placement, and (4) complication monitoring.

Diagnostic image quality in the thorax is enhanced by the inherent contrast between adjacent structures of varying density, e.g., air-filled lung and lung nodules or a mediastinal mass and adjacent mediastinal fat. Limitations to image quality include motion artifact, streak artifact from the arms, monitoring equipment or the biopsy device, and image noise due to low dose imaging parameters.

4 Patient Motion and Positioning

Motion artifact can be lessened by comfortable pre-procedure patient positioning and immobilization if necessary, conscious sedation if needed, and reproducible breathing instructions. The arms can be placed above the head to minimize streak artifact, if patient mobility allows. At the time of patient positioning, the space between the planned point of skin entry and the gantry should be wide enough to allow ingress of the intended procedure device without contacting the gantry. Patient position is determined by multiple factors; patient comfort, patient compliance, and target lesion location are important contributing factors to this decision. While in our experience, supine positioning appears to be most reproducible in terms of patient comfort, there are authors who advocate prone positioning for all biopsy procedures (Yankelevitz et al. 2000). The stated advantages to prone positioning include (i) decreased respiratory motion, (ii) reducing pneumothorax by placing the patient biopsy-side-down (i.e., supine) postprocedure (O'Neill et al. 2012), and (iii) performing the procedure out of the patient's field of view, so as to reduce anxiety (Yankelevitz et al. 2000). The reasoning for this approach is sound, particularly because the supine position is better tolerated by patients. However, other factors may override selection of a prone position. For example, if a posterior approach required transgression of the major fissure or a large bulla, a supine position may be more desirable in order to minimize the risk of pneumothorax. Furthermore, if a patient has an advanced airway, e.g., tracheostomy, the supine position may better enable the radiology nurse to aspirate secretions during the procedure.

If used, conscious sedation should be administered prior to performing the planning CT, as the target position and the depth of respiration may change as a result of altered patient consciousness. Pre-procedure and intraprocedural image acquisition and needle manipulation should be performed during the same phase of respiration, to ensure accurate needle placement. One such approach consists of patient coaching prior to the biopsy to perform suspended shallow respiration, when prompted. Needle manipulation is then either performed during shallow-held respiration or, if the patient is unable to obey commands, midway through patient exhalation. In our experience, shallow-held respiration and needle manipulation midway through patient exhalation

allow for reproducible and accurate device positioning without excessive reliance on patient compliance with instructions while sedated.

5 Radiation Dose

Opportunities for radiation dose reduction include limiting the imaged range of the pre-, intra- and post-procedure CT images, using a low milliamperage throughout the procedure and computer-based assistance in needle positioning (Chintapalli et al. 2012).

5.1 Pre-procedure Imaging

Prior imaging should be reviewed and will assist in procedure planning. A contrast-enhanced study is recommended prior to biopsy, to exclude a vascular lesion and to plan a safe biopsy path.

For the pre-procedure scan, the longitudinal scan length should be tailored to the region of interest as an excessive image volume can contribute unnecessarily to radiation dose (Chintapalli et al. 2012). Ideally, the localization grid should be applied prior to the pre-procedure CT, thus requiring only one scan prior to biopsy. The milliampere (mA) should be lower than that used for diagnostic CT scans. A low-mA setting of 30–100 mAs is suggested and can be adjusted according to patient size (Chintapalli et al. 2012). The absorbed dose also decreases linearly as photon fluence decreases (McNitt-Gray 2002). If the "auto mA" setting is used, it may increase the patient dose in order to achieve diagnostic quality images; therefore manually decreasing this setting may reduce patient dose and maintain adequate image quality (Sarti et al. 2012). Additionally, the highest pitch available should be selected to avoid unnecessarily high radiation dose, to which pitch is inversely related. Absorbed patient dose markedly decreases as beam energy decreases (McNitt-Gray 2002). Lower beam energy increases noise, but as diagnostic images have usually been acquired prior to biopsy, these images may be sufficient for procedure planning (McNitt-Gray 2002). Therefore, a kVp of 100 could be considered, if patient size permits.

5.2 Intraprocedure Imaging

Intermittent CT fluoroscopy using a small range, low mA, and 120 kVp (Chintapalli et al. 2012) is advantageous as it can almost halve procedure time (Gianfelice et al. 2000). Continuous use of fluoroscopy can result in twice the fluoroscopy time compared to intermittent fluoroscopy. The latter approach, whereby the operator intermittently steps on the fluoroscopy pedal, enabling a "quick check" of device position is therefore recommended, if CT fluoroscopy is used (Silverman et al. 1999).

If the biopsy needle approach is not in the axial plane, newer generation CT scanners can be used to tilt the gantry to follow the off-axis biopsy plane. Angling the gantry parallel to the needle path provides better guidance toward the target and decreases CT fluoroscopy time (Sarti et al. 2012). The required gantry angulation can be calculated by reconstructing the planning CT in the sagittal plane. Angulation of up to 30° is possible (Sarti et al. 2012).

Early data analyzing robotic devices to assist CT-guided procedures confirm their feasibility (Anzidei et al. 2015). Such a device consists of a machine with a robotic arm docked at the CT table. The operator can plan a biopsy or ablation procedure using inbuilt navigational software by selecting the intended device type and length, the target position, and skin entry site of the pre-procedure CT. The system software subsequently instructs the operator to move the CT table to a prescribed z-axis location and then prescribes the trajectory to the robotic arm (Koethe et al. 2014). An initial single operator comparative study of lung biopsies using either robot assistance or conventional CT-guided biopsy describes similar accuracy and reports a 40 % reduction in dose length product and a 36 % reduction in procedure time using robotic assistance.

Alternatives to CT fluoroscopy include intermittent conventional CT guidance and ultrasound guidance for the sampling of pleural lesions (Sarti et al. 2012). Both options minimize patient and operator dose. In fact, compared to CT fluoroscopy-guided biopsy (using either intermittent or continuous fluoroscopy), lung biopsy using conventional

CT biopsy mode results in a tenfold lower CT dose index (CTDI) levels with similar accuracy (Prosch et al. 2012). Ultrasound can be considered for peripheral or pleural lesions, if operator experience allows. One nonrandomized comparison study describes similar accuracy compared to CT-guided biopsy of peripheral or pleural lesions (Sconfienza et al. 2013).

5.3 Postprocedure Imaging

Postprocedure imaging should be acquired using similar principles. The CT range may be increased to assess for complications outside of the range of intraprocedural imaging such as pneumothorax. For procedures that involve transpleural passage, erect chest radiography is employed after the patient has left the procedure room to assess for delayed pneumothorax.

5.4 Radiation Dose to the Operator

CT-guided intervention leads to operator radiation exposure. CT fluoroscopy reduces procedure time but increases patient and operator dose. Operator hand radiation dose derived from a CT fluoroscopy phantom study is reported to range from 3 to 690 mcGy for 20 s of fluoroscopy time or a dose rate range of 0.16–39.5 mcGy/s using a tube voltage of 120 kVp, tube current of 50 mAs, and a tube rotation time of 0.5 s (Stoeckelhuber et al. 2005). Available dose reduction methods including needle holders (available in varying lengths), thin latex radiation protection gloves, and lead drapes under and on top of the patient (Stoeckelhuber et al. 2005), when used in combination, achieve a dose reduction to the operator of 99.6%, with lead drapes contributing the greatest to dose reduction. (18)F-fluorodeoxyglucose (FDG) positron emission tomography/computed tomography (PET-CT) guided procedures may confer a greater radiation dose to the operator due to the additional use of FDG to guide the procedure. A small study analyzing this effect concluded that personnel dose is not substantially altered by the use of PET-CT guidance, resulting in a median operator effective dose of 0.015 mSv when conventional CT was used and 0.06 mSv when real-time imaging guidance (CT fluoroscopy or ultrasound) was employed (Ryan et al. 2013).

6 Transthoracic Needle Biopsy

Transthoracic needle biopsy involves the insertion of a biopsy device into a lung, pleural, or mediastinal lesion for the purpose of a histologic diagnosis if malignancy is suspected or for microbiologic analysis or analysis of a genetic mutation that may guide therapy. Contraindications to transthoracic needle biopsy are relative and include uncorrected coagulopathy, deep lesions in patients with pulmonary hypertension, severe emphysema, and a large bulla along the biopsy path (Birchard 2011).

6.1 Technique

While many techniques exist and are effective, the standard technique in our institutions is described below.

Breathing instructions and patient position should be consistent and reproducible for each stage of the procedure. After acquisition of the pre-procedure scan, a safe percutaneous access point is marked prior to sterile skin preparation. The ideal access point allows (i) the avoidance of large vascular or osseous structures (e.g., ribs or scapula) (ii) in a plane that can be easily visualized on intraprocedural CT (ideally on one axial section) and (iii) minimization of pneumothorax risk. To avoid pneumothorax, the needle trajectory should avoid large bullae or fissures. Some operators prefer to access small subpleural lesions by passing the needle through a cuff of normal lung, as a direct approach can lead to inadequate anchoring of the guide needle and pneumothorax as a result of multiple pleural passes. Conversely, large subpleural lesions are

best approached directly without the traversal of aerated lung parenchyma.

Approximately 10 ml of 1 % lidocaine is injected into the subcutaneous fat and at the pleura for local anesthesia. A small skin incision is made with a scalpel. If used, a 17- or 19-gauge guide needle is placed at the chosen access point in the skin and secured in position with sterile towels or gauze; needle position is checked with conventional CT in biopsy mode prior to pleural puncture. Once accurate needle position has been confirmed, the guide needle is advanced across the pleura once during shallow exhalation. Guide needle position is checked using conventional CT. If minor needle tip deviation is observed, needle position can be corrected by applying torque to the needle hub in the direction opposite to the deviation (Yankelevitz et al. 2000). However, substantial needle tip deviation should be corrected by withdrawing the needle and redirecting it, ideally avoiding repeated pleural passes. Once the needle tip is in the correct location, biopsy is performed using an 18- or 20-gauge spring-loaded core biopsy gun or 20–23-gauge fine needle (Fig. 1). Such a selection is often based on operator preference.

If a fine needle aspirate is selected, the fine needle is inserted into the nodule while applying suction to the needle using a 10-ml syringe. Fine needle aspirate may lead to a lower diagnostic yield compared to core biopsy (78 % versus 93 % in one retrospective study (Anderson et al. 2003)) and has a comparable rate of pneumothorax. However, one study reports that the presence of a cytopathologist at the time of fine needle aspirate biopsy results in a diagnostic rate of 100 % compared to 80 % when a cytopathologist is absent.

If a spring-loaded core biopsy gun is selected, a variety of gauge devices are available, some with adjustable needle throw, with a 2-cm throw as standard. Both 18- and 20-gauge devices are used for lung biopsy. A small retrospective study reported a similar specimen adequacy (100 %) and pneumothorax rate (12.5 % compared to 13.3 %) using 18- and 20-gauge devices through 17- and 19-gauge guide needles, respectively, when specimens were tested for epidermal growth factor mutations (Cheung et al. 2010). However, a larger study of 4262 biopsies reported a chest tube insertion rate of 16.7 % for procedures performed with 18-gauge guide needles and 13.1 % for procedures performed with 19-gauge needles (Kuban et al. 2015). In the case of a pleural biopsy, it is common practice to select an 18G needle (Scott et al. 1995) with high reported rates of specimen adequacy (93 %)

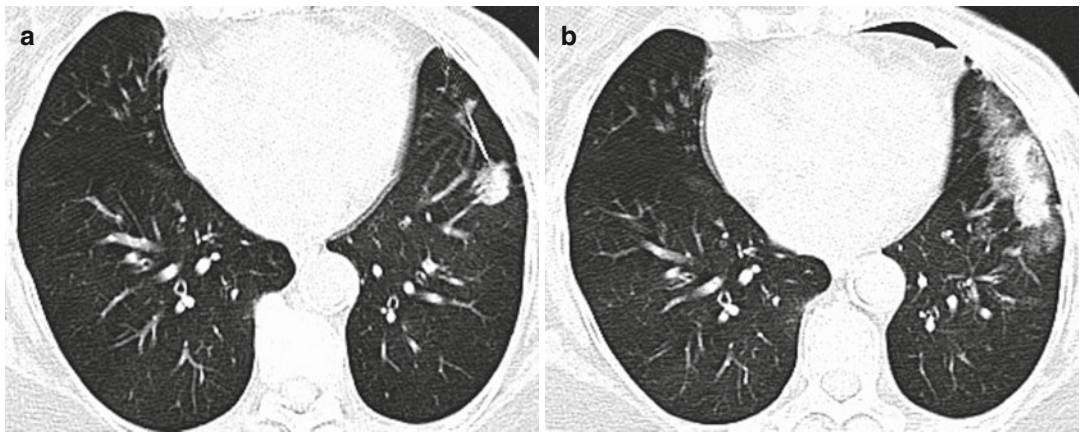

Fig. 1 (**a**) Axial CT image of a CT-guided lung biopsy of a 62-year-old female with breast carcinoma and a left upper lobe lung nodule. The needle tip is confirmed to be in the correct location, prior to biopsy with a 20-gauge spring-loaded core biopsy gun. Biopsy histology confirmed lung adenocarcinoma. (**b**) Post-biopsy CT demonstrates a small anteromedial pneumothorax and ground glass opacity along the biopsy tract due to the use of an autologous blood patch

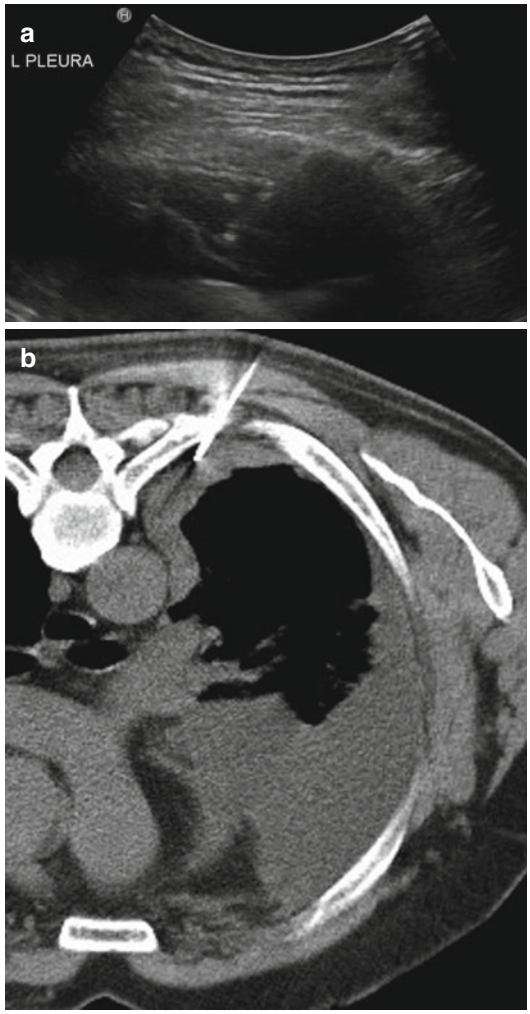

Fig. 2 (**a**) Ultrasound-guided pleural biopsy in a 52-year-old male with a growing left pleural mass. A transverse image demonstrates the tip of a 20-gauge biopsy needle in the pleural mass. Biopsy histology was inconclusive and the patient then underwent CT-guided biopsy. (**b**) Axial CT image of the same patient confirms correct position of a 17-gauge guide needle prior to pleural biopsy with an 18-gauge spring-loaded core biopsy gun. An 18-gauge biopsy needle was selected to ensure specimen adequacy. Biopsy histology confirmed malignant mesothelioma

(Scott et al. 1995) (Fig. 2). A small number of studies report the use of a 14-gauge core biopsy device for pleural or chest wall lesions without complication (Schubert et al. 2005). One pleural pass is ideal, as the risk of pneumothorax increases with the number of pleural passes. In terms of diagnosis, 2–3 coaxial passes are reported to lead to a sensitivity of 91.3–94 % compared to 78.6 % with just 1 coaxial pass. There is no evidence to suggest that an increased number of coaxial passes lead to a greater complication rate (Lim et al. 2013).

A number of maneuvers are reported to minimize complications after biopsy including aspiration of pneumothorax immediately after complicated biopsy, autologous intraparenchymal blood patch (Fig. 1b), tract sealing with an exogenous sealant, and rapid rollover after biopsy.

Upon completion of the biopsy, a chest radiograph is often obtained to detect a potential pneumothorax and serve as a comparison for a 2-h post-biopsy chest radiograph. If there is a small pneumothorax on the initial chest radiograph, the patient is observed clinically and assessed for progression of the pneumothorax on the 2-h-delayed chest radiograph; if progression is detected, chest tube placement may be indicated.

If the patient develops a pneumothorax during or after CT-guided lung biopsy, oxygen via nasal cannula or face mask should be administered at 2–4 L/min (Birchard 2011). Manual aspiration can be attempted immediately after biopsy; this technique is effective in small-volume pneumothoraces (<500 cc) (Yamagami et al. 2009). Autologous blood patch administration involves phlebotomy of approximately 10 mL of the patient's blood into a syringe or anticoagulant-free glass vacuum-sealed tube prior to the procedure. After the biopsy samples have been obtained, the blood is administered through the guiding needle as it is pulled back across each pleural surface from up to 2 cm inside the pleura to 1 cm outside the pleura (Fig. 1b). One randomized study of 242 patients undergoing lung biopsy using either a 17- or 19-gauge guide needle reports that the rate of pneumothorax reduced from 35 to 26 % ($p = 0.12$) and the rate of pneumothorax requiring chest tube placement reduced from 18 to 9 % ($p = 0.048$). Interestingly, the benefit was observed by the administration of a blood patch only after using a 19-gauge guide needle (Malone et al. 2013). A hydrogel expanding plug has also been assessed for efficacy as a pleural sealant. One such sealant consists of a 4-cm plug delivered to the pleural puncture site via a guide needle. In 287 randomized patients, the rate of

pneumothorax reduced from 31 to 18 %, and the rate of pneumothorax requiring chest tube placement reduced from 11 to 4 % after using the hydrogel sealant (Zaetta et al. 2010). Rapid rollover involves the rapid repositioning of the patient into the puncture-site-down position within 10 s of completion of lung biopsy (O'Neill et al. 2012; Kim et al. 2015a). Two randomized studies report a decrease in the need for chest tube placement with the use of this maneuver (1.6–4 %) (O'Neill et al. 2012; Kim et al. 2015a).

6.2 Complications

Serious complications of CT-guided lung biopsy include pneumothorax, hemoptysis, and air embolism. Pneumothorax is the most common complication. Factors increasing the risk of pneumothorax include increased patient age, obstructive lung disease, increased depth of lesion, multiple pleural passes, increased time of needle across the pleura, and traversal of a fissure (Birchard 2011; Kazerooni et al. 1996). The incidence of pneumothorax ranges from 15 to 42.3 % (Hiraki et al. 2010; Wiener et al. 2011), and the rate of chest tube placement ranges from 6.6 to 11.9 % (Hiraki et al. 2010; Wiener et al. 2011). Delayed pneumothorax (diagnosed more than 3 h after biopsy) is reported to occur in 3.3 % of patients undergoing CT-guided lung biopsy (Choi et al. 2004).

6.3 Chest Drain Placement

If a post-biopsy pneumothorax is large, there is mediastinal shift, or the patient is symptomatic, percutaneous needle decompression is indicated (Birchard 2011). In our institutions, the chest drain is placed by first inserting an apically directed 18-gauge needle attached to a 20-cc syringe containing 10 cc of normal saline into the pleura via the second intercostal space in the midclavicular line using a sterile technique. The needle is aspirated during insertion, and once air enters the syringe, it is disconnected from the needle and a 0.035-inch guidewire is inserted into the apical pleural space. A conventional short-range CT is obtained at this point to document adequate position. After appropriate tissue dilatation, an 8- or 10-Fr locking pigtail catheter is advanced into the pleural space such that the pigtail terminates in the lung apex. The catheter is then attached to an underwater seal device, and the pneumothorax is aspirated using a three-way stopcock. If a persistent air leak is noted, the underwater seal device may be connected to low wall suction of approximately −20 to −40 cmH_2O. A Heimlich valve is a lightweight one-way valve attached to conventionally placed chest tube that enables the ambulatory treatment of pneumothorax. Such a device enables early discharge and reduces patient discomfort. Its use for spontaneous and outpatient pneumothorax is reported to be successful in 85.8 % of patients in a pooled meta-analysis, and long-term outcomes appear to be similar to conventional therapy (Brims and Maskell 2013).

6.4 Hemorrhage

The average incidence of hemoptysis is 12 %, and the rate of parenchymal hemorrhage is 0.8 % (Yildirim et al. 2009). If severe hemoptysis is observed, the patient should be placed biopsy side down to prevent transbronchial aspiration of blood. Pulmonary hemorrhage incidence has not been found to differ depending on the use of a coaxial or non-coaxial technique (Nour-Eldin et al. 2014). The same study reported the risk factors associated with pulmonary hemorrhage which include a basal lesion location, increased lesion depth from pleura, and needle passage through vessels during biopsy (Nour-Eldin et al. 2014). The majority of cases of pulmonary hemorrhage are treated conservatively.

6.5 Air Embolism

Air embolism is an extremely rare but potentially fatal complication of lung biopsy, with a reported incidence of 0.5 % (Freund et al. 2012). Air may enter the pulmonary venous system by placement of the needle tip within a pulmonary vein, fol-

lowed by entry of air into the needle or by fistula formation between a pulmonary vein and bronchus as a result of needle placement (Birchard 2011) allowing passage of air into the pulmonary vein. Air emboli can cause cerebral infarction, myocardial infarction, and occasionally death with a mortality rate of 0.16 % (Freund et al. 2012). General anesthesia and prone positioning are reported risk factors for systemic air embolism. Treatment involves the administration of 100 % oxygen, immediate placement of the patient in the Trendelenburg or left lateral decubitus position, and hyperbaric oxygen therapy.

6.6 Success Rates

The diagnostic accuracy, sensitivity, and specificity of CT-guided lung biopsy of solitary pulmonary nodules are reported to be 92.9, 95.3, and 95.7 %, respectively (Yang et al. 2015). Fine needle aspiration without core biopsy has been reported to contribute to a nondiagnostic biopsy result (Choi et al. 2013).

7 Percutaneous Lung Abscess Drainage

A lung abscess develops as a result of necrosis of infected lung parenchyma. Anaerobic oral flora are the most common pathogens (Yu 2011). Rarely, a lung abscess can arise as a secondary phenomenon due to a centrally obstructing tumor, a foreign body, or an iatrogenic cause including radiation (Fig. 3) (Woody et al. 2010) and thermal ablation.

7.1 Indications

Lung abscesses are typically treated with antimicrobial therapy. If medical therapy fails, surgical or percutaneous intervention is considered. Lobectomy can be considered for patients who are considered good surgical candidates and in patients with extensive abscess (Schweigert et al. 2011). Percutaneous drainage is indicated for patients with localized abscesses (Schweigert et al. 2011). Such interventions are most suitable for patients with abscesses >6 cm and patients with a diminished cough reflex (Wali 2012).

7.2 Technique

The patient should undergo preoperative CT imaging with contrast, to exclude a bronchogenic neoplasm complicated by lung abscess and to guide drainage catheter insertion. The procedure is usually performed with conscious sedation using intravenous fentanyl and midazolam. In pediatric patients, general anesthesia may be required (Yu 2011). An 18-gauge access needle is inserted into the abscess cavity through the affected lung parenchyma. The path of drainage should avoid uninvolved lung, so as to prevent formation of a bronchopleural fistula and subsequent infection of the pleural space (Fig. 3) (Wali 2012). A Seldinger technique of catheter insertion over a 0.035 inch guidewire minimizes patient discomfort compared to a trocar technique (Yu 2011). Depending on the character of the aspirate, a 10- or 12-F locking pigtail catheter is placed over the guidewire after tissue dilatation. Once the catheter is locked and secured to the skin, it should be irrigated with normal saline and attached to an underwater seal. The catheter can be attached to low wall suction (e.g., 20 cm of water) to enhance drainage (Klein et al. 1995). Daily irrigation with 5-ml normal saline is suggested to maintain catheter patency and enhance drainage of purulent material.

7.3 Outcomes

A meta-analysis of pooled data of patients who underwent percutaneous drainage of lung abscess reports an overall success rate of 84 % (Wali 2012). Reported complications occur in approximately 16 % of patients and include catheter occlusion due to purulent fluid, pneumothorax, hemothorax, and hemoptysis. Reported deaths are few, with only one study published in the late 1990s describing mortality in 5 of 8 patients who

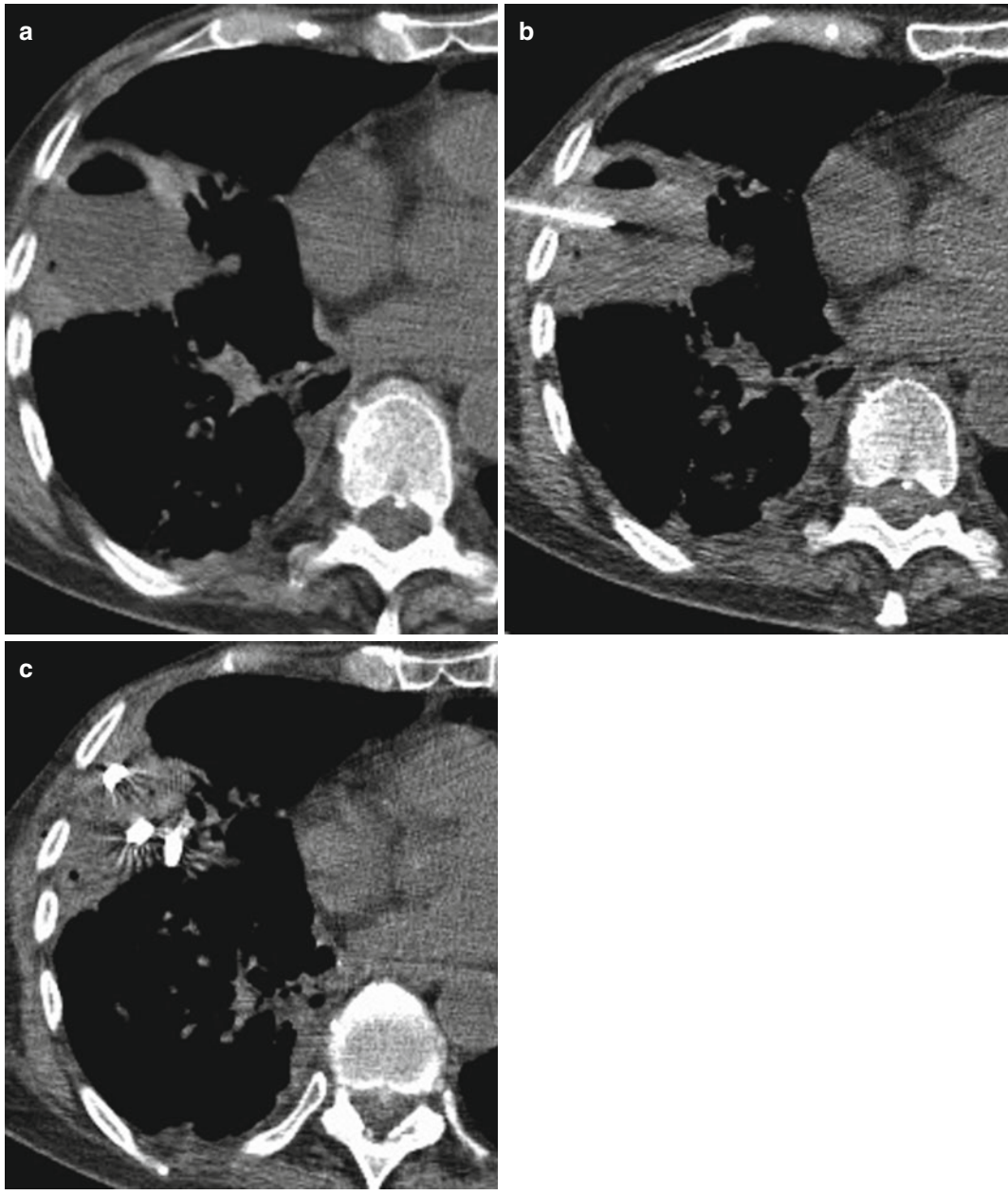

Fig. 3 (**a**) Axial CT image of a 72-year-old female with a prior history of right breast carcinoma, right mastectomy, and chest wall irradiation who presented with confusion and cough. CT confirmed a right upper lobe abscess. (**b**) Axial CT image demonstrating right upper lobe abscess access that avoids uninvolved lung, so as to prevent formation of a bronchopleural fistula and subsequent infection of the pleural space. (**c**) Axial CT image demonstrating a 12-Fr pigtail catheter advanced over a guidewire; adequate position within the abscess is confirmed

underwent drainage (Hirshberg et al. 1999). Host factors which predict a poor outcome include advanced age, debilitation, malnutrition, immunosuppression, malignancy, and duration of symptoms >8 weeks (Mwandumba and Beeching 2000). Lung abscesses >6 cm in the right lower lobe are also known to be resistant to treatment (Hirshberg et al. 1999).

8 Thermal Ablation

Heat-based ablation was first described in the liver in the 1990s using a modified Bovie knife and radiofrequency energy (McGahan et al. 1990; Rossi et al. 1990). This prompted further study of the technique in other organs (Buscarini et al. 1995; Fraker 1995). Its successful use in lung tumors in humans was described in patients with inoperable lung carcinoma in 2000 (Dupuy et al. 2000). These initial studies provided the impetus to further study thermal ablation as a safe method of treating inoperable lung tumors and metastases. Two other heat-based therapies, microwave ablation and cryoablation, have since come into clinical use.

8.1 Mechanism of Action

Radiofrequency ablation (RFA) is achieved through molecular friction created by an electrical current delivered to tumor cells surrounding the RFA probe tip, leading to a rise in tissue temperature named the Joule effect (Hong and Georgiades 2010). The temperature at the electrode tip should rise above 60° Celsius (C) to achieve cell death (Goldberg et al. 2000; Sapareto and Dewey 1984). Tissue immediately adjacent to the electrode is heated by electrical conduction, and the surrounding tissue is then heated by thermal conduction. If ablation temperatures are above 95 °C, tissue charring occurs and decreases ablation effectiveness (Cosman et al. 1984; Goldberg et al. 1995; Brace 2009). In order to avoid tissue charring, technical adaptations have been made to ablation probes including the use of multiple ablation probes (Siperstein et al. 1997), internally cooled probes (Goldberg et al. 1996), and pulsed RFA ablation systems (Goldberg et al. 1999).

Microwave energy causes the water molecules in human tissue to continuously realign with the applied field, when applied through a microwave ablation probe; this leads to an increase in local tissue temperature (Ahmed et al. 2011). Tissue destruction occurs when tissues are heated to lethal temperatures as high as 150 °C. Unlike RFA, microwave power penetrates tissues of low electrical conductivity such as lung and charred tissue.

Conversely, cryoablation involves rapid tissue cooling and resultant cell death at temperatures in the range of −50 °C. This is created by the release of argon from the tip of the cryoablation probe. Upon release, argon rapidly expands causing cooling of the adjacent tissues, known as the Joule-Thompson effect. Sequential warming and cooling increases the degree of cellular damage (Erinjeri and Clark 2010; Sharma et al. 2011). An ice ball forms during freezing, which is visible on CT, allowing the operator to monitor the ablation zone (Ahrar and Littrup 2012).

8.2 Indication

Indications for thermal ablation of lung tumors include T1N0M0 primary lung tumors and oligometastatic lung nodules in patients who are ineligible for surgical resection. Patients should be assessed by an interdisciplinary team, and the maximum tumor diameter should not exceed 3 cm in diameter (Pereira and Masala 2012). Thermal ablation can also be combined with surgery (Sano et al. 2008) or chemotherapy (Chua et al. 2010) with the intent of improving the chance of cure and sparing lung parenchyma.

Relative contraindications for treatment include underlying interstitial disease, such as pulmonary fibrosis due to the risk of severe pulmonary failure, and coagulopathy (Alexander and Dupuy 2013; Carrafiello et al. 2012). Lesions within 1 cm of sensitive structures such as the trachea, main bronchi, and esophagus are at higher risk of complications (Bargellini et al. 2011).

8.3 Technique

The thermal ablation probe is positioned under CT guidance in a manner similar to percutaneous lung biopsy. A guide needle is not typically used. The heat sink effect is an important factor when deciding whether and how to perform lung tumor ablation. The intention of thermal ablation is to deposit heat energy within the target lesion. If, however, the target lesion is located adjacent to a large vessel or airway, high pulmonary vascular flow and air exchange act as a “heat sink” to dis-

sipate heat from normal parenchyma and limit the concentration of lethal temperatures within the target lesion. Lesions within 1 cm of an airway or central vessel may often be incompletely ablated due to heat sink effect (Bargellini et al. 2011; Dupuy 2011). Hydrodissection or pneumodissection can be used to protect adjacent sensitive tissues from thermal damage (Fig. 4). Fluid or air is infused using a small (e.g., 5 Fr) catheter between the target tissue and the adjacent vulnerable structure. This creates a physical barrier between the zone of ablation and the neighboring tissue, which decreases heating of the vulnerable tissue. Five percent dextrose solution is the ideal choice for hydrodissection because it is isoosmolar and nonionic and therefore creates a physical and electrical barrier (Campbell et al. 2012; Laeseke et al. 2005; Brace et al. 2006). It can be combined with iodinated contrast for improved visibility at a concentration of 1 ml of 300 mg/ml iodine contrast in 50 ml of 5 % dextrose solution for optimal target visualization (Campbell et al. 2012).

8.4 Complications

Complications after lung RFA are reported to occur in 9.8 % of patients; the most frequently reported complications include pleuritis, pneumonia, abscess, hemorrhage, and refractory pneumothorax requiring pleurodesis (Carrafiello et al. 2012). Major complications include bronchopleural fistula, tumor seeding, and nerve (0.3 %) or diaphragmatic injury (Palussiere et al. 2013). Skin burns are rare with an incidence of 0.3 % (Wolf et al. 2008). Lung function is relatively preserved after thermal ablation. Lencioni and colleagues report a mild change at 3 months follow-up in forced vital capacity (FVC) of + 13.7 % and forced expiratory volume in 1 s (FEV_1) − 5.4 % (Lencioni et al. 2008).

8.5 Outcomes

Nine studies report recurrence rates after RFA of stage I lung carcinoma: the aggregate rate of local progression is 29 % (75/260 patients) (Dupuy et al. 2015; Ambrogi et al. 2011; Zemlyak et al. 2010; Pennathur et al. 2007; Hiraki et al. 2007; Hsie et al. 2009; Lanuti et al. 2009) and metastasis at any site is 31 % (42/137) (Ambrogi et al. 2011; Pennathur et al. 2007; Hsie et al. 2009; Lanuti et al. 2009). Reported 3- and 5-year survival ranges from 36 to 88 % (Zemlyak et al. 2010; Hiraki et al. 2007, 2011; Lanuti et al. 2009; Simon et al. 2007) and 19 to 27 %, respectively (Ambrogi et al. 2011; Zemlyak et al. 2010; Simon et al. 2007). Patients with synchronous and metachronous primary lung carcinoma are also reported to achieve similar local control rates and survival outcomes (Ridge et al. 2014). The cellular subtype bronchoalveolar carcinoma (now referred to as adenocarcinoma in situ or minimally invasive adenocarcinoma) may have a better prognosis after RFA. Lanuti and colleagues describe a 90 % local control rate of bronchoalveolar carcinoma after RFA compared to 68.5 % for all cell types (Lanuti et al. 2009). One report on the outcomes of patients with stage I lung carcinoma treated with microwave ablation describes a local recurrence rate of 26 % at a median follow-up of 12 months, but does not report survival data (Liu and Steinke 2013). Another study of patients with peripheral primary lung cancers describes a local recurrence rate of 24 % and 1- and 2-year survival rates of 91.3 and 82.6 %, respectively (Sun et al. 2015). Two small studies report outcomes of patients with stage I lung carcinoma treated with cryoablation and describe a local recurrence rate of 3–11 %, overall 3-year survival rates of 77–88 % (Zemlyak et al. 2010; Yamauchi et al. 2012) and a 3-year cancer-specific survival of 90.2 % (Zemlyak et al. 2010).

The literature analyzing outcomes after thermal ablation of metastases is limited by study size and patient heterogeneity. The largest trial to date reported the outcomes of patients with either primary or metastatic lung tumors treated with RFA in patients with colorectal metastases; overall survival at 1 and 2 years was 89 % and 66 % (Lencioni et al. 2008). Patients with metastases of other origin had a 1- and 2-year survival of 92 % and 64, respectively. Other published data analyzing the outcomes of ablation of colorectal lung metastases report 1-year survival ranging from 83.9 to 95 % and 3-year survival ranging from 46 to 59.6 % (Lencioni et al. 2008;

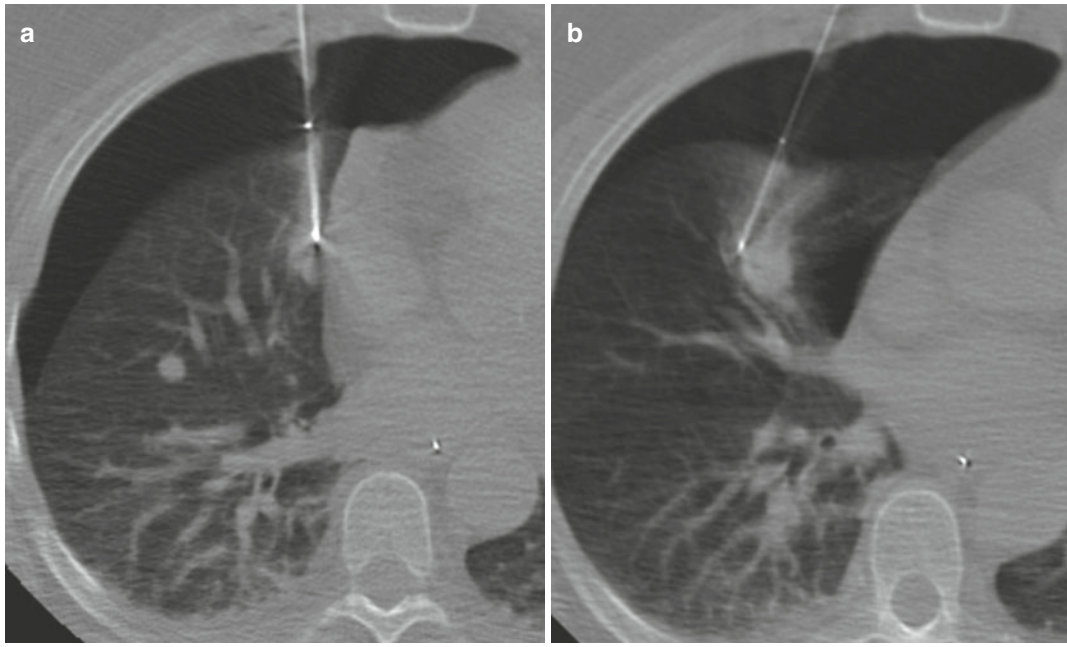

Fig. 4 (**a**) Axial CT image of a 67-year-old male with lung metastases from colorectal carcinoma; the image demonstrates a radiofrequency probe with a 3-cm active tip placed in a right middle lobe metastasis. A 5-Fr catheter has been introduced into the pleural space, and air has been insufflated to create an iatrogenic pneumothorax. (**b**) Axial CT image demonstrating radiofrequency probe tip deflection laterally to avoid injury to the heart. Insufflated air now lies between the right middle lobe and the heart

Yamakado et al. 2009; Yamauchi et al. 2011; Yan et al. 2006; Petre et al. 2013). Five-year survival of 34.9 % is reported by one group (Yamakado et al. 2009). Reported median survival ranges from 33 to 46 months (Yamakado et al. 2009; Yamauchi et al. 2011; Yan et al. 2006; Petre et al. 2013; Gillams et al. 2013). Reported local recurrence rates range from 13 to 38 % (Yamakado et al. 2009; Yamauchi et al. 2011; Yan et al. 2006; Petre et al. 2013; Gillams et al. 2013).

9 Mediastinal Biopsy

Mediastinal biopsy is indicated when a histologic diagnosis of a mediastinal lesion is required, particularly if the lesion cannot be safely accessed surgically, transbronchially, or endoscopically. Cervical mediastinoscopy is typically used to sample pretracheal, paratracheal, and anterior subcarinal lymph nodes in patients with lung carcinoma. Endoscopic or transbronchial US-guided needle biopsy may allow access to the paratracheal, subcarinal, aortopulmonary, and paraesophageal nodal stations. However, anterior mediastinal, prevascular, or paravertebral lesions may not be accessible using either approach; therefore percutaneous biopsy should be considered (Gupta et al. 2005). Mediastinal biopsy and drainage can be performed using either ultrasound or CT, depending on whether a sonographic window exists and local expertise.

Transgression of the pleura is ideally avoided during mediastinal biopsy, because of the related risk of pneumothorax. Possible percutaneous extrapleural routes of biopsy include the parasternal, paravertebral, transternal, and suprasternal approaches (Gupta et al. 2005). Procedure planning should include delineation of adjacent sensitive structures including the great vessels, the internal mammary vessels in the case of a parasternal approach, and knowledge of the expected locations of the vagus and phrenic

nerves, in the case of a prevascular lesion, and the thoracic duct, in the case of a left paravertebral lesion.

The parasternal approach involves passing a needle directly adjacent to the sternum, medial to the internal mammary vessels in order to avoid their injury. If the target lesion is more laterally located and contacts the anterior chest wall, a more lateral approach may be employed. An extrapleural approach requires a path that transgresses only extrapleural fat between the skin entry site and the target lesion.

The paravertebral approach is best performed by passing the access needle close to the vertebra outside the parietal pleura. The intercostal artery and nerve should also be avoided by employing a needle trajectory above the rib. Other techniques which may enable an extrapleural approach to lesions close to the pleura include hydrodissection and iatrogenic pneumothorax. Hydrodissection involves the placement of a 22-gauge needle along the planned trajectory and injection of saline into the extrapleural space to displace a sensitive structure or create an extrapleural path for needle placement. An iatrogenic pneumothorax is created by placing an 18G needle or 5-Fr catheter along the planned needle trajectory to the level of the parietal pleura, removing the stylet, advancing the blunt portion of the access device through the parietal pleural, and then insufflating air to create a potential space (Gupta et al. 2005). The pneumothorax should then be aspirated at the termination of the procedure. Inadvertent transgression of the pleura may lead to pneumothorax. The reported incidence of pneumothorax after mediastinal biopsy is 3.85–4.7 % (Kim et al. 2015b; Priola et al. 2008). Patients with emphysema are particularly at risk of pneumothorax and ongoing air leak. The reported diagnostic accuracy of mediastinal biopsy is 83.6 % (Priola et al. 2008).

10 Mediastinal Drainage

The commonest indications for percutaneous mediastinal drainage include mediastinal abscess and esophageal anastomotic leaks (McDermott et al. 2012), if surgical exploration is not possible. A retrospective study reports the most common indications for successful drainage including esophageal leak or postoperative abscess after surgical intervention (Arellano et al. 2011). The most common site of drainage is the posterior mediastinum. Reported mediastinal catheter size ranges from 8 to 16 Fr. In the author's institutions, a Seldinger approach is preferred. An 18-gauge needle is placed in the target collection under intermittent CT guidance. Once the needle tip is in the collection, a small fluid sample is obtained. A 0.038-inch guidewire is then advanced into the fluid collection and its position is confirmed on CT. A locking pigtail catheter is then advanced over the guidewire into the collection. The catheter is then secured to the skin and placed to gravity drainage (Arellano et al. 2011). The reported success rate for mediastinal drainage is 95.6 % (Arellano et al. 2011).

11 Fiducial Placement

Gold fiducials act as markers for the detection of tumor position throughout the respiratory cycle. Their placement allows the delivery of focused and accurate radiation to the tumor. Fiducials are typically implanted within primary or secondary lung malignancies prior to stereotactic body radiation therapy through an 18-gauge introducer needle within the center or margin of the target lesion under CT guidance. The applicator needle is loaded with the fiducial marker which ranges from 1 to 3 mm in length, a wax or rubber spacer at the end of the introducer is removed once the guide needle is correctly positioned, and the fiducial is then placed in the target lesion using a pusher device. For larger lesions, more than one fiducial can be placed (Fig. 5). Fiducial placement can also be performed concurrently with biopsy, without affecting accuracy or complication rate (Mendiratta-Lala et al. 2014). Placement accuracy is reported to be good. One retrospective study reports an intratumoral location in 60.1 % of patients, at the tumor margin in 15.6 %, and a mean distance of 4 mm outside the tumor in 24.3 % of cases (Trumm et al. 2014). Major com-

plications are rare. Reported complications include pneumothorax and hemothorax and transient hemoptysis. Pneumothorax requiring chest tube placement is reported to occur in 7 % of patients (Mendiratta-Lala et al. 2014; Trumm et al. 2014).

12 Wire Localization

Lung nodules located adjacent to the pleural margin are often considered for wedge resection for either histologic diagnosis or lung parenchyma sparing curative resection. These subpleural nodules are typically located by manual palpation. However, ground glass or small pulmonary nodules (diameter < 1 cm) located more than 1 cm from the pleural surface (Ichinose et al. 2013; Dendo et al. 2002) may not be palpable intraoperatively. Particularly if video-assisted thoracoscopic resection is performed, nodule localization by palpation for subcentimeter nodules may also be limited by small port size (Zaman et al. 2012). Wire localization is therefore indicated in these settings. The localization wire is placed via a guide needle under CT guidance. The guide needle is directed toward the target nodule; its tip is placed approximately 2 cm from the nodule margin in order to preserve the pathologic specimen (Dendo et al. 2002). The wire, which may have a hook or spiral configuration in order to maintain an intratumoral location, is then advanced into the nodule, and the guide needle is removed, leaving behind a wire in the nodule connected to the skin entry site by a suture. Reported accuracy ranges from 58 to 97.6 % (Dendo et al. 2002; Miyoshi et al. 2009; Pittet et al. 2007; Ciriaco et al. 2004; Chen et al. 2007; Gonfiotti et al. 2007). Reported complications include wire dislodgement (7.5–47 %) (Ciriaco et al. 2004; Gonfiotti et al. 2007; Bernard 1996; Mack et al. 1993) and pneumothorax (7.5–32 %) (Dendo et al. 2002; Ciriaco et al. 2004; Chen et al. 2007; Gonfiotti et al. 2007). Other radiologic techniques of nodule localization have been devised to minimize such complications. A technetium-99-labeled solution with iodinated contrast can be injected via a fine needle introduced into the target lesion under CT guidance. The nodule is then resected at video-assisted thoracoscopy using a gamma-ray detector (Chella et al. 2000). When compared to hook-wire localization, this technique is reported to lead to successful localization in 96–100 % of patients and a lower pneumothorax rate of 4–6 %, in two small prospective studies (Chella et al. 2000; Burdine et al. 2002). Nodule localization with microcoils has also been described. The microcoil is delivered via a fine needle under CT guidance and carries the advantage of less frequent displacement (3 %) compared to hook-wire localization (Mayo et al. 2009) and a success rate ranging from 86 to 100 % (Mayo et al. 2009; Eichfeld et al. 2005; Powell et al. 2004).

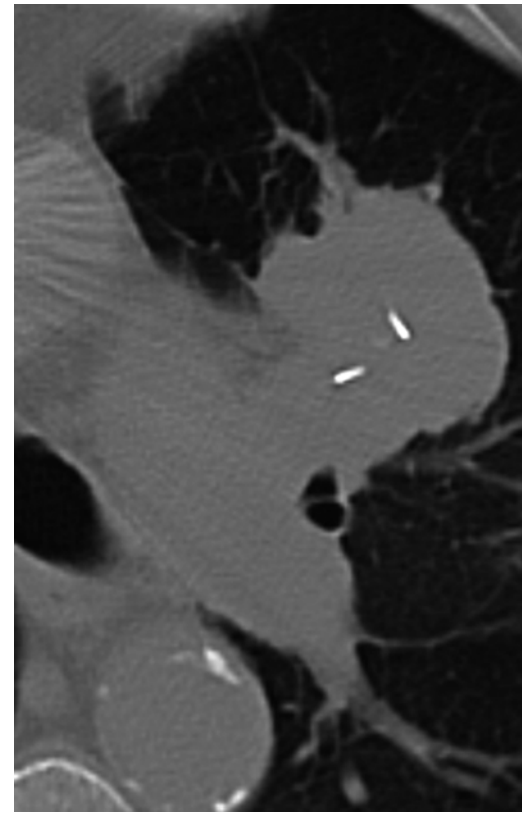

Fig. 5 Axial CT of a 75-year-old patient with a left upper lobe squamous cell carcinoma. Two gold fiducials have been placed within the tumor to act as markers for the detection of tumor position throughout the respiratory cycle. For larger lesions, more than one fiducial can be placed

13 Summary

CT-guided intervention in the thorax has vastly improved the minimally invasive management of benign and malignant thoracic pathologies. The advantages of CT-guided thoracic intervention include safe and accurate diagnosis in the case of biopsy, effective guidance of thermal ablation, avoidance of surgical intervention in the case of mediastinal or pulmonary abscess drainage, and successful localization of lung tumors prior to irradiation or resection. Radiologists should strive to achieve as low a radiation dose as possible and seek to minimize complications by accurate pre-procedure planning and appropriate intraprocedural monitoring.

References

Ahmed M, Brace CL, Lee FT Jr, Goldberg SN (2011) Principles of and advances in percutaneous ablation. Radiology 258(2):351–369

Ahrar K, Littrup PJ (2012) Is cryotherapy the optimal technology for ablation of lung tumors? J Vasc Interv Radiol 23(3):303–305

Alexander ES, Dupuy DE (2013) Lung cancer ablation: technologies and techniques. Semin Interv Radiol 30(2):141–150

Ambrogi MC, Fanucchi O, Cioni R, Dini P, De Liperi A, Cappelli C et al (2011) Long-term results of radiofrequency ablation treatment of stage I non-small cell lung cancer: a prospective intention-to-treat study. J Thorac Oncol 6(12):2044–2051

Anderson JM, Murchison J, Patel D (2003) CT-guided lung biopsy: factors influencing diagnostic yield and complication rate. Clin Radiol 58(10):791–797

Anzidei M, Argiro R, Porfiri A, Boni F, Anile M, Zaccagna F et al (2015) Preliminary clinical experience with a dedicated interventional robotic system for CT-guided biopsies of lung lesions: a comparison with the conventional manual technique. Eur Radiol 25(5):1310–1316

Arellano RS, Gervais DA, Mueller PR (2011) Computed tomography-guided drainage of mediastinal abscesses: clinical experience with 23 patients. J Vasc Interv Radiol 22(5):673–677

Bargellini I, Bozzi E, Cioni R, Parentini B, Bartolozzi C (2011) Radiofrequency ablation of lung tumours. Insights Imaging 2(5):567–576

Bernard A (1996) Resection of pulmonary nodules using video-assisted thoracic surgery. The Thorax Group. Ann Thorac Surg 61(1):202–204; discussion 204–205

Birchard KR (2011) Transthoracic needle biopsy. Semin Interv Radiol 28(1):87–97

Brace CL (2009) Radiofrequency and microwave ablation of the liver, lung, kidney, and bone: what are the differences? Curr Probl Diagn Radiol 38(3):135–143

Brace CL, Laeseke PF, Prasad V, Lee FT (2006) Electrical isolation during radiofrequency ablation: 5% dextrose in water provides better protection than saline. Conf Proc IEEE Eng Med Biol Soc 1:5021–5024

Brims FJ, Maskell NA (2013) Ambulatory treatment in the management of pneumothorax: a systematic review of the literature. Thorax 68(7):664–669

Burdine J, Joyce LD, Plunkett MB, Inampudi S, Kaye MG, Dunn DH (2002) Feasibility and value of video-assisted thoracoscopic surgery wedge excision of small pulmonary nodules in patients with malignancy. Chest 122(4):1467–1470

Buscarini L, Rossi S, Fornari F, Di Stasi M, Buscarini E (1995) Laparoscopic ablation of liver adenoma by radiofrequency electrocautery. Gastrointest Endosc 41(1):68–70

Campbell C, Lubner MG, Hinshaw JL, Munoz del Rio A, Brace CL (2012) Contrast media-doped hydrodissection during thermal ablation: optimizing contrast media concentration for improved visibility on CT images. AJR Am J Roentgenol 199(3):677–682

Carrafiello G, Mangini M, Fontana F, Di Massa A, Ierardi AM, Cotta E et al (2012) Complications of microwave and radiofrequency lung ablation: personal experience and review of the literature. Radiol Med 117(2):201–213

Chella A, Lucchi M, Ambrogi MC, Menconi G, Melfi FM, Gonfiotti A et al (2000) A pilot study of the role of TC-99 radionuclide in localization of pulmonary nodular lesions for thoracoscopic resection. Eur J Cardiothorac Surg 18(1):17–21

Chen YR, Yeow KM, Lee JY, Su IH, Chu SY, Lee CH et al (2007) CT-guided hook wire localization of subpleural lung lesions for video-assisted thoracoscopic surgery (VATS). J Formos Med Assoc 106(11):911–918

Cheung YC, Chang JW, Hsieh JJ, Lin G, Tsai YH (2010) Adequacy and complications of computed tomography-guided core needle biopsy on non-small cell lung cancers for epidermal growth factor receptor mutations demonstration: 18-gauge or 20-gauge biopsy needle. Lung Cancer 67(2):166–169

Chintapalli KN, Montgomery RS, Hatab M, Katabathina VS, Guiy K (2012) Radiation dose management: part 1, minimizing radiation dose in CT-guided procedures. AJR Am J Roentgenol 198(4):W347–W351

Choi CM, Um SW, Yoo CG, Kim YW, Han SK, Shim YS et al (2004) Incidence and risk factors of delayed pneumothorax after transthoracic needle biopsy of the lung. Chest 126(5):1516–1521

Choi SH, Chae EJ, Kim JE, Kim EY, Oh SY, Hwang HJ et al (2013) Percutaneous CT-guided aspiration and core biopsy of pulmonary nodules smaller than 1 cm: analysis of outcomes of 305 procedures from a tertiary referral center. AJR Am J Roentgenol 201(5):964–970

Chua TC, Thornbury K, Saxena A, Liauw W, Glenn D, Zhao J et al (2010) Radiofrequency ablation as an

adjunct to systemic chemotherapy for colorectal pulmonary metastases. Cancer 116(9):2106–2114
Ciriaco P, Negri G, Puglisi A, Nicoletti R, Del Maschio A, Zannini P (2004) Video-assisted thoracoscopic surgery for pulmonary nodules: rationale for preoperative computed tomography-guided hookwire localization. Eur J Cardiothorac Surg 25(3):429–433
Cosman ER, Nashold BS, Ovelman-Levitt J (1984) Theoretical aspects of radiofrequency lesions in the dorsal root entry zone. Neurosurgery 15(6):945–950
Dahlgren S (1966) Needle biopsy of intrapulmonary hamartoma. Scand J Respir Dis 47(3):187–194
Dendo S, Kanazawa S, Ando A, Hyodo T, Kouno Y, Yasui K et al (2002) Preoperative localization of small pulmonary lesions with a short hook wire and suture system: experience with 168 procedures. Radiology 225(2):511–518
Dupuy DE (2011) Image-guided thermal ablation of lung malignancies. Radiology 260(3):633–655
Dupuy DE, Zagoria RJ, Akerley W, Mayo-Smith WW, Kavanagh PV, Safran H (2000) Percutaneous radiofrequency ablation of malignancies in the lung. AJR Am J Roentgenol 174(1):57–59
Dupuy DE, Fernando HC, Hillman S, Ng T, Tan AD, Sharma A et al (2015) Radiofrequency ablation of stage IA non-small cell lung cancer in medically inoperable patients: results from the American College of Surgeons Oncology Group Z4033 (Alliance) trial. Cancer 121(19):3491–8
Eichfeld U, Dietrich A, Ott R, Kloeppel R (2005) Video-assisted thoracoscopic surgery for pulmonary nodules after computed tomography-guided marking with a spiral wire. Ann Thorac Surg 79(1):313–316; discussion 316–317
Erinjeri JP, Clark TW (2010) Cryoablation: mechanism of action and devices. J Vasc Interv Radiol 21(8 Suppl):S187–S191
Fraker DL (1995) Percutaneous radiofrequency interstitial thermal ablation. Cancer J Sci Am 1(1):30–31
Freund MC, Petersen J, Goder KC, Bunse T, Wiedermann F, Glodny B (2012) Systemic air embolism during percutaneous core needle biopsy of the lung: frequency and risk factors. BMC Pulm Med 12:2
Ghaye B, Dondelinger RF (2001) Imaging guided thoracic interventions. Eur Respir J 17(3):507–528
Gianfelice D, Lepanto L, Perreault P, Chartrand-Lefebvre C, Milette PC (2000) Effect of the learning process on procedure times and radiation exposure for CT fluoroscopy-guided percutaneous biopsy procedures. J Vasc Interv Radiol 11(9):1217–1221
Gillams A, Khan Z, Osborn P, Lees W (2013) Survival after radiofrequency ablation in 122 patients with inoperable colorectal lung metastases. Cardiovasc Intervent Radiol 36(3):724–730
Goldberg SN, Gazelle GS, Dawson SL, Rittman WJ, Mueller PR, Rosenthal DI (1995) Tissue ablation with radiofrequency: effect of probe size, gauge, duration, and temperature on lesion volume. Acad Radiol 2(5):399–404
Goldberg SN, Gazelle GS, Solbiati L, Rittman WJ, Mueller PR (1996) Radiofrequency tissue ablation: increased lesion diameter with a perfusion electrode. Acad Radiol 3(8):636–644
Goldberg SN, Stein MC, Gazelle GS, Sheiman RG, Kruskal JB, Clouse ME (1999) Percutaneous radiofrequency tissue ablation: optimization of pulsed-radiofrequency technique to increase coagulation necrosis. J Vasc Interv Radiol 10(7):907–916
Goldberg SN, Gazelle GS, Mueller PR (2000) Thermal ablation therapy for focal malignancy: a unified approach to underlying principles, techniques, and diagnostic imaging guidance. AJR Am J Roentgenol 174(2):323–331
Gonfiotti A, Davini F, Vaggelli L, De Francisci A, Caldarella A, Gigli PM et al (2007) Thoracoscopic localization techniques for patients with solitary pulmonary nodule: hookwire versus radio-guided surgery. Eur J Cardiothorac Surg 32(6):843–847
Gupta S, Seaberg K, Wallace MJ, Madoff DC, Morello FA Jr, Ahrar K et al (2005) Imaging-guided percutaneous biopsy of mediastinal lesions: different approaches and anatomic considerations. Radiographics 25(3):763–786; discussion 786–788
Hiraki T, Gobara H, Iishi T, Sano Y, Iguchi T, Fujiwara H et al (2007) Percutaneous radiofrequency ablation for clinical stage I non-small cell lung cancer: results in 20 nonsurgical candidates. J Thorac Cardiovasc Surg 134(5):1306–1312
Hiraki T, Mimura H, Gobara H, Shibamoto K, Inoue D, Matsui Y et al (2010) Incidence of and risk factors for pneumothorax and chest tube placement after CT fluoroscopy-guided percutaneous lung biopsy: retrospective analysis of the procedures conducted over a 9-year period. AJR Am J Roentgenol 194(3):809–814
Hiraki T, Gobara H, Mimura H, Toyooka S, Fujiwara H, Yasui K et al (2011) Radiofrequency ablation of lung cancer at Okayama University Hospital: a review of 10 years of experience. Acta Med Okayama 65(5):287–297
Hirshberg B, Sklair-Levi M, Nir-Paz R, Ben-Sira L, Krivoruk V, Kramer MR (1999) Factors predicting mortality of patients with lung abscess. Chest 115(3):746–750
Hong K, Georgiades C (2010) Radiofrequency ablation: mechanism of action and devices. J Vasc Interv Radiol 21(8 Suppl):S179–S186
Hsie M, Morbidini-Gaffney S, Kohman LJ, Dexter E, Scalzetti EM, Bogart JA (2009) Definitive treatment of poor-risk patients with stage I lung cancer: a single institution experience. J Thorac Oncol 4(1):69–73
Ichinose J, Kohno T, Fujimori S, Harano T, Suzuki S (2013) Efficacy and complications of computed tomography-guided hook wire localization. Ann Thorac Surg 96(4):1203–1208
Kazerooni EA, Lim FT, Mikhail A, Martinez FJ (1996) Risk of pneumothorax in CT-guided transthoracic needle aspiration biopsy of the lung. Radiology 198(2):371–375

Kim JI, Park CM, Lee SM, Goo JM (2015a) Rapid needle-out patient-rollover approach after cone beam CT-guided lung biopsy: effect on pneumothorax rate in 1,191 consecutive patients. Eur Radiol 25(7):1845–1853

Kim H, Park CM, Lee SM, Goo JM (2015b) C-arm cone-beam CT virtual navigation-guided percutaneous mediastinal mass biopsy: diagnostic accuracy and complications. Eur Radiol 25(12):3508–3517

Klein JS, Schultz S, Heffner JE (1995) Interventional radiology of the chest: image-guided percutaneous drainage of pleural effusions, lung abscess, and pneumothorax. AJR Am J Roentgenol 164(3):581–588

Koethe Y, Xu S, Velusamy G, Wood BJ, Venkatesan AM (2014) Accuracy and efficacy of percutaneous biopsy and ablation using robotic assistance under computed tomography guidance: a phantom study. Eur Radiol 24(3):723–730

Kuban JD, Tam AL, Huang SY, Ensor JE, Philip AS, Chen GJ et al (2015) The effect of needle gauge on the risk of pneumothorax and chest tube placement after percutaneous computed tomographic (CT)-guided lung biopsy. Cardiovasc Intervent Radiol 38(6):1595–1602

Laeseke PF, Sampson LA, Winter TC 3rd, Lee FT Jr (2005) Use of dextrose 5% in water instead of saline to protect against inadvertent radiofrequency injuries. AJR Am J Roentgenol 184(3):1026–1027

Lanuti M, Sharma A, Digumarthy SR, Wright CD, Donahue DM, Wain JC et al (2009) Radiofrequency ablation for treatment of medically inoperable stage I non-small cell lung cancer. J Thorac Cardiovasc Surg 137(1):160–166

Lencioni R, Crocetti L, Cioni R, Suh R, Glenn D, Regge D et al (2008) Response to radiofrequency ablation of pulmonary tumours: a prospective, intention-to-treat, multicentre clinical trial (the RAPTURE study). Lancet Oncol 9(7):621–628

Lim C, Lee KY, Kim YK, Ko JM, Han DH (2013) CT-guided core biopsy of malignant lung lesions: how many needle passes are needed? J Med Imaging Radiat Oncol 57(6):652–656

Liu H, Steinke K (2013) High-powered percutaneous microwave ablation of stage I medically inoperable non-small cell lung cancer: a preliminary study. J Med Imaging Radiat Oncol 57(4):466–474

Mack MJ, Shennib H, Landreneau RJ, Hazelrigg SR (1993) Techniques for localization of pulmonary nodules for thoracoscopic resection. J Thorac Cardiovasc Surg 106(3):550–553

Malone LJ, Stanfill RM, Wang H, Fahey KM, Bertino RE (2013) Effect of intraparenchymal blood patch on rates of pneumothorax and pneumothorax requiring chest tube placement after percutaneous lung biopsy. AJR Am J Roentgenol 200(6):1238–1243

Mayo JR, Clifton JC, Powell TI, English JC, Evans KG, Yee J et al (2009) Lung nodules: CT-guided placement of microcoils to direct video-assisted thoracoscopic surgical resection. Radiology 250(2):576–585

McDermott S, Levis DA, Arellano RS (2012) Chest drainage. Semin Interv Radiol 29(4):247–255

McGahan JP, Browning PD, Brock JM, Tesluk H (1990) Hepatic ablation using radiofrequency electrocautery. Invest Radiol 25(3):267–270

McNitt-Gray MF (2002) AAPM/RSNA physics tutorial for residents: topics in CT. Radiation dose in CT. Radiographics 22(6):1541–1553

Mendiratta-Lala M, Sheiman R, Brook OR, Gourtsoyianni S, Mahadevan A, Siewert B (2014) CT-guided core biopsy and percutaneous fiducial seed placement in the lung: can these procedures be combined without an increase in complication rate or decrease in technical success? Eur J Radiol 83(4):720–725

Miyoshi K, Toyooka S, Gobara H, Oto T, Mimura H, Sano Y et al (2009) Clinical outcomes of short hook wire and suture marking system in thoracoscopic resection for pulmonary nodules. Eur J Cardiothorac Surg 36(2):378–382

Mwandumba HC, Beeching NJ (2000) Pyogenic lung infections: factors for predicting clinical outcome of lung abscess and thoracic empyema. Curr Opin Pulm Med 6(3):234–239

Nour-Eldin NE, Alsubhi M, Naguib NN, Lehnert T, Emam A, Beeres M et al (2014) Risk factor analysis of pulmonary hemorrhage complicating CT-guided lung biopsy in coaxial and non-coaxial core biopsy techniques in 650 patients. Eur J Radiol 83(10):1945–1952

O'Neill AC, McCarthy C, Ridge CA, Mitchell P, Hanrahan E, Butler M et al (2012) Rapid needle-out patient-rollover time after percutaneous CT-guided transthoracic biopsy of lung nodules: effect on pneumothorax rate. Radiology 262(1):314–319

Palussiere J, Canella M, Cornelis F, Catena V, Descat E, Brouste V et al (2013) Retrospective review of thoracic neural damage during lung ablation – what the interventional radiologist needs to know about neural thoracic anatomy. Cardiovasc Intervent Radiol 36(6):1602–1613

Pennathur A, Luketich JD, Abbas G, Chen M, Fernando HC, Gooding WE et al (2007) Radiofrequency ablation for the treatment of stage I non-small cell lung cancer in high-risk patients. J Thorac Cardiovasc Surg 134(4):857–864

Pereira PL, Masala S, Cardiovascular, Interventional Radiological Society of E (2012) Standards of practice: guidelines for thermal ablation of primary and secondary lung tumors. Cardiovasc Intervent Radiol 35(2):247–254

Petre EN, Jia X, Thornton RH, Sofocleous CT, Alago W, Kemeny NE et al (2013) Treatment of pulmonary colorectal metastases by radiofrequency ablation. Clin Colorectal Cancer 12(1):37–44

Pittet O, Christodoulou M, Pezzetta E, Schmidt S, Schnyder P, Ris HB (2007) Video-assisted thoracoscopic resection of a small pulmonary nodule after computed tomography-guided localization with a hook-wire system. Experience in 45 consecutive patients. World J Surg 31(3):575–578

Powell TI, Jangra D, Clifton JC, Lara-Guerra H, Church N, English J et al (2004) Peripheral lung nodules: fluoroscopically guided video-assisted thoracoscopic resection after computed tomography-guided localization using platinum microcoils. Ann Surg 240(3):481–488; discussion 488–489

Priola AM, Priola SM, Cataldi A, Ferrero B, Garofalo G, Errico L et al (2008) CT-guided percutaneous transthoracic biopsy in the diagnosis of mediastinal masses: evaluation of 73 procedures. Radiol Med 113(1):3–15

Prosch H, Stadler A, Schilling M, Burklin S, Eisenhuber E, Schober E et al (2012) CT fluoroscopy-guided vs. multislice CT biopsy mode-guided lung biopsies: accuracy, complications and radiation dose. Eur J Radiol 81(5):1029–1033

Ridge CA, Silk M, Petre EN, Erinjeri JP, Alago W, Downey RJ et al (2014) Radiofrequency ablation of T1 lung carcinoma: comparison of outcomes for first primary, metachronous, and synchronous lung tumors. J Vasc Interv Radiol 25(7):989–996

Rossi S, Fornari F, Pathies C, Buscarini L (1990) Thermal lesions induced by 480 KHz localized current field in guinea pig and pig liver. Tumori 76(1):54–57

Ryan ER, Thornton R, Sofocleous CT, Erinjeri JP, Hsu M, Quinn B et al (2013) PET/CT-guided interventions: personnel radiation dose. Cardiovasc Intervent Radiol 36(4):1063–1067

Sano Y, Kanazawa S, Mimura H, Gobara H, Hiraki T, Fujiwara H et al (2008) A novel strategy for treatment of metastatic pulmonary tumors: radiofrequency ablation in conjunction with surgery. J Thorac Oncol 3(3):283–288

Sapareto SA, Dewey WC (1984) Thermal dose determination in cancer therapy. Int J Radiat Oncol Biol Phys 10(6):787–800

Sarti M, Brehmer WP, Gay SB (2012) Low-dose techniques in CT-guided interventions. Radiographics 32(4):1109–1119; discussion 1119–1120

Schubert P, Wright CA, Louw M, Brundyn K, Theron J, Bolliger CT et al (2005) Ultrasound-assisted transthoracic biopsy: cells or sections? Diagn Cytopathol 33(4):233–237

Schweigert M, Dubecz A, Stadlhuber RJ, Stein HJ (2011) Modern history of surgical management of lung abscess: from Harold Neuhof to current concepts. Ann Thorac Surg 92(6):2293–2297

Sconfienza LM, Mauri G, Grossi F, Truini M, Serafini G, Sardanelli F et al (2013) Pleural and peripheral lung lesions: comparison of US- and CT-guided biopsy. Radiology 266(3):930–935

Scott EM, Marshall TJ, Flower CD, Stewart S (1995) Diffuse pleural thickening: percutaneous CT-guided cutting needle biopsy. Radiology 194(3):867–870

Sharma A, Moore WH, Lanuti M, Shepard JA (2011) How I do it: radiofrequency ablation and cryoablation of lung tumors. J Thorac Imaging 26(2):162–174

Silverman SG, Tuncali K, Adams DF, Nawfel RD, Zou KH, Judy PF (1999) CT fluoroscopy-guided abdominal interventions: techniques, results, and radiation exposure. Radiology 212(3):673–681

Simon CJ, Dupuy DE, DiPetrillo TA, Safran HP, Grieco CA, Ng T et al (2007) Pulmonary radiofrequency ablation: long-term safety and efficacy in 153 patients. Radiology 243(1):268–275

Siperstein AE, Rogers SJ, Hansen PD, Gitomirsky A (1997) Laparoscopic thermal ablation of hepatic neuroendocrine tumor metastases. Surgery 122(6):1147–1154; discussion 1154–1155

Stoeckelhuber BM, Leibecke T, Schulz E, Melchert UH, Bergmann-Koester CU, Helmberger T et al (2005) Radiation dose to the radiologist's hand during continuous CT fluoroscopy-guided interventions. Cardiovasc Intervent Radiol 28(5):589–594

Sun YH, Song PY, Guo Y, Sheng LJ (2015) Computed tomography-guided percutaneous microwave ablation therapy for lung cancer. Genet Mol Res 14(2):4858–4864

Trumm CG, Haussler SM, Muacevic A, Stahl R, Stintzing S, Paprottka PM et al (2014) CT fluoroscopy-guided percutaneous fiducial marker placement for CyberKnife stereotactic radiosurgery: technical results and complications in 222 consecutive procedures. J Vasc Interv Radiol 25(5):760–768

vanSonnenberg E, Casola G, Ho M, Neff CC, Varney RR, Wittich GR et al (1988) Difficult thoracic lesions: CT-guided biopsy experience in 150 cases. Radiology 167(2):457–461

Wali SO (2012) An update on the drainage of pyogenic lung abscesses. Ann Thorac Med 7(1):3–7

Wiener RS, Schwartz LM, Woloshin S, Welch HG (2011) Population-based risk for complications after transthoracic needle lung biopsy of a pulmonary nodule: an analysis of discharge records. Ann Intern Med 155(3):137–144

Wolf FJ, Grand DJ, Machan JT, Dipetrillo TA, Mayo-Smith WW, Dupuy DE (2008) Microwave ablation of lung malignancies: effectiveness, CT findings, and safety in 50 patients. Radiology 247(3):871–879

Woody NM, Djemil T, Adelstein DJ, Mason DP, Rice TW, Videtic GM (2010) Severe local toxicity after lung stereotactic body radiation therapy: lesional abscess leading to bronchocutaneous fistula requiring surgical marsupialization. J Thorac Oncol 5(11):1874–1875

Yamagami T, Terayama K, Yoshimatsu R, Matsumoto T, Miura H, Nishimura T (2009) Role of manual aspiration in treating pneumothorax after computed tomography-guided lung biopsy. Acta Radiol 50(10):1126–1133

Yamakado K, Inoue Y, Takao M, Takaki H, Nakatsuka A, Uraki J et al (2009) Long-term results of radiofrequency ablation in colorectal lung metastases: single center experience. Oncol Rep 22(4):885–891

Yamauchi Y, Izumi Y, Kawamura M, Nakatsuka S, Yashiro H, Tsukada N et al (2011) Percutaneous cryoablation of pulmonary metastases from colorectal cancer. PLoS One 6(11):e27086

Yamauchi Y, Izumi Y, Hashimoto K, Yashiro H, Inoue M, Nakatsuka S et al (2012) Percutaneous cryoablation for the treatment of medically inoperable stage I non-small cell lung cancer. PLoS One 7(3):e33223

Yan TD, King J, Sjarif A, Glenn D, Steinke K, Morris DL (2006) Percutaneous radiofrequency ablation of pulmonary metastases from colorectal carcinoma: prognostic determinants for survival. Ann Surg Oncol 13(11):1529–1537

Yang W, Sun W, Li Q, Yao Y, Lv T, Zeng J et al (2015) Diagnostic accuracy of CT-guided transthoracic needle biopsy for solitary pulmonary nodules. PLoS One 10(6):e0131373

Yankelevitz DF, Vazquez M, Henschke CI (2000) Special techniques in transthoracic needle biopsy of pulmonary nodules. Radiol Clin North Am 38(2):267–279

Yildirim E, Kirbas I, Harman A, Ozyer U, Tore HG, Aytekin C et al (2009) CT-guided cutting needle lung biopsy using modified coaxial technique: factors effecting risk of complications. Eur J Radiol 70(1): 57–60

Yu H (2011) Management of pleural effusion, empyema, and lung abscess. Semin Interv Radiol 28(1):75–86

Zaetta JM, Licht MO, Fisher JS, Avelar RL, Bio-Seal SG (2010) A lung biopsy tract plug for reduction of postbiopsy pneumothorax and other complications: results of a prospective, multicenter, randomized, controlled clinical study. J Vasc Interv Radiol 21(8):1235–1243.e1–3

Zaman M, Bilal H, Woo CY, Tang A (2012) In patients undergoing video-assisted thoracoscopic surgery excision, what is the best way to locate a subcentimetre solitary pulmonary nodule in order to achieve successful excision? Interact Cardiovasc Thorac Surg 15(2):266–272

Zemlyak A, Moore WH, Bilfinger TV (2010) Comparison of survival after sublobar resections and ablative therapies for stage I non-small cell lung cancer. J Am Coll Surg 211(1):68–72

Medical-Legal Aspects of Multidetector CT

Jochen M. Grimm and Jim Potchen

Abstract

What are the medical-legal ramifications of multidetector CT? This chapter seeks to review the basis of medical-legal responsibility when advocating and implementing multidetector CT in the diagnosis of thoracic lesions. An example drawn from personal experience will be presented as a framework for analysis. This case exemplifies some legal issues that can embroil the practice of radiology. Medical malpractice litigation dominates the medical-legal ramifications of diagnostic imaging. Typically, radiologists are concerned about being sued for a failure to diagnose something that is subsequently demonstrated to have been present on the image, but it was either not observed or not correctly interpreted by the person who reported the film. In any diagnostic procedure, though mostly discussed in conjunction with "screening" procedures, a false-positive result can potentially injure the patient as much as a false-negative result. But also the diagnostic procedure itself may harm the patient, e.g., through an adverse reaction to contrast agent or through potentially carcinogenic effects of ionizing radiation. A different legal aspect may be encountered in cases of imaging for forensic rather than medical purposes, a field in which the application of ionizing radiation needs to be justified by other than medical reasons. Prominent examples of forensic indications are abdominal imaging in suspected drug couriers (body packers) or hand and wrist imaging in forensic age estimation; the thoracic region is only peripherally concerned, e.g., in age estimation by CT of the sternoclavicular joints. Last but not the least, postmortem MDCT for determining the cause of death in a deceased is becoming more widely used with completely different medical-legal implications.

J.M. Grimm, MD (✉)
Department of Medical Radiology, University Hospital Center and University of Lausanne, Lausanne, Switzerland

University Center of Legal Medicine Lausanne/Geneva, Lausanne, Switzerland
e-mail: jgrimm@imagomed-diagnostik.de

J. Potchen, MD
Department of Radiology, Michigan State University, 160 Radiology Building, East Lansing, MI 48824, USA

U.J. Schoepf, F.G. Meinel (eds.), *Multidetector-Row CT of the Thorax*, Medical Radiology,
DOI 10.1007/978-3-319-30355-0_27

1 Malpractice

1.1 The Diagnostic Dilemma

As with any diagnostic procedure, radiological reporting is susceptible to error. In most cases, a radiological diagnosis is not the gold standard for the final determination of the nature of a pathological condition, and often either a surgeon or pathologist or simply the development of a condition will prove the radiological diagnosis correct or incorrect. Apart from which findings the radiologist sees or fails to detect, his decisions on what to report and how to report it are often made under conditions of uncertainty. Human decisions under uncertainty have an error rate. The size of the error rate will likely decrease with increasing experience. What can be influenced independently from experience is the tendency toward false-positive or false-negative diagnostic errors. False-negative errors result in a delay of the correct diagnosis and adequate therapy with potential harm to the patient. False-positive errors result in unnecessary diagnostic and/or therapeutic procedures with potential harm to the patient and certain economic harm to the healthcare system. The question is which type of error is worse for whom. Both false-positive and false-negative errors can potentially harm or even kill the patient; so under the principle to cure the patient and avoid any unnecessary harm, no a priori decision on which type of error is preferable can be made. Despite this, the subjective effect of both errors on the patient is very different. With false-positive errors, actions are taken, the patient remains involved in the decision-making process, and the final result that there actually was no relevant pathology is a relief. False-negative errors result in passivity – at least for some time – and when the pathology is finally discovered, the patient will be unhappy with the bad news and the fact that something could have been done in the meantime. A patient is thus much more likely to seek malpractice litigation after a false-negative error than a false-positive one. Thus, it is psychologically reasonable for both the physician and the patient – the two parties who decide about the further course of action – to err on the false-positive rather than false-negative side. The effect is an increasingly "defensive" practice of medicine with huge economic consequences. Furthermore, if the false-positive error rate becomes too large, more patients are harmed than cured – an issue which has been broadly discussed in the context of screening programs (Swensen 2002). No general suggestion can be made on how to deal with ambiguous cases; the best solution depends on the individual situation. It is reasonable for the physician to be aware of risk and consequences of malpractice litigation. In case of doubt, it is reasonable to document the uncertainty in the written radiological report and discuss it with the referring physician. Communication with the patient is equally important, especially in cases where an error has already been discovered.

1.2 A Case of Lung Cancer

The problem of identifying early lung cancer on multidetector CT is well exemplified in a case where the CT was done to evaluate an abdominal problem. This eventually resulted in malpractice litigation for failure to classify properly an abnormality seen in the lung on the abdominal CT. The patient presented with acute abdominal pain and was ultimately diagnosed as having acute diverticulitis with subsequent peritonitis. The patient was in severe pain from her abdominal problem and an abdominal CT was performed (Fig. 1). The report associated with those images is as follows: Correlation is made with an abdominal ultrasound dated 4/22/97. A study is performed with 110 cc of Hypaque 60 contrast. Limited study through the lung bases demonstrates a 1.8 cm mass in the lingula of the left lung containing central calcification most consistent with a granuloma. The lung bases are otherwise clear with no evidence of pleural fluid. The pre-contrast study demonstrates focal area of amorphous low density in the pelvis which may represent multiple adherent unopacified bowel loops versus fluid around the bowel in the region of the sigmoid colon. There are also perirectal inflammatory changes in the mesentery. Though the contrast-enhanced study is obtained relatively delayed because of mechanical failure, this region is persistent and may represent sigmoid colonic diverticulitis. The inflammatory changes around the rectosigmoid region are again noted.

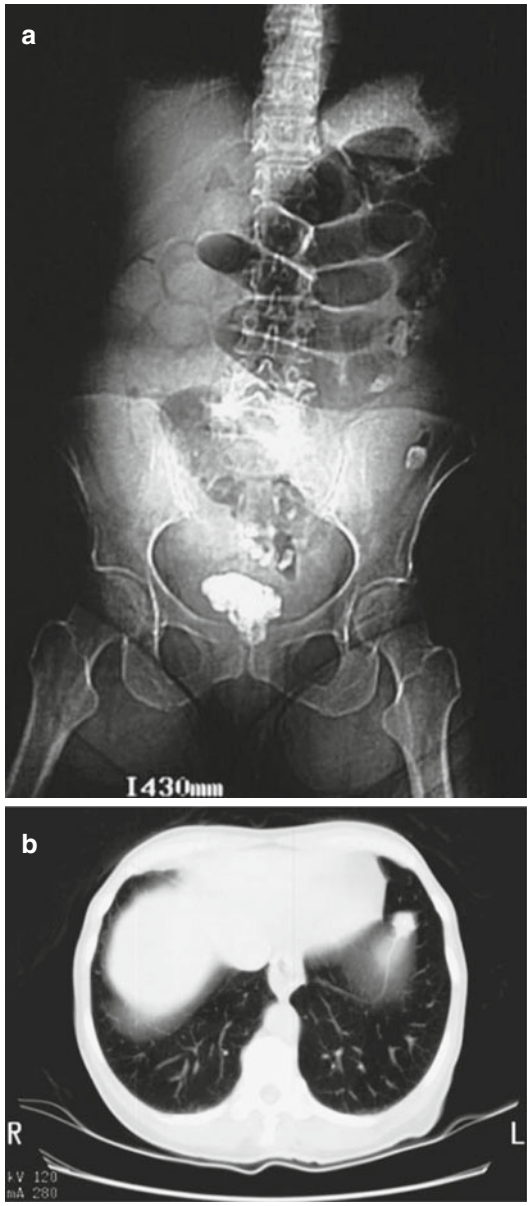

Fig. 1 (**a**) Initial abdominal CT in a patient ultimately diagnosed with acute diverticulitis and peritonitis. (**b**) This shows the lower portion of the chest, included in the initial abdominal CT, revealing an abnormality in the left lower lung field having the appearance of an irregular nodule with calcification

There are a cyst in the mid-pole of the right kidney and no free fluid in the upper abdomen. No free air is identified. There appears to be a calcification in the region of the right ureter with mild distension of the right renal collecting system and streaky opacification of the right kidney following contrast. This calcification, possibly intraureteral, may be partially occlusive. *Impression*: (1) There is perirectal and pericolonic mesenteric stranding possibly associated with fluid around the sigmoid colon. These findings may be related to diverticulitis. (2) Partially occlusive right ureteral calculus with mild right-sided hydronephrosis and streaky opacification of the right kidney. (3) Status post-hysterectomy. (4) A 1.85 cm granuloma in the left lung. (5) Right-sided renal cyst. On the basis of this CT image, the radiologist reported the presence of a 1.85 cm granuloma in the left lung. The referring surgeon therefore considered this to be a benign process. A subsequent CT study performed two days later, with contrast, stated that there were some nonspecific increased markings in the lung bases. Again, the CT primarily emphasized the abnormality in the abdomen for which the examination was performed. More than 1 year later, the patient presented with chest symptoms, and evidence of malignancy was found on CT. The case ultimately went to litigation. In this case, the lung abnormality was detected, but the interpretation of the abnormality was in question. The radiologists were not accused of a failure to detect the lesion; rather, the plaintiff complained of a failure by the radiologist to interpret correctly what was observed. The radiologist, who identified the abnormality, was not held responsible for malpractice, whereas the second radiologist, who did not comment on the abnormality, was found guilty. In the opinion of an expert called to testify, the first radiologist did what a reasonably prudent radiologist would do under the same or similar circumstances. Another expert considered the radiologist's action to be a breach of the standard of care, in that he believed the report should have been constructed to alert the surgeon that this abnormality might have been due to a lung cancer rather than a granuloma. The trial testimony revolved around whether the diagnostic impression of granuloma was a breach of the standard of care. Was the calcification central or eccentric? Was the pattern of the density consistent with a granuloma? In court, references taken from journal articles (Siegelman et al. 1986) were used in an attempt to teach the jury whether or not a reasonably

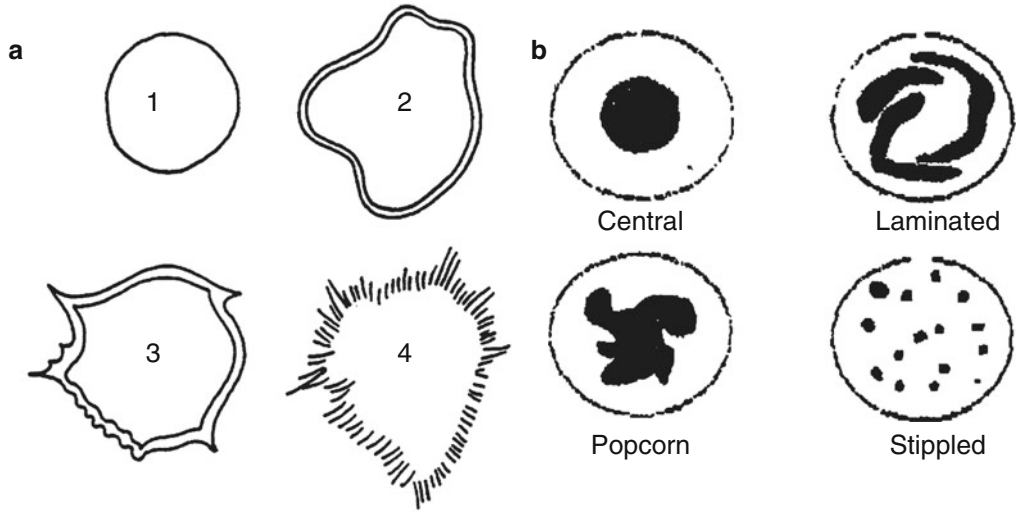

Fig. 2 (**a**) Figure taken from a radiologic text used in Court, by the Plaintiff, in an attempt to have the expert witness define specifically the nature and character of the nodular lesion seen in the lung. (**b**) Figure taken from a radiologic test used in Court, by the Plaintiff, in an effort to have the radiologic expert witness define the nature of the calcifications seen in the CT studyure 2b Figure taken from a radiologic test used in Court, by the Plaintiff, in an effort to have the radiologic expert witness define the nature of the calcifications seen in the CT study

prudent person would have concluded that this was a granuloma (Fig. 2). The jury was presented a detailed tutorial regarding the attributes used by radiologists to distinguish a granuloma from a malignancy when interpreting multislice CT images. They were instructed on the patterns of calcification and the subtleties of edge analysis that are applied in ascertaining whether the lesion was smooth, rounded, lobular, or spiculated. The details that are presented in jury instruction in such cases astound most radiologists who are being defended for potential malpractice litigation. In this instance, the plaintiff was seeking damages in excess of $5 million. Prior to litigation, the defendant had offered some $1 million in settlement, which was refused by the plaintiff. During the course of litigation, there was a concern early in the trial that the evidence was not sufficiently compelling for an acquittal of the defendant. The defendant's counsel agreed to increase the settlement. These offers were refused by the plaintiff. This is not unusual for cases where the plaintiff is confident that he or she will be victorious in the jury's decision. However, in this case, the last part of the testimony read to the jury was from the notes in the file of the defendant's expert. *Notes for File*: The patient presents with acute diverticulitis and a pericolonic abscess. A CT of the abdomen was performed, which clearly shows a substantial abnormality in the pelvis. There is an incidental peripheral note made of what may be a granuloma in the lingula of the left lung. The conclusion of the radiologist is that it was a granuloma. That is what a reasonably prudent physician may do under the same or similar circumstances. In this case, however, it appears to have been in error. Apparently, this turned out to be a carcinoma. I believe that one would not expect the surgeon to do anymore about this case once the definitive statement of granuloma is made and that statement may be slightly overreaching compared to what I would have said. However, in my opinion, it is not inconsistent with what a reasonably well-qualified physician may have done under the same circumstances. This testimony conveyed sufficient uncertainty for the jury to diminish the award below what had been offered to the plaintiff. The modulation in the magnitude of the award was, in part, due to the jury's awareness that a normally prudent radiologist may well have concluded this to be a granuloma. This case

raises many issues that are extremely common when reviewing multidetector CTs of the chest.

1.3 Malpractice in the USA

Reviews of American medical practice suggest that the number of malpractice cases filed is considerably fewer than the number of malpractice events that have occurred. There are far fewer malpractice claims filed in court than malpractice incidents which take place in the American healthcare system (Weller 1995). The median period between the occurrence of the malpractice incident and a payment for the injury is 3 years. In some 40 million patients hospitalized each year in the USA, it is estimated that 1.5 million suffer some kind of disabling injury on the basis of this medical encounter. Of these, approximately 400,000 involve negligence on the part of some provider. More than 100,000 involve fatal and serious permanent injuries. However, less than 50,000 malpractice suits are filed every year, fewer than half of the claimants receive any payments, and a sizable number of the remainder collect very little money because of the "tenuous quality of the claims." Twice the proportion (11 % vs. 5 %) of malpractice suits go to trial than do other types of personal injury suits. This is, in part, because the public, as a whole, has confidence in physicians, and many people realize that physicians, too, are human. If physicians believe this and act in a caring manner, malpractice litigation can often be avoided by the patient who believes that the physician did his or her best in any given situation. Indeed, the best protection against malpractice litigation, in addition to diminishing errors, is to have a favorable relationship with a patient. Most patients realize that medicine is imperfect. Physicians should also realize that. The arrogance of medicine does more to initiate malpractice litigation than any other single element. In fact, if one starts to trace the initial consideration of malpractice litigation from patients, the findings will point to the physician who did not respect the patient's concerns to the level that the patient felt was appropriate. The citizens and lawyers of the USA are not wantonly litigious. A nationwide RAND Institute survey found that of every 100 citizens who reported they were injured, only 19 considered legal action. Only seven of those consulted a lawyer, and only two of them found a lawyer willing to file a suit. In this instance, only one of those 100 collected any tort damage, whether by settlement or by verdict (Weller 1995). The frequency with which lung lesions are missed on chest X-ray has been well documented (Muhm et al. 1983). With the use of CT, there may be fewer missed lesions, but there are more likely to be more false-positive interpretations. While litigation for false-positive diagnosis is by no means as common as litigation for a diagnosis where the lesion is subsequently found, the fact is that thoracic multislice CT studies produce many more false-positive results, which occasionally injure the patient. This suggests that an overabundance of false-positive interpretations may become an increasing problem for the medical-legal system. In the NSCLC Study (US Public Health Service 1981; Potchen and Austin 1993), the correct diagnosis for 19 % of 259 patients with non-small cell lung cancer, which presented as a nodular lesion in the chest radiograph, was initially missed. It was only discovered on a later study. This miss rate was not dependent on location. Superimposing structures were more often present in the group of missed lesions, and, therefore, it is likely that CT will pick up many of these lesions not identified on plain chest films, at the cost of a higher false-positive error rate.

1.4 The Legal Basis for Malpractice Litigation

Even though the legal systems in different countries vary widely, the legal elements required in order for medical malpractice litigation to be successful are similar. Five requirements are found in most legislations:

1. A *duty* in relation to the patient. In medical malpractice litigation, the duty in question is regularly the physician's duty to practice to the standard of care. It can originate from a

law or from a contract between the patient and the physician or the hospital.

2. This duty must be *breached*. For example, the professional duty is breached when a physician does not practice to the standard of care. A breach requires an act that a responsible person would not do. What is a responsible person? An external standard is applied to the situation, i.e., unbiased experts have to conclude that the act done was or was not what a responsible person would do. The words used in evidence are "what a reasonably prudent person would do under the same or similar circumstances." Thus, the standard of care is not based on what an individual physician presumes is wrong or right in a specific case; rather, it relates to the contest of experts. The experts' arguments have to be sufficiently concise and complete to be believed by the independent trier of fact, either a judge or a jury. Most legislations also require a personal fault of the physician, i.e., there must not be any sufficient justification or exculpation for the actions taken or omitted by the physician.
3. There must be a *substantial injury* to the patient. This means that the patient must have suffered a greater than negligible physical, psychological, or economic harm compared to the hypothetical situation without a breach of duty.
4. The breach of duty must be the *proximate cause* of the injury. The requirement for proximate cause is often not understood by physicians being sued for medical malpractice. The legal thresholds of a causal relationship between an act and an injury begin with the "but for" doctrine. This means that but for the action of the physician, the patient would not have sustained an injury. While this is a necessary component of cause, it is insufficient. The legal term for the threshold required for a successful malpractice action by a plaintiff is "proximate cause." Not only would the injury not have occurred "but for" the actions of the physician, but there were no intervening causes between what the physician did and what happened to the patient. The negligent act must be the "proximate" cause of the injury. Often in malpractice litigation, even when the physicians are found to be in breach of a standard of care, they are not found guilty of negligence, because what they did was not the proximate cause of the injury sustained by the patient. All four elements (duty, breach, substantial injury, and proximate cause) are necessary before medical malpractice can be established. In some cases, even though there is an obvious breach of a duty, the patient is so ill at the time of the radiologic procedure that even if the diagnosis had been made at the time the radiologist missed the lesion, it would have had little or no effect on what eventually happened to the patient. In this instance, even an egregious error may not be considered to be the proximate cause of "a substantial injury." For example, in some cases of lung cancer, the disease is so far advanced at the time of the initial imaging procedure that the death of the patient would have occurred even had the radiologist been correct in the interpretation.

Many legal actions – especially in ambiguous cases – are decided by the burden of proof. In most legal systems, the patient has the burden of proof for all four of the stated requirements. Especially the proximity of the cause of the injury is often very difficult to prove, and many legal actions are unsuccessful for failure to prove this proximity. Therefore, some legislations modify the burden of proof regarding the causality of a breach of the standard of care in favor of the patient.

While the most common case of malpractice litigation regarding radiology is the failure to report something that was later seen by someone else or misinterpretation of findings, other cases go into litigation for failure to perform necessary diagnostic procedures or harm done to a patient during a diagnostic procedure. These cases follow the same general principles as misdiagnosis cases, with some differences in the details. Especially in recent times, an increasing number of legal actions against physicians are based on improper information of the patient prior to an intervention or incomplete documentation.

Without legally correct informed consent of the patient, most legislations consider medical interventions illegal infliction of bodily harm. Documentation is therefore an indispensable means of protection from litigation. What has not been documented has not happened, unless proven otherwise – a proof which is regularly very difficult and in most cases impossible.

2 Forensic Imaging in the Living

Forensic imaging in the living is to date mainly performed using ionizing radiation, mostly X-ray and CT. The associated – albeit small – risk of radiation-induced cancer can in forensic cases not be counterbalanced by a medical benefit for the examined person. Thus, the justification for potentially inflicting harm to a person is the functionality of the forensic system or, more generally, the welfare of the society as a whole. While the potential harm for the examined individual is large but unlikely, the benefit for society is not measurable for any individual case. It is therefore difficult to balance risk and benefit in these cases. Nonetheless, forensic imaging in the living using ionizing radiation is accepted and regularly performed in most legislations, even though most legal systems lack definite regulations. Both public and scientific attention to this issue are virtually nonexistent, which is owed to the fact that the practical relevance of this problem is equally low, considering the low incidence and long latency of radiation-induced cancer in conjunction with relatively low frequency of forensically examined persons seeking legal action against radiologists. Furthermore, this problem is likely to become smaller with technological advances, especially the increasing availability and utility of MRI.

3 Postmortem CT

Especially in recent years, the interest in postmortem imaging has increased considerably. Institutes of forensic pathology are beginning to install dedicated CT scanners for forensic imaging. Existing studies suggest that in some cases the cause of death of a person can be determined by imaging (Chevallier et al. 2013); some even suggest that the new gold standard for determining the cause of death in some cases is no longer autopsy but rather a combination of autopsy and (contrast-enhanced) postmortem imaging (Grabherr et al. 2014, 2015). Today, the lack of a dedicated subspecialty in forensic radiology keeps the subject interdisciplinary with an important role for radiologists. Advantages over invasive procedures like autopsy are numerous: The body stays intact, images can be archived and subjected to a "second look," 3D reconstructions make demonstrating lesions in court a lot easier than autopsy photographs, etc. Postmortem CT plays a role not only in solving forensic cases but also in clinical pathology, where it could become an important tool of medical quality management. While it is highly unlikely that imaging will completely replace autopsy at least in the near future, the subject can be expected to continue its rapid growth. In many cases the cause of death is to be found in the thoracic region, so interested radiologists should keep an eye on the development of postmortem CT and its potential applications.

References

Chevallier C, Doenz F, Vaucher P, Palmiere C, Dominguez A, Binaghi S, Mangin P, Grabherr S (2013) Postmortem computed tomography angiography vs. conventional autopsy: advantages and inconveniences of each method. Int J Legal Med 127(5):981–989. doi:10.1007/s00414-012-0814-3

Grabherr S, Grimm J, Dominguez A, Vanhaebost J, Mangin P (2014) Advances in post-mortem CT-angiography. Br J Radiol 87(1036):20130488. doi:10.1259/bjr.20130488

Grabherr S, Grimm J, Baumann P, Mangin P (2015) Application of contrast media in post-mortem imaging (CT and MRI). Radiol Med 120(9):824–34.

Muhm J, Miller WE, Fontana RS, Sanderson DR, Uhlenhopp MA (1983) Lung cancer detected during a screening program using four-month chest radiographs. Radiology 148:609–615

Natl Cancer Inst Monogr 57 Weller PC (1995) Fixing the tail: the place of malpractice in health care reform. Rudgers Law Review, Spring, p 1157

Potchen EJ, Austin JHM (1993) Problems and pitfalls in the diagnosis of early lung cancer. In: Potchen EJ, Granger RG, Greene R (eds) Pulmonary radiology. The Fleischner Society. Saunders, Philadelphia

US Public Health Service, Young JL Jr, Percy CL, Asire AJ (eds) (1981) Surveillance, epidemiology and end results program: incidence and mortality data, 1973–1977. Natl Cancer Inst Mongr 57:1–1082

Siegelman SS, Khouri NF, Leo FP, Fishman EK, Braverman RM, Zerhouni EA (1986) Solitary pulmonary nodules: CT assessment. Radiology 160: 307–312

Swensen S (2002) High false-positive rate seen with CT scans for lung. Am J Roentgenol 179:833–842

Future Developments for CT of the Thorax

Willi A. Kalender and Michael M. Lell

Abstract

This final chapter of the book discusses possible or likely developments in technology needed for the thoracic region, i.e. for lung, cardiac and even breast imaging by CT. Respective activities related to hardware, software and applications are addressed in the next two sections. Considerations on image quality and dose will point out some basic physics constraints that have to be kept in mind. Application-related aspects are taken into account throughout the chapter.

1 Introduction

What will the future bring? It is unnecessary to state that any prediction may prove to be wrong in the years to come or, in the worst case, as soon as the book is printed. Predictions or, better, the discussion of future developments can be based on what technology and physics may provide or it can be based on what the clinical demands are or will likely be. Future developments can be either technology driven or application driven or both. In any case, the most recent developments in CT technology will have to be reviewed and taken into account, in particular when they apply to organs of the thoracic region such as the lungs, heart, and breasts.

The development of spiral CT, which provided great advantages for CT of the thorax in the 1980s, serves as a good example for an innovation both application and technology driven. The project was initiated by the desire to detect pulmonary nodules reliably (Kalender et al. 1990; Vock et al. 1990). It became possible with the availability of slip-ring technology, which allowed for continuous scanning over many rotations. While it was easy to show early on that spiral CT allowed to provide the necessary performance in principle (Fig. 1a), it also became apparent immediately that other relevant technologies, in particular the available x-ray power

W.A. Kalender, PhD (✉)
Institute of Medical Physics, University of Erlangen-Nürnberg, Henkestr. 91, 91058 Erlangen, Germany
e-mail: willi@imp.uni-erlangen.de; http://www.imp.uni-erlangen.de

M.M. Lell, MD
Department of Radiology, Friedrich-Alexander University Erlangen-Nürnberg, Maximiliansplatz 1, 91054 Erlangen, Germany
e-mail: michael.lell@uk-erlangen.de

U.J. Schoepf, F.G. Meinel (eds.), *Multidetector-Row CT of the Thorax*, Medical Radiology,
DOI 10.1007/978-3-319-30355-0_28

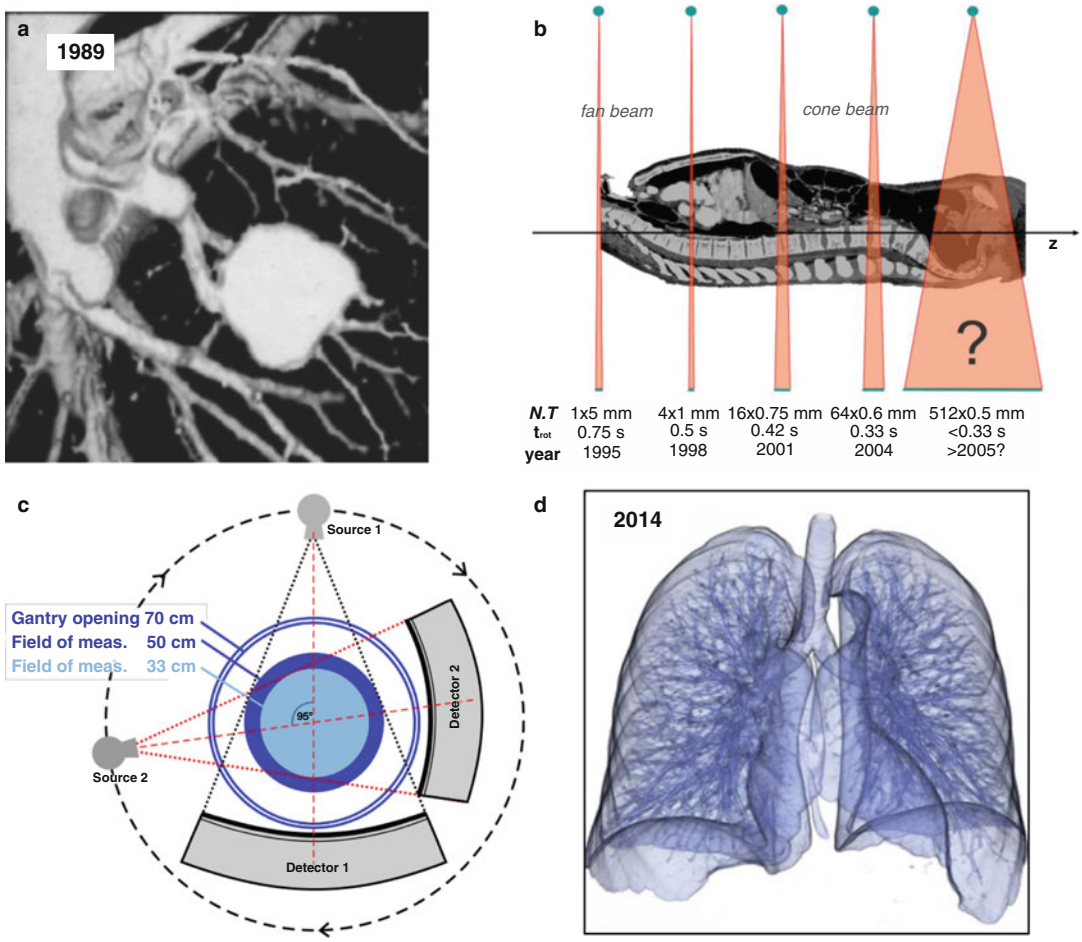

Fig. 1 The introduction of spiral scanning had tremendous impact on CT within the past 25 years. The first scan of the thorax in 1989 (**a**) was taken with a single-row scanner at 10 mm collimation. The availability of multi-row detector technology (**b**) since 1998 meant a big boost in image quality. The introduction of dual-source CT (**c**) only 10 years later brought about further increases in performance (**d**) (Figures **b** and **c** are taken from Kalender 2011)

and detector design, were insufficient to image complete organs of large sizes such as the lungs fast enough and with high spatial resolution. This defined the general goal of modern CT to image complete organs in a very short time and at high isotropic resolution and included all applications involving contrast medium administration and CT angiography. Tremendous technological developments such as higher-power x-ray tubes and generators and, above all, multi-row detector technology ensued.

The state of the art which has been reached after 25 years of spiral CT is documented well in this textbook and is represented by scanners which allow acquiring 64 and up to 320 slices of less than 1 mm each simultaneously (Fig. 1b) with gantry rotation times per 360° of 0.3 s or slightly less. A particular highlight was the introduction of dual-source CT scanners (Fig. 1c) in the late 2000s which offer particular advantages for the time-critical lung and cardiac imaging. This has led to the remarkable clinical results described in an excellent manner in the preceding chapters. Isotropic submillimeter spatial resolution and effective scan time per image of 0.1 s and below are essential features and routinely available. CT has apparently reached a very high level of performance, and it may seem that today's CT scanners already fulfill all clinical demands.

Is there still a need for further technical developments in CT? Will future developments be driven by technological advances or by application demands? Economical reason tells us that developments have to be application driven. From the preceding chapters, we may conclude that modern CT covers almost every need and demand already. Nevertheless, we observe many continuing successful research and development efforts in the field of CT, which are addressed in this final chapter of the book.

2 Technical Developments

Technical developments can be divided into those related to scanner mechanics, x-ray system, detector etc., the "hardware" as the first category, and into image reconstruction, data handling, dedicated processing and evaluation software, etc., and the "software" as the second category. We here discuss hardware-related aspects first, and software and application-related aspects follow in the next section.

It is obvious that the rotation frequency of mechanical gantries can be increased further; there are many technical instruments of similar sizes and masses which rotate much faster. However, there are particular challenges related to CT: the number and the complexity of subsystems such as integrated circuit boards, rotating x-ray tubes anodes, etc., demand specific adaptations to cope with the increasing centrifugal forces. This may mean increased or prohibitive cost and, in the worst case, susceptibility of the equipment to reduced lifetime and finally failure. Another important aspect is that it will be difficult to provide the necessary x-ray power, i.e., the necessary number of x-ray photons for sufficient image quality, in shorter and shorter rotation times. Electron beam CT in the 1990s showed that it was capable of performing scans within as low as 50 ms (Boyd and Lipton 1983); however, for high enough image quality and good low-contrast resolution, single sweeps had to be added up resulting in high effective scan times. The necessary x-ray flux could not be provided although directly cooled stationary ring anodes were used (Kalender 2011).

Today's clinical CT scanners are facing similar x-ray power challenges. Fortunately these have been relieved significantly by two developments: (1) multi-row detectors with their wider collimation use more of the available x-ray cone (the resulting multi-slice scans allow for higher-volume scan speed and thereby for shorter total scan times which in turn allow for higher anode burdening); and (2) modern dose management with several innovative approaches to dose reduction have become available lately (see Sect. 28.4) and allow working with reduced x-ray power.

Today's top scanner models have already proven that they can provide the necessary x-ray power needed for rotation times of below 0.3 s and adequate thoracic CT scanning results (Fig. 2a, b). Dual-source CT does so in a convincing manner due to its particular advantage of employing two sources simultaneously, i.e., presently with 2 times 120 kW power levels (Lell et al. 2015a).

Further reduction of rotation times is frequently requested for cardiac applications. Rotation times of down to 0.2 s are a target and would allow for effective scan times of clearly below 100 ms. Faster scanners dedicated to cardiac applications are likely to become available in the foreseeable future. The dose management efforts addressed in Sect. 28.4 will be helpful in this as they imply the neat side effect of lower x-ray power demands.

A question frequently asked in the past was: Will the slice race continue? All manufacturers tried to live up to customer demands and expectations, and consequently they came up with solutions for detectors with higher and higher numbers of detector rows (Fig. 1b) which aim at covering the organ or region of interest in a single view. The slice race has certainly slowed down meanwhile and should come to a stop with respect to z-coverage because wider and wider x-ray beams entail a number of disadvantages with respect to image quality (Kalender 2011). Whenever thinner slices are provided, i.e., higher resolution in the longitudinal direction is provided without the widening of the total beam, larger numbers of slices are very welcome. An exemplary solution for CT of the breast will be pointed out in the final section.

Improvements with respect to x-ray power, an old and mature technology, will not be dramatic;

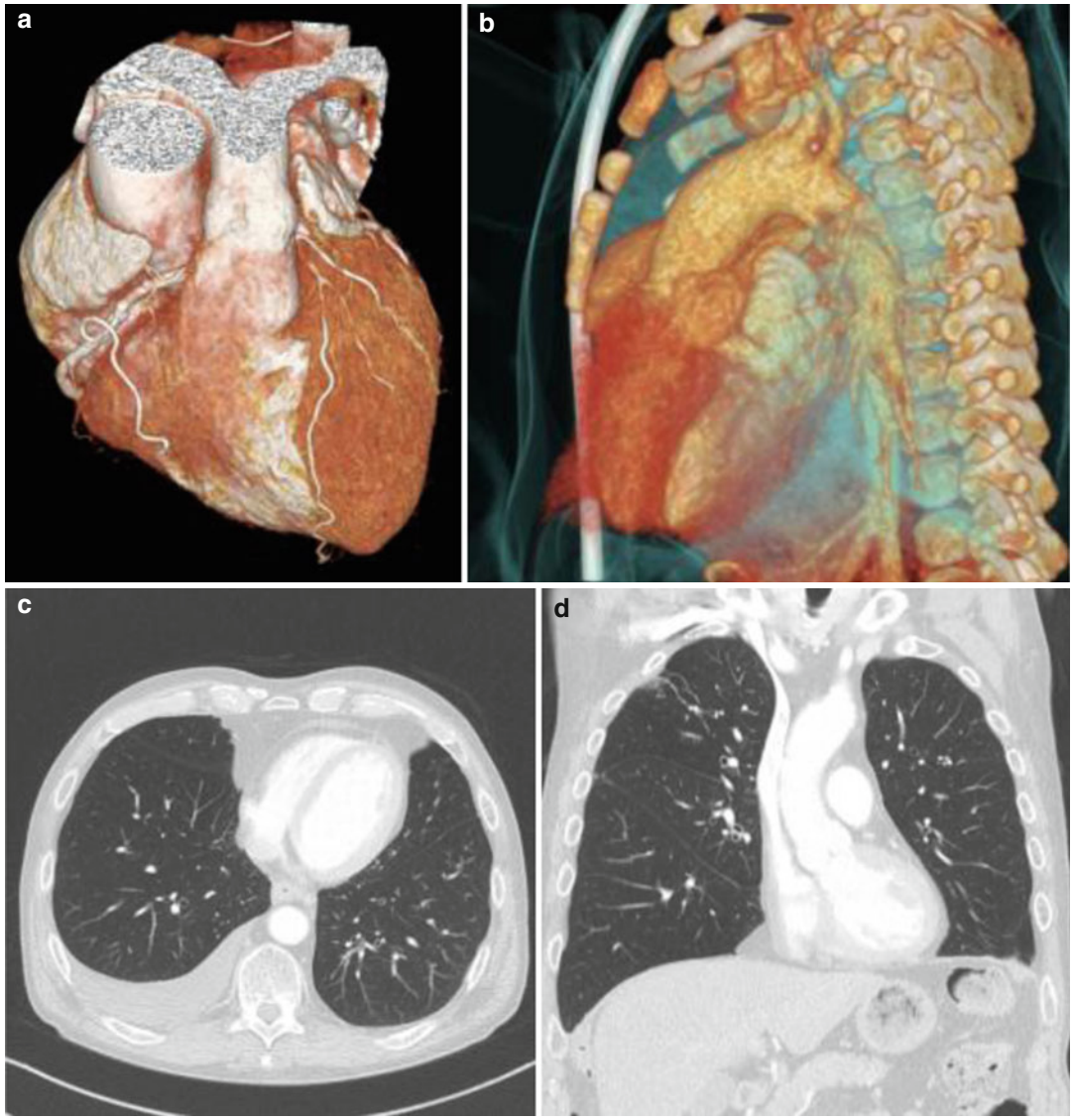

Fig. 2 Low-dose coronary CTA with atypical chest pain in a 70-year-old female patient with high-grade LAD stenosis (70 kV; effective dose 0.3 mSv) (**a**); CTA in a 3-month-old baby with complex CHD (Fallot tetralogy, right ventricular outflow obstruction, VSD, LPA stenosis; 70 kV, effective dose 0.29 mSv; no anesthesia) (**b**); non-ECG-gated high-pitch CT in a 77-year-old patient with shortness of breath. No motion artifacts in the lung parenchyma around the left ventricle (**c**, **d**)

tremendous improvements have already been provided since the introduction of spiral CT. The potential for further improvements appears limited and so is the motivation. The advent of multi-slice acquisition implied that the demand for long scan times and thereby for high average power diminished. Higher peak power ratings are of interest further on, in particular for cardiac CT with its short scan times. Availability of kV settings lower than 80 kV appears attractive as it allows reducing patient dose further without an impairment of image quality (Kalender et al. 2009; Lell et al. 2015b). Today most scanner models offer 80 kV, some even 70 kV. It may well be the case that, similar to traditional radiography, a wider range of selection and even 60 kV become available (Fig. 3).

With respect to further components, it is easy to predict that CT will benefit from general

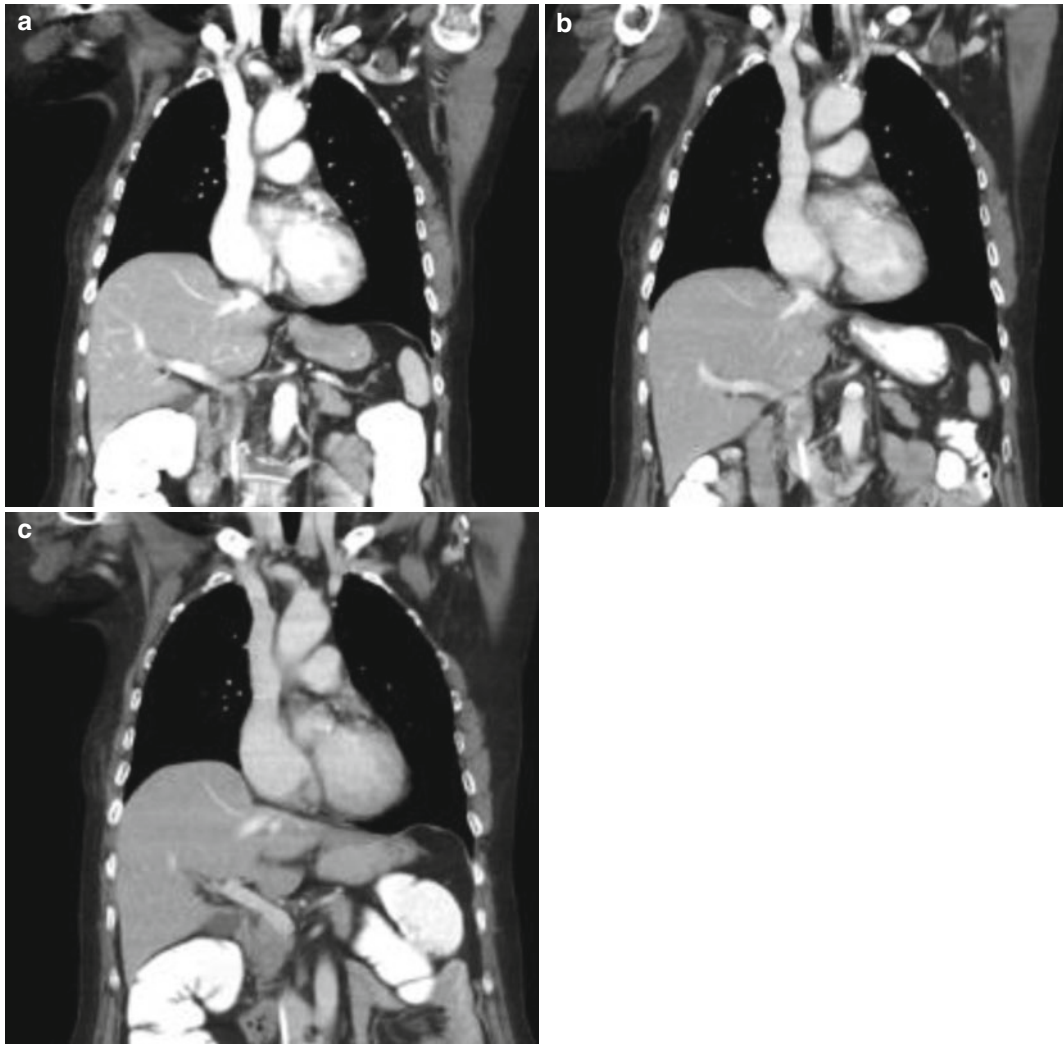

Fig. 3 (**a**–**c**) Follow-up examination of a 58-year-old female patient at different kV settings (**a**: 70 kV; **b**: 100 kV; **c**: 120 kV). The respective $CTDI_{vol}$ values were 5.56, 8.17, and 9.18 mGy

technical developments. For example, performance increases for computing power following Moore's law are likely. The same applies to data rendering and display technology.

3 Software and Application Developments

Some software developments have been addressed in previous chapters of this book already. No doubt, reconstruction approaches and speed of reconstruction will be improved further; model-based iterative reconstruction is and will remain a hot and very promising topic with further improvements to be expected. With increasing scan speed, decreasing slice thickness, and decreasing reconstruction times, the daily workload for radiologists will further increase. Data management algorithms will therefore be of increased importance in the future. In automatic detection of lung nodules, vessel stenoses, and vessel or bronchus labeling, registration with prior images is just the very basic beginning of such a task. Although such algorithms will not kick the radiologist out of business, they will probably group images into those with and those without pathologic findings and suggest

likely diagnoses enhancing both workflow and accuracy.

A relatively old problem in CT is artifacts from metal foreign bodies like fixation screws, prosthetic devices, wires, pacemakers, or ventricular assist devices (Fig. 4c, d). A number of different solutions have been advocated, but only recently these solutions became commercially available and can be routinely used to enhance image quality in CT (Meyer et al. 2012; Lell et al. 2012, 2013).

Subsecond chest CT became possible using the high-pitch mode and in pediatric imaging with large z-axis detector panels. This helps to reduce motion artifacts (Lell et al. 2009) and allows for exact anatomical mapping prior to surgery in neonates and small babies with congenital heart disease (CHD) without the need of anesthesia or sedation for imaging and at a very low radiation exposure (Fig. 2b) (Lell et al. 2011).

4D vascular imaging with high temporal resolution is beneficial in analyzing blood flow in complex vascular malformations and can help to plan interventional treatment or radiation therapy (Beijer et al. 2013). Similar to MR angiography, 4D CT angiography can improve results in peripheral arterial disease, where high-grade stenosis or occlusion may cause altered asymmetrical blood flow (Haubenreisser et al. 2015).

Dynamic contrast-enhanced CT (DCE-CT), often called perfusion CT, has been extensively evaluated in stroke imaging but also in oncologic imaging. Especially DCE-CT of bronchial carcinoma was limited by the small z-coverage in single-slice or early multi-slice CT, because of incomplete coverage and suboptimal means for reproducing image planes over a data collection time of 40 s or more (Ng et al. 2006; Klotz et al. 2015). Recent CT systems still face this problem with shuttle modes or wide detector panels. DCE-CT has demonstrated the potential of providing in vivo information about tumor vasculature and may depict specific perfusion changes in NSCLC in the early course of anti-angiogenic therapy, before tumor shrinkage occurs (Fraioli et al. 2013). Thus, DCE-CT can help to predict therapy response and act as a noninvasive tool for treatment monitoring (Tacelli et al. 2013). Cardiac DCE-CT has recently become a hot topic, because functional data complete the stenosis grading in

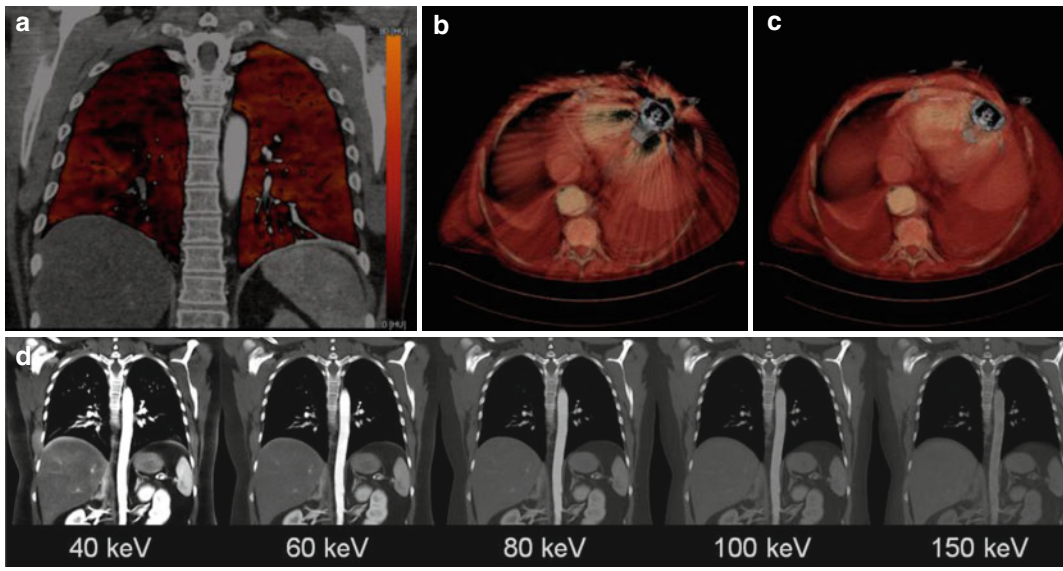

Fig. 4 (**a**–**d**) Iodine map demonstrating multiple perfusion defects in a patient with acute pulmonary embolism (**a**); patient with left ventricular assist device (**b**) and improvement of image quality using metal artifact reduction algorithms (**c**). Monoenergetic imaging with twin-beam dual energy at different keV settings to enhance vascular attenuation (**d**)

order to identify the hemodynamic relevance (George et al. 2009; Feuchtner et al. 2012; Rochitte et al. 2014).

Dual energy CT (DECT), a relatively old concept (Kalender et al. 1986), experienced a renaissance which started with the introduction of dual-source CT systems. DECT makes use of the fact that attenuation can be decomposed into two linearly independent functions of energy by using information from two different detected x-ray spectra. Meanwhile all major vendors provide DECT solutions: dual source (Siemens), rapid kV switching (GE), dual-layer detector (Philips), dual-rotation kV switching (Toshiba), and split-filter technique (Siemens). Photon counting detectors which can provide spectral x-ray information without the need to apply different x-ray tube voltages may provide an additional option; such detectors are also expected to improve tissue contrast, reduce image noise, and discriminate two or more energy windows (Lell et al. 2015a). DECT has a variety of applications in thoracic CT: monoenergetic imaging can be used to enhance the attenuation of perfused lung vessels; iodine maps allow to quantify the iodine distribution within tissue, for example, within the myocardium or lung tumors, or to indirectly detect perfusion defects related to pulmonary embolism. The quantification of pulmonary perfused blood volume in DECT may be used as an immediate, reader-independent parameter in acute PE, which inversely correlates with thrombus load, laboratory parameters, and the necessity for intensive care unit admission (Meinel et al. 2013). All these applications have to be developed and standardized further; it can be expected that they will provide additional information beyond the established Hounsfield values and increase the clinical value of CT.

4 Image Quality and Dose Considerations

Image quality and dose in CT are of fundamental importance, and they are closely related. We here consider noise, contrast, and spatial resolution as the most important image quality parameters. It is understood that we desire images to provide high-contrast and high spatial resolution at low dose.

The fundamental interdependence of image quality and dose is well known: noise σ varies inversely proportional to the square root of the dose D for otherwise unchanged scan and image reconstruction parameters: $\sigma \propto \sqrt{D}$. However, there are other interdependences such as the relationship between dose and spatial resolution which are not generally known but are of importance today and, in particular, for potential future high-resolution CT concepts. For better understanding, we will briefly review the present status of dose management and prospects for further increases of spatial resolution in future CT systems.

The general acceptance of CT is often linked to dose issues and potentially associated risks. It is a frequent and an amazing situation to find that CT is viewed and often termed as a “dangerous high-dose” modality. Therefore, it will be essential to provide information about patient dose values for any given CT examination further on. Information will help to counteract some of the unjustified fears.

Modern dose management including the innovative approaches listed in Table 1 ensures that the effective dose to the patient is kept low, typically at 0.1 to less than 10 mSv today for the thoracic region. Dose values on average will certainly drop further on for all CT applications as these modern technologies get into wider use. They form the basis for “sub-mSv CT” applications which was forecasted in 2009 as a likely development in CT for the decade 2010–2020 (Kalender 2011). Prospects are good that this development will continue.

The approaches listed in Table 1 all offer dose reduction without any compromising of image quality. Quite the opposite is the case; e.g., spectral optimization (Figs. 2 and 3) and iterative reconstruction (Fig. 5) offer clear improvements. Just the same, improved detector electronics and efficiency are always welcome and a necessity for imaging at very low dose, i.e., at low x-ray intensity and the resulting low signals. It can be predicted that average dose values will go down

Table 1 Innovative concepts and modern technology for dose reduction in CT provide, in combination, the potential for sub-mSv CT

Approach	Introduction	Typ. values (%)	References
Tube current modulation (TCM) Automatic exposure control (AEC)	1999 2004	10–60	Kalender et al. (1999) Greess et al. (2000)
Optimal choice of x-ray spectra	2009	10–70	Kalender et al. (2009) Schuhbaeck et al. (2013)
Elimination of z-overscanning effects	2009	5–30	Deak et al. (2009) Kalender (2011)
Dose-efficient image reconstruction	2010	20–80	Manufacturer reports
Improved detector technology	2012	10–40	Manufacturer reports

Based on table 8.2 (Kalender 2011)

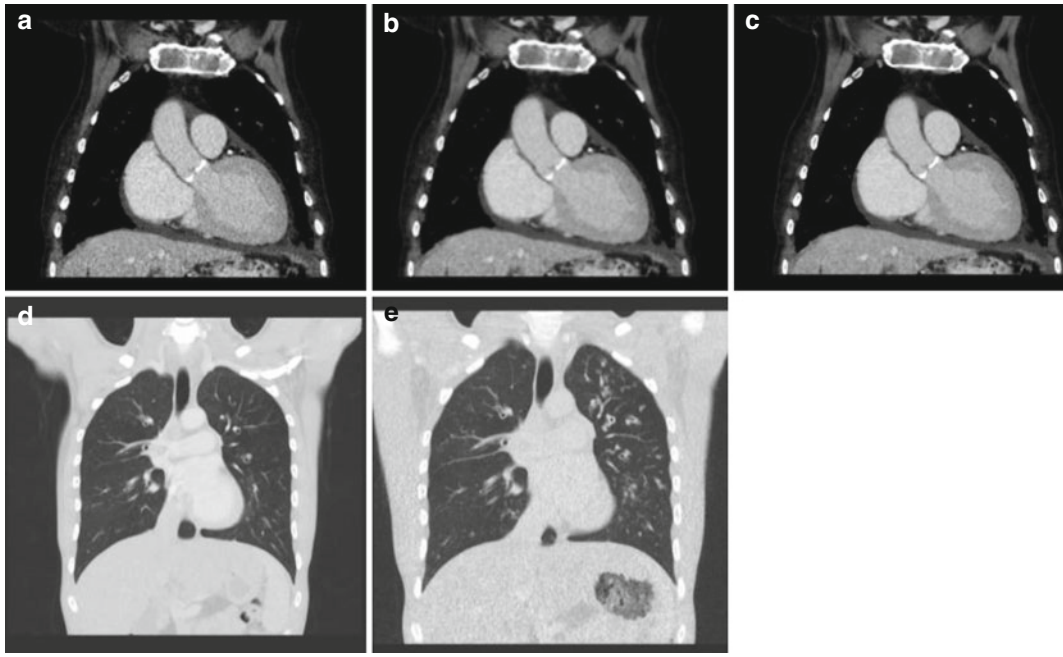

Fig. 5 Significant noise reduction with iterative image reconstruction in a 73-year-old patient with aortic valve replacement (**a**, FBP; **b**, ADMIRE 3; **c**, ADMIRE 5); low-dose chest CT in an 18-year-old patient with cystic fibrosis: 100 kV contrast-enhanced CT (**d**; $CTDI_{vol}$ 2.44 mGy) and follow-up 6 month later with 100 kV and tin filtration (**e**; $CTDI_{vol}$ 0.14 mGy), providing full 3D information at a dose comparable to conventional chest x-ray

further. Respective hopes and related risk assessments are addressed in the final section.

How about increases in spatial resolution? They are desired in many cases but certainly not dose neutral. Special high-resolution scan modes are offered on many scanners which employ post-patient collimation to reduce detector aperture size for special applications. This may be helpful and indicated with respect to spatial resolution, but it causes slight increases in dose. Caution is also indicated if stronger increases in spatial resolution are expected because there are limits set by physics. The mathematical background was elaborated already in the early days of CT; it was verified again lately both theoretically and experimentally in view of the new situation with high-resolution flat panel detectors (Fuchs and Kalender 2003). Image noise variance σ^2 and thereby the necessary dose to maintain image noise levels per voxel change with the

fourth power of the size of a cubic spatial resolution element with all other scan parameters unchanged (Kalender 2011). The message is that strongly increased spatial resolution is associated with strongly increased noise levels, reduced low-contrast resolution, and soft tissue discrimination and can only be counteracted by increasing dose strongly also.

"100 μm resolution" was sometimes quoted as a goal for clinical CT. Micro-CT scanners operate at such levels of resolution and even down to sub-μm resolution levels. They are in use for research with small objects such as biopsies or small animals and for nondestructive material testing. For research involving small animals such as mice, the implication of the increase in spatial resolution on dose may be tolerable as the object diameter, and thereby x-ray intensities and attenuation decrease by orders of magnitude. In clinical CT, as, for example, in isotropic resolution imaging of the thorax, increasing spatial resolution by a factor of 2 or 4 can mean an increase in dose of 16 or 256, respectively, if we expect to maintain the noise level as for a standard scan. This does not appear acceptable!

5 Summary and Conclusions

CT in general and, just the same, CT of the thorax have reached a very high level of performance. The technology can be considered mature, the dose levels are acceptable, and most clinicians are content. There is no doubt, however, that there will be further improvements: scan speed will be increased, and the size of detector arrays will be enlarged, while the size of single detector elements will be reduced moderately resulting in increases of spatial resolution. Reconstruction approaches, in particular model-based iterative reconstruction, and the speed of image reconstruction will be improved strongly.

Applications of CT in the thorax will be augmented by technological advances. Dynamic contrast-enhanced CT, e.g., for the determination of ventilation and perfusion of the lung and myocardial perfusion measurements are candidate applications which may initiate significant application-driven developments. The use of detector arrays wide enough to cover the complete heart offers fundamentally new possibilities.

CT of the breast is on the horizon and shall enhance the spectrum of thoracic CT applications. Imaging of the breast demands very high spatial resolution for assessing microcalcifications. First efforts with flat detector CT with about 300 μm resolution yielded good results for soft tissue and dynamic contrast-enhanced imaging but also the demand for higher resolution (Lindfors et al. 2008; O'Connell et al. 2010). This deficit may be overcome by novel detector technology employing sensor materials such as cadmium telluride which convert photons directly into electric charge. They omit the intermediate step of generating light which is the state of the art today with scintillating detectors. This technology provides advantages such as very high-dose efficiency and resolution, no electronic noise, and the option of single photon counting and energy discrimination; the feasibility for breast CT has been shown by simulations (Kalender et al. 2012) and in phantom measurements (Fig. 6). Detail resolution is higher than in mammography due to increased resolution in all directions; dose is maintained at levels prescribed for screening. The new detector technology may make various kinds of dedicated CT scanners even more attractive in the future.

Patient dose considerations will remain a critical topic, but there are some indications that dose issues may not remain the apparent "no. 1 topic" which they appeared to be in the past years. We have reached sub-mSv dose levels where even conservative assumptions of risk are termed "very low." For example, a 0.2 mSv scan would mean a risk of causing a lethal cancer in 1 out of 100,000 exposed according to the worst possible case scenario which follows the linear-no-threshold hypothesis. Taking into account that we operate at dose levels way below the natural background radiation level and that repair mechanisms are always in action the real risk may be assumed as insignificant. It appears crucial to make these facts and insights known to patients and to the public.

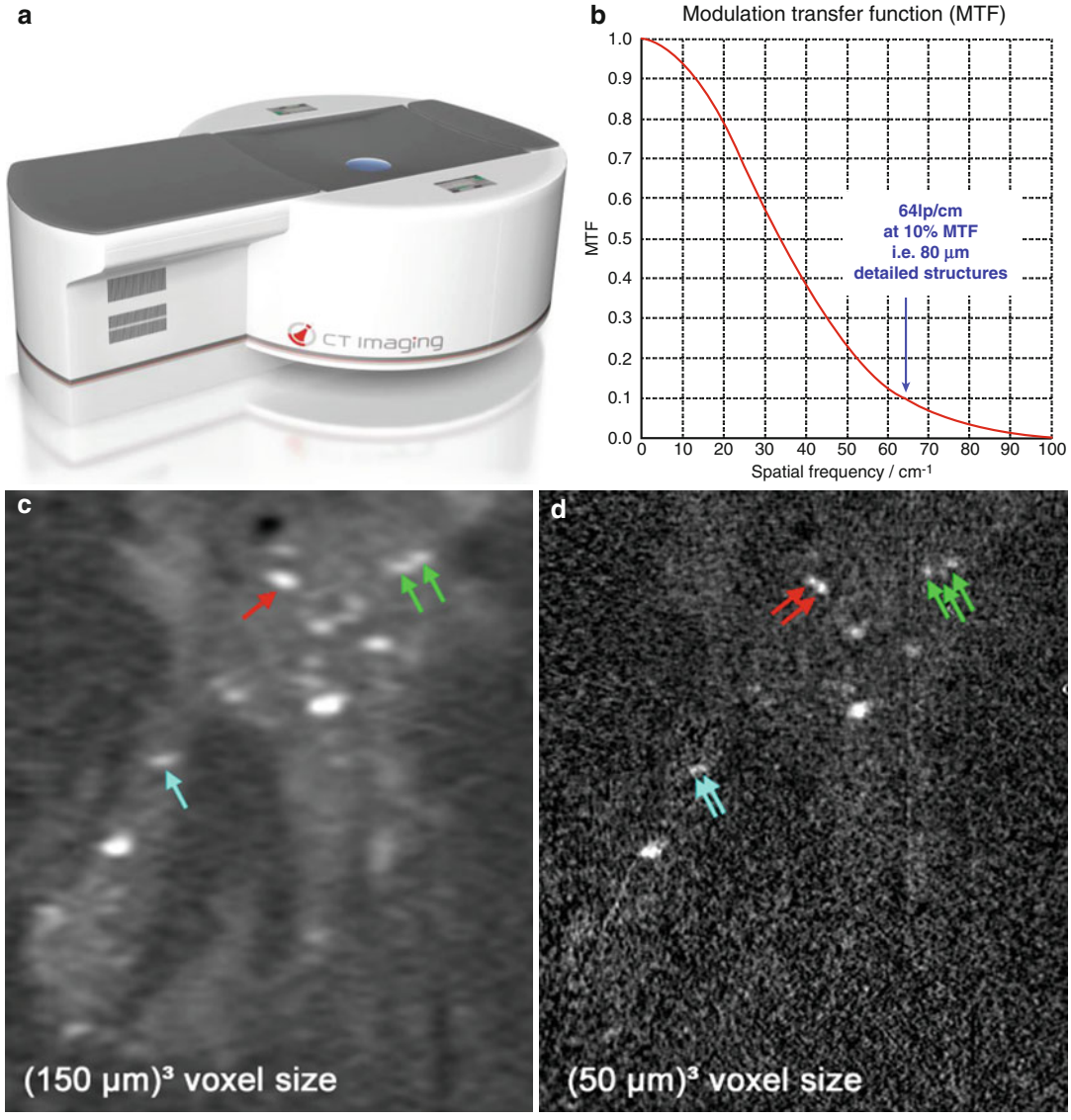

Fig. 6 High-resolution breast CT imaging may become a new option. (**a**) The patient is imaged in prone position one breast at a time; (**b**) the 512-row CdTe small-pixel detector provides spatial resolution of better than 100 µm as there is no spread of light involved; (**c**, **d**) specimen measurement showing minute calcifications in soft tissue mode (**c**) and in microcalcification high-resolution mode (**d**) (**a** Courtesy of CT Imaging GmbH, Erlangen)

References

Beijer TR, van Dijk EJ, de Vries J, Vermeer SE, Prokop M, Meijer FJ (2013) 4D-CT angiography differentiating arteriovenous fistula subtypes. Clin Neurol Neurosurg 115(8):1313–1316

Boyd DP, Lipton MJ (1983) Cardiac computed tomography. Proc IEEE 71:298–308

Deak P, Langner O, Lell M, Kalender WA (2009) Effects of adaptive slice collimation on patient dose in multi-slice spiral computed tomography. Radiology 252(1):140–147

Feuchtner GM, Plank F, Pena C et al (2012) Evaluation of myocardial CT perfusion in patients presenting with acute chest pain to the emergency department: comparison with SPECT-myocardial perfusion imaging. Heart 98(20):1510–1517

Fraioli F, Anzidei M, Serra G, Liberali S, Fiorelli A, Zaccagna F, Longo F, Anile M, Catalano C (2013) Whole-tumour CT-perfusion of unresectable lung cancer for the monitoring of anti-angiogenetic chemotherapy effects. Br J Radiol 86(1029):20120174

Fuchs T, Kalender WA (2003) On the correlation of pixel noise, spatial resolution and dose in computed tomography: Theoretical prediction and verification by simulation and measurement. Phys Med XIX(2):153–164

George RT, Arbab-Zadeh A, Miller JM et al (2009) Adenosine stress 64- and 256-row detector computed tomography angiography and perfusion imaging: a pilot study evaluating the transmural extent of perfusion abnormalities to predict atherosclerosis causing myocardial ischemia. Circ Cardiovasc Imaging 2(3):174–182

Greess H, Wolf H, Baum U, Lell M, Pirkl M, Kalender WA (2000) Dose reduction in computed tomography by attenuation-based online modulation of tube current: evaluation of six anatomical regions. Eur Radiol 10:391–394

Haubenreisser H, Bigdeli A, Meyer M, Kremer T, Riester T, Kneser U, Schoenberg SO, Henzler T (2015) From 3D to 4D: integration of temporal information into CT angiography studies. Eur J Radiol 84(12):2421–2424

Kalender WA (2011) Computed tomography. Fundamentals, system technology, image quality, applications, 3rd edn. Publicis, Erlangen

Kalender WA, Perman WH, Vetter JR et al (1986) Evaluation of a prototype dual-energy computed tomographic apparatus. I. Phantom studies. Med Phys 13:334–339

Kalender WA, Seissler W, Klotz E et al (1990) Spiral volumetric CT with single-breath-hold technique, continuous transport, and continuous scanner rotation. Radiology 176:181–183

Kalender WA, Wolf H, Suess C, Gies M, Greess H, Bautz WA (1999) Dose reduction in CT by on-line tube current control: principles and validation on phantoms and cadavers. Eur Radiol 9:323–328

Kalender WA, Deak P, Kellermeier M, van Straten M, Vollmar SV (2009) Application- and patient size-dependent optimization of x-ray spectra for CT. Med Phys 36(3):993–1007

Kalender WA, Beister M, Boone JM, Kolditz D, Vollmar SV, Weigel MC (2012) High-resolution spiral CT of the breast at very low does: concept and feasibility considerations. Eur Radiol 22:1–8

Klotz E, Haberland U, Glatting G, Schoenberg SO, Fink C, Attenberger U, Henzler T (2015) Technical prerequisites and imaging protocols for CT perfusion imaging in oncology. Eur J Radiol 84(12):2359–2367

Lell M, Hinkmann F, Anders K, Deak P, Kalender WA, Uder M, Achenbach S (2009) High-pitch electrocardiogram-triggered computed tomography of the chest: initial results. Invest Radiol 44(11):728–733

Lell MM, May M, Deak P, Alibek S, Kuefner M, Kuettner A, Köhler H, Achenbach S, Uder M, Radkow T (2011) High-pitch spiral computed tomography: effect on image quality and radiation dose in pediatric chest computed tomography. Invest Radiol 46(2):116–123

Lell MM, Meyer E, Kuefner MA, May MS, Raupach R, Uder M, Kachelriess M (2012) Normalized metal artifact reduction in head and neck computed tomography. Invest Radiol 47(7):415–421

Lell MM, Meyer E, Schmid M, Raupach R, May MS, Uder M, Kachelriess M (2013) Frequency split metal artefact reduction in pelvic computed tomography. Eur Radiol 23(8):2137–2145

Lell MM, Wildberger JE, Alkadhi H, Damilakis J, Kachelriess M (2015a) Evolution in computed tomography: the battle for speed and dose. Invest Radiol 50(9):629–644

Lell MM, Jost G, Korporaal JG, Mahnken AH, Flohr TG, Uder M, Pietsch H (2015b) Optimizing contrast media injection protocols in state-of-the art computed tomographic angiography. Invest Radiol 50(3):161–167

Lindfors KK, Boone JM, Nelson TR, Yang K, Kwan ALC, Miller DF (2008) Dedicated breast CT: initial clinical experience. Radiology 246:725–733

Meinel FG, Graef A, Bamberg F et al (2013) Effectiveness of automated quantification of pulmonary perfused blood volume using dual-energy CTPA for the severity assessment of acute pulmonary embolism. Invest Radiol 48(8):563–569

Meyer E, Raupach R, Lell M, Schmidt B, Kachelrieß M (2012) Frequency split metal artifact reduction (FSMAR) in computed tomography. Med Phys 39(4):1904–1916

Ng QS, Goh V, Fichte H, Klotz E, Fernie P, Saunders MI, Hoskin PJ, Padhani AR (2006) Lung cancer perfusion at multi-detector row CT: reproducibility of whole tumor quantitative measurements. Radiology 239(2):547–553

O'Connell A, Conover DL, Zhang Y et al (2010) Cone-beam CT for breast imaging: radiation dose, breast coverage, and image quality. Am J Roentgenol 195:496–509

Rochitte CE, George RT, Chen MY et al (2014) Computed tomography angiography and perfusion to assess coronary artery stenosis causing perfusion defects by single photon emission computed tomography: the CORE320 study. Eur Heart J 35(17):1120–1130

Schuhbaeck A, Achenbach S, Layritz C, Eisentopf J, Hecker F, Pflederer T, Gauss S, Rixe J, Kalender W, Daniel WG, Lell M, Ropers D (2013) Image quality of ultra-low radiation exposure coronary CT angiography with an effective dose <0.1 mSv using high-pitch spiral acquisition and raw data-based iterative reconstruction. Eur Radiol 23:597–606

Tacelli N, Santangelo T, Scherpereel A et al (2013) Perfusion CT allows prediction of therapy response in non-small cell lung cancer treated with conventional and anti-angiogenic chemotherapy. Eur Radiol 23(8):2127–2136

Vock P, Soucek M, Daepp M et al (1990) Lung: spiral volumetric CT with single-breath-hold technique. Radiology 176:864–867

Index

U.J. Schoepf, F.G. Meinel (eds.), *Multidetector-Row CT of the Thorax*, Medical Radiology,
DOI 10.1007/978-3-319-30355-0